

## FOREWORD

The world of nanotechnology has opened up a vast array of novel fundamental and applied frontiers in materials science and engineering. Nanotechnology is the control of matter at the nanometer-length scale and the exploitation of the novel properties and phenomena developed at that scale in the creation of practical materials, devices, and systems. Nanoscale materials and processes, especially biologically based ones, have always been around us, but it has only been in recent years that we have had the tools to identify these materials, to study and characterize them, and to manipulate in a controlled process. The relatively recent discoveries of buckminsterfullerene  $C_{60}$  and the carbon nanotube have created a whirlwind of exploration of both natural and man-made carbon nanomaterials and related nanotechnology.

For nearly 40 years, micron-size carbon fibers have been used for their high strength and stiffness and lightweight to reinforce polymeric materials for a variety of applications, ranging from tennis racquets to aircraft parts. Today, nanoscale carbon materials are being actively pursued for a large variety of applications such as household appliances, recreational sporting goods, biomedical devices, electronics, telecommunications, automobiles, aircraft, and space vehicles. In particular, it is envisioned that future aircraft and space vehicles will have a structure based on a material with a high strength-to-weight ratio, that is designed to withstand flight, launch, and landing loads, and also perform additional functions. The structure will incorporate various built-in miniaturized smart systems, including sensors, actuators, electronic and photonic devices. These smart systems will help to distribute loads and heat, sense environmental and load conditions, determine the state of health of the vehicle, provide electrical and magnetic fields for changing material properties, serve as a source of power, and offer sites for receiving, storing, processing, and transmitting information. However, today's conventional materials and designs cannot provide the desired multifunctionality. Because of their unusually high mechanical strength, high resilience, low density, excellent thermal and electronic properties, and tailorability, carbon nanotubes could provide multifunctional, super-strong, and light-weight composite structures for aircraft/aerospace and many other applications.

Recently, the nanoscale design and engineering of multifunctional materials and devices based on carbon nanotube composites have moved from a few empirical examples to a thriving, science-based activity. However, there are many challenges to overcome before carbon nanotechnology reaches its full potential. For instance, high-quality carbon nanotubes of a reproducible, uniform structure are not yet available in large quantities. Large quantities are essential to allow engineers to design, process, and test *structure*. If the price of carbon nanotubes remains as high as it is today, any large-scale application of carbon nanotubes will be unrealistic. Therefore, issues such as controlled syntheses of high-quality carbon nanotubes, new methods for functionalization of nanomaterials, and novel nanodevice design and integration are currently being actively investigated. The field of carbon

nanotechnology is expanding at a tremendous rate. With a comprehensive coverage of the recent development in the field, *Carbon Nanotechnology: Recent Developments in Chemistry, Physics, Materials Science and Device Applications*, edited by Liming Dai, is a timely and important addition to the currently available resources. It bridges the gap between the fundamental science of carbon nanomaterials and the development of practical devices through a broad treatment of key fields of work. Materials science and engineering, as well as device construction and application, are covered, with a large number of updated references and world-renowned experts' remarks. This book will be useful to both researchers who actively work with carbon nanomaterials and those merely curious about the possibilities that carbon nanomaterials offer. It can also be used both as a textbook and a critical reference by professionals and students in the disciplines of materials science, chemistry, physics, biology, and engineering.

Charles E. Browning  
Professor and  
Torley Chair in Composite Materials  
University of Dayton  
(Former Director of Materials and Manufacturing Directorate,  
The US Air Force Research Laboratory)



## PREFACE

Nanotechnology is no longer merely a topic of social conversation, but is beginning to affect the lives of everyone. Although nanotechnology, in general, covers many nanomaterials and processes, this book will focus on advances in carbon nanomaterials. Carbon has long been known to exist in three forms: amorphous carbon, graphite, and diamond. However, the Nobel Prize-winning discovery in 1985 of buckminsterfullerene  $C_{60}$ , which is a pure carbon molecule with a soccer ball-like structure consisting of 12 pentagons and 20 hexagons facing symmetrically, has created an entirely new branch of carbon chemistry. The subsequent discovery of carbon nanotubes in 1991 opened up a new era in materials science and nanotechnology.

A decade later, carbon nanotechnology has evolved into a truly interdisciplinary field encompassing chemistry, physics, biology, materials science, and engineering. This is a field, in which a huge amount of literature has been rapidly generated with the number of publications continuing to increase each year. Therefore, it is very important to cover the most recent developments in this field in a timely manner. To systematically manage a field of such breadth, *Carbon Nanotechnology* utilizes the expertise of many world-renowned experts and contributions from top researchers who have been actively working in the field. The reader will be exposed to a synopsis of the most cutting-edge research through comprehensive literature reviews in each chapter. This approach fosters an understanding of the scientific basis of carbon nanotechnology, and then extends this knowledge to the development, construction, and application of functional devices.

In order to cover a multidisciplinary field of such diversity, this book is divided into three major parts. The first part of the book, from Chapters 2 to 6, gives an overview of carbon nanomaterials. Then, Chapters 7 to 13 elucidate the basic science of nanocarbon chemistry and physics. The final part of the book, from Chapters 14 to 19, describes various device applications involving carbon nanomaterials. In addition, Chapter 1 gives a historical perspective of the field while Chapter 20 outlines some directions for the future development.

*Carbon Nanotechnology* is formatted to build off of a foundation of concepts fundamental to all fields of science. Therefore, it will be an essential reference for scientists, engineers, teachers, and students with backgrounds in physics, chemistry, biology, materials science, and engineering. While many self-explanatory illustrations could provide an overview understanding to those who are new to the field, the large number of updated references cited in each of the chapters should enable advanced readers to quickly review this challenging multidisciplinary field for the latest developments. Experienced academic and industrial professionals can use this book to broaden their knowledge of nanotechnology and/or to develop practical devices while graduate and senior undergraduate students can gain insight into a field of the future.

## ACKNOWLEDGMENTS

I would like to thank Donna de Weerd-Wilson for suggesting and encouraging me to edit this book and Anita Koch and Kristi Green at Elsevier for their enthusiasm, patience, and professional assistance throughout the whole course of the book project. I would also like to thank all the authors, who contributed to this book for their high quality and timely contributions. My great sympathy and special thanks go to Professor Richard E. Smalley at Rice University, who was very helpful and kindly agreed to write a *Foreword* for this book before he passed away on October 28, 2005. Many thanks also to my colleagues who contributed in one way or the other to the text and authors whose work was cited, in particular: Alexis Abramson, Wade Adams, Pulickel Ajayan, Chun-Li Bai, Yoseph Bar-Cohen, Bart Barthelemy, Sankar Basu, Ray Baughman, Jeff Baur, John Belk, David Benko, Patsy Bernal-Olson, Tia Benson-Tolle, Jon Borgwardt, Gail Brown, Charles Browning, Christopher Bunker, Timothy Bunning, Frank Chen, Stephen Z.D. Cheng, Long Chiang, Lee Chou, Ting Cing, Llayron Clarkson, Groeber Claudette, John Connell, Mary Connolly, Alan Crasto, Thomas Cruse, Daniel Curran, Greg Deiter, Lisa Denny, Dean Dunn, Michael Durstock, Thomas Eggemeier, Guliants Elena, Arthur Epstein, Frank Espinosa, Daniel Eylon, Barry Farmer, Jenny Finnell, Brian Frock, Yoshikazu Fujisawa, Lawrence Funke, Lloyd Goettler, Xiaoyi Gong, Michael Green, Mingming Guo, Adel Halasa, Abdou Hassanien, Joseph Haus, Pingang He, Dennis Holthaus, Xiaoyi Hong, Saber Hussain, Douglas Hutchens, Sadhan Jana, Michael Jin, Dave Johnson, Hisashi Kajiura, Alex Kawczak, Frank Kelley, Lafdi Khalid, Byung-Lip Lee, Charles Lee, James Lee, Kyung-Min Lee, John Leland, Renhe Lin, Samuel Lockhart, Andrew Lovinger, Jianping Lu, Weijie Lu, John Maguire, Russell Maquire, Benji Maruyama, Michael McCabe, Les McFawn, Albert Mau, Meyya Meyyappan, Sharell Mikesell, Saeed Mohammadi, Donald Moon, Edmund Moore, Charles Moorefield, Mary Morton, Paul Murray, Rajesh Naik, Danita Nelson, David Nelson, George Newkome, Jon Nieberding, Yoshio Nishi, Toshiyuki Ohashito, Eiji Osawa, Gregg Pamela, Janet Pastor, Kraft Peggy, Mark Pender, Gayle Peterman, Fred Pestello, Byron Pipes, Vikas Prakash, Coleen Pugh, Liangti Qu, M.S. Rajkumar, Bob Reichman, Brain Rice, John Rowe, Ajit Roy, Vincent Russo, Pachter Ruth, John Schlager, Joseph Saliba, Tony Saliba, Gordon Sargent, Amanda Schrand, Cheryl Seitz, Edward Silverman, John Starkovich, Chris Strauss, Morley Stone, Karla Strong, Jie Sun, Sam-Shajing Sun, Katie Thorp, Tsonis Panagiotis, Joseph Untener, Richard Vaia, Andrey Voevodin, Larrell Walters, Ben Wang, Zhong-Lin Wang, John White, Robert Wilkens, Thomas Wittberg, Ru Yu Wu, Ron Xu, Feng-Yu Yang, Tzzy-Lung Yu, Jeffrey Zabinski,

Qiwen Zhan, and Daoben Zhu. Last, but not the least, I thank my two sons, Quanbin Kevin Dai and Quanzhe Alvin Dai, for their love and my wife, Lin Zhu, for letting me to work overtime so often.

Liming Dai  
Wright Brothers Institute Endowed Chair Professor  
Department of Chemicals and Materials Engineering  
School of Engineering and UDRI  
University of Dayton  
Dayton, Ohio, USA  
November 2005.

## LIST OF CONTRIBUTORS

**Narayan R. Aluru**, Department of Mechanical & Industrial Engineering University of Illinois at Urbana-Champaign, IL, USA

**Tia Benson-Tolle**, AFRL/MLBC, Air Force Research Laboratory, Wright-Patterson AFB, OH, USA

**Davide Bonifazi**, Dipartimento di Scienze Farmaceutiche, Università degli Studi di Trieste, Trieste, Italy

**Ying Chen**, Department of Electronic Materials Engineering, Research School of Physical Sciences and Engineering, The Australian National University, Canberra, Australia

**Hui-Ming Cheng**, Shenyang National Laboratory for Materials Science, Institute of Metal Research, Chinese Academy of Sciences, Shenyang, China

**John W. Connell**, National Aeronautics and Space Administration, Langley Research Center, VA, USA

**Liming Dai**, Department of Chemical and Materials Engineering, School of Engineering and University of Dayton Research Institute, University of Dayton, OH, USA

**Michael Durstock**, Materials and Manufacturing Directorate, Air Force Research Laboratory, AFRL/MLBP, OH, USA

**K.A. Shiral Fernando**, Department of Chemistry and Laboratory for Emerging Materials and Technology, Clemson University, SC, USA

**Qiang Fu**, Department of Chemistry, Duke University, NC, USA

**A. Govindaraj**, CSIR-Centre of Excellence in Chemistry and Chemistry and Physics of Materials Unit, Jawaharlal Nehru Centre for Advanced Scientific Research, Bangalore, India

**Bruce Hinds**, Department of Chemical and Materials Engineering, University of Kentucky, KY, USA

**Michael H.-C. Jin**, Materials Science and Engineering Program, University of Texas, Arlington, TX, USA

**Kazuo Kajiwar**a, CNT-FED Research Consultant, Machida-shi, Tokyo, Japan

**Oleg I. Kiselev**, Institute of Influenza Russian Academy of Medical Sciences, Department of Molecular Virology and Genetic Engineering, Saint Petersburg, Russia

**Kyung Min Lee**, Department of Chemical and Materials Engineering, School of Engineering, University of Dayton, OH, USA

**Yi Lin**, Department of Chemistry and Laboratory for Emerging Materials and Technology, Clemson University, SC, USA

**Jie Liu**, Department of Chemistry, Duke University, NC, USA

**Aurelio Mateo-Alonso**, Dipartimento di Scienze Farmaceutiche, Università degli Studi di Trieste, Trieste, Italy

**A.I. Minett**, ARC Centre of Excellence for Electromaterials Science, Intelligent Polymer Research Institute, University of Wollongong, Wollongong, Australia

**S.E. Moulton**, ARC Centre of Excellence for Electromaterials Science, Intelligent Polymer Research Institute, University of Wollongong, Wollongong, Australia

**Toshiyuki Ohashi**, Honda Research Institute USA, Inc., OH, USA

**Eiji Ōsawa**, NanoCarbon Research Institute, Toudai Kashiwa Venture Plaza, Chiba, Japan

**Masaki Ozawa**, NanoCarbon Research Institute, Toudai Kashiwa Venture Plaza, Chiba, Japan

**L.B. Piotrovsky**, Institute of Experimental Medicine RAMS, Saint-Petersburg, Russia

**Maurizio Prato**, Dipartimento di Scienze Farmaceutiche, Università degli Studi di Trieste, Trieste, Italy

**Liangti Qu**, Department of Chemical and Materials Engineering, School of Engineering, University of Dayton, OH, USA

**C.N.R. Rao**, CSIR-Centre of Excellence in Chemistry and Chemistry and Physics of Materials Unit, Jawaharlal Nehru Centre for Advanced Scientific Research, Bangalore, India

**Yahachi Saito**, Department of Quantum Engineering, Nagoya University, Nagoya-shi, Japan

**Amanda M. Schrand**, Department of Chemical and Materials Engineering, School of Engineering and University of Dayton Research Institute, University of Dayton, OH, USA

**Susan B. Sinnott**, Department of Materials Science and Engineering, University of Florida, FL, USA

**Ya-Ping Sun**, Department of Chemistry and Laboratory for Emerging Materials and Technology, Clemson University, SC, USA

**G.G. Wallace**, ARC Centre of Excellence for Electromaterials Science, Intelligent Polymer Research Institute, University of Wollongong, Wollongong, Australia

**Li-Jun Wan**, Institute of Chemistry, Chinese Academy of Sciences, Beijing, China

**Wei Wang**, Department of Chemistry and Laboratory for Emerging Materials and Technology, Clemson University, SC, USA

**Kent A. Watson**, National Institute of Aerospace, VA, USA

**Quan-Hong Yang**, Shenyang National Laboratory for Materials Science, Institute of Metal Research, Chinese Academy of Sciences, Shenyang 110016, China

**Hui-Min Zhang**, Institute of Chemistry, Chinese Academy of Sciences, Beijing, China

## Chapter 1

# **From conventional technology to carbon nanotechnology: The fourth industrial revolution and the discoveries of C<sub>60</sub>, carbon nanotube and nanodiamond**

Liming Dai

Department of Chemical and Materials Engineering, School of Engineering,  
University of Dayton, Dayton, Ohio 45469-0240, USA

### **1. THE INDUSTRIAL REVOLUTIONS THAT CHANGED THE WORLD**

Since the development of the two-cylinder steam engine by James Watt in the 1760s, human-kind has experienced three industrial revolutions [1]. The first industrial revolution, as represented by the appearance of Watt's steam engine, employed various machines to replace human labor. The second industrial revolution began at the end of the 19th century and was characterized by the discovery of the internal combustion engine and electric generator [2], which lead to the increased usage of electrical appliances, automobiles, and petroleum products. The construction of the first computer in the 1940s led to the third industrial revolution, which was followed by the rapid development of information technology [2].

Although many of these inventions and developments provide innumerable benefits, they also pose new and sometimes unforeseeable risks. For example, the appearance of internal combustion engineering led to the wide-spread availability of electric power for lighting, home appliances, industrial machines, automobiles, and aerocrafts. However, it also has contributed to the levels of air pollution and accelerated global warming. With the rapid increase in population, consumption of natural resources, environmental pollution, and information overflow, the turn of this century witnessed the birth of nanotechnology. The demand for miniaturized and multifunctional systems has been a driving force for the development of nanotechnology.

### **2. NANOTECHNOLOGY—THE FOURTH INDUSTRIAL REVOLUTION**

Owing to the intriguing size-dependent properties of nanophase materials [3], the recent development of nanoscience and nanotechnology has opened up novel fundamental and applied frontiers in materials science and engineering. The concept of nanotechnology was first introduced by Nobel laureate Richard Feynman [4] in 1959 at the annual meeting of the American Physical Society at the California Institute of Technology (Caltech). In his classic lecture entitled: "There is a plenty room at the bottom", Feynman stated, "The principles of physics, as far as I can see, do not speak against the possibility of maneuvering things atom by atom". Later, Notio

Taniguchi from the Tokyo Science University first defined the nanotechnology as: (1) the creation of useful materials, devices, and systems through the control matter at the nanometer ( $10^{-9}$  m) length scale and (2) the exploitation of novel properties and phenomena developed at that scale [5]. The first scientific paper on nanotechnology was published in 1981 by Eric Drexler [6], a former student of Dr. Feynman at Caltech. Drexler's [7] idea of molecular manufacturing was followed by his book entitled: *Engines of Creation—The Coming Era of Nanotechnology* published in 1986. In this classic nanotechnology book, Drexler proposed the atom-stacking mechanism to produce machines smaller than a living cell and also presented some potential applications of nanotechnology. Although Drexler's publications have motivated researchers in the field of nanotechnology, the main breakthrough in nanotechnology occurred in 1981 when Binnig and Rohrer [8] at IBM Zurich invented the scanning tunneling microscope (STM)—the first instrument to generate real-space images of surfaces with atomic resolution. This discovery opened up the important new field of nanotechnology and was recognized by the 1986 Nobel Prize in Physics, along with the inventor of the electron microscope. Subsequently, Gerd Binnig, Christopher Gerber, and Calvin Quate of IBM devised the atomic force microscope (AFM) [9]. STM and AFM enabled not only the imaging of individual atoms, but also the manipulation of a single atom. Using STM, an IBM group precisely deposited 35 xenon atoms to spell out the name of IBM in April of 1990 [10]. Donald Eigler, the lead author on the *Nature* paper describing this work, saw clearly where all this is leading. Eigler [10] said, "For decades, the electronics industry has been facing the challenge of how to build smaller and smaller structures. For those of us who will now be using individual atoms as building blocks, the challenge will be how to build up structures atom by atom".

All matter is made up of atoms, with its properties depending strongly on how those atoms are arranged in space. If we could rearrange the atoms in coal, we could make diamond. If we could rearrange the atoms in sand (and add a few other trace elements), we could make computer chips. Consequently, nanotechnology, as defined to build materials and devices atom by atom, holds vast promise for innovation in virtually every industry and public sector, including health care, electronics, transportation, environment, and national security.

## 2.1. The bottom up vs. top down approaches

There are essentially two different approaches to creating very small structures or devices. As schematically illustrated in Fig. 1, individual atoms and/or molecules can be precisely placed where they are needed by scanning probe microscopy (e.g. AFM, STM, optical tweezers) or self-assembling [11]. This approach is designated as the "bottom up" because atomic or molecular building blocks are put together to create bigger objects. The second approach is called the "top down" approach, where macro-scale systems are converted into nanoscale ones by a series of sequential reduction operations to remove the unwanted portions away from the object that is wanted. The smallest features that can be created by the "top down" approach depend on the tools used and the system operator's experience and skills. In principle, there is no difference between the "top down" approach and the way a



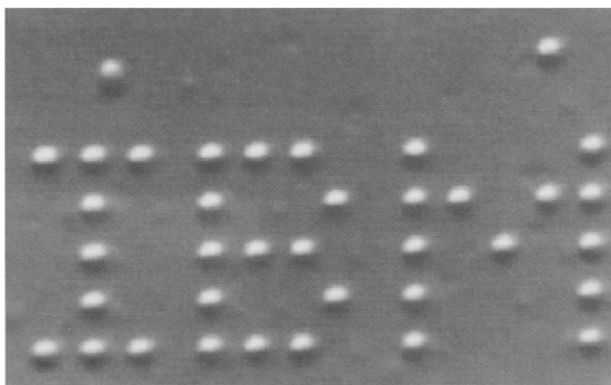


Figure 1. STM image of a patterned array of xenon atoms on a nickel surface (after Eigler and Schweizer [10]).

bronze-age scientist working with wood or stone. Evidently, the “top down” approach requires tedious work and produce considerable “waste”. In contrast, the “bottom up” approach is time and waste efficient. However, precision and scalability are still big challenges for the “bottom up” approach. The best model of systematically organizing matter at nanometer-length scale is in naturally occurring biological systems. For instance, proteins can self-assemble into working molecular machines that actively cut and splice other molecules or cause the contraction of muscles. Proteins can also join with other molecules to form huge assemblies both inside and outside of individual cells, such as cellular organelles and extracellular matrix, respectively. The supramolecular architectures and/or molecular machines that naturally exist have a complexity and efficiency that none of today’s synthetic systems can match. Therefore, there is considerable room for creating and tailoring new materials and devices by nanotechnology, as illustrated in those chapters in this book focusing on nanomanipulations.

## 2.2. The size and surface effects

Changes in the size-dependent properties can be observed in nanomaterials as the wave-like properties of electrons inside matter and atomic interactions are influenced by the size of materials at the nanometer scale [3]. Confinement of the deBroglie wavelength of charge carriers inside nanomaterials could also lead to new phenomena, such as the quantization effect [3]. When a gold nugget is converted into nanoparticles, for example, the color of the gold particles is changed to black. As the size decreases, the ratio of the surface atoms increases. These high energy surface atoms are very reactive. Due to the high surface-to-volume ratio associated with nanometer-sized materials, therefore, a tremendous improvement in chemical properties is also achievable through a reduction in size [3]. This is why

platinum nanoparticles can be used as efficient catalysts for many reactions whereas platinum bulk sheets are sufficiently inert as electrodes in electrochemistry. By creating nanostructures, therefore, new materials and advanced devices of desirable properties and functions can be developed for numerous applications, as detailed in many chapters related to nanomaterials preparation and applications.

### 3. CARBON NANOTECHNOLOGY

With the revolutionary discoveries of the  $C_{60}$  molecule [12] and carbon nanotubes [13], carbon nanotechnology has become the building block of the entire field of nanotechnology. Whether it is DNA or synthetic polymers, all are based on carbon backbones. The versatility of carbon materials can be experienced when we find it to be a good metal in the form of two-dimensional (2-D) graphite, super hard 3-D semiconductor in the form of diamond, a quantum dot fullerene molecules, and a 1-D quantum wire carbon nanotubes.

Carbon has long been known to exist in three forms: amorphous carbon, graphite, and diamond [14]. Depending on how the carbon atoms are arranged, their properties vary. For example, the most common form of carbon, graphite, is soft, black, and stable (Fig. 2a). In graphite, the carbon atoms are located at the corners of regular and fused hexagons arranged in parallel layers and its density is  $2.26 \text{ g/cm}^3$ . However, diamond is hard and transparent due to its regular repetitive pattern where each carbon atom is bound to four other carbon atoms (Fig. 2b) and its density of  $3.51 \text{ g/cm}^3$  is greater than that of graphite.

The Noble-Prize-winning discovery of buckminsterfullerene  $C_{60}$  (Fig. 2c) created an entirely new branch of carbon chemistry [12,15,16]. The subsequent discovery of carbon nanotubes (Fig. 2d) by Iijima [13] opened up a new era in materials science and nanotechnology [17–19]. These elongated nanotubes consist of carbon hexagons arranged in a concentric manner with both ends normally capped by fullerene-like structures containing pentagons (Fig. 2d). Nanodiamonds are the most recent additions to members of the carbon family (Fig. 2e). Having *conjugated* all-carbon structure with unusual molecular symmetries, fullerenes and carbon nanotubes show interesting electronic, photonic, magnetic, and mechanical properties attractive for various applications [19,20]. With the diamond structure at a nanometer scale, nanodiamonds also exhibit unique mechanical and optoelectronic properties useful for a variety of important applications, including field emission displays [21,22] and nanotribology [23,24], as discussed in relevant chapters of this book.

#### 3.1. The discovery of fullerene $C_{60}$

The visit of Kroto to Smalley and Curl at Rice University in 1985 led to the discovery of buckminsterfullerene  $C_{60}$ —a carbon molecule with a soccer-ball-like structure consisting of 12 pentagons and 20 hexagons facing symmetrically (Fig. 2c) [12]. This finding opened the important new field of carbon chemistry and was recognized by the 1996 Nobel Prize in Chemistry. Although Osawa [25] had theoretically predicted the structure of  $C_{60}$  in 1970 and Huffman [26] might have produced the  $C_{60}$  molecules in his “graphite smoke” as early as 1973, it was the 1985 discovery that generated a great deal of interest and created an entirely new branch of carbon chemistry.

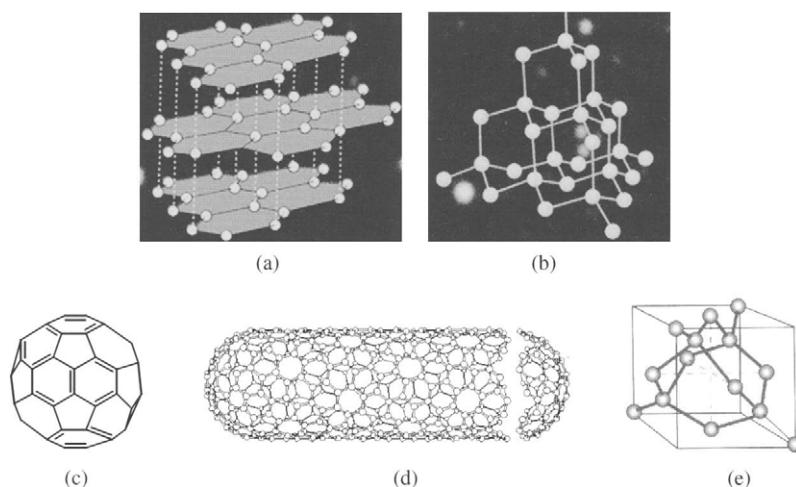


Figure 2. One-, two- and three-dimensional carbon materials: (a) graphite, (b) diamond, (c) buckminsterfullerene  $C_{60}$ , (d) [5,5] armchair single wall carbon nanotube, and (e) nanodiamond.

Shortly after the discovery of fullerene  $C_{60}$ , Krätschmer et al. [27] reported a simple way to produce macroscopic amounts of fullerenes in 1990. The large-scale production of fullerene  $C_{60}$  enabled scientists to study the physicochemical properties of the carbon clusters with all of the conventional spectroscopic methods and to use fullerenes as useful reagents in synthetic chemistry. Subsequently, other spherical fullerenes (collectively known as buckyballs) were synthesized with a different number of hexagonal faces. The fullerene buckyballs are hollow inside, indicating numerous possibilities for modifying the fullerene molecules both inside and outside. For instance, the insertion of a metal ion inside the fullerene cage [28] and metal-coated fullerenes [29] have been demonstrated. Chemically grafting fluorine (F) onto the  $C_{60}$  surface made it hydrophobic for use as a super-lubricant [30] while grafting it with OH rendered it hydrophilic for use as a free radical scavenger [31]. Mixing  $C_{60}$  with polymers either chemically [32] or physically [33] led to photoactive materials. Work has been reported on using fullerene  $C_{60}$  for various potential applications [34], including superconductors, hydrogen storage, high-efficiency solar cells, and chemical sensors. The detailed chemical modification and potential applications of pristine and modified  $C_{60}$  molecules can be found in several chapters in this book.

### 3.2. The discovery of carbon nanotube

Using transmission electron microscope (TEM) to examine carbon samples generated by an arc-discharge method similar to that used for the fullerene synthesis, Iijima [13] found needle-like tubes now popularly known as carbon nanotubes. This discovery of carbon nanotubes by Iijima in 1991 opened up a new era in material

science and nanotechnology. As schematically shown in Fig. 2(d), carbon nanotubes can be viewed as a graphite sheet that is rolled up into a nanoscale tube form (single-wall carbon nanotubes, SWNTs). There may be additional graphene tubes around the core of a SWNT to form the multi-wall carbon nanotubes (MWNTs) [19]. The first nanotube discovered by Iijima was multi-walled and his group produced single-walled carbon nanotubes in 1993 [35] while Donald Bethune et al. [36] independently reported the similar arc-discharge synthesis of SWNTs in the same year. An alternative methods for preparing SWNTs were reported by Smalley's group through laser evaporation [37] and Dai et al. [38] by chemical vapor deposition. Because the graphene sheet can be rolled up with varying degrees of twist along its length, carbon nanotubes have a variety of chiral structures [19]. Depending on their diameter and the helicity of the arrangement of graphite rings, carbon nanotubes can exhibit semiconducting or metallic behavior. Dissimilar carbon nanotubes may even be joined together to form molecular wires with interesting electronic, magnetic, nonlinear optical, and mechanical properties [19,39]. These properties allow carbon nanotubes to be used as new materials for the development of novel single-molecular transistor [40], scanning probe microscope tips [41], molecular computing elements [42], electron field emitting flat panel displays [43,44], gas and electrochemical storage [45], molecular-filtration membranes [46], artificial muscles [47], and sensors [48]. Most of the applications are discussed in details in relevant chapters in this book.

### 3.3. The discovery of nanodiamond

Single crystals of cubic diamond nanoparticles of an average size of 4–5 nm were first discovered in 1963 by a group of Soviet scientists, who performed detonation of an oxygen-deficient TNT/hexogen composition in inert media without involving any additional carbon source [49]. This historic discovery was kept secret for military security reasons until the first open report appeared in 1988 [50]. Since then, research in novel diamond nanoparticles has attracted considerable interest and some industrial production processes have even been devised [51]. Although the 1963 discovery has opened a new way to prepare nanodiamond particles, aggregation remained as a serious problem to preclude the possibility of their application. Recently, it has been demonstrated that disintegration of even extremely tight aggregation of nanodiamond particles can be achieved by stirred-media milling with micron-sized ceramic beads, leading to a stable, dark-colored aqueous colloidal solution of nanodiamond particles having diameters of 4–5 nm [52]. This finding provides an effective method for producing novel-dispersed ultrananocrystalline diamond [53].

Apart from their unusual mechanical properties and environmental stability, nanodiamonds possess a high dielectric constant (3.5 K), high electrical breakdown strength (787 V/ $\mu$ ), high operating temperature (>250 °C), and a low dissipation factor of 0.05% (at 25 °C, 1 kHz). These interesting properties make nanodiamonds a promising candidate material for a variety of important applications such as micro-electromechanical systems (MEMS) [54], field emission displays [21,22], electrochemical analysis [55], and energy storage, as described in relevant chapter(s).

As can be seen from the above discussions, the development of nanotechnology will surely someday change the world. Sooner or later, drug delivery will be accurate enough to target specific proteins within cells. Solar panels will be powerful enough to replace fossil fuels as our primary energy source. Chemical sensors will be small enough and cheap enough to be scattered in public spaces, detecting toxins before any damage is done. We will all be using a new class of super-strength nanomaterials as siding for our homes, protection for our cars and even our clothing. Some of these innovations are in the distant future, but the field is rapidly advancing. This book presents an in-depth view of the broad scope of carbon nanotechnology in a systematic approach from scientific fundamentals to practical applications with comprehensive references and remarks on cutting-age research all given by leading scientists in the field.

## REFERENCES

1. J. Gribbin, *The Scientists*, Random House, New York, 2004.
2. T. Philbin, *The 100 Greatest Inventions of All Time*, Kensington Publishing Corp., New York, 2003.
3. A. N. Goldstein, *Handbook of Nanophase Materials*, Marcel Dekker, Inc., New York, 1997.
4. R. P. Feynman, A lecture in engineering science, in California Institute of Technology, February, 1960.
5. <http://www.kheper.net/topics/nanotech/nanotech-history.htm>.
6. E. K. Drexler, *Proc. Natl. Acad. Sci. USA* **78** (1981) 5275.
7. E. K. Drexler, *Engines of Creation—The Coming Era of Nanotechnology*, Anchor Press/Doubleday, Garden City, N.Y., 1986.
8. G. Binnig and H. Rohrer, *Rev. Mod. Phys.* **59** (1987) 615.
9. R. Howard and L. Benatar, *A Practical Guide to Scanning Probe Microscopy*, Park Scientific Instruments, Sunnyvale, CA, USA.
10. D. M. Eigler and E. K. Schweizer, *Nature* **344** (1990) 524.
11. A. Aggeli, N. Boden and S. Zhang, *Self-assembling Peptide Systems in Biology, Medicine, and Engineering*, Kluwer Academic Publishers, Dordrecht, 2001.
12. H. W. Kroto, J. R. Heath, S. C. O'Brien, R. F. Curl and R. E. Smalley, *Nature* **318** (1985) 162.
13. S. Iijima, *Nature* **354** (1991) 56.
14. H. Marsh, *Introduction to Carbon Science*, Butterworths, London, 1989.
15. A. Hirsch, *The Chemistry of the Fullerenes*, Thieme, Stuttgart, 1994.
16. R. Taylor (Ed.), *The Chemistry of Fullerenes*, World Scientific, Singapore, 1995.
17. M. S. Dresselhaus, G. Dresselhaus and P. Eklund, *Science of Fullerenes and Carbon Nanotubes*, Academic, San Diego, 1996.
18. M. Meyyappan, *Carbon Nanotubes: Science and Applications*, CRC Press, Boca Raton, 2005.
19. P. J. F. Harris, *Carbon Nanotubes and Related Structures—New Materials for the Twenty-First Century*, Cambridge University Press, Cambridge, 2001.

20. L. Dai, *Intelligent Macromolecules for Smart Devices: From Materials Synthesis to Device Applications*, Springer-Verlag, New York, 2004.
21. D. Zhou, A. R. Krauss, T. D. Corrigan, T. G. McCauley, R. P. H. Chang, D. M. Gruen, *J. Electrochem. Soc.* **144** (1997) L224.
22. A. Ya Vul', E. D. Eidelman and A. T. Dideikin, in *Synthesis, Properties and Applications of Ultrananocrystalline Diamond*, Eds. D. M. Gruen, O. A. Shenderova and A. Ya Vul', Springer, Amsterdam, 2005.
23. A. Erdemir, C. Bindal, G. R. Fenske, C. Zuiker, A. Krauss and D. Gruen, *Diamond Relat. Mater.* **5** (1996) 923.
24. A. Erdemir, M. Halter, G. R. Fenske, C. Zuiker, R. Csencsits, A. R. Krauss and D. M. Gruen, *Tribol. Trans.* **40** (1997) 667.
25. E. Osawa, *Kagaku (Kyoto)* **25** (1970) 854.
26. K. L. Day and D. R. Huffman, *Nat. Phys. Sci.* **243** (1973) 50.
27. W. Krätschmer, L. D. Lamb, K. Fostiropoulos and D. R. Huffman, *Nature* **347** (1990) 354.
28. D. S. Bethune, R. D. Johnson, J. R. Salem, M. S. Devries and C. S. Yannoni, *Nature* **366** (1993) 123.
29. U. Zimmermann, N. Malinowski, U. Naher, S. Frank and T. P. Martin, *Phys. Rev. Lett.* **72** (1994) 3542.
30. J. H. Holloway and E. G. Hope, in *The Chemistry of Fullerenes*, Ed. R. Taylor, World Scientific, Singapore, 1995.
31. H. Jin, W. Q. Chen, X. W. Tang, L. Y. Chiang, C. Y. Yang, J. V. Schloss and J. Y. Wu, *J. Neurosci. Res.* **62** (2000) 600.
32. Y. Wang, *Nature* **356** (1992) 585.
33. G. Yu, J. Gao, J. C. Hummelen, F. Wudl and A. J. Heeger, *Science* **270** (1995) 1789.
34. K. Prassides, *Fullerene-Based Materials: Structures and Properties*, Springer: New York, 2004.
35. S. Iijima and T. Ichihashi, *Nature* **363** (1993) 603.
36. D. S. Bethune, C. H. Kiang, M. S. de Vries, G. Gorman, R. Savoy, J. Vasquez and R. Beyers, *Nature* **363** (1993) 605.
37. A. Thess, R. Lee, P. Nikolaev, H. Dai, P. Petit, J. Robert, C. Xu, Y. H. Lee, S. G. Kim, A. G. Rinzler, D. T. Colbert, G. E. Scuseria, D. Tomanek, J. E. Fischer and R. E. Smalley, *Science* **273** (1996) 483.
38. J. Kong, A. M. Cassell and H. Dai, *Chem. Phys. Lett.* **292** (1998) 567.
39. M. Endo, S. Iijima and M. S. Dresselhaus (Eds.), *Carbon Nanotubes*, Pergamon, New York, 1996.
40. S. J. Tans, A. R. M. Verschueren and C. Dekker, *Nature* **393** (1998) 49.
41. H. Dai, J. H. Hafner, A. G. Rinzler, D. T. Colbert and R. E. Smalley, *Nature* **384** (1996) 147.
42. T. Rueckers, K. Kim, E. Joselevich, G. Y. Tseng, C.-L. Cheung and C. M. Lieber, *Science* **289** (2000) 94.
43. W. A. de Heer, J.-M. Bonard, K. Fauth, A. Châtelain, L. Forró and D. Ugarte, *Adv. Mater.* **9** (1997) 87.
44. Y. Saito, K. Hamaguchi, T. Nishino, K. Hata, K. Tohji, A. Kasuya and Y. Nishina, *Jpn. J. Appl. Phys.* **36** (1997) L1340.

45. G. Che, B. B. Lakshmi, E. R. Fisher and C. R. Martin, *Nature* **393** (1998) 346.
46. B. J. Hinds, N. Chopra, T. Rantell, R. Andrews, V. Gavalas and L. G. Bachas, *Science* **303** (2004) 62.
47. R. H. Baughman, C. Cui, A. A. Zakhidov, Z. Iqbal, J. N. Barisci, G. M. Spinks, G. G. Wallace, A. Mazzoldi, D. De Rossi, A. G. Rinzler, O. Jaschinski, S. Roth and M. Kertesz, *Science* **284** (1999) 1340.
48. L. Dai, P. Soundarrajan and T. Kim, *Pure Appl. Chem.* **74** (2002) 1753; and references cited therein.
49. O. A. Shenderova, V. V. Zhirnov and D. W. Brenner, *Crit. Rev. Solid State Mater. Sci.* **27** (2002) 227.
50. A. Ya Vul', V. Dolmatov and O. Shenderova, *Bibliography Index of Detonation Nanodiamonds and Related Materials*, St. Petersburg, Ioffe Physico-Technical Inst., 2003.
51. O. A. Shenderova, V. V. Zhirnov and D. W. Brenner, *Crit. Rev. Solid State Mater. Sci.* **27** (2002) 227.
52. K. Krüger, F. Kataoka, M. Ozawa, T. Fujino, Y. Suzuki, A. E. Aleksenskii, A. Ya Vul' and E. Ósawa, *Carbon* **43** (2005) 1722.
53. D. Gruen, in *Perspectives of Fullerene Nanotechnology*, Ed. Ósawa, Kluwer Academic Publisher, Dordrecht, 2002.
54. A. R. Krauss, O. Auciello, D. M. Gruen, A. Jayatissa, A. Sumgnt, J. Tucek, D. C. Mancini, N. Moldovan, A. Erdemir, D. Ersoy, M. N. Gardos, H. G. Busmann, E. M. Meyer and M. Q. Ding, *Diam. Relat. Mater.* **10** (2001) 1952.
55. G. M. Swain, A. B. Anderson and J. C. Angus, *MRS Bull* (Sept.) **23** (1998) 56.

## Chapter 2

### Synthesis, growth mechanism and processing of carbon nanotubes

A. Govindaraj and C.N.R. Rao

CSIR-Centre of Excellence in Chemistry and Chemistry and Physics of Materials  
Unit, Jawaharlal Nehru Centre for Advanced Scientific Research, Jakkur P.O.,  
Bangalore 560 064, India

#### 1. INTRODUCTION

Ever since the discovery of the carbon nanotubes (CNTs) [1,2], several ways of preparing them have been explored. Besides multi-walled carbon nanotubes (MWNTs), single-walled carbon nanotubes (SWNTs) have been prepared by various methods, including electrochemical synthesis [3] and pyrolysis of precursor organic molecules [4]. The structure of CNTs has been extensively investigated by high-resolution electron microscopy (HREM) [5–7]. The nanotubes, prepared by arc vaporization of graphite, are closed at either end, but can be opened by various oxidants [8,9]. By employing CNTs as removable templates, oxidic, carbidic, and other nanostructures have been prepared. One of the developments is the synthesis of aligned nanotube bundles for specific applications. In this chapter, we provide a survey of the methods to synthesize multi-walled, single-walled and other types of CNTs and the methods of purification of the nanotubes. We also discuss the growth mechanisms of the nanotubes.

#### 2. SYNTHETIC STRATEGIES

##### 2.1. Multi-walled carbon nanotubes

CNTs are readily prepared by striking an arc between graphite electrodes in  $\sim 0.7$  atm ( $\sim 500$  Torr) of helium, considerably larger than the helium pressure used for the production of fullerene soot. The schematic diagram of the apparatus is shown in Fig. 1. A current of 60–100 A across a potential drop of about 25 V gives high yields of CNTs. The arcing process can be optimized such that the major portion of the carbon anode gets deposited on the cathode in the form of CNTs and graphitic nanoparticles [10a]. The arc evaporation of graphite has been carried out in various kinds of ambient gases (He, Ar, and  $\text{CH}_4$ ) [10b]. Hydrogen appears to be effective in producing MWNTs of high crystallinity. Arc-produced MWNTs in hydrogen also contain very few carbon nanoparticles. CNTs have been produced in large quantities by using plasma arc-jets by optimizing the quenching process in an arc between a graphite anode and a cooled copper electrode [11,12]. If both the electrodes are of graphite, MWNTs are the main products, although side products such as fullerenes, amorphous carbon, and graphite sheets are also formed.



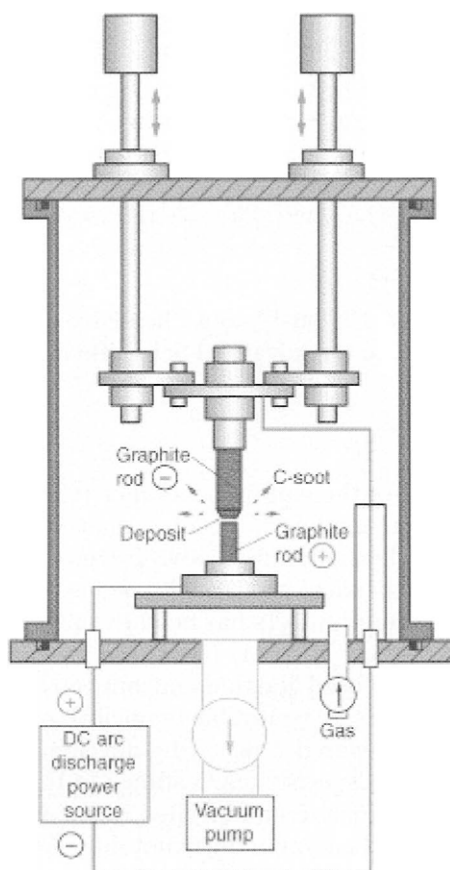


Figure 1. Schematic diagram of an arc-discharge apparatus. (Reproduced from Ando et al. [10b]).

A route to highly crystalline MWNTs is the arc-discharge method in liquid nitrogen [13]. In this method, vacuum is replaced with liquid nitrogen in the arc-discharge chamber. In a typical experiment, direct current was supplied to the apparatus using a power supply. The anode is a pure carbon rod of 8-mm diameter and the cathode is a pure carbon rod of 10-mm diameter. The Dewar flask is filled with liquid nitrogen and the electrode assembly immersed in nitrogen. Arc discharge occurs as the distance between the electrodes became less than 1 mm, and a current of  $\sim 80$  A flows between the electrodes. When the arc discharge is over, the carbon deposits near the cathode are recovered for analysis. Liquid nitrogen prevents the electrodes from contamination with unwanted gases and also lowers the temperature of the electrodes. Furthermore, CNTs do not stick to the wall of the chamber. The content of the MWNTs can be as high as 70% of the reaction product. Analysis with Auger-spectroscopy revealed that no nitrogen was incorporated in the MWNTs. Sano [14]

has recently synthesized various carbon nanostructures such as MWNTs, SWNTs, single-wall carbon nanohorns (SWNHs), multi-shelled nanoparticles and their metal-hybridized forms by a simple technique using arc discharge submerged in liquid. They consider this technique to be economical, as it does not require expensive components such as vacuum systems or a laser source.

Synthesis in a magnetic field gives defect-free and high purity ( $>95\%$ ) MWNTs, that can be used as nanosized electric wires for device fabrication [15]. In this case, the arc discharge is controlled by a magnetic field around the arc plasma created by using extremely pure graphite (purity  $>99.999\%$ ) electrodes (Figs. 2a and b). An economical route for the mass production of MWNTs is the synthesis by the plasma-rotating arc-discharge technique [16]. The centrifugal force caused by the rotation generates turbulence and accelerates the carbon vapor perpendicular to the anode (Fig. 2c). The rotation also distributes the microdischarges uniformly and generates a stable plasma. Consequently, it increases the plasma volume and raises the plasma temperature. At a rotation speed of 5000 rpm, a yield of 60% is obtained

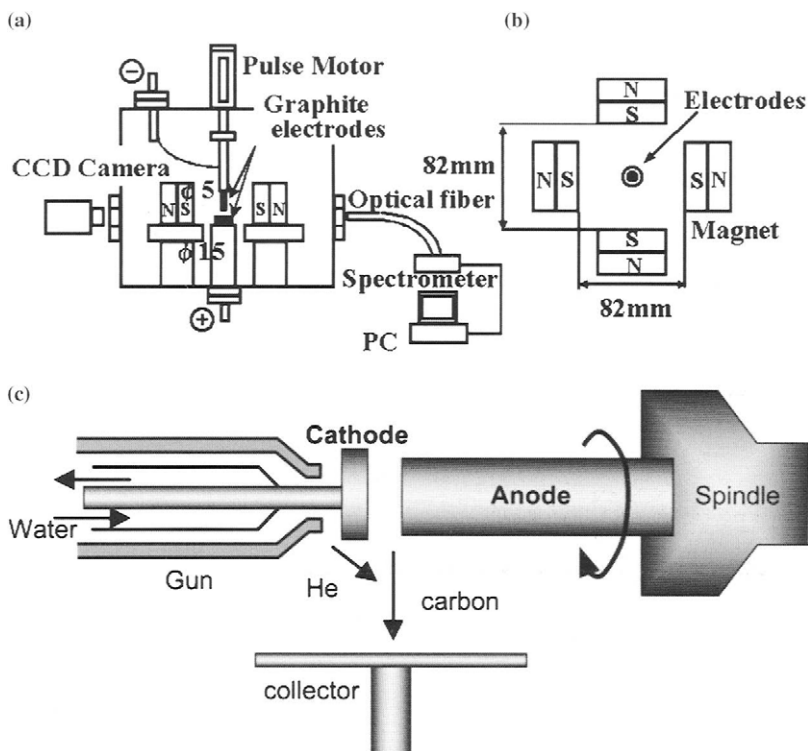


Figure 2. (a and b) Schematic diagrams of the system for the synthesis of MWNTs in a magnetic field (reproduced from Anazawa et al. [15]). (c) Schematic diagram of a plasma rotating electrode system. (Reproduced from Lee et al. [16].)

at a reaction temperature of 1025 °C (without the use of a catalyst). The yield increases up to 90% if the rotation speed is increased at a temperature of 1150 °C. The MWNTs obtained generally have an inner diameter of 1–3 nm and an outer diameter of ~10 nm.

Deposition of carbon vapor on cooled substrates of highly oriented pyrolytic graphite gives rise to tube-like structures [17]. CNTs are also produced by carrying out electrolysis in molten halide salts with carbon electrodes in an argon atmosphere [18a]. MWNTs with well-ordered graphitic structures have also been obtained under hydrothermal conditions around 800 °C under 60–100 MPa pressure using a polyethylene and water mixture in the presence of a nickel catalyst [18b]. CNT bundles with mesoporous structure are obtained by a simple one-step solvothermal reaction between Na and hexachlorobenzene (HCB) using  $\text{NiCl}_2$  as catalyst precursor [19]. Before the reaction,  $\text{NiCl}_2$  is dispersed ultrasonically in cyclohexane and pre-reduced by Na at 230 °C to produce small Ni particles. The nanotubes produced by this method have a uniform outer diameter of about 20 nm and an inner diameter of 4 nm; they occur as bundles with a 2-D hexagonal arrangement.

Besides the conventional arc-evaporation technique, CNTs are produced by chemical vapor deposition (CVD), by the decomposition of hydrocarbons such as  $\text{C}_2\text{H}_2$  under inert conditions around 700 °C over Fe/graphite [20], Co/graphite [21], or Fe/silica [22] catalysts. The presence of transition-metal particles is essential for the formation of nanotubes by the CVD or pyrolysis process, and the diameter of the nanotube is generally determined by the size of the metal particles [23].

### 2.1.1. Chemical vapor deposition

The CVD method uses a carbon source in the gas phase and a plasma or a resistively heated coil, to transfer the energy to the gaseous carbon molecule. The commonly used carbon sources are methane, carbon monoxide, and acetylene. The energy source cracks the molecule into atomic carbon. The carbon then diffuses toward the substrate, which is heated and coated with a catalyst (usually a first row transition metal such as Ni, Fe, or Co) and binds to it. CNTs are formed in this procedure if the proper parameters are maintained. Good alignment [24] as well as positional control on a nanometric scale [25] is achieved by using CVD. Control over the diameter as well as the growth rate of the nanotubes is also achieved by this method. Use of an appropriate metal catalyst permits the preferential growth of single-walled rather than multi-walled nanotubes [26].

CVD synthesis of nanotubes is essentially a two-step process, consisting of a catalyst preparation step followed by the actual synthesis of the nanotube. The catalyst is generally prepared by sputtering a transition metal onto a substrate and then using etching by chemicals such as ammonia or thermal annealing to induce the nucleation of catalyst particles. Thermal annealing results in metal cluster formation on the substrate, from which the nanotubes grow. The temperature for the synthesis of nanotubes by CVD is generally in the 650–900 °C range [24–27]. Typical nanotube yields from CVD are around 30%. A variety of CVD processes have been used for CNTs synthesis, which include plasma-enhanced CVD, thermal chemical CVD, alcohol catalytic CVD, aerogel-supported CVD, and laser-assisted CVD. In the

thermal CVD process, Fe, Ni, Co, or an alloy of these metals is initially deposited on a substrate. After the substrate is etched by a dilute HF solution, the substrate is placed in a quartz boat, positioned in a CVD reaction furnace. Nanometer-sized catalytic metal particles get formed after an additional etching of the catalytic metal film using  $\text{NH}_3$  gas at 750–1050 °C. The nanotubes grow on the fine catalytic metal particles by the CVD process [28].

### 2.1.2. Plasma-enhanced chemical vapor deposition

The plasma-enhanced CVD (PECVD) method involves a glow discharge in a chamber or a reaction furnace through a high-frequency voltage applied to both the electrodes. Fig. 3 shows a schematic diagram of a typical plasma CVD apparatus with a parallel plate electrode structure. A substrate is placed on the grounded electrode. In order to form a uniform film, the reaction gas is supplied from the opposite plate. Catalytic metals such as Fe, Ni, and Co are used on a Si,  $\text{SiO}_2$ , or glass substrate using thermal CVD or sputtering. After the nanoscopic fine metal particles are formed, the CNTs grow on the metal particles on the substrate by the glow discharge generated from a high-frequency power source. A carbon-containing gas, such as  $\text{C}_2\text{H}_2$ ,  $\text{CH}_4$ ,  $\text{C}_2\text{H}_4$ ,  $\text{C}_2\text{H}_6$ , or CO is supplied to the chamber during the discharge [29]. The catalyst has a strong effect on the nanotube diameter, growth

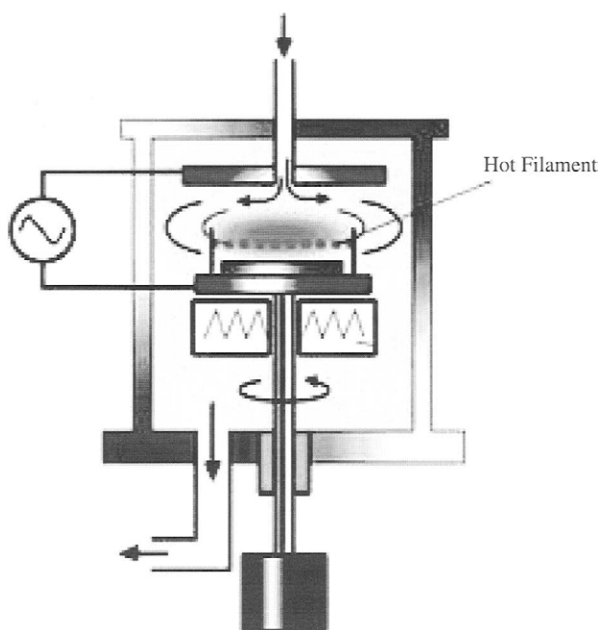


Figure 3. Schematic diagram of a plasma CVD apparatus. (Reproduced from Chen et al. [29].)

rate, wall thickness, morphology, and microstructure. Ni seems to be the most suitable catalyst for the growth of aligned MWNTs by this technique [30]. The diameter of the MWNTs is around 15 nm. The highest yield of CNTs achieved by Chen et al. [29] was about 50%, at a relatively low temperature ( $<330\text{ }^{\circ}\text{C}$ ).

### 2.1.3. Vapor-phase growth

Vapor-phase growth, pyrolysis, or the floating catalyst method is a method wherein the carbon vapor and the catalytic metal particles both get deposited in the reaction chamber without a substrate. The diameter of the CNTs by vapor-phase growth is in the range of 2–4 nm for SWNTs and between 70 and 100 nm for MWNTs. Using this technique, Sen et al. [31] prepared MWNTs as well as metal-filled onion-like and nanotube structures by the pyrolysis of metallocenes such as ferrocene, cobaltocene, and nickelocene under reducing conditions, wherein the precursor acts as the source of the metal as well as carbon. The pyrolysis setup consists of stainless steel gas flow lines and a two-stage furnace system fitted with a quartz tube as shown in Fig. 4, the flow rate of the gases being controlled by the use of mass flow controllers [32]. In a typical preparation, a known quantity (100 mg) of the metallocene (pre-sublimed 99.99% purity) is taken in a quartz boat and placed at the center of the first furnace, and a mixture of Ar and  $\text{H}_2$  of the desired composition is passed through the quartz tube. The metallocene is sublimed by raising the temperature of the first furnace to  $200\text{ }^{\circ}\text{C}$  at a controlled heating rate ( $20\text{ }^{\circ}\text{C}/\text{min}$ ). The metallocene vapor so generated is carried by the Ar- $\text{H}_2$  gas stream into the second furnace, maintained at  $900\text{ }^{\circ}\text{C}$ , where the pyrolysis occurs. The main variables in the experiment are the heating rate of ferrocene, the flow rate of Ar gas, and the pyrolysis temperature [32]. Fig. 5a shows a transmission electron microscopy (TEM) image of MWNTs obtained by the pyrolysis of mixture of  $\text{C}_2\text{H}_2$  and ferrocene. Ferrocene vapor carried by a 75% Ar + 25%  $\text{H}_2$  mixture at a flow rate of 900 sccm (standard cubic centimeter per minute) into the furnace yields large quantities of carbon deposits, mainly containing CNTs. Under similar conditions, nickelocene with benzene gave MWNTs (Fig. 5b). This procedure has been employed for large-scale production of CNTs [33].

Keller and Qadri [34] have obtained several ferrocenyl-aryl-acetylenic compounds and thermally converted them in situ to CNT-Fe nanoparticle compositions. Various shaped carbonaceous forms (solid, fiber, and film) containing large amounts of CNTs can be readily obtained from the precursor ferrocenyl compounds. Upon melting, the ferrocenyl compounds are cured to a shaped configuration through the acetylenic units. Further heating of the polymeric composition results in the decomposition of the ferrocene and the ultimate formation of Fe nanoparticles. During the carbonization process above  $500\text{ }^{\circ}\text{C}$  in an inert atmosphere, the Fe nanoparticles react with the developing carbon nanoparticles resulting in the formation of CNTs in high yield within the carbonaceous media.

Nebulized spray pyrolysis has been successfully employed for the synthesis of MWNTs [35]. Fig. 6 shows the schematic diagram of the experimental setup. Silicon substrates were placed in the regions I, II, III, and IV of the reactor to collect the product. In a typical synthesis, 2 g of metallocene was dissolved in 100 ml of a

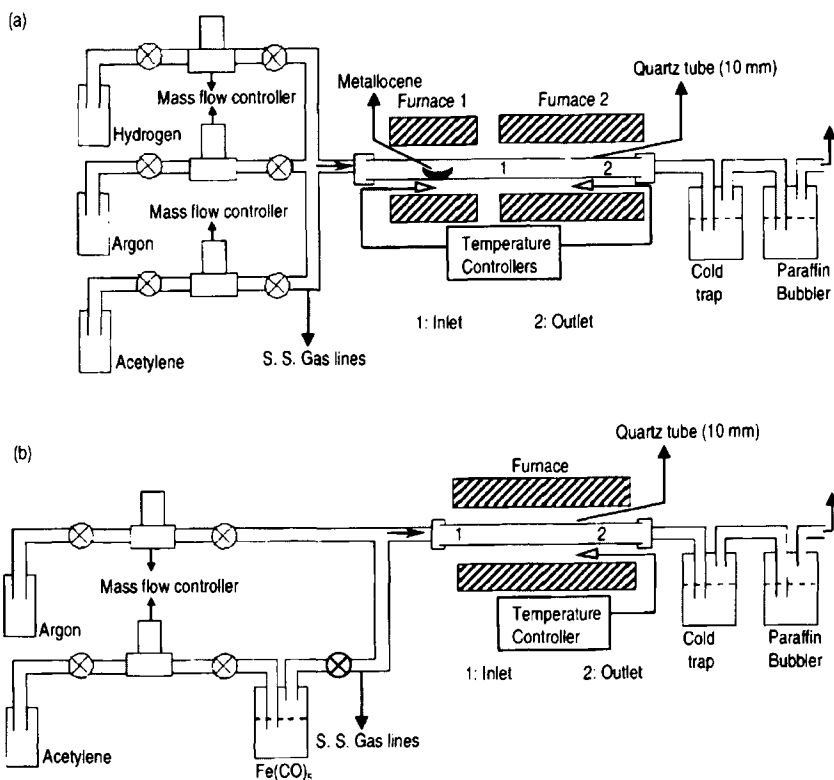


Figure 4. Apparatus employed for the synthesis of CNTs by the pyrolysis of mixtures of (a) metalocene +  $C_2H_2$  and (b)  $Fe(CO)_5$  +  $C_2H_2$ . Numbers 1 and 2 in the figure represent the inlet and outlet, respectively. (Reproduced from Rao et al. [32].)

hydrocarbon and the solution nebulized using a 1.54 MHz ultrasonic beam carried into a 25 mm quartz tube, placed in a SiC furnace maintained at the required temperature (800–1000 °C). Pure argon was used as the carrier gas and the gas flow rate was controlled using UNIT mass flow controllers. In a typical procedure, the carrier gas flow rate was kept at 1000 sccm and the pyrolysis was carried for 30 min. After the reaction, the furnace was allowed to cool. The products were collected after the tube cooled to room temperature. The average droplet size for the various solvents for 1.54 MHz frequency is  $\sim 2.2 \mu m$ . Ferrocene, cobaltocene, nickelocene, and iron pentacarbonyl were used as both catalysts and carbon sources. Acetylene, benzene, toluene, xylene, mesitylene, and *n*-hexane used as solvents for the catalysts, act as additional carbon sources. The TEM images in Fig. 7 shows the MWNTs obtained by this method. Random or aligned bundles of MWNTs with fairly uniform diameters are obtained depending on the flow rate and hydrocarbon solvent used

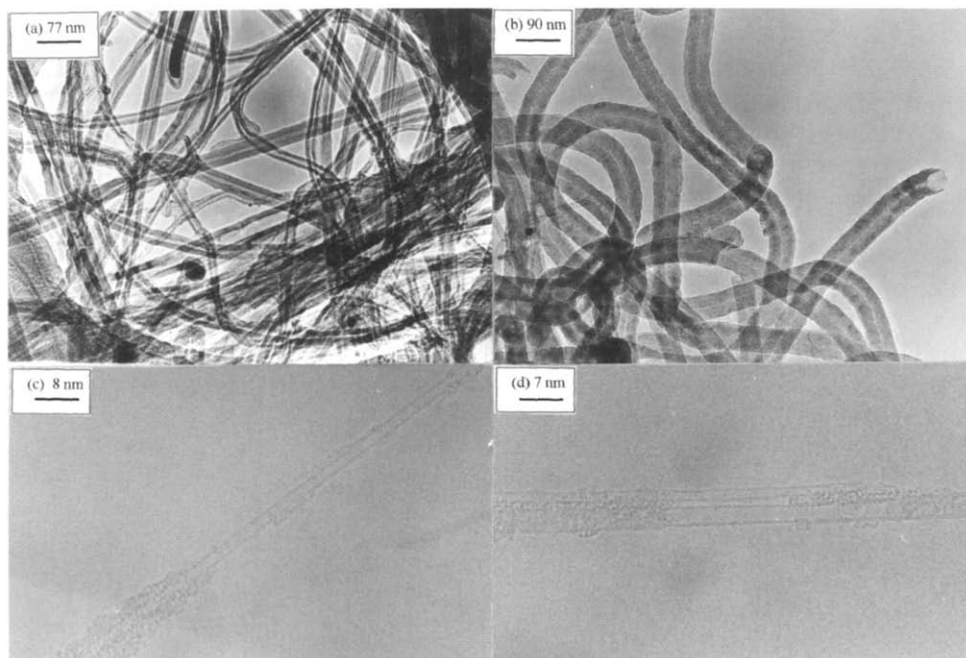


Figure 5. (a) TEM image of MWNTs obtained by the pyrolysis of a mixture of  $C_2H_2$  (25 sccm) and ferrocene at  $1100\text{ }^\circ\text{C}$  at 1000 sccm Ar flow. (b) TEM image of MWNTs obtained by the pyrolysis of a mixture of nickelocene and benzene at  $900\text{ }^\circ\text{C}$  in 85% Ar and 15%  $H_2$  mixture at a flow rate of 1000 sccm. (c) HREM image of a SWNT obtained by the pyrolysis of nickelocene and  $C_2H_2$  (50 sccm) at  $1100\text{ }^\circ\text{C}$  in a flow of Ar (1000 sccm). (d) HREM image of SWNTs obtained by the pyrolysis of ferrocene and  $CH_4$  at  $1100\text{ }^\circ\text{C}$  in a flow of Ar (990 sccm) and  $CH_4$  (10 sccm). (Reproduced from Sen et al. [31a], Rao et al. [32].)

for dissolving the metallocene. Well-graphitized MWNTs were obtained with a solution of ferrocene in xylene (inset in Fig. 7d). The quality of the product is dependent on the pyrolysis temperature, carrier gas flow rate, additional carbon sources used, and the catalyst precursor concentration. This procedure can be scaled up for continuous production of MWNTs.

## 2.2. Single-walled carbon nanotubes

The CNTs generally obtained by the arc method or hydrocarbon pyrolysis are multi-walled, having several graphitic sheets or layers. Depending on the exact technique, it is possible to selectively grow SWNTs or MWNTs. Two distinct methods of synthesis can be performed with the same arc-discharge apparatus. If SWNTs are required, the anode has to be doped with a metal catalyst based on Fe, Co, Ni, or

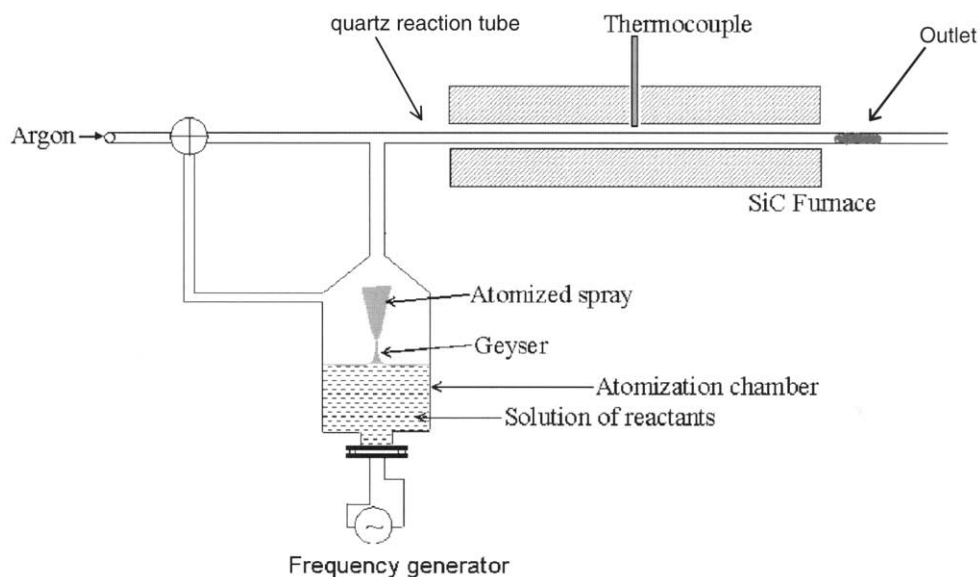


Figure 6. Schematic of the nebulized spray pyrolysis setup. (Reproduced from Vivekchand et al. [35].)

Mo. Several elements and mixtures of elements have been tested and the results vary considerably [36].

Single-walled nanotubes were first prepared by the metal-catalyzed dc arcing of graphite rods in a He atmosphere [1,2]. The graphite anode was filled with metal powders (Fe, Co, or Ni) and the cathode was of pure graphite. SWNTs generally occur in the web-like material deposited behind the cathode. Various metal catalysts have been used to make SWNTs by this route. Dai et al. [37] prepared SWNTs by the disproportionation of CO at 1200 °C over Mo particles of few nanometer diameter dispersed in a fumed alumina matrix. Saito et al. [38] compared SWNTs produced by using different catalysts and found that a Co or a Fe/Ni bimetallic catalyst gives rise to tubes forming a highway-junction pattern. SWNTs are also prepared by using various oxides  $Y_2O_3$ ,  $La_2O_3$ ,  $CeO_2$  as catalysts [39]. The arc-discharge technique, though cheap and easy to implement, gives low yields of SWNTs. Journet et al. [40] obtained ~80% yield of SWNTs in the dc arc, by using a mixture of 1 at.% Y and 4.2 at.% Ni as catalyst. Arc evaporation of graphite rods filled with Ni and  $Y_2O_3$  in a He atmosphere (660 torr) gives rise to web-like deposits on the chamber walls near the cathode, consisting of SWNT bundles [41]. HREM images show the presence of bundles consisting of 10–50 SWNTs forming highway junctions (Fig. 8a). The average diameter of the SWNTs was around 1.4 nm and the length extended upto 10  $\mu m$ . The quantity and quality of the nanotubes depend on various parameters such



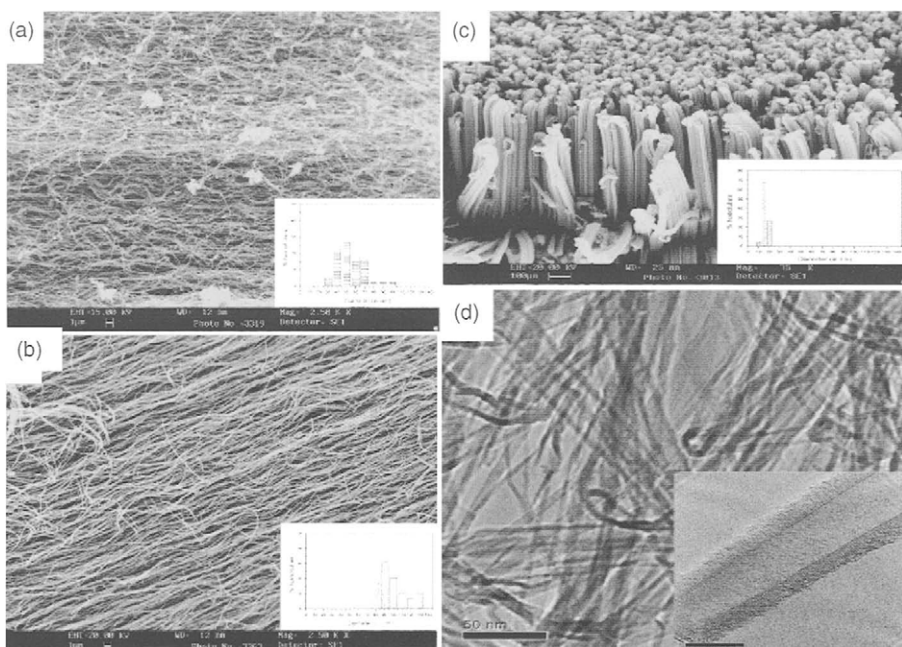


Figure 7. (a and b) SEM images of aligned MWNT bundles obtained by the nebulized spray pyrolysis of ferrocene along with benzene and mesitylene, respectively at 900 °C at an argon flow rate of 1000 sccm. (c and d) SEM and TEM images, respectively of aligned MWNTs obtained by the pyrolysis of a toluene solution of ferrocene (20 g/l) for 5 min and acetylene flow of 100 sccm for a duration of 30 min. Insets in Figs. (a–c) show diameter histograms. (Reproduced from Vivekchand et al. [35].)

as the metal concentration, inert gas pressure, kind of gas, the current and system geometry. In what follows, some of the ways to improve the process of arc discharge are discussed. Ohkohchi et al. [42] reported the synthesis of SWNTs by arc-discharge technique in a mixture of  $H_2$  and Ar, wherein they use a Fe catalyst and minimize the formation of nanoparticles.

A common problem with SWNT synthesis is that the product contains metal catalyst particles and defects, rendering purification difficult. On the other hand, an advantage is that the diameter can be controlled by changing the thermal transfer and diffusion, and hence the condensation of atomic carbon. This has been demonstrated in an experiment where different mixtures of inert gases were used [43]. Argon, with a lower thermal conductivity and diffusion coefficient, gives SWNTs with a diameter of  $\sim 1.2$  nm. A linear fit of the average nanotube diameter showed a 0.2-nm diameter decrease per 10% increase in argon–helium ratio, when nickel/yttrium was used (C/Ni/Y was 94.8:4.2:1) as catalyst.

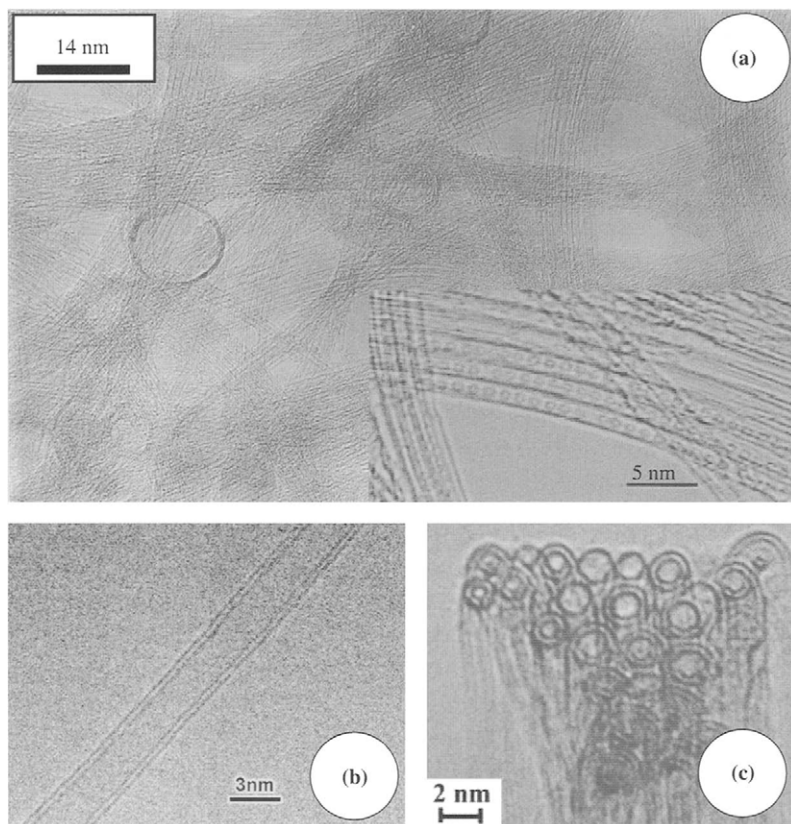


Figure 8. (a) HREM image of SWNTs obtained by arcing graphite electrodes filled with Ni and  $Y_2O_3$  under a He atmosphere (660 Torr). (Reproduced from Rao et al. [32] (inset reproduced from Smith et al. [88]).) (b and c) HREM images of DWNTs. Inset in (a): HREM image of fullerenes encapsulated inside the SWNTs (peapods); scale bar = 5 nm. (Reproduced from Flahaut et al. [98d].)

### 2.2.1. Optical plasma control

Here, the anode to cathode distance is adjusted in order to obtain strong visible vortices around the cathode. This enhances anode vaporization and improves nanotubes formation. Combined with suitable use of the argon–helium mixture, one can simultaneously control the macroscopic and microscopic parameters of the nanotubes formed [44]. With a nickel and yttrium catalyst (C/Ni/Y is 94.8:4.2:1), the optimum nanotube yield is found around 660 mbar for pure helium and 100 mbar for pure argon. The nanotube diameter ranges from 1.27 to 1.37 nm. Since CVD gives SWNTs with a diameter of 0.6–1.2 nm, different groups have used the same catalyst as in CVD in the arc-discharge method. Not all of the catalysts result in nanotubes.

Yet, there seems to be a relation between the diameter of SWNTs synthesized by CVD and arc discharge. As a result, the diameter could be lowered to a range of 0.6–1.2 nm with arc discharge, using a mixture of Co and Mo catalyst in high concentration. These diameters are considerably smaller than 1.2–1.4 nm found normally [36]. Green and co-workers [45] have studied the correlation of the diameter of SWNTs, using the same catalyst by the CVD and the arc-discharge methods.

### 2.2.2. Catalyst composition

Itkiss et al. [46] optimized the Ni–Y catalyst composition in bulk scale electric arc synthesis of SWNTs by using solution-phase near-infrared spectroscopy. By using this tool they found that a wide range of catalyst concentrations (3–6 at.% Ni and 1–2 at.% Y) allow efficient production of high-purity as-prepared SWNT soot. The broad window of acceptable synthetic parameters found in this study suggests that it may be possible to scale-up the electric arc-discharge synthesis of SWNTs. Significant deviations of the concentrations of either Ni or Y outside the optimum parameters result in a degradation in the quality and yield of the SWNT soot.

### 2.2.3. Improvement of oxidation resistance

There is some progress in improving the oxidation resistance of the SWNTs. A strong oxidation resistance is needed if the nanotubes are to be used for applications such as field emission displays. A modified arc-discharge method using a bowl-like cathode, is found to decrease the defects and yield cleaner nanotubes, with improved oxidation resistance. The anode rod contained the Ni and Y catalyst [47]. Open-air synthesis of SWNTs has been carried out with a modified welding arc-torch method [48]. A plate target made of graphite containing the Ni/Y catalyst (Ni/Y is 3.6:0.8 at.%), was fixed at the sidewall of a water-cooled, steel-based electrode. The torch arc aimed at the edge of the target and the soot was deposited on the substrate behind the target. The arc was operated at a direct current of 100 A and shielding argon gas flowed through the torch, enhancing the arc-jet formation beyond the target. In the soot, carbon nanohorns and bundles of SWNTs with an average diameter of 1.32 nm were found. However, the yield was lower than in the conventional low-pressure arc-discharge method. This is because the lighter soot escapes into the atmosphere in the open air synthesis. Secondly, the carbon vapor might be oxidized and emitted as carbon dioxide gas.

### 2.2.4. Laser vaporization

Smalley's [49] group reported the synthesis of CNTs by laser vaporization in 1995. The laser vaporization apparatus used by the Smalley group is shown in Fig. 9a. A pulsed [50,51] or continuous [52] laser is used to vaporize a graphite target in an oven at 1200 °C. The oven is filled with helium or argon gas in order to keep the pressure at 500 torr. A hot vapor plume forms, then expands and cools rapidly. As the vaporized species cool, small carbon molecules and atoms quickly condense to form larger clusters, possibly including fullerenes. The catalysts also begin to condense, but more slowly at first, and attach to carbon clusters and prevent their closing into cage structures [53]. Catalysts may even open cage structures when they attach to them. From these initial clusters, tubular molecules grow into single-wall

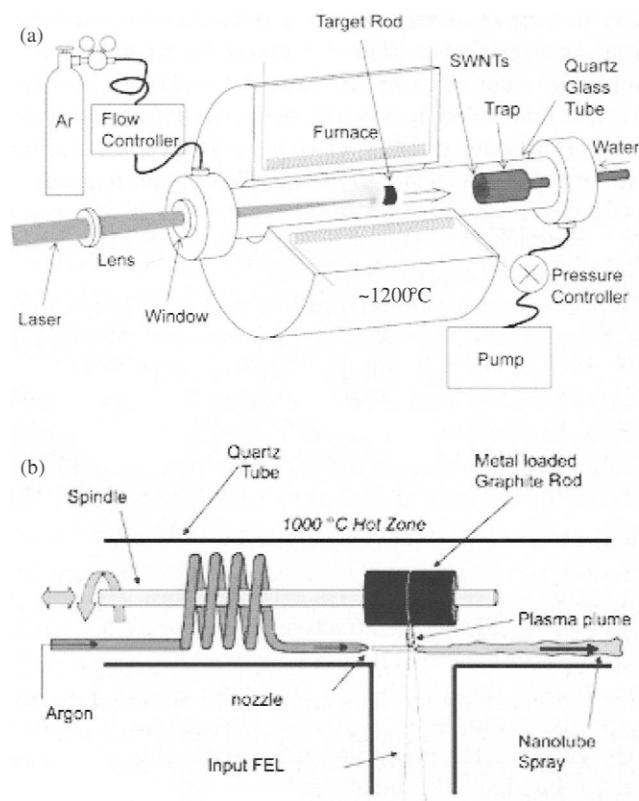


Figure 9. Schematic drawings of (a) a Smalley-type laser ablation apparatus (reproduced from Ando et al. [10b], Guo et al. [49]), (b) Ultrafast-pulsed laser ablation apparatus. (Reproduced from Eklund et al. [51].)

carbon nanotubes until the catalyst particles become too large, or until conditions have cooled sufficiently that carbon no longer can diffuse through or over the surface of the catalyst particles. It is also possible that the particles become that much coated with a carbon layer that they cannot absorb more and the nanotube stops growing. The SWNTs formed get bundled due to van der Waals forces. SWNTs have been produced in more than 70% yield by the condensation of a laser-vaporized carbon–nickel–cobalt mixture at  $1200^{\circ}\text{C}$  [54].

The condensates obtained by laser ablation are contaminated with CNTs and carbon nanoparticles. In the case of pure graphite electrodes, MWNTs are formed, but uniform SWNTs are obtained if a mixture of graphite with Co, Ni, Fe, or Y is used instead of pure graphite. SWNTs synthesized this way exist as ropes. The Ni/Y mixture catalyst (Ni/Y is 4.2/1) appears to give the best yield. With a Ni/Co catalyst

and a pulsed laser at 1470 °C, SWNTs with a diameter of 1.3–1.4 nm are obtained. When a continuous laser is used at 1200 °C with the Ni/Y catalyst (Ni/Y is 2:0.5 at.%), SWNTs with an average diameter of 1.4 nm are formed with 20–30% yield. Because of the good quality of nanotubes produced, there are efforts to scale-up laser ablation. However, the results are not yet as good as from the arc-discharge method. Laser vaporization results in a higher yield for SWNTs and the nanotubes have better properties and a narrower size distribution than the SWNTs produced by arc discharge. Nanotubes produced by laser ablation have greater purity (up to about 90% purity) than those by the arc-discharge process.

Zhang et al. [55] found that the simple introduction of Fe into a conventional NiCo catalyst enables the production of SWNTs with controlled diameter distributions by laser ablation. These workers find that the diameter of the as-grown SWNTs can be made larger by increasing the atomic percentage of Fe in the target without changing any other synthesis parameters. It seems Fe helps increase the aggregation rate of metal in laser ablation and enlarges the crystal lattice constant of metal catalysts because of a change in the crystal structure from Ni to Ni<sub>3</sub>Fe, NiFe, and NiFe<sub>2</sub>, which then results in the enlargement of metal particles and the growth of larger diameter SWNTs.

Ultrafast pulses from a free electron laser (FEL; pulse width is ~400 fs) with a pulse repetition rate of 75 MHz can be effectively used for SWNT synthesis [51]. Here, the intensity of the laser bundle behind the lens reaches  $\sim 5 \times 10^{11}$  W/cm<sup>2</sup>, which is about 1000 times greater than in the Nd:YAG laser systems. A jet of pre-heated (1000 °C) argon through a nozzle tip is situated close to the rotating graphite target, which contains the catalyst. The argon gas deflects the ablation plume approximately 90° away from the incident FEL beam direction, clearing away the carbon vapor from the region in front of the target. The SWNT soot is collected in a cold finger. This process can be seen in Fig. 9b. The yield is 1.5 g/h at 20% of the maximum power. With this method, the maximum achievable yield with the current lasers is 45 g/h (with a NiCo or NiY catalyst) in an argon atmosphere at 1000 °C at a wavelength of ~3000 nm. The SWNTs are in bundles. The number of tubes within a typical bundle varies from 8 to 200, with a length of 5–20 µm and a diameter of 1–1.4 nm.

A continuous wave laser-powder method has also been employed for SWNT synthesis, based on the laser ablation of mixed graphite and metallic catalyst powders by a 2-kW continuous wave CO<sub>2</sub> laser in an argon or nitrogen stream [52b]. Because of the use of micron-size particles, the thermal conductivity losses are significantly decreased compared with laser heating of the bulk solid targets in known laser techniques. As a result, more effective utilization of the absorbed laser power for material evaporation was achieved. The yield in this technique is 5 g/h with a Ni/Co catalyst (Ni/Co is 1:1) at a temperature of 1100 °C. The yield in SWNTs is 20–40% with a mean diameter of 1.2–1.3 nm. Arepalli [56] has reviewed the progress in the laser ablation process for SWNT production.

El Khakani and Yi [57] used an “all-laser” synthesis approach that permits the control of the lateral growth of SWNTs on SiO<sub>2</sub>/Si substrates at selected locations where nanoparticles catalysts were first deposited. This two-step growth process uses the same UV laser (KrF excimer;  $\lambda = 248$  nm) to deposit, in the first step, the

CoNi nanoparticle catalysts on patterned SiO<sub>2</sub>/Si substrates, and to grow SWNTs in a subsequent step. Atomic force microscopy and micro-Raman spectroscopy revealed that the “all-laser” process leads to the formation of horizontal random networks of SWNT bundles, which bridge two adjacent nanoparticle strips. The diameter of the SWNTs was found to be similar to 1.1 nm, while that of the bundles is generally in the 10–15 nm range.

### 2.2.5. Pyrolysis or vapor-phase deposition

Under controlled conditions of pyrolysis, dilute hydrocarbon–organometallic mixtures yield SWNTs [41,58a]. Pyrolysis of a metallocene–acetylene mixtures at 1100 °C yields SWNTs [58a], shown in TEM image in Fig. 5c. The diameter of the SWNT in Fig. 5c is 1.4 nm. In Fig. 5d, shows the SWNTs obtained similarly by the pyrolysis of ferrocene–CH<sub>4</sub> mixture at 1100 °C. It may be recalled that the pyrolysis of nickelocene in admixture with benzene under similar conditions primarily yields MWNTs. The bottom portion of the SWNT in Fig. 5c shows an amorphous carbon coating around the tube, common with such preparations. This can be avoided by reducing the proportion of the hydrocarbon C<sub>2</sub>H<sub>2</sub> and mixing hydrogen in the Ar stream. Pyrolysis of binary mixtures of metallocenes and acetylene also gives SWNTs, due to the beneficial effect of such binary alloys [58b]. Pyrolysis of acetylene in mixture with Fe(CO)<sub>5</sub> at 1100 °C gives good yields of SWNTs. Pyrolysis of ferrocene–thiophene mixtures also yield SWNTs, but the yield appears to be somewhat low. Pyrolysis of benzene and thiophene along with ferrocene gives a high yield of SWNTs [59].

### 2.2.6. Chemical vapor deposition

Compared with arc and laser methods, the main advantage of CVD is that it is a straightforward way to scale-up production to industrial levels. Colomer et al. [60] obtained SWNTs in high yield by the decomposition of methane over transition-metal-supported MgO substrates. Flahaut et al. [61a] have synthesized SWNTs by passing a H<sub>2</sub>–CH<sub>4</sub> mixture over transition metal containing oxide spinels, obtained by the combustion route. The quality of SWNTs has been characterized on the basis of adsorption measurements. Franklin and Dai [61b] used an enhanced CVD growth approach, by introducing a new conditioning step to grow high yield of SWNTs (150 μm length) with extensive networks of suspended SWNTs and a high degree of orientation. The conditioning step is a procedure that uses bulk amounts of catalyst materials (Fe–Mo/Al<sub>2</sub>O<sub>3</sub>) placed upstream of the catalytically patterned substrate in a CVD growth environment. The nanotubes form an extensive quasi-ordered network under methane flow (1000 sccm, 20 min) at 900 °C, with the nanotube orientations directed by the tower or pillar structures on the patterned substrate. They studied the effect of conditioning, which involves the generation of benzene molecules via catalytic conversion of methane by carrying out the mass spectral studies on effluent from the CVD growth reactions. They speculate that these catalytically generated highly reactive benzene molecules flows to the downstream substrate and provide an efficient carbon-feedstock for the growth of SWNTs.

Li et al. [62] studied the effect of hydrocarbon precursors on the formation of carbon nanotubes. However in their study they found that the morphology of carbon

deposits over MgO supported Fe catalyst during CVD process was closely related to the thermodynamic properties and chemical structures of the hydrocarbon precursors. They used six hydrocarbons (methane, hexane, cyclohexane, benzene, naphthalene, and anthracene) as carbon precursors in their study. Methane, which has a simple composition and is more stable seems to be favorable for the formation of high-purity SWNTs. For high-molecular weight hydrocarbons, the chemical structure rather than the thermodynamic properties of the carbon precursors plays a role in nanotube formation.

Paillet et al. [63] used discrete nickel catalyst nanoparticles to grow isolated SWNTs (1.45 nm dia.) by the use of CVD. Zheng et al. [64] have synthesized by CVD ultralong SWNTs (4-cm long) at a high growth rate of 11  $\mu\text{m/s}$ . Their results suggest the possibility of growing SWNTs continuously without any apparent length limitation. Song et al. [65] have obtained tough non-woven material of SWNTs with an area of up to several tens of square centimeters by a direct-floating CVD method followed by purification. The SWNT non-woven material exhibits an extremely high Young's modulus of ca. 0.4–0.7 TPa.

Li et al. [66] successfully synthesized SWNTs using the fluidized-bed method that involves fluidization of a catalyst/support at high temperatures by a hydrocarbon flow. By using nickel–nitrate coated silica-gel particles and methane, SWNTs were found to grow densely on the entire surface of the support particles at 760 °C. This approach seems to offer multiple advantages over the common fixed-bed process, such as uniform gas–solid mixture and avoids the sintering of catalyst particles. Li et al. [67] also obtained SWNTs by the rapid injection of a nickel formate/silica-gel catalyst/support into a hot fluidized-bed reactor.

Wang et al. [68] have studied the use of bimetallic catalysts such as Fe/Ru and Fe/Pt in the size range of 0.5–3 nm for the efficient growth of SWNTs on flat surfaces. They produced uniform Fe/Ru and Fe/Pt bimetallic nanoparticles by the chemical reduction under microwave irradiation with poly(*N*-vinyl-2-pyrrolidone) (PVP) as a protective agent. These nanoparticles were subsequently used as catalysts for the surface growth of SWNTs by CVD. When compared with single-component catalysts such as Fe, Ru, and Pt of similar size, bimetallic catalysts Fe/Ru and Fe/Pt produced 200% more SWNTs.

Mizuno et al. [69] studied the compatibility of various catalysts for ethylene and ethanol CVD synthesis of SWNTs on Si substrates. They found a strong selectivity between the catalyst elemental species and the carbon source; SWNT yield for Fe (Co) catalysts was much higher for ethylene (ethanol) CVD than for ethanol (ethylene) CVD.

Using spin-on catalyst, Pender et al. [70] synthesized SWNTs on various substrates from CVD of methane with hydrogen at 900 °C. The catalyst precursor used by them comprised of iron nitrate and a commercially available siloxane polymer solution. The siloxane matrix seems to help the controlled formation of catalytic nanoparticles via phase separation. Upon heating, a smooth, continuous film of  $\text{SiO}_x$ , which prevents catalyst coarsening and agglomeration at growth conditions is formed.

Zeolites containing one-dimensional channels have been employed for the synthesis of monosized SWNTs [71]. Endo et al. [72] have described a possible route for

the large-scale synthesis of SWNTs by a combination of a substrate (template) and floating catalyst. The template (nanosize zeolites), which has exposed pores act as anchoring sites for metal nanoparticles prohibiting the metal particle aggregation. Such optimized seeding results in high-purity SWNTs via suppression of impurity formation such as MWNTs and carbon nanoparticles. The three-dimensionally floated template in the reaction chamber makes it possible to produce nanotubes in the semicontinuous system, with a large variations in texture and a wide range of diameters (0.4–4 nm).

Hata et al. [73] have demonstrated an efficient CVD synthesis of SWNTs where the activity and lifetime of the catalysts are enhanced by water. Water-stimulated enhanced catalytic activity results in massive growth of superdense and vertically aligned nanotube forests with heights up to 2.5 mm that can be easily separated from the catalysts, providing nanotube material with carbon purity above 99.98%. Moreover, patterned, organized intrinsic nanotube structures are successfully fabricated. The water-assisted synthesis addresses some of the problems faced in CNT synthesis. Currently, complete control of selectively growing metallic or semiconducting SWNTs has not been achieved.

Okazaki and Shinohara [74] reported a simplified production method for SWNTs by hot-filament-assisted chemical vapor deposition (HFCVD) using pure alcohol vapor (ethanol, methanol, and 2-propanol) as a carbon source. Under optimized conditions, high-purity SWNTs were synthesized, the efficiency being further increased by the hot-filament-induced pyrolysis of carbon sources. Kato et al. [75] produced SWNTs using PECVD method. In this method, not only SWNTs in the form of thin bundles but also individually grown SWNTs are produced at a quite low-synthesis temperature (550 °C). Preferential growth of semiconducting SWNTs (>85%) has been observed in a PECVD process at 600 °C [76]. It is possible that preferential growth combined with postgrowth treatment and separation may solve the problem of obtaining metallic versus semiconducting nanotubes.

Peng et al. [77] have reported the synthesis of CNT cables: a form of compound single- and multi-walled carbon nanotubes, which could have the properties superior to both SWNTs and MWNTs. This compound form of CNT consists of a bundle of SWNTs formed into a MWNT, and the diameter of the inner most shell of the MWNT ranges from a few to tens nanometers.

### **2.2.7. Alcohol catalytic chemical vapor deposition**

Alcohol catalytic CVD is a technique that has been developed for possible of large-scale production of high-quality SWNTs at low cost. In this technique, evaporated alcohols (methanol and ethanol) are passed over iron and cobalt catalyst particles supported on zeolites at a relatively low temperature of 550 °C. It seems that hydroxyl radicals of the alcohol eliminate carbon atoms with dangling bonds, which are obstacles in forming high-purity SWNTs. The diameter of the SWNTs obtained by this method is ~1 nm [78]. The low reaction temperature and the high purity of the product suggest the possibility of upscaling the production. Furthermore, the low reaction temperature ensures that the technique is applicable for the direct growth of SWNTs on semiconductor devices patterned with aluminum.

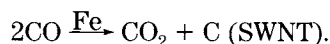


### 2.2.8. Laser-assisted thermal chemical vapor deposition

In the laser-assisted thermal CVD, a medium-power, continuous wave CO<sub>2</sub> laser, which is perpendicularly directed onto a substrate, pyrolyses sensitized mixtures of Fe(CO)<sub>5</sub> vapor and acetylene in a flow reactor. CNTs are formed by the catalyzing action of the small iron particles [79]. By using a reactant gas mixture of iron pentacarbonyl vapor, ethylene and acetylene, both single- and multi-walled carbon nanotubes are produced. Silica is used as substrate. The diameters of the SWNTs range from 0.7 to 2.5 nm. The diameter range of the MWNTs is 30–80 nm.

### 2.2.9. High-pressure CO disproportionation process

Nikolaev et al. [80] obtained SWNTs using a gas-phase catalytic method involving the pyrolysis of Fe(CO)<sub>5</sub> and CO. The decomposition of CO on a silica-supported Co–Mo catalyst also yields SWNTs [81]. The improvised technique, “High pressure CO” (HiPco) disproportionation process is a technique for catalytic production of SWNTs in a continuous-flow gas phase using CO as the carbon feedstock and Fe(CO)<sub>5</sub> as the iron-containing catalyst precursor. SWNTs are produced by flowing CO, mixed with a small amount of Fe(CO)<sub>5</sub> through a heated reactor. Fig. 10 shows the layout of CO flow-tube reactor. Size and diameter distribution of the nanotubes can be roughly selected by controlling the pressure of CO. This process is promising for bulk production of CNTs [80]. Nanotubes with a diameter as small as 0.7 nm, considered to be the smallest achievable chemically stable SWNTs, have been produced by this method [82]. The average diameter of HiPco SWNTs is ~1.1 nm. The yield that could be achieved is around 70%. SWNTs material with 97% purity can be produced at rates of up to 450 mg/h [83]. Nikolaev [84] has recently conducted a parametric study on the gas-phase production of SWNTs by the HiPco process. The latest process for producing large quantities of single-walled carbon nanotubes (SWNTs) is living up to its promise [83]. In the HiPco process, nanotubes grow in high-pressure, high-temperature flowing CO on catalytic clusters of iron. The catalyst is formed in situ by the thermal decomposition of Fe(CO)<sub>5</sub>, which is delivered intact within a cold CO flow and then rapidly mixed with hot CO in the reaction zone. Upon heating, the Fe(CO)<sub>5</sub> decomposes into atoms which condense into larger clusters. SWNTs nucleate and grow on these particles in the gas phase via CO disproportionation (Boudouard reaction) catalyzed by the Fe surface. The rate of the Boudouard reaction scales as a square of CO pressure, hence the importance of high-pressure CO for efficient SWNT production.



The concentration of CO<sub>2</sub> produced in this reaction is equal to that of carbon and can therefore serve as a useful real-time feedback parameter. The current production rates approach 450 mg/h (or 10 g/day), and nanotubes typically have no more than 7 mol% of iron impurities. The second-generation HiPco apparatus can run continuously for 7–10 days. The HiPco process is an attractive alternative gas-phase process that does not use pre-made catalyst particles, like other CVD techniques. To improve the yield and to avoid the release of CO exhaust into the atmosphere, a

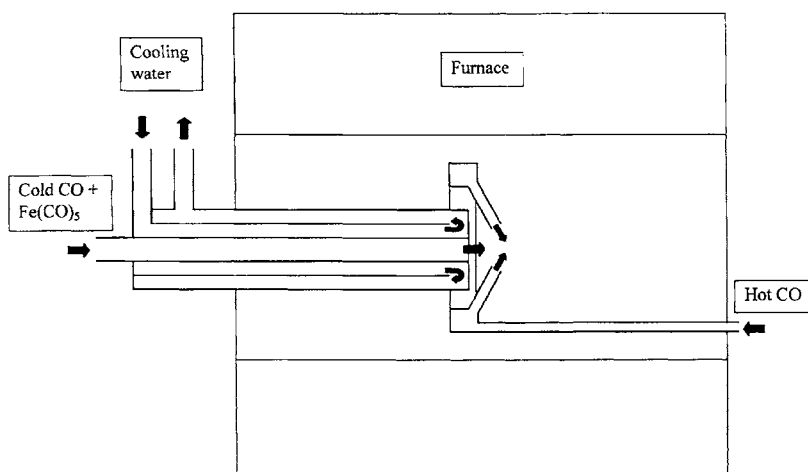


Figure 10. (a) Layout of a CO flow-tube reactor, showing water-cooled injector and ‘showerhead’ mixer. (Reproduced from Nikolaev et al. [80].)

closed-loop reactor has been developed. Here, CO is recirculated through the system using a compressor rather than being released into atmosphere.

#### 2.2.10. Flame synthesis

This method is based on the use of a controlled flame environment, wherein carbon atoms are formed from inexpensive hydrocarbon fuels along with aerosols of metal catalysts [85]. The SWNTs grow on metal islands in the same manner as in laser ablation and arc discharge. A submonolayer film ( $<10$  nm) of metal (cobalt) catalyst was applied to the stainless steel mesh (SS-304) by physical vapor deposition (PVD). In this manner, metal islands resembling droplets were formed upon the mesh support to serve as catalyst particles. These small islands become the aerosol when exposed to a flame. Another way is to create aerosol-type metal particles by burning a filter paper that is rinsed with a solution of metal ions (e.g., iron nitrate) [86]. A thermal evaporation technique in which the metal powder (e.g., Fe or Ni) is inserted in a trough and heated can also be used. A fuel gas is partially burnt under controlled conditions to attain a temperature of  $\sim 800$  °C to form the carbon atoms for the production of SWNTs. The optimization parameters are the fuel gas composition, the catalyst, catalyst carrier surface, and the temperature. The technique developed by Laplaze et al. [87] uses concentrated solar energy to vaporize graphite to synthesize SWNTs.

### 2.3. Peapods

Smith et al. [88] discovered fullerenes encased in single-walled carbon nanotubes (SWNTs) in acid-purified nanotubes prepared by the laser oven method [54] as shown in the inset of Fig. 8a. This material is called a *peapod*, because its structure

resembles miniature peas in a pod. The fullerenes of the peapod are arranged one-dimensionally with a constant intermolecular distance, which is slightly smaller (by 3%) than the nearest molecular distance of solid  $C_{60}$ .  $C_{60}$  peapods can be synthesized with high yields by means of the vapor-phase reaction of  $C_{60}$  with an acid-purified SWNT bundle [89a]. The reaction is carried out at 400 °C in a vacuum-sealed glass ampoule, the reaction time being normally a day or more to fill the tube with  $C_{60}$  (reaching a yield of almost 100%). Prior to taking the samples in the glass ampoule, it is necessary to heat the acid-purified SWNTs in dry air at 420–480 °C for 1 h in order to burn off contaminated carbon. This burning also guarantees open-ended tubes. The burning temperature depends on the cleanness of the tube surface. That is, if the rinsing step in the purification procedure for SWNTs is not sufficient to remove impurities, the burning temperature must be increased. Intact  $C_{60}$  molecules, thus arranged in the nanotube, start to merge together as the temperature is raised above ~800 °C in vacuum, and they finally form an inner tube. According to a TEM study of the merging process of  $C_{60}$  in the intermediate temperature range of 800–1000 °C, the internal tubes form as the result of a structural relaxation at the “bottleneck” area of the  $C_{60}$  dimers, trimers, tetramers, and so on. Once the fullerenes are in the nanotube space, they become stabilized, and it is rather difficult to remove them. Electronic structure calculations show that an energy of ~0.5 eV would be gained by peapod formation [90]. The encased  $C_{60}$  molecules are energetically stable and the dedoping of fullerenes is difficult and may not occur by heating. Metallofullerenes (endohedral fullerenes) have also been encapsulated in SWNTs and their structures investigated by TEM and other techniques [89b].

SWNTs encapsulating fullerenes, peapods such as  $C_{60}$  and metallofullerenes ( $Gd@C_{82}$ ) were synthesized by vapor-phase-doping technique, directly on Si substrates [91]. They used SWNTs grown on a  $SiO_2/Si$  substrate by dip-coating of metal acetate solution and alcohol CVD. The caps of the SWNTs were opened by annealing them in dry air before the vapor-phase deposition of fullerenes. They estimated from Raman scattering spectroscopy of synthesized peapods that the smallest diameters of the SWNTs capable of fullerene encapsulation were 1.28 nm for  $C_{60}$  and 1.43 nm for  $Gd@C_{82}$ . Chikkannanavar and Luzzi [92] has synthesized peapods using SWNTs and DWNTs grown by CVD, on substrates with windows etched into free-standing silicon nitride membranes. They oxidized the CVD-grown nanotubes in air, then filled with  $C_{60}$  molecules from the vapor phase. The windowed samples provide several important advantages for property measurements of peapods and other nanomaterials. Simon et al. [93] was successful in filling SWNTs with  $C_{60}$  and  $C_{70}$  by refluxing SWNTs with the respective fullerene solutions in *n*-hexane at temperatures as low as 69 °C for 2 h. They applied the same method to synthesize the temperature sensitive  $(N@C_{60}-C_{60})@SWNT$  and proved the encapsulation by electron spin resonance spectroscopy.

## 2.4. Double-walled carbon nanotubes

Double-walled carbon nanotubes (DWNTs) are obtained by the arc-discharge technique in an atmosphere of Ar and  $H_2$  mixture (1:1/v:v) at 350 torr [94]. The catalyst is prepared from a mixture of Ni, Co, Fe, and S powders heated in an inert

gas atmosphere at 500 °C for 1 h. The predominantly obtained DWNTs bundles have an outer diameter in the range of 1.9–5 nm and inner tube diameters in the range 1.1–4.2 nm. Li et al. [95] synthesized DWNTs in a large scale by a hydrogen arc-discharge method using composite rods made of graphite powders or MWNTs/carbon nanofibers (CNFs) as carbon feedstock with a co-catalyst composed of Fe/Co/Ni and Sulphur as growth promoter. They found that the DWNT product synthesized from MWNTs/CNFs had higher purity than that from graphite powders, with a yield of DWNTs of about 4 g/h. High-resolution TEM revealed that more than 80% of the CNTs were DWNTs, the rest being SWNTs, the outer and inner diameters ranging from 1.75 to 4.87 nm and 1.06 to 3.93 nm, respectively. The ends of the isolated DWNTs were uncapped. High-quality DWNTs are obtained by the high-temperature pulsed arc-discharge method with Y/Ni alloy catalysts at 1250 °C [96]. The optimum conditions of the DWNT synthesis are almost the same as those of SWNTs, indicating that the growth processes of DWNTs and SWNTs are closely related to each other. High-resolution TEM and Raman spectroscopy reveal that the DWNTs have an inner and outer diameters of 0.8–1.2 and 1.6–2.0 nm, respectively. DWNTs were prepared in quantitative amount from the chains of  $C_{60}$  molecules generated inside SWNTs [89a]. Heating at  $\sim 1200$  °C induces the coalescence between  $C_{60}$  and eventually the  $C_{60}$  molecules transform into a tubular structure.

Abe et al. [97] reported the X-ray diffraction (XRD) analysis of the structural transformation from SWNTs to DWNTs via  $C_{60}$ -encapsulated SWNTs ( $C_{60}$  peapods). They showed that the bundle structure of the starting SWNTs retained on this process and thermal expansion coefficients of DWNTs hardly changed from the pristine SWNTs. The intertube spacing between inner and outer tubes of DWNTs was obtained as  $0.36 \pm 0.01$  nm. This spacing was shown to be determined by the discreteness of the SWNT diameter under a turbostratic constraint between the inner and outer tubes of DWNT at synthesis temperatures.

Bandow et al. [89a] have reviewed the formation pathway to DWNTs from  $C_{60}$  encased within single-walled carbon nanotubes (peapods). High-quality DWNTs have been produced by catalytic CVD of carbon-containing molecules such as propanol, THF, hexane, benzene, alcohol around 900–1000 °C over Fe–Mo embedded  $MgO$  or  $Al_2O_3$  support material [98a–c]. Figs. 8b and c show TEM images of an isolated and of a bundle of DWNTs (77% yield), respectively, synthesized by the CVD of methane over a  $Mg_{1-x}Co_xO$  solid solution containing Mo oxide [98d]. The diameter of DWNTs so prepared was dependent on the process conditions and the carbon source. The DWNTs have inner tube diameters in the range of 0.6–3.4 nm and outer tube diameters in the 1.4–4.5 nm range.

Ramesh et al. [99a] selectively synthesized DWNTs over Fe/Co loaded mesoporous silica by CVD of alcohol. They investigated the use of several silica materials with desired pore diameter and morphology for the DWNT growth. The diameter distribution and selectivity of the DWNT are found to depend on the reaction temperature, pore size, and thermal stability of the support material. They achieved high yields of DWNTs at 900 °C over high-temperature stable mesoporous silica. Endo et al. [99b] has synthesized DWNTs by using a conditioning catalyst of molybdenum ( $Mo/Al_2O_3$ ) and a nanotube catalyst of iron (Fe/ $MgO$ ), which are kept at one

end and in the central part of the reactor, respectively. By feeding a mixture of methane-argon (1:1, 200 sccm) for 10 min into the reactor (maintained at 875 °C), they grow two sets of DWNT pairs having inner-to-outer diameter ratios of 0.77:1.43 and 0.90:1.60, respectively. They found that use of conditioning catalyst caused growth of more DWNTs than SWNTs, probably because of an increase in the amount of active carbon species, which provides an efficient carbon feedstock for the growth.

### 3. MECHANISM OF GROWTH

Several growth models have been proposed for the CNTs prepared by the pyrolysis of hydrocarbons on metal surfaces. Baker and Harris [100] suggested a four-step mechanism. In the first step, the hydrocarbon decomposes on the metal surface to release hydrogen and carbon, which dissolves in the particle. The second step involves the diffusion of the carbon through the metal particle and its precipitation on the rear face to form the body of the filament. The supply of carbon onto the front face is faster than the diffusion through the bulk, causing an accumulation of carbon on the front face, which must be removed to prevent the physical blocking of the active surface. This is achieved by surface diffusion and the carbon forms a skin around the main filament body, in step three. In the fourth step, overcoating and deactivation of the catalyst and termination of tube growth takes place. Oberlin et al. [101] proposed a mechanism where bulk diffusion is insignificant and carbon is transported around the particle by surface diffusion. Dai et al. [37] proposed a mechanism wherein carbon forms a hemispherical graphene cap (yarmulke) on the catalyst particle and the nanotubes grow from the cap. The diameter of the nanotube is controlled by the size of the catalytic particle, nanometer size particles yielding SWNTs. A crucial feature of this model is that it avoids dangling bonds at all stages of growth. SWNTs produced by arc vaporization may also be formed by the yarmulke mechanism.

Endo and Kroto [102], based on the observation of  $C_2$  ejection from  $C_{60}$  in mass spectrometry, suggested that the processes of formation of MWNTs involved the formation of fullerenes. Smalley [103], however, pointed out that only the growth of outer layers of multi-walled tubes would be permitted by such a mechanism. Iijima et al. [6] presented electron microscopy evidence for the open-ended growth of CNTs and suggested that the termination of incomplete layers of carbon seen on the tube surface may arise because of the extension and thickening of the nanotubes by the growth of graphite islands on the surfaces of existing tubes. The nucleation of pentagons and heptagons on the open tube ends results in a change in the direction of the growing tube and some novel morphologies, including one where the tube turns around 180° during the growth, have been observed. The growth is self-similar and fractal-like with the inner tubules telescoping out of the larger ones, with logarithmic scaling of the size.

Isotope scrambling experiments of Ebbesen et al. [104] showed that under the conditions of fullerene formation, the plasma has vaporized carbon atoms. Based on tube morphologies, a mechanism similar to that of Saito et al. [105], wherein the

carbonaceous material reaching the cathode anneals into polyhedral particles, was suggested. Given the right conditions, the tip might open and continue to grow. Such a growth could occur inwards from outside. Ebbesen et al. suggested the possibility of tubes forming directly from the closing of a large graphene sheet. Such a suggestion gains credence from the simulations of Robertson et al. [106] who examined the curling and closure of small graphitic ribbons. These workers found that the formation of cylinders is favored by both entropy and enthalpy. It is possible that this could serve to nucleate the growth of multilayers by cladding as in the mechanism of Iijima et al.

Amelinckx et al. [107] employ the concept of a spatial velocity hodograph to describe the extrusion of a carbon tubule from a catalytic particle. The model is consistent with the observed tubule shapes and explains how spontaneous plastic deformation of a tubule can occur. These workers propose a model in which the graphene sheets can form both concentric cylinders and scroll-type structures. The nanotubes nucleate from a large fullerene-type dome. In the case of SWNTs, produced by the arc method, two types of catalytic growth are observed: (a) one, wherein a large number of nanotubes grow radially from a single catalyst particle which has a size much larger than the nanotube diameter and (b) another where the metal particles are of the same size or even smaller than the tube diameter and a single tube grows from a metal particle. SWNT growth by mode (b) can be explained by the yarmulke mechanism [37] mentioned earlier. Based on molecular dynamics and total energy calculations, Maiti et al. [108] proposed a model for mode (a) growth wherein nanometer-sized protrusions on the metal particle surface lead to the nucleation of SWNTs. The metal particle is capped by a graphene sheet and nanometer size protrusions on the metal surface leave holes in the graphene sheet. Carbon atoms are added to the graphene sheet in the form of handles between a pair of nearest neighbor carbon atoms. These handles migrate along the graphene sheet till they reach the edge of the initial hole, where they form seven-membered rings to give rise to a geometry curving upward. The seven-membered rings get confined at this high-curvature region due to energetics and the hexagons grow further to form the body of the tube.

TEM examination of the carbonaceous products obtained in the pyrolysis of hydrocarbons and organometallic precursors suggests that the size of the catalyst particle plays a role, with regard to the nature of the product formed. The role of the size of the catalyst particle on the nature of the carbon nanostructure formed is shown schematically in Fig. 11. This should not be taken as a rule since nanotubes of diameters larger than 50 nm do occur. If the catalytic metal nanoparticle is around 1 nm in diameter, SWNTs are the predominant product [41,58]. The report of Dai et al. [37] that SWNTs are formed on Mo nanoparticles in the size range of 1–4 nm indicates that there can be a slight range in the size. In the case of organometallic precursors, it seems that metal nanoclusters of ~1 nm diameter are produced under controlled conditions. When the organometallic concentration is high, MWNTs are formed around the catalyst particles with sizes in the range of 5–20 nm. This is true of CNTs obtained by the metallocene route [31,32]. In the higher size range of  $\geq 50$  nm, mainly graphite-covered metal particles are formed [41].

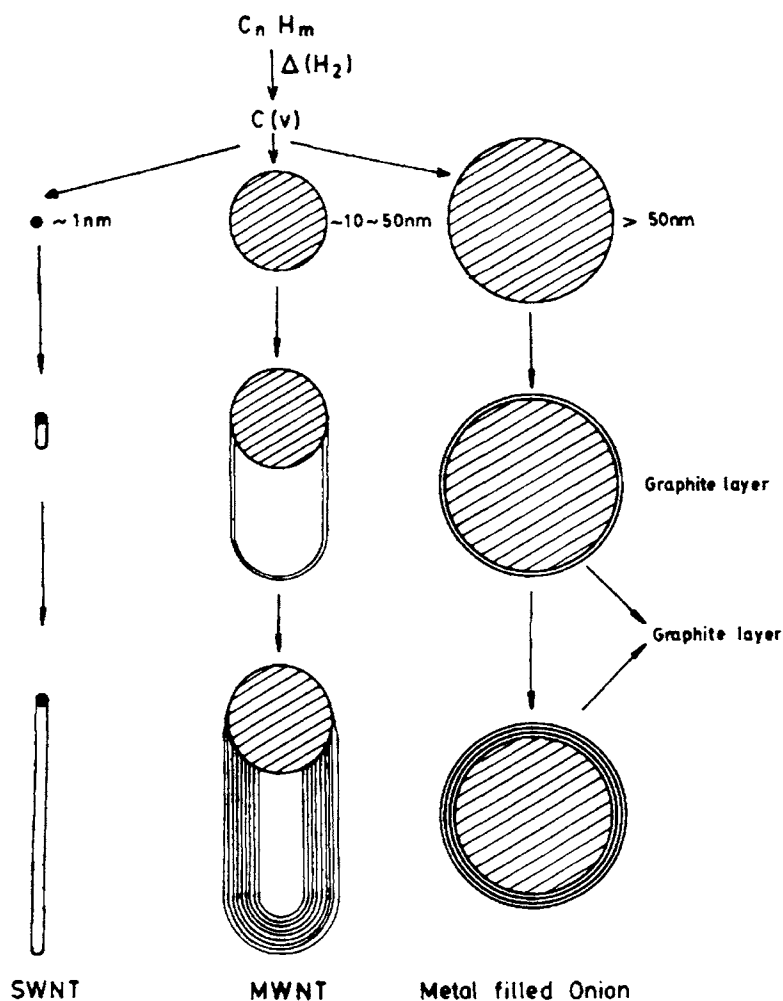


Figure 11. Schematic showing the dependence of the carbon nanostructure obtained by hydrocarbon pyrolysis on the size of the metal nanoparticles. (Reproduced from Rao et al. [41].)

Moisala et al. [109] has reviewed the progress in CVD and aerosol synthesis of SWNTs with an emphasis on the role of catalytic metal nanoparticles. They discuss the evolution of the catalyst particle size distribution due to collision, sintering, and evaporation of the metal during SWNT synthesis. The active catalyst has been demonstrated to be in a reduced metal form by comparison of the experimental data and calculations regarding the equilibrium concentration of carbon and oxygen in iron. The effect of the catalyst particle size on the melting temperature and

on carbon solubility in the metal is discussed. Furthermore, the maximum length of SWNTs of 1 and 2.5 nm diameter as a function of carbon solubility has been estimated to determine whether carbon dissolution and precipitation are simultaneous or subsequent process steps. The form of the precipitated carbon is dictated by the catalyst particle size, carbon feed rate, and reactor conditions. Also, the carbon precipitation rate affects the form of precipitated carbon in aerosol synthesis. In CVD, interactions between the catalyst particle and the support surface groups may be utilized in controlling the evolution of the particle size distribution. In aerosol synthesis, the velocity and temperature gradients in the flow reactor result in a distribution of particle sizes. The feed rate of carbon to the metal particles has to be controlled in order to selectively produce SWNTs and to avoid accumulation of amorphous carbon.

Ago et al. [110] studied by using TEM, the roles of metal-support interaction in growth of SWNTs and DWNTs with diameter-controlled iron particles supported on MgO. They found that the original iron particles became smaller during CVD and that these small particles gave SWNTs and DWNTs when reacted with methane. The decrease in the iron particle size was attributed to thermal diffusion of iron atoms into the MgO matrix, representing strong interaction between the iron particles and the MgO support. Reduction of the catalyst under a hydrogen flow at high temperature was found to suppress nanotube growth due to the increase in the particle size.

## **4. PURIFICATION AND SEPARATION OF CARBON NANOTUBES AND RELATED ASPECTS**

### **4.1. Purification and separation of carbon nanotubes**

As-synthesized CNTs contain carbonaceous impurities, typically amorphous carbon and graphitic nanoparticles, which may enclose the transition-metal catalyst in the case of SWNTs. A simple and successful strategy for the purification of arc-grown MWNTs is found to be high-temperature oxidation in air. Early attempts to apply such a method to the purification of SWNTs, however, failed. It has now become clear that the problem lies with the catalyst metal particles present in the material. In the presence of oxygen and other oxidizing gases, the metal particles catalyze the low-temperature oxidation of carbons indiscriminately, destroying the SWNTs. The first step before gas-phase oxidative purification is therefore the removal of the metal catalyst particles.

Most of the nanotube purification methods involve one or more of the following steps: gas- or vapor-phase oxidation, wet chemical oxidation/treatment, centrifugation, or filtration (including chromatographic methods). A combination of these steps is employed to achieve complete purification. Strong oxidation and acid refluxing have an effect on the structure of the tubes. Wet chemical purification methods (e.g., acid digestion of impurities) give rise to reaction products on the surface of a nanotube render it a natural surfactant. While the removal of the carbonaceous and catalyst impurities is a necessary in purification processes, it is not sufficient. The amorphous carbon is readily burnt away by heating the nanotubes in air around 300 °C. Hydrothermal treatment can be used to remove the amorphous carbon from the nanotube surface [111,112]. Bandow et al. [113] use microfiltration



to rid SWNTs of the other contaminants. Martinez et al. [114] use a combination of air oxidation and microwave acid digestion to purify arc-discharge SWNTs. High-temperature annealing of the purified samples is carried out in some procedures to remove the surface functional groups [115,116].

The need for the removal of metals was first pointed out by Chiang et al. [117,118]. Their method begins with long (18 h), low-temperature (225 °C) oxidative cracking of the carbonaceous shells encapsulating the metal particles. For this purpose, wet oxygen (20% O<sub>2</sub> in argon passed through a water-filled bubbler) was passed over the nanotubes in the hot zone of a flow-tube furnace. After this, the material was stirred in concentrated HCl to dissolve iron particles. After filtering the acid and drying, the oxidation and acid extraction cycle was repeated once more at 325 °C, followed by an oxidative bake at 425 °C. The 325 °C step may, however, be unnecessary.

Wiltshire et al. [119] reported comparative study on gas- and liquid-phase oxidative treatments of SWNTs, using a HiPCO produced raw material with a broad distribution of nanotube diameters. They found that the liquid-phase oxidation is a continuous diameter-selective process eliminating narrower SWNTs through oxidizing sidewalls of SWNTs. Gas-phase oxidation is a more discrete process requiring high activation energy for diameter-selective purification. Unlike liquid-phase oxidation, the gas-phase process preferentially oxidizes SWNTs without introducing sidewall defects.

Sen et al. [120] have examined the effect of oxidation conditions on the purity of the as-prepared SWNTs films prepared by the arc-discharge method. Purification was monitored by near-infrared spectroscopy. This technique also gives an estimate of the change in relative amounts of SWNTs and amorphous carbon impurities after each purification step, thereby providing control over the oxidation process. Oxidation was carried out by reaction in flowing oxygen at different temperatures and for different durations of time and the purity evaluated after each oxidation step. Optimization of the process allowed a three-fold improvement in purity with the quantitative retention of the SWNT portion of the sample. A purification efficiency is defined, which is expressed as the ratio of the fraction of SWNTs retained to the fraction of impurities retained in the sample after application of the purification process.

Vivekchand et al. [121] have developed a purification procedure involving high-temperature hydrogen heat-treatment of SWNTs or by etching the appropriate acid-treated CNTs with hydrogen at elevated temperatures [700–1000 °C]. The method has been effective in purifying both SWNTs and MWNTs. While acid washing dissolves the metal particles, the hydrogen treatment removes amorphous carbon as well as the carbon coating on the metal nanoparticles. Thus, it is possible to eliminate amorphous carbon and other carbonaceous materials in the SWNTs by this technique without the use of microfiltration, etc. It would be in order to compare this work with the other procedures reported in the literature. All the methods make use of acid washing to remove the metal particles present. In the procedures involving air oxidation, SWNTs are subjected to heat treatment in the 350–500 °C range depending on the method of synthesis. The method of Vivekchand et al., however,

employs hydrogen treatment around 1000 °C for most SWNTs and MWNTs, except for HiPCO SWNTs, which require a lower temperature. Whereas in air oxidation the amorphous carbon is converted into  $\text{CO}_2$ , it is converted to  $\text{CH}_4$  on hydrogen treatment. Electron microscope images corresponding to the hydrogen purification method are shown in Fig. 12. The TEM image in Fig. 12a shows the as-synthesized arc SWNTs bundles (13 nm dia.) containing amorphous carbon and metal nanoparticles. Most of the metal nanoparticles get dissolved on acid washing, but the nanotubes are covered with amorphous carbon as seen in the TEM image in Fig. 12b. The amorphous carbon is removed by high-temperature hydrogen treatment and the remaining small metal nanoparticles agglomerate into larger particles. The absence of amorphous carbon is revealed from the TEM image in Fig. 12c. TEM images also suggest that the bundles grow in size and have diameters in the range of 20–50 nm after the hydrogen treatment. The metal nanoparticles agglomerate in the 750–850 °C range (Fig. 12c) and are removed in the second acid treatment carried out for a

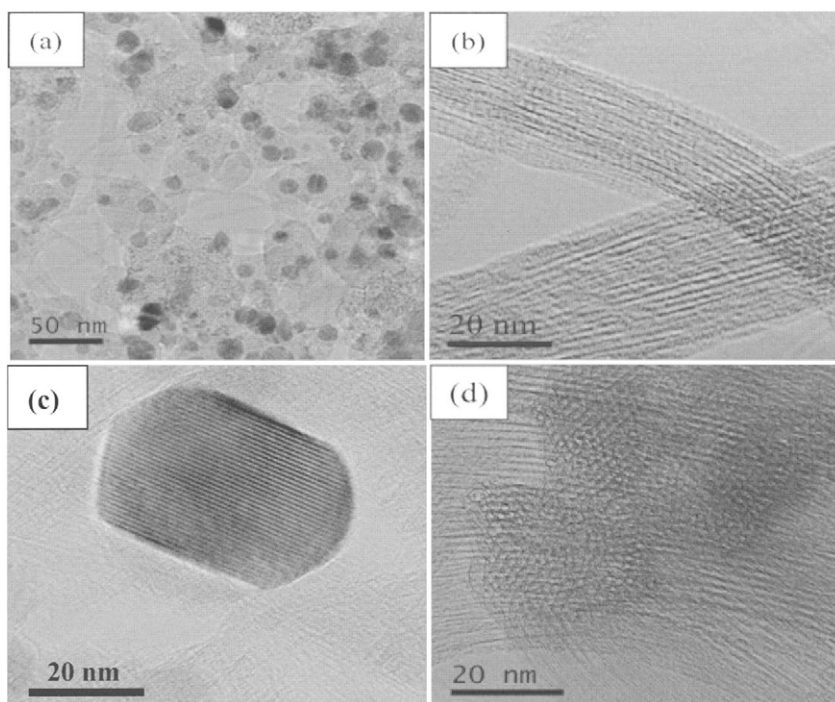


Figure 12. TEM images of (a) as-synthesized SWNTs obtained by the arc-discharge method, (b) after first acid treatment, (c) after first hydrogen treatment and before second acid treatment, and (d) after the second hydrogen treatment. (Reproduced from Vivekchand et al. [121].)

shorter duration. The second acid treatment is followed by the high-temperature hydrogen treatment at 1000 °C to obtain pure SWNTs. A TEM image of such purified SWNTs is shown in Fig. 12d. We do not see hollow onion-like structures often found in SWNTs purified by other methods.

CO<sub>2</sub> treatment at 800–1000 °C has been suggested for the removal of carbon covering over the metal nanoparticles by Gilbert [122]. Xu et al. [123] have outlined a controlled and scalable multi-step purification method to remove carbonaceous and metallic impurities from raw HiPco SWNTs. In this study, the carbon-coated iron nanoparticles were exposed and oxidized by multi-step oxidation at increasing temperatures; with the oxidized iron nanoparticles deactivated using either C<sub>2</sub>H<sub>2</sub>F<sub>4</sub> or SF<sub>6</sub>.

One of the problems in the purification of nanotubes is the evaluation of the purity of the final purified sample. Several techniques such as electron microscopy, thermogravimetric analysis (TGA), Raman spectroscopy, and visible-NIR spectroscopy have been employed for the determination for the purity of SWNTs. Itkis et al. [124] have pointed out the incapability of electron microscopy in the quantitative evaluation of purity of the bulk SWNTs. This is due to the small volume of the sample analyzed and the absence of algorithms to convert the images into numerical data. The use of solution-phase Raman spectroscopy and NIR spectroscopy for the quantitative evaluation of bulk purity has been strongly recommended by the authors. Clearly, any procedure or protocol for the purification of SWNTs should not only take into account the various steps referred to earlier, but also the methods of evaluation of purity as described by Itkis et al. Such an evaluation has been carried out on SWNTs treated with gases such as O<sub>2</sub>, CO<sub>2</sub>, and H<sub>2</sub> in addition to acid cleaning at different stages by Vivekchand et al. [125].

Vivekchand et al. [125] based on the comparative study established an effective purification protocol by improving the earlier procedure based on acid washing followed by air-oxidation at 300 °C, hydrogen treatment at 800 °C, and ending again by acid washing, which yielded only near-pure SWNTs containing a small amount of residues due to metal particles (~12%). Three procedures were examined for the purification of SWNTs synthesized by the arc-discharge process using the Ni–Y catalyst. In procedure A, the as-synthesized SWNTs were subjected to: 1, refluxing in 3 M HCl for 18 h, 2, CO<sub>2</sub> treatment at 800°C for 12 h followed by acid washing at room temperature, and 3, hydrogen treatment at 1200 °C for 5 h followed by acid washing. Procedure B involved the following steps: 1, refluxing in 3 M HCl for 18 h, 2, H<sub>2</sub> treatment at 800 °C for 12 h followed by acid washing, and 3, H<sub>2</sub> treatment at 1200 °C for 5 h followed by acid washing. Steps in procedure C were: 1, stirring in 3 M HCl for 18 h, 2, air oxidation at 300°C for 12 h, 3, CO<sub>2</sub> treatment at 800°C for 12 h followed by acid washing, and 4, H<sub>2</sub> treatment at 1200°C for 5 h followed by acid washing. At each step, the product was analyzed by TEM, TGA, Raman spectroscopy, and NIR spectroscopy. Based on the comparative study of the three procedures mentioned above, procedure B seems to provide an effective protocol for the purification SWNTs. While other purification protocols that may be equally effective, the simplicity of procedure B is noteworthy, specially because the H<sub>2</sub> treatment can be carried out at high temperatures unlike oxygen treatment.

A purification procedure for SWNTs prepared by the arc-discharge method employing a new step of potassium intercalation has been proposed [126]. The intercalation step is useful for exfoliating the graphitic shell structure that typically surrounds the metal catalyst particles that remain from the nanotube synthesis. By exfoliating the shell structure, subsequent treatments become more efficacious for removing the metal catalyst particles. With potassium intercalation, the number of purification steps can be reduced.

Fang et al. [127] used the electrochemical oxidation technique for the purification of SWNTs. They investigated the electrochemical cyclic voltammetric (CV) oxidation behavior of an arc-derived single-wall carbon nanotube (SWNT) sample in potassium hydroxide solution. Amorphous carbon in the as-grown SWNT sample was effectively removed by the CV oxidation, as confirmed by analyzing the  $sp^3/sp^2$  carbon ratio from C1s XPS spectra and HREM observations. The removal of the amorphous carbon led to the exposure of metal nanoparticles, hence facilitating the elimination of the metal impurities by subsequent HCl washing. The CV oxidation can be applied as an alternative oxidative treatment for the purification of SWNT samples. Redox peaks were observed during the CV oxidation. The redox peaks from the electrochemical redox reactions of Fe and Ni impurities can be considered as a benchmark for the removal extent of the amorphous carbon, and optimal electrochemical oxidation time for the purification of the as-grown SWNT sample can be determined in real time during the CV oxidation treatment.

Following the purification of the SWNTs to remove foreign materials such as catalyst, amorphous carbon, and carbon-coated nanoparticles, the sorting of the SWNTs according to their length becomes particularly important in light of their potential applications. Since SWNTs occur as large bundles with micron lengths, it is desirable to break them from the bundles, for purposes of further manipulations. Liu et al. [128] subjected SWNTs to ultrasound treatment in an acidic medium to break-up the bundles into open-ended small fragments of 100–300 nm length. The smaller fragments were functionalized. Various techniques have been employed for obtaining SWNTs sorted by length [129–133]. Chromatographic techniques are useful for the length fractionation of shortened SWNTs with sizes of less than 300 nm [129a,130,131,133]. For longer SWNTs, techniques such as capillary electrophoresis [130] and field-flow fractionation appear to be more applicable [132].

The stochastic nature of SWNT growth, generates mixtures of metallic and semiconducting SWNTs in a 1:2 ratio packed together in bundles and their separation is difficult [80]. There are several recent reports providing evidence for such separation. By exploring the complex physicochemical interactions of surfactant amines with carbon nanotubes, a purification approach for the bulk separation of the metallic SWNTs from the semiconducting SWNTs was achieved by using the enhanced chemical affinity of the semiconducting SWNTs to octadecylamine [ODA,  $\text{CH}_3(\text{CH}_2)_{17}\text{NH}_2$ ] [134]. Spectroscopic and thermogravimetric studies indicate that the amine interacts more strongly with the semiconducting than with the metallic SWNTs. This reduces the tendency of semiconducting SWNTs to aggregate as the concentration is increased. Based on these observations, as well as by utilizing resonance Raman spectroscopy, Samsonidze et al. [135] have developed

octadecylamine-assisted analytical method to provide quantitative evaluation of the separation efficiency between semiconducting and metallic SWNTs. The measured relative changes in the integrated intensities of the radial-breathing-mode region in the Raman spectrum provide a quantitative evaluation of the separation efficiency between semiconducting and metallic SWNTs along with diameter separation. They found that this separation technique provides an enrichment of semiconducting nanotubes by a factor of 5 for SWNTs prepared by high-pressure CO decomposition and higher enrichment of semiconducting SWNTs with diameters below 1 nm.

Metallic/semiconducting SWNT separation has been achieved by exposing an aqueous suspension of SWNTs in Triton X-100 surfactant to bromine solution, followed by centrifugation at 24 000 g for 12 h, led to enrichment of the supernatant in semiconducting nanotubes and the sediment in metallic nanotubes [136]. This separation relies on the important finding that *individual* nanotubes in aqueous surfactant suspension remain suspended during high-speed centrifugation, despite the fact that the specific gravities of the SWNTs are 20–40% greater than that of water [137]. As indicated by modeling, the micelles have a specific gravity that is lower than unity (ascribed to the exclusion of water from the region of the hydrophobic tails contacting the nanotubes), so that the combined object (SWNT plus micelle) acquires a specific gravity of close to 1.

Krupke et al. [138] have developed a method to separate metallic from semiconducting SWNTs from suspensions using ac dielectrophoresis. For the ac dielectrophoresis, the generator was operated at a frequency  $f$  of 10 MHz and a peak-to-peak voltage ( $V_{p-p}$ ) of 10 V range. The method takes advantage of the difference of the relative dielectric constants of the two species with respect to the solvent, resulting in an opposite movement of metallic and semiconducting tubes along the electric field gradient. Metallic tubes are attracted toward a microelectrode array, leaving semiconducting tubes in the solvent. Proof of the effectiveness of separation is given by a comparative Raman spectroscopy study on the dielectrophoretically deposited tubes and on a reference sample.

Strano et al. [139] have reported a selective reaction pathway of CNTs in which covalent chemical functionalization is controlled by differences in the nanotube electronic structure. They demonstrate the utility of these chemical pathways for manipulation of nanotubes of distinct electronic types by the selective functionalization of metallic nanotubes. They show that diazonium reagents functionalize single-walled carbon nanotubes suspended in aqueous solution with high selectivity and enable manipulation according to electronic structure. For example, the metallic nanotubes react to the exclusion of the semiconducting nanotubes under controlled conditions. Selectivity is dictated by the availability of electrons near the Fermi level to stabilize a charge-transfer transition state preceding bond formation. The chemistry is reversed by thermal treatment that restores the pristine electronic structure of the nanotubes.

Zheng et al. [140] report that single-stranded DNA (ssDNA) interacts strongly with CNTs to form a stable DNA–CNT hybrid that effectively disperses CNTs in aqueous solution. They also demonstrate that DNA-coated CNTs can be separated into fractions with different electronic structures by ion-exchange chromatography.

They have not discussed whether or not DNA wrapping on a CNT depends on the specific sequence of the DNA strand. Zheng et al. [141] have later shown that an oligonucleotide sequence that self-assembles into a highly ordered structure on CNTs, allowing not only markedly improved metal from semiconducting tube separation but also diameter-dependent separation. They found that anion-exchange chromatography provides a macroscopic means to assay for electrostatic properties of nanoscale DNA–CNT hybrids. More specifically, the outcome of anion-exchange-based DNA–CNT separation, as measured by optical absorption spectral changes from fraction to fraction, is dependent on the DNA sequence. A search of the ssDNA library selected a sequence  $d(GT)_n$ ,  $n = 10\text{--}45$  that self-assembles into a helical structure around individual nanotubes in such a manner that the electrostatics of the DNA–CNT hybrid depends on the tube diameter and the electronic properties, thereby enabling nanotube separation by anion-exchange chromatography. Optical absorption and Raman spectroscopy showed that early fractions are enriched in the smaller diameter and metallic tubes, whereas late fractions were enriched in the larger diameter and semiconducting tubes.

## REFERENCES

1. S. Iijima and T. Ichihashi, *Nature* **363** (1993) 603.
2. D. S. Bethune, C. H. Kiang, M. S. de Vries, G. Gorman, R. Savoy, J. Vazquez and R. Bayers, *Nature* **363** (1993) 605.
3. W. K. Hsu, J. P. Hare, M. Terrones, P. J. F. Harris, H. W. Kroto and D. R. M. Walton, *Nature* **377** (1995) 687.
4. M. Endo, K. Takeuchi, S. Igarashi, K. Kobori, M. Shiraishi and H. W. Kroto, *J. Phys. Chem. Solids* **54** (1993) 1841.
5. (a) P. M. Ajayan, T. Ichihashi and S. Iijima, *Chem. Phys. Lett.* **202** (1993) 384–388; (b) S. G. Louie, *Top. Appl. Phys.* **80** (2001) 113.
6. S. Iijima, P. M. Ajayan and T. Ichihashi, *Phys. Rev. Lett.* **69** (1992) 3100.
7. V. P. Dravid, X. Lin, Y. Wang, X. K. Wang, A. Yee, J. B. Ketterson and R. P. H. Chang, *Science* **259** (1993) 1601.
8. P. M. Ajayan, T. W. Ebbesen, T. Ichihashi, S. Iijima, K. Tanigaki and H. Hiura, *Nature* **362** (1993) 522.
9. S. C. Tsang, P. J. F. Harris and M. L. H. Green, *Nature*, **362** (1993) 520.
10. (a) T. W. Ebbesen and P. M. Ajayan, *Nature* **358** (1992) 220; (b) Y. Ando, X. Zhao, T. Sugai and M. Kumar, *Mater. Today* **7** (2004) 22; and the references therein.
11. N. Hatta and K. Murata, *Chem. Phys. Lett.* **217** (1994) 398.
12. D. T. Colbert, J. Zhang, S. M. McClure, P. Nikolaev, Z. Chen, J. H. Hafner, D. W. Owens, P. G. Kotula, C. B. Carter, J. H. Weaver and R. E. Smalley, *Science* **266** (1994) 1218.
13. S.-H. Jung, M.-R. Kim, S.-H. Jeong, S.-U. Kim, O.-J. Lee, K.-H. Lee, J.-H. Suh and C.-K. Park, *Appl. Phys. A-Mater. Sci. Process.* **76** (2003) 285.
14. N. Sano, *Chim. Oggi-Chem. Today* **22** (2004) 54.
15. K. Anazawa, K. Shimotani, C. Manabe, H. Watanabe and M. Shimizu, *Appl. Phys. Lett.* **81** (2002) 739.

16. S. J. Lee, H. K. Baik, J. Yoo and J. H. Han, *Diamond Relat. Mater.* **11** (2002) 914.
17. M. Ge and K. Sattler, *Science* **260** (1993) 515.
18. (a) W. K. Hsu, M. Terrones, J. P. Hare, H. Terrones, H. W. Kroto and D. R. M. Walton, *Chem. Phys. Lett.* **262** (1994) 161; (b) Y. Gogotsi, J. A. Libera and M. Yoshimura, *J. Mater. Res.* **15** (2000) 2591.
19. G. Hu, M. J. Cheng, D. Ma, X. H. Bao, *Chem. Mater.* **15** (2003) 1470.
20. M. Jose-Yacamán, M. Miki-Yoshida, L. Rendon and T. G. Santiesteban, *Appl. Phys. Lett.* **62** (1993) 202.
21. V. Ivanov, J. B. Nagy, Ph. Lambin, A. Lucas, X. B. Zhang, X. F. Zhang, D. Bernaerts, G. Van Tendeloo, S. Amelinckx and J. Van Landuyt, *Chem. Phys. Lett.* **223** (1994) 329.
22. K. Hernadi, A. Fonseca, J. B. Nagy, D. Bernaerts, J. Riga and A. Lucas, *Syn. Met.* **77** (1996) 31.
23. N. M. Rodriguez, *J. Mater. Res.* **8** (1993) 3233.
24. Z. F. Ren, Z. P. Huang, J. W. Xu, J. H. Wang, P. Bush, M. P. Siegel and P. N. Provencio, *Science* **282** (1998) 1105.
25. Z. F. Ren, Z. P. Huang, D. Z. Wang, J. G. Wen, J. W. Xu, J. H. Wang, L. E. Calvet, J. Chen, J. F. Klemic and M. A. Reed, *Appl. Phys. Lett.* **75** (1999) 1086.
26. S. B. Sinnott, R. Andrews, D. Qian, A. M. Rao, Z. Mao, E. C. Dickey and F. Derbyshire, *Chem. Phys. Lett.* **315** (1999) 25.
27. M. Yudasaka, R. Kikuchi, T. Matsui, Y. Ohki, S. Yoshimura and E. Ota, *Appl. Phys. Lett.* **67** (1995) 2477; M. Yudasaka, R. Kikuchi, Y. Ohki, E. Ota and S. Yoshimura, *Appl. Phys. Lett.* **70** (1997) 1817.
28. J.-B. Park, G.-S. Choi, Y.-S. Cho, S.-Y. Hong, D. Kim, S.-Y. Choi, J.-H. Lee and K.-I. Cho, *J. Cryst. Growth* **244** (2002) 211.
29. M. Chen, C. M. Chen and C. F. Chen, *J. Mater. Sci.* **37** (2002) 3561.
30. Z. P. Huang, D. Z. Wang, J. G. Wen, M. Sennett, H. Gibson and Z. F. Ren, *Appl. Phys. A: Mater. Sci. Process.* **74** (2002) 387.
31. (a) R. Sen, A. Govindaraj and C. N. R. Rao, *Chem. Phys. Lett.* **267** (1997) 276; (b) R. Sen, A. Govindaraj and C. N. R. Rao, *Chem. Mater.* **9** (1997) 2078.
32. C. N. R. Rao, A. Govindaraj, R. Sen and B. C. Satishkumar, *Mater. Res. Innov.* **2** (1998) 128.
33. C. J. Lee, S. C. Lyu, H.-W. Kim, C.-Y. Park and C.-W. Yang, *Chem. Phys. Lett.* **359** (2002) 109.
34. T. M. Keller and S. B. Qadri, *Chem. Mater.* **16** (2004) 1091.
35. S. R. C. Vivekchand, L. M. Cele, F. L. Deepak, A. R. Raju and A. Govindaraj, *Chem. Phys. Lett.* **386** (2003) 313.
36. C. Journet and P. Bernier, *Appl. Phys. A: Mater. Sci. Process.* **67** (1998) 1.
37. H. Dai, A. Z. Rinzler, P. Nikolaev, A. Thess, D. T. Colbert and R. E. Smalley, *Chem. Phys. Lett.* **260** (1996) 471.
38. Y. Saito, M. Okuda and T. Koyama, *Surf. Rev. Lett.* **3** (1996) 863.
39. Y. Saito, K. Kawabata and M. Okuda, *J. Phys. Chem.* **99** (1995) 16076.
40. C. Journet, W. K. Maser, P. Bernier, A. Loiseau, M. Lamy de la Chapelle, S. Lefrant, P. Deniard, R. Lee and J. E. Fischer, *Nature* **388** (1997) 756.

41. C. N. R. Rao, B. C. Satishkumar, A. Govindaraj and M. Nath, *ChemPhysChem* **2** (2001) 78.
42. M. Ohkohchi, X. L. Zhao, S. Inoue and Y. Ando, *Jpn. J. Appl. Phys. (Part 1)* **43** (2004) 8365.
43. S. Farhat, M. L. de La Chapelle, A. Loiseau, C. D. Scott, S. Lefrant, C. Journet and P. Bernier, *J. Chem. Phys.* **115** (2001) 6752.
44. I. Hinkov, S. Farhat, M. Lamy De La Chapelle, S. S. Fan, H. X. Han, G. H. Li and C. D. Scott, *Proceedings of the VI Appl. Diamond Conference/Sec. Frontier Carbon Technology Joint Conference*, Auburn, AL, August 6–10, 2001 and NASA Conference Publication (2001).
45. P. Costa, C. Xu, K. Coleman, J. Sloan and M. L. H. Green, *Trends in Nanotechnology Conference Proceedings (TNT2002)*, Santiago de Compostela, Spain, September 9–13, 2002.
46. M. E. Itkis, D. E. Perea, S. Niyogi, J. Love, J. Tang, A. Yu, C. Kang, R. Jung and R. C. Haddon, *J. Phys. Chem. B* **108** (2004) 12770.
47. H. J. Huang, J. Marie, H. Kajiura and M. Ata, *Nano Lett.* **2** (2002) 1117.
48. H. Takikawa, M. Ikeda, K. Hirahara, Y. Hibi, Y. Tao, P. A. Ruiz, T. Sakakibara, S. Itoh and S. Iijima, *Phys. B: Condens. Matter* **323** (2002) 277.
49. T. Guo, P. Nikolaev, A. Thess, D. T. Colbert and R. E. Smalley, *Chem. Phys. Lett.* **243** (1995) 49.
50. M. Yudasaka, R. Yamada, N. Sensui, T. Wilkins, T. Ichihashi and S. Iijima, *J. Phys. Chem. B* **103** (1999) 6224.
51. P. C. Eklund, B. K. Pradhan, U. J. Kim, Q. Xiong, J. E. Fischer, A. D. Friedman, B. C. Holloway, K. Jordan and M. W. Smith, *Nano Lett.* **2** (2002) 561.
52. (a) W. K. Maser, E. Munoz, A. M. Benito, M. T. Martinez, G. F. de la Fuente, Y. Maniette, E. Anglaret and J. L. Sauvajol, *Chem. Phys. Lett.* **292** (1998) 587; (b) A. P. Bolshakov, S. A. Uglov, A. V. Saveliev, V. I. Konov, A. A. Gorbunov, W. Pompe and A. Graff, *Diamond Relat. Mater.* **11** (2002) 927.
53. C. D. Scott, S. Arepalli, P. Nikolaev and R. E. Smalley, *Appl. Phys. A: Mater. Sci. Process.* **72** (2001) 573.
54. A. Thess, R. Lee, P. Nikolaev, H. Dai, P. Petit, J. Robert, C. Xu, Y. H. Lee, S. G. Kim, A. G. Rinzler, D. T. Colbert, G. E. Scuseria, D. Tomanek, J. E. Fischer and R. E. Smalley, *Science* **273** (1996) 483.
55. M. F. Zhang, M. Yudasaka and S. Iijima, *J. Phys. Chem. B* **108** (2004) 12757–12762.
56. S. Arepalli, *J. Nanosci. Nanotech.* **4** (2004) 318.
57. M. A. El Khakani and J. H. Yi, *Nanotechnology* **15** (Sp. Issue) (2004) S534–S539.
58. (a) B. C. Satishkumar, A. Govindaraj, R. Sen and C. N. R. Rao, *Chem. Phys. Lett.* **293** (1998) 47; (b) S. Seraphin and D. Zhou, *Appl. Phys. Lett.* **64** (1994) 2087.
59. H. M. Cheng, F. Li, G. Su, H. Y. Pan, L. L. He, X. Sun and M. S. Dresselhaus, *Appl. Phys. Lett.* **72** (1998) 3282.
60. J. F. Colomer, C. Stefan, S. Lefrant, G. van Tendeloo, I. Willems, Z. Konya, A. Fonseca, Ch. Laurent and J. B. Nagy, *Chem. Phys. Lett.* **317** (2000) 83.



61. (a) E. Flahaut, A. Govindaraj, A. Peigney, Ch. Laurent, A. Rousset and C. N. R. Rao, *Chem. Phys. Lett.* **300** (1999) 236; (b) N. R. Franklin and H. Dai, *Adv. Mater.* **12** (2000) 890.
62. Q. W. Li, H. Yan, J. Zhang and Z. F. Liu, *Carbon* **42** (2004) 829.
63. M. Paillet, V. Jourdain, P. Poncharal, J. L. Sauvajol, A. Zahab, J. C. Meyer, S. Roth, N. Cordente, C. Amiens and B. Chaudret, *J. Phys. Chem. B* **108** (2004) 17112.
64. L. X. Zheng, M. J. O'Connell, S. K. Doorn, X. Z. Liao, Y. H. Zhao, E. A. Akhadow, M. A. Hoffbauer, B. J. Roop, Q. X. Jia, R. C. Dye, D. E. Peterson, S. M. Huang, J. Liu and Y. T. Zhu, *Nat. Mater.* **3** (2004) 673.
65. L. Song, L. Ci, L. Lv, Z. P. Zhou, X. Q. Yan, D. F. Liu, H. J. Yuan, Y. Gao, J. X. Wang, L. F. Liu, X. W. Zhao, Z. X. Zhang, X. Y. Dou, W. Y. Zhou, G. Wang, C. Y. Wang and S. S. Xie, *Adv. Mater.* **16** (2004) 1529.
66. Y. L. Li, I. A. Kinloch, M. S. Shaffer, J. F. Geng, B. Johnson and A. H. Windle, *Chem. Phys. Lett.* **384** (2004) 98.
67. Y. L. Li, I. A. Kinloch, M. S. P. Shaffer, C. Singh, J. F. Geng, B. F. G. Johnson and A. H. Windle, *Chem. Mater.* **16** (2004) 5637.
68. X. Wang, W. B. Yue, M. S. He, M. H. Liu, J. Zhang and Z. F. Liu, *Chem. Mater.* **16** (2004) 799.
69. K. Mizuno, K. Hata, T. Saito, S. Ohshima, M. Yumura and S. Iijima, *J. Phys. Chem. B* **109** (2005) 2632.
70. M. J. Pender, L. A. Sowards, B. Maruyama, R. A. Vaia and M. O. Stone, *Chem. Mater.* **16** (2004) 2544.
71. H. D. Sun, Z. K. Tang, J. Chen and G. Li, *Appl. Phys. A* **69** (1999) 381.
72. M. Endo, T. Hayashi, Y. A. Kim, H. Muramatsu, M. Ezaka, P. C. P. Watts, K. Nishimura and T. Tsukada, *J. Nanosci. Nanotech.* **4** (2004) 132.
73. K. Hata, D. N. Futaba, K. Mizuno, T. Namai, M. Yumura and S. Iijima, *Science* **306** (2004) 1362.
74. T. Okazaki and H. Shinohara, *Chem. Phys. Lett.* **376** (2003) 606.
75. T. Kato, G. H. Jeong, T. Hirata, R. Hatakeyama, K. Tohji and K. Motomiya, *Chem. Phys. Lett.* **381** (2003) 422.
76. Y. M. Li, D. Mann, M. Rolandi, W. Kim, A. Ural, S. Hung, A. Javey, J. Cao, D. W. Wang, E. Yenilmez, Q. Wang, J. E. Gibbons, Y. Nishi and H. J. Dai, *Nano Lett.* **4** (2004) 317.
77. L. M. Peng, Z. J. Shi, Z. L. Zhang, L. Ouyang, Z. N. Gu, Z. Q. Xue and Q. D. Wu, *Ultramicroscopy* **98** (2004) 195.
78. (a) Y. Murakami, Y. Miyauchi, S. Chiashi and S. Maruyama, *Chem. Phys. Lett.* **374** (2003) 53; (b) S. Maruyama, S. Chiashi and Y. Miyauchi, 6th ASME/JSME Thermal Eng. Jt. Conf. (2003) A1-222.
79. R. Alexandrescu, A. Crunteanu, R. E. Morjan, I. Morjan, F. Rohmund, L. K. L. Falk, G. Ledoux and F. Huisken, *Infrared Phys. Technol.* **44** (2003) 43.
80. P. Nikolaev, M. Bronikowski, R. K. Bradley, F. Rohmund, D. T. Colbert, K. A. Smith and R. E. Smalley, *Chem. Phys. Lett.* **313** (1999) 91.
81. B. Kitiyanan, W. E. Alvarez, J. H. Harwell and D. E. Resasco, *Chem. Phys. Lett.* **317** (2000) 497.

82. R. E. Smalley and B. I. Yakobson, *Solid State Commun.* **107** (1998) 597.
83. M. J. Bronikowski, P. A. Willis, D. T. Colbert, K. A. Smith and R. E. Smalley, *J. Vac. Sci. Technol. A* **19** (2001) 1800.
84. P. Nikolaev, *J. Nanosci. Nanotech.* **4** (2004) 307.
85. R. L. V. Wal, L. J. Hall and G. M. Berger, *J. Phys. Chem. B* **106** (2002) 13122.
86. R. L. V. Wal, G. M. Berger and L. J. Hall, *J. Phys. Chem. B* **106** (2002) 3564.
87. D. Laplaze, P. Bernier, W. F. Maser, G. Flamant, T. Guillard and A. Loiseau, *Carbon* **36** (1998) 685.
88. B. W. Smith, M. Monthieux and D. E. Luzzi, *Nature* **396** (1998) 323.
89. (a) S. Bandow, K. Hirahara, T. Hiraoka, G. Chen, P. C. Eklund and S. Iijima, *MRS Bulletin*, April 2004, p. 260; and the references therein; (b) K. Suenaga, T. Okazaki, C. -R. Wang, S. Bandow, H. Shinohara and S. Iijima, *Phys. Rev. Lett.* **90** (2003) 055506.
90. (a) S. Okada, S. Saito and A. Oshiyama, *Phys. Rev. Lett.* **86** (2001) 3835; (b) S. Berber, Y. -K. Kwon and D. Tomanek, *Phys. Rev. Lett.* **88** (2002) 185502.
91. Y. Ohno, Y. Kurokawa, S. Kishimoto, T. Mizutani, T. Shimada, M. Ishida, T. Okazaki, H. Shinohara, Y. Murakami, S. Maruyama, A. Sakai and K. Hiraga, *Appl. Phys. Lett.* **86** (2005) 023109.
92. S. B. Chikkannanavar and D. E. Luzzi, *Nano Lett.* **5** (2005) 151.
93. F. Simon, H. Kuzmany, H. Rauf, T. Pichler, J. Bernardi, H. Peterlik, L. Korecz, F. Fulop and A. Janossy, *Chem. Phys. Lett.* **383** (2004) 362.
94. J. L. Hutchison, N. A. Kiselev, E. P. Krinichnaya, A. V. Krestinin, R. O. Loutfy, A. P. Morawsky, V. E. Muradyan, E. D. Obraztsova, J. Sloan, S. V. Terekhov and D. N. Zakharov, *Carbon* **39** (2001) 761.
95. L. X. Li, F. Li, C. Liu and H. M. Cheng, *Carbon* **43** (2005) 623.
96. T. Sugai, H. Yoshida, T. Shimada, T. Okazaki and H. Shinohara, *Nano Lett.* **3** (2003) 769.
97. M. Abe, H. Kataura, H. Kira, T. Kodama, S. Suzuki, Y. Achiba, K. Kato, M. Takata, A. Fujiwara, K. Matsuda and Y. Maniwa, *Phys. Rev. B* **68** (2003) 041405.
98. (a) S. C. Lyu, B. C. Liu, S. H. Lee, C. Y. Park, H. K. Kang, C.-W. Yang and C. J. Lee, *J. Phys. Chem. B* **108** (2004) 2192; (b) C.-J. Lee. (S. Korea), *PCT Int. Appl.* (2004) 19pp. (Patent No.: WO 2004083113); (c) S. H. Lee, S. I. Jung, C. B. Kong, T. J. Lee, S. K. Choi, M. H. Park, C. W. Yang, C. Y. Park and C. J. Lee, *Int. Conf. Sci. Appl. Nanotubes (Mexico)* (2004) 115; (d) E. Flahaut, R. Bacsá, A. Peigney and Ch. Laurent, *Chem. Commun.* **12** (2003) 1442.
99. (a) P. Ramesh, T. Okazaki, R. Taniguchi, J. Kimura, T. Sugai, K. Sato, Y. Ozeki and H. Shinohara, *J. Phys. Chem. B* **109** (2005) 1141; (b) M. Endo, H. Muramatsu, T. Hayashi, Y. A. Kim, M. Terrones and M. S. Dresselhaus, *Nature* **433** (2005) 476.
100. R. T. K. Baker and P. S. Harris, *Chemistry and Physics of Carbon*, Vol. 14, Eds. P. L. Walker and P. A. Thrower, Marcel Dekker, New York, 1978.
101. A. Oberlin, M. Endo and T. Koyama, *J. Cryst. Growth* **32** (1976) 335.
102. M. Endo and H. W. Kroto, *J. Phys. Chem.* **96** (1992) 6941.
103. R. E. Smalley, *Mat. Sci. Engg. B.* **19** (1993) 1.

104. T. W. Ebbesen, J. Tabuchi and K. Tanigaki, *Chem. Phys. Lett.* **191** (1992) 336.
105. Y. Saito, T. Yoshikawa, M. Inagaki, M. Tomita and T. Hayashi, *Chem. Phys. Lett.* **204** (1994) 277.
106. D. H. Robertson, D. W. Brenner and C. T. White, *J. Phys. Chem.* **96** (1992) 6133.
107. (a) S. Amelinckx, X. B. Zhang, D. Bernaerts, X. F. Zhang, V. Ivanov and J. B. Negy, *Science* **265** (1994) 635; (b) S. Amelinckx, D. Bernaerts, X. B. Zhang, G. Van Tendeloo and J. Van Landuyt, *Science* **267** (1995) 1334.
108. A. Maiti, C. T. Brabec and J. Bernholc, *Phys. Rev. B* **55** (1997) R6097.
109. A. Moisala, A. G. Nasibulin and E. I. Kaeuppinen, *J. Phys.: Condens. Matter* **15** (2003) S3011.
110. H. Ago, K. Nakamura, N. Uehara and M. Tsuji, *J. Phys. Chem. B* **108** (2004) 18908.
111. K. Tohji, T. Goto, H. Takahashi, Y. Shinoda, N. Shimizu, B. Jeyadevan, I. Matsuoka, Y. Saito, A. Kasuya, T. Ohsuna, K. Hiraga and Y. Nishina, *Nature* **383** (1996) 679.
112. K. Tohji, T. Goto, H. Takahashi, Y. Shinoda, N. Shimizu, B. Jeyadevan, I. Matsuoka, Y. Saito, A. Kasuya, S. Ito and Y. Nishina, *J. Phys. Chem.* **B101** (1997) 1974.
113. S. Bandow, A. M. Rao, K. A. Williams, A. Thess, R. E. Smalley and P. C. Eklund, *Phys. Chem. B* **101** (1997) 8839.
114. M. T. Martinez, M. A. Callejas, A. M. Benito, W. K. Maser, M. Cochet, J. M. Andres, J. Schreiber, O. Chauvet and J. L. G. Fierro, *Chem. Commun.* **9** (2002) 1000.
115. A. G. Rinzier, J. Liu, P. Nikolaev, C. B. Huffman, M. Rodrigues, P. J. Boul, A. H. Lu, D. Heymann, D. T. Colbert, R. S. Lee, J. E. Fischer, A. M. Rao, P. C. Eklund and R. E. Smalley, *Appl. Phys. A* **67** (1998) 29.
116. A. C. Dillon, T. Gennett, K. M. Jones, J. L. Alleman, P. A. Parilla and M. J. Heben, *Adv. Mater.* **11** (1999) 1354.
117. I. W. Chiang, B. E. Brinson, R. E. Smalley, J. L. Margrave and R. H. Hauge, *J. Phys. Chem. B* **105** (2001) 1157.
118. I. W. Chiang, B. E. Brinson, A. Y. Huang, P. A. Willis, M. J. Bronikowski, J. L. Margrave, R. E. Smalley and R. H. Hauge, *J. Phys. Chem. B* **105** (2001) 8297.
119. J. G. Wiltshire, A. N. Khlobystov, L. J. Li, S. G. Lyapin, G. A. D. Briggs and R. J. Nicholas, *Chem. Phys. Lett.* **386** (2004) 239.
120. R. Sen, S. M. Rickard, M. E. Itkis and R. C. Haddon, *Chem. Mater.* **15** (2003) 4273.
121. S. R. C. Vivekchand, A. Govindaraj, Md. Motin Seikh and C. N. R. Rao, *J. Phys. Chem. B* **108** (2004) 6935.
122. K. E. H. Gilbert, Removal of graphite encapsulated metal particles for the purification of SWNT materials, Purification, Separation and Characterization of Single-walled Carbon Nanotubes (SWNT's), 227th ACS National Meeting, Anaheim, CA, USA, March 28–April 1, 2004. Abstract can be found under <http://membership.acs.org/IEC/docs/Anaheim04-IEC-Separates.pdf>.
123. Y.-Q. Xu, H. Peng, R. H. Hauge and R. E. Smalley, *Nano. Lett.* **5** (2005) 163.

124. M. E. Itkis, D. E. Perea, R. Jung, S. Niyogi and R. C. Haddon, *J. Am. Chem. Soc.* **127** (2005) 3439.
125. S. R. C. Vivekchand, R. Jayakanth, A. Govindaraj and C.N.R. Rao, *Small* **1** (2005) 920.
126. A. Dailly, J. W. L. Yim, C. C. Ahn, E. Miura, R. Yazami and B. Fultz, *Appl. Phys. A (Mater. Sci. Processing)* **80** (2005) 717.
127. H. T. Fang, C. G. Liu, L. Chang, L. Feng, L. Min and H. M. Cheng, *Chem. Mater.* **16** (2004) 5744.
128. J. Liu, A. G. Rinzler, H. Dai, J. H. Hafner, R. K. Bradley, P. J. Boul, A. Lu, T. Iverson, K. Shelimov, C. B. Huffman, F. Rodriguez-Macias, Y. S. Shon, T. R. Lee, D. T. Colbert and R. E. Smalley, *Science* **280** (1998) 1253.
129. (a) G. S. Duesberg, J. Muster, V. Krstic, M. Burghard and S. Roth, *Appl. Phys. A* **67** (1998) 117; (b) G. S. Duesberg, W. Blau, H. J. Byrne, J. Muster, M. Burghard and S. Roth, *Synthetic Metals* **103** (1999) 2484.
130. S. K. Doorn, I. R. F. Fields, H. Hu, M. Hamon, R. C. Haddon, J. P. Selegue and V. Majidi, *J. Am. Chem. Soc.* **124** (2002) 3169.
131. D. Chattopadhyay, S. Lastella, S. Kim and F. Papadimitrakopoulos, *J. Am. Chem. Soc.* **124** (2002) 728.
132. B. Chen and J. P. Selegue, *Anal. Chem.* **74** (2002) 4774.
133. E. Farkas, M. Elizabeth Anderson, Z. Chen and A. G. Rinzler, *Chem. Phys. Lett.* **363** (2002) 111.
134. D. Chattopadhyay, I. Galeska and F. Papadimitrakopoulos, *J. Am. Chem. Soc.* **125** (2003) 3370.
135. Ge. G. Samsonidze, S. G. Chou, A. P. Santos, V. W. Brar, G. Dresselhaus, M. S. Dresselhaus, A. Selbst, A. K. Swan, M. S. Ünlü, B. B. Goldberg, D. Chattopadhyay, S. N. Kim and F. Papadimitrakopoulos, *Appl. Phys. Lett.* **85** (2004) 1006.
136. Z. Chen, X. Du, M.-H. Du, C. D. Rancken, H.-P. Cheng and A. G. Rinzler, *Nano Lett.* **3** (2003) 1245.
137. M. J. O'Connell, S. M. Bachilo, C. B. Huffman, V. C. Moore, M. S. Strano, E. H. Haroz, K. L. Rialon, P. J. Boul, W. H. Noon, C. Kittrell, J. Ma, R. H. Hauge, B. R. Weisman and R. E. Smalley, *Science* **297** (2002) 593.
138. R. Krupke, F. Hennrich, H. v. Löhneysen and M. M. Kappes, *Science* **301** (2003) 344.
139. M. S. Strano, C. A. Dyke, M. L. Usrey, P. W. Barone, M. J. Allen, H. Shan, C. Kittrell, R. H. Hauge, J. M. Tour and R. E. Smalley, *Science* **301** (2003) 1519.
140. M. Zheng, A. Jagota, E. D. Semke, B. A. Diner, R. S. McLean, S. R. Lustig, R. E. Richardson and N. G. Tassi, *Nat. Mater.* **2** (2003) 338.
141. M. Zheng, A. Jagota, M. S. Strano, A. P. Santos, P. Barone, S. G. Chou, B. A. Diner, M. S. Dresselhaus, R. S. Mclean, G. B. Onoa, G. G. Samsonidze, E. D. Semke, M. Usrey and D. J. Walls, *Science* **302** (2003) 1545.

## **Chapter 3**

### **Solid-state formation of carbon nanotubes**

Y. Chen

Department of Electronic Materials Engineering, Research School of Physical Sciences and Engineering, The Australian National University, Canberra, ACT 0200, Australia

This chapter reviews the research on synthesis of carbon nanotubes (CNTs) using a ball milling–annealing method, in which graphite powder is first treated using high-energy ball milling (HEBM) at room temperature to create a precursor structure, followed by a thermal annealing to activate nanotube growth. This chapter includes an introduction of the ball milling–annealing method, a comparison between the HEBM and traditional ball-milling techniques, a detailed description of the morphologic and structural changes of the graphite induced by HEBM, a presentation of the growth of various nanotubular structures during the annealing process, and a discussion of special solid-state formation mechanisms involved. The chapter aims to demonstrate a mass production method for CNTs and new solid-state formation mechanisms.

#### **1. INTRODUCTION OF A BALL MILLING–ANNEALING METHOD**

Carbon nanotubular materials have many new properties which the bulk materials do not have [1], as well as a large range of applications in almost all areas of our life [2,3]. Therefore, there is a strong demand for the CNTs with a high yield and also large quantities. Many synthesis methods have been developed during the last decade, including arc-discharge, laser ablation, chemical vapor deposition (CVD), ball milling–annealing, etc. [1]. The ball milling–annealing process, consisting of a pre-ball milling process and a subsequent thermal annealing process, was first discovered in 1999 [4,5], and is very different from the above vapor phase methods because there is no carbon vapor phase involved. Both single-walled nanotubes (SWNTs)[4] and multi-walled nanotubes (MWNTs) [5,6] have been produced using the ball milling–annealing method. One advantage of the method is the large production quantity because the milling capability can be readily increased up to the order of kilograms. Low production costs are also expected. The key to the successful mass production of nanotubes is a deep understanding of the formation mechanism involved. Fortunately, both the milling and the heating processes are fully controllable and at relatively low temperature ranges (less than 1400 °C) [4,5,7], which provide an excellent opportunity to investigate the nanotube formation process in terms of nucleation and growth. In addition, unlike other synthesis methods, the ball milling–annealing method has a solid-state formation process without the involvement of any vapor phase, and this has significant interest in understanding fundamental formation mechanisms.

The ball milling–annealing method can produce other nanotubes such as boron nitride (BN) nanotubes [8]. It actually becomes a successful method for large production of high-yield BN nanotubes [9]. Both nanotube size and structures (cylindrical and bamboo-type) can be controlled [10]. Commercial BN nanotubes have been produced using this method.

The ball milling–annealing method has also been used by many research groups in synthesis of different nanotubes. Tang et al. [11] obtained BN nanotubes and horns from a mixture of B and  $\text{Ga}_2\text{O}_3$  after first ball milling for 6 h and subsequent annealing up to 1550 °C in  $\text{NH}_3$  gas. Bae et al. [12] have produced BN nanotubes by first ball milling of B powder, followed by annealing in  $\text{NH}_3$  gas in the temperature range of 1000–1200 °C. Li et al. have [13] produced  $\text{TiTe}_2$  nanotubes by annealing the ball-milled mixture of Ti and Te powders, and they claim that the ball-milling treatment is essential for the nanotube formation. Multi-walled and open-ended  $\text{TiSe}_2$  nanotubes are also synthesized by using the ball milling–annealing method [14].

A large number of one-dimensional structures have also been produced using the same method. Urbietta et al. [15] found micro- and nanosized needles in the heated CdSe at 800–900 °C following a pre-ball milling treatment. SiC nanorods are obtained from the ball-milled mixtures of Si and amorphous C after annealing at 1200 °C in Ar gas [16]. Lee et al. [17] reported that  $\text{Ga}_2\text{O}_3$  nanobelts have been produced by ball milling and annealing of GaN powders in an oxygen atmosphere. Xiao et al. [18] demonstrated that  $\text{GaO}_2\text{H}$  nanorods are formed in the ball-milled GaN powders after a heat treatment. Yin et al. [19] first ball milled graphite in  $\text{NH}_3$  up to 120 h, in which a nitriding reaction between graphite and  $\text{NH}_3$  gas occurred with the formation of amorphous CN phase, and then annealed the milled in the range of 300–450 °C under a flow of  $\text{NH}_3$  gas to produce single-crystalline  $\beta$ -CN nanorods.

In addition to nanomaterial synthesis, ball-milling technique has been used widely for the processing of CNTs. Ball milling can be used as “scissors” to cut long nanotubes into short pieces or to open-capped nanotubes by “cutting” their tips off, as demonstrated by many researchers [20–24]. Opening of close-ended nanotubes allows a high absorption of hydrogen gas into the tubes [25–27], or increased intercalation of Li ions into nanotubes thereby resulting in an improved Li ion density in batteries [28,29]. Nanotubes shortened by ball milling are also reported to have better field-emission properties [30], an improved intimate mixing during composite formation, as well as enhanced dispersion and purification performances [31], because ball milling treatment not only cuts the nanotube length but also modifies its structures and creates more access windows and active sites [32].

Ball milling technique has been used successfully in assisting nanotube functionalizations. For example, ball milling of MWNTs in acid solutions [33] or in some specific atmospheres containing functional groups like thiol, amine, etc. can attach them onto fractured nanotubes [20]. Ball milling of SWNTs with agents such as trifluoromethane and trichloroethylene can effectively form radicals on the nanotube surfaces [34].

Many nanotube composite materials have been produced with the help of ball milling technique for mixing nanotubes into various matrix materials, including polyester–nanotube composites [35], nanotube–WC–Co composites [36], Mg–nanotube composites [24], alloy–nanotube composites with improved electrochemical properties [37].

The above research demonstrates that the ball milling technique, which is generally regarded as a traditional technique, with a history of at least several centuries, has become an important tool with many important applications in nanotube research. One reason is that most of the above research work uses actually a new ball milling technique: high-energy ball milling (HEBM), which is very different from the traditional ball milling techniques. The major differences between them will be discussed in detail in the next section.

## 2. HIGH-ENERGY BALL MILLING

Conventional ball milling is a traditional powder-processing technique, which is mainly used for reducing particle sizes and for the mixing of different materials. The technique is widely used in mineral, pharmaceutical, and ceramic industries, as well as scientific laboratories. The HEBM technique discussed in this chapter is a new technique developed initially for producing new metastable materials, which cannot be produced using thermal equilibrium processes, and thus is very different from conventional ball milling technique. HEBM was first reported by Benjamin [38] in the 1960s. So far, a large range of new materials has been synthesized using HEBM. For example, oxide-dispersion-strengthened alloys are synthesized using a powerful high-energy ball mill (attritor) because conventional ball mills could not provide sufficient grinding energy [38]. Intensive research in the synthesis of new metastable materials by HEBM was stimulated by the pioneering work in the amorphization of the Ni-Nb alloys conducted by Kock et al. in 1983 [39]. Since then, a wide spectrum of metastable materials has been produced, including nanocrystalline [40], nanocomposite [41], nanoporous phases [42], supersaturated solid solutions [43], and amorphous alloys [44]. These new phase transformations induced by HEBM are generally referred as mechanical alloying (MA). At the same time, it was found that at room temperature, HEBM can activate chemical reactions which are normally only possible at high temperatures [45]. This is called reactive milling or mechano-chemistry. Reactive ball milling has produced a large range of nanosized oxides [46], nitrides [47], hydrides [48], and carbide [49] particles.

The major differences between conventional ball milling and the HEBM are listed in the Table 1. The impact energy of HEBM is typically 1000 times higher than the conventional ball milling energy. The dominant events in the conventional ball milling are particle fracturing and size reductions, which correspond to, actually, only the first stage of the HEBM. A longer milling time is therefore generally required for HEBM. In addition to milling energy, the controls of milling atmosphere and temperature are crucial in order to create the desired structural changes or chemical reactions. This table shows that HEBM can cover most work normally performed by conventional ball milling, however, conventional ball milling equipment cannot be used to conduct any HEBM work.

Different types of high-energy ball mills have been developed, including the Spex vibrating mill, planetary ball mill, high-energy rotating mill, and attritors [50]. In the nanotube synthesis, two types of HEBM mills have been used: a vibrating ball mill and a rotating ball mill. The vibrating-frame grinder (Pulverisette O, Fritsch) is shown in Fig. 1a. This mill uses only one large ball (diameter of 50 mm) and the

Table 1  
Comparison between conventional ball milling and high-energy ball milling.

	Conventional ball milling	High-energy ball milling
Milling time	< 1 h	20–200 h
Milling mode	Rolling	Impact
Milling events	Fracturing	Fracturing, plastic deformation, welding
Impact energy (Wg <sup>-1</sup> ball <sup>-1</sup> )	0.001	0.2
Particle/cluster size range	μm	Sub-μm
Changes of crystalline structures	No	Yes
Chemical reactions	No	Yes
Milling atmosphere	Air	Vacuum, gases
Milling temperature	Ambient temperature	Liquid nitrogen –700 °C

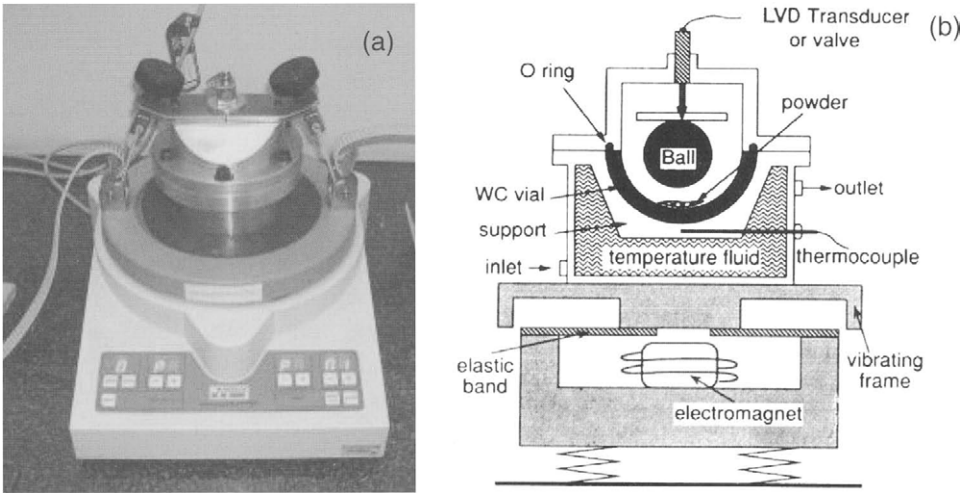


Figure 1. (a) Photo of a high-energy vibrating ball mill (Fritsch Pulverisette O). (b) A schematic representation of the high-energy vibrating ball mill [52].



media of the ball and vial can be stainless steel or ceramic tungsten carbide (WC). The milling chamber, as illustrated in Fig. 1b, is sealed with an O-ring so that the atmosphere can be changed via a valve. The pressure is monitored with an attached gauge during milling.

The milling energy and frequency can be adjusted by varying the vibrating amplitude and the ball mass [51,52]. By measuring the ball's movement, a milling intensity is defined as

$$I = M_b V_{\max} f / M_p,$$

where  $M_b$  is the mass of the milling ball,  $V_{\max}$  the maximum velocity of the vial,  $f$  the impact frequency, and  $M_p$  the mass of powder. The milling intensity is a very important parameter to MA and reactive ball milling. For example, a full amorphization of a crystalline NiZr alloy can only be achieved with a milling intensity above an intensity threshold of  $510 \text{ ms}^{-2}$  [52]. The amorphization process during ball milling can be seen from the images of transmission electron microscopy (TEM) in Fig. 2a, which were taken from samples milled for different lengths of time. The TEM images show that the size and number of NiZr crystals decrease with increasing milling time, and a full amorphization is achieved after milling for 165 h. The corresponding diffraction patterns in Fig. 2b confirm this gradual amorphization process. However, when milling below the intensity threshold, a mixture of nanocrystalline and amorphous phases is produced. This intensity threshold depends on milling temperature and alloy composition [52].

Fig. 3 shows a rotating steel mill and a schematic representation of milling action inside the milling chamber. The mill has a rotating horizontal cell loaded with several hardened steel balls. As the cell rotates, the balls drop onto the powder that is being ground. An external magnet is placed close to the cell to increase milling energy [53]. Different milling actions and intensities can be realized by adjusting the cell rotation rate and magnet position.

The atmosphere inside the chamber can be controlled, and adequate gas has to be selected for different milling experiments. For example, during the ball milling of pure Zr powder in the atmosphere of ammonia ( $\text{NH}_3$ ), a series of chemical reactions occur between Zr and  $\text{NH}_3$  [54,55]. The X-ray diffraction (XRD) patterns in Fig. 4 show the following reaction sequence as a function of milling time:

Stage 1: from beginning,	$\text{NH}_3 \rightarrow \text{N} + 3\text{H}_2$ ,	Decomposition of $\text{NH}_3$ ,
Stage 2: from 12 to 66 h,	$\text{Zr} + 2\text{H}_2 \rightarrow \text{ZrH}_2$ ,	Hydriding reaction,
Stage 3: from 46 to 288 h,	$\text{ZrH}_2 + \text{N} \rightarrow \text{ZrN} + \text{H}_2$ ,	Nitriding reaction.

Different reactions take place at the different stages of milling, with the formation of different products. The final end products are nanosized ZrN particles (diameter less than 20 nm) [54].

The mechanism of a HEBM process is quite complicated. During the HEBM, material particles are repeatedly flattened, fractured, and welded. Every time two steel

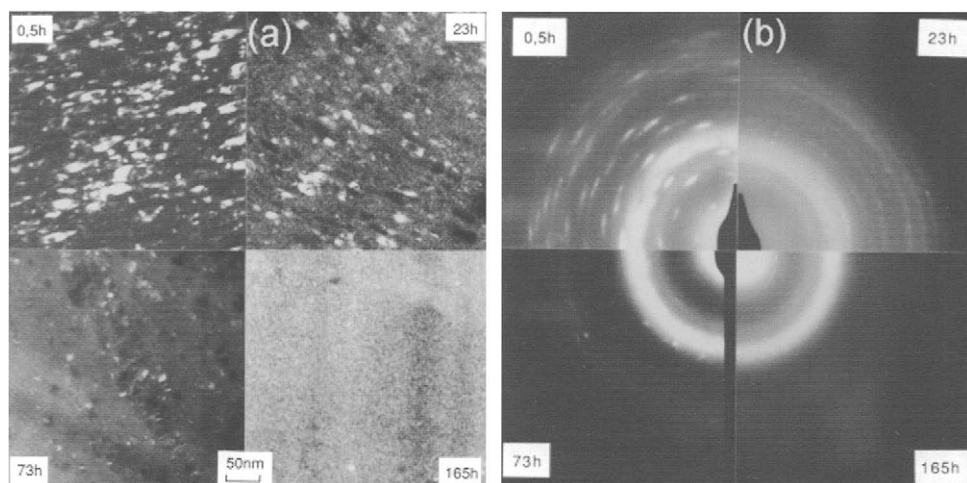


Figure 2. (a) Dark-field TEM image of  $\text{Ni}_{10}\text{Zr}_7$  alloy milled for 0.5, 23, 73, and 165 h in the vibrating ball mill with a milling intensity of  $940 \text{ ms}^{-2}$ . (b) Corresponding electron diffraction patterns [52].

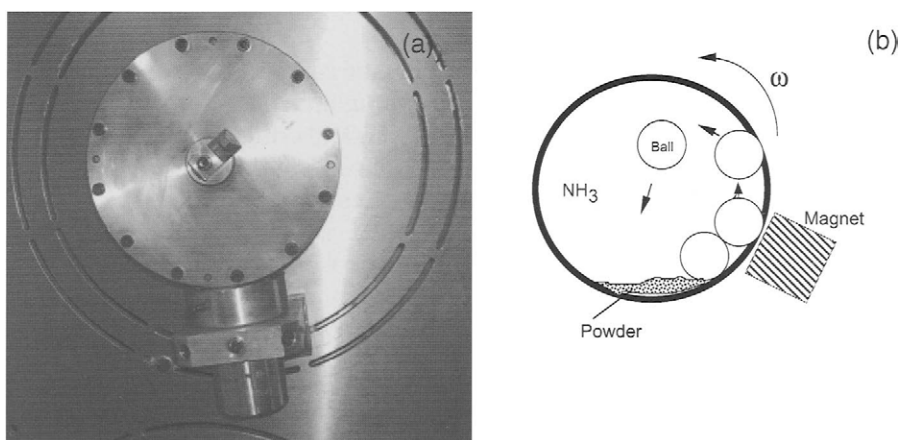


Figure 3. (a) Photo of a high-energy rotating steel ball mill. (b) Schematic representation of the rotating ball milling showing impact milling actions.

balls collide or one ball hits the chamber wall, they trap some particles between their surfaces. Such high-energy impacts severely deform the particles and create atomically fresh, new surfaces, as well as a high density of dislocations and other structural defects [44]. A high defect density induced by HEBM can accelerate the diffusion

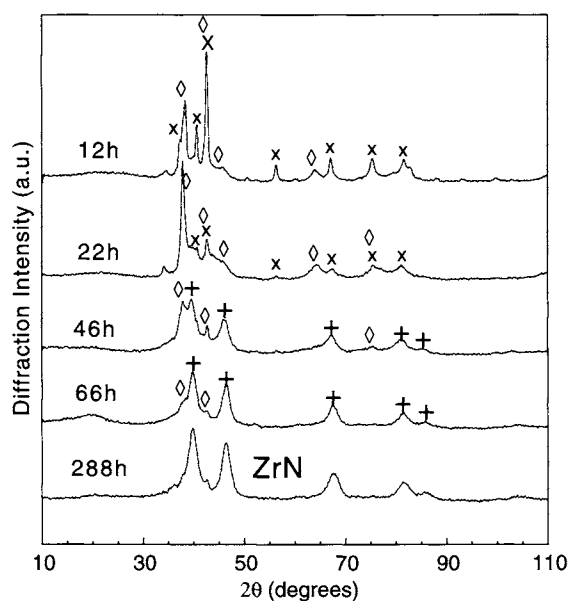


Figure 4. XRD patterns of Zr powder milled in the rotating ball mill for different times, (X) Zr, ( $\diamond$ )  $\text{ZrH}_2$ , and (+)  $\text{ZrN}$  [54].

process [56]. Alternatively, the deformation and fracturing of particles causes continuous size reduction and can lead to reduction in diffusion distances. This can at least reduce the reaction temperatures significantly, even if the reactions do not occur at room temperature [57,58]. Since newly created surfaces are most often very reactive and readily oxidize in air, the HEBM has to be conducted in an inert atmosphere. It is now recognized that the HEBM, along with other non-equilibrium techniques such as rapid quenching, irradiation/ion-implantation, plasma processing, and gas deposition, can produce a series of metastable and nanostructured materials, which are usually difficult to prepare using melting or conventional powder metallurgy methods [59,60]. In the next section, detailed structural and morphological changes of graphite during HEBM will be presented.

### 3. HIGH ENERGY BALL MILLING OF GRAPHITE

HEBM prepares a precursor for nanotube growth during subsequent annealing, and the precursor must contain nucleation structures and free C atoms for nanotube growth. These two structures in the milled graphite samples will be explored in this section. Hexagonal graphite powder of purity of 99.8% is selected as the starting material because amorphous carbon (e.g. activated carbon) is thermodynamically too stable to be converted to a different structure. The graphite powder is milled at room temperature using both the steel vertical-rotating ball mill and the ceramic

(WC) vibrating-frame grinder described in the previous section. Some graphite samples are also milled in a steel mill in a wet condition with 10 ml of ethanol to reduce particle agglomeration. The milled samples are analyzed using a large range of techniques, and the following new structures created by HEBM are found.

### 3.1. Microporous structures

The microporous structure is found in milled graphite samples using a Gemini 2375 surface area analyzer with the t-plot method [42]. It determines both the external surface area contributed by particles and macropores (diameter larger than 500 Å), and the internal surface area of micropores with a size smaller than 20 Å in diameter. The measurements are conducted using pure nitrogen gas at the liquid nitrogen temperature. Milled graphite samples need to be degassed at 200 °C for 1 h before the measurements are taken. Variations of the specific micropore internal surface ( $S_{\text{inter}}$ ), external surface ( $S_{\text{exter}}$ ) and the BET areas ( $S_{\text{BET}} = S_{\text{inter}} + S_{\text{exter}}$ ) as a function of milling time are illustrated in Fig. 5. It is found that the BET area increases to a maximum value of 589 m<sup>2</sup> g<sup>-1</sup> during the first 15 h of milling. It is important to note that more than 50% of this surface area is found to come from the nanosized pores with the specific internal area of 335 m<sup>2</sup> g<sup>-1</sup>, while the external surface area is 254 m<sup>2</sup> g<sup>-1</sup>. This reveals that a large number of micropores are created by HEBM. During further milling, the external surface decreases to about 102 m<sup>2</sup> g<sup>-1</sup> after 50 h and afterward remains constant up to 150 h. The increase in the external surface area during the first period of milling simply is a result of particle fracturing induced by ball impacts, and the later reduction in surface area is linked to agglomeration effects. The external surface area becomes constant when the particle fracturing is in balance with the formation of agglomerates. In contrast, the micropore area is apparently maintained at a high level during the extended milling, confirming that the formation of these micropores is due to HEBM. The nanoporous structure is

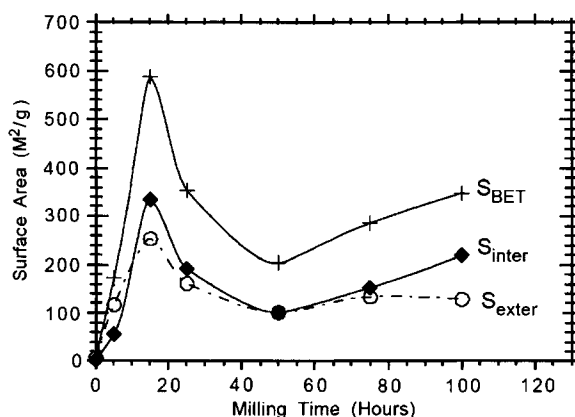


Figure 5. Surface area changes as a function of milling time for the graphite sample milled in a steel rotating mill without ethanol [42].

also found in samples milled for 150 h in the WC mill with a micropore area of  $284 \text{ m}^2 \text{ g}^{-1}$  and an external surface area of  $269 \text{ m}^2 \text{ g}^{-1}$ . Therefore, nanoporous carbon powders are produced using two different ball mills and are clearly unaffected by different milling contaminants. However, the milling conditions do affect the formation of the porous structure.

Fig. 6 shows different changes in the surface areas of the graphite samples during ball milling in the presence of ethanol. The BET surface area increases slowly to  $102 \text{ m}^2 \text{ g}^{-1}$  during 100 h of milling. The internal surface area is very low (only  $21 \text{ m}^2 \text{ g}^{-1}$ ). Hence, milling in a wet condition increases only the external surface as a result of fracturing of large particles. The new porous structure induced by HEBM contains a large number of structural defects and is probably fullerene-like in nature, which is important for nanotube formation.

### 3.2. Phase transformations

To understand the formation of the microporous structure, the milled samples are investigated thoroughly by means of both XRD using cobalt radiation ( $\lambda = 1.789 \text{ \AA}$ ) and TEM. Three typical XRD patterns taken from the graphite samples milled in the steel mill without ethanol for 10, 15, and 50 h are shown in Fig. 7. The hexagonal structure of graphite is still the dominant phase in the sample after milling for 10 h, but this phase is no longer present in the sample after milling for 15 h. Instead, a turbostratic structure with lattice spacings of  $d(002) = 3.46 \pm 0.05 \text{ \AA}$  and  $d(100) = 2.10 \pm 0.05 \text{ \AA}$  is found [42,61]. The asymmetric shape of the (002) peak is probably due to the possible presence of an amorphous carbon phase. A dominant amorphous phase is found in the sample after milling for 50 h. However, TEM reveals that carbon nanocrystallites can still be found in the sample. No further structural changes are detected by XRD in the samples after further milling up to 150 h [62]. The formation of a turbostratic structure suggests

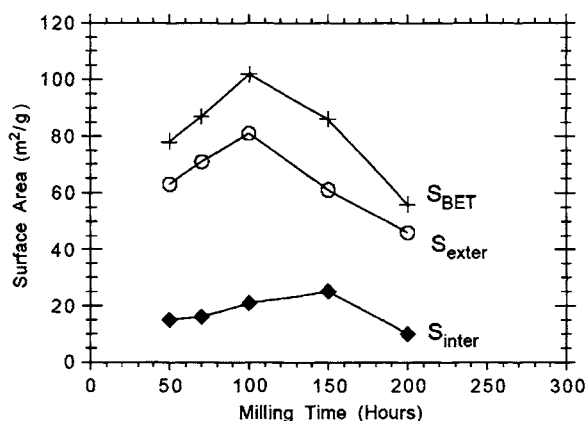


Figure 6. Surface area changes as a function of milling time for the graphite sample milled in the steel rotating mill with ethanol [42].

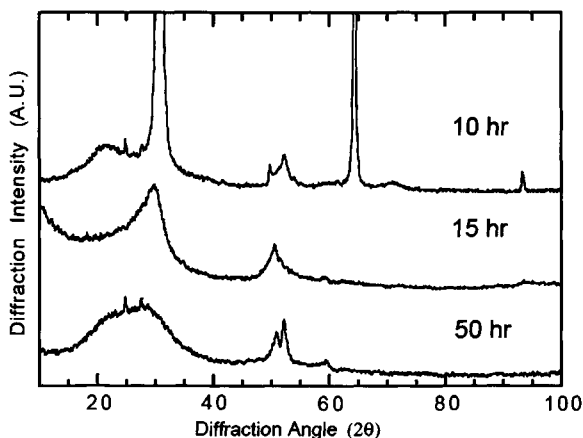


Figure 7. XRD patterns of a graphite sample milled in a steel ball milling without ethanol for different times [42].

fracturing of the hexagonal structure of graphite into small basal planes during the first period of milling. Further milling leads to broken-up graphene layers, which eventually transform to the amorphous structure. In the case of milling in a WC vibrating mill, the turbostratic structure is also found in the sample milled for 50 h, and the amorphous phase is dominant in the samples after 200 h of milling, as indicated by the XRD patterns in Fig. 8 [4]. Although milling contaminant WC is found in the sample, it seems to have no effect on the structural changes of the graphite during ball milling. In contrast, in the case of milling with ethanol, the hexagonal graphite structure remains stable even after 200 h of milling, suggesting that no disordered phases are produced during wet milling.

The above results suggest that the formation of the nanoporous structure is probably linked with the formation of the disordered structure such as the turbostratic and the amorphous phase. Micropores presumably form during agglomeration of fine carbon particles under the ball impacts. The porous structure could also be created by severe plastic deformation of large particles, similar to the crumpling of a piece of paper as shown in Fig. 9 [42].

Indeed, scanning electron microscopy (SEM) analysis reveals severely deformed graphite particles in milled graphite samples. Fig. 10a shows the typical morphology of the starting graphite powder with the flat chips of several micrometers thick and several ten-micrometers long; while Fig. 10b shows a different morphology of the sample after the ball milling treatment for 150 h. One large aggregate composed of many fine spherical particles can be seen. The significant shape and size changes induced by HEBM clearly indicate deformation of particles and (002) basal planes, which is in agreement with crystalline structural changes and the formation of nanoporous structures. In the case of wet milling, the low internal surface area is due to both much reduced plastic deformation and agglomeration of particles.

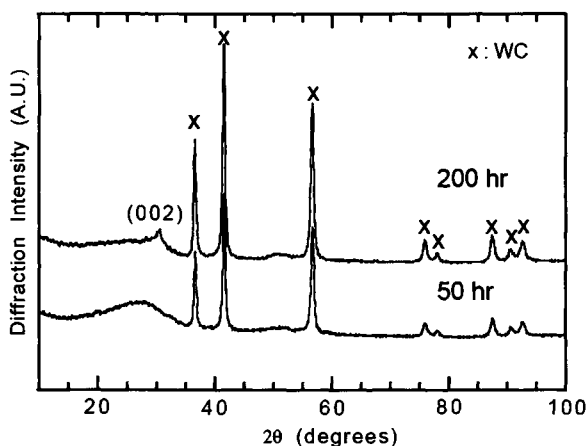


Figure 8. XRD patterns of a graphite samples milled in a WC vibrating mill for 50 and 200 h, (X) WC.

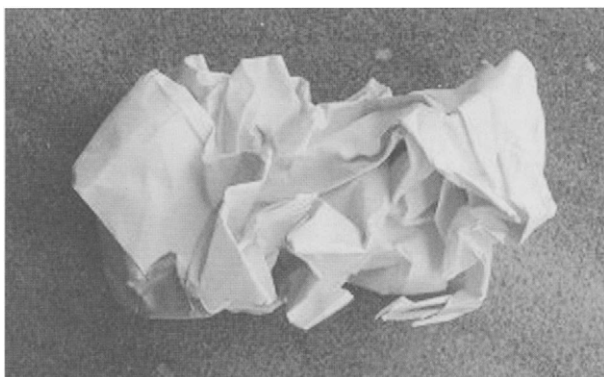


Figure 9. Photo of a crumpled paper.

TEM confirms the formation of the turbostratic and amorphous structures in the sample after ball milling for 15 h in the steel ball mill. The TEM image in Fig. 11 shows an agglomerate of milled graphite sample. Nanosized narrow ribbons (width of about 5 nm) with parallel fringes corresponding to (002) basal planes are characteristic of the turbostratic structure. Holes with different sizes and curved surfaces can also be observed in the agglomerate, revealing the porous structure, although the micropores cannot be observed directly in the TEM images. For samples milled for 50 h or longer, a more amorphous-like structure and fewer

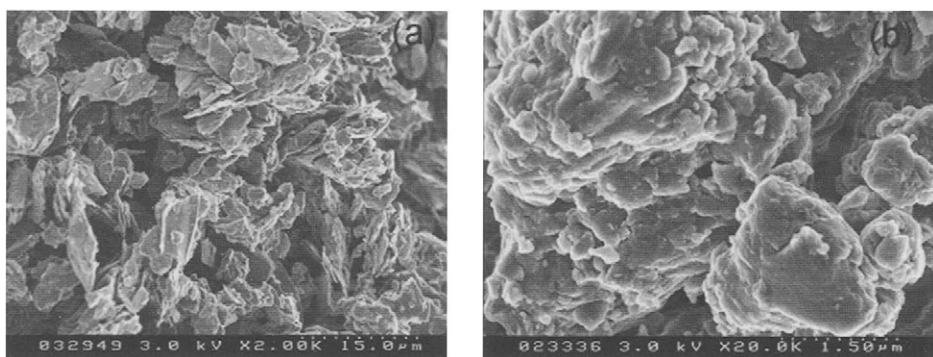


Figure 10. (a) SEM image of a graphite sample without ball-milling treatment. (b) SEM image of the graphite sample after ball milling for 150 h in a rotating mill.

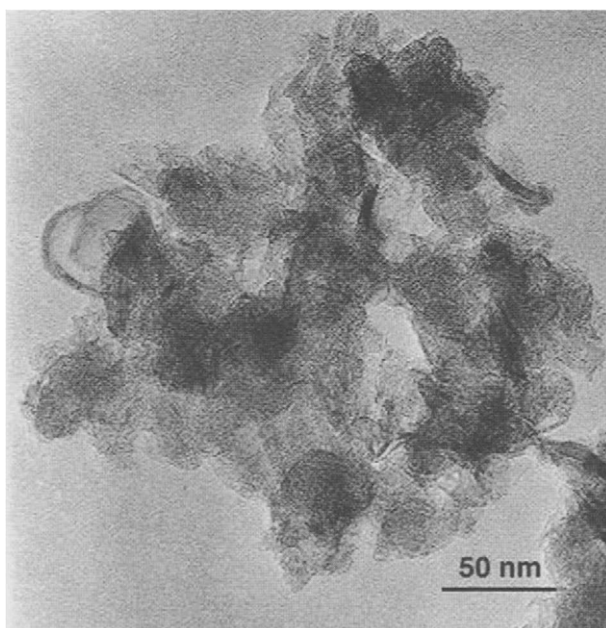


Figure 11. TEM image of the graphite sample after milling for 15 h in a steel mill [42].

nanosized ribbons are observed. The high-resolution TEM image in Fig. 12 shows a typical amorphous-like structure, and the deformed graphitic (002) planes can be seen in Fig. 13. Similar structures have also been observed by Tang et al. [63] and Shen et al. [64]. The high number of micropores in the milled samples suggests a



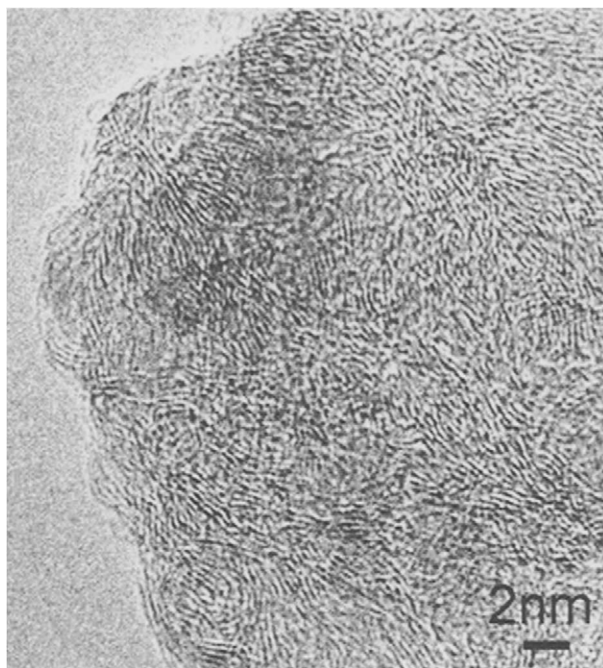


Figure 12. TEM image of the graphite sample milled for 150 h in the steel mill showing a typical amorphous structure induced by HEBM.

high number of Gaussian curved layers possibly due to the presence of pentagons, as in the well-known case of fullerenes. This disordered nanoporous structure is probably responsible for providing the precursors to homogenous nucleation for the growth of CNTs during subsequent annealing.

### 3.3. Metal particle inclusion

Like all other ball milling experiments, HEBM also introduces debris from the stainless steel container and hardened steel balls into graphite samples as milling contamination. X-ray dispersive spectroscopy (EDS) equipped with an Oxford ISIS EDXA analysis system can determine the level of metal contents in milled samples. The EDS spectra taken from the 150 h-milled sample are shown in Fig. 14. The sample contains approximately 5.4 at.% of Fe and 0.92 at.% of Cr. The average Fe and Cr contents increase gradually during the whole milling process, as shown in Fig. 15. Higher milling intensities result in higher Fe and Cr contents. TEM analysis confirms that the metal particles with sizes in the range of 10–100 nm disperse homogeneously in the disordered carbon. Nevertheless, the metal particles as milling contaminants have a positive catalytic role on nanotube formation in the current case [5,61], same as the case previously found in the arc-discharge process [65].

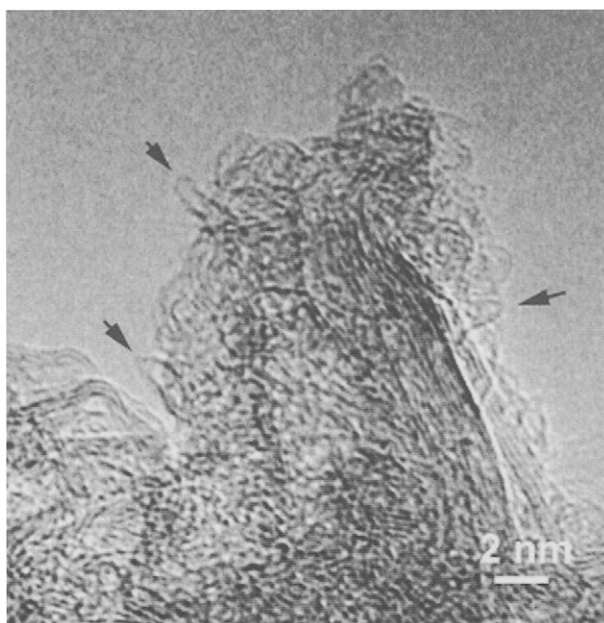


Figure 13. TEM image of the graphite sample after ball milling for 150 h. The arrows indicate heavily bent mamolayers [62].

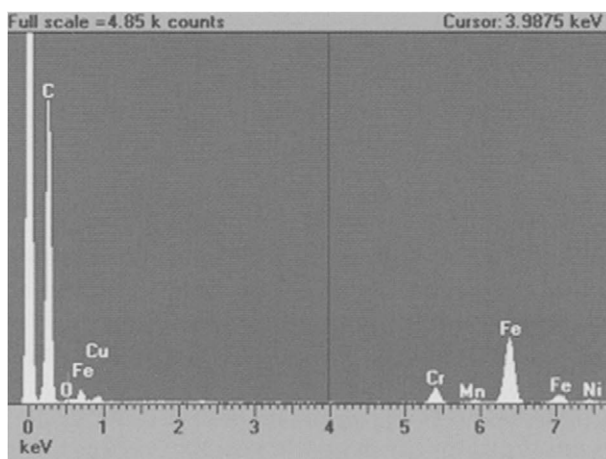


Figure 14. EDS spectra for the graphite sample after ball milling for 150 h in a steel mill, indicating the presence of Fe, Cr, Mn, Ni, and O elements as the milling contamination from the stainless steel container.

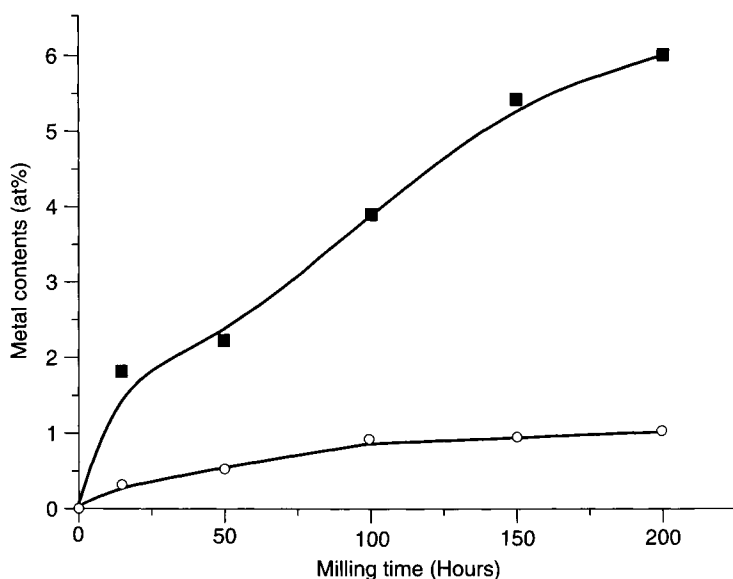


Figure 15. Metal content changes as a function of milling time for the milled graphite samples.

The above results show that disordered and nanoporous structures are produced by ball milling of graphite powder at room temperature. Micropores are formed through agglomeration of nanosized particles under ball impacts. The microporous structure is different from the porous structure of amorphous carbon, which has large and continuous surfaces. The milling contamination has no effect on the formation of this nanoporous structure, but will promote nanotube formation during subsequent annealing. No nanotube is formed in any of the above milled samples without further heat treatment. We presume that any well-ordered and crystalline structure is impossible to exist in such a violent mechanical grinding process.

#### 4. SOLID-STATE FORMATION PROCESS OF CNTs

Various structures grow out from the milled graphite samples during controlled annealing in a tube furnace under a flow of Ar or N<sub>2</sub> gas.

##### 4.1. Single-walled nanotubes

SWNTs are found in the sample milled for 150 h in a steel rotating mill, followed by heating at 1400 °C for 6 h in flowing nitrogen gas. A web-like structure of nanotubes can be seen on the TEM image in Fig. 16 [4]. The outer diameter of the nanotube boundless is less than 20 nm and nanotube size is about 1.5 nm. The dark particles observed are iron particles, which would seem to act as catalysts for the formation of

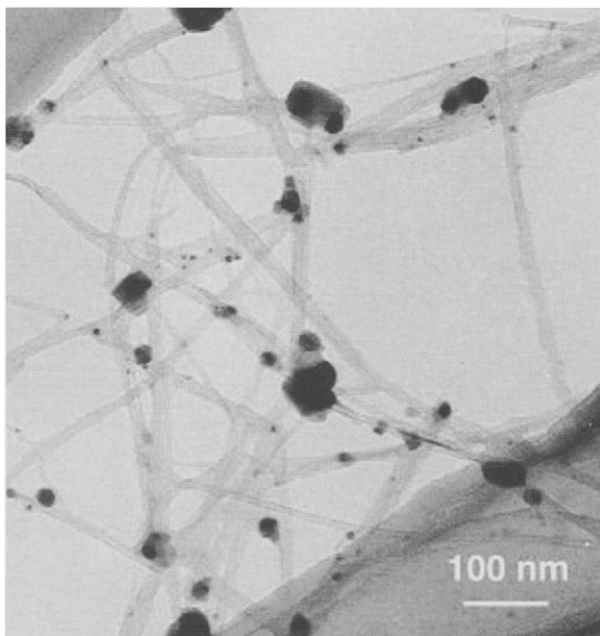


Figure 16. TEM image of the SWNTs formed in the graphite sample after first ball milling for 150 h and subsequent annealing at 1400 °C for 6 h [4].

the nanotubes. Like the SWNTs produced by arc-discharge method [65,66], SWNTs like to form bundles to minimize the total surface area. The yield of SWNTs is not high in the sample and no SWNTs are formed in the sample milled in WC mills, which might be due to different metal catalysts or to different milling intensities.

#### 4.2. Multi-walled nanotubes

A large quantity of MWNTs are produced in graphite samples milled in a steel mill for a long period of time (150–200 h) and subsequently annealed at 1400 °C [6,62]. A typical TEM image of the MWNTs is presented in Fig. 17a, and it shows groups of MWNTs with the outer diameter varying from 4 to 10 nm and the inner diameter of about 1.8 nm. The length is about several hundred nanometers. The multi-walled tubular structure of the observed CNTs is evidenced by the parallel fringes of the high-resolution image in Fig. 17b. Clearly, the tube end is closed by a hemispherical cap. However, it is worth pointing out that the two innermost atomic tubes have relatively flat caps (indicated by a black arrow). Most nanotubes have one free end (Fig. 17a), with the other connected to a cluster of carbon particles, suggesting that nanotubes grow out radially from the carbon clusters. Indeed, very small protuberances A and

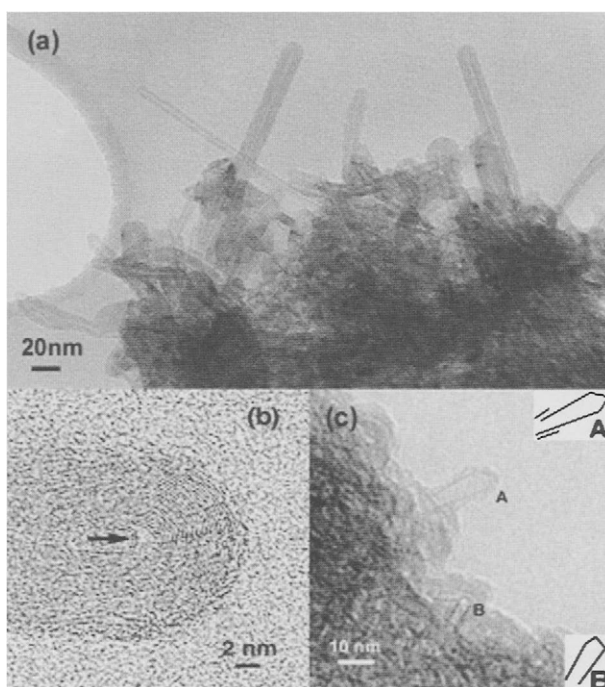


Figure 17. TEM images of the graphite sample after the ball milling and annealing treatment. (a) MWNTs and nanoparticles at the edge of a large sample cluster. (b) High-resolution image of the tip of one tube showing the typical paralleled-walled structure. (c) Two single-wall tubes with amorphous coating on the external surface. The possible faceted caps of each nanotube are illustrated [62].

B, which may be the precursors of SWNTs, can be found on the particle surface as shown in Fig. 17c. Tube A is only 20 nm long and appears to be capped with a polyhedron [67]. Small carbon clusters are observed to occur randomly on the external surface of the tube wall. A smaller “nanotube” B with a length of 10 nm and diameter of 2 nm also has a faceted cap. Compared with the flat caps in Fig. 17b, we suggest that the structures A and B may be the typical embryos of large MWNTs. In addition, no metal particles are found inside the thin MWNTs (Fig. 17a) or detected in the carbon cluster from which the nanotubes grow, although metal (mainly iron) particles are found in other carbon particles. The formation of MWNTs requires a long milling time (more than 150 h) and an annealing temperature above 1300 °C. Apparently, the quantity increases with a longer milling time and higher annealing temperatures.

#### 4.3. Bamboo-type nanotubes

Fig. 18 shows a bamboo-type tube formed in a sample after milling for 165 h and then annealing at 1300 °C for 4 h [6]. Two metal particles (dark spots) are encapsu-

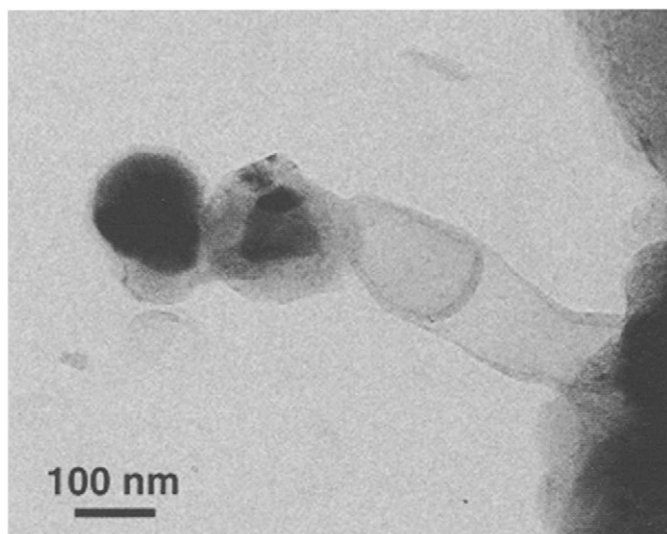


Figure 18. TEM image of a bamboo-type nanotube formed in the graphite sample. The dark particles encapsulated are Fe [6].

lated at the end of the tube and responsible for the formation of this special structure. Again, the other end is merged into a carbon cluster that served as carbon atom source. The short length and the thin wall of the tube indicate an early stage of growth. EDS reveals that the metal particles encapsulated are iron. The TEM image in Fig. 19 shows long bamboo-type nanotubes containing an iron particle at the tip [62]. In fact, all iron particles with clean surfaces in the milled sample have been covered by graphitic layers during annealing, suggesting a strong catalytic effect of metal particles on the growth. It is found that metal catalytic nanotubes in either cylindrical or bamboo structures have relatively large diameter ranging from 50 to 200 nm because the inner diameter is decided by the diameter of the metal particle [68]. The quantity of this type of tube increases with increasing iron content and annealing time. To further increase the yield, pure iron powder (1 at.%) can be added into the starting graphite sample. However, only some Fe particles produce tubular structures and others are just covered by the (002) layers.

#### 4.4. Nanoporous particles

Nanosized carbon clusters with a porous structure are found in many as annealed samples. The high-resolution TEM image in Fig. 20 shows a typical porous structure with mono- or double-curved graphitic layers in different shapes. Some stacks of parallel (002) planes start to form. Indeed, XRD patterns taken from the heated samples show a pronounced (002) diffraction peak, indicating growth of two-dimensional graphitic layers during the annealing (Fig. 21). Well-crystallized bulk hexagonal structure has not yet been established after annealing,

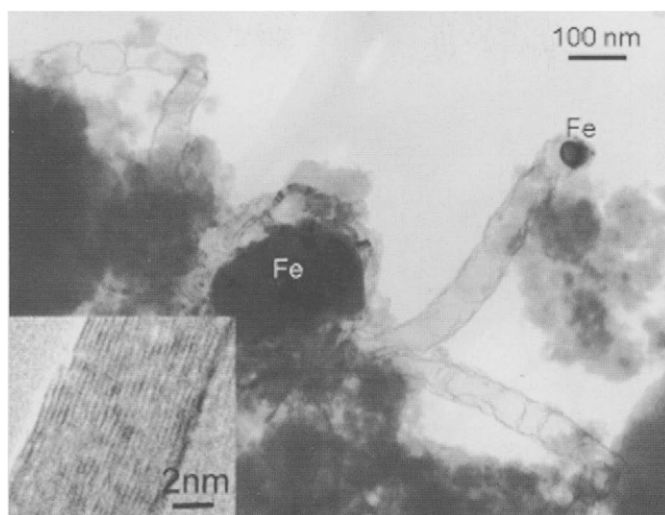


Figure 19. TEM image of the thick bamboo type nanotubes formed with the help of Fe catalyst particles. The insert high-resolution image was taken from the wall area [62].

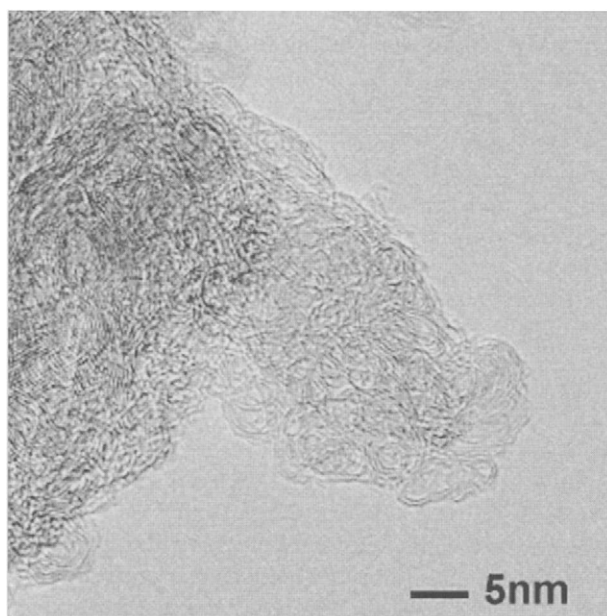


Figure 20. TEM of the nanoporous particles formed in the graphite sample after the ball milling and annealing treatment [6].

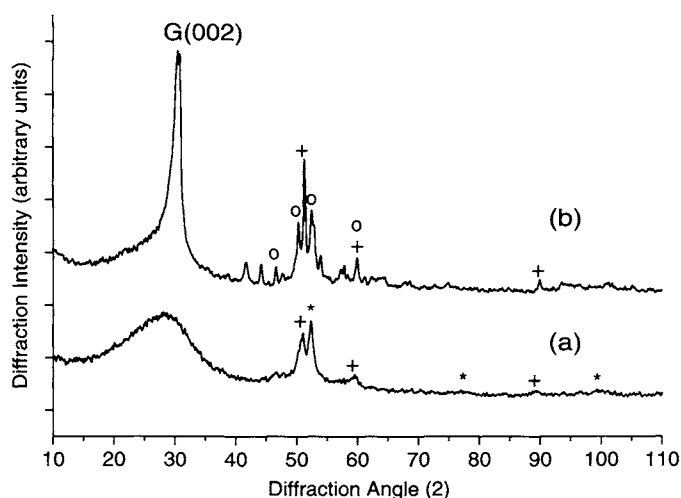


Figure 21. XRD patterns of the graphite samples (a) After ball milling for 150 h and (b) After subsequent annealing at 1400 °C for 3 h (+) Fe, (\*) Fe(C) stainless steel, (G) BN (002) planes, and (O)  $\text{Fe}_7\text{C}_3$  [62].

the dominant formation of graphitic layers is possibly due to the relatively low annealing temperature.

The temperatures of the above annealing experiments with the formation of various structures are less than 1500 °C, which are far below the melting/sublimation points for both graphite (3652 °C) and activated carbon (3697 °C) [69]. This suggests that no vapor phase should be present during the heat treatment. Hence, nanotubes probably grow by a solid-state process rather than condensation from a vapor phase involved in arc-discharge and laser-ablation methods [66,70]. Therefore, a new mechanism seems to be responsible for the solid-state nanotube formation in the milling-annealing process, which will be discussed in the next section.

## 5. FORMATION MECHANISMS

The formation mechanism of CNTs has received extensive attention since nanotubes were first discovered in 1991 [71]. An understanding of the formation mechanism is crucial in order to control the growth process, and to optimize the production of high-quality nanotubes. In the case of the arc-discharge method, multi-walled CNTs without metal catalysts are considered to have the same basic nucleation mechanism as fullerene. Free, highly chemically active carbon atoms in the vapor state collide to form clusters, chains, and rings by attaching to a hemispherical  $\text{C}_{60}$  [72–74]. This model is experimentally supported by the discovery of very small nanotubes with the inner diameters of only 0.4, 0.5, or 0.7 nm, corresponding to the size of  $\text{C}_{20}$ ,  $\text{C}_{36}$ , or  $\text{C}_{60}$  molecules, respectively [73–75]. For the



growth process itself, Iijima et al. [67,76] have suggested an open-end and layer-by-layer growth process based on TEM observations. The open tubes are closed by pentagons at the end of growth. Zhang et al. [72] suggested another growth model: when the first tube is formed, it serves as the substrate for second and third layers to nucleate and grow on the external surface. In the case of CVD process, the metal particles have an essential catalyst role in nanotube formation. The most popular vapor-liquid-solid (VLS) mechanism is illustrated in Fig. 22a. Carbon vapor dissolves into melt-catalyst particles forming an over-saturated solution at high temperatures, and then carbon precipitates out in the form of nanotubes or bamboo tubes when temperature is reduced [77]. The above models have been established based on a formation process involving carbon-vapor phase [78]. This section discusses special formation mechanisms involved in the ball milling-annealing process without the presence of a vapor phase.

### 5.1. Nucleation structures

Although nanotubes are not formed during the first ball milling process, the HEBM treatment is an essential step to the nanotube formation during subsequent annealing since direct heating of the graphite powders without any milling treatment does not produce nanotubes. The role of pre-ball milling treatment is to create a precursor containing nucleation structures/seeds and free carbon atoms. Two possible structures in the milled graphite samples promote the nucleation of CNTs: (1) metal catalytic particles. TEM observation has clearly revealed the typical catalytic effect of iron particles on the formation of thick MWNTs. Iron particles nucleate tubular structure and keep the tube open during growth. They are often encapsulated at tips of nanotubes when the growth terminates (Fig. 23). However, when the content of carbon in the solution reaches a high level so that carbides (e.g.  $\text{Fe}_7\text{C}_3$ ) are formed, precipitation does not occur at the end of the annealing [79]. The fundamental difference between CVD and the current case is that the possible dissolution and precipitation processes in the milling-annealing process should be a solid-liquid-solid (SLS) process, instead of the VLS process in other synthesis methods. A possible growth mechanism is illustrated in Fig. 22b. (2) Nanoporous structure containing graphene structures with defects (pentagons and heptanes), a large number of curved (002) layers have been produced by

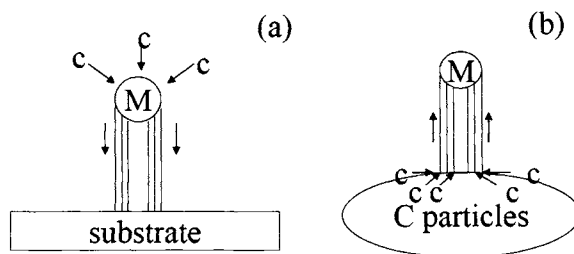


Figure 22. Schematic illustrations of the growth mechanism proposed for (a) CNTs produced by vapor deposition and (b) solid-state formation [5].

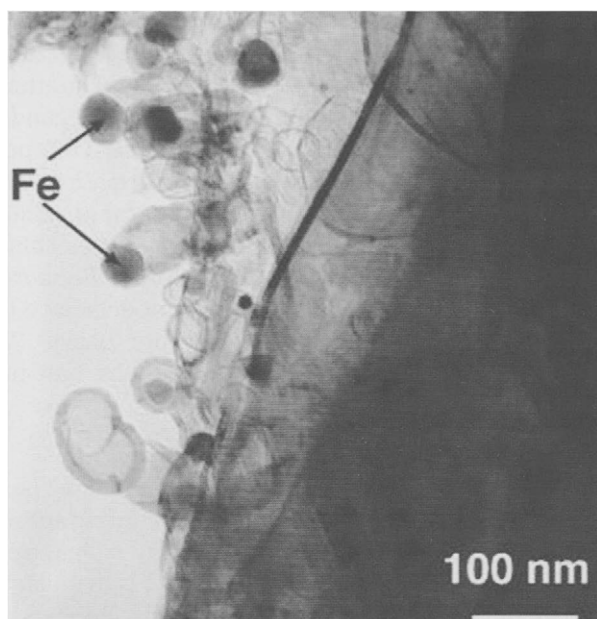


Figure 23. TEM image showing metal catalytic growth of CNTs in the ball milled and annealed graphite sample [5].

ball milling. These heavily bent layers contain a high density of pentagons and heptagons, and are metastable. They will transform to a more stable shape and geometry such as nanotubes when high mobility becomes possible on annealing. It has been reported that carbon onions and MWNTs are formed during heat treatment at a temperature between 2500 and 3500 K of carbon soot produced by arc-evaporation fullerene synthesis method [80].

The source of free available carbon atoms for nanotube formation must be disordered carbon, because no carbon vapor is available at such a low annealing temperature (1400 °C). The disordered phase with the nanosized carbon atom clusters, chains, and rings should serve as the carbon atom source for nanotube growth. Therefore, the ball-milled graphite provides nanotube nuclei and an available source of free carbon atoms, which is the ideal precursor for nanotube growth.

## 5.2. Solid-state growth process

The subsequent annealing process corresponds to the nanotube growth process as CNTs are only found in the final heated samples. Because the annealing temperature is much lower than the melting points of any known carbon materials, no vapor phase of carbon should be produced during the heating. As a consequence, the nanotube growth during the annealing should be a crystallization of the disordered phase, instead of condensation from carbon vapor phase.

XRD analysis reveals that crystallization of the disordered carbon takes place during the annealing. The XRD pattern in Fig. 21b, taken from the graphite sample annealed at 1400 °C for 3 h, shows a new pronounced diffraction peak superimposed on the broad amorphous peak. This sharp peak, corresponding to a lattice spacing of  $3.36 \pm 0.05$  Å, is indicative of the basal (002) planes of graphite and suggests a partial crystallization of the disordered carbon. TEM confirms the formation of a large number of the (002) layers instead of bulk graphite crystals, which is possibly associated with a relatively low annealing temperature and the low surface energy of the basal planes [81]. XRD also detects the appearance of the iron carbide ( $\text{Fe}_7\text{C}_3$ ) phase (Fig. 21b), suggesting reaction between carbon and some iron particles during the heating treatment. In a temperature range of 1000–1500 °C, thin MWNTs are found to form. No nanotubes are found below 1000 °C because the annealing temperature is too low for the crystallization. In contrast, only thick bamboo tubes and large crystals are formed after heating at 1800 °C.

The annealing temperature (1400 °C) is even lower than the crystallization temperature of amorphous structure (i.e. activated carbon, 2000 °C) [69]. Therefore, bulk and well-crystallized three-dimensional (3D) graphite structures are difficult to form. The newly formed thin layers have different nanostructures including nanotubes, nanocells, and nanoporous particles, each presumably originating from different nuclei. The TEM micrograph in Fig. 24 shows various structures growing out from the same carbon cluster. Metal particles (dense spots) can be seen clearly inside the carbon cluster. Along the edge, nanotubes (indicated by black arrows) and hollow particles (indicated by white arrows) are clearly observed [6].

Atomic diffusion of carbon from the disordered matrix is clearly essential for the low-temperature growth of nanotubes. At a temperature as low as 1400 °C, surface diffusion is the most likely mechanism for nanotube growth [7,82]. As suggested by the similar tip structure in Fig. 17b and c, small, single-wall tubes (which may be capped) could lengthen from the base through the accumulation of extra rows of carbon atom (diffusing from the particle cluster) into the tube root, as illustrated in Fig. 22b. A closed-tip growth has been experimentally tested [62]. Two milled graphite samples have been heated together for 4 h at 1400 °C and then cooled to 50 °C. After removing one sample from the furnace, one of the two samples is reheated for another 4 h (total 8 h) at 1400 °C. The two (4 h and 8 h-heated) samples are analyzed under SEM and the nanotube length is measured on SEM images. The length distributions for the two samples are compared in Fig. 25. The nanotubes of the 4 h-heated sample have shorter lengths compared with the 8 h-heated sample. About half of the nanotubes in the 4 h-heated sample are less than 400 nm including very short tubes of less than 200 nm, while only 15% of nanotubes are shorter than 400 nm in the 8 h-heated sample and no nanotube is less than 200 nm long. This suggests that short nanotubes formed during the first 4 h annealing continued to grow in length during the second 4 h heating with closed ends. TEM analysis confirms that the nanotubes in the 4 h-heated samples have closed tips. It is possible that the tube elongation is through the accumulation of extra rows of carbon atom (diffusing from the particle cluster) into the tube root.

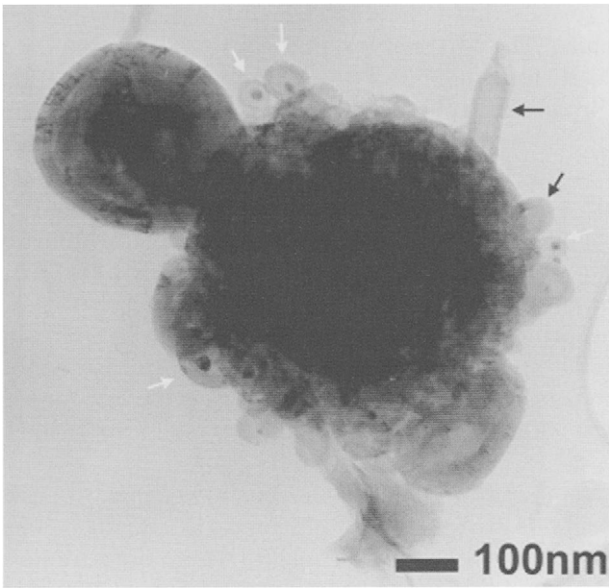


Figure 24. TEM image of a carbon cluster from the graphite sample after ball milling and annealing treatment. Dark arrows indicate nanotubes and light arrows indicate nanocells [6].

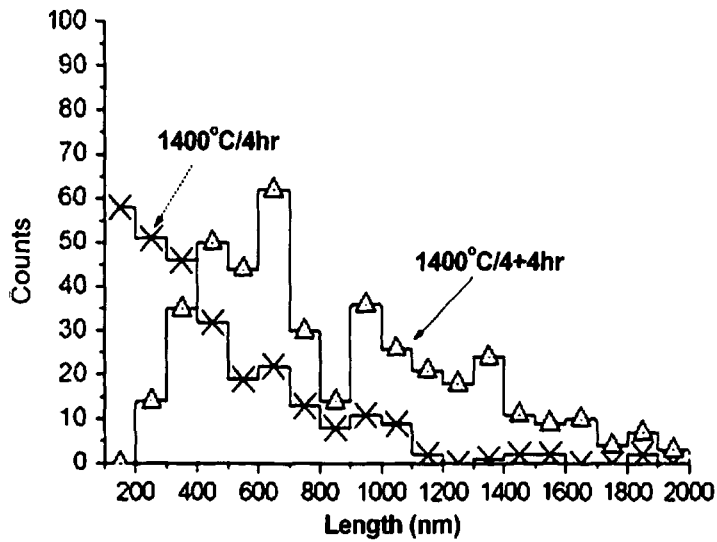


Figure 25. Length distributions of the MWNTs formed in two samples heated for different times, (X) 4 hours, and (Δ) 8 hours.

## 6. SUMMARY

CNTs with different structures have been produced from graphite by ball milling and annealing method. Mechanical milling produces a disordered and nanoporous structure, which provides nanotube nucleation sites. Subsequent annealing activates the growth of the (002) basal planes. Small SWNTs are first produced and serve as seeds for further growth into large MWNTs via fast surface diffusion along the external (002) surfaces. The method has the advantage for large-quantity production and low costs. New solid-state formation mechanisms are found. Like the products of the arc-discharge method, the end product does not contain pure nanotubes. At the current stage, a purification process is required for improving the nanotube yield. The method has great potential to become an industrial production method. In fact, it has been proven that the ball milling–annealing method is one of the best synthesis methods for high-yield BN nanotubes, which makes the first commercial production of BN nanotubes possible.

**Acknowledgments:** The author would like to thank colleagues Professor Jim S. Williams, Professor Lewis T. Chadderton, Dr John Fitz Gerald for their valuable discussions and important support. Grateful thanks also go to Dr Laurent Chaffron, Mr Martin Conway, and staff at the Electron Microscopy Unit for their experimental assistance. This work has been supported in part by the Australian Research Council under the Centre of Excellence and the Discovery programs.

## REFERENCES

1. M. S. Dresselhaus and M. Endo, Carbon Nanotubes: Synthesis, Structure, Properties, and Applications, Vol. 80, Eds. M. S. Dresselhaus, G. Dresselhaus and P. Avouris, Springer, Berlin, 2001.
2. R. H. Baughman, A. A. Zakhidov and W. A. de Heer, *Science* **297** (2002) 787.
3. P. M. Ajayan and O. Z. Zhou, Carbon Nanotubes, Vol. 80, Eds. M. S. Dresselhaus, G. Dresselhaus and P. Avouris, Springer, Berlin, 2001, p. 391.
4. Y. Chen, T. Fitz Gerald, L. T. Chadderton and L. Chaffron, *Mater. Sci. Forum* **312–314** (1999) 375.
5. Y. Chen, L. T. Chadderton, J. S. Williams and J. D. Fitz Gerald, *J. Metastable, Mechanically Alloyed Nanocrystalline Mater.* **343** (2000) 63.
6. Y. Chen, M. J. Conway and J. D. Fitz Gerald, *Appl. Phys. A-Mater. Sci. Process.* **76** (2003) 633.
7. L. T. Chadderton and Y. Chen, *Phys. Lett. A* **263** (1999) 401.
8. Y. Chen, J. D. Fitz Gerald, J. S. Williams and S. Bulcock, *Chem. Phys. Lett.* **299** (1999) 260.
9. Y. Chen, M. Conway, J. S. Williams and J. Zou, *J. Mater. Res.* **17** (2002) 1896.
10. J. D. Fitz Gerald, Y. Chen and M. J. Conway, *Appl. Phys. A-Mater. Sci. Process.* **76** (2003) 107.
11. C. C. Tang, Y. Bando and T. Sato, *Appl. Phys. A-Mater. Sci. Process.* **75** (2002) 681.
12. S. Y. Bae, H. W. Seo, J. Park, Y. S. Choi, J. C. Park and S. Y. Lee, *Chem. Phys. Lett.* **374** (2003) 534.

13. S. L. Li, Z. L. Tao, F. Gao and J. Chen, *Acta Chim. Sin.* **62** (2004) 634.
14. Z. L. Tao, S. L. Li, X. B. Fan and J. Chen, *Chin. J. Inorg. Chem.* **20** (2004) 99.
15. A. Urbietta, P. Fernandez and J. Piqueras, *Appl. Phys. Lett.* **85** (2004) 5968.
16. I. N. Kholmanov, A. Kharlamov, E. Barborini, C. Lenardi, A. Li Bassi, C. E. Bottani, C. Ducati, S. Maffi, N. V. Kirillova and P. Milani, *J. Nanosci. Nanotechnol.* **2** (2002) 453.
17. J. S. Lee, K. Park, S. Nahm, S. W. Kim and S. Kim, *J. Crystl. Growth* **244** (2002) 287.
18. H. D. Xiao, H. L. Ma, C. S. Xue, W. R. Hu, J. Ma, F. J. Zong, X. J. Zhang and F. Ji, *Mater. Lett.* **58** (2004) 3925.
19. L. W. Yin, Y. Bando, M. S. Li, Y. X. Liu and Y. X. Qi, *Adv. Mater.* **15** (2003) 1840.
20. Z. Konya, I. Vesselenyi, K. Niesz, A. Kukovecz, A. Demortier, A. Fonseca, J. Delhalle, Z. Mekhalif, J. B. Nagy, A. A. Koos, Z. Osvath, A. Kocsonya, L. P. Biro and I. Kiricsi, *Chem. Phys. Lett.* **360** (2002) 429.
21. Z. Konya, J. Zhu, K. Niesz, D. Mehn and I. Kiricsi, *Carbon* **42** (2004) 2001.
22. Y. B. Li, B. Q. Wei, J. Liang, Q. Yu and D. H. Wu, *Carbon* **37** (1999) 493.
23. N. Pierard, A. Fonseca, Z. Konya, I. Willems, G. Van Tendeloo and J. B. Nagy, *Chem. Phys. Lett.* **335** (2001) 1.
24. L. Chen, M. Z. Qu, G. M. Zhou, B. L. Zhang and Z. L. Yu, *Mater. Lett.* **58** (2004) 3737.
25. F. Liu, X. B. Zhang, J. P. Cheng, J. P. Tu, F. Z. Kong, W. Z. Huang and C. P. Chen, *Carbon* **41** (2003) 2527.
26. X. B. Yu, Z. Wu, B. J. Xia and N. X. Xu, *Phys. Lett. A* **333** (2004) 468.
27. F. X. Wang, X. P. Gao, Z. W. Lu, S. H. Ye, J. Q. Qu, F. Wu, H. T. Yuan and D. Y. Song, *J. Alloys Compd.* **370** (2004) 326.
28. B. Gao, A. Kleinhammes, X. P. Tang, C. Bower, L. Fleming, Y. Wu and O. Zhou, *Chem. Phys. Lett.* **307** (1999) 153.
29. B. Gao, C. Bower, J. D. Lorentzen, L. Fleming, A. Kleinhammes, X. P. Tang, L. E. McNeil, Y. Wu and O. Zhou, *Chem. Phys. Lett.* **327** (2000) 69.
30. Z. D. Tao, H. R. Geng, K. Yu, Z. X. Yang and Y. Z. Wang, *Mater. Lett.* **58** (2004) 3410.
31. Y. Wang, J. Wu and F. Wei, *Carbon* **41** (2003) 2939.
32. Y. A. Kim, T. Hayashi, Y. Fukai, M. Endo, T. Yanagisawa and M. S. Dresselhaus, *Chem. Phys. Lett.* **355** (2002) 279.
33. Z. J. Jia, Z. Y. Wang, J. Liang, B. Q. Wei and D. H. Wu, *Carbon* **37** (1999) 903.
34. R. Barthos, D. Mehn, A. Demortier, N. Pierard, Y. Morciaux, G. Demortier, A. Fonseca and J. B. Nagy, *Carbon* **43** (2005) 321.
35. H. M. Ma, J. J. Zeng, M. L. Realff, S. Kumar and D. A. Schiraldi, *Composites Sci. Technol.* **63** (2003) 1617.
36. F. M. Zhang, J. Shen and J. F. Sun, *Mater. Sci. Eng. A-Structu. Mater. Prop. Microstruct. Process.* **381** (2004) 86.
37. S. Li, G. L. Pan, X. P. Gao, J. Q. Qu, F. Wu and D. Y. Song, *J. Alloys Compd.* **364** (2004) 250.
38. J. S. Benjamin, *Metall. Trans.* **1** (1970) 2943.
39. C. C. Koch, O. B. Cavin, C. G. Mckamey and J. O. Scarbrough, *Appl. Phys. Lett.* **43** (1983) 1017.

40. C. Suryanarayana, *Bull. Mater. Sci.* **17** (1994) 307.
41. C. C. Koch, *Mater. Sci. Eng. A-Struct. Mater. Prop. Microstruct. Process.* **244** (1998) 39.
42. Y. Chen, J. D. Fitz Gerald, L. T. Chadderton and L. Chaffron, *Appl. Phys. Lett.* **74** (1999) 2782.
43. D. K. Mukhopadhyay, C. Suryanarayana and F. H. Froes, *Scr. Metal. Et Materialia* **30** (1994) 133.
44. C. C. Koch, *J. Non-Crystall. Solids* **117** (1990) 670.
45. G. B. Schaffer and P. G. McCormick, *Scr. Metal.* **23** (1989) 835.
46. G. B. Schaffer and P. G. McCormick, *Metall. Trans. A-Phys. Metall. Mater. Sci.* **21** (1990) 2789.
47. Y. Chen, A. Calka, J. S. Williams and B. W. Ninham, *Mater. Sci. Eng. A-Struct. Mater. Prop. Microstruct. Process.* **187** (1994) 51.
48. Y. Chen and J. S. Williams, *J. Alloys Compd.* **217** (1995) 181.
49. P. Matteazzi and G. Lecaer, *J. Am. Ceram. Soc.* **74** (1991) 1382.
50. C. Suryanarayana, *Prog. Mater. Sci.* **46** (2001) 1.
51. Y. Chen, R. Lehazif and G. Martin, *J. De Phys.* **51** (1990) C4273.
52. Y. Chen, M. Bibole, R. Lehazif and G. Martin, *Phys. Rev. B* **48** (1993) 14.
53. A. Calka and A. P. Radlinski, *Mater. Sci. Eng. A-Struc. Mater. Prop. Microstruct. Process.* **134** (1991) 1350.
54. Y. Chen and J. S. Williams, *J. Mater. Res.* **11** (1996) 1500.
55. Y. Chen and J. S. Williams, *Metastable, Mech. Alloyed Nanocryst. Mater.* **225** (1996) 545.
56. E. H. Zhou, C. Suryanarayana and F. H. Fores, *Mater. Lett.* **23** (1995) 27.
57. G. Lecaer and P. Matteazzi, *Hyperfine Interact.* **90** (1994) 229.
58. G. B. Schaffer and P. G. McCormick, *Appl. Phys. Lett.* **55** (1989) 45.
59. P. G. McCormick and F. H. Froes, *Jom-J. Miner. Met. Mater. Soc.* **50** (1998) 61.
60. C. C. Koch, *Nanostruct. Mater.* **9** (1997) 13.
61. Y. Chen, L. T. Chadderton, J. FitzGerald and J. S. Williams, *Appl. Phys. Lett.* **74** (1999) 2960.
62. Y. Chen, M. J. Conway, J. D. Fitz Gerald, J. S. Williams and L. T. Chadderton, *Carbon* **42** (2004) 1543.
63. J. Tang, W. Zhao, L. Li, A. U. Falster, W. B. Simmons, W. L. Zhou, Y. Ikuhara and J. H. Zhang, *J. Mater. Res.* **11** (1996) 733.
64. T. D. Shen, W. Q. Ge, K. Y. Wang, M. X. Quan, J. T. Wang, W. D. Wei and C. C. Koch, *Nanostruct. Mater.* **7** (1996) 393.
65. D. S. Bethune, C. H. Kiang, M. S. Devries, G. Gorman, R. Savoy, J. Vazquez and R. Beyers, *Nature* **363** (1993) 605.
66. S. Iijima and T. Ichihashi, *Nature* **363** (1993) 603.
67. S. Iijima, P. M. Ajayan and T. Ichihashi, *Phys. Rev. Lett.* **69** (1992) 3100.
68. L. T. Chadderton and Y. Chen, *J. Crystl. Growth* **240** (2002) 164.
69. A. Oberlin, *Chemistry and Physics of Carbon*, Marcel Dekker, New York, 1989.
70. J. C. Charlier and S. Iijima, *Carbon Nanotubes: Synthesis, Structure, Properties, and Applications*, Vol. 80, Eds. M. S. Dresselhaus, G. Dresselhaus and P. H. Avouris, Springer, Berlin, Germany, pp. 55–80, 2001.

71. S. Iijima, *Nature* **354** (1991) 56.
72. X. F. Zhang, X. B. Zhang, G. Vantendeloo, S. Amelinckx, M. O. Debeeck and J. Vanlanduyt, *J. Crystl. Growth* **130** (1993) 368.
73. L. C. Qin, X. L. Zhao, K. Hirahara, Y. Miyamoto, Y. Ando and S. Iijima, *Nature* **408** (2000) 50.
74. L. F. Sun, S. S. Xie, W. Liu, W. Y. Zhou, Z. Q. Liu, D. S. Tang, G. Wang and L. X. Qian, *Nature* **403** (2000) 384.
75. P. M. Ajayan and S. Iijima, *Nature* **361** (1993) 333.
76. S. Iijima, *Mater. Sci. Eng. B-Solid State Mater. Adv. Technol.* **19** (1993) 172.
77. J. Y. Dai, J. M. Lauerhaas, A. A. Setlur and R. P. H. Chang, *Chem. Phys. Lett.* **258** (1996) 547.
78. T. W. Ebbesen, *Annu. Rev. Mater. Sci.* **24** (1994) 235.
79. C. Laurent, E. Flahaut, A. Peigney and A. Rousset, *New J. Chem.* **22** (1998) 1229.
80. P. J. F. Harris, S. C. Tsang, J. B. Claridge and M. L. H. Green, *J. Chem. Soc.-Faraday Trans.* **90** (1994) 2799.
81. J. Abrahamson, *Carbon* **11** (1973) 337.
82. O. A. Louchev, Y. Sato and H. Kanda, *Appl. Phys. Lett.* **80** (2002) 2752.



## Chapter 4

### Catalytic chemical vapor deposition of single-walled carbon nanotubes

Q. Fu and J. Liu

Department of Chemistry, Duke University, Durham, NC27708

Since their discovery, carbon nanotubes (CNTs) have been widely studied in chemistry, physics and material science due to their unique structures and properties. The progresses of fundamental research and applications in the field are closely linked to the preparation of high-quality CNTs via controllable routes. Without the constantly improving methods of nanotube synthesis, many of the applications described in this book would not be possible. The aim of this chapter is to provide an introduction of recent developments of chemical vapor depositions (CVDs) of single-walled carbon nanotubes (SWNTs). A variety of CVD techniques have been introduced and related experimental issues are discussed. Additional challenges in the field of nanotube synthesis are also discussed.

#### 1. INTRODUCTION/BACKGROUND

Carbon nanotubes (CNTs) [1] are new materials, which are formed by self-assembling of carbon atoms. They are hollow cylinders with diameters in the nanometer scale and length of up to several centimeters (aspect ratio  $>10^4$ ). The tubular structures of carbon have actually been observed in carbon fibers in 1970s [2]. However, the structures started to attract intensive attention of researchers after Ijima observed multi-walled carbon nanotubes (MWNTs) under transmission electron microscopy (TEM) in 1991 [3]. In 1993, Ijima and Bethune independently observed SWNTs (Fig. 1) [4,5]. Since then, the unique structures and properties of CNTs have inspired researches in physics, chemistry and material science to exploit their synthesis and applications. Impressive progresses have been made over the years and new applications and properties are being discovered.

##### 1.1. Structure of SWNT

CNTs could be considered as seamless cylinders with sidewalls formed by rolling-up a section of two-dimensional graphene layers [13]. MWNTs have sidewalls with several layers of graphene sheet with diameters of 5–100 nm; SWNTs have only one layer of graphene as the sidewall with diameters of 0.7–10 nm. Properties of CNTs are determined by their structures. SWNTs are fundamentally more interesting and unique in electrical, mechanical and optical properties. They have great potential in broad applications such as electronic devices [6,7], field emitters [8,9], composite materials [10], nanoprobe tips [11–13] and chemical sensors [14]. In this section, we focus our discussion on SWNTs.

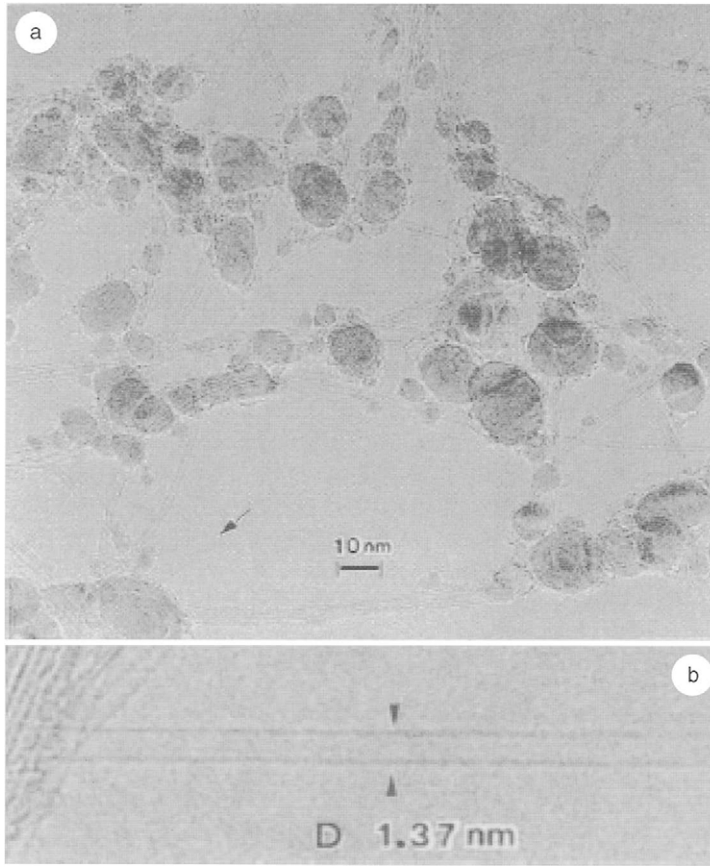


Figure 1. TEM images of SWNTs. Adapted with permission from Bethune et al. [4]. Copyright (1993) Nature Publishing Group.

Structure of an SWNT is characterized by a rolling-up vector on a graphite sheet [15,16],

$$C_h = na_1 + ma_2 = (n, m), \quad (1)$$

where  $a_1$  and  $a_2$  are the graphene primitive vectors and  $n, m$  are integers as shown in Fig. 2. In an SWNT,  $C_h$  corresponds to circumferential direction that is perpendicular to the axis. It determines the diameter and chiral angle of the SWNT. The diameter of an SWNT is given by  $L/\pi$ , where  $L$  is the circumferential length. For a  $(n, m)$  SWNT,

$$L = a\sqrt{3(n^2 + m^2 + nm)}, \quad (2)$$

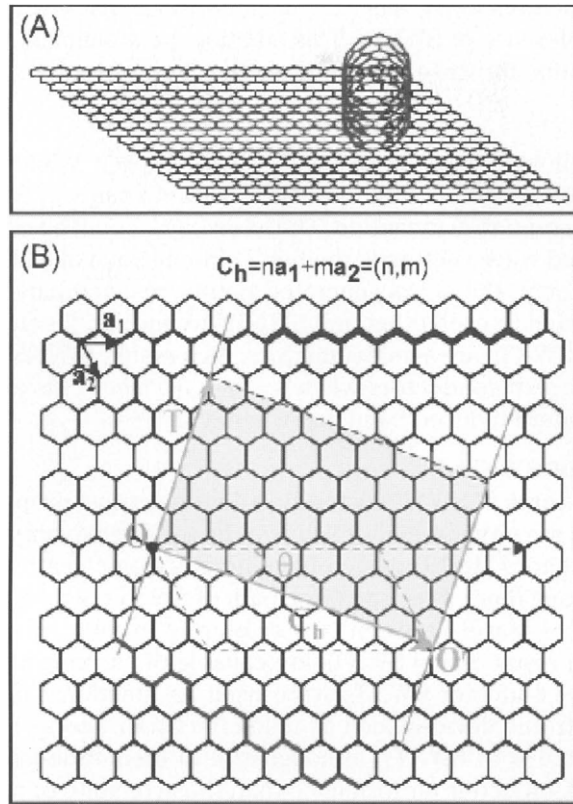


Figure 2. Schematic illustrations of rolling up a graphene sheet to form an SWNT. Adapted with permission from Ouyang et al. [15]. Copyright (2002) American Chemical Society.

where  $a$  is the length of the C–C bond in the graphene sheet. The chiral angle  $\theta$  in a  $(n, m)$  SWNT, which is the angle between  $C_h$  and  $a_1$ , is given by

$$\cos\theta = \frac{2n + m}{2\sqrt{n^2 + m^2 + nm}} \quad (3)$$

Structures of SWNTs determine their electronic band structures that subsequently control electrical properties. Basic electronic band structures of SWNTs can be derived from those of a graphene sheet [1,17]. Graphene is a semimetal with valence and conduction bands that are degenerated at six corners of hexagonal first Brillouin zone. Fermi surface of graphene is reduced to only six degenerate points.

For electronic structures of SWNTs, one must consider that electrons are confined around the circumference of SWNTs. This additional confinement introduces a new quantization condition for wave vectors along the circumferential direction,

$$K_1 C_h = 2\pi q, \quad (4)$$

where  $K_1$  is the allowed wave vector and  $q$  is an integer. While wave vectors  $K_2$  along axis direction remain continuous; only certain values of  $K_1$  will be allowed under the circumferential quantization. The allowed  $K_1$  could be represented by cutting lines of allowed wave vectors in the first Brillouin zone of a 2D graphene sheet. When  $K_1$  cuts through the six degenerated points, valence band and conduction band are degenerated to each other and SWNTs are metals. When  $K_1$  does not pass the Fermi points, SWNTs are semiconductors. As a result, SWNTs are metals when  $n = m$ ; SWNTs are semiconductors when  $n - m \neq 3i$ , where  $i$  is an integer. SWNTs have a small curvature-induced band gap when with  $n - m = 3i$ .

### 1.2. Properties of SWNTs

Electronic structures of SWNTs determine their electrical properties. Depending on  $(n, m)$ , SWNTs are either metal or semiconductor. High-quality SWNTs are ideal 1D ballistic conductors [18,19], which have no electronic scattering events when electrons move along them. Electrons free path of SWNTs, which describes the distance that electrons travel between two scattering events, can be up to several micrometers. As a result, metal SWNTs are capable of carrying a large current and act as wires; semiconductor SWNTs were used as functional elements for high-performance electronic devices such as field-effect transistors (FETs). For example, FETs fabricated with SWNTs, although still in their rudimentary states, have already demonstrated better performance than those of state-of-art silicon [19,20].

CNTs are strong and resilient. Young's modulus of SWNTs is on the order of 1 Tpa, which is much higher than most of existing materials. Tensile strength of SWNTs measured recently is about 20 Gpa [21]. Due to such high strength, SWNTs will buckle rather than distort or break when they are bent.

Because of their high-tensile strength and high-aspect ratio, SWNTs are used as high-resolution nanoprobe tips for atomic force microscopy (AFM). SWNTs could be mounted on the AFM cantilever or by direct growth [11,12]. Those tips showed capabilities for high-resolution AFM imaging, especially for biological molecules including DNA and proteins [13]. On the other side, mechanical properties of SWNTs, combined with their electronic properties, were also exploited for electromechanical devices [22].

### 1.3. Synthesis of SWNTs

SWNTs are generally formed by catalysis reaction on transitional metal particles with dimensions in nanometer scale. It is generally hypothesized that SWNT formation involves several basic steps: carbon atoms condense on the surface of metal catalyst nanoparticles; the condensed carbon atoms are dissolved and diffused into the metal nanoparticles; SWNTs nucleate and grow from the catalysts when the carbon concentration is saturated in the catalyst nanoparticles [23,24]. Those processes were supported by the observations of catalyst nanoparticles on one end of SWNTs and diameters of SWNTs are controlled by the size of the catalyst nanoparticles.

SWNT synthesis aims to provide large-quantity SWNTs with desired chemical structures, such as uniform length, diameter and chiral angle at low cost. Although more studies are still required to clarify detailed growth mechanisms, significant progress has been made in last decade. Productions of SWNTs have been much improved and scaled to commercial products. For instance, SWNTs are produced at a pound/day level using a process called High Pressure Decompositions of Carbon Monoxides (HiPCO) at Carbon Nanotechnology (Houston, Texas).

Arc-discharge [4,5,25], laser ablation [26] and chemical vapor deposition (CVD) [27] are three principal methods to produce SWNTs. Arc-discharge and laser ablation involve using high-power energy to vaporize solid-state carbon and form SWNTs at high temperature (thousands of Celsius); CVD uses carbon precursors from gas phase to form SWNTs that takes place at relatively low temperature (500–1000 °C). Gram-scale MWNTs and SWNTs are first synthesized by arc-discharge and laser ablation. However, both methods require delicate equipments and consume large energy, which limit them only at a lab scale. In addition, less control could be introduced in the reaction process. It is the CVD method that provides more accessible control in growth and could be scaled up to industry level.

## **2. CHEMICAL VAPOR DEPOSITION OF SWNT**

CVD is a heterogeneous catalysis process [28]. In a CVD process to produce SWNT, carbon precursors in gas phase pass through a high-temperature reaction chamber and decompose on solid catalysts to form SWNTs. Compared to arc-discharge and laser ablation, more parameters, including temperature, feeding gases, flow rate, catalyst components and heating rate, are accessible to control the growth process in CVD [29]. By changing growth conditions, one can control properties of the produced SWNTs such as length, orientation and diameter to some extent. External field, such as electrical field and magnetic field, could also be incorporated during the growth process to align SWNTs [30,31].

CVD has already been widely used to produce SWNTs for commercialization and fundamental research. A variety of CVD processes have been developed, which use different catalysts, different catalyst supports and various feeding gases. Based on forms of final products, CVD is divided into two categories: bulk growth and surface growth. Bulk growth use catalyst supported with porous materials or floating in gas phase to produce SWNTs. The produced SWNTs are black solid powders in which they are tangled with each other in forms of bundles. Surface growth directly produces SWNTs (as grown) with catalyst on a flat substrate; the produced SWNTs generally are attached to surface and extend along the surface in forms of isolate SWNTs or entangled thin film.

### **2.1. Bulk growth of SWNTs**

Bulk growth uses two types of distinctively different catalysts: supported catalysts and floating catalysts. Supported catalysts consist of catalyst nanoparticles impregnated in a porous material that acts as support for SWNT growth. SWNTs form within the solid support and require post treatments to separate them. Floating catalyst nanoparticles are formed in situ during the growth and SWNTs are formed in gas phase and collected on a solid substrate.

### 2.1.1. Growth on supported catalyst

In a typical growth on supported catalyst, catalyst is put into a chamber and heated up to high temperature. Carbon precursors such as methane ( $\text{CH}_4$ ), alcohols or carbon monoxide (CO) flow into the chamber, decompose and generate SWNTs. Supported catalysts are typically transition metal (Fe, Co, Ni) oxide nanoparticles dispersed in porous support materials. The goal of developing supported catalyst is to produce SWNTs with high yield at low cost. The raw products require separation process to isolate SWNTs from supports. Therefore, it is very important to have a porous support material that could be easily separated with SWNTs. Several preparation methods have been developed to prepare supported catalysts.

Direct impregnation is the easiest method to prepare supported catalyst, although the yield of SWNTs is limited. Typically, catalysts are prepared by mixing aqueous or alcohol solutions containing soluble precursors of the desired metal catalyst with inert porous materials, such as  $\text{Al}_2\text{O}_3$ ,  $\text{SiO}_2$  and  $\text{MgO}$  [32]. After the solvents are evaporated, the solid samples are calcinated at high temperature to transform metal precursors into metal oxide nanoparticles. Because it is very simple, catalysts prepared by impregnation were first used for CVD process. However, the yield is limited because the surface area of the catalyst is low.

High surface area supports can be prepared through a sol-gel approach, which significantly improved growth yield. Cassell and his coworkers prepared catalysts composed of metal nanoparticles supported on a  $\text{SiO}_2/\text{Al}_2\text{O}_3$  hybrids structure [33]. They observed that high-yield catalyst exhibits characteristics of high surface area and large mesoporous volume at elevated temperature. Scanning electron microscope (SEM) and transmission electron microscope (TEM) showed that SWNTs were clean and free of defects and amorphous carbon (Fig. 3). The yield was up to 30% (Fig. 4). Su et al. further improved this approach and prepared catalysts through an aerogel approach [34]. They dried their catalysts under supercritical condition to avoid collapse of pore structures in supports. They found that the yield of SWNTs increased with longer reaction time and could be up to 300% using methane as feeding gas, which might be scaled up for industry production (Fig. 4).

Recently, catalysts with high surface area are prepared by a combustion method, which are simple, fast and economical. Typically, transitional metal salts, certain organic compounds and precursors of the supports are mixed in an aqueous solution and heated up to evaporate all the solvents. When the mixture continues to be heated, it induces chemical reactions between organic compound and inorganic acid and releases large amount of gas, which make the solid support porous. For instance, Li et al. prepared  $\text{MgO}$ -supported Fe/Mo catalyst by decomposition of magnesita nitrate and alkaline magnesium carbonate at  $400^\circ\text{C}$  [35].  $\text{MgO}$  is the most widely used support in combustion synthesis and can be easily removed from CVD product by simple acid treatment, which greatly facilitates separation.

### 2.1.2. Growth on floating catalyst

In floating catalyst approach, metal nanoparticles are formed in gas phase by injecting volatile organometallic precursors into a high temperature zone. Once hydrocarbon is introduced, it decomposes on the metal nanoparticles, which subsequently

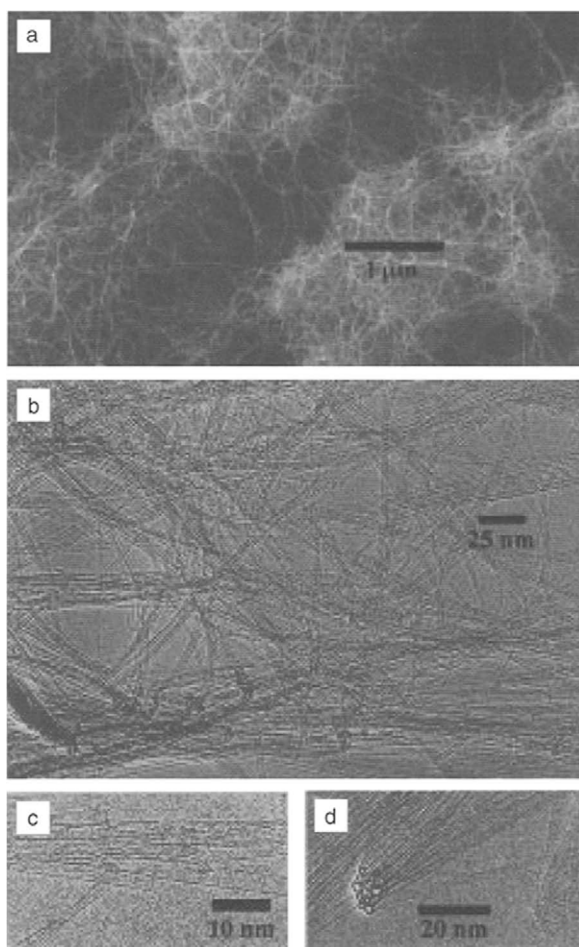


Figure 3. SWNTs grown from sol-gel catalyst using methane as carbon source. Adapted with permission from Kong et al. [32]. Copyright (1999) American Chemical Society.

nucleate and form SWNTs. SWNTs are then transported out of the reaction zone by the gas flow and collected on a cold plate. This approach is suitable for large-scale synthesis because the process could be carried out continuously and separation step might be avoided after growth because no catalyst supports are involved during the process.

Growth of SWNTs with floating catalyst is affected by a variety of factors, including feeding gases, flow rate, reaction temperature and reaction pressure. Cheng et al. carried out the first SWNT synthesis with floating catalysts [36]. They used vaporized ferrocene as a catalyst precursor and benzene as a carbon source to produce SWNTs

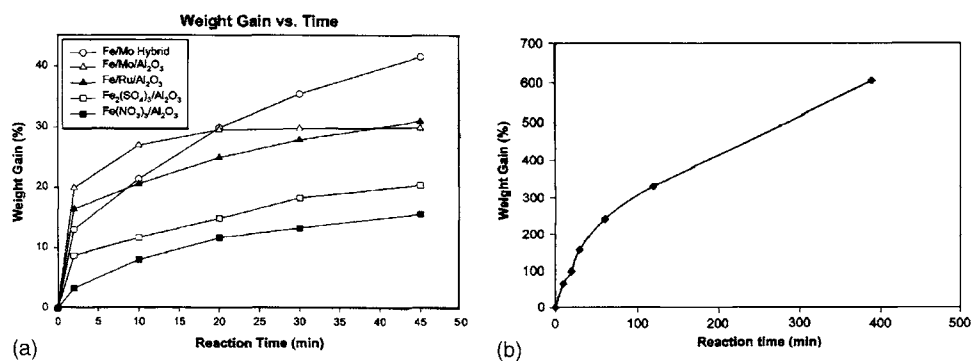


Figure 4. Weight gain versus time for (a) sol-gel catalyst and (b) aerogel catalyst. Adapted with permission from Kong et al. [32] and Cassell et al. [33]. Copyright (1999) American Chemical Society and (1999) Elsevier.

at 1200 °C. The product consists of many rope-like bundles with diameter ranging from 10 nm to 40 nm, which are formed by aligned SWNTs (Fig. 5). Other carbon sources and organometallic precursors have also been incorporated into this process. Among them, HiPCO process is probably the best-known floating catalyst process. It was developed at Rice University and commercialized by Carbon Nanotechnology Inc. in Houston. In this procedure, high pressure (30–100 atm) CO mixed with  $\text{Fe}(\text{CO})_5$  flow through a high temperature (1050 °C) reaction zone to produce high-quality SWNT at a rate of approximately 459 mg/h. The product consists of entangled SWNT bundles interspersed with Fe nanoparticles (Fig. 6) [37].

Several groups use vertical furnaces to carry out floating catalyst process. For example, Zhu et al. introduced hexane solution of ferrocene into a reaction zone using  $\text{H}_2$  as carrier gases in a vertical furnace, they produced SWNT strands with lengths of 20 cm (Fig. 7) [38]. Li et al. used a vertical heating furnace and alcohols as carbon source to produce SWNTs and MWNTs at 1050–1200 °C [39]. They found that SWNTs formed aerogel in the high-temperature zone and could be spun into a carbon fiber without apparent limit of length. Compared to supported catalyst growth, SWNTs synthesized with floating catalyst are free of solid supports and can be directly used after removal of catalyst nanoparticles.

## 2.2. Surface growth of SWNT

Surface growth is a method that directly synthesizes SWNTs on a flat substrate. It involves several key steps: catalyst nanoparticles are directly deposited on a flat substrate; the substrate is heated to a high temperature; SWNTs are formed when carbon precursors flow through the substrate. Reaction conditions, such as temperature, carbon precursors, catalysts, substrates, flowrate, heating speed, or an external field, could be adjusted to control the growth process.

There are several advantages to directly grow SWNTs on surface. SWNTs on a flat substrate could be directly used for property characterization and electrical device fabrication. No sonication or oxidative purification is involved in post treatments,



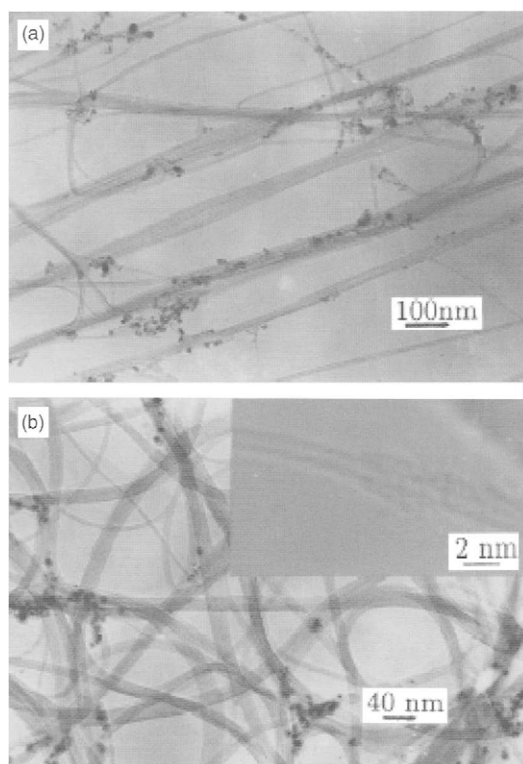


Figure 5. SWNTs synthesized from floating catalysts. Adapted with permission from Cheng et al. [36]. Copyright (1998) American Institute of Physics.

which greatly reduces the possibility to form defects. Catalysts could be patterned on surface by conventional lithography to define the location of SWNTs, which is essential to applications such as field emission, FETs and chemical sensors. Diameter of catalyst particles on surface could be synthesized in a predictable way, which could subsequently control the diameter of SWNTs. External guidance such as electrical field could be introduced to the substrate to direct SWNT orientation. Morphology and properties of as-grown SWNTs could be directly characterized by AFM, scanning electron microscopy (SEM) or Raman spectroscopy. Because of those benefits, surface growth has become an important approach to generate high-quality SWNTs for nano-electronic devices. Catalysts synthesis and growth conditions have been improved rapidly and more delicate controls in SWNT growth are expected in near future.

### 2.2.1. Catalyst preparation

Most of the catalysts used in surface growth of SWNT are transitional metals, including iron (Fe), cobalt (Co) and nickel (Ni). It is critical to prepare catalyst particles with size less than 5 nm on surface because diameter of SWNTs is controlled

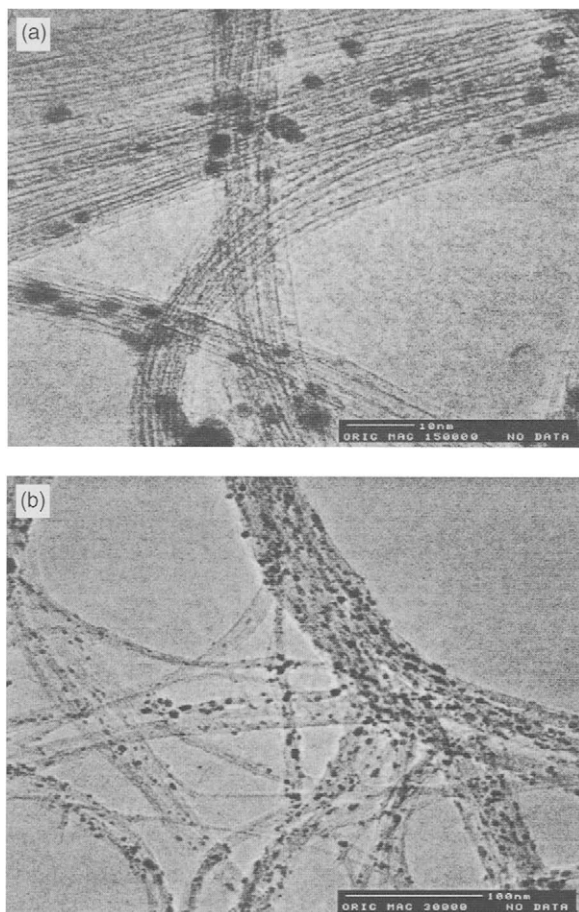


Figure 6. SWNTs grown from HiPco process. Adapted with permission from Bronikowski et al. [37]. Copyright (2001) Elsevier.

by the diameter of catalyst particles. A variety of methods have been developed to prepare catalyst nanoparticles on a flat substrate for SWNT growth.

Nanoparticles could be impregnated in a porous support and transferred to a surface. Dai and his coworkers at Stanford University carried out the first surface growth of SWNTs using an adapted catalyst for bulk synthesis [40]. They impregnated  $\text{FeCl}_3/\text{Mo}(\text{acac})_2$  into an  $\text{Al}_2\text{O}_3$  support by soaking and grounding, and deposited the catalysts on a substrate patterned with resists. After the resists were lifted off, the catalysts were confined on specific locations on the substrate. CVD was performed at 900 °C, using methane as carbon precursor. SWNTs were rooted in the catalyst patterns, some of which bridge two islands. AFM and TEM observations showed that SWNTs have diameters of 1–3 nm and length up to several micrometers

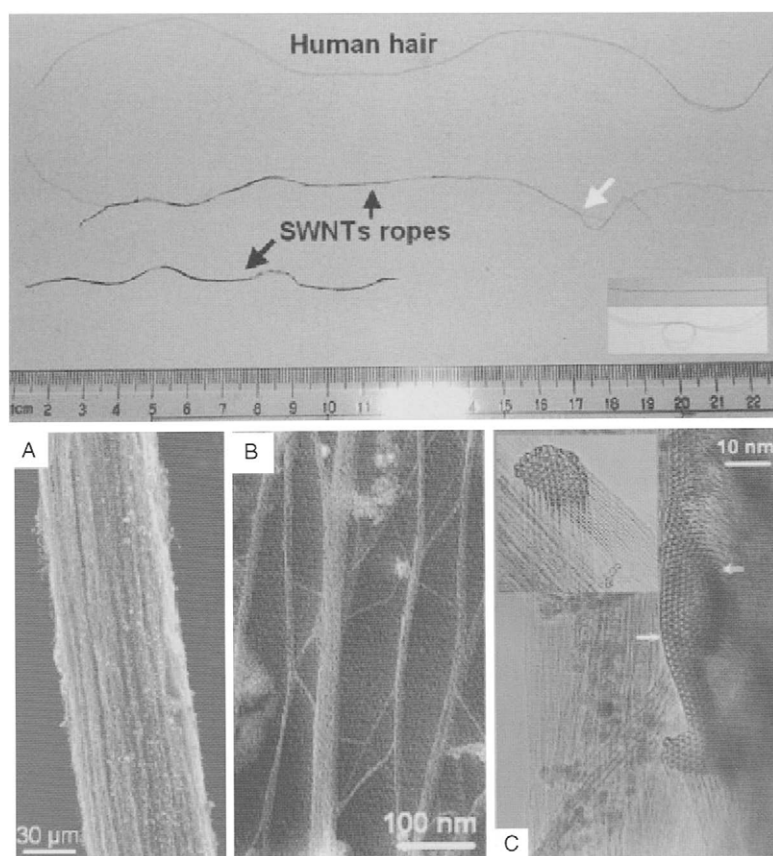


Figure 7. SWNT strands grown using floating catalyst. Adapted with permission from Zhu et al. [38]. Copyright (2002) Science.

(Fig. 8). Conductivity measurements on individual nanotubes have shown that the SWNTs are of similar quality as laser-grown SWNTs [41]. Because of the simplicity and high quality of produced SWNTs, this procedure was widely used to develop electrical interconnects and electrical devices. Growth on catalyst patterned on 4-inch wafers has also been achieved [42].

O'Brian group at Columbia University developed a sol-gel catalyst to direct the SWNT growth on surface [43,44]. They prepared catalyst supports composed of mesoscopic silica. Catalyst precursors such as  $\text{FeCl}_3$  or  $\text{CoCl}_2$  were incorporated in the silica during the sol-gel process. The sol-gel catalysts were transferred to a substrate using soft lithography and formed a thin film upon drying. The mesoscopic supports could maintain highly ordered porous structure at the growth temperature, which was believed to promote SWNT growth efficiency. Carbon precursors for CVD growth

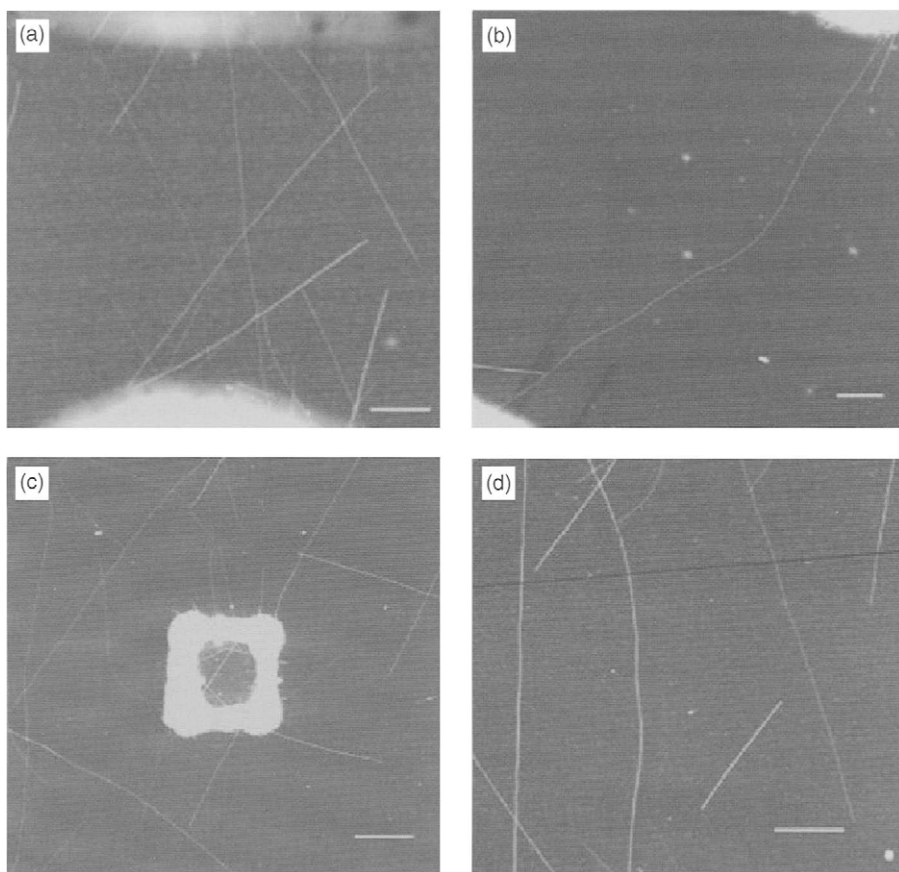


Figure 8. SWNTs grown from catalysts on surface. Reprinted with permission from Kong et al. [40]. Copyright (1998) Nature Publishing Group.

could be either methane [43] or alcohols [44]; SWNTs with controllable orientations and diameters were produced using methane, while superlong, horizontal aligned SWNTs were obtained when alcohol was used as a carbon precursor.

Metal film with thickness of several nanometers could be used as catalysts to grow SWNTs on surface. Generally, metal film (Fe, Co, Mo) could be formed with precisely controlled thickness on a substrate by thermal evaporation or sputtering. Prior to growth, metal films are annealed by heating up to several hundred degrees of Celsius. The metal films are disrupted and converted into nanoparticles. SWNTs are then grown from those nanoparticles using either methane or acetylene as carbon precursors. Growth temperatures are related to types of feeding gas. SWNT growth takes place at 900 °C using methane [45,46] and at 800 °C when using acetylene [47].

Multilayer catalyst systems showed better growth efficiency than a single layer of metal. For example, 10 nm Al/1.0 nm Fe/0.2 nm Mo gave better growth results than a single Fe film with same thickness (Fig. 9) [46]. It is very convenient to fabricate transition metal films on substrates by this procedure. However, it is difficult to precisely control the size of the catalyst particles, which limits applications of this physical deposition approach to prepare SWNTs.

Catalyst nanoparticles could also be prepared by wet chemistry approach. The most straightforward method is to directly impregnate metal salts onto a surface [12]. This approach was first developed by Hafner et al. at Harvard University to grow CNTs on AFM cantilevers. In this approach, a substrate is dipped into isopropanol or ethanol solutions of  $\text{FeCl}_3$  at extremely low concentration of  $\text{FeCl}_3$  (less than 150  $\mu\text{g/ml}$ ) to form isolated nanoparticles on the substrate. The substrate was then rinsed with hexane because it did not dissolve  $\text{FeCl}_3$ . Nanoparticles were formed after the substrate was annealed at 700–800 °C. SWNTs were grown with ethylene at 800 °C. Because it is very simple, this method is widely used to produce isolated SWNTs on surface and AFM cantilevers. It is also notable that some

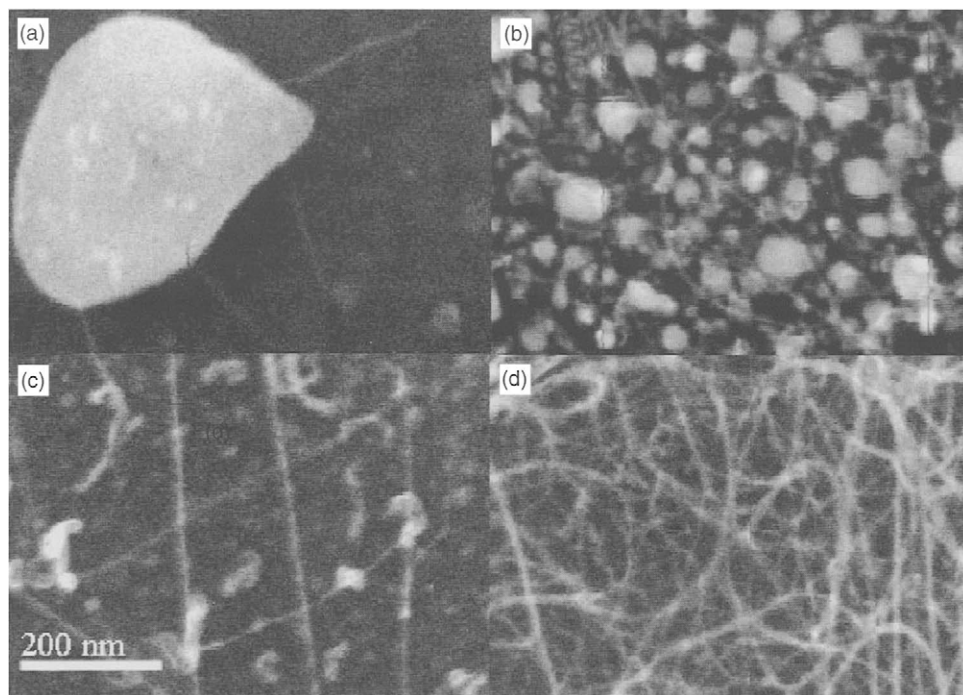


Figure 9. SWNTs grown on 1.0 nm Fe deposited on Si with an underlayer of (a) 0 nm, (b) 20 nm Ir, (c) 1 nm Al and (d) 10 nm Al. (c) and (d) also have 0.2 nm Mo as cocatalyst. Reprinted with permission from Delzeit et al. [46]. Copyright (2001) Elsevier.

nanotubes are about several hundred nanometers long and stand on the surface. Those nanotubes could be picked up when they are scanned by an AFM tip, which could serve as nanoprobe tips for high-resolution AFM imaging.

To control the size of catalyst nanoparticles, it is a more systematic approach to synthesize nanoparticles with defined diameter in solution and then transfer them onto a surface. Synthesis of nanoparticles by wet chemistry has been capable of producing nanoparticles with predictable structures [48–50]. Adjusting reactant ratio, protecting agents, temperature and other reaction conditions could precisely control the size, shape and components of nanoparticles. Such uniform nanoparticles could be transferred to a flat substrate and act as catalysts for SWNT growth. Liu et al. synthesized monodisperse Fe/Mo nanoparticles with diameter of about 3 nm by thermal decomposition of  $\text{Fe}(\text{CO})_5$  and  $\text{Mo}(\text{CO})_6$  [51]. Those nanoparticles could be transferred to a surface and catalyze SWNT growth. Cheung et al. further improved this approach and synthesized Fe nanoparticles with different diameters by adjusting the reactants [52]. Nanotubes with diameters of 3–7 nm were obtained from those nanoparticles. Dai et al. used ferritin, a protein incorporated with  $\text{FeCl}_3$ , to prepare  $\text{Fe}_2\text{O}_3$  nanoparticles on  $\text{SiO}_2$  substrates (Fig. 10) [53]. By controlling the amount of  $\text{FeCl}_3$  incubated in ferritin, nanoparticles with different diameters could be made. SWNTs with average diameter of 2 and 3 nm were obtained. Other uniform size catalysts for SWNT growth on surface include molecular clusters [54], dendrimer carriers [55], diblock copolymer micelles [56] and particles formed via surface reactions [57]. It is critical to prepare nanoparticles stable at high temperature or catalyst with improved growth efficiency at a low temperature in further development.

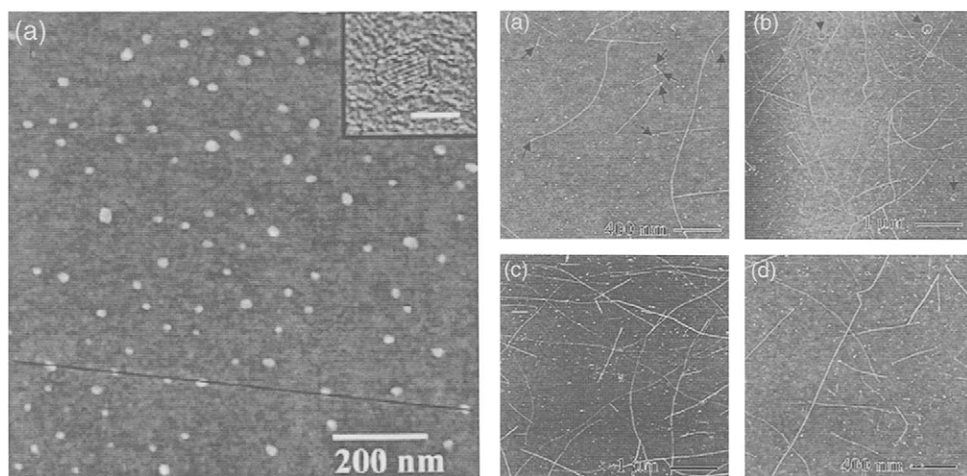


Figure 10. Discrete nanoparticles and SWNTs grown on surface. Adapted with permission from Li et al. [53]. Copyright (2001) American Chemical Society.

### 2.2.2. Carbon precursors

Surface growth of SWNT is very sensitive to components of feeding gases. Types of carbon precursors, carrier and additive gases could affect the growth process. So far, carbon precursors include methane [32], ethylene [58], carbon monoxide [59] and alcohols [60]. Hydrogen is widely used as an additive to prevent amorphous carbon deposition [42]. Other additives such as water and thiophen are also added in trace amounts to retain the activity of catalysts and promote growth efficiency [38,61].

Ethylene and methane are most widely used hydrocarbons for SWNT growth. Methane is used as a carbon precursor at high temperature (900–1000 °C) [32,33]. Ethylene as carbon source enable the growth to be carried out at a relatively low temperature (700–800 °C) [12,62]. Other than generating SWNTs from the catalyst nanoparticles, hydrocarbons could also take a self-pyrolysis path that forms amorphous carbon. Amorphous carbon could deposit on catalyst surface and disrupt its catalytic activity. To prevent catalysts from poisoning,  $H_2$  is normally mixed into feeding gases because it serves to decrease the rate of hydrocarbon decomposition by hydrogenating reactive carbon species. The hydrocarbon decomposition is slowed down because  $H_2$  is a product of the reaction. SWNTs only grow in a narrow range of the ratio between  $H_2$  and hydrocarbons. For example, best growth condition for  $Al_2O_3$  supported Fe/Mo catalysts is 90% to 70% of methane mixed with hydrogen [42]. Recently, water was found to be a very effective additive to promote growth efficiency. By adding a trace amount of water vapor into mixtures of ethylene, helium and hydrogen, SWNTs grow vertically and form dense forests on surface (Fig. 11). The yield is up to 50 000% [61]. The effect of water is due to the ability of water vapor to remove amorphous carbon and maintain catalyst activity during the growth.

Carbon monoxide (CO) is another carbon source used to produce SWNTs. Dai et al. performed the first CVD growth of SWNTs using molybdenum to catalyze disproportionation of CO at 1200 °C [27]. In bulk growth, SWNTs produced from CO have much less amorphous carbon than those from methane [63]. Zheng et al. used CO to grow SWNTs on surface [59]. They found that adding hydrogen could greatly enhance the growth efficiency. SWNTs could grow on surface in a relatively broad range of ratio between CO and  $H_2$ . The highest yield of SWNTs was achieved when the concentration of  $H_2$  was between 35% and 65% (Fig. 12). The effect of hydrogen could be understood by two possible explanations: (1) hydrogen directly reacts with CO, producing carbon and  $H_2O$  to promote SWNT growth; (2) hydrogen interacts with catalyst nanoparticles so that the activity toward CO disproportionation is enhanced.

Alcohols are new additions for SWNT CVD. Maruyama et al. first used alcohol vapors to grow SWNTs at 700–800 °C under low pressure. SWNTs formed on Fe/Co bimetallic catalysts supported on zeolites [60]. TEM and SEM showed that the products are clean SWNTs without amorphous carbon coating on sidewalls (Fig. 13). Thick mat and vertically aligned SWNT were also produced on surface using alcohols [64,65]. Alcohols appear to give better growth efficiency than methane or CO. It was hypothesized that OH radicals formed at high temperature from alcohol might remove amorphous carbon efficiently during the growth, leaving only pure SWNTs as product [66]. It was also believed that OH radicals help retain catalyst activity. Other groups rapidly adapted this approach because alcohols were safer, cheaper and simpler than CO and

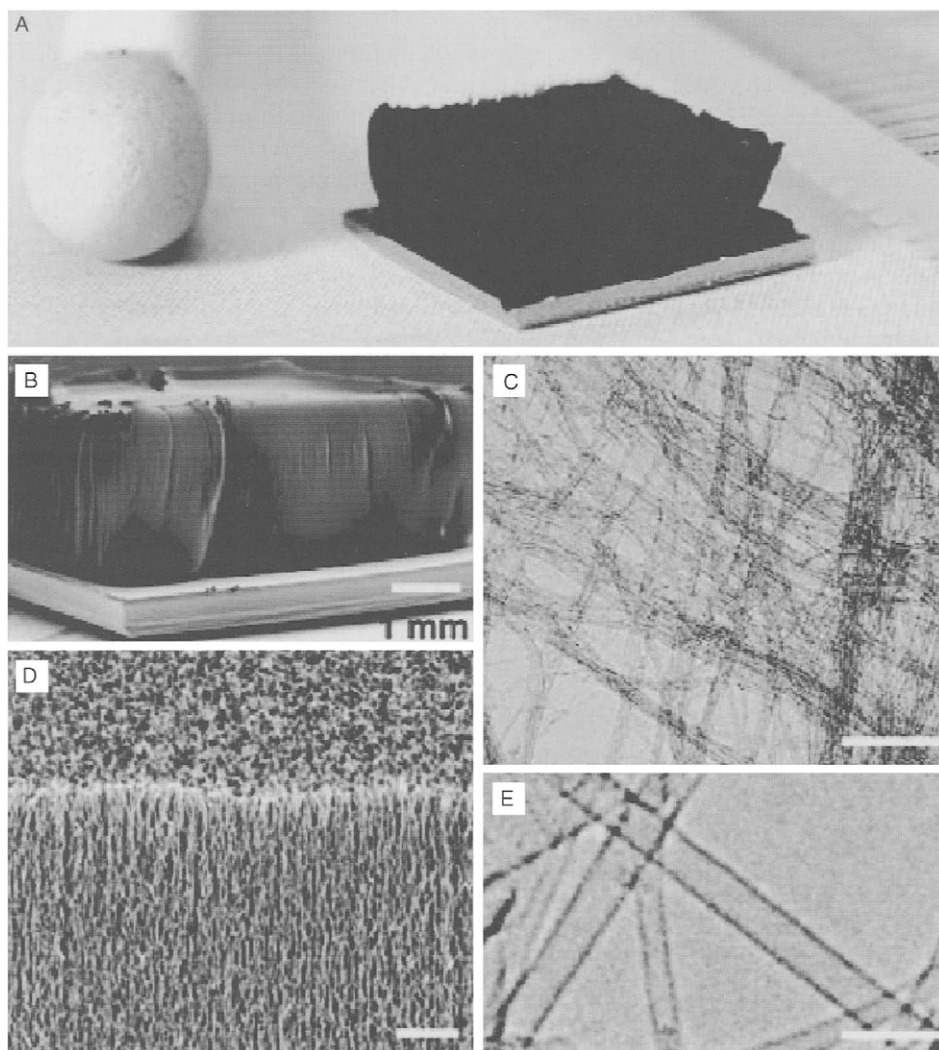


Figure 11. SWNT forest by water-assisted growth. Reprinted with permission from Hafner et al. [62]. Copyright (2004) Science.

methane. For instance, Huang et al. produced ultralong and flow-aligned SWNTs from mesoscopic silica catalyst with ethanol as carbon precursor [44]. Zheng et al. grew a single SWNT up to 4 cm long from iron catalyst with ethanol [67].

### 2.2.3. Substrate

Substrates for surface growth of SWNT must possess several properties: they must be thermally stable at growth temperature; they should not react with the



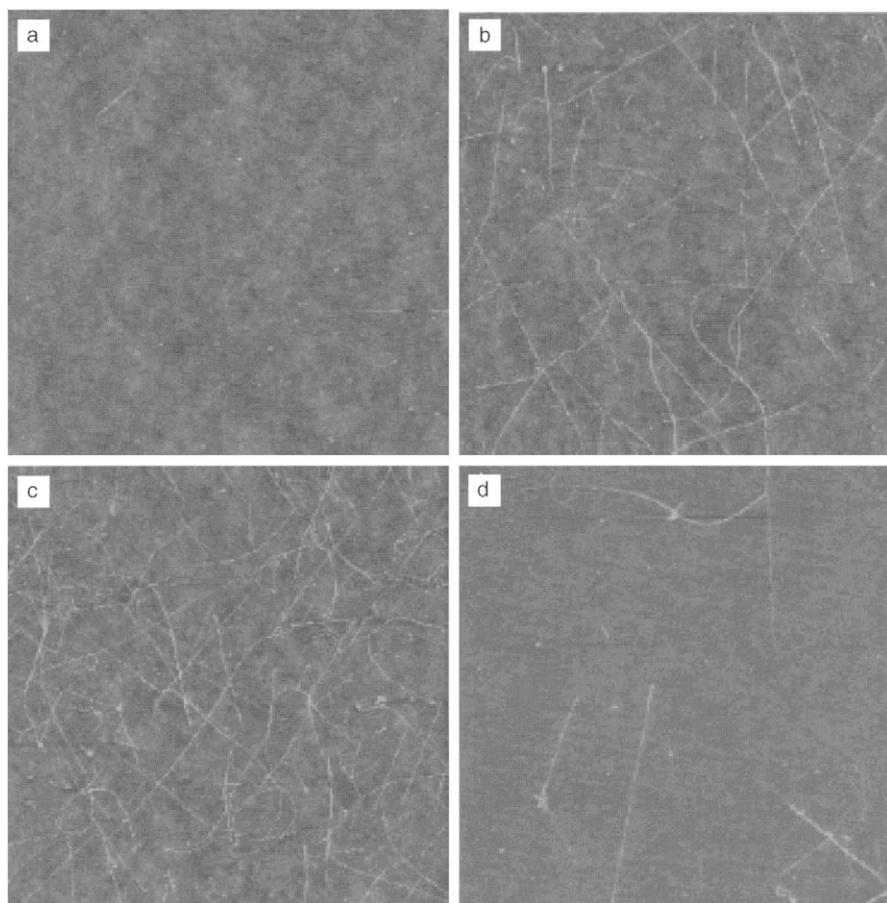


Figure 12. SWNTs grown on Si/SiO<sub>2</sub> surfaces at different hydrogen concentrations. (a) Pure CO, (b) 20% H<sub>2</sub> in CO, (c) 50% H<sub>2</sub> in CO and (d) 80% H<sub>2</sub> in CO. Reprinted with permission from Zheng et al. [59]. Copyright (2002) American Chemical Society.

catalysts under growth condition; they should be free of amorphous carbon deposition and they need to be flat enough for AFM or SEM characterization. Silicon is widely used as a substrate for SWNT growth because they meet the above requirements. Additionally, clean and flat wafers are commercially accessible at relatively low cost.

Other oxide substrates used for SWNT growth include Si<sub>3</sub>N<sub>4</sub>, sapphire, MgO and CaO. Substrate properties could affect growth result. For example, Hongo et al. found that orientation of the crystallographic face on a sapphire substrate greatly affected growth of SWNTs at 800 °C; the largest quantity of SWNTs were produced on A-face, followed by R- and C-face (Fig. 14) [68]. Other than oxide substrates,

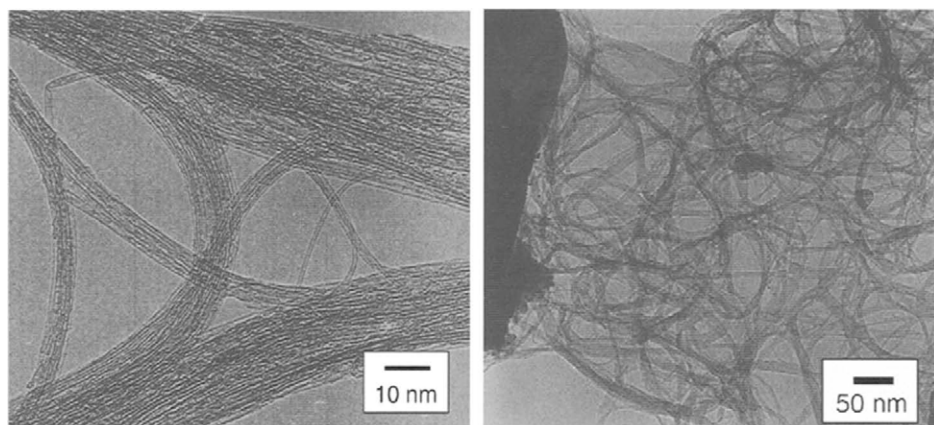


Figure 13. SWNTs grown from alcohol. Adapted with permission from Maruyama et al. [60]. Copyright (2002) Elsevier.

SWNT can also grow on metals with high melting point, such as molybdenum [69]. The metal substrate is essential to grow SWNTs under guidance of electric fields because metal electrodes are required to apply alignment voltage [30].

### 3. DISCUSSIONS

Critical to both fundamental research and industrial application of SWNTs is to gain control over growth. There are two aspects in controlling growth of SWNTs: morphology control and structure control. Morphology control focuses on manipulating the location, length and orientation of SWNT on surface; structure control aims to make SWNTs with predictable diameter and chiral angle. So far, much of the efforts have been focused on the morphology control and only a few studies have aimed to control the detailed structure of SWNTs.

#### 3.1. Diameter control

Diameter and chiral angle of an SWNT determine its electronic structure. Electronic structure of an SWNT could be restrained to some extent by just controlling its diameter. The diameter of an SWNT is controlled by the size of catalyst nanoparticles in CVD process. Dai et al. produced SWNTs of different diameters with iron oxide nanoparticles of different diameters. It was observed that controlling the diameter of catalyst nanoparticles regulates the diameter of SWNTs [53]. They also used dendrimers as carriers to form nanoparticles with sizes of about 1 nm to produce SWNTs with narrower diameter distribution [55]. Liu et al. found a type of catalyst containing molecular clusters to be good catalysts for CVD growth of SWNTs [54]. The nanoclusters have well-defined chemical compositions, with 84 Mo atoms and 30 Fe atoms. These nanoparticles were identical in diameters of about 1.3 nm after being

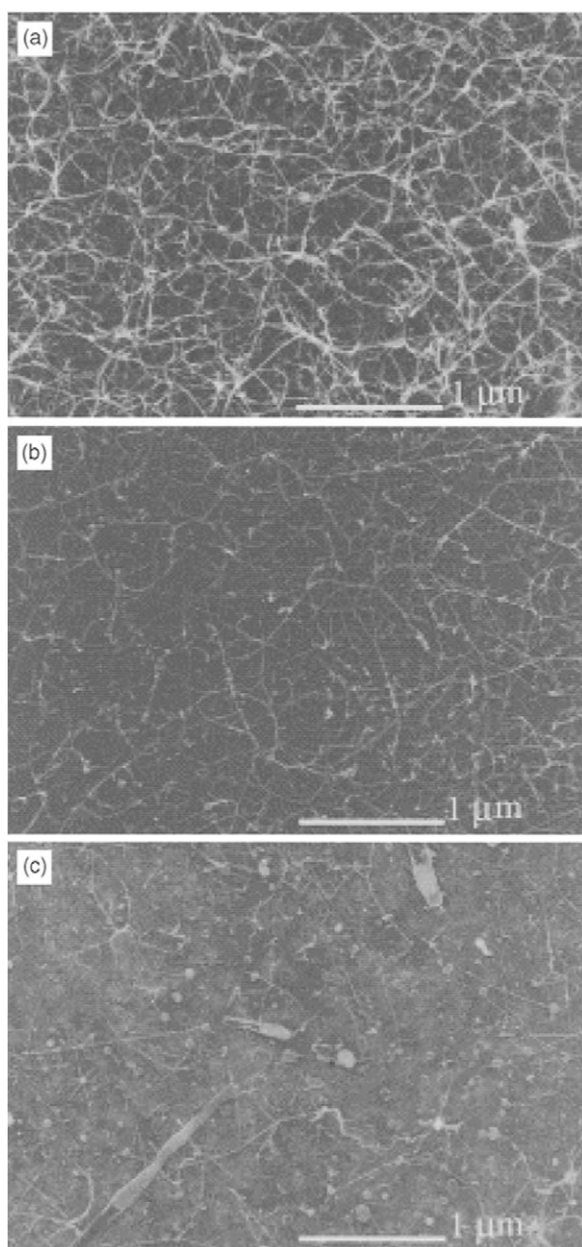


Figure 14. SWNTs grown on 0.2 nm Fe-coated sapphire substrates. (a) A-face, (b) R-face and (c) C-face orientation. Reprinted with permission from Franklin et al. [69]. Copyright (2002) Elsevier.

reduced with  $H_2$  at 900 °C. SWNTs could be grown by either methane or CO; the produced SWNTs have remarkable uniform diameter as revealed by AFM and Raman spectroscopy (Fig. 15). Nanoparticles were also prepared using diblock copolymers micelles, which produced uniformly dispersed nanoparticles over large area on surfaces [56]. Overall, significant progresses have been made in synthesizing catalyst nanoparticles for SWNT growth; however, there are still a number of challenges. For example, although nanoparticles made in solutions have uniform diameter distribution, they encountered severe evaporation and aggregation at growth temperature, which resulted in change of the size during the growth. Further development in diameter control would require catalyst nanoparticles that are stable at high temperature or new CVD process that could produce SWNT at low temperature.

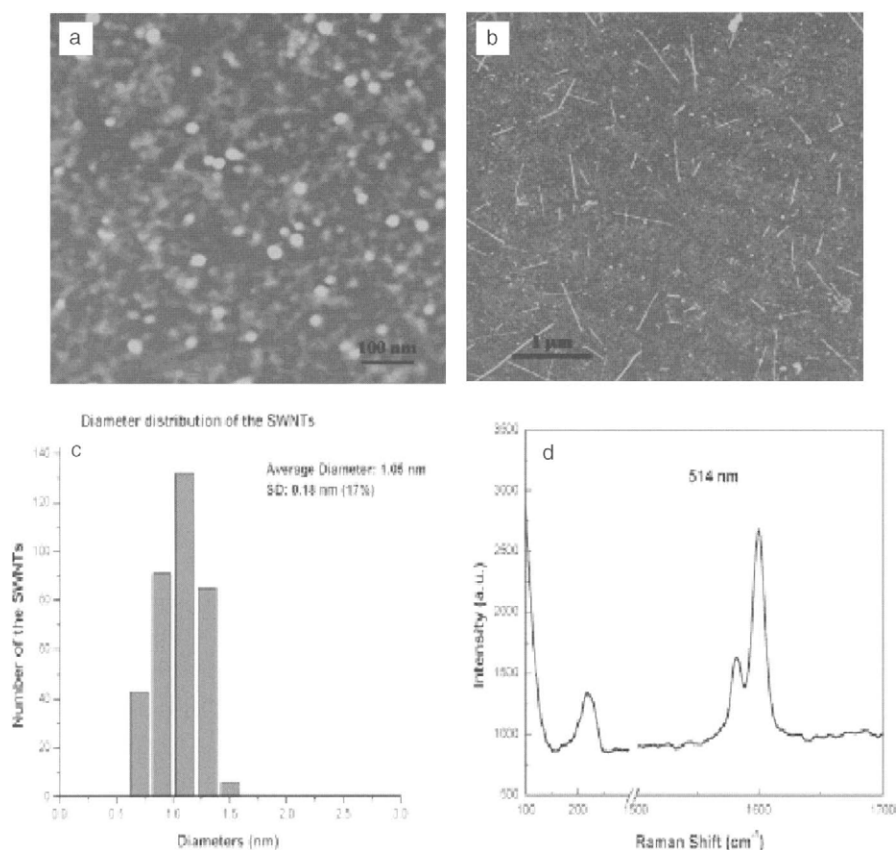


Figure 15. Fe/Mo clusters and SWNTs grown on surface. (a) AFM image of Fe/Mo nanoclusters, (b) AFM image of SWNTs, (c) diameter distributions of nanotubes and (d) Raman spectra of nanotubes. Adapted with permission from An et al. [54]. Copyright (2002) American Chemical Society.

### 3.2. Length control

It is more complicated to control length than diameter of SWNTs due to the lack of understandings of growth mechanism. The length of as-grown SWNTs on surface is related to feeding gases, heating speed, growth temperature and catalysts. Dai et al. used a mixture of  $C_2H_4$ ,  $CH_4$  and  $H_2$  as feeding gases to grow SWNTs up to 680  $\mu m$  long from iron oxide nanoparticles at 900 °C [70]. Those nanotubes had diameter of 2 nm, extended on surface and formed loop structures (Fig. 16). Electrical measurements showed that long nanotubes had similar electrical properties along the tube axis. It is believed that the nanotubes need to flow and wave in the gas during the growth to reach such length. Liu et al. developed a fast heating method to grow ultralong SWNT with length up to several millimeters [71,72]. They carried out the growth by heating up catalysts in a mixture of  $CO/H_2$  from room temperature to 900 °C in a few seconds. A single SWNT grown from Fe/Mo catalysts could be up to 1.5 cm long with growth time of 20 min. It is believed that those ultralong SWNTs grew with a tip-growth mechanism, which was supported by observations of catalyst particles at the end of SWNTs and facts that these long nanotubes could grow over barriers and across trenches.

### 3.3. Orientation control

In order to achieve orientation control, external guidance must be provided upon growth process. These external forces could be electrical field, magnetic field, gravity or mechanical interaction between grown SWNT with the feeding gas. Dai et al. at Stanford University first demonstrated aligned SWNTs grown under guidance of an electrical field. They applied a lateral electrical field during CVD growth, in which SWNTs were orientated along the electrical field (Fig. 17) [30,31]. This alignment originated from the high polarizability of SWNTs. Aligning torques and forces on the nanotubes were generated by an induced dipole moment. By growing SWNTs along electrical field under different directions, crossed nanotube structures were prepared.

Another promising approach to orientate SWNTs is to use feeding gas to align SWNTs along flow direction. This is normally associated with length control. The ultralong nanotubes discussed in last section are generally aligned by the gas flow. Gas-flow-aligned SWNT structure was achieved by the fast heating approach introduced in length control [71,72]. In this approach, Fe/Mo bimetallic nanoparticles were used as catalysts and a  $CO/H_2$  mixture was used as feeding gas. No electrodes were required to guide the growth direction of SWNTs. Multidimensional SWNT structures can be easily prepared by repeated growth on the sample along different directions. SWNTs were aligned with the gas flow direction and could be as long as several millimeters (Fig. 18). They were believed to grow with a tip-growth mechanism. In addition, the fast heating process was believed to cause convection of the gas flow due to the temperature difference between the substrate and feed gas. Such convection flow of the feed gas lifted the nanotubes upward and kept them floating and waving in the gas until they were caught by the laminar flow to the substrate. The actively growing nanotubes then floated in feeding gas and grew along the direction of the laminar flow. The extreme length achieved and control of orientation may prove their value in future nanoelectronic fabrications, since millions of devices could be built on just a single SWNT.

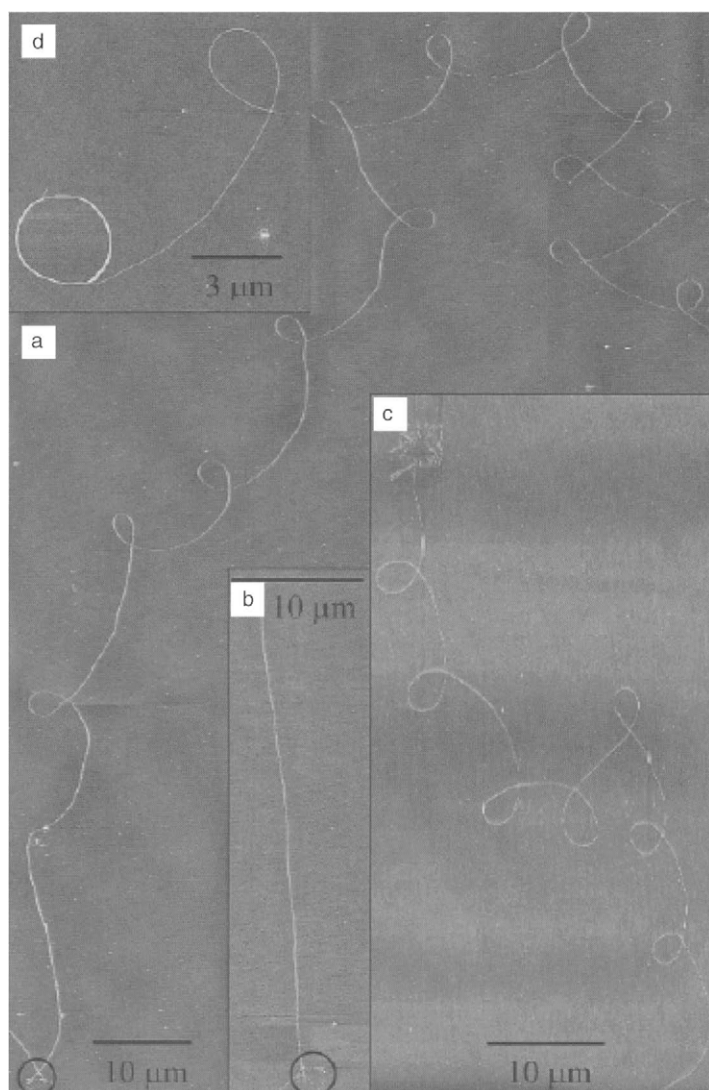


Figure 16. Ultralong SWNTs. Reprinted with permission from Huang et al. [71]. Copyright (2002) American Chemical Society.

#### 4. SUMMARIES AND OUTLOOKS

Overall, great progress has been made in developing CVD of SWNTs. A variety of catalysts have been synthesized and discovered. CVD condition has been continuously optimized to produce SWNTs with high quality and large quantity. Yield of CVD production was greatly improved. Diameter and orientation of SWNTs were

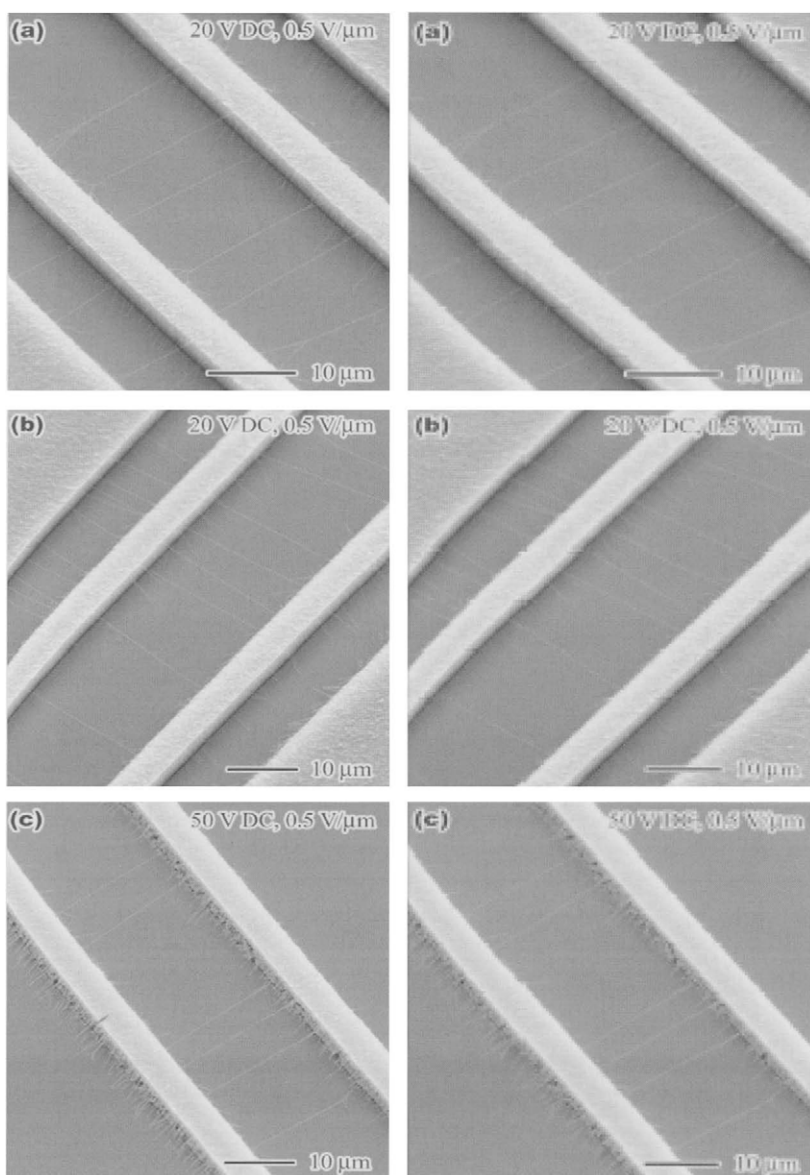


Figure 17. SWNTs aligned by electric field. Reprinted with permission from Zhang et al. [31]. Copyright (2001) American Institute of Physics.

controlled in the growth process. Such progress greatly facilitated fundamental research and practical application.

However, challenging issues still remain. To date, the structure of SWNTs synthesized varies from zigzag and armchair to all kinds of chiral forms. All those types

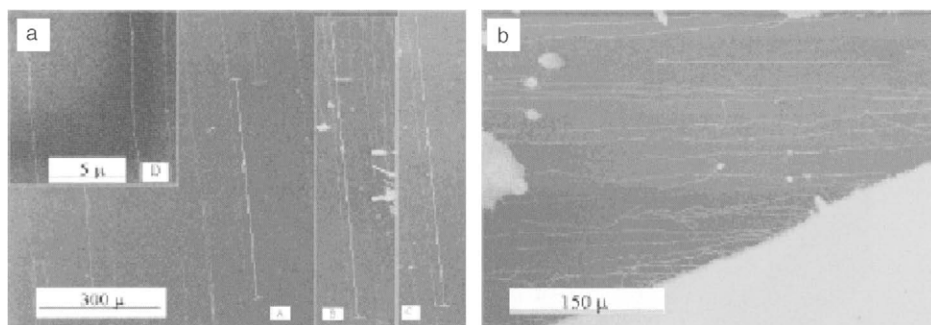


Figure 18. Aligned SWNTs grown on surface by fast heating methods. Reprinted with permission from Huang et al. [72]. Copyright (2003) American Chemical Society.

of nanotube coexist in the product. Complete control of selective growth or separation of metallic and semiconducting SWNTs has not been achieved. It is likely that the preferential growth [73] and postgrowth [74,75] treatment could possibly solve the problem to produce only semiconducting or metallic SWNTs. These remaining challenges, as well as the quest for better understanding of the nanotube growth mechanism, are going to be in the field of CVD of SWNTs.

## REFERENCES

1. P. Avouris, *Acc. Chem. Res.* **35** (2002) 1026.
2. A. Oberlin, M. Endo and T. Koyama, *Carbon* **14** (1976) 133.
3. S. Iijima, *Nature* **354** (1991) 56.
4. D. S. Bethune, C. H. Kiang, M. S. Devries, G. Gorman, R. Savoy, J. Vazquez and R. Beyers, *Nature* **363** (1993) 605.
5. S. Iijima and T. Ichihashi, *Nature* **363** (1993) 603.
6. R. Martel, T. Schmidt, H. R. Shea, T. Hertel and P. Avouris, *Appl. Phys. Lett.* **73** (1998) 2447.
7. S. J. Tans, M. H. Devoret, H. J. Dai, A. Thess, R. E. Smalley, L. J. Geerligs and C. Dekker, *Nature* **386** (1997) 474.
8. K. Matsumoto, S. Kinoshita, Y. Gotoh, T. Uchiyama, S. Manalis and C. Quate, *Appl. Phys. Lett.* **78** (2001) 539.
9. W. Zhu, C. Bower, O. Zhou, G. Kochanski and S. Jin, *Appl. Phys. Lett.* **75** (1999) 873.
10. H. Z. Geng, R. Rosen, B. Zheng, H. Shimoda, L. Fleming, J. Liu and O. Zhou, *Adv. Mater.* **14** (2002) 1387.
11. J. H. Hafner, C. L. Cheung and C. M. Lieber, *J. Am. Chem. Soc.* **121** (1999) 9750.
12. J. H. Hafner, C. L. Cheung, T. H. Oosterkamp and C. M. Lieber, *J. Phys. Chem. B* **105** (2001) 743.
13. J. H. Hafner, C. L. Cheung, A. T. Woolley and C. M. Lieber, *Prog. Biophys. Mol. Biol.* **77** (2001) 73.



14. J. Kong, N. R. Franklin, C. W. Zhou, M. G. Chapline, S. Peng, K. J. Cho and H. J. Dai, *Science* **287** (2000) 622.
15. M. Ouyang, J. L. Huang and C. M. Lieber, *Acc. Chem. Res.* **35** (2002) 1018.
16. R. Saito, G. Dresselhaus and M. S. Dresselhaus, *Physical Properties of Carbon Nanotubes*, Imperial College Press, London, 1998, p. 258.
17. T. W. Odom, J. L. Huang, P. Kim and C. M. Lieber, *J. Phys. Chem. B* **104** (2000) 2794.
18. W. J. Liang, M. Bockrath, D. Bozovic, J. H. Hafner, M. Tinkham and H. Park, *Nature* **411** (2001) 665.
19. A. Javey, J. Guo, Q. Wang, M. Lundstrom and H. J. Dai, *Nature* **424** (2003) 654.
20. S. J. Wind, J. Appenzeller, R. Martel, V. Derycke and P. Avouris, *Appl. Phys. Lett.* **80** (2002) 3817.
21. F. Li, H. M. Cheng, S. Bai, G. Su and M. S. Dresselhaus, *Appl. Phys. Lett.* **77** (2000) 3161.
22. T. W. Tombler, C. W. Zhou, L. Alexseyev, J. Kong, H. J. Dai, L. Lei, C. S. Jayanthi, M. J. Tang and S. Y. Wu, *Nature* **405** (2000) 769.
23. J. Gavillet, A. Loiseau, C. Journet, F. Willaime, F. Ducastelle and J. C. Charlier, *Phys. Rev. Lett.* **87** (2001) 275504-1–275504-4.
24. A. Maiti, C. J. Brabec and J. Bernholc, *Phys. Rev. B* **55** (1997) R6097.
25. T. W. Ebbesen and P. M. Ajayan, *Nature* **358** (1992) 220.
26. A. Thess, R. Lee, P. Nikolaev, H. J. Dai, P. Petit, J. Robert, C. H. Xu, Y. H. Lee, S. G. Kim, A. G. Rinzler, D. T. Colbert, G. E. Scuseria, D. Tomanek, J. E. Fischer and R. E. Smalley, *Science* **273** (1996) 483.
27. H. J. Dai, A. G. Rinzler, P. Nikolaev, A. Thess, D. T. Colbert and R. E. Smalley, *Chem. Phys. Lett.* **260** (1996) 471.
28. D. L. Smith, *Thin-Film Deposition: Principles and Practice*, McGraw-Hill, New York, 1995, p. xxiii.
29. J. Liu, S. S. Fan and H. J. Dai, *Mrs. Bull.* **29** (2004) 244.
30. A. Ural, Y. M. Li and H. J. Dai, *Appl. Phys. Lett.* **81** (2002) 3464.
31. Y. G. Zhang, A. L. Chang, J. Cao, Q. Wang, W. Kim, Y. M. Li, N. Morris, E. Yenilmez, J. Kong and H. J. Dai, *Appl. Phys. Lett.* **79** (2001) 3155.
32. J. Kong, A. M. Cassell and H. J. Dai, *Chem. Phys. Lett.* **292** (1998) 567.
33. A. M. Cassell, J. A. Raymakers, J. Kong and H. J. Dai, *J. Phys. Chem. B* **103** (1999) 6484.
34. M. Su, B. Zheng and J. Liu, *Chem. Phys. Lett.* **322** (2000) 321.
35. Q. W. Li, Y. Hao, X. H. Li, J. Zhang and Z. F. Liu, *Chem. Mater.* **14** (2002) 4262.
36. H. M. Cheng, F. Li, G. Su, H. Y. Pan, L. L. He, X. Sun and M. S. Dresselhaus, *Appl. Phys. Lett.* **72** (1998) 3282.
37. M. J. Bronikowski, P. A. Willis, D. T. Colbert, K. A. Smith and R. E. Smalley, *J. Vac. Sci. Technol. A* **19** (2001) 1800.
38. H. W. Zhu, C. L. Xu, D. H. Wu, B. Q. Wei, R. Vajtai and P. M. Ajayan, *Science* **296** (2002) 884.
39. Y. L. Li, I. A. Kinloch and A. H. Windle, *Science* **304** (2004) 276.
40. J. Kong, H. T. Soh, A. M. Cassell, C. F. Quate and H. Dai, *Nature* **395** (1998) 878.
41. H. T. Soh, C. F. Quate, A. F. Morpurgo, C. M. Marcus, J. Kong and H. J. Dai, *Appl. Phys. Lett.* **75** (1999) 627.

42. N. R. Franklin, Y. M. Li, R. J. Chen, A. Javey and H. J. Dai, *Appl. Phys. Lett.* **79** (2001) 4571.
43. L. Huang, S. J. Wind and S. P. O'Brien, *Nano Lett.* **3** (2003) 299.
44. L. M. Huang, X. D. Cui, B. White and S. P. O'Brien, *J. Phys. Chem. B* **108** (2004) 16451.
45. H. B. Peng, T. G. Ristorph, G. M. Schurmann, G. M. King, J. Yoon, V. Narayanamurti and J. A. Golovchenko, *Appl. Phys. Lett.* **83** (2003) 4238.
46. L. Delzeit, B. Chen, A. Cassell, R. Stevens, C. Nguyen and M. Meyyappan, *Chem. Phys. Lett.* **348** (2001) 368.
47. H. Cui, G. Eres, J. Y. Howe, A. Puretkzy, M. Varela, D. B. Geohegan and D. H. Lowndes, *Chem. Phys. Lett.* **374** (2003) 222.
48. L. M. Liz-Marzan, D. J. Norris, M. G. Bawendi, T. Betley, H. Doyle, P. Guyot-Sionnest, V. I. Klimov, N. A. Kotov, P. Mulvaney, C. B. Murray, D. J. Schiffrin, M. Shim, S. Sun and C. Wang, *MRS Bull.* **26** (2001) 981.
49. C. B. Murray, S. H. Sun, H. Doyle and T. Betley, *MRS Bull.* **26** (2001) 985.
50. C. B. Murray, S. H. Sun, W. Gaschler, H. Doyle, T. A. Betley and C. R. Kagan, *IBM J. Res. Dev.* **45** (2001) 47.
51. Y. Li, J. Liu, Y. Q. Wang and Z. L. Wang, *Chem. Mater.* **13** (2001) 1008.
52. C. L. Cheung, A. Kurtz, H. Park and C. M. Lieber, *J. Phys. Chem. B* **106** (2002) 2429.
53. Y. M. Li, W. Kim, Y. G. Zhang, M. Rolandi, D. W. Wang and H. J. Dai, *J. Phys. Chem. B* **105** (2001) 11424.
54. L. An, J. M. Owens, L. E. McNeil and J. Liu, *J. Am. Chem. Soc.* **124** (2002) 13688.
55. H. C. Choi, W. Kim, D. W. Wang and H. J. Dai, *J. Phys. Chem. B* **106** (2002) 12361.
56. Q. Fu, S. M. Huang and J. Liu, *J. Phys. Chem. B* **108** (2004) 6124.
57. H. C. Choi, S. Kundaria, D. W. Wang, A. Javey, Q. Wang, M. Rolandi and H. J. Dai, *Nano Lett.* **3** (2003) 157.
58. J. H. Hafner, C. L. Cheung and C. M. Lieber, *Nature* **398** (1999) 761.
59. B. Zheng, C. G. Lu, G. Gu, A. Makarovski, G. Finkelstein and J. Liu, *Nano Lett.* **2** (2002) 895.
60. S. Maruyama, R. Kojima, Y. Miyauchi, S. Chiashi and M. Kohno, *Chem. Phys. Lett.* **360** (2002) 229.
61. K. Hata, D. N. Futaba, K. Mizuno, T. Namai, M. Yumura and S. Iijima, *Science* **306** (2004) 1362.
62. J. H. Hafner, M. J. Bronikowski, B. R. Azamian, P. Nikolaev, A. G. Rinzler, D. T. Colbert, K. A. Smith and R. E. Smalley, *Chem. Phys. Lett.* **296** (1998) 195.
63. B. Zheng, Y. Li and J. Liu, *Appl. Phys. Mater. Sci. Process.* **74** (2002) 345.
64. Y. Murakami, S. Chiashi, Y. Miyauchi, M. H. Hu, M. Ogura, T. Okubo and S. Maruyama, *Chem. Phys. Lett.* **385** (2004) 298.
65. Y. Murakami, Y. Miyauchi, S. Chiashi and S. Maruyama, *Chem. Phys. Lett.* **377** (2003) 49.
66. S. Maruyama, Y. Murakami, Y. Shibuta, Y. Miyauchi and S. Chiashi, *J. Nanosci. Nanotechnol.* **4** (2004) 360.
67. L. X. Zheng, M. J. O'Connell, S. K. Doorn, X. Z. Liao, Y. H. Zhao, E. A. Akhadev, M. A. Hoffbauer, B. J. Roop, Q. X. Jia, R. C. Dye, D. E. Peterson, S. M. Huang, J. Liu and Y. T. Zhu, *Nat. Mater.* **3** (2004) 673.

68. H. Hongo, M. Yudasaka, T. Ichihashi, F. Nihey and S. Iijima, *Chem. Phys. Lett.* **361** (2002) 349.
69. N. R. Franklin, Q. Wang, T. W. Tombler, A. Javey, M. Shim and H. J. Dai, *Appl. Phys. Lett.* **81** (2002) 913.
70. W. Kim, H. C. Choi, M. Shim, Y. M. Li, D. W. Wang and H. J. Dai, *Nano Lett.* **2** (2002) 703.
71. S. M. Huang, X. Y. Cai and J. Liu, *J. Am. Chem. Soc.* **125** (2003) 5636.
72. S. M. Huang, B. Maynor, X. Y. Cai and J. Liu, *Adv. Mater.* **15** (2003) 1651.
73. Y. M. Li, D. Mann, M. Rolandi, W. Kim, A. Ural, S. Hung, A. Javey, J. Cao, D. W. Wang, E. Yenilmez, Q. Wang, J. F. Gibbons, Y. Nishi and H. J. Dai, *Nano Lett.* **4** (2004) 317.
74. M. S. Strano, C. A. Dyke, M. L. Usrey, P. W. Barone, M. J. Allen, H. W. Shan, C. Kittrell, R. H. Hauge, J. M. Tour and R. E. Smalley, *Science* **301** (2003) 1519.
75. R. Krupke, F. Hennrich, H. von Lohneysen and M. M. Kappes, *Science* **301** (2003) 344.

## Chapter 5

### Fabrication of fullerene nanostructures

H.-M. Zhang and L.-J. Wan

Institute of Chemistry, Chinese Academy of Sciences, Beijing 100080, China

#### 1. INTRODUCTION

Fullerenes and their derivatives have attracted considerable interest from both the scientific and technological points of view owing to their unique structural, chemical, and electronic properties. In this chapter, we present a summary of the recent works about the fabricating of fullerene and its derivative's nanostructures including surface two-dimensional assemblies, nanowires and nanotubes by electrochemical and self-assembly methods, and the electronic properties of several corresponding nanostructures. The structures of the various nanoarchitectures are characterized by scanning tunneling microscopy (STM), scanning electron microscopy (SEM), and transmission electron microscopy (TEM). Although most of the results are from our laboratory, apparently, many other research groups have made great contributions in this field. We expect more exciting achievements made by fellow scientists in the future.

#### 2. THE FORMATION OF HIGHLY-ORDERED C<sub>60</sub> AND C<sub>70</sub> ADLAYERS ON SINGLE-CRYSTAL SURFACES

STM, with its ability to image individual molecules, has been widely adopted as a tool to explore fullerene adlayers on surfaces [1]. With high-resolution STM, it was possible to determine the packing arrangements and even electronic structures of fullerene molecules adsorbed on various surfaces.

In 1990, the STM images of fullerene clusters on Au(111) and Au(110) were reported by Bethune and co-workers [2]. Since then, the adlayers of fullerenes, such as C<sub>60</sub> and C<sub>70</sub>, have been investigated on the surfaces of semiconductors (Si, GaAs, Ge) [3–5] and metals (Au, Ag, Cu, Pt) using STM in ultrahigh vacuum (UHV), in air and even in aqueous solution.

Weaver and co-workers [6] succeeded in the STM visualization of C<sub>60</sub> and C<sub>70</sub> layers prepared by solution-evaporation method on Au(111) and Au(110) surfaces in air and in aqueous 0.1 M HClO<sub>4</sub>. Hexagonal close-packed layers were obtained for both C<sub>60</sub> and C<sub>70</sub> on Au(111). The observed STM imaging properties of C<sub>70</sub> are consistent with the presence of groups of “standing-up” and “lying-down” orientations, with an effective height difference of 0.6–1.1 Å. While the fullerene layers are less ordered on Au(110), the molecules are more rigidly held and can yield STM images with resolved intramolecular carbon rings. Altman and Colton observed the growth of fullerene films by vapor deposition on Au(111) using UHV–STM. It was found that the molecules initially

adsorb at the intersections of multiple steps and edges of monatomic steps on narrow terraces[7]. As the coverage is increased, periodic arrays of short chains form at the steps separating wider terraces with the periodicity determined by the  $(2\sqrt{3} \times \sqrt{3})$ -Au(111) reconstruction. At higher coverage, hexagonal layers with a lattice constant of 1.0 nm grow out from the steps on both the upper and lower terraces, and the adsorption of the fullerenes lifts the reconstruction indicating a strong interaction between the fullerenes and Au(111), which is also elucidated by that the fullerene layer does not begin to desorb until 500 °C [8]. STM indicates two ordered commensurate structures,  $(2\sqrt{3} \times 2\sqrt{3})$  and  $(38 \times 38)$  in-phase structure.

Furthermore, Bard and co-workers [9] reported fullerene films prepared by the Langmuir–Blodgett (LB) method onto iodine-modified Pt(111). After that report, Uemura et al. [10] succeeded in preparing a well-defined epitaxial  $C_{60}$  adlayer on an Au(111) surface in aqueous  $HClO_4$  by transferring LB films of  $C_{60}$  and  $C_{70}$  onto bare and iodine-modified Au(111) electrodes. The fullerene films on air–water interfaces were prepared using Langmuir trough by means of spreading benzene solution. STM images show that both adlayers of  $C_{60}$  and the mixture of  $C_{60}$  and  $C_{70}$  on Au(111) surfaces in 0.1 M  $HClO_4$  possess hexagonal lattices. The commensurations of two  $C_{60}$  lattices can be assigned as  $(2\sqrt{3} \times 2\sqrt{3})$  and  $(7 \times 7)$ . The  $(2\sqrt{3} \times 2\sqrt{3})$  lattice seemed to be dominant in the film. Observed distances between hexagonally packed  $C_{60}$  molecules for both lattices are  $1.0 \pm 0.05$  nm. In the array of the mixture,  $C_{60}$  and  $C_{70}$  molecules can be clearly distinguished as individual dark and bright protrusions, which would be attributed to  $C_{60}$  and  $C_{70}$  molecules, respectively.  $C_{70}$  molecules with standing orientation are distributed randomly in the mixture adlayers. The experiment of electrochemical cyclic voltammogram (CV) shows that the epitaxial adlayers of fullerenes can be observed at whole double-layer potential range in 0.1 M  $HClO_4$ . Furthermore, the electrochemical replacement method has been proposed as a drastic improvement of the simple LB method to provide a high-quality epitaxial film with excellent uniformity [11]. In this method, fullerene adlayers on Au(111) are prepared by transferring them onto iodine-modified Au(111) (I/Au(111)), following the electrochemical replacement between the fullerene and iodine adlayers by the reductive desorption of iodine. Recently, the adsorption of fullerenes from non-aqueous solvents such as tetradecane [12], 1,2,4-trichlorobenzene (TCB) [13], and benzene [14] has independently come into use to prepare ordered adlayers of fullerenes on Au(111) in an epitaxial fashion. It should be noted that these various methods, including sublimation, the LB method, and adsorption from organic solvents, all provide essentially the same epitaxial lattices, either  $(2\sqrt{3} \times 2\sqrt{3})R30^\circ$  or the so-called “in-phase”  $C_{60}$  adlayers on Au(111). Fig. 1 is a typical STM image showing a  $(2\sqrt{3} \times 2\sqrt{3})R30^\circ$  structure of  $C_{60}$  molecules on Au(111) surface in 0.1 M  $HClO_4$  solution.

On Cu(111) surface, the  $C_{60}$  monolayers formed a  $(4 \times 4)$  structure in UHV [15,16]. On Ag(111) surface,  $C_{60}$  was found to show a stronger interaction with Ag atoms and form a  $(2\sqrt{3} \times 2\sqrt{3})R30^\circ$  structure [17]. Furthermore, it was found for both Ag(111) and Au(111), the same molecule in the same position on the surface could reversibly change contrast from bright to dim, due to the molecules bound in different rotational orientations on the surface (e.g. five-membered vs. six-membered ring on the surface) [18].

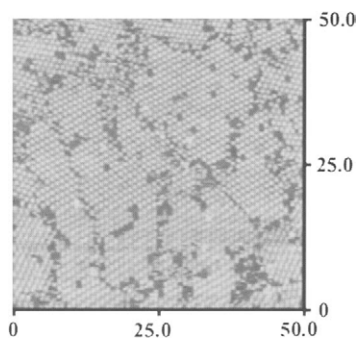


Figure 1. STM image of  $C_{60}$  on Au(111) surface in 0.1 M  $HClO_4$ .

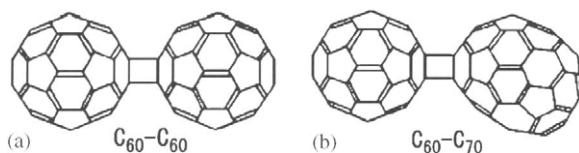


Figure 2. Chemical structures of [2+2]-type fullerene dimer ( $C_{60}-C_{60}$ ) (a) and the  $C_{60}-C_{70}$  cross-dimer ( $C_{60}-C_{70}$ ) (b).

As for fullerene dimers, Itaya and his co-workers used a unique synthetic method, based on a solid-state mechanochemical reaction, to prepare [2+2]-type fullerene dimers ( $C_{120}$ ) linked by two  $C_{60}$  cages and  $C_{60}-C_{70}$  cross-dimers ( $C_{130}$ ) linked by  $C_{60}$  and  $C_{70}$  cages shown in Fig. 2. They fabricated highly ordered adlayers on Au(111) by immersing the surface in benzene solution containing  $C_{120}$  or  $C_{130}$  molecules.  $(2\sqrt{3} \times 4\sqrt{3})R30^\circ$  and  $(2\sqrt{3} \times 5\sqrt{3})R30^\circ$  structures were observed in an aqueous  $HClO_4$  solution, while  $(2\sqrt{3} \times 4\sqrt{3})R30^\circ$ ,  $(2\sqrt{3} \times 5\sqrt{3})R30^\circ$ , and  $(7 \times 7)$  structures in UHV for the  $C_{120}$  dimer.  $C_{130}$  molecules were closely packed on the surface and each  $C_{60}$  or  $C_{70}$  monomer cage was discerned in the STM image of a  $C_{130}$  molecule [1,19].

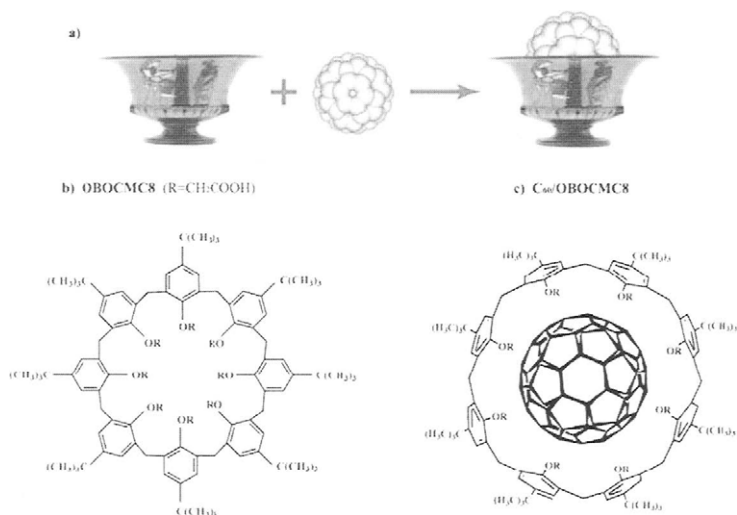
### 3. ADLAYERS OF CALIXARENE AND CALIXARENE/FULLERENE COMPLEX

Calixarenes and fullerenes have novel properties that make them ideal materials for nanoscale electronic devices. Calixarenes have a highly flexible molecular conformation, which is important in various chemical reactions and host-guest chemistry. If fullerenes are placed within a calixarene to form an ordered array, it could be possible to operate them and fabricate nanoscale circuits. As an essential

prerequisite, the configurations of calixarenes and fullerenes included within calixarene units at a solid surface should be understood to construct the nanoscalar architecture. We fabricated highly ordered adlayer of the inclusion of  $C_{60}$  in the calixarene [8] derivative OBOCMC8 ( $C_{104}H_{128}O_{24}$ ) under the potential control and revealed the configurations of OBOCMC8 and  $C_{60}$ /OBOCMC8 clearly by high-resolution STM images in 0.1 M  $HClO_4$  [20]. Scheme 1a illustrates the chemical insertion of the buckyball into the calix structure and the structures of the calixarene OBOCMC8 and the inclusion complex are shown in Scheme 1b and 1c, respectively. Well-ordered arrays of OBOCMC8 and  $C_{60}$ /OBOCMC8 can be constructed on an Au(111) surface only by their adsorption on Au(111) substrate.

### 3.1. The structure of highly ordered OBOCMC8 adlayer

After achieving the atomic resolution of an Au(111) substrate, a small amount of saturated OBOCMC8 solution was added into an STM cell containing 0.1 M  $HClO_4$  under the electrode potential control. Fig. 3a shows a typical large-scale STM image ( $20\text{ nm} \times 20\text{ nm}$ ) acquired in an OBOCMC8 adlayer. The electrode potential of Au(111) was held at 0.6 V (vs. RHE). A highly ordered OBOCMC8 array extends over the flat terrace of the Au(111) surface. The important features in the image are the well-ordered dark depressions. The structural details are revealed by a higher resolution STM image shown in Fig. 3b, which shows that the array consists of regular "calices." Each "calix," with an associated dark depression, can be clearly observed in the image. The chemical structure of OBOCMC8 suggests that it may be adsorbed on Au(111) through either the *tert*-butyl, carboxyl, or the



Scheme 1. (a) Schematic representation of the formation of the  $C_{60}$ /OBOCMC8 complex; (b, c) molecular structures of OBOCMC8 and  $C_{60}$ /OBOCMC8, respectively.

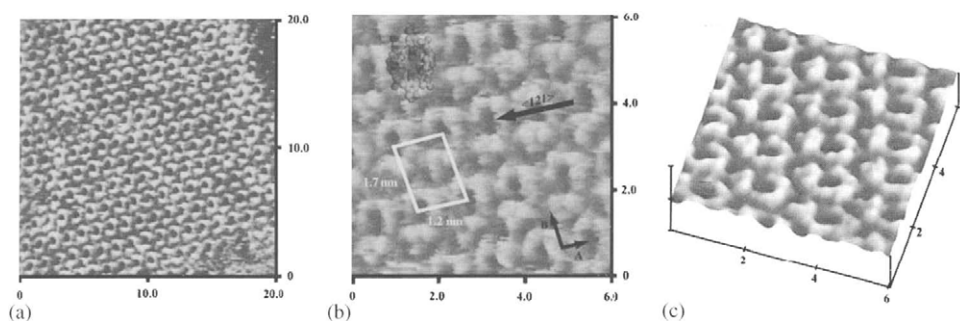


Figure 3. A typical large-scale STM image of an OBOCMC8 array on an (a) Au(111) surface, (b) a top view and (c) height-shaded surface plot of the same OBOCMC8 array, recorded using high-resolution STM. The bias voltage and tunneling current were 213 mV and 670 pA, respectively. The scales are given in nanometers.

phenyl groups. However, the carboxyl–gold interaction might be stronger than those of the phenyl and *tert*-butyl groups. The distance between the centers of the dark depressions is  $1.2 \pm 0.1$  nm along the A direction equivalent to the  $\langle 121 \rangle$  direction of underlying Au(111) substrate, and  $1.7 \pm 0.1$  nm along the B direction. The molecular rows in the A and B directions cross each other at an angle of  $95 \pm 2^\circ$ . These distances compare favorably to the size of the OBOCMC8 molecule and, therefore, each calix appearing in the STM image can be assigned as an individual OBOCMC8 molecule. The surrounding protrusion and dark depression can be attributed to the phenyl units and the molecular cavity, respectively. This feature can be more clearly seen in the height-shaded surface plot shown in Fig. 3c. OBOCMC8 molecules adsorb onto the substrate with an upright orientation.

### 3.2. The structure of highly ordered $C_{60}$ /OBOCMC8 adlayer

The same experimental procedure as that for construction of highly ordered OBOCMC8 adlayer was also applied to fabricate and investigate the array of  $C_{60}$ /OBOCMC8 on Au(111) in 0.1 M  $HClO_4$ . In the adlayer structure of the  $C_{60}$ /OBOCMC8 array, bright spots corresponding to  $C_{60}$  molecules can be clearly resolved in individual  $C_{60}$ /OBOCMC8 units. From Fig. 4a, it can be seen that the flat Au(111) surface is now covered by a highly ordered  $C_{60}$ /OBOCMC8 array, which is free of molecular defects over the whole  $25 \text{ nm} \times 25 \text{ nm}$ . This array extends over wide, flat terraces in an area more than  $50 \text{ nm} \times 50 \text{ nm}$ . An interesting feature of the  $C_{60}$ /OBOCMC8 array is the well-ordered bright spots, which can be clearly seen in the image. The feature is different from the dark depressions appearing in pure OBOCMC8 array shown in Fig. 3, demonstrating the existence of  $C_{60}$  associated with the OBOCMC8 molecule.



The higher resolution STM image in Fig. 4b shows that the molecular rows of the array are parallel to the  $\langle 121 \rangle$  direction of the underlying Au(111) substrate. The ordered molecular rows in different directions cross each other at an angle of either  $60^\circ$  or  $120^\circ$  within an experimental error of  $\pm 2^\circ$  and form a two-dimensional hexagonal lattice with associated bright spots. The structural symmetry of the  $C_{60}$ /OBOCMC8 array is significantly different from that of OBOCMC8. From careful observation, it can be seen that each individual bright spot indicated by the arrow in Fig. 4b, is surrounded by a circular protrusion. The nearest distance between the centers of the bright spots is approximately  $1.4 \pm 0.1$  nm, which is comparable to the size of the  $C_{60}$ /OBOCMC8 complex, as estimated from a molecular model. The molecular structure suggests that the carboxyl groups are responsible for this arrangement. Therefore, the bright spot and circular protrusion can be assigned as  $C_{60}$ , *tert*-butyl, and phenyl units, respectively. Thus, it is obvious that the cavity of the OBOCMC8 molecule is now filled with a  $C_{60}$  unit, observed as the additional bright spot in the STM image. Additionally, the STM images prove that the calix in  $C_{60}$ /OBOCMC8 complex still retains an upright configuration despite containing a

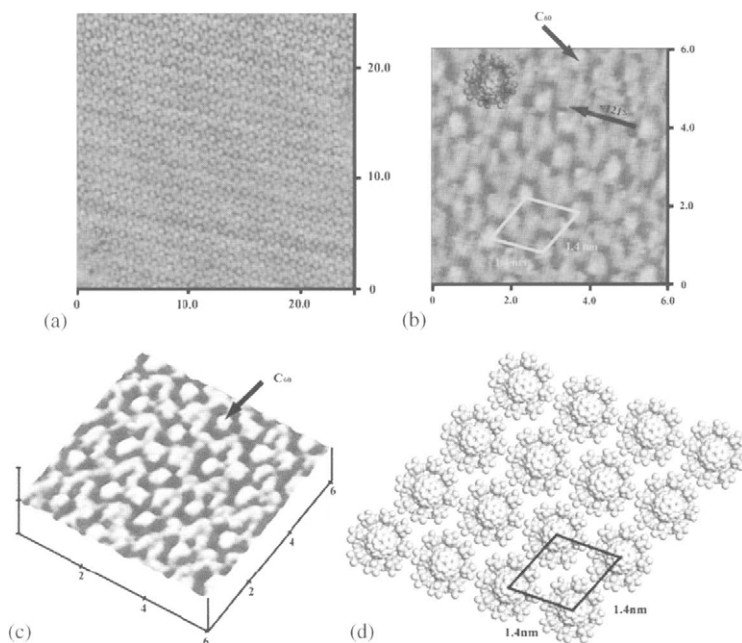


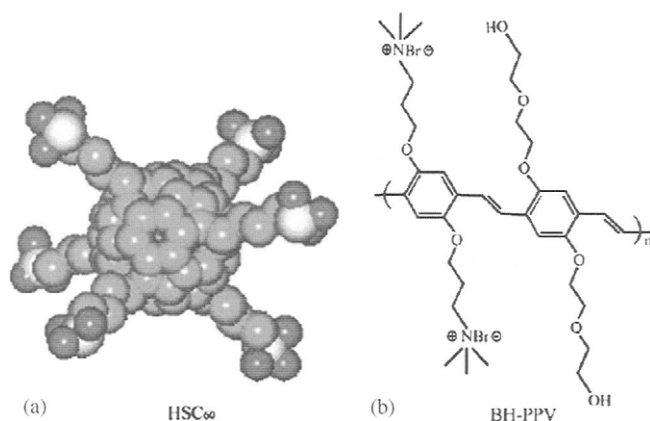
Figure 4. A typical large-scale STM image of a (a)  $C_{60}$ /OBOCMC8 array on an Au(111) surface, a (b) top view and (c) a height-shaded surface plot of the same  $C_{60}$ /OBOCMC8 array, recorded using high-resolution STM. The bias voltage and tunneling current were 140 mV and 1.0 nA, respectively. (d) A proposed structural model for the ordered array of  $C_{60}$ /OBOCMC8.

buckyball. This structural feature can be more clearly seen in the height-shaded surface plot shown in Fig. 4c.  $C_{60}$  molecules appear within protrusions throughout the array. On the basis of the STM results, a tentative model for the  $C_{60}$ /OBOCMC8 array was proposed in Fig. 4d, in which a unit cell with a parameter of 1.4 nm is outlined, which is comparable to the size of the  $C_{60}$ /OBOCMC8 complex. The results show a well-ordered array fabricated by  $C_{60}$ /OBOCMC8 molecules and provide direct structural evidence for this synthesized complex.

#### 4. ELECTROCHEMICAL CONSTRUCTION OF HIGHLY ORDERED $C_{60}$ DERIVATIVE/PPV COMPOSITE ADLAYER ON CU(111)

The fabrication of composite and multilayer structures is an important approach to improve performance and function of materials. The co-adsorption of functional molecules on metal surface under potential control should be one of the facile and powerful methods to fabricate controllable nanoscale film materials that possess promising properties, although many physical methods, such as MBE (molecular beam epitaxy) and LB, have been well used to prepare controllable thin films layer by layer. Here, we report the results that novel  $C_{60}$  derivative hexa (sulfobutyl) $C_{60}$  ( $HSC_{60}$ ) and BH-PPV (poly[(2,5-bis(3-bromotrimethylammonio-propoxy)-phenylene-1,4-divinylene)-*alt*-1,4-(2,5-bis(2-(2-hydroxyethoxy)ethoxy)) phenylene vinylene]) bimolecular composite adlayer was constructed by electrostatic interactions [21].

Scheme 2 shows the chemical structures of  $HSC_{60}$  and BH-PPV molecules. The incorporation of sulfobutyl chains with  $C_{60}$  cage improves the solubility and processability. PPV and its derivatives belong to one of the most extensively investigated conjugated polymers, which can be used for fabricating batteries,



Scheme 2. Chemical structures of (a)  $HSC_{60}$  ( $C_{84}H_{48}O_{18}S_6Na_6$ ) and (b) BH-PPV ( $C_{36}H_{56}O_8N_2Br_2$ )

sensors, and electrochromic devices as well as efficient and long-living electroluminescent devices. The use of conjugated polymers in devices has several advantages such as ease of fabrication and low cost. In addition, the fabrication of multilayer structure can be used to improve device performance or obtain higher device functionality, by combining two or more desirable properties.

#### 4.1. The adlayer structure of hexa(sulfobutyl) $C_{60}$

Fig. 5a is an STM image of the HSC<sub>60</sub> adlayer in 0.1 M HClO<sub>4</sub> + 1 mM HSC<sub>60</sub>. This image was acquired at  $-0.2$  V (vs. RHE). C<sub>60</sub> molecules can form ordered structure on the Cu(111) surface even at room temperature. There are almost no defects that can be seen in Fig. 5a. The molecular array is seen to extend over wide atomically flat terraces. The molecular rows cross each other at an angle of either 60° or 120° within an experimental error of  $\pm 2^\circ$ . By comparison with the Cu(111)-(1 × 1) atomic image, it is found that all molecular rows are parallel to the  $\langle 110 \rangle$  direction of underlying Cu(111) lattice. The intermolecular distances along the molecular rows were measured to be  $0.98 \pm 0.02$  nm, corresponding to four times the Cu(111) lattice distance. On the basis of the orientation of molecular rows and the intermolecular distance, it can be concluded that the observed HSC<sub>60</sub> adlayer is in a (4 × 4) structure with a surface coverage of 0.0625. A unit cell is superimposed in Fig. 5a. Fig. 5b is a high-resolution STM image of the HSC<sub>60</sub> adlayer. There exist two single molecular defects in the image, indicated by arrows where the molecules are missing. The features of the molecules can be clearly seen. Clearly, each spot corresponding to an HSC<sub>60</sub> molecule in the low-resolution image is now split into a set of three bright spots. They are believed to be the manifestation of the intramolecular structure of C<sub>60</sub> cage. It is clear from the observation that the C<sub>60</sub> cage dominates the molecular orientation, resulting in a stable adlayer. Because of the abundant electronic states of the C<sub>60</sub> core, the chains of the HSC<sub>60</sub> cannot be observed

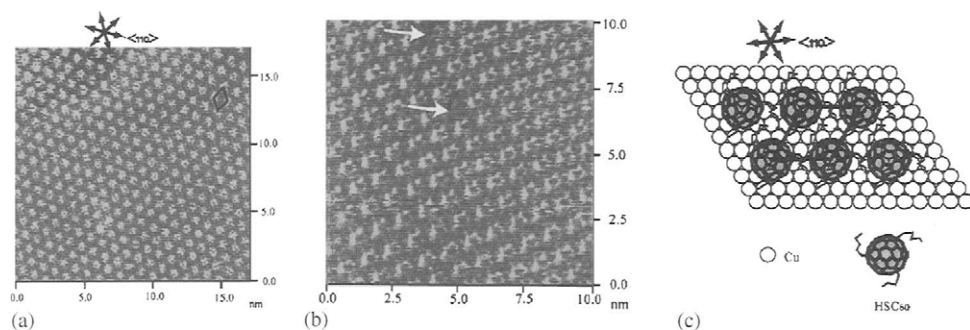


Figure 5. (a) Large-scale STM image of a Cu(111)-(4 × 4)-HSC<sub>60</sub> adlattice. Tunneling current was 2 nA. Scanning rate was 15.26 Hz. (b) High resolution STM image of HSC<sub>60</sub> adlayer on Cu(111). Tunneling current was 2 nA. Scanning rate was 20.35 Hz. (c) Proposed model of HSC<sub>60</sub> adlayer on Cu(111) surface.

clearly. A structural model for  $\text{HSC}_{60}$  adlayer on the  $\text{Cu}(111)$  surface is tentatively proposed in Fig. 5c. The molecular center is placed on the three-fold hollow site of the substrate. The three pentagonal rings surrounding one hexagonal ring of a  $\text{C}_{60}$  molecule are located on bridge sites. The side chains in  $\text{C}_{60}$  cage face down on the  $\text{Cu}(111)$  surface. In this model, there is a maximum coordination of  $\text{C}_{60}$  molecule to the  $\text{Cu}(111)$  substrate, yielding a stable adlayer. The ordered  $(4 \times 4)$  structure was consistently observed in the double-layer potential region from  $-0.30$  to  $0.1$  V.

#### 4.2. The adlayer structure of BH-PPV

BH-PPV molecule is positively charged in solution. The image shown in Fig. 6a is a typical STM image for the ordered BH-PPV adlayer formed on the  $\text{Cu}(111)$  surface. The image was acquired at  $-0.2$  V (vs. RHE) in a  $0.1$  M  $\text{HClO}_4$  solution containing  $1$  mM BH-PPV. The STM image in Fig. 6b shows more details of the packing arrangement and the internal structure of the BH-PPV adlayer. The two main spots along with side chains form a rectangle unit. The bright spots along with side chains in STM images are attributed to two benzene rings of a BH-PPV unit. The molecules form an ordered two-dimensional network. The width of each rectangle along direction  $a$  is  $\text{ca. } 1.0 \pm 0.05$  nm, and the length of the molecule along direction  $b$  is  $1.8 \pm 0.05$  nm, consistent with the results optimized by HyperChem. The angle between the two directions is  $90^\circ$  within an experimental error of  $\pm 2^\circ$ . A unit cell for the molecular adlayer is outlined in Fig. 6b. According to the intermolecular distance and orientation of molecular rows, the adlayer can be defined as a  $(4 \times 4\sqrt{3})$  structure. Fig. 6c shows a proposed schematic representation of BH-PPV on  $\text{Cu}(111)$  surface. It was tentatively proposed that the two benzene rings of the BH-PPV occupy at three-fold hollow sites.

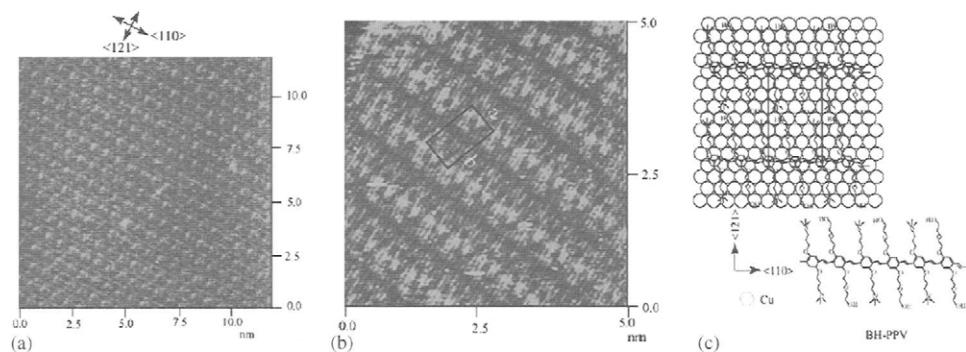


Figure 6. (a) STM image of BH-PPV molecules on  $\text{Cu}(111)$  in  $0.1$  M  $\text{HClO}_4$  containing  $1$  mM BH-PPV. Tunneling current was  $2$  nA. Scanning rate was  $15.26$  Hz. (b) Higher resolution STM image of BH-PPV from (a). Tunneling current was  $2$  nA. Scanning rate was  $20.35$  Hz. (c) Schematic representation for the  $(4 \times 4\sqrt{3})$  structure.

### 4.3. HSC<sub>60</sub> and BH-PPV composite adlayer

The alternating adsorption of oppositely charged adsorbates is a facile and powerful method to fabricate composite nanometer scale film layer by layer. The composite monolayer was prepared on Cu electrode surface by alternating adsorption of oppositely charged HSC<sub>60</sub> and BH-PPV. Briefly, a well-defined BH-PPV layer was first prepared on Cu(111) surface. Then, a HSC<sub>60</sub> solution was added over the BH-PPV layer. The experiments in an opposite order were also done, and results revealed by STM imaging were almost the same as those prepared by the previous order. Owing to their opposite charges, a composite monolayer of HSC<sub>60</sub>/BH-PPV was automatically formed.

Fig. 7a is a typical STM image of the composite adlayer on Cu(111) in 0.1 M HClO<sub>4</sub>. The appearance of the adlayer is completely different from that in Figs. 5 and 6, although the STM imaging conditions here are almost the same as those used in recording the adlayers in Figs. 5 and 6. A two-dimensional network with four-fold symmetry can be seen in the image shown in Fig. 7a. From the molecular structures in Scheme 2, it can be seen that the two molecules are positively and negatively charged. HSC<sub>60</sub> is negatively charged, while BH-PPV is positively charged. Owing to the static attraction, the side chains in the two kinds of molecules should be linked together by an electrostatic reaction, resulting in a composite adlayer. According to intermolecular distance and the orientation of the molecular rows to the underlying Cu(111) lattice, the composite adlayer has a  $(4 \times 4\sqrt{3})$  structure. This arrangement is a more densely packed phase than both of the single component adlayers. A unit cell is outlined in Fig. 7a. The bright spots in the STM image are assumed from C<sub>60</sub> cages

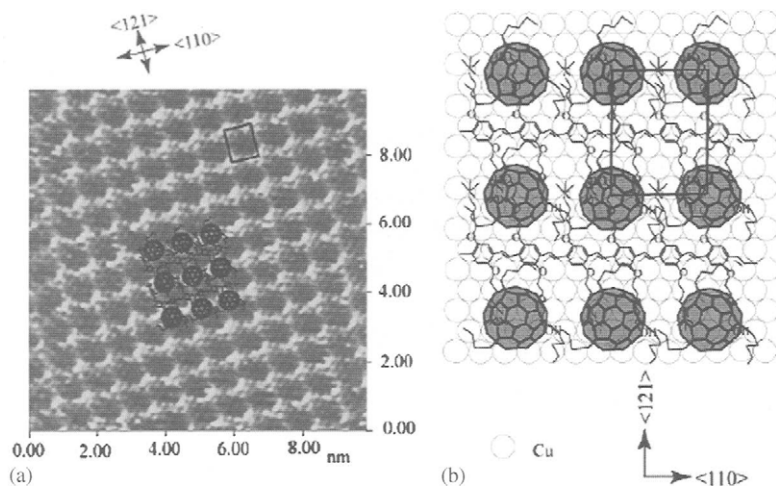


Figure 7. (a) Higher resolution STM image of the composite adlayer of HSC<sub>60</sub> and BH-PPV on Cu(111) in 0.1 M HClO<sub>4</sub>. Tunneling current was 2 nA. Scanning rate was 20.35 Hz. (b) Structural model for the composite adlayer (a).

based on the chemical structure difference in the two molecules. A tentative model for the composite adlayer on Cu(111) is proposed in Fig. 7b.

#### 4.4. Current-voltage features of HSC<sub>60</sub> adlayer, BH-PPV adlayer, and their composite adlayer

The composite adlayer prepared by BH-PPV and HSC<sub>60</sub> will produce different electronic and electroluminescent property from their single component adlayer.

Fig. 8 shows typical current-voltage ( $I$ - $V$ ) curves of the three types of adlayers measured by the method of capillary tunnel junction [22]. From Fig. 8, nonlinear characteristics have been observed in all junctions of the three types of molecular film. The tunneling between the substrate and molecular layer is generally a function of the electronic state of molecules. The asymmetric  $I$ - $V$  characteristics of these molecules suggest that they have a potential application in nanometer scale electronic devices such as rectifier. As shown in Fig. 8, rectified behavior was clearly observed for these adlayers. The rectified region of HSC<sub>60</sub> in Fig. 8a is extended from  $-0.5$  to  $0.5$  V and BH-PPV from  $-2$  to  $2$  V. However, the rectified region of the composite monolayer in Fig. 8c is extended from  $-5$  to  $5$  V, broader than that of in Figs. 8a and b. This result is likely due to the interaction between the HSC<sub>60</sub> and BH-PPV molecules. The interactions enhance the potential barrier of the composite adlayer and the energy gap broadened.

### 5. THE FABRICATION OF FULLERENE NANOWIRES

Although individual fullerene molecules can form well-ordered adlayers with defined symmetry in two-dimension surface, in order to easily construct a functional circuit in tailoring a device structure and interconnect, pre-designed and controllable molecular arrays should be achieved in fullerene application. Thus, great effort has been made to prepare single-wall carbon nanotubes (SWCNTs) and multi-wall carbon nanotubes (MWCNTs) with various special functions, though the exact control in length, diameter, and chirality of carbon nanotubes (CNTs) still remain a major hurdle for large-scale applications.

To explore the possibility of making nanomaterials with fullerene, we fabricated controllable fullerene nanowire arrays with well-defined diameter, structure, and

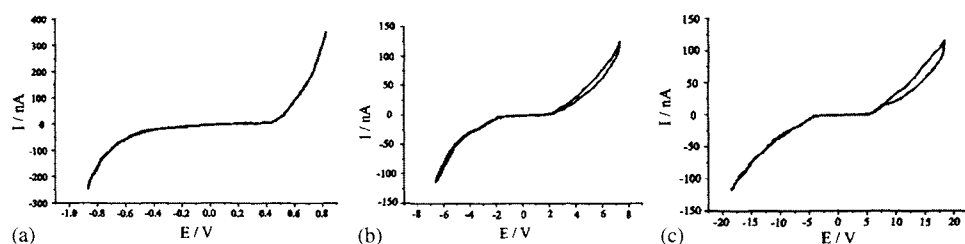


Figure 8. The current-voltage characteristics of the adlayers of (a) HSC<sub>60</sub>, (b) BH-PPV, and (c) HSC<sub>60</sub> and BH-PPV.

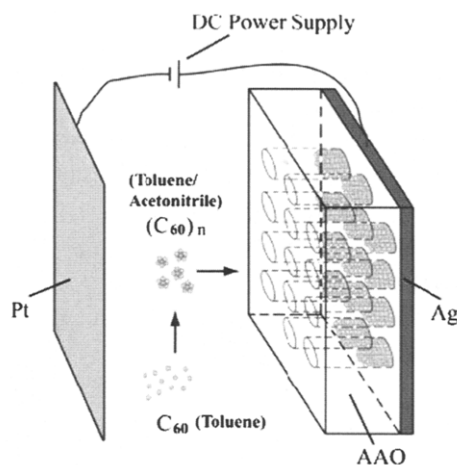
length by introducing fullerene molecules such as  $C_{60}$  derivatives into the pores of anodic aluminum oxide (AAO) templates under a direct current (DC) electric field and then polymerizing them in the pores [23]. Scheme 3 is a schematic illustration of the electrodeposition process of  $C_{60}$  nanowires. Briefly, under a DC electric field, the charged  $C_{60}$  molecules will aggregate at the electrode and then form highly ordered  $C_{60}$  nanowires.

### 5.1. The morphology of $C_{60}$ nanowires

Fig. 9 is an SEM image of the  $C_{60}$  nanowires prepared by DC electrodeposition in AAO template with a pore diameter of 45 nm. A well-defined aligned  $C_{60}$  nanowire array with a uniform length of ca. 19  $\mu\text{m}$  is observed in the image. The length of the wire is dependent on the thickness of the AAO template. Individual  $C_{60}$  nanowires can be seen in Fig. 9 indicated by an arrow. From the TEM image shown in Fig. 10a, it can be seen that the nanowire is with a smooth wall/surface and a uniform diameter. The average diameter of these nanowires is ca. 45 nm. The winding shapes of these nanowires demonstrate the flexibility of the so-prepared  $C_{60}$  nanowires. The typical high-resolution TEM image in Fig. 10b shows that the  $C_{60}$  nanowires are polycrystalline (see the arrow in the upper right corner of Fig. 10b). From the HRTEM image in Fig. 10c, nanocrystals with diameter ca. 6 nm, indicated by circles, can be observed.

### 5.2. The conductivity of $C_{60}$ nanowires

The conductivity of  $C_{60}$  nanowires is characterized by  $I$ - $V$  curve. The  $I$ - $V$  characteristic of  $C_{60}$  nanowires at room temperature is shown in Fig. 11. The conductivity deduced from the curve is  $\sim 6 \times 10^{-6}$  S/m. This value suggests that the electrochemically deposited  $C_{60}$  nanowire may have semiconductor properties. The low conductivity may be contributed to the polycrystalline structure of the  $C_{60}$



Scheme 3. Schematic illustration of the preparation of fullerene nanowire arrays by using AAO membranes as templates.

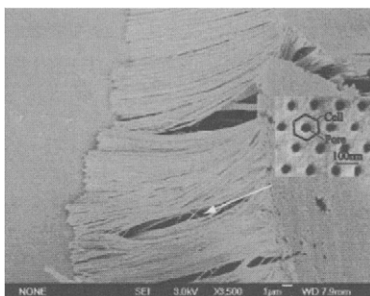


Figure 9. Typical SEM image of the prepared C<sub>60</sub> nanowire array. The inset is a typical SEM image of the AAO template used in the fabrication of nanowires.

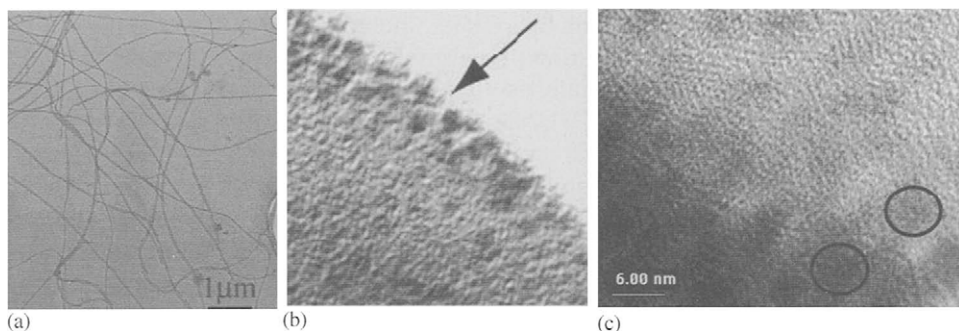


Figure 10. (a) TEM image of dispersed C<sub>60</sub> nanowires. (b) and (c) HRTEM images of as-prepared C<sub>60</sub> nanowires.

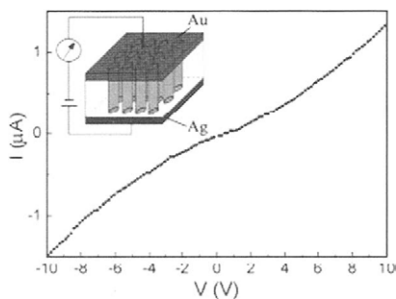


Figure 11.  $I$ - $V$  characteristics of C<sub>60</sub> nanowires at room temperature. The inset schematically shows the circuit used in the measurement.



nanowires, which causes lowering of the conduction across grain boundaries. But proper modification such as doping in the nanowires may enable adjustment of the conductivity like that performed on the CNTs [24] and hence the nanowires could be used in the development of nanodevices.

Therefore, by using an AAO membrane as the template, various arrays of fullerene derivatives and endohedral fullerenes, which are more easily manipulated in designing nanodevices, could be fabricated into nanowires and nanotubes by the technique of electrodeposition. The diameter and length of the nanowires are easily controllable by tailoring the pore size and the thickness of the template. On the other hand, the morphology of the so-prepared could also be controlled by adjusting the parameters of electrodeposition such as applied voltage and current.

## 6. THE ELECTROCHEMISTRY OF MULTI-WALL CARBON NANOTUBE FILM

The discovery of fullerenes has sparked a great research effort in the area of carbon related nanomaterials, such as CNTs, including SWCNTs and MWCNTs. MWCNTs are the materials featuring predetermined functionality, thus forming an essential bridge between industrially useful graphite fibers of a micrometer size and fullerenes of a molecular size. MWCNTs combine high electrical conductivity with mechanical strength and chemical inertness.

With regard to their electrochemical properties, CVs of MWCNTs are measured as shown in Fig. 12 [25]. The nanotubes were deposited on glass carbon substrate as a film by drop coating method. The CV of the freshly prepared nanotube film electrode was measured in a pH 7.1 PBS buffer solution. Although the carboxylic acid groups were introduced on the open ends of empty nanotubes during shortened process of the nanotubes, no redox peaks can be seen as shown in the curve a of

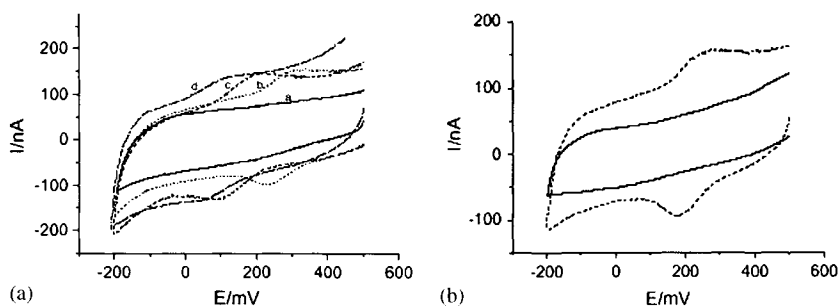


Figure 12. (a) CVs of freshly prepared empty nanotube film electrode in pH 7.1 buffer solution (curve a) and after being exposed to air for 12 h in pH 4.3 (curve b), pH 7.1 (curve c) and pH 9.1 (curve d) PBS buffer solution at a scan rate of 0.1 V/s. (b) CVs of the tobulene-filled nanotube film electrode freshly prepared (—) and after being exposed to air for 12 h (---) in pH 7.1 PBS buffer solution at a scan rate of 0.1 V/s.

Fig. 12a. This is different from that of carboxyl-terminated SWCNT film electrode, which shows a pair of reduction/oxidation waves associated with the carboxylic acid groups [26]. When the nanotube film electrode was exposed to air for 12 h, the CV in pH 7.1 PBS buffer showed a pair of stable and well-defined redox peaks as shown in curve c of Fig. 12a. The peak potentials and currents remained almost the same after the second cycle. The removal of dissolved oxygen did not affect the features of the CV. Prolonging the exposed time does not bring about any change of the peaks. In a comparison, bare Au electrode was also exposed to air for the same time. But no any single redox peak could be addressed. So the pair of peaks in curve c was ascribed to the redox reaction of empty nanotube film. We measured the CV at a scan rate of 0.1 V/s and the cathodic and anodic peak potentials were 0.1135 V and 0.2025 V, respectively. The peak currents are found to be linearly dependent on scan rate, showing characteristic of thin-layer electrochemical behavior. The background current of empty nanotube film was apparently large, which might be attributed to the increased surface charge. On the other hand, the peak potential was pH dependent. In the pH range from 4.3 to 9.1, the peak potentials shift to the negative direction (see the curves b–d in Fig. 12a). The pair of redox peaks is assigned to the reduction/reoxidation of the surface oxygen-containing functional groups. When the nanotube film was exposed to air, oxygen molecules adsorb on the surface of nanotubes and cannot be removed again.

Using CNTs as nanoreactors filled by metallic [27–29] and inorganic [30–32] materials, and even fullerene molecules [33], special materials could be prepared. The presence of the atoms and molecules filled into nanotubes will influence the properties. For example, toluene-filled nanotube film was fabricated [25]. As shown in Fig. 12b, the film has the same electrochemical behavior as that of empty nanotube film. However, it is found that the toluene-filled nanotube film can enhance the electrochemical response of biomolecules such as dopamine (DA) and epinephrine

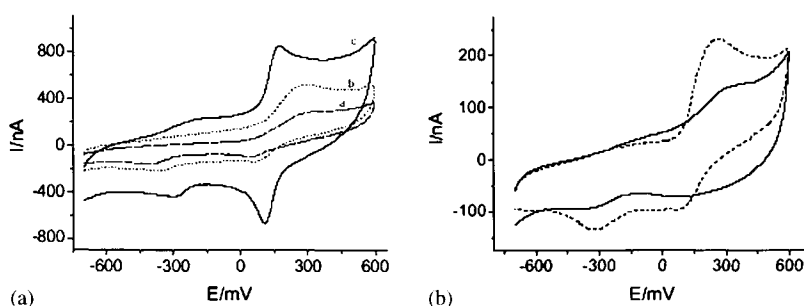


Figure 13. (a) CVs of bare Au electrode (curve a), empty nanotube film electrode (curve b), and toluene-filled nanotube film electrode (curve c) in a pH 7.1 PBS buffer solution containing 0.1 mM DA at a scan rate of 0.1 V/s. (b) CVs of bare Au electrode (—) and toluene-filled nanotube film electrode (---) in a pH 7.1 PBS buffer solution containing 0.1 mM EP at a scan rate of 0.1 V/s.

(EP), which exhibits large cathodic and anodic peak currents and small peak separation in comparison with that at bare Au electrode. However, the empty MWCNT film without toluene shows less electrocatalytic activity to these biomolecules shown in Fig. 13. This result suggests that filled nanotubes have some particular properties compared to empty MWCNT.

## REFERENCES

1. M. Matsumoto, J. Inukai, E. Tsutsumi, S. Yoshimoto, K. Itaya, O. Ito, K. Fujiwara, M. Murata, Y. Murata and K. Komatsu, *Langmuir* **20** (2004) 1245; and references cited therein.
2. R. J. Wilson, G. Meijer, D. S. Bethune, R. D. Johnson, D. D. Chambliss, M. S. de Vries, H. E. Hunziker and H. R. Wendt, *Nature* **384** (1990) 621.
3. Y. Z. Li, J. C. Patrin, M. Chander, J. H. Weaver, L. P. F. Chibante and R. E. Smalley, *Science* **252** (1991) 547.
4. Y. Z. Li, M. Chander, J. C. Patrin, J. H. Weaver, L. P. F. Chibante and R. E. Smalley, *Science* **253** (1991) 429.
5. Y. Z. Li, M. Chander, J. C. Patrin, J. H. Weaver, L. B. F. Chibante and R. E. Smalley, *Phys. Rev. B* **45** (1992) 13837.
6. Y. Zhang, X. Gao and M. J. Weaver, *J. Phys. Chem.* **96** (1992) 510.
7. E. I. Altman and R. J. Colton, *Surf. Sci.* **279** (1992) 49.
8. E. I. Altman and R. J. Colton, *J. Vac. Sci. Technol. B* **12**(3) (1994) 1906.
9. C. Jehoulet, Y. S. Obeng, Y.-T. Kim, F. Zhou and A. J. Bard, *J. Am. Chem. Soc.* **114** (1992) 4237.
10. S. Uemura, A. Ohira, T. Ishizaki, M. Sakata, M. Kunitake, I. Taniguchi and C. Hirayama, *Chem. Lett.* **4** (1999) 279; **6** (1999) 535 (correction).
11. S. Uemura, M. Sakata, I. Taniguchi, M. Kunitake and C. Hirayama, *Langmuir* **17** (2002) 5.
12. A. Marchenko and J. Cousty, *Surf. Sci.* **513** (2002) 233.
13. S. Uemura, P. Samorý, M. Kunitake, C. Hirayama and J. P. Rabe, *J. Mater. Chem.* **12** (2002) 3366.
14. S. Yoshimoto, R. Narita, E. Tsutsumi, M. Matsumoto, K. Itaya, O. Ito, K. Fujiwara, Y. Murata and K. Komatsu, *Langmuir* **18** (2002) 8518.
15. K. Motai, T. Hashizume, H. Shinohara, Y. Saito, H. W. Pickering, Y. Nishina and T. Sakurai, *Jpn. J. Appl. Phys.* **32** (1993) L450.
16. T. Hashizume, K. Motai, X. D. Wang, H. Shinohara, Y. Saito, Y. Maruyama, K. Ohno, Y. Kawazoe, Y. Nishina, H. W. Pickering, Y. Kuk and T. Sakurai, *Phys. Rev. Lett.* **71** (1993) 2959.
17. E. I. Altman and R. J. Colton, *Surf. Sci.* **295** (1993) 13.
18. E. I. Altman and R. J. Colton, *Phys. Rev. B* **48** (1993) 18244.
19. S. Yoshimoto, R. Narita, E. Tsutsumi, M. Matsumoto, K. Itaya, O. Ito, K. Fujiwara, Y. Murata and K. Komatsu, *Langmuir* **18** (2002) 8518.
20. G. Pan, J. Liu, H. Zhang, L. Wan, Q. Zheng and C. Bai, *Angew. Chem. Int. Ed.* **42** (2003) 2747.

21. M. Han, L. Wan, S. Lei, H. Li, X. Fan, Ch. Bai, Y. Li and D. Zhu, *J. Phys. Chem. B* **108** (2004) 965.
22. X. L. Fan, C. Wang, D. L. Yang, L. J. Wan and C. L. Bai, *Chem. Phys. Lett.* **361** (2002) 465.
23. Y. Guo, C. Li, L. Wan, D. Chen, C. Wang, C. Bai and Y. Wang, *Adv. Funct. Mater.* **13** (2003) 626.
24. A. M. Rao, P. C. Eklund, S. Bandow, A. Thess and R. E. Smalley, *Nature* **388** (1997) 257.
25. H. Zhang, X. Wang, L. Wan, Y. Liu and C. Bai, *Electrochim. Acta* **49** (2004) 715.
26. H. Luo, Z. Shi, N. Li, Z. Gu and Q. Zhuang, *Anal. Chem.* **73** (2001) 915.
27. P. M. Ajayan and S. Iijima, *Nature* **361** (1993) 333.
28. P. M. Ajayan, T. W. Ebbesen, T. Ichihashi, S. Iijima, K. Tanigake and H. Hiura, *Nature* **362** (1993) 522.
29. R. M. Lago, S. C. Tsang, K. L. Lu, Y. K. Chen and M. L. H. Green, *J. Chem. Soc. Chem. Commun.* **13** (1995) 1355.
30. D. Ugarte, A. Chalelain and W. A. Heer, *Science* **274** (1996) 1897.
31. P. M. Ajayan, O. Stephen, P. Redlich and C. Colliex, *Nature* **375** (1995) 564.
32. J. Sloan, S. J. Grosvenor, S. Friedrichs, A. Kirkland, J. L. Hutchison and M. L. H. Green, *Angew. Chem. Int. Ed.* **41** (2002) 1156.
33. B. W. Smith, M. Monthieux and D. E. Luzzi, *Nature* **396** (1998) 323.

## Chapter 6

### Carbon blacks as the source materials for carbon nanotechnology

Masaki Ozawa and Eiji Ōsawa

NanoCarbon Research Institute, Toudai Kashiwa Venture Plaza, 5-4-19 Kashiwa-no-ha, Kashiwa, Chiba 277-0882, Japan

The structure and formation/growth mechanism of soot particles (carbon blacks) have recently been elucidated by TEM experiments, and this study led to a surprising conclusion that the primary particles of carbon blacks are highly defective multi-shell fullerenes. The conclusion further led us to propose new synthesis of  $C_{60}$  by pyrolysis, and improved preparation of carbon nano-onions and nano- to submicron-diamonds, at very low cost. Smallest members of nano-onions are obtainable as by-products from the pyrolytic synthesis of  $C_{60}$ , and considered as the potential starting material for superhard carbons, Mackay crystals.

#### 1. INTRODUCTION

If it were not for the discoveries of  $C_{60}$  in 1985 and carbon nanotube in 1991, the emergence of nanotechnology [1] may have been delayed by at least a few decades. The impact was so big that  $C_{60}$  and carbon nanotube continued to occupy major positions in the international research arena until long after the initiative in nanotechnology was taken over on national scales [2]. However, the problem of forbiddingly high production cost gradually caught up with the glory of fullerene carbons. A brief summary on the production cost of fullerenes and carbon nanotubes is given in the first four entries in Table 1. Even though the second-generation combustion method is supposed to improve  $C_{60}/C_{70}$  ratio to a very high level and to reduce the cost to one-tenth of the present level, \$500/kg for the  $C_{60}/C_{70}$  mixture is still too high. HiPco method is so far the only practicable method of producing single-wall carbon nanotubes (SWCNTs) of acceptable quality in macroscopic quantities [2], but its price level is simply too high to seriously consider any industrial applications. The current cost level of \$150/kg for producing multi-wall carbon nanotubes (MWCNTs) by chemical vapor deposition (CVD) method is certainly acceptable, but their application is rather limited [3].

We may have been pre-occupied by the bright prospect of these fullerenes for long. After a decade of continued failure in the search of better production methods, it is perhaps time to think of alternatives. The purpose of this Chapter is to shed light on the cost problem from a new angle. The central issue is to consider *carbon blacks*, being produced on the very large scale all over the world, as the new source materials for carbon nanoparticles [4,5]. The proposal is based on our own work on the structure and formation mechanism of soot, which will be disclosed in

Table 1  
Production costs of major nano-carbon materials.

	Starting materials	Method	Products	Production costs (\$10 /kg)	Notes
1	Hydrocarbons	First-generation combustion method	Mixture of $C_{60}/C_{70}$ (6 /4)	500	40 ton /year under operation
2	Hydrocarbons	Second-generation combustion method	Mixture of $C_{60}/C_{70}$ (>10)	50	Under development
3	CO/Fe	HiPCO	SWCNTs + catalysts	100,000	Under test operation
4	Hydrocarbons	CVD	MWCNTs	15	Operation has started
5	Carbonaceous industrial wastes	Pyrolysis	Carbon blacks	0.1	Matured industry
6	Carbon blacks	Electron beam irradiation	Carbon nano-onions	0.2	Being planned
7	Carbon nano-onions	Electron beam irradiation at high temperatures	Nano-diamonds	1.0	Being planned

some detail below, but the definitive advantage can be immediately understood by looking at the lower half of Table 1. Carbon blacks are prepared at a rate of \$1/kg in high yield by pyrolysis of carbonaceous industrial waste like the distillation residue from the cracking of crude oil.

## 2. REVIEW OF SOOT AND CARBON BLACKS

Carbon blacks are the established industrial intermediates [2]. Taking a number of distinguished features including inexhaustible starting material, extremely low production cost, and almost perfect purity and homogeneity (Table 2) into accounts, we consider them qualified in the first requirement for the source material of carbon industry. Perhaps the readers are curious about the reason why one can produce such pure and uniform carbon at such a low cost. Before discussing the second requirement, which is a list of potential applications, we will briefly mention the production of carbon blacks, a topic rarely discussed recently.

Essentially carbon blacks are the pure soot, and produced by pyrolysis of carbonaceous industrial wastes. The pyrolysis furnace, the core of the whole process, is a huge empty tube several dozen meters in length, ca. 2 m in diameter, and made of heat-resistant bricks as illustrated in Fig. 1. Coal gas or natural gas is mixed with air and the mixed gas is introduced from one end of the tube, compression-ignited, and the high-temperature flame (1800–2000 °C in the highest case) thus generated is blown at a

Table 2  
Characteristics of carbon blacks as industrial materials.

Items	Values	Notes
Carbon content	97–99 wt%	By-contents are H and O
Bonding states of carbon	sp <sup>2</sup> carbon	High degree of purity
Microstructures	Bunched agglutinates of spherical primary particles	The less agglutinative for the larger primary particles
Homogeneity of microstructures	100%	Common feature in high temperature pyrolysis
Starting materials	Carbonaceous industrial wastes	Oil cokes or residual oil
Production method	Mainly furnace black method	Fluidized continuous pyrolysis
Production costs	~\$1 /kg	Stable
Production /year	~10 M ton	Distributed plants in the world
Products	Black granulated powder	Mainly used as reinforcement of rubber and black toner

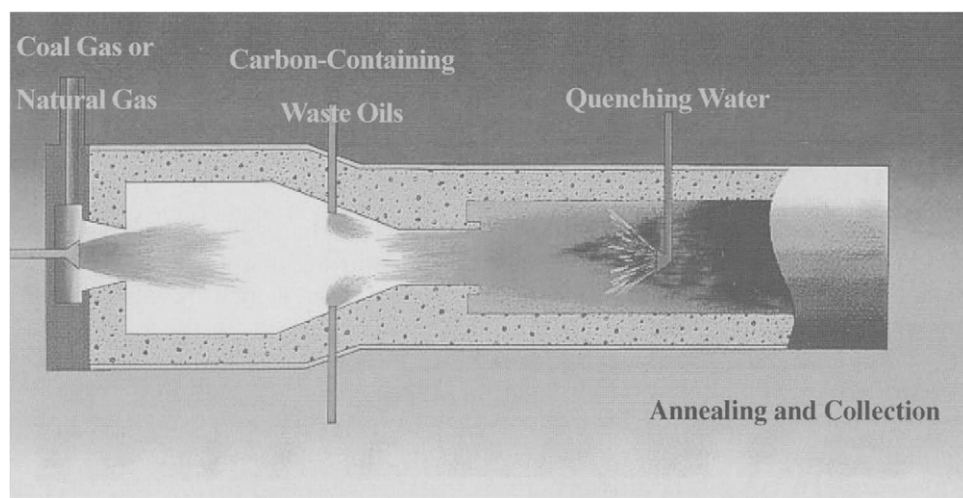


Figure 1. Pyrolysis furnace for carbon blacks. Classical process produces chemically pure carbon, which turned to be a sort of fullerene.

supersonic flow toward the other end. A little downstream, carbon-containing industrial wastes like oil cokes or residual oil, fluidized by preheating at 200–300 °C, is sprayed into the high-temperature current of flame to produce soot through cracking. When the soot thus produced grew to a desired size, water is sprayed in further downstream to extinguish combustion and suspend the cracking processes and the soot is gathered after cooling by passing through a long vertical pipe.

One should not misunderstand at this point the main sooting process as incomplete combustion of the starting materials. On the contrary, the combustion taking place in the furnace is complete combustion of the fuel gas, and the role of high-temperature supersonic flow thus generated in the first segment of furnace is to supply heat for the cracking process of the industrial waste. The cracking reaction may appear quite simple, but the chemistry of soot formation involving self-assembly of the atoms or atomic fragments, clustering, network formation, and growth processes into soot particles is actually highly complicated. Only a rough picture has been indicated here [6].

The largest drawback of carbon blacks as industrial materials is the low crystalline nature: carbon blacks are categorized as amorphous carbon. Nevertheless, the application for the reinforcement of tires began at the beginning of the 20th century and proved to be a great success. Demand for this single market grew rapidly with the expansion of vehicular transport. More than 10 million tons of carbon blacks are produced annually in automated plants all over the world [4,5]. However, science of carbon blacks has remained almost 'black', even the structure of primary particles had defied elucidation for a long time until Rosalind Franklin presented a



famous model based on X-ray diffraction analysis, wherein crystallites of graphite are assembled into turbostratic spherical structure [7].

Science of carbon blacks revived after the discovery of  $C_{60}$  at the end of 20th century [8]. Our work on the mechanism of  $C_{60}$  formation led us to the problem of soot structure, and by luck we could reveal all the basic aspects of structure and formation mechanism of primary soot particles [7]. As our present proposal is based on this fundamental study, the next section is devoted to its brief summary.

### 3. THE STRUCTURE AND FORMATION MECHANISM OF CARBON BLACKS

#### 3.1. Crystallization of carbon blacks without heating

When a large number of molecules or atoms are ordered into three-dimensional arrangements, chemists call the states as crystals. The better crystallinity generally gives the higher melting point and less pronounced defects. On the other hand, material scientists say 'crystals' or 'with good crystallinity' even for partly ordered arrangements in bulk materials. The latter case will be followed for these terms in this chapter.

High-resolution transmission electron micrographs (HRTEM) of carbon blacks generally display very low crystallinity as shown Fig. 2a. Although the average diameter of the primary particles in this photograph is given as 14 nm by the producer, it is clearly difficult to reach this number from this picture alone. It is naturally desirable to increase the crystallinity.

We find that primary particles of carbon blacks can be converted into carbon nano-onions upon irradiation with electron beam focused to a current density as high as  $150 \text{ A/cm}^2$  in a HRTEM [6]. The experiments are quite similar to those carried out by Ugarte [9] originally using polyhedral carbon nanoparticles as the target. Ugarte [9] refers in his paper to his preliminary experiments on amorphous carbons including carbon black, but it seems that he did not have much luck in this direction. We later observed that carbon black samples with low crystallinity often fail to produce clear-cut conversion into nano-onion but decompose into undefinable structures. We were lucky enough to have started with the right sample having rather good crystallinity. The major factor responsible for such morphological modification in microscopes is the knock-on effect [10] of the electron beam. Hence, an acceleration voltage high enough to displace carbon atoms from the lattice is necessary for the nano-onion structure to improve.

The micrograph of nano-onions in Fig. 2b demonstrates the following characteristics:

- (1) Larger nano-onions have more structural defects than smaller onions, which appear to have almost perfect structure.
- (2) The outermost graphitic layers extending over more than one primary particle appear to have been mostly removed under electron beam irradiation, while some of the extended layers still remain in this picture.
- (3) The innermost shell is  $C_{60}$ .

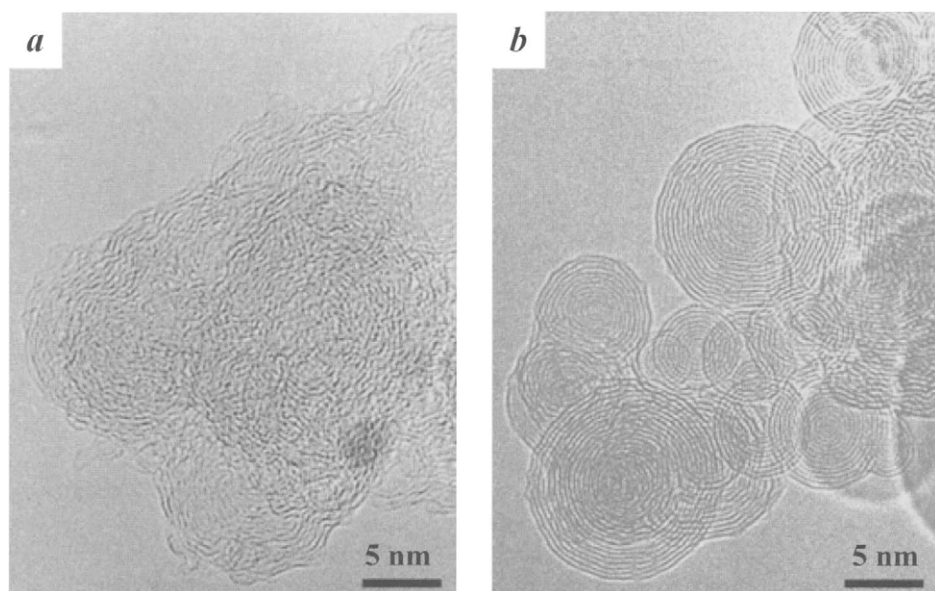


Figure 2. Crystallization of carbon black structure by intensive electron beam bombardment (JEOL, JEM-2010 at 200 keV,  $\sim 150$  A/cm<sup>2</sup>) onto Toka Black #8500F, claimed to have an average diameter of 14 nm in the primary particles. (a) Pristine structure shows numerous defects and ambiguous grain boundaries. (b) After irradiation for 20 min at this spot spherical contours and inner-layers of carbon nano-onions clearly appeared.

- (4) Some particles have spiral layers instead of concentrically nested ones. A spiral image with 12 nm in diameter located in the upper center of Fig. 2b provides an example of non-onion particle, a spiroid.

### 3.2. Discovery of spiroid intermediates

An astonishing phenomenon was then observed, when electron bombardment was kept going for a longer time in order to achieve conversion into perfect nano-onions: every primary particles of carbon blacks always metamorphose to spiral intermediates during the structural evolution into nano-onions. In addition, the transformation between a spiral intermediate and a nano-onion is reversible as shown in Fig. 3, and sometimes occurs repeatedly with gradual change of the contour.

Carbon nano-onions are in general spherical, and their centers filled. However, it is known that the shape changes at high temperatures into faceted polyhedral nanoparticle, often with void in the center [11]. Similar 'carbon nanoparticles' are also formed as by-products, when fullerenes are produced by the arc-discharge method. Polyhedral carbon nanoparticles are presumed to be more stable than

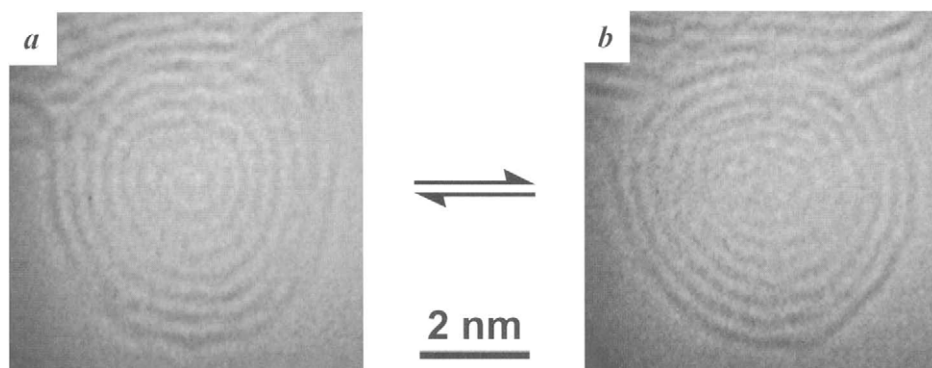


Figure 3. Reversible transformation between the intermediate spiral particle (spiroid) (a) and the carbon nano-onion (b) observed under electron beam irradiation onto primary particles of carbon blacks.

spherical carbon nano-onions. However, the premise has never been proven experimentally because of the difficulty in isolation and purification of these nanoparticles.

On the other hand, it has been suggested by theoretical calculations that one particular onion series,  $C_{60}@C_{240}@C_{540}@C_{960}@C_{1500}@ \dots @C_{60n}@ \dots$ , is exceptionally stable irrespective of the number of layers,  $n$ , among large number of other homologous series [12]. In this series, intershell spacing is always nearly equivalent to those of graphite, and moreover, each giant fullerene shell takes the most stable  $\pi$ -electronic structure. It is likely that the spiral intermediates observed here are used for attaining this ideal structure.

The most difficult part of the present proposal was to conceive an acceptable molecular model of the spiral intermediates. The term 'spiral' generally refers to a path of a point on a plane winding around a fixed center point with continuously increasing distances from it, and does not fit to three-dimensional spherical shapes. At first a path of a semicircle winding around a fixed axis was examined, but we soon realized that exact Archimedean spiral projection produced high strain along the rotation axis. We eventually found that a discretely growing arc, where the height increases with the rotation angle and the width increases at every  $2\pi$  rotation, gives a more convincing structure.

A three-dimensional spiral molecular model of a carbon nanoparticle with a spiral projection thus generated contains discontinuous points, which are assigned to free radical centers. Additional free radical centers exist at the innermost and outermost ends of the spirals. These radicals are all stabilized by delocalization with conjugated carbon network (Fig. 4). Such hypothetical species were given a temporary name of 'spiroids'. Spiroid-to-onion transformation may occur if one assumes interlayer valence isomerization involving delocalized radical centers to propagate radially in a zipper-like fashion (Fig. 5) [6]. The series of spiroid-to-onion transformation must

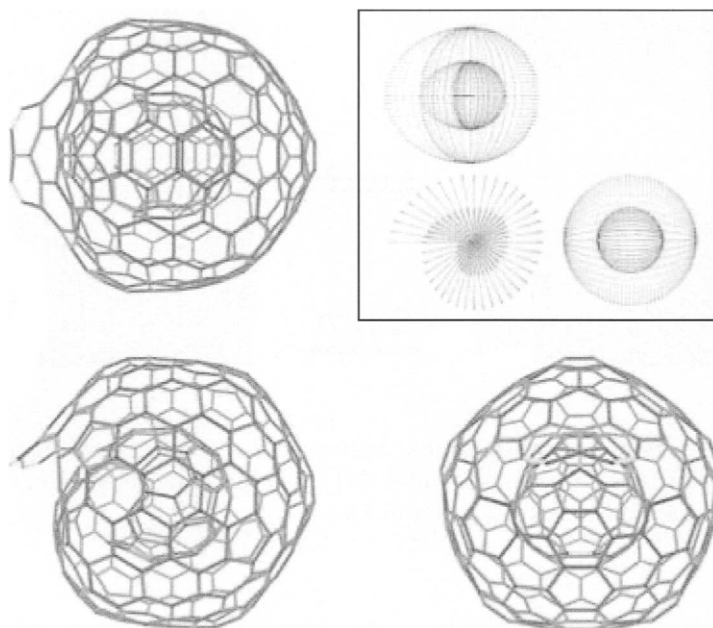


Figure 4. Molecular and numerical (inset) models of a three-dimensional double-layer spiral particle (spiroid),  $C_{300}$ .

constitute a large exothermic reaction as a whole. Under constant input of large electron energy the reverse series of valence isomerization, namely the zipper-like onion-to-spiroid transformations will occur, probably assisted by the release of strain energy.

### 3.3. Formation of carbon nano-onions and Homann mechanism

According to our mechanistic assumption, onion shells achieve the most stable structures from inside toward outside by repeating reversible spiroid-to-onion and onion-to-spiroid transformations accompanied by in-plane valence isomerization like Stone–Wales rearrangements. Carbon nano-onions and nanospiroids are likely to give the idealized models of primary soot particles, which have been a long-pending problem. It is exciting to realize the fact that soot, with which human beings have been so familiar since they discovered fire, is a sort of fullerene.

Previously, Kroto [8] and Homann [13] studied the mechanism of fullerene formation in flame. Kroto's mechanism, called icospiral nucleation process, is the closest to ours, but he apparently thought of logarithmic rather than Archimedean spiral, and did not suggest any reasonable connection between spiral and onion structures. Homann intensively investigated the relationship between soot and fullerenes experimentally for 10 years since 1987 when he found  $C_{60}$  in combustion flame of hydrocarbons. At the end of his career, he proposed a new mechanism of fullerene formation in soot,

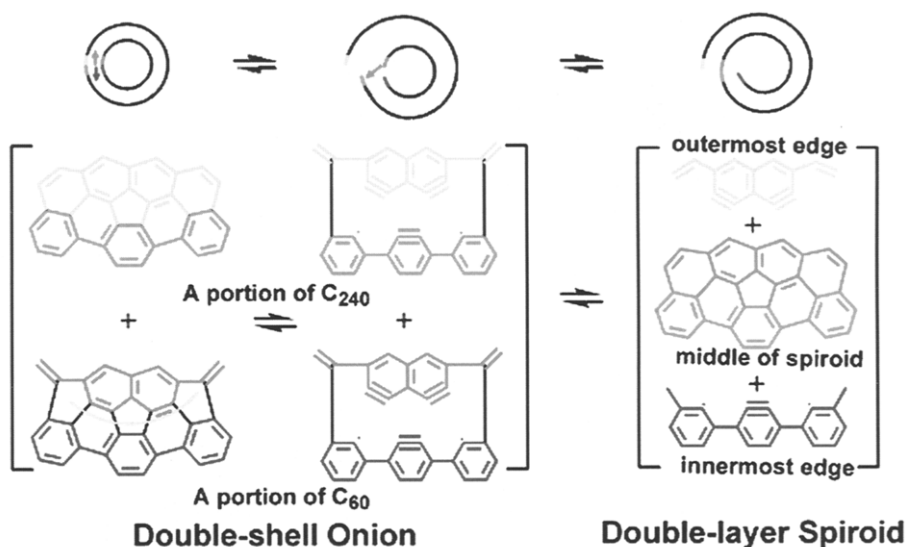


Figure 5. Presumed reaction scheme of the reversible transformation between a double-layer carbon spiroid,  $C_{300}$ , and a double-shell carbon nano-onion  $C_{60}@C_{240}$ . Cleavage of onion-shell starts at weak C–C bonds at structural defects, fused pentagons, etc., and prompts interlayer valence-bond isomerization.

wherein the small unidentified species from pyrolysis of carbonaceous fuel grow through a series of well-identified species: polycyclic aromatic hydrocarbons (PAHs), their *syn*-dimers, and then fullerenes by intra-dimer cyclization (Fig. 6). It is assumed that buckminsterfullerene  $C_{60}$  is formed only when the *syn*-dimer contained 60 carbon atoms. Dimers of PAH that do not give rise to  $C_{60}$  grow to oligomers by adding more PAH molecules, and eventually become soot. Negatively charged aromatic oligomers (aromers) including those having 60 carbon atoms have been identified by mass spectrometry. His scheme considered only the single-shell fullerenes like  $C_{60}$ .

### 3.4. Unified mechanism of soot and fullerene formation

We believe that *syn*-oligomerization of a discretionary pair of PAHs should be a more likely initiation process of primary particle formation than Homann's intramolecular cyclization of *syn*-dimers (Fig. 7). Subsequently, the products undergo reversible spiroid-onion transformation involving in-plane rearrangements under the high-temperature conditions. Continuous rearrangement process leads, like adamantane rearrangement [14], to thermodynamically the most stable  $60n^2$  ( $n = 1, 2, 3, \dots$ ) configuration of the infinite carbon nano-onion series with  $C_{60}$  ( $n = 1$ ) in the center. Thus, concomitant formation of soot particles and fullerenes can be understood within the framework of a single collective mechanism. Single-layer

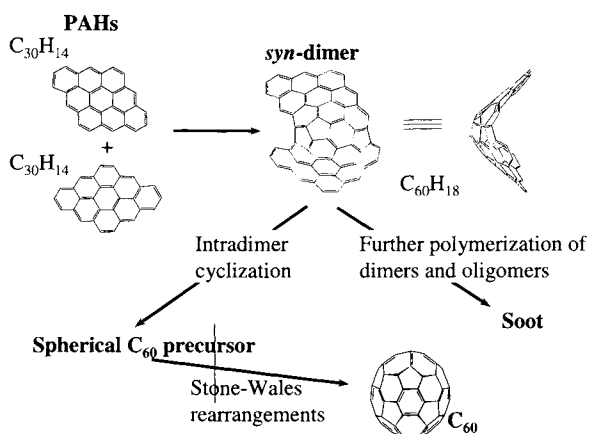


Figure 6. Chemical transformations in the incomplete combustion process of hydrocarbon proposed by Homann. The first intermediates PAH polymerize into *syn-dimer* and other oligomers (aromers), but only the *syn-dimer* of 30-carbon PAH is transformed into  $C_{60}$ , while all the other aromers grow into soot.

fullerenes are formed only when *syn*-oligomerization of PAH happened to lead to closure to a spherical polyhedral solid during the first spiral turn. Even in such a case, total number of carbon atoms will be adjusted by the one-layer version of onion-spiroid transformation. Otherwise, continuous *syn*-addition of small carbon radicals, such as  $C_2$ , PAH, and aromer radicals onto the radical terminal at the outermost layer of spiroids lead to primary particles of soot.

### 3.5. Secondary structure of soot by agglutination of primary particles

Chemistry of soot is complicated by the appearance of the secondary structures, or the so-called 'aggregate' superstructure of the spherical primary particles (Fig. 8). Let us speculate on how the superstructure evolves. Primary particles may have been well dispersed immediately after explosion and their formation, but the particles become aggregated as the pressure and temperature decrease, depending upon the size of particles (the smaller the particles, the higher the tendency to aggregation). Under the incomplete combustion conditions of furnace black processes, concentrations of  $C_2$ , PAHs, and aromer radicals are abundant at this point and the radical addition process continues at the outermost layer on the surface of aggregate to form deformed graphene layers extending over the entire surface of aggregate. As the aggregation and radical addition proceed simultaneously, the product will have complex structure, in which deformed graphene layers will be found not only on the surface but also in the inside of aggregates.

The deformed graphene layers that bind primary particles together by both physical and chemical forces will be much more resistant to weak perturbations like strong agitation than aggregates simply bound by van der Waals attraction force

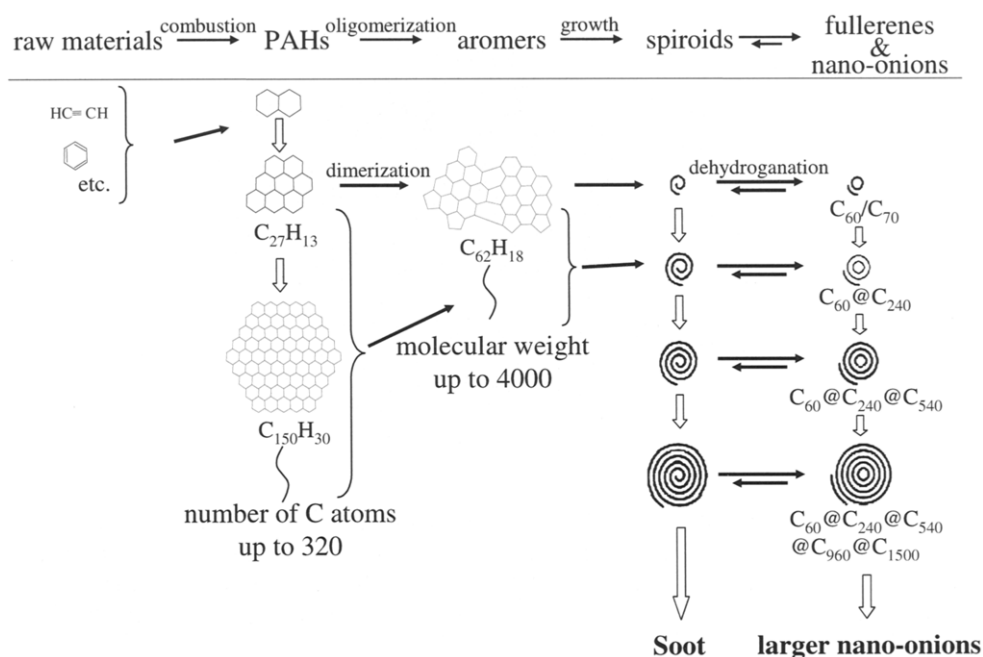


Figure 7. Unified mechanism of formation/growth of soot,  $C_{60}$  and nano-onions. Some PAHs and only one aromer out of numerous structures are depicted as examples.

alone, but tend to break down readily by high-energy treatments with strong oxidants or even special mechanical impacts because of the abundant structural defects. It would be interesting to correlate the curvature properties of deformed graphene sheets with chemical and mechanical stability.

An important aspect of the above speculation is about the definition of aggregation. The word aggregation has been used primarily to the mass of particles assembled through physical force, namely van der Waals attraction. Van der Waals force is generally weak, and such aggregates can be easily dispersed by giving physical perturbation like grinding and mixing. On the other hand, forces that bind particles together within the 'aggregate' structure of carbon blacks are those of chemical bonds, hence the current terminology of using the same word of aggregation to two different kinds of assembly is confusing. For this reason, we suggest to call chemical aggregates as 'agglutinates' [15].

#### 4. CARBON BLACKS AS INDUSTRIAL MATERIALS

With the knowledge on the formation mechanism and on the structure of primary as well as secondary particles of carbon blacks, we now have some perspectives on their potential as the carbon materials.

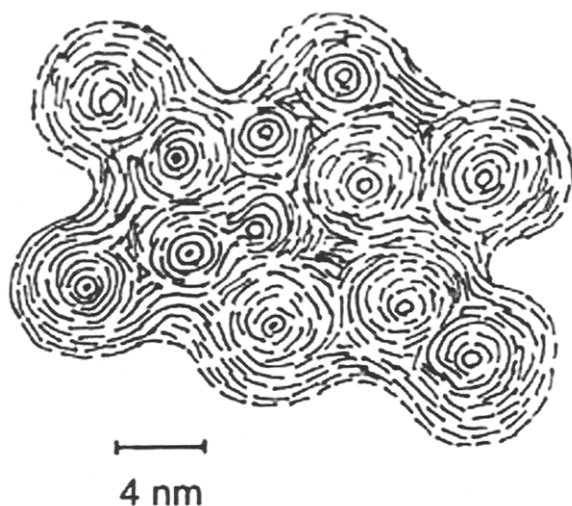


Figure 8. Model of core agglutinate of a high-structure carbon black. Primary particles are believed to contain  $C_{60}$  or its congener in its center. Outer layers are merged into large deformed and defective graphene sheets that hold the assembly of primary particles, which are highly defective multi-shell fullerenes or its spiroidal counterpart.

*Crystallinity.* The most outstanding defect of carbon blacks as the industrial carbon source is their low crystallinity. How can we improve the degree of crystallization? In the past, heating has been traditionally used to increase crystallinity of poorly crystalline or amorphous carbons. The process is also called graphitization because graphite was the goal of the highest crystalline carbon. Now that fullerenes are recognized as another crystalline form of carbon, which attains stability due to the closed structure and favorable disposition of pentagonal defects, we have a new strategy to increase the crystallinity of non-graphitizing carbon: to convert carbon black into the most stable isomer of corresponding fullerene analog. In our case, the goal is carbon nano-onion with  $60n^2$  ( $n = 1, 2, 3, \dots$ ) configuration.

Heating strategy has long been adopted to carbon blacks by heating carbon blacks above  $3000^\circ\text{C}$  [4,5]. The products of heating have been commercialized under the trade name of 'graphitized carbon black', but without much success. In our opinion, this is because the agglutination remained unchanged in the graphitized carbon blacks, even though primary particles were changed into giant polyhedral multi-layered fullerenes with void in the center. Thus, the results of heating sharply contrasts with those of electron-beam irradiation (Fig. 2), wherein agglutination are destroyed and primary particles are crystallized into nano-onions without any void.



Annealing of carbon black at high temperature is much slower process than irradiation of high-current electron beam to give different products. Clearly, the polyhedral particles with pentagonal defects aligned vertically to absorb uneven interlayer steric interactions are more stable than the carbon nano-onion where interlayer steric energy is absorbed by skeletal deformations to a sphere. Situation is much less clear about the fate of deformed outer layers under these two different modes of annealing; the slow heating probably crystallized the outermost layers as well, which should then become more resistant against destruction. On the contrary, rapid absorption of high-density electron beam at the surface of agglutinate must have led to destruction rather than crystallization.

Only the high-density electron beam is mentioned, but high-energy beams of atoms like proton and carbon should give similar but more pronounced effects compared to the former.

*Dispersity.* If we succeed in isolating carbon nano-onions or any other form of multi-shell fullerenes from carbon black, it would be the highest concern to keep them dispersed in order to appreciate the effect of nano-sized primary particles to full extent. The problem and countermeasures will be discussed elsewhere [16].

*Homogeneity and uniformity.* Even though the structural homogeneity of carbon blacks is almost perfect (Table 1), the structure itself is of low crystallinity. Furthermore, the nanostructure of carbon black is not uniform, consisting of highly defective primary particles and deformed outer layers on the surface of agglutinates.

## 5. CARBON NANO-ONIONS

We found that irradiation of convergent electron beam onto carbon blacks leads to remarkable improvements in the crystallinity of the primary particles and at the same time to disintegration of agglutinate structures (Fig. 2). This novel transformation, listed in the 6th row of Table 1, deserves more attention and will be analyzed in some detail in this section.

In spite of the characteristic structure equivalent to MWCNTs with zero length, carbon nano-onions have never been isolated in macroscopic amounts, impeding physical or chemical characterization of bulk or dispersion properties. However, their atomistic structures are well investigated by calculation [12], and their bulk forms have often been observed under electron microscopes [9]. All the shells in an onion structure are akin irrespective of its size. In this regard, a mixture of nano-onions having a size distribution is similar to homologous mixtures of hydrocarbons like kerosene and gasoline. Nano-fractionation of the particles according to diameter must be a challenging subject, once they are isolated.

Why cannot we apply the focused electron beam upon carbon blacks to isolate carbon nano-onions? This is simply due to the technical reason, that electron beam sources with large apertures working at high voltage and high density comparable to 200 keV and 150 A/cm<sup>2</sup>, respectively, was not available. We knew the method of isolation, but the tool was missing. In this regard, carbon nano-onions were no more than painted delicacies. However, currently such a super-electron gun is gradually gaining reality. It has been already known since 1966 when the explosive electron

emission was discovered in Russia by Mesyats/Fursey that high-density pulse electron beam is producible up to 1 MA/cm<sup>2</sup> even under the condition of low voltages [17]. A prototype of explosive electron emission devices was first produced in 2002 in Japan, by Uemura, and appeared on the market from Nagata Seiki Co., Ltd. in the following year under the commercial name of 'Corrosion Resistant System' (for metals) [18,19]. Irradiation of pulsed electron beam of ultra-high density under a relatively low acceleration voltage of 20 keV upon metallic objects like metal mold quickly produces polishing effects. Despite large irradiation area of about 100 cm<sup>2</sup>, the acceleration voltage is by far lower than the threshold of electron energy for displacement of *sp*<sup>2</sup> carbon atoms to trigger the formation of nano-onions. Nevertheless, the subsequent developments enabled to attain 250 keV of acceleration voltage and 500 ns of pulse width at High Voltage Research Institute in Tomsk, Russia.

There will be a number of potential applications worth examining, once carbon nano-onions are produced. While some have made a 'sour grapes'-like explanation that bunched agglutinates of carbon blacks are favorable for reinforcing rubber by tangling well with the polymer backbones, it is also likely that nano-dispersion of primary particles provides even a better effect due to the incomparably larger total surface area. The unique structures composed of nested fullerenes will give rise to novel properties suitable for solid-state optical limiter, solar heat storage, or in general as the substitute of graphite micropowder.

## 6. PRODUCTION OF DIAMOND FROM SOOT

When carbon nano-onions are exposed to convergent electron beam irradiation under heating above 400 °C (the upper limit has not been determined) in a HRTEM, diamond cores are nucleated. Further irradiation in the temperature range 300–1000 °C propagates the diamond phases, converting the nano-onions into nanodiamond particles as demonstrated in Fig. 9 [10,20]. This phenomenon was found by Banhart already

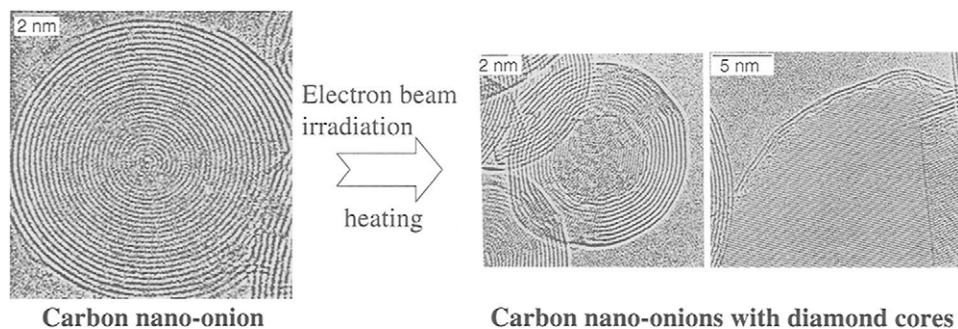


Figure 9. Nucleation and growth of diamond cores in carbon nano-onions induced by high-voltage high-density electron beam irradiation at >400 °C.

in 1996 [21] (the 7th row in Table 1). If carbon blacks are treated in this way subsequent to the crystallization into separate particles of carbon nano-onions (Fig. 2), the overall change would be the direct conversion of soot particles into much more valuable nanodiamond particles via one-pot two-stage dry reaction.

The mechanism of onion-diamond transition under the irradiation of electron beam in high vacuum is still not well understood, but represents one of the mild syntheses of diamond. Displacement of carbon atoms from onion-shells takes place by knock-on collisions of high-energy electron beam, creating interstitial-vacancy pairs. At high temperatures the vacancies are quickly relaxed by recombination with interstitial atoms or in-plane rearrangements of the fullerene shells. This effective relaxation process plays an essential role in the onion-to-diamond transition in addition to the displacement itself. The in-plane rearrangements induced by the knock-on collisions lead to the formation of pentagon-heptagon pairs while the creation of interstitial-vacancy pairs some reduction of onion shells in size. Nano-onions undergoing these changes have more spherical shapes and smaller intershell spacing [10,21–23], especially at inner shells, than those with the ideal configuration of  $C_{60}@C_{240}@C_{540}@C_{960}@C_{1500}@ \dots @C_{60n}^2@ \dots$ . This self-compression creates pressures high enough to nucleate diamond cores at the centers of the onions. Once nucleation takes place, the graphite-to-diamond transformation, a transition from a stable to a metastable phase, proceeds even at zero pressure until all the onion shells are converted due to the lower displacement threshold of graphite than that of diamond [24].

We will begin producing nanodiamond particles from carbon nano-onions as soon as the high-density high-voltage electron gun is ready. As shown in Fig. 9, bucky diamond particles will be obtained as the primary products, wherein the spherical diamond particles are wrapped with a few layers of giant fullerene. The surfaces of such particles are susceptible to chemical reconstruction, for example hydrogenation or functionalization. Carbon blacks have a big advantage in this production besides the low cost: various types of commercial carbon blacks have average sizes ranging between 14 and 1000 nm, hence it should be possible to produce diamond particles having different sizes, each being considerably smaller than the starting onion particles because of the higher density of diamond and the displacement of carbon atoms during the irradiation process.

Single crystals of diamond having an average diameter of  $4.4 \pm 0.3$  nm have been recently obtained in dispersed form from their agglutinates by stirred-media milling with micron-sized ceramic beads [15,25,26]. Crude agglutinates are produced by detonation of an oxygen-imbalanced explosive like Composition B consisting of TNT and hexogen: about one half of the soot weight that results from the incomplete combustion in the explosion is nanodiamond. This fact has been known since almost 40 years ago [27]. Thus, when the conversion of carbon blacks into diamond is realized to give double-digit-nano to submicron diamonds, we will have a whole range of diamondoid carbons starting from adamantane ( $C_{10}H_{16}$ ), diamantane ( $C_{14}H_{20}$ ), and higher diamondoid hydrocarbons [28] through single-digit nanodiamond by detonation (ultranano-crystalline diamond), double-digit-nano- to submicron-diamond (from carbon blacks), artificial micron-sized diamond (by the static high-pressure high-temperature synthesis) to gem diamond larger than millimeters.

## 7. PRODUCTION OF $C_{60}/C_{70}$ AND SMALL CARBON NANO-ONIONS BY PYROLYSIS

A close look at Fig. 7 indicates several possibilities of developing the furnace black process into a few interesting variations. According to our hypothesis, all primary particles of carbon blacks contain one  $C_{60}$  molecule or counter spiroid in the center (Fig. 8). This means that  $C_{60}$  can be produced using pyrolysis method at a price as low as \$1/kg, if the growth process of soot can be quenched at a very early stage (the 8th row, Table 1). The possibility of pyrolytic synthesis of  $C_{60}$  was conceived in this way [29]. It would be difficult to exclude contamination of the  $C_{60}$  fraction by the smaller members of carbon nano-onions such as  $C_{60}@C_{240}$  and  $C_{60}@C_{240}@C_{540}$ . However, these smaller onions are appealing not only as novel additions to fullerene family, but also as the starting materials for Mackay crystals or superfullerene conceived by Mackay in 1991 [31–39].

### 7.1. Pyrolytic synthesis of $C_{60}$

The second-generation combustion method of  $C_{60}$  synthesis developed by Howard is counted as one of the hot topics in the production of fullerenes [32]. Whereas the details of this method still remain undisclosed, the new method allegedly succeeded in entirely suppressing soot formation in contrast to the previous method, which was accompanied by large excess of soot.

Nonetheless, we note here a few essential contradictions that we found when analyzing the combustion method [33]

- (1) The whole process, which must be similar to that given in Fig. 8, takes place under extremely hostile environment of flame. Considerably high proportion of the product may have been lost by burning.
- (2) Similarly, the whole complex process must be completed within a few seconds while in the flame. Considerably high proportion of the product may have been lost due to insufficient time.
- (3) For the reactions to proceed fast enough, the flame temperature must be kept high, close or equal to 2000 °C, and more and more fuel must be burnt under good supply of air, leaving less and less carbon atoms for fullerene formation.
- (4) With violent oxidation reactions of combustion going on in the close vicinity of reaction zone, only a few controllable factors are available.
- (5) As the result, close to 97.5% of fuel are burnt out and only 2.5% remain available for soot formation, among which only 10–20% proceed to fullerene.

On reflection, we must admit that flame is used only for the purpose of supplying heat for thermal decomposition of fuel to occur and for fullerene forming reaction sequences to proceed. However, heat can be supplied separately from other source as well, e.g., electrical resistance under non-oxidative conditions [29].

In this regard, the furnace black process is worth examining as an archetype of pyrolytic fullerene synthesis. Fig. 1 will be employed to expound the draft. Hot fluidic heat supply, which consists of carbon dioxide and steam, is prepared by

complete combustion of cheap fuel in the combusting zone colored yellow with a *proviso* that slight excess of oxygen should be left unburned in this zone for removing the surface hydrogen of raw materials sprayed afterwards. In the red-colored soot-growth region, clustering of pyrolyzed carbon atoms takes place in the order PAHs, aromers, and spiroids. In the course, the intermediate reactants must be correctly quenched in order to obtain structurally homogeneous product. Ensuing annealing process is also critical to complete the cyclization reaction and the transformation into onion-like cage structures. Finally the hot gas stream is extinguished. In order to maximize the yields of desired products, the reaction conditions must be properly modified.

The merits of pyrolytic synthesis of  $C_{60}/C_{70}$  are as follows: (1) low-cost but rational production of fullerenes, (2) low yields of by-products, and (3) many adjustable reaction conditions. Probably some of the readers will wonder why mass production is necessary at the time when fullerenes are hardly seen in the nanocarbon market. On the contrary,  $C_{60}$  is one of the best-studied materials in the world among more than 10 million molecules investigated in chemistry, and consequently an astonishingly wide variety of applications have already been discovered and compiled [34]. Low cost of production is hence the only remaining key factor to promote applications on the industrial scale.

## 7.2. Preliminary approach toward the synthesis of Mackay crystals

As mentioned, according to the soot formation scheme of Fig. 7, the pyrolytic synthesis of fullerenes will be accompanied by considerable amounts of  $C_{60}@C_{240}$  and  $C_{60}@C_{240}@C_{540}$  as the by-products. Once the fullerene production conditions are found double- or triple-shell nano-onions will be quickly accumulated. It is desirable to have a clear perspective on the use of these by-products. Here we explore the possibility of making Mackay crystals from the small nano-onions.

Preliminary theoretical calculations suggest that  $C_{60}@C_{240}$  and  $C_{60}@C_{240}@C_{540}$  tend to take spherical shapes rather than polyhedral structures, therefore showing properties similar to fullerenes rather than graphite [35]. We also expect that these onions form face-centered cubic (fcc) or body-centered cubic (bcc) crystals like  $C_{60}$  [36]. On the other hand, it has been known that  $C_{60}$  crystals transform themselves into various polymers via  $[2 + 2]$  cyclo-addition reactions under high pressure between 3 and 8 GPa and high temperatures as displayed in Fig. 10 [37,38]. Among these polymers, Blank discovered a few remarkably hard carbons, even harder than diamond, formed at around 13 GPa and 670–820 K [39]. Rietveld analysis was performed on one of these superhard carbons [40,41], and the following notable features of the structure were revealed as represented in Fig. 11:

- (1) Three-dimensional network is firmly constructed by forming 14 single-bond bridges from each  $C_{60}$ -derived unit.
- (2) An especially interesting feature is a bridge of cyclobutane ring aligned perpendicularly along *b*-axis and connecting  $C_{60}$  unit along this axis.

When Rietveld analysis was attempted on the amorphous powder of superhard carbon, an unusually small inter- $C_{60}$  unit distance, about 0.86 nm, was found.

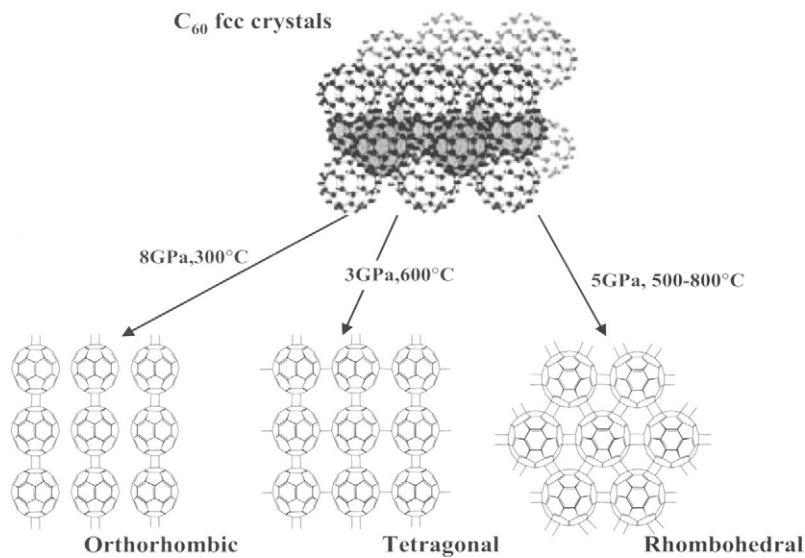


Figure 10. One- and two-dimensional [2 + 2] polymers obtained by high-temperature high-pressure treatments of  $C_{60}$  crystals.

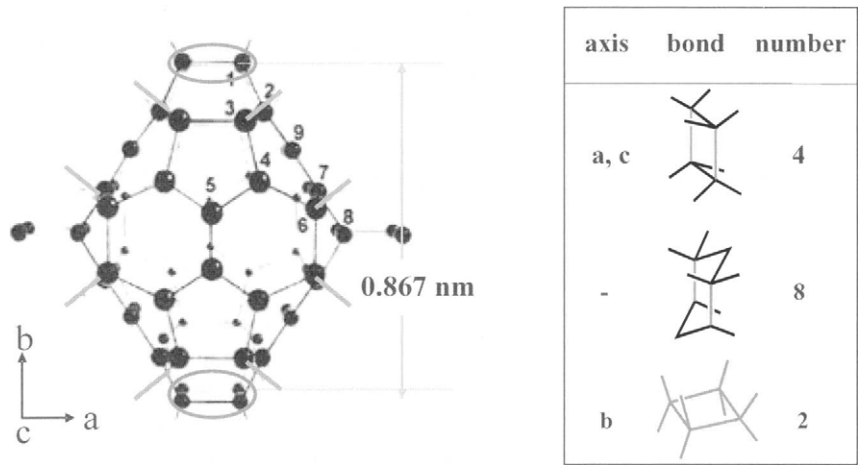


Figure 11.  $C_{60}$ -derived asymmetric unit with its bonding patterns with neighboring units in the body-centered orthorhombic lattice of the superhard three-dimensional polymer of  $C_{60}$ .

Incidentally, this short distance coincided with the inter- $C_{60}$  unit distance in the optimized geometry of structure (B) of Fig. 12, which depicts the first three  $C_{120}$  intermediate structures, hand-generated in a study on the likely course of Stone–Wales rearrangement sequence starting from  $[2 + 2]$   $C_{60}$  dimer (A) [42]. When the optimized structure (B) was fit to the subsequent Rietveld analysis, the crystal structure of the superhard carbon could be solved with a satisfactory fitness level.

Upon inspection of the resulting crystal structure, we felt that a key factor contributing to the particularly high hardness of this carbon must be those strong bridges of double-sided cyclobutane ring formed along *b*-axis in each  $C_{60}$ -derived unit. According to this assumption, even harder carbon materials will be obtained if three-dimensional  $C_{60}$  polymers having wide and stronger bridges were made.

Later, we wrote a program to deduce the shortest Stone–Wales rearrangement pathways starting from  $[2 + 2]$   $C_{60}$  dimer and reaching the shortest carbon nanotube  $C_{120}$  (24, Fig. 13) [43]. In this long sequence, we found a number of intermediates having thick and wide bridges as mentioned above, but we were puzzled to realize that the structure B with double-sided cyclobutane ring in the center was missing in this route. In our previous hand-driven pathway (Fig. 12), the intermediate C, which corresponds to the molecule 4 in Fig. 13, is the precursor of B. However, 4 changed into 5, then into 6 and so on, never yielding B. The reason is two-fold. First, structure B is a dead end, from whence there is no Stone–Wales pathway to evolve into stable

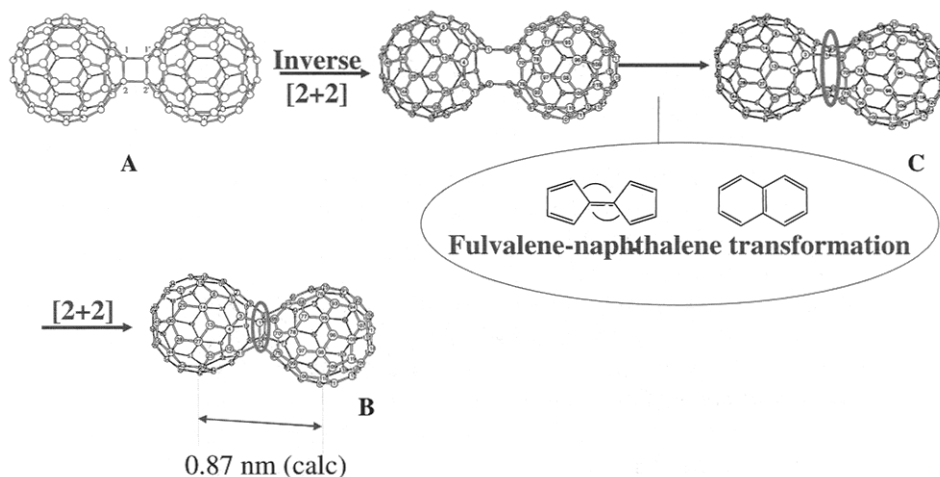


Figure 12. Three-step transformation pathway of  $[2 + 2]$   $C_{60}$  dimer (A) into a fused structure (B), which has been found in the superhard  $C_{60}$  three-dimensional polymer having double-sided cyclobutane bridges along *b*-axis. The pathway was derived by hand.

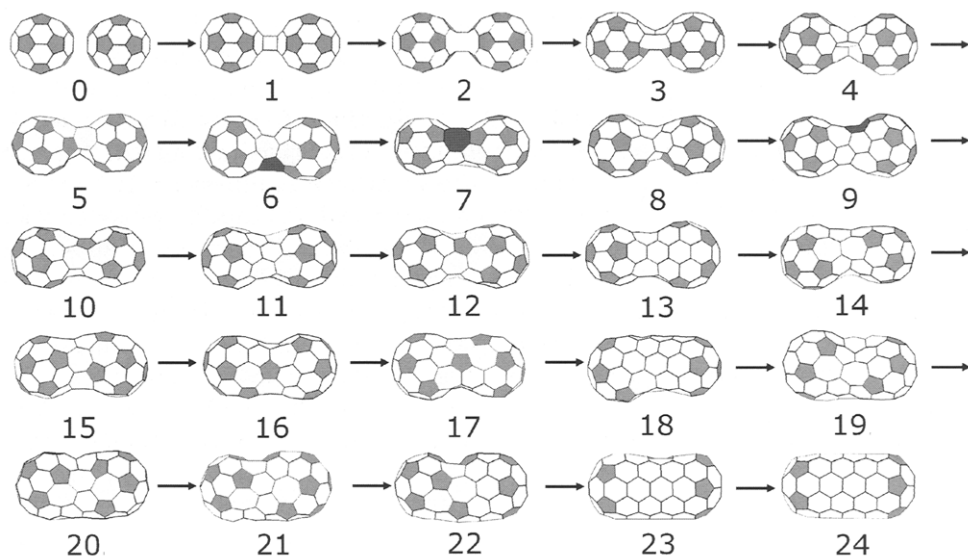


Figure 13. Computer-generated shortest pathway from  $[2 + 2]$   $C_{60}$  dimer (1) to the shortest  $C_{120}$  carbon nanotube (24) through Stone–Wales rearrangements. Hexagons, pentagons, heptagons, and octagons are colored white, pale black, white, and black, respectively.

isomers. The other reason is that in crystal  $C_{60}$  molecule is bonded with the other neighboring  $C_{60}$  units; hence, only a few carbon atoms are left for bridging even at this early stage. In other words, we need fullerenes much larger than  $C_{60}$  in order to create still harder carbon materials wherein it is desirable that each fullerene unit is bonded to at least six neighboring fullerene units by thick and strong bridges.

Giant fullerenes like  $C_{100}$  are, however, hardly available. Hereby, we believe that  $C_{60}@C_{240}$  and  $C_{60}@C_{240}@C_{540}$  can be potential candidates for the superhard materials. Having almost spherical outershell, these fullerenes will form a similar crystal of multi-dimensional polymers by  $[2 + 2]$  addition reaction like  $C_{60}$  upon heating the crystals under high pressure. At some point during the evolution of inter-unit bridges, the shrinking outershell will exert high pressure upon inner shells and eventually destroy them so that many carbon atoms will become available for constructing stronger, wider, and thicker bridges. The final result of high-pressure high-temperature treatment of these multi-layered fullerene crystals will be hard carbons having jungle gym skeleton made of wide bridges and fullerene-like joints. Strain will be minimized by Stone–Wales rearrangements in the network to create smooth curved surface having negative Gaussian curvatures. Then, we have Mackay crystals.



### 7.3. Plausible properties of Mackay crystals

As mentioned above, Mackay crystals (Table 3) [30,31] are novel carbon structures conceived by Mackay as the topological counterpart of  $C_{60}$ . The most prominent feature of the crystals is that any points on the curved surfaces are saddle points with negative Gaussian curvatures ( $K < 0$ ). Whereas no surface having constant negative  $K$  converges in the real space, periodically curved surfaces are possible with varying  $K$ . Some of such surfaces were discovered in the 19th century by Schwarz, and named Schwarz surfaces. In analogy with mineral crystals, they are often called Schwarzites. Patchwork of graphitic tiles consisting of 4- to 8-membered rings onto the surfaces of Schwarzites gives the Mackay crystals. We have also used a similar strategy to generate a hypothetical superdiamond structure [44–46].

Unlike the times of Schwarz and Mackay, the practical syntheses of these crystals are actually forthcoming as argued in the precedent section. A sketch of synthetic scheme for a Mackay crystal based on the simplest p-type Schwarzite is depicted in

Table 3  
Topological comparison between  $C_{60}$  and Mackay crystal.

Comparative items	$C_{60}$	Mackay crystals
Gaussian curvature	$K > 0$ constant	$K \leq 0$ variable
Average of curvature	$H > 0$ constant	$H = 0$ minimal surface
Singularity	Center point	Omphalos
Symmetry	$I_h$	Repeating unit of p-type is $O_h$
Primary factor for discreteness	5-,6-, (7-) membered rings	6-,7-,8-membered rings 4-,9-,10-membered rings are also possible
Pores	No	Yes p-type has 6 pores per unit cell
Number of C	60	$\infty$ crystal
Structural rigidity	High	—
Thermodynamic stability	High energy minimum	Unknown low energy minimum?
Spatial division by surface	Uneven division	Equivalent division zeolite-like
Surface shape	Spherical	Schwarz surface p-, d-, g-types, etc.
Synthesis	Relatively easy	Possible?

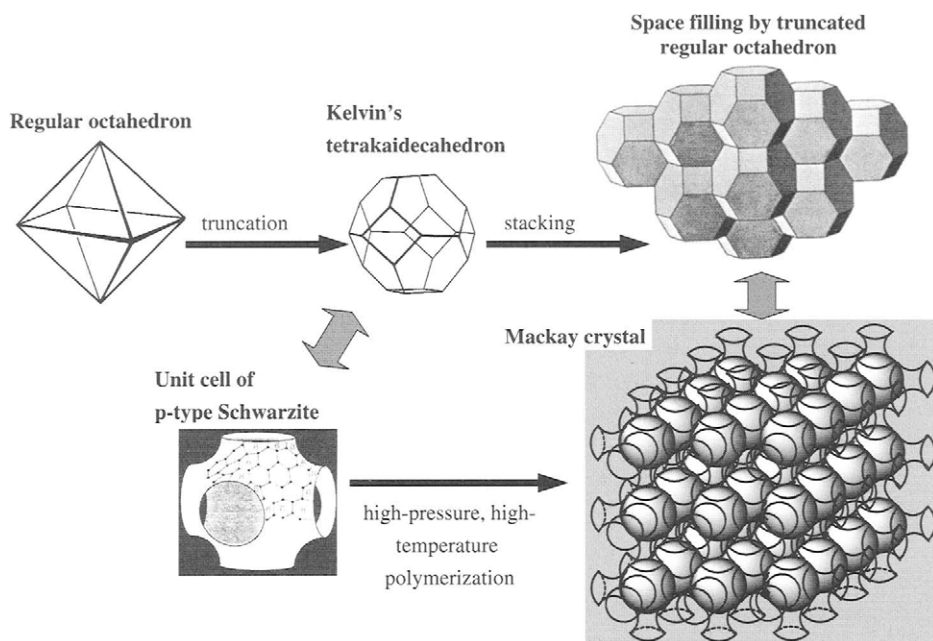


Figure 14. Mackay crystal consisting of p-type Schwarzite.

Fig. 14. Numerous applications can be proposed for a Mackay crystal in view of its remarkable characteristics predicted, like superhardness, nano-porosity, and novel electronic structures inherent to the unique continuous network structure. Especially, there are uncountable applications of superhard materials like diamond. It would be a wonderful material of boring drills or cutters for the investigation of underground. Not only exploration of natural resources in relatively shallow underground, say down to 5 km, but also collecting geological information of somewhat deeper underground like 30 km, are evidently important and rewarding subjects of research. Another interesting aspect of Mackay crystal may be worthwhile a brief mention here. If heptagons and/or octagons, essential for the negative curvatures of the Schwarzites, are completely oriented in the infinite translational repetition of the unit cells in Mackay crystal, they might cause strong ferromagnetism [47].

## 8. A TENTATIVE PROPOSAL FOR CARBON BLACKS-DERIVED NANO-CARBON INDUSTRIES

Among the conceivable nano-carbon industries related to carbon blacks, those plans that are already taking concrete shape are presented in Fig. 15. The two rows on the lower half signify direct utilization of carbon blacks, while the other two will need some modification in the reactor system of furnace blacks. All these plans were

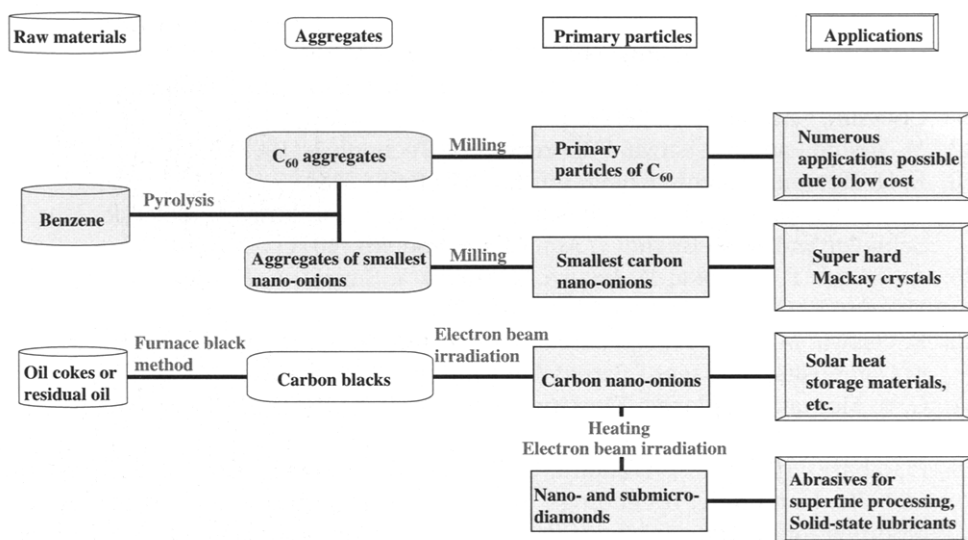


Figure 15. Nanocarbon industry that uses carbon blacks and their precursors as the raw materials.

given solid background ever since we reconfirmed Kroto's original proposal that primary particles of soot are defective carbon nano-onions (Fig. 8). We still have a long way to go, and actually the important phases discussed in the Sections 5 and 6 have been examined only in very preliminary experiments. However, it is delightful to look forward to the new materials and to what they will bring in our lives.

## REFERENCES

1. <http://www.nano.gov/>
2. E. Ōsawa (Ed.), *Perspectives of Fullerene Nanotechnology*, Kluwer Academic, Dordrecht, Netherlands, 2002.
3. A. M. Thayer, *C&EN* **83** (2005) 17.
4. J.-B. Donnet, R. C. Bansal and M.-J. Wang (Eds.), *Carbon Blacks*, 2nd ed., Dekker, New York, 1993.
5. T. Kato, G. Akiyama, Y. Akiyama, T. Nakahara, T. Hayasaka, B. Hoshino and T. Yamasaki (Eds.), *Carbon Black Handbook*, 3rd ed., Carbon Black Association, Tokyo, 1995.
6. M. Ozawa, H. Goto, M. Kusunoki and E. Ōsawa, *J. Phys. Chem. B* **106** (2002) 7135.
7. R. E. Franklin, *Proc. Roy. Soc. A* **209** (1951) 196.
8. H. R. Kroto, K. Prassides, R. Taylor and D. R. M. Walton, in *The Chemical Physics of Fullerenes 10 (and 5) Years Later*, Ed. W. Andreoni, Kluwer Academic, Dordrecht, Netherlands, 1995, p. 3.

9. D. Ugarte, *Nature* **359** (1992) 707.
10. F. Banhart, *Rep. Prog. Phys.* **62** (1999) 1181.
11. E. D. Obratsova, M. Fujii, S. Hayashi, V. L. Kuznetsov, Yu. V. Butenko and A. L. Chuvilin, *Carbon* **36** (1998) 821.
12. M. Yoshida and E. Ōsawa, *Fullerenes Sci. Technol.* **1** (1993) 55.
13. K. H. Homann, *Angew. Chem. Int. Ed.* **37** (1998) 2434.
14. E. Ōsawa, K. Aigami, N. Takaishi, Y. Inamoto, Y. Fujikura, Z. Majerski, P. v. R. Schleyer and E. M. Engler, *J. Am. Chem. Soc.* **99** (1977) 5361.
15. A. Krüger, F. Kataoka, M. Ozawa, T. Fujino, Y. Suzuki, A. E. Aleksenskii, A. Ya. Vul' and E. Ōsawa, *Carbon* **43** (2005) 1722.
16. E. Ōsawa, M. Ozawa, M. Inakuma and M. Takahashi, *Dispersing Nanoparticles in Composites*, Japanese Patent Application 2005-309948.
17. G. A. Mesyats, *Explosive Electron Emission*, URO-Press, Ekaterinburg, Russia, 1998.
18. P. Raharjo, H. Wada, Y. Nomura, G. E. Ozur, D. I. Proskurovsky, V. P. Rotshtein and K. Uemura, *Proceedings of the 6th International Conference on Modification of Materials with Particle Beams and Plasma Flows*, Tomsk Tech. Univ., Tomsk, Russia, 2002, pp. 679–682.
19. A. Okada, Y. Uno, N. Yabushita, K. Uemura and P. Raharjo, *International Conference on Large Edge Manufacturing in the 21st Century*, Niigata Univ., Niigata, Japan, 2003, pp. 1023–1028.
20. M. Zaiser and F. Banhart, *Phys. Rev. Lett.* **79** (1997) 3680.
21. F. Banhart and P. M. Ajayan, *Nature* **382** (1996) 433.
22. H. Terrones and M. Terrones, *J. Phys. Chem. Solids* **58** (1997) 1789.
23. K. R. Bates and G. E. Scuseria *Theor. Chem. Acc.* **99** (1998) 29.
24. M. Zaiser, Y. Lyutovich and F. Banhart, *Phys. Rev. B.* **62** (2000) 3058.
25. E. Ōsawa, in *Synthesis, Properties and Applications of Ultrananocrystalline Diamond*, Eds. D. M. Gruen, O. A. Shenderova and A. Ya. Vul', Springer, Dordrecht, Netherlands, 2005.
26. E. D. Eidelman, V. I. Siklitsky, L. V. Sharonova, M. A. Yagovkina, A. Ya. Vul', M. Takahashi, M. Inakuma and E. Ōsawa, *Diamond & Rel. Mater.* **14** (2005) 1765.
27. O. A. Shenderova, V. V. Zhirnov and D. W. Brenner, *Crit. Rev. Solid State Mater. Sci.* **27** (2002) 227.
28. J. E. Dahl, S. G. Liu, R. M. K. Carlson, *Science* **299** (2003) 96.
29. E. Ōsawa, Japanese Kokai Patent 2005-8500, Appl. 2003-177403.
30. A. L. Mackay and H. Terrones, *Nature* **352** (1991) 762.
31. A. L. Mackay and H. Terrones, *Phil. Trans. R. Soc. Lond. A* **343** (1993) 113.
32. J. B. Howard and D. F. Kronholm, *Nanotechnology Forum*, National Taiwan University, Taipei, Taiwan, 2003.
33. M. Ozawa, P. Deota and E. Ōsawa, *Fullerene Sci. Technol.* **7** (1999) 387.
34. K. M. Kadish and R. S. Ruoff (Eds.), *Fullerenes: Chemistry, Physics and Technology*, Wiley, New York, 2000.
35. Unpublished results.

36. M. S. Dresselhaus, G. Dresselhaus and P. C. Eklund, *Science of Fullerenes and Carbon Nanotubes*, Chapt. 7, Academic Press, San Diego, 1995.
37. Y. Iwasa, T. Arima, R. M. Fleming, T. Siegrist, O. Zhou, R. C. Haddon, L. J. Rothberg, K. B. Lyons, H. L. Carter, Jr., A. F. Hebard, R. Tycko, G. Dabbagh, J. J. Krajewski, G. A. Thomas and T. Yagi, *Science* **264** (1994) 1570.
38. M. Nuñez-Regueiro, L. Marques, J.-L. Hodeau, O. Béthoux and M. Perroux, *Phys. Rev. Lett.* **74** (1995) 278.
39. V. Blank, S. Buga, G. Dubitsky, N. Serebryanaya, M. Popov and V. Prokhorov, in *Perspectives of Fullerenes Nanotechnology*, Ed., E. Ōsawa, Academic, Dordrecht, Netherlands, 2002, pp. 223–233.
40. L. A. Chernozatonskii, N. R. Serebryanaya and B. N. Mavrin, *Chem. Phys. Lett.* **316** (2000) 199.
41. N. R. Serebryanaya and L. A. Chernozatonskii, *Solid State Commun.* **114** (2000) 537.
42. S. Ōsawa, E. Ōsawa and Y. Hirose, *Fullerene Sci. Technol.* **3** (1995) 565.
43. H. Ueno, S. Ōsawa, E. Ōsawa and K. Takeuchi, *Fullerene Sci. Technol.* **6** (1998) 319.
44. E. Ōsawa, M. Yoshida and M. Fujita, *MRS Bull.* **19** (1994) 33.
45. M. Fujita, T. Umeda, M. Yoshida and E. Ōsawa, *Synth. Metals* **71** (1995) 1897.
46. M. Fujita, M. Yoshida and E. Ōsawa, *Fullerene Sci. Technol.* **3** (1995) 937.
47. T. Makarova, B. Sundqvist, R. Höhne, P. Esquinazi, Y. Kopelevich, P. Scharff, V. A. Davydov, L. S. Kashevarova and A. V. Rakhmanina, *Nature* **413** (2001) 716.

## Chapter 7

### Functionalization and applications of [60]fullerene

A. Mateo-Alonso, D. Bonifazi and M. Prato

Università degli Studi di Trieste, Dipartimento di Scienze Farmaceutiche, Piazzale Europa 1, 34127 Trieste, Italy

This section reviews the different synthetic methodologies for the covalent functionalization of [60]fullerene along with the most significative examples in advanced materials-oriented applications.

#### 1. INTRODUCTION

##### 1.1. Structure of [60]fullerene

Fullerenes are polyhedral carbon cages in which  $sp^2$ -carbons are directly bonded to three neighbors in an arrangement of five- and six-membered rings. Among all fullerenes,  $C_{60}$  has been the most extensively studied since its discovery in 1985 [1] due to its  $I_h$ -symmetrical structure and bulk production in 1990 [2,3]. The structure includes two different types of bonds, namely those at the junction of two hexagons (6–6 junctions, mean C–C distance = 1.391 Å) and those at the junction of a pentagon and a hexagon (5–6 junctions, mean C–C distance = 1.449 Å) [4,5]. The measured bond lengths clearly show that the formal double bonds correspond to the 6–6 junctions and, thus, there are no double bonds in the pentagons. The mean diameter of the sphere is  $\sim 7.1$  Å. Taking into account the van der Waals radius of the carbon atoms, the external diameter is  $\sim 10.4$  Å, while the inner diameter is  $\sim 3.5$  Å. The crystal structure of  $C_{60}$  revealed low-electron delocalization over the spherical surface, and the bond alternation clearly shows a preference for the resonance structure with the 30 double bonds localized at 6–6 junctions. The low delocalization is explained by considering the partial rehybridization of the  $sp^2$ -C-atoms leading to a higher contribution from the s-orbitals. As a consequence, the double bonds are located exocyclic to the pentagons, providing [5]radialene nature to the five-membered rings and 1,3,5-cyclohexatriene nature to the six-membered rings (see Fig.1).

Such rehybridization is also partially responsible for the fairly high electron affinity of  $C_{60}$  (2.7 eV), since it allows a lowering of the LUMO (lowest-unoccupied molecular orbital) energy level [6]. Thus,  $C_{60}$  cannot be considered a “superarene” as it was previously imagined, but rather a weakly conjugated, very strained, and electron-deficient polyene. Although the Hückel Molecular Orbital (HMO) theory is inadequate to calculate the overall stability of  $C_{60}$  since the total energy of fullerene molecules gets a significant contribution from the strain of the  $\sigma$ -bonds, it describes well the frontier orbitals in accordance with the experimental reactivity. The HMO theory thus allowed the calculation of the electronic configuration of pristine

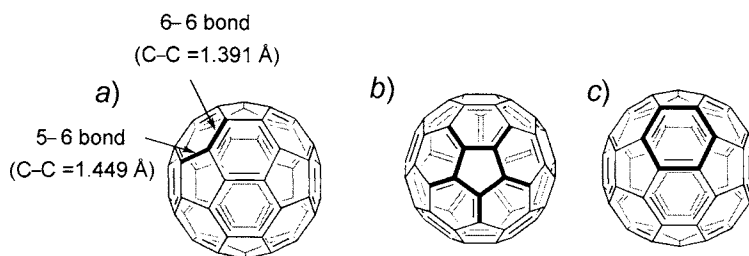


Figure 1. (a) The different types of bonds in C<sub>60</sub>; (b) the [5] radialene and (c) 1,3,5-cyclohexatriene substructures.

buckminsterfullerene, comprising a fivefold degenerate HOMO (highest-occupied molecular orbital) (*hu*) and a low-lying triply degenerate LUMO level (*t<sub>1u</sub>*) [7–11]. This threefold-degeneracy together with the small energy gap between the HOMO and the LUMO ( $\sim 1.8$  eV) make C<sub>60</sub> a fairly good electron acceptor with the ability of gaining reversibly up to six electrons upon reduction [12,13]. The facile reduction contrasts with its difficult oxidation. Only the first three reversible oxidation waves have been observed [14]. HMO-based calculations correctly predict the bond localization in C<sub>60</sub> and also the observed high electron affinity and the electrochemical behavior of buckminsterfullerene.

### 1.2. Physical and electronic properties of [60]fullerene

Due to the  $I_h$ -symmetry of C<sub>60</sub>, only electronic  ${}^1T_{1u} \rightarrow {}^1A_g$  transitions are allowed. The UV/VIS spectrum of C<sub>60</sub> shows strong absorption bands that are due to symmetry-allowed excitations from the HOMO to the LUMO+1, and to a smaller extent from the HOMO–1 to the LUMO. These excitations give rise to three broad main bands at 211 nm ( $\epsilon \sim 158\,000\text{ M}^{-1}\text{ cm}^{-1}$ ), 256 nm ( $\epsilon \sim 174\,000\text{ M}^{-1}\text{ cm}^{-1}$ ), and 328 nm ( $\epsilon \sim 52\,500\text{ M}^{-1}\text{ cm}^{-1}$ ), and to a weaker band at 404 nm ( $\epsilon \sim 2950\text{ M}^{-1}\text{ cm}^{-1}$ ). On the other hand, the absorption in the visible region is associated with the lowest-energy electronic transitions. It is weak because of the highly symmetric closed-shell electronic configuration of the HOMO, and characterized by a weak broad band ( $\epsilon \leq 750\text{ M}^{-1}\text{ cm}^{-1}$ ) between 440 and 635 nm with two main maxima located at 598 and 543 nm [15–17]. The longest-wavelength absorption attributed to the energetically lowest  $S_0 \rightarrow S_1$  HOMO–LUMO transition appears at 620 nm [18]. C<sub>60</sub> shows a very weak fluorescence with low-quantum yield, most likely due to the short lifetime of the singlet excited state and the symmetry-forbidden character of the lowest-lowest energy transition.

The major drawback of fullerenes is their low solubility in organic solvents, which decreases substantially their processability. The solubility of C<sub>60</sub> has been studied in a wide variety of solvents [19]. The solvation of C<sub>60</sub> requires the disruption of many solvent–solvent interactions, which are not adequately compensated by the interactions between solvent and C<sub>60</sub> due to the rigid geometry of the latter

and the lack of permanent dipole moment. In fact,  $C_{60}$  is almost completely insoluble in protic or dipolar aprotic solvents like MeOH, MeCN, tetrahydrofuran (THF), and dimethylsulfoxide (DMSO). It is scarcely soluble in alkanes, with the solubility increasing from pentane to decane. Octane is the only exception in this series, being a worse solvent than heptane. The solubility in haloalkanes is generally higher than in alkanes, and tetrachloroethylene and 1,1,2,2-tetrachloroethane are the best solvents among the common halogenated hydrocarbons. Aromatic hydrocarbons are substantially better solvents. Since  $C_{60}$  is a good electron acceptor, it can easily form charge-transfer complexes with solvents possessing electron donating properties such as tertiary amines and anilines substituted with electron donor groups [20,21]. For instance, the solubility of  $C_{60}$  at 298 K in aniline, *N*-methylaniline, and -*N,N'*-dimethylaniline is 1.05, 1.16, and 3.89 mg mL<sup>-1</sup>, respectively [22]. A notable exception to these trends is CS<sub>2</sub>, which solubilizes  $C_{60}$  quite well even though it is neither very large nor strongly interacting with the all-carbon chromophore.

### 1.3. Chemical reactivity of [60]fullerene

As mentioned above,  $C_{60}$  possesses two different types of bonds, the 5–6 and 6–6 bonds with the latter having a higher double bond character. Due to the low-lying degenerate LUMO level which accounts for its low reduction potential, the chemical reactivity of the formal double bonds is close to that of a strained, electron-deficient alkene [23] and  $C_{60}$  does not behave as an aromatic hydrocarbon. Chemical transformations of  $C_{60}$  generally involve reactions at the 6–6 bonds [24–26]. The main driving force for addition to fullerenes is the relief of strain due to a change in hybridization at the reacting carbons on the spherical surface from  $sp^2$  to  $sp^3$ . Since the additions to  $C_{60}$  are generally exothermic and exergonic, it is often difficult to stop a reaction at the monoadduct stage, unless a large excess of  $C_{60}$  is used. In recent years, the field of fullerene functionalization was mostly aiming at the preparation of fullerene derivatives suitable for materials applications. The most significant reactions directly related to the topic discussed in the context of the material application will be presented here. Specifically, two main class of reactions are mainly used for the organic derivatization of  $C_{60}$  for material application: cycloadditions and nucleophilic additions [27,28].

## 2. CYCLOADDITIONS REACTIONS

[60]Fullerene behaves as a  $2\pi$  electron-deficient dienophiles and 1,3-dipolarophiles undergoing a variety of cycloaddition reactions. Four main types of cycloaddition reactions have been largely investigated: [1+2], [2+2], [3+2], and [4+2]. All reactions typically take place on the 6–6 ring double-bond junctions of the fullerene skeleton. The number of compounds that have been prepared through cycloaddition reactions is too vast to be described in detail, consequently only a few numbers of selected examples are shown to be representative of the general reactions (see Fig. 2).

### 2.1. [1+2]Cycloadditions

Fullerenes undergo [1+2]cycloaddition reactions with divalent species such as carbenes, nitrenes, and silylenes [29] leading to a very large series of methanofullerene



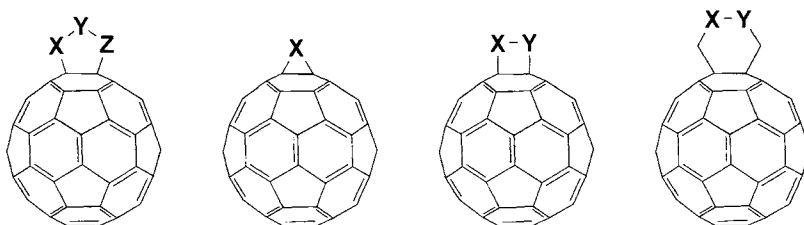


Figure 2. Fullerene cycloadducts.

and their heteroanalogs, respectively. However, addition of carbon has been the most studied to date, through addition of nitrogen (which lead to azafullerenes) has also gained importance.

#### 2.1.1. Addition of carbenes: Synthesis of methanofullerenes

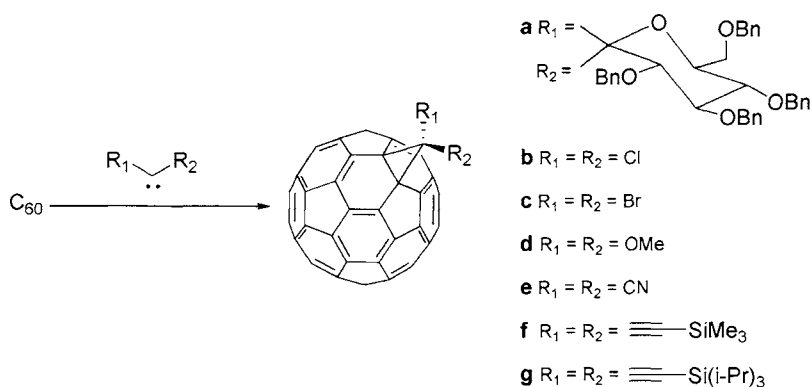
The [2+1]cycloaddition of carbenes with  $C_{60}$  occurs at the 6–6 bond in a single step (Scheme 1). In general the reactions proceed cleanly and only the products of 1,2-addition at the 6–6 ring junction form. The first addition of a carbene has been accomplished preparing a fullerene–sugar type conjugate by addition of sugar-derived spirodiazirines to  $C_{60}$  [30]. In principle, any method generating carbenes can be employed for the transformation of  $C_{60}$  to methano[60]fullerenes. Addition of dihalocarbenes, [31] dimethoxycarbene, [32,33] diethynyl carbenes [34,35], or dicyanocarbene [36] have also been described (Scheme 1).

#### 2.1.2. Addition of nitrenes: Synthesis of [60]fulleroaziridines

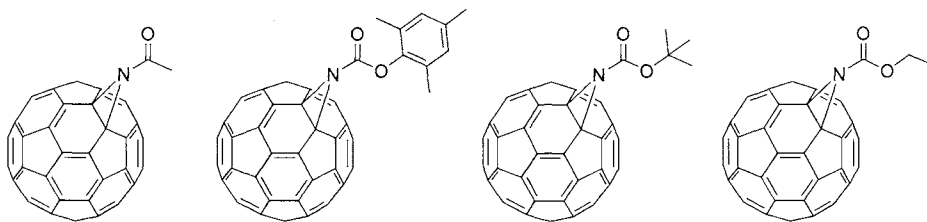
Addition of nitrene intermediates leads to the 6–6-closed isomers. Under the reaction conditions, the stabilized nitrene intermediates are formed and react with  $C_{60}$  on double bonds in a cycloaddition fashion [37–40]. For example, after heating  $C_{60}$  with several substituted azidoformates at 147°C in 1,1,2,2-tetrachloroethane, the [60]fulleroaziridines shown in Scheme 2 were isolated as a consequence of the formation of the nitrene reactive species [38].

Fulleroaziridines were also prepared by additions of nitrenes generated from  $Pd(OAc)_4$ -induced oxidation of *N*-aminophthalimide [41] or photochemically [42] from *N*-succinimidyl-4-azido-2,3,5,6-tetrafluorobenzoate.

Very interestingly, the high regioselectivity addition of two nitrene units resulted also in a very powerful reaction employed for the controlled opening of the fullerene shells. In a typical example, after the initial monoadduct formation, the second addition of the nitrene occurs primarily at the *cis*-1 position, which is very unusual, due to the inaccessibility of this site in other cycloadditions. The first aziridine nitrogen is small enough to allow addition of the incoming nitrene at the *cis*-1 site, partly helped by the favorable HOMO coefficient at this double bond. Remarkably, the fullerene bisadduct open up to afford the first example of a system having the 6–6 ring junction broken.



Scheme 1. Examples of [2+1]cycloaddition reactions between various carbene derivatives and  $\text{C}_{60}$ .

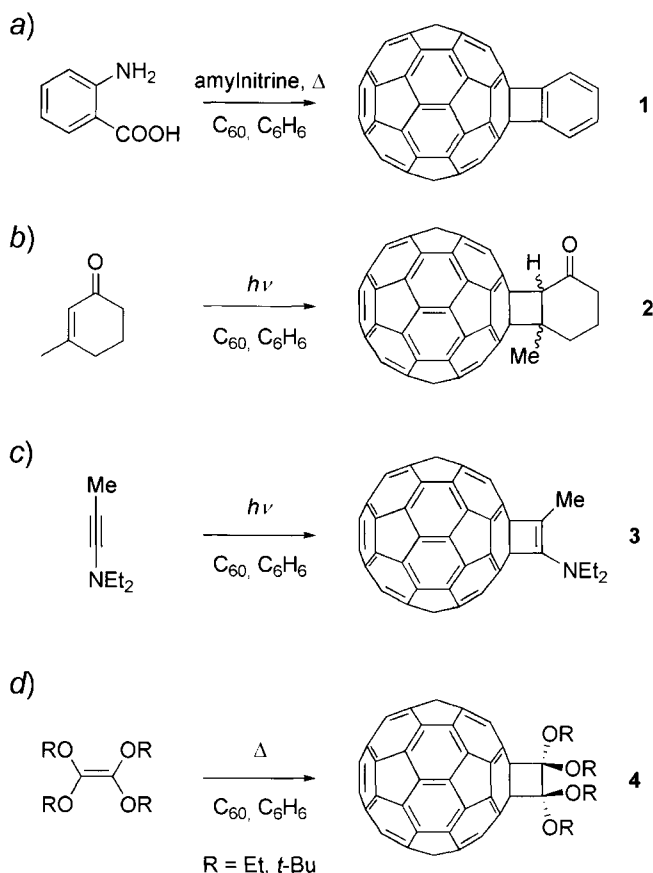


Scheme 2. [60]Fulleroaziridines prepared by addition of nitrene intermediates to  $\text{C}_{60}$ .

## 2.2. [2+2]Cycloadditions

### 2.2.1. Addition of alkenes and alkynes

Thermal- and photoinduced [2+2]cycloadditions occur as 1,2-addition at the 6–6 bonds leading to fullerene adducts bearing a four-membered ring fused to the carbon cage. Addition of benzyne to  $\text{C}_{60}$  at room temperature affords the [2+2]cycloaddition product **1** (Scheme 3a) [43,44]. Cyclic enones and 1,3-diones undergo photochemical [2+2]cycloaddition to  $\text{C}_{60}$ , with the mechanism presumably involving stepwise addition of the excited enone triplet state to the fullerene ground state (Scheme 3b, molecule **2**) [45–48]. Electron-rich alkynes and alkenes readily give photochemical reactions with fullerenes. In the case of electron-rich alkynes (Scheme 3c), such as *N,N*-diethylpropynylamine, photochemical [2+2]cycloaddition reaction yields the fullerene derivative **3** which easily undergo oxidation yielding the corresponding oxoamide or amide upon exposure to air or  $\text{H}_2\text{O}/\text{SiO}_2$ , respectively.

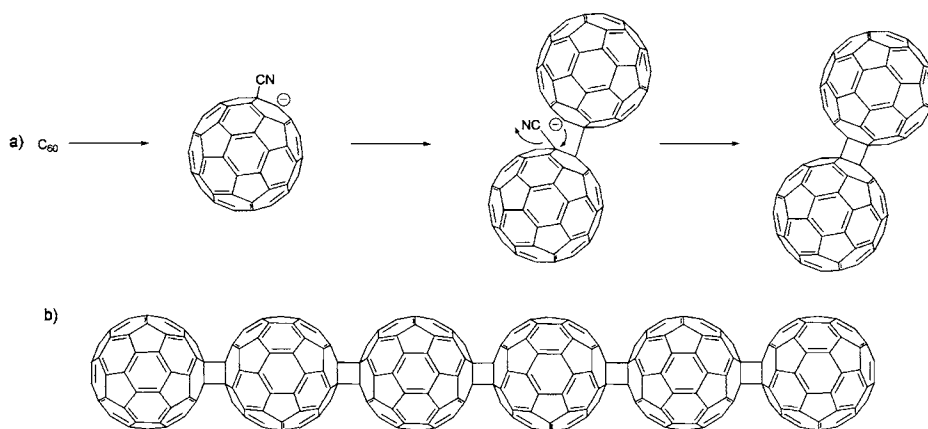


Scheme 3. Example of [2+2]cycloaddition reaction with alkenes and alkynes.

From the synthetic view point, the most interesting [2+2]cycloaddition reaction with  $C_{60}$  probably is the addition of electron-rich alkenes and alkynes [49–51]. In the case of alkynes such as ynamines, photochemical cycloaddition gives adducts that easily undergo further reaction. In the case of tetraalkoxyethenes (TEA), the addition occurs thermally, affording monoadduct **4** (Scheme 3d) in a very good yield [49]. The resulting bisketals are photochemically unstable compounds, and easily undergo cycloreversion to  $C_{60}$  upon irradiation with visible or UV light in high yields. Owing to the ease of addition and retro-reaction and the high yields, such TEA derivatives have a good potential as protecting groups for fullerene double bonds [52].

### 2.2.2. [60]Fullerene oligomers

The preparation of the [2+2]fullerene dimer was accomplished in the solid state under high-speed vibration milling conditions with  $C_{60}$  in the presence of KCN



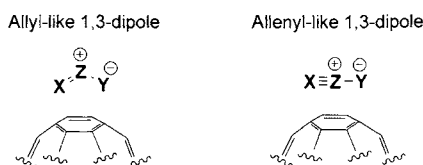
Scheme 4. [60]Fullerene oligomerization *via* [2+2]cycloaddition.

(Scheme 4) [53]. The dimerization is believed to occur by first addition of CN<sup>-</sup> to a C<sub>60</sub> molecule to form an anionic intermediate **6** (CNC<sub>60</sub><sup>-</sup>), which then reacts with a closely located C<sub>60</sub> molecule in a 1,4-addition mode (Scheme 4a). A successive intramolecular nucleophilic reaction of intermediate **7** yields the resulting [60]fullerene dimer [53]. The dimerization protocols affording [2+2]C<sub>70</sub> [54] and C<sub>60</sub>=C<sub>70</sub> [55] dimers have been also reported. Photopolymerization of C<sub>60</sub> in the solid state, was also proposed to occur *via* photochemical [2+2] reaction between double bonds of adjacent molecules (Scheme 4b) [56]. However, pressure-induced dimerization of C<sub>60</sub> to produce C<sub>60</sub>=C<sub>60</sub> is not efficient in co-crystallite. The oligomerization mechanism is proposed to proceed *via* the long-lived fullerene triplet state *T*<sub>1</sub>, when two double bonds on adjacent molecules are oriented parallel to one another and separated by less than ca. 4.2 Å.

### 2.3. [3+2]Cycloaddition reaction with [60]fullerene

[60]Fullerene behaves as a 2π electron-deficient 1,3-dipolarophiles undergoing a variety of [3+2]cycloaddition reactions. Among the 1,3-dipoles used, diazo compound, azomethine ylides, and azides were the first to be discovered to react with C<sub>60</sub>. The 1,3-dipolar cycloaddition reaction is one of the most common synthetic approaches for the construction of heterocyclic five-membered rings on the fullerene surface. Concerted cycloaddition reactions are the reactions of both allyl anion-type and propargyl/allenyl anion-type 1,3-dipoles, as shown in Scheme 5.

Depending on the structure of the 1,3-dipole, up to two new chiral centers can be formed in the five-membered ring. Parent 1,3-dipoles consist of molecules containing elements from the second row and the central atom of the dipole is limited to N or O. Thus, a limited number of structures can be formed by permutations of N, C, and O. Among the possible 1,3-cycloaddition reactions on fullerenes, the six types of 1,3-dipoles shown in Fig. 3 have mainly been explored.



Scheme 5. Concerted [3+2]cycloaddition reactions with C<sub>60</sub> involving allyl and propargyl/allenyl anion-type 1,3-dipoles.

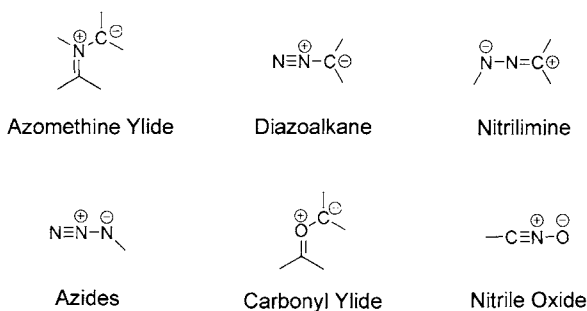


Figure 3. 1,3-Dipole intermediates utilized for the [3+2]cycloaddition reaction with C<sub>60</sub>.

Most studies in this field have been conducted with azomethine ylides [57]. Although azomethine ylides are unstable and must be prepared *in situ*, several methods have been developed for the synthesis, such as proton abstraction from imine derivatives of  $\alpha$ -amino acids [57], thermolysis or photolysis of aziridines [57], and dehydrohalogenation of imonium salts. Carbonyl ylides are a less common type of 1,3-dipole, which have found only limited application in fullerene synthesis [58]. Nitrile oxides on the other hand are, in close competition with nitrones, very commonly applied 1,3-dipoles for the synthesis of five-membered fullerene functionalized derivatives [59]. They are easily available from aldoximes or primary nitro compounds, but most nitrile oxides must be prepared *in situ*, because of high reactivity and rapid dimerization [60].

### 2.3.1. [3+2]Cycloaddition of azomethine ylides

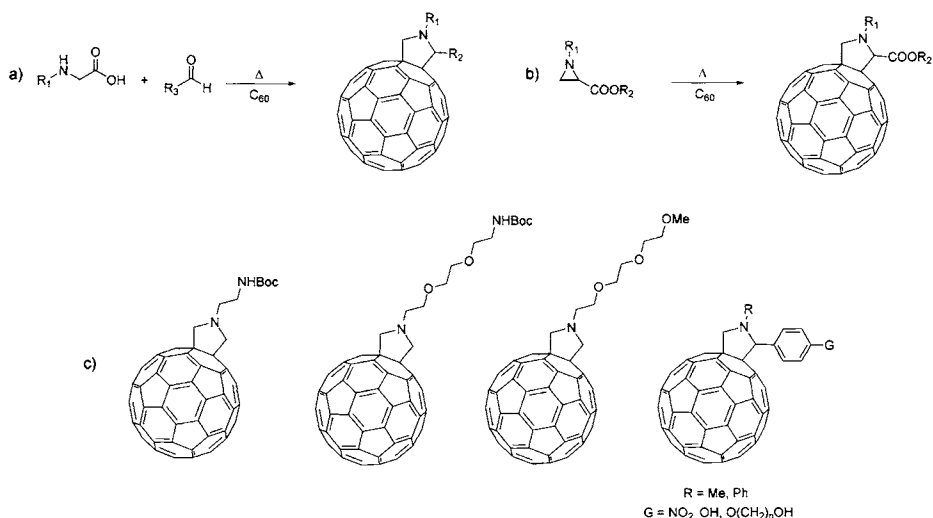
The 1,3-dipolar cycloaddition of azomethine ylides has become as one of the most versatile tools for functionalization of fullerenes [26,57,61–63]. Azomethine ylides are generated *in situ* either by decarboxylation of immonium salts derived from thermal condensation of  $\alpha$ -amino acids and aldehydes (alternatively ketones,

Scheme 6a) or by thermal ring opening of aziridines (Scheme 6b). 1,3-Dipolar addition of azomethine ylides to  $C_{60}$  yields fulleropyrrolidines that are formed across the 6–6 junction of the fullerene core. The utilization of functionalized aldehydes leads to the formation of 2-substituted fulleropyrrolidines whereas utilization of *N*-substituted glycines affords *N*-substituted fulleropyrrolidines.

By controlling the stoichiometry of the reagents and the reaction conditions mono-, bis-, tris-, etc., adducts of fulleropyrrolidines are formed. The isolation and full analytical characterization of the whole series of the pyrrolidine bisadducts (*trans*-1, *trans*-2, *trans*-3, *trans*-4, *e*, *cis*-3, *cis*-2, and *cis*-1) was achieved following this methodology (Fig. 4) [64]. Although some of these patterns had been partly characterized before [65–67], the never observed *cis*-3, *cis*-2, and *cis*-1 fulleropyrrolidine isomers were isolated for the first time. Following this strategy, nine different trisadducts have been synthesized [68].

### 2.3.2. [3+2]Cycloaddition reaction of hydrazone derivatives *via* nitrilimine intermediates

The formal cycloaddition of nitrilimines to a double bond of  $C_{60}$  results in the formation of [60]fulleropyrazoline derivatives (Scheme 7a) [69–71]. [60]Fulleropyrazolines are triazoline analogs, in which the  $sp^2$ -hybridized nitrogen has been substituted with a  $sp^2$ -carbon atom. In the first protocol, the 1,3-substituted-2-pyrazoline ring-fused [60]fullerene derivatives were prepared *via* thermally induced [3+2]cycloaddition between  $C_{60}$  and 1,3-substituted nitrilimine species, which are prepared *in situ* starting from the *N*-chlorobenzylidene precursors in the presence of



Scheme 6. 1,3-Dipolar cycloaddition reaction of azomethine ylides with  $C_{60}$ .

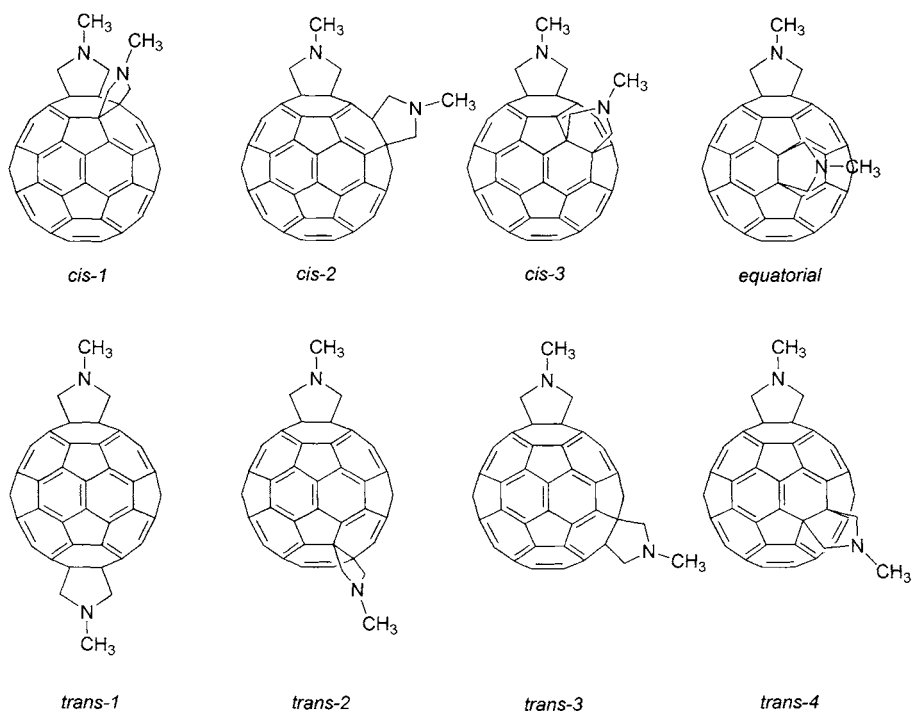
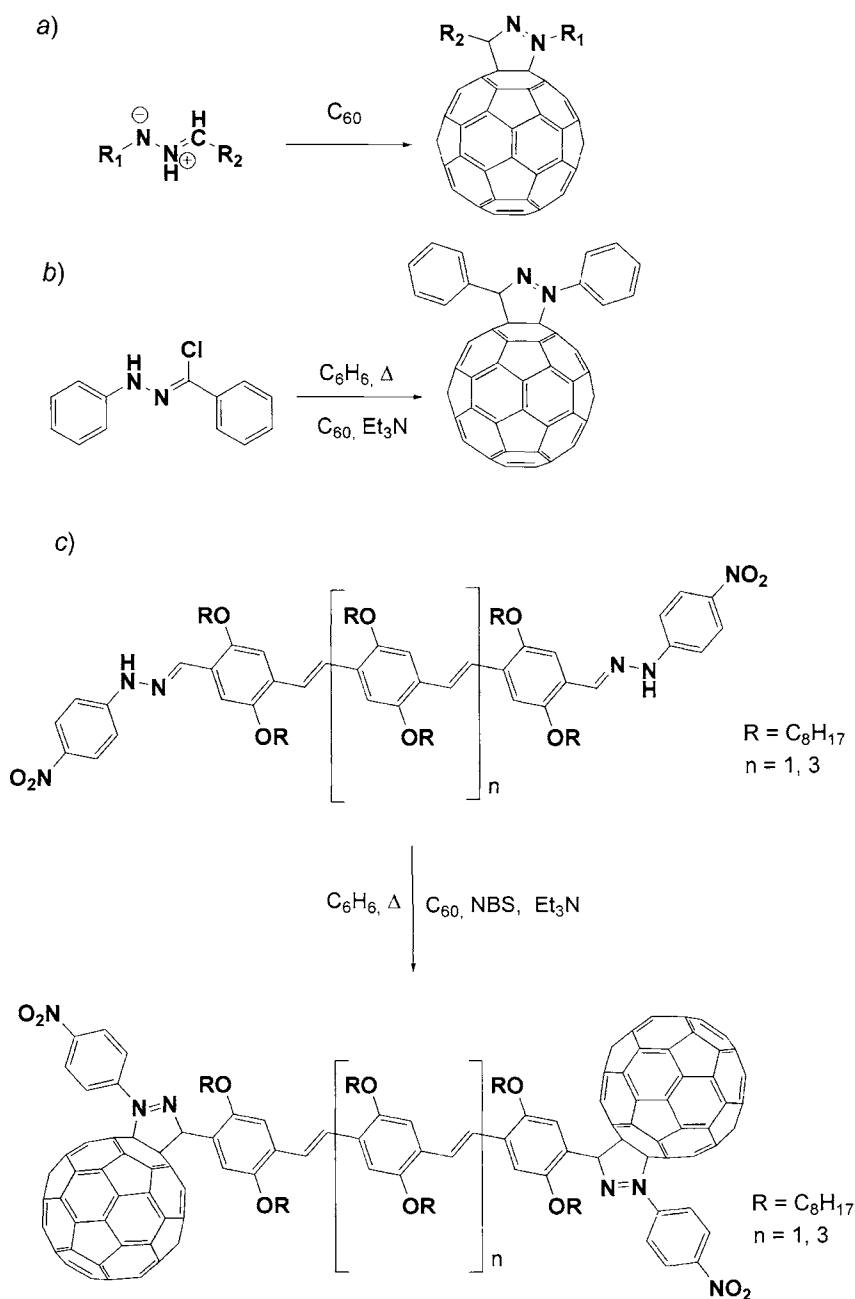


Figure 4. Fulleropyrrolidine bisadducts.

$\text{Et}_3\text{N}$  under refluxing conditions (Scheme 7b). A convenient modification of this protocol consists of preparing the 1,3-nitrilimine species *in situ* starting from the corresponding hydrazone precursors in the presence of NBS and  $\text{Et}_3\text{N}$  under microwave irradiation (Scheme 7c). This modified procedure allows the reaction to proceed under mild conditions and can be used in the presence of a wide range of chemical groups. The main advantages of this fullerene functionalization are: (i) the starting hydrazones are easily available in one step synthesis from aldehydes with almost quantitative yield, (ii) the cycloadditions are obtained in good yields, (iii) absence of stereoisomer, and (iv) retention of the fundamental physical properties of  $\text{C}_{60}$ .

Despite the fact that several *N*-substituted [60]fulleropyrazoline derivatives have been prepared, the best results have been obtained with electron withdrawing groups. The main restriction of this reaction is that the *N*-functionalization is limited by the availability of the starting hydrazine precursor. [60]Fulleropyrazoline derivatives are now increasingly attracting attention due to their intrinsic charge-separation properties and chemical versatility for the construction of photo- and electrochemical-active molecular building blocks for advanced material applications (Scheme 7c) [72].

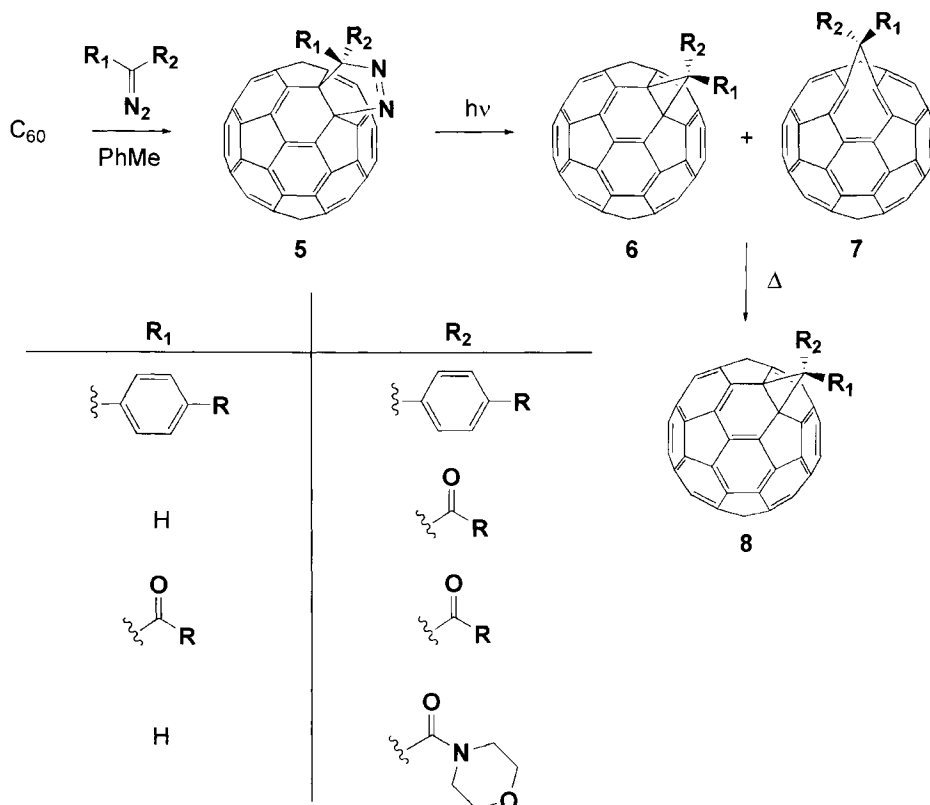


Scheme 7. Examples of microwave-induced [3+2]cycloaddition: (a) general reaction, (b) with *N*-( $\alpha$ -chlorobenzylidene)-*N'*-phenylhydrazine, (c) with OPV-bearing hydrazone derivatives.



### 2.3.3. [3+2]Cycloaddition reactions of diazo compounds

Diazo compounds cycloadd to 6–6 bonds to give the cyclic pyrazoline intermediate **5** as primary product, which then undergo thermal or photochemical  $N_2$  extrusion leading to a mixture of 6–6-closed **6** (methanofullerene) and 5–6-open **7** (homofullerene) (Scheme 8). In most cases, the initially formed homofullerene **7** can be rearranged into the thermodynamically more stable 6–6-closed isomer either by heating the product mixtures [73], by an electrochemical process [74], or by a photochemical isomerization presumably through a 1,5-sigmatropic-like rearrangement [75]. The pyrazoline intermediates are usually unstable under the reaction conditions and rapidly lose  $N_2$  under formation of isomeric mixtures of 5–6-open and 6–6-closed cyclopropane adducts. However, in the case of diazomethane addition, the pyrazoline intermediate could be isolated and characterized [76]. Interestingly, the 5–6-open adduct, does not rearrange to the 6–6-closed



Scheme 8. [3+2]Cycloaddition reaction between diazo compounds and C<sub>60</sub>, followed by dinitrogen extrusion and di- $\pi$ -rearrangement.

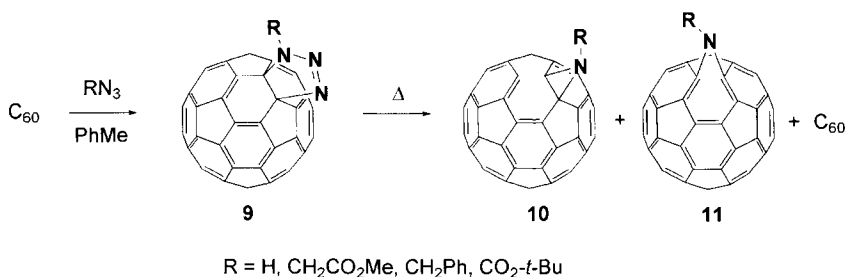
methanofullerene isomer by any methods, and thus a final mixture of 6-6-closed and 5-6-open adducts is obtained.

### 2.3.4. [3+2]Cycloaddition reaction of azides

The thermal [3+2]cycloaddition of azides to  $C_{60}$  [77–79] should be highlighted as it is the first step toward aza[60]fullerenes [80–82]. When the reaction was carried out at temperatures under  $80^\circ\text{C}$ , the cycloaddition takes place preferentially at the 6-6 ring junctions, affording thermally labile [60]fullerenetriazoline **9** (Scheme 9). Due to the  $D_{5h}$  symmetry of  $C_{70}$  as compared to  $I_h$ -symmetrical  $C_{60}$ , the regiochemistry of [3+2]cycloadditions of azides to  $C_{70}$  gives isomeric mixture of [70]fullerenetriazolines derivatives that can be eventually separated and serve as precursors in the synthetic route to aza[70]fullerenes [83–85]. Upon heating, the triazoline adduct loses  $N_2$  and rearranges to the 6-5-open (azahomofullerenes) **10** and the 6-6-closed **11** monoadduct. Under the reaction condition, the triazoline intermediate partly undergoes cycloreversion to  $C_{60}$ , which makes azides as potential protecting groups for the fullerene double bond, although the yields are quite low. Contrary to homofullerene derivatives (see Section 2.3.3, molecule **7**), the azahomofullerene **11** rearranges to the 6-6-closed isomer. Therefore, the addition of azides holds a great potential in the preparation of the functional fullerene derivatives in which the physical properties of  $C_{60}$  are maintained unaltered (due to the fact that the 60 electrons of the  $\pi$ -system remain intact). The characteristics of the fullerene skeleton combined with the properties of the substituents, leads to the construction of several fullerene derivatives for materials application with novel optical and electrochemical properties. A particularly interesting development in the field of fullerene synthetic chemistry is the cage opening *via* the azahomofullerene intermediates (see also Section 2.1.2).

### 2.4. [4+2]Cycloaddition: Diels–Alder reactions

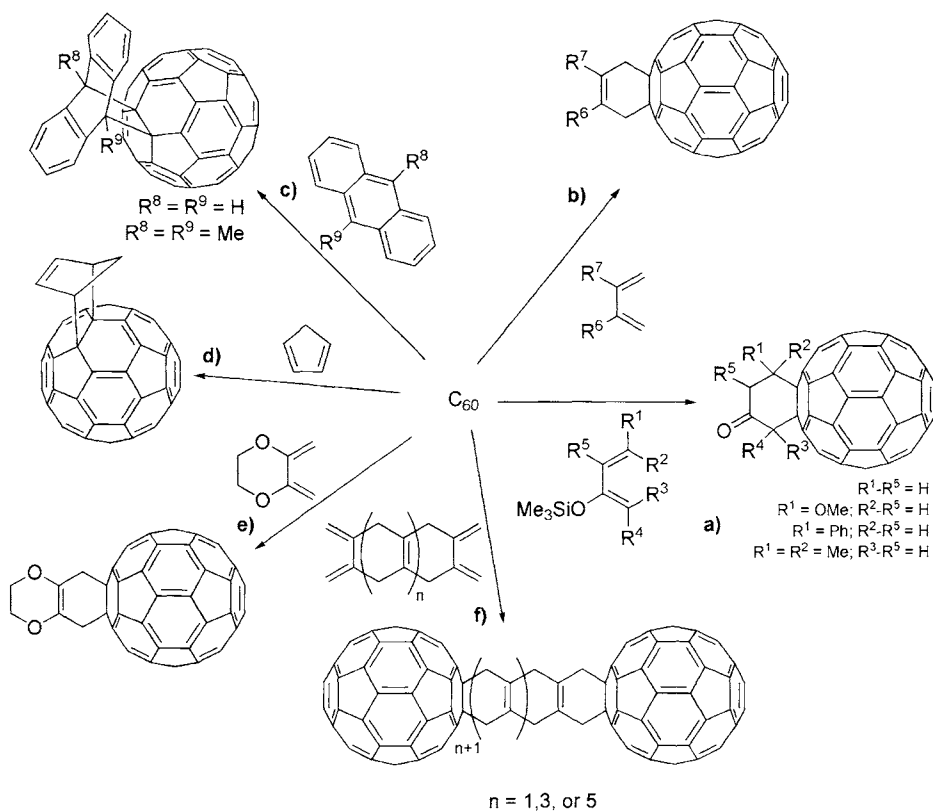
As electron deficient dienophiles, fullerenes undergo Diels–Alder cycloadditions with 1,2-dienes. The reaction occurs at the 6-6 bond leading to 1,2-addition products in which a cyclohexene ring is fused to the 6-6 junction. No fullerene



Scheme 9. [3+2]Cycloaddition of azides to  $C_{60}$ , yielding after extrusion of  $N_2$ , a mixture of 6-5-open and 6-6-closed isomers.

cycloadducts have been isolated where the fullerene moiety acts as the diene component. The stability of the cycloadduct against the retro-Diels–Alder reaction strongly depends on the electronic nature of the diene substituents. Specifically, thermal and chemical instability has been reported for a number of Diels–Alder adducts which can undergo thermal-induced retro-Diels–Alder reaction or self-photooxidation in the presence of  $O_2$ . Diels–Alder derivatives of  $C_{60}$  have been prepared using acyclic (Scheme 10a, b), endocyclic (Scheme 10c, d), and exocyclic 1,3-dienes (Scheme 10e, f).

The addition of several analogs of *Danishesky* dienes yielded fullerene-fused cyclohexanones [86]. Other *Diels–Alder* reactions with electron-deficient dienes involved tropones [87], 1,3-butadienes substituted with electron-withdrawing groups [88] as well as 2-pyrone [89]. By using an excess of the reactive 1,2-diene, multiadducts could be obtained, such as the hexakis fullerene derivatives prepared upon cycloaddition of 2,3-dimethyl-1,3-butadiene to  $C_{60}$  [90,91].



Scheme 10. Some examples of Diels–Alder adducts of  $C_{60}$ .

Solid state [4+2] reactions between  $C_{60}$  and aromatic compounds, including anthracene, tetracene, pentacene, and naphtho[2,3-a]pyrene were carried out under high-speed vibrating milling (HSVM) conditions [92]. In the case of anthracene, the same adduct as in solution was obtained [93–95], but with higher yields. With pentacene the reaction yielded a different adduct to the one obtained in solution, in which the pentacene backbone was attached to two-carbon sphere, leading to a dumbbell fullerene dimer.

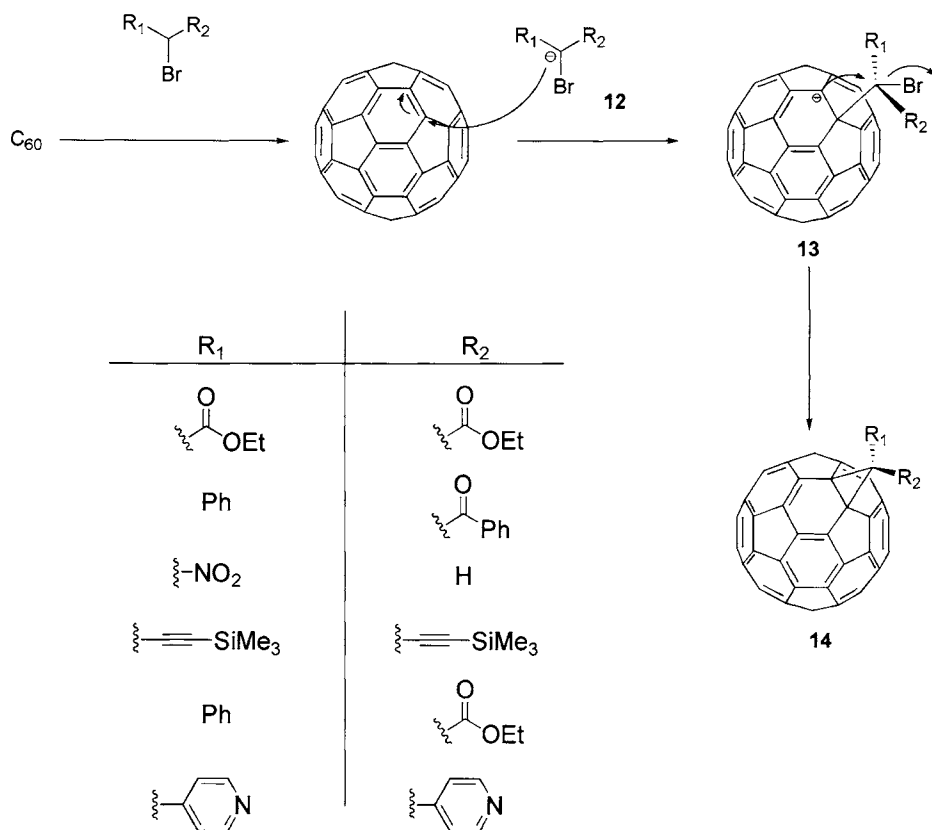
Diels–Alder cycloadditions have been also achieved by *in situ* generation of the reactive diene species. Some examples include reactive *o*-quinodimethanes species generated by thermolysis of cyclic sulfones [96], substituted cyclo- [96, 97], benzo-cyclo-butanones [98], and 1,4-elimination of dibromides [98]. This methodology was also applied to  $C_{70}$  and  $C_{76}$  [99–101], which leads to isomeric mixtures due to their lower molecular symmetry. The reaction of *o*-benzoquinone [102] obtained by oxidation of the readily available 2-methoxy phenols, [103] yielded highly functionalized bicyclo[2.2.2]octenone-fused fullerenes. Nevertheless, most attention has been paid to their generation *via* chelotropic elimination of  $SO_2$  from heteroaromatic-fused 3-sulfolenes and 1,4 elimination from the corresponding  $\alpha,\alpha'$ -dihalides [104–108]. In this respect, a porphyrin-stoppered rotaxane bearing a butadiene sulfone moiety on the macrocycle was reported to react with  $C_{60}$  *via in situ* generation of the 1,3-butadiene species by chelotropic elimination of  $SO_2$  [109].

Bisadducts with different substitution patterns containing crown ethers have been prepared by 1,4-dihalide elimination [110]. Various properties of these derivatives with potential applications in the field of molecular sensors, including complexation, electrochemical, and fluorescence emission behaviors were studied.

### 3. NUCLEOPHILIC ADDITION TO [60]FULLERENE

#### 3.1. Addition of $\alpha$ -carbanions: *Bingel*-type reactions

The original conditions for the Bingel reaction involve the treatment of diethyl bromomalonate with NaH in the presence of  $C_{60}$ . A simple mechanistic view considers such reaction a two-step process [111]. First, a deprotonation of the  $\alpha$ -bromomalonate derivative affords the  $\alpha$ -halocarbanion **12** that adds to  $C_{60}$ , giving the anionic fullerene intermediate **13**; in the second step a displacement of bromide by an intramolecular nucleophilic substitution yields methanofullerene **14** (Scheme 11). NaH or DBU can be used as a base due to their low nucleophilicity, which prevents any additions to the fullerene surface. The Bingel reaction exclusively proceeds at the 6–6 bonds. However, when complex structures need to be attached to the fullerene core, the synthesis of the corresponding bromomalonate precursor is rather difficult and reduces overall yields. A convenient modification of this reaction protocol, introduced by Bingel, [112] it consists in preparing the  $\alpha$ -halomalonate *in situ* from the corresponding malonate in the presence of  $I_2$  and a non-nucleophilic base (DBU) [113]. Another modification uses DBU and  $CBr_4$  as bromine source for the *in situ* formation of  $\alpha$ -bromomalonates [114]. All the modified Bingel reactions proceed under mild conditions and can be employed in the presence of a wide range of functional groups. The *Bingel*-type methanofullerenes are thermally



Scheme 11. Cyclopropanation of  $C_{60}$  by nucleophilic addition of  $\alpha$ -bromomalonate carbanions (Bingel reaction) Nucleophilic cyclopropanation by addition of various  $\alpha$ -halocarbanions to  $C_{60}$ .

stable, and the cyclopropane ring is rigid with a well-defined directionality of the ester groups. This reaction can be extended to the preparation of a large variety of methanofullerenes including  $\alpha$ -chloroketones,  $\alpha$ -bromonitromethanes,  $\alpha$ -bromocyanoacetates, and 3-bromopenta-1,4-dynes (Scheme 11) [24,26,115,116].

Despite the many synthetic advantages of the Bingel cyclopropanation over other functionalization methods, its use in materials applications is very limited due to the lability of the fullerene-fused di(alkoxycarbonyl)cyclopropane ring under reductive conditions. It has been showed that di(alkoxycarbonyl)methanofullerenes are chemically unstable under the conditions of reductive electrochemistry, undergoing the so-called retro-Bingel reaction [117–119]. The reaction results in the removal of the malonate addends yielding the parent fullerene and the starting malonate as products [120,121]. The reaction was also observed to proceed smoothly using amalgamated

magnesium [122]. Nevertheless, due to the high versatility and easy experimental protocol, the modified Bingel reaction has been used as a synthetic method to prepare a lot of the methanofullerene derivatives.

### 3.2. Addition of ylides

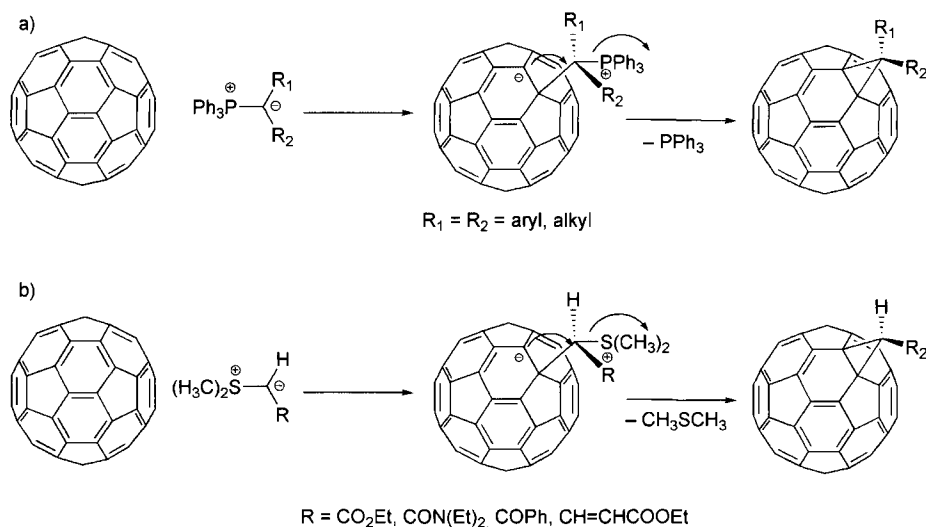
The reaction of phosphonium ylides with  $C_{60}$  also affords methanofullerenes in a two-step mechanism. The first step involves a nucleophilic addition of the carbanionic center to the 6–6 bonds followed by an intramolecular nucleophilic substitution,  $S_Ni$ , leading to a cyclopropane ring (Scheme 12a) [123]. The reaction yields are in the range between 15% and 25%. A similar synthetic method employing sulfonium ylides (Scheme 12b) revealed to be more efficient in terms of yield (30–87%) [124].

## 4. MATERIALS-ORIENTED APPLICATIONS

### 4.1. Hydrophilic [60]fullerene derivatives

When [60]fullerene is derivatized with hydrophilic residues, fullerene-based amphiphilic derivatives are obtained. The solubility in water of these derivatives allowed exploring its properties in physiological media medicinal chemistry, bio-, and nanotechnology.

Fulleropyrrolidines bearing suitable hydrophilic addends have been found to form highly organized *Langmuir* films that can be successively transferred onto



Scheme 12. Cyclopropanation of  $C_{60}$  by nucleophilic addition of (a) phosphonium and (b) sulfonium ylides, followed by an intramolecular nucleophilic substitution.

solid substrates (*Langmuir–Blodgett*, LB). The formation of LB films could not be obtained with analogous hydrophobic chains [125–141].

*N*-substituted fulleropyrrolidines can be *N*-alkylated to give fulleropyrrolidinium salts. The insertion of positive charges substantially increases the solubility of fullerene-containing compounds in aqueous media, giving rise to a new variety of compounds with applicability in a wide variety of fields. *N*-functionalization with oligoethylene glycol chains bearing terminal ammonium salts revealed to be a suitable functional residue for the construction of supramolecular architectures. The polar chains enhanced the solubility in water, while the fullerene–fullerene interactions were responsible for aggregation due to the high cohesive fullerene–fullerene energy interaction. The combination of these properties led to the formation of spheres, nanorods, or nanotubules in water (Fig. 5) [142].

The positively charged fulleropyrrolidines were introduced into the interlayer space of smectite clays by cation exchange, replacing the charge-balancing cations, leading to a new family of organic–inorganic nanocomposites [143].

These fulleropyrrolidinium salts can also form *Langmuir–Shäfer* films with porphyrins bearing anionic groups (Fig. 5) [144]. The films revealed to be robust enough to be deposited on indium-tin-oxide (ITO) electrodes leading to devices for photocurrent generation.

These amphiphilic positively charged bisadducts could also form organic–inorganic nanoensembles with CdTe nanoparticles. The experiments showed rapid

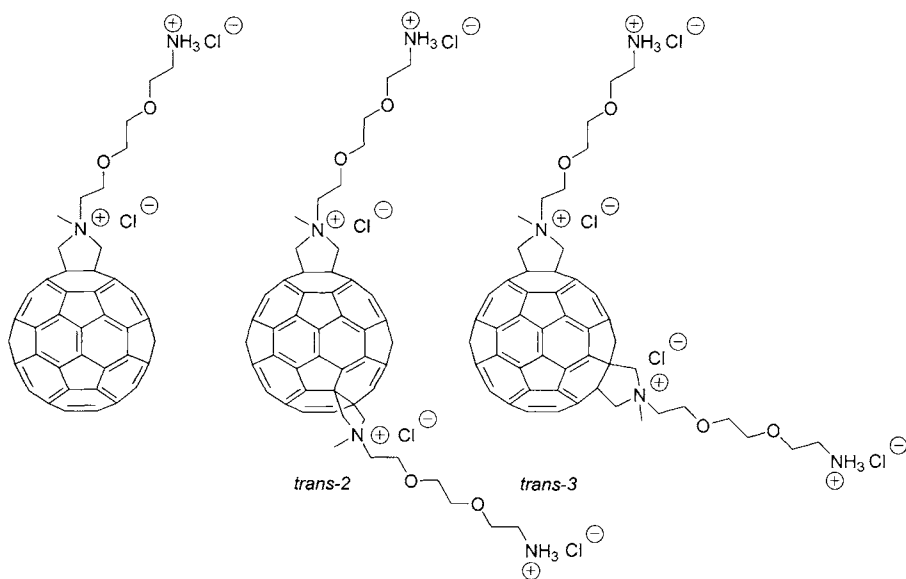


Figure 5. Water-soluble ammonium-bearing fullerene derivatives.

photoinduced electron transfer between the two units due to the electrostatic binding (Fig. 5) [145].

The influence on the reduction potentials of the different substitution patterns in bisadducts of both fulleropyrrolidines and fulleropyrrolidinium salts was studied [146]. It was found that fulleropyrrolidinium ions are much better acceptors than fulleropyrrolidines. This concept was efficiently extended to the preparation of molecules for other applications, such as cation recognition [147]. Bisfunctionalized crown ethers have been attached very close to the fullerene sphere using 1,3-dipolar additions. An electrochemical signal is obtained from the variation of the redox potentials of the fullerene when different cations are bonded. The responses were favorable showing reduction potential shifts between 15–38 mV depending on the cationic species.

In a recent paper [148], fulleropyrrolidine bisadducts were prepared and separated by HPLC. It should be noted that *trans*-2, *trans*-3, and *cis*-3 enantiomers display  $C_2$  symmetry and are chiral due to their addition pattern. Then, each couple of these enantiomers was separated by chiral HPLC. The resulting enantiomerically pure isomers were transformed into fulleropyrrolidinium salts. The *trans*-3 enantiomers were used successfully to induce chiral helicity, in opposite directions, of negatively charged polymer backbones.

A dendrimeric anthracene unit was also successfully covalently attached to  $C_{60}$  using Diels–Alder cycloaddition [149], providing fullerene derivatives with a great solubility in water as well as in physiological media. The chemical reversibility of the reaction allowed the possibility of selective photocleavage of the solubilizing dendrimer function, with the ultimate effect of releasing pristine  $C_{60}$ .

#### 4.2. Biologically active [60]fullerene derivatives

Again the functionalization with polar side-chains [150] and with positively charged groups [151] enhanced the solubility to sufficiently high concentrations ( $10^{-4}$ – $10^{-5}$  M) to study the biological activity of fulleropyrrolidines (Fig. 5) [63]. The *trans*-2, *trans*-3, *trans*-4, and *equatorial* bisadducts [152] were prepared and purified by HPLC, which showed an increase of solubility in water of a 100 times compared with the corresponding monoadducts. The cytotoxic and hemolytic effects [153] of a series of positively charged bisadducts were also studied as well as their potential use as HIV inhibitors [154] and neuroprotective agents [155].

Fulleropyrrolidine-based steroid hybrids were synthesized and found to decrease both the ATP hydrolysis and  $Ca^{2+}$ -uptake activity of SR  $Ca^{2+}$ -ATPase while the inhibitions were concentration-dependent [156].

Recently, a range of fullerene–flavanoid dyads were synthesized [157–159], since flavanoids possess significant antioxidant activity, can act as anticarcinogens, and express beneficial effects in inflammatory and immunomodulatory systems.

1,3-Dipolar additions have been also used to prepare fulleroproline, the biggest unnatural amino acid [160], which comprises a natural  $\alpha$ -amino acid proline condensed to a 6–6 ring junction of  $C_{60}$ . [161] Fulleroprolines can be also obtained *via* the thermal ring opening of aziridines [162]. Di- and tri-peptides have already been prepared incorporating fulleroproline at their *N*- or *C*-terminal parts [163–165].



In order to prepare more complex fullerene-modified peptides, a protocol for the solid-phase using the fulleropyrrolidino-glutamic acid, was developed. It allowed the introduction of a series of different peptides including Leu-enkephalins analogs and antimicrobial sequences (Fig. 6) [166].

Recently, the synthesis of a functionalized fullerene having a deoxyribonucleic acid (DNA) minor groove binder and an oligonucleotide chain covalently linked to a fullerene cage *via* a fused pyrrolidine ring was reported [167–169]. The design of the latter synthesis was based on an already established idea that coupling of fullerenes to a minor groove binder leads to higher affinity and specificity of the derivatives toward target DNA [170]. The construction of fullerene-DNA hybrid materials allows transmission electron microscopy (TEM) imaging of DNA without the use of any heavy metal. Recently, such compounds became available and showed to bind to DNA through electrostatic interactions with the phosphate groups providing excellent contrast for imaging individual DNA molecules [171].

#### 4.3. Hydrogen-bonded fullerene ensembles

The introduction of substituents that can form hydrogen bonds with other species allows fullerenes to form complex supramolecular architectures with other systems. This field has been recently reviewed [172].

Hummelen [173] and Martin [174] introduced self-complementary hydrogen bond patterns in functionalized fullerenes. Quadrupole hydrogen bond motifs based on 2-uridopyrimidin-4-ones, were used to prepare self-assembled fullerene dimers (Fig. 7a). The dimers were successfully assembled and a high association constant

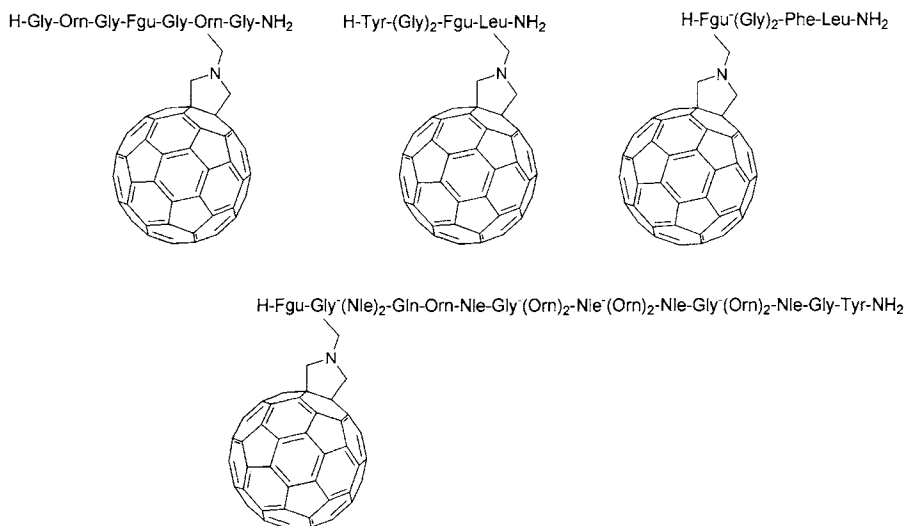


Figure 6. Fullerene derivatives functionalized with antimicrobial sequences.

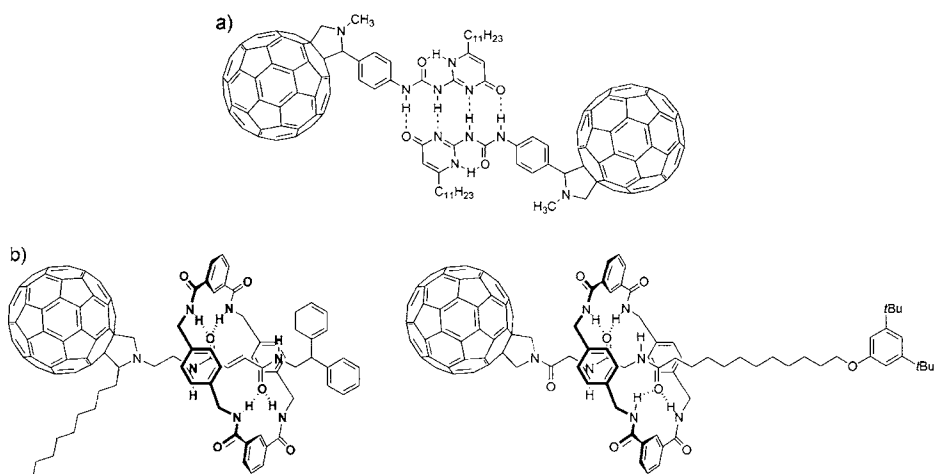


Figure 7. Supramolecular fullerene assembled directed by hydrogen bond interactions.

was measured ( $K_a = 1 \times 10^6 \text{ M}^{-1}$ ) [173]. Moreover, a fluorescence quench of 50% was observed in the assembled dimer [174], while an enhancement of the fluorescence was detected when disrupting hydrogen bond solvents were added.

Several fullerene-stoppered rotaxanes have been prepared by hydrogen bond-directed cyclization [175,176].  $\text{C}_{60}$  was functionalized with different templates that assisted the clipping of benzylic amide macrocycle around the thread. Functionalization with the right substituents is crucial in these systems in order to provide solubilization of the fullerene-thread in chloroform, one of the most important requirements for the preparation of the rotaxanes (Fig. 7b).

When  $\text{C}_{60}$  was derivatized using a glycyglycine and a long hydrophobic chain [175], it was possible to switch the macrocycle along the thread when changing from non-disrupting hydrogen bonds solvents such as chloroform to high polar solvents such as DMSO. The switching could be monitored by NMR and transient absorption spectroscopy.

#### 4.4. Substitution with electron donors

Photoactive systems with applicability in photovoltaics and nanosensing can be produced when the electron-accepting fullerenes are coupled with electron-donors. Photoinduced electron transfer (PET) can take place between both units leading to radical pairs where the energy is stored. Fullerenes have been linked to different electron donors to increase the lifetimes of the radical pairs in order to produce efficiently chemical energy.

1,3-Dipolar addition was used to prepare architectures bearing porphyrins in position 2 of fulleropyrrolidines (Fig. 8) [177–179]. These systems have shown the

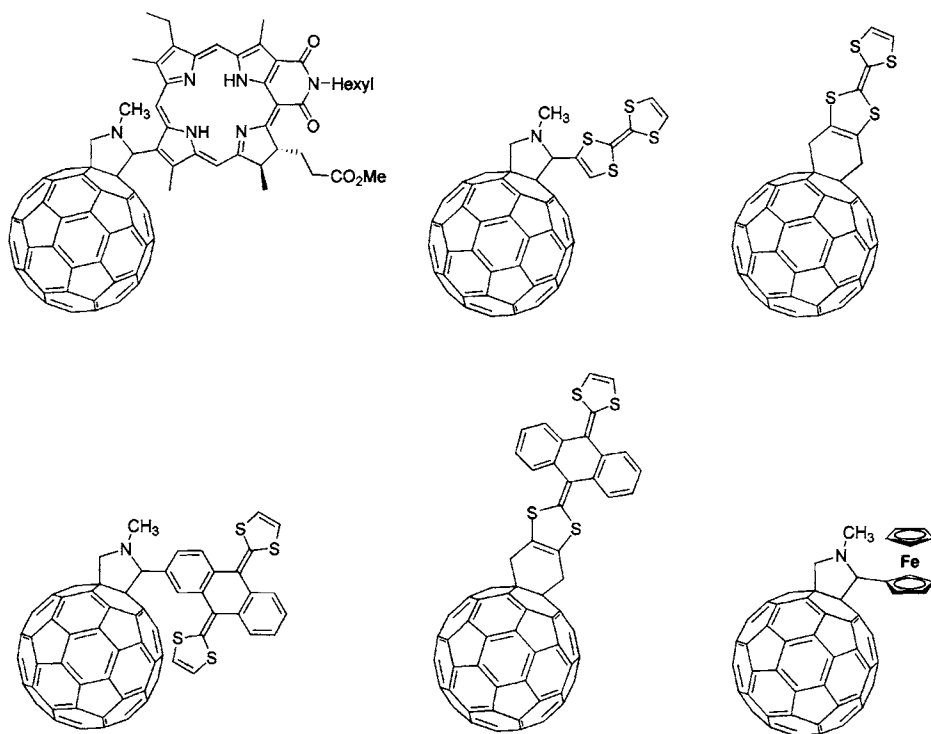


Figure 8. Electron donor–fullerene dyads.

longest lifetimes reported in dyads to the moment (230  $\mu$ s at 25  $^{\circ}$ C)[179] and have been highlighted for their simplicity and effectiveness [180]. Analogous systems have been prepared with phthalocyanines [181–183], tetrathiafulvalene [184,185], vinyl spacers bearing tetrathiafulvalene (TTF) moieties [186,187], along with azides bearing TTF [188],  $\pi$ -extended-TTF units [189,190], and ferrocene [161,185,191–194].

Strapped and parachute-like fullerene-porphyrin architectures have been prepared *via* Bingel reaction with flexible linkers that allow the porphyrin to get very close to the fullerene [195–199].

Novel  $C_{60}$ -based [4+2] adducts were recently synthesized through 1,4-dihalide elimination, giving fused TTF- $C_{60}$  dyads,  $C_{60}$ -TTF- $C_{60}$  triads [200–203], and  $\pi$ -extended-TTF- $C_{60}$  dyads [190], leading to efficient electron and energy transfer through the covalent bonds (Fig. 8).

More complicated systems containing various electron-donor units for multistep electron or energy transfer have been prepared and successfully attached to  $C_{60}$  by 1,3-dipolar addition. A wide variety of systems containing combinations of  $C_{60}$ , porphyrins ( $H_2P$ ), Zn-porphyrins (ZnP), and ferrocene (Fc) were synthesized and studied by Imahori and collaborators. In a very elegant work, ZnP- $H_2P$ - $C_{60}$  was synthesized

and investigated [204,205]. After photostimulation energy transfer took place from the ZnP to the H<sub>2</sub>P followed by an electron transfer from the excited H<sub>2</sub>P to C<sub>60</sub> giving a long distance charge separated state. Analogous Fc-ZnP-C<sub>60</sub> and Fc-H<sub>2</sub>P-C<sub>60</sub> triads that contain a terminal ferrocene unit [204–206] were prepared and examined. When irradiated, two consecutive electron transfers took place. First from the porphyrin to C<sub>60</sub> and then from the ferrocene to the porphyrin leading to the charge separated state. By combination of these two systems, a tetrad was reported (Fig. 9) [207], which showed the longest charge separated state to date, as the product of a sequence of energy and multistep electron transfer events. Analogous porphyrin-C<sub>60</sub> triads bearing terminal TTF [208] and  $\pi$ -extended-TTF [209] moieties have been prepared and studied.

Novel multicomponent polyads have been prepared and analyzed, based on linear [210,211] multiporphyrin polyads (Fig. 9b).

A series of triads containing both a terminal  $\pi$ -extended-TTF [212] or a porphyrin [213] unit linked to C<sub>60</sub> through a polyphenylenevinylene (PPV) molecular wire have been recently reported. After light irradiation, electron transfer occurred between the units, leading to a long distance charge separated state that revealed a small attenuation factor (Fig. 9c).

If the proper functionalization is introduced, fullerene can be linked to the electron-donor by means of non-covalent interactions, such as metal-induced and hydrogen-bonding coordination. C<sub>60</sub> was functionalized with a pyridine moiety to form an axial complex with a ZnP by metal coordination (Fig. 10) [214–218]. Similar fulleropyrrolidine complexes, including also porphyrins covalently linked to C<sub>60</sub> have been reported [214,215,219].

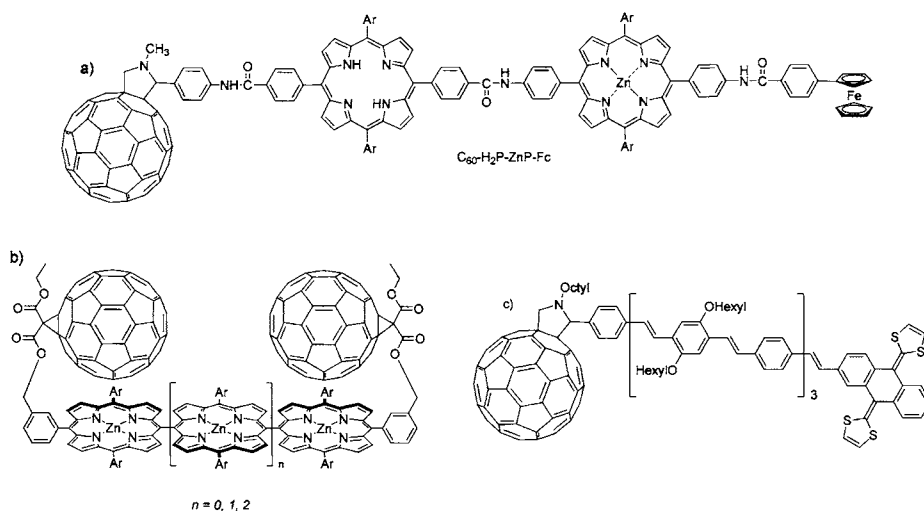


Figure 9. Fullerene-containing polyads.

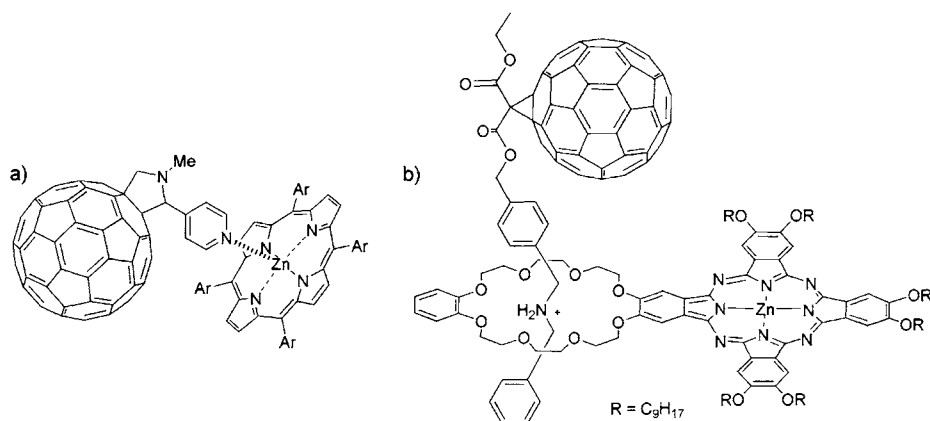


Figure 10. Various fullerene-containing supramolecular dyads.

Complexation have also been applied to prepare fullerene-subphthalocyanine complexes, by introducing 2-phenoxy substituents in  $C_{60}$  [220,221]. The peripheral substitution in the subphthalocyanine moiety, led to the tuning of the electron-donating properties of the dyads.

Schuster and co-workers have successfully used the metal-templated strategy to produce interlocked architectures based on Sauvage-type rotaxanes. Rotaxane containing fullerenes as stoppers with a porphyrin unit attached to the macrocycle was first synthesized [222]. In a different article [223], an analogous rotaxane was prepared in which the fullerenes and the porphyrins were swapped. In the latter, the new structural distribution allowed the preparation of novel catenane systems by complexation of the two terminal Zn-porphyrins when one equivalent of a bidentate ligands such as DABCO and 4,4'-bipyridine, were used. A subsequent addition of one extra-equivalent of the bidentate ligand converted the 1:1 catenane supramolecular complex into a 2:1 rotaxane complex.

Pseudorotaxane architectures have been prepared by Torres and collaborators through coordination of fullerene ammonium salts with phthalocyanine crown ethers (Fig. 10) [224–225]. These assemblies are not interlocked so both the thread and the macrocycle are free to dissociate. An interesting feature regarding the reversibility of these systems should be highlighted. When the fullerene ammonium salt was complexed by the phthalocyanine crown ether, the fluorescence of the macrocycle was quenched by proximity of the fullerene. In the presence of a base the two units are disassembled, restoring (switching “on”) the fluorescence of the system.

Other rotaxanated dyads have been assembled by hydrogen bonding, the thread was introduced in the macrocycle and stoppered by two porphyrins [109]. The macrocycle functionalized with the hydrogen bond template and butadiene sulfone. Then,  $C_{60}$  was added to the macrocycle using Diels–Alder cycloaddition, as 1,3-butadiene was generated *in situ* from butadiene sulfone.

A wide variety of fullerene-TTF systems has been prepared by *Martin* et al. [226] by means of complementary recognition between carboxylates and guanidinium salts by donor-donor/acceptor-acceptor hydrogen bond motifs. Intramolecular electron transfer occurred between the two units but this was not observed when solvents that disrupt hydrogen bonds were added. Alternatively intermolecular electron transfer was detected.

#### 4.5. Functionalization with dendrimers and conjugated oligomers

The general use of the 1,3-dipolar addition protocol becomes more evident when very big and branched dendrimeric addends can be attached directly to  $C_{60}$ . Dendrimers can serve as building blocks for the construction of organized materials with nanosize precision due to the well-defined three-dimensional structure they possess. A wide variety of fullerodendrimers containing oligoethylene glycol chains have been prepared since they have shown a great potential not only for optical limiting applications [227–230] but also as liquid crystalline electron-donor systems (Fig. 11a) [231].

Ultrafast photoinduced electron transfer has been observed between conjugated polymers and fullerenes [232]. An issue of great importance has been to incorporate

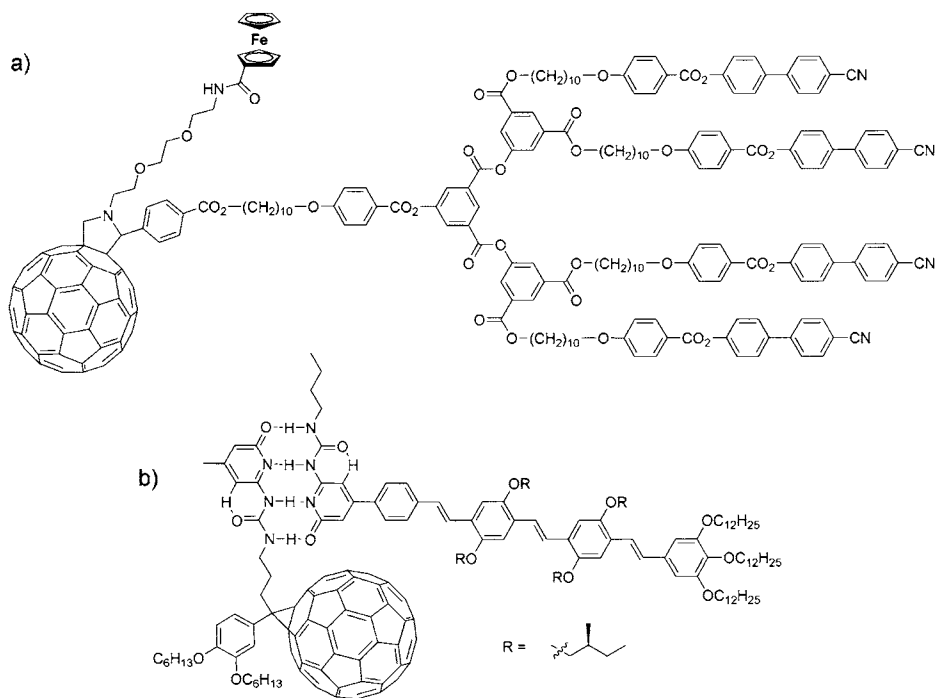


Figure 11. Fullerene-bearing dendrimers.

conjugated oligomers for the preparation of photovoltaic devices. By using the corresponding azomethine ylide, a variety of linear mixed naphthalene/thiophene conjugated polymers [233], linear and ramified oligophenylenevinylene (OPPV), and linear oligophenyleneethynylene (OPE) units have been coupled with  $C_{60}$  [227–230,234].

More sophisticated systems have been prepared following the quadrupole hydrogen bond strategy. Fullerenes were assembled with oligo(*p*-phenylenevinylene)s (OPVs), the photo- and electrochemical properties of these new materials [235] with applications in the field of plastic solar cells, were studied (Fig. 11b) [236]. Additionally,  $C_{60}$  was functionalized with two 2-uridopyrimidin-4-one moieties, which self-assembled as a linear supramolecular fullerene polymer [237] as well as other motifs with bisfunctional OPVs [238].

## REFERENCES

1. H. W. Kroto, J. R. Heath, S. C. O'Brien, R. F. Curl and R. E. Smalley, *Nature* **318** (1985) 162.
2. W. Krätschmer, L. D. Lamb, K. Fostiropoulos and D. R. Huffman, *Nature* **347** (1990) 354.
3. R. E. Haufler, J. Conceicao, L. P. F. Chibante, Y. Chai, N. E. Byrne, S. Flanagan, M. M. Haley, S. C. O'Brien, C. Pan, Z. Xiao, W. E. Billups, M. A. Ciufolini, R. H. Hauge, J. L. Margrave, L. J. Wilson, R. F. Curl and R. E. Smalley, *J. Phys. Chem.* **94** (1990) 8634.
4. H.-B. Bürgi, E. Blanc, D. Schwarzenbach, S. Liu, Y. Lu, M. M. Kappes and J. A. Ibers, *Angew. Chem. Int. Ed.* **31** (1992) 640.
5. K. Hedberg, L. Hedberg, D. S. Bethune, C. A. Brown, H. C. Dorn, R. D. Johnson and M. De Vries, *Science* **254** (1991) 410.
6. R. C. Haddon, *Philos. Trans. R. Soc. Lond. Ser. A: Phys. Sci. Eng.* **343** (1993) 53.
7. R. C. Haddon, L. E. Brus and K. Raghavachari, *Chem. Phys. Lett.* **125** (1986) 459.
8. P. W. Fowler and J. Woolrich, *Chem. Phys. Lett.* **127** (1986) 78.
9. J. Dias, *J. Chem. Educ.* **66** (1989) 1012.
10. W. B. Brown, *Chem. Phys. Lett.* **136** (1987) 128.
11. M. Bühl and A. Hirsch, *Chem. Rev.* **101** (2001) 1153.
12. F. Arias, L. Echegoyen, S. R. Wilson and Q. Lu, *J. Am. Chem. Soc.* **117** (1995) 1422.
13. L. Echegoyen and L. E. Echegoyen, *Acc. Chem. Res.* **31** (1998) 593.
14. C. Bruno, I. Doubitski, M. Marcaccio, F. Paolucci, D. Paolucci and A. Zaopo, *J. Am. Chem. Soc.* **125** (2003) 15738.
15. Y.-P. Sun, G. E. Lawson, J. E. Riggs, B. Ma, N. X. Wang and D. K. Moton, *J. Phys. Chem. A* **102** (1998) 5520.
16. B. Ma, C. E. Bunker, R. Guduru, X. F. Zhang and Y.-P. Sun, *J. Phys. Chem. A* **101** (1997) 5626.
17. B. Ma and Y.-P. Sun, *J. Chem. Soc., Perkin Trans. 2* (1996) 2157.
18. Y.-P. Sun, in *Optical and Electronic Properties of Fullerenes and Fullerene-based Materials*, Eds. J. Shinar, Z. V. Vardeny and Z. H. Kafafi, Marcel Dekker Inc., New York, 2000, p. 43.

19. M. V. Korobov and L. M. Allan, in *Fullerenes: Chemistry, Physics, and Technology*, Eds. K. M. Kadish and R. S. Ruoff, Wiley Interscience, New York, 2000, p. 53.
20. P.-M. Allemand, A. Koch, F. Wudl, Y. Rubin, F. Diederich, M. M. Alvarez, S. J. Anz and R. L. Whetten, *J. Am. Chem. Soc.* **113** (1991) 1050.
21. R. J. Sension, A. Z. Szarka, G. R. Smith and R. M. Hochstrasser, *Chem. Phys. Lett.* **185** (1991) 179.
22. Y. Kubozono, H. Maeda, Y. Takabayashi, K. Hiraoka, T. Nakai, S. Kashino, S. Emura, S. Ukita and T. Sogabe, *J. Am. Chem. Soc.* **118** (1996) 6998.
23. R. C. Haddon, *Science* **261** (1993) 1545.
24. A. Hirsch in *The Chemistry of the Fullerenes*, Thieme Verlag, Stuttgart, 1994.
25. A. Hirsch, *Angew. Chem. Int. Ed.* **32** (1993) 1138.
26. S. R. Wilson, D. I. Schuster, B. Nuber, M. S. Meier, M. Maggini, M. Prato and R. Taylor, in *Fullerenes: Chemistry, Physics, and Technology*, Eds. K. M. Kadish and R. S. Ruoff, Wiley Interscience, New York, 2000, p. 91.
27. M. Prato, *J. Mat. Chem.* **7** (1997) 1097.
28. M. Prato, *Top. Curr. Chem.* **199** (1999) 173.
29. T. Akasaka, K. Komatsu, Y. Murata and M. Shiro, *J. Am. Chem. Soc.* **115** (1997) 1605.
30. A. Vasella, P. Uhlmann, C. A. A. Waldruff, F. Diederich and C. Thilgen, *Angew. Chem. Int. Ed.* **1992** (1992) 1388.
31. M. Tsuda, T. Ishida, A. Nogami, S. Kurono and M. Ohashi, *Tetrahedron Lett.* **34** (1993) 2335.
32. L. Isaacs and F. Diederich, *Helv. Chim. Acta* **76** (1993) 2454.
33. W. W. Win, M. Kao, M. Eiermann, J. J. McNamara, F. Wudl, D. L. Pole, K. Kassam and J. Warkentin, *J. Org. Chem.* **59** (1994) 5871.
34. H. L. Anderson, R. Faust, Y. Rubin and F. Diederich, *Angew. Chem. Int. Ed.* **33** (1994) 1366.
35. P. Timmerman, H. L. Anderson, R. Faust, J.-F. Nierengarten, T. Habicher, P. Seiler and F. Diederich, *Tetrahedron* **52** (1996) 4925.
36. M. K. Keshavarz, B. Knight, R. C. Haddon and F. Wudl, *Tetrahedron* **52** (1996) 5149.
37. A. Ishida, K. Tanaka and A. Nogami, *Chem. Lett.* (1994) 561.
38. G. Schick, A. Hirsch, H. Mauser and T. Clark, *Chem. Eur. J.* **2** (1996) 935.
39. M. R. Banks, J. I. G. Cadogan, I. Gosney, P. K. G. Hodgson, P. R. R. Landgridge-Smith and D. W. H. Rankin, *J. Chem. Soc., Chem. Comm.* (1994) 1365.
40. M. R. Banks, J. I. G. Cadogan, I. Gosney, P. K. G. Hodgson, P. R. R. Landgridge-Smith and D. W. H. Rankin, *J. Chem. Soc., Chem. Comm.* (1995) 885.
41. S. Kuwashima, M. Kubota, K. Kushida, T. Ishida, M. Ohashi and T. Nogami, *Tetrahedron Lett.* **35** (1994) 4371.
42. M. Yan, S. X. Cai and J. F. W. Keana, *J. Org. Chem.* **59** (1994) 5951.
43. S. H. Hoke II, J. Molstad, D. Dilettato, M. J. Jay, D. Carlson, B. Kahr and R. G. Cooks, *J. Org. Chem.* **57** (1992) 5069.
44. M. Tsuda, T. Ishida, T. Nogami, S. Kurono and M. Ohashi, *Chem. Lett.* (1992) 2333.
45. A. W. Jensen, A. Khong, M. Saunders, S. R. Wilson and D. I. Schuster, *J. Am. Chem. Soc.* **119** (1997) 7303.



46. D. I. Schuster, J. R. Cao, N. Kaprinidis, Y. H. Wu, A. W. Jensen, Q. Y. Lu, H. Wang and S. R. Wilson, *J. Am. Chem. Soc.* **118** (1996) 5639.
47. S. R. Wilson, N. Kaprinidis, Y. H. Wu and D. I. Schuster, *J. Am. Chem. Soc.* **115** (1993) 8495.
48. S. R. Wilson, Y. H. Wu, N. A. Kaprinidis, D. I. Schuster and C. J. Welch, *J. Org. Chem.* **58** (1993) 6548.
49. X. Zhang, A. Fan and C. S. Foote, *J. Org. Chem.* **61** (1996) 5456.
50. X. Zhang and C. S. Foote, *J. Am. Chem. Soc.* **117** (1995) 4271.
51. X. Zhang, A. Romero and C. S. Foote, *J. Am. Chem. Soc.* **115** (1993) 11024.
52. M. S. Meier and M. Poplawska, *J. Org. Chem.* **58** (1993) 4524.
53. G. W. Wang, K. Komatsu, Y. Murata and M. Shiro, *Nature* **387** (1997) 583.
54. G. S. Forman, N. Tagmatarchis and H. Shinohara, *J. Am. Chem. Soc.* **124** (2002) 178.
55. N. Tagmatarchis, G. S. Forman, A. Taninaka and H. Shinohara, *Synlett* (2002) 235.
56. A. M. Rao, P. Zhou, K.-A. Wang, G. T. Hager, J. M. Holden, Y. Wang, W.-T. Lee, X.-X. Bi, P. C. Ecklund, D. S. Cornett, M. A. Duncan and I. J. Amster, *Science* **259** (1993) 955.
57. M. Maggini, G. Scorrano and M. Prato, *J. Am. Chem. Soc.* **115** (1993) 9798.
58. N. Jagerovic, J. Elguero and J. L. Aubagnac, *J. Chem. Soc., Perkin Trans. 1* (1996) 499.
59. T. Da Ros, M. Prato, F. Novello, M. Maggini, M. De Amici and C. De Micheli, *Chem. Commun.* (1997) 59.
60. M. S. Meier and M. Poplawska, *Tetrahedron Lett.* **52** (1996) 5043.
61. M. Prato and M. Maggini, *Acc. Chem. Res.* **31** (1998) 519.
62. N. Tagmatarchis and M. Prato, *Synlett* (2003) 768.
63. K. Kordatos, T. Da Ros, S. Bosi, E. Vázquez, M. Bergamin, C. Cusan, F. Pellarini, V. Tomberli, B. Baiti, D. Pantarotto, V. Georgakilas, G. Spalluto and M. Prato, *J. Org. Chem.* **66** (2001) 4915.
64. K. Kordatos, S. Bosi, T. Da Ros, A. Zambon, V. Lucchini and M. Prato, *J. Org. Chem.* (2001) 2802.
65. Q. Lu, D. I. Schuster and S. R. Wilson, *J. Org. Chem.* **61** (1996) 4764.
66. L. Pasimeni, A. Hirsch, I. Lamparth, A. Herzog, M. Maggini, M. Prato, C. Corvaja and G. Scorrano, *J. Am. Chem. Soc.* **119** (1997) 12896.
67. G. Schick, M. Levitus, L. Kvetko, B. A. Johnson, I. Lamparth, R. Lunkwitz, B. Ma, S. I. Khan, M. A. Garcia-Garibay and Y. Rubin, *J. Am. Chem. Soc.* **121** (1999) 3246.
68. S. Marchesan, T. Da Ros and M. Prato, *J. Org. Chem.* **70** (2005) 4706.
69. S. Muthu, P. Maruthamuthu, R. Ragunathan, P. R. V. Rao and C. K. Mathews, *Tetrahedron Lett.* (1994) 1763.
70. Y. Matsubara, H. Tada, S. Nagase and Z. Yoshida, *J. Org. Chem.* **60** (1995) 5372.
71. Y. Matsubara, H. Muraoka, H. Tada and Z. Yoshida, *Chem. Lett.* (1996) 373.
72. F. Langa, M. J. Gomez-Escalonilla, J.-M. Rueff, T. M. Figueira Duarte, J.-F. Nierengarten, V. Palermo, P. Samorì, Y. Rio, G. Accorsi and N. Armaroli, *Chem. Eur. J.* **11** (2005) 4405.
73. L. Isaacs, A. Wehrsig and F. Diederich, *Helv. Chim. Acta* **76** (1993) 1231.

74. M. Eiermann, F. Wudl, M. Prato and M. Maggini, *J. Am. Chem. Soc.* **116** (1994) 8364.
75. H. E. Zimmerman, in *Rearrangements in Ground and Excited States*, Ed. P. de Mayo, Academic Press, New York, 1980, p. 875.
76. T. Suzuki, Q. Li, K. C. Khemani, F. Wudl and Ö. Almarsson, *J. Am. Chem. Soc.* **114** (1992) 7300.
77. T. Grösser, M. Prato, V. Lucchini, A. Hirsch and F. Wudl, *Angew. Chem. Int. Ed.* **34** (1995) 1343.
78. J. C. Hummelen, M. Prato and F. Wudl, *J. Am. Chem. Soc.* **117** (1995) 7003.
79. M. Prato, Q. Li, F. Wudl and V. Lucchini, *J. Am. Chem. Soc.* **115** (1993) 1148.
80. J. C. Hummelen, C. Bellavia-Lund and F. Wudl (Eds.), in *Fullerenes and Related Structures*, Springer, 1999, p. 93.
81. J. C. Hummelen, B. Knight, J. Pavlovich, R. Gonzalez and F. Wudl, *Science* **269** (1995) 1554.
82. I. Lamparth, B. Nuber, G. Schick, A. Skiebe, T. Grosser and A. Hirsch, *Angew. Chem. Int. Ed.* **34** (1995) 2257.
83. C. Bellavia-Lund and F. Wudl, *J. Am. Chem. Soc.* **119** (1997) 943.
84. B. Nuber and A. Hirsch, *Fullerene Sci. Technol.* **4** (1996) 715.
85. N. Tagmatarchis, *Synlett* (2001) 1761.
86. M. Ohno, T. Azuma, S. Kojima, Y. Shirakawa and S. Eguchi, *Tetrahedron* **52** (1996) 4983.
87. A. Mori, Y. Takamori and H. Takeshita, *Chem. Lett.* (1997) 395.
88. M. Ohno, Y. Shirakawa and S. Eguchi, *Synthesis* (1998) 1812.
89. S. Mori, T. Karita, K. Komatsu, N. Sugita and T. S. M. Wan, *Synth. Commun.* **27** (1997) 1475.
90. B. Krautler and J. Maynollo, *Tetrahedron* **52** (1996) 5033.
91. B. Kräutler and J. Maynollo, *Angew. Chem. Int. Ed.* **34** (1995) 87.
92. Y. Murata, N. Kato, K. Fujiwara and K. Komatsu, *J. Org. Chem.* **64** (1999) 3483.
93. K. Komatsu, Y. Murata, N. Sugita, K. Takeuchi and T. S. M. Wan, *Tetrahedron Lett.* **34** (1993) 8473.
94. J. A. Schlueter, J. M. Seaman, S. Taha, H. Cohen, K. R. Lykke, H. H. Wang and J. M. Williams, *J. Chem. Soc., Chem. Commun.* (1993) 972.
95. M. Tsuda, T. Ishida, T. Nogami, S. Kurono and M. Ohashi, *J. Chem. Soc., Chem. Commun.* (1993) 1296.
96. M. Walter, A. Gugel, J. Spickermann, P. Belik, A. Kraus and K. Mullen, *Fullerene Sci. Technol.* **4** (1996) 101.
97. J. Mattay, G. Torres-Garcia, J. Averdung, C. Wolff, I. Schlachter, H. Luftmann, C. Siedschlag, P. Luger and M. Ramm, *J. Phys. Chem. Solids* **58** (1997) 1929.
98. Y. Nakamura, T. Minowa, S. Tobita, H. Shizuka and J. Nishimura, *J. Chem. Soc., Perkin Trans.* **2** (1995) 2351.
99. A. Hermann, *Helv. Chim. Acta.* **77** (1994) 1689.
100. P. Seiler, A. Herrmann and F. Diederich, *Helv. Chim. Acta.* **78** (1995) 344.
101. M. F. Meidine, A. G. Avent, A. D. Darwish, H. W. Kroto, O. Ohashi, R. Taylor and D. R. M. Walton, *J. Chem. Soc., Perkin Trans.* **2** (1994) 1189.
102. C. C. Liao and R. K. Peddinti, *Acc. Chem. Res.* **35** (2002) 856.

103. C. F. Yen, R. K. Peddinti and C. C. Liao, *Org. Lett.* **2** (2000) 2909.
104. M. AlHariri, K. Jouve, F. Pautet, M. Domard, B. Fenet and H. Fillion, *J. Org. Chem.* **62** (1997) 405.
105. C. Boulle, M. Cariou, M. Bainville, A. Gorgues, P. Hudhomme, J. Orduna and J. Garin, *Tetrahedron Lett.* **38** (1997) 81.
106. J. H. Liu, A. T. Wu, M. H. Huang, C. W. Wu and W. S. Chung, *J. Org. Chem.* **65** (2000) 3395.
107. J. L. Segura and N. Martin, *Chem. Rev.* **99** (1999) 3199.
108. A. C. Tome, R. F. Enes, J. A. S. Cavaleiro and J. Elguero, *Tetrahedron Lett.* **38** (1997) 2557.
109. N. Watanabe, N. Kihara, Y. Furusho, T. Takata, Y. Araki and O. Ito, *Angew. Chem. Int. Ed.* **42** (2003) 681.
110. Y. Nakamura, A. Asami, T. Ogawa, S. Inokuma and J. Nishimura, *J. Am. Chem. Soc.* **124** (2002) 4329.
111. C. Bingel, *Chem. Ber.* **126** (1993) 1957.
112. C. Bingel, Presentation at the meeting New Perspectives in Fullerene Chemistry and Physics, Rome, 1994.
113. J.-F. Nierengarten, V. Gramlich, F. Cardullo and F. Diederich, *Angew. Chem. Int. Ed.* **35** (1996) 2101.
114. X. Camps and A. Hirsch, *J. Chem. Soc., Perkin Trans.* **1** (1997) 1595.
115. F. Diederich and C. Thilgen, *Science* **271** (1996) 317.
116. F. Diederich and R. Kessinger, *Acc. Chem. Res.* **32** (1999) 537.
117. R. Kessinger, J. Crassous, A. Herrmann, M. Rüttimann, L. Echegoyen and F. Diederich, *Angew. Chem. Int. Ed.* **37** (1998) 1919.
118. C. Boudon, J. P. Gisselbrecht, M. Gross, A. Herrmann, M. Rüttimann, J. Crassous, F. Cardullo, L. Echegoyen and F. Diederich, *J. Am. Chem. Soc.* **120** (1998) 7860.
119. M. W. J. Beulen, L. Echegoyen, J. A. Rivera, M. A. Herranz, A. Martín-Domenech and N. Martín, *Chem. Commun.* (2000) 917.
120. M. A. Herranz, C. T. Cox and L. Echegoyen, *J. Org. Chem.* **68** (2003) 5009.
121. M. A. Herranz, J. A. Rivera, R. J. Alvarado, N. Martin, C. Thilgen, F. Diederich and L. Echegoyen, *J. Supramol. Chem.* **1** (2001) 299.
122. N. N. P. Moonen, C. Thilgen, L. Echegoyen and F. Diederich, *Chem. Commun.* (2000) 335.
123. H. J. Bestmann, D. Hadawi, B. Roder and C. Moli, *Tetrahedron Lett.* **35** (1994) 9017.
124. Y. Wang, J. Cao, D. I. Schuster and S. R. Wilson, *Tetrahedron Lett.* **38** (1995) 6843.
125. G. Angelini, P. De Maria, A. Fontana, M. Pierini, M. Maggini, F. Gasparrini and G. Zappia, *Langmuir* **17** (2001) 6404.
126. M. Carano, P. Ceroni, T. Da Ros, K. Kordatos, V. Tomberli, F. Paolucci, M. Prato and S. Roffia, *Electrochim. Acta* **46** (2000) 265.
127. X. Z. Ge, *Thin Solid Films* **368** (2000) 147.
128. Z. X. Ge, Y. L. Li, Z. X. Guo, Z. Q. Shi and D. B. Zhu, *Tetrahedron Lett.* **40** (1999) 5759.
129. Z. Guo, *Appl. Phys. B* **71** (2001) 545.
130. Z. Guo, J. Yan, Y. Li, Z. Ge and D. Zhu, *Synth. Met.* **102** (1999) 1567.

131. Z. Guo, *Synth. Commun.* **28** (1998) 1957.
132. Z. Guo, Y. Li, J. Yan, F. Bai, F. Li, D. Zhu, J. Si and P. Ye, *Appl. Phys. B* **70** (2000) 257.
133. M. P. Hernandez, *Langmuir* **17** (2001) 3317.
134. L. Leo, G. Mele, G. Rosso, L. Valli, G. Vasapollo, D. M. Guldi and G. Mascolo, *Langmuir* **16** (2000) 4599.
135. H. Murakami, M. Shirakusa, T. Sagara and N. Nakashima, *Chem. Lett.* (1999) 815.
136. N. Nakashima, T. Ishii, M. Shirakusa, T. Nakanishi, H. Murakami and T. Sagara, *Chem. Eur. J.* **7** (2001) 1766.
137. J. F. Nierengarten, *Chem. Eur. J.* **6** (2000) 3667.
138. Y. Rio, J. F. Nicoud, J. L. Rehspringer and J. F. Nierengarten, *Tetrahedron Lett.* **41** (2000) 10207.
139. P. Wang, B. Chen, R. M. Metzger, T. Da Ros and M. Prato, *J. Mater. Chem.* **7** (1997) 2397.
140. P. Wang, R. M. Metzger and B. Chen, *Thin Solid Films* **329** (1998) 96.
141. S. Zhang, L. Gan and C. Huang, *Chem. Phys. Lett.* **331** (2000) 143.
142. V. Georgakilas, F. Pellarini, M. Prato, D. M. Guldi, M. Melle-Franco and F. Zerbetto, *Proc. Natl. Acad. Sci. U S A.* **99** (2002) 5075.
143. D. Gournis, V. Georgakilas, M. A. Karakassides, T. Bakas, K. Kordatos, M. Prato, M. Fanti and F. Zerbetto, *J. Am. Chem. Soc.* **126** (2004) 8561.
144. S. Conoci, D. M. Guldi, S. Nardis, R. Paolesse, K. Kordatos, M. Prato, G. Ricciardi, M. G. H. Vicente, I. Zilbermann and L. Valli, *Chem. Eur. J.* **10** (2004) 6523.
145. D. M. Guldi, I. Zilbermann, G. Anderson, N. A. Kotov, N. Tagmatarchis and M. Prato, *J. Am. Chem. Soc.* **126** (2004) 14340.
146. M. Carano, T. Da Ros, M. Fanti, K. Kordatos, M. Marcaccio, F. Paolucci, M. Prato, S. Roffia and F. Zerbetto, *J. Am. Chem. Soc.* **125** (2003) 7139.
147. P. M. Smith, A. L. McCarty, N. Y. Nguyen, M. E. Zandler and F. D'Souza, *Chem. Commun.* (2003) 1754.
148. T. Nishimura, K. Tsuchiya, S. Ohsawa, K. Maeda, E. Yashima, Y. Nakamura and J. Nishimura, *J. Am. Chem. Soc.* **126** (2004) 11711.
149. Y. Takaguchi, T. Tajima, K. Ohta, J. Motoyoshiya, H. Aoyama, T. Wakahara, T. Akasaka, M. Fujitsuka and O. Ito, *Angew. Chem. Int. Ed.* **41** (2002) 817.
150. V. Tomberli, T. Da Ros, S. Bosi and M. Prato, *Carbon* **38** (2000) 1551.
151. S. Bosi, T. Da Ros, S. Castellano, E. Banfi and M. Prato, *Bioorg. Med. Chem. Lett.* **10** (2000) 1043.
152. S. Bosi, L. Feruglio, D. Milic and M. Prato, *Eur. J. Org. Chem.* (2003) 4741.
153. S. Bosi, L. Feruglio, T. Da Ros, G. Spalluto, B. Gregoretti, M. Terdoslavich, G. Decorti, S. Passamonti, S. Moro and M. Prato, *J. Med. Chem.* **47** (2004) 6711.
154. S. Bosi, T. Da Ros, G. Spalluto, J. Balzarini and M. Prato, *Bioorg. Med. Chem. Lett.* **13** (2003) 4437.
155. C. Cusan, T. Da Ros, G. Spalluto, S. Foley, J. M. Janto, P. Seta, C. Larroque, M. C. Tomasini, T. Antonelli, L. Ferraro and M. Prato, *Eur. J. Org. Chem.* (2002) 2928.
156. H. S. Li, *J. Chem. Soc., Perkin Trans. 1* (2000) 617.
157. M. D. L. de la Torre, *Tetrahedron Lett.* **43** (2002) 1689.

158. M. D. L. de la Torre, *Tetrahedron Lett.* **43** (2002) 4617.
159. M. D. L. de la Torre, *Tetrahedron* **60** (2004) 3581.
160. A. B. Holmes and G. R. Stephenson, *Chem. Ind.* (1994) 303.
161. M. Maggini, A. Karlsson, G. Scorrano, G. Sandona, G. Farnia and M. Prato, *J. Chem. Soc., Chem. Commun.* (1994) 589.
162. A. Bianco, F. Gasparrini, M. Maggini, D. Misiti, A. Polese, M. Prato, G. Scorrano, C. Toniolo and C. Villani, *J. Am. Chem. Soc.* **119** (1997) 7550.
163. A. Bianco, M. Maggini, G. Scorrano, C. Toniolo, G. Marconi, C. Villani and M. Prato, *J. Am. Chem. Soc.* **118** (1996) 4072.
164. A. Bianco, V. Lucchini, M. Maggini, M. Prato, G. Scorrano and C. Toniolo, *J. Pept. Sci.* **4** (1998) 364.
165. A. Bianco, T. Bertolini, M. Crisma, G. Valle, C. Toniolo, M. Maggini, G. Scorrano and M. Prato, *J. Pept. Res.* **50** (1997) 159.
166. D. Pantarotto, A. Bianco, F. Pellarini, A. Tossi, A. Giangaspero, I. Zelezetsky, J. P. Briand and M. Prato, *J. Am. Chem. Soc.* **124** (2002) 12543.
167. M. Bergamin, T. Da Ros, G. Spalluto, A. Boutorine and M. Prato, *Chem. Commun.* (2001) 17.
168. T. Da Ros, M. Bergamin, E. Vázquez, G. Spalluto, B. Baiti, S. Moro, A. Boutorine and M. Prato, *Eur. J. Org. Chem.* (2002) 405.
169. T. Da Ros, G. Spalluto, A. Boutorine and M. Prato, *Aust. J. Chem.* **54** (2001) 223.
170. E. Nakamura, H. Tokuyama, S. Yamago, T. Shiraki and Y. Sugiura, *Bull. Chem. Soc. Jpn.* **69** (1996) 2143.
171. A. M. Cassell, W. A. Scrivens and J. M. Tour, *Angew. Chem. Int. Ed.* **37** (1998) 1528.
172. L. Sanchez, N. Martin and D. M. Guldi, *Angew. Chem. Int. Ed.* **44** (2005) 2.
173. M. T. Rispens, L. Sanchez, J. Knol and J. C. Hummelen, *Chem. Commun.* (2001) 161.
174. J. J. Gonzalez, S. Gonzalez, E. M. Priego, C. P. Luo, D. M. Guldi, J. de Mendoza and N. Martin, *Chem. Commun.* (2001) 163.
175. T. Da Ros, D. M. Guldi, A. F. Morales, D. A. Leigh, M. Prato and R. Turco, *Org. Lett.* **5** (2003) 689.
176. A. Mateo-Alonso and M. Prato, *Tetrahedron* (2006) in press.
177. D. M. Guldi, I. Zilbermann, G. A. Anderson, K. Kordatos, M. Prato, R. Tafuro and L. Valli, *J. Mater. Chem.* **14** (2004) 303.
178. Y. Kashiwagi, K. Ohkubo, J. A. McDonald, I. M. Blake, M. J. Crossley, Y. Araki, O. Ito, H. Imahori and S. Fukuzumi, *Org. Lett.* **5** (2003) 2719.
179. K. Ohkubo, H. Kotani, J. G. Shao, Z. P. Ou, K. M. Kadish, G. L. Li, R. K. Pandey, M. Fujitsuka, O. Ito, H. Imahori and S. Fukuzumi, *Angew. Chem. Int. Ed.* **43** (2004) 853.
180. A. Harriman, *Angew. Chem. Int. Ed.* **43** (2004) 2.
181. D. M. Guldi, A. Gouloumis, P. Vazquez and T. Torres, *Chem. Commun.* (2002) 2056.
182. M. A. Loi, P. Denk, H. Hoppe, H. Neugebauer, C. Winder, D. Meissner, C. Brabec, N. S. Sariciftci, A. Gouloumis, P. Vazquez and T. Torres, *J. Mater. Chem.* **13** (2003) 700.
183. A. Sastre, A. Gouloumis, P. Vazquez, T. Torres, V. Doan, B. J. Schwartz, F. Wudl, L. Echegoyen and J. Rivera, *Org. Lett.* **1** (1999) 1807.

184. N. Martin, L. Sanchez, C. Seoane, R. Andreu, J. Garin and J. Orduna, *Tetrahedron Lett.* **37** (1996) 5979.
185. M. Prato, M. Maggini, C. Giacometti, G. Scorrano, G. Sandona and G. Farnia, *Tetrahedron* **52** (1996) 5221.
186. N. Martin, L. Sanchez, M. A. Herranz and D. M. Guldi, *J. Phys. Chem. A* **104** (2000) 4648.
187. N. Martin, L. Sanchez, B. Illescas, S. Gonzalez, M. A. Herranz and D. M. Guldi, *Carbon* **38** (2000) 1577.
188. D. M. Guldi, S. Gonzalez, N. Martin, A. Anton, J. Garin and J. Orduna, *J. Org. Chem.* **65** (2000) 1978.
189. S. Gonzalez, N. Martin, A. Swartz and D. M. Guldi, *Org. Lett.* **5** (2003) 557.
190. M. C. Diaz, M. A. Herranz, B. M. Illescas, N. Martin, N. Godbert, M. R. Bryce, C. Luo, A. Swartz, G. Anderson and D. M. Guldi, *J. Org. Chem.* **68** (2003) 7711.
191. T. Chuard and R. Deschenaux, *Helv. Chim. Acta* **79** (1996) 736.
192. D. M. Guldi, C. P. Luo, T. Da Ros, S. Bozi and M. Prato, *Chem. Commun.* (2002) 2320.
193. D. M. Guldi, C. P. Luo, D. Koktysh, N. A. Kotov, T. Da Ros, S. Bosi and M. Prato, *Nanoletters.* **2** (2002) 775.
194. D. M. Guldi, M. Maggini, G. Scorrano and M. Prato, *J. Am. Chem. Soc.* **119** (1997) 974.
195. E. Dietel, A. Hirsch, E. Eichhorn, A. Rieker, S. Hackbarth and B. Roder, *Chem. Commun.* (1998) 1981.
196. P. Cheng, S. R. Wilson and D. I. Schuster, *Chem. Commun.* (1999) 89.
197. D. I. Schuster, P. Cheng, S. R. Wilson, V. Prokhorenko, M. Katterle, A. R. Holzwarth, S. E. Braslavsky, G. Klihm, R. M. Williams and C. P. Luo, *J. Am. Chem. Soc.* **121** (1999) 11599.
198. L. R. Sutton, M. Scheloske, K. S. Pirner, A. Hirsch, D. M. Guldi and J. P. Gisselbrecht, *J. Am. Chem. Soc.* **126** (2004) 10370.
199. D. I. Schuster, P. Cheng, P. D. Jarowski, D. M. Guldi, C. P. Luo, L. Echegoyen, S. Pyo, A. R. Holzwarth, S. E. Braslavsky, R. M. Williams and G. Klihm, *J. Am. Chem. Soc.* **126** (2004) 7257.
200. D. Kreher, M. Cariou, S. G. Liu, E. Levillain, J. Veciana, C. Rovira, A. Gorgues and P. Hudhomme, *J. Mater. Chem.* **12** (2002) 2137.
201. J. Llacay, M. Mas, E. Molins, J. Veciana, D. Powell and C. Rovira, *Chem. Commun.* (1997) 659.
202. J. Llacay, J. Veciana, J. Vidal-Gancedo, J. L. Bourdelande, R. Gonzalez-Moreno and C. Rovira, *J. Org. Chem.* **63** (1998) 5201.
203. M. Mas-Torrent, R. A. Rodriguez-Mias, M. Sola, M. A. Molins, M. Pons, J. Vidal-Gancedo, J. Veciana and C. Rovira, *J. Org. Chem.* **67** (2002) 566.
204. H. Imahori, K. Tamaki, D. M. Guldi, C. P. Luo, M. Fujitsuka, O. Ito, Y. Sakata and S. Fukuzumi, *J. Am. Chem. Soc.* **123** (2001) 2607.
205. C. Luo, D. M. Guldi, H. Imahori, K. Tamaki and K. Sakata, *J. Am. Chem. Soc.* **122** (2000) 6535.
206. M. Fujitsuka, O. Ito, H. Imahori, K. Yamada, H. Yamada and Y. Sakata, *Chem. Lett.* (1999) 721.

207. H. Imahori, D. M. Guldi, K. Tamaki, Y. Yoshida, C. P. Luo, Y. Sakata and S. Fukuzumi, *J. Am. Chem. Soc.* **123** (2001) 6617.
208. P. A. Liddell, G. Kodis, L. de la Garza, J. L. Bahr, A. L. Moore, T. A. Moore and D. Gust, *Helv. Chim. Acta* **84** (2001) 2765.
209. G. Kodis, P. A. Liddell, L. de la Garza, A. L. Moore, T. A. Moore and D. Gust, *J. Mater. Chem.* **12** (2002) 2100.
210. D. Bonifazi, M. Scholl, F. Y. Song, L. Echegoyen, G. Accorsi, N. Armaroli and F. Diederich, *Angew. Chem. Int. Ed.* **42** (2003) 4966.
211. D. Bonifazi and F. Diederich, *Chem. Commun.* (2002) 2178.
212. F. Giacalone, J. L. Segura, N. Martin and D. M. Guldi, *J. Am. Chem. Soc.* **126** (2004) 5340.
213. G. de la Torre, F. Giacalone, J. L. Segura, N. Martin and D. M. Guldi, *Chem. Eur. J.* **11** (2005) 1267.
214. F. D'Souza, G. R. Deviprasad, M. S. Rahman and J. P. Choi, *Inorg. Chem.* **38** (1999) 2157.
215. F. D'Souza, N. P. Rath, G. R. Deviprasad and M. E. Zandler, *Chem. Commun.* (2001) 267.
216. T. Da Ros, M. Prato, D. Guldi, E. Alessio, M. Ruzzi and L. Pasimeni, *Chem. Commun.* (1999) 635.
217. T. Da Ros, M. Prato, D. M. Guldi, M. Ruzzi and L. Pasimeni, *Chem. Eur. J.* **7** (2001) 816.
218. S. R. Wilson, S. MacMahon, F. T. Tat, P. D. Jarowski and D. I. Schuster, *Chem. Commun.* (2003) 226.
219. F. D'Souza, G. R. Deviprasad, M. E. El-Khouly, M. Fujitsuka and O. Ito, *J. Am. Chem. Soc.* **123** (2001) 5277.
220. D. Gonzalez-Rodriguez, T. Torres, D. M. Guldi, J. Rivera, M. A. Herranz and L. Echegoyen, *J. Am. Chem. Soc.* **126** (2004) 6301.
221. D. Gonzalez-Rodriguez, T. Torres, D. M. Guldi, J. Rivera and L. Echegoyen, *Org. Lett.* **4** (2002) 335.
222. K. Li, D. I. Schuster, D. M. Guldi, M. A. Herranz and L. Echegoyen, *J. Am. Chem. Soc.* **126** (2004) 3388.
223. D. I. Schuster, K. Li, D. M. Guldi and J. Ramey, *Org. Lett.* **6** (2004) 1919.
224. M. V. Martinez-Diaz, N. S. Fender, M. S. Rodriguez-Morgade, M. Gomez-Lopez, F. Diederich, L. Echegoyen, J. F. Stoddart and T. Torres, *J. Mater. Chem.* **12** (2002) 2095.
225. D. M. Guldi, J. Ramey, M. V. Martinez-Diaz, A. de la Escosura, T. Torres, T. Da Ros and M. Prato, *Chem. Commun.* (2002) 2774.
226. M. Segura, L. Sanchez, J. de Mendoza, N. Martin and D. M. Guldi, *J. Am. Chem. Soc.* **125** (2003) 15093.
227. J. F. Nierengarten, *New J. Chem.* **28** (2004) 1177.
228. J. F. Nierengarten, *C. R. Chim.* **6** (2003) 725.
229. J. F. Nierengarten, *Top. Curr. Chem.* **228** (2003) 87.
230. J. F. Nierengarten, N. Armaroli, G. Accorsi, Y. Rio and J. F. Eckert, *Chem. Eur. J.* **9** (2003) 37.

- 231. S. Campidelli, E. Vazquez, D. Milic, M. Prato, J. Barbera, D. M. Guldi, M. Marcaccio, D. Paolucci, F. Paolucci and R. Deschenaux, *J. Mater. Chem.* **14** (2004) 1266.
- 232. N. S. Sariciftci, L. Smilowitz, A. J. Heeger and F. Wudl, *Science* **258** (1992) 1474.
- 233. D. M. Guldi, C. P. Luo, A. Swartz, R. Gomez, J. L. Segura, N. Martin, C. Brabec and N. S. Sariciftci, *J. Org. Chem.* **67** (2002) 1141.
- 234. S. Campidelli, R. Deschenaux, J. F. Eckert, D. Guillon and J. F. Nierengarten, *Chem. Commun.* (2002) 656.
- 235. M. T. Rispens, L. Sanchez, E. H. A. Beckers, P. A. van Hal, A. Schenning, A. El-ghayoury, E. Peeters, E. W. Meijer, R. A. J. Janssen and J. C. Hummelen, *Synth. Met.* **135** (2003) 801.
- 236. E. H. A. Beckers, P. A. van Hal, A. Schenning, A. El-ghayoury, E. Peeters, M. T. Rispens, J. C. Hummelen, E. W. Meijer and R. A. J. Janssen, *J. Mater. Chem.* **12** (2002) 2054.
- 237. L. Sanchez, M. T. Rispens and J. C. Hummelen, *Angew. Chem. Int. Ed.* **41** (2002) 838.
- 238. E. H. A. Beckers, A. Schenning, P. A. van Hal, A. El-ghayoury, L. Sanchez, J. C. Hummelen, E. W. Meijer and R. A. J. Janssen, *Chem. Commun.* (2002) 2888.



## Chapter 8

### Functionalization and applications of carbon nanotubes

Liangti Qu, Kyung Min Lee and Liming Dai

Department of Chemical and Materials Engineering, School of Engineering and UDRI, The University of Dayton,  
300 College Park, Dayton, Ohio 45469-0240, USA

Carbon nanotubes (CNTs) can be viewed as graphite sheet(s) that have been rolled up into a tiny tube form. These elongated nanotubes usually have a diameter in the range from few angstroms to tens of nanometers and a length of up to centimeters. The ends of CNTs are normally capped by fullerene-like structures containing pentagons. It has been demonstrated that the tips of CNTs are more reactive than sidewalls with the seamless arrangement of hexagon rings. Judicious application of site-selective reactions to non-aligned and aligned CNTs has opened up a rich field of carbon nanotube chemistry for chemical functionalization of the nanotube tips, inner- and/or outer-walls. This chapter provides a summary of the recent progress in the research on functionalization of CNTs for multifunctional materials and device applications.

#### 1. INTRODUCTION

The discovery of fullerenes has provided an exciting new insight into carbon nanostructures built from  $sp^2$  carbon units [1]. Carbon nanotubes (CNTs) can be viewed as elongated fullerenes, in which the walls of the tubes consist of cylindrical graphite sheet(s) with their ends capped by fullerene hemispheres [2]. There are two types of CNTs: multi-walled carbon nanotubes (MWNTs) and single-walled carbon nanotubes (SWNTs). MWNT consists of two or more concentric cylindrical shells of graphene sheets coaxially arranged around a central hollow core, and SWNT comprises a single graphene cylinder. Although graphite is a semiconductor, CNTs can be either metallic or semi-conducting, depending upon their diameter and the helicity of the arrangement of graphite rings [3–5]. Due to the unique mechanical, electrical, magnetic, optical and thermal properties, CNTs have been used in many areas, such as electron emitter in field emission display, reinforcement fillers in nanocomposite materials, scanning probe microscopy tips, actuators and sensors, and molecular scale components in micro-/nano-electronic devices [6].

The use of CNTs, either in aligned or non-aligned form, for many applications, including as the reinforcement agent for making advanced polymer composites and as biosensors/artificial mussels in biomedical devices, inevitably requires modification of their surface characteristics to meet the specific requirements for particular applications [7–9]. Many physical and/or chemical methods have been devised for functionalization of aligned and non-aligned CNTs. In this chapter, we will present

an overview on the functionalization of CNTs, covering both the covalent and non-covalent reactions at the tips, outerwalls, and innerwalls of SWNTs and MWNTs. Some potential applications of functionalized CNTs are also discussed.

## **2. COVALENT FUNCTIONALIZATION OF CARBON NANOTUBES**

### **2.1. End functionalization**

#### **2.1.1. Oxidation of carbon nanotubes**

Early work to modify the defective site of carbon nanotube surface is the oxidation reaction of CNTs at high temperature above 700 °C in the presence of air, yielding hemispherical end-caps opening in CNTs [10]. This indicates that the hemispherical end-tips are more reactive than the sidewalls of CNTs. The CNTs, with opened end-caps, can be filled with foreign materials such as metal oxide nanoparticles into the hollow tubes. Niu et al. [11] reported the gas-phase reaction with CNTs by using CO<sub>2</sub>, N<sub>2</sub>O, NO, NO<sub>2</sub>, O<sub>3</sub> and ClO<sub>2</sub> and the purification of CNTs, and observed that amorphous carbon impurities are more susceptible to gas-phase oxidation than CNTs.

Compared with the above works, solution chemical oxidation is more efficient for the purification and/or modification of CNTs. Since Tsang et al. [12] reported the liquid-phase oxidation of CNTs in HNO<sub>3</sub>, various strong acids, such as HNO<sub>3</sub> [13–15] HNO<sub>3</sub> + H<sub>2</sub>SO<sub>4</sub> [16], HClO<sub>4</sub> [17], H<sub>2</sub>SO<sub>4</sub> + K<sub>2</sub>Cr<sub>2</sub>O<sub>7</sub> [18,19], H<sub>2</sub>SO<sub>4</sub> + KMnO<sub>4</sub> [20], remained as the main class of oxidants used.

The oxidation reactions discussed above generate the various functional groups, such as –COOH, –OH, –C = O, at the opened end or defect sites of the CNTs. Fig. 1 shows the typical defects in an SWNT, and these defects could be oxidized by strong acids, which modified nanotube surface with functional groups, such as carboxylic acid, ketone, alcohol, and ester groups [21]. As shown in Fig. 2, a small amount of sulfur-containing functional groups can also be introduced by oxidizing CNTs with HNO<sub>3</sub>/H<sub>2</sub>SO<sub>4</sub> [16].

The degree of oxidation depends on the nature of the oxidant and the reaction conditions. The oxidation reaction in SWNTs takes place at nanotube end-tips and the outer layer of the bundle [14], while oxidation reaction in MWNTs, which starts from the nanotube tips and/or the defect sites, moves gradually from the outermost graphitic layer toward the nanotube core, resulting in a successive removal of the grapheme cylinders and the thinner nanotubes [10,12,22]. Many techniques such as FTIR, UV/VIS/NIR, Raman, [23,24] vibration spectroscopic NEXAFS, [25] SEM/TEM, [26] EDS, STM, [27] XPS, [16] and X-ray diffractometry [11] to characterize the oxidized nanotubes have been used.

#### **2.1.2. Covalent coupling via the oxidized nanotubes ends**

Oxidized nanotubes have carboxyl and hydroxyl functional groups, and these functional groups can be further used to chemically attach other small molecules or macromolecules through reactions characteristic of the oxidation-induced functional groups [28,29]. One of the most common chemical reactions with oxidized nanotubes is the amidation reaction, in which amide bond between the nanotube and the amine group moieties is formed, as shown in Scheme 1. The attached long hydrocarbon chains onto nanotubes improved the nanotube solubility significantly [30,31] and the modified

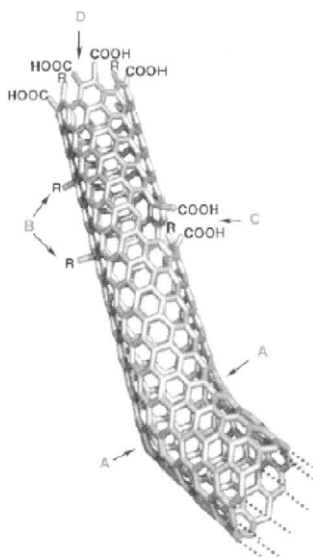


Figure 1. Typical defects in an SWNT: (A) Five- or seven-membered rings in the carbon framework, instead of the normal six-membered ring, leads to a bend in the tube. (B)  $sp^3$ -hybridized defects ( $R=H$  and  $OH$ ). (C) Carbon framework damaged by oxidative conditions, which leaves a hole lined with  $-COOH$  groups. (D) Open end of the SWNT, terminated with  $-COOH$  groups. Besides carboxy termini, the existence of which has been unambiguously demonstrated, other terminal groups such as  $-NO_2$ ,  $-OH$ ,  $-H$  and  $=O$  are possible. (Adapted from Hirsh [21].)

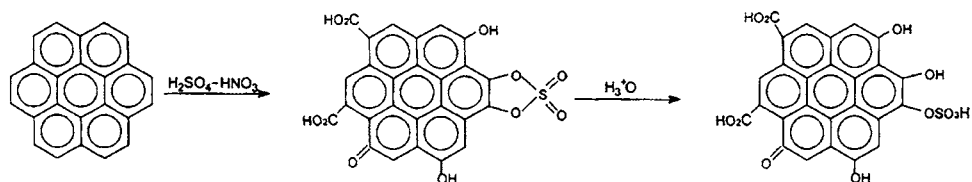


Figure 2. Surface modification of carbon nanotubes with a mixture of  $HNO_3$ - $H_2SO_4$ , yielding various functional groups such as carboxyl, carbonyl, and phenolic groups. (Adapted from Yu et al. [16].)

SWNTs can be purified by the conventional chromatographic method [32]. Polymers with amino side groups, such as poly(propionylethylenimine-*co*-ethylenimine) (PPEI-EI), can also be grafted onto the oxidized nanotubes through the amide formation in Fig. 3, leading to a high solubility in most organic solvents and water [33–35]. Alkyl chains with amine groups can be covalently attached onto the oxidized nanotubes using a carboxylate-ammonium salt, which also improves the solubility of nanotubes [31,36].

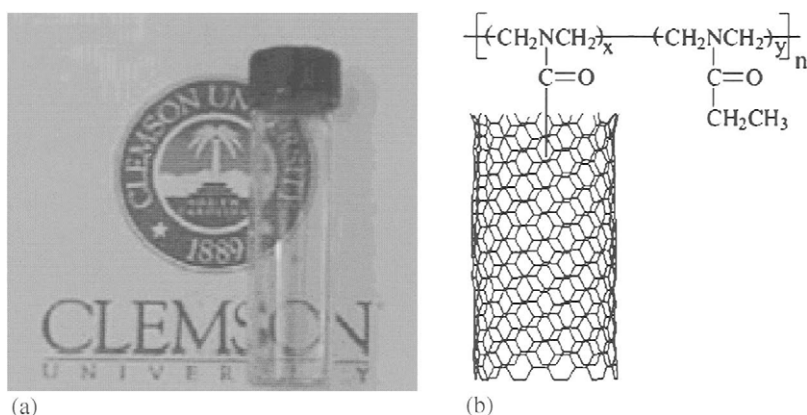
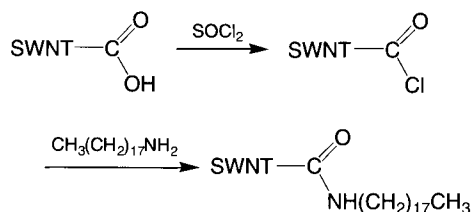


Figure 3. (a) Suspension of functionalized nanotube with  $\sim 0.5$  wt% of SWNTs. (b) Idealized cartoon of the PPEI-EI attachment. (Adapted from Czerw et al. [33].)



Scheme 1. Amidation reaction of an oxidized nanotube with amine molecule. (Adapted from Chen et al. [30].)

Apart from the amide linkage, the etherification reaction has also been used to covalently attach alkyl groups and polymers onto oxidized CNTs. For instance, etherification reaction of the octadecyl alcohol [37] and poly(vinyl acetate-*co*-vinyl alcohol) (PVA-VA) [34] with oxidized nanotubes have been reported.

Furthermore, dendrimers or dendrons (e.g. the tenth generation of poly(ami-doamine) (PAMAM) starburst dendrimer (G10)) have also been grafted onto the oxidized CNTs to form nanotube stars [38], as were lipophilic and hydrophilic dendrons that terminated with long alkyl chains and poly(ethylene glycol) oligomers [39,40]. Interestingly enough, Sano et al. [41] reported the ring formation from the oxidized SWNTs through the esterification reaction (Fig. 4a) between carboxylic groups and hydroxyl end-groups at the nanotube tips in the presence of condensation reagent, 1,2-dicyclohexylcarbodiimide (DCC). Fig. 4b shows the average diameter of 540 nm and narrow size distribution of nanotube rings.

Nanotube hetero-junctions with two nanotubes joined in either end-to-side or end-to-end configuration have also been made through a bifunctionalized amine linkage [42], as shown in Fig. 5.

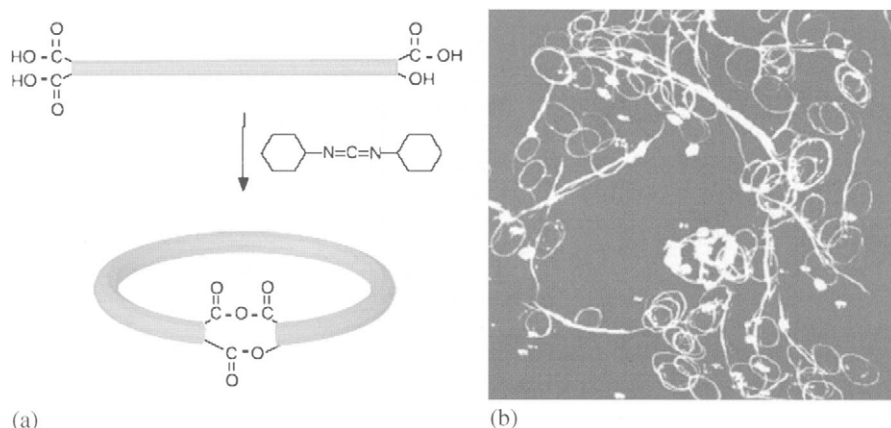


Figure 4. (a) A possible scheme for the ring-closure reaction with DCC, and (b) a typical AFM image of carbon nanotube rings. (Adapted from Sano et al. [41].)

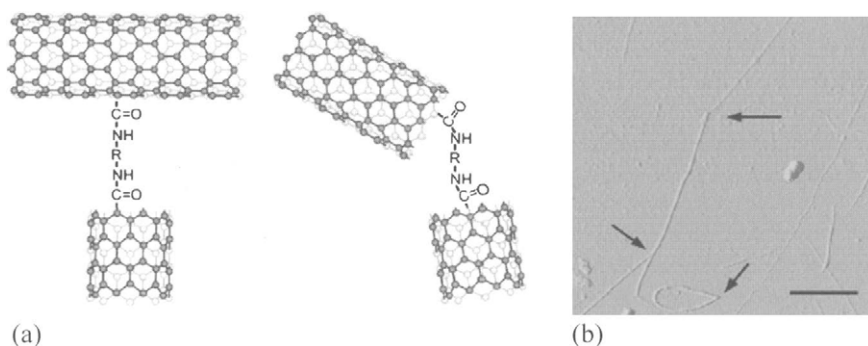


Figure 5. (a) Schematic representation of SWNT intermolecular junctions. The left side shows an end-to-side junction connected via two amide linkages and the right side shows an end-to-end configuration, where  $\text{R} = (\text{CH}_2)_3\text{NH}(\text{CH}_2)_3\text{NH}(\text{CH}_2)_3$ . (b) AFM image of interconnected SWNTs. (Adapted from Chiu et al. [42].)

Of particular interest, Hinds' and Dai's groups have independently achieved the asymmetric end-functionalization of CNTs recently [43,44]. Hinds et al. [43] used a vertically aligned array of CNTs impregnated with polystyrene to independently functionalize each end of the CNTs. The presence of the polystyrene matrix prevents side-wall oxidation of the CNTs, resulting in carboxylate derivatization at one side of the CNT tips by plasma oxidation. The other side of CNT tips can be further functionalized with different groups. On the other hand, Dai et al. [44] reported a simple and effective photochemical approach to directly grafting different chemical reagents onto the opposite tube-ends of individual CNTs, as schematically shown in Fig. 6.

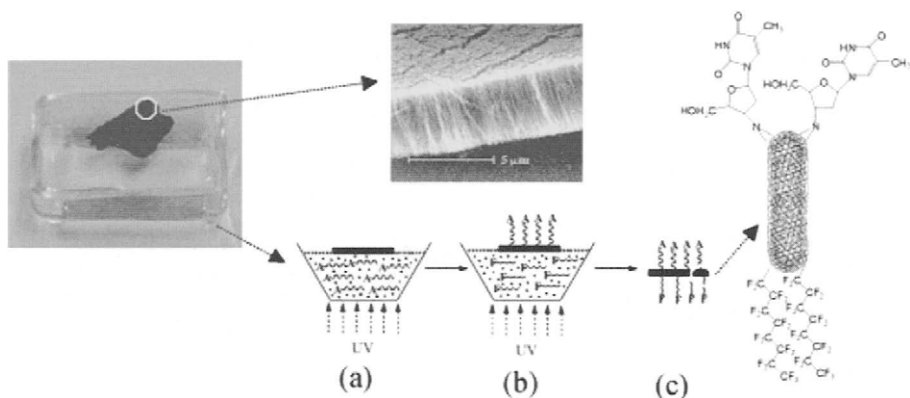


Figure 6. A free-standing film of aligned MWNTs floating on the top surface of (a) an AZT solution in ethanol for UV irradiation at one side of the nanotube film, and (b) a perfluorooctyl iodide solution in TCE for UV irradiation at the opposite side of the nanotube film (c) the asymmetrically end-functionalized carbon nanotube film. (Adapted from Lee et al. [44].)

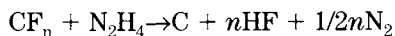
## 2.2. Functionalization of carbon nanotube outerwall

It is well known that sidewall of nanotubes is less reactive than tip-areas of nanotubes, however, three types of covalent sidewall functionalization reaction of the nanotubes have been achieved (Fig. 7) [45].

### 2.2.1. Sidewall fluorination of carbon nanotubes

Although CNTs are generally known to be inert toward fluorine at room temperature, chemical fluorination of CNTs has been achieved at relatively high temperatures. For instance, Nakajima et al. [46] have demonstrated the chemical fluorination of CNT wall within the temperature range between 250 and 400 °C. Fluorination of SWNTs has also been carried out following the same way as that for fluorination of graphite, [47] indicating there was considerable room for chemical functionalization of CNTs under appropriate conditions. Fluorination at a temperature above 400 °C was found to cause the decomposition of the tube structure. Although, fluorination between 250 and 400 °C does not damage the structure to that extent, it reduces the conductivity of the SWNTs due to the partial destruction of the graphitic structure. As a result, the fluorinated SWNTs differ dramatically from their unmodified counterparts in electronic properties. The presence of covalently bonded fluorine in the fluorinated CNT sample was confirmed by the appearance of FTIR peaks over 1220–1250 cm<sup>-1</sup>. The TEM elemental images given in Fig. 8 further indicate that fluorine atoms are homogeneously attached onto the nanotube wall.

The covalently bonded fluorine was found to be removable from the fluorinated nanotube surface by reacting with N<sub>2</sub>H<sub>4</sub>:



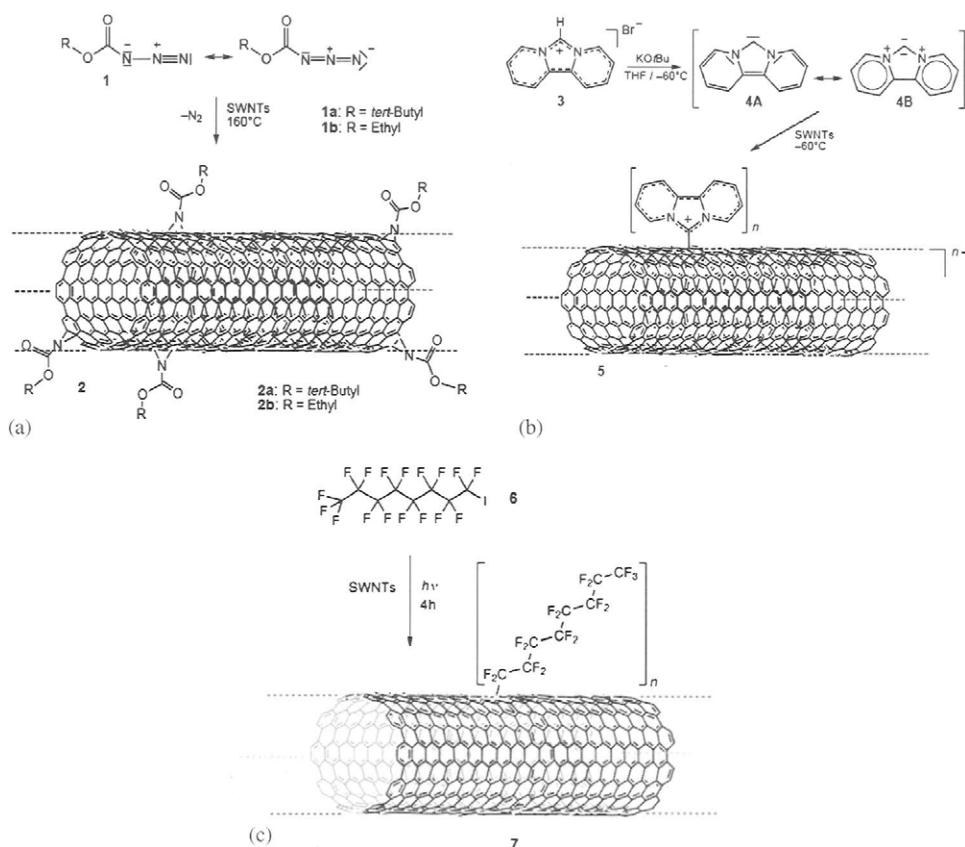


Figure 7. Sidewall functionalization by the (a) [2 + 1] cycloaddition of nitrenes, (b) addition of nucleophilic carbenes and (c) the addition of a radical. (Adapted from Holzinger et al. [45].)

The above fluorination reaction is of considerable interest because further functionalization of CNTs can be carried out through the fluorine intermediate. In this context, it was demonstrated that the covalently-bonded fluorine could be replaced by alkyl groups through the alkylation reaction [48]. For this purpose, alkyl lithium or Grignard reagent can be used as an alkylation reagent. Interestingly, these alkyl groups can also be removed by heating the alkylated nanotubes at ~250 °C, leading to the recovery of the pure SWNTs. Various physicochemical properties of the fluorinated SWNTs, including high-resolution electron energy loss [49], thermal recovery behavior [50], and solvation in alcohol solvents [51], have been investigated. Furthermore, Yudanov and coworkers [52] have recently demonstrated the fluorination of MWNTs at room temperature by using BrF<sub>3</sub> as the fluorination reagent, though only the outside shell of the MWNT was modified.

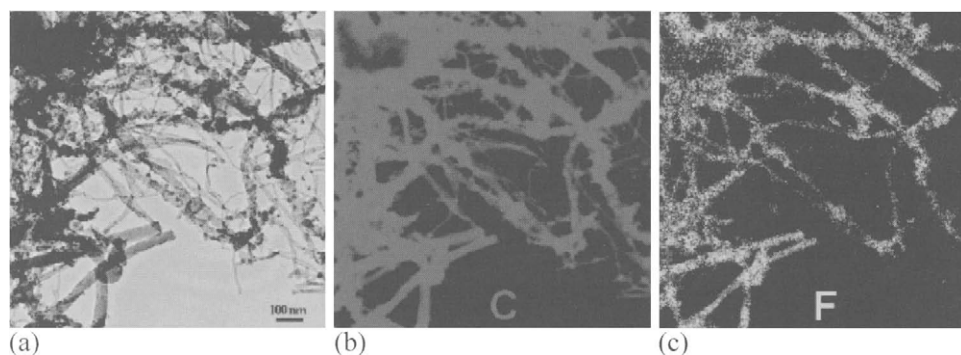


Figure 8. (a) TEM image of fluorinated CNTs, (b) elemental C mapping of the image (a), and (c) elemental F mapping of the image (a). (Adapted from Hayashi et al.[49].)

### 2.2.2. The attachment of dichlorocarbene to the sidewall of carbon nanotubes

Chen and coworkers [30] modified the SWNTs and MWNTs by using 1,1-dichlorocarbene generated from different sources, including NaOH/chloroform and Hg complex. It is well known that 1,1-dichlorocarbene can attack the C=C bond connecting two adjacent six-membered carbon rings to produce 1,1-dichlorocyclopropane. XPS measurement was used to investigate the surface chemical state of elements C and O in the carbonated nanotubes [53]. It was found that a large number of amorphous carbon attached onto the tubular wall, leading to a question whether the dichlorocarbene was attached onto the sidewall of nanotube or just reacting with the amorphous carbon [54]. Like fullerene C<sub>60</sub>, 1,3-dipolar cycloaddition of azomethine ylides can also take place between the graphite sidewall of SWNTs at the C=C bond connecting two adjacent six-membered rings and an  $\alpha$ -amino acid or an aldehyde molecule, resulting in high solubility in chloroform up to 50 mg mL<sup>-1</sup> [55].

Recently, Ajayan and coworkers [56] reported a single-step in-situ synthesis of polystyrene-grafted SWNT composites without disrupting the original structure by using anionic polymerization method as shown in Fig. 9. This approach does not require nanotube pretreatment with debundling of SWNTs and polymer attachment occurred in one-step, leading to a homogeneous dispersion of CNTs.

A somewhat related, but different, approach to attach the poly(*n*-butyl methacrylate) (PnBMA) onto nanotubes was reported by using atomic transfer radical polymerization (ATRP) method, yielding polymer brushes coated SWNTs (Fig. 10) [57]. In this case, carboxylic groups on SWNTs were generated by nitric acid oxidation. The ATRP initiators were then covalently attached onto SWNTs by esterification of 2-hydroxyethyl 2'-bromopropionate with carboxylic acid groups, followed by the addition of monomer molecules (*n*-butyl methacrylate, nBMA). The PnBMA-functionalized SWNTs can be dissolved in several organic solvents, including 1,2-dichlorobenzene, chloroform and tetrahydrofuran.



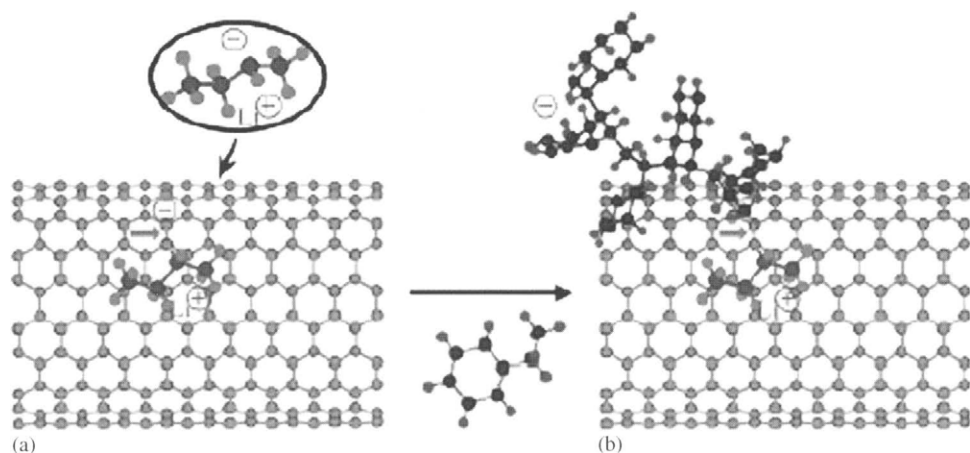


Figure 9. Schematic (not to scale) of carbanion formation and subsequent initiation of polymerization: (a) section of SWNT sidewall showing *sec*-butyllithium addition to a double bond (green arrow indicates the bond to which it adds) and formation of anion via transfer of charge; (b) the carbanion attacks the double bond in styrene and, in turn, transfers the negative charge to the monomer. Successive addition of styrene results in the formation of a living polymer chain. (Adapted from Viswanathan et al. [56].)

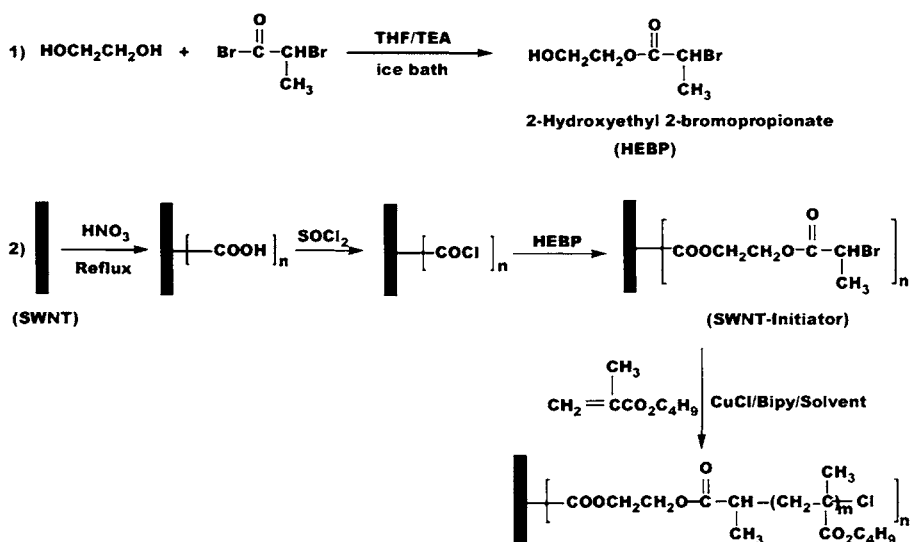


Figure 10. Schematic presentation of polymer brushes from the SWNT by functionalizing the ends and sidewalls of the tube with ATRP initiators and subsequent grafting of poly(*n*-butyl methacrylate) (PnBMA). (Adapted from Qin et al. [57].)

Sun et al. [58] reported the strong interaction of nanotubes with aniline. Figs. 11a and b show the UV/Vis and fluorescence spectra for the nanotubes dissolved in aniline, exhibiting a new UV-Vis absorption peak at  $\sim 540$  nm and a new fluorescence peak at  $\sim 620$  nm, respectively. In general, aniline quenches the fluorescence emission due to its strong electron affinity, however, they proposed the possible chemical reaction between the SWNTs and aniline to explain the unusual phenomena, as shown in Fig. 11c.

Having demonstrated the modification of a glassy carbon electrode by electrochemical reduction of an aryl diazonium salt, Tour and coworkers [59] were able to demonstrate that this process was also possible with the nanotube electrode. This reaction involves the attachment of aryl cations onto the sidewall of SWNTs, and Fig. 12 shows various diazonium salts attached onto the nanotube wall. Those aryl cations with long alkyl chains at the *para*-position of the benzyl ring can significantly improve the solubility of the nanotubes in organic solvents. Again, these grafted molecules can be removed by heating the modified nanotubes in an inert atmosphere at  $500^\circ\text{C}$ .

### 2.3. Functionalization of carbon nanotube innerwall

For the innerwall modification, CNTs have been synthesized via template technique [60]. Until now, most modification of nanotubes has been done for the outerwall, and innerwall modification of nanotubes has been less discussed in the literature. This is because the innerwall modification often requires the opening nanotube tip(s) and the protection of the outerwall; both of the processes are uneasy and tedious. In this regard, CNTs synthesized by the template technique possess advantages toward the innerwall modification [60].

The template-synthesized CNTs are made by direct deposition of CNTs or precursor polymer nanotubes followed by high temperature graphitizing within the pores of

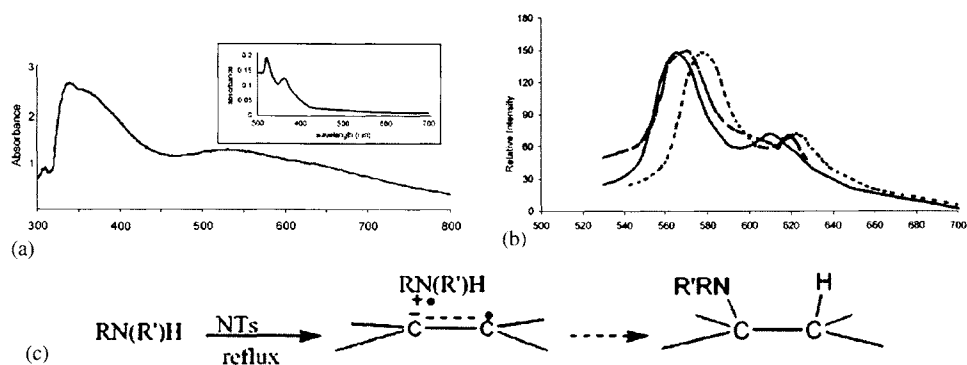


Figure 11. (a) UV/Vis absorption spectrum of carbon nanotube dissolved in aniline. The inset shows the corresponding UV/Vis spectrum for the carbon nanotube/aniline solution diluted with acetone; (b) Fluorescence emission spectra of the carbon nanotube/aniline solution diluted in different solvents: acetone (—), toluene (---), and methanol (· · ·); all samples were excited at 500 nm; (c) Proposed reaction mechanism between nanotubes and aromatic amines. (Adapted from Sun et al. [58].)

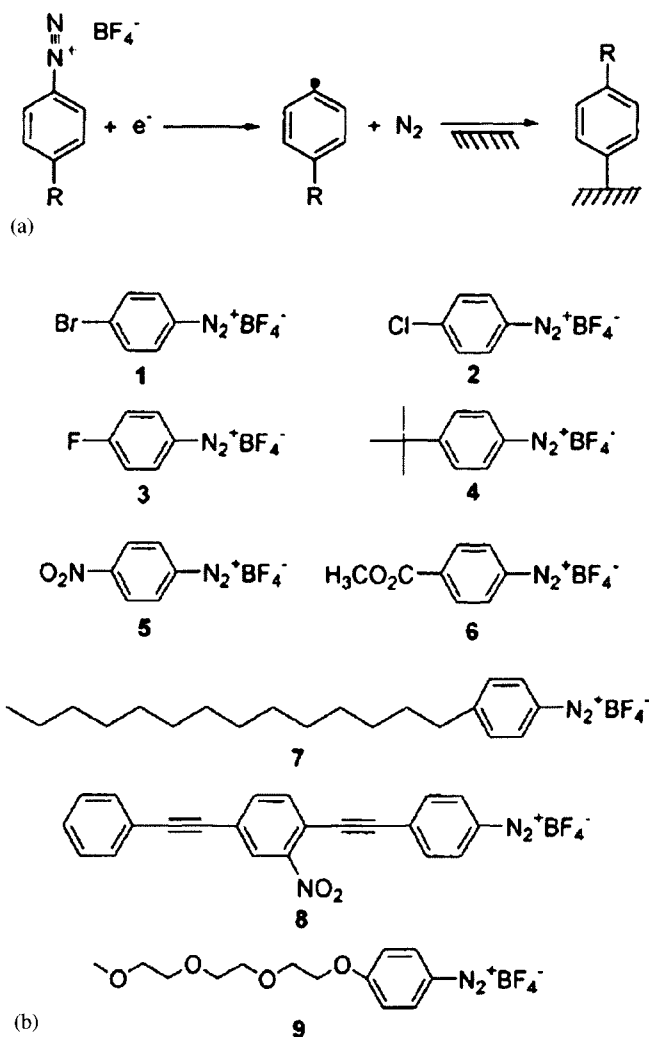


Figure 12. (a) Electrochemical reduction of aryl diazonium salts, giving a reactive radical that covalently attaches to a carbon surface; (b) Aryl diazonium salts used to derivatize the SWNTs. (Adapted from Bahr et al. [59].)

a nanoporous template. This nanoporous template is aluminum membrane or mesoporous zeolite. The advantage of template technique is the production of monodispersed CNTs with opened ends, controllable diameters, length and orientation. The aligned CNTs are synthesized in the nanoporous alumina membrane [61,62], and CNTs are also prepared by high-temperature graphitizing of the polyacrylonitrile (PAN) nanotubules within the pores of an alumina template membrane or zeolite nanochannels [63–65]. Kyotani and coworkers [60] reported successful nitric acid oxidation of nanotube innerwalls within the nanoporous  $\text{Al}_2\text{O}_3$  pores with the alumina

template membrane, which acts as the protection layer for the nanotube outerwall. After complete oxidation of nanotube innerwalls, the template was dissolved in the HF solution to release the innerwall-modified nanotubes, as shown in Fig. 13.

### 3. NON-COVALENT FUNCTIONALIZATION OF CARBON NANOTUBES

#### 3.1. Physical wrapping

Compared to covalently modified nanotubes, one of main advantage of non-covalently functionalized nanotubes with macromolecules is to conserve the nanotube electronic structures by preventing rupture of nanotube  $sp^2$  conjugated structure. Some research groups reported that high-molecular weight-polymers, especially conjugated polymers, could wrap CNTs [21,66,67]. These nanotubes wrapped by polymers show the reduced van der Waals interaction between CNTs, resulting in increased solubility of SWNTs. The driving force to wrap the carbon nanotube sidewall with polymer chains, such as poly(*m*-phenylene vinylene) (PmPV), is strong  $\pi$ - $\pi$  interaction between carbon nanotube and conjugated polymer [20]. Poly(vinyl pyrrolidone) (PVP) or poly(styrene sulfonate) (PSS) can also be wrapped onto the CNTs as shown in Fig. 14 [68].

The wrapping of conjugated polymer around the nanotube sidewall is evidenced, at least partially, by the broadening of UV/Vis absorption bands. Fig. 15 shows the UV-Vis absorption bands of PmPV at 329 and 410 nm, and the appearance of a new broad absorption band over 650–900 nm from the SWNTs/PmPV complexes [69].

Xu and Tang [70] showed the in-situ polymerization of phenylacetylene, PA, in the presence of the shortened SWNTs to prepare the SWNTs wrapped by conjugated polymer. This resulting material was characterized by several characterization tools, such as GPC, NMR, UV, FL, SEM/TEM and XRD, and revealed that the PPA chains thickly wrapped nanotubes. These SWNT/PPA composites show a high solubility in organic solvents, good photostability even under harsh laser irradiation, and excellent optical limiting properties.

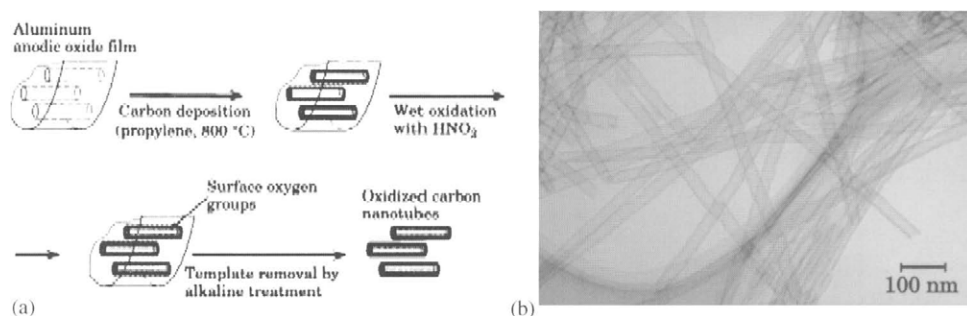


Figure 13. (a) Oxidation process to the inner surface of carbon nanotube and (b) TEM image of the carbon nanotube prepared from the  $HNO_3$ -treated carbon coated alumina film. (Adapted from Kyontani et al. [60].)

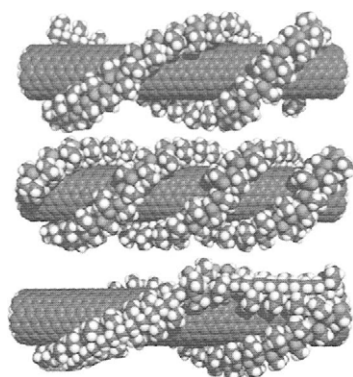


Figure 14. Some possible wrapping arrangement of poly(vinyl pyrrolidone) (PVP) on an 8,8 SWNT. A double helix (top) and a triple helix (middle). Backbone bond rotation can induce switch-backs, allowing multiple parallel wrapping strands to come from the same polymer chain (bottom). (Adapted from O'Connell, [68].)

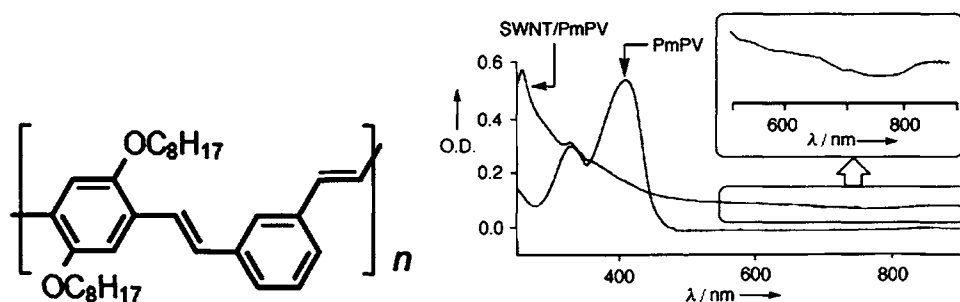


Figure 15. Molecular structure of poly(metaphenylenevinylene) (PmPV) and UV/Vis spectra of PmPV and SWNT/PmPV complex. (Adapted from Star et al. [69].)

### 3.2. Encapsulation — physical attachment onto carbon nanotube sidewall

Recently, certain aromatic molecules with a planar  $\pi$  moiety such as a pyrenyl group could strongly interact with the basal plane of graphite on the nanotube sidewall via  $\pi$ - $\pi$  stacking [9]. The aromatic molecule is strongly adsorbed onto the hydrophobic surface of the nanotubes, yielding a stable self-assembled structure in aqueous solution. As shown in Fig. 16A, the end-adsorbed long alkyl chains onto nanotube surface via  $\pi$ - $\pi$  stacking could significantly improve the solubility of the nanotubes. Biologically active molecules, such as DNA and protein chains, could be attached strongly onto the sidewall of SWNTs through appropriate anchoring molecules. Chen and coworkers [9] reported that some bioactive molecules containing amine group, such as ferritin, tavidine and biotiny-3,6-dioxactanediamine, have been attached onto the sidewall of SWNTs through nucleophilic substitution of the amino

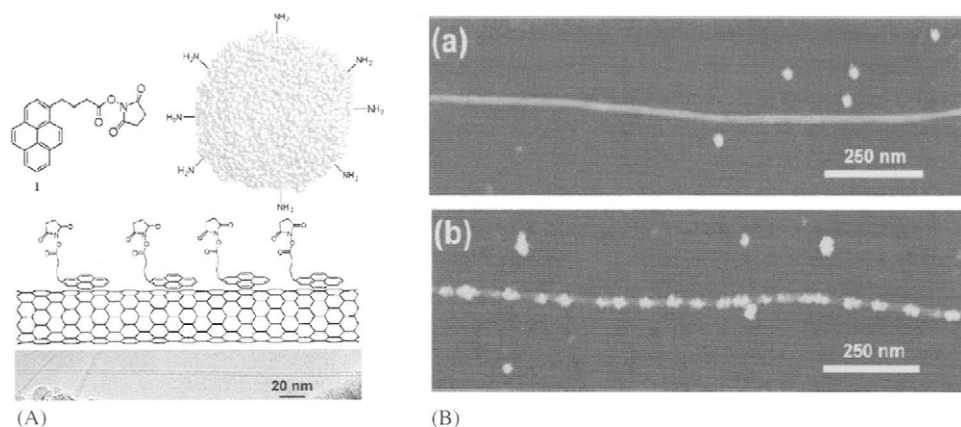


Figure 16. (A) 1-Pyrenebutanoic acid, succinimidyl ester 1 irreversibly adsorbing onto the sidewall of an SWNT via  $\pi$ -stacking. (B) (a) An AFM image showing a SWNT bundle (diameter = 4.5 nm) free of adsorbed ferritin after incubation in a ferritin solution and (b) ferritin molecules (apparent height  $\sim 10$  nm) adsorbed on an SWNT bundle (diameter = 2.5 nm) functionalized by 1 and incubated in a ferritin solution. (Adapted from Chen et al. [9].)

functionality by an N-hydroxysuccinimide group, which were pre-anchored onto the nanotube via a succinimidyl ester linkage by pyrenylene, as shown in Fig. 16B.

#### 4. FUNCTIONALIZATION OF CARBON NANOTUBES WITH OTHER PHYSICAL CHEMICAL METHODS

##### 4.1. Modification of carbon nanotubes via mechanochemical reactions

Mechanochemistry refers to processes in which mechanical motions/energy control chemical reactions [71]. Specifically, the mechanochemical reaction involves highly reactive centers generated by the mechanical energy (e.g. ultrasonication, ball-milling) imparted to the reaction system. Certain organic reactions have been demonstrated to take place efficiently in the solid-state phase [72].

Ultrasonication has been demonstrated to significantly enhance many chemical reactions, including the acid oxidation of CNTs [73]. It was envisaged that the strong vibration arising from the ultrasonication created many defect sites on the SWNT sidewalls (both the inner and outer ones), which could not only facilitate the oxidation reaction but also cut the SWNTs into short segments. Ultrasonication has also been found to induce a chemical reaction between SWNTs and monochlorobenzene in the presence of poly (methyl methacrylate) (PMMA) [74]. In particular, SWNTs could be separated from carbonaceous impurities and cut into short by ultrasonication of SWNTs and PMMA in monochlorobenzene [74]. As evidenced by the appearance of new peaks at 1729, 2848, and 2920  $\text{cm}^{-1}$ , characteristic of C=C, C=O, and C-H

bond stretching vibration, respectively, in solid state diffuse reflectance FTIR spectra, the above polymer-assisted ultrasonication purification process was accompanied by a chemical reaction between the SWNT and monochlorobenzene [75]. PMMA might have enhanced the solubility of SWNTs in monochlorobenzene, and hence facilitated the reaction. High-resolution TEM imaging revealed that a large number of defects formed on the sidewall of SWNTs, which became holes upon heating in oxygen [76].

Another closely related observation is that certain SWNTs folded back under ultrasonication to form nanotube coils with a narrow distribution of radii (300–400 nm, Fig. 17) [77]. Although the ultrasonication-induced nanotube ring formation unlike those nanotube rings formed by the end-to-end ester linkage discussed above (Fig. 4) [41], it seemed to be largely a physical process; some interesting chemical interactions between the nanotube ends might involved as very smooth junctions were observed.

Apart from the ultrasonication, various other physicochemical processes, including microwave [78] and ball-milling [79], have also been investigated. In particular, ball-milling of CNTs in the presence of acid was reported to cut the nanotube into 200–300 nm ropes [79].

#### 4.2. Modification of carbon nanotubes via electrochemical deposition

Owing to the good electronic properties intrinsically associated with CNTs [80], electrochemical modification of individual carbon nanotube bundles has been attempted. For instance, Kooi et al. [81] have electrochemically polymerized a thin polymer layer onto the individual SWNT bundle (Fig. 18A), which was pre-coated on a microelectrode. The resultant polymer layer was directly observed to be of 6 nm thick by in-situ AFM imaging (Fig. 18B).

Electrochemistry is also a powerful technique for the deposition of metal nanoparticles onto CNTs, which allows the chemist to easily control the nucleation and growth of metal nanoparticles [82–85]. By varying the deposition potential, substrate and deposition time one can control the size and distribution of metal nanoparticles. The deposited nanoparticles are mainly limited to such noble metals

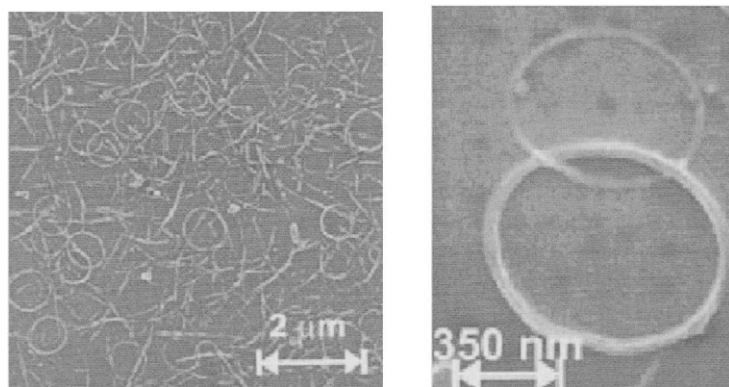


Figure 17. Nanotube rings formed by ultrasonication. (Adapted from Martel et al. [77].)

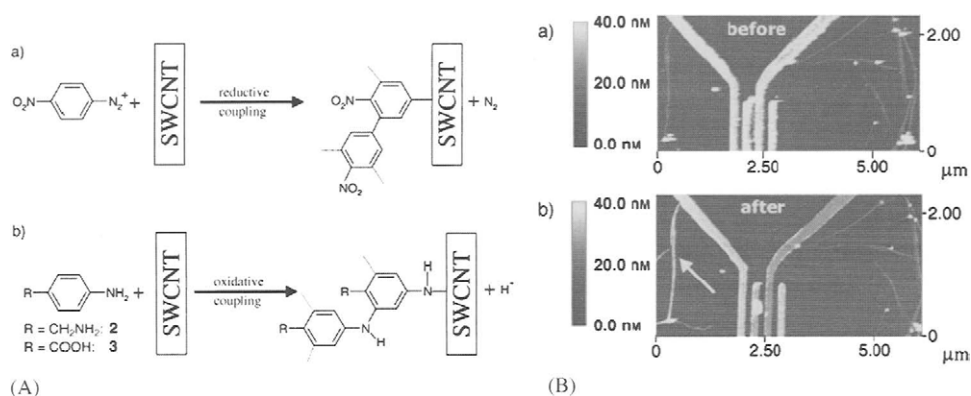


Figure 18. Scheme of electrochemically polymerized a thin polymer layer onto the individual SWNT bundle (A) and AFM image of SWNTs before (B, a) and after (B, b) reductive coupling with polymer. (Adapted from Kooi et al. [81].)

as Pd [82,83,86], Pt [84–88] Au [86], and Ag [84,89]. The related literature has been summarized in a recent review [90].

#### 4.3. Modification of carbon nanotubes via electroless deposition

Unlike the electrochemical reduction discussed above, electroless deposition methods rely on a chemical process, whereby a substrate with a lower redox potential than that of the metal species to be reduced provides the driving force for reducing the metal ions onto the substrate. Such methods have been used to form nanoparticles between certain metal pairs, including Pt and CNTs [91–95], Au and Ag [95], Ni and Pd [91] and Cu and Ni [96]. Of particular interest, Qu and Dai have developed a reductant-free electroless deposition method called substrate-enhanced electroless deposition, or SEED [97,98]. They discovered that by supporting the CNTs on a metal substrate with a lower redox potential than that of the metal ions to be reduced, spontaneous deposition of the metal nanoparticles onto the CNTs could occur. In so doing, they deposited metal nanoparticles of Cu, Ag, Au, Pt, and Pd onto both SWNTs and MWNTs, as exemplified by Fig. 19 [98].

### 5. SELF-ASSEMBLY OF MODIFIED CARBON NANOTUBES

Just as the chemically and non-covalently modified CNTs have significantly facilitated the characterization of their physicochemical properties at the molecular level and their efficient incorporation into devices, an aligned/micropatterned form of CNTs has been demonstrated to be highly desirable for device applications [99]. However, so far, ordered structures have been only constructed from a few of the end-functionalized CNTs on certain pre-treated substrates. For instance, Liu et al. [100] have prepared aligned SWNTs by self-assembling of nanotubes end-functionalized with thiol groups on a gold substrate (Fig. 20).



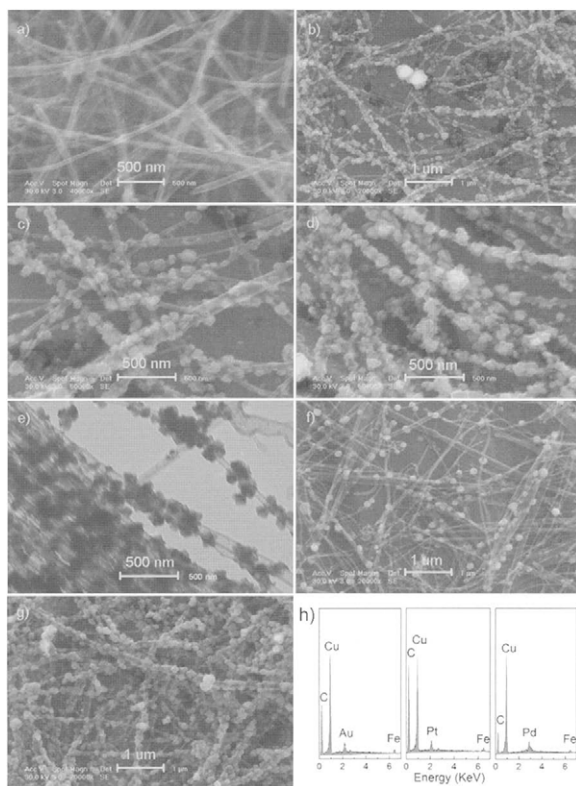


Figure 19. SEM images of MWNTs supported by a Cu foil after being immersed into an aqueous solution of  $\text{HAuCl}_4$  (3.8 mM) for different periods of time: (a) 0 s, (b) 10 s, (c) same as for (b) under a higher magnification, (d) 30 s. (e) A transmission electron microscopic (TEM) image of Au nanoparticle-coated MWNTs, (f) the Cu-supported MWNTs after being immersed into an aqueous solutions of  $\text{K}_2\text{PtCl}_4$  (4.8 mM) for 10 s, and (g) the Cu-supported MWNTs after being immersed into an aqueous solution of  $(\text{NH}_4)_2\text{PdCl}_4$  (7.0 mM) for 10 s. (h) EDX spectra for the Au, Pt, and Pd nanoparticle-coated MWNTs on Cu foils. (Adapted from Qu and Dai [98].)

As seen in Fig. 20, the carboxyl-terminated short SWNTs prepared by acid oxidation were used as the starting material for further functionalization with thiol-containing alkyl amines through the amide linkage. Then, the self-assembly of aligned SWNTs was obtained by dipping a gold (111) ball into the thiol-functionalized SWNT suspension in ethanol, followed by ultrasonication and drying in high-purity nitrogen.

Given that carboxylic acids could be deprotonated by various metal oxides (e.g. Ag, Al, Cu), Liu and coworkers [101] have investigated the formation of aligned nanotube array by self-assembling  $\text{COOH}$ -terminated CNTs onto certain metal oxide substrates (e.g. Ag). The deprotonation between the carboxylic groups on nanotubes and the metal surface effectively led to the anchoring of aligned CNTs on

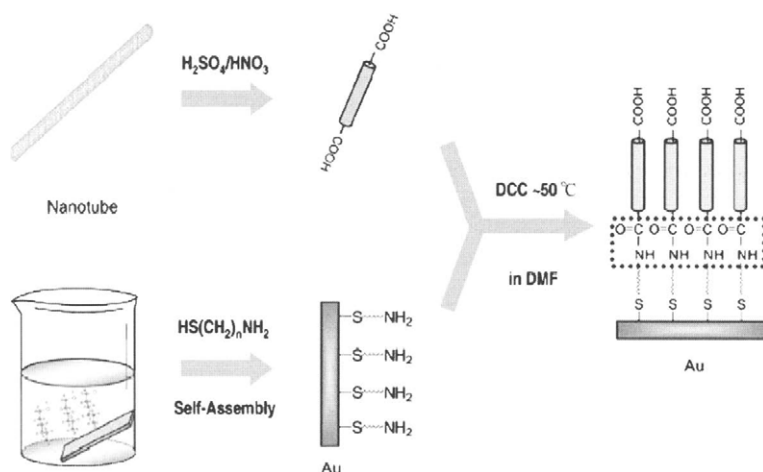


Figure 20. Schematic illumination of the self-assembling process of modified CNTs on Au. (Adapted from Nan et al. [102].)

the metal substrate via their carboxylated anion head groups by Coulombic force. Raman spectroscopic measurements confirmed the process shown in Fig. 21 [101].

Recently, Nan et al. [102] have demonstrated that individual acid oxidized SWNTs can be deposited onto a gold substrate pre-treated with  $\text{NH}_2(\text{CH}_2)_{11}\text{SH}$  to form an aligned nanotube array on gold through the amide linkage. In this case, the micro-contact printing ( $\mu\text{CP}$ ) technique was used to pre-pattern the thiol self-assembled monolayer on the gold surface for region-specific deposition of the aligned CNTs. As shown in the optical microscope image (Fig. 22a), the dark dot regions are covered by CNTs. The corresponding AFM image given in Fig. 22b clearly shows the aligned structure.

Pan et al. [103] have also reported that SWNTs can react with potassium hydroxide (KOH) through a solid-phase mechanochemical reaction at room temperature to produce the single-walled carbon nanotubols (SWNTols) with multiple hydroxyl, as shown in Fig. 23. These SWNTols are highly soluble in water and can be self-assembled into aligned arrays through strong surface hydrogen bond interactions.

## 6. FUNCTIONALIZATION OF ALIGNED CARBON NANOTUBES

Owing to the rather harsh conditions involved, most of the above-mentioned solution reactions would cause detrimental damage to aligned CNTs. Given that the alignment is an additional advantage for the use of CNTs in many devices, a particularly attractive option is the surface modification of CNTs while largely retaining their structural integrity. Various techniques have been developed for the functionalization of aligned carbon nanotubes without destruction of the alignment.

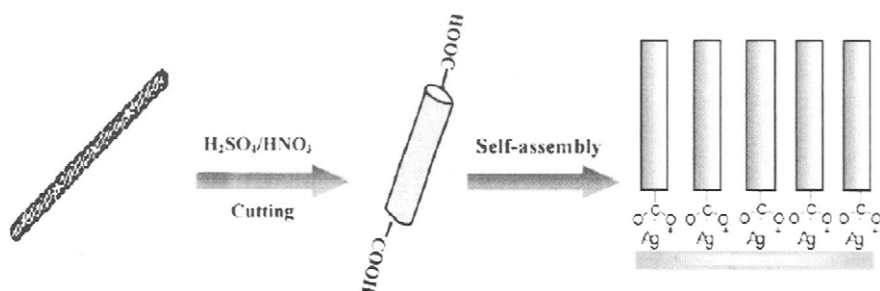


Figure 21. Schematic illumination of the self-assemble process of modified CNTs on Ag. (Adapted from Wu et al. [101].)

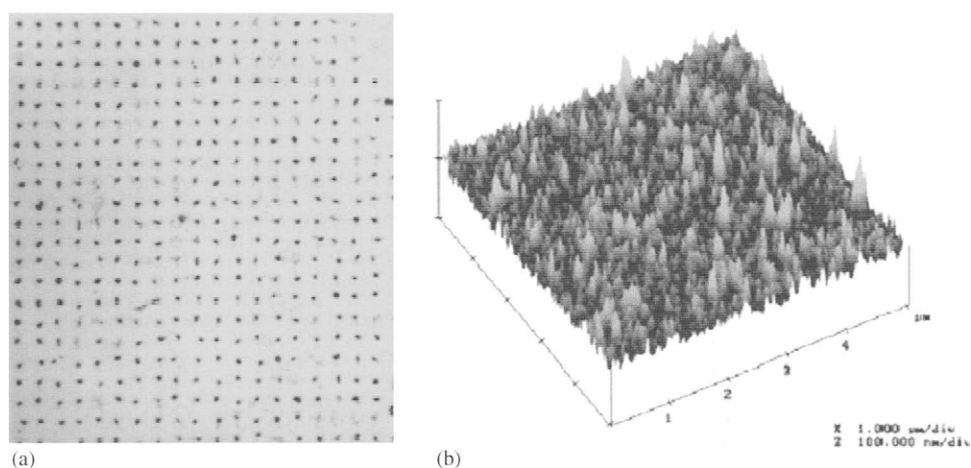


Figure 22. Aligned CNTs formed by self-assembling of  $\text{COOH}$ -terminated nanotubes onto a gold surface pre-patterned with thiol molecules. (a) Optical microscope image and (b) AFM image. (Adapted from Nan et al. [102].)

### 6.1. Spin-on glass process

One approach to protect the nanotube alignment is to have the pre-aligned nanotubes infiltrated with protected coating before further modification. In this aspect, Nguyen and coworkers [104] have developed an effective method to protect the alignment structure by filling the gaps between the aligned nanotubes with a spin-on glass (SOG) prior to the oxidative reaction (Fig. 24).

Fig. 25 shows the oxidation-induced changes in alignment for the aligned CNTs with and without the SOG protection. Comparing Fig. 25C with Fig. 25B indicates that the SOG film provides structural support to the aligned CNTs. After having successfully functionalized the tips of the aligned CNTs with carboxylic groups, these

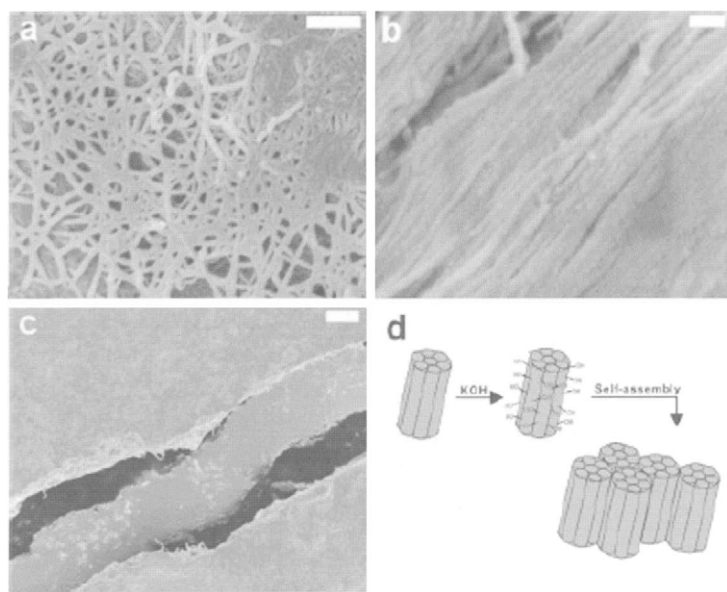


Figure 23. SEM images of (a) the starting SWNT sample (scale bar, 100 nm); (b) cross-sectional view of the self-assembled SWNTol sample shown in (c) (scale bar, 100 nm); (c) top view of the self-assembled SWNTol sample (scale bar, 1000 nm); and (d) schematic representation of the self-assembling process. (Adapted from Pan et al. [103].)

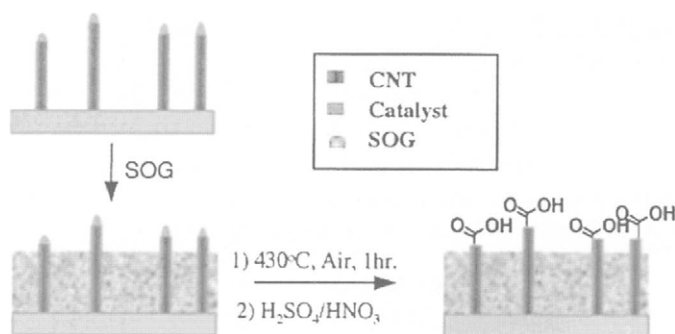


Figure 24. Schematic representation of the fabrication and pretreatment of carbon nanoelectrode arrays for functionalization. (Adapted from Nguyen et al. [104].)

authors demonstrated accomplishments in chemical coupling of nucleic acids to the aligned nanotube array using the standard water-soluble coupling reagents [i.e. 1-ethyl-3-(3-dimethylaminopropyl) carbodiimide hydrochloride, EDC, and *N*-hydrocysulfo-succinimide, sulfo-NHS], as schematically shown in Fig. 25E.

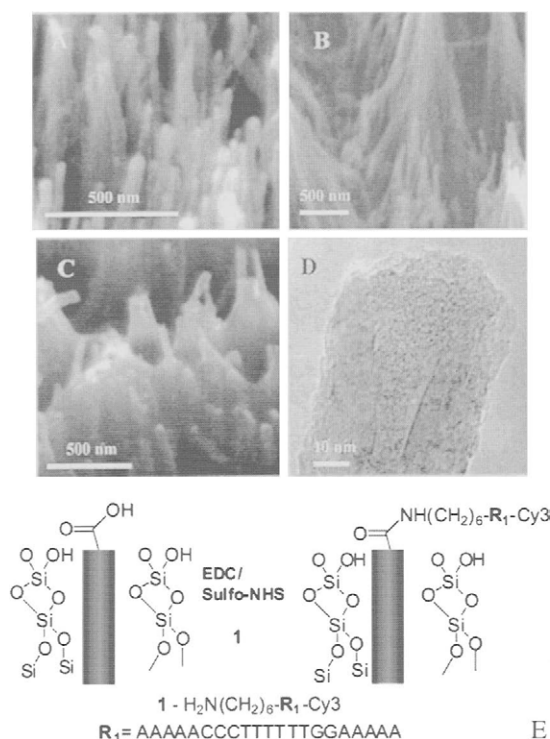


Figure 25. Electron microscope images. (A) Vertically aligned multi-walled CNT arrays with length about 1 μm. (B) Collapsed CNT arrays after purification process. (C) CNT arrays with SOG after purification and tip opening process. (D) High-resolution transmission electron microscope image of an opened CNT end. (E) Schematic illustration of chemical coupling of nucleic acid to aligned carbon nanotube array. (Adapted from Nguyen et al. [104].)

To prepare nanoelectrode arrays (NEAs) with each of the aligned CNTs that acts as an individual nanoelectrode, Ren and coworkers [105] have developed a method to grow low-density aligned CNTs, along with a polymer-spun-on process to support the aligned structure (Fig. 26).

Well-ordered nanoporous membrane can also be prepared by the polymer spinning on aligned CNTs [106]. Fig. 27A shows an SEM image of well-aligned CNTs. When the space between the CNTs is filled with a continuous polymer film and the normally closed ends of the CNTs are etched open, one can obtain an ideal membrane structure with nanoscale pores (Fig. 27B). Fig. 27C shows a free-standing membrane of aligned CNTs infiltrated by polystyrene (PS) matrix. H<sub>2</sub>O plasma-enhanced oxidation process was used to remove the thin layer of excess polymer on the top surface and to open the CNT tips, leading to well-ordered nanoporous membrane useful for gas flow and ion transport.

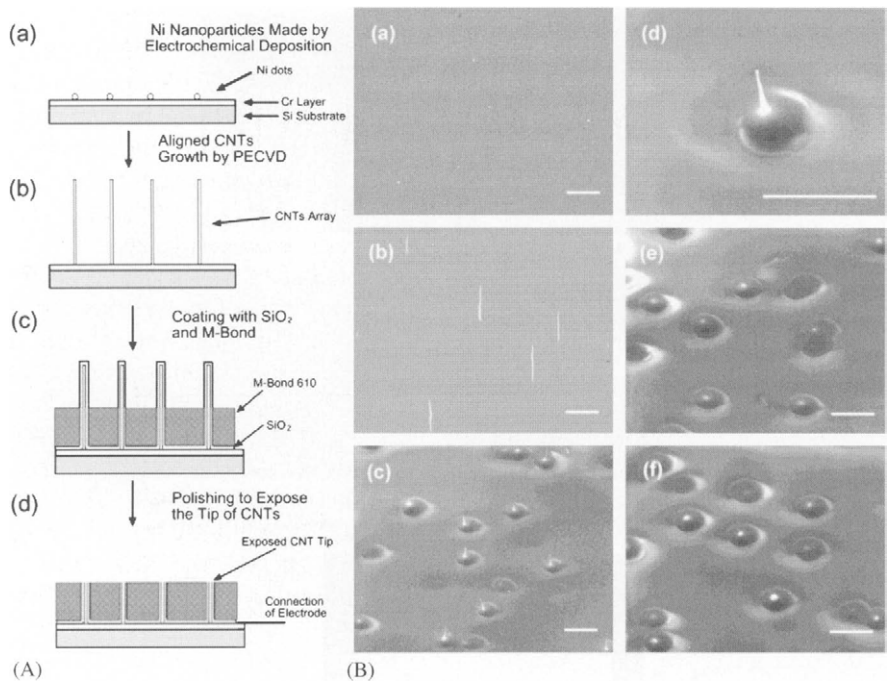


Figure 26. Fabrication scheme of the NEAs (A) and SEM images of the corresponding surface. (a) Top view; (b–f) from a 45° side view. All of the scale bars represent 5  $\mu\text{m}$ . (a) Electrodeposited Ni nanoparticles; (b) low site density aligned CNTs array; (c) CNTs array coated with SiO<sub>2</sub> and an epoxy layer, (d) close-up look at a single half-embedded CNT; (e) CNTs after polishing; and (f) second electrodeposition of Ni nanoparticles on the broken CNTs only. (Adapted from Tu et al. [105].)

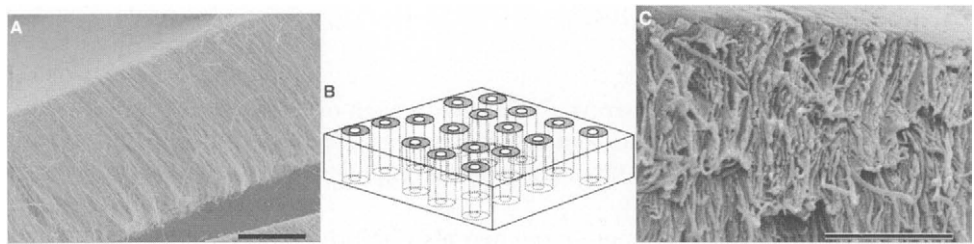


Figure 27. (A) An as-grown, dense, multi-walled CNT array produced. (scale bar, 50  $\mu\text{m}$ ). (B) Schematic of the target membrane structure. With a polymer embedded between the CNTs, a viable membrane structure can be readily produced, with the pore being the rigid inner-tube diameter of the CNT. (C) The cleaved edge of the CNT-PS membrane after exposure to H<sub>2</sub>O plasma oxidation. The PS matrix is slightly removed to contrast the alignment of the CNTs across the membrane (scale bar, 2.5  $\mu\text{m}$ ). (Adapted from Hinds et al. [106].)

## 6.2. Plasma activation

Radio frequency glow discharge plasma has been widely used for surface activation of various materials, ranging from organic polymers to inorganic ceramics and metals [107–109]. Dai and coworkers [110,111] have also developed a novel plasma approach for the chemical modification of aligned CNTs. For instance, they have successfully immobilized polysaccharide chains onto acetaldehyde-plasma-activated CNTs through the Schiff-base formation, followed by reductive stabilization of the Schiff-base linkage with sodium cyanoborohydride in water under mild conditions (Fig. 28).

Fig. 29a shows a typical SEM micrograph for the aligned CNTs. By plasma polymerization of acetaldehyde, a concentric layer of plasma polymer film was homogeneously deposited onto each of the constituent aligned CNTs (Fig. 29b). The SEM image for the plasma polymer-coated nanotubes given in Fig. 29b shows the similar features as the aligned nanotube array of Fig. 29a, but with a larger tubular diameter and smaller inter-tube distance due to the presence of the plasma coating. The TEM images of the constituent nanotube before and after the plasma treatment clearly shows the presence of a homogeneous plasma coating along the nanotube sidewall. The resulting amino-dextran grafted nanotubes showed very low advancing (ACA), sessile (SCA), and receding (RCA) air/water contact angles. For example, the ACA ( $155^\circ$ ), SCA ( $146^\circ$ ), and RCA ( $122^\circ$ ) for an untreated aligned carbon nanotube film were found to

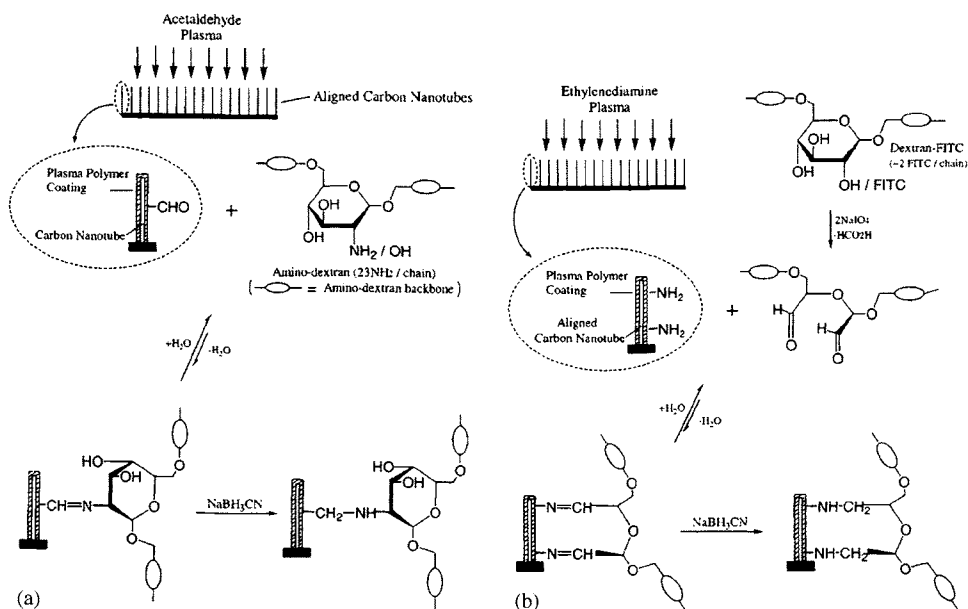


Figure 28. (a) Reaction scheme for the covalent immobilization of amino-dextran chains onto acetaldehyde-plasma activated CNTs. (b) Reaction scheme for the periodate oxidation of fluorescein isothiocyanate (FITC)-labeled dextran (designated as dextran-FITC), followed by covalent immobilization onto ethylenediamine-plasma activated CNTs. (Adapted from Chen et al. [110].)

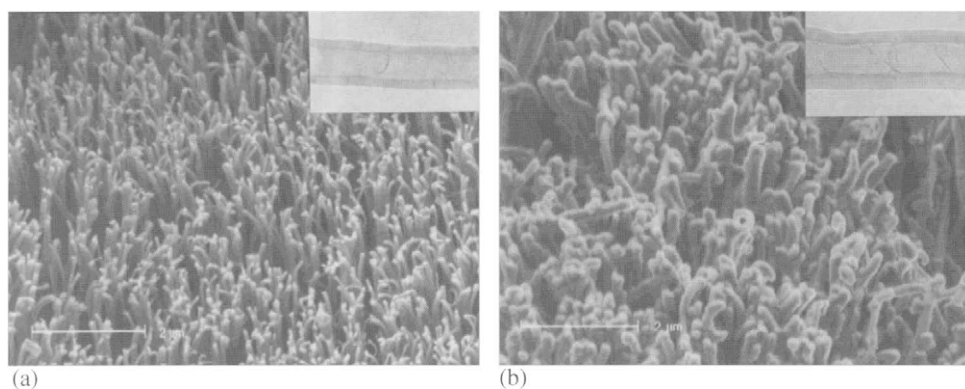


Figure 29. SEM micrographs of the aligned CNTs (a) before and (b) after the plasma polymerization of acetaldehyde. The insets show TEM images of an individual nanotube (a) before and (b) after being coated with a layer of the acetaldehyde-plasma-polymer. (Adapted from Chen et al. [110].)

be reduced to values of  $90^\circ$ ,  $78^\circ$ , and  $45^\circ$ , respectively, by the acetaldehyde plasma treatment. Subsequent immobilization of amino-dextran chains led to such a highly hydrophilic surface with a  $0^\circ$  air/water contact angles. The highly hydrated and biologically benign amino-dextran coating should facilitate the use of the aligned CNTs for many biologically related applications (e.g. as biosensors and artificial muscles) [112,113]. The glucose units within the surface grafted amino-dextran chains can be converted into dialdehyde moieties by periodate oxidation [114,115], thereby allowing for further chemical modification. Similarly, Khare et al. [116] have recently reported the treatment of SWNTs with cold hydrogen-plasma. In addition, plasma polymerization provides a facile and effective approach to uniformly coat aligned CNTs with different materials. Shi and coworkers [117] have successfully modified the aligned CNTs with a carbonfluorine thin coating.

### 6.3. Electrochemical polymerization

Electrochemical polymerization along the aligned CNTs is another interesting area for the synthesis of the coaxial aligned nanowires of polymers and CNTs. In this regard, Dai and coworkers [118] have used the aligned carbon nanotubes as nano-electrodes for making novel conducting coaxial nanowires by electrochemically depositing a concentric layer of an appropriate conducting polymer uniformly onto each of the aligned nanotubes to form the aligned conducting polymer-coated carbon nanotube coaxial nanowires (CP-NT). The SEM image for these CP-NT coaxial nanowires given in Fig. 30b shows the same features as the aligned nanotube array of Fig. 30a, but the former has a larger tubular diameter due to the presence of the newly-electropolymerized polypyrrole coating. Similarly, Ren and coworkers [119,120] have also reported the deposition of polypyrrole along the aligned CNTs. The coaxial structure allows the nanotube framework to provide mechanical stability and efficient



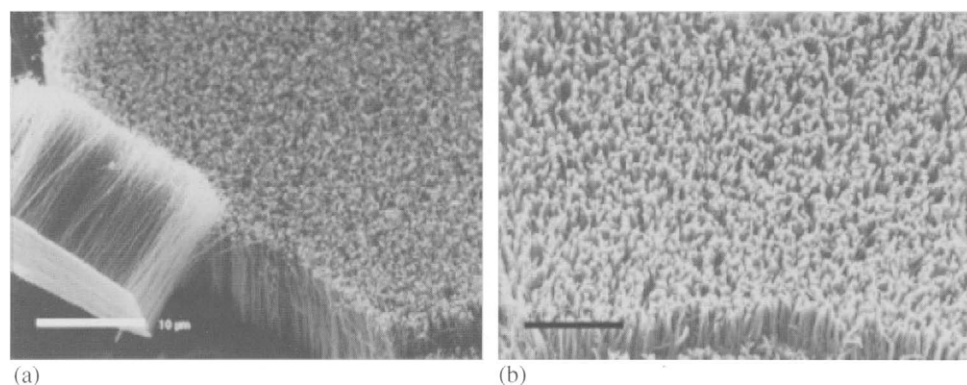


Figure 30. (a) Aligned nanotubes and (b) CP-NT coaxial nanowires — scale bar is 10  $\mu\text{m}$ . (Adapted from Gao et al. [118].)

thermal and electrical contact with the conducting polymer layer. The large interfacial surface area per unit mass obtained for the nanotube-supported conducting polymer layer is potentially useful in many optoelectronic applications, for example, in sensors, organic light-emitting diodes, and photovoltaic cells where the charge injection and separation are strongly limited by the interfacial area available in more conventional devices. In addition, the composite of aligned CNTs and polypyrrole offers an exciting combination of exceptional charge storage capacities and improved device response times relative to pure polypyrrole film [121].

#### 6.4. Chemical polymerization

Direct chemical polymerization of monomer onto the aligned CNTs is another approach to well-ordered polymer functionalized CNTs. Feng et al. [122] reported that aligned MWNT films can be used to fabricate ordered polyaniline-carbon nanotube composite films by in-situ polymerization of aniline, as shown in Fig. 31.

Similarly, Ajayan and coworkers [123] have also reported an approach to simultaneously control the nanotube alignment and the nanotube dispersion in polymer film by infiltrating monomer molecules into the pre-aligned arrays of nanotubes, followed by in-situ polymerization. The resulting composite films have a controllable distribution, dispersion, and alignment of nanotubes in a polymer matrix. The CNTs also provide reinforcement in the out-of-plane direction.

### 7. POTENTIAL APPLICATIONS OF THE MODIFIED CARBON NANOTUBES

#### 7.1. Chemical force sensors

CNTs have been demonstrated to be promising as AFM/STM tips because of their small size and high mechanical elasticity. Although these sharp nanotube tips offer advantages for high-resolution imaging, the unmodified nanotube tips, like most of

the commercial tips, do not provide information about the chemical nature of the surface. The use of functionalized CNTs as the scanning probe offers the possibility for chemically sensitive mapping at molecular resolution. For example, Lieber and coworkers [124] have introduced  $\text{-COOH}$  groups at the opened end of an SWNT tip by acid oxidation (Fig. 32). They then demonstrated the possibility to chemically attach an amine molecule,  $\text{RNH}_2$  (e.g. benzylamine) onto the terminal  $\text{-COOH}$  group through the amide-linkage.

To demonstrate the chemically sensitive force mapping, they first used a  $\text{-COOH}$  terminated SWNT AFM tip to image a micropatterned surface consisting of  $10\text{-}\mu\text{m}$  squares of a hexadecanethiol SAM (i.e.  $\text{CH}_3$  rich surface) surrounded by a 16-mercaptohexadecanoic acid SAM (i.e.  $\text{-COOH}$  rich surface). As shown in Fig. 33a, the tapping mode image recorded in ethanol shows a greater phase lag for tip- $\text{COOH}$ /sample- $\text{COOH}$  vs. tip- $\text{COOH}$ /sample- $\text{CH}_3$  regions due to the stronger adhesion force for the former. The corresponding image obtained with the benzylamine-modified SWNT AFM tip shows the patterned feature, but with the opposite

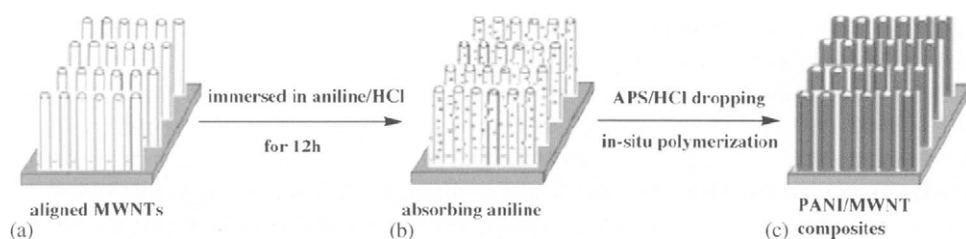


Figure 31. Preparation procedures of organizing PANI/MWNT films. (a) Aligned MWNT film grown on a quartz substrate. (b) Aligned MWNT film immersed into aniline/HCl solution at  $0\text{--}8\text{ }^{\circ}\text{C}$  for 12 h. (c) Polymerization takes place on the MWNT surface and forms an ordered PANI/MWNT NCT film. (Adapted from Feng et al. [122].)

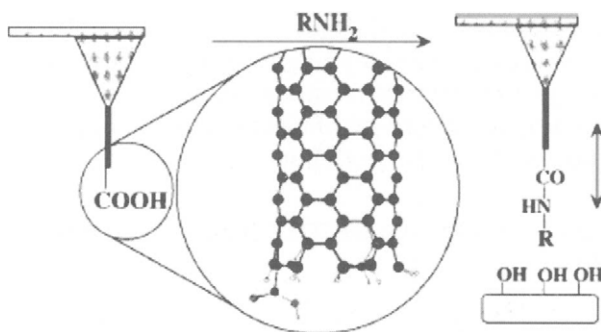


Figure 32. Modified CNTs as AFM tips. The replacement of the conventional AFM tip by the acid-oxidized carbon nanotube. (Adapted from Wong et al. [124].)

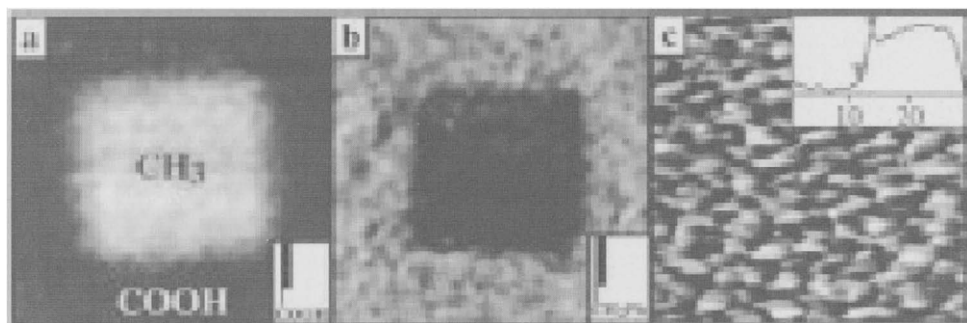


Figure 33. (a) Tapping mode phase image of a patterned sample in ethanol recorded with an unmodified SWNT tip ( $-\text{COOH}$ -terminated). (b) Analogous image of a patterned sample with a benzylamine-functionalized SWNT tip. Darker regions indicate greater phase lag; the contrast in (a) and (b) corresponds to phase variations of  $1.3^\circ$  and  $1.1^\circ$ , respectively. The images are  $16\text{ }\mu\text{m} \times 16\text{ }\mu\text{m}$ . (c) Tapping mode phase image recorded on a partial bilayer structure. The image is  $100\text{ nm} \times 100\text{ nm}$ . (inset) Variation of the phase vs. position along the line in (c); the numbers correspond to the distance in nanometers. Inverted triangles indicate the distance ( $3.3\text{ nm}$ ) separating adjacent chemically distinct regions. (Adapted from Wong et al. [124].)

phase contrast (Fig. 33b) as this particular tip interacts more strongly with the  $-\text{CH}_3$  rich surface in respect to the  $-\text{COOH}$  region. These results clearly demonstrate that chemically modified nanotube AFM tips can be used as sensing probes for chemically sensitive surface recognition.

Apart from the replacement of the conventional AFM tip by the acid-oxidized carbon nanotube, a wet chemical approach based on condensation reactions between  $-\text{NH}_2$  groups of a self-assembled monolayer, SAM, on the AFM tip and carboxylic groups on the oxidized SWNTs, has also been used to attach the SWNT probes onto an AFM tip (Fig. 34) [125].

## 7.2. Chemical and biological sensors

The high surface area, small size, hollow geometry, and chemical inertness are the remarkable properties of CNTs that make them attractive for demanding applications in the field of sensing. Many studies on possible applications of CNTs have been focused either on individual single-walled CNTs as sensitive materials toward  $\text{O}_2$ ,  $\text{NO}_2$ , and  $\text{NH}_3$  [126–129] or on MWNT mats as  $\text{NH}_3$ ,  $\text{CO}$ ,  $\text{CO}_2$  humidity, and  $\text{O}_2$  gas sensors [130–132]. Nanotube sensors offer significant advantages over conventional metal-oxide-based electrical sensor materials in terms of sensitivity and small sizes needed for miniaturization and construction of massive sensor arrays. Nevertheless, it also was found that nanotubes are not sensitive to many types of molecules (i.e.  $\text{CO}$ ,  $\text{H}_2$ ,  $\text{HCl}$ ), indicating an apparent lack of specific interactions between nanotube and these molecules. So, based on the valuable platform of carbon nanotubes, the functionalized CNTs with macromolecules or polymers offer further scope for improving the sensor performance.

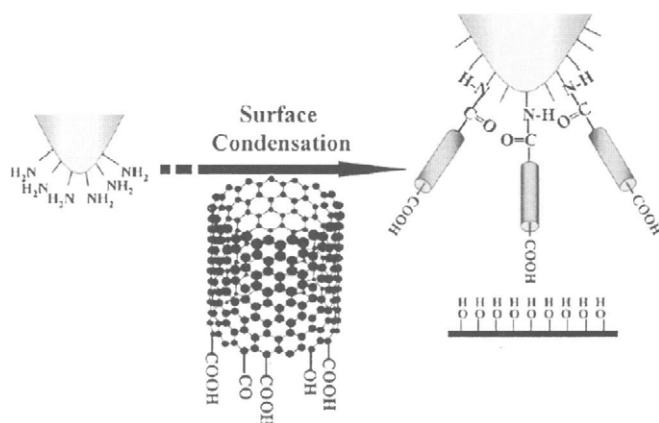


Figure 34. Schematic illustration of the preparation of SWNT AFM tips and measurement of force titration. (Adapted from Yang et al. [125].)

Polymer functionalization of CNTs has been demonstrated to impart high sensitivity and selectivity to the sensors. For example, polyethyleneimine (PEI) coating affords *n*-type SWNT devices capable of detecting  $\text{NO}_2$  at  $\leq 1$  ppm (parts-per-billion) concentrations while being insensitive to  $\text{NH}_3$  [129]. Coating Nafion (a polymeric perfluorinated sulfonic acid ionomer) on nanotubes blocks  $\text{NO}_2$  and allows for selective sensing of  $\text{NH}_3$  (Fig. 35). Multiplex functionalization of a nanotube sensor array is carried out by microspotting. Detection of molecules in a gas mixture is demonstrated with the multiplexed nanotube sensors [129].

The diagnosis and management of diabetes mellitus requires a tight monitoring of blood glucose levels. Electrochemical biosensors for glucose play a leading role in this direction. In this case, CNT-modified electrodes indicate great promise for the biosensing of glucose. In particular, the use of aligned CNTs provides a novel electrode platform for inherently conducting polymer-based biosensors. An example to highlight the usefulness of such a platform is the polypyrrole-based glucose oxidase system for the detection of glucose [133]. The use of these three-dimensional electrodes offers advantages in that large accessible enzyme loadings can be obtained within an ultrathin layer. It has also been found that the detection of  $\text{H}_2\text{O}_2$  at these new electrode structures containing iron loaded nanotube tips can be achieved at low anodic potentials. The result is a sensitive and selective glucose sensor. Recently, Lin and coworkers [134] developed glucose biosensors based on carbon nanotube (CNT) nanoelectrode ensembles (NEEs) for the selective detection of glucose. Glucose oxidase was covalently immobilized on CNT NEEs via carbodiimide chemistry by forming amide linkages between their amine residues and carboxylic acid groups on the CNT tips. The catalytic reduction of hydrogen peroxide liberated from the enzymatic reaction of glucose oxidase upon the glucose and oxygen on CNT NEEs leads to the selective detection of glucose. The biosensor effectively performs a selective electrochemical analysis of glucose in the presence of common interferents (e.g. acetaminophen, uric and

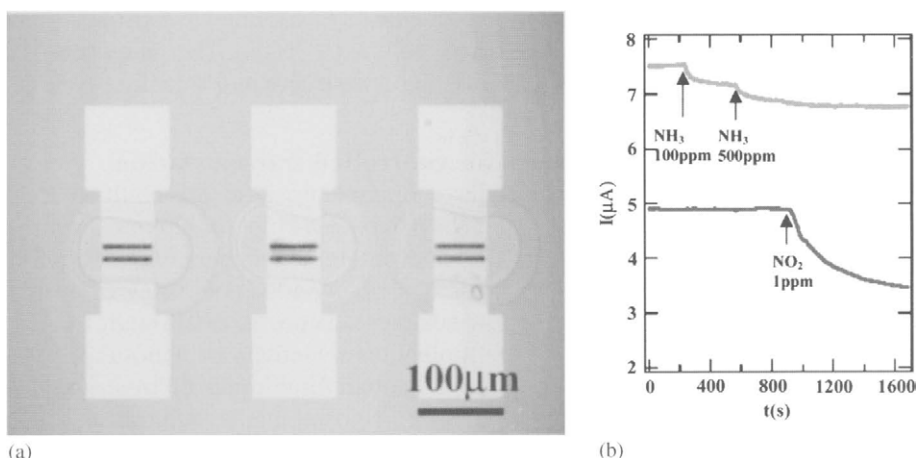


Figure 35. (a) Optical image showing three multiple tube devices after microspotting with droplets of polymer solutions. (b) Red (top) curve: a device coated with Nafion exhibits response to 100 and 500 ppm of  $\text{NH}_3$  in air, and no response when 1 ppm of  $\text{NO}_2$  was introduced to the environment. Blue (bottom) curve: a PEI-coated device exhibiting no response to 100 and 500 ppm of  $\text{NH}_3$  and large conductance decrease to 1 ppm of  $\text{NO}_2$ . (Adapted from Qi et al. [129].)

ascorbic acids), avoiding the generation of an overlapping signal from such interferers. Such an operation eliminates the need for permselective membrane barriers or artificial electron mediators, thus greatly simplifying the sensor design and fabrication. The low-potential ( $-0.2$  V vs. SCE) reductive detection of the hydrogen peroxide product led to highly selective amperometric monitoring of the glucose substrate, along with linearity up to 30 mM glucose and a detection limit of 0.08 mM. Willner's group [135] demonstrated that aligned reconstituted GOx on the edge of SWCNT can be linked to an electrode surface. The electrons were transported along distances higher than 150 nm with the length of the SWCNT controlling the rate of electron transport. Such enzyme reconstitution on the end of CNT represents an extremely efficient approach for 'plugging' an electrode into GOx.

DNA biosensors, based on nucleic acid recognition processes, are rapidly being developed toward the goal of rapid, simple, and inexpensive testing of genetic and infectious diseases. The performance of such devices can greatly benefit from the use of CNT. Such improvements are attributed to enhanced detection of the target guanine or of the product of an enzyme label, as well as to the use of CNT carrier platforms. Highly sensitive bioelectronic protocols for detecting of proteins and DNA have been described recently based on the coupling of several CNT-derived amplification processes [136].

On the other hand, the use of aligned CNTs provides additional advantages for a maximized access of the nanotube electrode surface and an efficient device construction. Dai and coworkers [137] report a simple, but effective, method for preparing

aligned carbon nanotube–DNA sensors by chemically coupling DNA probes on both the tip and wall of *plasma-activated* aligned CNTs. The nanotube–DNA electrochemical sensors thus produced are highly sensitive and selective even in the absence of any electron mediator.

### 7.3. Carbon nanotube membranes for controlled transportation

Novel microfabrication techniques have opened up new possibilities for the development of small-scale devices, such as a ‘lab-on-a-chip’ for chemical synthesis and analysis [138–140]. Fluid flow in such micrometer-level channels has been relatively well studied [141]. At even smaller scales, open-ended nanotubes offer unique possibilities as conduits for flow of low-surface-tension fluids through their rigid cylindrical pores [142]. To enhance the molecular selectivity of nanotubes beyond steric effects, their surface can be modified through functionalized treatment [143]. Applications of nanotubes or nanopores in (bio)molecule separation devices [144–146], in biocatalysis [146], in molecule detection [147], as encapsulation media for storage and delivery [148,149], and as pores for selective and rapid gas flow [150] have been either proposed or already demonstrated.

An aligned array of CNTs impregnated in a polystyrene matrix can form a membrane structure with well-ordered, nanometer-scale pores by the spin-on process [106]. This membrane structure is suitable for the gas flow and ionic transport studies. The open tips of the CNTs in this membrane terminate in carboxylates that can be easily derivatized with a molecule that binds to a bulky receptor, which subsequently can be used to open/close the pore entrance. Recently, Hinds and coworkers have achieved the reversible Biochemical Switching of Ionic Transport by end functionalization of carbon nanotube films [151]. They switched on the functionalized nanopore membranes between handoff states reversibly by attaching and releasing the receptor in a controlled fashion (i.e. receptor-stimulated switching). They have used a desthiobiotin derivative that binds reversibly to streptavidin to modify the entrance of the through pores of membrane-embedded CNTs, thereby enabling a reversible on/off system (Fig. 36). Transport through the nanotube pores is switched off when streptavidin binds to the functionalized membrane and turned on when streptavidin is released (Fig. 37). Similar results were also reported in Ref. [152].

Martin et al. [153] developed a method which entailed coating the inside walls of the CNTs within the carbon nanotube membrane (CNM) with redox-active polymer films. The redox polymer, poly(vinylferrocene), can be reversibly electrochemically switched between an electrical neutral and a polycationic form. This provides a way for controlling both the magnitude and the sign of the surface charge on the nanotube walls, which in turn allows for control of both the rate and direction of Electroosmotic flow (EOF) through the CNM.

### 7.4. Changes of the p- and n-type semiconducting states by surface modification

CNTs are known to be susceptible to oxygen adsorption [127]. A layer of oxygen molecules often adsorb on the SWNT surface in air. Due to the strong electron affinity of O<sub>2</sub> molecules, CNTs often exhibit p-type characters in air with holes as main charge carriers. When SWNTs are wrapped by amine-rich polymer (e.g. PEIs),

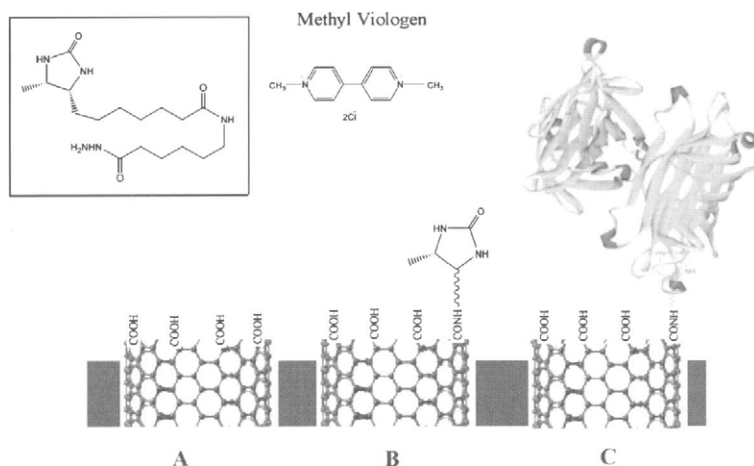


Figure 36. Schematic demonstrating the binding of streptavidin to DSB-functionalized tips of CNTs at the surface of the CNT-polystyrene composite membrane. (A) Open tips of CNT with carboxylic end groups, (B) DSB-X biotin hydrazide functionalized tip of CNT, and (C) streptavidin bound to the functionalized membrane. The structures of DSB-X biotin hydrazide and methyl viologen are shown in an inset. (Adapted from Nednoor et al. [151].)

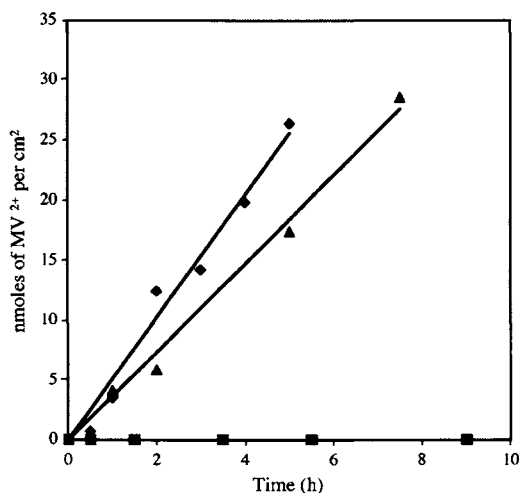


Figure 37. Flux data of methyl viologen (MV<sup>2+</sup>) through the pores of CNT membrane. (◆) DSB-functionalized CNT membrane, (■) streptavidin bound to DSB-CNT membrane, and (▲) after biotin incubation, to release streptavidin from the CNT pore entrance. (Adapted from Nednoor et al. [151].)

however, the nanotube can change into an *n*-type semiconductor with electrons as main carriers [154]. As shown by the  $I$ - $V_g$  curves given in Fig. 38a, a single pure SWNT field-effect transistor, FET, reveals that a positive  $V_g$  shifts the Fermi energy level away from the valence band and deplete hole carriers in the system. After the PEI absorption (Fig. 38b), however, the SWNT FET exhibits a clear *n*-type behavior; the conductance of the device increases as  $V_g$  moves to more positive value.

### 7.5. Enhanced carbon nanotube fluorescence by grafting with polymer chains

As mentioned above, fluorescence emission has been observed for individual SWNTs. Grafting shortened SWNTs with polymer chains, such as poly(propionylethylenimine-*co*-ethylenimine), PPEI-EI, and poly(vinyl acetate-*co*-vinyl alcohol), PVA-VA, via amide and ester linkage, respectively, was also found to enhance the fluorescence emission from the soluble component (Fig. 39). The fluorescence spectra and quantum yields depend on the excitation wavelength in a progressive fashion. The same order of magnitude in the luminescence yield was observed for both SWNTs and MWNTs [34]. Two possible emission mechanisms have been suggested for the luminescence of the functionalized nanotube. One of them takes account of the trapping of excitation energy at defect sites as similar as the emission of the semiconductor particle. The other attributes the emission to the extended electronic structure of the shortened nanotube that is isolated as a result of nanotube surface functionalization.

### 7.6. Optoelectronic devices

The combination of CNTs with polymers offers an attractive route not only to reinforce polymer films but also to introduce new electronic properties based on

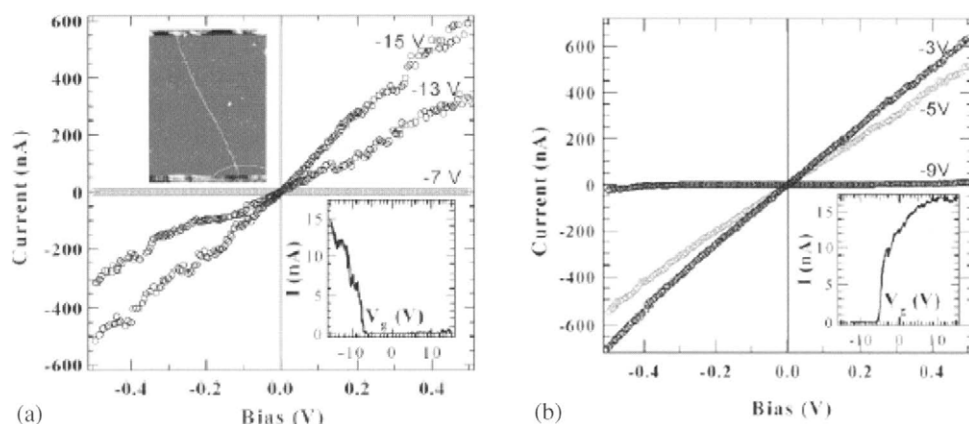


Figure 38. Current vs. voltage characteristic of SWNTs before (a) and after (b) PEI functionalization. The lower right insets are the corresponding current vs. gate voltage plots measured at 10 mV bias. The upper left inset in part (a) is an AFM image ( $2 \times 3 \mu\text{m}$ ) of the actual SWNT device. (Adapted from Shim et al. [154].)



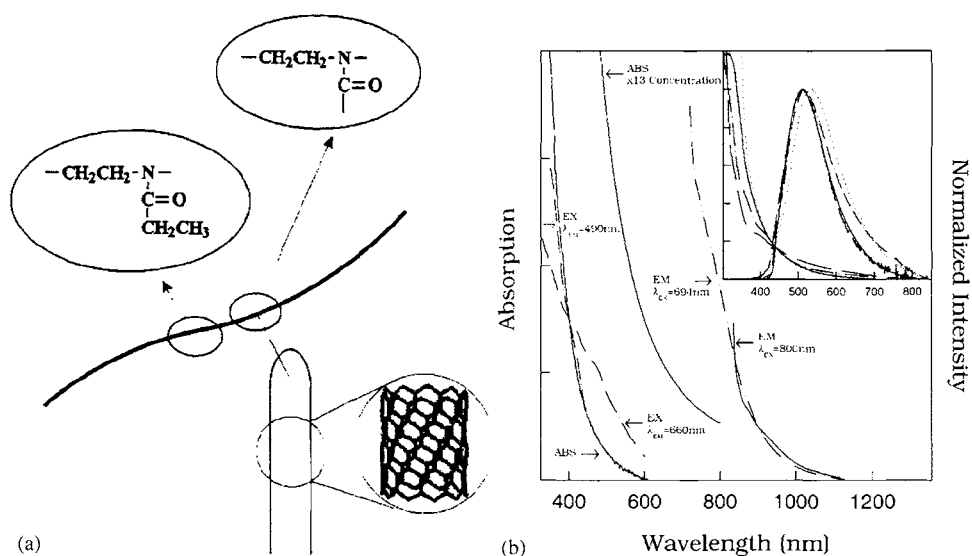


Figure 39. (a) A cartoon illustration of the PPEI-EI polymer-bound carbon nanotube. (b) Absorption (ABS), luminescence (EM) and luminescence excitation (EX) spectra of the PPEI-EI polymer-bound S-MWNT in room temperature chloroform. Inset: A comparison of absorption and luminescence (440 nm excitation) spectra of s-MWNT-PPEI-EI (-), S-MWNT-PVA-VA (...), s-SWNT-PPEI-EI (-.-.) and SWNT-PPEI-EI (- - -) in homogeneous chloroform solution at room temperature. (Adapted from Riggs et al. [34].)

morphological modification or electronic interaction between the two components. In particular, the combination of CNTs with  $\pi$ -conjugated polymers is of interest because their  $\pi$ -conjugation enables the polymers to be used as an active material for light-emitting diodes (LEDs) [155], field-effect transistors (FETs) [156] and photovoltaic devices [157].

In 1998, Curran and coworkers [158] incorporated CNTs into poly(*m*-phenylenevinylene-*co*-2,5-dioctoxy-*p*-phenylenevinylene) and found an increase in conductivity by a factor of  $10^8$  for such low concentrations of nanotubes. A LED device was fabricated and electroluminescence was observed (Fig. 40), which uncovered a new application field of CNTs.

The power of nanotubes as field emitters has been apparent from their inception, [159–165] since they show very low turn-on fields and high current densities. Recently, Star et al. [166] have combined carbon nanotube field effect transistor devices with a photosensitive polymer, poly{(*m*-phenylenevinylene)-*co*-[(2,5-dioctyloxy-*p*-phenylene)vinylene]} (PmPV), to fabricate an optoelectronic memory device. Electric charges are created upon optical illumination by the polymer nanotube element of the structure, and charge storage occurs in the nanotube transducer. The read and erase functions are performed by a voltage applied across the

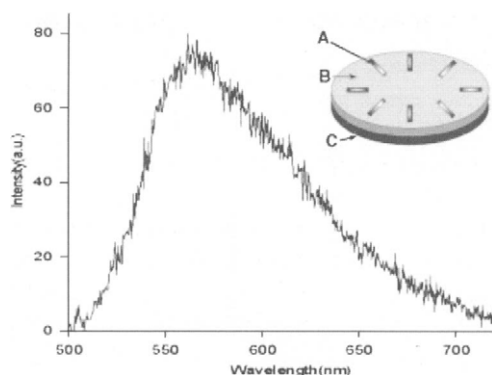


Figure 40. Electroluminescence spectrum taken from the composite LED. The inset shows a typical LED constructed from the composite and tested in air: (A), aluminum top contact; (B), PmPV/nanotube composite; (C), indium tin oxide bottom contact. (Adapted from Curram et al. [158].)

nanotube channel. Spectral response of the device is adjusted by utilizing different polymers with different absorption characteristics.

Kymakis and Amaratunga [167] have demonstrated a photovoltaic device based on SWNTs and a conjugated polymer, poly(3-octylthiophene) (P3OT). SWNTs doping was found to dramatically improve the photovoltaic performance of P3OT devices revealing a photocurrent larger than two orders of magnitude compared to that of the pristine diodes, and a doubling of the open-circuit voltage. The results show that the conjugated polymer-SWNTs composite represents an alternative class of organic semiconducting material that can be used to manufacture organic photovoltaic cells with improved performance.

Despite of the well known fact that CNTs possess unusual optoelectronic properties, the recent report on ignition of some dry and fluffy SWNTs in air by the camera flashlight is rather intriguing [168]. In view of the highly efficient absorption of light by CNTs, the observed ignition may be resulted from a rapid temperature increase within the nanotube sample upon exposure to the camera flashlight (it was estimated to be up to at least 1500 °C in a very short time), which is well above the temperature required for ignition when oxygen is present. While the mechanism of ignition by camera flashlight in this system deserves further investigation, such an interesting photochemical reaction may find its application in the remote light triggering combustion or explosive [168].

Closely related to the above discussion, band gap fluorescence emission from individual SWNTs has also been observed. For instance, O'Connell et al. [169] obtained individual nanotubes through ultrasonication of an aqueous dispersion of raw SWNTs in sodium dodecyl sulfate, followed by centrifuging to remove tube bundles, ropes, and residual catalyst. They found that individual semiconducting CNTs could show fluorescence emission directly across the band gap whereas aggregation of nanotubes into bundles quenches the fluorescence through interactions with

metallic tubes and substantially broaden the absorption spectra. More recently, incandescent light emission has also been observed from certain CNTs upon the application of a DC voltage [170]. Continued research efforts in this embryonic field could give birth to a flourishing area of nanotube optoelectronic technologies.

### 7.7. Fluorinated carbon nanotubes as cathodes in lithium electrochemical cells

Similar to carbon monofluoride ( $\text{CF}_x$ ), fluorinated nanotubes could also be used as cathodes in lithium electrochemical cells, [171] as schematically shown in Fig. 41.

Comparing with carbon monofluoride cells, the fluorotube cell shows a higher voltage ( $\sim 0.7$  V higher) and discharge curves with a steeper slope (Fig. 42). Smaller nanotubes in diameter show a higher potential due to their larger surface area. During the discharge, the cell potential drops more rapidly for the fluorotube cell than carbon monofluoride cell due to the difference in their carbon-fluorine bond energies.

### 7.8. Carbon nanotubes used for multifunctional nanocomposites

CNTs are unique nanostructured materials with remarkable physical and mechanical properties [172–175]. These properties have inspired interest in using CNTs as a filler in polymer composite systems to obtain ultra-light structural materials with enhanced electrical, thermal, and optical characteristics [176,177]. The prospect of obtaining advanced nanocomposites with multifunctional features, e.g. materials used for structures and electrical conductors, has attracted the efforts of researchers in both academia and industry [178, 179]. Industry in particular recognizes many potential applications such as electrostatically dissipative materials and aerospace structural materials [178–182].

One of the outstanding features of the composite of polymers and carbon nanotubes is that the mechanical properties can be greatly improved. For example, Safadi et al. [183] found that at  $\leq 1$  vol% of nanotubes, there is a 40% increase in strength of PS/MWNT film composites. The modulus improves by a factor of 2 with respect to the neat polymer when 2.49 vol% of CNTs are added. Alignment of CNTs in a PP matrix resulted in higher tensile strength but had no effect on the modulus [184].

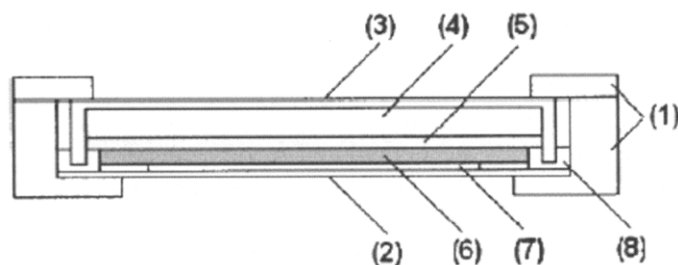


Figure 41. Schematic illustration of a lithium/fluorotube electrochemical cell. (1) Teflon holder, (2) stainless steel (anode), (4) lithium foil, (5) porous polyethylene membrane soaked with electrolyte, (6) fluorotubes, (7) Ti current collector, (8) rubber separator. (Adapted from Peng et al. [171].)

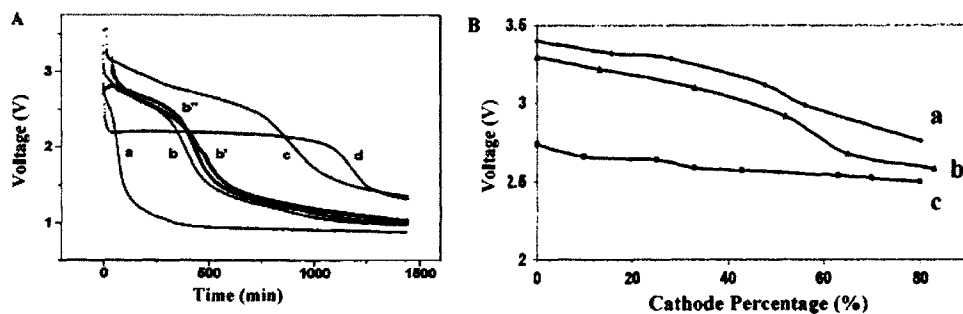


Figure 42. Discharging curves of fluorotubes (L-SWNTs) and carbon monofluoride electrochemical cell. (A) Trace a: discharging curve of 6 mg fluorotube cell at 2 k $\Omega$ ; Trace b: discharging curve of 20 mg fluorotube cell at 2 k $\Omega$ ; Trace b': discharging curve of 20 mg fluorotubes cell at 2 k $\Omega$ ; Trace c: discharging curve of 40 mg fluorotube cell at 2 k $\Omega$ ; Trace d: discharging curve of 20 mg CFx cell at 2 k $\Omega$ . In traces a, b and c, fluorotubes were mixed with same amount of graphite as cathodes; in trace b', only fluorotubes were used; in traces b' and d, fluorotube and CFx were mixed with the same amount of SWNTs. (B) Trace a: open circuit voltage of fluorinated L-SWNTs vs. cathode percentage; Trace b: open circuit voltage of fluorinated H-SWNTs vs. cathode percentage; Trace c: open circuit voltage of CFx vs. cathode percentage. (Adapted from Peng et al. [171].)

The excellent electrical and thermal properties of nanotubes are particularly important in nanocomposites. Conductivity can be obtained in a CNT/polymer composite at extremely low CNT contents because of the large CNT aspect ratio. These composites exhibit percolation-type behavior [185–189]. The CNTs make conjugated polymers mechanically stronger, more conductive and less susceptible to thermal degradation [190]. Composite materials based on CNTs in PmPV exhibited nearly an eightfold increase in electrical conductivity compared to the neat polymer, without impairing the photo- and electro-luminescence properties of the polymer [69].

CNT/epoxy composites show increases in thermal conductivity,  $K$ , of 110%–120% when 1% of SWNTs [192,193]. The coefficient of thermal expansion in the longitudinal direction of flow (CTE) is significantly reduced when the nanocomposite is injection molded [194]. CTE reduction enables reduced cure shrinkage and hygrothermal instability in these systems, resulting in better dimensional stability of the material [178]. The nanotubes delay the onset of thermal degradation of the polymer—for example, PMMA [195] or PVOH [196,197]. Thermal stability may be affected by the presence of the nanotubes, which interfere with the mobility and crystallization of the polymer chains, and enable the composite to be used for high temperature applications [198].

## 8. CONCLUSIONS

Different applications of CNTs require varied, tailored modifications to improve nanotube processability, accessibility, and performance. Thus, different functionalization methods are developed to meet different requirements. Covalent chemical functionalization of nanotubes provides a remarkable and powerful potential to tune the surface properties of CNTs. Compared with covalently modified nanotubes, one of main advantages of non-covalently functionalized nanotubes with macromolecules is to conserve the nanotube electronic structures by preventing rupture of nanotube  $sp^2$  conjugated structure. On the other hand, aligned CNTs modified with active reagents provide unique advantages for some special applications (e.g. electrochemical sensor) compared with non-aligned CNTs.

Recently, some interesting reactions have also been devised for chemical modification of both the inner and outer nanotube walls, each of the ends of one nanotube with different chemical group. Judicious application of these site-selective reactions to non-aligned and aligned CNTs has open up the rich field of carbon nanotube chemistry. Due to the fascinating properties of CNTs and the recent achievement of functionalizing the CNTs, some important and possible applications, such as multi-functional nanocomposite, chemical and biological sensor, optoelectronic devices, have attracted academic and industrial interest. Great breakthrough is being expected in the near future.

**Acknowledgments:** We are grateful for the financial support from the American Chemical Society (ACS-PRF 39060-AC5M), National Science Foundation (NSF-CCF-0403130), AFOSR, and the Materials and Manufacturing Directorate of the Air Force Research Laboratory, The Dayton Development Coalition, and Wright Brothers Institute.

## REFERENCES

1. H. W. Kroto, J. R. Heath, S. C. O'Brien, R. F. Curl and R. E. Smalley, *Nature* **318** (1985) 162.
2. S. Iijima, *Nature* **354** (1991) 56.
3. H. Dai, E. W. Wong and C. M. Lieber, *Science* **272** (1996) 523.
4. T. W. Ebbesen, *Annu. Rev. Mater. Sci.* **24** (1994) 235.
5. T. W. Ebbesen, H. J. Lezec, H. Hiura, J. W. Bennett, H. F. Ghaemi and T. Thio, *Nature* **382** (1996) 54.
6. L. Dai, *Intelligent Macromolecules for Smart Devices*, Springer, Berlin, 2004.
7. J. P. Salvetat, J. M. Bonard, N. H. Thomson, A. J. Kulik, L. Forro, W. Benoit and L. Zuppiroli, *Appl. Phys. A: Mater. Sci. Process* **69** (1999) 255.
8. P. Calvert, *Nature* **399** (1999) 210.
9. R. J. Chen, Y. Zhang, D. Wang and H. Dai, *J. Am. Chem. Soc.* **123** (2001) 3838.
10. P. M. Ajayan, T. Ichihashi and S. Iijima, *Chem. Phys. Lett.* **202** (1993) 384.
11. Z. J. Niu, Z. Y. Yuan, W. Zhou, L. M. Peng and Z. Xu, *Phys. Chem. Chem. Phys.* **3** (2001) 2518.

12. S. C. Tsang, Y. K. Chen, P. J. F. Harris and M. L. H. Green, *Nature* **372** (1994) 159.
13. A. C. Dillon, T. Gennett, K. M. Johns, J. L. Alleman, P. A. Parilla and M. J. Heben, *Adv. Mater.* **11** (1999) 1354.
14. E. Dujardin, T. W. Ebbesen, A. Krishnan and M. M. Treacy, *Adv. Mater.* **10** (1998) 611.
15. S. Nagasawa, M. Yudasaka, K. Hirahara, T. Ichihashi and S. Iijima, *Chem. Phys. Lett.* **328** (2000) 374.
16. R. Yu, L. Chen, Q. Liu, J. Lin, K.-L. Tan, S. C. Ng, A. S. O. Chan, G.-Q. Xu and T. S. A. Hor, *Chem. Mater.* **10** (1998) 718.
17. S. Delpeux, K. Metenier, R. Benoit, F. Vivet, L. Boufendi, S. Bonnamy and F. Begui, *AIP Conf. Proc.* **486** (1999) 470.
18. X. Li, Z. Yang, Z. Chen, H. Wang, N. Sheng and J. Li, *Xinxing Tan Cailiao* **14** (1999) 32.
19. Z. H. Yang and H. Q. Wu, *Gaodeng Xuexiao Huaxue Xuebao* **22** (2001) 446.
21. H. Hiura, T. W. Ebbesen and K. Tanigaki, *Adv. Mater.* **7** (1995) 275.
21. A. Hirsh, *Angew. Chem. Int. Ed.* **41** (2002) 1853.
22. P. J. F. Harris and M. L. H. Green, *Nature* **362** (1993) 520.
23. A. Koshio, M. Yudasaka and S. Iijima, *Chem. Phys. Lett.* **341** (2001) 461.
24. Z. Yu and L. E. Brus, *J. Phys. Chem. A* **104** (2000) 10995.
25. A. Kuznetsova, A. Popova, J. T. Yates Jr., M. J. Bronikowski, C. B. Huffman, J. Liu, R. E. Smalley, H. H. Hwu and J. G. Chen, *J. Am. Chem. Soc.* **123** (2001) 10699.
26. L. Vaccarini, C. Goze, R. Aznar, V. Micholet, C. Journet and P. Bernier, *Synth. Met.* **103** (1999) 2492.
27. L. P. Biro, N. Q. Khanh, Z. Vertesy, Z. E. Horvath, Z. Osvath, A. Koos, J. Gyulai, A. Kocsonya, Z. konya, X. B. Zhang, G. Van Tendeloo, A. Fonseca and J. B. Nagy, *Mater. Sci. Eng. C: Biomi. Supramol. Sys.* **C19** (2002) 9.
28. Y. P. Sun, K. F. Fu, Y. Lin and W. J. Huang, *Acc. Chem. Res.* **35** (2002) 1096.
29. Y. Sun, S. R. Wilson, S. MacMahon and D. I. Schuster, *Proc. Electrochem. Soc.* **2000** (2000) 282.
30. J. Chen, M. A. Hamon, H. Hu, Y. Chen, A. M. Rao, P. C. Eklund and R. C. Haddon, *Science* **282** (1998) 95.
31. M. A. Amon, J. Chen, H. Hu, Y. Chen, M. E. Itkis, A. M. Rao, P. C. Eklund and R. C. Haddon, *Adv. Mater.* **11** (1999) 834.
32. S. Niyogi, H. Hu, M. A. Hamon, P. Bhomik, B. Zhao, S. M. Rozenzhak, J. Chen, M. E. Itkis, M. S. Meier and R. C. Haddon, *J. Am. Chem. Soc.* **123** (2001) 733.
33. R. Czerw, Z. Guo, P. M. Ajayan, Y.-P. Sun and D. L. Carroll, *Nano Lett.* **1** (2001) 423.
34. J. E. Riggs, Z. Guo, D. L. Carroll and Y. P. Sun, *J. Am. Chem. Soc.* **122** (2000) 5879.
35. J. E. Riggs, D. B. Walker, D. L. Carroll and Y. P. Sun, *J. Phys. Chem. B* **104** (2000) 7071.
36. J. Chen, A. M. Rao, S. Lyuksyutov, M. E. Itkis, M. A. Hamon, H. Hu, R. W. Cohn, P. C. Eklund, D. T. Colbert, R. E. Smalley and R. C. Haddon, *J. Phys. Chem. B* **105** (2001) 2525.
37. M. A. Hamon, H. Hui, P. Bhowmik, H. M. E. Itkis and R. C. Haddon, *Appl. Phys. A: Mater. Sci. Pro.* **74** (2002) 333.

38. M. Sano, A. Kamino and S. Shinkai, *Angew. Chem. Int. Ed.* **40** (2001) 4661.
39. Y. P. Sun, W. Huang, Y. Lin, K. Fu, A. Kitaygorodskiy, L. A. Riddle, Y. J. Yu and D. L. Carroll, *Chem. Mater.* **13** (2001) 2864.
40. K. Fu, W. Huang, Y. Lin, L. A. Riddle, D. L. Carroll and Y. P. Sun, *Nano Lett.* **1** (2001) 439.
41. M. Sano, A. Kamino, J. Okamura and S. Shinkai, *Science* **293** (2001) 1299.
42. P. W. Chiu, G. S. Duesberg, U. Dettlaff-Weglikowska and S. Roth, *Appl. Phys. Lett.* **80** (2002) 3811.
43. N. Chopra, M. Majumder and B. J. Hinds, *Adv. Funct. Mater.* **15** (2005) 858.
44. K. Lee, L. Li and L. Dai, *J. Am. Chem. Soc.* **127** (2005) 4122.
45. M. Holzinger, O. Vostrowsky, A. Hirsch, F. Hennrich, M. Kappes, R. Weiss and F. Jellen, *Angew. Chem. Int. Ed.* **40** (2001) 4002.
46. T. Nakajima, S. Kasamatsu and Y. Matsuo, *Eur. J. Inorg. Chem.* **33** (1997) 831.
47. E. T. Mickelson, C. B. Huffman, A. G. Rinzier, R. E. Smalley, R. H. Hauge and J. L. Margrave, *Chem. Phys. Lett.* **296** (1998) 88.
48. P. J. Boul, J. Liu, E. T. Mickelson, C. B. Huffman, L. M. Ericson, I. W. Chiang, K. A. Smith, D. T. Colbert, R. H. Hauge, J. L. Margrave and R. E. Smalley, *Chem. Phys. Lett.* **310** (1999) 367.
49. T. Hayashi, M. Terrones, C. Scheu, Y. A. Kim, M. Ruehle, T. Nakajima and M. Endo, *Nano Lett.* **2** (2002) 491.
50. W. Zhao, C. Song, B. Zheng, J. Liu and T. Viswanathan, *J. Phys. Chem. B* **106** (2002) 293.
51. E. T. Mickelson, I. W. Chiang, J. L. Zimmerman, P. J. Boul, J. Lozano, J. Liu, R. E. Smalley, R. H. Hauge and J. L. Margrave, *J. Phys. Chem. B* **103** (1999) 4318.
52. N. F. Yudanov, A. V. Okotrub, Y. V. Shubin, L. I. Yudanov, L. G. Bulusheva, A. L. Chuvilin and J. M. Bonard, *Chem. Mater.* **14** (2002) 1472.
53. W. H. Lee, S. J. Kim, W. J. Lee, J. G. Lee, R. C. Haddon and P. J. Reucroft, *Appl. Surf. Sci.* **181** (2001) 121.
54. Y. Chen, R. C. Haddon, S. Fang, A. M. Rao, P. C. Eklund, W. H. Lee, E. C. Dickey, E. A. Grulke, J. C. Pendergrass, A. Chavan, B. E. Haley and R. E. Smalley, *J. Mater. Res.* **13** (1998) 2423.
55. V. Georgakilas, K. Kordatos, M. Proto, D. M. Guldi, M. Holzinger and A. Hirsh, *J. Am. Chem. Soc.* **124** (2002) 760.
56. G. Viswanathan, N. Chakrapani, H. Yang, B. Wei, H. Chung, K. Cho, C. Y. Ryu and P. M. Ajayan, *J. Am. Chem. Soc.* **125** (2003) 9258.
57. S. Qin, D. Qin, W. T. Ford, D. E. Resasco and J. E. Herrera, *J. Am. Chem. Soc.* **126** (2004) 170.
58. Y. Sun, S. R. Wilson and D. I. Schuster, *J. Am. Chem. Soc.* **123** (2001) 5348.
59. J. L. Bahr, J. Yang, D. V. Kosynkin, M. L. Bronikowski, R. E. Smalley and J. M. Tour, *J. Am. Chem. Soc.* **123** (2001) 6536.
60. T. Kyotani, S. Nakazaki, W. H. Xu and A. Tomita, *Carbon* **39** (2001) 782.
61. T. Kyotani, L.-F. Tsai and A. Tomita, *Chem. Mater.* **8** (1996) 2109.
62. W. J. Li, S. S. Xie, L. X. Qian, B. H. Chang, B. S. Zou, W. Y. Zhou, R. A. Zhao and G. Wang, *Science* **274** (1996) 1701.

63. T. Kyotani, T. Nagai, S. Inoue and A. Tomita, *Chem. Mater.* **9** (1997) 609.
64. T. Kyotani, L. F. Tsai and A. Tomita, *Chem. Commun.* **7** (1997) 701.
65. R. Parthasarathy, K. L. M. Phani and C. R. Martin, *Adv. Mater.* **7** (1995) 896.
66. J. L. Bahr and J. M. Tour, *J. Mater. Chem.* **12** (2002) 1952.
67. S. Niyogi, M. A. Hamon, H. Hu, B. Zhao, P. Bhowmik, R. Sen, M. E. Itkis and R. C. Haddon, *Acc. Chem. Res.* **35** (2002) 1105.
68. M. J. O'Connell, P. Boul, L. M. Ericson, C. Huffman, Y. Wang, E. Haroz, C. Kuper, J. Tour, K. D. Ausman and R. E. Smalley, *Chem. Phys. Lett.* **342** (2001) 265.
69. A. Star, J. F. Stoddart, D. Steuerman, M. Diehl, A. Boukai, E. W. Wong, X. Yang, S.-W. Chung, H. Choi and J. R. Heath, *Angew. Chem. Int. Ed.* **40** (2001) 1721.
70. H. Xu and B. Z. Tang, *Polym. Mater. Sci. Eng.* **80** (1999) 408.
71. K. E. Drexler, *Nanosystems: Molecular Machinery, Manufacturing, and Computation*, Wiley, New York, 1992.
72. K. Tanaka and F. Toda, *Chem. Rev.* **100** (2000) 1025.
73. M. T. Martinez, M. A. Callejas, A. M. Benito, W. K. Maser, M. Cochet, J. M. Andres, J. Schreiber, O. Chauvet and J. L. G. Fierro, *Chem. Commun.* **9** (2002) 1000.
74. M. Yudasaka, M. Zhang, C. Jabs and S. Iijima, *Appl. Phys. A: Mater. Sci. & Proc.* **71** (2000) 449.
75. A. Koshio, M. Yudasaka, M. Zhang and S. Iijima, *Nano Lett.* **1** (2001) 361.
76. M. Zhang, M. Yudasaka, A. Koshio, C. Jabs, T. Ichihashi and S. Iijima, *Appl. Phys. A: Mater. Sci. & Proc.* **74** (2002) 7.
77. R. Martel, H. R. Shea and P. Avouris, *J. Phys. Chem. B* **103** (1999) 7551.
78. A. R. Harutyunyan, B. K. Pradhan, J. Chang, G. Chen and P. C. Eklund, *J. Phys. Chem. B* **106** (2002) 8671.
79. J. Liu, A. G. Rinzier, H. Dai, J. H. Hafner, R. K. Bradley, P. J. Boul, A. Lu, T. Iverson, K. Shelimov, C. B. Huffman, F. Rodriguez-Macias, Y.-S. Shon, T. R. Lee, D. T. Colbert and R. E. Smalley, *Science* **280** (1998) 1253.
80. L. Dai and A. W. H. Mau, *Adv. Mater.* **13** (2001) 899.
81. S. E. Kooi, U. Schlecht, M. Burghard and K. Kern, *Angew. Chem. Int. Ed.* **41** (2002) 1353.
82. D. J. Guo and H. L. Li, *Electrochem. Commun.* **6** (2004), 999.
83. D. J. Guo and H. L. Li, *J. Colloid & Interface Sci.* **286** (2005) 274.
84. T. M. Day, P. R. Unwin, N. R. Wilson and J. V. Macpherson, *J. Am. Chem. Soc.* **127** (2005) 10639.
85. D. J. Guo and H. L. Li, *J. Electroanal. Chem.* **573** (2004) 197.
86. B. M. Quinn, C. Dekker and S. G. Lemay, *J. Am. Chem. Soc.* **127** (2005) 6146.
87. J. Qu, Y. Shen, X. Qu and S. Dong, *Chem. Commun.* **1** (2004) 34.
88. H. F. Cui, J. S. Ye, W. D. Zhang, J. Wang and F. S. Sheu, *J. Electroanal. Chem.* **577** (2005) 295.
89. K. Sivakumar, S. Lu and B. Panchapakesan, *Mater. Res. Soc. Symp. Proc.* **818** (2004) 341.
90. G. G. Wildgoose, C. E. Banks and R. G. Compton, *Small* (2005) <http://www3.interscience.wiley.com/cgi-bin/abstract/112217571/ABSTRACT>
91. L. M. Ang, T. S. A. Hor, G. Q. Xu, C. H. Tung, S. Zhao and J. L. S. Wang, *Chem. Mater.* **11** (1999) 2115.



92. H. C. Choi and H. Dai, Abstracts of Papers, 225th ACS National Meeting, New Orleans, LA, United States, March 23–27, 2003.
93. S. C. Mu, H. L. Tang, M. Pan, R. Z. Yuan and J. Wuhan, Univ. Tech., Mater. Sci. Ed. **18** (2003) 33.
94. B. Rohland, M. Pietrzak, S. Moeller, M. C. Bunesu, M. Wienecke, T. Barfels and M. C. Bunesu, Fullerenes, Nanotubes, and Carbon Nanostructures **13** (2005) 511.
95. B. C. Satishkumar, E. M. Vogl, A. Govindaraj and C. N. R. Rao, J. Phys. D: Appl. Phys. **29** (1996) 3173.
96. L. M. Ang, T. S. A. Hor, G. Q. Xu, C. H. Tung, S. P. Zhao and J. L. S. Wang, Carbon **38** (2000) 363.
97. H. C. Choi, M. Shim, S. Bangsaruntip and H. Dai, J. Am. Chem. Soc. **124** (2002) 9058.
98. L. Qu and L. Dai, J. Am. Chem. Soc. **127** (2005) 10806.
99. A. Mau, L. Dai, S. Huang, Y. Y. Yang and H. Z. He, WO Patent 0073203, 20001207.
100. Z. Liu, Z. Shen, T. Zhu, S. Hou, L. Ying, Z. Shi and Z. Gu, Langmuir **16** (2000), 3569.
101. B. Wu, J. Zhang, Z. Wei, S. Cai and Z. Liu, J. Phys. Chem. B **105** (2001) 5075.
102. X. Nan, Z. Gu and Z. Liu, J. Colloid & Interface Sci. **245** (2002) 311.
103. H. Pan, L. Liu, Z.-X. Guo, L. Dai, F. Zhang, D. Zhu, R. Czerw and D. L. Carroll, Nano Lett. **3** (2003) 29.
104. C. V. Nguyen, L. Delzeit, A. M. Cassell, J. Li, J. Han and M. Meyyappan, Nano Lett. **2** (2002) 1079.
105. Y. Tu, Y. H. Lin and Z. F. Ren, Nano Lett. **3** (2003) 107.
106. B. J. Hinds, N. Chopra, T. Rantell, R. Andrews, V. Gavalas and L. G. Bachas, Science **303** (2004) 62.
107. L. Dai, J. Macromol. Sci, Rev. Macromol. Chem. Phys. C **39** (1999) 237.
108. L. Dai, H. J. Griesser and A. W. H. Mau, J. Phys. Chem. **101** (1997) , 9548.
109. Q. Chen and L. Dai, Appl. Phys. Lett. **76** (2000) 2719.
110. Q. Chen, L. Dai, M. Gao, S. Huang and A. Mau, J. Phys. Chem. B **105** (2001), 618.
111. S. Huang and L. Dai, J. Phys. Chem. B **106** (2002) 3543.
112. R. H. Baughman, C. Changxing, A. A. Zakhidov, Z. Iqbal, J. N. Barisci, B. M. Spinks, G. G. Wallace, A. Mazzoldi, D. De Rossi, A. G. Rinzler, O. Jaschinski, S. Roth and M. Kertesz, Science **284** (1999) 1340.
113. L. Dai and A. W. H. Mau, J. Phys. Chem. B **104** (2000) 1891.
114. L. Dai, P. Zientek, H. A. W. St. John, P. Pasic, R. C. Chatelier and H. J. Griesser, in Surface Modification of Polymeric Biomaterials, Eds. B. D. Ratner and D. G. Castner, Plenum Press, New York, 1996.
115. L. Dai, H. A. W. St. John, J. Bi, P. Zientek, R. C. Chatelier and H. J. Griesser, Surf. Interface Anal. **29** (2000) 46.
116. B. N. Khare, M. Meyyappan, A. M. Cassell, C. V. Nguyen and J. Han, Nano Lett. **2** (2002) 73.
117. P. He, D. L. Shi, J. Lian, L. M. Wang, R. C. Ewing, W. van Ooij, W. Z. Li and Z. F. Ren, Appl. Phys. Lett. **86** (2005) 043107.
118. M. Gao, S. Huang, L. Dai, G. Wallace, R. Gao and Z. Wang, Angew. Chem. Int. Ed. **39** (2000) 3664

119. J. H. Chen, Z. P. Huang, D. Z. Wang, S. X. Yang, W. Z. Li, J. G. Wen and Z. F. Ren, *Synth. Met.* **125** (2002) 289.
120. J. H. Chen, Z. P. Huang, D. Z. Wang, S. X. Yang, J. G. Wen and Z. R. Ren, *Appl. Phys. A* **73** (2001) 129.
121. M. Hughes, M. S. P. Shaffer, A. C. Renouf, C. Singh, G. Z. Chen, D. F. Fray and A. H. Windle, *Adv. Mater.* **14** (2002) 382.
122. W. Feng, X. D. Bai, Y. Q. Lian, J. Liang, X. G. Wang and K. Yoshino, *Carbon* **41** (2003) 1551.
123. N. R. Raravikar, L. S. Schadler, A. Vijayaraghavan, Y. P. Zhao, B. Q. Wei and P. M. Ajayan, *Chem. Mater.* **17** (2005) 974.
124. S. S. Wong, A. T. Woolley, E. Joselevich, C. L. Cheung and C. M. Lieber, *J. Am. Chem. Soc.* **120** (1998) 8557.
125. Y. Yang, J. Zhang, X. Nan and Z. Liu, *J. Phys. Chem. B* **106** (2002) 4139.
126. J. Kong, N. R. Franklin, C. Zhou, M. G. Chapline, S. Peng, K. Cho and H. Dai, *Science* **287** (2000) 622.
127. P. G. Collins, K. Bradley, M. Ishigami and A. Zettl, *Science* **287** (2000) 1801.
128. J. Li, Y. Lu, Q. Ye, M. Cinke, J. Han and M. Meyyappan, *Nano Lett.* **3** (2003) 929.
129. P. Qi, O. Vermesh, M. Grecu, A. Javey, Q. Wang, H. Dai, S. Peng and K. J. Cho, *Nano Lett.* **3** (2003) 347.
130. K. G. Ong, K. Zeng and C. A. Grimes, *IEEE Sensors J.* **2** (2002) 82.
131. O. K. Varghese, P. D. Kichamber, D. Cong, K. G. Ong and E. A. Grimes, *Sens. Actuators B* **81** (2001) 32.
132. S. Chopra, A. Pham, J. Gaillard, A. Parker and M. Rao, *Appl. Phys. Lett.* **80** (2002) 4632.
133. M. Gao, L. Dai and G. G. Wallace, *Electroanalysis* **15** (2003) 1089.
134. Y. Lin, F. Lu, Y. Tu and Z. Ren, *Nano Lett.* **4** (2004) 191.
135. F. Patolsky, Y. Weizmann and I. Willner, *Angew. Chem. Int. Ed.* **43** (2004) 2113.
136. J. Wang, G. Liu and M. Jan, *J. Am. Chem. Soc.* **126** (2004) 3010.
137. P. He and L. Dai, *Chem. Commun.* **3** (2004) 348.
138. W. D. Volkmuth and R. H. Austin, *Nature* **358** (1992) 600.
139. H. Gau, S. Herminghaus, P. Lenz and R. Lipowsky, *Science* **283** (1999) 46.
140. M. W. J. Prins, W. J. J. Welters and J. W. Weekamp, *Science* **291** (2001) 277.
141. G. M. Whitesides and A. D. Stroock, *Phys. Today* **54** (2001) 42.
142. E. Dujardin, T. W. Ebbeson, H. Hiura and K. Tanigaki, *Science* **265** (1994) 1850.
143. S. S. Wong, E. Joselevich, A. T. Woolley, C. L. Cheung and C. M. Lieber, *Nature* **394** (1998) 52.
144. K. B. Jirage, J. C. Hulteen and C. R. Martin, *Science* **278** (1997) 655.
145. S. A. Miller, V. Y. Young and C. R. Martin, *J. Am. Chem. Soc.* **123** (2001) 12335.
146. D. T. Mitchell, S. B. Lee, L. Trofin, N. Li, T. K. Nevanen, H. Soderlund and C. R. Martin, *J. Am. Chem. Soc.* **124** (2002) 11864.
147. D. W. Deamer and M. Akeson, *Trends Biotechnol.* **18** (2000) 147.
148. P. M. Ajayan and S. Iijima, *Nature* **361** (1993) 333.
149. P. M. Ajayan, O. Stephan, P. Redlich and C. Colliex, *Nature* **375** (1995) 564.
150. A. I. Skoulidas, D. M. Ackerman, J. K. Johnson and D. S. Sholl, *Phys. Rev. Lett.* **89** (2002) 185901.

151. P. Nednoor, N. Chopra, V. Gavalas, L. G. Bachas and B. J. Hinds, *Chem. Mater.* **17** (2005) 3595.
152. M. Majumder, N. Chopra and B. J. Hinds, *J. Am. Chem. Soc.* **127** (2005) 9062.
153. S. A. Miller and C. R. Martin, *J. Am. Chem. Soc.* **126** (2004) 6226.
154. M. Shim, A. Javey, N. W. S. Kam and H. Dai, *J. Am. Chem. Soc.* **123** (2001) 11512.
155. J. H. Burroughes, D. D. C. Bradley, A. R. Brown, R. N. Marks, K. Mackay, R. H. Friend, P. L. Burns and A. B. Holmes, *Nature* **347** (1990) 539.
156. H. Koezuka, A. Tsumura and T. Ando, *Synth. Met.* **18** (1987) 699.
157. R. N. Marks, J. J. M. Halls, D. D. C. Bradley, R. H. Friend and A. B. Holmes, *J. Phys.: Condens. Mater.* **6** (1994) 1379.
158. S. A. Curran, P. M. Ajayan, W. J. Blau, D. L. Carroll, J. N. Coleman, A. B. Dalton, A. P. Davey, A. Drury, B. McCarthy, S. Maier and A. Strevens, *Adv. Mater.* **10** (1998) 1091.
159. C. Schonenberger and L. Forro, *Phys. World* **13** (2000) 37.
160. E. J. Lerner, *The Industrial Physicist* **5** (1999) 22.
161. J. M. Bonard, J. P. Salvetat, T. Stockli, L. Forro and A. Chatelain, *Appl. Phys. A* **69** (1999) 245.
162. C. H. Poa, S. R. P. Silva, P. C. P. Watts, W. K. Hsu, H. W. Kroto and D. R. M. Walton, *Appl. Phys. Lett.* **80** (2002) 3189.
163. Y. W. Jin, J. E. Jmg, Y. J. Park, J. H. Choi, D. S. Jung, H. W. Lee, S. H. Park, N. S. Lee, J. M. Kim, T. Y. Ko, S. J. Lee, S. Y. Hwang, J. H. You, J. B. Yoo and C. Y. Park, *J. Appl. Phys.* **92** (2002) 1065.
164. S. Hoffman, C. Ducati, B. Kleinsorge and J. Robertson, *Appl. Phys. Lett.* **83** (2003) 4661.
165. E. E. Donaldson, M. F. Durstock, B. E. Taylor, D. W. Tomlin, L. C. Richardson and J. W. Baur, *Proceedings of the SPIE – The International Society for Optical Engineering, San Diego*, **85** (2001) 4465.
166. A. Star, Y. Lu, K. Bradley and G. Gruner, *Nano Lett.* **4** (2004) 1587.
167. E. Kymakis and G. A. J. Amaratunga, *Appl. Phys. Lett.* **80** (2002) 112.
168. P. M. Ajayan, M. Terrones, A. de la Guardia, V. Huc, N. Grobert, B. Q. Wei, H. Lezec, G. Ramanath and T. W. Ebbesen, *Science* **296** (2002) 705.
169. M. J. O'Connell, S. M. Bachilo, C. B. Huffman, V. C. Moore, M. S. Strano, E. H. Haroz, K. L. Rialon, P. J. Boul, W. H. Noon, C. Kittrell, J. Ma, R. H. Hauge, R. B. Weisman and R. E. Smalley, *Science* **297** (2002) 593.
170. K. Jiang, Q. Li and S. Fan, *Nature* **419** (2002) 801.
171. H. Peng, Z. Gu, J. Yang, J. L. Zimmerman, P. A. Willis, M. J. Bronikowski, R. E. Smalley, R. H. Hauge and J. L. Margrave, *Nano Lett.* **1** (2001) 625.
172. P. M. Ajayan and O. Z. Zhou, *Carbon Nanotubes: Synthesis, Structure, Properties, and Applications*, Chap. 13, Eds. M. S. Dresselhaus, G. Dresselhaus and Ph. Avouris, Springer, Berlin, 2000.
173. R. Saito, G. Dresselhaus and M. S. Dresselhaus, *Physical Properties of Carbon Nanotubes*, Imperial College Press, London, 1999.
174. C. A. Grimes, C. Mungle, D. Kouzoudis, S. Fang and P. C. Eklund, *Chem. Phys. Lett.* **319** (2000) 460.

175. B. S. Files and B. M. Mayeaux, *Adv. Mater. Proc.* **156** (1999) 47.
176. P. M. Ajayan and L. S. Schadler, *Polym. Prep.* **42** (2001) 35.
177. E. Barrera, *JOM* **52** (2000) 38.
178. B. Maruyama and K. Alam, *SAMPE J.* **38** (2002) 59.
179. A. Allaoui, S. Bai, H. M. Cheng and J. B. Bai, *Comp. Sci. Technol.* **62** (2002) 1993.
180. Z. Jin, K. P. Pramoda, G. Xu and S. H. Goh, *Chem. Phys. Lett.* **337** (2001) 43.
181. C. Park, Z. Ounaies, K. A. Watson, K. Pawlowski, S. E. Lowther, J. W. Connell, E. J. Siochi, J. S. Harrison and T. L. St. Clair, *Making Functional Materials with Nanotubes Symposium, Mater. Res. Soc. Symp. Proc.* 706 (2002) 91.
182. R. Vajtai, B. Q. Wei, Z. J. Zhang, Y. Jung, G. Ramanath and P. M. Ajayan, *Smart Mater. Struct.* **11** (2002) 691.
183. B. Safadi, R. Andrews and E. A. Grulke, *J. Appl. Polym. Sci.* **84** (2002) 2660.
184. R. J. Kuriger, M. K. Alam, D. P. Anderson and R. L. Jacobsen, *Comp. Pt. A* **33** (2002) 53.
185. R. Andrews, D. Jacques, M. Minot and T. Rantell, *Macromol. Mater. Eng.* **287** (2002) 395.
186. K. Yoshino, H. Kajii, H. Araki, T. Sonoda, H. Take and S. Lee, *Fullerene Sci. Technol.* **7** (1999) 695.
187. J. M. Benoit, B. Corraze, S. Lefrant, W. J. Blau, P. Bernier and O. Chauvet, *Synth. Met.* **121** (2001) 1215.
188. P. C. P. Watts, W. K. Hsu, D. P. Randall, H. K. Kroto and D. R. M. Walton, *Phys. Chem. Chem. Phys.* **4** (2002) 5655.
189. J. Benoit, B. Corraze and O. Chauvet, *Phys. Rev. B.* **65** (2002) 241405R.
190. G. B. Blanchet, C. R. Fincher and F. Gao, *Appl. Phys. Lett.* **82** (2003) 1290.
191. B. E. Kilbride, J. N. Coleman, J. Fraysse, P. Fournet, M. Cadek, A. Drury, S. Hutzler, S. Roth and W. J. Blau, *J. Appl. Phys.* **92** (2002) 4024.
192. M. J. Biercuk, M. C. Llaguno, M. Radosavljevic, J. K. Hyun, A. T. Johnson and J. E. Fischer, *Appl. Phys. Lett.* **80** (2002) 2767.
193. J. Hone, M. C. Llaguno, M. J. Bierck, A. T. Johnson, B. Batlogg, Z. Benes and J. E. Fischer, *Appl. Phys. A* **74** (2002) 339.
194. D. J. Burton, D. G. Glasgow, M. L. Lake, C. Kwag and J. C. Finegan, *46th International SAMPE Symposium and Exhibition: Materials and Processes Odyssey*, Long Beach, CA, 2001.
195. J. Sandler, M. S. P. Shaffer, Y. M. Lam, C. A. Keun, J. Nastalczyk, G. Broza, K. Schulte and A. H. Windle. <http://www.msm.cam.ac.uk/polymer/members/js364/js364Composites.pdf>.
196. Z. Jin, K. P. Pramoda, S. H. Goh and G. Xu, *Mater. Res. Bull.* **37** (2002) 271.
197. J. N. Coleman, W. J. Blau, A. B. Dalton, E. Munoz, S. Collins, B. G. Kim, J. Raazal, M. Selvidge, G. Vieiro and R. H. Baughman, *Appl. Phys. Lett.* **82** (2003) 1682.
198. J. R. Wood, Q. Zhao, M. D. Frogley, E. R. Meurs, A. D. Prins, T. Peijs, D. J. Dunstan and H. K. Wagner, *Phys. Rev. B* **62** (2000) 7571.

## Chapter 9

### Biological activity of pristine fullerene C<sub>60</sub>

L. B. Piotrovsky

Institute of Experimental Medicine RAMS,  
12 Acad. Pavlov Str., Saint-Petersburg, 197376, Russia

#### 1. INTRODUCTION

Fullerenes are very attractive compounds. At first sight, it seems that the structure of their molecules, which are geodesic, is nonbiological and is the play of human imagination. That is why the original name of these molecules was “buckminsterfullerene’s”, which comes from the name of the architect Buckminster Fuller, who was the first to propose the project of geodesic domes. However, fullerene C<sub>60</sub> can be found in our environment though in very small amounts, e.g. in the soot produced by free burning of hydrocarbons like benzene and cyclohexane, as well as in charcoal [1]. Moreover similar geodesic structures can also be found in the living nature: e.g. “fullerene-like” organization of the envelope of some viruses [2,3].

The interest in the investigations of the biological activity of fullerenes appeared practically after they became available in real amounts as a consequence of the elaboration of the preparative method of their synthesis in 1991 [4]. The first works on the investigations of toxicity of fullerene C<sub>60</sub> [5] and the use of its derivatives in medicinal chemistry [6,7] appeared as early as in 1993.

These quickly developing studies were brought out in many reviews devoted to the investigations of the biological activity of fullerenes [8–13]. However, owing to the well-known insolubility of fullerenes in polar media, the most part of these works were done using water-soluble derivatives of fullerenes, mostly fullerene C<sub>60</sub>. In the present work, we will take into account only pristine fullerene as the source of biological activity.

#### 2. WHY PRISTINE FULLERENE C<sub>60</sub>?

First, from the theoretical point of view, it is necessary to clear up the properties of the parent compound. These data would help to elucidate the role of fullerene core itself and the input of substituents into different biological properties, which in turn would help to plan more rationally the design on new biologically active compounds of this series.

Secondly, from the formal point of view, fullerene derivatives are not fullerenes. According to the International Union of Pure and Applied Chemistry (IUPAC) nomenclature, a fullerene is “a compound composed solely of an even number of carbon atoms which form a cage-like fused-ring polycyclic system with 12 five-membered

rings and the rest six-membered rings”, and all derivatives must be called fulleranes or fulleroids [14]. While we do not want to be more saintly than the Pope, we would also not insist that the study of the biological activity of fullerene derivatives is always the study of the biological activity of pristine fullerene. It is necessary to state that if the substituent (or substituents) in the derivative is much larger in volume than fullerene core, or practically totally shields it sterically, then the biological action of this compound will be defined not by the fullerene core, but by other structural fragments on the surface of the molecule. Even in the case of simple derivatives, some of their biological parameters will differ from the similar ones of pristine fullerene. For example, there is no doubt that intracellular distribution of the negatively charged “dicarboxy-fullerene”  $C_{61}(CO_2H)_2$  [15], will differ from the distribution of fullerene itself.

Thirdly, from the commercial point of view, the use of pristine fullerene  $C_{60}$  in biology and medicine can be more profitable because to date, and probably in the near future, it is much more available and is cheaper than other fullerenes and its derivatives. For the producers of fullerene, it is also necessary to know the biological and toxic properties of pristine fullerene in order to determine its safety for people and the environment.

### 3. WHAT CAN BE INTERESTING IN PRISTINE FULLERENE FOR MEDICINAL CHEMISTRY?

What physicochemical properties of fullerene can be useful for drug design?  
These are:

- ability of fullerene  $C_{60}$  to produce the singlet oxygen with high quantum yields under illumination [16];
- high affinity of fullerene core to electron donors, causing its ability to react with free radicals [17];
- high lipophilicity of  $C_{60}$  molecule [18].

Therefore, in biology and medicine fullerene  $C_{60}$  can be used as:

- oxidant [by production of various reactive oxygen species (ROS)] or photosensibilizer for photodynamic therapy;
- antioxidant (radical scavenger);
- membranotropic agent.

Let us observe the mechanism of each of these effects estimating also the influence of the substituents on the properties of the fullerene core. Upon illumination, fullerene  $^1C_{60}$  is excited to a short-lived singlet state  $^1C_{60}^*$ , which converts almost quantitatively into a longer-lived triplet state  $^3C_{60}^*$ . The triplet state transfers energy very efficiently to molecular oxygen, generating singlet oxygen with almost unitary yield (Fig. 1) [19]. Since the latter is a powerful oxidizing agent [20,21], the fullerene in the presence of oxygen and under illumination will be the oxidant.

The peculiarity of this process is that the fullerene molecule does not undergo any chemical modifications and can participate in this cycle multiple times, being a catalyst of the reaction of singlet oxygen generation. It is necessary to state that this property of fullerene molecule differs from other known photosensitizers, for

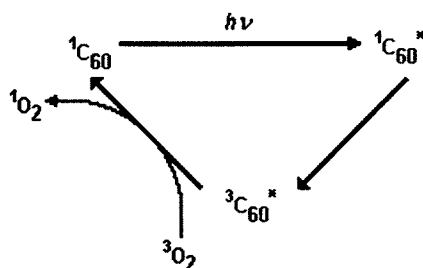


Figure 1. The production of singlet oxygen by fullerene  $C_{60}$  during photoexcitation.

which singlet oxygen is generated as a result of the destruction of the initial molecule. Fullerene  $C_{60}$  is a more efficient photosensitizer than rose Bengal, methylene blue and eosin yellowish [22].

The ability of fullerene to behave as an oxidant, especially in biological systems, is not connected only with its property to generate singlet oxygen. Both excited states ( ${}^1C_{60}^*$ ) and ( ${}^3C_{60}^*$ ) are powerful electron acceptors, more powerful than ground state  ${}^1C_{60}$ , and therefore can interact with various electron donors [17,23–25]. That is why in the presence of compounds with electron-donating groups (amines, various antioxidants, etc.) the state ( ${}^3C_{60}^*$ ) can be reduced up to the anion-radical  $C_{60}^{\bullet-}$  [26]. Formation of this anion-radical under illumination was confirmed by electron spectroscopy and EPR data [27]. This anion-radical in the presence of oxygen can transfer one electron to  $O_2$ , converting it into superoxide-anion radical  $O_2^{\bullet-}$ . As a whole, “interrelationships” of fullerene and oxygen molecules are shown in Fig. 2 [9]. Therefore, the oxidative activity of fullerene is connected with its ability to produce different ROS.

Molecular mechanism of the antioxidant activity of fullerenes in biological systems is caused by high electronegativity of these molecules. Fullerene molecule is an olefin with conjugated  $\pi$ -electron system, therefore the reagents with unpaired electron (e.g. hydroxyl or superoxide radicals) are added to olefin fragments of  $C_{60}$  molecule with the formation of multisubstituted derivatives (Fig. 3).

It was shown that one  $C_{60}$  molecule can add 34 methyl radicals, and this allowed the authors to call this molecule “radical sponge” [17]. As in biological systems, the reactions with free radicals are mainly the reactions of oxidation, then one of the biological properties of fullerene  $C_{60}$  must be its antioxidant activity.

Photodynamic and chemical properties of fullerene are defined by the presence of conjugated double bond system in the molecule. Substitution of the fullerene core leads to the diminishing of conjugation system, number of  $sp^2$  carbon atoms, and eventually to fullerene derivatives (especially in the case of multisubstitution) that slightly resemble pristine fullerene. It was shown that the presence of the substituents in the fullerene core decreases the ability of the compounds to generate singlet oxygen [28]. The decrease of quantum yield of singlet oxygen with the decrease of conjugation area is shown in [29]. The ability to add free radicals also

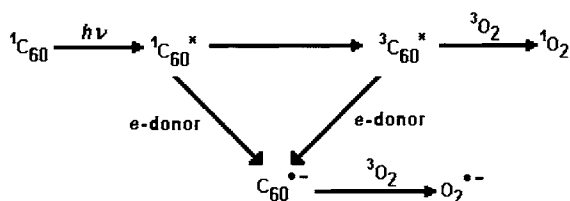


Figure 2. Generation of different types of ROS under irradiation of fullerene  $\text{C}_{60}$  in the presence of electron donors.

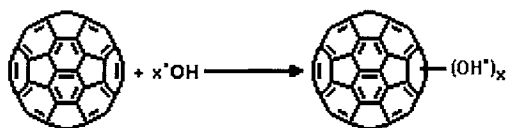


Figure 3. Reaction of pristine  $\text{C}_{60}$  with free radicals.

decreases though a bit less, and this effect is more pronounced in the case of multisubstituted derivatives [30].

It is necessary to stress again that during the production of ROS, fullerene molecule undergoes only reversible changes of its physical state, while in the reaction with free radicals its chemical nature is changed. So it is possible to say that in the first case  $\text{C}_{60}$  molecule plays the role of a catalyst, and in the second of a reagent. The ability of both fullerene  $\text{C}_{60}$  and its derivatives to play the role of radical scavenger and ROS generator brings out the fact that the same compound in biological systems shows properties of both antioxidant and oxidant. Such combination of two types of biological actions (antioxidant and oxidant) is another example of the peculiarity of a fullerene molecule. These properties are most vividly expressed for pristine fullerene, and this is one of the reasons for studying the biological activity of pristine fullerene, considered to be most “inconvenient” for practical use.

#### 4. PRISTINE FULLERENE $\text{C}_{60}$ PREPARATIONS FOR BIOLOGY AND MEDICINE

Though it is “inconvenient”, nothing is impossible for the investigator, and pristine fullerene can be used (and is used) in biological studies in the form of:

- dispersions (crystalline or colloidal)
- water-soluble complexes with polymers (or inclusion complexes)
- fullerene-coated surfaces.



In all these preparations we have fullerene  $C_{60}$  itself, but they essentially differ from one another. First of all, these differences are due to the degree of association of molecules, which is an important factor influencing the manifestation of various properties of fullerene core. As fullerene core is highly hydrophobic, the degree of association of fullerene molecules in the solutions is rather high. This tendency of fullerene core to aggregation is expressed so strongly that the addition of only one polar chain into the core appears to be insufficient to avoid clustering, and hydrophobic carbon spheres stick together, leaving the hydrophilic chains on the outside of the aggregate [31,32]. As a consequence of this aggregation, for example, the lifetime of the excited triplet state is reduced by several orders of magnitude [33,34], and negatively charged fullerene clusters are effectively shielded against reduction by electron transfer [35]. The differences in the degree of association also influence the appearance of other biological properties (e.g. only lowly associated molecules will possess membranotropic effects). We shall try to show below how this ability to association influences the effects shown by pristine fullerene in biological systems.

For example, fullerene-containing ointments, the basis of which is high branched and unbranched alkanes ( $C_{16}$ – $C_{24}$ ), accelerate wound healing. The ointment, which is a saturated solution of fullerene  $C_{60}$  in this alkane mixture, appeared to be more effective than the ones prepared by triturating of solid fullerene with the ointment base, in spite of the fact that the quantity of fullerene in them is higher [36].

#### 4.1. Dispersions

In this part we shall describe two types of dispersions, namely, suspensions of solid (micronized) fullerene in water and stable aqueous colloidal solutions of fullerene  $C_{60}$  (ACSF).

In earlier works it was shown that pristine fullerene in solid state did not possess any pronounced biological activity. For example, a suspension of micronized  $C_{60}$  in water did not give any visible biological effects in *in vivo* tests performed on Swiss mice [37]. One of the first examples of the application of fullerene with biological purposes was the use of its suspension for virus inactivation [38]. It was shown that Semliki Forest virus and vesicular stomatitis virus were effectively inactivated in the presence of micronized fullerene  $C_{60}$  and oxygen after 4–5 h of illumination of these mixtures. This process was clearly dependent on the presence of oxygen. Addition of glutathione or hydroquinone (scavengers of free radicals) in the assay had no effect on virus inactivation by  $C_{60}$ , which allowed us to suggest that no radical mechanism is involved in the inactivation process and the main active species is singlet oxygen. In these conditions, enveloped viruses are inactivated more readily than nonenveloped ones.

ACSF was prepared for the first time by Scrivens et al. [39] by a complicated procedure using the sequence of organic solvents and their mixtures (benzene, tetrahydrofuran (THF) and acetone). Deguchi et al. [40] prepared ACSF by simple injecting of saturated solution of fullerene in THF into water. The other method proposed by Andrievsky et al. [41] consists in ultrasonification of the mixture of toluene solution of fullerene and water. All these methods use organic solvents, the

removal of which from the final preparations can be of a problem. This is the reason why in the paper [39] it is stated that the peaks for small amounts of residual organic solvents were negated by filtering ACSF and by using the filtrate as a blank. Lately, a method was proposed that excluded the use of organic solvents, and ACSF was prepared by prolonged stirring of suspension of solid  $C_{60}$  in water [42]. All these methods gave nearly the same results [43].

In ACSF the molecules of fullerene  $C_{60}$  form highly polydisperse particles, they are slightly anisotropic and have a characteristic size of  $\sim 70$  nm [43]. These particles are charged negatively, which makes the system highly stable (in pure water, see below) [40,44]. According to [45], ACSF (named by the authors as  $C_{60}$ FWS) is a molecular–colloid system, containing both single fullerene  $C_{60}$  molecules and their fractal clusters in a hydrated state (i.e. the fullerene aggregates are covered by a strong hydrated shell). The smallest stable spherical  $C_{60}$  cluster with a diameter of 3.4 nm contains 13  $C_{60}$  molecules. More detailed theoretical and experimental studies of the structure of ACSF can be found in [46–49]. The presence of the negatively charged envelope brings out the fact that fullerene cannot be extracted by toluene [39,41,50]. In spite of crystalline (solid) forms ACSF cannot produce ROS because the hydrate shell does not allow molecular oxygen to sorb at the surface of the fullerene molecule.

Biological action of ACSF is described in a number of papers. For example, it was shown that an aqueous suspension of  $^{14}C$ - $C_{60}$  has no effects on the proliferation rate of keratinocytes and fibroblasts [39]. Different biological effects of ACSF *in vitro* and *in vivo* were listed in [51]. It was also stated that ACSF shows anti-atherosclerotic activity [52]. In the studies of the direct action of ACSF, prepared according to the method [41], on the morphology of influenza virions [virus A/PR/8/34 (H1N1)] with and without illumination, we found that only under UV-irradiation ACSF caused expressed damaging of influenza virions [53]. Such influence of illumination allows us to suppose that in this case we have come across the action of ROS (singlet oxygen?), produced by fullerene  $C_{60}$  under illumination.

It was also found that low UV-irradiation is sufficient to induce the pro-oxidant activity of ACSF [54]. The same authors proposed that the photoirradiated water solutions of fullerene  $C_{60}$  may be potentially useful for photodynamic therapy of tumors as ROS catalytic system [55]. The cytotoxicity of “nano- $C_{60}$ , fullerene aggregates that readily forms when pristine  $C_{60}$  is added to water”, was also shown in [56]. But, ACSF does not obtain photodynamic activity and the fullerene in them is not able to play the role of photosensitizer. Then why was it observed in the experiments mentioned above?

The most probable explanation is that ACSF was stable only in pure aqueous media. The changes in ionic strength and pH value of the media in physiological range caused the coagulation of fullerene [42,44]. The addition of saline to ACSF led to the formation of brown amorphous precipitate (most probably amorphous fullerene), which is an effective photosensitizer [57].

Therefore, it is the instability of ACSF in physiological media which is the reason for the changes of its properties. In other words, when ACSF is introduced in physiological media, the negatively charged clusters of stable colloidal suspension are

deconstructed and we observe the biological action of fullerene itself: oxidant (under illumination) or antioxidant (in darkness).

#### 4.2. Water-soluble complexes with polymers (or inclusion complexes)

Various methods for dissolving fullerene  $C_{60}$  in water using various hydrophilic organic compounds were developed in order to overcome its insolubility in this media (for reviews see [8,9,13]). Among them it is necessary to mention the inclusion complex  $C_{60}/\gamma$ CD ( $\gamma$ -cyclodextrin)  $C_{60}$  [58], inclusion of fullerene  $C_{60}$  into liposomes [59] and the complex with polyvinylpyrrolidone ( $C_{60}$ /PVP complex) [60].

The inclusion complex  $C_{60}/\gamma$ CD (1:2) was prepared by boiling water solution of  $\gamma$ CD with fullerene  $C_{60}$  [58]. As we know, this inclusion complex is a rare example when it was undoubtedly shown that a fullerene molecule is in isolated nonaggregated state but practically nothing is known about the biological properties of this complex. At such shielding of fullerene core as in this complex, the main input in the biological activity is defined by the host molecules. However, it was shown both in physical and biological experiments [28,61] that in this complex in particular fullerene possesses photodynamic properties, while free radicals (e.g.  $\cdot$ OH) react exclusively with the macromolecular host  $\gamma$ CD [28]. In the case of the transfer of fullerene  $C_{60}$  into the aqueous phase by inclusion into liposomes, it shows antioxidant activity similar or even higher than natural antioxidant vitamin E [59].

The biological properties of  $C_{60}$ /PVP complexes with fullerene concentration  $\sim 0.8$  wt.% (with which it is possible to obtain aqueous solutions with the concentration of  $C_{60}$  up to  $4.1 \times 10^{-5}$  M) can be studied much better [60]. The preparation of this complex with higher content of fullerene (1.1–2.7 wt.%) was described in [62]. This complex was already examined in several *in vitro* biological tests [60,63–67]. However, physicochemical properties of this complex are investigated to be much worse. This complex is formed by weak donor–acceptor interactions [68]. The interactions between  $C_{60}$  and polymer vehicle is not very strong, and fullerene can be easily extracted by toluene from aqueous solution. According to the data,  $^{13}\text{C}$ -NMR in  $\text{D}_2\text{O}$  in the complex significantly changes the electronic state of the carbon atoms  $\text{C}^{(1)}$  and  $\text{C}^{(4)}$  of pyrrolidone cycle and  $\text{C}^{(5)}$  of the monomeric unit of PVP, nearest to the nitrogen atom [69].  $C_{60}$ /PVP complex, as it was shown by static and dynamic light scattering, forms aggregates with high molecular masses in aqueous solutions [70,71].

The degree of aggregation of fullerene molecules in this complex seems to be low, but it was not determined. This property of fullerene  $C_{60}$  can be monitored, for example, by UV–VIS spectrophotometry. In the range of 320–350 nm, the clustering causes the bathochromic shift of the absorption band with the decrease of extinction coefficient [72]. The analyses of several dozens of UV spectra of  $C_{60}$ /PVP complexes, which differ in the content of fullerene and the molecular mass of PVP, shows that the use of PVP with low molecular mass leads to a low degree of association of fullerene molecules in the complexes. For samples with low association, the band is at 331–333 nm, whereas for the other ones it is shifted to 340 nm. Antibasis decreases the values of extinction coefficient (from  $\sim 1.0 \times 10^{-5}$  to  $\sim 0.4 \times 10^{-5} \text{ M}^{-1}\text{cm}^{-1}$ ). Such complexes can be prepared only with a relatively low content of fullerene (about 0.1–0.2 wt.% to PVP mass) and PVP of low molecular mass (10,000 Da). The degree

of association of fullerene molecules in such preparations changes in time during storage for about several months. Certainly, it is not good that fullerene concentration in  $C_{60}$ /PVP complexes is rather low (usually  $\sim 0.5$ – $0.6$  wt.%), but let us remind ourselves that the effective antiviral dose of fullerene itself in the complex is also not high. The active quantity of fullerene, calculated neglecting the polymer vehicle, against the influenza virus is about  $7 \mu\text{M}$  [73].

At the beginning of the studies of fullerene action on influenza virus reproduction, it seemed that the mechanism of fullerene action will be similar to that of lipophilic antiviral drug derivatives of such framework compounds as adamantane [74]. Though the inhibitory activity of the complex is comparable to the antiviral activity of such reference as anti-influenza drug such as rimantadine, there are distinct differences. First of all,  $C_{60}$ /PVP complex did not specifically inhibit any stage of the virus replication cycle, including absorption [75]. The complex is active, in contrast to rimantadine, against both types of influenza virus (A and B), as well as other RNA- and DNA-containing viruses (e.g. herpes simplex and human parainfluenza virus) [76]. It was proposed that  $C_{60}$ /PVP complex interferes with the late membrane-dependent stages of morphogenesis of enveloped viruses and so it can be classified as membranotropic antiviral compound [77].  $C_{60}$ /PVP complex influences the morphology of influenza virions predominantly in light-independent manner [53]. Some virions in  $C_{60}$ /PVP-virion mixture look like the aggregates with polymer complexes (Fig. 4). It is possible to assume that this image corresponds to the moment of the fusion between the complex and the virion. The fraction of such particles was not large (about 1–3%), this can be the evidence of rather quick interaction of the complex with virions [78].

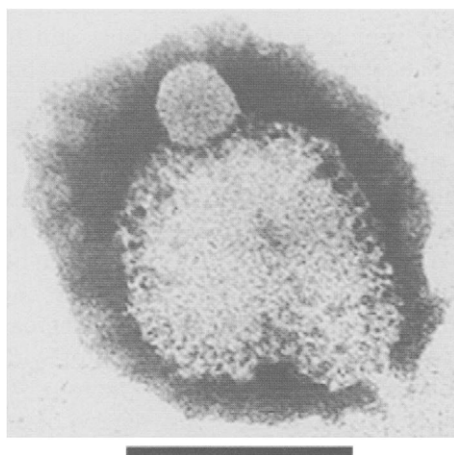


Figure 4. TEM image of fusion of  $C_{60}$ /PVP complex with influenza virion envelope. Scale 100 nm.

On the basis of these data it is possible to speculate that fullerene  $C_{60}$  attached to the polymer vehicle by weak donor–acceptor bonds, can easily move from the complex to the lipid bilayer of the envelope of virion. The transition of fullerene molecules into the lipid bilayer was shown directly with the use of erythrosine as a probe, while pyrene as a probe showed that the fluidity of membranes increases [79].

The obtained data proved the conclusion made earlier about the membranotropic mechanism of antiviral action of  $C_{60}$ /PVP [77]. From this point of view the most vulnerable stage in the cycle of influenza virus reproduction is budding, because at this stage the fluidity of the lipid bilayer and the ability of viral glycoproteins to form patches with the regular structure are of great importance [80]. So, the penetration of fullerene molecules into the membrane will change its properties, and will disturb the assembly of virions (Fig. 5A). When the fluidity of the cell membrane increases, the processes of the virion assembly proceed wrongly and damage the noninfectious particles formed (Fig. 5B).

It is not surprising that owing to high lipophilicity of fullerene the penetration of its molecules into membrane, their interactions with bilayer components will lead to the damage of the regular structure and to the formation of the pores in the virion envelope. However, it can be possible only in the case of single fullerene molecules or low associated aggregates, which are smaller than the membrane thickness (5 nm). However, the small increase of virucidal effect of  $C_{60}$ /PVP complex during illumination [78] allows us to suppose that there is also the input of the second, light-dependent mechanism [81].

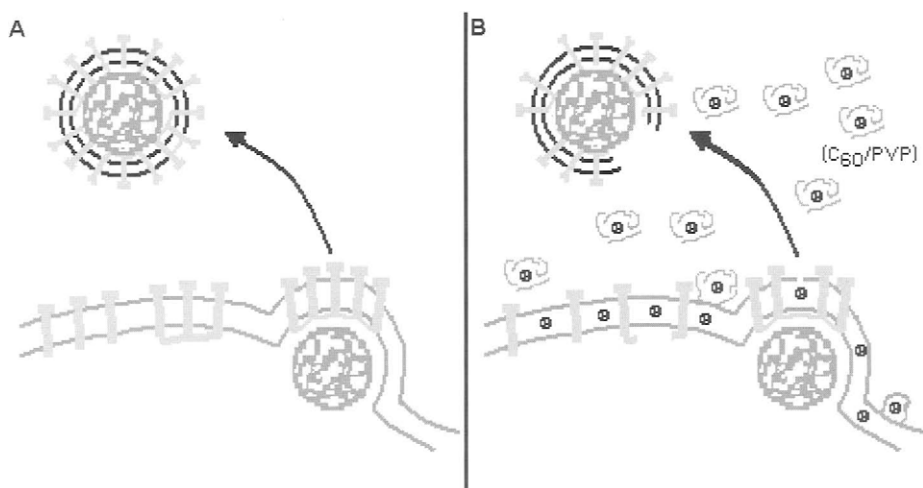


Figure 5. The scheme of the late membrane dependent stages of influenza virus replication (A – normal; B – in the presence of  $C_{60}$ /PVP complex).

### 4.3. Fullerene-coated surface

The third form of pristine fullerene  $C_{60}$  that can be used in biological experiments is the fullerene-coated surface. There are two possibilities of immobilization of fullerenes on a surface:

- by absorption interactions
- by covalent linkers.

A surface coated by fullerene, obtained by evaporation of solution of  $C_{60}$  in benzene, was proposed for the first time in 1994 “to be used in the methods of growing cells as a substrate for cell growth, and for immobilizing biological materials including cells, macromolecules, drugs, aromatic molecules, and aliphatic substances” [82]. The surfaces with covalently linked fullerene moieties are also described. For example,  $C_{60}$  can be anchored or modified by aminopropyl moiety silica [83]. The UV spectra indicate the chemical sorption of fullerenes through the aminopropyl linkers. The aminopropylsilica-based composites were obtained with concentration of fullerenes from 60 to 240  $\mu\text{mol g}^{-1}$ . In the same conditions on the bare silica, the maximum concentration of fullerenes has reached 140  $\mu\text{mol g}^{-1}$ . The studies of bioactivity of the aminopropylsilica-based composites showed that they possess the properties of a pro-oxidant. The same pro-oxidant effect and its increase under UV and X-ray irradiation were described in [84].

The fulleroproline derivative, immobilized on silica gel, represents the new stationary phase for high pressure liquid chromatography (HPLC) column chromatography. This phase can be used in either organic or aqueous solutions for selective separation of some compounds (e.g. calixarenes or cyclodextrins) or to investigate the binding affinities of potential hosts for the immobilized fullerene core [11]. Strong host–guest interaction between the nonapeptide Bz-Aib-Tyr(ferrocenoyl)-Aib<sub>2</sub>-Gly-Aib<sub>2</sub>-Tyr(ferrocenoyl)-Aib-OMe (where Aib is 1-aminoisobutyric acid residue) and fullerene spheroid was shown in [85].

The fullerene-coated surfaces can also be prepared on polypropylene layer by evaporation of the saturated solution of fullerene  $C_{60}$  in hexane. When concentration of fullerene  $C_{60}$  on the surface is about 10  $\mu\text{g cm}^{-2}$  it looks like a light brown film. But in reality, as it was shown by the data of light spectroscopy, it is not a film because fullerene molecules form separate clusters on the surface. According to the data of TEM on such freshly prepared surface, it is possible to conclude that these clusters are mostly amorphous and only in some regions there can be observed something like crystal structure.

This fullerene-coated surface in the cell free system showed the pro-oxidant activity (the reduction of 2',7'-dichlorofluorescein, which is one of the most direct techniques of the indication of ROS [86,87]). In the cell free system, which contained different concentrations of  $\text{H}_2\text{O}_2$  and 2',7'-dichlorofluorescein, the pristine fullerene  $C_{60}$  showed antioxidant properties. As it was awaited the ability of pristine  $C_{60}$  to be an antioxidant is limited (in this reaction it acts as a reagent) [88].

This fullerene-coated surface is useful for the study of cell cultures growth, because it has a good adhesion for the cells in the culture, which forms a normal monolayer on it [88]. In this study a powerful photodynamic effect of fullerene  $C_{60}$

on M-104 cells (line of kidney epithelium of African green monkey) was observed. Practically all the cells died probably owing to their damage by ROS, generated by  $C_{60}$  during 30 min illumination. This effect is time dependent, and the comparison of the sensitivity of malignant cells [A-549 (line derived from human lung carcinoma) and HeLa (line derived from human cervical carcinoma)] to phototoxic action of fullerenes in comparison to normal ones [MA-104 (spontaneously transformed, conditionally normal line) and embryonic human lung fibroblasts (completely normal cells)] showed that the malignant cells under illumination on the fullerene surface were inactivated with higher speed than the normal ones [88].

As far as we know, these are the first data on relative selectivity of pristine  $C_{60}$  phototoxicity against tumor-derived cells. In the earlier published example of photodynamic tumor therapy not pristine fullerene, but chemically conjugated  $C_{60}$  with polyethyleneglycol (PEG) [89] was used. According to the opinion of the authors, this modification was the reason why  $C_{60}$ -PEG conjugate was accumulated to a greater extent and retained for a longer time in the tumor tissue than in the normal one.

$C_{60}$  phototoxicity is actually correlated to the generation of ROS, because the introduction of Hypoxene (Na salt of poly(2,5-dihydroxyphenyl)-4-thiosulfonate), the antioxidant with non-specific direct mechanism of action, into the media completely blocked the phototoxic effect of  $C_{60}$ . The absence of the protective effect of superoxide dismutase and glutathione is an additional proof that the real damaging agent of photodynamic effect of  $C_{60}$  in the fullerene-coated surface is singlet oxygen and not other ROS.

## 5. IS PRISTINE FULLERENE $C_{60}$ TOXIC?

In spite of the recent paper [90], the question whether pristine fullerene  $C_{60}$  is toxic is still open. There are rather many data in the reviews [8,9] showing at least very low toxicity of fullerene itself. As it was mentioned earlier *in vivo* tests, performed on Swiss mice with a dispersion of micronized  $C_{60}$  in water, did not show any lethality, toxicity, or growth inhibition [37]. It was also found that  $C_{60}$  can be phagocytized by human leukocytes [91] and monocytes [92]. However, the associated usual increase of interleukin IL-1b release was not observed. This effect is not clear but it seems to be correlated with the lack of inflammatory response observed after  $C_{60}$  administration in Swiss mice [93]. The data in the other papers also show the absence of fullerene  $C_{60}$  toxicity [e.g. 94–96]. However, several data showed that fullerene can cause some nuisances. High ability of unsaturated fullerene core to cycloaddition reactions appears in biological conditions in that it reacts *via* Diels–Alder addition with vitamin A [97]. The influence of  $C_{60}$  (as  $C_{60}$ /PVP complex) on embryogenesis was also shown *in vivo* and *in vitro* [64,65].

Concerning the influence of pristine fullerene on central nervous system in ordinary conditions, it is difficult to imagine how fullerene can penetrate into the brain because this organ is quite well protected by different barriers, first of all by blood–brain barrier. If such lipophilic compound as fullerene still reaches this lipophilic structure then, most probably, it will stay in a lipid layer and would not be able to pass into the brain. In the charged form fullerene also cannot pass this

barrier. The penetration of the charged molecules into the brain is possible only with the help of special transport systems, which seems unreal in the case of fullerene (in any case, it has not been found till now). Secondly, there are two papers devoted to direct administration of pristine fullerene into brain as  $C_{60}$ /PVP complex [98] and as ACSF [99]. In the first case it was shown that injection of  $C_{60}$ /PVP into the hippocampus prevents the development of amnesia induced by protein synthesis blockade in the rat brain, in the second, it was shown that the infusion of  $C_{60}$  as ACSF into the lateral ventricles of the brain did not disturb the cognitive abilities of intact rats. Moreover this infusion before the administration of amyloid- $\beta_{25-35}$  peptide prevented the spatial memory disturbances caused by the latter. There were no acute toxic manifestations in the experiments cited above.

Thus, at present we do not possess any reliable data on acute toxic action of pristine fullerene on central nervous system. Moreover there are some indications that pristine  $C_{60}$  in rodents (which are more commonly used as test animals for relating the toxicity to the humans than fish, earthworms, or bacteria) after oral and intraperitoneal administration of the large doses (2 to 5 g kg<sup>-1</sup> of body weight) is not only toxic but that it actually protects living systems against oxidative stress [8]. Therefore on the basis of the known data it is possible to state now that pristine fullerene does not have acute or sub-acute toxicity. Nevertheless the existing data do not allow us to say that there cannot be any toxic manifestations during prolonged exposition, including respiration. It must be taken into account that pristine  $C_{60}$  and fullerene black are taken up by alveolar and HL-60 macrophages and induce the release of pro-inflammatory cytokines *in vitro* [100]. The release of such chemical signals is the indication of an attempt to protect against some cellular threat. On the other hand, the damaging action of some nanoparticles on respiratory system (and after the penetration into the blood to the whole organism) is rather well known [101,102].

## 6. CONCLUSION

The data given above show that pristine fullerene  $C_{60}$  in biological systems manifests all its possible properties, namely, as a photosensitizer, radical scavenger, and influence on membrane-depending processes. The appearance and efficacy of any of these properties depend both on the way it comes into contact with the biological system and on the way it is delivered to the living organism. The aggregation state of pristine fullerene, the method of its preparation and conditions of biological experiments are also of great importance.

The most biologically inactive fullerene is *solid fullerene*. Its activity strictly depends on the illumination and manifests in oxidative action owing to the production of singlet oxygen. Solid fullerene itself cannot penetrate into the biological tissues and therefore must be used in the external devices for the production of ROS or as applications for local photodynamic therapy.

It is difficult to discuss the entire data on the biological action of ACSF as a whole because of inaccessibility of detailed description of experiments listed in [51]. However, the set of enumerated effects is rather wide, and the antioxidant effects



of such preparations are rather well documented. There is, however, one snag – we must remember every time about the instability of this preparation in the physiological media. In this case, we return to the solid fullerene, but with other delivery system.

Pristine fullerene as *water-soluble complexes* is much more accessible for biological systems, because it can distribute more or less evenly in the organism and penetrate in various tissues and organs. That is why its serious harmful effect was found only with the use of  $C_{60}$ /PVP complex [e.g. 65]. The list of activities of  $C_{60}$ /PVP complex, the preparation with the lowest aggregated state of fullerene molecules, is much wider than for any other ones. At low degree of aggregation, the effects connected with the action on the membranes appear. It is quite natural that the fullerene molecule aggregates of the sizes larger than the sizes of biological molecules and their supramolecular associates cannot interact with the latter. Depending on the external conditions, therefore, pristine fullerene can show opposite effects, for example, from the support of the cell growth (in darkness) up to their total destruction (at illumination). Duality of the mechanisms of action, the existence of both photoactivity and membranotropic action is observed also for fullerene derivatives. For example, “carboxyfullerene” C3 in the concentration of 10  $\mu\text{M}$  inhibits the virus Dengue-2 reproduction at illumination, while at the concentration of 40  $\mu\text{M}$  it practically totally suppresses its replication in darkness. In the latter case the virus absorption is suppressed as a result of hydrophobic interaction of this compound with the virus lipid envelope. It is confirmed by the comparative investigation of antiviral activity of two isomeric *tris*-malonic derivatives of  $C_{60}$  (C3 и D3) (Fig. 6) [103].

More lipophilic isomer C3 inhibits the virus replication in a dose-dependent manner and is much more active than the second more hydrophilic one D3 [104].

The data given above show that pristine fullerene  $C_{60}$  in biological systems manifests all its possible properties, namely, as photosensitizer, radical scavenger and membranotropic compound. The appearance and efficacy of any of these properties would depend on the aggregation state of pristine fullerene, method of its preparation and conditions of biological experiments. On the other hand, we have previously emphasized that based only on the examples of antiviral action of

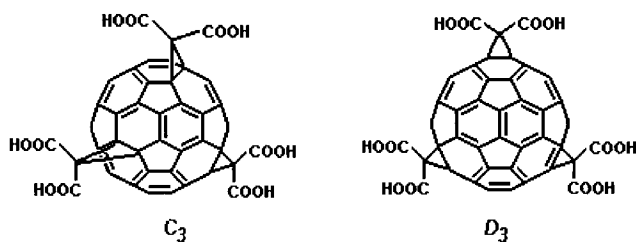


Figure 6. The structures of two isomeric *tris*-malonic derivatives of  $C_{60}$ .

fullerene  $C_{60}$  and its derivative the three main mechanisms of drug action, namely, unspecific, specific interaction of ligand–receptor type, and membranotropic can be obtained [77]. This conclusion is drawn from virus inactivation by singlet oxygen (unspecific) [38], inhibition of HIV protease (specific ligand–receptor interaction) [7] and from our results on the antiviral activity of  $C_{60}$ /PVP complexes (membranotropic action) [77] (Fig. 7).

At present we can say that this conclusion is confirmed not by the data on antiviral activity only. Earlier as an example of specific ligand–receptor interaction, the data was obtained not with the use of pristine fullerene, but its derivative. At present there are data to support that pristine fullerene itself shows its own biological activity, which means that it is able to show complementary interaction with biological targets. The results of [105] can be interpreted in the ways fullerene can interact with the biological macromolecule–target directly, playing the role of the real active origin. The nonapeptide with electron-rich, hydrophobic and wide cavity, formed by aromatic residues, which is able to host fullerene  $C_{60}$ , is described [106]. It is also known that 1,2–(dimethoxymethano)fullerene is able to inhibit the earlier stages of  $\beta$ -amyloid peptide aggregation by specific binding with central hydrophobic motif KLVFF of  $A\beta$  peptide [107]. The role of the substituent in these experiments is most probably in the transfer of fullerene core into aqueous media and its delivery to the target. After that, the fitting of fullerene core into the lipophilic cavity is formed by benzene rings of phenylalanine residues and then binding with peptides occurs. This conclusion is supported by the direct binding of

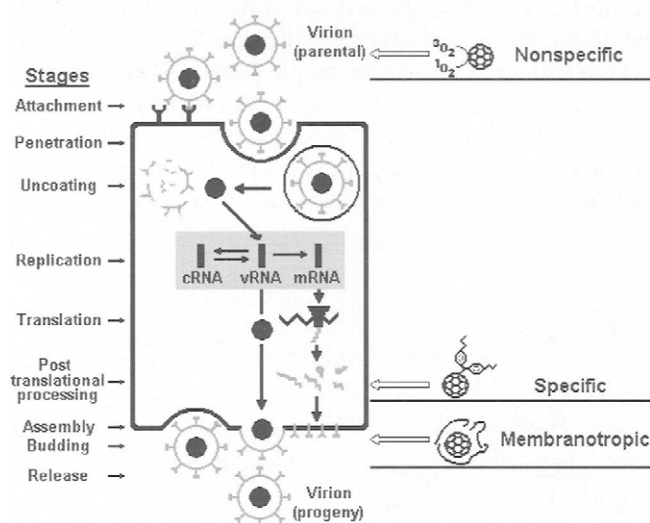


Figure 7. Scheme of the reproduction cycle of enveloped viruses and targets for fullerene  $C_{60}$  and its derivatives.

pristine fullerene by proteins shown in [108]. Although these experiments on binding of pristine fullerene and its derivatives were done *in vitro*, it is possible to foresee that similar interactions of  $C_{60}$  with biological target would be found *in vivo* (if a suitable delivery system to bring pristine fullerene into the cell, across the membranes, is found).

**Acknowledgments:** I would like to thank Professor Eiji Ōsawa (Nano-Carbon Research Institute, Japan) and Professor Alexander Vul' (Ioffe Physico-Technical Institute RAS, Russia) for their attention to our work and helpful discussions. I would like to acknowledge Professor Motoi Sakamoto (Tohoku University, Japan) for his support. This work was supported by ISTC grant #2592.

## REFERENCES

1. M. Shibuya, M. Kato, M. Ozawa, P. H. Fang and E. Osawa, *Full. Sci. Technol.* **7** (1999) 181.
2. M. Nermut, D. J. Hockley, J. B. M. Jowett, I. M. Jones, M. Garreau and D. Thomas, *Virology* **198** (1994) 288.
3. B. K. Ganser, S. Li, V. Y. Klishko, J. T. Finch and W. I. Sundquist, *Science* **283** (1999) 80.
4. W. Kratschmer, L. D. Lamb, K. Fostiropoulos and D. R. Huffman, *Nature* **347** (1990) 354.
5. M. A. Nelson, F. E. Domann, G. T. Bowden, S. B. Hooser, Q. Fernando and D. E. Carter, *Toxicol. Ind. Health* **9** (1993) 623.
6. S. H. Friedman, D. L. DeCamp, R. P. Sijbesma, G. Srdanov, F. Wudl and G. L. Kenyon, *J. Am. Chem. Soc.* **115** (1993) 6506.
7. R. Sijbesma, G. Srdanov, F. Wudl, J. A. Castoro, C. Wilkins, S. H. Friedman, D. L. DeCamp and G. L. Kenyon, *J. Am. Chem. Soc.* **115** (1993) 6510.
8. A. W. Jensen, S. R. Wilson and D. L. Schuster, *Bioorg. Med. Chem.* **4** (1996) 767.
9. T. Da Ros and M. Prato, *J. Chem. Soc., Chem. Commun.* (1999) 663.
10. T. Da Ros, G. Spalluto and M. Prato, *Croatica Chemica Acta* **74** (2001) 743.
11. A. Bianco, T. Da Ros, M. Prato and C. Toniolo, *J. Pept. Sci.* **7** (2001) 208.
12. S. Bosi, T. Da Ros, G. Spalluto and M. Prato, *Eur. J. Med. Chem.* **38** (2003) 913.
13. L. B. Piotrovsky, in *Fundamentalnye Napravleniya Molekulyarnoi Medicini*, Rostock, St.-Petersburg, 2005 (in Russian), pp. 195–268.
14. W. H. Powell, F. Cozzi, G. P. Moss, C. Thilgen, R. J.-R. Hwu and A. Yerin, *Pure Appl. Chem.* **74** (2002) 629.
15. S. Foley, C. Crowley, M. Smaih, C. Bon, B. F. Erlanger, P. Seta and C. Larroque, *Biochem. Biophys. Res. Commun.* **294** (2002) 116.
16. J. W. Arbogast, A. P. Darmanyan, C. S. Foote, F. N. Diederich, Y. Rubin, F. Diederich, M. M. Alvarez and S. J. Anz, *J. Phys. Chem.* **95** (1991) 11.
17. P. J. Krusic, P. N. Wasserman, P. N. Keizer, J. R. Morton and K. F. Preston, *Science* **254** (1991) 1183.
18. A. Bagnò, S. Claeson, M. Maggini, M. L. Martini, M. Prato and G. Scorrano, *Chem. Eur. J.* **8** (2002) 1016.

19. A. S. Foote, *Top. Curr. Chem.* **169** (1994) 347.
20. H. Barry and M. C. John, *Free Radical in Biology and Medicine*, 2nd ed., Clarendon Press, Oxford, 1982.
21. K. Briviba, L. O. Klotz and H. Sies, *Biol. Chem.* **378** (1997) 1259.
22. T. Nagano, K. Arakane, A. Ryu, T. Masunaga, K. Shinmoto, S. Mashioko and M. Hirobe, *Chem. Pharm. Bull.* **42** (1994) 2291.
23. J. W. Arbogast, C. S. Foote and M. J. Kao, *J. Am. Chem. Soc.* **114** (1992) 2277.
24. V. Ruebsam, K.-P. Dinse, M. Plueschau, J. Fink, W. Kratchmer, K. Fostiropoulos and C. Taliani, *J. Am. Chem. Soc.* **114** (1992) 10059.
25. K. C. Hwang and D. Mauserall, *J. Am. Chem. Soc.* **114** (1992) 9705.
26. A. S. D. Sandanayaka, Y. Araki, C. Luo, M. Fujitsuka and O. Ito, *Bull. Chem. Soc. Jpn.* **77** (2004) 1313.
27. V. Brezova, A. Stasko, P. Raptá, G. Domschke, A. Bartl and L. Dunsch, *J. Phys. Chem.* **99** (1995) 16234.
28. D. M. Guldi and K.-D. Asmus, *Radiat. Phys. Chem.* **56** (1999) 449.
29. F. Prat, R. Stackow, R. Bernstein, W. Quian, Y. Rubin and C. S. Foote, *J. Phys. Chem.* **103** (1999) 7230.
30. R. V. Bensasson, M. Brettreich, J. Frederiksen, H. Gottinger, A. Hirsch, E. J. Land, S. Leach, D. J. McGarvey and H. Schonberger, *Free Rad. Biol. Med.* **29** (2000) 26.
31. D. M. Guldi and M. Prato, *Acc. Chem. Res.* **33** (2000) 695.
32. V. Georgakilas, F. Pellarini, M. Prato, D. M. Guldi, M. Melle-Franco and F. Zerbetto, *Proc. Natl. Acad. Sci. USA* **99** (2002) 5075.
33. J. Eastoe, E. Crooks, A. Beeby and R. Heenan, *Chem. Phys. Lett.* **245** (1995) 571.
34. D. M. Guldi, *J. Phys. Chem. A* **101** (1997) 3895.
35. D. M. Guldi, H. Hungerbühler and K.-D. Asmus, *J. Phys. Chem.* **99** (1995) 13487.
36. O. I. Kiselev, L. V. Krylova, G. I. Djachuk and L. B. Piotrovsky, unpublished work (2000).
37. F. Moussa, F. Trivin, R. Céolin, M. Hadchouel, P.-Y. Sizaret, V. Greugny, C. Fabre, A. Rassat and H. Szwarc, *Fullerene Sci. Technol.* **4** (1996) 21.
38. F. Kasermann and C. Kempf, *Antiviral Res.* **34** (1997) 65.
39. W. A. Scrivens, J. M. Tour, K. E. Creek and L. Pirisi, *J. Am. Chem. Soc.* **116** (1994) 4517.
40. S. Deguchi, R. G. Alargova and K. Tsujii, *Langmuir* **17** (2001) 6013.
41. G. V. Andrievsky, M. V. Kosevich, O. M. Vovk, V. S. Shelkovsky and L. A. Vaschcenko, *J. Chem. Soc., Chem. Commun.* (1995) 1281.
42. J. Labille, J. Brant, F. Villiéras, J. Rose, M. Wiesner and J.-V. Bottero, *Book of Abstracts 7th Bienalle International Workshop "Fullerenes and Atomic Clusters"*, St.-Petersburg, Russia, 2005, p. 47.
43. M. V. Avdeev, A. A. Khokhryakov, T. V. Tropin, G. V. Andrievsky, V. K. Klochkov, L. I. Derevyanchenko, L. Rosta, V. M. Garamus, V. B. Priezzhev, M. V. Korobov and V. L. Aksenov, *Langmuir* **20** (2004) 4363.
44. N. O. Mchedlov-Petrosyan, V. K. Klochkov and G. V. Andrievsky, *J. Chem. Soc., Faraday Trans.* **93** (1997) 4343.
45. G. V. Andrievsky, V. K. Klochkov, E. L. Karyakina and N. O. Mchedlov-Petrosyan, *Chem. Phys. Lett.* **300** (1999) 92.

46. Yu. Prilutski, S. Durov, L. Bulavin, V. Pogorelov, Yu. Astashkin, V. Yashchuk, T. Ogul'chansky, E. Buzaneva and G. Andrievsky, *Mol. Gryst. Liq. Cryst.* **324** (1998) 65.
47. L. Bulavin, I. Adamenko, Yu. Prilutskyy, S. Durov, A. Graja, A. Bogucki and P. Scharff, *Phys. Chem. Chem. Phys.* **2** (2000) 1627.
48. I. I. Adamenko, K. O. Moroz, S. S. Durov, Yu. I. Prilutskyy, P. Scharff and T. Braun, *High Pressure Research* **23** (2003) 271.
49. P. Scharff, K. Risch, L. Carta-Abelman, I. M. Dmytruk, M. M. Bilyi, O. A. Golub, A. V. Khavryuchenko, E. V. Buzaneva, V. L. Aksenov, M. V. Avdeev, Yu. I. Prilutskyy and S. S. Durov, *Carbon* **42** (2004) 1204.
50. G. V. Andrievsky, V. K. Klochkov, A. Bordyuh and G. I. Dovbeshko, *Chem. Phys. Lett.* **364** (2002) 8.
51. G. V. Andrievsky, Book of Abstracts 7th Bienalle International Workshop "Fullerenes and Atomic Clusters", St.-Petersburg, Russia, 2005, p. 235.
52. G. V. Andrievsky, V. Yu. Galchinskaya, V. K. Klochkov, I. K. Kondakov and G. B. Shitova, Book of Abstracts 7th Bienalle International Workshop "Fullerenes and Atomic Clusters", St.-Petersburg, Russia, 2005, p. 236.
53. L. B. Piotrovsky, A. K. Sirotkin, V. V. Zarubaev, L. N. Poznyakova, T. D. Muravyeva, T. K. Krisko, I. M. Belousova and O. I. Kiselev, Book of Abstracts 7th Bienalle International Workshop "Fullerenes and Atomic Clusters", St.-Petersburg, Russia, 2005, p. 240.
54. P. Scharff, L. Carta-Abelman, O. P. Matyshevskaya, S. V. Prylutska, T. V. Koval, A. A. Golub, V. M. Yaschchuk, K. M. Kushnir and Yu. I. Prilutskyy, *Carbon* **42** (2004) 1199.
55. A. P. Burlaka, Y. P. Sidorik, S. V. Prilutska, O. P. Matyshevskaya, O. A. Golub, Yu. I. Prilutskyy and P. Scharff, *Exp. Oncol.* **26** (2004) 326.
56. C. M. Sayes, A. M. Gobin, K. D. Ausman, J. Mendez, J. L. West and V. L. Colvin, *Biomaterials* **26** (2005) 7587.
57. I. M. Belousova, Personal Communication, Institute of Laser Physics, St.-Petersburg, Russia.
58. T. Andersson, K. Nilsson, M. Sundahl, G. Westman and O. Wennerstrom, *J. Chem. Soc., Chem. Commun.* (1992) 604.
59. I. C. Wang, L. A. Tai, D. D. Lee, P. P. Kanakamma, C. K.-F. Shen, T.-Y. Luh, C. H. Cheng and K. C. Hwang, *J. Med. Chem.* **42** (1999) 4614.
60. Y. N. Yamakoshi, T. Yagami, K. Fukuhara, S. Sueyoshi and N. Miyata, *J. Chem. Soc., Chem. Commun.* (1994) 517.
61. J. P. Kamat, T. P. A. Devasagayam, K. I. Priadarsini, H. Mohan and J. P. Mittal, *Chem. Biol. Interact.* **114** (1998) 145.
62. M. G. Krakovjak, E. V. Anufrieva, L. B. Piotrovsky, T. D. Anan'eva, and T. N. Nekrasova, Russian Patent RU 2 255 942, 10.07.2005.
63. T. Tsuchiya, Y. N. Yamakoshi and N. Miyata, *Biochem. Biophys. Res. Commun.* **206** (1995) 885.
64. T. Tsuchiya, I. Ogiri, Y. N. Yamakoshi and N. Miyata, *Full. Sci. Technol.* **4** (1995) 989.
65. T. Tsuchiya, I. Ogiri, Y. N. Yamakoshi and N. Miyata, *FEBS Lett.* **393** (1995) 377.

66. A. Sakai, Y. N. Yamakoshi and N. Miyata, *Full. Sci. Technol.* **3** (1995) 377.
67. N. Sera, H. Tokiwa and N. Miyata, *Carcinogenesis* **10** (1996) 2163.
68. C. Ungurenasu and A. Airinei, *J. Med. Chem.* **43** (2000) 3186.
69. L. V. Vinogradova, E. Yu. Melenevskaya, A. S. Chahaturov, E. E. Kever, L. S. Litvinova, A. V. Novokreschenova, M. A. Sushko, S. I. Klenin and V. N. Zgonnik, *Khim. Vysokomol. Soedinen.* **40** (1998) 1854 (in Russian).
70. M. L. Sushko, S. I. Klenin, M. A. Dumpis and L. B. Piotrovsky, *Tech. Phys. Lett.* **25** (1999) 778.
71. M. L. Sushko, H. Tenhu and S. I. Klenin, *Polymer* **43** (2002) 2769.
72. R. V. Bensasson, E. Bienvenue, M. Dellinger, S. Leach and P. Seta, *J. Phys. Chem.* **98** (1994) 3492.
73. L. B. Piotrovsky, K. N. Kozeletskaya, N. A. Medvedeva, M. A. Dumpis, L. N. Poznyakova and O. I. Kiselev, *Voprosy virusologii* No 3 (2001) 38 (in Russian).
74. L. B. Piotrovsky, O. I. Kiselev, K. N. Kozeletskaya, E. Yu. Melenevskaya, L. V. Vinogradova, E. E. Kever, S. I. Klenin, V. N. Zgonnik and M. A. Dumpis, *Dokl. Akad. Nauk* **362** (1998) 547 (in Russian).
75. O. I. Kiselev, K. N. Kozeletskaya, E. Yu. Melenevskaya, L. V. Vinogradova, E. E. Kever, S. I. Klenin, V. N. Zgonnik, M. A. Dumpis and L. B. Piotrovsky, *Mol. Mat.* **11** (1998) 121.
76. L. B. Piotrovsky, M. A. Dumpis, L. N. Poznyakova, O. I. Kiselev, K. N. Kozeletskaya, M. Yu. Eropkin and A. O. Monaenkov, *Mol. Mat.* **13** (2000) 41.
77. L. B. Piotrovsky and O. I. Kiselev, *Fullerenes, nanotubes, and carbon clusters* **12** (2004) 397.
78. A. K. Sirotkin, L. B. Piotrovsky, L. N. Poznyakova and O. I. Kiselev, *Voprosy biologicheskoy, medicinskoy i farmacevticheskoy khimii* N3(2005)21–24, 2005 (in Russian).
79. L. B. Piotrovsky, R. V. Romanov, R. A. Kotelnikova, G. I. Bogdanov and A. I. Kotelnikov, *Fundamental problems of pharmacology (Thesis of the 2nd congress of Russian scientific pharmacological society)* **2** (2003) 84, Moscow.
80. R.A. Lamb and R. M. Krug, in *Fields Virology*, 4th ed., Eds. D. M. Knipe and P. M. Howley, Lippincott-Raven, Philadelphia, PA., 2001, pp. 1487–1531.
81. Y. Yamakoshi, N. Umezawa, A. Ryu, K. Arakane, N. Miyata, Y. Goda, T. Mazumizu and T. Nagano, *J. Am. Chem. Soc.* **125** (2003) 12803.
82. R. C. Richmond and U. J. Gibson, *US Patent* **5**, 310 669 (May 10, 1994).
83. A. Golub, O. Matyshevskaya, S. Prilutskaya, V. Sysoyev, L. Ped, V. Kudrenko, E. Radchenko, Yu. Prilutsky, P. Scharff and T. Braun, *J. Mol. Liq.* **105** (2003) 141.
84. Yu. I. Prilutskyy, V. M. Yashchuk, K. M. Kushnir, A. A. Golub, V. A. Kudrenko, S. V. Prilutskaya, I. I. Grynyuk, E. V. Buzaneva, P. Scharff, T. Braun and O. P. Matyshevskaya, *Mater. Sci. Eng. C* **23** (2003) 109.
85. D. Guldi, M. Maggini, G. Scorrano, M. Prato, A. Bianco and C. Toniolo, *J. Inf. Rec.* **24** (1998) 33.
86. D. A. Bass, J. W. Parce and L. R. Dechatelet, *J. Immunol.* **130** (1983) 1910.
87. R. Clothier, G. Starzec and L. Pradel, *ATLA* **30** (2002) 493.
88. M. Yu. Eropkin and E. M. Eropkina, unpublished work (2005).
89. Y. Tabata and Y. Ikada, *Pure Appl. Chem.* **71** (1999) 2047.

90. E. Oberdörster, *Environmental Health Perspectives* **112** (2004) 1058.
91. F. Moussa, P. Chretien, P. Dubois, L. Chuniaud, M. Dessante, F. Trivin, P.Y. Sizaret, V. Agafonov, R. Ceolin, H. Szwarc, V. Greugny, C. Fabre and A. Rassat, *Fullerene Sci. Technol.* **3** (1995) 333.
92. F. Moussa, P. Chrétien, M. Pressac, F. Trivin, H. Szwarc and R. Céolin, *Fullerene Sci. Technol.* **5** (1997) 503.
93. F. Moussa, F. Trivin, R. Céolin, M. Hadchouel, P-Y. Sizaret, V. Greugny, C. Fabre, A. Rassat and H. Szwarc, *Fullerene Sci. Technol.* **4** (1996) 21.
94. M. Satoh, K. Matsuo, Y. Takanashi and I. Takayanagi, *Gen. Pharmacol.* **26** (1995) 1533.
95. T. Baierl, E. Drosselmeyer, A. Seidel and S. Hippeli, *Exp. Toxicol. Pathol.* **48** (1996) 508.
96. L. P. Zakharenko, I. K. Zakharov, E. A. Vasiunina, T. V. Karamysheva, A. M. Danilenko and A.A. Nikiforov, *Genetika* **33** (1997) 405.
97. F. Moussa, S. Roux, M. Pressac, E. Génin, M. Hadchouel, F. Trivin, A. Rassat, R. Céolin and H. Szwarc, *New J. Chem.* (1998) 989.
98. I. Ya. Podolsky, E. V. Kondrat'eva, I. V. Schheglov, M. A. Dumpis and L. B. Piotrovsky, *Phys. Solid States* **44** (2002) 552.
99. I. Ya. Podolski, E. A. Kosenko, E. A. Mugantseva, E. G. Makarova, Yu. G. Kaminsky, G. V. Andrievsky, V. K. Klochkov and L. I. Derevyanchenko, *Book of Abstracts 7th Bienalle International Workshop "Fullerenes and Atomic Clusters"*, St.-Petersburg, Russia, 2005, p. 241.
100. T. Baierl, A. Siedel, *Fullerene Sci. Technol.* **4** (1996) 1073.
101. P. J. A. Born, *Inhalation Toxicology* **14** (2002) 311.
102. E. Bermudez, J. B. Magnum, B. A. Wong, B. Asgharian, P. M. Next, D. B. Warheit and J. I. Everitt, *Toxicol. Sci.* **77** (2004) 347.
103. I. Lamparth and A. Hirsch, *J. Chem. Soc., Chem. Commun.* (1994) 1727.
104. Y.-L. Lin, H.-Y. Lei, T.-Y. Luh, C.-K. Chou and H.-S. Liu, *Virology* **275** (2000) 258.
105. M. Iwata, T. Mukai, Y. N. Yamakoshi, S. Hara, T. Yanase, M. Shoji, T. Endo and N. Miyata, *Full. Sci. Techn.* **6** (1998) 213.
106. A. Bianco, C. Corvaja, M. Crisma, D. M. Guldi, M. Maggini, E. Sartori and C. Toniolo, *Chem. Eur. J.* **8** (2002) 1544.
107. J. E. Kim and M. Lee, *Biochem. Biophys. Res. Commun.* **303** (2003) 576.
108. C. R. Prabha, R. Patel and C. N. Murthy, *Fullerenes, nanotubes, and carbon nanoclusters* **12** (2004) 405.

## Chapter 10

### Separation of metallic and semiconducting single-walled carbon nanotubes

Yi Lin, K. A. Shiral Fernando, Wei Wang and Ya-Ping Sun

Department of Chemistry and Laboratory for Emerging Materials and Technology,  
 Clemson University, Clemson, South Carolina 29634-0973, USA

#### 1. INTRODUCTION

Carbon nanotubes are one-dimensional carbon allotropes. They are cylindrical hollow structures, with the conjugated carbon network forming one or multiple concentric atomic layers of thin walls, known as single-walled carbon nanotubes (SWNT) or multiple-walled carbon nanotubes (MWNT), respectively. An SWNT (or an MWNT layer) may be formed conceptually by rolling up a graphene sheet into cylindrical structure [1–3]. This requires a chiral vector  $C_h$ , consisting of two primitive vectors ( $C_h = n\mathbf{a}_1 + m\mathbf{a}_2$ ), to match the graphitic carbon atoms from edge to edge (Fig. 1). The chiral vector, often referred to as the chiral index ( $n, m$ ) (or chirality, helicity), uniquely defines the diameter ( $d$ ) and the chiral angle ( $\theta$ ) of the SWNT:

$$d = \frac{\sqrt{3}a_{c-c}}{\pi} \sqrt{n^2 + nm + m^2} \quad (1)$$

$$\theta = \tan^{-1}[\sqrt{3}m/(2n + m)] \quad (2)$$

where  $a_{c-c}$  ( $\sim 0.142$  nm) is the nearest-neighbor C–C distance.

It is now well established, both theoretically and experimentally, that a SWNT can be either semiconducting or metallic (including semi- or quasi-metallic) in nature, which is referred to as “metallicity”. The SWNT metallicity depends upon its chirality: if  $n - m \neq 3q$  ( $q$  is an integer), its electronic density of states (DOS) exhibits a significant band-gap near the Fermi level, and the SWNT is semiconducting; if  $n - m = 3q$ , the conductance and valence bands overlap, and the SWNT is metallic (semi-metallic when  $n \neq m$ ). Thus, the ratio of semiconducting and metallic SWNTs in a statistically as-grown mixture is 2:1. In fact, a tiny difference in the nanotube chirality could result in distinctively different properties. For example, (10,10) and (11,9) SWNTs have almost identical diameters (1.356 vs. 1.358 nm) and minor differences in their chiral angles ( $30^\circ$  vs.  $26.7^\circ$ ), but they are metallic (continuous DOS near Fermi level) and semiconducting (a band-gap of  $\sim 0.64$  eV), respectively.



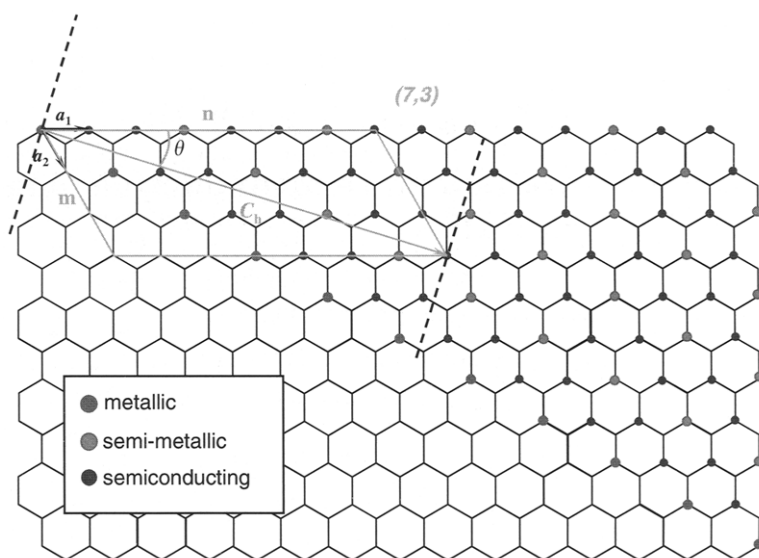


Figure 1. The conceptual SWNT formation by rolling up a graphene sheet. As an example, the dashed lines represent the two edges that will merge in the rolling up of a (7,3) semiconducting SWNT.

There have been many reports and predictions on the superior materials properties of carbon nanotubes, including those relevant to their potential electrical, mechanical, thermal, optical, and other applications [4,5]. Many of these applications depend strongly on the metallic and semiconducting characteristics of carbon nanotubes. For example, semiconducting SWNTs are necessary in field-effect transistor (FET) devices [6] (including those for chemical [7] and biological sensors [8]) and electroluminescent and photovoltaic materials [9–11]. Metallic SWNTs are required for nano-circuitry [12], transparent conductive coatings, and polymeric nanocomposites of unique electrical properties [13,14]. Therefore, the availability of SWNT samples of desired metallic or semiconducting characteristics for their respective applications is of paramount importance.

Semiconducting and metallic SWNTs differ not only in their electrical conductivities, but also in other physical and chemical aspects, such as static polarizability, doping properties, chemical reactivities, and some other electronic structure-induced characteristics. Conversely, the different properties between the two types of SWNTs make possible their identification and separation. As first reported by the IBM group in 2001 [15], metallic SWNTs could be selectively eliminated via current-induced electrical breakdown to leave behind semiconducting SWNTs for FET devices. Since then, there has been great interest in the research community in preparing nanotube samples containing only metallic or semiconducting SWNTs. Significant progress has been achieved in the development of

methodologies and merits for metallic/semiconducting enrichment in nanotube production or post-production separation, projecting a promising future for the research field.

In this chapter, we will review most of the currently available strategies and experimental methods for enriched metallic or semiconducting SWNTs and provide a perspective on the further development. We will begin with a brief introduction on the techniques that are commonly used or required for the differentiation and characterization of metallic and semiconducting SWNTs.

## 2. IDENTIFICATION AND CHARACTERIZATION

A number of micro- and macroscopic techniques have been used for the characterization and differentiation of semiconducting vs. metallic SWNTs in a given sample. Qualitative information on whether a sample is enriched with one kind of SWNT could usually be obtained rather conveniently. However, despite much effort and recent advances, a quantitative evaluation of either mixed or enriched samples is by no means a trivial task. Summarized here are some commonly used characterization techniques. Their advantages and disadvantages, especially with respect to the more challenging quantitative evaluation, are discussed.

### 2.1. Microscopic techniques

Microscopic techniques are those based on “counting” individual nanotubes, in which the semiconducting or metallic SWNTs are identified one by one to build a data set for statistical analysis. Among the most sophisticated are the uses of microscopy methods to image each SWNT at atomic resolution to determine its chirality (Fig. 2). Unfortunately, this is hardly straightforward experimentally for routine practices, even in light of the recent rapid advances in scanning tunneling microscopy (STM), scanning tunneling spectroscopy (STS) [16,17], and high-resolution transmission electron microscopy (HR-TEM) [18,19] instrumentations. High-resolution electron diffraction technique has been used in the characterization of bundled SWNTs, but its applicability to the determination of nanotube chirality is probably limited [20,21].

Other methods in this category include those based on direct electrical measurement of individual nanotubes. For example, the  $I$ - $V$  relationship of nanotube devices can be determined, with the assistance of atomic force microscopy (AFM), to identify the metallic or semiconducting nature of the underlying nanotube [22]. Alternatively, selective current-induced electrical breakdown could be used [22] (Sec. 3.2). In this method, the electrodes are bridged with multiple SWNTs. By ramping the current at controlled gate voltage (so that no current is passed through semiconducting SWNTs), metallic SWNTs are burned off one by one, providing individual abrupt changes (counts) in the electrical signal. The semiconducting SWNTs are then turned on and similarly burned off one-by-one, providing the other data set of counting (Fig. 3).

In the use of electrical counting methods, especially those based on the electrical breakdown, the controlled fabrication of microelectrodes that are in excellent contact with the nanotubes is a significant technical challenge. Other issues also

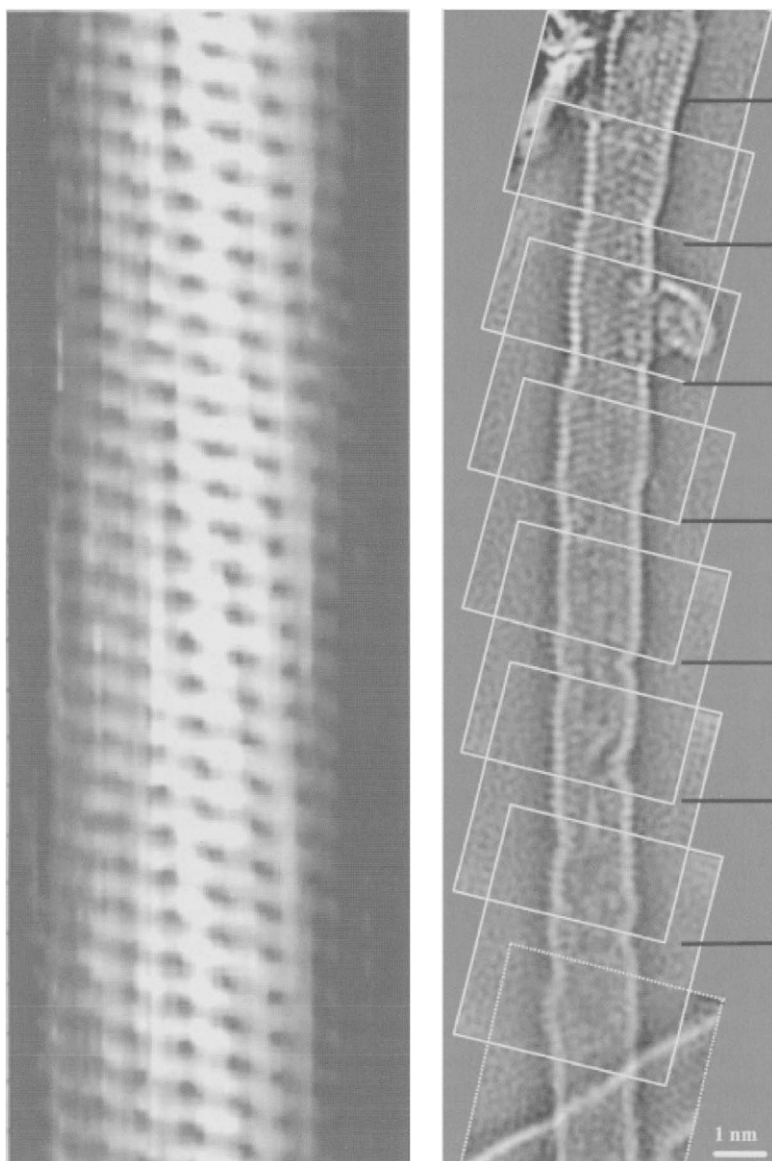


Figure 2. High-resolution STM (left) and TEM (right) images of SWNT. (Reproduced from Refs. [3] and [19], respectively, with permission. Copyright © 1999 American Chemical Society and 2003 The Royal Microscopical Society.)

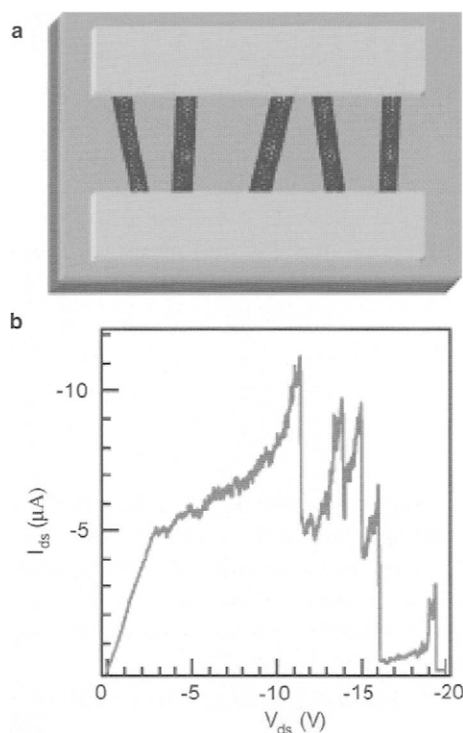


Figure 3. (a) Schematic drawing of a five-SWNT-in-parallel transistor device. (b)  $I_{ds}$  vs.  $V_g$  showing sequential electrical breakdown of the SWNTs in the device. (Reproduced from [22] with permission. Copyright © 2004 American Chemical Society.)

include the presence of semi-metallic SWNTs in the sample [23], the interference owing to strong current oscillations for semiconducting SWNTs at current saturation and high source-drain biases [23], and the bundling of nanotubes [15]. For bundling, in particular, it is inevitable that some of the semiconducting SWNTs will be sacrificed in the devices containing bundled SWNTs before metallic SWNTs can all be destroyed (counted) [15]. Therefore, when the counting technique is applied to a bulk sample, exhaustive solution processing is often required to exfoliate the nanotube bundles [24,25].

## 2.2. Macroscopic techniques

Macroscopic characterization techniques measure the properties of an assembly of nanotubes. These include various spectroscopic methods, and certainly, bulk electrical conductivity measurements.

### 2.2.1. Optical absorption

Both semiconducting and metallic SWNTs have optical signatures in the visible and near-IR wavelength regions, corresponding to their respective electronic transitions. Because of the quantum confinement effect, the DOS of SWNT is characterized by well-defined spike-like features, known as van Hove singularities [1,2]. In a simple tight-binding model, the energy separation of each van Hove singularity pair is inversely related to the nanotube diameter  $d$  and weakly dependent upon the chiral angle  $\theta$ . The energy gaps in semiconducting ( $S_{ii}$ ) and metallic SWNTs ( $M_{ii}$ ) can be approximately expressed as follows [26]:

$$S_{11} = 2\gamma_0 a_{c-c} / d; S_{22} = 4\gamma_0 a_{c-c} / d; \dots \quad (3)$$

$$M_{11} = 6\gamma_0 a_{c-c} / d; \dots \quad (4)$$

where  $\gamma_0$  is C–C tight-binding overlap energy ( $\sim 2.4$ – $3.0$  eV),  $a_{c-c}$  is the nearest neighbor C–C distance ( $\sim 0.142$  nm), and  $d$  the nanotube diameter. The inverse relationship between the band-gap energies and the tube diameter was concisely presented as a comprehensive plot by Kataura and coworkers (“Kataura Plot”, Fig. 4) [27]. The plot has subsequently been modified on the basis of available experimental energy gap data for semiconducting SWNTs [28–32].

According to the tight-binding approximation (Formulas (3) and (4)), the diameter of SWNTs is in the range of  $\sim 0.7$ – $1.8$  nm, thus  $S_{11}$  of 1–0.4 eV (1240–3100 nm),  $S_{22}$  of 2–0.8 eV (620–1550 nm), and  $M_{11}$  of 3–1.2 eV (410–1030 nm). For currently available samples from different production methods, these optical absorption features are distinctive without severe overlapping if SWNTs in the sample are in a relatively narrow diameter range (Fig. 5). The optical density of each nanotube transition obeys Beer’s Law [33]. However, the relationship between the absorption cross-sections of different SWNTs and their chiralities is still unclear. Experimentally, technical issues, such as the necessary corrections for the effect of light scattering (due to the aggregation of nanotubes) and for the  $\pi$ -plasmon background, should be carefully considered when optical absorption is used in the quantitative evaluation of metallic and semiconducting SWNTs [33,34]. The doping of nanotube surface (either covalently or non-covalently) may significantly suppress or diminish  $S_{11}$  and in some cases  $S_{22}$  transitions [35–39].

The DOS of metallic (“armchair”,  $n=m$ ) SWNTs in bundles and semi-metallic ( $n-m=3q$ ,  $n \neq m$ ) ones exhibit only a small gap at milli-electronvolt level, and thus optical transitions in the far-IR region [40]. This small energy gap in the metallic SWNTs may disappear upon chemical alteration of the conjugated carbon structure, such as in carbene addition [41,42], in addition to its extreme sensitivity toward various doping effects. The far-IR absorption feature may serve as a qualitative tool in the probing of reactions with metallic SWNTs, as demonstrated by Haddon and coworkers [40–42]. Its potential in quantitative evaluations is yet to be explored.

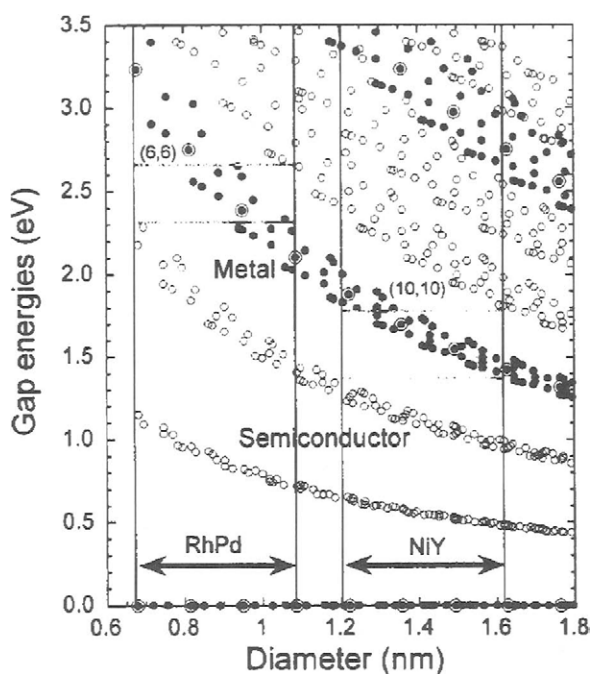


Figure 4. The original Kataura plot: the relationship of SWNT band-gap energies with the nanotube diameter ( $\bullet$ : metallic SWNTs;  $\circ$ : semiconducting SWNTs). Arrows indicate the diameter distribution of SWNTs produced from two different catalysts. Two horizontal lines in each catalyst area define the “metallic window” in which the optical transitions are from the metallic SWNTs only. (Reproduced from Ref. [27] with permission. Copyright © 1999 Elsevier Science S. A.)

### 2.2.2. Fluorescence spectroscopy

Well-dispersed semiconducting SWNTs exhibit weak but distinctive band-gap fluorescence (Fig. 6) [24]. The excitation and emission energy contour plot follows a characteristic pattern, making it possible to directly determine the  $(n,m)$  values of semiconducting SWNTs present in the sample [28]. Conversely, the  $S_{11}$  and  $S_{22}$  energies have been determined from the experimental excitation–emission data [29]. Metallic SWNTs are practically non-fluorescent, which somewhat limits the applicability of the characterization technique. The fluorescence in semiconducting SWNTs is vulnerable to quenching associated with inter-tube interactions in bundled nanotubes. A sample preparation procedure involving ultrasonication and ultracentrifugation in the presence of surfactant is typically required [24]. Since only a tiny fraction of the bulk sample under consideration is “extracted” in the procedure, there is need for caution in the extrapolation of the observed fluorescence properties to the entire sample.

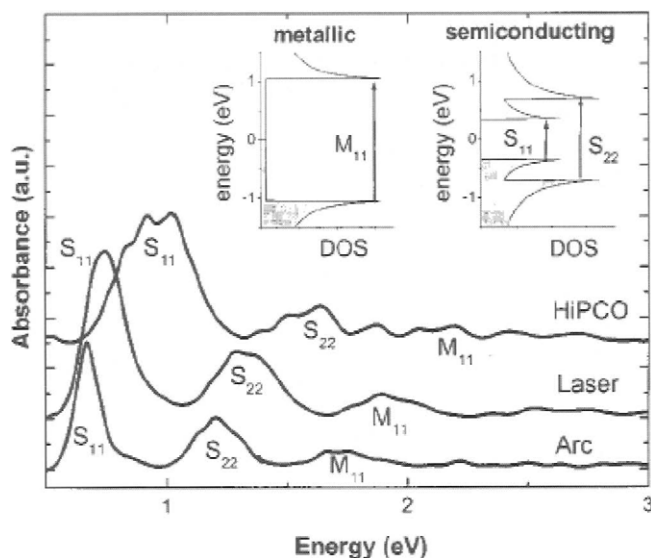


Figure 5. Absorption spectra (after baseline correction) of films of SWNTs from HiPco, laser ablation, and arc-discharge methods. Insets are schematic DOS plots for metallic and semiconducting SWNTs. (Reproduced from Ref. [26] with permission. Copyright © 2001 American Chemical Society.)

### 2.2.3. Raman spectroscopy

In Raman measurements of SWNTs, the nanotube signals are resonantly enhanced when the excitation wavelength is close to the optical transitions (usually  $S_{22}$ ,  $S_{33}$ ,  $M_{11}$ ) [43,44]. In other words, metallic or semiconducting SWNTs of certain diameters are sensitive only to selected Raman excitation wavelengths. There are three sets of Raman signals for SWNTs that reveal the most information:  $G$ -band at  $\sim 1550\text{--}1600\text{ cm}^{-1}$  from vibrations of graphitic  $\text{sp}^2$  carbons (tangential and parallel to the tube axis),  $D$ -band at  $\sim 1350\text{ cm}^{-1}$  from disordered  $\text{sp}^3$  carbons, and radial breathing mode (RBM, tubular carbon vibrations in the radial direction) peaks in the low-frequency region of  $\sim 100\text{--}300\text{ cm}^{-1}$ . The  $G$ -band and RBM peaks are more useful to both qualitative and quantitative evaluations of metallic and semiconducting SWNTs.

The two kinds of SWNTs have different  $G$ -band line-shapes [45,46]. The two components of the  $G$ -signal,  $\omega_G^-$  at lower frequency ( $\sim 1560\text{ cm}^{-1}$ ) and  $\omega_G^+$  at higher frequency ( $\sim 1590\text{ cm}^{-1}$ ), are related to vibrations at the tangential direction and parallel to the tube axis, respectively. The  $\omega_G^-$  component is similar in both metallic and semiconducting SWNTs, a sharp Lorentzian peak narrow in line width. The  $\omega_G^+$  component in semiconducting SWNTs is also Lorentzian in shape, but the same component in metallic SWNTs is asymmetrical and much broader, known as Breit-Wigner-Fano (BWF) lineshape (Fig. 7). Thus, at a given Raman excitation

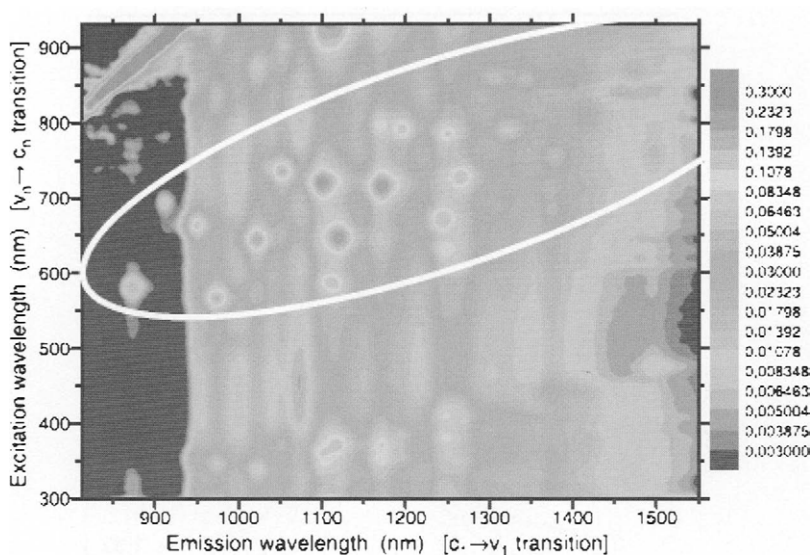


Figure 6. Contour plot of band-gap fluorescence intensity vs. excitation and emission wavelengths for an SDS-assisted SWNT dispersion in D<sub>2</sub>O. (Reproduced from Ref. [28] with permission. Copyright © 2002 The American Association for the Advancement of Science.)

wavelength, the observation of BWF lineshape for the *G*-band is commonly used as a qualitative indicator for the presence of metallic SWNTs.

The position of a nanotube RBM signal is inversely proportional to its diameter:

$$\omega_{\text{RBM}} = c_1/d + c_2 \quad (5)$$

where  $d$  is the diameter of the SWNT and  $c_1$  and  $c_2$  empirical parameters available in various reports [28,30,44,47,48]. Thus, by using the RBM region in a Raman spectrum, one can easily estimate the diameter distribution of the SWNTs that are in resonance with the excitation wavelength. In single-molecule Raman spectroscopy, where only one SWNT is detected, it is possible to assign the nanotube chirality [49,50]. There have also been similar chirality assignments based on Raman results of surfactant-assisted individual SWNT dispersions [28,30].

In the evaluation of metallic and semiconducting SWNTs, it is important to know the electronic types and diameters of SWNTs that are resonant with the given Raman excitation wavelength. A particularly useful guide is the Kataura Plot, which visually depicts the relationship between the nanotube diameters and their corresponding transition energies [27–32]. Several precautions are also advised with respect to the use of Raman RBM modes in determining the metallic or semiconducting enrichment in a sample. First, multiple excitation wavelengths are always necessary to obtain



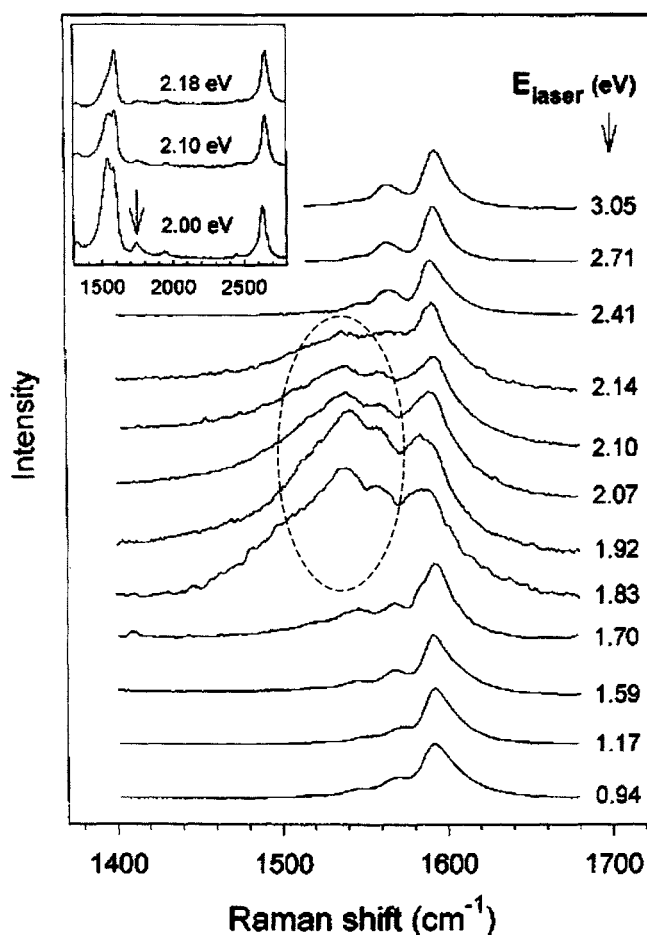


Figure 7. Raman tangential mode spectra of SWNTs obtained with several different laser lines. The BWF G-band features (in the dashed ellipse) are obvious at laser energies of 1.83–2.14 eV. The inset shows low-resolution Raman spectra in 1300–2800  $\text{cm}^{-1}$  in the critical range of laser energies 2.00–2.18 eV. (Reproduced from Ref. [45] with permission. Copyright © 1998 The American Physical Society.)

overall information on a given sample because of the resonance effect. The construction of total RBM maps is helpful if (quasi-) continuous Raman excitations are available (Fig. 8) [51]. Second, RBM is very sensitive to the nanotube bulk morphology, namely that the same SWNT sample with a distribution of chiralities (diameters) after different processing procedures could have different relative RBM intensities for the various tubes that are in resonance [52,53]. Third, the relative RBM intensities of

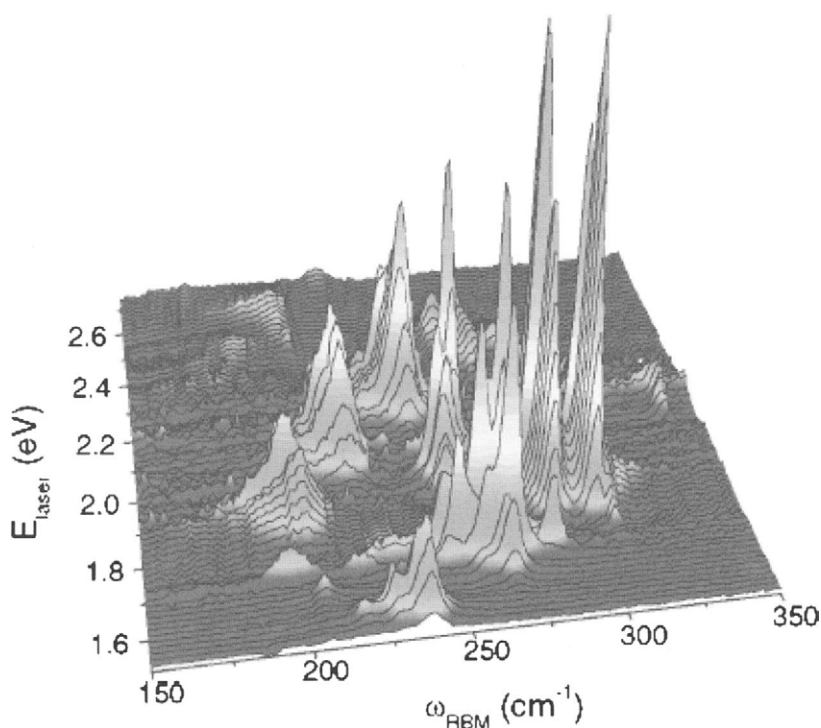


Figure 8. A Raman RBM “map” obtained with 76 different laser lines for HiPco-SWNTs dispersed in aqueous SDS solution. (Reproduced from Ref. [51] with permission. Copyright © 2004 The American Physical Society.)

different nanotubes in a Raman spectrum do not quantitatively represent their relative abundance because of the resonance effect, although each signal itself may be comparable in different samples providing the sample morphology is strictly controlled. Recently, several comprehensive and quantitative evaluations of nanotube diameter selectivity and metallic/semiconducting enrichment in SWNT samples have been reported [54,55].

#### 2.2.4. NMR spectroscopy

As predicted theoretically, the chemical shifts of nanotube carbons in metallic and semiconducting SWNTs are different, with the latter  $\sim 12$  ppm up-field shifted (lower in chemical shift value) owing to the effect of localized ring current [56]. In a recent NMR investigation of functionalized SWNTs ( $^{13}\text{C}$  enriched) in both solution and solid state, Kitaygorodskiy et al. [57] observed two resolved nanotube carbon signals (Fig. 9). The two signals are separated by 10–15 ppm, consistent with those of metallic and semiconducting SWNTs. Separately, the relaxation times of the

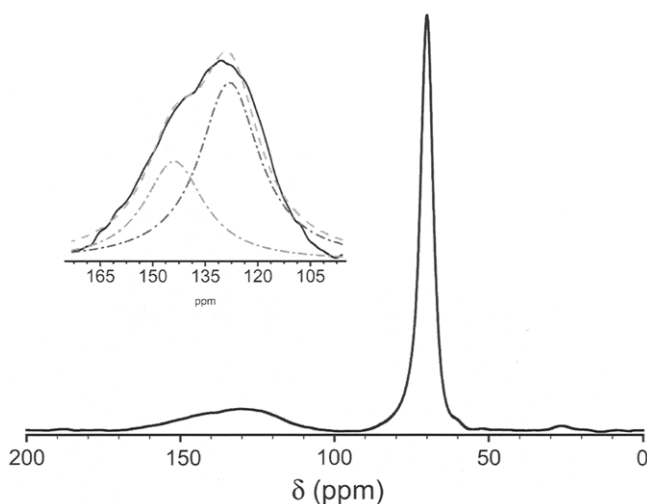


Figure 9. The  $^{13}\text{C}$  NMR spectrum of a functionalized  $^{13}\text{C}$ -enriched SWNT sample in  $\text{D}_2\text{O}$  solution. Shown in the inset is a deconvolution based on two Lorentzian peaks, tentatively assigned to metallic (higher  $\delta$ ) and semiconducting (lower  $\delta$ ) SWNTs. (Reproduced from Ref. [57] with permission. Copyright © 2005 American Chemical Society.)

carbons in metallic and semiconducting SWNTs are known to be different, with the former being much shorter [58]. Thus, the carbon NMR technique based on more accurate determination of chemical shifts and/or relaxation times may find increasing applications in qualitative and quantitative evaluations of metallic and semiconducting SWNTs in mixed or enriched samples.

### 2.2.5. Bulk conductivity

The electrical conductivity of bulk SWNT samples is commonly measured by using the classical four-point probe technique [59]. However, the absolute values of electrical conductivity thus measured are easily affected by some external factors in the experiments, so that caution is necessary in the data interpretation. On the other hand, the relative conductivity values for different samples are generally comparable if measured under the same conditions, which thus allows for a meaningful evaluation of samples enriched with metallic or semiconducting SWNTs at different levels [60,61]. Tetrahertz conductivity measurements have also been applied for similar purposes [62–64].

## 3. ENRICHMENT AND SEPARATION

Three major production methods for SWNTs are arc-discharge [65], laser ablation [25], and chemical vapor deposition [66–68] (CVD, including the HiPco or

high-pressure carbon monoxide disproportionation method [69]). The nanotube samples from these production methods are widely considered as containing the statistical distributions of metallic (1/3) and semiconducting (2/3) SWNTs. There have been claims for enriched content of armchair nanotubes in the laser ablation samples, but the available experimental evidence is hardly conclusive. The nanotubes produced by the arc-discharge and laser ablation methods have relatively narrower diameter distributions, with means at  $\sim 1.5$  and  $1.4$  nm, respectively. The nanotubes from the HiPco process have smaller but broadly distributed diameters ( $0.7$ – $1.2$  nm).

The arc-discharge and laser ablation methods are similar in the way that SWNTs form as a result of the organization of gaseous carbon atoms in the presence of proper metal catalysts, where the carbon evaporation is achieved in the high-energy bombardment of graphite targets by arcing and laser, respectively. In the CVD production, SWNTs are grown on catalyst nanoparticles (floating or on substrates) in a flow of precursor gas. Thus, the CVD method generally allows more flexibility in the experimental configuration and control over the conditions for the nanotube formation. Discussed next are reports on the use of CVD for selectivity in the growth of a certain nanotube type or nanotubes of metallic or semiconducting characteristics.

### 3.1. Selective growth in production

Bachilo et al. [70] reported that a narrow chirality distribution of SWNTs could be achieved by using silica-supported Co–Mo catalysts in carbon monoxide CVD (CoMoCAT SWNTs). The distribution was visualized in terms of a contour excitation–emission spectrum of the as-produced sample (Fig. 10), which suggested significant enrichment in (6,5) and (7,5) SWNTs (semiconducting). Interestingly, Miyauchi et al. [71] used a completely different combination of carbon source and catalysts (alcohol CVD with zeolite-supported Fe/Co catalysts) to produce samples of similar chirality selectivity, enriched in near-armchair tubes, especially (6,5) and (7,5) SWNTs. These CVD conditions are apparently in favor of small-diameter armchair-like nanotubes, but their selectivity toward metallic vs. semiconducting SWNTs was not reported.

The selective growth of semiconducting SWNTs has been reported by Li et al. [22]. These authors used plasma-enhanced methane CVD with uniform iron catalysts to synthesize SWNTs on silica substrates. According to evaluations of direct electrical measurements by AFM and the current-induced electrical breakdown method, the sample was found to contain almost 90% semiconducting SWNTs. The diameter distribution in these nanotubes was relatively broad ( $0.7$ – $1.5$  nm), and the average diameter could be altered by tuning the plasma power. The samples with smaller average diameters were found to be richer in semiconducting SWNTs [72]. According to their density functional theory calculation, semiconducting SWNTs may have lower formation energies per unit length than metallic SWNTs of similar diameters, and the difference may be more pronounced in the smaller-diameter regime [72].

There have been reports on utilizing atomically ordered structure of substrates to template the nanotube formation for aligned SWNTs or MWNTs with some

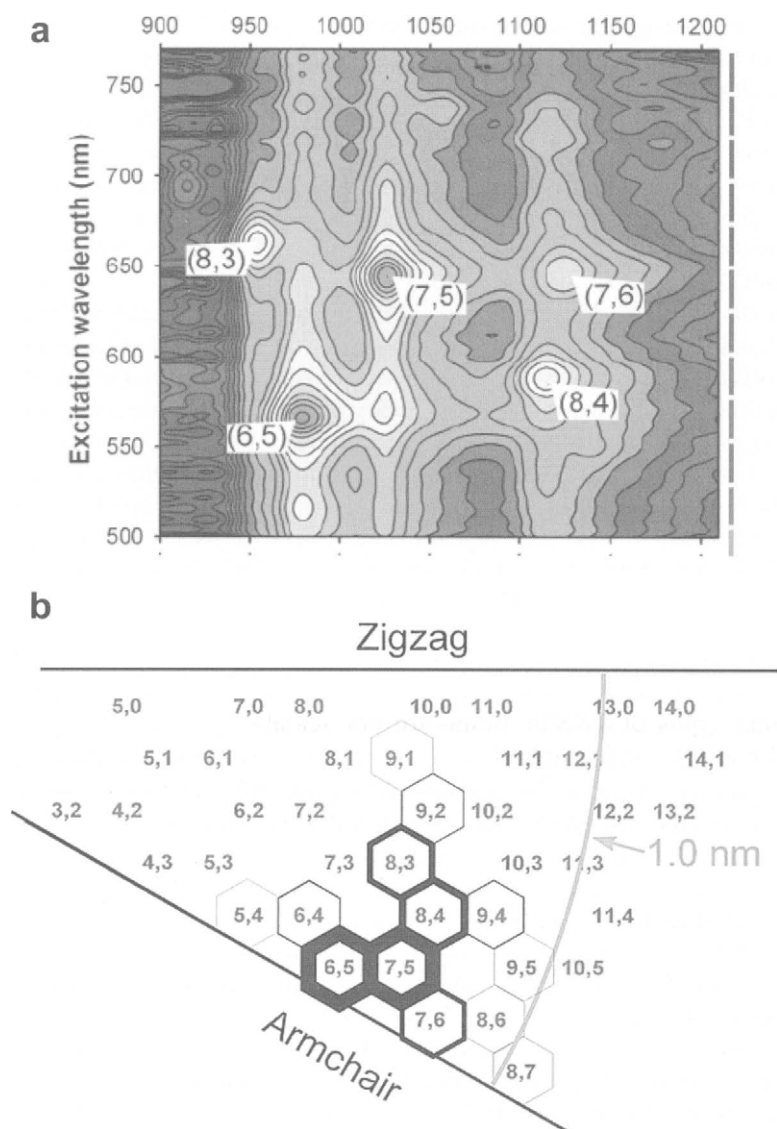


Figure 10. Contour plots of (top) normalized fluorescence intensities and (bottom) the corresponding  $(n,m)$ -abundance map for the CoMoCAT-SWNTs. Only semiconducting SWNTs are showed. For the  $(n,m)$  map, the thickness of each hexagon cell is proportional to the observed fluorescence intensity for that structure. (Reproduced from Ref. [70] with permission. Copyright © 2003 American Chemical Society.)

chirality selectivity [73,74], suggesting a possibility that SWNTs of a desired chirality might be prepared by engineering the substrate [75].

External electric field has also been used to influence the growth of one kind of SWNTs [76,77]. For example, the axial polarizability values of semiconducting SWNTs (inversely proportional to the square of tube diameter) are much smaller than those of metallic SWNTs (infinitely large) [78]. In addition, the static polarizability of SWNTs in the axial direction is much higher than that in the cross-sectional direction. Thus, when the nanotubes were allowed to rotate freely during growth (not in contact with substrate), short metallic SWNTs could be preferentially aligned in an external electric field during growth, as observed by Joselevich and Lieber [76]. The merit of such an *in situ* differentiation method is somewhat similar to the post-production separation methods discussed below in that the strategy is to differentiate one electronic type from the other by taking advantage of their difference in properties.

### 3.2. Post-production enrichment

The post-production enrichment and separation methodologies developed in the past few years took advantage of the different physical (different conductive behavior and static polarizability) or chemical (preferential non-covalent and covalent reactions) properties of metallic and semiconducting SWNTs. Some of the methods allow the collection of one type of SWNTs by physically altering (or even destroying) the other type, while others facilitate the enrichment or separation of both types of SWNTs. Some are not scalable (sub-milligram quantity or less) and might be only applicable at device level, while others have been practiced at bulk level from milligrams to grams. Because of their more significant practical implications, the bulk separation methods will be discussed separately in Sec. 3.3.

#### 3.2.1. Current-induced electrical breakdown

Current-induced electrical breakdown was first used by Collins et al. [15,79] as a post-production method to selectively obtain semiconducting SWNTs for FET devices. In the practice, bundled SWNTs were deposited across the source/drain microelectrodes. On the basis of the assumption that metallic and semiconducting SWNTs in the bundle were in equally efficient contact with the electrodes, electrical current was applied at controlled gate voltage ( $V_g$ ) such that the current could pass through metallic but not semiconducting SWNTs. At high enough current level, defects formed and propagated along the metallic SWNTs because of self-heating-induced oxidation (in air), eventually leading to their breakdown (Fig. 11). Semiconducting SWNTs, on the other hand, remained insulating at the applied  $V_g$  and thus left behind. The same strategy was applied to the fabrication of FET devices from MWNTs, whose metallic layers could be stripped off until a semiconducting one became available for transport [15].

Recently, it was demonstrated that the current-induced electrical breakdown could also be applicable to devices containing multiple individual SWNTs bridging the electrodes. According to Li et al. [22] (see also Secs. 2 and 3.1), wide source/drain

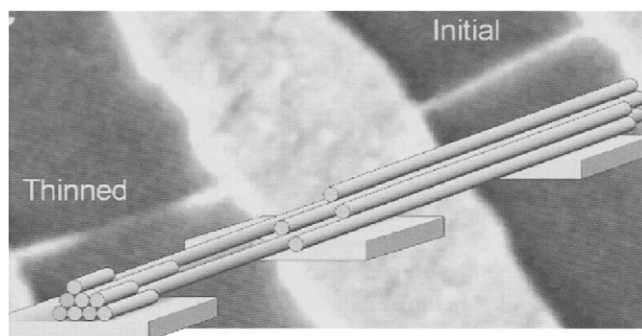


Figure 11. An SEM image, overlaid by a schematic drawing, illustrates the partial electrical breakdown of a SWNT bundle. (Reproduced from Ref. [15] with permission. Copyright © 2001 The American Association for the Advancement of Science.)

electrodes were fabricated on top of individual SWNTs grown on  $\text{SiO}_2/\text{Si}$  substrate from plasma-enhanced CVD. The  $V_g$  was held at + 10 V to deplete the semiconducting SWNTs (predominantly *p* type). When the bias was increased, the individual bridging metallic SWNTs preferentially failed, sending abrupt changes in the electrical output (Fig. 3).

The electrical breakdown mechanism is not unique to metallic SWNTs. It works for semiconducting SWNTs as well if there is sufficiently high current passing through the nanotubes with the control of  $V_g$  sign (usually negative) and bias magnitude. In fact, this is the basis for the statistical counting of SWNTs in terms of their electrical type, as discussed earlier (Sec. 2.1).

### 3.2.2. Alternating current dielectrophoresis

The initial purpose of alternating current dielectrophoresis (ac DEP) was to deposit suspended carbon nanotubes between electrodes for their alignment [80,81]. Because of their much higher polarizability, metallic SWNTs could be preferentially aligned under ac field [82], an effect somewhat similar to the electric field-induced alignment of metallic SWNTs during their growth [76] (see Sec. 3.1). As reported by Krupke et al. [82], a drop of a surfactant-assisted individual SWNT dispersion was placed on an ac DEP chip operated at 10 MHz. Directional nanotube deposition between the electrodes was observed (Fig. 12). When compared to the sample of SWNTs deposited on Si without ac DEP, the results from Raman characterization seemed to suggest that the electrode-deposited SWNTs were enriched with metallic SWNTs.

Baik et al. [83] essentially repeated the same experiment and found similar changes in Raman features. However, they suspected that the morphological difference of the samples contributed, at least in part, to the observed RBM signal profile “change”. For example, the RBM profile in the spectrum of the sample from ac DEP

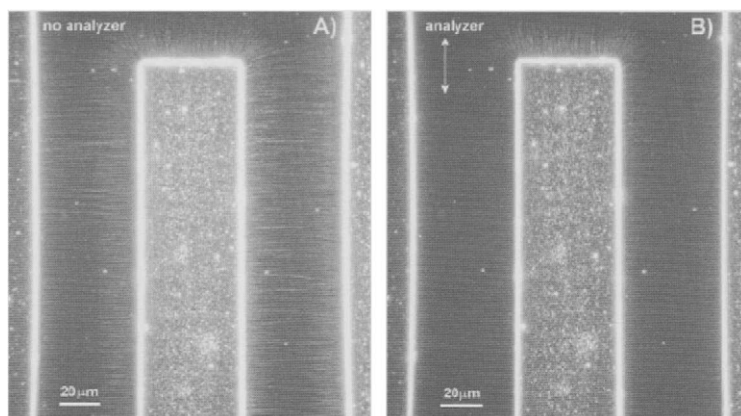


Figure 12. Rayleigh scattered light from the dielectrophoretically deposited SWNTs and the electrodes, recorded with an incident-light dark-field microscope. The scattered light from the aligned SWNTs appears green to the eye (A) and is polarized perpendicular to the electrodes (B). (Reproduced from Ref. [82] with permission. Copyright © 2003 The American Association for the Advancement of Science.)

(supposedly with enriched metallic SWNTs) was almost identical to that of a sample without ac DEP (Fig. 13). Therefore, it might make more sense to compare Raman spectra of the nanotube dispersion before and after ac DEP (enriched with semiconducting SWNTs as a result of preferential deposition of metallic SWNTs) [84] since fewer morphological problems are expected.

The preferential deposition of metallic SWNTs occurs only at certain frequencies where semiconducting SWNTs experience negative DEP force (repelled by electrodes) while metallic ones experience positive DEP force (attracted toward electrodes) [82,85,86]. At low enough ac frequency, semiconducting SWNTs can also be attracted toward the electrodes, although with a somewhat less positive DEP force compared to that for metallic SWNTs [85,87]. Dimaki and Bøggild suggested that even under such conditions, reasonably enriched deposition of metallic SWNTs could be expected if a microfluid device was used [87]. The crossover frequency for semiconducting SWNTs (DEP force = 0) was found to be around 10 MHz at a surfactant concentration between 0.1 and 1% [85]. In other words, only at frequencies above 10 MHz, metallic SWNTs can be selectively attracted toward the electrodes.

The quantities of the separated samples by ac DEP are currently at nanogram level at best [82] since an individual SWNT dispersion is necessary to achieve enough differentiation between the two nanotube types. The deposition efficiency from a single ac DEP experiment is also low, in which only  $\sim 0.1\%$  of the starting SWNT material is collected at electrodes [82]. Thus, recycling the SWNT dispersion for deposition is definitely needed for improved separation [86,87].



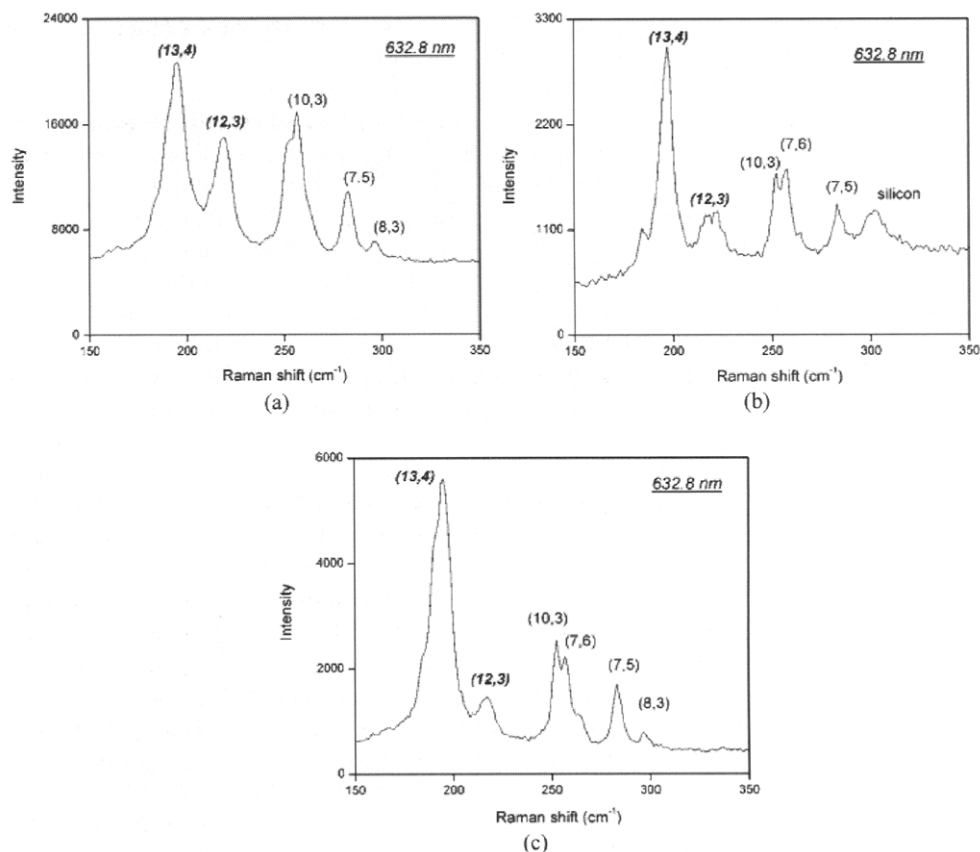


Figure 13. Raman spectra (the RBM region, 632.8 nm excitation) of specimens starting from an SDS-assisted HiPco-SWNT dispersion: (a) material dried on a glass slide; (b) dielectrophoretically deposited material; and (c) acetone-induced precipitates. (Reproduced from Ref. [83] with permission. Copyright © 2003 American Chemical Society.)

### 3.2.3. DNA-assisted separations

Zheng et al. [88] found that single-stranded DNAs (ssDNAs), such as those with enriched thymidine (T) units (polyT) and specially alternative guanine (G) and T units (poly(G/T)) [89], readily adsorb onto the nanotube surface and efficiently disperse SWNTs upon ultrasonication. After ultracentrifugation, dispersions enriched with individual nanotubes could be obtained, as evidenced by the presence of well-resolved bands in their adsorption and fluorescence spectra. ssDNAs are negatively charged species and thus express linear negative charge on the wrapped SWNTs. Based on the theoretical conclusion that metallic and semiconducting SWNTs have

different polarizabilities, resulting in different linear charge densities in the ssDNA-wrapped SWNTs, Zheng et al. injected the dispersion into an anionic exchange column for separation. The optical absorption (Fig. 14) and Raman results were consistent with the expectation that the early fractions were enriched with metallic SWNTs.

The elution in ion-exchange chromatography is based on charge density, not the total charge. Therefore, unlike other chromatography techniques [90–97], this method is not suited for sorting in terms of nanotube lengths. On the other hand, smaller-diameter semiconducting SWNTs are of higher polarizabilities and thus relatively lower charge density when wrapped by ssDNAs [89,98,99]. Therefore, these SWNTs are also eluted in early fractions (Fig. 14). Since the diameter effect is more pronounced for smaller-diameter nanotubes, the ssDNA-assisted ion exchange chromatography technique is in principle more suitable for starting SWNTs of a larger average diameter. Nevertheless, the diameter selectivity did allow the isolation of predominantly (6,5) semiconducting SWNTs from the nanotube sample produced by the CoMoCAT method [100–102].

Arnold et al. [103] recently used centrifugation to separate ssDNA-wrapped SWNTs in solutions with a density gradient media. Upon the centrifugation, the nanotubes formed discrete colored bands in the centrifuge tubes. Optical absorption studies showed that these discrete bands were due to ssDNA-wrapped SWNTs of different average diameters. It seemed that the larger the diameter of the semiconducting nanotube, the higher the hybrid density (in the range of 1.11–1.17 g/mL). A (6,5)-enriched fraction was also obtained from CoMoCAT SWNTs.

For either ion-exchange chromatography or density gradient centrifugation, the use of ssDNAs for preparative separation is probably cost prohibitive. In fact, ssDNAs have no preferential interactions with different types of SWNTs, serving only as an effective nanotube dispersion agent in the separation method. In principle, it may be possible to replace ssDNAs with other molecules as dispersion agents for the same functions. For example, polyelectrolytes that can non-covalently disperse SWNTs and express uniform charge density on the nanotubes might be used in the ion-exchange chromatography. Many surfactant-assisted SWNT dispersion [24,104,105] or different soluble functionalized SWNTs [106–112] might be explored in the separation based on density gradient centrifugation.

### 3.2.4. Preferential doping

Halogens, such as bromine, are known to readily complex with carbon nanotubes [35,36,113,114]. Furthermore, theoretical calculations suggested that the binding energies of bromine with metallic SWNTs are larger than those with semiconducting ones [115,116]. Chen et al. [115] added diluted bromine solution to a surfactant-assisted individual SWNT dispersion, stirred vigorously, and separated immediately in ultracentrifugation. If the same density ( $1.0 \text{ g/cm}^3$ ) for all of the initial surfactant-coated individual SWNTs is assumed, the preferential doping of bromines on metallic SWNTs should result in higher relative densities of the corresponding complexes. It was found that the sediment was enriched to some degree with metallic SWNTs according to optical absorption characterization after the

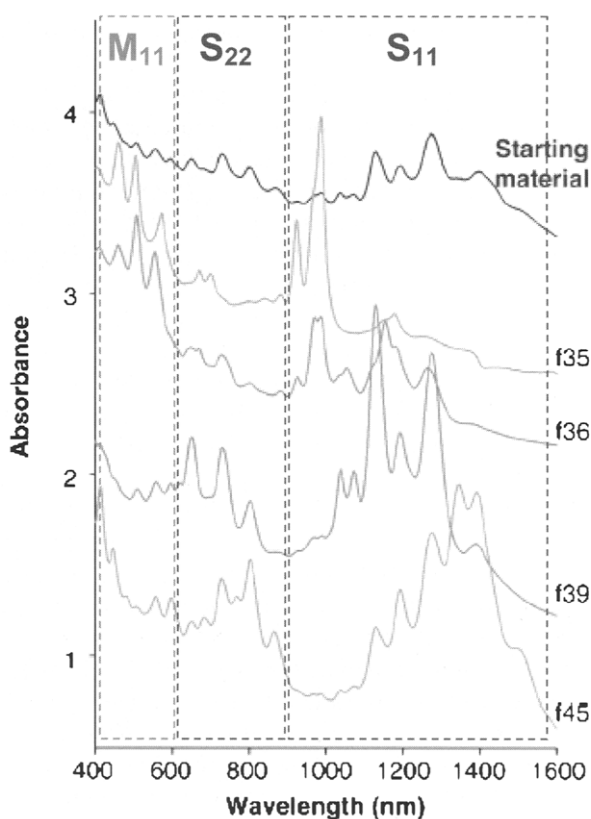


Figure 14. Absorption spectra of starting DNA-wrapped HiPco-SWNTs and fractionated samples from anionic exchange chromatography. The dashed rectangles define approximate regions for metallic and semiconducting optical transitions. (Reproduced from Ref. [89] with permission. Copyright © 2003 The American Association for the Advancement of Science.)

de-doping via annealing at a high temperature (Fig. 15). The supernatant, on the other hand, was enriched with semiconducting SWNTs.

For semiconducting SWNTs, many doping reactions are in fact band-gap dependent. Dopants such as protons [24,38] and some small inorganic and organic molecules [100,117] preferentially interact with larger-diameter semiconducting SWNTs, which have smaller band-gaps, according to optical absorption and fluorescence studies. However, no related fractionation or separation effort has been reported.

### 3.2.5. Preferential covalent functionalization

Covalent sidewall chemistries of SWNTs have been attributed largely to the curvature-induced pyramidization and  $\pi$ -orbital misalignment [109]. The nanotube

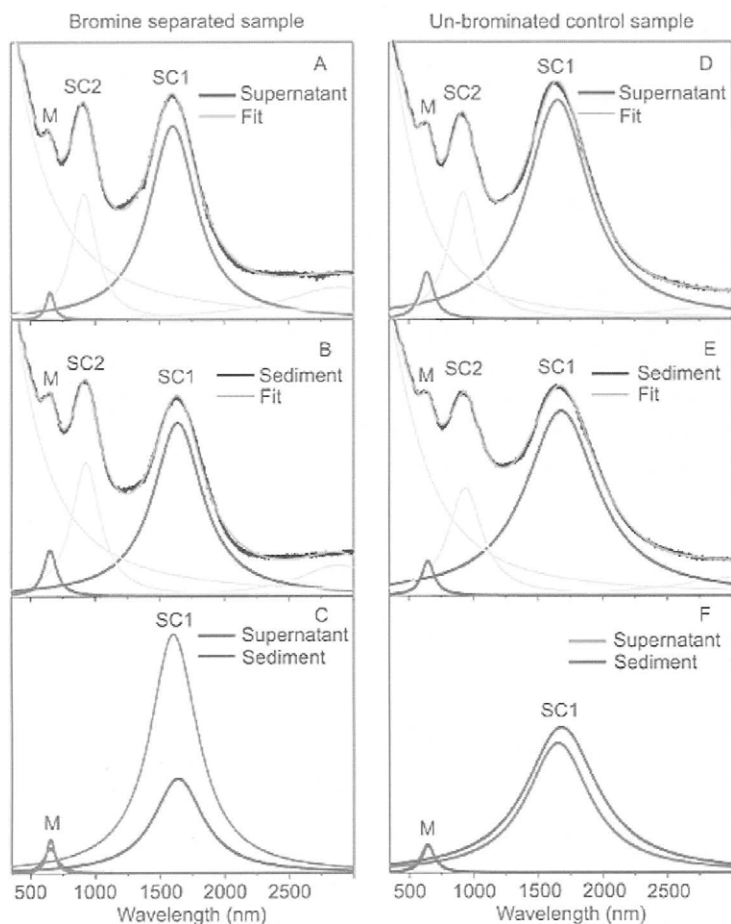


Figure 15. An absorption spectroscopic analysis for the Br-assisted enrichment of metallic SWNTs. (A) Absorption spectrum for a Br-separated supernatant sample overlaid fit to five Lorentzians. The two Lorentzians corresponding to the metallic ( $M: M_{11}$ ) and semiconducting (SC1:  $S_{11}$ ) bands are highlighted. (B) The same for the corresponding sediment sample. (C) Comparison of the Lorentzians from A and B normalized to the same underlying metallic band areas. (D–F) Corresponding spectra, fits, and comparison for a control sample (no Br). (Reproduced from Ref. [115] with permission. Copyright © 2003 American Chemical Society.)

functionalization strategies reported so far resemble those of either fullerenes or graphite [106–111]. Some of these reactions were recently found to be in favor of metallic SWNTs over their semiconducting counterparts, which have been rationalized by considering the metallic nanotubes as better electron donors [118,119].

Tour and co-workers applied the diazonium chemistry, previously known for graphite derivatization, to the sidewall functionalization of SWNTs [37,107]. Recently, Strano et al. [120] titrated a surfactant-assisted SWNT aqueous dispersion with an aryl diazonium reagent, 4-chlorobenzenediazonium tetrafluoroborate and found a gradual decrease in the  $M_{11}$  band in the optical absorption spectra (Fig. 16). Raman results also supported that the metallic SWNTs were preferentially reacted with the diazonium compound [32,120]. However, whether the reaction involves a charge-transfer mechanism (aryl cations) seems still a subject of debate [121].

Semiconducting SWNTs are also reactive with diazonium compounds, though with a lower reactivity, which makes the separation less effective at least at the bulk level. Dyke et al. [122] carefully derivatized SWNTs with the controlled addition of diazonium compounds containing different polar and non-polar addends for the purpose that the functionalized metallic and semiconducting SWNTs would have polarity difference due to the different addend composition and/or density.

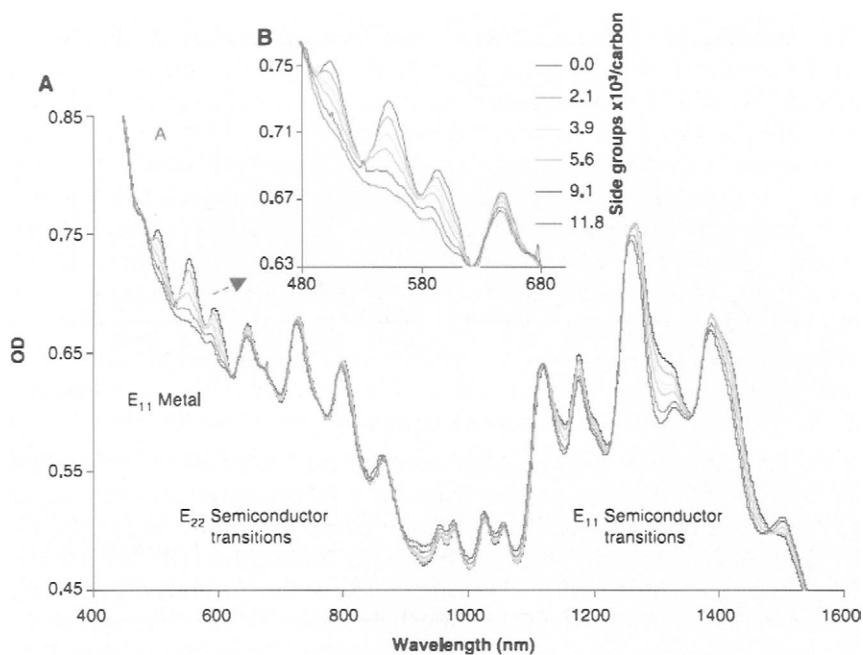


Figure 16. (A) The evolution of absorption spectrum of SDS-assisted SWNT dispersion after the addition of various amounts of 4-chlorobenzenediazonium tetrafluoroborate (in mol/1000 mol carbon). (B) Expanded view of the metallic region. (Reproduced from [120] with permission. Copyright © 2003 The American Association for the Advancement of Science.)

The soluble product was then separated via silica gel chromatography according to the polarity difference, but the resulting enrichments in the separated metallic and semiconducting fractions were marginal.

Preferential sidewall addition of nitronium cations to SWNTs, similarly derived from graphite chemistry, were also evaluated in terms of the selectivity toward metallic and semiconducting nanotubes and the nanotube diameters. An et al. [64] used rather extreme reaction conditions (60 °C for 4 weeks or sonication for 24 h) in the reaction of a nitronium compound with SWNTs. According to Raman (Fig. 17) and optical absorption results, most metallic SWNTs (smaller diameter in particular) were destroyed to become soluble carbonaceous species, whereas the reaction for semiconducting SWNTs was to a considerably lesser extent so that their tubular structures were largely preserved and could be recovered upon thermal defunctionalization. A sample enriched in semiconducting SWNTs could thus be obtained by simple filtration to remove soluble carbonaceous species (from destroyed metallic SWNTs) followed by heat removal of functional groups [64].

Banerjee and Wong suggested that metallic SWNTs are more reactive than their semiconducting counterparts in another type of covalent SWNT functionalization reaction—the solution-phase osmylation reaction with  $\text{OsO}_4$  under narrow UV illumination [123]. The rationale was that the selectivity is likely due to the well-known electron-accepting behavior of  $\text{OsO}_4$ , as found in the reactions with alkenes or arenes [124,125]. They argued that  $\text{OsO}_4$  might have formed a charge-transfer intermediate (short-lived ion pair) with SWNTs in the initial step of reaction (similar to the diazonium [120] and nitronium [64] additions), for which the availability of electrons at the Fermi level in metallic SWNTs is probably more favorable.

The selectivity in sidewall functionalization reactions has found useful application in the fabrication of SWNT-based devices of dominating semiconducting behavior. For example, An et al. [126] reported that the metallic behavior in the devices could be effectively removed by the controlled addition of a diazonium reagent and also recovered by subsequent thermal treatment to defunctionalize the modified SWNTs. In another report, Balasubramanian et al. [127] used an electrochemical approach for the selective reaction of a diazonium compound with metallic SWNTs by turning the semiconducting SWNTs to the insulating state. The purpose of these studies was to obtain high-performance FET devices.

In most of the sidewall covalent reactions, that the reactivity is curvature-induced and diameter-dependent (more reactive for the smaller-diameter SWNTs) is a significant issue. It complicates the use of such reactions for the purpose of metallicity separation. For example, in the nitronium addition, only small-diameter metallic SWNTs were destroyed in the process [64]. In some cases, the diameter-selectivity could be predominant, as found in the solution-phase ozonolysis [128].

### 3.2.6. Other merits

There are theoretical calculations suggesting that some other chemical processes may be selective toward one chirality/metallicity. For example, according to the density functional calculations of Seo et al. [129],  $\text{CO}_2$  should selectively be adsorbed on the open edge of semiconducting zigzag SWNTs ( $m = 0$ , e.g. (10,0)) over that of

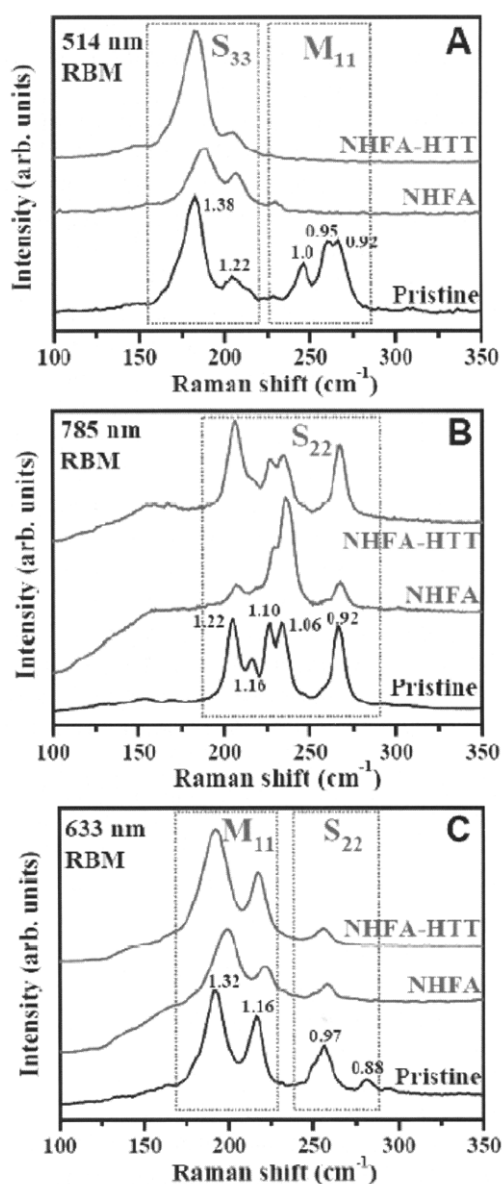


Figure 17. Raman spectra (the RBM region) of pristine SWNTs, the residual sample on the filter after the nitronium treatment (NHFA), and the residual sample with further heat treatment at 1000 °C in vacuum (NHFA-HTT) with excitations of (A) 514, (B) 785, and (C) 633 nm. The resonantly enhanced RBM regions are enclosed with rectangles and denoted to be corresponding to the respective absorption features. (Reproduced from Ref. [64] with permission. Copyright © 2005 American Chemical Society.)

metallic armchair tubes ( $n = m$ , e.g. (5,5)). Such  $\text{CO}_2$  adsorption will eventually etch away the carbons from the zigzag tubes, while armchair ones remain intact. Similar selective adsorption will not happen with the use of other oxygen-containing gases, such as  $\text{O}_2$ ,  $\text{CO}$ ,  $\text{NO}$ , and  $\text{NO}_2$ , also according to the calculations [129].

Several uncommon experimental methods and merits have been reported for selectively obtaining or eliminating certain types of SWNTs. For example, Hassanien et al. [130] claimed that hydrogen plasma was selective toward metallic SWNTs according to Raman and STM studies. In another report, Tan et al. [131] applied optical tweezer technology to trap SWNTs at the center of the laser beam. The electric field component of the laser induces a dipole in a nanotube, which pushes the nanotube in the direction of optical density gradient toward the center of the laser beam. The authors suggested that semiconducting SWNTs are more prone to such optical trapping force, which may result in a minor enrichment in semiconducting nanotubes in the isolated trapped sample. Separately, Maehashi et al. [132] proposed an interesting method to use a high-energy laser beam to selectively eliminate SWNTs of certain chiralities. As discussed earlier, when the band-gap transition energies of SWNTs match with the laser excitation wavelengths, the Raman signals for the respective nanotube vibration modes are resonantly enhanced [44] (Fig. 18). Similarly, the resonance with the high-energy laser irradiation may result in the depletion of the corresponding types of nanotubes. This could apparently be achieved at moderate laser power ( $10 \text{ kW/cm}^2$ ) according to Raman characterization of the affected sample [132].

### 3.3. Toward bulk separation

Most of the available methods for the post-production separation of metallic and semiconducting SWNTs are limited by their ability to handle only a very small quantity of sample. The methods based on covalent functionalization have additional issues of being invasive, and thus there are concerns about the potential for damage to the nanotube electronic structures. To achieve effective separation for samples in bulk quantities, highly selective but less invasive techniques are obviously more desirable. In addition, the final products should also be easily distinguishable by their relatively simple physical characteristics. Several methods satisfying some of these requirements have been developed, which show promise of being scalable toward bulk separation.

#### 3.3.1. Separation with amines

Prolonged heating of a mixture of nitric acid-treated SWNTs and octadecylamine (ODA) melt, first reported by Chen et al. [133], is a simple functionalization reaction for the nanotube solubilization. Mechanistically, it was proposed that the interaction is primarily zwitterionic between the amines and the nanotube broken end/surface defect-derived carboxylic acids [133]. However, Chattopadhyay et al. [60] noticed that after a thorough washing to remove free unbound molecules, the amount of ODA functionalities incorporated was much larger than what would have been possible even if all carboxylic acid moieties on acid-treated SWNTs (usually <5%) were converted into zwitterions with the amines. In light of the reports on surface self-organization behavior of ODA [134,135] and the ready amine physisorption



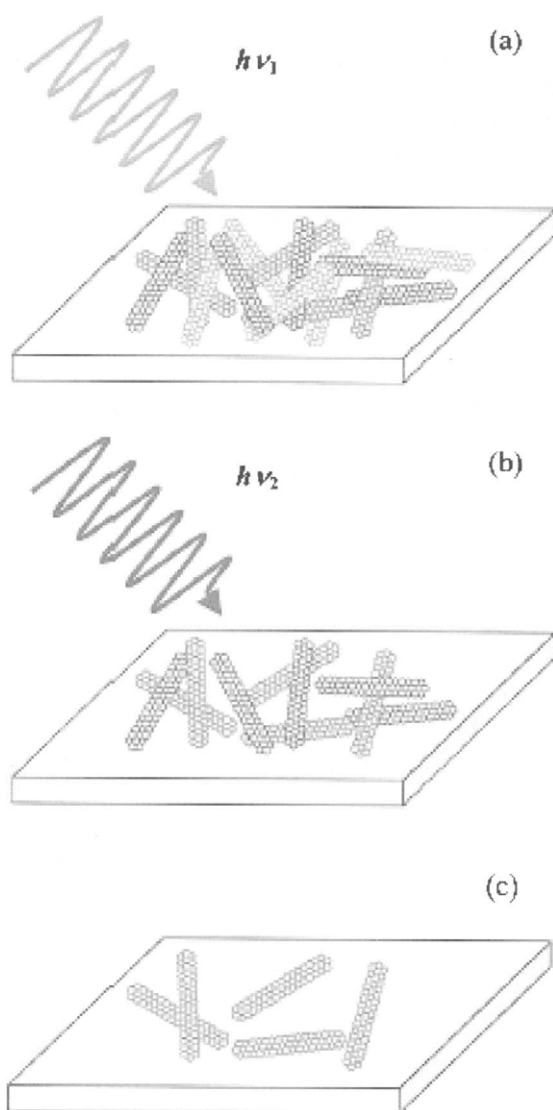


Figure 18. Schematic illustration of the laser resonance chirality selection method. The SWNTs with specific chirality that are at resonance with the energy of the excitation laser beam (indicated by color match) are selectively removed after the intense laser irradiation. (Reproduced from Ref. [132] with permission. Copyright © 2004 American Institute of Physics.)

on SWNTs [136], these authors made an intuitive suggestion that there was massive ODA adsorption on the nanotube surface and the adsorption was stable enough to sustain the solvent extraction [60]. Separately, it was demonstrated that the adsorption of small amine molecules on semiconducting SWNT FET devices could change the nanotube transport properties from *p*- to *n* type, while the metallic nanotube devices were not sensitive to the amine exposure [7,137]. According to Kong et al. [137], the wide energy continuum of DOS near the Fermi level in metallic SWNTs likely made them insensitive toward the charge-transfer effects induced by amine species. On the basis of these experimental facts and their own observation, Chattopadhyay et al. [60] suggested that the massive ODA functionalities on the nanotube surface beyond the zwitterionic interaction would apply only to semiconducting SWNTs (Fig. 19). As a result, ODA-functionalized semiconducting SWNTs should possess much higher solubility than their metallic counterparts, allowing the separation of the two types of nanotubes in terms of their solubility difference in a solvent like THF.

The Raman spectroscopy and electrical conductance results were supportive of the conclusion that the two separated samples were each enriched with either metallic (the less soluble fraction) or semiconducting SWNTs (the more soluble fraction). In a more quantitative evaluation of the enrichment in the separated fractions, Samsonidze et al. [54] carried out Raman measurements by using two laser wavelengths, with one (2.33 eV, or 532 nm) exciting small-diameter metallic (resonant with higher-energy  $M_{11}$ ) and large-diameter semiconducting (lower-energy  $S_{33}$ ) SWNTs (from HiPco method) and the other (1.96 eV or 632 nm) for the opposite (resonant with lower-energy  $M_{11}$  and higher-energy  $S_{22}$ ). The spectral deconvolution of the Raman RBM peaks (Fig. 20) allowed the identification of the metallic and semiconducting nanotube signals according to the Kataura plot (energy-diameter dependence). By assuming a starting metallic-to-semiconducting ratio of 1:2, the same ratios for the separated less- and more-soluble fractions were 1.14:2 and 1:10.4, respectively, further supporting the enrichment conclusion. The separation method is in principle scalable to larger sample quantities.

For SWNTs produced from the HiPco process, there is a wide distribution of nanotube diameters. ODA was found to be highly selective toward smaller-diameter SWNTs (average  $\sim 0.9$  nm) [54,55]. Poor enrichment result was also obtained for SWNTs produced from the laser-ablation method (average diameter  $\sim 1.4$  nm). Therefore, the ODA separation of metallic and semiconducting SWNTs is more suitable for smaller-diameter nanotubes. One may speculate that the curvature in smaller-diameter semiconducting SWNTs enhances the amine adsorption.

### 3.3.2. Separation with planar aromatic molecules

The non-covalent attachment of planar aromatic molecules like pyrene to SWNTs has been well established. It was proposed that the pyrene moieties readily anchor on the nanotube graphitic surface via  $\pi$ - $\pi$  stacking interactions [138]. For the functionalization and solubilization of carbon nanotubes based on the non-covalent interactions, various oligomeric and polymeric compounds containing pyrene [39,139–143] and tetraazaannulenes [144,145] (including porphyrins [61,146–148]

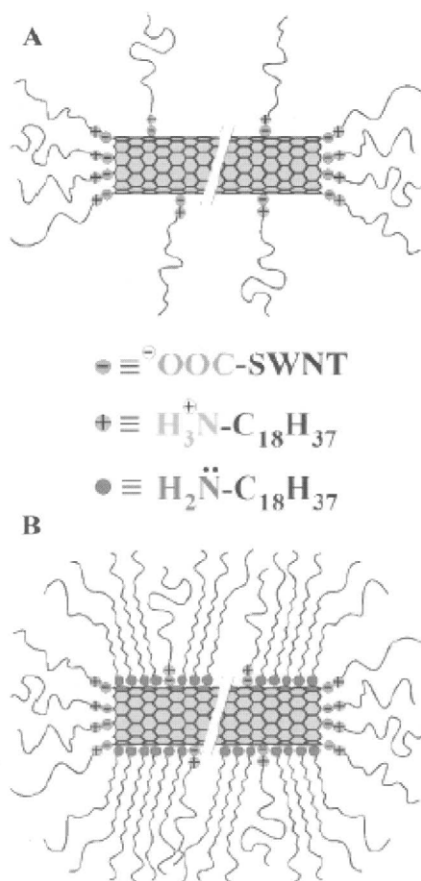


Figure 19. Schematic illustration of the interaction modes of ODA with purified SWNTs with defect attached carboxylic acids: (A) zwitterion formation only for metallic SWNTs and (B) both zwitterion formation and adsorption-assisted organization of ODA on SWNT sidewalls for semiconducting SWNTs. (Reproduced from Ref. [60] with permission. Copyright © 2003 American Chemical Society.)

and phthalocyanines [149,150]) or even some rigid conjugated polymers [151] have been used successfully.

Li et al. [61] employed a free-base porphyrin compound with four tethered long alkyl chains, 5,10,15,20-tetrakis (hexadecyloxyphenyl)-21*H*,23*H*-porphine (THPP), for the solubilization of SWNTs via the non-covalent interactions. Interestingly, however, the experiments yielded a considerably more significant finding that the solubilization was selective toward semiconducting SWNTs—namely that the soluble fraction was enriched with semiconducting SWNTs and the insoluble residue was enriched with metallic SWNTs (Fig. 21). The conclusion was supported by all

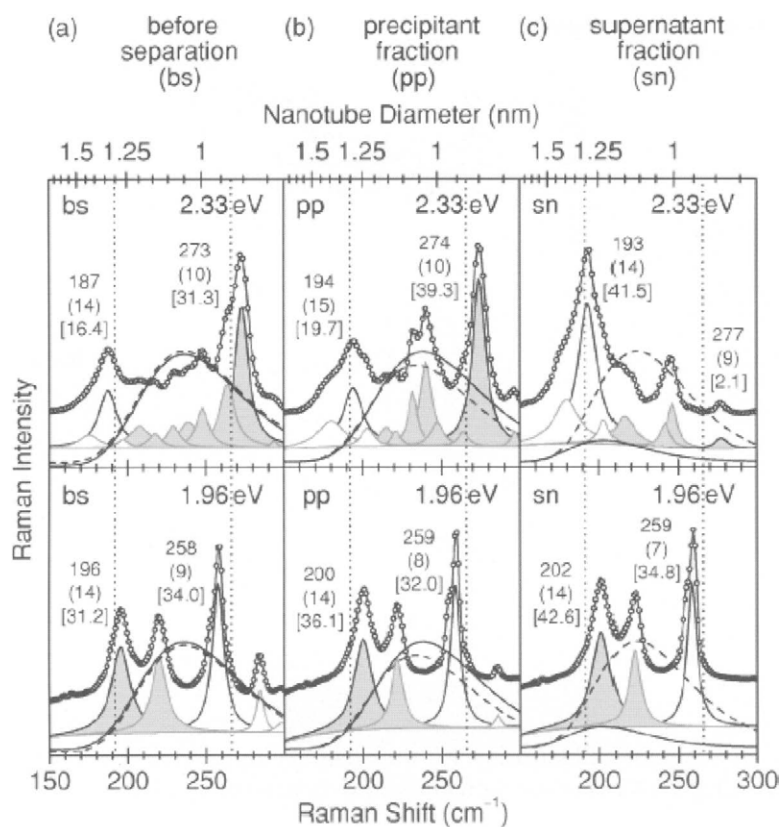


Figure 20. A Raman analysis (based on RBM features) of the ODA-assisted enrichment by using two excitation wavelength (top: 2.33 and bottom: 1.96 eV). Each spectrum was deconvoluted into Lorentzians that were individually assigned to RBM features from either metallic (grey) or semiconducting (white) SWNTs, according to Kataura Plot. (Reproduced from Ref. [54] with permission. Copyright © 2004 American Institute of Physics.)

of the results from optical absorption, Raman, and bulk conductivity measurements [61]. The fact that the porphyrins in the soluble fraction could readily be removed via simple solvent extraction for the recovery of clean semiconducting SWNTs was consistent with the interactions being non-covalent in nature. The separation method is simple, amenable to scale-up, and also effective. In addition to porphyrins, other planar aromatic molecules, such as those containing pyrene moieties (for example, 1-docosyloxymethyl-pyrene or DomP [152]), were also found to be effective in selectively solubilizing semiconducting SWNTs. According to the subsequent experimental results, sample fractions containing at least 80%

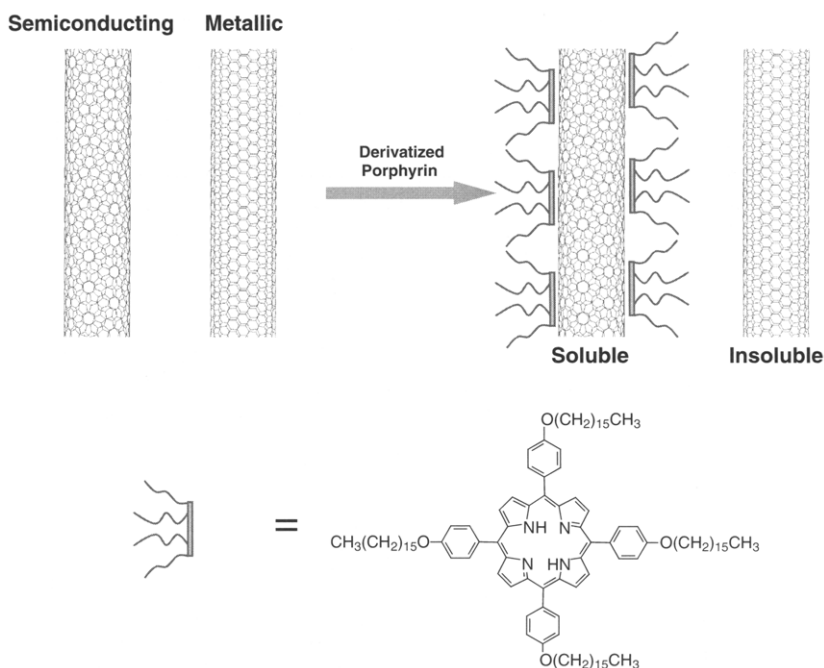


Figure 21. A schematic illustration for the selective interactions of porphyrin with semiconducting SWNTs for the semiquantitative separation [61,152].

metallic or 85% semiconducting SWNTs can be obtained from the separation (Fig. 22) [152].

Mechanistically, Li et al. [61] proposed that the two types of SWNTs, those with intrinsic defects or those from the oxidative treatment in their purification, should have different surface properties. The surface of a semiconducting SWNT in the presence of solvent might be viewed as being similar to those of radical ion pairs, favorable to interactions with relatively large planar aromatic molecules. The presence of such interactions, strong in some respect, was reflected by the dramatic changes in the optical absorption of the semiconducting SWNTs upon the attachment of the aromatic moieties. As shown in Fig. 23, while the attachment of DomP made the nanotubes soluble, it also diminished both  $S_{11}$  and  $S_{22}$  transitions characteristic of semiconducting SWNTs [39]. In this sense, the non-covalent interactions between pyrene moieties and the nanotube may be considered as complexation. The nanotube-complexed pyrenes could be removed via non-invasive means, such as dialysis or solvent extraction, and the removal of pyrene moieties from the nanotube surface resulted in the recovery of the characteristic  $S_{11}$  and  $S_{22}$  absorption features (Fig. 23). The complexation of porphyrins with semiconducting SWNTs resulted in the same diminishing of optical absorption bands, which similarly recovered upon

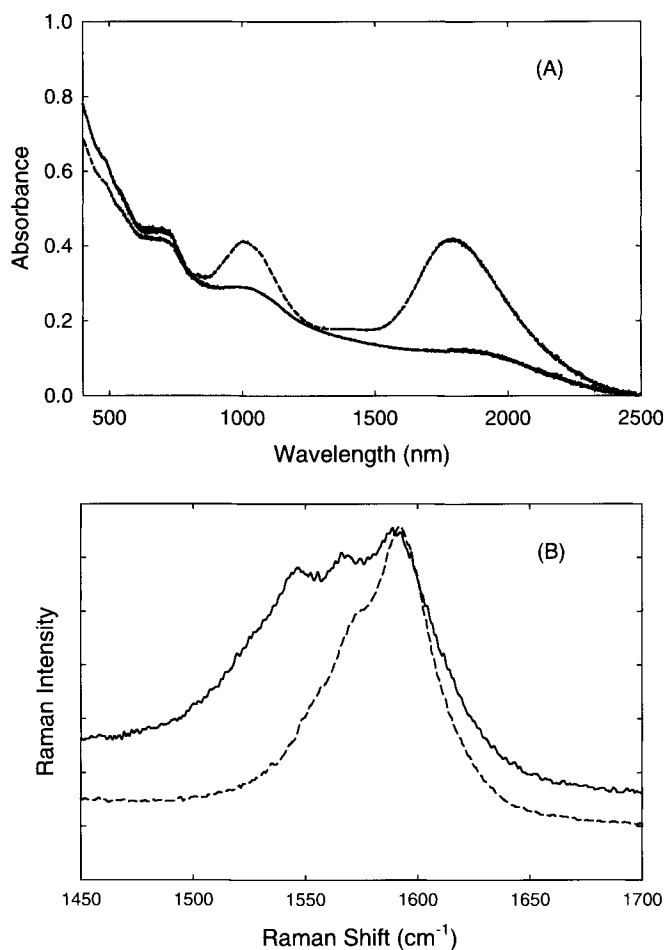


Figure 22. Absorption (A) and Raman spectra (G-band) (B) of samples enriched with metallic (—) and semiconducting (----) SWNTs from the separation with DomP [152].

the removal of the porphyrins [152]. The effects on optical absorption associated with the complexation of the planar aromatic species with semiconducting SWNTs are different from those with the covalent modification of the nanotube sidewalls [37] or the doping by halogens or protons (affecting only  $S_{11}$ ) [35,36,38]. As proposed by Fernando et al. [39], the complex of a semiconducting SWNT with (a monolayer of) pyrenes may be viewed as a double-walled carbon nanotube (Fig. 24) [39], whose outer layer is not only highly defected (incomplete surface coverage) but also of mixed “chiralities” (different pyrene stacking configuration). The SWNT-pyrene complex may in fact be analogous to a MWNT, which has

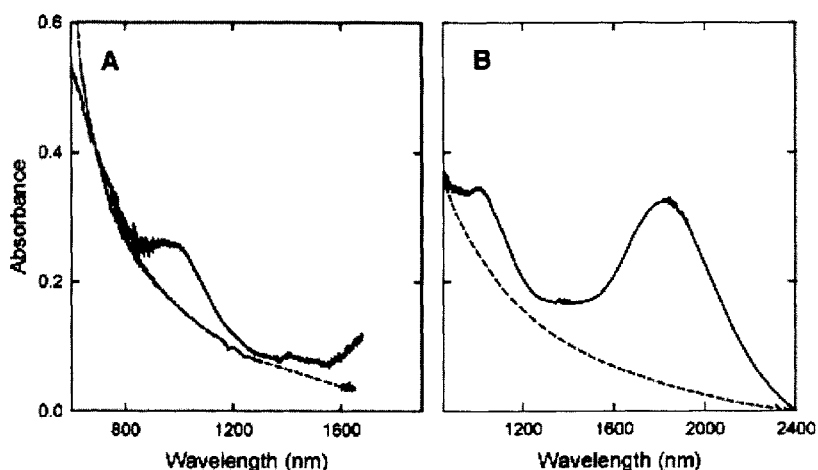


Figure 23. (A) Absorption spectra of the DomP-solubilized SWNT sample in THF (---) and in SDS-assisted D<sub>2</sub>O suspension after the removal of DomP via dialysis (—), with the nanotube-equivalent concentration in the former being at least five times higher than that in the latter. (B) Similarly, absorption spectra of the sample in the solid state before (---) and after (—) the removal of DomP. (Reproduced from Ref. [39] with permission. Copyright © 2004 American Chemical Society.)

featureless absorption because of broad hybridizations of different band-gap transitions.

Basiuk [145] suggested on the basis of computational results that Co(II)-complexed tetraaza[14]annulene adopts bent structures when approaching the SWNT surface and that it is more affinitive toward a zigzag (8,0) SWNT than an armchair (5,5) SWNT, with formation energies of  $-54.7$  and  $-7.0$  kcal/mol, respectively (Fig. 25). These results are, to some extent, consistent with the experimental observation on selective interactions of THPP or other similarly large planar aromatic molecules with semiconducting SWNTs [61,152]. Basiuk [145] also suggested that Co-complexed tetraazaannulenes should have more efficient adsorption on SWNTs than their free-base forms. However, the experimental results reported by Li et al. [61] have proven otherwise. In fact, the Zn-complexed THPP was found to be incapable of solubilizing SWNTs via the non-covalent interactions. On the other hand, there was a report on another Zn-complexed acidic porphyrin (protoporphyrin IX zinc (II) complex, or 3,7,12,17-tetramethyl-8,13-divinyl-2,18-porphinedipropionic acid) solubilizing SWNTs [146]. Further investigations are required to resolve such discrepancies.

The starting sample typically contains severely bundled SWNTs. The separated fractions from the non-covalent interactions with porphyrins, pyrenes, or other

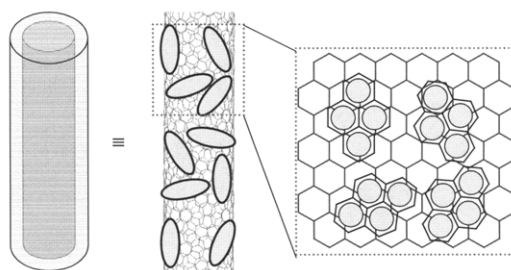


Figure 24. A schematic representation of a semiconducting SWNT covered by a monolayer of pyrenes, which is conceptually similar to a double-walled carbon nanotube.

planar aromatic molecules are probably composed of individual nanotubes as well as thin bundles (from partial exfoliation). These bundles may in principle contain mixtures of metallic and semiconducting nanotubes, responsible in part for the incomplete separation. Therefore, repeated functionalization/separation experiments on the separated fractions [153,154] to further exfoliate the bundled SWNTs represents a strategy to obtain samples of better metallic or semiconducting purity. The effectiveness of such a strategy was demonstrated preliminarily in the report of Li et al. [61]. Subsequent experiments to use the repeated non-covalent functionalization strategy confirmed that improved separation of metallic and semiconducting for their respective better-enriched samples could be achieved [152].

#### 4. OUTLOOK

There is some excitement in the nanotube research community associated with the recent development of methodologies for separated metallic and semiconducting SWNTs [155–159]. Despite some success with the approach of in-production control, selective production of a specific type of SWNTs may prove to be a very difficult task. The post-production separation appears more promising and realistic, at least in the near term. However, a number of issues, some of which are common to most available methods, remain to be addressed. Some examples are: (1) Impurity: The typical starting nanotube sample contains impurities such as amorphous carbons and carbon particles (also with embedded metal residues from the catalysts), which may interfere with the separation that is based on small difference in interactions. The likely presence of defective and “mutated” SWNTs (those containing multiple metallicity/chirality segments connected with kinks or defects) should also be considered. (2) Diameter selection: The diameter selection accompanying the metallic-semiconducting separation represents a complication, sometime a rather troublesome one. For SWNTs of a wide diameter distribution (such as those produced from the HiPco process), some methods may be applicable only to a certain



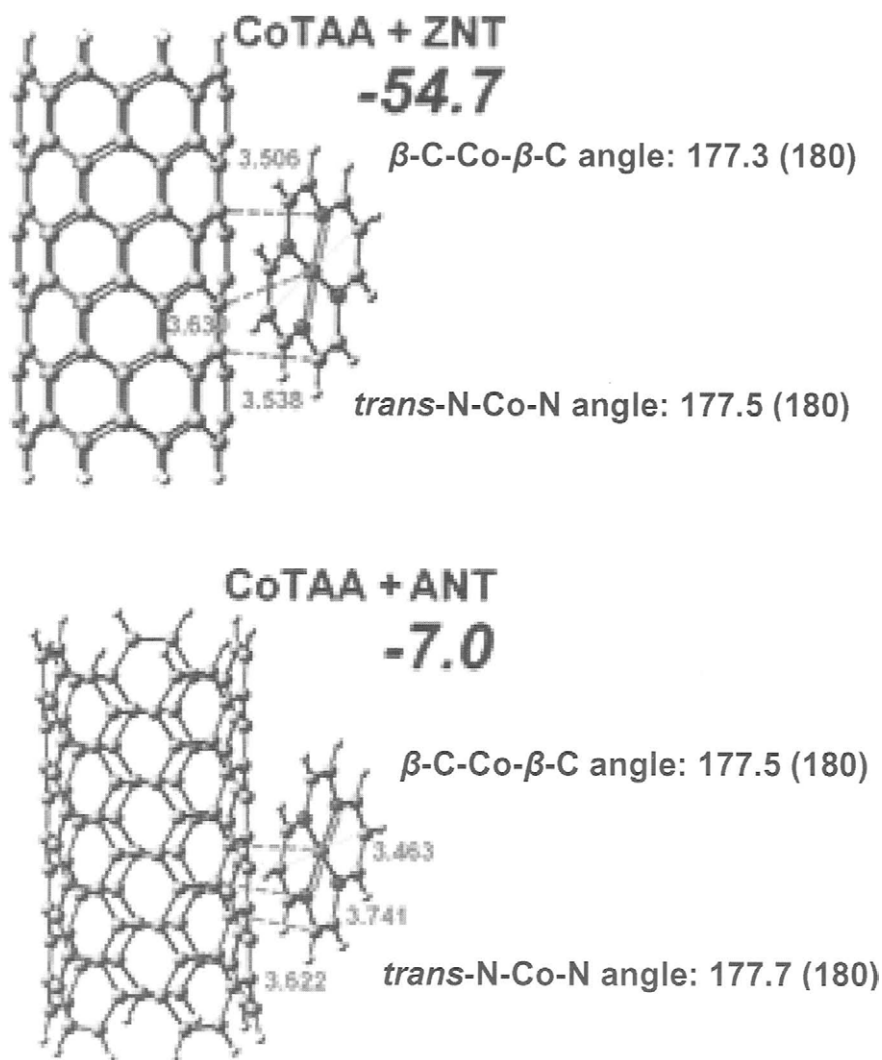


Figure 25. Optimized structures of a (8,0) semiconducting SWNT (ZNT) and a (5,5) metallic SWNT (ANT) complexes with Co-complexed tetraaza[14]annulene. The closest distances (in Å) between the annulene molecule and SWNT sidewalls are shown. *trans*-N-Co-N and  $\beta$ -C-Co- $\beta$ -C angles and their values in the NT complexes are also noted with the corresponding values for isolated optimized Co-complexed tetraaza[14]annulene in parenthesis. Binding energy values (in bold italics) are in kcal/mol. (Reproduced from Ref. [145] with permission. Copyright © 2004 American Chemical Society.)

diameter range. Thus, possible distortions to the quantitative relationships between nanotubes of different diameters should be considered. (3) Quantification: Relatively simple and reliable analytical techniques to directly quantify the separated samples are still in demand. Among the most promising in the near term are probably significant improvements in Raman and optical absorption spectroscopy techniques. (4) Mechanism: The mechanistic understanding of a separation method is critical to its optimization experimentally. This will be particularly valuable to the methods that are promising for bulk separation.

The available experimental results have already demonstrated that substantially enriched metallic and semiconducting SWNTs can be obtained. We are optimistic that better and wider uses of the currently most promising post-separation methods will result in enriched samples in larger quantities, from which exciting technological breakthroughs at the nanotube-based device level may be expected.

**Acknowledgment:** Financial support from NSF, NASA, and Center for Advanced Engineering Fibers and Films (NSF-ERC at Clemson University) is gratefully acknowledged.

## REFERENCES

1. M. S. Dresselhaus, G. Dresselhaus and P. C. Eklund, *Science of Fullerenes and Carbon Nanotubes*, Academic Press, San Diego, 1996.
2. R. Saito, M. Fujita, G. Dresselhaus and M. S. Dresselhaus, *Appl. Phys. Lett.* **60** (1992) 2204.
3. P. M. Ajayan, *Chem. Rev.* **99** (1999) 1787.
4. R. H. Baughman, A. A. Zakhidov and W. A. de Heer, *Science* **297** (2002) 787.
5. W. A. de Heer, *MRS Bull.* **29** (2004) 281.
6. S. J. Tans, A. R. M. Verschueren and C. Dekker, *Nature* **393** (1998) 49.
7. J. Kong, N. R. Franklin, C. Zhou, M. G. Chapline, S. Peng, K. Cho and H. Dai, *Science* **287** (2000) 622.
8. R. J. Chen, S. Bangsaruntip, K. A. Drouvalakis, N. W. S. Kam, M. Shim, Y. Li, W. Kim, P. J. Utz and H. Dai, *Proc. Nat. Acad. Sci. USA* **100** (2003) 4984.
9. J. A. Misewich, R. Martel, P. Avouris, J. C. Tsang, S. Heinze and J. Tersoff, *Science* **300** (2003) 783.
10. A. Fujiwara, Y. Matsuoka, H. Suematsu, N. Ogawa, K. Miyano, H. Kataura, Y. Maniwa, S. Suzuki and Y. Achiba, *Jpn. J. Appl. Phys.* **40** (2001) L1229.
11. M. Freitag, Y. Martin, J. A. Misewich, R. Martel and P. Avouris, *Nano Lett.* **3** (2003) 1067.
12. P. L. McEuen and J. -Y. Park, *MRS Bull.* **29** (2004) 272.
13. A. Nogales, G. Broza, Z. Roslaniec, K. Schulte, I. Sics, B. S. Hsiao, A. Sanz, M. C. Garcia-Gutierrez, D. R. Rueda, C. Domingo and T. A. Ezquerra, *Macromolecules* **37** (2004) 7669.
14. J. G. Smith, J. W. Connell, D. M. Delozier, P. T. Lillehei, K. A. Watson, Y. Lin, B. Zhou and Y.-P. Sun, *Polymer* **45** (2004) 825.
15. P. G. Collins, M. S. Arnold and P. Avouris, *Science* **292** (2001) 706.

16. J. W. G. Wildoer, L. C. Venema, A. G. Rinzler, R. E. Smalley and C. Dekker, *Nature* **391** (1998) 59.
17. T. W. Odom, J. -L. Huang, P. Kim and C. M. Lieber, *Nature* **391** (1998) 62.
18. D. Golberg, Y. Bando, L. Bourgeois and K. Kurashima, *Carbon* **37** (1999) 1858.
19. R. R. Meyer, S. Friedrichs, A. I. Kirkland, J. Sloan, J. L. Hutchison and M. L. H. Green, *J. Microsc.* **212** (2003) 152.
20. J. W. Cowley, P. Nikolaev, A. Thess and R. E. Smalley, *Chem. Phys. Lett.* **265** (1997) 379.
21. L.-C. Qin, S. Iijima, H. Kataura, Y. Maniwa, S. Suzuki and Y. Achiba, *Chem. Phys. Lett.* **268** (1997) 101.
22. Y. Li, D. Mann, M. Rolandi, W. Kim, A. Ural, S. Hung, A. Javey, J. Cao, D. Wang, E. Yenilmez, Q. Wang, J. F. Gibbons, Y. Nishi and H. Dai, *Nano Lett.* **4** (2004) 317.
23. R. V. Seidel, A. P. Graham, B. Rajasekharan, E. Unger, M. Liebau, G. S. Duesberg, F. Kreupl and W. Hoenlein, *J. Appl. Phys.* **96** (2004) 6694.
24. M. J. O'Connell, S. M. Bachilo, C. B. Huffman, V. C. Moore, M. S. Strano, E. H. Haroz, K. L. Rialon, P. J. Boul, W. H. Noon, C. Kittrell, J. Ma, R. H. Hauge, R. B. Weisman and R. E. Smalley, *Science* **297** (2002) 593.
25. A. Thess, R. Lee, P. Nikolaev, H. Dai, P. Petit, J. Robert, C. Xu, Y. H. Lee, S. G. Kim, A. G. Rinzler, D. T. Colbert, G. E. Scuseria, D. Tománek, J. E. Fischer and R. E. Smalley, *Science* **273** (1996) 483.
26. M. A. Hamon, M. E. Itkis, S. Niyogi, T. Alvaraez, C. Kuper, M. Menon and R. C. Haddon, *J. Am. Chem. Soc.* **123** (2001) 11292.
27. H. Kataura, Y. Kumazawa, Y. Maniwa, I. Umez, S. Suzuki, Y. Ohtsuka and Y. Achiba, *Synth. Met.* **103** (1999) 2555.
28. S. M. Bachilo, M. S. Strano, C. Kittrell, R. H. Hauge, R. E. Smalley and R. B. Weisman, *Science* **298** (2002) 2361.
29. R. B. Weisman and S. M. Bachilo, *Nano Lett.* **3** (2003) 1235.
30. M. S. Strano, S. K. Doorn, E. H. Haroz, C. Kittrell, R. H. Hauge and R. E. Smalley, *Nano Lett.* **3** (2003) 1091.
31. A. Hagen and T. Hertel, *Nano Lett.* **3** (2003) 383.
32. M. S. Strano, *J. Am. Chem. Soc.* **125** (2003) 16148.
33. B. Zhou, Y. Lin, H. Li, W. Huang, J. W. Connell, L. F. Allard and Y. -P. Sun, *J. Phys. Chem. B* **107** (2003) 13588.
34. B. Zhao, M. E. Itkis, S. Niyogi, H. Hu, J. Zhang and R. C. Haddon, *J. Phys. Chem. B* **108** (2004) 8136.
35. S. Kazaoui, N. Minami, R. Jacquemin, H. Kataura and Y. Achiba, *Phys. Rev. B* **60** (1999) 13339.
36. S. Kazaoui, N. Minami, N. Matsuda, H. Kataura and Y. Achiba, *Appl. Phys. Lett.* **78** (2001) 3433.
37. C. A. Dyke and J. M. Tour, *J. Phys. Chem. A* **108** (2004) 11151.
38. M. S. Strano, C. B. Huffman, V. C. Moore, M. J. O'Connell, E. H. Haroz, J. Hubbard, M. Miller, K. Rialon, C. Kittrell, S. Ramesh, R. H. Hauge and R. E. Smalley, *J. Phys. Chem. B* **107** (2003) 6979.

39. K. A. S. Fernando, Y. Lin, W. Wang, S. Kumar, B. Zhou, S. -Y. Xie, L. T. Cureton and Y.-P. Sun, *J. Am. Chem. Soc.* **126** (2004) 10234.
40. M. E. Itkis, S. Niyogi, M. E. Meng, M. A. Hamon, H. Hu and R. C. Haddon, *Nano Lett.* **2** (2002) 155.
41. K. Kamaras, M. E. Itkis, H. Hu, B. Zhao and R. C. Haddon, *Science* **301** (2003) 1501.
42. H. Hu, B. Zhao, M. A. Hamon, K. Kamaras, M. E. Itkis and R. C. Haddon, *J. Am. Chem. Soc.* **125** (2003) 14893.
43. A. M. Rao, E. Richter, S. Bandow, B. Chase, P. C. Eklund, K. A. Williams, S. Fang, K. R. Subbaswamy, M. Menon, A. Thess, R. E. Smalley, G. Dresselhaus and M. S. Dresselhaus, *Science* **275** (1997) 187.
44. M. S. Dresselhaus, G. Dresselhaus, R. Saito and A. Jorio, *Phys. Rep.* **409** (2005) 47.
45. M. A. Pimenta, A. Marucci, S. A. Empedocles, M. G. Bawendi, E. B. Hanlon, A. M. Rao, P. C. Eklund, R. E. Smalley, G. Dresselhaus and M. S. Dresselhaus, *Phys. Rev. B* **58** (1998) R16016.
46. S. D. M. Brown, A. Jorio, P. Corio, M. S. Dresselhaus, G. Dresselhaus, R. Saito and K. Kneipp, *Phys. Rev. B* **63** (2001) 155414.
47. H. Kuzmany, W. Plank, M. Hulman, C. Kramberger, A. Gruneis, T. Pichler, H. Peterlik, H. Kataura and Y. Achiba, *Eur. Phys. J. B* **22** (2001) 307.
48. A. Kukovecz, C. Kramberger, V. Georgakilas, M. Prato and H. Kuzmany, *Eur. Phys. J. B* **28** (2002) 223.
49. A. Jorio, R. Saito, J. H. Hafner, C. M. Lieber, M. Hunter, T. McClure, G. Dresselhaus and M. S. Dresselhaus, *Phys. Rev. Lett.* **86** (2001) 1118.
50. M. S. Dresselhaus, G. Dresselhaus, A. Jorio, A. G. Souza, M. A. Pimenta and R. Saito, *Acc. Chem. Res.* **35** (2002) 1070.
51. C. Fantini, A. Jorio, M. Souza, M. S. Strano, M. S. Dresselhaus and M. A. Pimenta, *Phys. Rev. Lett.* **93** (2004) 147406.
52. D. A. Heller, P. W. Barone, J. P. Swanson, R. M. Mayrhofer and M. S. Strano, *J. Phys. Chem. B* **108** (2004) 6905.
53. Z. Luo, R. Li, S. N. Kim and F. Papadimitrakopoulos, *Phys. Rev. B* **70** (2004) 245429.
54. G. G. Samsonidze, S. G. Chou, A. P. Santos, V. W. Brar, G. Dresselhaus, M. S. Dresselhaus, A. Selbst, A. K. Swan, M. S. Ünlü, B. B. Goldberg, D. Chattopadhyay, S. N. Kim and F. Papadimitrakopoulos, *Appl. Phys. Lett.* **85** (2004) 1006.
55. V. W. Brar, G. G. Samsonidze, A. P. Santos, S. G. Chou, D. Chattopadhyay, S. N. Kim, F. Papadimitrakopoulos, M. Zheng, A. Jagota, G. B. Onoa, A. K. Swan, M. S. Ünlü, B. B. Goldberg, G. Dresselhaus and M. S. Dresselhaus, *J. Nanosci. Nanotech.* **5** (2005) 209.
56. C. Goze-Bac, S. Latil, P. Lauginie, V. Jourdain, J. Conard, L. Duclaux, A. Rubio and P. Bernier, *Carbon* **40** (2002) 1825.
57. A. Kitaygorodskiy, W. Wang, S. -Y. Xie, Y. Lin, K. A. S. Fernando, X. Wang, L. Qu, B. Chen and Y. -P. Sun, *J. Am. Chem. Soc.* **127** (2005) 7517.

58. X.-P. Tang, A. Kleinhammes, H. Shimoda, L. Fleming, K. Y. Bennoune, S. Sinha, C. Bower, O. Zhou and Y. Wu, *Science* **288** (2000) 492.
59. R. H. Baughman, C. Cui, A. A. Zakhidov, Z. Iqbal, J. N. Barisci, G. M. Spinks, G. G. Wallace, A. Mazzoldi, D. D. Rossi, A. G. Rinzler, O. Jaschinski, S. Roth and M. Kertesz, *Science* **284** (1999) 1340.
60. D. Chattopadhyay, I. Galeska and F. Papadimitrakopoulos, *J. Am. Chem. Soc.* **125** (2003) 3370.
61. H. Li, B. Zhou, Y. Lin, L. Gu, W. Wang, K. A. S. Fernando, S. Kumar, L. F. Allard and Y. -P. Sun, *J. Am. Chem. Soc.* **126** (2004) 1014.
62. T. -I. Jeon, K. -J. Kim, C. Kang, S. -J. Oh, J. -H. Son, K. H. An, D. J. Bae and Y. H. Lee, *Appl. Phys. Lett.* **80** (2002) 3403.
63. T. -I. Jeon, K. -J. Kim, C. Kang, I. H. Maeng, J. -H. Son, K. H. An, J. Y. Lee and Y. H. Lee, *J. Appl. Phys.* **95** (2004) 5736.
64. K. H. An, J. S. Park, C. -M. Yang, S. Y. Jeong, S. C. Lim, C. Kang, J. -H. Son, J. S. Jeong and Y. H. Lee, *J. Am. Chem. Soc.* **127** (2005) 5196.
65. C. Journet, W. K. Maser, P. Bernier, A. Loiseau, M. L. de la Chapelle, S. Lefrant, P. Deniard, R. Lee and J. E. Fishcher, *Nature* **388** (1997) 756.
66. J. Kong, H. T. Soh, A. M. Cassell, C. F. Quate and H. Dai, *Nature* **395** (1998) 878.
67. J. H. Hafner, M. J. Bronikowski, B. R. Azamian, P. Nikolaev, A. G. Rinzler, D. T. Colbert, K. A. Smith and R. E. Smalley, *Chem. Phys. Lett.* **296** (1998) 195.
68. J. Kong, A. M. Cassell and H. Dai, *Chem. Phys. Lett.* **292** (1998) 567.
69. P. Nikolaev, M. J. Bronikowski, R. K. Bradley, F. Rohmund, D. T. Colbert, K. A. Smith and R. E. Smalley, *Chem. Phys. Lett.* **313** (1999) 91.
70. S. M. Bachilo, L. Balzano, J. E. Herrera, F. Pompeo, D. E. Resasco and R. B. Weisman, *J. Am. Chem. Soc.* **125** (2003) 11186.
71. Y. Miyauchi, S. Chiashi, Y. Murakami, Y. Hayashida and S. Maruyama, *Chem. Phys. Lett.* **387** (2004) 198.
72. Y. Li, S. Peng, D. Mann, J. Cao, R. Tu, K. J. Cho and H. Dai, *J. Phys. Chem. B* **109** (2005) 6968.
73. M. Kusunoki, T. Suzuki, C. Honjo, T. Hirayama and N. Shibata, *Chem. Phys. Lett.* **366** (2002) 458.
74. A. Ismach, L. Segev, E. Wachtel and E. Joselevich, *Angew. Chem. Int. Ed.* **43** (2004), 6140.
75. J. Liu, S. Fan and H. Dai, *MRS Bull.* **29** (2004) 244.
76. E. Joselevich and C. M. Lieber, *Nano Lett.* **2** (2002) 1137.
77. Y. Matsunaga, T. Kato and T. Hatori, *J. Appl. Phys.* **95** (2004) 8149.
78. L. X. Benedict, S. G. Louie and M. L. Cohen, *Phys. Rev. B* **52** (1995) 8541.
79. P. G. Collins, M. Hersam, M. Arnold, R. Martel and P. Avouris, *Phys. Rev. Lett.* **86** (2001) 3128.
80. K. Yamamoto, S. Akita and Y. Nakayama, *J. Phys. D* **31** (1998) L34.
81. X. Q. Chen, T. Saito, H. Yamada and K. Matsushige, *Appl. Phys. Lett.* **78** (2001) 3714.
82. R. Krupke, F. Hennrich, H. v. Löhneysen and M. M. Kappes, *Science* **301** (2003) 344.
83. S. Baik, M. Usrey, L. Rotkina and M. Strano, *J. Phys. Chem. B* **108** (2004) 15560.

84. D. S. Lee, D. W. Kim, H. S. Kim, S. W. Lee, S. H. Jhang, Y. W. Park and E. E. B. Campbell, *Appl. Phys. A* **80** (2005) 5.
85. R. Krupke, F. Hennrich, M. M. Kappes and H. v. Löhneysen, *Nano Lett.* **4** (2004) 1395.
86. S. W. Lee, D. S. Lee, H. Y. Yu, E. E. B. Campbell and Y. W. Park, *Appl. Phys. A* **78** (2004) 283.
87. M. Dimaki and P. Bøggild, *Nanotechnology* **15** (2004) 1095.
88. M. Zheng, A. Jagota, E. D. Semke, B. A. Diner, R. S. Mclean, S. R. Lustig, R. E. Richardson and N. G. Tassi, *Nat. Mater.* **2** (2003) 338.
89. M. Zheng, A. Jagota, M. S. Strano, A. P. Santos, P. Barone, S. G. Chou, B. A. Diner, M. S. Dresselhaus, R. S. Mclean, G. B. Onoa, G. G. Samsonidze, E. D. Semke, M. Usrey and D. J. Walls, *Science* **302** (2003) 1545.
90. G. S. Duesberg, J. Muster, V. Krstic, M. Burghard and S. Roth, *Appl. Phys. A* **67** (1998) 117.
91. S. Niyogi, H. Hu, M. A. Hamon, P. Bhowmik, B. Zhao, S. M. Rozenzhak, J. Chen, M. E. Itkis, M. S. Meier and R. C. Haddon, *J. Am. Chem. Soc.* **123** (2001) 733.
92. B. Zhao, H. Hu, S. Niyogi, M. E. Itkis, M. A. Hamon, P. Bhowmik, M. S. Meier and R. C. Haddon, *J. Am. Chem. Soc.* **123** (2001) 11673.
93. D. Chattopadhyay, S. Lastella, S. Kim and F. Papadimitrakopoulos, *J. Am. Chem. Soc.* **124** (2002) 728.
94. B. Chen and J. P. Selegue, *Anal. Chem.* **74** (2002) 4774.
95. S. K. Doorn, R. E. Fields, H. Hu, M. A. Hamon, R. C. Haddon, J. P. Selegue and V. Majidi, *J. Am. Chem. Soc.* **124** (2002) 3169.
96. S. K. Doorn, M. S. Strano, M. J. O'Connell, E. H. Haroz, K. L. Rialon, R. H. Hauge and R. E. Smalley, *J. Phys. Chem. B* **107** (2003) 6063.
97. D. A. Heller, R. M. Mayrhofer, S. Baik, Y. V. Grinkova, M. L. Usrey and M. S. Strano, *J. Am. Chem. Soc.* **126** (2004) 14567.
98. S. R. Lustig, A. Jagota, C. Khripin and M. Zheng, *J. Phys. Chem. B* **109** (2005) 2559.
99. M. S. Strano, M. Zheng, A. Jagota, G. B. Onoa, D. A. Heller, P. W. Barone and M. L. Usrey, *Nano Lett.* **4** (2004) 543.
100. M. Zheng and B. A. Diner, *J. Am. Chem. Soc.* **126** (2004) 15490.
101. S. G. Chou, H. B. Ribeiro, E. B. Barros, A. P. Santos, D. Nezich, G. G. Samsonidze, C. Fantini, M. A. Pimenta, A. Jorio, F. P. Filho, M. S. Dresselhaus, G. Dresselhaus, R. Saito, M. Zheng, G. B. Onoa, E. D. Semke, A. K. Swan, M. S. Ünlü and B. B. Goldberg, *Chem. Phys. Lett.* **397** (2004) 296.
102. S. G. Chou, F. Plentz, J. Jiang, R. Saito, D. Nezich, H. B. Ribeiro, A. Jorio, M. A. Pimenta, G. G. Samsonidze, A. P. Santos, M. Zheng, G. B. Onoa, E. D. Semke, G. Dresselhaus and M. S. Dresselhaus, *Phys. Rev. Lett.* **94** (2005) 127402.
103. M. S. Arnold, S. I. Stupp and M. C. Hersam, *Nano Lett.* **5** (2005) 713.
104. M. F. Islam, E. Rojas, D. M. Bergey, A. T. Johnson and A. G. Yodh, *Nano Lett.* **3** (2003) 269.
105. V. C. Moore, M. S. Strano, E. H. Haroz, R. H. Hauge and R. E. Smalley, *Nano Lett.* **3** (2003) 1379.

106. J. Chen, M. A. Hamon, H. Hu, Y. Chen, A. M. Rao, P. C. Eklund and R. C. Haddon, *Science* **282** (1998) 95.
107. J. L. Bahr and J. M. Tour, *J. Mater. Chem.* **12** (2002) 1952.
108. A. Hirsch, *Angew. Chem., Int. Ed.* **41** (2002) 1853.
109. S. Niyogi, M. A. Hamon, H. Hu, B. Zhao, P. Bhowmik, R. Sen, M. E. Itkis and R. C. Haddon, *Acc. Chem. Res.* **35** (2002) 1105.
110. Y.-P. Sun, K. Fu, Y. Lin and W. Huang, *Acc. Chem. Res.* **35** (2002) 1096.
111. D. Tasis, N. Tagmatarchis, V. Georgakilas and M. Prato, *Chem. Eur. J.* **9** (2003) 4000.
112. Y. Lin, S. Taylor, H. Li, K. A. S. Fernando, L. Qu, W. Wang, L. Gu, B. Zhou and Y. -P. Sun, *J. Mater. Chem.* **14** (2004) 527.
113. A. M. Rao, P. C. Eklund, S. Bandow, A. Thess and R. E. Smalley, *Nature* **388** (1997) 257.
114. R. S. Lee, H. J. Kim, J. E. Fischer, A. Thess and R. E. Smalley, *Nature* **388** (1997) 255.
115. Z. Chen, X. Du, M.-H. Du, C. D. Rancken, H.-P. Cheng and A. G. Rinzler, *Nano Lett.* **3** (2003) 1245.
116. N. Park, Y. Miyamoto, K. Lee, W. I. Choi, J. Ihm, J. Yu and S. Han, *Chem. Phys. Lett.* **403** (2005) 135.
117. M. J. O'Connell, E. E. Eibergen and S. K. Doorn, *Nat. Mater.* **4** (2005) 412.
118. E. Joselevich, *Angew. Chem. Int. Ed.* **43** (2004) 2992.
119. E. Joselevich, *ChemPhysChem* **5** (2004) 619.
120. M. S. Strano, C. A. Dyke, M. L. Usrey, P. W. Barone, M. J. Allen, H. Shan, C. Kittrell, R. H. Hauge, J. M. Tour and R. E. Smalley, *Science* **301** (2003) 1519.
121. C. A. Dyke, M. P. Stewart, F. Maya and J. M. Tour, *Synlett* (2004) 155.
122. C. A. Dyke, M. P. Stewart and J. M. Tour, *J. Am. Chem. Soc.* **127** (2005) 4497.
123. S. Banerjee and S. S. Wong, *J. Am. Chem. Soc.* **126** (2004) 2073.
124. J. J. Wallis and J. K. Kochi, *J. Org. Chem.* **53** (1988) 1679.
125. J. J. Wallis and J. K. Kochi, *J. Am. Chem. Soc.* **110** (1988) 8207.
126. L. An, Q. Fu, C. Lu and J. Liu, *J. Am. Chem. Soc.* **126** (2004) 10520.
127. K. Balasubramanian, R. Sordan, M. Burghard and K. Kern, *Nano Lett.* **4** (2004) 827.
128. S. Banerjee and S. S. Wong, *Nano Lett.* **4** (2004) 1445.
129. K. Seo, C. Kim, Y. S. Choi, K. A. Park, Y. H. Lee and B. Kim, *J. Am. Chem. Soc.* **125** (2003) 13946.
130. A. Hassanien, M. Tokumoto, P. Umek, D. Vrbancic, M. Mozetic, D. Mihailovic, P. Venturini and S. Pejovnik, *Nanotechnology* **16** (2005) 278.
131. S. Tan, H. A. Lopez, C. W. Cai and Y. Zhang, *Nano Lett.* **4** (2004) 1415.
132. K. Maehashi, Y. Ohno, K. Inoue and K. Matsumoto, *Appl. Phys. Lett.* **85** (2004) 858.
133. J. Chen, A. M. Rao, S. Lyuksyutov, M. E. Itkis, M. A. Hamon, H. Hu, R. W. Cohn, P. C. Eklund, D. T. Colbert, R. E. Smalley and R. C. Haddon, *J. Phys. Chem. B* **105** (2001) 2525.
134. L. Piculell, K. Thuresson and B. Lindman, *Polym. Adv. Technol.* **12** (2001) 44.
135. R. W. Meulenberg and G. F. Strouse, *J. Phys. Chem. B* **105** (2001) 7438.

136. E. V. Basiuk, V. A. Basiuk, J. G. Banuelos, J. M. Saniger-Blesa, V. A. Pokrovskiy, T. Y. Gromovoy, A. V. Mischanchuk and B. G. Mischanchuk, *J. Phys. Chem. B* **106** (2002) 1588.
137. J. Kong and H. Dai, *J. Phys. Chem. B* **105** (2001) 2890.
138. R. J. Chen, Y. Zhang, D. Wang and H. Dai, *J. Am. Chem. Soc.* **123** (2001) 3838.
139. N. Nakashima, Y. Tomonari and H. Murakami, *Chem. Lett.* **31** (2002) 638.
140. P. Petrov, F. Stassin, C. Pagnouille and R. Jerome, *Chem. Commun.* (2003) 2904.
141. L. Liu, T. Wang, J. Li, Z. -X. Guo, L. Dai, D. Zhang and D. Zhu, *Chem. Phys. Lett.* **367** (2003) 747.
142. D. M. Guldi, G. M. A. Rahman, N. Jux, N. Tagmatarchis and M. Prato, *Angew. Chem. Int. Ed.* **43** (2004) 5526.
143. H. Paloniemi, T. Aaritalo, T. Laiho, H. Liuke, N. Kocharova, K. Haapakka, F. Terzi, R. Seeber and J. Lukkari, *J. Phys. Chem. B* **109** (2005) 8634.
144. E. V. Basiuk, E. V. Rybak-Akimova, V. A. Basiuk, D. Acosta-Najarro and J. M. Saniger, *Nano Lett.* **2** (2002) 1249.
145. V. A. Basiuk, *J. Phys. Chem. B* **108** (2004) 19990.
146. H. Murakami, T. Nomura and N. Nakashima, *Chem. Phys. Lett.* **378** (2003) 481.
147. A. Satake, Y. Miyajima and Y. Kobuke, *Chem. Mater.* **17** (2005) 716.
148. J. Chen and C. P. Collier, *J. Phys. Chem. B* **109** (2005) 7605.
149. X. Wang, Y. Liu, W. Qiu and D. Zhu, *J. Mater. Chem.* **12** (2002) 1636.
150. L. Cao, H. -Z. Chen, H. -B. Zhou, L. Zhu, J. -Z. Sun, X. -B. Zhang, J. -M. Xu and M. Wang, *Adv. Mater.* **15** (2003) 909.
151. J. Chen, H. Liu, W. A. Weimer, M. D. Halls, D. H. Waldeck and G. C. Walker, *J. Am. Chem. Soc.* **124** (2002) 9034.
152. K. A. S. Fernando, Y. Lin, X. Wang and Y. -P. Sun, Unpublished results.
153. Y. Lin, S. Taylor, W. Huang and Y. -P. Sun, *J. Phys. Chem. B* **107** (2003) 914.
154. W. Huang, S. Fernando, Y. Lin, B. Zhou, L. F. Allard and Y. -P. Sun, *Langmuir* **19** (2003) 7084.
155. M. S. Dresselhaus, *Nat. Mater.* **3** (2004) 665.
156. R. B. Weisman, *Nat. Mater.* **2** (2003) 569.
157. R. C. Haddon, J. Sippel, A. G. Rinzler and F. Papadimitrakopoulos, *MRS Bull.* **29** (2004) 252.
158. S. Banerjee, T. Hemraj-Benny and S. S. Wong, *J. Nanosci. Nanotech.* **5** (2005) 841.
159. R. Krupke and F. Hennrich, *Adv. Eng. Mater.* **7** (2005) 111.



## Chapter 11

### Electrochemical properties of carbon nanotubes

S.E. Moulton, A.I. Minett, and G.G. Wallace

ARC Centre for Nanostructured Electromaterials,  
Intelligent Polymer Research Institute, University of Wollongong,  
Northfields Avenue, Wollongong, NSW 2522, Australia

#### 1. INTRODUCTION

Carbon materials have attracted the interest of those of us involved in the development of new electrode materials for some time. Carbon in appropriate forms is highly conductive, electrochemically inert over a wide potential range and amenable to chemical functionalisation to modify electrochemical behaviour. The most widely exploited form of carbon as an electrode, to date, is glassy carbon [1]. Glassy carbon has a wide electrochemical potential window and is a dense glassy material impervious to gas or liquids. Reticulated vitreous carbon is a glassy carbon material with an open porous honeycomb like structure inducing high-surface area: volume ratios [2,3]. Both carbon cloth [4] and carbon felt [5] have also been used as electrode materials. Carbon fibres have been used to produce microelectrodes with extraordinary properties in terms of their utilisation in low-ionic strength media and the ability to operate at very high-potential scan rates.

Since their discovery in 1991 by Iijima [6], carbon nanotubes (CNTs) have generated an immense amount of interest. Over the last 12 years the number of publications detailing their electrical, mechanical, electromechanical and chemical properties as well as potential areas of application has risen exponentially. Studies into the use of CNTs as electrode materials are gaining momentum and it is this aspect of these fascinating materials that is discussed here.

#### 2. CARBON NANOTUBE-BASED ELECTRODES

CNTs have been used as electrodes in different forms. The simplest and perhaps most elegant is their use as single nanotube structures [7]. CNTs have also been packed into appropriate constructions to form microelectrodes [8]. Alternatively adherent CNT films have been cast (as films) from a volatile solvent onto an appropriate electrode substrate such as glassy carbon (Fig. 1) [9].

Perhaps the most robust form of CNT electrodes is in the form of so called bucky paper. This is usually formed using a simple filtration procedure (as depicted in Scheme 1).

The papers may stand-alone or may be retained as a film on a platinised membrane. CNT papers with thickness in the range 10–100  $\mu\text{m}$  are easily prepared.

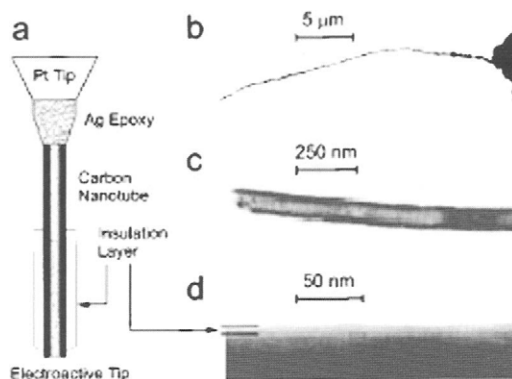
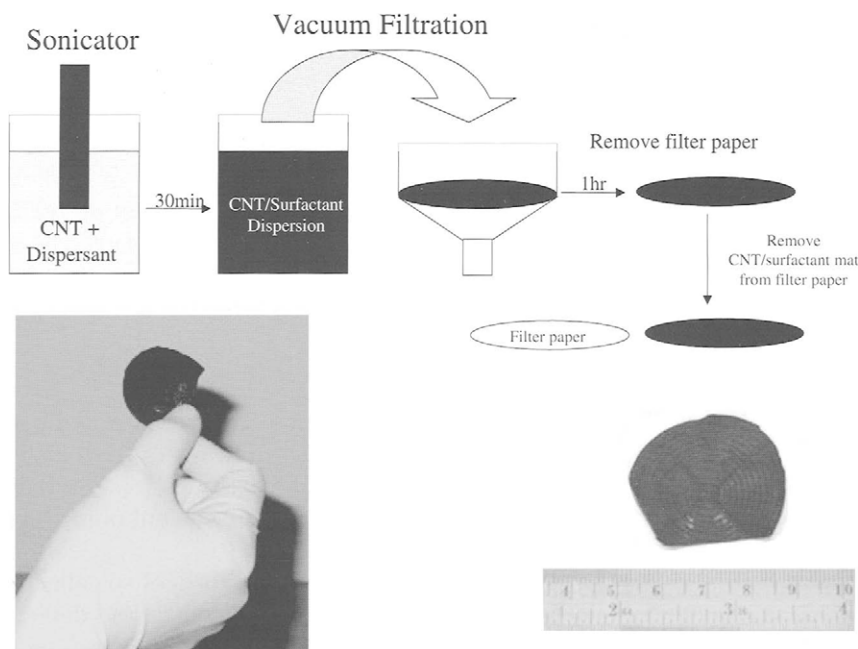


Figure 1. (a) Schematic representation of a partially insulated carbon nanotube electrode. (b–d) TEM images of mounted nanotubular electrodes showing; (b) a 30 μm long electrode; (c) the tip of a ~100 nm diameter uninsulated nanoelectrode; (d) a ~10 nm thick insulation layer of polyphenol on a ~220 nm diameter nanotube. Adapted from Campbell et al. [7].



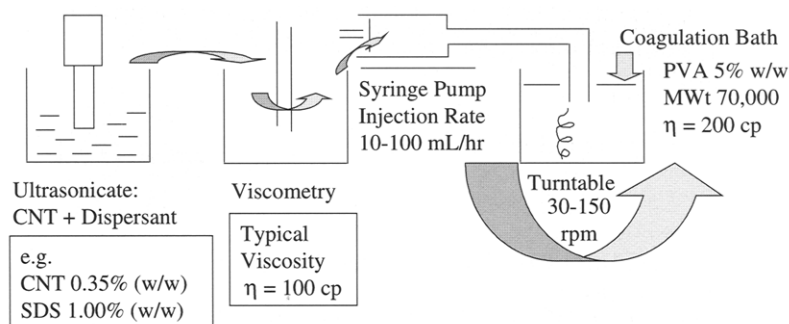
Scheme 1. Formation of CNT paper.

Baughman et al. [10] have produced CNT papers having Young's modulus of  $\sim 1.2$  GPa and electrical conductivity of 100 S/cm.

An alternative electrode configuration involves the use of wet spinning techniques to produce CNT fibres [11] (Scheme 2). This method provides a route to produce fibres, which exhibit a maximum tensile strength of 1.8 GPa [12] and electrical conductivities ranging from 10 to 200 S/cm depending on the CNT dispersing agent and coagulant [13]. The dispersant used in the initial stages of the wet spinning process has a profound effect on the mechanical, electronic and electrochemical properties of the resultant fibre.

Another way to produce fibre structures incorporating CNTs is via the electrospinning method (Fig. 2) [14–16]. Electrospinning has long been an effective method to produce polymer nanofibres [17], which has been utilized in a variety of applications. Electrospinning produces tangled arrays of nanofibres resulting in the formation of a polymeric entangled web. CNTs may be incorporated into these nanofibres to improve their mechanical and electrical properties. Seoul et al. [18] showed the percolation threshold for the insulator-to-conductor transition was 0.04 wt% CNTs for a CNT/PVDF electrospun fibre mat. They explained this low-percolation threshold to be a consequence of the large aspect ratio of the CNTs used resulting in entanglement of the CNTs at low concentrations. The incorporation of 20 wt% CNT into polyacrylonitrile nanofibres resulted in a 144% increase in the nanofibres tensile modulus (1.8 GPa at 0 wt% – 4.4 GPa at 20 wt%) [15].

A very elegant way to produce CNT electrodes is via the formation of aligned CNT arrays (Fig. 3), either horizontally or vertically aligned [19]. Typically, horizontal arrays are formed by either deposition of CNTs via filtration of suspensions [20] or by direct growth of the CNTs wires between controlled surface sites by catalyst patterning [21]. The large-scale synthesis of vertically aligned CNTs was first reported by Xie and co-workers [22]. In recent times many research groups [23–25] have produced vertically aligned CNT arrays using a variety of techniques.



Scheme 2. Spinning carbon nanotube fibres.

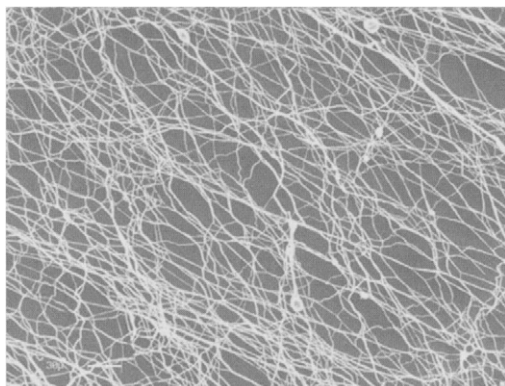


Figure 2. SEM micrographs of the electrospun fibers from 0.3 wt% SWCNT/3 wt% PEO blends in chloroform (Scale = 30  $\mu\text{m}$ ). Acknowledgement: SEM supplied by Yong Liu and Violeta Misoska (IPRI).

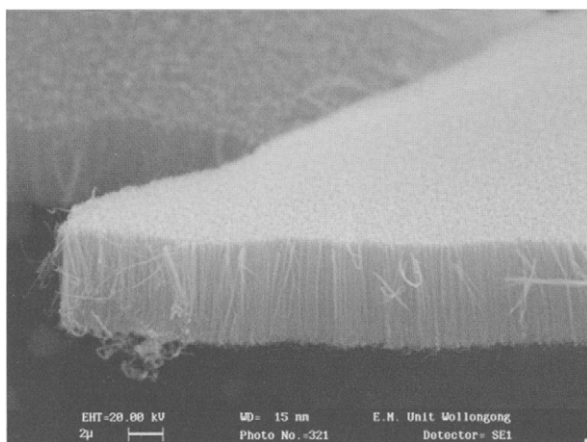


Figure 3. SEM micrograph of aligned CNTs.

### **3. CARBON NANOTUBE FUNCTIONALISATION**

To function in a wide range of sensing applications it will be necessary to incorporate molecular recognition and/or electrocatalytic properties into CNTs. Reviews covering the (covalent) functionalisation of CNTs have appeared recently [26–28]. Both covalent (Table 1) and non-covalent (Table 2) attachment of CNTs have been explored.

Table 1.

Examples of covalent attachment of functional groups to CNTs.

	Functional group	Reference
SWNT	Carboxylic acid	[29-31]
	Ester	[32]
	Amines	[3, 33-35]
	Thiols	[36]
	Proteins	[37, 38]
	DNA	[39-41]
	Enzymes	[42]
	Glucose	[43]
	Alkylation	[44]
	Fluorination	[45]
	Nucleophilic carbenes	[46]
	Phenyl groups	[47]
MWNT	Carboxylic acid	[48, 49]
	Polyethylenimine	[50]

Table 2.

Examples of non-covalent attachment of functional groups to CNTs.

	Functional group	References
SWNT	Sodium dodecylsulfonate	[51]
	Triton-X 100	[52]
	Sodium dodecylbenzene sulfonate	[53, 54]
	Porphyrin	[55]
	Poly(metaphenylenevinylene)	[56, 57]
	Poly(vinyl alcohol)	[58 (and references therein), 59]
	Nafion	[60]
	DNA	[61, 62]
	Proteins	[34 63-68]
	Peptides	[69]
	Enzymes	[70]
	Polysaccharide	[71]
MWNT	Poly(lactic acid)	[72]
	DNA	[34, 73]
	Chitosan, hyaluronic acid	[45]
	Proteins	[74]

Covalent attachment involves direct attachment to the CNTs via the formation of chemical bonds, whereas non-covalent attachment involves CNT-molecule interactions involving electrostatic, van der Waals and/or hydrophobic interactions.

## 4. ELECTROCHEMICAL PROPERTIES

The electrochemical properties of CNTs as electrode materials are now received under selected areas of application.

### 4.1. Sensors

Sensors based on CNTs have recently attracted considerable attention. A major area of application for nanotubes is likely to be the sensing of important molecules, either for medical or environmental health purposes [75]. Recent studies have demonstrated that CNTs can enhance the electrochemical reactivity of biomolecules and promote the electron-transfer reactions of proteins [76]. CNTs have been shown to promote direct electron transfer from haeme containing proteins such as myoglobin [77] and cytochrome *c* [78] due to their ability to access the haeme centre of these biomolecules (usually electrically insulated by the protein shell), something conventional glassy carbon electrodes have difficulty doing [78].

An added advantage of incorporating CNTs into current electrochemical sensors is the ability of CNTs, in some cases, to lower the overpotential of electrode processes [79]. Furthermore, their ultra high surface-to-volume ratios make their electrical properties extremely sensitive to surface-adsorbed species [80].

The reported superiority of CNT-based electrodes over traditional carbon electrodes has resulted in their use to study the electrochemistry of many organic molecules such as catechol [81], dopamine [82], glucose oxidase [83] and serotonin [84]. As the need and desire to monitor our health and environment in real time increases, correspondingly the demand for reliable miniature sensors that can measure a wide range of molecules also increases [85]. CNTs are emerging as an ideal material for such applications and have been used to sense a range of molecules such as glucose [86], cholesterol [87], antibodies [88] and even organophosphorus nerve agents [89].

Much work has gone into developing the optimal electrode configuration to match biosensing needs. These configurations range from, disordered arrays formed by drop casting CNT dispersions to form films [90] to, the more elegant aligned CNT 'forests' [91] formed using the chemical vapour deposition (CVD) technique. These structures are at times further functionalised to complete the biosensor fabrication process. Sotiropoulou et al. [92] grew an array of aligned multi-wall CNTs on a platinum substrate that were subsequently functionalised by oxidation to allow the efficient immobilization of the enzyme glucose oxidase. The carboxylated open ends of nanotubes were used for the immobilization of the enzymes, while the platinum substrate provided the direct transduction platform for signal monitoring (Fig. 4). This glucose oxidase functionalised MWNT biosensor was used to detect various amounts of glucose. In devices such as these the CNTs play a dual role; a substrate to attach biologically significant molecules and as the transducer component of the biosensor.

A great deal of the early CNT biosensor work has involved the development of enzyme-based CNT electrodes. Guiseppi-Elie et al. [83] showed that glucose oxidase spontaneously adsorbed onto the walls of CNTs and exhibited quasi-reversible one-electron transfer. This and other similar studies [91, 93] led to the development

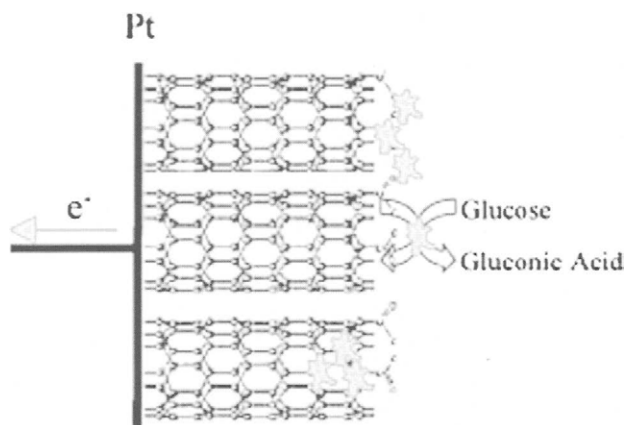


Figure 4. Schematic diagram of the carbon nanotube array biosensor. The enzyme immobilization allows for the direct electron transfer from the enzyme to platinum transducer. With permission Sotiropoulou et al. [92].

of blood glucose sensors based on CNTs. CNTs have also been used as the dopant for the conducting polymer polypyrrole, to form a biosensor for the detection of glucose [94]. Wallace and co-workers [91] coated vertically aligned CNTs with polypyrrole to develop a glucose biosensor. The PPy was doped with glucose oxidase (GOX), while the CNT acted as a wire to transport the detection signal of the liberated hydrogen peroxide ( $\text{H}_2\text{O}_2$ ) upon interaction with glucose. This electrode configuration resulted in a low-potential detection of the  $\text{H}_2\text{O}_2$  compared to a PPy-GOX biosensor. A MWNT nano-enzymatic glucose sensor was developed by Ye et al. [95] that exhibited a +400 mV decrease in the over voltage of the glucose oxidation reaction was observed at electrodes. This decrease was attributed to the presence of the MWNTs.

The Human Genome Project is providing large amounts of genetic information that should revolutionise the understanding and diagnosis of genetic diseases. As a result, the development of a DNA-based biosensor with the potential for genomic sequencing, mutation/damage detection and pathogen identification is extremely important. The development of such a sensor has led researchers to harness electromechanically robust CNTs with the specificity of DNA. Cai et al. [90] have described for the first time the development of a novel and sensitive electrochemical DNA biosensor using MWNTs functionalised with a carboxylic acid group for covalent DNA immobilisation with enhanced hybridisation detection (Fig. 5). The hybridisation reaction between the 5'-amino groups and the DNA of interest is detected by differential pulse voltammetry (DPV), utilising daunomycin as an electroactive hybridisation marker. They found that CNTs provide an intimate connection between the nucleic acid system and the electronic transducer, a vital component for the viability of DNA-based sensors.

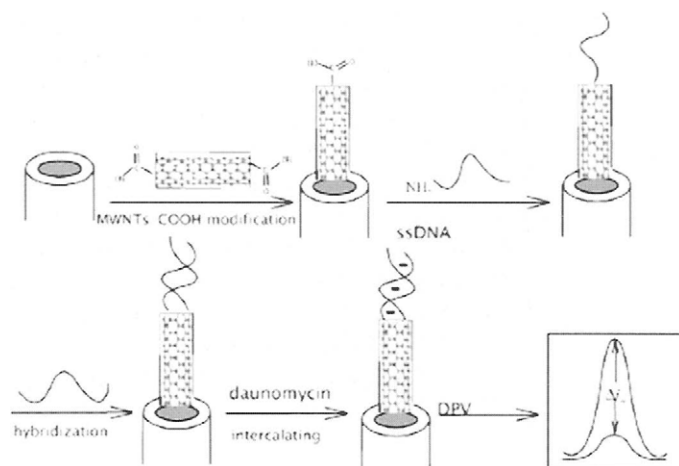


Figure 5. Schematic representation of the enhanced electrochemical detection of DNA hybridization based on the MWNTs-COOH constructed DNA biosensor. With permission from Cai et al. [90].

The use of MWNTs in the biosensor design afforded Cai's team to reach detection limits of  $1 \times 10^{-10} \text{ molL}^{-1}$  of the complementary DNA sequence, providing a superior sensitivity to that reported by Marrazza et al. [96], whose biosensor design did not utilise CNTs. This increased sensitivity has tentatively been attributed to the MWNTs-COOH acting as a promoter to enhance the electrochemical reaction, increasing the rate of heterogeneous electron transfer between the electrode and the redox active daunomycin. Also, they could increase the effective surface area of the electrode, resulting in significantly increased detection currents.

Yemini et al. [97] developed a novel electrochemical biosensing platform based on biocompatible, well-ordered and self-assembled diphenylalanine peptide nanotubes. The incorporation of CNTs into the biosensor was evaluated using voltammetry and time-based amperometry, with the findings showing an improvement on the electrochemical parameters of graphite electrodes. Chicharro et al. [98] also demonstrated CNTs to be highly useful as detectors in flow injection analysis and capillary electrophoresis. They found that compared to classical graphite paste electrodes CNTs improved the detection limits of dopac, ascorbic acid, dopamine, norepinephrine and epinephrine.

Wang et al. [99] demonstrated the use of CNTs for dramatically amplifying enzyme-based bioaffinity electrical sensing of proteins and DNA. A schematic diagram of the biosensor is shown in Fig. 6. In brief: the alkaline phosphatase-loaded CNT is captured (A) and tags to the streptavidin-modified magnetic beads by a sandwich DNA hybridization (A) or Ab-Ag-Ab interaction (B). Following this event an enzymatic reaction occurs forming a product that is electrochemically detected (C).



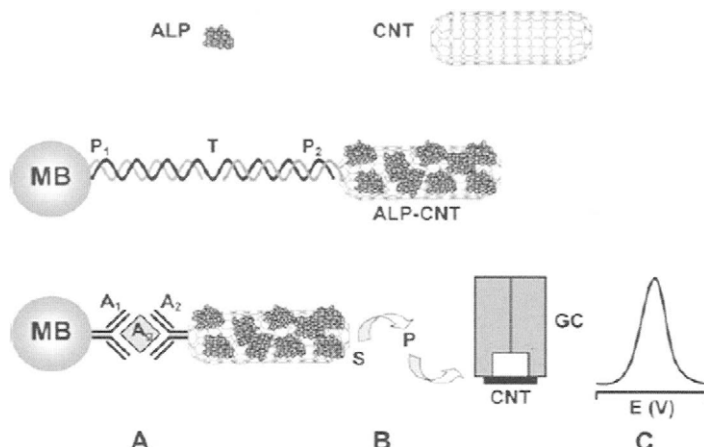


Figure 6. MB, Magnetic beads; P<sub>1</sub>, DNA probe 1; T, DNA target; P<sub>2</sub>, DNA probe 2; Ab<sub>1</sub>, first antibody; Ag, antigen; Ab<sub>2</sub>, secondary antibody; S and P, substrate and product, respectively, of the enzymatic reaction; GC, glassy carbon electrode; CNT, carbon nanotube layer. With permission from Wang et al. [99].

#### 4.2. Energy storage

The high-surface area (up to 1,600 m<sup>2</sup>/g) of CNTs along with the high conductivities attainable makes their use in energy storage applications attractive. Specific capacitance values as high as 283 F/g have been reported [100]. As expected the values attainable are critically dependent on the configuration of the electrode. For example, in the extreme, tightly aligned CNTs on surfaces give rise to electrochemical behaviour similar to a flat electrode, while a CNT mat (bucky paper) gives true 3-D electrochemical behaviour [101]. Pre-treatment of the tubes including thermal annealing [102], acid treatment [103] and electrochemical activation [104] have all been shown to have a significant effect on capacitance.

Lefrant et al. [105] used surface enhanced Raman Spectroscopy to clearly demonstrate the breakdown of CNTs into smaller fragments under oxidative electrochemical conditions in H<sub>2</sub>SO<sub>4</sub>, have all been shown to have significant effects on the subsequent electrochemical properties.

In order to store maximum amounts of energy the electrodes should be stable over a wide potential range. This range is, of course, usually determined by the electrolyte employed.

As expected in ionic liquid electrolytes such as those shown below (1) and (2) very wide electrochemical potential windows are available [106]. However, as with all new electromaterials the chemical interactions with the electrolyte need to be taken into consideration. A recent study [107] has shown that ionic liquid electrolytes can swell CNT bucky paper electrodes decreasing mechanical properties.

The use of ionic liquid electrolytes has the advantage of high environmental stability since they have an extremely low-vapour pressure.

In pursuit of even greater energy storage capabilities in the form of capacitors a number of workers have investigated the use of composites containing CNTs and other electroactive materials. For example, Park et al. [108] showed that heat treatment of ruthenium ethoxide in the presence of CNTs results in formation of  $\text{RuO}_2$  nanoparticles as small as 1 nm, which adhere well to the CNT matrix. Specific capacitance values as high as 900 F/g were obtained. Others [109] have coated CNTs with  $\text{MnO}_2$  using an in-situ chemical oxidation process. While increases in capacitance were observed, values were not as high as the  $\text{RuO}_2$  nanocomposites discussed above.

Composite electrodes containing the conducting polymer polypyrrole and sulfonated CNTs were obtained by chemical oxidation of pyrrole in the presence of the tubes [110]. These studies revealed that while CNT papers consisted primarily of microprobes (pore width <2 nm) the PPy composite material was composed of meso (2–50 nm) and macro (>50 nm) pores. Despite this compromise in surface area due to loss of small pores the capacitance was increased by a factor of 7 for the PPy containing materials. Obviously not just surface area but also electrochemical accessibility is important.

CNT-PPy composite electrodes for capacitance applications have also been formed by electrochemical polymerisation of pyrrole in the presence of oxidised tubes [111] or by direct electropolymerisation of pyrrole on top of a preformed bucky paper electrode [112].

### 4.3. Batteries

CNT electrodes have also attracted some attention for their potential use as anodes in lithium batteries. Given the use of more conventional graphite materials, capable of Li intercalation during the required redox processes this is perhaps not surprising.

The use of graphite rather than Li metal electrodes results in a reduction in specific capacity from 3860 to 372 mA hr/g. However, the use of Li electrodes is not practical due to safety concerns. Hence, the interest in alternative electrodes. The use of CNT electrodes is attractive in that Li can potentially intercalate into the interstitial value between tubes and possibly into the interior volume of the tubes as well. However, a number of early studies [113–115] revealed that capacities were only 25% higher than for graphite itself. More recent studies have shown that the use of chemical etching or ball milling of the CNTs effects composites more significantly with values up to ~1,000 mA hr/g obtained [116,117].

Barisci et al. [118] used cyclic voltammetry and electrochemical quartz crystal microbalance to study Li intercalation into CNT paper electrodes. Electrochemical impedance spectroscopy studies showed behaviour typical of a porous electrode structure. The fact that electrochemical behaviour was almost independent of the electrolyte used was attributed to the pores being on the meso–macro in nature with little access to internal tube volumes being obtained.

Yang et al. used impedance spectroscopy to show that open-ended CNTs had a greater capacity for Li intercalation than closed tubes [119].

CNT composites with polyethylenedioxythiophene (PEDOT) (3) have been prepared using chemical or electrochemical polymerisation or by simple mixing of the compounds [120]. The protocol used to obtain the composites was shown to have a significant impact on the capacitance values obtainable with the highest obtained using the electrochemical approach.

#### 4.4 Electro-mechanical actuators

In many systems, an external energy source can trigger changes in the internal state of a structure, leading to a mechanical response much larger than the initial input. In particular, the isothermal conversion of chemical energy into mechanical work underlies the motility of all living systems—i.e. *natural muscles*. In this section, the use of electrochemical processes occurring at CNT electrodes to induce actuation (strain and/or stress) is reviewed.

Known as *artificial muscles*, lying under the category of electro-chemo-mechanical devices, whereby the transformation of chemical energy into mechanical energy is triggered by either an electrical signal or a *dc* bias. They generally operate as a result of double layer (i.e. the electrochemical double layer) charge injection in electrodes having very high-gravimetric surface area and gravimetric/specific capacitance and the output of the actuator may be a mechanical displacement that can be used to accomplish mechanical work [121].

Researchers have explored the use of both single- and multi-wall nanotubes in actuators and shape-memory systems, motivated by the discovery of bond extension in charged nanotubes (i.e. the piezoelectric (PZT) effect in nanotubes). Various different types of CNT-based actuators have been discussed in the literature [122], from the development of soft, wet devices [123], to torsional actuators [124] and to reinforced ionomeric actuators [125]. The modification of existing shape-memory plastics [126] is another area that can be included into the broad title of actuators.

Studies have shown from intercalated graphite that the graphene sheets expand if extra charges are injected on them. Graphite can be intercalated by inserting oxidising or reducing species between the carbon layers, resulting in a change in the charge on the individual layers. Such experiments can be carried out on graphite single crystals and the expansion of the graphitic honeycomb lattice can be studied by X-ray diffraction. Similarly, CNTs stretch if they are charged. This effect is used in nanotube actuators. This actuation effect can be explained in simpler terms: neutral graphene is optimised both in bond strength and length. If electrons are removed or added, bonding states are depopulated or non-bonding states are populated, hence the bonds weaken and the lattice expands. The expansion is fairly large,  $\Delta L/L \sim 1\%$ , which in comparison is much larger than for common PZT actuators [127].

However, the discussion that follows focuses on the electrochemical actuation of CNT materials and composites made from them.

##### 4.4.1. Single-wall carbon nanotube actuators

The property of single-wall CNTs acting as a nano-mechanical actuator was first described in 1999, by Baughman et al. [123], who reported the first use of nanostructured carbon for the conversion of electrical energy into mechanical

energy. The actuator is based on sheets of single-walled CNTs as electrolyte filled electrodes of a super-capacitor. The two electrodes are typically separated by an electronically insulating material, which is ionically conducting in electrochemical devices. The nanostructure of the electrode sheets are that of CNTs packed tightly into ropes and bundles, which is commonly termed '*bucky-paper*' (see Scheme 1).

Changing the applied voltage injects electronic charge into the nanotubes [128], which is compensated at the nanotube–electrolyte interface by electrolyte ions, forming the so-called double layer. No dopant intercalation is required, but dimensional changes in covalently bonded directions caused by the charge injection, which originate from quantum chemical and double-layer electrostatic effects, are responsible for device operation (see Fig. 7a and b)[129].

The capacitance for an ordinary planar sheet capacitor inversely depends on the inter-electrode separation. In contrast, the capacitance for an electrochemical device depends on the separation between the charge on the electrode and the counter-charge in the electrolyte [130]. For the case of CNTs in bundles and ropes, the inter-tube separation is in the order of about a nanometre, as compared with the micrometre or larger separations in ordinary dielectric capacitors. When CNTs are used as the basis of an electrode material, very large reported capacitances result from the high-nanotube surface area accessible to the electrolyte. These capacitances (typically between  $\sim 15$  and  $\sim 200$  F/g, depending on the surface area of the nanotube array) result in large amounts of charge injection when only a few volts are applied [123,131,132].

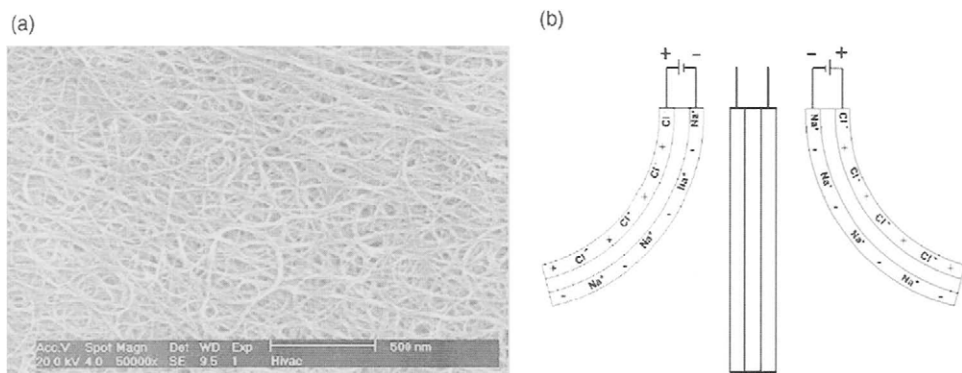


Figure 7. (a) Scanning electron micrograph of carbon nanotube '*bucky paper*'. (b) Schematic representation of bucky paper bimorph actuator showing double-layer charge compensation from ionic species in the electrolyte. (Reprinted with permission from Baughman et al. [123]. Copyright (1999) American Association for the Advancement of Science.)

Researchers have improved on these initial performances by demonstrating that resistance compensation coupled with potential pulses, can provide significant improvement in the charging rate, and consequent actuation strain rate, for CNT sheets operated in an organic electrolyte [133]. The researchers reported that strain rate increased with increasing potential pulse amplitudes when a more negative potential limit was applied. Additionally, the amount of strain produced also increased with longer pulse times.

The highest strain rate achieved was 0.6%/s, which produced a strain amplitude of 0.3% in 0.5 s. The improvements in strain rate are somewhat offset when large negative potential limits are used. This is largely due to the introduction of Faradaic reactions in the electrolyte medium that do not contribute to the actuation mechanism. Efficiency of operation is, therefore, reduced under such conditions [133].

As we have seen the ability of an electrochemical material to store charge determines the performance capabilities in electro-mechanical actuators. This storage ability is directly dependant on the inert potential window that is electrochemically available. Depending on the electrolyte used, carbon-based electrode materials generally exhibit a small available potential window.

The use of an organic electrolyte, such as 1 M tetra-butylammonium hexafluorophosphate in acetonitrile, is one technique employed to overcome this disadvantage [106]. This electrolyte has a high-voltage stability electrochemical window, however, it has been found that the nature of the organic electrolyte degrades CNT '*bucky paper*'.

Switching from conventional electrolytes to the use of ionic liquids as electrolytes for electrochemical applications also offers the possibility of improving on these initial studies. Recently, it has been reported that ionic liquids are highly effective electrolytes with a wide electrochemical potential window [134,135]. Reports have shown for CNT-based electrodes, high conductivity and wide potential windows (up to 5.5 V) are indeed possible [136]. The researchers conclude that the overall good electrochemical behaviour of the CNT electrodes, coupled with the wide potential window and non-volatility of the ionic liquid electrolytes, suggests potential new avenues for electro-mechanical actuators.

#### 4.4.2. Pneumatic actuation

Some applications of electro-mechanical actuators require the generation of large displacements, rather than large forces. Spinks et al. [137] report extremely high strains and strain rates with the description of a new mechanism of CNT actuation-pneumatic actuators.

The researchers describe a surprising observation for un-annealed CNT sheets during electrochemical cycling at high-redox potentials in aqueous electrolytes. Normally, only non-Faradaic mechanisms associated with double-layer charge injection are observed during square-wave cycling at high potentials (+1.5 V). It was found that after approximately 12 cycles, the voltage switched in-plane strain progressively increased to ~3% (Fig. 8A). Fig. 8B shows that upon exceeding potentials of +1.2 V in the positive direction, much larger actuator responses are observed. At the higher applied voltages, a second mechanism for actuation is

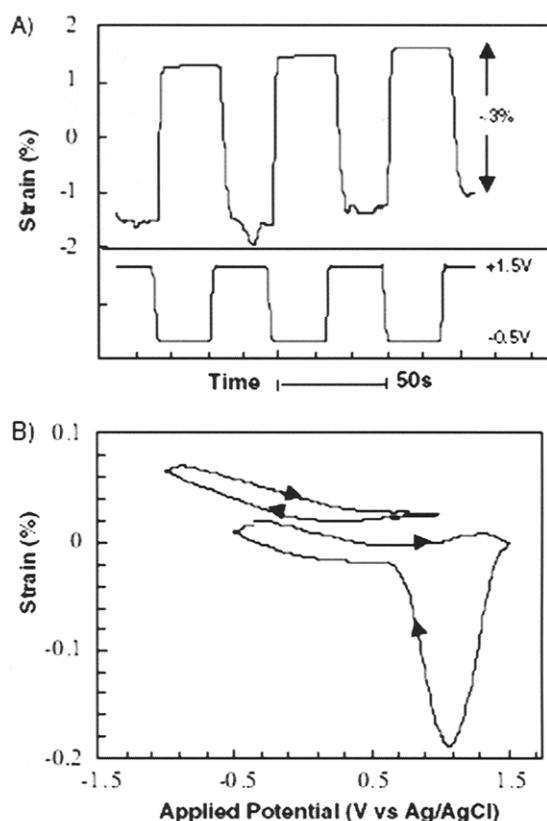


Figure 8. (A) Actuator strain measured in the Faradaic regime, where pneumatic actuation occurs. An aqueous 5 M NaCl electrolyte was used for square wave potential cycling between  $-0.5$  V and  $+1.5$  V with a 60 s period. (B) The strain of a nanotube sheet measured in aqueous electrolyte (1 M NaCl). The applied potential was cycled either between  $+1$  V and  $-1$  V (where the response is non-Faradaic) or between  $-0.5$  V and  $+1.5$  V (where a Faradaic response occurs at high-positive potentials). The scan rate was  $50$  mV/s<sup>1</sup>. Arrows indicate the scan direction. (Reprinted with permission from Spinks et al. [137]. Copyright (1999) American Association for the Advancement of Science.)

responsible for an in-plane contraction at large positive potentials. This response is markedly different to the superimposed charge injection process shown.

Fig. 9A shows optical microscopy images of before and after this *extreme* actuation where the thickness directional strain ( $\sim 300\%$ ) is two orders of magnitude higher than the in-plane strain. The authors suggest a pneumatic mechanism for the giant actuation at potentials that cause gas evolution at high positive potentials in aqueous electrolytes (Fig. 9B).

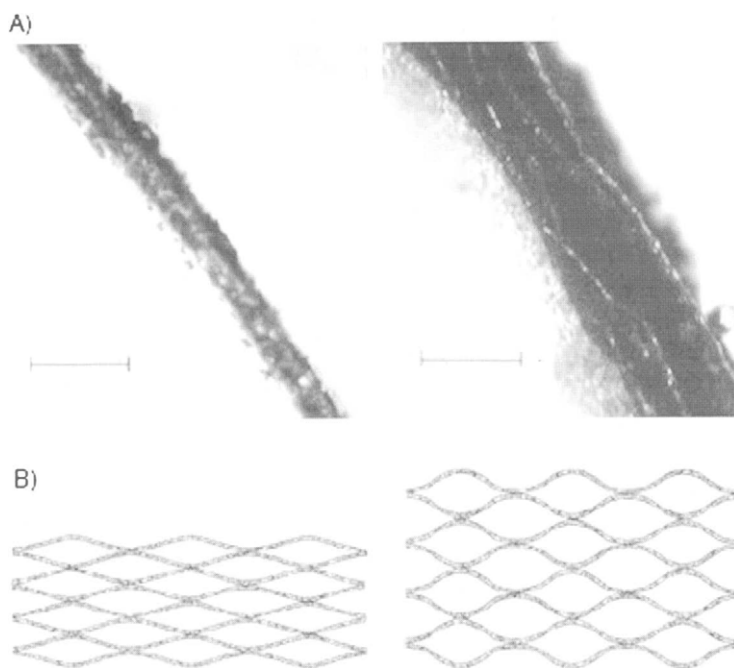


Figure 9. (A) Edge-view optical photographs showing the thickness of a carbon nanotube sheet before (left) and after (right) Faradaic actuation in 5 M NaCl. (B) Schematic diagram of partially collapsed (left) and highly extended (right) states of the idealised structure that is used for modelling the pneumatic actuation process. Disk-like microcracks in the nanotube-sheet structure serve as pneumatic chambers that expand as gas is electrochemically produced within the carbon nanotube sheet. Like the deformations of a nearly collapsed wine rack or accordion, the pressure driven increase in the volume of the nanotube sheet is associated with an in-plane contraction and a greatly amplified thickness-direction expansion. (Reprinted with permission from Spinks et al. [137]. Copyright (1999) American Association for the Advancement of Science.)

The disadvantages of this type of actuation include inefficient energy conversion, cycle rate and work-per-cycle values, which are not competitive with current ferro-electric or electro-strictive materials [138,139], or that for non-Faradaic actuation processes in CNT-based materials. The advantages include the high 300% (thickness direction) actuator stroke and the low-operating voltages required to achieve them.

#### 4.4.3. Measuring the actuation force of a single nanotube

Although the performance of the demonstrator *bucky-paper* actuator described above was impressive, the results did not meet expected theoretical results for

CNTs. Part of this results from the fact that most theoretical predictions are made for single CNTs. It is generally accepted that the demonstrator was not an optimised system.

Several attempts have been made to demonstrate a *single* single-walled CNT actuator [140] by measuring both the Young's modulus and force of actuation using an atomic force microscope cantilever. To remove surface effects, methods were developed to obtain suspended nanotubes between two metal contacts.

Several methods have been trialled in an attempt to obtain suspended nanotubes that are metal contacted at either end. Simple deposition and shadow masking or E-beam metal contact deposition proved unreliable [141]. More successful were attempts to grow nanotubes across pre-designed trenches made from laser ablation of catalyst material or micro-contact printed catalyst islands [142]. In both cases the nanotubes were grown via chemical vapour deposition (CVD) techniques.

The methods described above generally suffer from reproducibility problems and the task of trying to locate individual nanotubes on surfaces. A novel approach [143] was developed where co-ordinate patterned markers were first deposited onto the silicon wafer before consecutive sacrificial layers of PMMA and nano-objects were deposited. Subsequent E-beam lithography and selective patterning produced suspended [144] nano-objects with metal contacted leads (Fig. 10a). The advantage of using the co-ordinate marker system allows the deposited entities (tubes or fibres) to be located easily for multiple analyses.

By manipulating the nanotube with the tip of an AFM and observing the change in cantilever deflection versus  $Z$ -direction height, the researchers were able to determine the force, according to the following expression. If the spring constant of the cantilever is calibrated:  $F = k_c \Delta Z_c$ , where  $F$  is the force against the cantilever and the nanotube,  $k_c$  the spring constant and  $\Delta Z_c$  the cantilever deflection.

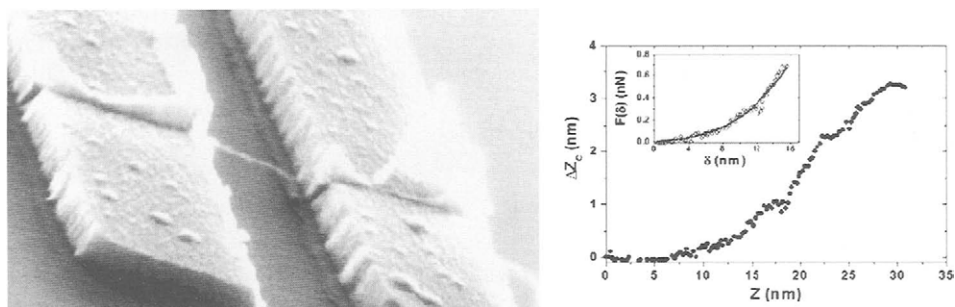


Figure 10. (a) SEM image of a suspended carbon nanotube (or small bundle) between two metallic contacts. (b) Plot showing the change in cantilever deflection versus  $Z$ -direction height. Inset: force determination plot. (Reprinted with permission from Kim et al. [144]. Copyright American Institute Physics.)



Manipulation of the suspended nanotube in Fig. 10a resulted in the curves obtained in Fig. 10b, where the change in cantilever deflection versus  $Z$ -direction height and from this the force determination,  $F(\delta)$ , plot was shown [144].  $F(\delta) = 8YA (\delta/l)^3$  where  $Y$  is Young's modulus,  $A$  is the cross-sectional area,  $\delta$  the deflection and  $l$  the suspended tube length. The vertical displacement of the nanotube ( $\delta$ ) can be readily obtained by subtracting the cantilever deflection,  $Z - Z_0$ , where  $Z$  is the current height and  $Z_0$  is the height when the AFM tip touches the nanotube. From this determination, the authors estimated the Young's modulus to be  $\sim 0.6$  TPa, which is in good approximation with values reported in the literature [145–147]. It was hypothesised that the strain could also be determined using:  $\sigma = [(4\delta^2 + l^2) (l/2 - l)] / l$  where  $\sigma$  is the strain of the tube and  $l$  the suspended tube length. Subsequent experiments found that the electrostatic forces between the atomic force microscope tip and the suspended CNT were too great to overcome to obtain reliable and reproducible actuation force measurements.

#### 4.4.4. Multi-wall actuators

The actuation of multi-wall CNTs was initially found to be quite difficult to demonstrate due to the inability to produce *bucky-paper* type examples of multi-wall nanotubes with any mechanical robustness. One of the first demonstrators was described by Spinks et al. [148] where multi-wall nanotube forests [149] were produced on flexible gold substrates immersed into an electrolyte solution. Upon application of a switching potential, the uni-morph actuator bent in opposite directions. The mechanism of this actuation was thought to be electrostatic in nature, where electrostatic repulsion of the unanchored nanotube ends of the forest was occurring during the application of the potential.

Interestingly, free-standing mats of multi-wall CNTs can undergo a similar quantum-chemical and double-layer capacitance actuation mechanism as those described for single-wall nanotube produced mats. This was demonstrated only recently by Hughes et al. [150] who were able to overcome the problem of producing macroscopic sheets of multi-walls with sufficient mechanical robustness for testing. The acid-treated [151] multi-walls were filtered using a pressure-assisted apparatus, before being temperature annealed prior to testing.

Their multi-wall mats were capable of maximum strains of about 0.2%, which is comparable to those obtained for their single-wall cousins ( $\sim 0.06$ –0.2%). Combined with the reported profiles for strain versus applied potential and strain versus nominal charge per carbon, it was concluded that the similarities between these mats and those reported for single-wall nanotube mats [123] indicate that the mechanism of actuation is likely to be the same in both cases.

The researchers hypothesise that the performance of multi-wall nanotube mats would be superior to those made from single-walls due to the superior processability of multi-walls compared to single-walls. Primarily, that advantage is a reflection of the benefits arising from the avoidance of nanotube bundling typically found with single-wall nanotube materials. Control over purity, chirality and electrical properties of single-walls are also limiting factors. It is thought that the bundling of single-wall nanotubes into small bundles and ropes is the main reason to date that single-wall

nanotube actuators have underperformed compared to their theoretical limits. It has been assumed that using common electrochemical electrolytes and the existence of the nanotubes in bundles and ropes, limits the available surface area for charge injection to those nanotubes on the outer surface of the bundles and not those of the inner surfaces. Consequently, any quantum-chemical and double-layer effects are limited to the outer nanotubes that are at the interface with the electrolyte.

The actuation of nanotube electro-mechanical actuators functioning at a few volts compares favourably with the  $\sim 100$  V used for PZT stacks and the  $\sim 1000$  V used for electrostrictive actuators. Nanotube actuators have been operated at temperatures up to  $350^{\circ}\text{C}$ , and operation above  $1,000^{\circ}\text{C}$  could be possible, based on the thermal stability of single-wall CNTs [152]. From reported nanotube actuator strains that can exceed a few percent, order-of-magnitude advantages over commercial actuators in work per cycle and stress generation capabilities are predicted if the mechanical properties of nanotube sheets can be increased to close to the inherent mechanical properties of the individual nanotubes. The maximum observed isometric actuator stress of SWNT actuators is presently  $\sim 10$  times the stress initially reported for CNT actuators and  $\sim 100$  times that of the stress generation capability of natural muscle. These values are also approaching the stress generation capability of high-modulus commercial ferroelectrics ( $\sim 40$  MPa).

The success of electrochemical actuator technology based on CNTs will depend upon improvements in the mechanical properties of nanotube sheets and fibres. By increasing nanotube alignment (therefore increasing surface area) and the binding between nanotubes (to stop creep), CNT actuation may then approach theoretical expectations [130].

## 5. CONCLUSIONS AND FUTURE DIRECTION

The advent of CNTs and various electrode structures containing them has resulted in a number of advances in the field of electrochemistry. The high-surface area and catalytic nature of CNT-based electrode materials has resulted in new electrochemical sensing technologies, improved energy storage systems (capacitors and batteries) and electro-mechanical actuators.

As methods for synthesis of CNTs are improved and functionalisation methods refined further impact in other electrochemical fields can be expected. By commencing with more uniform nanocomponents better performing electrodes can be expected. The use of functionalisation approaches that allow biomolecules, to be effectively integrated is expected to further impact on the area of electrochemical biosensors as well as biofuel cells and electrode platforms for mammalian cell culturing. The attachment of light harvesting molecules is expected to have an impact in the area of photo electrochemical cells and catalytic systems.

## REFERENCES

1. T. Nagaoka and T. Yoshino, *Anal. Chem.* **58** (1986) 1037–1042; J. Wang and P. Tuzhi, *Anal. Chem.* **58** (1986) 1787–1790; M. Noel and P. N. Anantharaman, *Analyst* **110** (1985) 1095–1103.

2. D. J. Curran and T. P. Tougas, *Anal. Chem.* **56** (1984) 672–678.
3. A. N. Strohl and D. J. Curran, *Anal. Chem.* **51** (1979) 353–357.
4. D. Yaniv and M. Ariel, *J. Electroanal. Chem.* **129** (1998) 301–313.
5. F. Tobaling, F. Pariente, L. Hernandez, H. D. Abruna and E. Lorenzo, *Anal. Chim. Acta* **358** (1998) 15–25.
6. S. Iijima, *Nature* **354** (1991) 56–58.
7. J. K. Campbell, L. Sun and R. M. Crooks, *J. Am. Chem. Soc.* **121** (1999) 3779–3780.
8. P. J. Britto, K. S. V. Santhanam, A. Rubio, J. A. Alonso and P. M. Ajayan, *Adv. Mater.* **11** (1999) 154–157.
9. H. Luo, Z. Shi, N. Li, Z. Gu and Q. Zhuang, *Anal. Chem.* **73** (2001) 915–920.
10. R. H. Baughman, C. X. Cui, A. A. Zakhidov, Z. Iqbal, J. N. Barisci, G. M. Spinks, G. G. Wallace, A. Mazzoldi, D. De Rossi, A. G. Rinzler, O. Jaschinski, S. Roth and M. Kertesz *Science* **284** (1999) 1340–1344.
11. B. Vigolo, A. Penicaud, C. Coulon, C. Sauder, R. Pailler, C. Journet, P. Bernier and P. Poulin, *Science* **290** (2000) 1331–1334.
12. A. B. Dalton, S. Collins, E. Muñoz, J. M. Razal, V. H. Ebron, J. P. Ferraris, J. N. Coleman, B. G. Kim and R. H. Baughman, *Nature* **423** (6941) (2003) 703.
13. E. Muñoz, D. –S. Suh, S. Collins, M. Selvidge, A. B. Dalton, B. G. Kim, J. M. Razal, G. Ussery, A. G. Rinzler, M. T. Martínez and R. H. Baughman *Adv. Mater.* **17** (2005) 1064–1067.
14. R. Sen, B. Zhao, D. Perea, M. E. Itkis, H. Hu, J. Love, E. Bekyarova and R. C. Haddon, *Nano Lett.* **4**(3) (2004) 459–464.
15. H. Hou, J. J. Ge, J. Zeng, Q. Li, D. H. Reneker, A. Greiner and S. Z. D. Cheng, *Chem. Mater.* **17** (2005) 967–973.
16. J. Jason, J. J. Ge, H. Hou, Q. Li, M. J. Graham, A. Greiner, D. H. Reneker, F. W. Harris and S. Z. D. Cheng, *J. Am. Chem. Soc.* **126** (2004) 15754–15761.
17. D. H. Reneker and I. Chun, *Nanotechnology* **7** (1996) 216–223.
18. C. Seoul, Y. T. Kim and C. K. Baek, *J. Polym. Sci., Part B Polym. Phys.* **41** (2003) 1572–1577.
19. L. M. Dai, A. Patil, X. Gong, Z. Guo, L. Liu, Y. Liu and D. Zhu, *Chem. Phys. Chem.* **4** (2003) 1150–1169.
20. W. A. de Heer, J. M. Bonard, K. Fauth, A. Chatelain, L. Forro and D. Ugarte, *Adv. Mater.* **9** (1997) 87–89.
21. A. M. Cassell, N. R. Franklin, T. W. Tombler, E. M. Chan, J. Han and H. Dai, *J. Am. Chem. Soc.* **121** (1999) 7975–7976.
22. W. Z. Li, S. S. Xie, L. X. Qian, B. H. Chang, B. S. Zou, W. Y. Zhou, R. A. Zhao and G. Wang, *Science* **274** (1996) 1701–1703.
23. S. H. Tsai, C. T. Shiu, S. H. Lai, L. H. Chan, W. Hsieh and H. C. Shih, *J. Mater. Sci. Lett.* **21** (2002) 1709–1711.
24. X. Nan, Z. Gu and Z. J. Liu, *Colloid Interface Sci.* **245** (2002) 311–318.
25. Y. Yang, S. Huang, H. He, A. W. H. Mau and L. Dai, *J. Am. Chem. Soc.* **121** (1999) 10832–10833.
26. T. Lin, V. Bajpai, T. Ji and L. M. Dai, *Aust. J. Chem.* (2003) 635–651.
27. S. Banerjee, T. Hemraj-Benny and S. S. Wong, *Adv. Mater.* (2005) 17–29.

28. Y. Lin, S. Taylor, H. P. Li, K. A. S. Fernando, L. W. Qu, W. Wang, L. R. Gu, B. Zhou and Y. P. Sun, *J. Mater. Chem.* **14** (2004) 527–541.
29. D. B. Mawhinney, V. Naumenko, A. Kuznetsova, J. T. Yates, J. Liu and R. E. Smalley, *Chem. Phys. Lett.* **324** (2000) 213–216.
30. H. Hu, P. Bhowmik, B. Zhao, M. A. Hamon, M. E. Itkis and R. C. Haddon, *Chem. Phys. Lett.* **345** (2001) 25–28.
31. T. Ramanathan, F. T. Fisher, R. S. Ruoff and L. C. Brinson, *Chem. Mater.* **17**(6) (2005) 1290–1295.
32. M. A. Hamon, H. Hui, P. Bhowmik, H. E. Itkis and R. C. Haddon, *Appl. Phys. A: Mater. Sci. Process* **74** (2002) 333–338.
33. J. E. Riggs, D. B. Walker, D. L. Carroll and Y. P. Sun, *J. Phys. Chem. B* **104** (2000) 7071–7076.
34. P. W. Chiu, G. S. Duesburg, U. Dettlaff-Wegiikowska and S. Roth, *Appl. Phys. Lett.* **80** (2002) 3811–3813.
35. F. Frehill, J. G. Vos, S. Benrezzak, A. A. Koos, Z. Konya, M. G. Ruther, W. Blau, A. Fonseca, J. B. Nagy, L. P. Biro, A. I. Minett and M. in het Panhuis, *J. Am. Chem. Soc.* **124** (2002) 13694–13695.
36. J. K. Lim, W. S. Yun, M. H. Yoon, S. K. Lee, C. H. Kim, K. Kim and S. K. Kim, *Synth. Met.* **139** (2003) 521–527.
37. K. Fu, W. Huang, Y. Lin, D. Zhang, T. W. Hanks, A. M. Rao and Y. P. Sun, *J. Nanosci. Nanotech.* **2** (2002) 457–461.
38. W. Huang, S. Taylor, K. Fu, Y. Lin, D. Zhang, T. W. Hanks, A. M. Rao and Y. P. Sun, *Nano Lett.* **2** (2002) 311–314.
39. K. A. Williams, P. T. M. Veenhuizen, B. G. de la Torre, R. Eritja and C. Dekker, *Nature* **420** (2002) 761.
40. C. Dwyer, M. Guthold, M. Falvo, S. Washburn, R. Superfine and D. Erie, *Nanotechnology* **13** (2002) 601–604.
41. C. S. Lee, S. E. Baker, M. S. Marcus, W. S. Yang, M. A. Eriksson and R. J. Hamers, *Nano Lett.* **4**(9) (2004) 1713–1716.
42. J. Q. Liu, A. Chou, W. Rahmat, M. N. Paddon-Row and J. J. Gooding, *Electroanalysis* **17**(1) (2005) 38–46.
43. F. Pompeo and D. E. Resasco, *Nano Lett.* **2** (2002) 369–373.
44. P. J. Boul, J. Liu, E. T. Mickelson, C. B. Huffman, L. M. Ericson, I. W. Chiang, K. A. Smith, D. T. Colbert, R. H. Hauge, J. L. Margrave and R. E. Smalley, *Chem. Phys. Lett.* **310** (1999) 367–372.
45. V. N. Khabashesku, W. E. Billups and J. L. Margrave, *Acc. Chem. Res.* **35** (2002) 1087–1095.
46. M. Holzinger, O. Vostrowsky, A. Hirsch, F. Hennrich, M. Kappes, R. Weiss and F. Jellen, *Angew. Chem. Int. Edit.* **40** (2001) 4002–4005.
47. S. E. Kooi, U. Schlecht, M. Burghard and K. Kern, *Angew. Chem. Int. Edit.* **41** (2002) 1353–1355.
48. H. Hu, Y. Ni, V. Montana, R. C. Haddon and V. Parpura, *Nano Lett.* **4**(3) (2004) 507–511.
49. H. Kong, C. Gao and D. Y. Yan, *Macromolecules* **37**(11) (2004) 4022–4030.

50. Y. Liu, D. C. Wu, W. D. Zhang, X. Jiang, C. B. He, T. S. Chung, S. H. Goh and K. W. Leong, *Angew. Chem. Int. Edit.* **44**(30) (2005) 4782–4785.
51. X. F. Zhang, T. Liu, T. V. Sreekumar, S. Kumar, V. C. Moore, R. H. Hauge and R. E. Smalley, *Nano Lett.* **3** (2003) 1285–1288.
52. M. in het Panhuis, C. Salvador-Morales, E. Franklin, G. Chambers, A. Fonseca, J. B. Nagy, W. J. Blau and A. I. Minett, *J. Nanosci. Nanotech.* **3** (2003) 209–213.
53. M. F. Islam, E. Rojas, D. M. Bergey, A. T. Johnson and A. G. Yodh, *Nano Lett.* **3** (2003) 269–273.
54. M. J. O'Connel, S. M. Bachilo, C. B. Huffman, V. C. Moore, M. S. Strano, E. H. Haroz, K. L. Rialon, P. J. Boul, W. H. Noon, C. Kittrell, J. Ma, R. H. Hauge, R. B. Weisman and R. E. Smalley, *Science* **297** (2002) 593.
55. H. Murakami, T. Nomura and N. Nakashima, *Chem. Phys. Lett.* **378** (2003) 481–485.
56. A. Star, J. F. Stoddart, D. Steuerman, M. Diehl, A. Boukai, E. W. Wong, X. Yang, S. W. Chung, H. Choi and J. R. Heath, *Angew. Chem. Int. Edit.* **40** (2001) 1721–1725.
57. J. N. Coleman, A. B. Dalton, S. Curran, A. Rubio, A. P. Davey, A. Drury, B. McCarthy, B. Lahr, P. M. Ajayan, S. Roth, R. C. Barklie and W. J. Blau, *Adv. Mater.* **12** (2000) 213–216.
58. V. C. Moore, M. S. Strano, E. H. Haroz, R. H. Hauge and R. E. Smalley, *Nano Lett.* **3** (2003) 1379–1382.
59. X. F. Zhang, T. Liu, T. V. Sreekumar, S. Kumar, V. C. Moore, R. H. Hauge and R. E. Smalley, *Nano Lett.* **3**(9) (2003) 1285–1288.
60. J. Wang, M. Musameh and Y. H. Lin, *J. Am. Chem. Soc.* **125** (2003) 2408–2409.
61. M. S. Arnold, S. I. Stupp and M. C. Hersam, *Nano Lett.* **5**(4) (2005) 713–718.
62. Z. Guo, P. J. Sadler and S. C. Tsang, *Adv. Mater.* **10** (1998) 701–703.
63. K. Fu, W. Huang, Y. Lin, D. Zhang, T. W. Hanks, A. M. Rao and Y. P. Sun, *J. Nanosci. Nanotech.* **2** (2002) 457–461.
64. R. J. Chen, Y. G. Zhang, D. Wang and H. J. Dai, *J. Am. Chem. Soc.* **123** (2001) 3838–3839.
65. F. Belavoine, P. Schultz, C. Richard, V. Mallouh, T. W. Ebbesen and C. Mioskowski, *Angew. Chem. Int. Edit.* **38** (1999) 1912–1915.
66. J. J. Davis, K. S. Coleman, B. R. Azamian, C. B. Bagshaw and M. H. Green, *Chem. Eur. J.* **9** (2003) 3732–3739.
67. S. Q. Wang, E. S. Humphreys, S. Y. Chung, D. F. Delduco, S. R. Lustig, H. Wang, K. N. Parker, N. W. Rizzo, S. Subramoney, Y. M. Chiang and A. Jagota, *Nature Mater.* **2** (2003) 196–200.
68. O. K. Kim, J. T. Je, J. W. Baldwin, S. Kooi, P. E. Pehrsson and L. J. Buckley, *J. Am. Chem. Soc.* **125** (2003) 4426–4427.
69. D. Pantarotto, C. D. Partidos, R. Graff, J. Hoebeke, J. P. Briand, M. Prato and A. Bianco, *J. Am. Chem. Soc.* **125** (2003) 6160–6164.
70. P. J. Britto, K. S. V. Santhanam and P. M. Ajayan, *Bioelectrochem. Bioener.* **41** (1996) 121–125.
71. R. Bandyopadhyaya, E. Nativ-Roth, O. Regev and R. Yerushalmi-Rozen, *Nano Lett.* **2** (2002) 25–28.

72. P. R. Supronowicz, P. M. Ajayan, K. R. Ullmann, B. P. Arulanandam, D. W. Metzger and R. Bizios, *J. Biomed. Mater. Res.* **59**(3) (2002) 499–506.
73. S. E. Moulton, A. I. Minett, R. Murphy, K. P. Ryan, D. McCarthy, J. N. Coleman, W. J. Blau and G. G. Wallace, *Carbon* **43**(9) (2005) 1879–1884.
74. F. Balavoine, P. Schultz, C. Richard, V. Mallouh, T. W. Ebbesen and C. Mioskowski, *Angew. Chem. Int. Edit.* **38** (1999) 1912–1915.
75. M. Law, H. Kind, B. Messer, F. Kim and P. D. Yang, *Angew. Chem. Int. Edit.* **41** (2002) 2405–2408.
76. M. Valcarcel, B. Simonet, S. Cardenas and B. Suarez, *Anal. Bioanal. Chem.* published on line 11th July (2005)
77. C. C. Zhao, L. Zhang, X. W. Wei and Z. S. Yang, *Electrochem. Commun.* **5** (2003) 825–829.
78. J. Wang, M. Li, L. Z. Shi, N. Li and Z. Gu, *Anal. Chem.* **74** (2002) 1993–1997.
79. M. Zhang and W. Gorski, *Anal. Chem.* **77** (2005) 3960–3965.
80. R. J. Chen, N. R. Franklin, J. Kong, J. Cao, T. W. Tomblor, Y. G. Zhang and H. J. Dai, *Appl. Phys. Lett.* **79** (2001) 2258–2260.
81. Z. Xu, X. Chen, X. H. Qu and S. J. Dong, *Electroanalysis* **16**(8) (2004) 684–687.
82. Y. F. Zhao, Y. Q. Gao, D. P. Zhan, H. Liu, Q. Zhao, Y. Kou, Y. H. Shao, M. X. Li, Q. K. Zhuang and Z. W. Zhu, *Talanta* **66**(1) (2005) 51–57.
83. A. Guiseppi-Elie, C. H. Lei and R. H. Baughman, *Nanotechnology*, **13**(5) (2002) 559–564.
84. K. B. Wu, J. J. Fei and S. S. Hu, *Anal. Bioch.* **318**(1) (2003) 100–106.
85. P. P. Joshi, S. A. Merchant, Y. D. Wang and D. W. Schmidtke, *Anal. Chem.* **77**(10) (2005) 3183–3188.
86. Y. Q. Dai and K. K. Shiu, *Electroanalysis* **16**(20) (2004) 1697–1703.
87. X. Tan, M. Li, P. Cai, L. Luo and X. Zou, *Anal. Biochem.* **337** (2005) 111–120.
88. R. J. Chen, S. Bangsaruntip, K. A. Drouvalakis, N. W. S. Kam, M. Shim, Y. M. Li, W. Kim, P. J. Utz and H. J. Dai, *Proc. Nat. Acad. Sci.* **100** (2003) 4984–4989.
89. K. A. Joshi, J. Tang, R. Haddon, J. Wnag, W. Chen and A. Mulchandani, *Electroanalysis* **17**(1) (2005) 54–58.
90. H. Cai, X. N. Cao, Y. Jiang, P. G. He and Y. Z. Fang, *Anal. Bioanal. Chem.* **375**(2) (2003) 287–293.
91. M. Gao, L. Dai and G. G. Wallace, *Synth. Met.* **137**(1–3) (2003) 1393–1394.
92. S. Sotiropoulou and N. A. Chaniotakis, *Anal. Bioanal. Chem.* **375**(1) (2003) 103–105.
93. M. Gao, L. M. Dai and G. G. Wallace, *Electroanalysis*, **15**(13) (2003) 1089–1094.
94. J. Wang and M. Musameh, *Anal. Chim. Acta* **539**(1–2) (2005) 209–213
95. J. S. Ye, Y. Wen, W. D. Zhang, L. M. Gan, G. O. Xu and F. S. Sheu, *Electrochem. Commun.* **6** (2004) 66–70.
96. G. Marrazza, I. Chinanella and M. Mascini, *Anal. Chim. Acta* **387** (1999) 297.
97. M. Yemini, M. Reches, J. Rishpon and E. Gazit, *Nano Lett.* **5**(1) (2005) 183–186.
98. M. Chicharro, A. S'anchez, E. Bermejo, A. Zapardiel, M. A. Rubianes and G. A. Rivas, *Anal. Chim. Acta* **543** (2005) 84–91.
99. J. Wang, G. J. Liu and M. R. Jan, *J. Am. Chem. Soc.* **126** (2004) 3010–3011.

100. C. Liu, A. J. Bard, F. Wudl, I. Weitz and J. R. Heath, *Electrochem. Solid-State Lett.* **2** (1999) 577–578.
101. J. Li, A. Cassell, L. Delzeit, J. Han and M. Meyyappan, *J. Phys. Chem. B* **106** (2002) 9299–9305.
102. K. H. An, W. S. Kim, Y. S. Park, Y. C. Choi, S. M. Lee, D. C. Chung, D. J. Bae, S. C. Lim and Y. H. Lee, *Adv. Mater.* **13** (2001) 497–500.
103. J. N. Barisci, G. G. Wallace and R. H. Baughman, *J. Electroanal. Chem.* **488** (2000) 92–98.
104. M. Musameh, N. S. Lawrence and J. Wang, *Electrochem. Commun.* **7** (2005) 14–18.
105. S. Lefrant, M. Baibarac, I. Baltog, J. Y. Mevellec, L. Mihut and O. Chauvet, *Synth. Met.* **144** (2004) 133–142.
106. J. N. Barisci, G. G. Wallace, D. Chattopadhyay, F. Papadimitrakopoulos and R. H. Baughman, *J. Electrochem. Soc.* **150** (2003) E409–E415.
107. P. G. Whitten, G. M. Spinks and G. G. Wallace, *Carbon* **43** (2005) 1891–1896.
108. J. H. Park, J. M. Ko and O. O. Park, *J. Electrochem. Soc.* **150**(7) (2003) A 864–A 867.
109. M. Deng, B. Yang, S. Shang and Y. Hu, *J. Mater. Sci.* **40** (2005) 1017–1018.
110. C. Zhou, S. Kumar, C. D. Doyle and J. M. Tour, *Chem. Mater.* **17** (2005) 1997–2002.
111. M. Hughes, G. Z. Chen, M. S. P. Shaffer, D. J. Fray and A. H. Windle, *Chem. Mater.* **14** (2002) 1610–1613.
112. K. Jurewicz, S. Delpeux, V. Bertagna, F. Beguin and E. Frackowiak, *Chem. Phys. Lett.* **347** (2001) 36–40.
113. G. Maurin, Ch. Bousquet, F. Henn, P. Bernier, R. Almairac and B. Simon, *Chem. Phys. Lett.* **312** (1999) 14–18.
114. B. Gao, A. Kleinhammes, X. P. Tang, C. Bower, L. Fleming, Y. Wu and O. Zhou, *Chem. Phys. Lett.* **307** (1999) 153–157.
115. A. S. Claye, J. E. Fischer, C. B. Huffman, A. G. Rinzler and R. E. Smalley, *J. Electrochem. Soc.* **147**(8) (2000) 2845–2852.
116. H. Shimoda, B. Gao, X. P. Tang, A. Kleinhammes, L. Fleming, Y. Wu and O. Zhou, *Phys. Rev. Lett.* **88** (2002) 015502-1–015502-4.
117. B. Gao, C. Bower, J. D. Lorentzen, L. Fleming, A. Kleinhammes, X. P. Tang, L. E. McNeil, Y. Wu and O. Zhou, *Chem. Phys. Lett.* **327** (2000) 69–75.
118. J. N. Barisci, G. G. Wallace and R. H. Baughman, *J. Electrochem. Soc.* **147**(12) (2000) 4580–4583.
119. Z. H. Yang and H. Q. Wu, *Chem. Phys. Lett.* **343** (2001) 235–240.
120. K. Lota, V. Khomenko and E. Frackowiak, *J. Phys. Chem. Solids* **65** (2004) 295–301.
121. S. Gupta, M. Hughes, A. H. Windle and J. Robertson, *J. App. Phys.* **95** (2004) 2038–2048.
122. V. Richard, *Nature Mater.* **4** (2005) 429–430.
123. R. H. Baughman, C. X. Cui, A. A. Zakhidov, Z. Iqbal, G. M. Spinks, G. G. Wallace, A. Mazzoldi, D. De Rossi, A. G. Rinzler, O. Jaschinski, S. Roth and M. Kertesz, *Science* **284** (1999) 1340–1344.

124. A. M. Fennimore, T. D. Yuzvinsky, W. Q. Han, M. S. Fuhrer, J. Cumings and A. Zettl, *Nature*, **424** (2003) 408–410.
125. B. J. Landi, R. P. Raffaele, M. J. Heben, J. L. Alleman, W. VanDerveer and W. Gennett, *Nano Lett.* **2** (2002) 1329–1332.
126. H. Koerner, G. Price, N. A. Pearce, M. Alexander and R. A. Vaia, *Nature Mater.* **3** (2004) 115–119.
127. A. I. Minett, K. S. Atkinson and S. Roth, Carbon Nanotubes, in *Handbook of Porous Solids*, Eds. F. Schueth, K. Sing and J. Weitkamp, Wiley-VCH, Weinheim, 2002.
128. M. Kertesz, G. Sun, J. Kurti and R. H. Baughman, *Abs. of Papers of the American Chemical Society*, 22 August (1999).
129. G. Sun, G. Sun, M. Kertesz, J. Kurti and R. H. Baughman, *Abs. Papers of the American Chemical Society* 20 August (2000).
130. R. H. Baughman, A. A. Zakhidov and W. A. de Heer, *Science* **297** (2002) 787–792.
131. C. Niu, E. K. Sickel, R. Hoch, D. Moy and H. Tennent, *App. Phys. Lett.* **70** (1997) 1480–1482.
132. K. H. An, W. S. Kim, Y. S. Park, J. M. Moon, D. J. Bae, S. C. Lim, Y. S. Lee and Y. H. Lee, *Adv. Funct. Mater.* **11** (2001) 387–392.
133. J. N. Barisci, G. M. Spinks, G. G. Wallace, J. D. Madden and R. H. Baughman, *Smart Mater. Struct.* **12** (2003) 549–555.
134. P. A. Z. Suarez, V. M. Selbach, J. E. L. Dullius, S. Einloft, C. M. S. Piatnicki, D. S. Azambuja, R. F. de Souza and S. Dupont, *Electrochimica. Acta* **42**(16) (1997) 2533–2535.
135. J. Sun, M. Forsyth and D. R. MacFarlane, *J. Phys. Chem. B.* **102** (1998) 8858–8864.
136. J. N. Barisci, G. G. Wallace, D. R. MacFarlane and R. H. Baughman, *Electrochem. Commun.* **6** (2004) 22–27.
137. G. M. Spinks, G. G. Wallace, L. S. Fifield, L. R. Dalton, A. Mazzoldi, D. De Rossi, I. Khayrullin and R. H. Baughman, *Adv. Mater.* **14** (2002) 1728–1732.
138. R. Pelrine, R. Kornbluh, Q. Pei and J. Joseph, *Science* **287** (2000) 836–839.
139. Q. M. Zhang, V. Bharti and X. Zhao, *Science* **280** (1998) 210–2104.
140. J. Fraysse, A. I. Minett, G. Gu, S. Roth, A. G. Rinzler and R. H. Baughman, *Curr. App. Phys.* **1** (2001) 407–411.
141. A. I. Minett, J. Fraysse, G. Gu and S. Roth, *Electronic Properties of Molecular Materials*, Vol. 591, Eds. H. Kuzmany, J. Fink, M. Mehring and S. Roth, AIP, New York, 2001, pp. 585–589.
142. G. Gu, G. Philipp, X. Wu, M. Burghard, A. M. Bittner and S. Roth, *Adv. Funct. Mater.* **11** (2001) 295–298.
143. G. T. Kim, U. Waizmann and S. Roth, *App. Phys. Lett.* **79** (2001) 3479–3499.
144. G. T. Kim, G. Gu, U. Waizmann and S. Roth, *App. Phys. Lett.* **80** (2002) 1815–1817.
145. M. M. J. Treacy, T. W. Ebbesen and J. M. Gibson, *Nature* **381** (1996) 678–680.
146. E. W. Wong, P. E. Sheehan and C. M. Lieber, *Science* **277** (1997) 1971–1975.



147. J. P. Salvetat, J. M. Bonard, N. H. Thomson, A. J. Kulik, L. Forro, W. Benoit and L. Zuppiroli, *App. Phys. A* **69** (1999) 255–260 (and references stated within).
148. G. M. Spinks, G. G. Wallace, R. H. Baughman and L. M. Dai, in *Electroactive Polymer (EAP) Actuators as Artificial Muscles: Reality, Potential and Challenges*, 2nd ed., Ed. Y. Bar-Cohen, SPIE Press, Bellingham, WA, 2001, Ch. 8. 223–246.
149. S. Huang, L. M. Dai and A. W. H. Mau, *J. Phys. Chem. B* **103** (1999) 4223–4227.
150. M. Hughes and G. M. Spinks, *Adv. Mater.* **17** (2005) 443–446.
151. M. S. P. Shaffer, X. Fan and A. H. Windle, *Carbon* **36** (1998) 1603–1612.
152. W. I. Milne, K. B. K. Teo, G. A. J. Amaratunga, P. Legagneux, L. Gangloff, J. P. Schnell, V. Semet, V. T. Binh and O. Groening, *J. Mater. Chem.* **14** (2004) 933–943.

## Chapter 12

### Carbon nanotubes: Surface, porosity, and related applications

Q.-H. Yang<sup>a,b</sup> and H.-M. Cheng<sup>a</sup>

<sup>a</sup>Shenyang National Laboratory for Materials Science, Institute of Metal Research, Chinese Academy of Sciences, Shenyang 110016, China

<sup>b</sup>Institute of Multidisciplinary Research for Advanced Materials, Tohoku University, Sendai 980-8577, Japan

Carbon nanotube (CNT) is a kind of novel porous materials with a multi-modal porous structure and energy-dispersive surface. Its porous structure can be divided into fundamental inner cavity and several kinds of secondary porosities. The secondary porosities include interstices between single- and double-walled carbon nanotubes (SWNTs and DWNTs) in a bundle, aggregated pores among nanotube bundles or among multi-walled carbon nanotubes (MWNTs), and “carbon island” structure in large diameter MWNTs. Two typical physicochemical processes, adsorption in all types of porosities and filling in inner cavities, are discussed in detail, and two aspects of applications, filling-related nano-reactors and adsorption-related hydrogen storage media, electrode materials and sensors, are reviewed. The theoretical predictions and experimental results show that the multi-modal porous structure and surface characteristics of CNTs exert different influences on their applications and CNTs can be expected to be a promising candidate for energy storage media, especially as new electrode materials to improve the performance of rechargeable batteries and high-capacity double-layer electric capacitors.

#### 1. INTRODUCTION

Carbon nanotubes (CNTs) possess many distinguished properties and potential applications some of which are related to adsorption and capillarity in CNTs [1]. The theoretical and experimental investigations have proved that adsorption and capillarity may occur in either quasi-one-dimensional (1D) interiors of CNTs or other secondary porous structures [1]. CNTs, especially single-walled carbon nanotubes (SWNTs), are regarded as an ideal model for searching unfamiliar properties and performance of real 1D system. In this aspect, the inner cavities of SWNTs afford a wonderful and unique example of 1D confined space, and may serve as “nano-tanks” and “nanosized test tubes”, in which many unexpected physicochemical processes may occur [2]. In this chapter, adsorption and filling in the inner channel of CNTs are discussed in detail, since many interesting properties are stemmed from either of them. The secondary porous structures of CNTs include

interstices between individual CNTs in a bundle, aggregated pores between CNTs or CNT bundles, and separation zones between “carbon islands”. Different secondary porous structures are characterized by different properties, and consequently result in different performance. Furthermore, we should note that the surface area of CNTs exerts impact on many properties, and the surface defects of CNTs also influence their adsorption behaviors, which have been extensively investigated. Therefore, the exploration of the porous structure and surface characteristics of CNTs is very important for the interpretation of their adsorption performance and other related properties. In addition, we also review the latest advances in control and modification of the porous structure and surface characteristics of CNTs.

Nowadays, energy resource depletion and environmental pollution are the major two severe challenges human beings have to face. Since their birth in 1991 [3], CNTs have been regarded as one of the most possible alternatives for energy storage media [4] and promising in energy-related applications due to their unique surface characteristics and porous structures. Therefore, we also introduce some potential applications of CNTs, such as hydrogen storage, electrode materials, sensors, and nanosized test tubes, which are related to adsorption and other physicochemical processes occurred in the porous structures and surface defects of CNTs.

## 2. ADSORPTION IN CARBON NANOTUBES

### 2.1. Adsorption in inner channels of carbon nanotubes

Adsorption of gases in nanospaces is characterized as strong adsorption due to the overlap of force field from the opposite pore walls [5–7]. Calculated adsorption potential for micropores (pore size less than 2 nm) is enhanced by a factor of up to 2 compared with that for a planar surface, showing adsorbed molecules in micropores are subject to a strong adsorption force field. Theoretical predictions and experimental verifications have revealed that in these micropores, the assembly of adsorbed molecules and atoms is apparently different from that on a planar surface [5,6], and consequently quite many interesting physicochemical processes, which hardly occur on a planar surface, can be initiated.

It is well accepted that the fundamental porous structure of CNTs is inner hollow cavities (interiors). Open CNTs (e.g. SWNTs), with 1D cylindrical micro- or small meso-porous structures, have stronger force field than carbon slit-pores with similar pore size, as shown in Fig. 1 [8], which also makes CNTs an ideal substrate for adsorption studies.

In the past several years, many intriguing adsorption properties have been found for the interiors of CNTs. Experimental results and some theoretical calculations revealed that CNTs have high hydrogen adsorption capacities [9–16], and some researchers argue that inner cavities are important adsorption sites for  $H_2$  [9,17]. Gadd et al. reported that at 923 K, argon gas was squeezed into inner hollow cavities of closed CNTs (BET surface area:  $9.91 \text{ m}^2$ ) under 170 MPa, and the pressure of the sealed Ar in these nanotubes was estimated to be 60 MPa at room temperature. The Ar trapped nanotubes would not leak over several months until 1400 s of exposure to electron beam, so that CNTs can be regarded as the smallest gas cylinders [18].

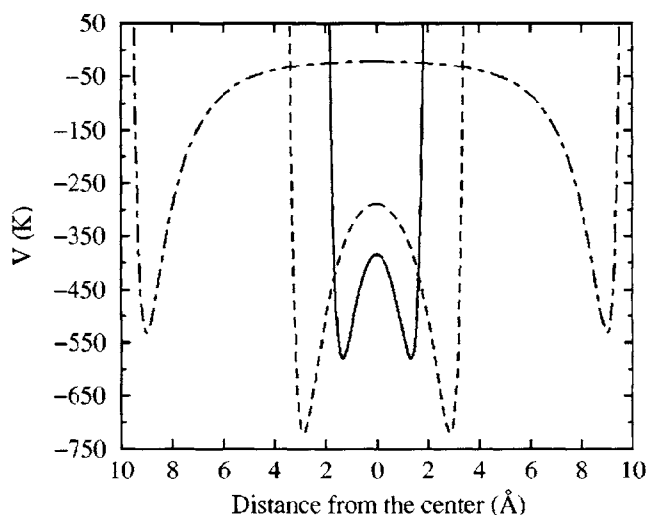


Figure 1. Adsorption potentials for hydrogen in tube arrays and idealized slit pores. The solid line denotes the idealized carbon slit pore with a pore width of 9 Å. The dashed line is the potential for a (9,9) tube array, and the dot-dashed line represents a (18,18) tube array [8]. Reprinted with permission from Wang and Johnson, Copyright 1999, American Institute of Physics.

Adsorption of other gases, such as noble gases [19,20] and oxygen [21], has also been investigated, and it is indicated that many curious properties of CNTs are related to gas adsorption properties.

Dillon et al. [9] investigated the adsorption of  $H_2$  in SWNT soots by temperature-programmed desorption (TPD) spectroscopy, and the results suggested that physisorption of hydrogen mainly occurred within the cavities of SWNTs with a binding energy four times higher than that for the planar graphite. Fujiwara [21] arrived at a conclusion that the inside cavity of nanotube has strong affinity for gas adsorption, and the affinity is larger than that in the interstitial channels of CNT bundles. It is revealed that the nitrogen cryo-adsorption amount in CNTs is enhanced with opening of nanotube caps, indicating that inner cavities are important adsorption sites for CNTs [22,23]. Yang et al. [24] investigated the adsorption behaviors of CNTs, and proved that the classical adsorption theory is still valid for the long and narrow nanotube pores with a huge aspect ratio. Nitrogen adsorption in open SWNTs is characterized by micropore-filling, while adsorption in open multi-walled carbon nanotubes (MWNTs) is typical capillarity and condensation, as shown in Fig. 2 [22].

Physicists pour their enthusiasms into the realization of quasi-1D fluids in the inner channels of CNTs. Many simulations and calculations show that some kinds of quasi-1D fluids may form in the inner hollow cavities [25–33]. Stan and Cole [30] conducted a theoretical exploration of the adsorption of noble gases in CNTs and found that there is a strong potential energy field in the nanoscale channel, as a consequence

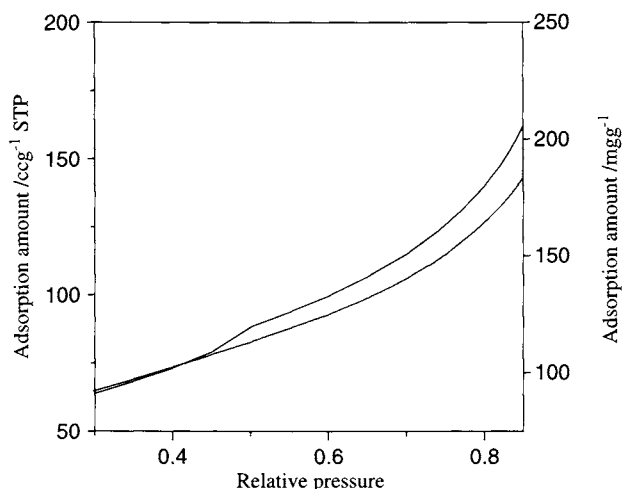


Figure 2. Nitrogen cryo-adsorption isotherm (medium pressure range) in MWNTs [22].

much stronger binding of the adsorbate in the channel than at the planar surface of graphite, leading to the ideal realization of 1D system. Their results also indicated that the adsorption potential inside MWNTs is a little higher than that inside SWNTs with a similar inner diameter, possibly due to the more overlapped force field from the coaxial multilayers of MWNTs. Helium is an ideal candidate for investigations of 1D system due to its low molecular weight, and some results revealed that  $^4\text{He}$  quasi-1D liquid could be formed in small-diameter SWNTs [26,31]. Gordillo et al. reported the Monte Carlo calculations for He [26] and  $\text{H}_2$  [32] adsorption in SWNTs, which showed that inside a (5,5) SWNT, the binding energy of liquid  $^4\text{He}$  is approximately three times larger than that on planar graphite, and  $^4\text{He}$  and  $\text{H}_2$  in a nanotube exist as a quasi-1D quantum fluid.  $\text{H}_2$  in the nanotube is well maintained in a large density range, closer to an ideal 1D fluid than liquid  $^4\text{He}$  in the same setup.

In the past several years, there appears another kind of novel 1D carbon nanomaterials except CNTs, e.g. carbon nanohorns [34], which also have quasi-1D interiors for adsorption and other physicochemical processes. Single-walled carbon nanohorns (SWNHs) are in fact one special type of SWNTs with cone caps resembling a horn, and SWNH aggregates can be produced by  $\text{CO}_2$  laser vaporization of carbon. A single aggregate can take either a “dahlia-like” or “bud-like” form. The interiors can be opened by partially burning them in an  $\text{O}_2$  [34,35] or  $\text{CO}_2$  [36] atmosphere (physical activation). As shown in Fig. 3, nanohorns usually have single walls and the inner diameter is about 2 nm [35].

In some cases, ends of CNTs are open or partially open, and the inner cavities of SWNTs and MWNTs possess micro- and meso-porous characteristics in adsorption measurements, respectively [24,37–39]. The pristine SWNTs, prepared by hydrogen arc discharge method [40], are proved with partially open ends since their isotherm shows

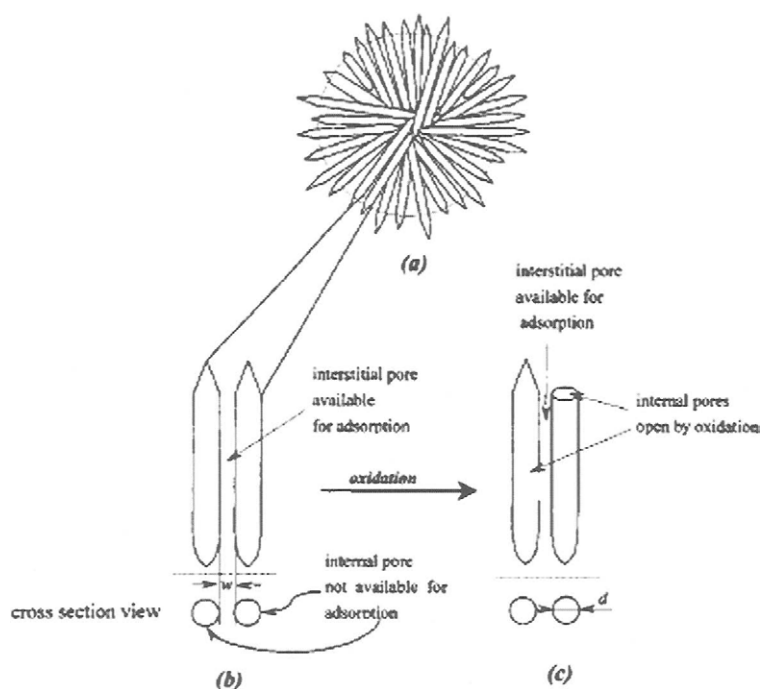


Figure 3. (a) A schematic representation of a bundle of SWNHs, (b) two adjacent SWNHs creating interstitial pore in as-prepared SWNH, (c) and internal pores in oxidized SWNHs with open windows [35]. Reprinted with permission from Bekyarova et al., Copyright 2003, American Chemical Society.

obvious microporous characteristics (Type I isotherm) [24]. The results based on TPD [9] and FTIR [41] also indicate that the adsorption occurs in the inside channels of partially opened SWNTs. Template-synthesized CNTs can be intentionally controlled to be with one or both ends opened [42–44]. Recently, Yang et al. [45] also explored the pore structure of template-synthesized CNTs, which were characterized by completely open ends and single-modal porosity attributed by uniform inside channels. The isotherm was characterized by a hysteresis loop with a sharply increased adsorption branch at the high relative pressure and stepwise desorption in a wide pressure range. The average pore diameter (22.5 nm) of the inner cavities, obtained by the analyses of the isotherm using Barrett–Joyner–Halender (BJH) method, coincides with the high-resolution transmission electron microscopy (HRTEM) observation (about 22 nm). The measured surface area of the CNTs was 365 m<sup>2</sup>/g, which is well consistent with the predicted value for the open-end CNTs (discussed below). Kaneko and co-workers [37] investigated the adsorption characteristics of MWNTs with one end opened and the adsorption isotherm was found to have no hysteresis loop, which is consistent with the theoretical prediction. In general, experiments and calculations show that the interiors

of CNTs can hold atoms or molecules through capillarity and adsorption, which thus brings out the unique possibility of using CNTs as nanosized super-adsorbents, nanosized reactors (offering possibility of experimental realization of a quasi-1D system) [2] and templates [46–48] for the fabrication of novel 1D nanomaterials such as nanowires.

However, for most real CNTs and nanohorns, the ends are usually capped with a half fullerene molecule, and therefore the inner cavities of CNTs are not fully available for adsorption and capillarity in most cases. Thus, researchers have been endeavoring to remove ends of CNTs [49–50] or open “windows” on the sidewalls of CNTs to enhance the adsorption and capillarity in their inner cavities [34,35].

## 2.2. Adsorption in interstices among nanotubes in a bundle

The interstices among individual nanotubes in a bundle are regarded as one kind of secondary porosity, which results from the closely packed SWNTs and DWNTs [51–56]. The smallest inter-tube spacing is usually slightly larger than the interlayer spacing in graphite, and the inter-tube spacing in DWNTs, in most cases, is a little larger than that in SWNTs. In crystalline SWNT ropes, individual SWNTs self-organize into “ropes”, which consist of 100–500 SWNTs in a 2D triangular lattice with uniform inter-tube spacing [57]. Some simulations were performed to determine the adsorption behavior of gas atoms or molecules such as He, Ar, Kr, H<sub>2</sub>, Xe, and N<sub>2</sub> in the interstices of a SWNT bundle and the results revealed that quasi-1D liquid of these gases may also be formed in the interstices between nanotubes [25,31,33]. However, for the cases of common SWNTs or DWNTs, due to their small diameter, this kind of porosities is hard to be confirmed by experimental adsorption measurements. Like interlayer spacing in conventional graphite materials, the interstices are believed to be domains holding some doped ions in charge-transfer systems. Rao et al. [58] proved that the halogen and alkaline-earth metal ions were inserted into the spacing and some electron transfer occurred between the dopants and the host SWNTs.

The interstices in SWNHs are relatively larger (about ~1 nm) compared with the common SWNTs, and have been proved by nitrogen adsorption as an important domain for adsorption before ends-opening process [35,59]. Yang et al. [60] prepared large-diameter SWNTs with a larger inter-tube spacing around 1 nm by the chemical vapor deposition (CVD) method as schematically represented in Fig. 4. It is shown that this kind of porosity is wedge-shaped porosity. Regrettably, the amount of the sample was too low to carry out adsorption measurement, and optimization of the synthesis technique is highly needed. MWNTs usually do not exist as bundles except for aligned nanotubes [61], leading to the absence of this type of porosity.

## 2.3. Adsorption in aggregated pores in carbon nanotubes

Aggregated pores are the third kind of porosity in CNTs and another secondary porous structure for adsorption as discussed in ref. [22]. In the nitrogen cryo-adsorption isotherm of MWNTs as shown in Fig. 5, an apparent hysteresis loop is shown in Part IV in the pressure range of  $p/p_0 = 0.85–0.99$ . The adsorption amount of nitrogen sharply increases from 160 to 750 mg/g, resulting from an enhanced capillary

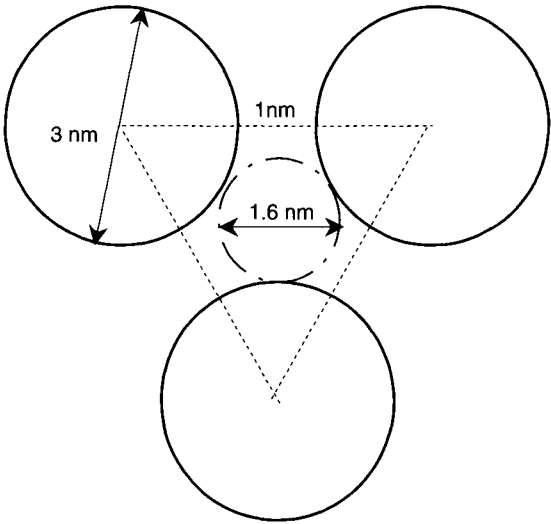


Figure 4. Schematic model for inter-tube cavity in a large-diameter SWNT bundle. Herein, the SWNTs are of 3.0 nm in diameter, the inter-tube distance is 1.0 nm, and accordingly, dimension of the cavity formed within the bundle lies in micropore range [60]. Reprinted with permission from Yang et al., Copyright 2003, Wiley-VCH.

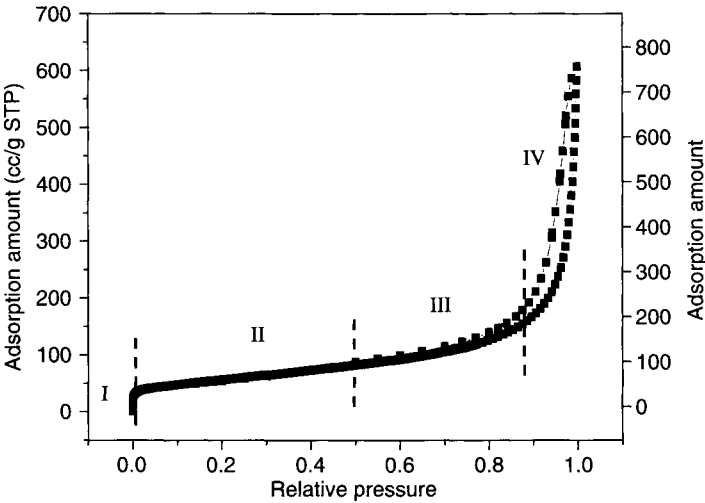


Figure 5. Nitrogen cryo-adsorption isotherm of MWNTs (above curve: desorption branch; below: adsorption branch) [22].



condensation in larger pores, which represents 78.5% of the total adsorption amount. According to the Kelvin equation, the corresponding pore size is about 20–40 nm (widely distributed porosity), which is likely to be contributed by the so-called aggregated pores (confined pores formed in an aggregated structure), since there are no CNTs with so large an inner cavity to form such inner porosity. The isolated nanotubes of different diameters and orientations interact to form an aggregated structure by inter-molecular force, and the so-called aggregated pores are formed among the isolated nanotubes in a relatively stable aggregated structure (see Fig. 6). This observation experimentally proved the existence of the third kind of pores—“aggregated pores”, which plays an important role in the adsorption and capillarity behavior of MWNTs. Due to the wide size distribution and large volume, the aggregated pores in MWNTs make greater contribution to capillary condensation than the CNT inner cavities. This kind of porosity is also important for SWNTs, which attributes the capillarity at high relative pressures [17,62]. For SWNTs, these pores are formed by the interaction between SWNT bundles and can be divided into ordered inter-bundle pores and disordered inter-bundle pores, whose sizes range from several nanometers to several hundred nanometers [17]. Alain et al. [63] also reported a nitrogen adsorption isotherm of SWNTs with a slight hysteresis loop at high relative pressures, but they did not discuss the origin of the hysteresis. These pores were also found in aggregated SWNHs and were formed between the SWNH assemblies, and the pore size was in the range of 5–20 nm [25].

The aggregated pores are not very stable and a relatively strong foreign force exerted on the CNTs can destroy these structures since these disorder pores are not intrinsic structural cavities like the inner cavities of nanotubes. For example, a cold-pressing process can greatly decrease the volume of the aggregated pores [22,63]. In Fig. 7, we compare the isotherms of the purified MWNTs before and after cold-pressing under a pressure of 6 MPa, and it is revealed that this kind of porosity is greatly diminished after pressing, resulting in a reduction of the corresponding hysteresis [22].

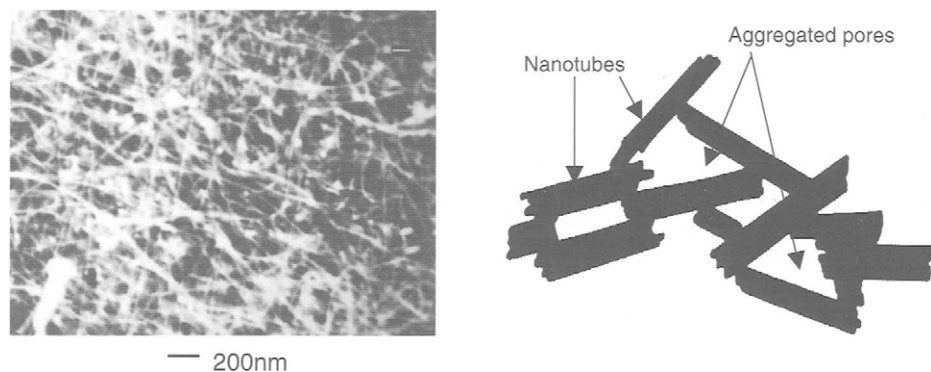


Figure 6. SEM image of the aggregated MWNTs (left) and schematic structural model for the aggregated pores (right) [22].

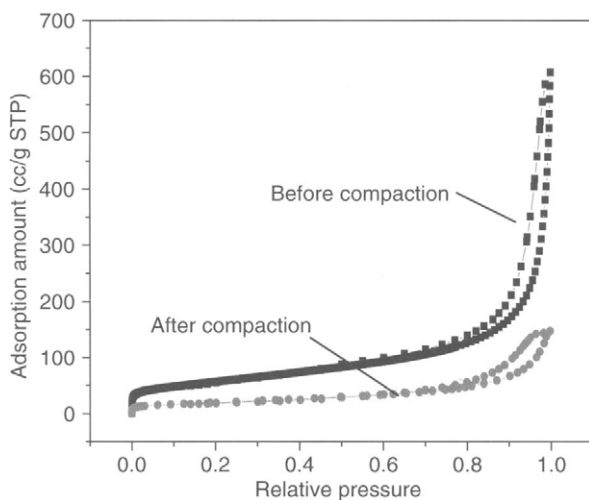


Figure 7. Comparison of nitrogen cryo-adsorption isotherms of MWNTs before and after cold-pressing under high pressure [22].

Although the aggregated pores in CNTs are not very stable, in some cases, they play a much greater role in adsorption than their inner cavities since nanotubes are popular with both ends closed. Thus, not only the opening-up of the nanotubes but also the control of their aggregated pore texture is important for the enhancement of adsorption and capillarity of CNTs.

#### 2.4. Adsorption in inter- and intra- “carbon island” spacing

The interlayer spacing of rolled graphene sheets in MWNTs is also thought to possibly behave as adsorption space for some kinds of small molecules. By HRTEM observation as shown in Fig. 8, it is apparent that the sidewalls of less crystallized CNTs are composed of discontinuous graphene stacks, which we defined as “carbon island” [64]. For this kind of structure, graphene layers are roughly aligned with each other to form “carbon islands”, and these “carbon islands” are surrounded by cavities and defect areas like a “sea”. The interlayer spacing between the wavy adjacent graphene sheets in “carbon islands” is too small for  $N_2$  to enter, but they are possible adsorption domain for some smaller molecules. The “sea” including defects or cavities around the “carbon islands” would not only provide a pathway or entrance for adsorbate molecules to enter the interiors of the graphene layers and but also behave as another adsorption sites. Hou et al. [65] argued that this kind of structure plays an important role in hydrogen adsorption of CNTs.

In the past several years, chemical activation processes applicable for the preparation of activated carbons were employed for the preparation of high specific surface area CNTs (activated CNTs, over  $1000 \text{ m}^2/\text{g}$ ) [66]. The activation processes are in fact to destroy and remove cavities and defect zones surrounding the “carbon islands” to enlarge the separation (“sea” around “island”) and produce more defects.

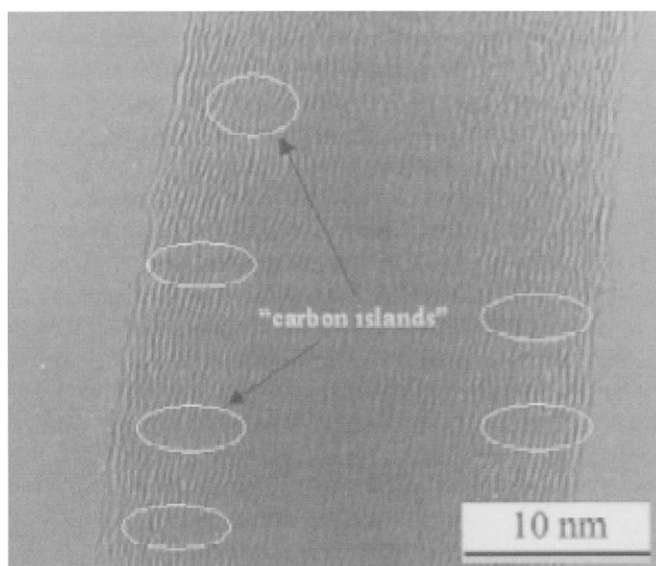


Figure 8. HRTEM image of MWNTs with “carbon island” structure [64,65].

These enhanced separations between “carbon islands” are in a micropore range. All these micropores are easily accessible since the diameter of CNTs is very small and the diffusion length of gas adsorbates to reach these pores is short compared with other activated carbon materials. It is obvious that these pores between “carbon islands” are one kind of defect-related secondary pores and can be enlarged by activation processes.

## 2.5. Adsorption in surface structural defects

The surface defects (thereafter referred to as physical defects resulted from geometry differences) of sidewalls of less crystallized CNTs contribute to a “carbon island” structure. In fact, even those CNTs with good crystallinity (e.g. SWNTs or DWNTs), also possess a certain concentration of defects on the surface of their sidewalls. These defects contain dangling bonds, pentagon–heptagon defect pairs in the lattice, pentagons at the nanotube tips and curvature, and doped foreign atoms. These surface defects will contribute to some surface adsorption, and this kind of adsorption determines some important performances, such as gas sensing, of CNTs. Experimental results suggest that the electronic conduction of semiconducting SWNTs is dependent upon gas adsorption on defective sites of their carbon wall [67,68].

Surface geometry influences adsorption process to some extent, and Williams and Eklund [69] concluded based on calculations that there are many kinds of adsorption sites with different surface geometry and energy coexisting in SWNT bundles and “grooves” (the wedge-shaped channel running along the outer surface of the rope where two nanotubes meet), which may have very high adsorption potentials

comparable to the interstices in nanotube bundles. These results suggest that the treatment of the outer surface of SWNT ropes is important not only for the obvious geometrical reasons (high surface area), but also for energetic reasons as well, since typical ropes possess many “wedge” channels on their exterior surface. Yang et al. [17] also conducted surface energy distribution investigations based on the nitrogen adsorption isotherm of highly crystalline SWNTs and the results confirm the existence of heterogeneous surface in the SWNTs. Sun et al. [70] conducted the fractal investigations on CNTs using nitrogen adsorption isotherm and small angle X-ray spectroscopy (SAXS) results. It was shown that the surface of SWNTs is fractal and energetically dispersive, coinciding to Eklund and Yang's results. Generally, CNTs have a wide surface energy distribution, showing the existence of multi-model surface structures and multiple-types of adsorption sites.

### 3. POROUS STRUCTURE OF CARBON NANOTUBES

Many kinds of gases, vapors, and liquids have been employed as adsorbates to probe adsorption behaviors, porous and surface structures of CNTs. Among them, nitrogen is the most commonly used adsorbate. Fig. 5 shows a multi-stage nitrogen cryo-adsorption isotherm of MWNTs, which indicates a multi-modal pore structure [22]. The significant characteristic for this isotherm is a hysteresis loop in Parts III and IV (Type IV characteristics), which is associated with capillary condensation in mesopores. As stated above, Part III corresponds to capillary condensation occurring in the inner cavities of some nanotubes with open tips at the medium relative pressure range and Part IV represents the condensation process in larger aggregated pores in the high relative pressure range. SWNTs and SWNHs have a similar multi-stage adsorption isotherm, also indicating the multi-modal porous structure.

Combining adsorption results with other results (HRTEM, XRD, etc.), a simple model for the multi-types of porosity in CNTs was proposed by Yang et al. [64,71]. In comparison to the slit-pore system of conventional activated carbons, the schematic representation of this mode is shown in Fig. 9 [64]. Illustrated in this representation are the fundamental porosity, quasi-1D inner channels, and secondary porous structures including interstices between individual CNTs in a bundle, aggregated pores between CNTs or CNT bundles. It should be noted that “carbon island” and the related surface microporosity are not included in this model. Due to the diversity of the geometrical characteristics for different porosities, the detailed adsorption natures are different from fundamental internal pores to secondary pores, from SWNTs, SWNHs to MWNTs. Related investigations have been extensively conducted in different areas from different point of views.

Three additional points should be pointed out. Firstly, except for the common porous structures, activated CNTs [66] contain abundant microporosity on their sidewalls, and this kind of porosity is most important for adsorption and other physicochemical process. Secondly, aligned CNTs or CNT ropes may be considered as multi-stage porous materials containing ordered porous textures not only in nanoscale, but also in mesoscale and macroscale [61]. Thirdly, the interstices and aggregate pores are very important for the SWNH assemblies [34].

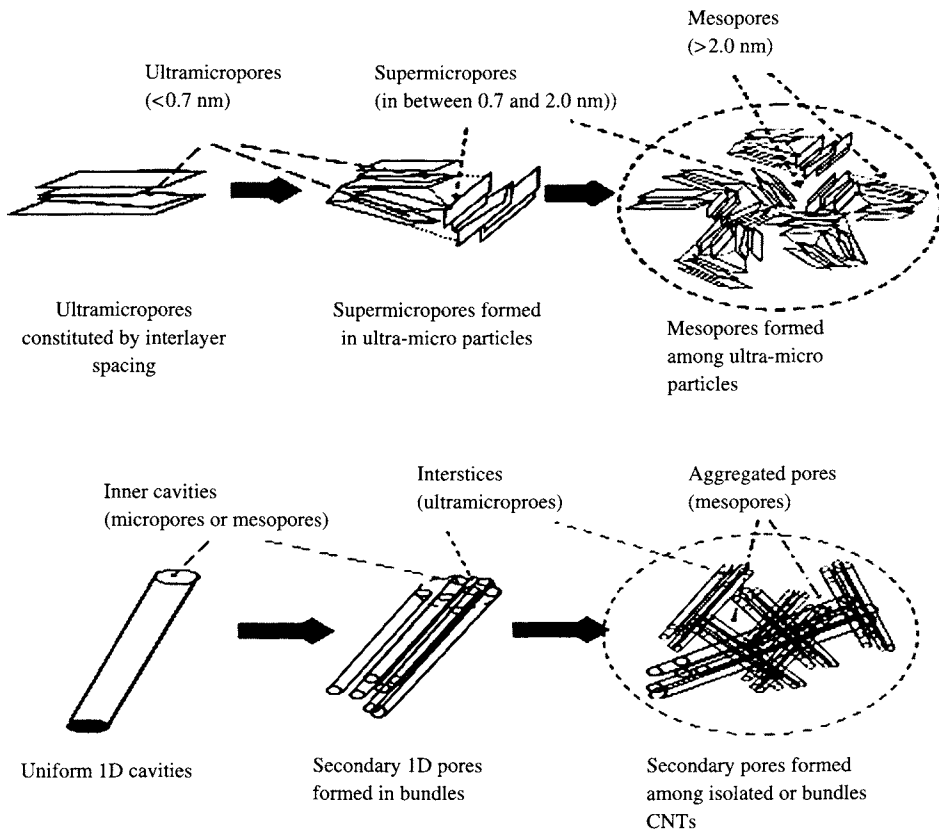


Figure 9. Schematic representation of proposed pore formation model in carbon nanostructures (upper: porous carbon; lower: carbon nanotubes) [64].

#### 4. SURFACE CHARACTERISTICS OF CARBON NANOTUBES

As stated above, both surface area and surface characteristics of a porous material are essential factors for its adsorption behavior. CNTs are regarded as high surface area materials. Isolated SWNTs with open tips are predicted to have very high surface area ( $S_{\max} = 2630 \text{ m}^2/\text{g}$ ) [64,71]. In this case, every carbon atom is on the surface. However, in fact, the real SWNTs show much lower specific surface area (measured by gas adsorption method) than the predicted value because SWNTs usually aggregate into bundles and most of the SWNTs are capped with hemi-fullerene molecules. Therefore, for real SWNTs, the surface area ( $S$ ) is a function of three parameters, purity ( $p$ ), tube number ( $n$ ) in one bundle, and the ratio ( $r$ ) of the number of open tubes versus that of overall tubes [64]. The correlation can be expressed in the following equation,

$$S = S_{\max} f(p, n, r) \quad (1)$$

Higher purity (larger  $p$ ) and higher open tube ratio ( $r$ ) but smaller bundle (low  $n$ ) result in higher surface area ( $S$ ). Peigney et al. [72] and Williams and Eklund [69] gave a similar correlation between  $r$  and  $S$  that delaminating of nanotube ropes should increase the specific surface area. Bacsá et al. prepared a mixture of SWNTs and DWNTs with relatively high surface area ( $\sim 950 \text{ m}^2/\text{g}$ ) using CVD method. Nanotubes (90%) are individual rather than bundled, leading to a much larger surface area compared with common SWNTs, accessible to nitrogen in adsorption measurement [73].

For MWNTs with both ends open, the surface area is only dependent on their wall number, the correlation is shown in Eq. (2) [64].

$$S = 2630/n \text{ (m}^2/\text{g)} \text{ (} n \text{ is the wall number)} \quad (2)$$

The template-synthesized MWNTs with open tips accord the correlation between surface area and diameter very well. The CNTs with an average diameter of 30 nm and wall number of 8 layers have the measured surface area of  $356 \text{ m}^2/\text{g}$ , consistent with the calculated value of  $329 \text{ m}^2/\text{g}$  [45].

For the MWNTs prepared by conventional techniques, their surface area is related to purity ( $p$ ), the wall number ( $n$ ), tube diameter ( $d$ ), and the ratio ( $r$ ) of the number of opening tubes relative to that of the overall tubes. Peigney et al. [72] gave a correlation between the specific surface area and tube wall number and tube diameter, as indicated in Fig. 10. Based on these correlations, we can obtain one parameters from the other, and thus we can have a preliminary estimation on the structure parameters and purity of CNTs. Yang et al. [56] compared the aggregation characteristics of DWNTs with those of SWNTs, prepared by a similar method, by the specific surface area (the specific surface area of DWNTs is half that of SWNTs) and proved that the SWNTs and DWNTs have similar bundle characteristics (average number of nanotube in a bundle).

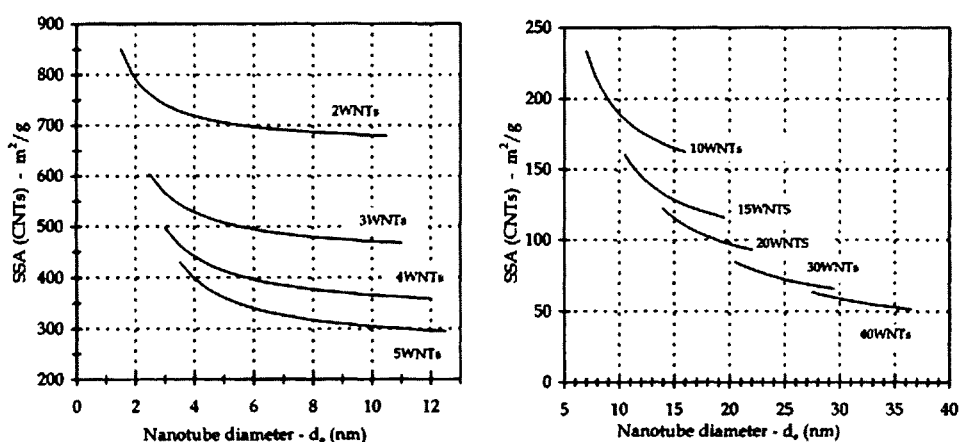


Figure 10. Specific surface area of closed CNTs versus their diameter and number of walls [72].

Gas adsorption on solid surfaces and in pore spaces is a complex process between adsorptive molecules and adsorbent surface molecules, involving mass and energy interaction. Not only pore structure but also surface structure determines adsorption process as stated above, and adsorption isotherms provide a great deal of information not only for pore structure but also for surface energy distribution [17]. Williams and Eklund [69] have reached the conclusion that there are many kinds of adsorption sites with different surface energy coexisting in SWNT bundles: inner surface of cylindrical cavities, outer surface of SWNT bundles and isolated nanotubes, and interstice in nanotube bundles, which is hard to be characterized by nitrogen adsorption method. The multi-stage characteristics of the isotherm also suggest that there are several adsorption sites with different surface energy; for instance, adsorption sites on micropore surface, adsorption sites on smaller mesopore surface responsible for capillarity (possibly ordered inter-bundle pores) and outer surface of bundles. In other words, the adsorption isotherm conveys a great deal of information about the energetic heterogeneity of solid adsorbent and provides a sensitive indicator of surface properties.

The integral adsorption isotherm can be interpreted as a convolution of a distribution of the adsorbate-adsorbent interaction intensity with a local isotherm for which the interaction (resulted from surface energy) is a parameter. The local isotherm can be calculated by the modified density functional theory (DFT) and the measured integral isotherm can be inverted into surface energy distribution [68]. Accordingly, Yang et al. [17,64] obtained multi-model surface area distribution  $f(\epsilon)$  for SWNTs and MWNTs with respect to surface energy  $\epsilon$ . Fig. 11 [64] shows a wide surface energy distribution of two SWNTs, suggesting the existence of heterogeneous surface in these SWNTs. Similarly, MWNTs are also proved to have a multi-distributed surface energy.

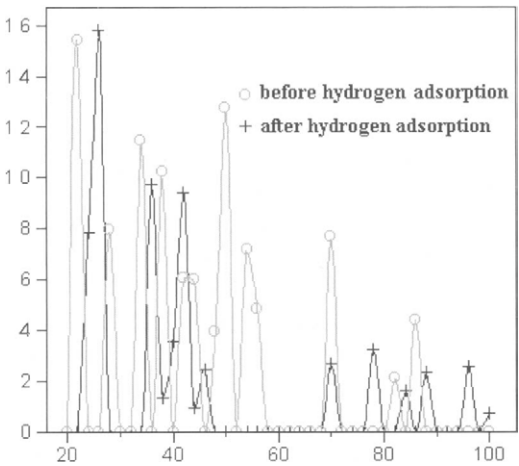


Figure 11. Surface energy distribution of SWNT bundles before and after hydrogen ad-desorption cycle [64].

In general, CNTs have a wide surface energy distribution, showing the existence of multi-type surface structures and multi-type adsorption sites.

## 5. CAPILLARITY AND FILLING IN CARBON NANOTUBES

Except for adsorption and capillarity of gas and vapor into porous structure of CNTs, another fundamental process in these porous structures is capillarity and filling of liquid and molten solid. Soon after the discovery of CNTs, on the basis of computer simulations, Pederson and Broughton [74] predicted that liquid may fill into open CNTs by capillary effect. That is to say, the inner channels of CNTs possibly behave as storage media not only for gases and vapors but also for liquid and solid transformed from liquid or gas through nano-reaction. Ajayan and Iijima [75] first reported that molten lead can be trapped in the inside channel of MWNTs. In the past several years, the successful encapsulation of metal compounds in SWNTs [76] and the discovery of peapods [77] opened up a new era for nanotube filling.

Filling in CNTs is an effective tool to construct nanocomposites, build nanodevices, and synthesize nanowires and nanorods. Filling and encapsulation of some foreign materials in CNTs can be achieved by several methods: (1) inclusion in the interior of CNTs in preparation process; (2) physical filling (two successive steps comprising opening of nanotubes and capillary filling of foreign liquid); and (3) chemical filling (opening of nanotubes and filling of foreign elements occur simultaneously).

Wetting carbon surface by a foreign liquid is the basis of capillary filling, and this process is only applicable to the liquids with low surface tension and is also determined by nanotube diameters [78–80]. Materials with high surface tension can be encapsulated in CNTs only by chemical filling routes. Chemical filling routes can be divided into two categories: wet chemistry solution method [50] and molten medium method [75]. For the former, CNTs are treated with diluted nitric acid in which a metal salt is dissolved, and when nanotube caps are removed by the acid, metal salts simultaneously enter into the inner cavities. The typical procedure for the latter is filling of the molten salt into CNTs in an oxidized atmosphere at relatively high temperatures, characterized by simultaneous opening of nanotube caps by oxygen and filling of molten metal compounds. For example, when lead and CNTs are annealed in the presence of oxygen at 673 K, Pb salt will enter the inner cavities of CNTs. However, the Pb salt cannot fill the inner cavities when the calcination occurs in inert atmosphere or in vacuum [49,75]. Likewise, bismuth and CNTs were co-heated at 1123 K in the oxidized atmosphere to form Bi-filled CNTs [49]. Pure metals or metal compounds with high surface tension fill into CNTs only in an oxidized atmosphere possibly due to the fact that low-surface-tension oxides are formed in the oxidized atmosphere [79].

Both molten medium and wet chemistry solution methods have been used to introduce substances into the hollow cavities of MWNTs. However, the agglomeration state of filled materials is highly dependent upon the techniques used. Wet chemistry method tends to result in filling, which consists of discrete crystallites; whereas molten medium method tends to give long, continuous single crystals [83].



Many researchers carried out chemical reactions inside the filled tubes to modify the properties of filled materials, such as the reduction of encapsulated oxides to metals. The big drawback for both methods is low-filling effectiveness, which possibly results from the diameter dependence of filling and capillarity [80].

The research on filling in CNTs can also be stretched to some new areas: preparation of nanocomposites combining host CNTs with guest filling materials, fabrication of 1D nanowires, and reaction in nanochannels of CNTs.

Green and co-workers [76,81–88] have published many reports in the research field of filling CNTs since they reported filling MWNTs by wet chemistry solution method in 1994 [50]. In 1998, they first realized the filling of  $\text{RuCl}_3$  in SWNTs [76] and subsequently made precise investigations on filled SWNTs. They observed filling of  $\text{C}_{60}$  molecules in SWNTs [84]. The peculiar crystallization behavior of filled species is enforced by 1D inner cavities of CNTs, and they prepared and verified bilayer KI 1D crystals included in 1.4-nm diameter SWNTs (Fig. 12) [85]. Therefore, CNTs, especially SWNTs, are ideal templates for the formation of nanowires and 1D nanocomposites with many unexpected structure and properties.

Reported in 1998, Luzzi and co-workers [77] proved the existence of peapod chains (formed by encapsulation of  $\text{C}_{60}$  in SWNTs, named by Luzzi et al. as  $\text{C}_{60}@\text{SWNTs}$ ), as shown in Fig. 13, in purified SWNTs prepared by pulsed laser vaporization method. The peapods in chain are 1.0 nm apart, center-to-center, and the diameter of peapod is about 0.7 nm, near to the size of  $\text{C}_{60}$ . So far, they have realized the controlled syntheses of carbon peapod with a high yield of 50–100% [89], and made further investigations for the properties of carbon peapod [90–93] and other kinds of metallo-fullerence molecules such as  $\text{La}_2@\text{C}_{80}@\text{SWNTs}$  [94]. They found that peapods can make remarkable deformation when exposure to electron-beam irradiation within an electron microscope [77,90]. They also found that inserting of  $\text{C}_{60}$  molecules into SWNTs modifies the local electronic structure of both nanotubes and  $\text{C}_{60}$ , giving rise to a novel hybrid material with some extraordinary properties such as tunable electronic properties [92].

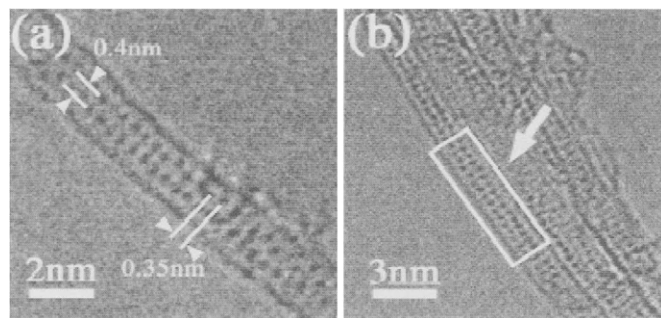


Figure 12. HRTEM images of two-atom thick crystals formed within (a) a 1.4-nm diameter SWNT, (b) a SWNT bundle [85]. Each dark spot corresponds to a two-atom K–I (or I–K) column. The inter-spot spacing along the tubule is ca. 0.35 nm, while the spacing across the tubule is ca. 0.4 nm.

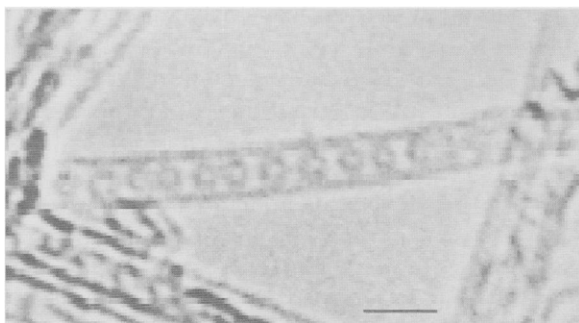


Figure 13. HRTEM image of peapods. The closed cycles in the SWNT are C<sub>60</sub> molecules. Scale bar = 2.0 nm [77]. Reprinted with permission from Smith et al., Copyright 1998, Nature publishing group.

It should be mentioned that Kyotani and co-workers [100] prepared various nanowires and nanocrystals by filling CNTs. They prepared CNTs with open ends and evenly distributed diameters by chemical vapor deposition of hydrocarbons in the nanochannels of anodic alumina oxide (AAO) films, filled CNTs with some species followed by removing the AAO templates, and finally obtained nanowires or nanoribbons in CNTs with a uniform diameter.

## 6. CONTROL AND MODIFICATION OF SURFACE CHARACTERISTICS AND POROUS STRUCTURE OF CARBON NANOTUBES

Both porous structure and surface characteristics are critical for generating unique physicochemical processes in CNTs, and it is necessary to precisely tailor these parameters using physical or chemical routes to control these physicochemical processes.

### 6.1. Diameter control of carbon nanotubes

The diameter of CNTs is believed as one of the controlling parameters for surface area and internal pore size of CNTs. However, the controlled growth of CNTs, especially SWNTs with a very narrow or uniform diameter distribution, still remains a challenging issue up to date. SWNTs with the peak diameter of about 1.2–1.4 nm can be grown by a conventional pulse laser vaporization method [101] and electric arc method [102]. Ajayan and Iijima [103] observed a single isolated nanotube with a diameter of C<sub>60</sub> on the surface of a MWNT. Sun et al. [104] succeeded in the preparation of MWNTs with the inner diameter of 0.5 nm (the same as the diameter of a C<sub>36</sub> molecule) by a modified electric arc technique. Several years ago, mono-sized (0.4 nm) SWNTs were prepared by a template technique of pyrolysis of tripropylamine molecules in the channels of porous zeolite [105]. Cheng et al. [106–107] developed a catalytic decomposition method of hydrocarbons to synthesize SWNTs with mean diameter of  $1.69 \pm 0.34$  nm. Liu et al. [108] prepared SWNTs and SWNT ropes with a mean diameter of  $1.72 \pm 0.2$  nm by the hydrogen electric arc method

[38]. Kiang [109] synthesized SWNTs with average diameter around 2 nm by a modified electric arc method with addition of some kinds of promoters. Labedkin et al. [110] succeeded in preparing SWNTs with diameter distribution of 2–6 nm by laser vaporization. By precise control of the synthesis parameters, Yang et al. [60,111] prepared large diameter SWNTs over 3 nm with a narrow diameter distribution and SWNT macroscopic fibers (aligned not only microscopically, but also mesoscopically and macroscopically) with average individual diameter over 2 nm by floating catalytic CVD of hydrocarbons. Different groups prepared DWNTs using diverse methods [51–56,112–115] and their diameter often has a wider distribution than that of the SWNTs prepared by the similar preparation method. Recently, Endo et al. [51] reported a CVD synthesis and a two-step purification to obtain DWNTs with high purity, whose double coaxial walls varying little in diameter. Most recently, Ren and Cheng [113] have synthesized aligned DWNT ropes with a narrow diameter distribution by sulfur assisted floating catalytic decomposition of methane. The outer and inner tube diameters of DWNTs are narrowly distributed in the range of 1.7–2.0 and 1.0–1.3 nm, respectively. Kyotani et al. [116] invented a template technique to prepare MWNTs with controlled inner and outer diameters, and the most striking feature of their method is to allow one to produce monodispersed CNTs with uniform length, diameter, and thickness.

## 6.2. Activation of carbon nanotubes

In the cases of conventional activated carbons, activation is employed to open the closed pores existed in the pristine materials or introduce new defects to carbon layer. The activation methods can be divided into two categories: physical or chemical activation. The two categories of activation methods have been used to prepare high surface area 1D carbon nanomaterials.

Physical activation is used for end-opening and side-wall erosion of CNTs or SWNHs by  $O_2$  [34,35,41,50] and  $CO_2$  [36,49]. In most cases, CNTs have both ends closed, and hence the activation to remove their tips is critical for the interior to behave as adsorption domain. In 1993, Ajayan et al. [49] and Tsang et al. [50] removed the tube tips by activation (heat-treating CNTs in  $CO_2$  and air atmosphere, respectively). Nowadays, it is not difficult to obtain open tubes by physical activation. Fig. 14 reveals that the purification process can remove part of tips from both ends of MWNTs [22], and the diameter of the opened inner cavities is around 3.0–4.0 nm. Correspondingly, as shown in Fig. 15, the pristine MWNTs (close ends) have no mid-pressure capillarity (no hysteresis loop on the isotherm), while the purified MWNTs (some fraction of ends opened) appear an apparent hysteresis loop, indicative of a strong capillary condensation. Therefore, it is the inner hollow cavities in MWNTs that are responsible for capillarity in a mid-pressure range.

Nanowindows were donated to the walls of SWNHs by oxidation in oxygen [35] at relatively low temperature (lower than 700 K). It was shown that He, Ar,  $N_2$ ,  $CH_4$ ,  $SF_6$ , and  $C_{60}$  can enter the interiors of SWNHs through the nanowindows, imparting the nanohorns a molecular sieving effect. Heat-treatment in  $CO_2$  at 1273 K provides a sufficient opening for nanowindows in the walls of bud-type SWNHs [39]. The size of nanowindows can be precisely controlled by varying the treatment conditions.

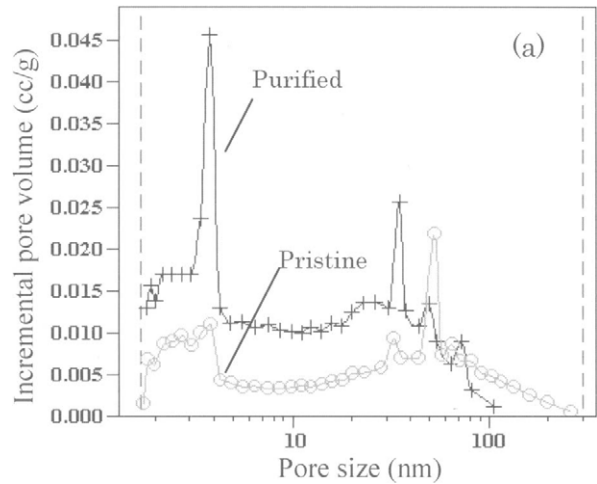


Figure 14. Pore size distributions of the aggregated MWNTs before and after purification [22].

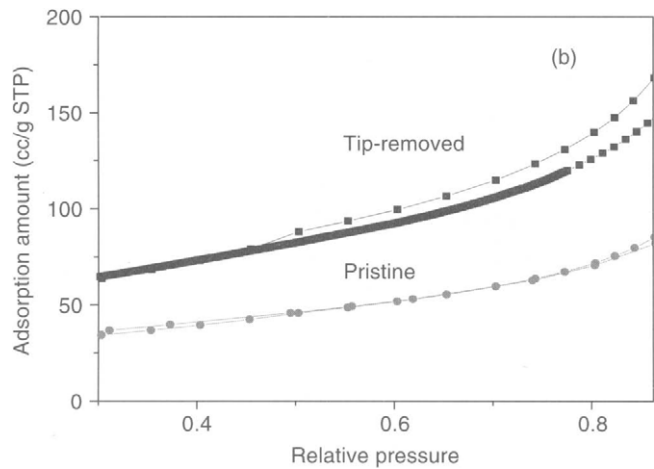


Figure 15. Nitrogen adsorption isotherm of the aggregated MWNTs before and after purification [22].

SWNHs, after pore-opening by oxidization treatment, shows a higher surface area of about 800 m<sup>2</sup>/g and pore size of the internal tube spacing is about 2 nm, consistent with the HRTEM observations.

In the case of MWNTs, activation to introduce defects and porosities into side-walls produces activated CNTs with a high surface area [66,117,118]. Raymundo-Pinero [66] first produced this kind of CNTs with a specific surface area of

1000 m<sup>2</sup>/g using chemical activation. The results show that KOH is a very effective chemical activation agent to develop the porosity on sidewalls of CNTs. It is revealed from TEM images (Fig. 16) that the activation process introduces high concentration of defects and disordered carbon in the sidewalls. In other words, the activation modifies the “carbon island” structure in sidewalls of MWNTs in the following way: not only etch the edge carbons but also destroy less-ordered carbon layers and enlarge the “sea” area when activation proceeds, leaving more and

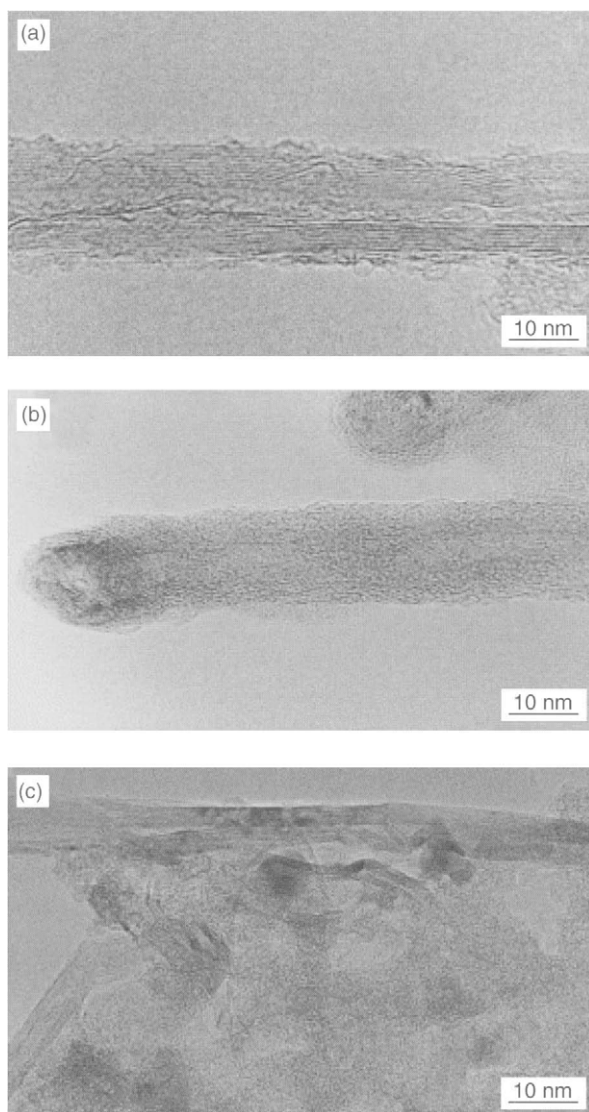


Figure 16. TEM images of activated carbon nanotubes [66].

larger inter- and intra-island pores. Compared with conventional activated carbons and activated carbon fibers, the activated CNTs have relatively lower surface area (too high activation rate will destroy the sidewall thoroughly) but higher adsorption rate since the tube diameter is so small that the diffusion path is much shorter. The activated CNTs are investigated for their applications as gas storage media or electrode materials [117,118].

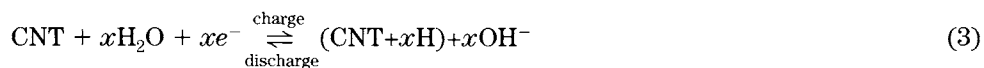
### 6.3. Modification of inner surface characteristics of carbon nanotubes

Since the interiors of CNTs are the fundamental adsorption domain, and the adsorption and other physicochemical processes are strongly dependent on the surface characteristics of their inner surface. The tailoring of inner surface characteristics of CNTs is much more difficult than that of outer surface. This tailoring and control of inner surface can be accomplished in the preparation process (in-situ process) or after synthesis (post-treatment). We take the template-synthesized CNTs as examples to explain how to modify the surface characteristics of CNTs. Xu et al. [119] and Yang et al. [120] prepared double coaxial CNTs with N-doped and undoped multiwalls using a two-step template technique (one step of propylene CVD and another step of acetonitrile CVD), and the prepared CNTs have different outer and inner surface composition and chemical activities. The inner surface characteristics can be controlled by the deposition of undoped or N-doped layer, and N-content in the inner layer can be adjusted through controlling the composition of feedstocks. Kyotani and co-workers [121,122] prepared CNTs by an AAO template technique, and modified the inner surface nature before removing the template. After the dissolution of the template, the CNTs were obtained with entirely different surface properties for inner or outer surface. They obtained CNTs with inner hydrophobic surface by fluorination [121] and with hydrophilic surface by oxidation using nitric acid [122] before removing AAO templates, leaving the outer surface not modified. After template being removed for liberation of the outer surface, CNTs with different inner and outer surface properties were prepared, possibly behaving as nanoscale test tubes with controlled properties. For instance, for nitric acid-treated CNTs, the inner cavities are hydrophilic while the outer surface of CNTs is hydrophobic, becoming nanoreactors with entirely reverse surface characteristics.

## 7. RELATED APPLICATIONS

### 7.1. Hydrogen storage in carbon nanotubes

In 1997, Dillon et al. [9] first claimed that SWNTs have a high reversible hydrogen storage capacity of 5–10 wt% at room temperature. Thereafter, many research groups started to carry out hydrogen storage studies (not only gas storage but also electrochemical storage) experimentally or theoretically [8,10–17,123–142]. Nützenadel et al. [123], for the first time, gave an electrochemical hydrogen storage capacity of SWNTs at room temperature (110 mAh/g, corresponding to 0.41 wt%). The charge–discharge behaviors of hydrogen into CNTs can be represented as follows [124]:



where hydrogen ions enter CNTs during charging and released during discharging.

The gas adsorption and electrochemical storage amount in CNTs show a big scattering by experimental results ranging from 0.1 to 67 wt% [9–13,123–139] and the simulation and calculation results from 0 to 33 wt% [8,14–16,140–142]. Up to date, no commonly agreed understanding is achieved for hydrogen storage in CNTs. In order to understand the nature of  $H_2$ –CNT interaction, one of the key points is to search for adsorption sites and understand how the adsorption sites work during hydrogen storage.

Dresselhaus et al. [142] presented a simple geometrical representation for the physical filling of  $H_2$  in a rope (crystalline lattice) of SWNTs (Fig. 17). Using the geometrical model with close-packing of hydrogen molecules within the core of a (10,10) tube, 3.3 wt% hydrogen adsorption within the tube and 0.7 wt% adsorption within the interstitial space, or a total of 4.0 wt% hydrogen adsorption is obtained (see Fig. 17). This model gives us two possible adsorption sites for hydrogen: interiors and interstices.

Lee and Lee [16] proposed another model for hydrogen–carbon chemical interaction to explain the hydrogen electrochemical storage in SWNTs by density functional calculations (Fig. 18), and proposed that the adsorption of hydrogen in SWNTs is a chemisorption process. Their calculation predicts that the hydrogen storage capacity in (10,10) nanotubes can exceed 14 wt% ( $160 \text{ kgH}_2/\text{m}^3$ ). This model also gave us two potential adsorption sites for hydrogen, endo- or exo-surface, which in fact represent two adsorption processes in interiors (inner surface of SWNTs) and interstices (outer surface of SWNTs).

In fact, the above two possible sites have been involved in most discussions on the hydrogen adsorption sites of CNTs. Recent advances in effect of tube diameter

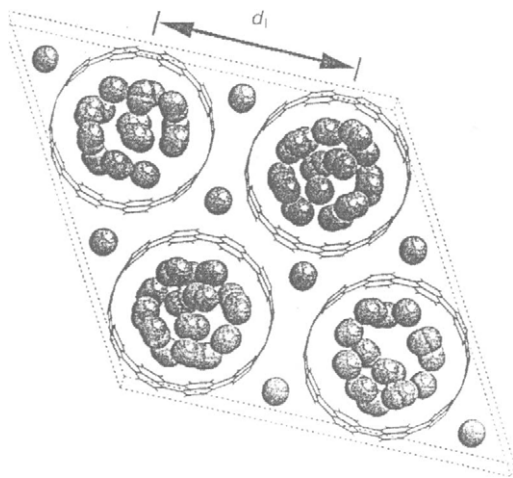


Figure 17. A typical configuration of  $H_2$  molecules adsorbed on a triangular array of carbon nanotubes based on classical Monto Carlo simulation (10 MPa, 50 K) [14,142]. Reprinted with permission from Williams and Eklund.

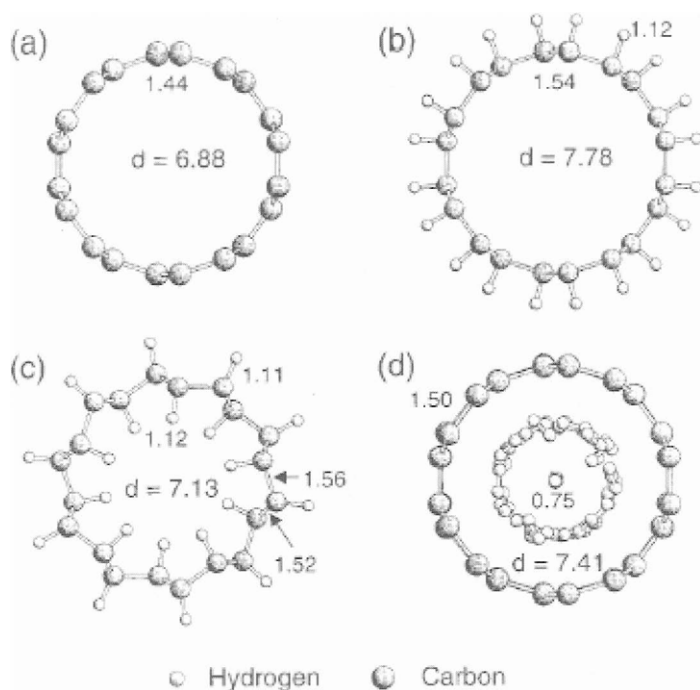


Figure 18. Top views of various hydrogen adsorptions in the (5,5) nanotube with ball-and-stick forms. (a) Pristine, (b) *arch*-type, (c) *zigzag* type, and (d) the molecular hydrogen inside the CNT with coverage to 1.0 [16]. The  $d$  indicates an average diameter of the CNT. Bond lengths are in units of Å. Reprinted with permission from Lee and Lee, Copyright 2000, American Institute of Physics.

on hydrogen storage, hydrogen storage in aligned CNTs, and impacts of pretreatment on hydrogen storage have given us some worthy hints for clarification of hydrogen adsorption mechanism. These results imply that inner cavities, interstices in SWNT bundles, interlayer spacing, and aggregated pores in aligned CNTs might be responsible for hydrogen adsorption.

Firstly, inner hollow cavities are primary hydrogen adsorption sites. Many simulations reveal that the inner hollow cavities can hold hydrogen molecules in a relatively high density due to the strong adsorption potential from overlapped tube walls of SWNTs and MWNTs (with small diameter) [8,14–16]. Experimental results also proved that cutting and tip-removing process [126,127,143,144] can improve the hydrogen storage capacities of CNTs.

Secondly, some simulations proved that interstices among large diameter SWNTs (e.g. (18,18) SWNTs) have strong adsorption potentials toward hydrogen [8]. Therefore, to adjust inter-tube spacing will enhance hydrogen storage capacity of



CNTs. Simulations by Yin et al. [15] show that small diameter SWNTs (tube diameter 0.6 nm) with inter-tube spacing of 3.0 nm have surprisingly high hydrogen physisorption capacity of 33 wt% at 77 K under 7 MPa. Shiraishi et al. [145] deduced that the inter-tube space in bundles is the main hydrogen adsorption site from a comparative study of desorption process of molecular hydrogen from SWNT bundles and peapods using the TPD method.

Thirdly, smaller aggregated pores (several nanometer) between CNTs or CNT bundles are responsible for part of hydrogen uptake. Fig. 19 [64] represents the pore size distribution curves of SWNTs (prepared by the hydrogen arc discharge method) before and after hydrogen ad-desorption, where ordered inter-bundle pores (small aggregated pores) of 3 nm in diameter, responsible for hydrogen adsorption, disappeared after the first run of hydrogen storage experiment, leading to lower hydrogen uptake capacity at the second run. This unstable ordered inter-bundle pores formed in course of bundled SWNT interaction with each other into the ropes [17,64]. Experimental results showed that the small aggregated pores among the aligned CNTs would be more stable and responsible for several runs of hydrogen ad-desorption [146–147].

Fourthly, large aggregated pores (tens of nanometers) have no contribution to hydrogen adsorption. Liu et al. [148] found that macroscopically long-aligned SWNT ropes synthesized by a hydrogen/argon arc discharge method showed excellent molding properties and they could be easily cold pressed into tablets without using any binders. The pressed tablets showed a hydrogen storage capacity of 4.0 wt% at 11 MPa and ambient temperature, corresponding to a volumetric hydrogen storage capacity of 68 kgH<sub>2</sub>/m<sup>3</sup>. After compaction, the large aggregated pores of diameters in 20–40 nm in SWNTs, leading to high-pressure capillarity, disappeared, while the hydrogen adsorption capacity kept stable. Hou et al. [149] also had a similar finding

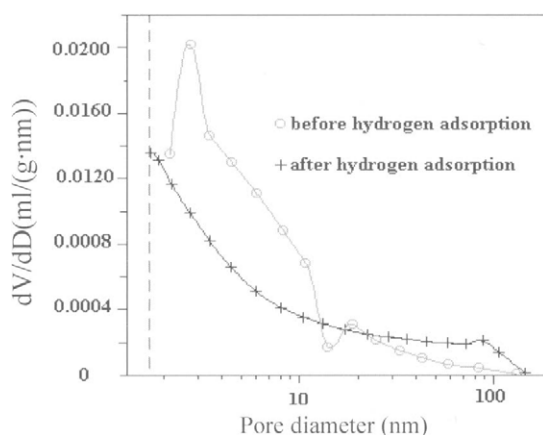


Figure 19. Pore size distributions of SWNT bundles before and after hydrogen adsorption cycle [64].

for the MWNTs that the cold-pressing decreased the volume of large diameter aggregated pores, but not changing the hydrogen adsorption amount apparently.

Fifthly, the spacing around “carbon island” structure (inter- and intra- “carbon island” spacing) in less crystallized CNTs are possibly domains for hydrogen adsorption. Hou et al. [65] considered that the “carbon island” structure was another main domain for hydrogen storage: The defects provide smooth channels for hydrogen entering the graphitic layers of the well-oriented small nano-islands. They argued that the increase of hydrogen storage capacity with the diameter increase of the MWNTs was attributed to the rich “carbon island” structures formed on the walls of larger diameter MWNTs. After graphitization, the graphitic layers of the MWNTs became very flat and smooth and their spacing significantly decreased compared to the “carbon island”-rich MWNTs before graphitization. As a result, the hydrogen storage capacity of the pretreated MWNTs before and after graphitization was greatly changed from 2.5 to 0.8 wt%. Therefore, it is reasonable to assume that the so-called “carbon island” structure that cannot be characterized by nitrogen adsorption may provide a larger potential energy field for hydrogen adsorption in MWNTs and become a major adsorption site.

At last, surface characteristics are also important for hydrogen adsorption. As shown in Fig. 10 (Sec. 4) [17], the transformation of surface energy distribution during hydrogen ad-desorption indicates changes of the surface characteristics of SWNTs. After hydrogen ad-desorption, there are much more changes in the zone of high surface energy than low-surface-energy zone.

Generally, both recent experimental and theoretical results have proved that the surface and porous structures play important roles in hydrogen adsorption. However, it is still difficult to elucidate fully the detailed hydrogen adsorption process unless the hydrogen–carbon interaction mechanism can be well understood.

## 7.2. Lithium storage in carbon nanotubes

Carbon materials including graphite materials, mesophase-pitch-based materials, and porous carbon materials are widely investigated as Li-ion battery electrode materials. Usually, the surface, interlayer spacing and porous nanospace in carbon materials are regarded as potential sites for lithium storage. CNTs are also considered to be a candidate for high-performance electrode material of Li-ion batteries due to their abundant nanosized pore structures.

Che et al. [150] first reported a reversible lithium intercalation capacity of 490 mAh/g for template-synthesized MWNTs in 1998. Up to now, most results on lithium storage capacity of MWNTs ranges from 300 to 1200 mAh/g depending on the preparation method and treatment process, and almost all cases showed high irreversible capacity [151–155]. Only a few results on SWNTs used as Li-ion electrode materials were reported [156–158]. Gao et al. [156] reported that the reversible saturation of Li-ion composition increased from  $\text{Li}_{1.7}\text{C}_6$  to  $\text{Li}_{2.7}\text{C}_6$  (1000 mAh/g) after 10 min ball milling treatment of the purified SWNTs, and their irreversible capacity decreased from  $\text{Li}_{3.2}\text{C}_6$  to  $\text{Li}_{1.3}\text{C}_6$ .

Many efforts have been made to understand the Li-ion charge-discharge mechanism in CNTs theoretically and experimentally. Almost all kinds of porosities discussed

above, including inner channels [151,152,154,157,158], surface defects including “carbon island” structures [156,159–161] and aggregated pores [153], are believed to be the storage sites or transmit channels for Li-ions. Shimoda et al. [157] found that the reversible Li storage capacity increased from  $\text{LiC}_6$  in close-ended SWNTs to  $\text{LiC}_3$  after etching treatment (end-opening and increasing defect concentration), which is twice the value observed in intercalated graphite. The enhanced capacity is attributed to Li diffusion into the interior of the SWNTs through the opened ends and sidewall defects. The surface defects are another domain for Li-ion adsorption, since they possibly behave as transmitting route for Li-ion into the interiors. Meunier et al. [159] also proposed, based on *ab initio* simulations, that topological defects are important for Li-ion diffusion into interior of CNTs. It was suggested that the higher lithium storage capacity of the MWNTs grown at lower temperature could be attributed to the extra lithium trapped into micro-cavities, the edges of graphitic layers (“carbon island” structures) and the surface of single graphitic layers in addition to the interlayer spacing of graphitic planes [152]. In summary, tip-removing (end-opening) treatment and activation treatment to increase surface defect concentration may be effective to enhance lithium storage in CNTs.

However, CNT-based anode materials have some drawbacks that may hinder their practical application in commercialized lithium-ion batteries: large irreversible capacity, the hysteresis between discharge and charge potentials, and cyclability. All these drawbacks are closely related to their pore structure. Frackowiak et al. [137] reported that the irreversible capacity of CNTs was linearly proportional to their mesopore volume, and small micropores were a desirable structure for limiting the fading of reversible capacity during cycling. Therefore, optimization on the structure, composition, and fabrication process of the CNT-containing electrodes may be possible ways to overcome the above limitations. Besides, two other approaches were employed to overcome these drawbacks.

On one hand, doped CNT or CNT-based composites were investigated as anode materials [162–166]. It was found that, compared with the pristine CNTs, the composites have an improved lithium storage capacity and low irreversible capacity. Another approach is to use CNTs as an effective additive of the electrodes, instead of serving as the primary anode material. The quasi-1D CNTs/CNFs (carbon nanofibers) can form a network inside the electrode, whose conductivity and mechanical properties can be improved due to the enhancement effect of the CNTs, leading to longer cycle life and higher charge/discharge rates.

MWNT/natural graphite and CNF/natural graphite anode composites for Li-ion battery were recently prepared at our group, in which MWNTs were dispersed into natural graphite spherical particles or CNFs were directly grown on the surface of natural graphite spherical particles, respectively. Both materials have good overall performance for Li-ion battery, and the latter is even better than the former. With the advantage of technical feasibility and cost effectiveness, the above electrode additive route may accelerate the practical application of CNTs/CNFs in lithium ion batteries.

### 7.3. Carbon nanotube-based electrode materials for supercapacitors

Investigations on porous carbon materials as an electrode of supercapacitors (electrochemical double layer capacitors) have also been widely performed. Large

specific surface area and high mesopore (2–50 nm) volume are believed to be very critical for the performance of carbon materials. CNTs are one kind of novel porous carbons with unique pore structure, and hence CNTs as an electrode of supercapacitors attracts many attentions. Niu et al. [167] first reported their related results, and the employed MWNTs had a narrow diameter distribution centered at 8 nm, and large specific surface area of 430 m<sup>2</sup>/g. A maximum capacitance of 113 F/g and a power density of 8 kW/kg were reported. Many results appeared thereafter and most of them were in the range of 80–200 F/g [168–175].

Surface area and surface characteristics exert great influences on the performance of electrode materials. A NH<sub>3</sub> plasma treatment on MWNTs increased the capacitance of the integrated electrode remarkably from 38.7 to 207.3 F/g, which could be attributed to the enhanced surface area and wettability of the MWNTs subjected to ammonia pretreatment [171]. Lee et al. [176] proved that fluorinated SWNT-based supercapacitor has almost unchanged surface area and modified surface characteristics compared with the as-prepared one and have entirely different specific capacitance.

Porous structure is also a critical factor to determine the capacitance, and small mesopores are believed to be responsible for the improved performance. Electrochemical oxidation method [177] was used to enhance the specific capacitance of SWNT-based supercapacitors [178]. A specific capacitance of 163 F/g was obtained for the electrochemically oxidized SWNTs compared to only 20 F/g for the as-prepared SWNTs. The increased specific capacitance was due to the increase of small mesopore (3.0–5.0 nm) volume during the electrochemical oxidation process.

Aggregated pores between CNTs and CNT bundles are very important for the specific capacitance. It is revealed that this kind of networks favor the formation of 3D electrical double layers. Niu et al. [167] reported that in an electrode made of free-standing mats of entangled nanotubes, the aggregated pore network was highly desirable for high power and long cycle life electrochemical capacitors. An entangled network of MWNT-based nanocomposite favored the formation of 3D electrical double layers, allowing a more effective contribution of the pseudo-faradaic property of polypyrrole [179].

Many groups tend to use CNT-based nanocomposites to build a real electrode to approach the practical applications. Yoon et al. [171] and Chen et al. [172] synthesized MWNTs directly on a nickel foil, which subsequently served as the current collector of the integrated electrode for a supercapacitor. Jurewicz et al. [179] electrochemically deposited a homogeneous layer of polypyrrole with 5 nm in thickness on the surface of MWNTs synthesized by CVD. Several groups studied the performance of supercapacitors based on MWNTs [137,175,180] and SWNTs [181] deposited with conducting polymers. These composite electrodes show a very good specific capacitance (higher than 150 F/g) and very long cycling life. Recently, DWNT/polyaniline (DWNT/PAn) was in-situ polymerized and used in electrochemical capacitors. It was found that DWNT/PAn had a drastic higher specific capacitance of 250 F/g, much higher than that of pure DWNTs (ca. 36 F/g) and pure PAn (ca. 90 F/g) [182].

#### 7.4. Carbon nanotube-based sensors

The electronic properties of semiconducting SWNTs are intimately related to the gas molecule adsorption properties, which makes CNTs, especially SWNTs, potential as a new generation of gas sensors [28,29,183]. CNTs can adsorb some kinds of gases even at very low concentration (ppm), and some of the trace adsorbates partly change the electronic structure by donating/accepting a small amount of electrons to/from nanotube wall. Collins reported that electronic conductance of SWNTs is highly sensitive to oxygen adsorption when exposure to environmental molecular oxygen. The conductance of bulk SWNTs increases when oxygen adsorption is enhanced, and the change rate of the conductance is consistent with the oxygen adsorption rate on nanotube surface. The electron transfer between the adsorbed molecular oxygen and nanotubes is believed to be the main reason leading to the conductance sensitivity toward oxygen adsorption [28]. Kong et al. [29] also found that the conductance of semiconducting SWNTs greatly increases with exposure to trace amount of  $\text{NO}_2$  (ppm), while the conductance apparently decreases when exposure to  $\text{NH}_3$  (2%). Kong et al. [183] have made some further progress about nanotube sensors, and they coated semiconducting SWNTs with nanosized Pa and found that the conductance of the new material is extremely sensitive to molecular hydrogen. In short, SWNTs show high gas sensitivity when the interaction with target gas is strong. As for the other gases having weak interaction with CNTs, one can modify the nanotube surface to enhance the affinity toward the target gas.

#### 7.5. Carbon nanotube-based nanosized test tubes

1D inner cavities of CNTs, with the diameters of  $\sim 0.4\text{--}50$  nm, are indeed nanosized test tubes [2], in which nanoscale chemical reaction can occur. The characteristics of nanosized test tubes are summarized as follows: Firstly, the nanosized test tubes provide a 1D environment, in which reactants and resultants are confined within 1D channel and enforced to adopt 1D morphology. Secondly, the CNTs have particularly high surface to volume ratio, and adsorbed or filled species have a correspondingly high coverage and high activities compared with macroscopic systems. Thirdly, CNT walls are composed of rolled graphene sheets with high density  $\pi$  electrons, generating special chemical activities. Furthermore, there is usually electron transfer between the filled materials and carbon atoms in the tube wall, leading to some modifications to the reactivity of filled materials. Fourthly, CNTs may be regarded as a high-pressure nanocontainer or nanoreactor and can be subject to ultrahigh pressure. Finally, the inner surface of CNTs may be chemically modified and tailored to generate different chemical reactions.

As stated in Sec. 2, CNTs may sustain ultrahigh argon pressure, and are regarded as the smallest gas cylinders. Ugarte et al. [2] found that silver nitrate was decomposed when exposure to the electron beam, leading to the formation of discrete pure silver nanobeads. The chains of silver particles fitted tightly in the nanotube and were separated by several domains with extremely high gas pressure (evaluated over 1000 bar) resulted from liberation of a great amount of gases during the decomposition of  $\text{AgNO}_3$ . It should be noted that the tube was intact at the tube-particle interface. In contrast, the tube wall in the gas domains was eroded by the evolved corrosive gases during the decomposition of  $\text{AgNO}_3$  [2].

The nanospace of CNTs has chemical activities greatly different from a planar graphite surface, and possibly generates many curious physicochemical processes. 1D PbO nanowire can be obtained and exist stably in nanochannels of CNTs at 450 °C, while the bulk PbO is obtained only above 550 °C [82,184]. Britto et al. [185] found that the pentagon- or heptagon-defects on the nanotube wall improved the reduction of oxygen of microelectrode for fuel cells.

One of the potential applications for nanoreactors is to prepare 1D materials by the nanoscale reaction of filled substances. The typical procedure is to fill metallic salt in the 1D channel of CNTs, and ignite chemical reaction to produce unique low dimensional nanostructures (for most cases, metals or metallic compounds in reduction state) such as nanowires, nanoparticles, nanorods or nanoribbons according to different nanotube diameter and detailed reaction conditions [2,47,80,87,98,184,186]. In this regard, silver chloride filled in SWNTs can transform into pure silver (reduction state) nanowires when exposure to electron beam [87]. Calcination of MWNTs with PbO<sub>2</sub> at 450 °C led to the formation of very long PbO (reduction state) nanowires [184].

The nanostructures prepared in CNTs are normally of periodic structure greatly different from macroscopic cases (e.g. KI presented above and NiO below). Furthermore, it should be emphasized that the 1D nanostructure may exist not only in cylindrical shaped nanowires or nanorods but also planar nanoribbons. Fig. 20 shows a NiO nanoribbon, with the thickness of 20 nm and the width of 20 nm,

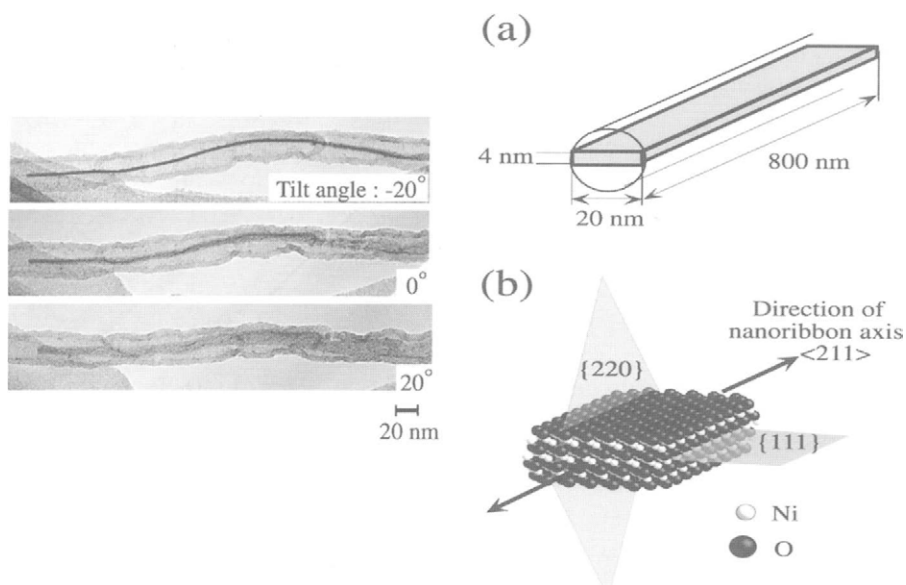


Figure 20. TEM image of a NiO nanoribbon in the cavity of carbon nanotube and the structural model of the nanoribbons [98]. Reprinted with permission from Matsui et al., Copyright 2003, American Chemical Society.

formed in CNTs prepared by a template technique, in which, CNT is not used as a shape template but a size template [98].

In some cases, nanoparticles or nanowires filled in nanotubes and the nanotubes can behave as host-guest supramolecular system (also called nanocomposites), contributing to some interesting properties such as electromagnetic or catalytic properties. Metallic compounds filled in nanotubes exist as different morphologies under different ambient conditions, and consequently form different nanocomposites with different properties. For instance, silver nitride is transformed into discrete silver nanoparticles when exposed to electron beam, while transformed to long silver nanowires during 673 K heat-treatment, constituting different Ag-CNT composites [2].

## 8. CONCLUDING REMARKS

CNTs are unique in their structure, and in particular, they possess a multi-modal porous structure and energy-dispersive surface, imparting this novel material diverse physicochemical properties and a great number of potential applications. The different porosities of CNTs have entirely different characteristics and result in different physicochemical (adsorption or filling) processes. Fundamental inner cavity and secondary porosities, such as interstices in a bundle, aggregated pores, "carbon island" structure, and surface defects, play different and important roles in the performance of CNTs in specific applications such as hydrogen storage, Li-ion secondary battery, supercapacitors, sensors, and nanosized reactors. Deep understanding on correlation between the porous structure and surface characteristics of CNTs and performance and consequently optimizing these structural parameters are critical for the final realization of practical applications of CNTs in a wide range of fields such as clean energy and environment protection, etc.

**Acknowledgments:** We acknowledge the financial supports from the Special Funds for State Major Basic Research Projects of China (No. G20000026403), NSFC (No. 50328204), and CAS.

## REFERENCES

1. Q.-H. Yang, L. X. Li, H.-M. Cheng and M. Z. Wang, *Chin. Sci. Bul.* **48** (2003) 2395.
2. D. Ugarte, A. Chatelain and W. A. de Heer, *Science* **274** (1996) 1897.
3. S. Iijima, *Nature* **354** (1991) 56.
4. H.-M. Cheng, Q.-H. Yang and C. Liu, *Carbon* **39** (2001) 1447.
5. Q.-H. Yang, J. T. Zheng, M. Z. Wang and B. J. Zhang, *Chin. J. Mater. Res.* **14** (2000) 112.
6. K. Kaneko, *Colloid Surf.* **109** (1996) 319.
7. B. McEnaney, *Carbon* **26** (1988) 267.
8. Q. Y. Wang and J. K. Johnson, *J. Chem. Phys.* **110** (1999) 577.
9. A. C. Dillon, K. M. Jones, T. A. Bekkedahl, C. H. Kiang and D. S. Bethune, *Nature* **386** (1997) 377.

10. Y. Ye, C. C. Ahn, C. Witham, B. Fultz, J. Liu, A. G. Rinzler, D. Colbert, K. A. Smith and R. E. Smalley, *Appl. Phys. Lett.* **74** (1999) 2307.
11. Y. Y. Fan, B. Liao, M. Liu, Y. L. Wei, M. Q. Lu and H.-M. Cheng, *Carbon* **37** (1999) 1649.
12. C. Liu, Y. Y. Fan, M. Liu, H. T. Cong, H.-M. Cheng and M. S. Dresselhaus, *Science* **286** (1999) 1127.
13. P. Chen, X. Wu, J. Lin and K. L. Tan, *Science* **285** (1999) 91.
14. K. Williams and P. C. Eklund, *Chem. Phys. Lett.* **320** (2000) 352.
15. Y. F. Yin, T. J. Mays and B. McEnaney, *Langmuir* **16** (2000) 10521.
16. S. M. Lee and Y. H. Lee, *Appl. Phys. Lett.* **76** (2000) 2877.
17. Q.-H. Yang, C. Liu, M. Liu, Y. Z. Fan, H.-M. Cheng and M. Z. Wang, *Sci. in China Ser. E* **45** (2002) 561.
18. G. E. Gadd, M. Blackford, S. Morica, N. Webb, P. J. Evans, A. N. Smith, G. Jacobsen, S. Leung, A. Day and Q. Hua, *Science* **277** (1997) 933.
19. A. Kuznetsova, J. T. Yates, J. Liu and R. E. Smalley, *J. Chem. Phys.* **112** (2000) 9590.
20. M. C. Gordillo, J. Boronat and J. Casulleras, *Phys. Rev. B* **61** (2000) R878.
21. A. Fujiwara, K. Ishii, H. Suematsu, H. Kataura, Y. Maniwa, S. Suzuki and Y. Achiba, *Chem. Phys. Lett.* **336** (2001) 205.
22. Q.-H. Yang, P. X. Hou, S. Bai, M. Z. Wang and H.-M. Cheng, *Chem. Phys. Lett.* **345** (2001) 18.
23. P. X. Hou, S. Bai, Q.-H. Yang, C. Liu and H.-M. Cheng, *Carbon* **40** (2002) 81.
24. Q.-H. Yang, F. Li, P. X. Hou, C. Liu, M. Liu and H.-M. Cheng, *Chin. Sci. Bull.* **46** (2001) 1317.
25. M. Calbi, M. W. Cole, S. M. Gatica, M. J. Bojan and G. Stan, *Rev. Mod. Phys.* **73** (2001) 857.
26. M. W. Cole, V. H. Crespi, G. Stan, C. Ebner, J. M. Hartman, S. Moroni and M. Boninsegni, *Phys. Rev. Lett.* **84** (2000) 3883.
27. G. Stan, S. M. Gatica, M. Boninsegni, S. Curtarolo and M. W. Cole, *Am. J. Phys.* **67** (1999) 1170.
28. P. G. Collins, K. Bradley, M. Ishigami and A. Zettl, *Science* **87** (2000) 1801.
29. J. Kong, N. R. Franklin, C. W. Zhou, M. G. Chapline, S. Peng, K. Cho and H. Dai, *Science* **287** (2000) 622.
30. G. Stan and M. W. Cole, *Surf. Sci.* **395** (1998) 280.
31. W. Teizer, R. B. Hallock, E. Dujardin and T. W. Ebbesen, *Phys. Rev. Lett.* **82** (1999) 5305.
32. M. C. Gordillo, J. Boronat and J. Casulleras, *Phys. Rev. Lett.* **85** (2000) 2348.
33. S. M. Gatica, M. J. Bojan, G. Stan and M. W. Cole, *J. Chem. Phys.* **114** (2001) 3765.
34. D. Kasuya, M. Yudasaka, K. Takahashi, F. Kokai and S. Iijima, *J. Phys. Chem. B* **106** (2002) 4947.
35. E. Bekyarova, K. Kaneko, D. Kasuya, K. Murata, M. Yudasaka and S. Iijima, *Langmuir* **18** (2002) 4138.
36. E. Bekyarova, K. Kaneko, M. Yudasaka, D. Kasuya, S. Iijima, A. Huidobro and F. Rodriguez-Reinoso, *J. Phys. Chem. B* **107** (2003) 4479.



37. S. Inoue, N. Ichikuni, T. Suzuki, T. Uematsu and K. Kaneko, *J. Phys. Chem. B* **102** (1998) 4689.
38. M. Eswaramoorthy, R. Sen and C. N. R. Rao, *Chem. Phys. Lett.* **304** (1999) 207.
39. H. Gao, X. B. Wu, J. T. Li, G. T. Wu, J. Y. Lin, K. Wu and D. S. Xu, *Appl. Phys. Lett.* **83** (2003) 3389.
40. C. Liu, H. T. Cong, F. Li, P. Tan, H.-M. Cheng, K. Lu and B. L. Zhou, *Carbon* **37** (1999) 1865.
41. A. Kuznetsova, D. B. Mawhinney, V. Naumenko, J. T. Yates, J. Liu and R. E. Smalley, *Chem. Phys. Lett.* **321** (2000) 292.
42. T. Kyotani, L. F. Tsai and A. Tomita, *Chem. Mater.* **8** (1996) 2109.
43. Q.-H. Yang and T. Kyotani, unpublished work (2005).
44. T. Kyotani, L. F. Tsai and A. Tomita, *Chem. Mater.* **7** (1995) 1427.
45. Q.-H. Yang, P. X. Hou and T. Kyotani, unpublished work (2005).
46. W. Q. Han, S. S. Fan, Q. Q. Li, B. L. Gu, X. B. Zhang and D. P. Yu, *Appl. Phys. Lett.* **71** (1997) 2271.
47. W. Q. Han, S. S. Fan, Q. Q. Li and Y. D. Hu, *Science* **277** (1997) 1287.
48. Y. Q. Zhu, W. K. Hsu, H. W. Kroto and D. R. Walton, *Chem. Comm.* **7** (2001) 2184.
49. P. M. Ajayan, T. W. Ebbesen, T. Ichihashi, S. Iijima, K. Tanigaki and H. Hiura, *Nature* **262** (1993) 522.
50. S. C. Tsang, Y. K. Chen, P. J. F. Harris and M. L. H. Green, *Nature* **372** (1994) 159.
51. M. Endo, H. Muramatsu, T. Hayashi, Y. A. Kim, M. Terrones and M. S. Dresselhaus, *Nature* **433** (2005) 476.
52. J. L. Hutchison, N. A. Kiselev, E. P. Krinichnaya, A. V. Krestinin, R. O. Loutfy, A. P. Morawsky, V. E. Muradyan, E. D. Obraztsova, J. Sloan, S. V. Terekhov and D. N. Zakharov, *Carbon* **39** (2001) 761.
53. W. C. Ren, F. Li, J. Chen, S. Bai and H.-M. Cheng, *Chem. Phys. Lett.* **359** (2002) 196.
54. L. X. Li, F. Li, C. Liu and H.-M. Cheng, *Carbon* **43** (2005) 623.
55. W. Z. Li, J. G. Wen, M. Sennett and Z. F. Ren, *Chem. Phys. Lett.* **368** (2003) 299.
56. Q.-H. Yang, Y. Tong, C. Liu, F. Li and H.-M. Cheng, *Carbon* **43** (2005) 2027.
57. A. Thess, R. Lee, P. Nikolaev, H. J. Dai, P. Petit, J. Robert, C. H. Xu, Y. H. Lee, S. G. Kim, A. G. Rinzler, D. T. Colbert, G. E. Scuseria, D. Tomanek, J. E. Fischer and R. E. Smalley, *Science* **273** (1996) 483.
58. A. M. Rao, P. C. Eklund, S. Bandow, A. Thess and R. E. Smalley, *Nature* **388** (1997) 257.
59. A. J. Zambano, S. Talapatra, K. Lafdi, M. T. Aziz, W. McMillin, G. Shaughnessy, A. D. Migone, M. Yudasaka, S. Iijima, F. Kokai and K. Takahashi, *Nanotechnology* **13** (2002) 201.
60. Q.-H. Yang, S. Bai, J. L. Sauvajol and J. B. Bai, *Adv. Mater.* **15** (2003) 792.
61. T. W. Ebbesen, H. Hiura, J. Fujita, Y. Ochiai, S. Matsui and K. Tanigaki, *Chem. Phys. Lett.* **209** (1993) 83.
62. C. Liu, Q.-H. Yang, Y. Tong, H. T. Cong and H.-M. Cheng, *Appl. Phys. Lett.* **80** (2002) 2389.

63. E. Alain, Y. F. Yin, T. Mays and M. McEnaney, *Stud. Surf. Catal.* **128** (2000) 313.
64. Q.-H. Yang, Surface, pore structure of carbon nanotubes and its influence on hydrogen storage, Post-PhD Report, Institute of Metal Research, Chinese Academy of Sciences, 2001.
65. P. X. Hou, S. T. Xu, Z. Ying, Q.-H. Yang, C. Liu and H.-M. Cheng, *Carbon* **41** (2003) 2471.
66. E. Raymundo-Pinero, A. Cazorla-Amoros, S. Delpeux, E. Frackowiak, K. Szostak and F. Beguin, *Carbon* **40** (2002) 1614.
67. P. G. Collins, K. Bradley, M. Ishigami and A. Zettl, *Science* **87** (2000) 1801.
68. J. Kong, N. R. Franklin, C. W. Zhou, M. G. Chapline, S. Peng, K. Cho and H. J. Dai, *Science* **287** (2000) 622.
69. K. A. Williams and P. C. Eklund, *Chem. Phys. Lett.* **320** (2000) 352.
70. C. H. Sun, F. Li, Z. Ying, C. Liu and H.-M. Cheng, *Phys. Rev. B* **69** (2004) 033404-1.
71. Q.-H. Yang, M. Liu, H.-M. Cheng and M. Z. Wang, *Chin. J. Mater. Res.* **15** (2001) 375.
72. A. Peigney, C. Laurent, E. Flahaut, R. R. Bacsá and A. Rousset, *Carbon* **39** (2001) 507.
73. R. R. Bacsá, C. Laurent, A. Peigney, W. S. Bacsá, T. Vaugien and A. Rousset, *Chem. Phys. Lett.* **323** (2000) 566.
74. M. R. Pederson and J. Q. Broughton, *Phys. Rev. Lett.* **69** (1992) 2689.
75. P. M. Ajayan and S. Iijima, *Nature* **361** (1993) 333.
76. J. Sloan, J. Hammer, M. Zwiefka-Sibley and M. L. H. Green, *Chem. Comm.* (1998) 347.
77. B. W. Smith, M. Monthieux and D. E. Luzzi, *Nature* **396** (1998) 323.
78. C. Guerretpiecourt, Y. Lebouar, A. Loiseau and H. Pascard, *Nature* **372** (1994) 761.
79. E. Dujardin, T. W. Ebbesen, H. Hiura and K. Tanigaki, *Science* **265** (1994) 1850.
80. D. Ugarte, T. Stockli, J. Bonard, A. Chatelain and W. A. DeHeer, Capillarity in carbon nanotubes, in *The Science and Technology of Carbon Nanotubes*, Eds., K. Tanaka, T. Yamabe and K. Fukui, 136, Elsevier, Netherlands, 1999.
81. J. Sloan, A. I. Kirkland, J. L. Hutchison and M. L. H. Green, *Chem. Comm.* (2002) 1319.
82. J. Sloan, S. J. Grosvenor, S. Friedrichs, A. I. Kirkland, J. L. Hutchison and M. L. H. Green, *Angew. Chem.* **114** (2002) 1204.
83. E. Philp, J. Sloan, A. I. Kirkland, R. R. Meyer, S. Friedrichs, J. Hutchison and M. L. H. Green, *Nat. Mater.* **12** (2003) 788.
84. J. Sloan, R. E. Dunin-Borkowski, J. L. Hutchison, K. S. Coleman, V. C. Williams, J. B. Claridge, A. P. E. York, C. Xu, S. R. Bailey, G. Brown, S. Friedrichs and M. L. H. Green, *Chem. Phys. Lett.* **316** (2000) 191.
85. J. Sloan, M. C. Novotny, S. R. Bailey, G. Brown, C. Xu, V. C. Williams, S. Friedrichs, E. Flahaut, R. L. Callender, A. P. E. York, K. S. Coleman, M. L. H. Green, R. E. Dunin-Borkowski and J. L. Hutchison, *Chem. Phys. Lett.* **329** (2000) 61.
86. R. R. Meyer, J. Sloan, R. E. Dunin-Borkowski, A. I. Kirkland, M. C. Novotny, S. R. Bailey, J. L. Hutchison and M. L. H. Green, *Science* **289** (2000) 1324.

87. J. Sloan, D. M. Wright, H. G. Woo, S. Bailey, G. Brown, A. P. E. York, K. S. Coleman, J. L. Hutchison and M. L. H. Green, *Chem. Comm.* (1999) 699.
88. A. Rothschild, J. Sloan, A. P. E. York, M. L. H. Green, J. L. Hutchison and R. Tenne, *Chem. Comm.* (1999) 363.
89. B. W. Smith, R. M. Russo, S. B. Chikkannanavar and D. E. Luzzi, *J. Appl. Phys.* **91** (2002) 9333.
90. B. W. Smith, M. Monthieux and D. E. Luzzi, *Chem. Phys. Lett.* **315** (1999) 31.
91. B. W. Smith and D. E. Luzzi, *Chem. Phys. Lett.* **321** (2000) 169.
92. D. J. Hornbaker, S. J. Khang, S. Misra, B. W. Smith, A. T. Johnson, E. J. Mele, D. E. Luzzi and A. Yazdani, *Science* **295** (2002) 828.
93. B. Bouteaux, A. Claye, B. W. Smith, M. Monthieux, D. E. Luzzi and J. E. Fischer, *Chem. Phys. Lett.* **310** (1999) 21.
94. B. W. Smith, D. E. Luzzi and Y. Achiba, *Chem. Phys. Lett.* **331** (2000) 137.
95. T. Kyotani, L. F. Tsai and A. Tomita, *Chem. Comm.* (1997) 701.
96. B. K. Pradhan, T. Toba, T. Kyotani and A. Tomita, *Chem. Mater.* **10** (1998) 2510.
97. B. K. Pradhan, T. Kyotani and A. Tomita, *Chem. Comm.* (1999) 1317.
98. K. Matsui, B. K. Pradhan, T. Kyotani and A. Tomita, *J. Phys. Chem. B* **105** (2001) 5682.
99. K. Matsui, T. Kyotani and A. Tomita, *Adv. Mater.* **14** (2002) 1216.
100. K. Matsui, T. Kyotani and A. Tomita, *Mol. Cryst. Liq. Cryst.* **387** (2002) 225.
101. A. Thess, R. Lee, P. Nikolaev, H. Dai, P. Petit, J. Robert, C. Xu, Y. H. Lee, S. G. Kim, D. T. Colbert, G. Scuseria, D. Tomaneck, J. E. Fisher and R. E. Smalley, *Science* **273** (1996) 483.
102. C. Journet, W. K. Maser, P. Bernier, A. Loiseau, M. Lamydelachapelles, S. Lefrant, P. Deniard, R. Lee and J. E. Fischer, *Nature* **388** (1997) 756.
103. P. M. Ajayan and S. Iijima, *Nature* **358** (1992) 23.
104. L. F. Sun, S. S. Xie, W. Liu, W. Y. Zhou, Z. Q. Liu, D. S. Tang, G. Wang and L. X. Qian, *Nature* **403** (2000) 384.
105. N. Wang, Z. K. Tang, G. D. Li and J. S. Chen, *Nature* **408** (2000) 50.
106. H.-M. Cheng, F. Li, G. Su, H. Y. Pan, L. L. He, X. Sun and M. S. Dresselhaus, *Appl. Phys. Lett.* **72** (1998) 3282.
107. H.-M. Cheng, F. Li, X. Sun, S. D. M. Brown, M. A. Pimenta, A. Marucci, G. Dresselhaus and M. S. Dresselhaus, *Chem. Phys. Lett.* **289** (1998) 602.
108. C. Liu, H.-M. Cheng, H. T. Cong, F. Li, G. Su, B. L. Zhou and M. S. Dresselhaus, *Adv. Mater.* **12** (2000) 1190.
109. C. H. Kiang, *J. Phys. Chem. A* **104** (2000) 2454.
110. S. Lebedkin, P. Schweiss, B. Renker, S. Malik, F. Hennrich, M. Neumaier, C. Stoermer and M. Kappes, *Carbon* **40** (2002) 417.
111. Q.-H. Yang, S. Bai, T. Fournier, F. Li, G. Wang, H.-M. Cheng and J. R. Bai, *Chem. Phys. Lett.* **370** (2003) 274.
112. B. W. Smith, M. Monthieux and D. E. Luzzi, *Chem. Phys. Lett.* **315** (1999) 31.
113. W. C. Ren and H.-M. Cheng, *J. Phys. Chem. B* **109** (2005) 7169.
114. L. J. Ci, Z. L. Rao, Z. P. Zhou, D. S. Tang, Y. Q. Yan, Y. X. Liang, D. F. Liu, H. J. Yuan, W. Y. Zhou, G. Wang, W. Liu and S. S. Xie, *Chem. Phys. Lett.* **359** (2002) 63.
115. E. Flahaut, R. Bacsa, A. Peigney and C. Laurent, *Chem. Comm.* (2003) 1442.

116. T. Kyotani, B. K. Pradhan and A. Tomita, *Bull. Chem. Soc. Jpn.* **72** (1999) 1952.
117. Q. Jiang, M. Z. Qu, B. L. Zhang and Z. L. Yu, *Carbon* **40** (2002) 2743.
118. S. H. Yoon, S. Lim, Y. Song, Y. Ota, W. M. Qiao, A. Tanaka and I. Mochida, *Carbon* **42** (2004) 1723.
119. W. H. Xu, T. Kyotani, B. K. Pradhan, T. Nakajima and A. Tomita, *Adv. Mater.* **15** (2003) 1087.
120. Q.-H. Yang, W. H. Xu, A. Tomita and T. Kyotani, *Chem. Mater.* **17** (2005) 2940.
121. Y. Hattori, Y. Watanabe, S. Kawasaki, F. Okino, B. K. Pradhan and T. Kyotani, *Carbon* **37** (1999) 1033.
122. T. Kyotani, S. Nakazaki, W. Xu and A. Tomita, *Carbon* **39** (2001) 782.
123. C. Nützenadel, A. Züttel, D. Chartouni and L. Schlapbach, *Electrochem. Solid State Lett.* **2** (1999) 30.
124. A. K. M. F. Kibria, Y. H. Mo, K. S. Park, K. S. Nahm and M. H. Yun, *Inter J. Hydrogen Energy* **26** (2001) 823.
125. A. Chambers, C. Park, R. T. K. Baker and N. M. Rodriguez, *J. Phys. Chem. B* **102** (1998) 4253.
126. A. C. Dillon, T. Gennett, J. Z. L. Alleman, K. M. Jones, P. A. Parilla and M. J. Heben, *Proceedings of the 1999 U.S. DOE Hydrogen Program Review*, Golden, Colorado (1999).
127. A. C. Dillon and M. J. Heben, *Appl. Phys. A* **72** (2001) 133.
128. C. Park, P. E. Anderson, A. Chambers, C. D. Tan, R. Hidalgo and N. M. Rodriguez, *J. Phys. Chem. B* **103** (1999) 10572.
129. R. T. Yang, *Carbon* **38** (2000) 623.
130. M. Hirscher, M. Becher, M. Haluska, U. Dettlaff-Weglikowska, A. Quintel, G. S. Duesberg, Y. M. Choi, P. Downes, M. Hulman, S. Roth, I. Stepanek and P. Bernier, *Appl. Phys. A* **72** (2001) 129.
131. B. K. Gupta, R. S. Tiwari and O. N. Srivastava, *J. Alloys Compd.* **381** (2004) 301.
132. G. Q. Ning, F. Wei, G. H. Luo, Q. X. Wang, Y. L. Wu and H. Yu, *Appl. Phys. A* **78** (2004) 955.
133. R. Bacsá, C. Laurent, R. Morishima, H. Suzuki and M. L. Lay, *J. Phys. Chem. B* **108** (2004) 12718.
134. Y. P. Zhou, K. Feng, Y. Sun and L. Zhou, *Chem. Phys. Lett.* **380** (2004) 526.
135. G. P. Dai, M. Liu, D. M. Chen, P. X. Hou, Y. Tong and H.-M. Cheng, *Electrochem. Solid State Lett.* **5** (2002) E13.
136. G. P. Dai, C. Liu, M. Liu, M. Z. Wang and H.-M. Cheng, *Nano Lett.* **2** (2002) 503.
137. E. Frackowiak and F. Beguin, *Carbon* **40** (2002) 1775.
138. K. Jurewicz, E. Frackowiak and F. Beguin, *Appl. Phys. A* **78** (2004) 981.
139. H.-M. Cheng, Q.-H. Yang and C. Liu, *Carbon* **39** (2001) 1447.
140. Q. Y. Wang and J. K. Johnson, *J. Phys. Chem. B* **103** (1999) 4809.
141. J. R. Cheng, X. H. Yuan, L. Zhao, D. C. Huang, M. Zhao, L. Dai and R. Ding, *Carbon* **42** (2004) 2019.
142. M. S. Dresselhaus, K. A. Williams and P. C. Eklund, *MRS Bull.* **24** (1999) 45.
143. J. M. Skowronski, P. Scharff, N. Pfander and S. Cui, *Adv. Mater.* **15** (2003) 55.
144. M. R. Smith, E. W. Bittner, W. Shi, J. K. Johnson and B. C. Bochrath, *J. Phys. Chem. B* **107** (2003) 3752.

145. M. Shiraishi, T. Takenobu, A. Yamada, M. Ata and H. Kataura, *Chem. Phys. Lett.* **358** (2002) 213.
146. A. Y. Cao, H. W. Zhu, X. F. Zhang, X. S. Li, D. B. Ruan, C. L. Xu, B. Q. Wei, J. Liang and D. H. Wu, *Chem. Phys. Lett.* **342** (2001) 510.
147. Y. Chen, D. T. Shaw, X. D. Bai, E. G. Wang, C. Lund, W. M. Lu and D. D. L. Chung, *Appl. Phys. Lett.* **78** (2001) 2128.
148. C. Liu, Q.-H. Yang, Y. Tong, H. T. Cong and H.-M. Cheng, *Appl. Phys. Lett.* **80** (2002) 2389.
149. P. X. Hou, Q.-H. Yang, S. Bai, S. T. Xu, M. Liu and H.-M. Cheng, *J. Phys. Chem. B* **106** (2002) 963.
150. G. L. Che, B. B. Lakshmi, E. R. Fisher and C. R. Martin, *Nature* **393** (1998) 346.
151. E. Frackowiak, S. Gautier, H. Gaucher, S. Bonnamy and F. Beguin, *Carbon* **37** (1999) 61.
152. G. T. Wu, M. H. Chen, G. M. Zhu, J. K. You, Z. G. Lin and X. B. Zhang, *J. Solid State Electrochem.* **7** (2003) 129.
153. G. X. Wang, J. H. Ahn, J. Yao, M. Lindsay, H. K. Liu and S. X. Dou, *J. Power Sources*, 119–121 (2003) 16.
154. J. Y. Eom, H. S. Kwon, J. Liu and O. Zhou, *Carbon* **42** (2004) 2589.
155. S. H. Yoon, C. W. Park, H. Yang, Y. Korai, I. Mochida, R. T. K. Baker and N. M. Rodriguez, *Carbon* **42** (2004) 21.
156. B. Gao, C. Bower, J. D. Lorentzen, L. Fleming, A. Kleinhammes, X. P. Tang, L. E. McNeil, Y. Wu and O. Zhou, *Chem. Phys. Lett.* **327** (2000) 1999.
157. H. Shimoda, B. Gao, X. P. Tang, A. Kleinhammes, L. Fleming, Y. Wu and O. Zhou, *Phys. Rev. Lett.* **88** (2002) 015502.
158. R. S. Morris, B. G. Dixon, T. Gennett, R. Raffaele and M. J. Heben, *J. Power Sources* **138** (2004) 277.
159. V. Meunier, J. Kephart, C. Roland and J. Bernholc, *Phys. Rev. Lett.* **88** (2002) 075506.
160. Y. Liu, H. Yukawa and M. Morinaga, *Computational Mater. Sci.* **30** (2004) 50.
161. Z. H. Yang, Z. F. Li, H. Q. Wu and B. Simard, *Mater. Lett.* **57** (2003) 3160.
162. Z. Zhou, X. P. Gao, J. Yan, D. Y. Song and M. Morinaga, *J. Phys. Chem. B* **108** (2004) 9023.
163. Z. Zhou, X. P. Gao, J. Yan, D. Y. Song and M. Morinaga, *Carbon* **42** (2004) 2677.
164. M. H. Chen, Z. C. Huang, G. T. Wu, G. M. Zhu, J. K. You and Z. G. Liu, *Mater. Res. Bull.* **38** (2003) 831.
165. W. X. Chen, J. Y. Lee and Z. L. Liu, *Carbon* **41** (2003) 959.
166. T. P. Kumar, R. Ramesh, Y. Y. Lin and G. T. K. Fey, *Electrochem. Comm.* **6** (2004) 520.
167. C. M. Niu, E. K. Sichel, R. Hoch, D. Moy and H. Tennent, *Appl. Phys. Lett.* **70** (1997) 1480.
168. E. Frackowiak, K. Metenier, V. Bertagna and F. Beguin, *Appl. Phys. Lett.* **77** (2000) 2421.
169. B. Zhang, J. Liang, C. L. Xu, B. Q. Wei, D. B. Ruan and D. H. Wu, *Mater. Lett.* **51** (2001) 539.

170. Ch. Emmenegger, Ph. Mauron, P. Sudan, P. Wenger, V. Hermann, R. Gallay and A. Zuttel, *J. Power Sources* **124** (2003) 321.
171. B. J. Yoon, S. H. Jeong, K. H. Lee, H. S. Kim, C. G. Park and J. H. Han, *Chem. Phys. Lett.* **388** (2004) 170.
172. J. H. Chen, W. Z. Li, D. Z. Wang, S. X. Yang, J. G. Wen and Z. F. Ren, *Carbon* **40** (2002) 1193.
173. K. H. An, W. S. Kim, Y. S. Park, Y. C. Choi, S. M. Lee, D. C. Chung, D. J. Bae, S. C. Lim and Y. H. Lee, *Adv. Mater.* **13** (2001) 497.
174. K. H. An, W. S. Kim, Y. S. Park, J. M. Moon, D. J. Bae, S. C. Lim, Y. S. Lee and Y. H. Lee, *Adv. Funct. Mater.* **11** (2001) 387.
175. E. Frackowiak, K. Jurewicz, S. Delpeux and F. Beguin, *J. Power Sources* 97–98 (2001) 822.
176. J. Y. Lee, K. H. An, J. K. Heo and Y. H. Lee, *J. Phys. Chem. B* **107** (2003) 8812.
177. H. T. Fang, C. G. Liu, C. Liu, F. Li, M. Liu and H.-M. Cheng, *Chem. Mater.* **16** (2004) 5744.
178. C. G. Liu and H.-M. Cheng, Frequency response characteristic of single-walled carbon nanotubes as electrode material in electrochemical capacitors, 2nd Japan–China–Korea Joint Symposium on “Carbon Materials to Save the Earth”—Devices and Materials for New Energies, Fukuoka, Japan, 6–9 September, 2004.
179. K. Jurewicz, S. Delpeux, V. Bertagna, F. Beguin and E. Frackowiak, *Chem. Phys. Lett.* **347** (2001) 36.
180. Q. F. Xiao and X. Zhou, *Electrochim. Acta* **48** (2003) 575.
181. K. H. An, K. K. Jeon, J. K. Heo, S. C. Lim, D. J. Bae and Y. H. Lee, *J. Electrochem. Soc.* **149** (2002) A1058.
182. L. X. Li, Synthesis of double-walled carbon nanotubes and carbon nanotube/conducting polymer composite as electrode material in electrochemical capacitor, Doctoral thesis, Institute of Metal Research, Chinese Academy of Sciences (2005).
183. J. Kong, M. Chapline and H. J. Dai, *Adv. Mater.* **13** (2001) 1384.
184. D. Ugarte, T. Stockli, J. Bonard, A. Chatelain and W. A. de Heer, *Appl. Phys. A* **67** (1998) 101.
185. P. J. Britto, K. S. V. Santhanam, A. Rubio, A. Alonso and P. M. Ajayan, *Adv. Mater.* **11** (1999) 154.
186. J. Mittal, M. Monthieux, H. Allouche and O. Stephan, *Chem. Phys. Lett.* **339** (2001) 311.

## Chapter 13

### Carbon nanotubes as nanoelectromechanical systems components

Susan B. Sinnott<sup>a</sup> and Narayan R. Aluru<sup>b</sup>

<sup>a</sup> Department of Materials Science and Engineering, University of Florida, Gainesville, FL 32611-6400, USA

<sup>b</sup> Department of Mechanical and Industrial Engineering, University of Illinois at Urbana-Champaign, Urbana, IL 61801, USA

Carbon nanotubes (CNTs) have attracted much interest since their discovery because of their unique structures and properties. In particular, they can function as metallic or semiconducting conductors, have great stiffness in the axial direction, are excellent thermal conductors, and readily absorb gases and liquids into their hollow interiors. This combination of properties makes CNTs natural components for future nanoelectromechanical systems (NEMS). This chapter reviews recent computational and experimental work that investigates and establishes the properties of nanotubes that will be relevant to their use in NEMS devices. The focus is on nanofluidic behavior of gases and liquids confined to CNT or bundle interiors, the mechanical and thermal properties of CNTs, and electronic transport in CNTs. Lastly, the challenges and opportunities inherent in producing NEMS devices from CNT components are discussed.

#### 1. INTRODUCTION

Carbon nanotubes (CNTs) have been the focus of much study since their discovery by Iijima in 1991 [1]. They can be thought of as nanometer-scale diameter, rolled up sheets of graphite, the hollow, tubular analogs of buckyballs [2], and smaller, structurally more perfect versions of carbon fibers [3–5]. As a consequence of their one-dimensional (1D), hollow, graphitic structure, CNTs have unique structural, chemical, mechanical, electrical, and thermal properties [6–14].

Over this same time period advances in nanotechnology as well as in nanomachining techniques have enabled development of novel nanoelectromechanical systems (NEMS) [15,16]. NEMS devices are defined as nanometer-scale sensors, actuators, and similar devices and systems with critical feature sizes ranging from several hundreds of nanometers to only a few nanometers. The central feature of NEMS is miniaturization, and the characteristics of NEMS obey the scaling laws of the physical world. The effective masses, heat capacities, and power consumption are proportional to the critical feature size, either linearly or non-linearly, while the fundamental frequencies, mass/force sensitivities, and mechanical quality factors are inversely proportional to

the critical feature size. Using state-of-the-art surface and bulk nanomachining techniques [16], NEMS can now be built with masses approaching a few attograms ( $10^{-18}$  g) and with cross-sections of about 10 nm [17]. The extremely small size of NEMS provides fundamental frequencies in the microwave range, mechanical quality factors in the tens of thousands, force sensitivities at the attonewton level, active masses in the femtogram range, mass sensitivity at the level of individual molecules, and heat capacities far below a yoctocalorie [15–19].

The aim of this chapter is to review the carbon nanotube literature with an emphasis on those properties that make them promising components for NEMS and related devices. The chapter also provides an outlook on the challenges and opportunities inherent in pursuing the development of NEMS from these materials.

### 1.1. Carbon nanotubes

Nanotubes can be produced in two varieties. In the first, the CNT contains only one wall or shell and is therefore called a single-walled nanotube (SWNT). Several SWNTs are shown in Figs. 1a and b. The second variety of the CNT contains multiple tubes, or shells, one within another and is called a multiwalled nanotube (MWNT). In particular, MWNTs are composed of larger diameter nanotubes surrounding smaller nested nanotubes, where each successive outer shell has a larger diameter but retains the characteristic rolled graphene structure, as shown in Fig. 1c. The diameter of a SWNT is typically several nanometers whereas the diameter of a MWNT can be as large as 100 nm.

Both SWNTs and MWNTs can be grown in tangled structures or ordered close-packed structures (see Fig. 2) using fabrication methods that include carbon-arc discharge, laser ablation of carbon, or chemical vapor deposition (CVD) [14,21]. They are usually produced with capped ends that can be round, half-spheres of buckyballs, or tapered if pentagonal defects are introduced at the end [22].

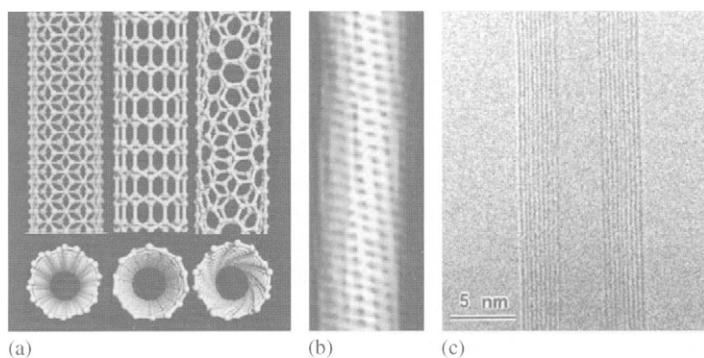


Figure 1. (a) SWNTs of various chiralities (from left to right: armchair, zigzag, and chiral). (b) STM image of a SWNT. (c) A TEM image of a MWNT. Reprinted with permission from [R. H. Baughman, A. A. Zakhidov and W. A. d. Heer, *Science* **297** (2002) 787]. Copyright (2002) American Association for the Advancement of Science.



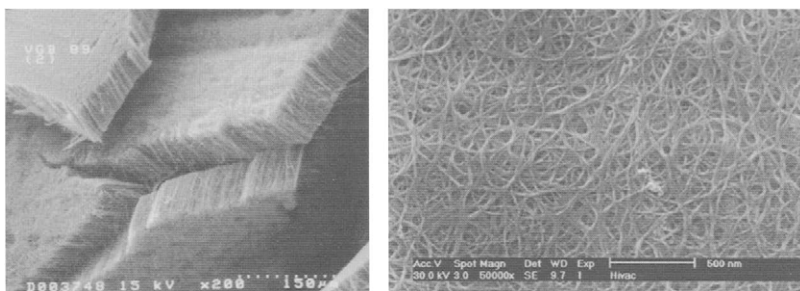


Figure 2. Left-hand side: MWNTs grown by CVD in ordered closed backed arrays (image courtesy of D. Jacques). Right-hand side: SWNTs grown by pulsed laser deposition from Ref. [25]. Reused with permission from R. Smalley, *J. Chem. Phys.* **115**, 6691 (2001). Copyright 2001, American Institute of Physics.

Chemical methods have been developed for the opening of capped CNTs [23,24] that leave functional groups at the opened ends.

The bonding within the CNT walls is covalent [26] and van der Waals bonding typically exists between CNTs in a bundle or between CNTs arranged in a MWNT structure. The ideal van der Waals spacing between shells in a MWNT ranges from 0.34 to 0.39 nm, and changes as the nanotube diameters vary [27]. Larger inter-shell spaces occur in smaller diameter nanotubes because of the increased repulsive forces associated with the higher curvature of the walls.

Nanotubes are usually round, as illustrated in Fig. 1, but at large diameters (around 15 nm) [27] they can deform and facet, especially when they are placed on a surface [28]. Fig. 3 illustrates how this deformation changes with the diameter of SWNTs and the number of shells in MWNTs. The driving force for this deformation is maximization of the van der Waals interactions between the CNT and the surface. The calculated binding energies of SWNTs and MWNTs with surfaces are shown in Fig. 4. The strain energy associated with forming the cylindrical shape is predicted to vary as the inverse of the CNT radius squared [29] and is not predicted to depend on the helical structure of the CNT. Calculations of the stability of circular and collapsed SWNTs of various helical structures [30] show that at radii  $<1.0$  nm, only nanotubes with circular cross-sections are stable, while at radii  $>1.0$  and  $<3.0$  nm, both circular CNTs and CNTs with collapsed cross-sections are stable. At radii  $>3.0$  nm, the calculations indicate that only tubes with collapsed cross-sections are stable because of the substantial energy gain from van der Waals bonding across the collapsed tube.

In addition to CNT diameters, the helical arrangement of carbon atoms in nanotubes can affect their behavior, especially their electronic properties. It is therefore important to be able to unambiguously identify the diameter and atomic structure of an individual CNT. Such a system has been developed and is illustrated in Fig. 5. The integer lattice vectors shown in the figure,  $\mathbf{m}$  and  $\mathbf{n}$ , are added together and the tail and head of the resulting vector are placed on top of each other in

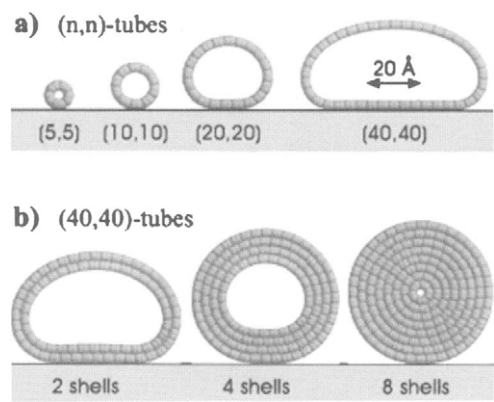


Figure 3. Schematic indicating how large diameter SWNTs and thin MWNTs deform on solid surfaces to maximize their interaction with the surface. However, if the MWNTs are thick (i.e., have a large number of shells), they are too stiff in the radial direction to deform. Courtesy of P. Avouris, IBM Research, and the American Physical Society. From Ref. [28]. Copyright (1998) the American Physical Society.

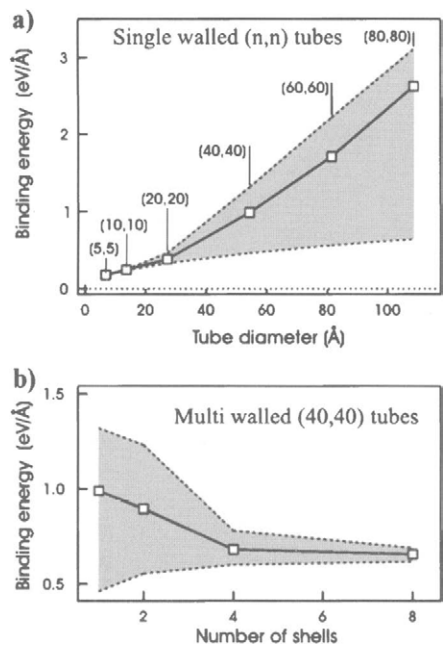


Figure 4. The calculated binding energies of CNTs adsorbed on a surface as a function of (a) their diameter or (b) number of shells (thickness). Courtesy of P. Avouris, IBM Research, and the American Physical Society. From Ref. [28]. Copyright (1998) the American Physical Society.

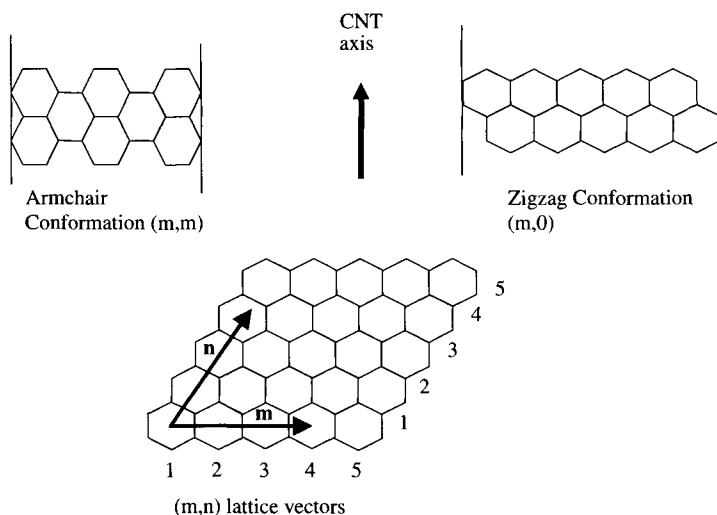


Figure 5. Illustration of arrangements of helical CNT structures. The integer lattice vectors  $\mathbf{m}$  and  $\mathbf{n}$  are added together and the tail and head of the resulting vector are placed on top of each other in the final CNT structure. The structures of the two achiral (armchair and zigzag) CNTs are shown. All other  $(\mathbf{m},\mathbf{n})$  combinations yield chiral CNTs.

the final nanotube structure. Zigzag nanotubes have  $(\mathbf{n},0)$  lattice vector values, while armchair nanotubes have  $(\mathbf{n},\mathbf{n})$  lattice vector values. These are the only two achiral confirmations; all other  $(\mathbf{m},\mathbf{n})$  lattice vector values yield chiral nanotubes [6,31]. The SWNTs in Fig. 1a are, from left to right, armchair, zigzag, and chiral.

Because the chirality and diameter of nanotubes are so important for their properties, achieving sufficient control to produce only SWNTs of one achiral type (zigzag or armchair) is a goal of many researchers that has not yet been achieved. Rather, SWNTs of mixed chirality are produced using all known synthesis approaches, and MWNTs usually contain shells that differ from one another in helical symmetry [32]. Complicating matters is the fact that there is no general agreement on whether SWNTs with particular chiralities are more stable than similarly sized SWNTs with different chiral structures [33–35]. Experimentally, CNT diameters are determined with transmission electron microscopy (TEM) [1,36] and their chiralities are determined with scanning tunneling microscopy (STM) [37–39], Raman spectroscopy [40,41], and Raleigh spectroscopy [42]. Importantly, new methods have been recently developed to separate SWNTs with differing chiralities from one another [43,44].

## 1.2. Nanoelectromechanical systems

Semiconductor materials such as silicon, silicon carbide, and gallium arsenide have been used to build NEMS for a variety of applications. SWNTs and MWNTs are also being heavily explored as components in NEMS [20]. CNTs have high electrical conductivity [45], high thermal conductivity ( $>3000$  W/m K), high Young's modulus

( $\sim 1$  TPa), and a high tensile strength ( $\sim 63$  GPa). These unique attributes of CNTs offer opportunities for new CNT NEMS applications.

Broadly defined, CNT NEMS currently being pursued can be classified into three categories: nanomechanical, resonant, and nanofluidic systems. In a CNT nanomechanical system, CNTs typically act as structural components of the system, which deform or move according to external forces (e.g., electrostatic, magnetic, thermal, optical, chemical, or biological). Typical examples of this class of devices are mass/force sensors, torsional springs [47], nanogears [48], and bearing systems [49] (see Fig. 6). In CNT-based resonant systems, CNTs are actuated to vibration by the applied electrical or other signals. Nanoscale resonant systems can be used to detect adsorbed mass. The principle of sensing is based on the resonant frequency shift of a CNT resonator [50] when it is subjected to a strain resulting from external loading. Another class of CNT NEMS applications is nanofluidic systems, where CNTs can function as ion channels and the fluid transport can be controlled by the applied electrical field. Nanoscale drug delivery/release system [51] is a typical example of this class of NEMS. Beyond these major application areas, new applications of CNTs continue to emerge. For example, CNTs have been used in artificial muscles [52] and in hydrogen storage [21,49].

NEMS offer tremendous opportunities in various areas ranging from fundamental research to health care, from conventional sensing and actuating technology to nanorobotics. With further advances in nanofabrication technology, CNT NEMS with unprecedented complexity and functionality are expected to appear in the near future.

## **2. MECHANICAL PROPERTIES OF CARBON NANOTUBES**

This section discusses the mechanical properties of CNTs, including Young's moduli and responses of CNTs to deformation. The focus is on CNT properties rather than methodology.

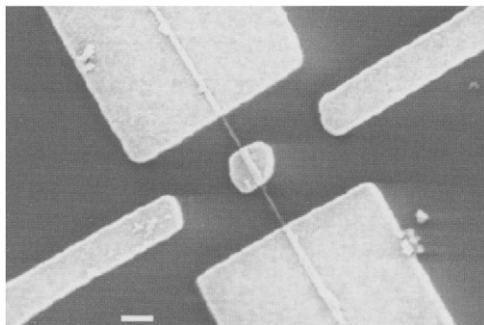


Figure 6. An MWNT bearing system. From Ref. [46]. Reprinted with permission from A. Zettl and Nature. Copyright (2003) Macmillan Magazines, Inc.

## 2.1. Carbon nanotubes in tension and compression

### 2.1.1. Elastic responses: Young's modulus determination and radial deformation

It is well established that the carbon bonds within graphene sheets are among the strongest known. It is therefore not surprising that shortly after the discovery of CNTs, there was interest in the mechanical properties of these tubular graphene forms of carbon. Table 1 lists some of the reported Young's moduli from computational and experimental studies with an indication of the way in which the values were obtained.

The different ways in which these studies take into account the wall thickness of the nanotubes is responsible for the considerable variation in the calculated moduli ( $\sim 5$  versus  $\sim 1$  TPa) [73]. Specifically, SWNTs are one carbon atom (0.066 nm) thick but, as discussed in the last section, they have a van der Waals radius of 0.34 nm. Most calculations require a wall thickness, and the value that is used affects the reported Young's modulus value. In particular, when a wall thickness equal to the van der Waals radius is used, continuum elasticity theory predicts a Young's modulus of 1 TPa but also predicts a bending stiffness that is about 25 times lower than that predicted by classical mechanics. On the other hand, if a wall thickness of 0.066 nm is used, the correct classical bending stiffness is obtained, but the Young's modulus is  $\sim 5$  TPa. It should be pointed out that this issue not only affects the computational results; most of the experimental data also requires inclusion of a wall thickness for the determination of a value for Young's modulus. This quandary perfectly illustrates the complications inherent in applying continuum elasticity theory and classical mechanics to nanotubes, which are not only hollow "pipes" and large aspect ratio "beams," but also have only single-atom thickness and can be thought of as single, seamless molecules.

It has been pointed out [90] that the product of the Young's modulus and the wall thickness of SWNTs is surprisingly consistent at  $0.3685 \pm 0.0055$  TPa nm. Some studies have avoided the issue of what wall thickness to use by calculating the elastic constant per unit mass rather than the Young's modulus, and found that this value does not depend on the geometry of the CNT systems and is quite similar for CNTs and graphite [91]. The carbon-carbon bond strength in SWNTs have been analyzed from melting data and estimated to correspond to a Young's modulus that is 2.5 times the value of graphite [90]. However, if the moduli of SWNTs are calculated by simply scaling the modulus of graphene with density when it is close-packed in a hexagonal arrangement with hollow interior volumes, Young's moduli values of about 600 GPa are obtained for SWNTs [76].

There have been several studies that have explored other aspects involved in using classical models to extract the Young's modulus of CNTs. For example, an analysis by Ru [92] indicates that the bending stiffness of SWNTs are much lower than those calculated with the classical, elastic shell model. In contrast, the bending stiffness of MWNTs is in good agreement with the classical bending stiffness model if the friction barrier between the adjacent CNT shells is high enough that interlayer slipping is prohibited. However, inter-shell sliding is known to occur, as discussed in more

detail below. An analysis by Govindjee and Sackman [93] indicates that for the study of nanobeam bending or buckling, the nanobeam must consist of a large number of atomic layers for the continuum cross-section assumption to be valid. Furthermore, Sudak [94] pointed out that the most important aspect of this problem is that at small length scales, the length of the internal aspects of the CNT, such as inter-shell spacing in MWNTs, are important but are not taken into account in classical continuum models. Similar conclusions were reached by Zhang et al. [95].

There are other variations in the calculated results shown in Table 1. For example, in the case of Ref. [58] the values are independent of chiralities and diameters, while in the case of Ref. [59] the values are independent of helical structure but the onset of plastic deformation depends significantly on helical structure (zigzag SWNTs have a larger elastic limit than armchair SWNTs). However, the effects of curvature are not included in Ref. [58], which could explain the fact that the results are independent of diameter. Universal force field calculations [62] that include torsional energy terms yield Young's moduli that decrease as the SWNT diameter increases and also as the degree of helicity increases. Furthermore, some continuum shell model calculations [96] predict that under compression, zigzag SWNTs are stiffer than armchair SWNTs of comparable diameters, but that under tension, armchair SWNTs are stiffer than armchair SWNTs. In contrast, some molecular dynamics (MD) simulations [68] find that under large strain conditions (defined as 15% or greater) zigzag SWNTs are stiffer under tension, while armchair SWNTs are stiffer under compression.

On the experimental side, several different methods are used to determine the Young's modulus of CNTs. One approach is to subject the CNT to radial compression with an atomic force microscope (AFM) tip, as shown in Fig. 7. The compressibility of SWNTs is determined to be reversible up to 4 GPa after which the lattice is destroyed [97]. Some of the data obtained with this approach is illustrated in Fig. 8, which compares the radial compressive elastic modulus of MWNTs and graphite [98]. The CNTs are seen to be much stiffer than the graphite in the radial direction, and quite resistant to plasticity overall, in agreement with the findings of others studies [99,100]. When this approach is used to compare the mechanical properties of pinned MWNTs and silicon carbide nanorods, the MWNTs are determined to be twice as stiff as the silicon carbide [78]. A subsequent study [101] using X-ray diffraction of SWNTs under hydrostatic pressures up to 13 GPa found that the nanotube bundle lattice does not disappear until applied stresses of about 10 GPa, at which point a phase transformation occurs. Interestingly, symmetry returns even after pressures of 13 GPa have been applied. An even more recent study using Raman spectroscopy to characterize SWNTs under hydrostatic pressure found a critical pressure of  $2.1 \pm 0.2$  GPa for nanotube collapse [102].

The differences in the amount of pressure needed to irreversibly damage nanotube samples could be due to the difference between volume compression under quasi-hydrostatic pressures in Ref. [101], and volume compression under non-hydrostatic stresses in Ref. [97]. Furthermore, the collapse of SWNT bundles under hydrostatic pressures is generally agreed to be dependent on the SWNT diameters [104]. However, different computational studies do not predict formation of the same

Table 1  
Summary of published Young's moduli for CNTs along their axis as determined by the indicated theoretical and experimental approaches. MD, molecular dynamics.

Young's modulus (TPa)	Material	Method	Reference
0.414	SiC	—	[53]
1.035	Diamond	—	[53]
0.72—1.12	SWNTs, various chiralities and diameters (range 0.688–0.738 nm)	Ab initio calculations	[54]
0.764	SWNTs	Ab initio calculations	[55]
0.930	SWNTs with diameters of 1.4 nm	Ab initio calculations	[56]
1.22–1.26	SWNTs of various chiralities and diameters (range 0.791–2.034 nm)	Tight-binding calculations	[57]
0.971–0.975	SWNTs of various chiralities and diameters (0.68–27 nm)	Tight-binding calculations	[58]
1.0–1.7	SWNTs more details	Tight-binding calculations	[59]
1.4	SWNTs of various chiralities and diameters (0.2–1.6 nm)	Tight-binding calculations	[60]
0.969–1017	SWNTs of various chiralities and diameters (0.63–1.10 nm)	Tight-binding and ab initio calculations	[61]
1.0–1.1	Armchair SWNTs of various diameters (range 0.4–3.4 nm)	Universal force field calculations	[62]
1.002	SWNTs of various chiralities and diameters (range 0.41–2.06 nm)	Lattice-dynamics model-derived calculations	[63]
1.05±0.05	MWNTs	Molecular structural mechanics	[64]

(Continued)

Table 1 (Continued)

Young's modulus (TPa)	Material	Method	Reference
0.48–0.61	SWNTs with diameters in the range of 1.0–1.5 nm	Continuum shell model calculations	[65]
4.70	SWNTs	Classical elasticity theory	[66]
1.04–4.70	MWNTs of various diameters	Classical elasticity theory	[66]
0.50	SWNTs of various helical symmetries and diameters of 0.4–2.2 nm	MD simulations	[67]
0.980	SWNTs	MD simulations	[68]
3.62	SWNTs with diameters of 1.2 nm	MD simulations	[69]
1.350±0.012	SWNTs of various chiralities	MD simulations	[70]
1.238±0.006	and diameters		
1.25–1.48	SWNTs of various chiralities with diameters of 0.5–1.7 nm	MD simulations	[71]
5.5	SWNTs	Theoretical considerations	[72]
5.1	SWNTs	Band structure calculations	[73]
0.850–2.55	SWNTs under various levels of strain (0.003–0.04 for the lowest value, less than 0.003 for the highest value); diameter of 0.69 nm	MD simulations and ab initio calculations	[74]
0.670–0.700	SWNTs of various diameters and chiralities	MD simulations and continuum theory	[75]
0.600	SWNTs	Graphene density analysis calculations	[76]
0.989	SWNTs	Analytic analysis of a graphene sheet	[77]
1.28±0.59	MWNT	Experimental proximal probe tip indentation	[78]



1	SWNT rope	Experimental proximal probe tip indentation	[79]
0.045±0.007 (lower bound)	SWNT rope	Experimental proximal probe tip indentation	[80]
0.320–1.470	SWNT rope	Experimental tensile test	[81]
0.270–0.950	MWNTs	Experimental tensile test	[82]
1.81	MWNTs of various diameters and containing different numbers of shells	Experimental TEM analysis of vibrations	[83]
1.25±0.45	SWNTs with diameters of 1.0–1.5 nm	Experimental TEM analysis of vibrations	[84]
5	SWNTs	Experimental analysis of CNTs strained while embedded in epoxy	[85]
1.8	MWNTs	Experimental analysis of CNTs strained while in epoxy	[85]
0.100	SWNTs	Experimental Raman spectra, deformation by liquid surface tension	[86]
(at low strains)			
0.91	MWNTs	Experimental tension and bending test	[87]
0.016	Aligned MWNT strands with two shells and diameters of 3–20 µm	Experimental stress–strain puller	[88]
0.076±0.004	SWNT bundles with diameters of 15–70 nm	Mechanical resonance with TEM	[89]

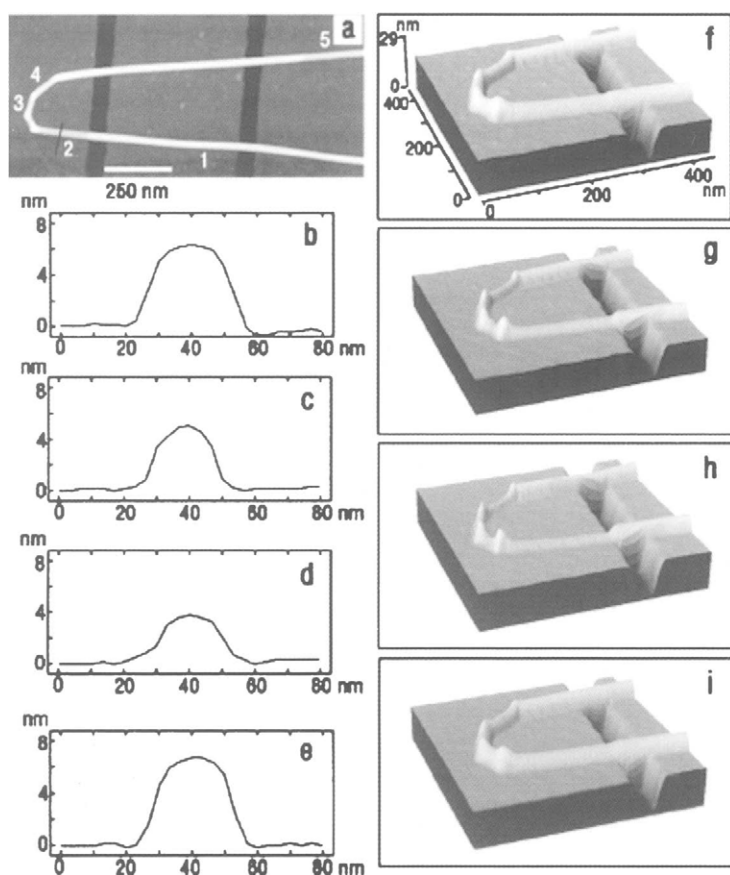


Figure 7. AFM images of the deformability of an MWNT positioned on a patterned silicon wafer. The darker shades indicate deeper features. (a) Large area view of an MWNT bent into a hairpin shape. (b)–(e) Height profiles taken along the thin marked line in (a) from images taken at set point values of (b) 1.0, (c) 0.7, (d) 0.5, (e) 1.0. (f)–(i) Three-dimensional images of the curved region of the MWNT acquired at the set point values indicated in (b)–(e). Reprinted with permission from R. S. Ruoff and the American Physical Society. From Ref. [103]. Copyright (2000) the American Physical Society.

collapsed structure, which is thought to depend on loading rate, size, and compression rate, among other variables [105,106]. Tight-binding calculations indicate that a reversible  $sp^2$ – $sp^3$  transition can occur in SWNTs under relatively low hydrostatic stresses [107,108]. However, *ab initio* calculation studies [109,110] do not predict  $sp^3$  bonding across deformed SWNTs to occur up to high stress levels of 20 GPa [110].

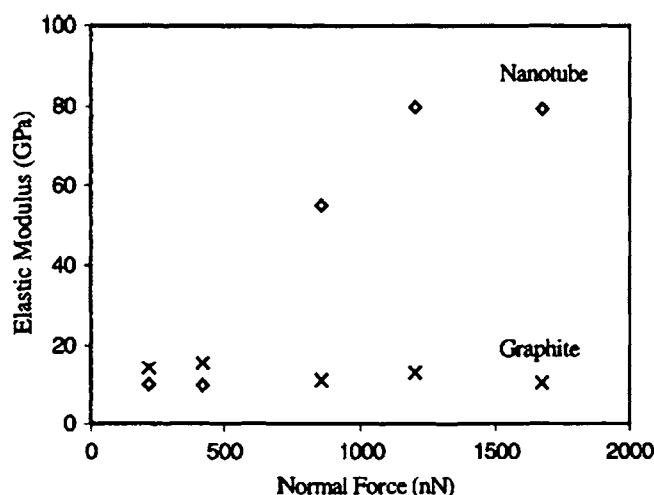


Figure 8. Experimentally measured radial compressive elastic moduli of CNTs and graphite under an increasing normal force. Reprinted with permission from W. C. Shen and the American Physical Society. From Ref. [98]. Copyright (2000) the American Physical Society.

Another experimental approach used to extract the Young's modulus of nanotubes involves subjecting the CNTs to tensile loading by attaching them at one end to a AFM tip and the other end to a piezo actuator or another AFM tip, as illustrated in Fig. 9. Fig. 10 shows measured stress–strain curves for several samples of SWNT ropes (Fig. 10a) and individual MWNTs (Fig. 10b) measured in this manner. In this case, the stress was calculated by using the cross-sectional area of the sample and the forces were measured by the AFM tip. The stress–strain curves in Fig. 10 are not perfectly linear over their entire length, although the curves for the individual MWNTs are significantly more linear than the curves for the SWNT ropes. This is most likely because not all the SWNTs in the rope are carrying the load equally, whereas each MWNT is being fully probed.

An additional experimental method of measuring Young's modulus of individual CNTs is by monitoring their vibrations with a TEM [83,84]. Fig. 11a shows thermal vibrations of freestanding CNTs, while Fig. 11b illustrates electric field-driven resonance of a CNT. Analytic expressions have been developed to better understand the vibrations of CNTs from theory [111] and simulation studies [112–114]. The vibrational behavior of CNTs is found to depend on temperature, CNT length, and on whether the sample under consideration consists of MWNTs or SWNTs (weak inter-layer interactions in MWNTs increases energy dissipation in vibrating MWNTs). The oscillatory behavior of MWNTs deflected at the end of AFM cantilevers [115] is consistent with a nanospring.

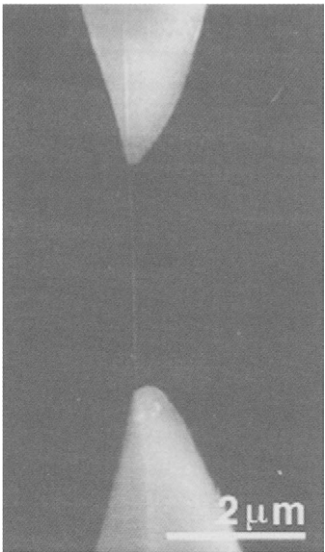


Figure 9. A magnified SEM image of an MWNT between two AFM tips. From Ref. [82]. Copyright (2000) American Association for the Advancement of Science.

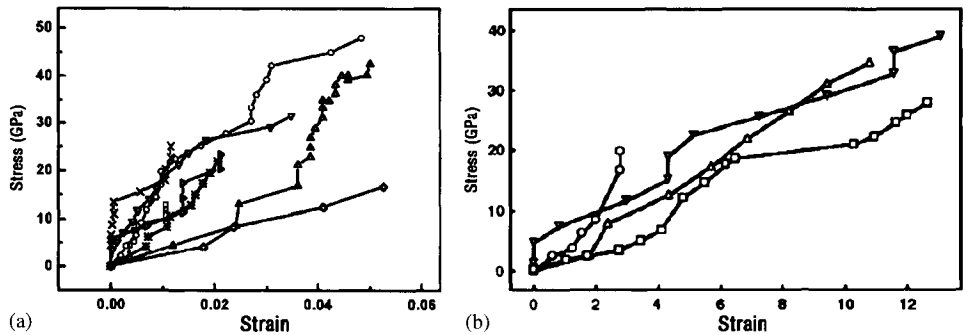


Figure 10. (a) Measured stress–strain curves from tensile-loading experiments on individual SWNT ropes. Each rope diameter is measured with an SEM within an accuracy of a few nanometers. The stress values are calculated using the cross-sectional area of the perimeter SWNTs. Reprinted with permission from R. S. Ruoff and the American Physical Society. From Ref. [81]. Copyright (2000) the American Physical Society. (b) Plot of stress versus strain for individual MWNTs. The measured Young’s moduli are 954 GPa for the circles, 470 and 300 GPa for the first and second upswings of the curve represented by squares, and 335 and 274 GPa for the whole curves of triangles pointing up and down, respectively. From Ref. [82]. Copyright (2000) American Association for the Advancement of Science.

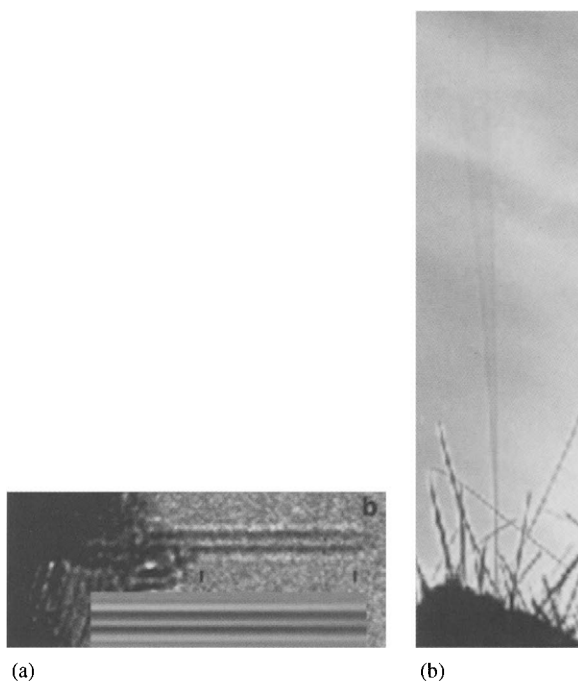


Figure 11. (a) TEM image of a vibrating SWNT. Reprinted with permission of M. M. J. Treacy and the American Physical Society. From Ref. [84]. Copyright (1998) the American Physical Society. (b) Electric field driven resonance of an MWNT. From Ref. [116]. Copyright (1999) American Association for the Advancement of Science.

Calculations [117] have been useful for identifying the differences in the vibrations of SWNTs and double-walled MWNTs; in particular, they showed that the fundamental frequencies of the MWNTs were about 10% lower than those of SWNTs of the same diameter and length. Subsequent studies examined the thermally driven vibrations of clamped and suspended straight [118] and coiled [119] CNTs. When the CNTs were attached at the clamped ends to gold contacts the contacts were sensitive to the CNT vibrations in a piezoelectric manner and were able to detect the fundamental resonances of the suspended CNT [119].

Lastly, the moduli of CNTs have been determined by embedding them in an epoxy matrix, varying the system temperature to induce contractions and expansions, characterizing the tubes with micro-Raman spectroscopy [85]. A related approach monitors the change in Raman spectra when the CNTs are immersed in various liquids and deformed by the liquids' surface tension [86].

The axial buckling of MWNTs is generally thought to require more force as the number of shells increases. This is illustrated in Fig. 12 from non-linear structural mechanics model calculations [120]. However, at some thickness the effective

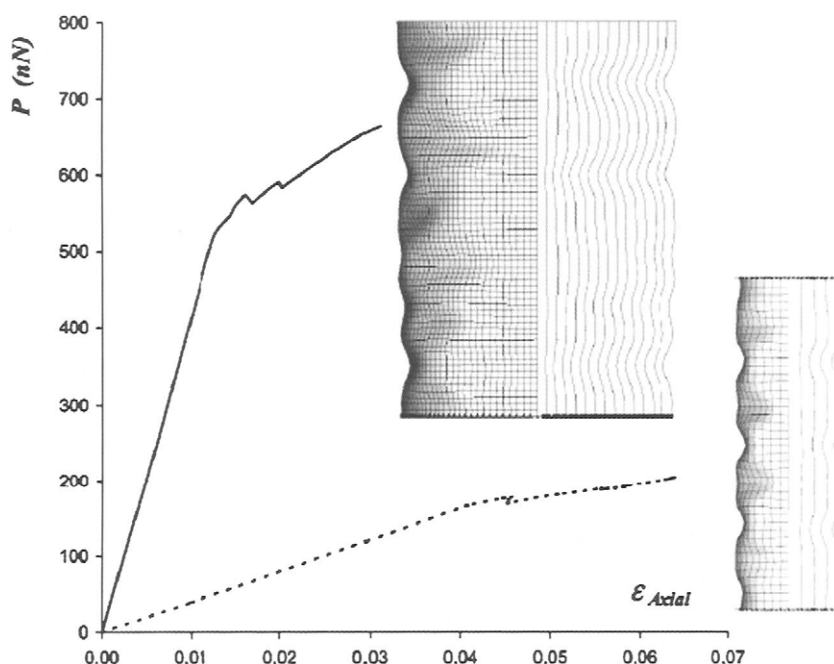


Figure 12. Predicted axial compression of MWNTs with 4 and 14 shells. From Ref. [120]. Reprinted with permission from D. M. Parks and the American Physical Society. Copyright (2003) the American Physical Society.

bending stiffness of MWNTs decreases. This was investigated with generalized local quasi-continuum calculations [121], which indicated that thick MWNTs (with, e.g., 34 shells) deform by rippling of the walls during bending and twisting, which leads to an overall non-linear response. For these reasons, linear elasticity approaches are not appropriate for the study of these systems. Similar rippling is observed in MD simulations of bent MWNTs [122].

Chemical functionalization of SWNTs has been shown to affect their mechanical properties. For instance, the buckling forces of SWNTs of various diameters and chiralities were shown to be reduced by about 15% when they were heavily functionalized relative to pristine tubes [123]. In addition, the relative strain of SWNTs was shown to change with chemical modification of the tube walls [124].

Nanotubes can be filled with materials other than smaller diameter nanotubes. One of the most famous examples is fullerene-filled nanotubes [125–129], which are widely known as “peapods”. MD simulations were used to compare the compressibility of SWNTs and peapods of comparable diameters and helical structures [130]. The simulations indicate that after a critical filling density is reached, peapods buckle at a larger force than comparable SWNTs, but that the slope of the

force versus strain plots for these two systems are the same, indicating that the Young's modulus of the SWNT is not affected by filling with  $C_{60}$ . However, the effect of temperature on the buckling force is significantly different between the empty SWNTs and the peapods. In particular, the effect of temperature on the buckling force decreases appreciably at high temperatures, as illustrated in Fig. 13. A similar study of the deformation of empty SWNTs and peapods through compression, tension, and torsion [131] found peapods to be slightly softer, or more easily deformable, than the empty SWNTs, possibly due to the fact that the fullerenes in the peapods were separated by 1.00–1.05 nm, rather than the 0.35 nm separation used in Ref. [130]. A study where organic polymers were inter-collated into sheets

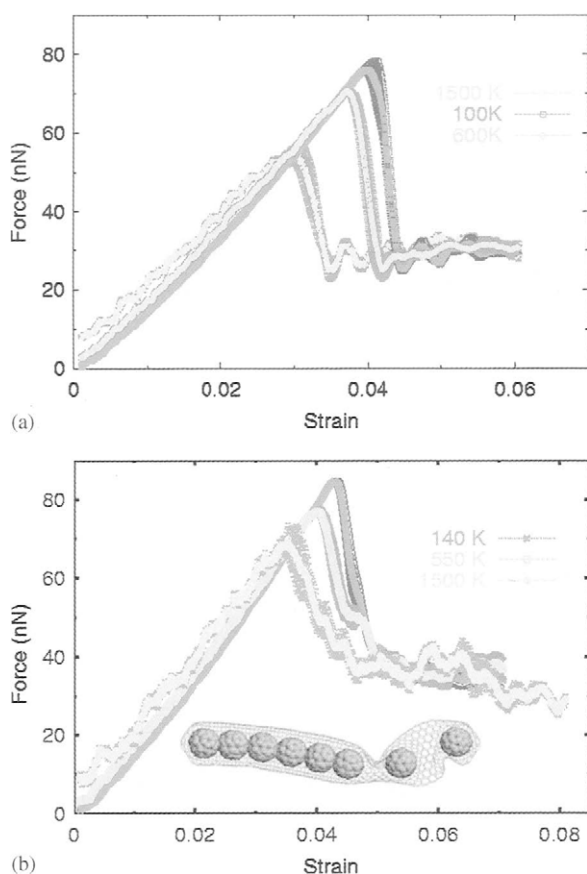


Figure 13. Dependence of buckling force with filling and temperature. (a) Buckling of empty (10,10) SWNTs at indicated temperatures. (b) Buckling of (10,10) SWNTs filled with  $C_{60}$  as a function of temperature. Inset in (b) is of the buckled peapod system at 300 K.

of SWNTs [132] found that by filling the free volume with polymer, improved load transfer occurs in the sheets that significantly increase their Young's modulus, strength, and toughness.

There have also been several studies of the mechanical properties of SWNTs filled with metallic and carbon-based nanowires, which, unlike CNTs, are solid rather than hollow. MD studies by Trotter et al. [133] predicted that the buckling behavior of double-walled MWNTs and SWNTs filled with diamond nanowires with the same outer diameters are nearly identical. Interestingly, MD studies by Danailov et al. [134] found that SWNTs filled with metal nanowires that were bent had suppressed buckling instabilities and damped oscillations not predicted to occur for MWNTs.

Because of their high moduli, small diameters, and electrical conductivity, CNTs can be used as AFM or STM tips [135] or extensions of AFM silicon cantilevers [136]. CNT tips are either formed by gluing the CNTs to the cantilever [135] or by growing them there directly through a CVD process [137]. Such tips are used to image fine details on surfaces [138–140] and, when a current is running between the tip and sample, to etch the sample [141]. The buckling behavior of CNT AFM tips have been modeled in MD simulations and shown to have similarities and differences to the buckling of freestanding SWNTs and MWNTs [142–145]. In related studies, CNTs were used as nanotweezers to manipulate nanoclusters [146] and not only moved the nanocluster from one location to another but also probed its electronic structure. Such configurations could lead to the development of sensors and electronic devices.

While all the results shown in Table 1 indicate that CNTs have high stiffness along their tubular axis, CNTs are known to have a much lower modulus in the direction perpendicular to the tube axis, which is calculated to be about 9.3 GPa for SWNTs [147]. The elastic modulus of CNTs in the radial direction decreases as the CNT diameter increases. Structural mechanics method calculations predicted values of 1.5–11 GPa for SWNTs with diameters of 2.0–0.6 nm [148]. These low radial moduli were verified by AFM experiments [149] that indicated that CNT–substrate interactions can not only induce the radial deformation of CNTs, but also stabilize the collapsed CNT over long times. When the radius-to-thickness ratio is larger than 4, a MWNT with  $N$ -shells requires approximately  $N$  times the critical pressure of a SWNT to buckle in the radial direction [150].

### **2.1.2. Plastic responses and failure of carbon nanotubes**

Nanotubes have high tensile strengths of about 0.15 TPa [87] and failure strengths of 13–52 GPa [81]. However, the presence of point defects in CNT walls can reduce the measured modulus and could be a factor in the experimental results discussed so far. This reduction could be quite significant. It was estimated to be a 10-fold decrease [151] or a decrease of 30–50% [152] and found to be dependent on the loading conditions and chirality and diameter of the tube [152]. Other studies [75] predicted a two-fold decrease in the tensile strength and critical strain at which SWNTs fail in the presence of individual wall vacancies, and noted that CNTs are able to heal defects by rebonding, which influences the results. However, multiple or clustered defects are predicted to have a more significant effect on the strength. In addition, computational studies suggest that electronically excited SWNTs with



monatomic vacancies can result in new bond formation that heals vacancies even more aggressively [153]. *Ab initio* calculations predicted that the activation energy for the formation of Stone-Wales defects in CNTs to be very high (about 3–10 eV) and to form more readily in smaller diameter SWNTs and at higher strains [154].

The presence of additional dimers on a SWNT that is subject to tension leads to defects within the CNT walls that change the helicity of the CNT for a short section [155]. CNTs modified in this manner are able to respond to induced tensile strain in a plastic manner at points where the unmodified CNTs undergo brittle failure [155]. Comparison of critical strain energies and elastic responses for SWNTs with a range of diameters obtained from atomistic and continuum models indicates that for diameters greater than about 1.0 nm the two approaches agree well with each other [156]. However, for smaller diameters the results of the two are in poor agreement.

The way in which the CNTs under study are synthesized and/or cleaned can affect their defect density. This was illustrated in a recent study [157] that found that MWNTs synthesized by the arc method exhibited plastic deformation when bent beyond the elastic limit, whereas MWNTs synthesized by CVD exhibited brittle fracture under the same conditions. While this could be due to differences in the diameters and number of shells in the two types of MWNTs, differences in the defect density are undoubtedly a contributing factor.

MD simulations of the tensile loading of SWNTs indicated that while the behavior is elastic under normal conditions, plasticity can occur in some cases [158–160]. Fig. 14 shows snapshots from MD simulations that elucidate the mechanisms by which non-elastic responses occur in SWNTs. In particular, plastic flow is predicted at high temperature and brittle failure at low temperatures. The mechanism in both cases starts off with the creation of a dislocation dipole of Stone-Wales defect structures that move away from each other along the CNT axis in a helical path. The simulations predicted that CNTs are strained to about 30–40% before failure occurs, with the results showing some dependence on tube diameter, rate of strain, and system temperature. Fig. 15 illustrates the way in which brittle versus ductile responses depends on the diameter and helical symmetry of SWNTs. When the SWNTs are pulled in tension to a greater extent, they dissociate into carbon chains, illustrated in Fig. 16 [158]. Only a few discrete cracking modes are predicted to dominate the brittle failure of SWNTs [161].

A combined TEM experimental and MD simulation study [163] found that fracture of SWNTs under tension is controlled by the rate of strain, temperature, and the number of defects. At high temperatures and high defect densities, plastic deformation dominates and chains of carbon atoms were observed (as illustrated in Fig. 17) in good agreement with the results shown in Fig. 16. Similar findings of necking, plastic deformation, and brittle fracture were also observed in Ref. [164]. Eventually, the chains break and the new CNT ends are capped, as illustrated in Fig. 17. The presence of defects is predicted to enhance plastic deformation under conditions where perfect nanotubes fail in a brittle manner [163], although computational studies predict that even with wall defects, SWNT failure can still be brittle [165].

An analytic model was developed that predicts plastic yield strain as a function of temperature and time [166]. MD simulation studies [167,168] predicted that the tensile

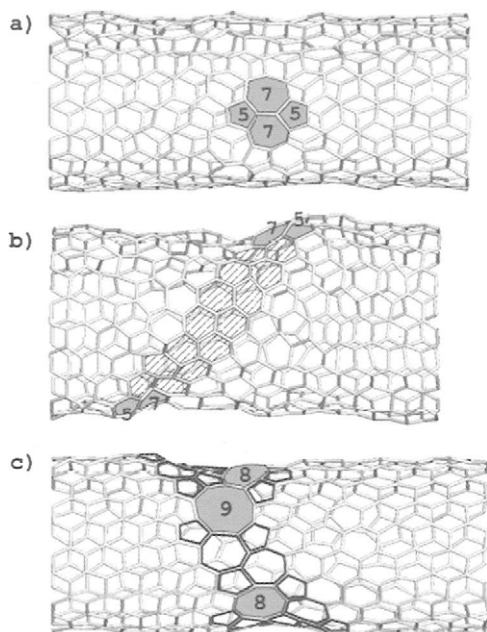


Figure 14. Snapshots from MD simulations of a (10,10) SWNT under axial strain. (a) Formation of a Stone-Wales defect at 2000 K and 10% strain. (b) Plastic flow after about 2.5 ns at 3000 K and 3% strain. (c) Nucleation of large open rings and brittle relaxation after about 1.0 ns at 1300 K and 15% strain. From Ref. [162]. Courtesy of J. Bernholc and the American Physical Society. Copyright (1998) the American Physical Society.

yielding of MWNTs and SWNTs depends significantly on the rate of strain. In particular, these studies identified a critical strain rate above which the yielding strain of MWNTs is larger than SWNTs, and below which the yielding strain of MWNTs is smaller than SWNTs [167]. For instance, at a strain rate of 1%/h at 300 K, the yield strain of MWNTs is 3–4% higher than the yield strain of SWNTs under the same conditions. These simulations also predicted that larger diameter, defect-free SWNTs yield at a 2–3% higher strain than smaller diameter SWNTs [168]. Another way in which the SWNTs and MWNTs differ is that when SWNTs buckle, their strain energy decreases, while in the case of MWNTs that buckle, the potential energy increases as chemical bonds within the MWNT change from  $sp^2$ - to  $sp^3$ -hybridization [169]. Interestingly, repeated application of torsional strains to MWNTs causes them to stiffen relative to pristine MWNTs [170]. It was hypothesized that this is because the repeated straining is creating cross-links between the MWNTs or, alternatively, destroying wall defects and allowing better inter-shell atomic registry [170].

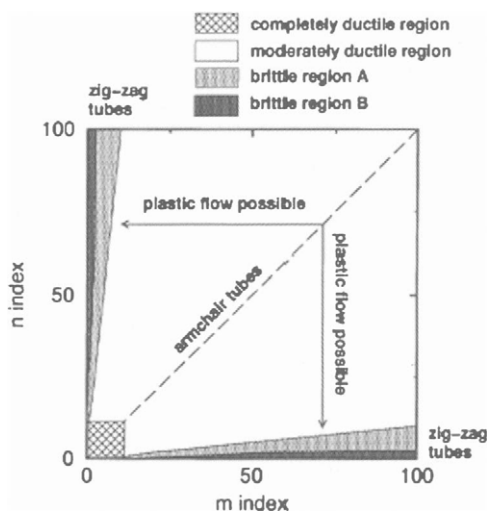


Figure 15. A domain map showing the ductile to brittle domains for SWNTs with diameters up to 13 nm. From Ref. [162]. Courtesy of J. Bernholc and the American Physical Society. Copyright (1998) the American Physical Society.

When MWNTs fracture in a brittle manner, frequently it is only the outer shell that breaks while the inner shells remain intact. This is the so-called “sword-in-sheath” failure mechanism for MWNTs where the inner shells (the “sword”) can be extended from the broken outer shell (the “sheath”) relatively easily and reversibly [49,82,171]. However, as discussed below, several factors can influence the ease with which this sliding occurs, including the degree of commensurability between the sliding shells, the wall defect density, and the interactions of the outer shell broken ends with the inner shells. For example, TEM studies [172] showed that chemical bonds form between the broken outer shells of MWNTs and the intact inner shells. This finding led to the proposal of a “breakage-sliding-fusion” model to describe the breaking of MWNTs, which is a variation of the sword-in-sheath mechanism. In addition, MD simulations that considered a double-walled MWNT with covalent cross-links between the shells predicted that these inter-shell bonds prevent sword-in-sheath failure. Under high strain rate conditions, experiments found dynamic nanofragmentation of MWNTs [173]. The ends have irregular cross-sections that suggest that elastic deformation, plasticity, and failure occurs, in agreement with computational studies.

Because of these unique inter-shell interactions, double-walled MWNT systems have been proposed as gigahertz oscillators [50]. MD simulations [174] indicated that these nanooscillators are stable when the radii differences between the inner and outer tubes are around 0.34 nm. In these cases, shown in Fig. 18, the simulations predicted frequencies as large as 38 GHz. MD studies [175,176] also indicated that the

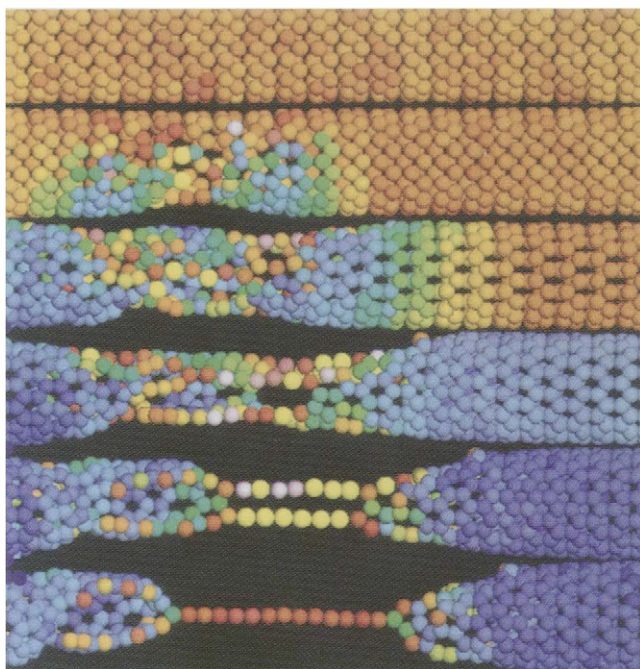


Figure 16. Snapshots from MD simulations of a SWNT in the different stages of tensile fracture. From Ref. [158]. Reprinted from B. I. Yakobson, M. P. Campbell, C. J. Brabec and J. Bernholc, High strain rate fracture and C-chain unraveling in carbon nanotubes, *Comp. Mat. Sci.* **8**, 341 (1997) with the permission from J. Bernholc and Elsevier Science.

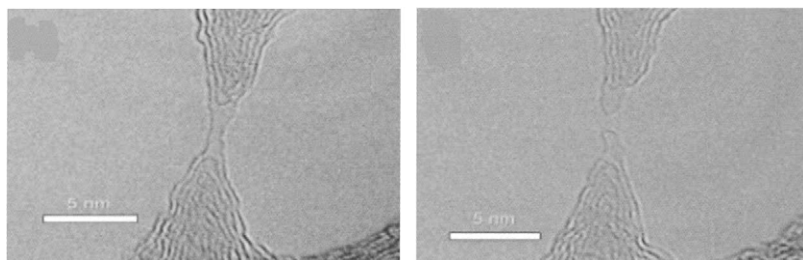


Figure 17. TEM images of CNTs under strain that are thinned (left-hand side) and that then break (right-hand side). Reprinted with permission from [163]. Copyright (2004) American Chemical Society.

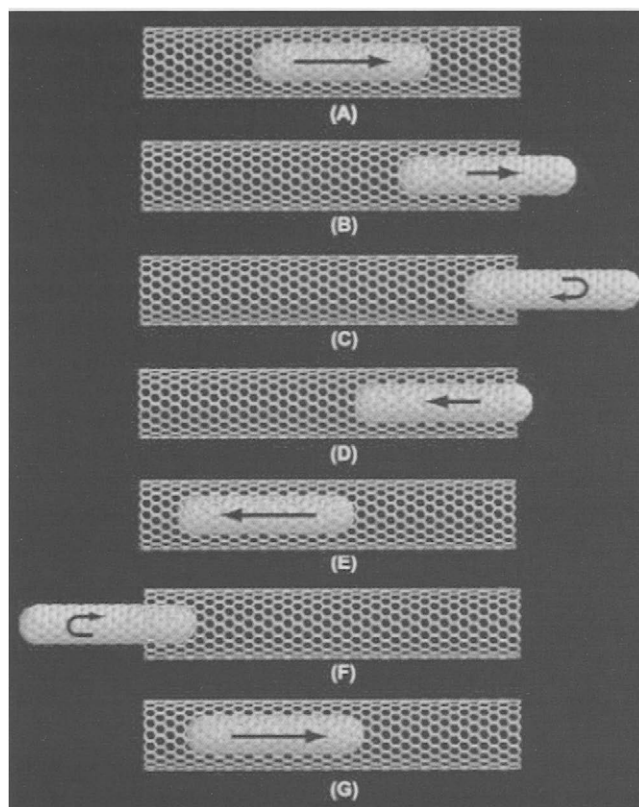


Figure 18. Snapshots from MD simulations showing the oscillatory behavior of a (9,0) SWNT inside a (18,0) SWNT. From Ref. [174]. Reprinted with permission from D. S. Galvao and the American Physical Society. Copyright (2003) the American Physical Society.)

oscillations damp out over time, and showed that the time that elapses until the oscillations go to 0 is linearly dependent on the lengths of the CNTs. In addition, MD simulations [177] predicted that energy dissipation in commensurate, double-walled CNTs oscillators is substantially higher than in incommensurate oscillators. Consequently, incommensurate system oscillators take much longer to damp out than commensurate system oscillators. When the temperature of the system increases, the MD simulations predicted that friction increases as a result of thermal fluctuations [175].

## 2.2. Deformation of carbon nanotubes

### 2.2.1. Bending and twisting

Nanotubes can be deformed easily by bending, twisting, or related motions [72,178,179]. Fig. 19 is a high resolution electron microscopy (HREM) figure of a

bent CNT [179] that can be simulated in MD simulations. The simulations indicated that when the CNT is returned to its original position there is no plastic deformation as a result of the bending [179]. Fig. 20 shows snapshots from MD simulations where SWNTs were twisted through the application of torsional forces [72]. Again this is a remarkably elastic phenomenon that is predicted to be reversible.

Interestingly, molecular mechanics calculations and MD simulations indicated that twisting a SWNT bundle enhances load transfer between neighboring nanotubes [180]. It also leads to deformation of the cross-sections of the SWNTs, as illustrated in Fig. 21. This effect is determined to depend on the twist angle as the load transfer depends to a great extent on the contact between the CNTs in the bundle, as illustrated in Fig. 22.

When *ab initio* calculations were used to study the bending of SWNTs under mechanical loads at the ends (either in a manner similar to that shown in Fig. 19 or

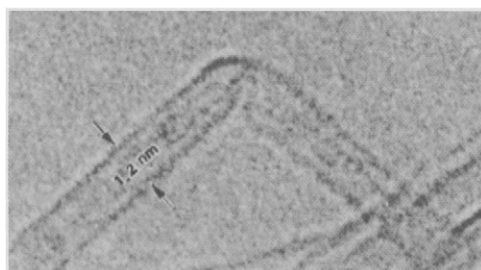


Figure 19. High-resolution electron microscopy image of a bent SWNT that has a diameter of 1.2 nm. The gap between the kink and the upper wall is about 0.4 nm. From Ref. [179]. Used with permission from J. Bernholc and the American Institute of Physics.



Figure 20. Snapshots from an MD simulation of a (13,0) SWNT being twisted under applied torsion forces. From Ref. [72]. Reprinted with permission from J. Bernholc and the American Physical Society. Copyright (1996) the American Physical Society.

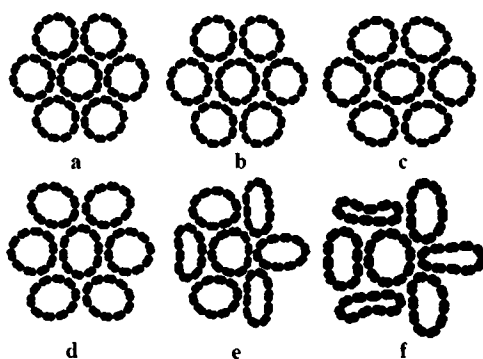


Figure 21. Snapshots from MD simulations of a rope of SWNTs being twisted. The perspective is along the nanotube axis. The images indicate how the cross-sections of the SWNTs change as the twisting progresses from image (a) to image (f). From Ref. [180]. Reprinted with permission from R. S. Ruoff and Elsevier Science.

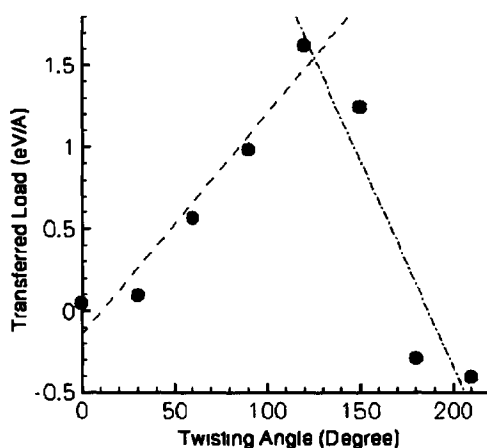


Figure 22. Predicted transfer of load in a bundle of SWNTs that is being twisted in MD simulations, as illustrated in Fig. 21, a function of twist angle. The lines are the linear fits of the predicted data. From Ref. [180]. Reprinted with permission from R. S. Ruoff and Elsevier Science.

by deforming them with an AFM tip) [181], the results show that SWNTs bent mechanically retain their bonding structure to relatively high bending angles, while those bent by AFM tips develop “inward, cone-like structures” followed by four-fold coordination and rupture. The calculations further predicted that these bent SWNTs

will return to their original structures when the AFM tip is removed. However, if the SWNT was constrained from bending by, for example being held in place, then plastic failure occurred in the simulations [182].

### 2.2.2. Shear and tribological deformation

The shear modulus of a SWNT rope has been measured to be quite low [79] at around 0.001 TPa. Calculations predict slightly higher shear moduli for individual CNTs that are still quite low. Reported values include  $0.40 \pm 0.05$  [64], 0.5 [58], 0.27–0.30 [65], 0.492 [70], and 0.490 TPa [56].

There have also been several studies of the tribological properties of CNTs, which are quite interesting. For example, MD simulations by Buldum and Lu [183] and Schall and Brenner [184] indicated that when forces are applied to SWNTs on graphite, the SWNTs roll when their honeycomb lattice is “in registry” with the honeycomb lattice of the graphite. However, if the SWNT and the graphite are not in registry, the SWNT responds to the applied forces from, e.g., an AFM tip, by sliding. This behavior is summarized in Fig. 23. These MD simulation findings were simultaneously confirmed in experimental studies by Falvo et al. [185].

An experimental study by Miura et al. [186] of nanotube bundles being pushed around on a potassium chloride surface with an AFM tip indicated that bundles of SWNTs can be induced to roll in a manner that is similar to the rolling observed for MWNTs. MD simulations by Ni and Sinnott [187,188] predicted more complex behavior for bundles of SWNTs as a function of orientation. The movement of the SWNTs in response to the shear forces is simple sliding when they are arranged horizontally or vertically relative to the sliding surfaces. In contrast to the experimental findings of Miura et al., the simulations do not predict rolling of the horizontally arranged CNTs even when they are aligned with each other in two- and three-layer structures. Rather, at low compressive forces the SWNT bundles slide as a single unit, and at high compressive forces, the deformed SWNTs closest to the topmost moving surface start to slide in a motion reminiscent of the movement of a tank or bulldozer wheel belt. However, when these moving SWNTs would have turned the

Out-of-registry: “slide-roll-slide”

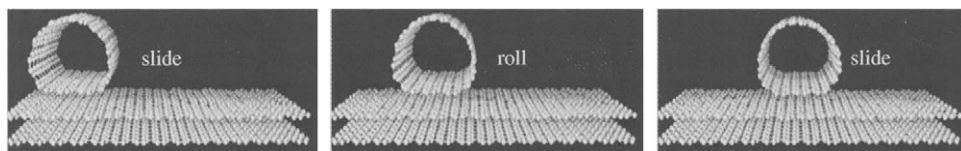


Figure 23. Snapshots from an MD simulation of a (10,10) SWNT being pushed from left to right by external forces on a graphite surface. When the SWNT and graphite plane are out of registry, the nanotube slides as it slow down from the initial impulse of applied force. However, when the SWNT is oriented such that it is in registry with the graphite, it rolls and slides. Figure courtesy of D. W. Brenner.



first corner at the top of the ellipse, they encounter the neighboring SWNT and cannot slide past it. This causes them to deform even further, form cross-links with one another, and, in some cases, move in the reverse direction to the sliding motion of the diamond surface. This causes the large oscillations in the normal and lateral forces, as shown in Fig. 24.

The simulations of Ni and Sinnott [187,188] further predicted that the responses of the horizontally arranged SWNTs are substantially different from the responses of the vertically arranged SWNTs at high compression. This is obvious through a comparison of Figs. 24 and 25. In particular, the vertical, capped SWNTs are flexible and buckle in response to applied compressive forces. As the buckle is forming, the normal force decreases then levels off after the buckled structure forms. As the topmost surface slides, the buckled SWNTs swing around the buckle “neck” and this process helps dissipate the applied stresses. For this reason, the magnitudes of the lateral forces are not significantly different for the vertical nanotubes at low and high compression, as indicated in Fig. 25. Recent experiments by Dickrell et al. [189] show good agreement with these predictions, as summarized in Fig. 26.

### 3. ELECTRONIC PROPERTIES OF CARBON NANOTUBES

This section discusses the electronic properties of CNTs. In particular, the manner in which their electronic properties depend on their chirality, diameter, and

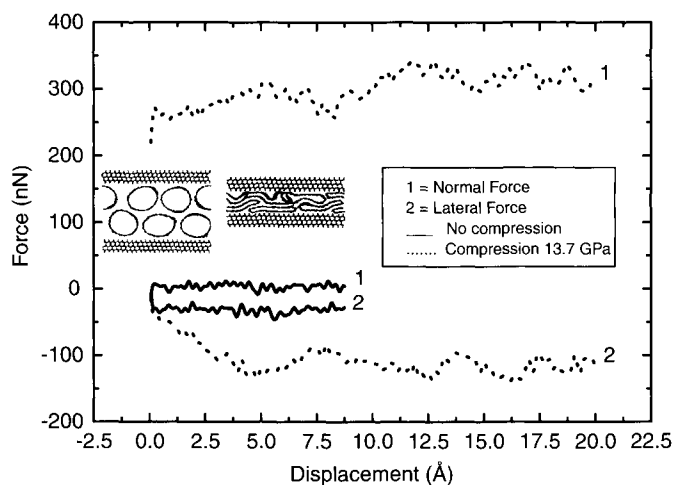


Figure 24. Plots of the normal and lateral components of force during the sliding of a hydrogen-terminated diamond surface on horizontally arranged SWNTs as a function of the lateral displacement of the top diamond surface obtained from MD simulations. Insets are snapshots from the simulations. The left inset is at a pressure of  $\sim 0$  GPa and the right inset is at a pressure of 13.7 GPa.

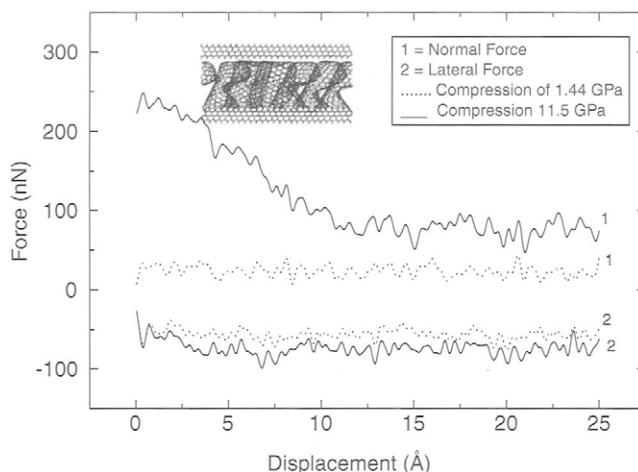


Figure 25. Plots of the normal and lateral components of force during the sliding of a hydrogen-terminated diamond surface on vertically arranged SWNTs as a function of the lateral displacement of the top diamond surface obtained from MD simulations. The inset is a snapshot from the simulations at a pressure of 11.5 GPa.

purity are addressed. Importantly, the relationship between the mechanical and electrical properties of CNTs is reviewed. In addition, their use in electronic devices is discussed.

### 3.1. Dependence of the electronic properties of carbon nanotubes on their structure

#### 3.1.1. Single-walled carbon nanotubes

The electronic properties of CNTs are determined by their atomic structure, described by the chiral angle and diameter specified by the lattice indices ( $m, n$ ) illustrated in Fig. 5. In early *ab initio* calculations by Mintmire et al. [190], the electronic structure of SWNTs was examined and the calculations predicted that SWNTs could be metallic conductors. One of the most important conclusions of this study is that Peierls [191] distortions do not produce a gap at the Fermi level to destroy the metallic character of some SWNTs, as occurs in other 1D materials, such as polyacetylene [190,192,193]. The calculations also indicated that the band gap of SWNTs decreases as the SWNT diameter increases. Most importantly, they estimated that the carrier concentration is on the order of that of typical metal conductors (about  $10^{22} \text{ cm}^{-3}$ ).

In subsequent studies, Saito et al. [194] and Hamada et al. [195] simultaneously considered, for the first time, the effects of chirality and helical structure of SWNTs

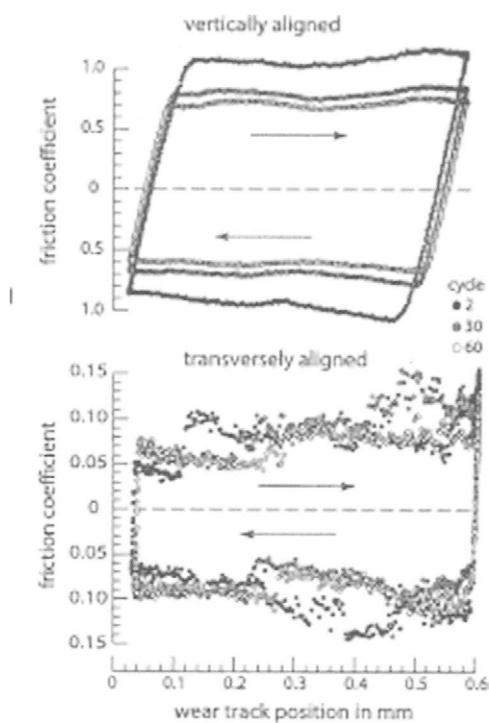


Figure 26. Coefficient of friction data versus track position collected for one full cycle of reciprocating sliding for SWNTs that are vertically and transversely aligned. Reprinted with permission from *Tribology Letters*, **18**, P. L. Dickrell, S. B. Sinnott, D. W. Hahn, N. R. Raravikar, L. S. Schadler, P. M. Ajayan, and W. G. Sawyer, Frictional anisotropy of oriented carbon nanotube surfaces, 59–62. Copyright (2005) Springer Science and Business Media B.V.

on their electronic properties. Additionally, they derived simple, predictive rules for determining the conductivity of SWNTs. These rules can be written as

$$2\mathbf{n} + \mathbf{m} = 3q, \quad (1)$$

where  $\mathbf{n}$  and  $\mathbf{m}$  are the integral lattice vectors described above and defined in Fig. 5, and  $q$  is an integer. When this rule is analyzed in more detail, it is clear that all arm-chair SWNTs are metallic, and all zigzag SWNTs where  $\mathbf{n}$  is a multiple of 3 are metallic. All other SWNTs chiralities have a band gap in their electronic structure and so are semiconducting.

Experimental verification that some SWNTs are metallic conductors came in a report by Tans et al. [196], where the conductivity of a nanotube draped across

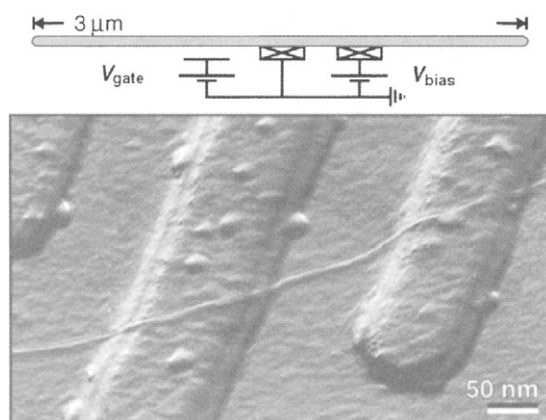


Figure 27. An SWNT draped across platinum electrodes. From Ref. [196]. Reprinted with permission from Nature. Copyright (1997) Macmillan Publishers Ltd.

platinum electrodes, as shown in Fig. 27, was measured. Interestingly, the experimental measurements indicated that SWNTs conduct as coherent quantum wires, as illustrated in Fig. 28. Put another way, the current flowing through an SWNT goes through distinct and discrete electron states that are quantum-mechanically coherent from one contact point to the other. Later experimental papers [37,39,197,198] confirmed the theoretical prediction that the electronic properties of SWNTs, as measured by STM, change significantly with variations in tube diameter and chirality; this finding is summarized in Fig. 29 from Ref. [197].

In one study, the resistance of metallic SWNTs was found to vary with temperature from about 12 k $\Omega$  at 2 K to about 20 k $\Omega$  at 300 K (with  $-10$  V gate bias) [199]. When the gate voltage varied from  $-100$  to  $100$  V, metallic SWNTs were found to conduct over the entire range with no periodic Coulomb oscillations. Results of comparable experiments on semiconducting SWNTs [199] indicated that the room temperature resistance of the large diameter semiconducting SWNT vary from about 200 to about 500 k $\Omega$ . SWNTs with the smaller diameters ( $d \leq 1.5$  nm) were shown to have room temperature resistances in the M $\Omega$  range or higher. However, at low temperatures (4 K), the tubes were insulating with gaps up to  $\pm 1000$  mV on the  $I/V$  curves. These gaps increased in size as the SWNT diameter decreased [199].  $I/V$  curve analysis confirmed that semiconducting SWNTs can function as hole-doped p-type transistors [199].

Calculations [200] predicted that electrical conductivity in metallic SWNTs is ballistic (largely free from scattering). Subsequent experimental studies [201] confirmed ballistic transport in SWNTs over distances of thousands of atoms. Importantly, metallic SWNTs have low electron backscattering, although phonon vibrations cause backscattering as temperatures increase [202,203].

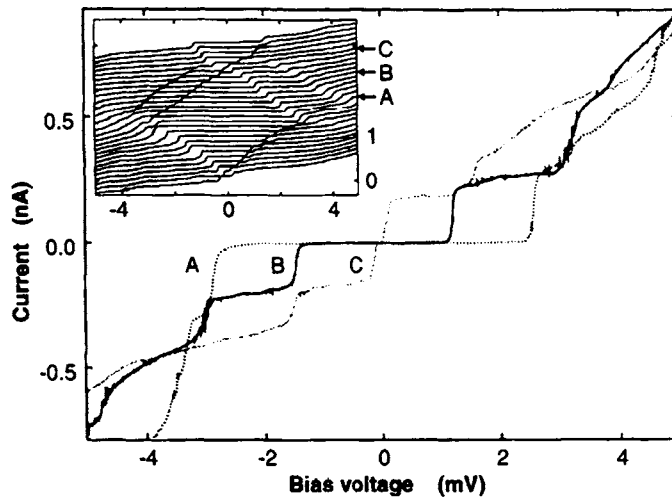


Figure 28. Measured  $I/V$  curves for the SWNT/platinum system shown in Fig. 27 at different trace voltages. Trace voltage A, B, and C are 88.2, 104.1, and 120 meV, respectively. The inset shows  $I/V$  (bias) curves for different trace values of  $V_{gate}$ . The graphs are vertically offset for clarity and range from  $V_{gate}=50$  meV for the top curve, to  $V_{gate}=136$  meV for the bottom curve. From Ref. [196]. Reprinted with permission from Nature. Copyright (1997) Macmillan Publishers Ltd.

The band-gap behavior of semiconducting SWNTs was found to depend to a great degree on the tube diameter. In particular, the energy gap decreases as the SWNT diameter increases. The behavior can be described by

$$E_g = 2\gamma_0 a_{C-C} / d, \quad (2)$$

where  $d$  is the nanotube diameter,  $a_{C-C}$  is the carbon-carbon distance in the nanotube wall, and  $\gamma_0$  is 2.45 eV [204]. Gaps can also be produced in SWNTs by the application of an external electric field [205], where the size of the gap depends on the electric field and the diameter of the SWNT.

The length of a given nanotube was also shown to affect its electronic properties. For example, it was shown [206] that band gaps are produced in short (<10 nm) metallic SWNTs, and that the size of the gap varies with changes in the length of the tube. However, this effect disappears at lengths of about 10 nm or greater, after which the electronic behavior of the SWNT is independent of its length. Factors that modulate the length dependence of SWNT electronic properties was shown to include the aromatic character and chirality of the tube [207]. In addition, analytically derived expressions have been developed to describe the discrete energy levels in finite metallic SWNTs [208].

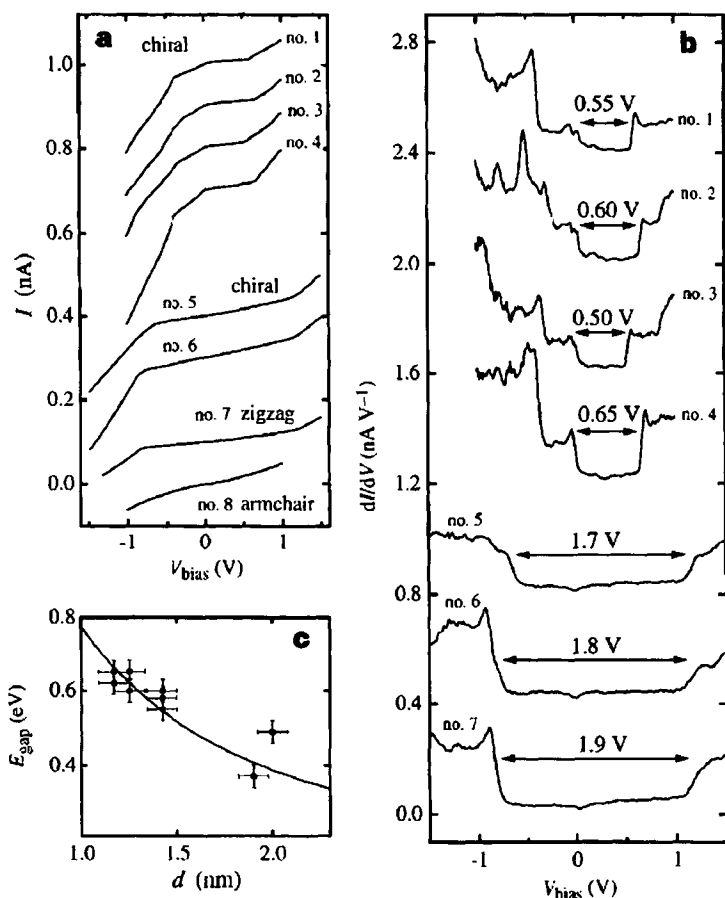


Figure 29. Experimental measurements of the electrical conductivity of a wide range of SWNTs. Nanotubes 1–6 are chiral, nanotube 7 is zigzag, and nanotube 8 is armchair. (a) The  $I/V$  curves for these SWNTs. Many of the chiral tubes have several kinks in the  $I/V$  curves but the armchair tube has none between  $-1$  and  $+1$  V. (b) The  $dI/dV$  and estimated band gaps. (c) Band gaps of the SWNTs (points) and a comparison with the theoretical predictions (curve). From Ref. [197]. Reprinted with permission from Nature. Copyright (1998) Macmillan Publishers Ltd.

Transport through these short SWNTs was shown to be free of substantial scattering from acoustic or optical phonons [209]. Consequently, under high-bias voltage conditions transport is ballistic, while under low-bias voltage conditions transport is quasi-ballistic [209]. Remarkably, experiments demonstrated that currents as high as  $70 \mu\text{A}$  can flow through short SWNTs [209]. However, at very high fields the SWNTs eventually break down. Non-linear dependence of nanotube conductance

on tube length was observed in experiments [210] and shown to be an intrinsic property of 1D conductors [211]. This behavior is summarized in Fig. 30. Recent studies indicate that good bulk conductivity of SWNTs can extend over hundreds of nanometers [212], several micrometers [213], and tenths of a centimeter [214], although this behavior was shown to depend on whether the SWNT is semiconducting or metallic [213].

### 3.1.2. Effects of intrinsic defects on the electronic properties of carbon nanotubes

In metallic SWNTs, backscattering due to the presence of long-range disorder is much smaller than in the case of semiconducting SWNTs [202,203]. When more severe defects are produced in metallic SWNTs through ion implantation [215], such as large holes and vacancies at a higher densities than in as-created SWNTs, it was found, not surprisingly, that the defects lead to increased resistance in the SWNT. In particular, the defects produced this way were shown to act as a gate-tunable barrier [215]. When a voltage was applied to a MWNT rope that was simultaneously scanned with an AFM, it was possible to match the locations of nanotube surface defects with the source(s) of tube failure due to applied voltage [216]. The results indicate that current-induced failure is localized to regions of large defects, and that these defects can substantially lower the maximum current density the nanotube can carry prior to failure. Interestingly, SWNT wall vacancies are predicted to enhance the density of occupied states near the Fermi energy in these systems

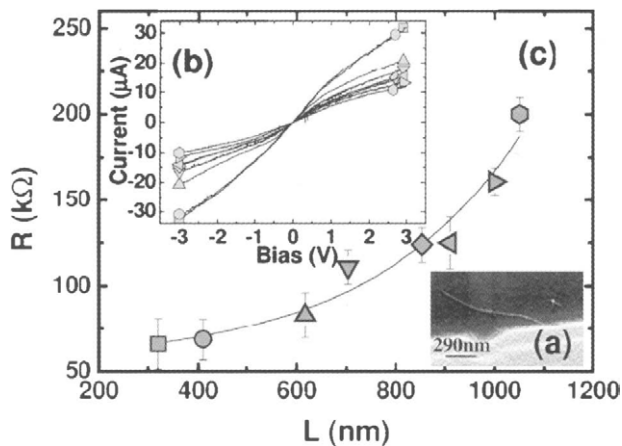


Figure 30. (a) SWNT of 1.5 nm diameter in contact with gold electrodes. (b) Several  $I/V$  curves taken along the SWNT. Note the linear region around 0 V. For large voltages a saturation effect is observed. (c) Resistance versus SWNT length that exhibits a non-linear behavior. A contact resistance of 54 kΩ is obtained by extrapolation. From Ref. [210]. Reprinted with permission from A. M. Baro and the American Physical Society. Copyright (2002) the American Physical Society.

[217]. In addition, the degree of localization increases as the number of vacancies increases. These results indicate that vacancies could cause both armchair and zigzag SWNTs to function as narrow-gap semiconductors or ferromagnetic materials, assuming that the interaction of ambient gases with the vacancies (which was not included in the calculations) does not greatly alter the amount of localization.

STM studies of the  $I/V$  characteristics of SWNT bundles [218] indicated that they have semimetallic behavior that is similar to graphite, as illustrated in Fig. 31. The resulting curves are reproducible for a fixed tip position, but as shown in the figure, vary with small displacements in tip position as a result of slight alterations of the electronic coupling at the probe interface. This type of behavior is representative for large numbers of nanotubes at room temperatures.

However, some nanotube ropes do have  $I/V$  characteristics that deviate from this behavior [218], as illustrated in Fig. 32. In particular, the transport current changes sharply at some point-contact positions from a graphitic response to a highly non-linear, asymmetric response that includes rectification. This response is indicative of a region of the nanotube rope that no longer acts as a wire but instead behaves as a Schottky barrier or other form of heterojunction. This finding is in agreement with the results of predictions for the effects of a Stone-Wales defects [218–220].

The effect of wall defects, such as pentagons and heptagons instead of the usual hexagons, on nanotube curvature was examined quite soon after the discovery of CNTs [221,222]. These studies discovered that pentagons cause inward curvature of the otherwise straight nanotube, while heptagons cause outward curvature of the tube. Importantly, pentagon/heptagon pairs, also as known as Stone-Wales or 5/7

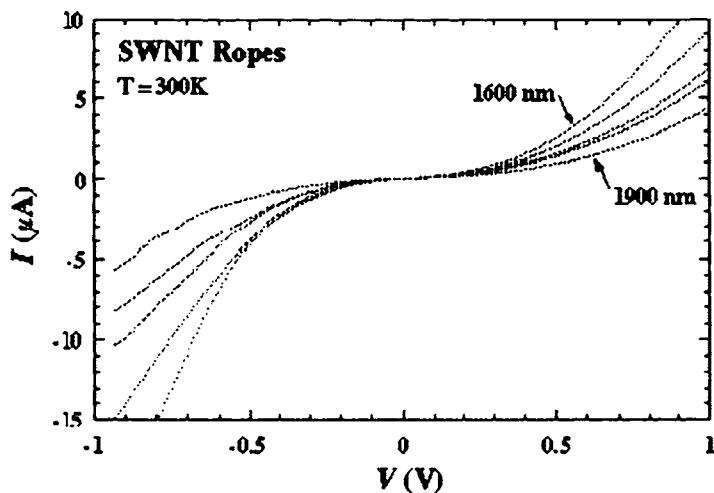


Figure 31.  $I$ - $V$  curves measured at contact points at different heights along a CNT rope. From Ref. [218]. P. G. Collins, H. Bando and A. Zettl, *Nanoscale electronic devices on carbon nanotubes*, *Nanotechnology* **9**, 153 (1998). Reprinted with permission from A. Zettl and the Institute of Physics Publishing, Inc.



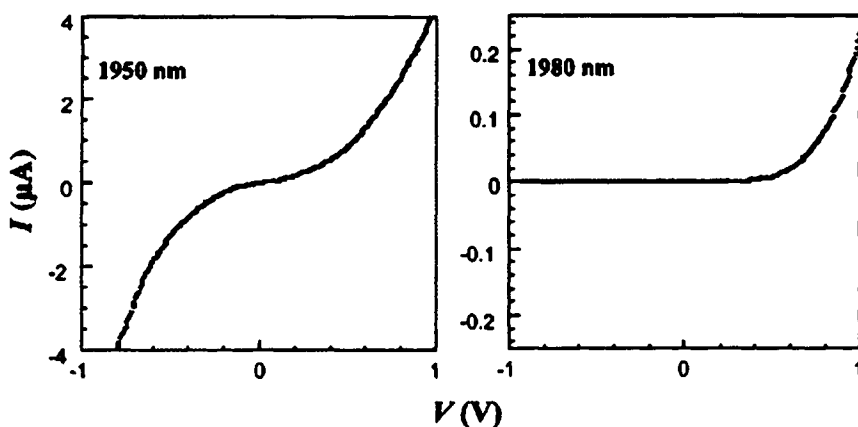


Figure 32.  $I/V$  curves measured on a nanotube sample using a STM tip. There is an abrupt transition as a result of dominant semimetallic behavior. The curve on the left-hand side is from the beginning of the experiment until the transition point, while the curve on the right-hand side starts from the transition point. This transition point occurred when the STM tip movement changed by a few nanometers. From Ref. [218]. Reprinted with permission from A. Zettl and the Institute of Physics Publishing, Inc.

defects, are necessary for forming seamless junctions between SWNTs with different chiralities and/or diameters [219,222–224].

The effect of Stone-Wales defects on the electronic behavior of SWNTs was therefore found to be important [218,219]. For example, calculations [224] indicated that Stone-Wales defects in zigzag SWNTs that are positioned along the cylindrical axis are more stable than when they are distributed around the circumference. It is interesting to note that only in a zigzag SWNT can the Stone-Wales defect be perfectly aligned with the nanotube axis and thus cause a change in diameter but no change in helicity. If the Stone-Wales defect is perpendicular to the nanotube axis, the result is a tube with the same diameter but enantiomeric segments, and so the tube bends slightly in the vicinity of the defect. Lastly, for all other defect orientations, changes in both SWNT diameter and chirality result [224].

### 3.1.3. Effect of doping on the electronic properties of carbon nanotubes

One route to controlled electronic properties in nanotubes is the introduction of heteroatom impurities. For instance, SWNT mats have been doped with cesium and potassium [225]. As the cesium doping progressed, the mat resistance decreased and then increased; in contrast, as the potassium doping increased, the mat resistance increased monotonically before saturating. SWNT ropes doped with potassium [226] had an overall decrease in resistance. In a related study, SWNTs doped with potassium [227] exhibited n-type behavior with the conductance increasing as

the gate voltage increased, as shown in Fig. 33. In contrast, the conductance of the undoped nanotubes decreased with increasing gate voltage, which is p-type behavior. Thus, doping with potassium changes the carriers in the nanotube ropes from holes to electrons, with typical carrier densities of 100–1000 electrons/ $\mu\text{m}$ . The effective mobility of the electrons is 20–60  $\text{cm}^2/\text{V}\cdot\text{s}$ , similar to the hole effective mobility reported by others [228].

Avouris and co-workers [203] showed that p-type character of as-prepared CNTs was determined by the nature of carrier injection to the SWNT at the contacts. Specifically, p-type behavior of as-produced SWNTs can, depending on the conditions, be due to contact doping, doping through cleaning with acids, and adsorption of oxygen from the atmosphere [203,229]. If these tubes are annealed in an inert environment or vacuum, they become ambipolar field effect transistors (FETs) where they can operate as switches for electrons or holes depending on the sign of the gate voltage [203,229,230]. However, experiments [231] found that in the n-type region of a semiconducting SWNT, the ends of the tube remained p-type because of doping by the metal contact. As a result, a small p–n junction formed near the CNT junction.

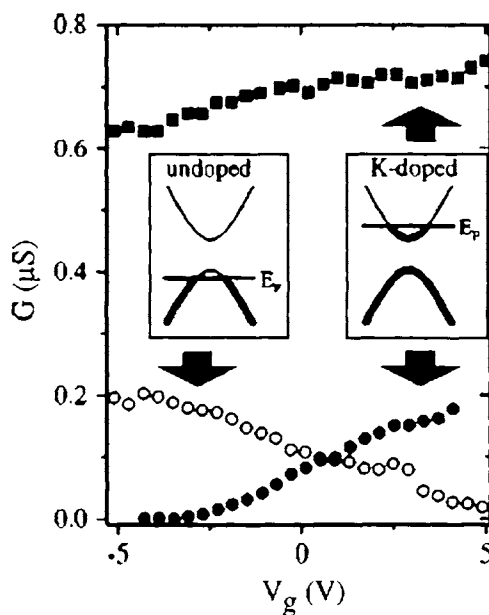


Figure 33. Conductance as a function of gate voltage for an SWNT rope that is undoped (open circles), potassium-doped (filled squares), and potassium-doped after a cycle of deintercalation and reintercalation at a lower doping level. From Ref. [227]. Reprinted with permission from R. E. Smalley and the American Physical Society. Copyright (1999) the American Physical Society.

SWNTs that are a mixture of carbon and boron nitride have been produced [232,233] that have properties that are intermediate [234,235] between those of CNTs and boron nitride [236–240] nanotubes. One of the unique properties of boron nitride nanotubes is the independence of their electronic structure to changes in the diameter or chirality of the tube. In the case of doped carbon SWNTs, adding even a small percentage of boron or nitrogen dopants can affect the electronic structure of the tube. For example, calculations predicted that less than 0.5% of boron or nitrogen dopants can significantly modify electronic transport in an SWNT [241]. In addition, experiments indicated that SWNTs doped with boron and potassium have substantially lower resistivity than undoped SWNTs at room temperature [242].

These doped SWNT systems are being explored for use in electronic devices but face unique challenges. For example, calculations [243] indicate that in p–n junctions created with a single SWNT through selective doping, the depletion length varies exponentially with inverse doping. As a result, at low doping densities the depletion length can extend for micrometers, while, at high doping densities, the depletion length is short enough to effectively short-circuit the junction. One interesting application reported recently uses a zigzag SNWT doped with nitrogen on one side and phosphorous on the other. This system was shown to have non-linear rectifying behavior and therefore might function as a nanometer-scale diode [241].

Doped MWNTs were also shown to have unique properties. For instance, when pure MWNTs were compared with boron-doped MWNTs [244], it was found that both systems are p-type semiconductors. However, the boron-doped tubes had reduced resistivities relative to the pure tubes ( $7.4 \times 10^{-7} - 7.7 \times 10^{-6} \Omega\text{m}$  for the boron-doped system,  $5.3 \times 10^{-6} - 1.9 \times 10^{-5} \Omega\text{m}$  for the pure system, both at room temperature) [244]. Another study of boron-doped MWNTs [245] found that substitutional boron-doping lowers the Fermi energy and increases the conductivity of the MWNTs without increasing scattering.

### **3.1.4. Effects of chemical functionalization on the electronic properties of carbon nanotubes**

The chemical modification of CNTs has been extensively explored for several reasons, including nanotube solubilization in solvents and the engineering of nanotube–polymer interfaces in composites [246]. Studies show that chemically modifying nanotube walls can alter their electronic properties. For example, calculations predict the covalent attachment of hydrocarbons to metallic zigzag SWNTs opens a band gap near the Fermi energy [247]. Similarly, the attachment of fluorocarbons to semiconducting SWNTs alters the nanotube's band gap [248]. In another example, the functionalization of semiconducting SWNTs with fluorine was predicted to yield several different structures that, while close to one another in energy, behave as metals, semiconductors, or insulators, depending on the atomic arrangement of the functionalized structure [248].

Currently, much effort is being focused on experimentally producing SWNTs with uniform electrical properties (i.e., metallic or semiconducting). While no group has been successful to date at synthesizing nanotubes with uniform chiralities, recently

there has been success in separating metallic and semiconducting SWNT from heterogeneous mixture of nanotubes [249,250] using selective, non-covalent chemical functionalization techniques.

### 3.2. Carbon nanotube junctions

#### 3.2.1. With other carbon nanotubes

One goal of researchers working to build nanometer-scale electronic devices is to be able to use as building blocks not individual SWNTs, but a series of either metallic or semiconducting SWNTs that are connected to one another at seamless junctions. In this way, for example, nanometer-scale transistors could be constructed by connecting a metallic SWNT to each end of a semiconducting SWNT.

The electronic properties of two-nanotube junctions were investigated in calculations by several groups [219,223,224]. The results indicate that the junctions possess resonant tunneling conduction properties and effectively function as nanometer-scale electronic devices.

AFM tips were usually used to manipulate nanotubes to create junctions from buckled or crossed CNTs and investigate the electronic transport properties of individual SWNT connected to metallic electrodes [251]. This work clearly showed that it is possible to artificially produce nanotube junctions that behave as electronic tunnel junctions. The conductance of crossed nanotubes shows power-law behavior as a function of bias voltage and temperature, as illustrated in Fig. 34, which can be modeled by as a Luttinger liquid to describe tunneling between nanotube segments separated by the proximal probe induced junction. In Ref. [252], calculations indicated that the inter-tube conductance of crossed CNT junctions depends on the overall deformation of the junction. At medium contact forces, greater inter-tube conductance was predicted at smaller contact distances.

An example junction system is shown in Fig. 35 between two SWNTs with different chiralities [219]. Heptagons and pentagons are formed at the junction and are indicated by large gray spheres in Fig. 35. Figs. 36a and b shows the predicted density of states (DOS) for the system starting at the junction and moving away down each SWNT. The data indicates that the junction has a more significant effect on the semiconducting SWNT, with electronic states appearing in its gap region. In the case of the metallic SWNT, the primary effect of the junction is the smearing of some Van Hove singularities [219]. The effects of the junction diminish rapidly as one moves away from the junction in either direction. Experiments [253] indicated that metal SWNTs and semiconductor SWNTs form electronically sharp junctions without localization, while metal SWNT-metal SWNT junctions have a more diffuse interface with low energy states. Additional experiments [254] found that there are discrete drops in conduction across CNT networks that are attributed to metal-semiconducting CNT junctions.

Menon and Srivastava [255,256] considered the electronic properties of more complex structures, such as Y- and T-junctions, two of which are illustrated in Fig. 37. The calculated DOS of the T-junction presented in Fig. 37 are shown in Fig. 38. The calculations predicted that the presence of structural defects at the neck region between the SWNTs (heptagons in this case) cause the appearance of

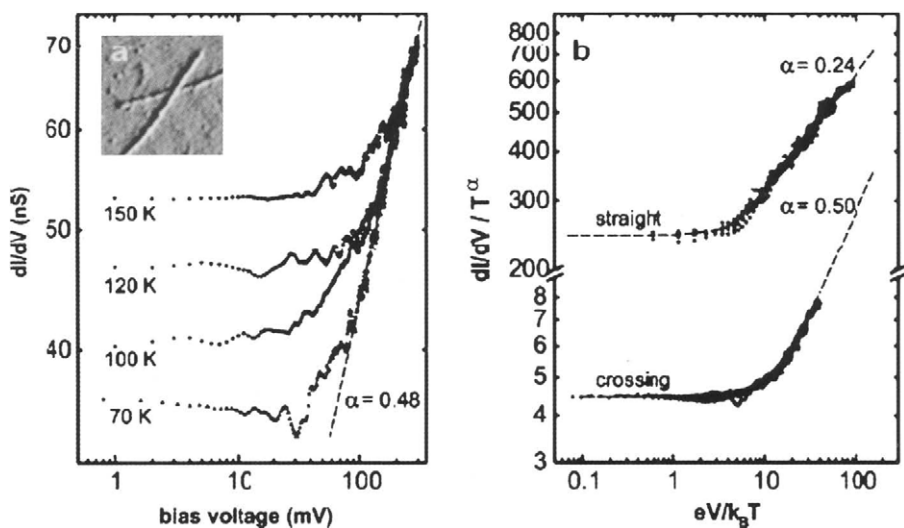


Figure 34. Measured differential conductance of crossed CNTs as a function of applied voltage at several temperatures. In this case, the Coulomb blockade effect suppresses the conductance below 70 K. The inset of (a) shows an AFM image of the crossing. (b) A scaled plot of  $dI/dV$  as a function of  $eV/k_B T$  for a crossed segment and for a straight segment of the CNT. From Ref. [251]. Reprinted with permission from C. Dekker and the American Physical Society. Copyright (2000) the American Physical Society.

localized states in the gap of the semiconducting SWNT that may act to pin the system Fermi level. Similar results were found for the Y-junctions considered by these authors.

The rectifying behavior of Y-junctions were also considered [257–259], where the ends of all three SWNTs were assumed to be in contact with nickel electrodes. The calculated current as a function of applied voltage for one of these systems is shown in Fig. 39, which indicates that this Y-junction acts as a rectifying device. In other words, current flows when the applied voltage is negative, but does not flow for positive applied voltages. Subsequent calculations [260] indicated that the rectifying behavior of Y-junctions is not intrinsic to the junction, but is due to the interface between the CNT branches and the metallic leads as a result of scattering by the interfacial states. These states are closely related to the Schottky barrier at metal–CNT contacts and depend to a large degree on the geometry of the contact. Similar findings are expected for other, non-symmetric Y- and T-junctions. Experimental measurement of room temperature electrical conduction through Y-junctions of SWNTs produced in nanoporous templates [261] or through pyrolysis [262] exhibits the same rectifying behavior calculated in Refs. [257–259].

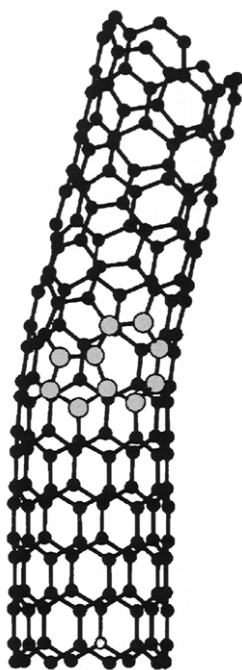


Figure 35. A junction between an (8,0) SWNT and a (7,1) SWNT. The large gray spheres serve to emphasize the Stone-Wales type defect at the junction. From Ref. [219]. Reprinted with permission from M. L. Cohen and the American Physical Society. Copyright (1996) the American Physical Society.

MD simulations [263,264] revealed the likely mechanisms by which electron irradiation welds together nanotubes to form junctions. In particular, defects were predicted to form in the SWNT walls that cause the damaged tubes to weld together. Predicted electronic properties of X-shaped nanotube junctions produced through electron irradiation in these simulations [264,265] are significantly different from the properties of ideal junctions or of crossed SWNTs with covalent attachments. The top part of Fig. 40 shows that the irradiated junctions are significantly more disordered than the ideal junctions illustrated in Fig. 37. This disorder leads to the localization of electronic states indicated in the bottom part of Fig. 40, which effectively makes the irradiated SWNT junctions into quantum dots. Covalent bonds are predicted to form between crossed SWNTs [266] under compression, especially in the presence of wall defects and dopants. In the case of crossed SWNTs, the contact resistance between the tubes depends on the structure of the contact [267]. In particular, optimal electronic transport occurs when the tubes are in atomic-scale registry.

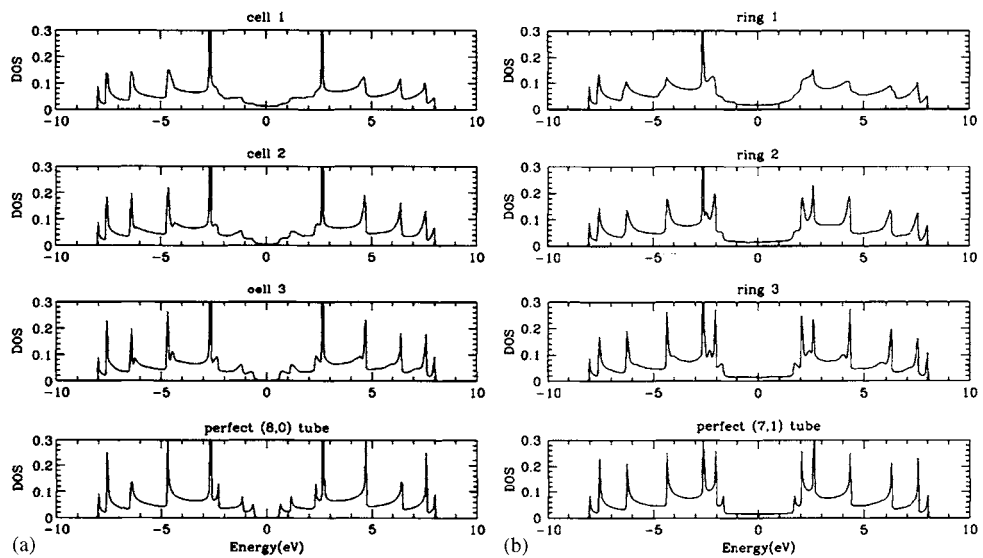


Figure 36. Calculated local DOS plots for the system shown in Fig. 35. (a) The local DOS of (8,0) SWNT as one moves away from the junction and for a pristine (8,0) SWNT. (b) The local DOS of the (7,1) SWNT as one moves away from the junction and for a pristine (7,1) SWNT. In both cases, cell 1 is closest to the junction. From Ref. [219]. Reprinted with permission from M. L. Cohen and the American Physical Society. Copyright (1996) the American Physical Society.

### 3.2.2. With metal contacts

Most electronic devices that are created with CNTs involve carbon–metal interactions, as illustrated in Fig. 27 [196]. For this reason, it is important to fully understand the effect of nanotube–metal interactions on the conductivity of CNTs. Calculations [268] indicate that within an idealized calculation, an armchair SWNT and a free-electron metal in contact with one another have a very high contact resistance. The calculations also indicate several methods by which this contact resistance can be reduced, including using a metal with a high Fermi wave vector, using a zigzag SWNT rather than an armchair SWNT at the contact point, and inducing electron scattering in the nanotube [268]. Experimentally, control of the contact can be achieved by, e.g., burying the CNT ends under metal contact pads [269].

The transistor behavior of SWNT FETs was explained as being due to a Schottky barrier across the metal–SWNT contact [270]. The gate produces an electric field at the contact and this field controls both the width of the barrier and the current flow. Changes in the work function at the contact through such processes as gas adsorption can affect the Schottky barrier as will be discussed in more detail in Sec. 5.2.

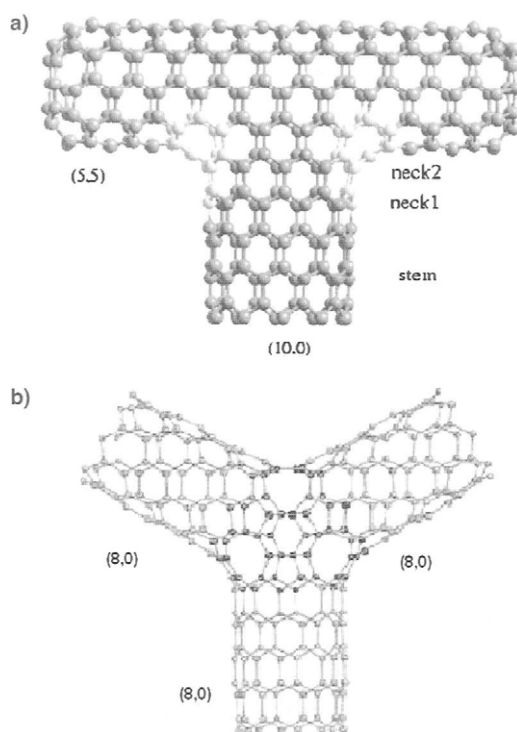


Figure 37. (a) T-junction made up of (5,5)–(10,0)–(5,5) SWNTs. From Ref. [255]. Reprinted with permission from D. Srivastava and the American Physical Society. Copyright (1997) the American Physical Society. (b) Y-junction made up of three (8,0) SWNTs. From Ref. [256]. Reprinted with permission from D. Srivastava and the Materials Research Society. M. Menon and D. Srivastava: Carbon nanotube based molecular electronic devices, *J. Mater. Res.* **13** (9), 2357 (1998). In both figures the lighter atoms denote atoms making up the heptagon–pentagon pairs.

*Ab initio* calculations [271] indicated that the contact between semiconducting SWNTs and metal electrodes depends on the type of metal used in the electrode. For example, a semiconducting SWNT is only weakly bound to gold. Consequently, there is little charge rearrangement and a finite barrier forms at the contact. On the other hand, semiconducting SWNTs interact strongly with molybdenum and this leads to substantial charge transfer across the contact; the subsequent deformation of the SWNT lowers the barrier at the contact. Furthermore, when wide-diameter semiconducting SWNTs are in contact with palladium, the Schottky barrier at the metal–CNT contact is greatly reduced or eliminated [272]. This is thought to be due to the fact that the palladium is a noble metal with a high work function that readily wets the SWNT. Consequently, ballistic CNT FETs with zero Schottky barriers can be produced.



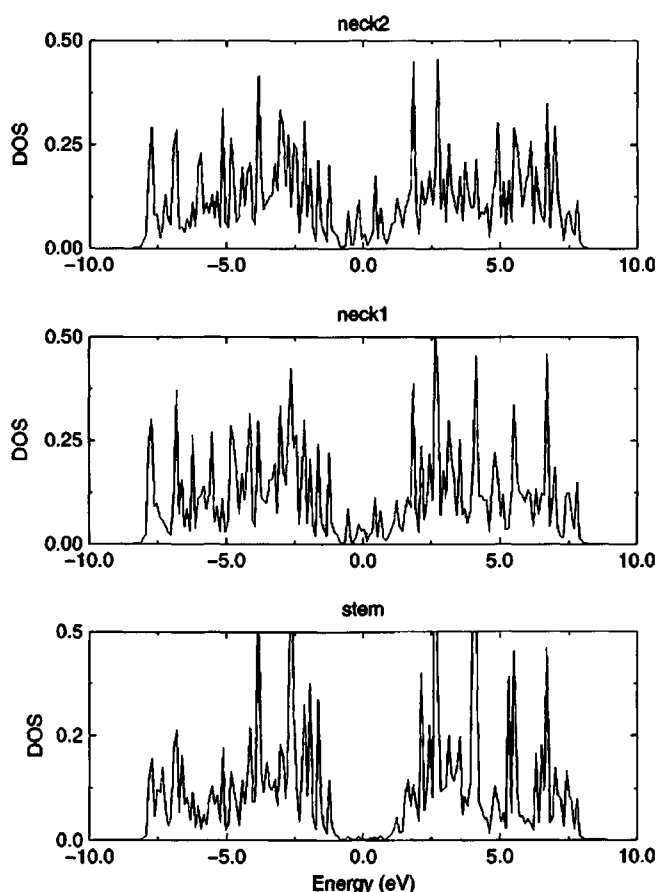


Figure 38. The calculated local DOS plots at different points on the T-junction shown in Fig. 38(a). Defect induced gap states move from the “stem” to the “neck.” From Ref. [256]. Reprinted with permission from D. Srivastava and the American Physical Society. Copyright (1997) the American Physical Society.

Tight-binding calculations [273,274] indicated that the transport properties of metal–semiconducting SWNT interfaces depends strongly on the metal work function and much less strongly on the details of the interface. A subsequent experimental study [275] found that gold also makes a good contact with the p-type region of a semiconducting SWNT with no Schottky barrier; in contrast, a large contact resistance was found with the n-type region of the semiconducting SWNT. However, *ab initio* calculations [276] predicted that gold, platinum, and palladium all form Schottky barriers when in contact with a small-diameter, zigzag semiconducting SWNT, but the height of the barrier depends on the type of metal and its

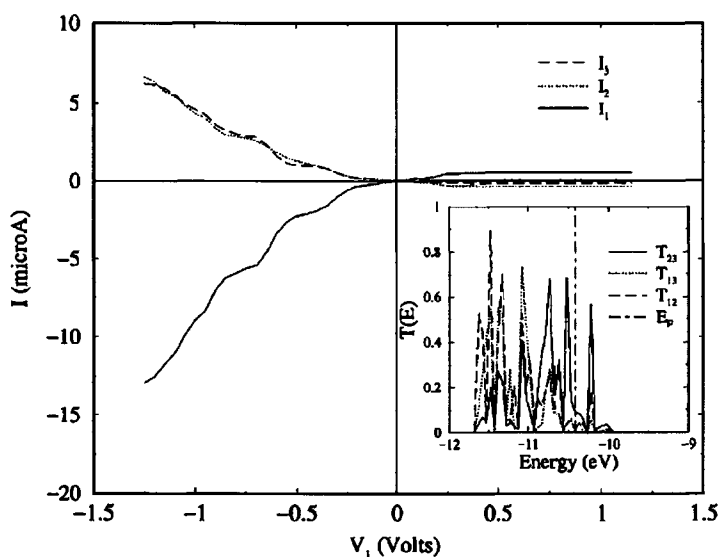


Figure 39. The predicted rectifying behavior of a Y-junction consisting of a (14,0) CNT branching into two (7,0) CNTs. Figure printed from Ref. [258]. Reprinted with permission from D. Srivastava and the American Physical Society. Copyright (2001) by the American Physical Society.

surface orientation relative to the SWNT. Importantly, palladium was predicted to have the lowest barrier. The chirality of the nanotube might be an important factor in these measurements. For instance, metallic zigzag SWNTs were shown to have better total electron transmission when in contact with gold electrodes than metallic armchair SWNTs [277].

In the case of metal contacts with short SWNTs [278], the shape of the potential barrier was found to depend on the long-range tail of the charge transfer. This leads to an injection barrier thickness that is equal to half of the SWNT length for short nanotubes. The conductance of the junction transitions from tunneling to a thermally activated process as the CNT length increases [278]. Experiments [279] indicated that as the temperature increases, transport at a semiconducting SWNT/metal contact changes from tunneling through a reverse biased metal-tube junction to a thermal activated process. However, variation in the shape of the  $I/V$  curve for a semiconducting SWNT/metal contact was explained by a change from thermal-activation to tunneling behavior across the junction [280].

Recently, CNT FETs were created using ohmic metal (palladium)-tube contacts and high dielectric constant hafnium oxide gate insulators [281]. The electrostatically doped CNTs acted as sources and drain electrodes. These FETs have high “on” currents and low “off” currents. Importantly, ambipolar conduction is suppressed in these devices.

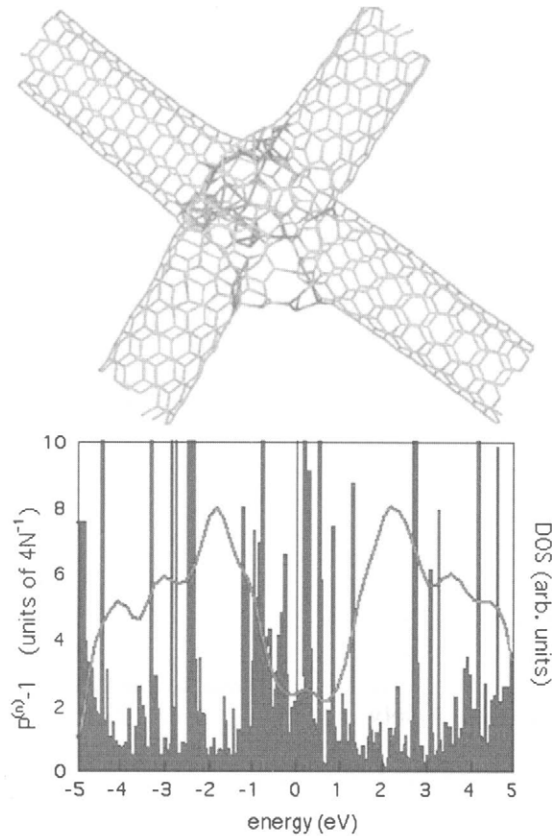


Figure 40. Top: X-junction formed in MD simulations of the electron-beam irradiation of two crossed (5,5) SWNTs. Bottom: DOS (curve) and eigenvalue participation ratio (histogram) around the Fermi energy, which is shifted at  $E=0$ . From Ref. [265]. Reprinted with permission from S. B. Sinnott and the American Physical Society. Copyright (2004) the American Physical Society.

### 3.3. Relationship between electronic and mechanical properties of carbon nanotubes

Electromechanical changes can occur in CNT systems when mechanical deformation results in a change in the tubes electronic properties, or vice versa, when changes to the CNTs' electronic structure result in mechanical deformation.

In the case of the effect of mechanical deformation on the electrical properties of nanotubes, the first kind of deformation that will be considered is radial compression. As discussed in Sec. 2.1.1, nanotubes are much less stiff in the radial direction than in the axial direction. This is especially true of SWNTs and MWNTs with few shells (see, e.g., Fig. 3). When nanotubes are "squashed," the process has a profound influence

on their electronic properties. For example, when a semiconducting SWNT is radially deformed, calculations predicted that the band gap decreases and eventually disappears in the compressed region of the tube, but remains at its normal value in the uncompressed portions of the tube [282–285]. Therefore, it was hypothesized that selectively compressing portions of a long SWNT could lead to the production of self-contained quantum well structures within an individual SWNT [283,285]. In the case of radially deformed metallic SWNTs, calculations [286] predicted that the electronic structure of  $(n,n)$  and  $(3n,0)$  SWNTs is more sensitive to radial deformation than SWNTs with other chiralities because of the presence of degenerate low-energy electronic states in these systems. In particular, a metal-to-semiconductor transition was predicted to occur as a result of the breaking of symmetry and/or the formation of bonds across the flattened faces [282,287]. Calculations [288] indicated, however, that at least in the case of deformed armchair SWNTs, metal–semiconductor–metal transitions only occur when the deformed length is greater than or equal to a critical value. Smaller deformed lengths do not exhibit clear transitions as a result of quantum tunneling. Experimental data indicated that the electronic properties of suspended SWNTs are not the same as the properties of SWNTs in a bundle or on a substrate [289,290]. This is because the interactions between the substrate and the SWNT lead to radial deformation of the SWNT.

As discussed in Sec. 2, CNTs may be deformed in a variety of ways besides “squashing”. Tight-binding calculations and simulations indicated that the electronic structures of deformed SWNTs varies considerably depending on the chirality of the tubes and the deformation mode, which can include stretching, compression, torsion, and bending [61,247,291–294], as summarized in Fig. 41. Interestingly, the calculations indicated that the effects of stretching and compression on the DOS can be ignored when the effects of strain are averaged over the SWNT circumference and effectively cancel each other. The calculations further predicted that under uniaxial and torsional strain, the magnitude of the slope of the band gap as a function of strain has an almost universal behavior that depends to a substantial degree on the chiral angle of the SWNT. Changes in band gap versus strain were predicted to be smallest for armchair tubes, largest for zigzag tubes, and to decrease as the chiral angle increases. Experimentally, the electronic properties of suspended SWNTs under tensile stretching were measured [295]. The results indicate that small band-gap semiconducting SWNTs that are quasi-metallic prior to deformation exhibit the largest resistance changes when under strain. In fact, the experimental data suggests that these SWNTs have piezoelectric gauge factors of about 600–1000, which is substantially greater than the gauge factor of about 200 for doped silicon [295,296]. In contrast, the electronic properties of metallic SWNTs are shown to have a weaker (but non-zero) sensitivity to strain.

The band structure of nanotubes also changes when they are in tension [297], as shown in Fig. 42. In this study, the AFM applied strain to the CNT and at the same time gated the system. The applied strain opened a band gap in metallic SWNTs and modified the band gap of semiconducting SWNTs. The measured values are consistent

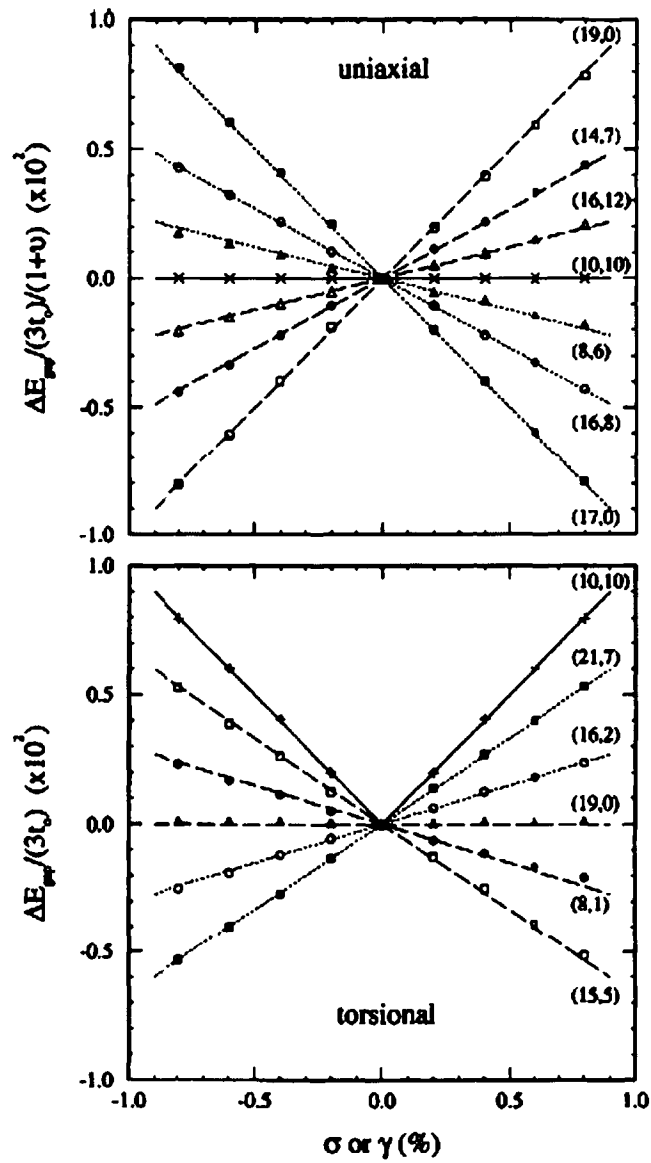


Figure 41. Predicted band gap change of SWNTs with diameters of 0.8–2.0 nm under uniaxial strain (defined to be  $>0$  for tension and  $<0$  for compression) and torsional strain (defined to be  $>0$  for net bond stretching and  $<0$  for net bond compression). The lines are from theory and the symbols are from simulations. From Ref. [293]. Reprinted with permission from J. Han and the American Physical Society. Copyright (2000) the American Physical Society.

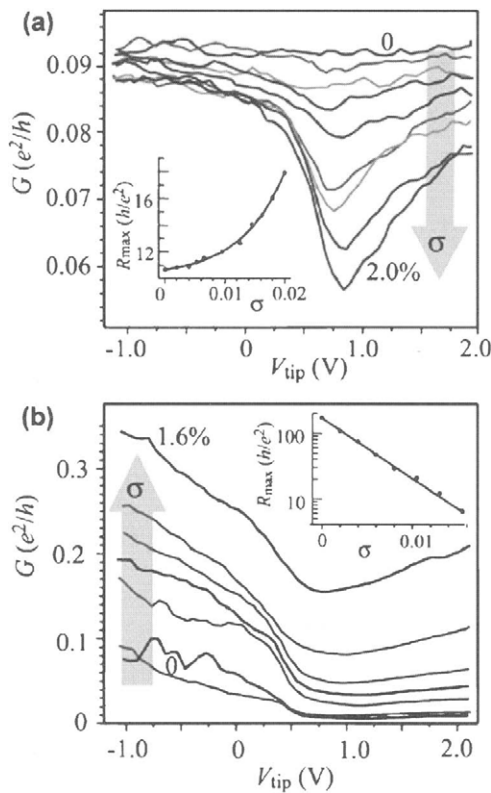


Figure 42.  $G$  is conductance and  $V_{\text{tip}}$  is the voltage on the AFM tip that is straining the SWNT. (a) Metallic SWNT with diameter  $3 \pm 0.5$  nm and length of  $1.4 \pm 0.1$   $\mu\text{m}$ . Strain is 0, 0.5, 0.7, 1.0, 1.2, 1.4, 1.6, 1.8, and 2.0%. (b) Semiconducting SWNT with diameter  $4 \pm 0.5$  nm and length of  $1.1 \pm 0.1$   $\mu\text{m}$ . Strain is 0, 0.2, 0.6, 0.8, 1.1, 1.3, and 1.6%. The closed circles in the insets show maximum device resistance as a function of strain; solid lines in the insets show fit curves. From Ref. [297]. Reprinted with permission from P. L. McEuen and the American Physical Society. Copyright (2003) the American Physical Society.

with the theoretical prediction of band gap changes of  $\pm 100$  meV per 1% stretch (depending on the chirality of the SWNT).

Changes in the electronic properties of bent CNTs are measured experimentally by draping the nanotube across a trench and indenting it with an AFM tip. When such a study was carried out on MWNTs [298] the resistance was found to remain unchanged within the signal-to-noise ratio until the lateral force increased to a critical value, beyond which the force abruptly drops. This is an indication of failure of the nanotube, either by plastic deformation or brittle fracture. At this point, the

resistance sharply increased to 143 k $\Omega$ . Similar findings were obtained when suspended SWNTs were deflected with an AFM tip [107]. In particular, the conductivity of SWNTs is reduced by two orders of magnitude when they are deformed but, when the applied stresses are relieved, the conductivity is the same as for the unstressed SWNTs.

The reduction of conductivity was explained [107,108] as arising from the reversible formation of covalent bonds across the buckle point of the bent tube. Additionally, *ab initio* calculations [299] predicted that bending a semiconducting SWNT causes the formation of a four-member carbon ring at the sharpest point of the kink with strong  $sp^3$  character. Localized electron states were found at the bend that decreases the resistivity [299]. However, subsequent *ab initio* calculations [109] predicted that SWNTs remain  $sp^2$ -hybridized coordinated when bent by an AFM tip. The calculations further indicated that armchair SWNTs should have no significant drop in conductivity when bent, but that zigzag tubes should experience a drop in conductivity of several orders of magnitude. In the latter case, this drop in conductivity was predicted to be due to stretching of the carbon-carbon bonds in the tip at the buckle site rather than to the reversible formation of  $sp^3$ -coordinated carbon atoms at the buckle site. Other studies indicate that zigzag tubes are stiffer than armchair tubes of the same diameters such that, at the same bias, current in the metallic tubes decreases with increased bending, while current in the semiconducting tubes increases [300]. As illustrated in Fig. 43. Some of the differences in these findings could be due to differences in the bent nanotube geometry being probed. The structures shown in Fig. 43a are not necessarily representative of the structures that form during AFM tip indentation of a suspended nanotube.

In any case, all studies agree that bending SWNTs leads to scattering of conduction electrons and electron localization [301,302]. In addition, it was predicted that metallic armchair SWNTs develop a band gap that initially scales linearly with twist angle and then reaches a constant value because of structural transition to a flattened helical structure.

When the many-channel Landauer formalism was used to describe the electron transport in bent nanotubes and nanotubes with vacancies [303], the current was predicted to increase in a stepwise manner with the applied voltage. Moderate bending of the nanotube was predicted to shift the single-particle levels without affecting overall current. For large bending, the  $\pi$  electron system becomes more disturbed, which yields a large decrease in tube conductivity, as shown in Fig. 44. In addition, a single carbon vacancy in the nanotube was predicted to have very little effect on the metallic conductivity, while large vacancy concentrations greatly decrease the conductivity.

In the case of strained MWNTs [304] small elastic strains were found to cause no change to their electronic properties. Under large strain, MWNTs experienced drastic electronic heterogeneity, which was explained [304] as being due to relaxation of the outermost layer of the tube. Changes in the electrical conductivity of strained MWNTs is found to be reversible within the elastic limit, but irreversible after plasticity or the formation of lattice defects [305]. When MWNTs fail by the sword-and-sheath

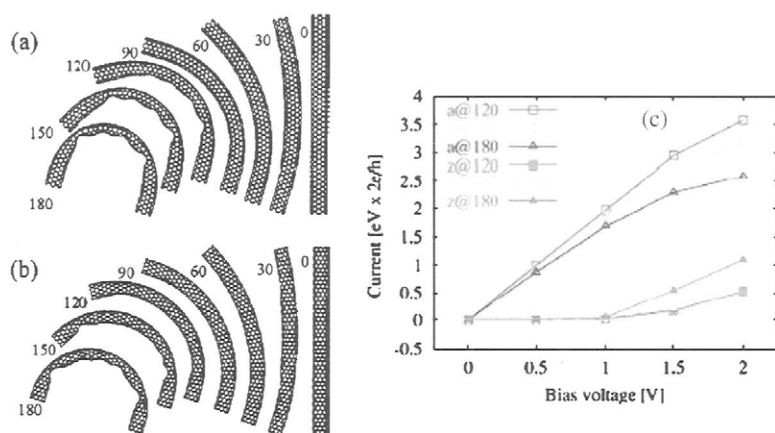


Figure 43. (a) Relaxed configurations of a (6,6) armchair and (b) (10,0) zigzag SWNTs at different bending angles. (c) Predicted  $I/V$  curve of (6,6) and (10,0) tubes at different bending angles. From Ref. [300]. Reprinted with permission from Y. Kawazoe and the American Physical Society. Copyright (2003) the American Physical Society.

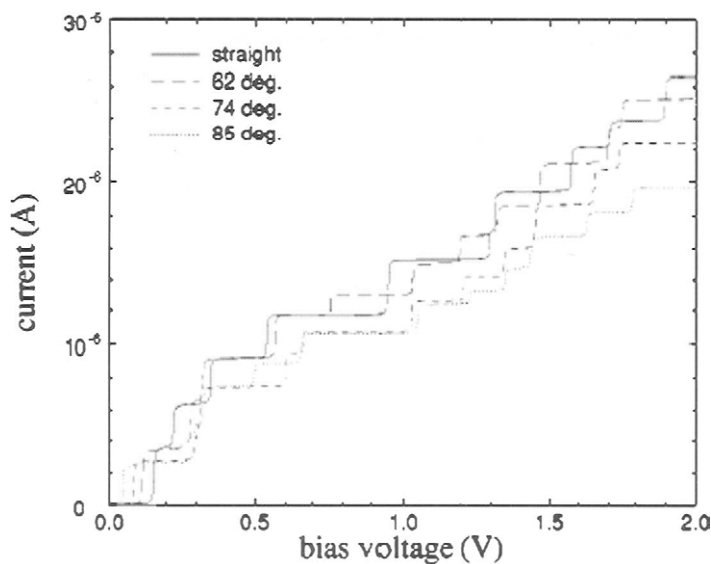


Figure 44. Measured  $I-V$  curves of CNTs that are straight (solid line), bent at an angle of  $62^\circ$  (long dashed lines), bent at an angle of  $74^\circ$  (dashed line), and bent at an angle of  $85^\circ$  (dotted line). From Ref. [303]. Reprinted with permission from S. Stafstrom and the American Physical Society. Copyright (2000) the American Physical Society.



mechanism discussed in Sec. 2.1.2, the “telescoping” of the shells affects electronic properties of the system in a manner that depends on the chirality of the CNTs [306].

The mechanical properties of nanotubes can also be changed by altering their electronic structure. A theoretical study of doubly clamped and suspended SWNTs found that the capacitance between the SWNT and the gate depended on the distance between them [307]. Interestingly, the position of the tube changes in a discrete manner each time an electron tunnels into it. This could be related to the fact that, as charge is injected into SWNTs [308], the carbon–carbon bond lengths in the SWNTs change. At low-level charge injection levels, the SWNTs deform in an anisotropic manner that depends on the nanotube structure. In particular, SWNTs expand on electron injection [309], but respond differently to hole injection, depending on their structure. For example, hole injection causes metallic SWNTs to display non-monotonic behavior as the lattice constant contracts, then expand as the hole density increases [309]. In contrast, semiconducting SWNTs with diameters  $\leq 2.0$  nm always expand in response to hole injection, while semiconducting SWNTs with diameters  $> 2.0$  nm display behavior that is intermediate between the behavior of metallic and large-gap CNTs [309].

When armchair and zigzag SWNTs were exposed to external electric fields [310], they experienced induced axial strains  $> 10\%$  for field strengths of around  $1 \text{ V/\AA}$ . Most impressively, volumetric and gravimetric work capacities were predicted to be three–six orders of magnitude higher than those of ferroelectrics, electrostrictive, magnetostrictive materials, and elastomers, respectively. An example of this response is the actuation behavior of SWNTs embedded in polymer in response to applied electric fields [311], as summarized in Fig. 45.

### 3.4. Carbon nanotube-based electronic devices

In addition to the approach for separating metallic and semiconducting SWNTs summarized in Sec. 3.1.4, another process for the isolation of SWNTs with uniform chiralities was developed by Avouris and co-workers [203,312] that is termed “constructive destruction”. In this technique, arrays of CNT FETS are fabricated from SWNT bundles without first separating metallic from semiconducting tubes. Then, a gate voltage is applied to the SWNT bundle that depletes all semiconducting SWNTs of their carriers. A source-drain bias is then applied that causes current to flow only through the metallic SWNTs. At appropriately high voltages, the metallic SWNTs break down and the semiconducting SWNTs remain intact. This process is illustrated in Fig. 46. Using a similar procedure, the shells in MWNTs can be selectively “peeled” to obtain CNTs with the desired electrical properties [203,312].

Much interest surrounds the use of nanotubes for electronic circuitry and devices [20,203,313–315]. These can consist primarily of individual nanotubes or nanotubes used in combination with conventional silicon-based electronic devices [316]. One of the first simple CNT electronic devices to be experimentally studied is shown in Fig. 27 [196]. By spin-coating a nanotube suspension onto a silicon/silica surface with 15 nm thick platinum electrodes, it was possible to bridge across two of the electrodes with a single SWNT and measure its electron transport properties. This experiment found that the SWNT acted as a molecular quantum wire. SWNTs were

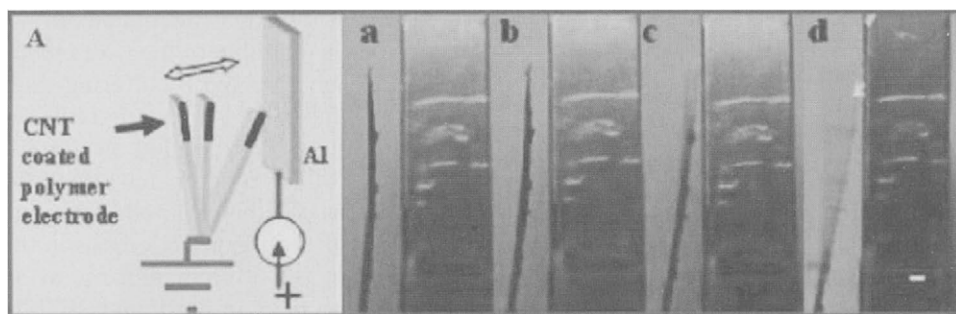


Figure 45. (A) Schematic of an SWNT-coated polymer strip under an applied external field as a micro-cantilever actuator. The strip was grounded with respect to a positive aluminum electrode. (a)–(d) is a sequence of experimental microscopy images taken as the external voltage increases from 0 V in (a) to 900 V in (d). By (d) the strip is vibrating at high frequency as it comes into contact with the counterelectrode. The scale is 1 mm. Reprinted with permission from P. M. Ajayan and American Scientific Publishers from [311]. N. Koratkar, A. Modi, J. Kim, B. Q. Wei, R. Vajtai, S. Talapatra and P. M. Ajayan, *J. Nanosci. Nanotech.* **4**, 69 (2004). Copyright (2004) American Scientific Publishers, <http://www.aspbs.com>.

subsequently examined for possible use as “nanowires” or molecular “power-lines”, as shown in Fig. 47 [199].

Molecular devices can also be formed from SWNT ropes. In one example [228], a ring superstructure that consisted of bundles of metallic and semiconducting SWNTs was used. Fig. 48 shows the ring structure (inset) as well as its transport properties as a function of temperature, bias voltage, and applied magnetic field. The rings were found to function as metals at low temperatures with some quantum interference effects. The resistance decreases with increasing temperature and this behavior is linear at low temperatures (4 K), as illustrated in Fig. 48b.

The electrical performance of crossed SWNTs was also explored as possible electrical gates for semiconductor devices or as quantum dots [317]. Fig. 49 shows the  $I/V$  characteristics for a metal–metal and a metal–semiconductor SWNT cross. The  $I/V$  characteristics of the metal–metal SWNT cross exhibit linear regions at  $|V| < 300$  mV and  $|V| > 400$  mV, with resistances of 600 and 400 k $\Omega$ , respectively. STM-induced gating of the two SWNTs in the metallic cross (Fig. 49a, inset) did not produce a change in conductance for tip-gate voltages up to 10 V, which confirms that both SWNTs are metallic. As metallic SWNTs resistances are typically in the range of 15–200 k $\Omega$ , the high resistance measured for this set of crossed SWNTs is most likely due to contact resistance. The  $I/V$  characteristics of a comparable metal–semiconductor SWNT cross exhibits diminished conductance as backgate voltage is increased from 0 to 8 V, and thus functions as a FET. STM-induced gating of the metallic SWNT had no effect on the conductance of the cross system (see Fig. 49b, upper inset), but gating of

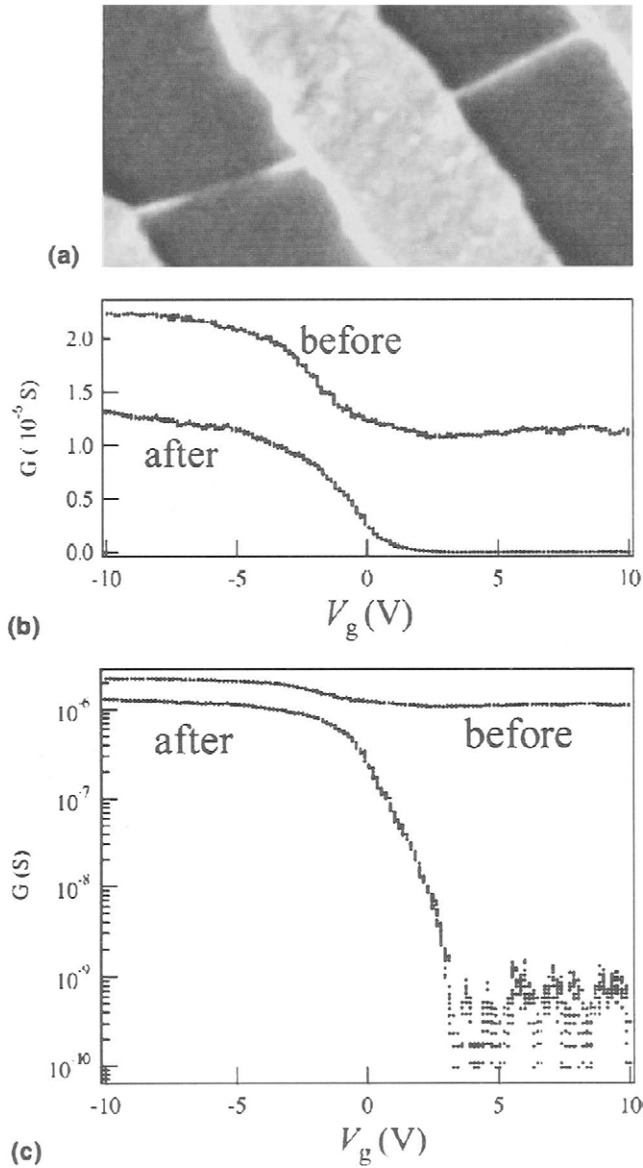


Figure 46. (a) AFM image of an SWNT bundle before and after thinning by selective breakdown of the metallic tubes as described in the text. (b) The conductance of the bundle before and after thinning. (c) The conductance of the bundle before and after thinning plotted on a log scale. From Ref. [203]. Reprinted with permission from Ph. Avouris, IBM Research, and Elsevier Science.

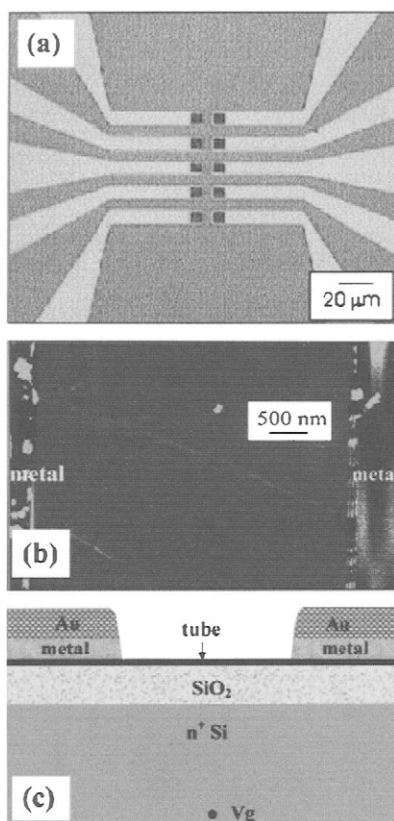


Figure 47. (a) Optical image of SWNT integrated circuits. (b) AFM image of an individual SWNT device. (c) Schematic view of the device structure. From Ref. [199]. Reprinted with permission from L. Dai, Stanford University, and the American Chemical Society. Copyright (1999) the American Chemical Society.

the semiconducting SWNT exhibited periodic oscillations under a tip voltage of 10 V (see Fig. 49b, lower inset) [317]. Additional studies (see, e.g., [318]) have similarly explored the production of FETs from individual SWNTs.

A more complex, integrated circuit along the length of an individual CNT was produced that functions as an intramolecular logic circuit [203], as illustrated in Fig. 50. Potassium was used to dope half of the CNT through the window created in the polymer coating over the SWNT bundle in contact with gold electrodes. The potassium doping produced an n-type CNT FET while the half protected by the polymer was p-type. The gain of the device shown in Fig. 50 is about 1.6 and it is shown to depend on the characteristics of the CNTs. Improvements in gain might be achieved through better contacts and reduced gate oxide thicknesses.

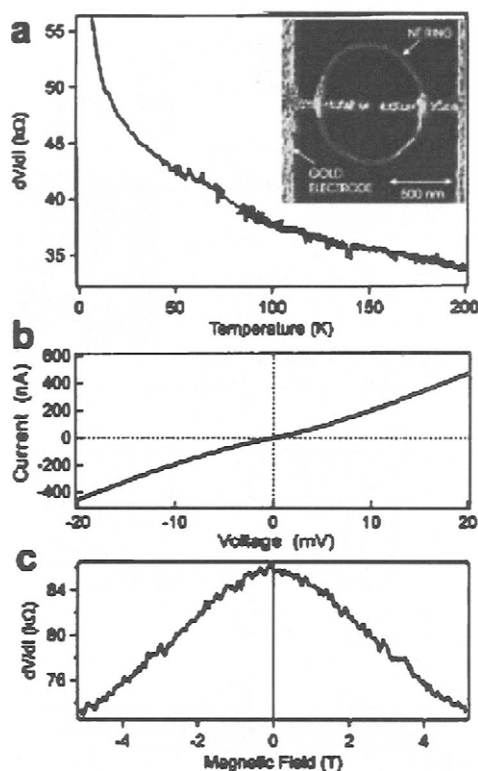


Figure 48. (a) Resistance as a function of temperature for an SWNT ring. The inset is an AFM image of the SWNT ring on top of gold electrodes. The diameter of the ring is  $0.82 \mu\text{m}$ . (b)  $I/V$  curve across the ring at 4 K. (c) Differential resistance of the nanotube ring as a function of the magnetic field applied perpendicular to the plane of the ring. From Ref. [228]. Reprinted with permission from Ph. Avouris, IBM Research, and the American Chemical Society. Copyright (1999) the American Chemical Society.

#### 4. THERMAL PROPERTIES OF CARBON NANOTUBES

The thermal properties of CNTs display a wide range of behavior which stems from their relation to  $\text{sp}^2$  bonded two-dimensional (2D) graphite sheets and their unique structure and small size. We review here the current status of knowledge about the specific heat, thermal conductivity, thermal expansion, and thermopower of CNTs.

##### 4.1. Specific heat

While the specific heat  $C$  consists of contributions from phonons,  $C_{\text{ph}}$ , and electrons,  $C_{\text{e}}$ ,  $C = C_{\text{ph}} + C_{\text{e}}$ , for CNTs the phonon contribution,  $C_{\text{ph}}$ , is dominant, as in

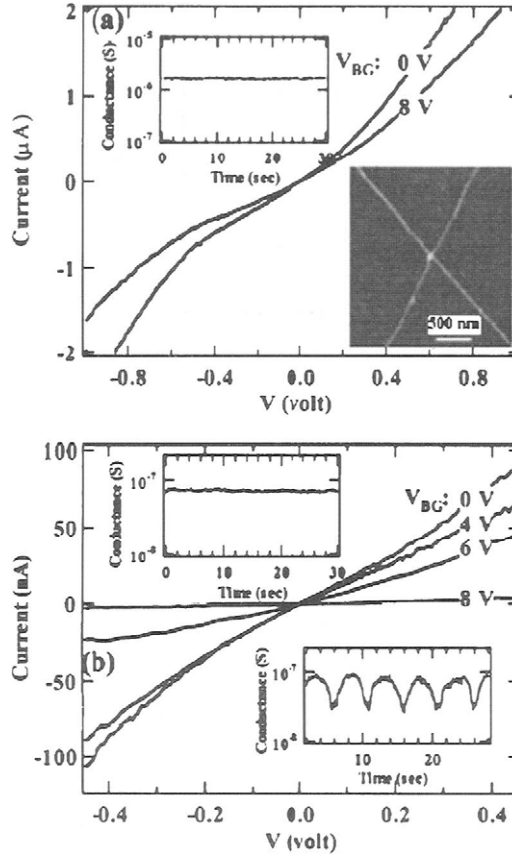


Figure 49. (a) Measured  $I/V$  curves of crossed metal/metal SWNTs. The left inset is a scanning-probe gating result on one of the SWNTs. The right inset is the AFM image of the cross. (b) Measured  $I/V$  curves of crossed metal-semiconductor SWNTs. The right and left insets are scanning-probe gating results of the metallic SWNT and the semiconducting SWNT, respectively. From Ref. [317]. Used with permission from H. Dai, Stanford University, and the American Institute of Physics.

graphite.  $C_{\text{ph}}$  is obtained by integrating over the phonon density of states with a factor that reflects the energy and occupation of each phonon state [319]:

$$C_{\text{ph}} = \int_0^{\omega_{\text{max}}} k_B \left( \frac{\hbar\omega}{k_B T} \right)^2 = \frac{e^{\hbar\omega/k_B T} \rho(\omega) d\omega}{(e^{\hbar\omega/k_B T} - 1)^2}, \quad (3)$$

where  $\rho(\omega)$  is the phonon density of states and  $\omega_{\text{max}}$  the highest phonon energy of the material and is related to the Debye temperature ( $\Theta_D$ ), which is defined as the

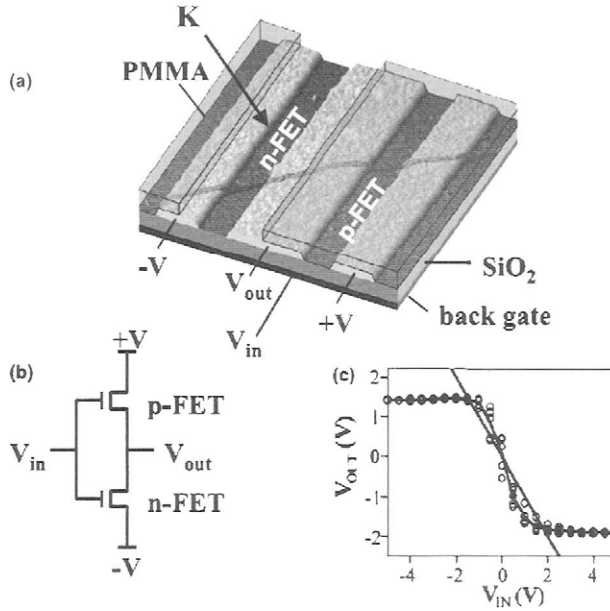


Figure 50. (a) AFM image showing the design of an intramolecular logic gate. An SWNT bundle is positioned over the gold electrodes to produce two p-type CNT FETs in series. Polymer (polymethyl-methacrylate) resist is then deposited on top and a window is opened by electron-beam lithography to expose part of the tube. (b) Schematic of the inverter. (c) Electrical characteristics of the intramolecular voltage inverter. Open circles are raw data for five individual measurements on the same device (voltage of  $\pm 2$  V) and the solid line is the average of these measurements. The thin straight line is the output/gain of one measurement. From Ref. [202]. Reprinted with permission from Ph. Avouris and Elsevier Science.

temperature of a crystal's highest normal mode of vibration. At low temperature ( $T \ll \Theta_D$ ),  $\omega_{\max} \rightarrow \infty$  and if  $C_{ph}$  is dominated by a single acoustic mode, then for a 2D graphite [320],

$$C_{ph} = \frac{3Ak_B T^2}{2\pi\hbar^2 v^2} \times (7.212), \quad T \ll \Theta_D. \quad (4)$$

Hence, at low temperatures,  $C_{ph} \propto T^2$  for a 2D graphite system, where the factor 2 accounts for the dimensionality of the system.

At room temperature, when many of the phonon subbands of the nanotube are occupied, the specific heat is similar to that of a 2D graphite sheet. At low temperatures, however, both the quantized phonon structure and the stiffening of the acoustic modes cause the specific heat of a nanotube to differ from that of graphite.

In the low- $T$  regime, only the acoustic bands are populated, and thus the specific heat is expected to be that of a 1D system, showing a linear  $k$  dependence for the acoustic phonons  $\omega(k)$ . In this limit,  $T \ll \hbar v / k_B R$ , where  $R$  is the nanotube radius and the above equation can be evaluated analytically, yielding a linear  $T$  dependence for the specific heat [320]:

$$C_{\text{ph}} = \frac{3Lk_B^2 T}{\pi \hbar v} \times (3.292), \quad T \ll \frac{\hbar v}{k_B R}, \quad (5)$$

where  $L$  is the tube length and  $v$  the acoustic phonon velocity. Thus, at low temperature, we observe a heat capacity (mJ/gK) of 0.3 for a (10,10) SWNT, approximately 0 for a SWNT bundle and graphite, and 2–10 for a MWNT bundle. However, when  $T > 100$  K, a SWNT, SWNT bundle, or MWNT have heat capacities that are similar to the heat capacity of graphite, about 700 mJ/g K [321,322] with  $C_{\text{ph}} \propto T^2$  [320].

As discussed in Sec. 3, a metallic SWNT is a 1D metal with a non-zero density of states at the Fermi level. The electronic specific heat is linear in temperature [320]:

$$C_e = \frac{4\pi Lk_B^2 T}{3\hbar v_F}, \quad (6)$$

for  $T \ll \hbar v_F / k_B R$  where  $v_F$  is the Fermi velocity. The ratio between the phonon and the electron contributions to the specific heat is  $(C_{\text{ph}} / C_e) \approx (v_F / v) \approx 10^2$  [320], so that even for a metallic SWNT, phonons dominate the specific heat all the way down to  $T=0$ . The electronic specific heat of a semiconducting tube should vanish roughly exponentially as  $T \rightarrow 0$  [323].

#### 4.2. Thermal conductivity of carbon nanotubes

In CNTs, generally two physical mechanisms contribute to the thermal conduction: (i) electron–phonon interactions, which mainly depend on the electronic band structure and the electron scattering process, and (ii) phonon–phonon interactions, which depend on the vibrational modes of the lattice. For semiconductor CNTs at room temperature, phonon–phonon interactions dominate the overall thermal conductivity and electron–phonon interactions have only a small contribution due to the large band gap and low density of free charge carriers [324]. In graphite, the thermal conductivity is generally dominated by phonons, and limited by the small crystallite size within a sample. In solids, macroscopic thermal conductivity is defined by the Fourier law of heat flow:

$$\vec{J}_q = k \nabla T, \quad (7)$$

where  $k$  is the thermal conductivity tensor and  $\vec{J}_q$  the heat flux due to the temperature gradient. Since the dominant carriers of thermal energy are the low-frequency phonons, the thermal conductivity along the nanotube axis is determined by the kinetic theory as:

$$k = \frac{1}{3} \int C v \Lambda dq \quad (8)$$



where  $q$ ,  $C$ ,  $v$ , and  $\Lambda$  are the phonon wave vector, specific heat, group velocity, and the mean free path of a given phonon state, respectively, and the sum is over all phonon states. From the above equation we see that the thermal conductivity is most sensitive to the states with the highest band velocity and the largest mean free path. Since the thermal conductivity along the tube axis is at least two orders of magnitude larger than that normal to the tube axis, we would expect that the magnitude and temperature dependence of the thermal conductivity of an SWNT bundle or of an isolated MWNT should be close to those of their constituent tubes, though some inter-tube thermal conduction could occur.

#### 4.2.1. Variation with temperature: Experimental studies of SWNTs and MWNTs

Measurements were reported on the thermal conductivity of a SWNT bundle [325] and a MWNT [326]. For an SWNT bundle sample with a diameter range estimated to be 10–100 nm, thermal conduction measurements were made between 14.5 and 320 K with a peak observed at about 310 K [325], as shown in Fig. 51 (left).

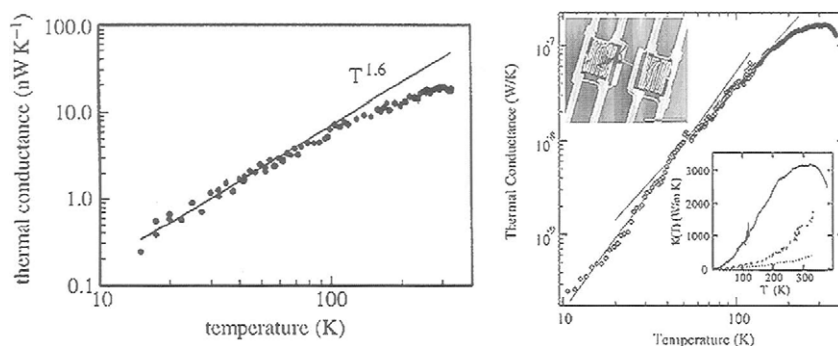


Figure 51. (Left) Measured temperature dependence of the thermal conductivity of a single bundle of SWNTs from 15 to 330 K plotted on a log–log plot. Reproduced from Refs. [319,325]. Figure 14b from M. S. Dresselhaus, G. Dresselhaus, J. C. Charlier and E. Hernandez, Electronic, thermal and mechanical properties of carbon nanotubes, *Phil. Trans. R. Soc. Lond. A* **362**, 2065–2098, (2004) the Royal Society. Reprinted with permission from M. Dresselhaus and the Royal Society. (Right) Measured temperature dependence of the thermal conductance of an individual MWNT of 14 nm in diameter. The solid lines represent linear fits of the data in a logarithmic scale at different temperature ranges. The slopes of the line fits are 2.50 and 2.01, respectively. Lower inset: Solid line represents  $\kappa(T)$  of an individual MWNT ( $d = 14\text{ nm}$ ). Broken and dotted lines represent small ( $d = 80\text{ nm}$ ) and large bundles ( $d = 200\text{ nm}$ ) of MWNTs, respectively. Upper inset: SEM image of the suspended islands within the individual MWNT. The scale bar is  $10\mu\text{m}$ . From [328]. Reprinted with permission from P. L. McEuen and the American Physical Society. Copyright (2001) the American Physical Society.

The functional form of  $\kappa(T)$  exhibits a  $T^{1.6}$  dependence, clearly lower than that for graphite (which exhibits a  $T^{2.3}$  dependence) [327]. The departure from a linear  $T$  dependence may be due to the coupling to optical phonons and to the tube–tube scattering/conduction processes. The peak at 310 K suggests that phonon–phonon scattering becomes important near room temperature for SWNT bundle samples, but this effect is much weaker than in graphite, possibly reflecting the much smaller number of available scattering states for a 1D system.

Measurements of  $\kappa(T)$  for an individual MWNT (14 nm diameter) show very high values of  $\kappa$  (over 3000 W/m/K) and a maximum in  $\kappa(T)$ , which is indicative of significant phonon–phonon scattering at high  $T$  [325]. The slope of  $\kappa(T)$  for the low- $T$  data is 2.0, indicative of a 2D system, while the corresponding slope of  $\kappa(T)$  at larger  $T$  (e.g., 77 K) is  $\sim 2.5$ , indicative of the many nanotube phonons that are activated in this  $T$  range, which is to be compared with a slope of 2.3 for graphite.

#### 4.2.2. Variation with temperature: Molecular dynamics simulations

Since the phonon–phonon contribution to thermal conduction is much more dominant than the electron–phonon interaction, thermal conductivity can be studied by classical MD simulations as well. Three main approaches have been used in the literature.

The first is direct calculation. This is done directly using Fourier's Law but the non-linear effects could result from using large temperature gradients. Using this approach Osman and Srivastava [329] found that  $k$  shows a peak in conductivity around 2700 W/m K before falling off at higher temperatures due to the onset of *Umklapp* scattering, defined as a three-phonon process which causes thermal resistance.

The second is the equilibrium Green–Kubo (EGK) method. Using this approach, the conductivity is calculated as

$$k = \frac{1}{3Vk_B T^2} \int_0^\infty \langle J(t) \cdot J(0) \rangle dt, \quad (9)$$

where  $V$  is the volume,  $k_B$  the Boltzmann constant, and  $J$  the microscopic heat flux vector which is a function of the binding energies, positions, and velocities of atoms. Che et al. [330] reported a value of 2980 W/m K using this approach.

The third is the homogenous non-equilibrium Green–Kubo method. Berber et al. [331] claimed that the results obtained by the EGK method may be affected by the initial conditions. They proposed the homogenous non-equilibrium Green–Kubo (HNEGK) method, which is computationally more efficient and obtained an unusually high value of  $k$  of 6600 W/m K for a (10,10) CNT using the Tersoff potential at room temperature. Using the same method, Zhang et al. [332] calculated a  $k$  value of about 2200 W/m K based on the Brenner potential instead of the Tersoff potential.

#### 4.2.3. Variation with length

Since the phonon mean free path in the axial direction of CNT is estimated to be very large, ranging from about 100 nm to 1  $\mu$ m, and much longer than that of other materials, the thermal conductivity of CNTs, which are shorter than a few micrometers, may have ballistic transport features compared to the infinitely long tube. Maruyama [333] claimed that the finite size constrains the phonon motion and causes the thermal conductance to vary with the CNT length. Maruyama observed that the thermal conductivity of a (10,10) CNT was almost constant and independent

of the tube length, but the conductivity of a (5,5) CNT varies as a power of 0.32 at 300 K,  $k = aL^{0.32}$ . Yao et al. [334] and Che et al. [330] found that the thermal conductivity of CNTs becomes constant when their length is greater than 10 nm (Fig. 52). Moreland et al. [335] simulated armchair SWNTs with lengths ranging from 50 nm to 1  $\mu\text{m}$ , which showed a strong dependence of thermal conductivity on length.

#### 4.2.4. Variation with chirality and diameter

Osman and Srivastava [329] and Zhang et al. [332] suggested that the *Umklapp process* takes place more easily in small-diameter nanotubes because its axial component remains independent of tube diameter. But in smaller diameter nanotubes, the radial and azimuthal components are larger than those in larger diameter nanotubes. Thus, the thermal conductivity of the (10,10) nanotube is lower than the (11,11) nanotube (see Fig. 53).

In armchair and chiral SWNTs, the sigma bonds along the circumference are strongly strained compared to the zigzag nanotube and this can limit the phonon mean free path due to scattering and lower the thermal conductivity. Thus, the conductivities of armchair and chiral nanotubes are lower than that of the zigzag nanotube. In armchair and zigzag nanotubes, the atom chains are parallel to the axis, but in chiral nanotubes, the atom chains are in a helix. Thus the vibration of the atomic chains in chiral nanotubes may easily transfer the momentum to the radial direction, which causes the low thermal conductivity of chiral nanotubes in the axial direction [332] (Fig. 53).

#### 4.2.5. Effect of physical and chemical modifications

Shenogin et al. [336] studied the variation of the conductivity of CNTs with chemical functionalization using MD simulations. In functionalized tubes, randomly selected atoms were covalently bonded with additional carbon atoms residing just outside the tube wall. This led to  $\text{sp}^3$ -hybridized “defects” in the tube wall. The conductivity for a (10,10) tube is shown in Fig. 54. With increasing degree of

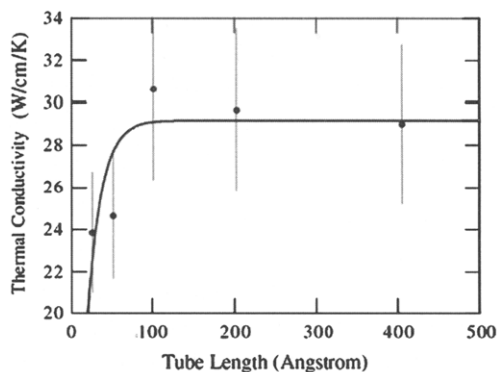


Figure 52. Convergence of thermal conductivity. From Ref. [330]. Reprinted with permission from W. A. Goddard III and the Institute of Physics Publishing, Inc.

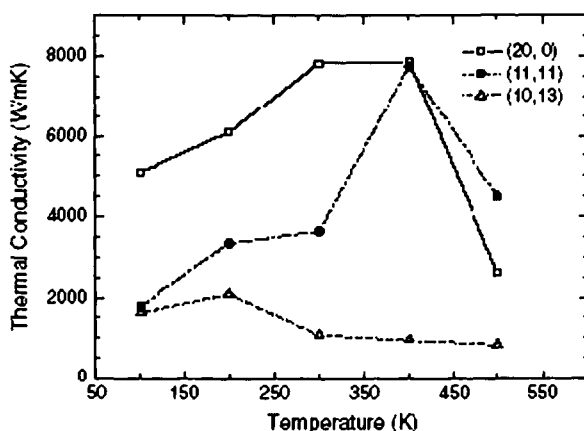


Figure 53. Thermal conductivity of (20,0): open squares, (11,11): solid circles, and (10,13): open triangles, nanotubes. From Ref. [332]. Reprinted with permission from Z. Wang and the Institute of Physics Publishing, Inc.

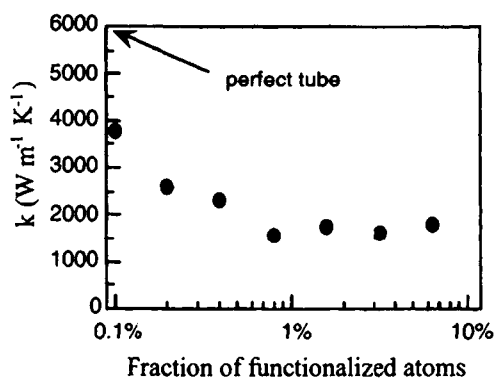


Figure 54. Carbon nanotube conductivity versus fraction of functionalized tube carbon atoms. Reproduced from Ref. [336]. Used with permission from P. Keblinski and the American Institute of Physics.

functionalization, the conductivity drops significantly [336]. However, once about 1% of carbon atoms are functionalized, further increase in defect density does not affect thermal conductivity, which remains essentially constant at around 1700 W/m/K. As defects are introduced, the mean free path of phonons is reduced, so conductivity decreases. However, long wavelength phonons are only weakly scattered

by local defects and they are likely responsible for the plateau value of the conductivity at high defect concentration.

The thermal conductivity of (10,10) SWNTs filled with  $C_{60}$  fullerenes (or peapods) was computed by Noya et al. [337] using MD simulations. The temperature-dependent thermal conductivity of the peapod, while showing qualitatively similar behavior to that of an unfilled SWNT, was found to be higher than the unfilled nanotube at all temperatures (Fig. 55). This result is in agreement with recent experimental observations by Vavro et al. [338,339] who observed a 20% increase in thermal conductivity when (10,10) tubes were filled with fullerenes. Since thermal conduction in CNTs is primarily governed by phonon–phonon interactions, the increase in thermal conductivity in the peapod was explained through the low-frequency radial vibration coupling of the phonon–phonon interactions between fullerene and CNT phonon modes. The combined spectra of the CNT and fullerene contributions in a peapod show an overall enhancement with respect to that of an empty nanotube. Second, energy transfer along the peapod axis due to fullerene–fullerene collisions also contributes to the enhancement in conductivity.

Using picosecond transient absorption, Huxtable et al. [340] measured the interfacial conductance of SWNTs encased in cylindrical micelles of sodium dodecyl sulfate (SDS). The nanotube–hydrophobic alkane interface was found to have an exceptionally low interface conductance of  $12 \text{ MW/m}^2/\text{K}$ . Using MD simulations to

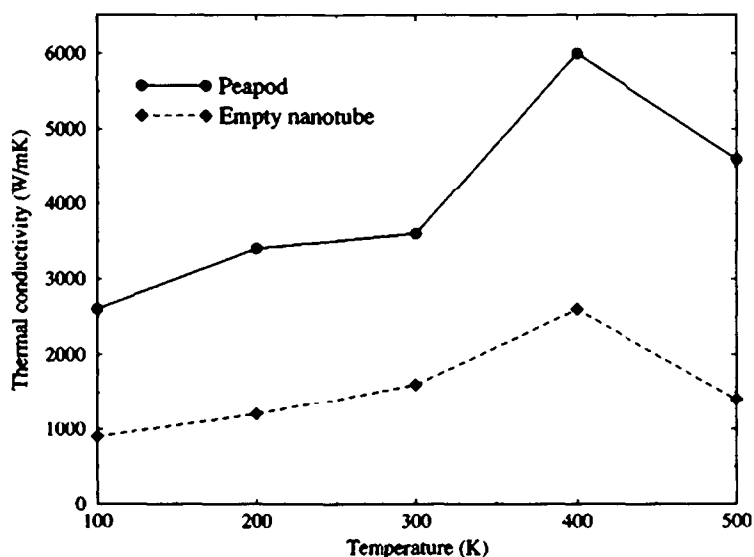


Figure 55. Temperature dependence of peapod thermal conductivity as compared with that of an empty SWNT. Reproduced from Ref. [337]. Reprinted with permission from L. A. Chernozatonskii and the American Physical Society. Copyright (2004) the American Physical Society.

corroborate their experiments, they attributed the low conductance to the fact that the surfactant and the nanotube are coupled by low-frequency vibrational modes. The lowest-frequency phonon present in a 3.5-nm-long nanotube has essentially the same temperature as the surfactant. By contrast, high-frequency phonons have temperatures close to the average nanotube temperature. Thus, energy contained in high-frequency phonon modes within the CNTs must first be transferred to the low-frequency modes through phonon–phonon coupling before it can be exchanged with the surrounding medium. This frequency difference leads to high interfacial resistance for the heat flow between the tubes and the other elements. In summary, interface conductance between nanotubes and molecular fluids is controlled by phonon–phonon coupling within the nanotube.

#### **4.3. Thermal expansion**

X-ray diffraction techniques [341] were used to measure the thermal expansion of a SWNT bundle. Consistent with expectations based on studies of graphite, extremely small thermal expansion in the axial direction ( $-0.15 \pm 0.20 \times 10^{-5} \text{ K}^{-1}$ ), but a value of  $0.75 \pm 0.25 \times 10^{-5} \text{ K}^{-1}$  in the radial direction were found for the thermal expansion over a range of temperatures (300–950 K). The measurements show large anharmonicity and temperature dependence of the inter-tube gap for an SWNT bundle ( $4.2 \pm 1.4 \times 10^{-5} \text{ K}^{-1}$ ) relative to graphite ( $2.6 \pm 1.4 \times 10^{-5} \text{ K}^{-1}$ ). The very small thermal expansion coefficient of the tube diameter is a sign of the strong in-plane carbon–carbon bonds in nanotubes. The various thermal expansion coefficients affect the temperature dependence of the observed phonon modes. Also, significant strain is introduced when nanotubes are mixed with other constituents to form composites for various applications, because of the difference in the thermal expansion properties between SWNTs and other materials.

#### **4.4. Thermopower**

In early studies [342], thermopower was dominated by ensemble averaging effects, inter-tube interactions and oxygen doping effects. Subsequent studies showed the thermopower or Seebeck coefficient of SWNT bundles to be very sensitive to exposure to oxygen and other gaseous species [343], because oxygen adsorption causes SWNTs to become p-type, and to yield quite high thermopower values. This high sensitivity of the thermopower to gas adsorption has potential for the development of gas sensors [344]. However, for quantitative measurements of the temperature dependence of the intrinsic thermopower of SWNTs, the removal of adsorbed gases is essential. The Seebeck coefficient is sensitive to charge transfer effects, motion of the Fermi level and various other effects, which can potentially be used to characterize SWNTs, but at the same time, requires great care with sample preparation for the measurement of intrinsic behavior in SWNTs. For example, the insertion of  $\text{C}_{60}$  inside SWNTs to form peapods leads to a decrease in the positive value of the Seebeck coefficient for all temperatures [338,339], which may perhaps be related to charge transfer. It is further found that the phonon drag term is not important in SWNTs, and that the thermopower is dominated by the diffusion term down to low temperatures [319]. The effects of the Coulomb blockade and of

electron–electron interaction can be seen in metallic SWNTs. The thermopower of semiconducting SWNTs appears to be qualitatively different from that of metallic SWNTs [319].

## 5. INTERACTION BETWEEN GASES AND CARBON NANOTUBES

In this section, we review the interaction of gases and particles with CNTs. Specifically, static properties such as adsorption behavior and dynamic properties such as transport and separation, and related concepts are reviewed.

### 5.1. Adsorption of gases to carbon nanotube walls

Carbon materials are widely used for filtering and adsorption of gases. For instance, activated carbon is an important industrial material that is used for separation and purification of gases [345], and graphite is known to be a good hydrogen sink. Because CNTs have curved exterior walls, and hollow interiors, they would be expected to have different interactions with gas molecules than graphite and other forms of carbon.

#### 5.1.1. Hydrogen adsorption

The adsorption of hydrogen in CNT interiors and bundles has been the focus of much study [21,346]. This is motivated by the need for solid-state, hydrogen storage materials to facilitate the use of hydrogen in place of fossil fuels in energy and transportation applications to increase efficiency and decrease emission of pollutants [347]. However, the study of hydrogen storage in CNTs has been fraught with controversy [348]. Reported hydrogen storage densities in undoped CNTs range from about 0.25 to about 8 wt% [349–352]. In the case of CNTs doped with alkali metals, hydrogen storage densities of 14–20 wt% [353] were reported, but subsequent studies suggested that water contamination may have been a factor in the result [354]. Neutron energy loss results for hydrogen interacting with capped SWNTs show that it is similar to, and with a stability in between, what is predicted for hydrogen interaction with graphite and bulk  $C_{60}$  [355]. Monte Carlo (MC) simulations predicted substantial quantum sieving in SWNTs [356], where heavy isotopes are preferentially adsorbed over light isotopes of a given molecular system. In particular, smaller diameter SWNTs (diameters  $\leq 0.7$  nm) show strong selectivity for sieving of hydrogen/tritium molecules.

Several computational studies have been carried out of hydrogen interactions with CNTs, but none have predicted significant hydrogen adsorption densities [357–360] unless under high temperatures and pressures [361] or by forming dense structures [362–365]. The details of the theoretical approach were shown to have a significant effect on the results. Importantly, small changes in the spacing between SWNTs or in SWNT diameters were predicted to have a significant effect on hydrogen absorption by SWNT bundles [366]. Several studies also considered hydrogen chemisorption and the electrochemical storage of hydrogen in CNT-based systems [21,346].

#### 5.1.2. Adsorption isotherms for gaseous interactions with carbon nanotubes

The determination of adsorption isotherms for gases in CNT systems is important because it not only reveals much about the interaction of nanotubes with gas

molecules, it also can be used to characterize the diameters of nanotube interiors and bundle interstitial channels.

Adsorption isotherms for methane in SWNT bundles with closed ends at low temperatures (78–110 K) and pressures ( $10^{-6}$ –1 Torr) [367] are shown in Fig. 56, which also includes comparisons to the isotherm of methane on graphite. A comparison of adsorption on these two systems indicates that the gas is forming single layers on the exterior of the bundle. Similar results were obtained for krypton.

The binding energy of methane to the exterior of a SWNT bundle (with closed ends) was determined to be about 0.22 eV at 150–200 K, which is about 76% higher than on graphite [368]. In this case, the increase was attributed to either the insertion of the methane into the channels between the SWNTs or their adsorption to ridges on the bundle exterior. When quasi-electron neutron scattering was used to characterize the condensation of methane on SWNTs [369], both a strongly bound, solid-like phase and a more weakly bound liquid-like phase were observed, depending on the system temperature, which varied between 70 and 120 K. At temperatures below 50 K, the methane solidified.

Cole and co-workers [370–374] used MC and energy minimization calculations to analyze the adsorption of gases such as argon, krypton, neon, and methane on the exteriors of bundles of SWNTs. They found that at low gas pressures (low chemical potential), gas molecules form a quasi-1D phase within the groove between two neighboring CNTs in the bundle. As the pressure (chemical potential) increases, a “three-stripe” phase is formed in the direction that is parallel to this groove for all

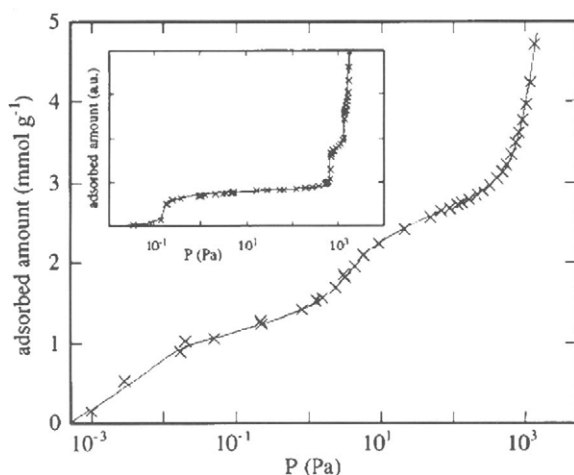


Figure 56. Adsorption isotherm of methane in SWNT bundles at 78.7 K. The inset shows the comparable isotherm for graphite at 80 K. From Ref. [367]. Reprinted with permission from N. Dupont-Pavlovsky and the American Chemical Society. Copyright (2000) American Chemical Society.



the gases considered except for xenon. At higher pressures, monolayer and multi-layer phases are most stable. Xenon was predicted to transition directly from the 1D phase within the groove to a “five stripe” monolayer structure. This different behavior was attributed to xenon’s larger size and, consequently, stronger interaction with other xenon atoms than with the CNT walls. As the temperature in these studies was increased, the molecular layers spread out more but the number of atoms or molecules adsorbed to the CNT remains about the same until desorption occurs. Importantly, experimental measurements for xenon and argon at low pressures [375], and neon, methane, xenon [376], and argon [377] at higher pressures show overall good agreement with these calculation results.

Computational studies indicate that, as a general rule, small atoms and molecules are easily absorbed inside opened tubes [378,379]. However, larger atoms and molecules can only adsorb to CNT exteriors when the nanotube diameter is large enough to accommodate them without steric hindrance. There is experimental evidence that gases enter the interiors of CNTs. For example, adsorption of xenon in CNTs increases when the CNT ends are chemically opened and the resulting functional groups at the opening are removed [380]. The measured binding energies are  $26.8 \pm 0.6$  kJ/mol, which agree with the theoretical estimate of 22.6 kJ/mol [381] for xenon adsorption in the interior of SWNTs. A similar study found that opened SWNTs with no functional groups at the openings and placed on graphitized gold surfaces preferentially adsorb  $\text{CCl}_4$  [382].

When adsorption isotherms of benzene in closed and opened SWNTs are compared [383], significant differences are observed, as shown in Fig. 57. In particular, the uptake of benzene increases dramatically between the opened and closed SWNTs, with about three times more benzene adsorbing in the opened tubes compared to the closed tubes [383]. Similarly, large differences in methanol adsorption isotherms for opened and closed tubes were observed in this study, but much more modest increases were observed for nitrogen [383]. This reflects the differences in the nature of the interactions of these gases with the nanotubes. In particular, the benzene has strong van der Waals interactions with the nanotube walls [384,385] because of the delocalized, aromatic bonding in both the benzene and CNT wall. The methanol is a polarizable molecule that also interacts strongly with the nanotube walls. In contrast, nitrogen is a relatively inert gas that fills the nanotube interior but interacts much more weakly with the nanotube walls. Similar reasons are responsible for the observed significant increase in adsorption of methane and ethane, and small increase in adsorption of oxygen in cut SWNTs [386].

There is evidence that the polar oxidized groups, such as  $-\text{COOH}$  and  $-\text{COOR}$ , at nanotube openings (at the ends and on the walls at defect sites) interferes with gas adsorption, especially in the case of smaller openings and larger gas atoms (xenon) [25]. These groups can be removed by heating [380], but heating to too high of a temperature can close the openings [387] and retard the amount of adsorption, as illustrated in Fig. 58.

When MC simulations were used to compare the adsorption and desorption behavior of argon and nitrogen gases in the interiors of SWNTs and small MWNTs of varying inner diameters, substantial differences were predicted to occur [388], as

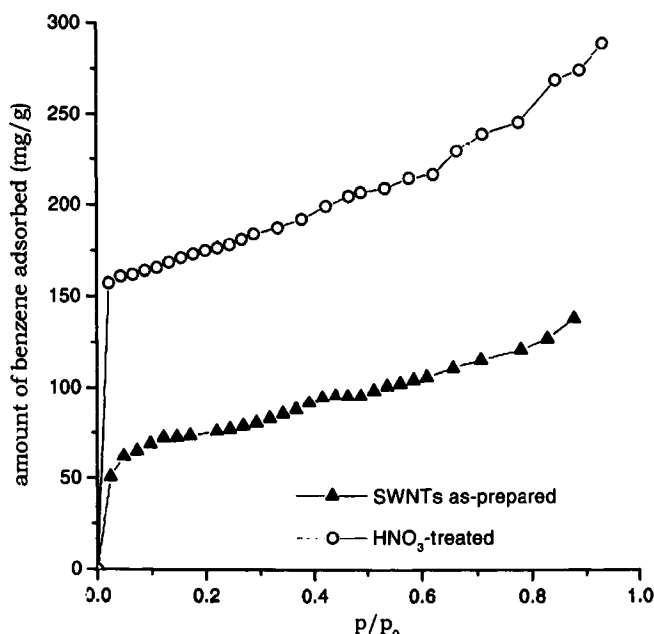


Figure 57. Adsorption isotherms for benzene in SWNTs at 298 K. From Ref. [383]. Reprinted with permission from C. N. R. Rao and Elsevier Science.

shown in Fig. 59. The simulations indicated that these differences are related to the qualitative differences in adsorption between these two systems. Specifically, adsorption in a 1D manner was predicted to occur for the SWNT and layering was predicted to occur in the MWNT. Fig. 59 also indicates that argon is adsorbed more strongly in the SWNT system because more of the smaller argon atoms can be packed into the SWNT interior than the larger nitrogen molecules. In contrast, in the MWNT, there are fewer differences in behavior between these gases, as both are predicted to form layers on the interior walls.

A combined experimental and computational study by Byl et al. [389] showed that infrared spectroscopy can be used to distinguish between carbon tetrafluoride adsorbed on the exterior of SWNTs and in SWNT interiors. This difference is illustrated in Fig. 60, where MC simulations were used to help interpret the experimental data. Interestingly, this study found that xenon selectively displaces the carbon tetrafluoride in the CNT interiors. Follow up studies by Matranga et al. [390,391] found that infrared spectroscopy can similarly be used to distinguish carbon dioxide adsorbed inside opened SWNTs and on the exterior of the tubes. They further found that carbon dioxide preferentially fills interstitial channels before filling the interiors of the CNTs. In addition, xenon preferentially displaces the carbon dioxide in a sequential manner, first from the interior nanotube sites and then from the groove/external sites.

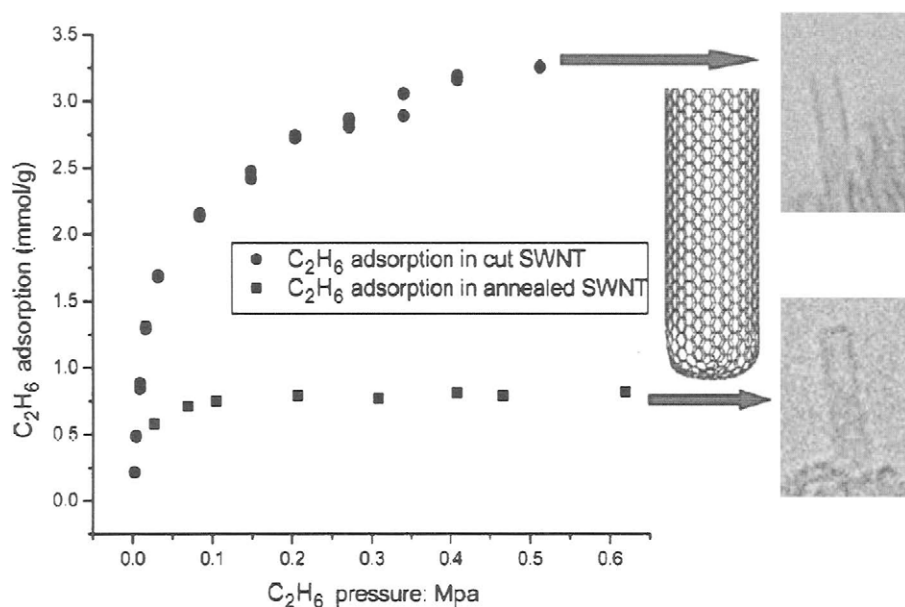


Figure 58. Pressure dependence of the intensities of the broad peaks of the  $^1H$  NMR spectra of SWNTs that are cut before annealing and after annealing at  $800^\circ C$ . The spectra were measured at room temperature. The TEM insets indicate that the annealed SWNTs are closed and the pre-annealed SWNTs are open. From Ref. [387]. Reprinted with permission from O. Zhou and Elsevier Science.

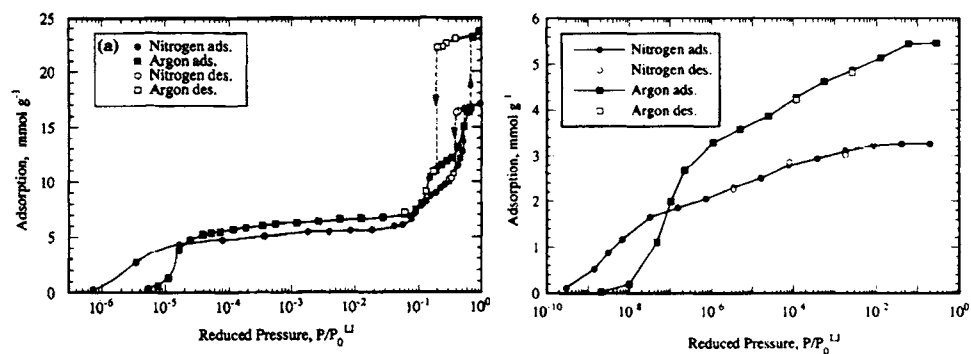


Figure 59. Predicted adsorption isotherms for nitrogen and argon in a 1.02-nm SWNT (left-hand side) and 4.78-nm doubled-walled MWNT (right-hand side). The results are from MC simulations at 77 K. From Ref. [388]. Reprinted with permission from M. W. Maddox and the American Chemical Society. Copyright (1995) American Chemical Society.

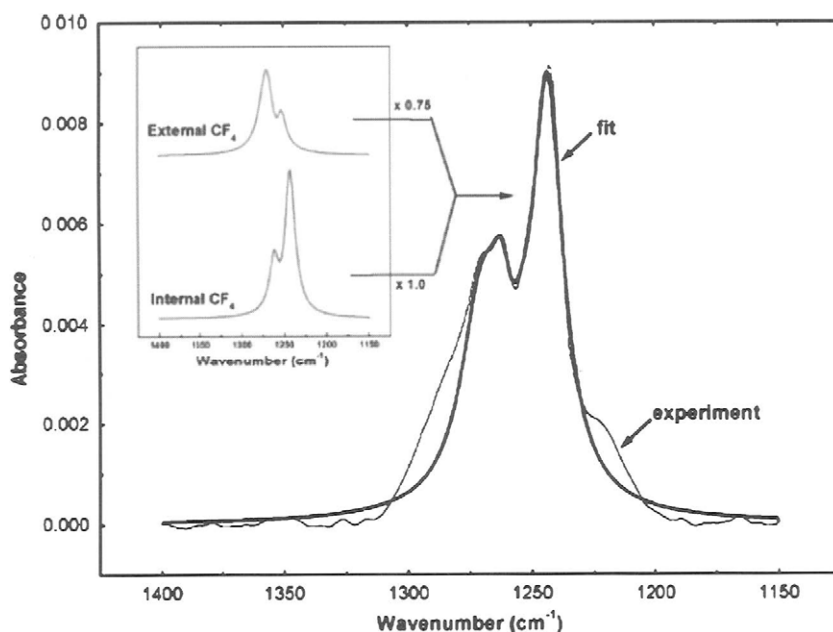


Figure 60. Experimental and simulated infrared spectra of the adsorption of carbon tetrafluoride on the external and internal sites of SWNTs in a bundle. From Ref. [389]. Reprinted with permission from J. T. Yates, Jr., and the American Chemical Society. Copyright (2003) the American Chemical Society.

The experimentally measured smaller increases in adsorption isotherms for nitrogen gas interacting with opened and closed SWNTs are reflected in the results of MC simulations [392], as illustrated in Fig. 61. In particular, the simulations found more significant differences in adsorption as the separation between the CNTs in the bundle vary. Specifically, as the separation between the nanotubes increases, the amount of nitrogen uptake also increases, as indicated in Fig. 61. This is because there is more room for the molecules to pack the interstitial channels, as shown in Fig. 62.

This interstitial adsorption was predicted to cause dilation of the CNT bundle, an increase in the breathing mode frequency of the tubes, and a reduced threshold pressure for gas adsorption [393]. The predicted gas densities, CNT lattice constants, and chemical potential at the threshold for gas uptake for a uniform, regular array of SWNTs is shown in Table 2. The table also indicates the value of the chemical potential for the system without any dilation of the CNT bundle. The results indicate that lattice dilation has a significant effect on the chemical potential for hydrogen, argon, and methane, and a less significant effect for helium and neon,

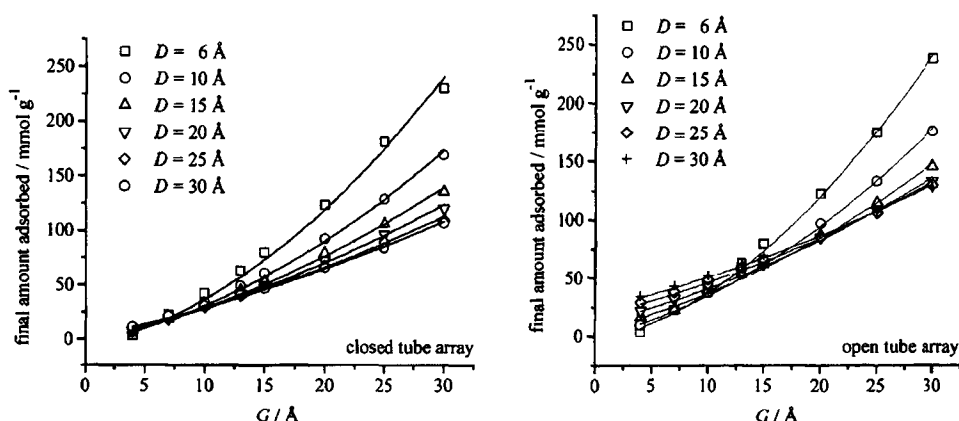


Figure 61. Predicted nitrogen adsorption of nitrogen in SWNT bundles, where the nanotubes are closed (left-hand side) and opened (right-hand side) and arranged in a square array, as the diameter of the nanotubes ( $D$ ) and the separation between them ( $G$ ) is varied. The results are from MC simulations. From Ref. [392]. Reprinted with permission from T. Mayes and the American Chemical Society. Copyright (1999) American Chemical Society.

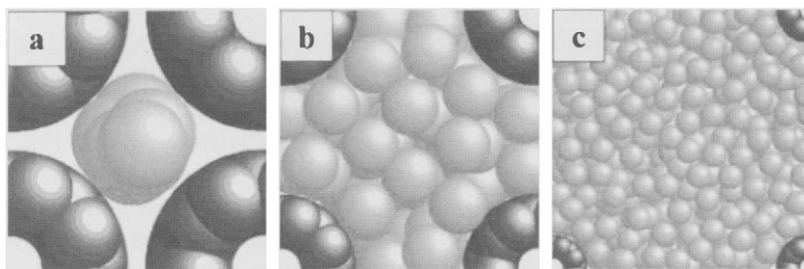


Figure 62. Snapshots of nitrogen adsorption in the interstitial channels between SWNTs in a bundle from MC simulations at 77 K and 760 Torr. The diameter of the tubes in these snapshots is 0.6 nm and the separations are (a) 0.4 nm, (b) 1.0 nm, and (c) 3.0 nm. From Ref. [392]. Reprinted with permission from T. Mayes and the American Chemical Society. Copyright (1999) American Chemical Society.

which are small enough to fit in the undistorted interstitial channels without any lattice dilation.

Experiments and calculations [394–396] for the adsorption of hydrogen, methane, argon, oxygen, and carbon dioxide on irregular, closed-end SWNTs did not find

Table 2

Gas density ( $\rho_c$ ), CNT lattice constant ( $d_c$ ), and chemical potentials ( $\mu_c$  is the chemical potential after lattice dilation,  $\mu_{\text{undil}}$  is the chemical potential without any lattice dilation) for gases interacting with a regular array of uniform SWNTs. .

	$^4\text{He}$	Ne	$\text{H}_2$	$\text{D}_2$	Ar	$\text{CH}_4$
$\rho_c$ ( $\text{\AA}^{-3}$ )	0.215	0.327	0.277	0.275	0.273	0.270
$d_c$ ( $\text{\AA}$ )	17.024	17.069	17.166	17.154	17.330	17.373
$\mu_c$ (K)	-380.7	-927.5	-480.7	-621.4	-1270	-1290
$\mu_{\text{undil}}$ (K)	-378.0	-895.6	-281.5	-446.9	227.6	787.1

Source: From Ref. [393].

solid evidence of lattice dilation. This may be affected by the irregularity of the lattice, which may experience local swelling but not exhibit detectable global swelling. Path-integral MC simulations by Gordillo et al. [397] of neon interactions with bundles of closed- and open-end SWNTs indicated that the interstitials should be filled in the case of closed-end tubes, and that substantial filling occurs in the case of opened-end tubes. They speculated that the reasons for the lack of experimental observance of neon in bundle interstitial channels could, in some instances, be due to entropic barriers or impurities that are blocking the interstitial channels in the experimental samples.

The binding energy of helium in SWNT bundles at temperatures of 14–23 K was experimentally determined by Teizer et al. [398,399] to be too high for 2D adsorption, but consistent with 1D adsorption in the bundle interstitial channels or grooves. However, they did not report on the issue of lattice dilation. Subsequent measurements of the specific heat of helium with SWNT bundles at temperatures of 0.001–6 K [400] indicated that 1D confinement occurs in smaller bundles at lower densities, while 2D adsorption occurs on larger bundles and at higher densities. Calculations by Cole et al. [401] indicated that helium adsorbed in interstitial channels can form an anisotropic phase that is characterized by strong localization of the helium and strong specific heats.

The computational studies described above assume regular arrays of identical CNTs in the bundles. Shi and Johnson [402] performed MC simulations of the adsorption of methane, xenon, and argon in two bundles of closed-end SWNTs, one of which was regular and uniform, and one which contained a distribution of nanotube diameters and, as a consequence, interstitial site diameters. The latter case is closer to experimental conditions, where CNTs are almost always synthesized with an array of diameters (see, for example Ref. [403]). The simulation results for the irregular bundle showed much better agreement with experimental data than the results for the regular bundle, as illustrated in Fig. 63. This indicates that including irregularities in the nanotube bundle structure is important to fully capture gases adsorption in nanotube bundles.

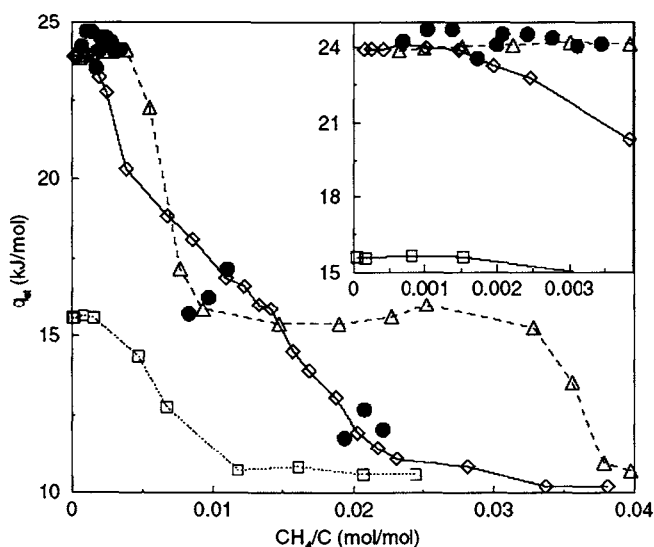


Figure 63. Calculated isosteric heats of adsorption for methane interacting with regular and irregular bundles of closed shell, SWNTs, with an average diameter of 1.24 nm. The circles are experimental data, the diamonds are MC simulation data for adsorption on the heterogeneous bundle, the squares are MC simulation data for adsorption on the homogeneous bundle, and the triangles are MC simulation data for adsorption on the homogeneous bundle where the solid-gas potential is increased by 45%. The low coverage region is shown in the inset for clarity. From Ref. [402]. Reprinted with permission from J. K. Johnson and the American Physical Society. Copyright (2003) the American Physical Society.

## 5.2. Effects of molecular/fullerene adsorption on the electrical conductivity of carbon nanotubes

### 5.2.1. Gaseous interactions with nanotubes

The consequences of gaseous adsorption on CNTs have been of considerable interest. Nowhere is this more true than with regards to the electronic properties of nanotubes. The electrical conductivity of SWNTs was predicted to change when exposed to ammonia and nitrogen dioxide [404,405]. This finding suggests that CNTs might find application as chemical sensors. Fig. 64 shows the behavior of a single semiconducting SWNT when it is exposed to these gases. Part A is an AFM image of the nanotube between two metal contacts. This CNT was determined to be p-type prior to gas exposure. When it was exposed to ammonia, the conductivity was depleted, as shown in part B of Fig. 64. Conversely, when this CNT was under a gate voltage of  $V_g = +4$  V, which would normally make the CNT into an insulator, and exposed to nitrogen dioxide gas, a substantial increase in the

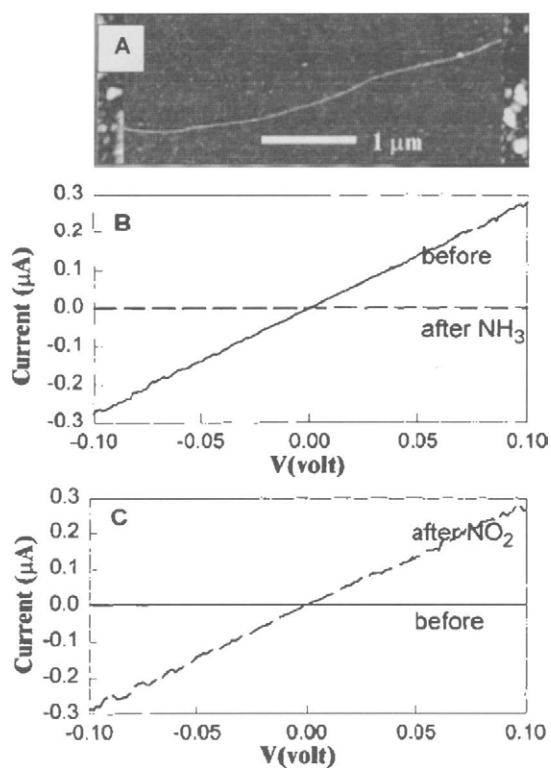


Figure 64. (a) AFM image of SWNT that is between two metal contacts. (b) Normally p-type SWNT loses carriers when exposed to  $\text{NH}_3$ . Under a gate voltage of +4 V this SWNT is normally an insulator. However, when exposed to  $\text{NO}_2$  the conductivity drastically changes, as shown in part (c). From Ref. [404]. Reprinted with permission from H. Dai and Stanford University. Copyright (2000) American Association for the Advancement of Science.

conductivity was measured. This was hypothesized to be due to an excess of p-type carriers in the SWNT.

Subsequent experiments by Collins et al. [406] found that semiconducting SWNTs were similarly sensitive to oxygen gas. In particular, they showed that a normally semiconducting SWNT was transformed into a metallic conductor when exposed to oxygen. Since these findings were reported there has been an intense debate on the role of oxygen in modulating the electrical conductivity of CNTs. For example, questions have been raised about whether a physisorbed molecule can drastically alter CNT conductivity, and what the effects of CNT wall defects are on the process.

The initial claim concerning the conductance change of the semiconducting SWNT shown in Fig. 64 was that it occurred through direct interaction of oxygen with the



nanotube walls that may have been pristine and also contained wall defects [404–406]. This argument was supported by both *ab initio* calculations [407–410] and experiments [406]. However, this claim was not supported by a variety of theoretical [411–416] and experimental [249,414,417–421] studies that found that direct contact between oxygen and SWNTs does not cause changes in electrical conductivity.

Experiments by Avouris and co-workers [203,420] that examined the behavior of FETs made from SWNTs revealed that when the transistors were exposed to oxygen, the conductivity changed as shown by Collins et al. [406]. However, when the metal/CNT contacts within the transistor were protected from exposure to oxygen, no measurable change in conductance was observed. They concluded that direct contact between oxygen and SWNT walls does not play a significant role in changing the conductivity of the nanotube. Instead, they hypothesized that the oxygen changes the barrier height at the metal/CNT contact. In a related study, Goldoni et al. [421] found that oxygen exposure changed the conductivity of as synthesized SWNTs that contained sodium and nickel contaminants. When these sodium contaminants were removed through annealing, there was no measurable conductance change in the SWNT bundle on exposure to oxygen. This is consistent with a hypothesis by Collins et al. [406] that charge transfer from the oxygen to the nanotube could occur through a metal contaminant.

Calculations by Ricca and Drocco [422] found that oxygen can weakly physisorb to sites on the interior and exterior walls of small (9,0) SWNTs. They further found that stronger chemisorption can also occur, such as might be expected to influence the nanotube conductivity, but has a high activation barrier (about 65 kcal/mol). Experiments and calculations [396] of oxygen and carbon dioxide adsorption on closed-shell SWNT bundles at higher pressures found that physisorption in the groove channels occurs. In the case of oxygen, at higher coverage adsorption on the outer nanotube wall was also predicted to occur, while for carbon dioxide, adsorption was only observed at the groove channels.

Experiments [423] also suggested that water acts as a donor dopant to the p-type semiconducting SWNT so that it becomes n-type in the presence of a large concentration of water. Water degrades the performance of CNT FETs [424] when the metal–CNT contacts are protected and only the CNT is exposed to the water. This is thought to be due to charge transfer between the water and the CNT or to a change in gate coupling strength.

Goldoni et al. [421] did not find contaminants to be responsible for SWNT bundle conductivity changes due to exposure to ammonia and nitrogen dioxide. However, Bradley et al. [425] found that the electrical conductivity of SWNTs that were annealed in vacuum did not change on exposure to ammonia. Interestingly, this was not the case when ammonia was introduced in an aqueous or a humid environment. They therefore concluded that water vapor under ambient conditions must play a role in altering the conductivity of SWNTs exposed to ammonia. This is consistent with the original predictions of Kong et al. [404] that the change in CNT conductivity as a result of exposure to ammonia is most likely an indirect process because strong binding between the two was not found in their *ab initio* calculations. A subsequent study by Bradley et al. [426] considered passivation of the metal/CNT contacts as was done in

the oxygen experiments in Refs. [203,420]. Unlike the findings for oxygen, Bradley et al. found that the conductivity changed by only a few percent a result of passivation of the metal/CNT contact. They therefore concluded that the interaction causing the conductivity change was in the CNT region rather than the contact region.

It is interesting to note that all the experimental and theoretical studies appear to agree that nitrogen dioxide directly alters the electrical conductivity of SWNTs. This is not surprising, as nitrogen dioxide interacts strongly with SWNTs. In particular, the binding energy of nitrogen dioxide to a semiconducting SWNT was calculated to be equivalent to 0.1 electrons of charge transfer [404]. It is therefore likely that nitrogen dioxide alters the electrical conductivity of SWNTs by direct charge transfer. There have been some indications that the electrical conductivity change is due to chemisorption or other mechanisms [427]. However, the ideal nitrogen dioxide physisorption studies provide the clearest evidence that physisorption is responsible. Specifically, Kong et al. [404] showed that the physisorbed  $\text{NO}_2$  changes the conductivity of SWNTs by taking electrons away from the nanotube and adding a carrier state near the top of the nanotube valence band [404,405,428]. Later studies clearly showed that there was a new state near the Fermi energy in the density of states plot for this system [408,429–431]. Lastly, adsorbed gases are thought to be responsible for the large, bias-dependent  $1/f$  noise exhibited by SWNT [432].

It is not surprising that there is so much more disagreement among various theoretical and experimental studies of gas interactions with CNTs. This is because it is non-trivial to rule out contaminating effects in the experiments, and challenging to quantitatively model systems where dispersion interactions are important [433].

### 5.2.2. Interaction of fullerenes and organic molecules with carbon nanotubes

The interaction of buckyballs and metallofullerenes with the interiors of SWNTs is also predicted to alter their electronic structure [434]. For instance,  $\text{C}_{60}@(10,10)$  SWNTs were predicted to be metallic [435,436] with the carriers distributed along either the nanotube or the chain of fullerenes. The rotations and collisions of the fullerenes with the SWNTs walls were shown to affect the SWNT conductivity, but not enough to open a band gap in the DOS [436]. In addition, some measurements and calculations indicated that peapods have a hybrid electronic structure, with components from the SWNT and fullerene electronic structures [437]. The electronic behavior of peapods was also found to depend on the relative orientations of the fullerenes with respect to the nanotube, the diameter of the tube, and the degree of packing of the fullerenes [436,438,439].

There is also evidence of charge transfer between the fullerenes and the SWNTs in peapods [440]. For example, calculations and experiments [338,441,442] indicated that peapods composed of ordinarily semiconducting SWNTs have enhanced electrical conductivity (narrower band gaps) relative to the empty SWNTs. This enhancement was thought to be due to charge transfer from the nanotube to the fullerene. The degree of charge transfer is also modulated by the creation of peapods from metallofullerenes (charge-donating metal atoms, such as potassium, inside the fullerene molecules) and SWNTs [440,443–447].

However, other experiments found that the electrical responses of SWNTs and peapods are very similar [448]. In cases where the electronic properties of peapods were electrochemically tuned [449,450], the results indicated that capacitive double-layer charging occurs that is very similar to what occurs in empty SWNTs. Some of the disparities between the studies listed above may be due to the fact that the degree to which fullerenes affects the electronic properties of the host SWNT, and the degree to which charge transfer occurs, is strongly dependent on the SWNT diameter [451]. In particular, the smaller diameter SWNTs that are the focus of most computational studies experience more charge transfer from the fullerenes than larger diameter SWNTs that are most commonly examined in the experiments. If nothing else, the presence of the fullerenes prevents the adsorption of other gases and increases phonon scattering [338].

Metallofullerenes-doped SWNTs were also proposed as a unique, nanometer-scale memory device called a bucky-shuttle [452]. Unlike normal metallofullerenes-doped SWNTs and peapods that can be several micrometers long, the entire system would be only a few nanometer in length, as shown in Fig. 65. The different states required to store memory in a binary fashion would rely on the movement of the charged  $K@C_{60}$  molecule from one end of the capped CNT to the other, as illustrated in Fig. 65.

Related approaches explored the integration of organic electronics with CNT electronics by encapsulation of organic molecules that are amphoteric carriers inside SWNTs [453]. This would allow for the carrier doping to be adjusted by modifying the electron affinity and ionization energy of the organic molecules and provide an important link between CNT electronics and organic electronics.

### 5.3. Molecular transport through carbon nanotubes

There has been considerable study of molecular transport through nanoporous materials, including zeolites [454]. Computational studies helped determine the mechanisms by which molecular transport occurs in these materials. Some of the mechanisms that have been characterized are normal-mode diffusion (see Fig. 66), where molecules pass each other as they move through the pore [455], single-file diffusion (shown in Fig. 66), where molecules are unable to pass each other [456,457], and a mode that is in between these two that is called transition-mode diffusion [458]. Some of these same molecular transport modes are predicted to occur in CNTs, as discussed below.

#### 5.3.1. Non-equilibrium transport

When gas atoms or molecules, such as argon, helium, and methane, were given high transport velocities through the interiors of SWNT, non-equilibrium MD simulations indicated that the molecules rapidly slow down as a result of their strong interactions with the CNT walls [459,460]. This is not surprising given the adsorption behaviors discussed in the previous section. However, non-equilibrium MD simulations also indicate that mass transport occurs through the interiors of CNTs, primarily through diffusion.

Non-equilibrium MD simulations by Sinnott and co-workers [460–462] indicated that the transport of methane from a reservoir and through opened SWNTs, as illustrated in Fig. 67, varies considerably over time and as the diameter of the SWNT

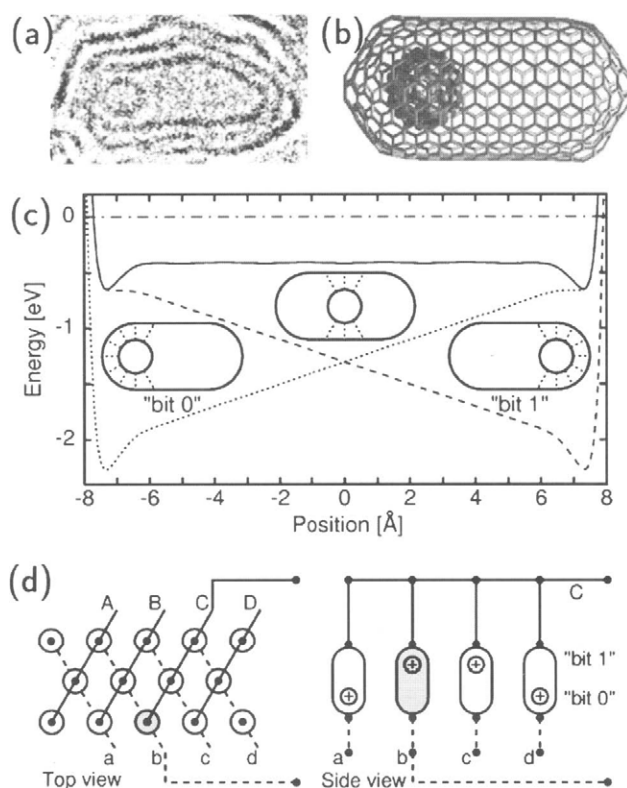


Figure 65. (a) TEM image of a bucky-shuttle system. (b) Computational representation of the system seen in (a). Part (c) illustrates the possible bit configurations and the energetics of the  $C_{60}$  molecule in the SWNT, and the energetics of the structure under bias. (d) Possible configuration for high-density memory. From Ref. [452]. Reprinted with permission from S. Iijima and the American Physical Society. Copyright (1999) by the American Physical Society.

changes. In particular, as the molecules begin to flow from the reservoir into the SWNT, their motion is far from steady state and is driven by the density gradient that exists across the length of the tube. When these initial molecules have flowed all the way down the length of the SWNT interior and approach the vacuum region outside the open exit, the significant attraction between the molecules and the nanotube wall causes them to reverse direction and head back toward the reservoir. In the meantime, molecules have continued to flow from the reservoir into the nanotube. Thus, this stage of the molecular transport process is highly chaotic. Finally, near-steady-state stage diffusion is reached where for every molecule that

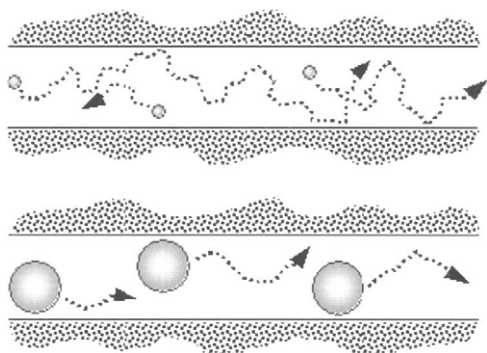


Figure 66. Schematic of normal-mode diffusion (top) and single-file diffusion (bottom).

enters the nanotube from the reservoir, a molecule exits the far open end into the vacuum area with a minimum of direction reversal. These three stages of transport are observed in all the zigzag and armchair SWNTs considered in Refs. [460,461], as illustrated in Fig. 68.

Significant differences were predicted in the nature of the final steady-state transport mechanism as a function of nanotube diameter, but not chirality. In particular, in the case of the larger diameter nanotubes ( $0.69 \text{ nm} \geq \text{diameters} \geq 0.55 \text{ nm}$ ), the steady-state transport mode is consistent with normal-model diffusion, while in the case of the smallest diameter SWNTs considered (diameters  $\approx 0.4 \text{ nm}$ ), the steady-state transport mode is intermediate between normal-mode diffusion and ballistic transport. This intermediate state, termed anomalous or superdiffusion [463–465], is indicative of the interference of the CNT wall corrugation with the molecular transport motion. This interference is significant for the smallest diameter SWNTs and decreases in importance as the diameter increases and the molecules interact less strongly with the nanotube walls.

Similar molecular transport behavior is predicted to occur for the non-equilibrium transport of oxygen through SWNTs [462,466]. In addition, equilibrium MD simulations by Bhide and Yashonath [467] found that normal-pentane and iso-pentane molecules follow similar anomalous transport mechanisms through opened SWNTs. Several arguments were proposed to explain this behavior, including changes in levitation, conformation, and potential energy. Another computational study by Supple and Quirke [468] predicted molecular transport by ballistic motion for decane molecular flowing through rigid SWNTs. The ballistic transport mode was attributed to the high driving force of convection. The fact that the walls were rigid may have contributed to this behavior, however.

The effect of Stone-Wales defects and kinks in the structure of SWNTs on the diffusion of rare gases was determined in MD simulations by Roth and Messentseva

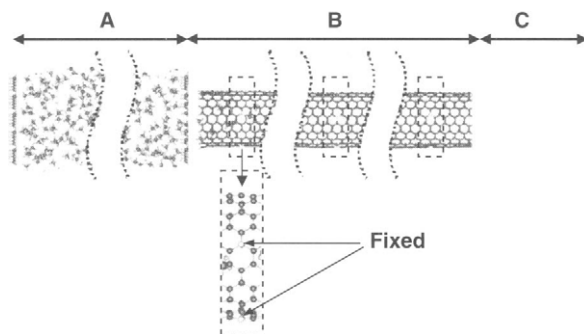


Figure 67. Snapshot of system used to investigate non-equilibrium transport through SWNTs. Methane molecules flow into the open, hydrogen-terminated (10,10) SWNT. Region A is a gas reservoir, region B is nanotube region, and region C is initially vacuum. From Ref. [461]. Reprinted with permission from S. B. Sinnott and the American Chemical Society. Copyright (2004) the American Chemical Society.

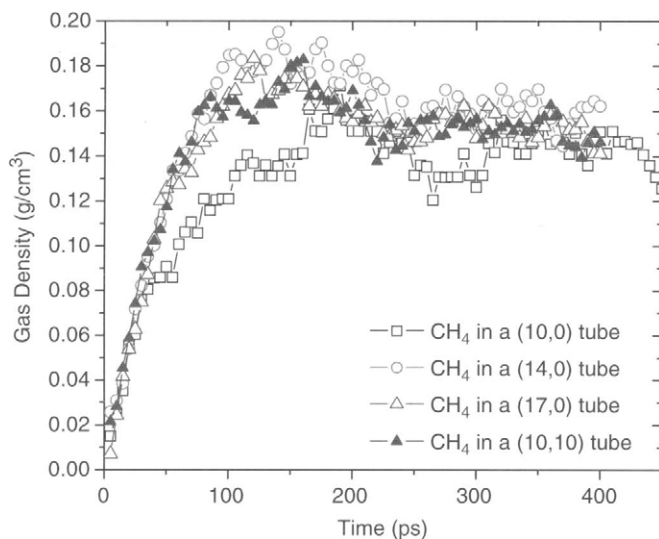


Figure 68. Plot of the change in methane density inside SWNTs of varying diameter and helical structure as a function of time. From Ref. [461]. Reprinted with permission from S. B. Sinnott and the American Chemical Society. Copyright (2004) the American Chemical Society.

[469]. They found that irregularities in the tube structure have a more significant effect on some of the gases than others, and that chaotic motion with intermittent reversals occurs.

Other studies of the transport of shorter non-equilibrium molecules, such as ethane and ethylene, through SWNTs predicted that they follow substantially different mass transport behavior. In particular, at very low densities they were predicted to follow spherical paths along the inner circumference of the SWNTs [470]. As illustrated in Fig. 69, the spiral path followed depends on the chiral structure of the SWNT. MD simulations by Roth and Messentseva [469] also predicted that at low densities, rare-gas-atom transport through SWNTs occurs along a spiral path.

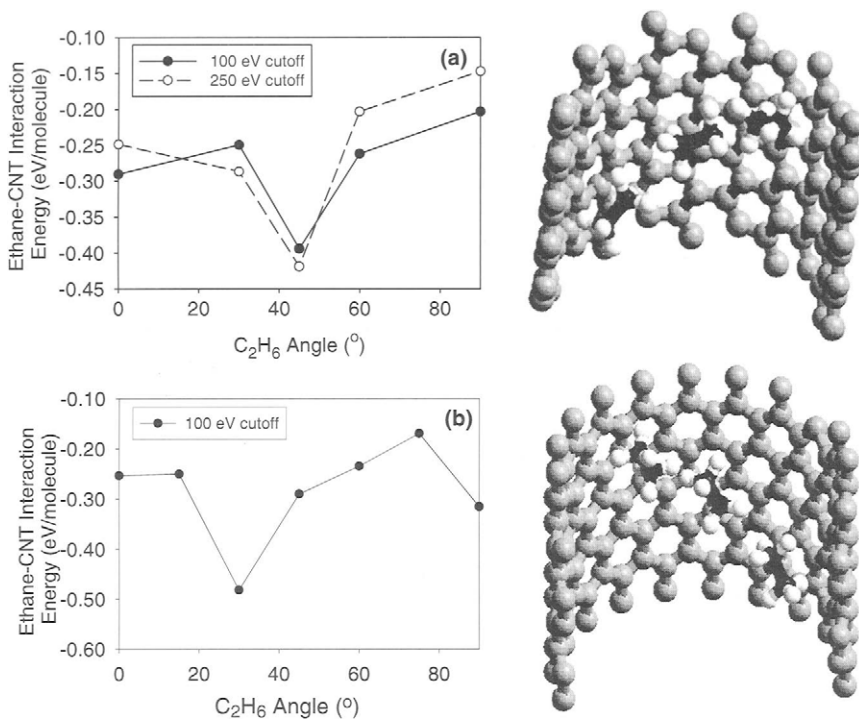


Figure 69. Molecule-SWNT interaction energies and snapshots from the ab initio (density functional theory) calculations of ethane molecules oriented along the axis of a (a) (10,10) and (b) (19,0) SWNT. Pseudopotential cutoff energies used in the calculations are indicated. The energies are for the ethane in various orientations while the snapshots show the optimal configurations predicted by the calculations. The distance between the molecule and the nanotube wall was 0.35–0.45 nm. From Ref. [470]. Reprinted with permission from S. B. Sinnott and the American Physical Society. Copyright (2002) the American Physical Society.

Power et al. [471] used hybrid MC simulations to investigate whether chiral SWNTs might be used to preferentially interact with enantiospecific adsorbants, or separate out molecules based on their chirality. They concluded that the differences in the isosteric heats of adsorption for various molecular enantiomers are too small to make this a viable application for SWNTs.

At larger molecular densities, ethane and ethylene were predicted to follow near-steady-state behavior that is consistent with transition-mode diffusion [460]. Interestingly, these molecules were also predicted to follow this type of molecular transport in zeolites in MD simulations [458], although this mechanism has not been experimentally observed.

### 5.3.2. Equilibrium transport

The self-diffusivities and transport diffusivities of argon and neon in CNTs were recently predicted by Sholl and co-workers [472,473] to be larger by, at most, three orders of magnitude relative to flow in zeolites. This is illustrated in Fig. 70. These equilibrium MD simulations showed that the exceptionally high flux light gas atoms and molecules through CNTs is due to the smoothness of the CNT walls, which are very different from the corrugated structure of zeolite walls. When artificial scattering was included in the simulations, the diffusivities decreased significantly. Similar results were found by Sokhan et al. [474] for nitrogen flowing through several SWNTs. Cao and Wu [475] found that the diffusivities of nitrogen through rigid SWNTs depends significantly on the conditions. For instance, at subcritical temperatures, the diffusion coefficient is dependent on the loading of nitrogen and the diameter of the nanotube, while at supercritical temperatures, the diffusion coefficient decreases as

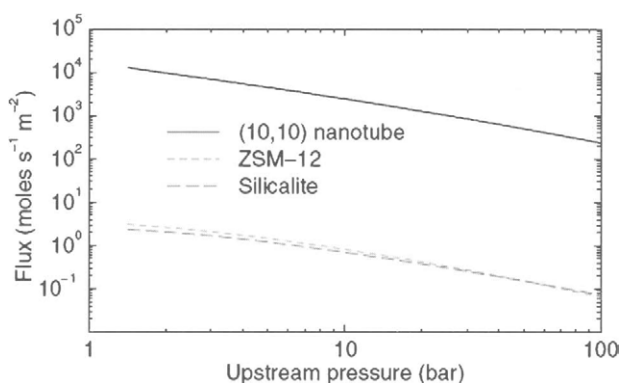


Figure 70. The flux of methane through a membrane that is composed of the stated materials and is 10  $\mu\text{m}$  in width as a function of the inlet pressure. The outlet pressure is 1.38 bar lower than the inlet pressure. From Ref. [472]. Reprinted with permission from D. S. Sholl and the American Physical Society. Copyright (2002) the American Physical Society.



the gas loading increases and then reaches a plateau that is independent of the diameters of the SWNTs. These results were explained by the differing ordering of the molecules in the nanotube interiors under the various conditions [475].

Near-equilibrium MD simulations examined the motion of linear decanes inside SWNTs [476]. They indicated that the molecules closest to the nanotube walls adsorb and form a single layer there at most molecular densities [476]. The resulting structures are anisotropic and show a strong dependence on position relative to each other and to the walls. Most of the molecular transport takes place in the center of the nanotube where the molecules are not strongly attracted by the nanotube wall.

Ordered structures were observed to form during equilibrium MD simulations of transport through SWNTs. For instance, in the case of nitrogen [477] and oxygen [466] interacting with SWNTs of various diameters, single and double layers form around the inner walls of the nanotube, as illustrated in Fig. 71. The molecules that are in the inner most core of these structures have a higher mobility than the molecules that are closest to the nanotube walls. Likewise, the simulations [477] predicted that the nitrogen molecules with the highest diffusivities are found in the SWNTs with the smallest diameters, where the nitrogen molecules are confined closer to the nanotube core and farther from the nanotube walls as a result of the curvature of the tubes. In the case of larger diameter SWNTs, a semiordered nitrogen structure was predicted to form in the nanotube core near saturation pressures at 100 K [477]; this structure effectively blocks transport through the SWNT interior.

As the diameter of the SWNTs increases, the simulations predicted that the transport of oxygen [466] through the log of the mean-square displacement (MSD) as a function of the log of time varies from being highly non-linear for small nanotube

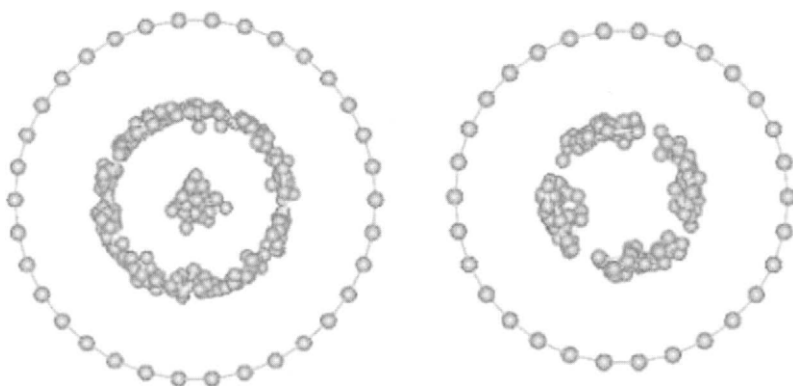


Figure 71. Snapshots at equilibrium of nitrogen in a (17,0) (left) and (15,0) (right) SWNT at 100 K at saturation coverage of the nanotube interiors. From Ref. [477]. Reprinted with permission from S. I. Sandler and the American Chemical Society. Copyright (2004) the American Chemical Society.

diameters, to being highly linear and consistent with normal-mode diffusion, as illustrated in Fig. 72. The non-linearity in the smallest diameter case is indicative of the formation, dissolution, and reformation, of a more ordered structure in the nanotube core. Similar ordering was also predicted to occur for carbon dioxide in nanometer-scale carbon pores [478] and methane in SWNTs at subcritical and supercritical conditions [475], where at supercritical temperatures layering only occurs very close to the nanotube walls, while at subcritical temperatures multi-layers form, as shown in Fig. 71.

Experiments of the transport of methane through buckypaper (a membrane of open-end SWNTs) showed that there is a strong pressure dependence on the diffusion rates [479]. Interestingly, the diffusion rates were measured to be independent of time. The explanation for this phenomenon was that the membrane elastically deforms under higher pressures, which allows increased flow between the nanotubes in the membrane. Such a membrane has the potential to operate as a check valve.

#### 5.4. Gaseous separations in carbon nanotubes

MC simulations by Ayappa [480] were used to study the behavior of binary gas mixtures in CNTs. Molecules with larger radii are able to adsorb to the walls more easily than smaller diameter molecules because they are able to get closer to the

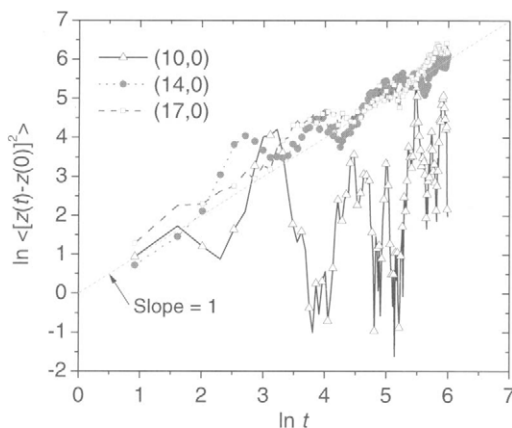


Figure 72. Log-log plots of average square displacement versus time of  $O_2$  molecules entering various nanotubes. The data points are the average value from 10 cases arbitrarily chosen; the straight diagonal line denotes  $\ln\langle[z(t) - z(0)]^2\rangle = \ln t$  line, which is parallel to the relationship of any normal mode diffusion. From Ref. [466]. Reprinted with permission from S. B. Sinnott and the American Chemical Society. Copyright (2005) the American Chemical Society.

CNT walls. Thus, molecular mixtures that contained molecules of differing sizes can be separated on exposure to CNTs [480]. However, for molecular mixtures where the molecules are of similar sizes, such as methane/ethane mixtures, separation is not possible [480].

This result was also seen in classical MD simulations by Mao and Sinnott [481] that predicted significant separation of methane/butane mixtures but little separation of methane/ethane mixtures. The separation of methane and butane is more pronounced in smaller diameter SWNTs but is substantial for all the tubes considered, as illustrated in Fig. 73. Similar molecular separation dependences on diameter for carbon dioxide/methane mixtures in generic carbon nanopores were predicted [482].

## 6. INTERACTION BETWEEN WATER/ELECTROLYTES AND CARBON NANOTUBES

In this section, we review the interaction of water and electrolytes with CNTs. Specifically, the wetting behavior, static properties such as density distribution, dipole

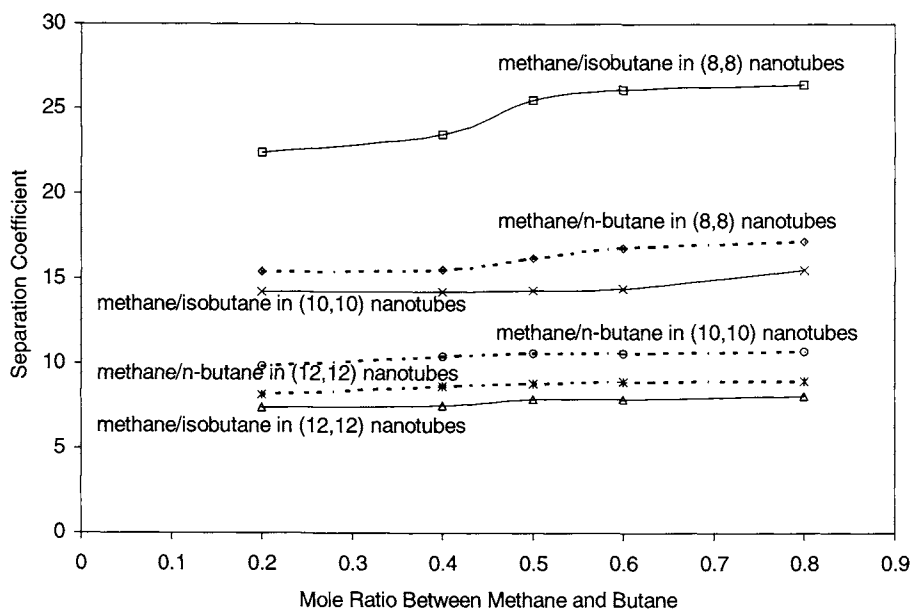


Figure 73. The separation coefficients versus the mole ratio of two types of molecules in molecular mixtures of methane/isobutane and methane/*n*-butane in (8,8), (10,10), and (12,12) SWNTs at 300 K. From Ref. [481]. Reprinted with permission from S. B. Sinnott and the American Chemical Society. Copyright (2001) the American Chemical Society.

orientation, and hydrogen bonding (HB), dynamic properties such as reorientation dynamics, diffusion, filling and emptying kinetics, the effect of surface charge and functionalization on fluid transport, and other concepts are reviewed.

### 6.1. Wetting of carbon nanotube interiors

It is important to know when the CNTs are wet and liquid fills their interiors. According to several recent studies on the wetting and capillarity of CNTs, only relatively low-surface-tension materials can be drawn into the nanotubes [483], and typically a surface tension of 0.1–0.2 N/m is low enough for water and organic solvents to wet and fill the interior of the CNT. Simple experiments on placing a water droplet (surface tension 0.073 N/m) on top of the ground-closed nanotubes showed that water is readily sucked into the capillary channels, eventually leaving a dry surface [484]. More interestingly, Hummer et al. [485] and Berezhkovskii and Hummer [486] showed that water conducts through a subnanometer SWNT (0.81 nm in diameter) by forming a single water wire. Since this size is comparable to the size of a biological ion channel [487], studies on water/electrolyte and CNT interaction have gained more attention because of their potential applications in biological nanosystems. Fig. 74 is a typical experimental TEM photograph of a CNT system enclosing a liquid and a gas [488]. Fig. 75 shows the water occupancy in the nanotube during a 66 ns MD simulation and

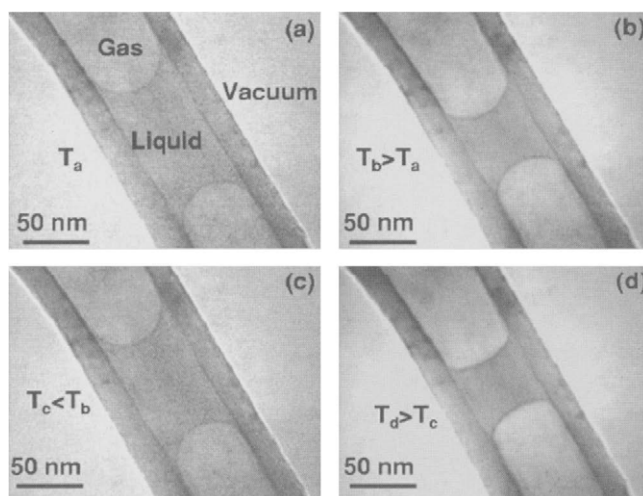


Figure 74. TEM micrograph sequence of a typical CNT portion showing the reversible volume contraction/expansion of a liquid entrapment upon heating/cooling achieved by manipulating the illuminating electron beam. (a) Initial shape of liquid at temperature  $T_a$ , (b) inclusion gets thinner upon heating at  $T_b > T_a$ , (c) liquid returns to its initial size upon cooling at  $T_c < T_b$ , (d) heating is repeated ( $T_d > T_c$ ), resulting in a renewed contraction of the liquid volume. From Ref. [488]. Used with permission from Y. Gogotsi and the American Institute of Physics.

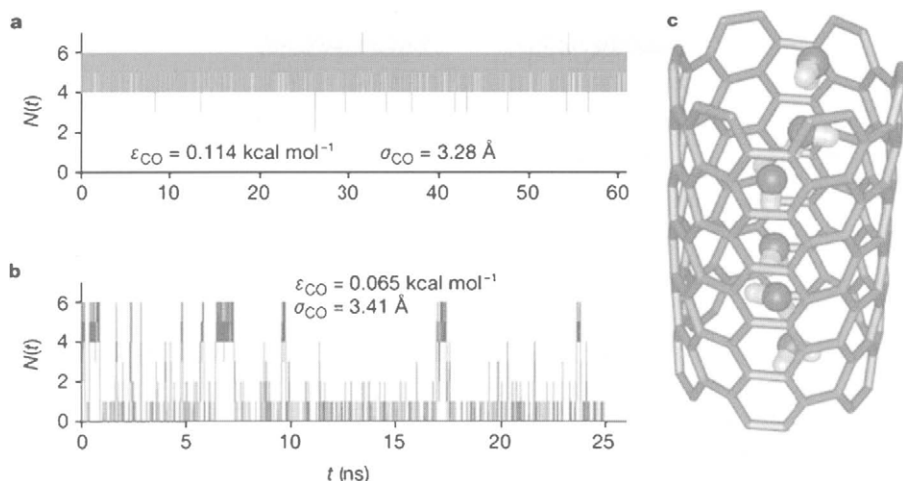


Figure 75. Water occupancy in a (6,6) SWNT. (a) and (b) Number,  $N$ , of water molecules inside the nanotube as a function of time for  $\text{sp}^2$  carbon parameters (a) and reduced carbon–water attractions (b). (c) Structure of the hydrogen-bonded water chain inside the nanotube. From Ref. [485]. Reprinted with permission from G. Hummer and Nature. Copyright (2001) Macmillan Magazines, Inc.

the water “nanowire” that is formed. In contrast to intuition, the initially empty CNT is rapidly filled by water from the surrounding reservoir, and remains occupied with about five water molecules during the entire simulation time of 66 ns. This can be understood quantitatively by computing the local excess chemical potential,  $\mu_{\text{NT}}^{\text{ex}}$ , which is defined on average as the negative of the free energy of removing a water molecule from the channel. This free energy is dominated not by how strongly bound a water molecule is on average, but by how populated weakly bound states are. Even though the binding energy of water molecules inside the nanotube is unfavorable compared to bulk water, the binding energy inside the nanotube is more sharply distributed, and high-energy states dominating the free energy are less frequently occupied (see Fig. 76). As a result, though the water molecules inside the nanotube lose about 2 kcal/mol in energy due to HB, they have a lower excess chemical potential of  $\mu_{\text{NT}}^{\text{ex}} \approx -6.87 \pm 0.07$  kcal/mol, compared to that of bulk water of  $\mu_{\text{NT}}^{\text{ex}} \approx -6.05 \pm 0.02$  kcal/mol.

## 6.2. Interaction between water and carbon nanotubes

Although a single water molecule has a simple structure, the properties of water are quite complex due to its HB nature [489]. In this section, we will summarize some recent results on water/CNT interaction. The results are categorized into static and dynamics properties of water, effect of surface charge on water, water transport through a CNT membrane, and the electronic response of CNT due to its interaction with water.

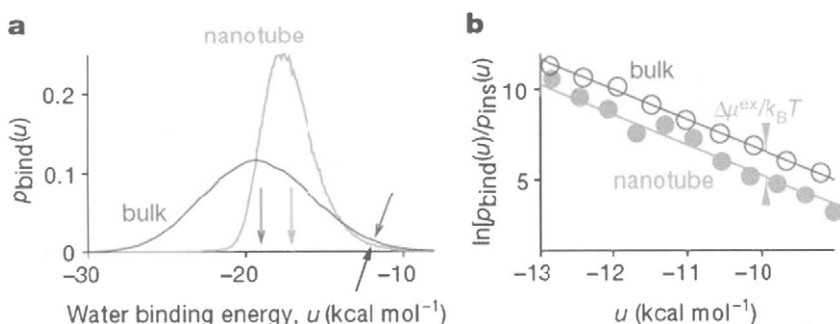


Figure 76. Water binding energies. (a) Probability distribution  $p_{\text{bind}}(u)$  of binding energies  $u$  for bulk water (blue) and water inside the nanotube (red; with a cylindrical volume of radius 0.8 Å from the nanotube axis and a height of about 13.4 Å). Vertical arrows indicate average binding energies. Tilted black arrows indicate the crossover region, in which weakly bound states are more populated in bulk water. (b)  $\ln[p_{\text{bind}}(u)/p_{\text{ins}}(u)]$  for water inside the nanotube (filled circles) and in bulk TIP3P water (open circles), fitted to  $\beta(\mu_w^{\text{ex}} - u)$  (lines). The vertical distance between the parallel lines of slope  $-\beta$  gives the difference in the excess chemical potentials,  $\beta(\mu_w^{\text{ex}} - \mu_{\text{NT}}^{\text{ex}})$ , as indicated by green arrows. From Ref. [485]. Reprinted with permission from G. Hummer and Nature. Copyright (2001) Macmillan Magazines, Inc.

### 6.2.1. Static properties of water

In the examination of static properties of water in a CNT, we will focus on how the water structure and its HB are influenced by the CNT confinement.

When water is confined inside a CNT, there is a phase transition into a solid-like pentagonal or square ice structure. This was shown to occur under normal conditions ( $T = 300$  K and  $p = 1$  bar [490]; see Fig. 77), at high axial pressure conditions ( $p = 50$  MPa [491]) or even at an elevated temperature ( $T = 515$  K [492]). Fig. 77 indicates that in the narrowest nanotube the water molecules adopt a single-file formation with 1D HB, as reported by Hummer et al. [485], whereas in the wider nanotubes they appear to be more disordered. However, in the small-diameter SWNT (diameter of 0.86 nm), the water molecules form a highly ordered lattice filling the hydrophobic cavity. Even though the water molecules are highly ordered exhibiting ice-like behavior, movement of water was still observed [493].

Fig. 78 shows how the density distribution inside CNTs depend on the size and chirality [494]. The orientational distribution of water in CNT is better understood by investigating the orientational distribution of dipole moments as shown in Fig. 79 [494]. The angles are defined by an angle between the dipole moment of water and the positive axial direction (ODDM) and between OH-bond and the positive

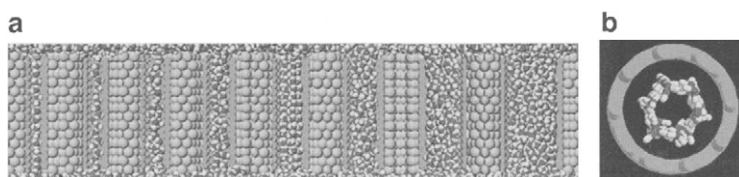


Figure 77. Snapshots from MD simulations at 300 K. (a) Composite image of all systems with nanotube size increasing from left to right. In narrow nanotubes, the water adopts a single-file arrangement but becomes more disordered in a fashion similar to that of bulk water in wider nanotubes. Confined within a nanotube of a “critical” diameter (fifth from left), the water spontaneously orders into a regular array. (b) Cross-sectional view of water inside the critical-sized 0.86-nm-diameter nanotube showing a multicolumnar water structure. Images were derived from visualizations using RasMol. From Ref. [490]. Used with permission from N. Aluru and the American Chemical Society.

axial direction (ODOH). The distribution within narrow tubes is more concentrated than that in the wider tubes, because water molecules tend to form ordered single-file water wires. The small fluctuations in the angle are representative of a strong hydrogen bonded, preferentially aligned water wire. With the increase in tube diameter, any value between  $0^\circ$  and  $180^\circ$  becomes possible, which may be caused by two different reasons. One is that water molecules tend to become more disordered in wider CNTs, as in bulk water. The other is that the flipping of the water dipole becomes more frequent inside wider CNTs.

Since many interesting properties of water originate from the HB, it is important to investigate the HB of water inside a CNT. Two water molecules are considered to be hydrogen bonded if their inter-oxygen distance is smaller than 0.35 nm, and the angle between the O–O axis and one of O–H bond is less than  $30^\circ$  [489]. Fig. 80 shows the variation of the average number of hydrogen bonds (nHB) with the tube size. From this plot, we can observe that nHB does not approach the bulk value even for a tube of 1.8 nm diameter. Second, nHB in narrower CNTs, such as (5,5), (10,0), and (6,6) SWNTs, is significantly smaller than that of the bulk value. Third, in wider CNTs, such as (8,8) and (18,0) SWNTs, nHB does not vary significant in spite of big variation in the diameter. From these results, we can conclude that nanoscale confinement can significantly reduce nHB and the effect of chirality on nHB can be small.

In experiments, the water structure is identified through the vibrational and rotational spectra. Martí and Gordillo [495] investigated the rotational and vibrational spectra of water in CNT and this is shown in Fig. 81. The comparison of the absorption line shapes with the corresponding ones for liquid bulk water presents significant shifts in the positions of the spectral bands directly related to the tube radii. The HB network of constrained water was revealed to be weaker than the

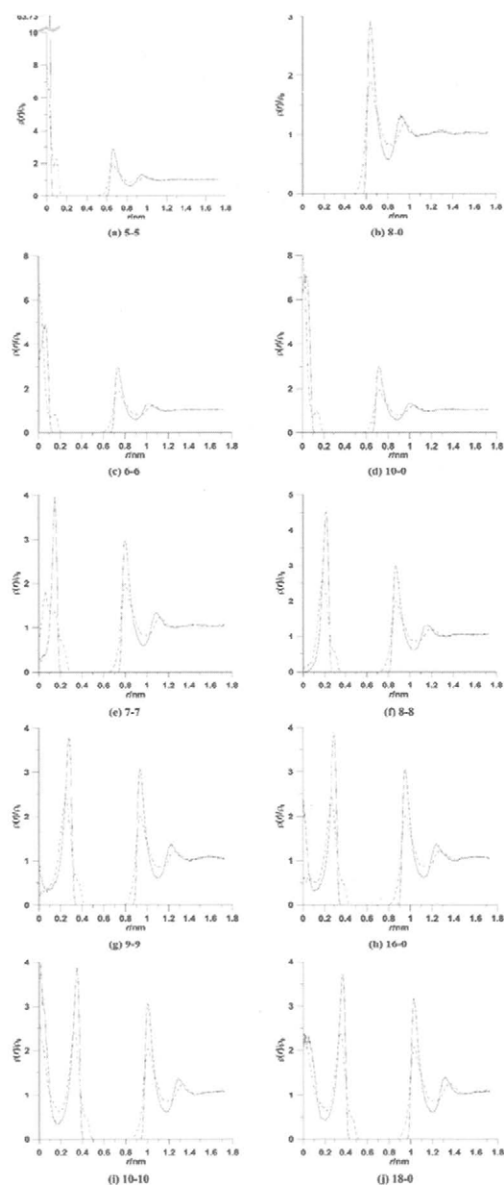


Figure 78. Radial density profiles of oxygen and hydrogen for various CNTs. Full lines represent radial density of oxygen and dashed lines represent radial density of hydrogen. The  $x$ -axis represents radial position from tube center. The  $y$ -axis represents the radial density of O and H ( $\rho(r)$ ) in units of corresponding bulk density ( $\rho_0$ ). From Ref. [494]. [J. Wang, Y. Zhu, J. Zhou and X.-H. Lu, *Phys. Chem. Chem. Phys.* **6**, 829 (2004)]. Reproduced with permission from J. Wang and the PCCP owner societies.



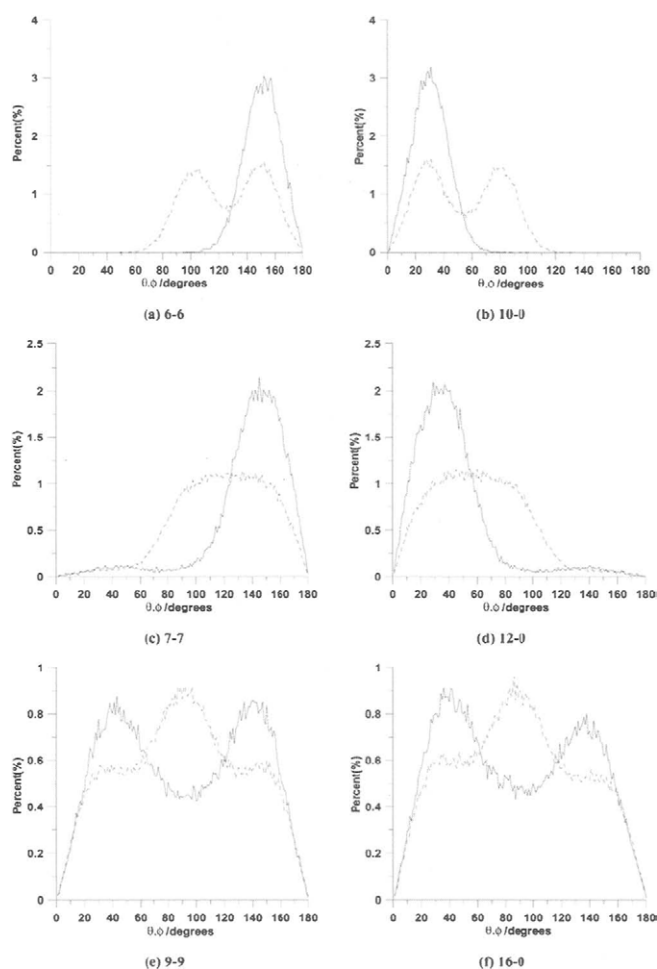


Figure 79. Orientation distributions of water molecules within various tube segments. Full lines represent orientation distribution of dipole moment (ODDM) and dashed lines orientation distribution of the OH bond (ODOH). From Ref. [494]. Reprinted with permission from J. Wang and the Royal Society of Chemistry. Copyright (2004) the Royal Society of Chemistry.

network of bulk water at all simulated temperatures. The narrow tubes do not allow complex HB structures and, in many cases, the absorbed water molecules inside form long linear chains. One relevant fact is the detection of a high vibrational frequency in the stretching spectral region of all constrained water samples that is absent in the bulk.

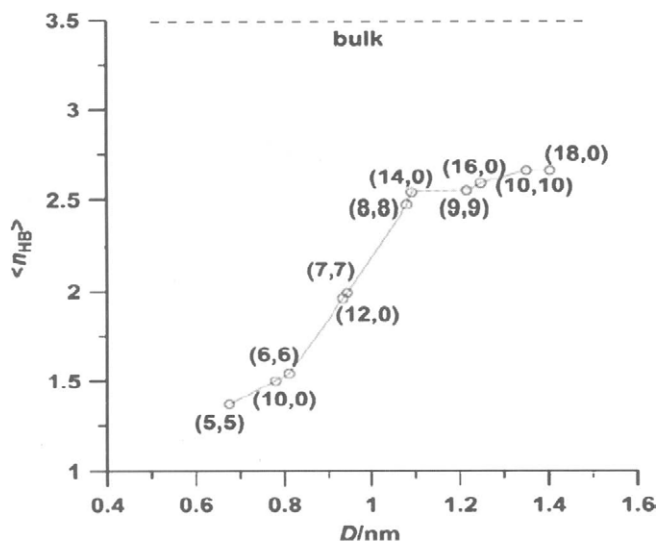


Figure 80. Average  $n_{HB}$  as a function of tube diameter  $D$ . From Ref. [494]. Reprinted with permission from J. Wang and the Royal Society of Chemistry. Copyright (2004) the Royal Society of Chemistry.

### 6.2.2. Dynamic properties of water

Understanding the dynamic behavior of water is critical for many biological nano-device applications. For example, the study of the diffusion of water molecules through nanochannels can help explain the operating mechanism of water channels, which are responsible for many important biological processes in the cell. In this section, we review the dynamic properties of a single water molecule (e.g., reorientation dynamics, residence time, and dipole correlation), the diffusion properties of water, and the filling and emptying kinetics of water in a CNT.

The reorientational motion of water molecules is characterized by the dipole moment reorientation time,  $\tau_{1,2}^\mu$ , where (1,2) denotes the first and second Legendre polynomials. A smaller  $\tau$  corresponds to a faster reorientational motion of a water molecule. Martí et al. [496] studied the reorientation time of water molecules confined in CNTs of various diameters. Fig. 82 shows the reorientation time of the water dipole moment at different temperatures and in different sized nanotubes. We observe that, at room temperature, the narrower the nanotube, the faster the reorientational motion and in the largest nanotube (diameter: 1.26 nm), the reorientational time approaches that of bulk water. Such behavior can be attributed to the partial breakdown of the tetrahedral HB network when the water is confined in small diameter tubes.

The mean time spent by a water molecule in its first coordination shell can be characterized by a residence time function,  $C_{res}(t)$ . Usually, an exponential-like

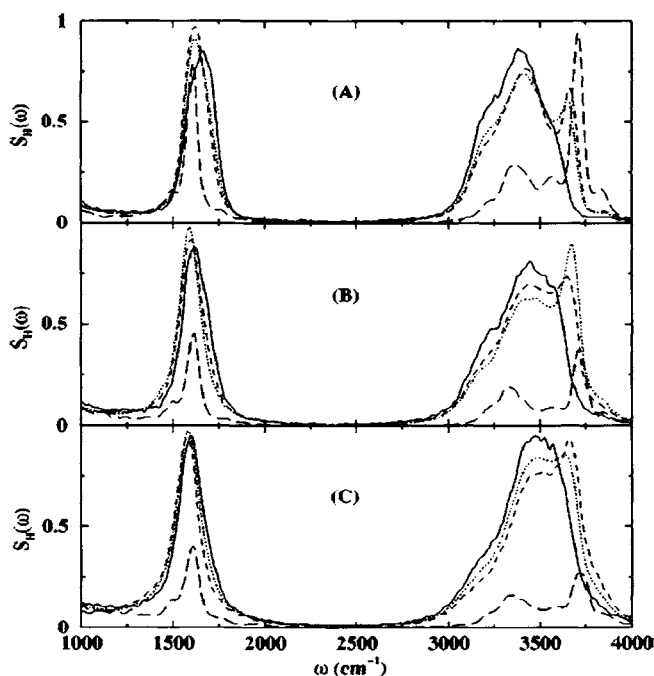


Figure 81. Hydrogen spectral densities for a CNT at different temperatures in high-frequency range (1000–4000  $\text{cm}^{-1}$ ). (A) 298 K, (B) 400 K, (C) 500 K. Bulk is represented by full lines at ambient conditions, (6,6) SWNT is represented by long dashed lines, (8,8) SWNT is represented by dashed lines, and (10,10) SWNT is represented by dotted lines. Bulk has been computed at 298, 403, and 523 K. From Ref. [495]. Reprinted with permission from M. C. Gordillo and the American Physical Society. Copyright (2001) the American Physical Society.

behavior of  $C_{\text{res}}(t)$  is observed, and a residence time,  $\tau_{\text{res}}$ , can be obtained from the fitting of  $C_{\text{res}}(t)$  to a single exponential:

$$C_{\text{res}}(t) \approx c \exp(-t / \tau_{\text{res}}). \quad (10)$$

A longer residence time suggests that water molecules form a more stable structure. Fig. 83 shows the residence time,  $\tau_{\text{res}}$ , of a water molecule in its first coordination shell as a function of the temperature in different sized nanotubes. We observe that at room temperature, the residence time  $\tau_{\text{res}}$  increases as the nanotube diameter decreases, indicating that a water molecule inside a narrow pore will spend a longer time in its neighborhood than in larger pores. As the temperature

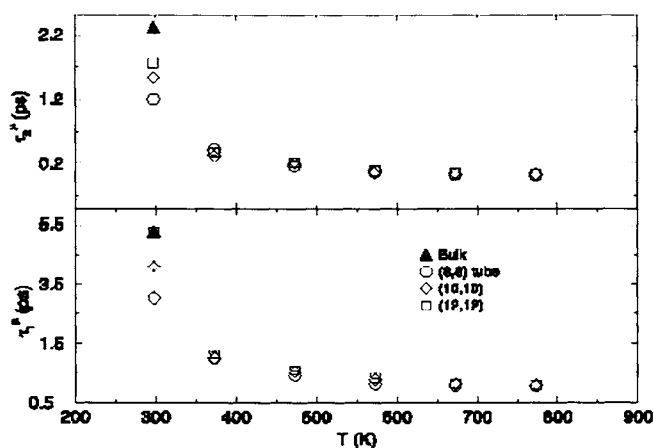


Figure 82. Molecular dipole moment reorientation times  $\tau_{1,2}^\mu$  as a function of temperature at a density of  $0.83 \text{ g/cm}^3$ . Computation with first (bottom) and second (top) Legendre polynomials. From Ref. [496]. Reprinted with permission from M. C. Gordillo and Elsevier Science.

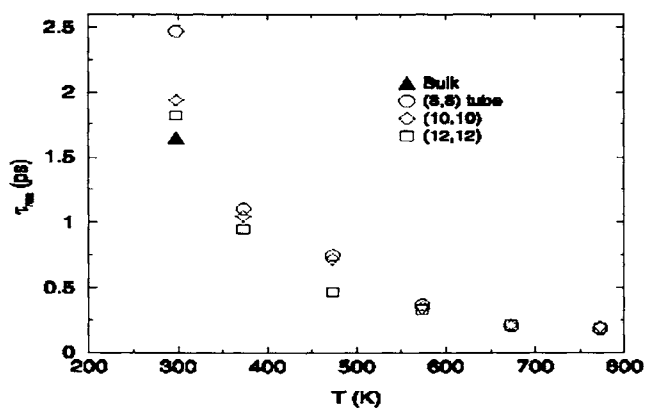


Figure 83. Residence time of a water molecule in its first coordination shell as a function of temperature at a density of  $0.83 \text{ g/cm}^3$ . From Ref. [496]. Reprinted with permission from M. C. Gordillo and Elsevier Science.

increases, the residence time decreases sharply and the deviation of  $\tau_{\text{res}}$  in different sized tubes also decreases.

The reorientation ability of water inside a nanotube can be characterized by using an autocorrelation function (ACF) of water dipoles. The ACF is defined as  $C(t) = \langle \mathbf{p}_i(0) \cdot \mathbf{p}(t) \rangle / \langle p^2 \rangle$ , where  $\mathbf{p}$  is the water–water dipole moment and the angle

brackets denote averages over time,  $t$ , and molecules. Mashl et al. [490] studied the reorientability of water molecules inside the CNTs and Fig. 84 shows the ACF of water inside CNTs of various diameters. They observed that for water in wide nanotubes, the ACFs generally take a bulk-like character. However, for smaller nanotubes, the appearance of a plateau suggests that the hydrogen bonds tends to form very rapidly and are maintained for much longer times compared to that in the bulk. An interesting observation is that the water molecules in the 0.86 nm nanotube show the largest degree of rotational immobilization, while the ACF of water molecules inside nanotubes that are slightly narrower or wider show almost bulk-like behavior.

An important aspect of water behavior at the nanoscale is to understand how its transport is affected by confinement. Since in nanoscale systems diffusion is usually the dominant transport mechanism, the diffusion of water in nanometer systems has been studied extensively. For example, Mashl et al. [490] studied the diffusion of water inside CNTs of different diameters. Fig. 85 shows the MSD and diffusion coefficient of water molecules inside different sized nanotubes. The water molecules are “immobilized” in the 0.86-nm-diameter nanotube in which a stable HB network is observed (recall the panel (b) of Fig. 77). Even under these extreme conditions, water motion is observed. In a related work, Kolesnikov et al. [493] experimentally showed that inside a SWNT with a diameter of about 1.4 nm, the nanotube ice exhibits a continuous transition from solid to liquid state upon heating

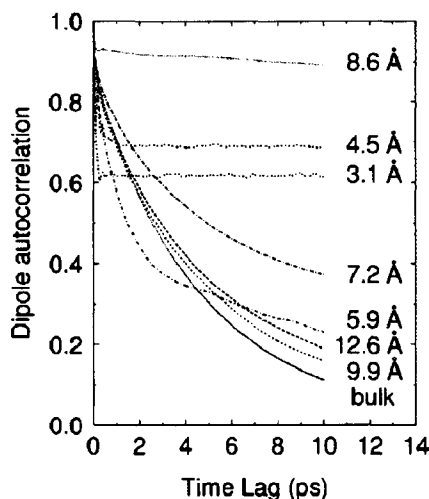


Figure 84. Water reorientation dynamics inside nanotubes at 300 K. Shown is the water dipole ACF for various nanotubes. Data for the 1.81 nm nanotube was indistinguishable from that of the bulk. From Ref. [490]. Reprinted with permission from E. Jakobsson and the American Chemical Society. Copyright (2003) the American Chemical Society.

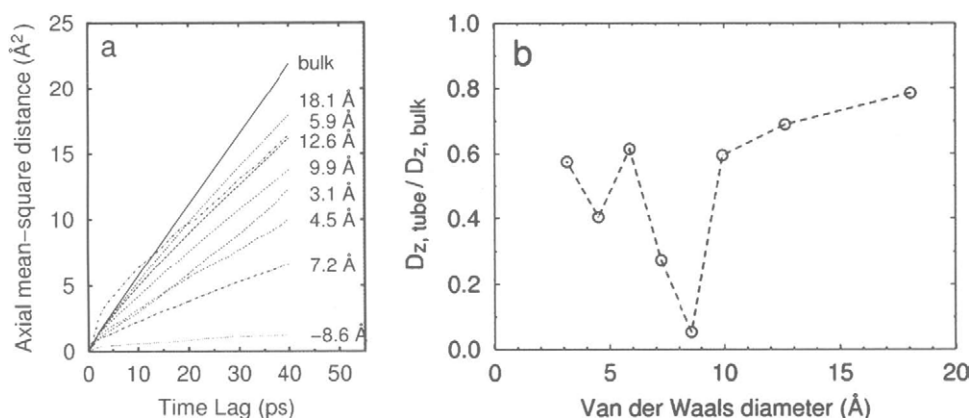


Figure 85. Water mobility inside nanotubes at 300 K. (a) Mean-square displacement of water traveled along the nanotube axis for the various nanotubes. (b) Axial diffusion coefficient of water, normalized to bulk ( $2.69 \times 10^{-5} \text{ cm}^2/\text{s}$ ), derived from panel (a). From Ref. [490]. Reprinted with permission from E. Jakobsson and the American Chemical Society. Copyright (2003) the American Chemical Society.

from 8 to 300 K, unlike bulk ice that has a transition temperature at 273 K. The measured displacement of hydrogen atoms in the nanotube is four times that of normal ice at 8 K.

As mentioned earlier in this section, water diffusion in a confined geometry is strongly affected by the nHB. The dependence of nHB on nanotube diameter can have a strong influence on diffusion rates of confined water molecules. Typically, the diffusion rate of confined water must be determined by a competition between confinement induced by CNTs and the break-up of HB networks. As confinement increases, the water molecules are more constrained and the diffusion rate drops. But as the nHB per water molecule decreases, the water molecules can move more freely relative to each other resulting in an increase of the diffusion coefficient. This gives rise to an anomalous behavior where at a critical diameter, of 0.86 nm, the diffusion coefficient has very low value that immobilizes the water (Fig. 85). Above this diameter, the diffusion coefficient increases until it reaches the bulk value of water.

Hummer et al. [485] found that not only do the water molecules penetrate, but they can also conduct through the nanotube. For a (6,6) CNT, on average, about 17 water molecules pass through the nanotube per nanosecond. Fig. 86 shows the water flow through the nanotube. The water conduction occurs in a burst-like manner. This is because it is energetically costly to rupture the tight HB network inside the nanotube. However, once the HB network is ruptured, the water chain moves with little resistance through the nanotube, resulting in a burst of the water flow. Filling and emptying occurs predominantly by sequential addition of water to, or

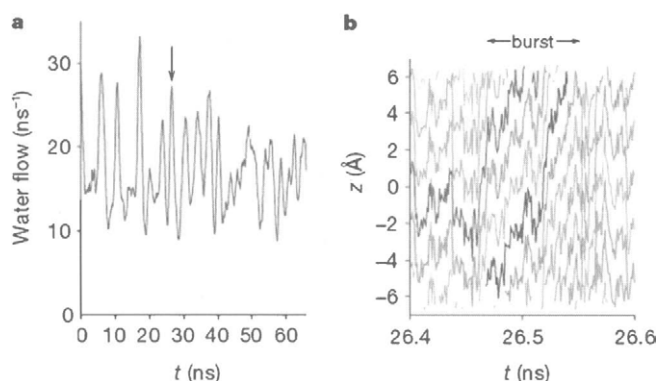


Figure 86. Flow of water through the nanotube. (a) Number of water molecules leaving the nanotube at time  $t$  that entered the nanotube from the other side. Individual water conduction events are smoothed with a 1-ns-wide (at half-maximum) triangular filter. (b) Motions,  $z(t)$ , of individual water molecules shown as colored lines, inside the nanotube along the nanotube axis during the conduction “burst” at 26.5 ns. From Ref. [485]. Reprinted with permission from G. Hummer and Nature. Copyright (2001) Macmillan Magazines, Inc.

removal from, a single-file chain inside the nanotube. The water chains in the nanotube are orientationally ordered as shown in Fig. 87. This precludes simultaneous filling from both tube ends, and forces chain rupturing to occur at the tube end where a water molecule donates a hydrogen bond to the bulk fluid. A detailed investigation of filling/emptying kinetics of water in a CNT [497] suggested that: (1) though filling of the tube can be initiated from either side of the nanotube, it can progress only from the side where it was initiated, with the possible exception of the last water molecule completing the single-file chain; (2) emptying of a filled nanotube starts from the side with the hydrogen bond pointing outward; and (3) filling and emptying occurs mainly by the sequential addition of water to or removal from a single-file chain inside the nanotube.

Proton conduction through membranes is fundamental to many biological and technological processes ranging from ATP synthesis to electrical power generation in hydrogen fuel cells. 1D chains of hydrogen-bonded water molecules provide excellent conductors for protonic currents through pores across membranes. Dellago et al. [498] studied the proton transfer along 1D water wires in CNT. As shown in Fig. 88, the proton mobility along the water wire exceeds that of bulk water by a factor of 40, but is reduced if orientational defects are present. When both protons and HB defects are present, the protons experience long-range electrostatic interactions with the defects, which leads to coupled motion of the protons and the defects that ultimately reduces the diffusion coefficient of the protons.

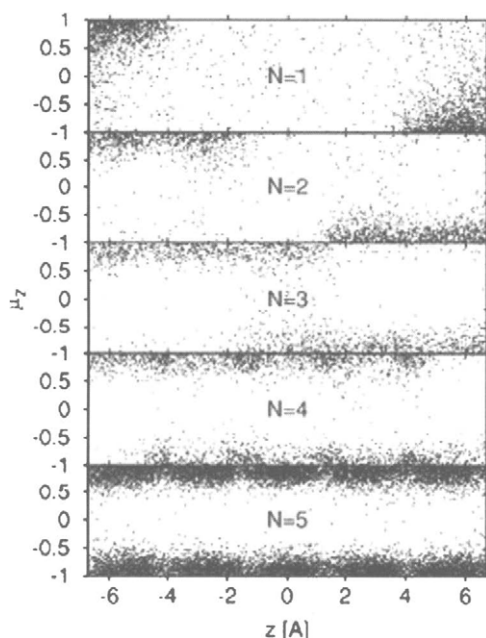


Figure 87. Normalized dipole of water molecules inside the tube projected onto the tube axis as a function of the position  $z$  of the water oxygen atom along the tube axis. Each point corresponds to one water molecule in a saved configuration. The results are separated for  $N=1-5$  water molecules inside the tube (top to bottom). From Ref. [497]. Reprinted with permission from G. Hummer and the American Institute of Physics.

### 6.2.3. Effect of surface charge

Once a charge is introduced to a CNT, the water structure and its transport through the CNTs can be remarkably affected [499]. Fig. 89 compares the water structure with/without surface charge for a (10,10) CNT. In the absence of charge, a cylindrical shell composed of water is formed outside the tube [485]. Inside the tube, water molecules form an obscure water tubule and a central water core, in which water molecules are randomly distributed due to thermal movement (Fig. 89(a)). In the exterior water shell surrounding the CNT, the local density of water molecules is higher than that of bulk water. However, if the CNT is charged, the density distribution is altered significantly. For instance, in the charged case, the water molecules in the shells are highly polarized with all the hydrogen atoms pointing toward the wall of the CNT. Due to the surface charge, the water molecules in the exterior shell become more ordered as a result of the electrostatic interaction with the CNT when compared to the case with no charge.



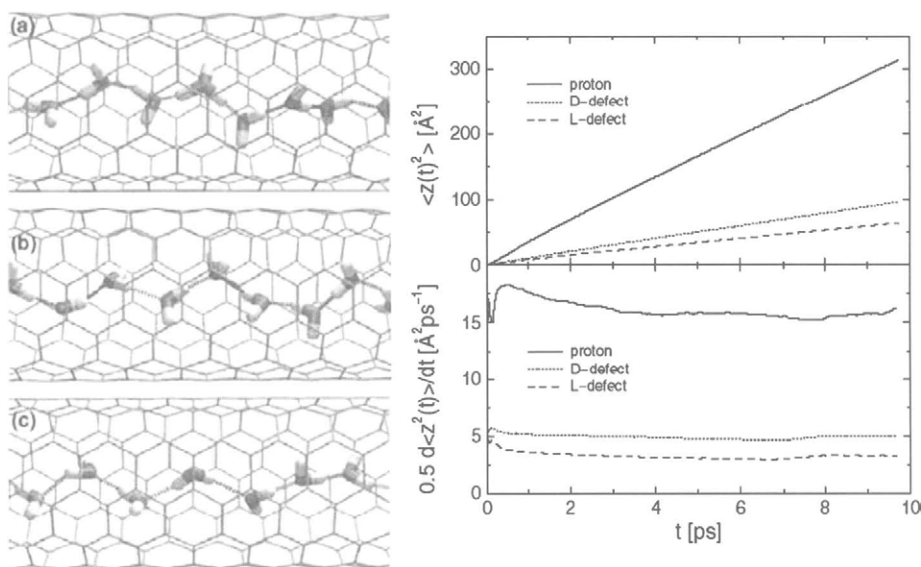


Figure 88. (left) Typical defect configurations: (a) eigen cation, (b) D defect, (c) L defect; (right) Top: mean-square displacement in  $z$ -direction for the excess proton, a D defect, and an L defect in open CNTs containing 120 water molecules. Bottom: time derivative of the mean-square displacement divided by 2. From Ref. [498]. Reproduced with permission from G. Hummer and the American Physical Society. Copyright (2003) the American Physical Society.

In transport phenomena studies, in contrast to the case of a neutral CNT, water molecules were found to be sucked into the negatively charged CNT very quickly, filling up the CNT within a few picoseconds from both the tube ends, as shown in Fig. 90(b). Once the water molecules enter the CNT, the electrostatic and the van der Waals interactions confine the water molecules in the cavity of the CNT. The movement of the water molecules is restricted to inside the CNT, as shown in Fig. 90(b). In the case of  $-0.05e$  charged SWNT, as shown in Fig. 90(c), water molecules flow into the nanotube cavity faster than in the case of the neutral SWNT, but slower compared to the case of  $-0.115e$  charged SWNT. The  $-0.05e$  charged SWNT also restricts the motions of the water molecules considerably. Only six water molecules were found leaving the  $-0.05e$  charged SWNT during the 250 ps period.

#### 6.2.4. Water transport through a carbon nanotube membrane

Kalra et al. [500] examined water transport through CNT membranes as schematically shown in Fig. 91. Two parallel self-assembled membranes of hexagonally packed CNTs separate two compartments, one filled with pure water and the other with an aqueous solution of sodium chloride at an initial concentration of 5.8 M. The

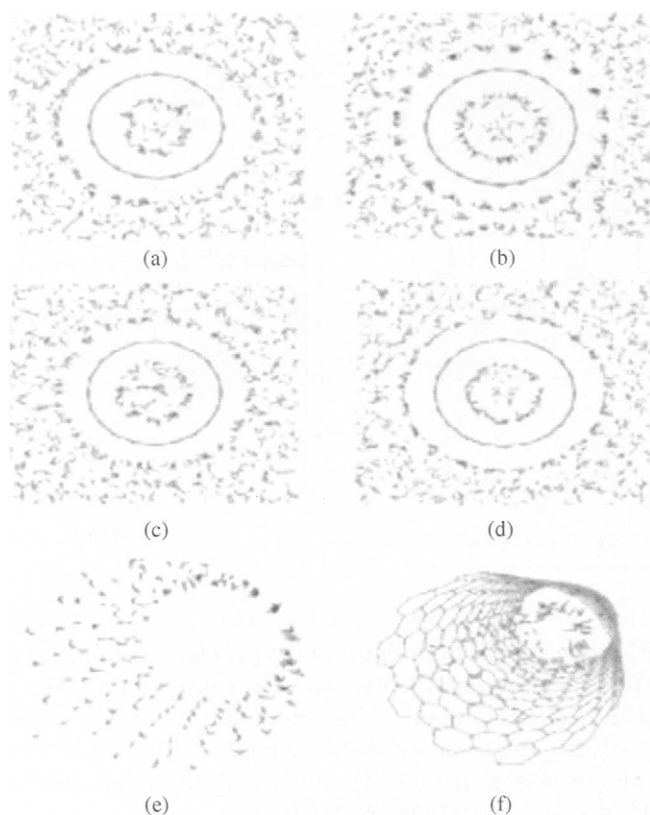


Figure 89. Top view of the molecular structures for (10,10) SWNTs soaked in water (a) neutral SWNT; (b)  $-0.115e$  charged SWNT, (c)  $-0.05e$  charged SWNT, (d)  $+0.115e$  charged SWNT, (e) the perspective side view of the water tubule formed outside the  $-0.115e$  charged SWNT, and (f) the perspective side view of the  $-0.115e$  charged SWNT and the inner water tubule. From Ref. [499]. Used with permission from C. Song and the American Institute of Physics.

subnanometer pores of the CNTs permit transport of water molecules between the two compartments, but not that of hydrated sodium or chloride ions. Similar processes occur in living organisms where lipid membranes separate compartments of different molarity, thus driving the transport of water and solutes through membrane-inserted pores. The resulting osmotic imbalance drives water to flow from the pure-water compartment to the salt-solution compartment, thus gradually draining the pure-water compartment.

The nature of the specific osmotic setup allows the study of not only the transport of water through molecule-sized pores but also the structural and thermodynamic

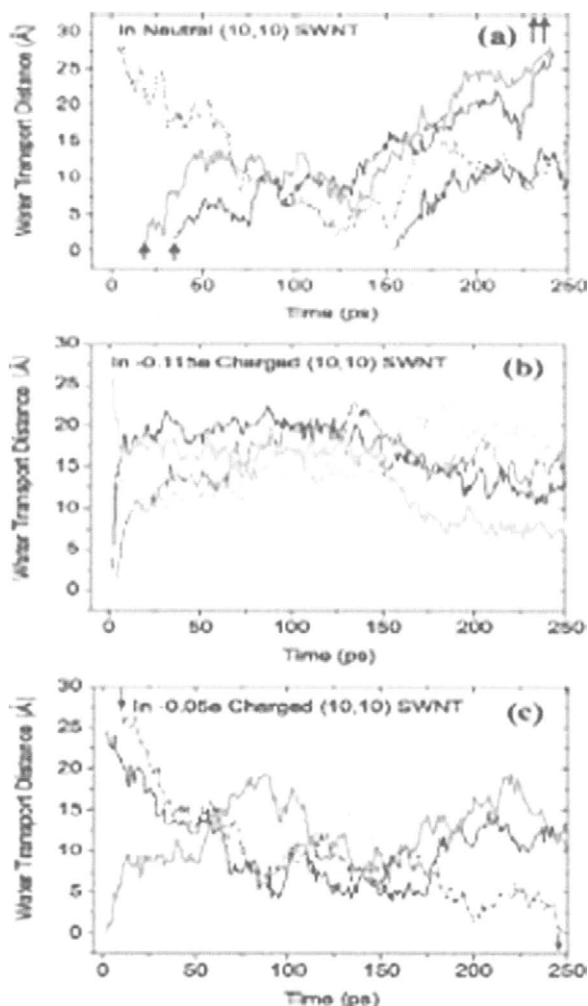


Figure 90. Transport distance of water molecules from the SWNT tips as a function of time inside SWNTs (a) for a neutral (10,10) SWNT, (b) for a  $-0.115e$  charged (10,10) SWNT, and (c) for a  $-0.05e$  charged (10,10) SWNT. Reproduced from Ref. [499]. Used with permission from C. Song and the American Institute of Physics.

aspects of water sheets sandwiched between the CNT membranes as shown in Fig. 92. The results suggest that: (1) water flows through arrays of open-ended nanotubes with negligible friction; (2) water transport is influenced by microscopic fluctuations and can be described by a 1D continuous time random-walk model; (3) the

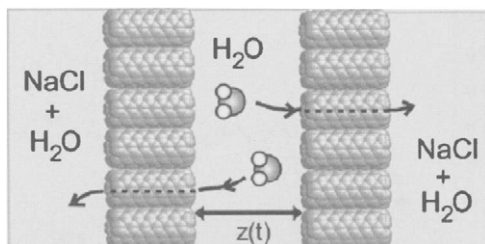


Figure 91. Schematic of the two-compartment system. Driven by the osmotic imbalance, water flows from the pure-water compartment into the salt-solution compartment through the two CNT membranes, reducing the membrane-membrane separation,  $z(t)$ , with time. Reproduced from Ref. [500]. Reprinted with permission from G. Hummer and the National Academy of Sciences, USA. Copyright (2003) the National Academy of Sciences, USA.

observed flow rates are comparable to those measured for biological water channels (aquaporin); (4) water can form remarkably (meta)-stable one- and two-water sheets sandwiched between the membranes; and (5) CNTs can be used for partitioning of molecular species.

Hinds et al. [501] fabricated membrane structures that take advantage of the as-deposited alignment of multiwalled CNTs to form a well-controlled nanoporous membrane structure and used this for molecular transport through the CNT pores. CNTs with inner diameters of  $6 \pm 2$  nm were aligned within a composite of polystyrene (PS) and toluene to form a film of 5–10  $\mu\text{m}$  thickness. Transport measurements of nitrogen and aqueous ionic species  $[\text{Ru}(\text{NH}_3)_6^{3+}]$  through the inner core of the CNTs gave a permeance of  $2.6 \mu\text{mol}/(\text{m}^2 \text{ s Pa})$  for nitrogen and a flux of  $0.9 \mu\text{mol cm}^{-2}/\text{h}$  for  $[\text{Ru}(\text{NH}_3)_6^{3+}]$  after hydrochloric acid treatment. Membranes with CNT tips that were functionalized with biotin showed a reduction in  $[\text{Ru}(\text{NH}_3)_6^{3+}]$  flux by a factor of 15 when bound with streptavidin, thereby demonstrating the ability of CNT-PS membranes for chemical separations and sensing (Fig. 93(D)).

Ionic flux through the CNT-PS membrane structure was studied as a function of chemical end groups at the entrance to CNTs [502]. As seen previously in the simulations of Joseph et al. [503], the overall chemical flux through CNT membranes is largely limited by chemical interactions of functional molecules at the CNT core entrances. The transport through the membrane of two different sized but equally charged molecules  $[\text{Ru}(\text{bipy})_2^{2+}]$  and  $[\text{MV}^{2+}]$  was quantified in a U-tube permeation cell by UV-vis spectroscopy. Relative selectivity of the molecules varied from 1.7 to 3.6 as a function of tip-functionalization chemistry. Use of anionically charged dye molecules

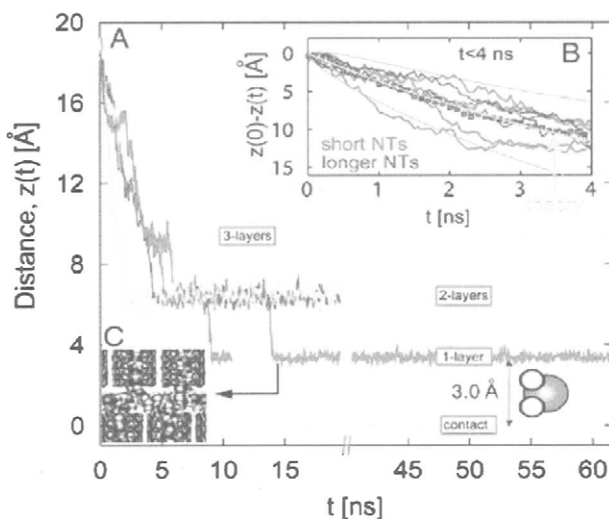


Figure 92. Osmotic flow of water through CNT membranes. (A) CNT membrane separation of the water compartment,  $z(t)$ , as a function of time  $t$  for five independent non-equilibrium simulations (colored lines). Horizontal lines indicate metastable water layers separated by  $\sim 3$  Å, the diameter of a water molecule. (B) Observed water flow measured as  $z(0)-z(t)$  through membranes comprising short ( $L=13.4$  Å; light gray lines) and long ( $L=27$  Å; dark gray lines) nanotubes compared with the prediction of the random-walk model of water transport (darkest gray lines). The average of the five simulations of short-tube membranes is shown by symbols. The shaded area covers the predicted variation of the net flow (two standard deviations from the average value). (C) Side view of a single water sheet confined between two porous CNT membranes. From Ref. [500]. Reprinted with permission from G. Hummer and the National Academy of Sciences, USA. Copyright (2003) the National Academy of Sciences, USA.

as gatekeepers dramatically improved cationic transport through the membrane due to columbic attraction.

#### 6.2.5. Electric dipole moment of water inside CNTs

The high polarizability of a CNT can significantly alter the electronic properties (e.g., the electric dipole moment) of an encapsulated water wire. Mann and Halls [504] investigated the dipole moment of a water wire segment consisting of 6 or 12 water molecules inside a SWNT. Table 3 shows the components of the electric dipole vectors and the net dipole moment of two different water-filled nanotube segments, along with the corresponding values in the absence of the SWNT. The average dipole moment per water molecule is found to be approximately 0.75 D

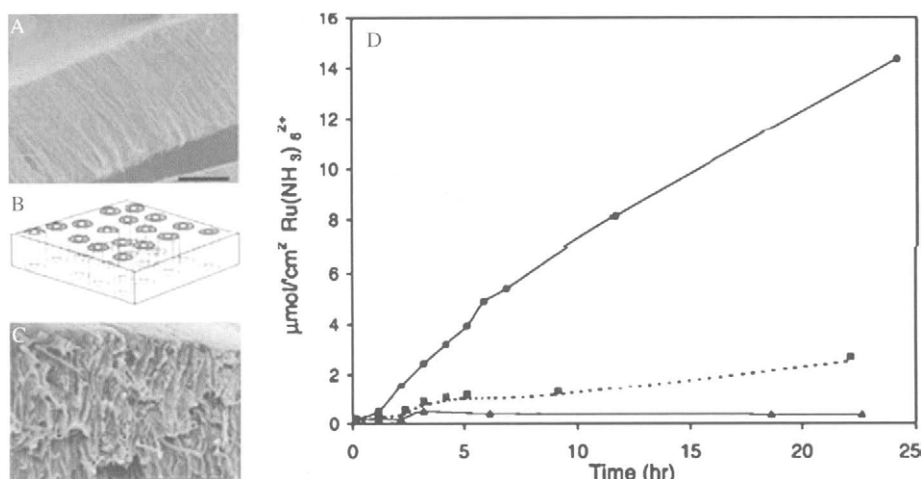


Figure 93. (A) An as-grown, dense, multiwalled CNT array produced with an Fe-catalyzed CVD process. Scale bar=50  $\mu\text{m}$ . (B) Schematic of the membrane structure. (C) The cleaved edge of the CNT-PS membrane. Scale bar=2.5  $\mu\text{m}$ . (D)  $\text{Ru}(\text{NH}_3)_6^{3+}$  flux through a CNT membrane structure after HCl treatment (circles), after biotin functionalization (squares), and after streptavidin coordination (triangles). From Ref. [501]. Reprinted with permission from B. Hinds. Copyright (2004) American Association for the Advancement of Science.

for the water-filled nanotubes, significantly smaller than the average of 2.7 D for water wires in the absence of the nanotube. The water wire interacting with its image dipole induced on the CNT effectively reduces the dipole moment of the composite system. The net result is a length-dependent dipole moment of approximately 0.36 D/Å. An excess proton injected into the water wire is found to be significantly stabilized, relative to the gas phase, due to the high polarizability of the CNT.

### 6.3. Interaction between an electrolyte and a carbon nanotube

In this section, we review the electrolyte–CNT interaction. An electrolyte can interact with the CNT either inside or outside. The study of electrolytic transport through CNTs has great potential for providing insight into biological nanosystem applications and nanofluidic systems. Considering that a CNT is comparable in size to a biological ion channel [487], a proper understanding of the behavior of electrolytes inside CNTs paves the way toward artificial devices mimicking living systems. External interaction between an electrolyte and a CNT typically generates an electrical response in the CNT and a fundamental understanding of this interaction has the potential for nanoscale sensor development, electrochemical control of

Table 3

Dipole moments and dipole moment vectors of the water-filled (6,6) SWNT segments.

H <sub>2</sub> O wire length <sup>1</sup>	$\mu_x$ <sup>2</sup>	$\mu_y$ <sup>2</sup>	$\mu_z$ <sup>2</sup>	$ \mu ^2$
6 0.05 –0.15	4.53	4.53		
6 (no CNT) <sup>3</sup>	0.49	–0.79	16.07	16.09
12	0.08	–0.22	9.00	9.00
12 (no CNT) <sup>3</sup>	0.61	–0.79	32.63	32.65

<sup>1</sup> Number of molecules in the 1D water wire.<sup>2</sup> In units of debye.<sup>3</sup> Water wire in the absence of CNT.

Source: Reproduced from Ref. [504].

nanodevices, energy conversion, etc. However, very few studies have been performed so far on electrolyte/CNT interaction and in this section we summarize some of these studies.

### 6.3.1. Electrolytic transport

Joseph et al. [503] explored the transport of an electrolytic solution (potassium chloride) through a CNT by MD simulations. It is observed that ion occupancy is very low in a (16,16) 1.34 nm long CNT in 1.85 M KCl solution, because the non-electrostatic forces between the CNT and the ions are not strong enough to overcome the attractive force between potassium and chloride in the bulk solution. However, they also proposed a novel method to increase the ion occupancy in CNTs by attaching functional groups with partial charges to the CNT rims. When the partial charges were placed on the rim atoms of the tube and an external electric field was applied, it was found that the ion occupancy increased significantly.

### 6.3.2. Effect of surface charge on the electroosmotic transport

Qiao and Aluru [505] investigated atypical electroosmotic transport through a CNT and how it depended on surface charge. They considered the electroosmotic flow of NaCl in a (20,20) SWNT. As shown in Fig. 94, if the SWNT surface is negatively charged, a significant amount of sodium ions are contact adsorbed on the nanotube wall and immobilized, resulting in negligible electroosmotic transport. However, if the SWNT surface is positively charged, the contact adsorption of the chloride ion is moderate and the adsorbed chloride ions are not immobilized, thus generating a significant electroosmotic transport and a velocity slip on the CNT surface. The observed dependence of electroosmotic transport on the surface charge is significantly different from the results obtained using conventional continuum theories, which predict that the electroosmotic transport will simply reverse its direction if the surface charge density is flipped. This anomalous dependence of electroosmotic transport on the surface charge is mainly caused by the different adsorption behavior of the counterions, which depends on the size of the counterion,

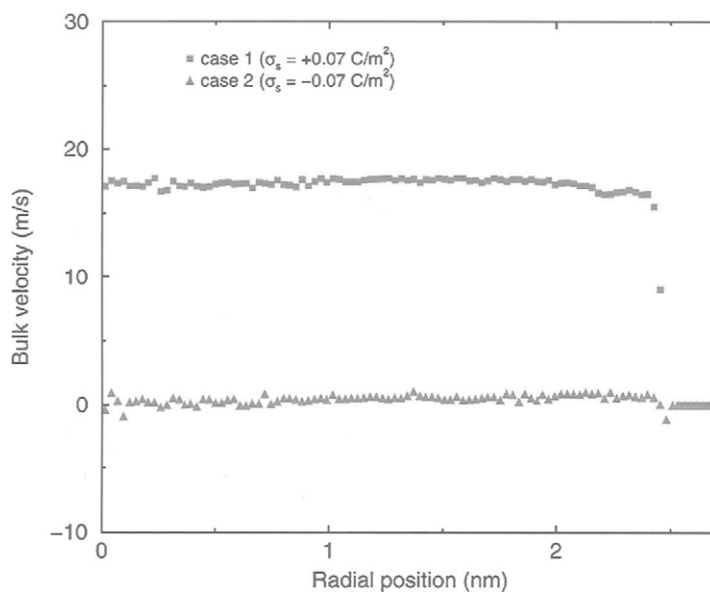


Figure 94. Bulk water velocity profile across the channel for a positively charged surface (shown as ■) and a negatively charged surface (shown as ▲). From Ref. [505]. Reprinted with permission from N. Aluru and the American Chemical Society. Copyright (2003) the American Chemical Society.

the local electrostatic interactions between ion-water and ion-charged surface atoms, and on the external electric field.

### 6.3.3. Electrical response of CNT due to electrolyte/CNT interaction

Krüger et al. [506] measured systematically the electrical responses of MWNTs for different electrolyte environments ( $\text{LiClO}_4$ ,  $\text{KCl}$ ,  $\text{KMnO}_4$ , and  $\text{H}_3\text{PO}_3$ ) as well as in different gas (ambient air, hydrogen, and oxygen) environments. As shown in Fig. 95, they considered an electrochemically gated CNT transistor circuit [507] and investigated the responses of MWNTs to different electrolytes and gate voltages. Fig. 96 compares the measured normalized resistance as a function of the electrochemical gate voltage,  $U_g$ , for three 0.01 M solutions of  $\text{LiClO}_4$ ,  $\text{KMnO}_4$ , and  $\text{H}_3\text{PO}_3$  at pH 6. The dependence of the resistance on the electrolyte shows that water alone is not the only factor that determines the doping state of the CNTs; the electrochemical environment matters. It also shows that a relatively strong oxidizing agent ( $\text{KMnO}_4$ ) shifts the Fermi level deeper into the valence band, hence oxidizing the CNT. In contrast, a strong reducing agent ( $\text{H}_3\text{PO}_3$ ) does the opposite. However, the role of water is also crucial, as is strikingly demonstrated by a measurement in a non-aqueous electrolyte, i.e.,  $\text{LiClO}_4$  in propylene carbonate (PC). The relevant  $R(U_g)$  is shown in Fig. 96. The shape of the curve is similar to the



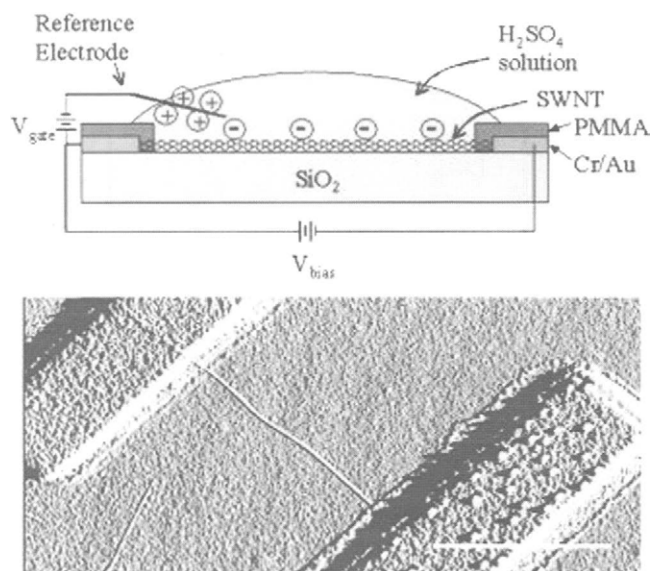


Figure 95. Schematic diagram of electrochemical gating of ions in a solution on one CNT (upper panel). AFM image of metal electrodes on a CNT (lower panel). Scale bar = 1  $\mu\text{m}$ . From Ref. [507]. Used with permission from B. B. Goldberg and the American Institute of Physics.

$\text{LiClO}_4\cdot\text{H}_2\text{O}$  case, but the peak positions differ markedly—the resistance maximum is close to  $U_g = 0$  V in PC, as compared to in water. Hence, in the non-aqueous solvent, the CNT is undoped, demonstrating that water is a prerequisite for the p-doped state of CNTs.

If the applied gate voltage is kept small ( $U_g \leq 1.0$  V), the measured samples can be recycled, i.e., flushed in water, dried and re-immersed, even in a different solvent. Hence, the oxidized state of the CNTs (p-doped state) cannot originate from the oxidation of the carbon–carbon bonds with a corresponding loss of the graphitic network, which would be irreversible and associated with a permanent resistance increase. This means that a polarized or a charged layer is specifically adsorbed on the nanotube surface. Since water is a prerequisite for the p-state in electrolytes,  $\text{H}_2\text{O}$  may adsorb in the form of an oriented dipole layer, inducing a partial charge transfer. In addition to water, anions, e.g.,  $\text{OH}^-$ ,  $\text{Cl}^-$ ,  $\text{ClO}_4^-$ , and  $\text{MnO}_4^-$ , may adsorb specifically and increase the effective p-doping.

#### 6.4. Induced voltage due to a moving electrolyte

The transport of liquid past a CNT can induce a voltage on the CNT [508,509]. Ghosh et al. [509] experimentally confirmed that the flow of a liquid on CNT bundles induces a voltage in the sample along the direction of the flow. As shown in Fig. 97, the voltage is developed in the CNT as a function of water velocity. The

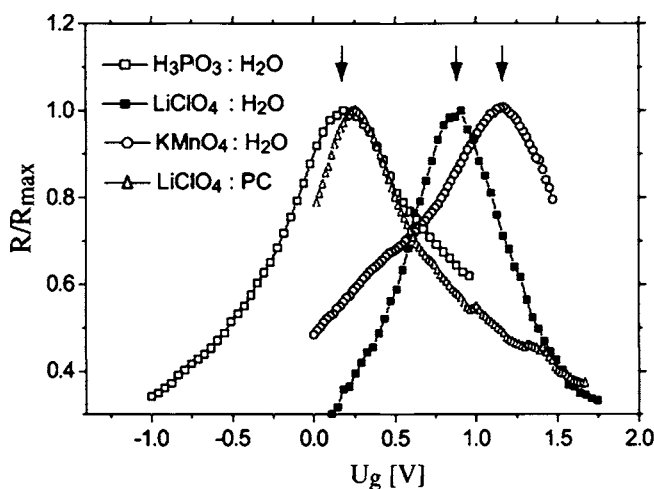


Figure 96. Comparison of electrochemical gating in different aqueous solutions ( $\text{LiClO}_4$ : ■,  $\text{KMnO}_4$ : ○, and  $\text{H}_3\text{PO}_3$ : □), all 0.01 M at pH=6. Note that the peak is shifted to the right (left) for  $\text{KMnO}_4$  ( $\text{H}_3\text{PO}_3$ ) relative to the position in  $\text{LiClO}_4$ . Also shown is a measurement in a non-aqueous electrolyte, i.e., in 0.3 M  $\text{LiClO}_4$  in PC. Reproduced from Ref. [506]. Reprinted with permission from C. Schönenberger and the Institute of Physics Publishing, Inc.

resulting voltage fits a logarithmic velocity dependence over nearly six decades of velocity. The magnitude of the voltage is sensitive to the ionic conductivity and to the polar nature of the liquid. The measurements suggest that the dominant mechanism responsible for this highly non-linear response involves a direct forcing of the free charge carriers in the nanotubes by the fluctuating Coulombic field of the liquid flowing past the nanotube. The dependence of the induced voltage on the ionic strength of the flowing liquid suggests that the mechanism involving fluctuating Coulombic fields dominates that of the phonon-mediated electron drag. The most notable feature of the experimental data is the slow, nearly saturating growth of the induced electric voltage (current) with the increasing flow velocity. Also, the electric current and the fluid were flowing in the same direction.

## 7. CHALLENGES AND OPPORTUNITIES IN THE DEVELOPMENT OF NEMS FROM CARBON NANOTUBES

The previous sections reviewed the properties of CNTs that make them attractive materials for a variety of applications, including NEMS. Progress has been made in exploring precursors to actual, functioning NEMS devices based on CNTs [20]. For example, Baughman et al. [52] studied electromechanical actuators that consisted of sheets of SWNTs. These actuators were reported to generate higher stresses than

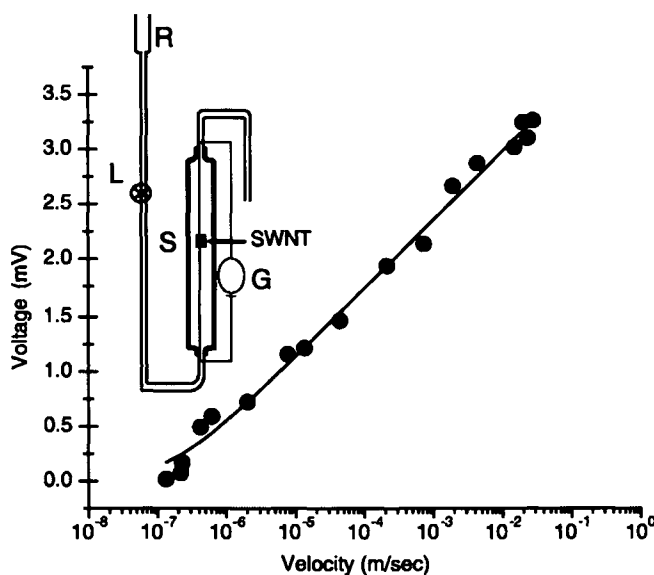


Figure 97. Variation of voltage ( $V$ ) developed as a function of velocity ( $u$ ) of water. Solid line is a fit to functional form as  $V = \alpha \log(u\beta + 1)$ , where  $\alpha$  and  $\beta$  are constants. Inset shows experimental setup where  $R$  is the reservoir,  $L$  the valve controlling the liquid flow,  $S$  the cylindrical glass flow chamber, and  $G$  the voltmeter. From Ref. [509]. Reprinted with permission from A.K. Snood and the American Association for the Advancement of Science. Copyright 2002 American Association for the Advancement of Science.

natural muscles and higher strains than ferroelectrics. The mechanism by which these actuators functioned is through expansion as a result of electrochemical double-layer charging of the system.

In another recent example, Sazonova et al. [510] examined tunable electro-mechanical oscillators created from suspended, doubly clamped CNTs in contact with gold electrodes. In particular, the electrical actuation and detection of the “guitar-string-like” oscillation modes of the CNT were detected and “tuned.” The study showed that the resonance frequency of the suspended CNT could be modulated over a wide range by varying the gate voltage and ultimately used to transducer very small forces [510]. The process therefore includes an electronic way of adjusting the “tension” of the vibrating CNT. Interestingly, the motion of the nanotube was detected using the variation in its electrical conductance as it moved through the electric field of the gate electrode. However, the CNT oscillations damp relatively quickly in vacuum and even more rapidly in the presence of low pressures of ambient gases. In a related study, Papadakis et al. [47] examined nanometer-scale resonators consisting of a MWNT used

as a torsional spring that was actuated electrostatically, as shown in Fig. 98. The deflection of the MWNT at both low frequency and on resonance was then detected optically.

Potential NEMS devices have also been designed and tested computationally. For example, Kang and Hwang [511] designed and computationally studied a NEMS device where CNTs were used as oscillators, motors, channels, and nozzles, as illustrated in Fig. 99.

Despite this considerable progress exploring and designing electromechanical and fluidic confinement properties of CNTs, there are many challenges to the routine production of fully functioning NEMS devices that remain to be overcome.

### 7.1. Understanding and controlling the physics of NEMS

While MEMS devices are now routinely manufactured, this is not the case for NEMS devices. This is due to the fact that while NEMS are three orders of magnitude

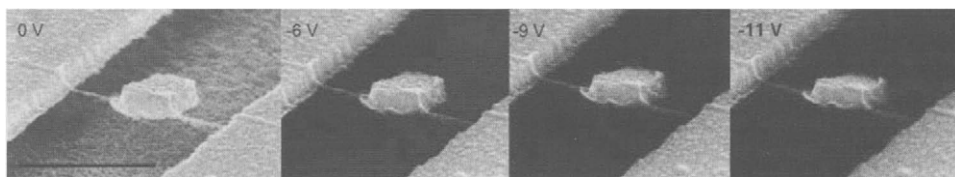


Figure 98. Electrostatic deflection of a nanometer-scale resonator device composed of an MWNT in SEM. Scale bar=1  $\mu$ m. Negative voltage is applied to the substrate that causes the darkening of the substrate in the images. From Ref. [47]. Reprinted with permission from S. Washburn and the American Physical Society. Copyright (2004) the American Physical Society.

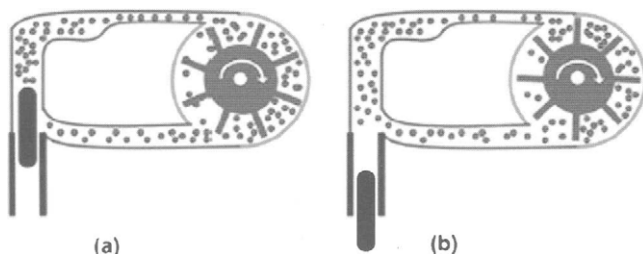


Figure 99. NEMS device composed of CNTs designed and studied using computational tools. The proposed engine, actuator, channel, nozzle, and motor are all composed of CNTs. From Ref. [511]. Reprinted with permission from H. J. Hwang and the Institute of Physics Publishing, Inc.

smaller than MEMS, they can also be orders of magnitude more complex. This is in large part due to the physics that is inherent to the nanometer scale.

For example, quantum and atomistic behavior that may not be significant at macroscopic length scales becomes significant at nanometer scales. As a result, macroscopic theories may not be directly applicable for analysis of NEMS. Thus, the development of physical theories that are accurate for NEMS is critical for rapid advances in NEMS.

In addition, interfacial phenomena are much more significant at nanometer scales than micro and macroscales. A proper understanding of interfacial issues and development of physical theories and models that can accurately describe interfacial phenomena is necessary to fully develop NEMS devices.

Furthermore, defects can play an important role in the operation of NEMS. Physical theories accounting for defects and atomically imperfect structures is important. Producing defect-tolerant devices may be ultimately more important than completely defect-free systems.

## **7.2. Developing computational methods and experiments to guide the design of NEMS**

As shown in the previous sections, computational chemical and physical methods are important and widely used in the study of CNTs and the design of NEMS. However, the development of computational tools to fully design and study NEMS devices is challenging because of the presence of several mixed-energy domains (mechanical, electrical, fluidic, chemical, biological, and optical). This is especially true in the case of heterogeneous material systems. What is needed is fast and accurate simulation tools for quantum, atomistic, mesoscopic and continuum modeling of the various components of NEMS and their application in the device. In addition, techniques are needed to seamlessly combine quantum, atomistic, mesoscopic, and continuum length scales to develop efficient multiscale simulation tools.

Despite the impressive experimental studies discussed above, there is relatively little experimental data available to assist in the development or validation of computational tools. This will undoubtedly change as more experimental studies are carried out on better characterized samples. In particular, experiments are needed to measure a variety of macroscopic properties, such as current–voltage relationships and force–displacement curves. Furthermore, experiments are needed to measure material properties, and surface and interfacial properties and phenomena in a quantitative and reproducible manner. Most importantly, canonical problems need to be developed and examined to benchmark both computational and experimental data for the purposes of NEMS development.

## **7.3. Challenges of integrated system design**

The integration of electrical, mechanical, optical, and fluidic components on a chip enables design of revolutionary integrated systems. Analogous to very large scale integration of electronic components on a chip, system-level design tools for integrated nanosystem technology can enable revolutionary advances in rapid system level design. Critical research issues that need to be addressed include the development of structured design methodologies for integrated nanosystem design,

compact or reduced-order models for nanomechanical, nanofluidic, optical, electronic, and other components, and the development of SPICE-like [512] simulation tools for integrated microsystems.

**Acknowledgments:** The authors gratefully acknowledge the support of the National Science Foundation funded Network for Computational Nanotechnology (EEC-02288390). S.B.S. thanks Mr. P. Chiu and Ms. A. Holt for their assistance assembling materials for this chapter. N.R.A. thanks Drs. J. Park, G. Li, C. Won, and S. Joseph with help on some of the material presented in this chapter.

## REFERENCES

1. S. Iijima, *Nature* **354** (1991) 56.
2. H. W. Kroto, J. R. Heath, S. C. O'Brien, R. F. Curl and R. E. Smalley, *Nature* **318** (1985) 162.
3. A. Oberlin, M. Endo and T. Koyama, *Carbon* **14** (1976) 133.
4. S. Iijima, *J. Cryst. Growth* **55** (1980) 675.
5. G. G. Tibbetts, *J. Cryst. Growth* **66** (1984) 632.
6. M. S. Dresselhaus, G. Dresselhaus and P. C. Eklund, *Science of Fullerenes and Carbon Nanotubes*, Academic Press, San Diego, 1996.
7. M. Endo, S. Iijima and M. S. Dresselhaus, *Carbon Nanotubes*, Pergamon, Tarrytown, NY, 1996.
8. T. W. Ebbesen, *Carbon Nanotubes: Preparation and Properties*, CRC Press, Boca Raton, 1997.
9. P. M. Ajayan, *Chem. Rev.* **99** (1999) 1787.
10. K. Tanaka, T. Yamabe and K. Fukui, *The Science and Technology of Carbon Nanotubes*, Elsevier, Oxford, 1999.
11. P. J. F. Harris, *Carbon Nanotubes and Related Structures: New Materials for the 21st Century*, Cambridge University Press, New York, 1999.
12. M. S. Dresselhaus, G. Dresselhaus and P. Avouris, *Carbon Nanotubes: Synthesis, Structure, Properties, and Applications*, Springer, New York, 2000.
13. L. P. Biro, *Carbon Filaments and Nanotubes: Common Origins, Differing Applications?* Kluwer, Boston, 2001.
14. S. B. Sinnott and R. Andrews, *Crit. Rev. Solid State Mater. Sci.* **26** (2001) 145.
15. M. L. Roukes, *Proceedings of Solid-State Sensor and Actuator Workshop 2000*, Hilton Head Island, SC, USA, 2000.
16. H. G. Craighead, *Science* **290** (2000) 1532.
17. M. L. Roukes, *Physical World* **14** (2001) 25.
18. Z. J. Davis, G. Abadal, O. Kuhn, O. Hansen, F. Grey and A. Boisen, *J. Vac. Sci. Technol. B*, **18** (2000) 612.
19. A. Husain, J. Hone, H. W. C. Postma, X. M. H. Huang, T. Drake, M. Barbic, A. Scherer and M. L. Roukes, *Appl. Phys. Lett.* **83** (2003) 1240.
20. R. H. Baughman, A. A. Zakhidov and W. A. d. Heer, *Science* **297** (2002) 787.
21. R. G. Ding, G. Q. Lu, Z. F. Yan and M. A. Wilson, *J. Nanosci. Nanotech.* **1** (2001) 7.
22. V. H. Crespi, *Phys. Rev. Lett.* **82** (1999) 2908.

23. J. Liu, A. G. Rinzler, H. Dai, J. H. Hafner, R. K. Bradley, P. J. Boul, A. Lu, T. Iverson, K. Shelimov, C. B. Huffman, F. Rodriguez-Macias, Y.-S. Shon, T. R. Lee, D. T. Colbert and R. E. Smalley, *Science* **280** (1998) 1253.
24. S. S. Wong, E. Joselevich, A. T. Woolley, C. L. Cheung and C. M. Lieber, *Nature* **394** (1998) 52.
25. A. Kuznetsova, J. J. T. Yates, V. V. Simonyan, J. K. Johnson, C. B. Huffman and R. E. Smalley, *J. Chem. Phys.* **115** (2001) 6691.
26. O. Stephan, P. M. Ajayan, C. Colliex, F. Cyrot-Lackmann and E. Sandre, *Phys. Rev. B* **53** (1996) 13824.
27. C.-H. Kiang, M. Endo, P. M. Ajayan, G. Dresselhaus and M. S. Dresselhaus, *Phys. Rev. Lett.* **81** (1998) 1869.
28. T. Hertel, R. E. Walkup and P. Avouris, *Phys. Rev. B* **58** (1998) 13870.
29. D. H. Robertson, D. W. Brenner and J. W. Mintmire, *Phys. Rev. B* **45** (1992) 12592.
30. G. Gao, T. Cagin and W. A. Goddard, III, *Nanotechnology* **9** (1998) 184.
31. C. T. White, D. H. Robertson and J. W. Mintmire, *Phys. Rev. B* **47** (1993) 5485.
32. P. Lambin, V. Meunier, L. Henrard and A. A. Lucas, *Carbon* **38** (2000) 1713.
33. Y. H. Lee, S. G. Kim and D. Tomanek, *Phys. Rev. Lett.* **78** (1997) 2393.
34. D.-H. Oh and Y. H. Lee, *Phys. Rev. B* **58** (1998) 7407.
35. S. Zhang, S. Zhao, J. Lu and M. Xia, *Phys. Rev. B* **61** (2000) 12693.
36. A.-L. Hamon, A. L. Marraud and B. Jouffrey, *Phil. Mag. B* **81** (2001) 1779.
37. T. W. Odom, J.-L. Huang, P. Kim, M. Ouyang and C. M. Lieber, *J. Mater. Res.* **13** (1998) 2380.
38. T. W. Odom, J.-L. Huang, P. Kim and C. M. Lieber, *J. Phys. Chem. B* **104** (2000) 2794.
39. L. C. Venema, V. Meunier, P. Lambin and C. Dekker, *Phys. Rev. B* **61** (2000) 2991.
40. R. Saito, A. Jorio, J. H. Hafner, C. M. Lieber, M. Hunter, T. McClure, G. Dresselhaus and M. S. Dresselhaus, *Phys. Rev. B* **64** (2001) 085312.
41. A. Jorio, C. Fantini, M. A. Pimenta, R. B. Capaz, G. G. Samsonidze, G. Dresselhaus, M. S. Dresselhaus, J. Jiang, N. Kobayashi, A. Grüneis and R. Saito, *Phys. Rev. B* **71** (2005) 075401.
42. M. Y. Sfeir, F. Wang, L. Huang, C.-C. Chuang, J. Hone, S. P. O'Brien, T. F. Heinz and L. E. Brus, *Science* **306** (2004) 1540.
43. R. Krupke, F. Hennrich, H. v. Löhneysen and M. M. Kappes, *Science* **301** (2003) 344.
44. M. Zheng, A. Jagota, M. S. Strano, A. P. Santos, P. Barone, S. G. Chou, B. A. Diner, M. S. Dresselhaus, R. S. Mclean, G. B. Onoa, G. G. Samsonidze, E. D. Semke, M. Usrey and D. J. Walls, *Science* **302** (2003) 1545.
45. T. W. Ebbesen, H. J. Lezec, H. Hiura, J. W. Bennett, H. F. Ghaemi and T. Thio, *Nature* **382** (1996) 54.
46. A. M. Fennimore, T. D. Yuzvinsky, W. Han, M. S. Fuhrer, J. Cumings and A. Zettl, *Nature* **424** (2003) 408.
47. S. J. Papadakis, A. R. Hall, P. A. Williams, L. Vicci, M. R. Falvo, R. Superfine and S. Washburn, *Phys. Rev. Lett.* **93** (2004) 146101.
48. A. Globus, C. W. Bauschlicher Jr., J. Han, R. L. Jaffe, C. Levit and D. Srivastava, *Nanotechnology* **9** (1998) 192.

49. J. Cumings and A. Zettl, *Science* **289** (2000) 602.
50. Q. Zheng and Q. Jiang, *Phys. Rev. Lett.* **88** (2002) 045503.
51. B. C. Regan, S. Aloni, R. O. Ritchie, U. Dahmen and A. Zettl, *Nature* **428** (2004) 924.
52. R. H. Baughman, C. Cui, A. A. Zakhidov, Z. Iqbal, J. N. Barisci, G. M. Spinks, G. G. Wallace, A. Mazzoldi, D. D. Rossi, A. G. Rinzler, O. Jaschinski, S. Roth and M. Kertesz, *Science* **284** (1999) 1340.
53. Y.-M. Chiang, D. Birnie III, and W. D. Kingery, *Physical Ceramics: Principles for Ceramic Science and Engineering*, Wiley, New York, 1997.
54. G. V. Lier, C. V. Alsenoy, V. V. Doren and P. Geerlings, *Chem. Phys. Lett.* **326** (2000) 181.
55. G. Zhou, W. Duan and B. Gu, *Chem. Phys. Lett.* **333** (2001) 344.
56. S. Reich, C. Thomsen and P. Ordejon, *Phys. Rev. B* **65** (2002) 153407.
57. E. Hernandez, C. Goze, P. Bernier and A. Rubio, *Phys. Rev. Lett.* **80** (1998) 4502.
58. J. P. Lu, *Phys. Rev. Lett.* **79** (1997) 1297.
59. P. Zhang, P. E. Lammert and V. H. Crespi, *Phys. Rev. Lett.* **81** (1998) 5346.
60. J. M. Molina, S. S. Savinsky and N. V. Khokhriakov, *J. Chem. Phys.* **104** (1996) 4652.
61. S. Ogata and Y. Shibutani, *Phys. Rev. B* **68** (2003) 165409.
62. N. Yao and V. Lordi, *J. Appl. Phys.* **84** (1998) 1939.
63. V. N. Popov and V. E. V. Doren, *Phys. Rev. B* **61** (2000) 3078.
64. C. Li and T.-W. Chou, *Compos. Sci. Technol.* **63** (2003) 1517.
65. T. Natsuki, K. Tantrakarn and M. Endo, *Carbon* **42** (2004) 39.
66. Z.-C. Tu and Z.-C. Ou-Yang, *Phys. Rev. B* **65** (2002) 233407.
67. T. Halicioglu, *Thin Solid Films* **312** (1998) 11.
68. T. Ozaki, Y. Iwasa and T. Mitani, *Phys. Rev. Lett.* **84** (2000) 1712.
69. Z. Yao, C.-C. Zhu, M. Cheng and J. Liu, *Comp. Mater. Sci.* **22** (2001) 180.
70. Y. Jin and F. G. Yuan, *Compos. Sci. Technol.* **63** (2003) 1507.
71. Y. Wang, X.-X. Wang, X.-G. Ni and Y.-A. Wu, *Comp. Mater. Sci.* **32** (2005) 141.
72. B. I. Yakobson, C. J. Brabec and J. Bernholc, *Phys. Rev. Lett.* **76** (1996) 2511.
73. Z. Xin, Z. Jianjin and O.-Y. Zhong-can, *Phys. Rev. B* **62** (2000) 13692.
74. Y. Xia, M. Zhao, Y. Ma, M. Ying, X. Liu, P. Liu and L. Mei, *Phys. Rev. B* **65** (2002) 155415.
75. M. Sammalkorpi, A. Krashenninnikov, A. Kuronen, K. Nordlund and K. Kaski, *Phys. Rev. B* **70** (2004) 245416.
76. A. G. Rinzler, personal communication, University of Florida, 2001.
77. D. Qian, W. K. Liu and R. S. Ruoff, *J. Phys. Chem. B* **105** (2001) 10753.
78. E. W. Wong, P. E. Sheehan and C. M. Lieber, *Science* **277** (1997) 1971.
79. J.-P. Salvetat, G. A. D. Briggs, J.-M. Bonard, R. R. Bacsá, A. J. Kulik, T. Stockli, N. A. Burnham and L. Forro, *Phys. Rev. Lett.* **82** (1999) 944.
80. D. A. Walters, L. M. Ericson, M. J. Casavant, J. Liu, T. Colbert, K. A. Smith and R. E. Smalley, *Appl. Phys. Lett.* **74** (1999) 3803.
81. M.-F. Yu, B. S. Files, S. Arepalli and R. S. Ruoff, *Phys. Rev. Lett.* **84** (2000) 5552.
82. M.-F. Yu, O. Lourie, M. J. Dyer, K. Moloni, T. F. Kelly and R. S. Ruoff, *Science* **287** (2000) 637.



83. M. M. J. Treacy, T. W. Ebbesen and J. M. Gibson, *Nature* **381** (1996) 678.
84. A. Krishnan, E. Dujardin, T. W. Ebbesen, P. N. Yianilos and M. M. J. Treacy, *Phys. Rev. B* **58** (1998) 14013.
85. O. Lourie and H. D. Wagner, *J. Mater. Res.* **13** (1998) 2418.
86. J. R. Wood and H. D. Wagner, *Appl. Phys. Lett.* **76** (2000) 2883.
87. B. G. Demczyk, Y. M. Wang, J. Cumings, M. Hetman, W. Han, A. Zettl and R. O. Ritchie, *Mater. Sci. Eng. A* **334** (2002) 173.
88. Y. Li, K. Wang, J. Wei, Z. Gu, Z. Wang, J. Luo and D. Wu, *Carbon* **43** (2005) 31.
89. P. Jaroenapibal, D. E. Luzzi, S. Evoy and S. Arepalli, *Appl. Phys. Lett.* **85** (2004) 4328.
90. C. Q. Sun, H. L. Bai, B. K. Tay, S. Li and E. Y. Jiang, *J. Phys. Chem. B* **107** (2003) 7544.
91. D. Sanchez-Portal, E. Artacho, J. M. Soler, A. Rubio and P. Ordejon, *Phys. Rev. B* **59** (1999) 12678.
92. C. Q. Ru, *Phys. Rev. B* **62** (2000) 9973.
93. S. Govinkdjee and J. L. Sackman, *Solid State Commun.* **110** (1999) 227.
94. L. J. Sudak, *J. Appl. Phys.* **94** (2003) 7281.
95. Y. Q. Zhang, G. R. Liu and J. S. Wang, *Phys. Rev. B* **70** (2004) 205430.
96. T. Natsuki and M. Endo, *Carbon* **42** (2004) 2147.
97. J. Tang, L.-C. Qin, T. Sasaki, M. Yudasaka, A. Matsushita and S. Iijima, *Phys. Rev. Lett.* **85** (2000) 1887.
98. W. Shen, B. Jiang, B. S. Han and S.-s. Xie, *Phys. Rev. Lett.* **84** (2000) 3634.
99. M. R. Falvo, G. J. Clary, R. M. Taylor II, V. Chi, J. F. P. Brooks, S. Washburn and R. Superfine, *Nature* **389** (1997) 582.
100. W. H. Knechtel, G. S. Dusberg, W. J. Blau, E. Hernandez and A. Rubio, *Appl. Phys. Lett.* **73** (1998) 1961.
101. S. M. Sharma, S. Karmakar, S. K. Sikka, P. V. Teredesai, A. K. Sood, A. Govindaraj and C. N. R. Rao, *Phys. Rev. B* **63** (2001) 205417.
102. J. Sandler, M. S. P. Shaffer, A. H. Windle, M. P. Halsall, M. A. Montes-Moran, C. A. Cooper and R. J. Young, *Phys. Rev. B* **67** (2003) 035417.
103. M.-F. Yu, T. Kowalewski and R. S. Ruoff, *Phys. Rev. Lett.* **85** (2000) 1456.
104. J. a. Elliott, J. K. W. Sandler, A. H. Windle, R. J. Young and M. S. P. Shaffer, *Phys. Rev. Lett.* **92** (2004) 095501.
105. X. H. Zhang, Z. F. Liu and X. G. Gong, *Phys. Rev. Lett.* **93** (2004) 149601.
106. J. A. Elliott, J. K. W. Sandler, A. H. Windle, R. J. Young and M. S. P. Shaffer, *Phys. Rev. Lett.* **93** (2004) 149602.
107. T. W. Tombler, C. Zhou, L. Alexseyev, J. Kong, H. Dai, L. Liu, C. S. Jayanthi and S. Y. Wu, *Nature* **405** (2000) 769.
108. L. Liu, C. S. Jayanthi, M. Tang, S. Y. Wu, T. W. Tombler, C. Zhou, L. Alexseyev, J. Kong and H. Dai, *Phys. Rev. Lett.* **84** (2000) 4950.
109. A. Maiti, A. Svizhenko and M. P. Anantram, *Phys. Rev. Lett.* **88** (2002) 126805.
110. S.-P. Chan, W.-L. Yim, X. G. Gong and Z.-F. Liu, *Phys. Rev. B* **68** (2003) 075404.
111. G. D. Mahan, *Phys. Rev. B* **65** (2002) 235402.
112. C.-Y. Li and T.-W. Chou, *Nanotechnology* **15** (2004) 1493.
113. H. Jiang, M.-F. Yu, B. Liu and Y. Huang, *Phys. Rev. Lett.* **93** (2004) 185501.

114. K.-H. Lee, P. Koblinski and S. B. Sinnott, *Nano Lett.* **5** (2005) 263.
115. M. A. Poggi, J. S. Boyles, L. A. Bottomley, A. W. McFarland, J. S. Colton, C. V. Nguyen, R. M. Stevens and P. T. Lillehei, *Nano Lett.* **4** (2004) 1009.
116. P. Poncharal, Z. L. Wang, D. Ugarte and W. A. de Heer, *Science* **283** (1999) 1513.
117. C. Li and T.-W. Chou, *Appl. Phys. Lett.* **84** (2004) 121.
118. B. Babic, J. Furer, S. Sahoo, S. Farhangfar and C. Schonenberger, *Nano Lett.* **3** (2003) 1577.
119. A. Volodin, D. Buntinx, M. Ashlskog, A. Fonseca, J. B. Nagy and C. V. Haesendonck, *Nano Lett.* **4** (2004) 1775.
120. A. Pantano, M. C. Boyce and D. M. Parks, *Phys. Rev. Lett.* **91** (2003) 145504.
121. M. Arroyo and T. Belytschko, *Phys. Rev. Lett.* **91** (2003) 215505.
122. D. Qian, W. K. Liu, S. Subramoney and R. S. Ruoff, *J. Nanosci. Nanotech.* **3** (2003) 185.
123. A. Garg and S. B. Sinnott, *Chem. Phys. Lett.* **295** (1998) 273.
124. D. W. Brenner, O. A. Shenderova, D. A. Areshkin, J. D. Schall and S.-J. V. Frankland, *Comp. Model. Eng. Sci.* **3** (2002) 643.
125. B. W. Smith, M. Monthioux and D. E. Luzzi, *Nature* **396** (1998) 323.
126. B. W. Smith, M. Monthioux and D. E. Luzzi, *Chem. Phys. Lett.* **315** (1999) 31.
127. R. Smith, K. Beadmore and J. Belbruno, *J. Chem. Phys.* **111** (1999) 9227.
128. B. Bouteaux, A. Claye, B. W. Smith, M. Monthioux, D. E. Luzzi and J. E. Fischer, *Chem. Phys. Lett.* **310** (1999) 21.
129. M. Monthioux, *Carbon* **40** (2002) 1809.
130. B. Ni, S. B. Sinnott, P. T. Mikulski and J. A. Harrison, *Phys. Rev. Lett.* **88** (2002) 205505.
131. A. A. Farajian and M. Mikami, *J. Phys.: Condens. Mater.* **13** (2001) 8049.
132. J. N. Coleman, W. J. Blau, A. B. Dalton, E. Munoz, S. Collins, B. G. Kim, J. Razal, M. Selvidge, G. Veiuro and R. H. Baughman, *Appl. Phys. Lett.* **82** (2003) 1682.
133. H. Trotter, R. Phillips, Y. Hu, B. Ni, S. B. Sinnott, P. Mikulski and J. A. Harrison, *J. Nanosci. Nanotech.* **5** (2005) 536.
134. D. Danailov, P. Koblinski, S. Nayak and P. M. Ajayan, *J. Nanosci. Nanotech.* **2** (2002) 503.
135. H. Dai, J. H. Hafner, A. G. Rinzler, D. T. Colbert and R. E. Smalley, *Nature* **384** (1996) 147.
136. S. B. Arnason, A. G. Rinzler, Q. Hudspeth and A. F. Hebard, *Appl. Phys. Lett.* **75** (1999) 2842.
137. C. L. Cheung, J. H. Hafner, T. W. Odom, K. Kim and C. M. Lieber, *Appl. Phys. Lett.* **76** (2000) 3136.
138. S. S. Wong, A. T. Woolley, T. W. Odom, J.-L. Huang, P. Kim, D. V. Vezhenov and C. M. Lieber, *Appl. Phys. Lett.* **73** (1998) 3465.
139. G. Nagy, M. Levy, R. Scarmozzino, J. R. M. Osgood, H. Dai, R. E. Smalley, C. A. Michaels, G. W. Flynn and G. F. McLane, *Appl. Phys. Lett.* **73** (1998) 529.
140. G. Nagy, M. Levy, R. Scarmozzino, J. R. M. Osgood, H. Dai, R. E. Smalley, C. A. Michaels, E. T. Sevy, G. W. Flynn and G. F. McLane, *Appl. Phys. Lett.* **73** (1998) 1448.

141. H. Dai, N. Franklin and J. Han, *Appl. Phys. Lett.* **73** (1998) 1508.
142. J. A. Harrison, S. J. Stuart, D. H. Robertson and C. T. White, *J. Phys. Chem. B* **101** (1997) 9682.
143. N. Yao and V. Lordi, *Phys. Rev. B* **58** (1998) 12649.
144. A. Garg, J. Han and S. B. Sinnott, *Phys. Rev. Lett.* **81** (1998) 2260.
145. F. N. Dzegilenko, D. Srivastava and S. Saini, *Nanotechnology* **10** (1999) 253.
146. P. Kim and C. M. Lieber, *Science* **286** (1999) 2148.
147. J. Tersoff and R. S. Ruoff, *Phys. Rev. Lett.* **73** (1994) 676.
148. C. Li and T.-W. Chou, *Phys. Rev. B* **69** (2004) 073401.
149. M.-F. Yu, T. Kowalewski and R. S. Ruoff, *Phys. Rev. Lett.* **86** (2001) 87.
150. C. Y. Wang, C. Q. Ru and A. Mioduchowski, *J. Nanosci. Nanotech.* **3** (2003) 199.
151. R. Gao, Z. L. Wang, Z. Bai, W. A. d. Heer, L. Dai and M. Gao, *Phys. Rev. Lett.* **85** (2000) 622.
152. N. Chandra, S. Namilae and C. Shet, *Phys. Rev. B* **69** (2004) 094101.
153. Y. Miyamoto, S. Berber, M. Yoon, A. Rubio and D. Tomanek, *Chem. Phys. Lett.* **392** (2004) 209.
154. Q. Zhao, M. B. Nardelli and J. Bernholc, *Phys. Rev. B* **65** (2002) 144105.
155. D. Orlikowski, M. B. Nardelli, J. Bernholc and C. Roland, *Phys. Rev. Lett.* **83** (1999) 4132.
156. C. F. Cornwell and L. T. Wille, *J. Chem. Phys.* **109** (1998) 763.
157. T. Kuzumaki, S. Kitakata, K. Enomoto, T. Yasuhara, N. Ohtake and Y. Mitsuda, *Carbon* **42** (2004) 2343.
158. B. I. Yakobson, M. P. Campbell, C. J. Brabec and J. Bernholc, *Comp. Mater. Sci.* **8** (1997) 341.
159. M. B. Nardelli, B. I. Yakobson and J. Bernholc, *Phys. Rev. B* **57** (1998) R4277.
160. B. I. Yakobson, *Appl. Phys. Lett.* **72** (1998) 918.
161. T. Xiao, Y. Ren and K. Liao, *Nano Lett.* **4** (2004) 1139.
162. M. B. Nardelli, B. I. Yakobson and J. Bernholc, *Phys. Rev. Lett.* **81** (1998) 4656.
163. M. A. L. Marques, H. E. Troiani, M. Miki-Yoshida, M. Jose-Yacamán and A. Rubio, *Nano Lett.* **4** (2004) 811.
164. H. E. Troiani, M. Miki-Yoshida, G. A. Camacho-Bragado, M. A. L. Marques, A. Rubio, J. A. Ascencio and M. Jose-Yacamán, *Nano Lett.* **3** (2003) 751.
165. T. Belytschko, S. P. Xiao, G. C. Schatz and R. S. Ruoff, *Phys. Rev. B* **65** (2002) 235430.
166. T. Dumitrica and B. I. Yakobson, *Appl. Phys. Lett.* **84** (2004) 2775.
167. C. Wei, K. Cho and D. Srivastava, *Appl. Phys. Lett.* **82** (2003) 2512.
168. C. Wei, K. Cho and D. Srivastava, *Phys. Rev. B* **67** (2003) 115407.
169. K. M. Liew, C. H. Wong, X. Q. He, M. J. Tan and S. A. Meguid, *Phys. Rev. B* **69** (2004) 115429.
170. P. A. Williams, S. J. Papadakis, A. M. Patel, M. R. Falvo, S. Washburn and R. Superfine, *Phys. Rev. Lett.* **89** (2002) 255502.
171. M.-F. Yu, B. I. Yakobson and R. S. Ruoff, *J. Phys. Chem. B* **104** (2000) 8764.
172. G. L. Hwang and K. C. Hwang, *Nano Lett.* **1** (2001) 435.

173. C. Daraio, V. F. Nesterenko, J. F. Aubuchon and S. Jin, *Nano Lett.* **4** (2004) 1915.
174. S. B. Legoas, V. R. Coluci, S. F. Braga, P. Z. Coura, S. O. Dantas and D. S. Galvao, *Phys. Rev. Lett.* **90** (2003) 055504.
175. J. L. Rivera, C. McCabe and P. T. Cummings, *Nano Lett.* **3** (2003) 1001.
176. J. L. Rivera, C. McCabe and P. T. Cummings, *Nanotechnology* **16** (2005) 186.
177. W. Guo, Y. Guo, H. Gao, Q. Zheng and W. Zhong, *Phys. Rev. Lett.* **91** (2003) 125501.
178. C. F. Cornwell and L. T. Wille, *Solid State Commun.* **101** (1997) 555.
179. S. Iijima, C. Brabec, A. Maiti and J. Bernholc, *J. Chem. Phys.* **104** (1996) 2089.
180. D. Qian, W. K. Liu and R. S. Ruoff, *Compos. Sci. Technol.* **63** (2003) 1561.
181. A. Maiti, *Chem. Phys. Lett.* **331** (2000) 21.
182. D. Srivastava, M. Menon and K. Cho, *Phys. Rev. Lett.* **83** (1999) 2973.
183. A. Buldum and J. P. Lu, *Phys. Rev. Lett.* **83** (1999) 5050.
184. J. D. Schall and D. W. Brenner, *Mol. Simulat.* **25** (2000) 73.
185. M. R. Falvo, J. Steele, R. M. Taylor II and R. Superfine, *Phys. Rev. B* **62** (2000) R10664.
186. K. Miura, T. Takagi, S. Kamiya, T. Sahashi and M. Yamauchi, *Nano Lett.* **1** (2001) 161.
187. B. Ni and S. B. Sinnott, *Surf. Sci.* **487** (2001) 87.
188. B. Ni and S. B. Sinnott, *Nanotubes and Related Materials*, Materials Research Society, Pittsburgh, PA, 2001, pp. A17.3.1–A17.3.5.
189. P. L. Dickrell, W. G. Sawyer, D. W. Hahn, S. B. Sinnott, B. Yurdumakan, A. Dhinojwala, N. R. Raravikar, L. S. Schadler and P. M. Ajayan, *Tribol. Lett.* **18** (2005) 59.
190. J. W. Mintmire, B. I. Dunlap and C. T. White, *Phys. Rev. Lett.* **68** (1992) 631.
191. R. E. Peierls, *Quantum Theory of Solids*, Oxford University Press, New York, 1955.
192. W. P. Su, J. R. Schrieffer and A. J. Heeger, *Phys. Rev. Lett.* **42** (1979) 1698.
193. W. P. Su, J. R. Schrieffer and A. J. Heeger, *Phys. Rev. B* **22** (1980) 2099.
194. R. Saito, M. Fujita, G. Dresselhaus and M. S. Dresselhaus, *Appl. Phys. Lett.* **60** (1992) 2204.
195. N. Hamada, S.-I. Sawada and A. Oshiyama, *Phys. Rev. Lett.* **68** (1992) 1579.
196. S. J. Tans, M. H. Devoret, H. Dai, A. Thess, R. E. Smalley, L. J. Geerligs and C. Dekker, *Nature* **386** (1997) 474.
197. J. W. G. Wildöer, L. C. Venema, A. G. Rinzler, R. E. Smalley and C. Dekker, *Nature* **391** (1998) 59.
198. L. C. Venema, J. W. G. Wildoer, J. W. Janssen, S. J. Tans, H. L. J. T. Tuinstra, L. P. Kouwenhoven and C. Dekker, *Science* **283** (1999) 52.
199. H. Dai, J. Kong, C. Zhou, N. Franklin, T. Tombler, A. Cassell, S. Fan and M. Chapline, *J. Phys. Chem. B* **103** (1999) 11246.
200. C. T. White and T. N. Todorov, *Nature* **393** (1998) 240.
201. W. Liang, *Nature* **411** (2001) 665.
202. T. Ando, *Solid State Commun.* **127** (2003) 69.

203. P. Avouris, *Chem. Phys.* **281** (2002) 429.
204. L. P. Biro, S. Lazarescu, P. Lambin, P. A. Thiry, A. Fonseca, J. B. Nagy and A. A. Lucas, *Phys. Rev. B* **56** (1997) 12490.
205. X. Zhou, H. Chen and O.-Y. Zhong-can, *J. Phys.: Condens. Mater.* **13** (2001) L635.
206. A. Rochefort, D. R. Salahub and P. Avouris, *J. Phys. Chem. B* **103** (1999) 641.
207. L. Liu, C. S. Jayanthi and S. Y. Wu, *Chem. Phys. Lett.* **357** (2002) 91.
208. J. Jiang, J. Dong and D. Y. Xing, *Phys. Rev. B* **65** (2002) 245418.
209. A. Javey, J. Guo, M. Paulsson, Q. Wang, D. Mann, M. Lundstrom and H. Dai, *Phys. Rev. Lett.* **92** (2004) 106804.
210. P. J. de Pablo, C. Gomez-Navarro, J. Colchero, P. A. Serena, J. Gomez-Herrero and A. M. Baro, *Phys. Rev. Lett.* **88** (2002) 036804.
211. A. N. Andriotis, M. Menon and L. Chernozatonskii, *Nano Lett.* **3** (2003) 131.
212. S. J. Wind, J. Appenzeller and P. Avouris, *Phys. Rev. Lett.* **91** (2003) 058301.
213. A. Bachtold, M. S. Fuhrer, S. Plyasunov, M. Forero, E. H. Anderson, A. Zettl and P. L. McEuen, *Phys. Rev. Lett.* **84** (2000) 6082.
214. S. Li, Z. Yu, C. Rutherglen and P. J. Burke, *Nano Lett.* **4** (2004) 2003.
215. J. W. Park, J. Kim, J.-O. Lee, K. C. Kang, J.-J. Kim and K.-H. Yoo, *Appl. Phys. Lett.* **80** (2002) 133.
216. P. J. de Pablo, S. Howell, S. Crittenden, B. Walsh, E. Graugnard and R. Reifenberger, *Appl. Phys. Lett.* **75** (1999) 3941.
217. V. V. Belavin, L. G. Bulusheva and A. V. Okotrub, *Int. J. Quantum Chem.* **96** (2004) 239.
218. P. G. Collins, H. Bando and A. Zettl, *Nanotechnology* **9** (1998) 153.
219. L. Chico, V. H. Crespi, L. X. Benedict, S. G. Louie and M. L. Cohen, *Phys. Rev. Lett.* **76** (1996) 971.
220. M. B. Nardelli and J. Bernholc, *Phys. Rev. B* **60** (1999) R16338.
221. S. Iijima, T. Ichihashi and Y. Ando, *Nature* **356** (1992) 776.
222. B. I. Dunlap, *Phys. Rev. B* **49** (1994) 5643.
223. R. Saito, G. Dresselhaus and M. S. Dresselhaus, *Phys. Rev. B* **53** (1996) 2044.
224. J.-C. Charlier, T. W. Ebbesen and P. Lambin, *Phys. Rev. B* **53** (1996) 11108.
225. L. Grigorian, G. U. Sumanasekera, A. L. Loper, S. Fang, J. L. Allen and P. C. Eklund, *Phys. Rev. B* **58** (1998) R4195.
226. R. S. Lee, H. J. Kim, J. E. Fischer, J. Lefebvre, M. Radosavljevic, J. Hone and A. T. Johnson, *Phys. Rev. B* **61** (2000) 4526.
227. M. Bockrath, J. Hone, A. Zettl, P. L. McEuen, A. G. Rinzler and R. E. Smalley, *Phys. Rev. B* **61** (1999) R10606.
228. R. Martel, H. R. Shea and P. Avouris, *J. Phys. Chem. B* **103** (1999) 7551.
229. V. Derycke, R. Martel, J. Appenzeller and P. Avouris, *Nano Lett.* **1** (2001) 453.
230. V. Derycke, R. Martel, J. Appenzeller and P. Avouris, *Appl. Phys. Lett.* **80** (2002) 2773.
231. J. Park and P. L. McEuen, *Appl. Phys. Lett.* **79** (2001) 1363.
232. K. Suenaga, C. Colliex, N. Demoncey, A. Loiseau, H. Pascard and F. Willaime, *Science* **278** (1997) 653.
233. Y. Zhang, H. Gu, K. Suenaga and S. Iijima, *Chem. Phys. Lett.* **279** (1997) 264.

- 234. D. Golberg, Y. Bando, M. Eremets, K. Takemura, K. Kurashima and H. Yusa, *Appl. Phys. Lett.* **69** (1996) 2045.
- 235. D. Yu, X. S. Sun, C. S. Lee, I. Bello, S. T. Lee, H. D. Gu, K. M. Leung, G. W. Zhou, Z. F. Dong and Z. Zheng, *Appl. Phys. Lett.* **72** (1998) 1966.
- 236. A. Rubio, J. L. Corkill and M. L. Cohen, *Phys. Rev. B* **49** (1994) 5081.
- 237. N. G. Chopra, R. J. Luyken, K. Cherrey, V. H. Crespi, M. L. Cohen, S. G. Louie and A. Zettl, *Science* **269** (1995) 966.
- 238. A. Loiseau, F. Willaime, N. Demoncy, G. Hug and H. Pascard, *Phys. Rev. Lett.* **76** (1996) 4737.
- 239. W. Han, Y. Bando, K. Kurashima and T. Sato, *Appl. Phys. Lett.* **73** (1998) 3085.
- 240. J. Cumings and A. Zettl, *Chem. Phys. Lett.* **316** (2000) 211.
- 241. S. Latil, S. Roche, D. Mayou and J.-C. Charlier, *Phys. Rev. Lett.* **92** (2004) 256805.
- 242. R. S. Lee, H. J. Kim, J. E. Fischer, A. Thess and R. E. Smalley, *Nature* **388** (1997) 255.
- 243. F. Leonard and J. Tersoff, *Phys. Rev. Lett.* **83** (1999) 5174.
- 244. B. Wei, R. Spolenak, P. Kohler-Redich, M. Ruhle and E. Arzt, *Appl. Phys. Lett.* **74** (1999) 3149.
- 245. K. Liu, P. Avouris, R. Martel and W. K. Hsu, *Phys. Rev. B* **63** (2001) 161404.
- 246. S. B. Sinnott, *J. Nanosci. Nanotech.* **2** (2002) 113.
- 247. D. W. Brenner, J. D. Schall, J. P. Mewkill, O. A. Shenderova and S. B. Sinnott, *J. Br. Inter. Soc.* **51** (1998) 137.
- 248. G. Seifert, T. Kohler and T. Frauenheim, *Appl. Phys. Lett.* **77** (2000) 1313.
- 249. M. S. Strano, C. B. Huffman, V. C. Moore, M. J. O'Connell, E. H. Haroz, J. Hubbard, M. Miller, K. Rialon, C. Kittrell, S. Ramesh, R. H. Hauge and R. E. Smalley, *J. Phys. Chem. B* **107** (2003) 6979.
- 250. Z. Chen, X. Du, M.-H. Du, C. D. Rancken, H.-P. Cheng and A. G. Rinzler, *Nano Lett.* **3** (2003) 1245.
- 251. H. W. C. Postma, M. d. Jonge, Z. Yao and C. Dekker, *Phys. Rev. B* **62** (2000) R10653.
- 252. Y.-G. Yoon, M. S. C. Mazzoni, H. J. Choi, J. Ihm and S. G. Louie, *Phys. Rev. Lett.* **86** (2001) 688.
- 253. M. Ouyang, J.-L. Huang, C. L. Cheung and C. M. Lieber, *Science* **291** (2001) 97.
- 254. M. Stadermann, S. J. Papadakis, M. R. Falvo, J. Novak, E. Snow, Q. Fu, J. Liu, Y. Fridman, J. J. Boland, R. Superfine and S. Washburn, *Phys. Rev. B* **69** (2004) 201402(R).
- 255. M. Menon and D. Srivastava, *Phys. Rev. Lett.* **79** (1997) 4453.
- 256. M. Menon and D. Srivastava, *J. Mater. Res.* **13** (1998) 2357.
- 257. A. N. Andriotis, M. Menon, D. Srivastava and L. Chernozatonskii, *Appl. Phys. Lett.* **79** (2001) 266.
- 258. A. N. Andriotis, M. Menon, D. Srivastava and L. Chernozatonskii, *Phys. Rev. Lett.* **87** (2001) 066802.
- 259. A. N. Andriotis, M. Menon, D. Srivastava and L. Chernozatonskii, *Phys. Rev. B* **65** (2002) 165416.

- 260. V. Meunier, M. B. Nardelli, J. Bernholc, T. Zacharia and J.-C. Charlier, *Appl. Phys. Lett.* **81** (2002) 5234.
- 261. C. Papadopoulos, A. Rakitin, J. Li, A. S. Vedeneev and J. M. Xu, *Phys. Rev. Lett.* **85** (2000) 3476.
- 262. B. C. Satishkumar, P. J. Thomas, A. Govindaraj and C. N. R. Rao, *Appl. Phys. Lett.* **77** (2000) 2530.
- 263. M. Terrones, F. Banhart, N. Grobert, J.-C. Charlier, H. Terrones and P. M. Ajayan, *Phys. Rev. Lett.* **89** (2002) 75505.
- 264. I. Jang, S. B. Sinnott, D. Danailov and P. Keblinski, *Nano Lett.* **4** (2004) 109.
- 265. F. Cleri, P. Keblinski, I. Jang and S. B. Sinnott, *Phys. Rev. B* **69** (2004) 121412.
- 266. S. Dag, R. T. Senger and S. Ciraci, *Phys. Rev. B* **70** (2004) 205407.
- 267. A. Buldum and J. P. Lu, *Phys. Rev. B* **63** (2001) 161403.
- 268. J. Tersoff, *Appl. Phys. Lett.* **74** (1999) 2122.
- 269. P. J. de Pablo, E. Graugnard, B. Walsh, R. P. Andres, S. Datta and R. Reifengerger, *Appl. Phys. Lett.* **74** (1999) 323.
- 270. S. Heinze, J. Tersoff, R. Martel, V. Derycke, J. Appenzeller and P. Avouris, *Phys. Rev. Lett.* **89** (2002) 106801.
- 271. S. Dag, O. Gulseren, S. Ciraci and T. Yildirim, *Appl. Phys. Lett.* **83** (2003) 3180.
- 272. A. Javey, J. Guo, Q. Wang, M. Lundstrom and H. Dai, *Nature* **424** (2003) 654.
- 273. Y. Xue and M. A. Ratner, *Phys. Rev. B* **69** (2004) 161402(R).
- 274. Y. Xue and M. A. Ratner, *Nanotechnology* **16** (2005) 5.
- 275. Y. Yaish, J.-Y. Park, S. Rosenblatt, V. Sazonova, M. Brink and P. L. McEuen, *Phys. Rev. Lett.* **92** (2004) 046401.
- 276. B. Shan and K. Cho, *Phys. Rev. B* **70** (2004) 233405.
- 277. M. P. Anantram, *Appl. Phys. Lett.* **78** (2001) 2055.
- 278. Y. Xue and M. A. Ratner, *Appl. Phys. Lett.* **83** (2003) 2429.
- 279. C. Zhou, J. Kong and H. Dai, *Appl. Phys. Lett.* **76** (2000) 1597.
- 280. T. Nakanishi, A. Bachtold and C. Dekker, *Phys. Rev. B* **66** (2002) 073307.
- 281. A. Javey, J. Guo, D. B. Farmer, Q. Wang, D. Wang, R. G. Gordon, M. Lundstrom and H. Dai, *Nano Lett.* **4** (2004) 447.
- 282. C.-J. Park, Y.-H. Kim and K. J. Chang, *Phys. Rev. B* **60** (1999) 10656.
- 283. C. Kilic, S. Ciraci, O. Gulseren and T. Yildirim, *Phys. Rev. B* **62** (2000) R16345.
- 284. M. S. C. Mazzoni and H. Chacham, *Appl. Phys. Lett.* **76** (2000) 1561.
- 285. O. Gulseren, T. Yildirim, S. Ciraci and C. Kilic, *Phys. Rev. B* **65** (2002) 155410.
- 286. P. E. Lammert, P. Zhang and V. H. Crespi, *Phys. Rev. Lett.* **84** (2000) 2453.
- 287. J.-Q. Lu, J. Wu, W. D. Duan, F. Liu, B.-F. Zhu and B.-L. Gu, *Phys. Rev. Lett.* **90** (2003) 156601.
- 288. J.-Q. Lu, J. Wu, W. Duan and B.-L. Gu, *Appl. Phys. Lett.* **84** (2004) 4203.
- 289. M. Ouyang, J.-L. Huang, C. L. Cheung and C. M. Lieber, *Science* **292** (2001) 702.
- 290. A. Hassanien and M. Tokumoto, *Carbon* **42** (2004) 2649.
- 291. R. Heyd, A. Charlier and E. McRae, *Phys. Rev. B* **55** (1997) 6820.
- 292. L. Yang, M. P. Anantram, J. Han and J. P. Lu, *Phys. Rev. B* **60** (1999) 13874.
- 293. L. Yang and J. Han, *Phys. Rev. Lett.* **85** (2000) 154.
- 294. J. W. Ding, X. H. Yan, J. X. Cao, D. L. Wang, Y. Tang and Q. B. Yang, *J. Phys.: Condens. Mater.* **15** (2003) L439.

295. J. Cao, Q. Wang and H. Dai, *Phys. Rev. Lett.* **90** (2003) 157601.
296. J. Fraden, *Handbook of Modern Sensors*, Springer-Verlag, New York, 1996.
297. E. D. Minot, Y. Yaish, V. Sazonova, J.-Y. Park, M. Brink and P. L. McEuen, *Phys. Rev. Lett.* **90** (2003) 156401.
298. S. Paulson, M. R. Falvo, N. Snider, A. Heiser, T. Hudson, A. Seeger, R. M. Taylor, R. Superfine and S. Washburn, *Appl. Phys. Lett.* **75** (1999) 2937.
299. M. S. C. Mazzoni and H. Chacham, *Phys. Rev. B* **61** (2000) 7312.
300. A. A. Farajian, B. I. Yakobson, H. Mizuseki and Y. Kawazoe, *Phys. Rev. B* **67** (2003) 205423.
301. A. Rochefort, D. R. Salahub and P. Avouris, *Chem. Phys. Lett.* **297** (1998) 45.
302. A. Rochefort, P. Avouris, F. Lesage and D. R. Salahub, *Phys. Rev. B* **60** (1999) 13824.
303. A. Hansson, M. Paulsson and S. Stafstrom, *Phys. Rev. B* **62** (2000) 7639.
304. D. Tekleab, D. L. Carroll, G. G. Samsonidze and B. I. Yakobson, *Phys. Rev. B* **64** (2001) 035419.
305. T. Kuzumaki and Y. Mitsuda, *Appl. Phys. Lett.* **85** (2004) 1250.
306. D.-H. Kim and K. J. Chang, *Phys. Rev. B* **66** (2002) 155402.
307. S. Sapmaz, Y. M. Blanter, L. Gurevich and H. S. J. van der Zant, *Phys. Rev. B* **67** (2003) 235414.
308. Y. N. Gartstein, A. A. Zakhidov and R. H. Baughman, *Phys. Rev. Lett.* **89** (2002) 045503.
309. M. Verissimo-Alves, B. Koiller, H. Chacham and R. B. Capaz, *Phys. Rev. B* **67** (2003) 161401.
310. W. Guo and Y. Guo, *Phys. Rev. Lett.* **91** (2003) 115501.
311. N. Koratkar, A. Modi, J. Kim, B. Q. Wei, R. Vajtai, S. Talapatra and P. M. Ajayan, *J. Nanosci. Nanotech.* **4** (2004) 69.
312. P. G. Collins, M. S. Arnold and P. Avouris, *Science* **292** (2001) 706.
313. G. Y. Tseng and J. C. Ellenbogen, *Science* **294** (2001) 1293.
314. G. A. J. Amaratunga, *Science* **297** (2002) 1657.
315. R. F. Service, *Science* **302** (2003) 1310.
316. M. Stoneham, *Nat. Mater.* **3** (2004) 3.
317. T. W. Tomblor, C. Zhou, J. Kong and H. Dai, *Appl. Phys. Lett.* **76** (2000) 2412.
318. S. Rosenblatt, Y. Yaish, J. Park, J. Gore, V. Sazonova and P. L. McEuen, *Nano Lett.* **2** (2002) 869.
319. M. S. Dresselhaus, G. Dresselhaus, J.-C. Charlier and E. R. Hernández, *Phil. Trans. R. Soc. Lond. A* **362** (2004) 2065.
320. L. Benedict, S. G. Louie and M. L. Cohen, *Solid State Commun.* **100** (1996) 177.
321. J. Hone, B. Batlogg, Z. Benes, A. T. Johnson and J. E. Fischer, *Science* **289** (2000) 1730.
322. W. Yi, L. Lu, D.-L. Zhang, Z. W. Pan and S. S. Xia, *Phys. Rev. B* **59** (1999) 9015.
323. N. W. Ashcroft and N. D. Mermin, *Solid State Physics*, Harcourt Brace, New York, 1976.
324. B. T. Kelly, *Physics of Graphite*, Applied Science, New Jersey, 1981.
325. D. Li, *Thermal transport in individual nanowires and nanotubes*, PhD Thesis, University of California, 2002.



- 326. J. P. Small, L. Shi and P. Kim, *Solid State Commun.* **127** (2003) 181.
- 327. J. Heremans and C. P. Beetz, *Phys. Rev. B* **32** (1985) 1981.
- 328. P. Kim, L. Shi, A. Majumdar and P. L. McEuen, *Phys. Rev. Lett.* **87** (2001) 215502.
- 329. M. A. Osman and D. Srivastava, *Nanotechnology* **12** (2001) 21.
- 330. T. Che, T. Cagin and W. A. Goddard III, *Nanotechnology* **11** (2000) 65.
- 331. S. Berber, Y.-K. Kwon and D. Tomanek, *Phys. Rev. Lett.* **84** (2000) 4613.
- 332. W. Zhang, Z. Zhu, F. Wang, T. Wang, L. Sun and Z. Wang, *Nanotechnology* **15** (2004) 936.
- 333. S. Maruyama, *Physica B* **323** (2002) 193.
- 334. Z. Yao, J.-S. Wang, B. Li and G.-R. Liu, *Phys. Rev. B* **71** (2005) 085417.
- 335. J. F. Moreland, J. B. Freund and G. Chen, Abstract submitted for MECT-2002, 2002.
- 336. S. Shenogin, A. Bodapati, L. Xue, R. Ozisik and P. Keblinski, *Appl. Phys. Lett.* **85** (2004) 2229.
- 337. E. G. Noya, D. Srivastava and L. A. Chernozatonskii, *Phys. Rev. B* **70** (2004) 115416.
- 338. J. Vavro, M. C. Llaguno, B. C. Satishkumar, D. E. Luzzi and J. E. Fischer, *Appl. Phys. Lett.* **80** (2002) 1450.
- 339. J. Vavro, M. C. Llaguno, B. C. Satishkumar, R. Haggenmueller, K. I. Winey, D. E. Luzzi, J. E. Fischer, G. U. Sumanasekera and P. C. Eklund, in *Proceedings of AIP*, Eds., H. Kuzmany, J. Fink, M. Mehring and S. Roth, AIP Conference Proceedings, Vol. 633, 2002, 127pp.
- 340. S. T. Huxtable, D. G. Cahill, S. Shenogin, L. Xue, R. Ozisik, P. Barone, M. Usrey, M. S. Strano, G. Siddons, M. Shim and P. Keblinski, *Nat. Mater.* **2** (2003) 731.
- 341. Y. Maniwa, R. Fujiwara, H. Kira, H. Kataura, S. Suzuki, Y. Achiba, E. Nishibori, M. Takata, M. Sakata, A. Fujiwara and H. Suematsu, *Phys. Rev. B* **64** (2001) 241402.
- 342. K. Bradley, S.-H. Jhi, P. G. Collins, J. Hone, M. L. Cohen, S. G. Louie and A. Zettl, *Phys. Rev. Lett.* **85** (2000) 4361.
- 343. G. G. Samsonidze, R. Saito, A. Jorio, A. G. S. Filho, A. Grüneis, M. A. Pimenta, G. Dresselhaus and M. S. Dresselhaus, *Phys. Rev. Lett.* **90** (2003) 027403.
- 344. G. G. Samsonidze, R. Saito, A. Jorio, M. A. Pimenta, A. G. S. Filho, A. Grüneis, G. Dresselhaus and M. S. Dresselhaus, *J. Nanosci. Nanotech.* **3** (2003) 431.
- 345. S. Polarz and B. Smarsly, *J. Nanosci. Nanotech.* **2** (2002) 581.
- 346. H.-M. Cheng, Q.-H. Yang and C. Liu, *Carbon* **39** (2001) 1447.
- 347. G. W. Crabtree, M. S. Dresselhaus and M. V. Buchanan, *Phys. Today*, December 2004, p. 39.
- 348. C. Zandonella, *Nature* **410** (2001) 734.
- 349. A. C. Dillon, K. M. Jones, T. A. Bekkedahl, C. K. Kiang, D. S. Bethune and M. J. Heben, *Nature* **386** (1997) 377.
- 350. C. Liu, Y. Y. Fan, M. Liu, H. T. Cong, H. M. Cheng and M. S. Dresselhaus, *Science* **286** (1999) 1127.
- 351. Y. Ye, C. C. Ahn, C. Witham, B. Fultz, J. Liu, A. G. Rinzler, D. Colbert, K. A. Smith and R. E. Smalley, *Appl. Phys. Lett.* **74** (1999) 2307.

- 352. X. B. Wu, P. Chen, J. Lin and K. L. Tan, *Int. J. Hydrogen Energ.* **25** (2000) 261.
- 353. P. Chen, X. Wu, J. Lin and K. L. Tan, *Science* **285** (1999) 91.
- 354. Y. T. Yang, *Carbon* **38** (2000) 623.
- 355. C. M. Brown, T. Yildirim, D. A. Neumann, M. J. Heben, T. Gennett, A. C. Dillon, J. L. Alleman and J. E. Fischer, *Chem. Phys. Lett.* **329** (2000) 311.
- 356. Q. Wang, S. R. Challa, D. S. Sholl and J. K. Johnson, *Phys. Rev. Lett.* **82** (1999) 956.
- 357. V. V. Simonyan, P. Diep and J. K. Johnson, *J. Chem. Phys.* **111** (1999) 9778.
- 358. M. Rzepka, P. Lamp and M. A. d. I. Casa-Lillo, *J. Phys. Chem. B* **102** (1998) 10894.
- 359. Q. Wang and J. K. Johnson, *J. Phys. Chem. B* **103** (1999) 4809.
- 360. Q. Wang and J. K. Johnson, *J. Chem. Phys.* **110** (1999) 577.
- 361. Y. F. Yin, T. Mays and B. McEnaney, *Langmuir* **16** (2000) 10521.
- 362. S. M. Lee and Y. H. Lee, *Appl. Phys. Lett.* **76** (2000) 2877.
- 363. M. S. Dresselhaus, K. A. Williams and P. C. Eklund, *MRS Bull.* **24** (1999) 45.
- 364. P. A. Gordon and R. B. Saeger, *Ind. Eng. Chem. Res.* **38** (1999) 4647.
- 365. F. Darkrim and D. Levesque, *J. Chem. Phys.* **109** (1998) 4981.
- 366. F. Darkrim and D. Levesque, *J. Phys. Chem. B* **104** (2000) 6773.
- 367. M. Muris, N. Dufau, M. Bienfait, N. Dupont-Pavlovsky, Y. Grillet and J. P. Palmari, *Langmuir* **16** (2000) 7019.
- 368. S. E. Weber, S. Talapatra, C. Journet, A. Zambano and A. D. Migone, *Phys. Rev. B* **61** (2000) 13150.
- 369. M. Bienfait, B. Asmussen, M. Johnson and P. Zeppenfeld, *Surf. Sci.* **460** (2000) 243.
- 370. S. M. Gatica, M. J. Bojan, G. Stan and M. W. Cole, *J. Chem. Phys.* **114** (2001) 3765.
- 371. M. M. Calbi, S. M. Gatica, M. J. Bojan and M. W. Cole, *J. Chem. Phys.* **115** (2001) 9975.
- 372. M. M. Calbi, M. W. Cole, S. M. Gatica, M. J. Bojan and G. Stan, *Rev. Mod. Phys.* **73** (2001) 857.
- 373. M. M. Calbi and M. W. Cole, *Phys. Rev. B* **66** (2002) 115413.
- 374. M. K. Kostov, M. M. Calbi and M. W. Cole, *Phys. Rev. B* **68** (2003) 245403.
- 375. S. Talapatra and A. D. Migone, *Phys. Rev. Lett.* **87** (2001) 206106.
- 376. S. Talapatra, V. Krungleviciute and A. D. Migone, *Phys. Rev. Lett.* **89** (2002) 246106.
- 377. S. Talapatra, D. S. Rawat and A. D. Migone, *J. Nanosci. Nanotech.* **2** (2002) 467.
- 378. M. R. Pederson and J. Q. Broughton, *Phys. Rev. Lett.* **69** (1992) 2689.
- 379. J. Breton, J. Gonzalez-Platas and C. Girardet, *J. Chem. Phys.* **101** (1994) 3334.
- 380. A. Kuznetsova, D. B. Mawhinney, V. Naumenko, J. T. Yates, J. Liu and R. E. Smalley, *Chem. Phys. Lett.* **321** (2000) 292.
- 381. G. Stan and M. W. Cole, *Surf. Sci.* **395** (1998) 280.
- 382. P. Kondratyuk and J. T. Yates, *Chem. Phys. Lett.* **383** (2004) 314.
- 383. M. Eswaramoorthy, R. Sen and C. N. R. Rao, *Chem. Phys. Lett.* **304** (1999) 207.

- 384. G. U. Sumanasekera, B. K. Pradhan, H. E. Romero, K. W. Adu and P. C. Eklund, *Phys. Rev. Lett.* **89** (2002) 166801.
- 385. D. L. Irving, S. B. Sinnott and A. Lindner, *Chem. Phys. Lett.* **389** (2004) 96.
- 386. A. Kleinhammes, S.-H. Mao, X.-J. Yang, X.-P. Tang, H. Shimoda, J. P. Lu, O. Zhou and Y. Wu, *Phys. Rev. B* **68** (2003) 075418.
- 387. H. Z. Geng, X. B. Zhang, S. H. Mao, A. Kleinhammes, H. Shimoda, Y. Wu and O. Zhou, *Chem. Phys. Lett.* **399** (2004) 109.
- 388. M. W. Maddox and K. E. Gubbins, *Langmuir* **11** (1995) 3988.
- 389. O. Byl, P. Kondratyuk, S. T. Forth, S. A. FitzGerald, L. Chen, J. K. Johnson and J. J. T. Yates Jr., *J. Am. Chem. Soc.* **125** (2003) 5889.
- 390. C. Matranga, L. Chen, M. Smith, E. Bittner, J. K. Johnson and B. Bockrath, *J. Phys. Chem. B* **107** (2003) 12930.
- 391. C. Matranga, L. Chen, B. Bockrath and J. K. Johnson, *Phys. Rev. B* **70** (2004) 165416.
- 392. Y. F. Yin, T. Mays and B. McEnaney, *Langmuir* **15** (1999) 8714.
- 393. M. M. Calbi, F. Toigo and M. W. Cole, *Phys. Rev. Lett.* **86** (2001) 5062.
- 394. S. Talapatra, A. Z. Zambano, S. E. Weber and A. D. Migone, *Phys. Rev. Lett.* **85** (2000) 138.
- 395. M. Bienfait, P. Zeppenfeld, N. Dupont-Pavlovsky, J.-P. Palmari, M. R. Johnson, T. Wilson, M. DePies and O. E. Vilches, *Phys. Rev. Lett.* **91** (2003) 035503.
- 396. M. Bienfait, P. Zeppenfeld, N. Dupont-Pavlovsky, M. Muris, M. R. Johnson, T. Wilson, M. DePies and O. E. Vilches, *Phys. Rev. B* **70** (2004) 035410.
- 397. M. C. Gordillo, L. Brualla and S. Fantoni, *Phys. Rev. B* **70** (2004) 245420.
- 398. W. Teizer, R. B. Hallock, E. Dujardin and T. W. Ebbesen, *Phys. Rev. Lett.* **82** (1999) 5305.
- 399. W. Teizer, R. B. Hallock, E. Dujardin and T. W. Ebbesen, *Phys. Rev. Lett.* **84** (2000) 1844.
- 400. J. C. Lasjaunias, K. Biljakovic, J. L. Sauvajol and P. Monceau, *Phys. Rev. Lett.* **91** (2003) 025901.
- 401. M. W. Cole, V. H. Crespi, G. Stan, C. Ebner, J. M. Hartman, S. Moroni and M. Boninsegni, *Phys. Rev. Lett.* **84** (2000) 3883.
- 402. W. Shi and J. K. Johnson, *Phys. Rev. Lett.* **91** (2003) 015504.
- 403. S. B. Sinnott, R. Andrews, D. Qian, A. M. Rao, Z. Mao, E. C. Dickey and F. Derbyshire, *Chem. Phys. Lett.* **315** (1999) 25.
- 404. J. Kong, N. R. Franklin, C. Zhou, M. G. Chapline, S. Peng, K. Cho and H. Dai, *Science* **287** (2000) 622.
- 405. S. Peng and K. J. Cho, *Nanotechnology* **11** (2000) 57.
- 406. P. G. Collins, K. Bradley, M. Ishigami and A. Zettl, *Science* **287** (2000) 1801.
- 407. M. Grujicic, G. Cao and R. Singh, *Appl. Surf. Sci.* **211** (2003) 166.
- 408. J. J. Zhao, A. Buldum, J. Han and J. P. Lu, *Nanotechnology* **13** (2002) 195.
- 409. S. H. Jhi, S. G. Louie and M. L. Cohen, *Phys. Rev. Lett.* **85** (2000) 1710.
- 410. A. Rochefort and P. Avouris, *J. Phys. Chem. A* **104** (2000) 9807.
- 411. S. Dag, O. Gulseren, T. Yildirim and S. Ciraci, *Phys. Rev. B* **67** (2003)
- 412. S. Dag, O. Gulseren and S. Ciraci, *Chem. Phys. Lett.* **380** (2003) 1.
- 413. P. Giannozzi, R. Car and G. Scoles, *J. Chem. Phys.* **118** (2003) 1003.

- 414. H. Ulbricht, G. Moos and T. Hertel, *Phys. Rev. B* **66** (2002).
- 415. D. C. Sorescu, K. D. Jordan and P. Avouris, *J. Phys. Chem. B* **105** (2001) 11227.
- 416. A. Ricca, C. W. Bauschlicher Jr., and A. Maiti, *Phys. Rev. B* **68** (2003) 035433.
- 417. R. Larciprete, A. Goldoni and S. Lizzit, *Nucl. Instrum. Meth. Phys. B* **200** (2003) 5.
- 418. H. Ulbricht, G. Moos and T. Hertel, *Surf. Sci.* **532** (2003) 852.
- 419. S. Heinze, J. Tersoff, R. Martel, V. Derycke, J. Appenzeller and P. Avouris, *Phys. Rev. Lett.* **89** (2002) 106801.
- 420. V. Derycke, R. Martel, J. Appenzeller and P. Avouris, *Appl. Phys. Lett.* **80** (2002) 2773.
- 421. A. Goldoni, R. Larciprete, L. Petaccia and S. Lizzit, *J. Am. Chem. Soc.* **125** (2003) 11329.
- 422. A. Ricca and J. A. Drocco, *Chem. Phys. Lett.* **362** (2002) 217.
- 423. A. Zahab, L. Spina, P. Poncharal and C. Marliere, *Phys. Rev. B* **62** (2000) 10000.
- 424. T. Sameya, P. Kim and C. Nuckolls, *Appl. Phys. Lett.* **82** (2003) 2338.
- 425. K. Bradley, J. C. P. Gabriel, M. Briman, A. Star and G. Gruner, *Phys. Rev. Lett.* **91** (2003) 218301.
- 426. K. Bradley, J. C. P. Gabriel, A. Star and G. Gruner, *Appl. Phys. Lett.* **83** (2003) 3821.
- 427. L. Valentini, F. Mercuri, I. Armentano, C. Cantalini, S. Picozzi, L. Lozzi, S. Santucci, A. Sgamellotti and J. M. Kenny, *Chem. Phys. Lett.* **387** (2004) 356.
- 428. S. Peng and K. J. Cho, *Nano Lett.* **3** (2003) 513.
- 429. H. Chang, J. D. Lee, S. M. Lee and Y. H. Lee, *Appl. Phys. Lett.* **79** (2001) 3863.
- 430. S. Santucci, S. Picozzi, F. Di Gregorio, L. Lozzi, C. Cantalini, L. Valentini, J. M. Kenny and B. Delley, *J. Chem. Phys.* **119** (2003) 10904.
- 431. W. L. Yim, X. G. Gong and Z. F. Liu, *J. Phys. Chem. B* **107** (2003) 9363.
- 432. P. G. Collins, M. S. Fuhrer and A. Zettl, *Appl. Phys. Lett.* **76** (2000) 894.
- 433. D. L. Irving, S. B. Sinnott and A. Lindner, *Chem. Phys. Lett.* **392** (2004) 567.
- 434. R. F. Service, *Science* **292** (2001) 45.
- 435. S. Okada, S. Saito and A. Oshiyama, *Phys. Rev. Lett.* **86** (2001) 3835.
- 436. J. Chen and J. Dong, *J. Phys.: Condens. Mater.* **16** (2004) 1401.
- 437. D. J. Hornbaker, S.-J. Kahng, S. Misra, B. W. Smith, A. T. Johnson, E. J. Mele, D. E. Luzzi and A. Yazdan, *Science* **295** (2002) 828.
- 438. D.-H. Kim, H.-S. Sim and K. J. Chang, *Phys. Rev. B* **64** (2001) 115409.
- 439. S. Okada, M. Otani and A. Oshiyama, *Phys. Rev. B* **67** (2003) 205411.
- 440. Y. Cho, S. Han, G. Kim, H. Lee and J. Ihm, *Phys. Rev. Lett.* **90** (2003) 106402.
- 441. T. Miyake and S. Saito, *Solid State Commun.* **125** (2003) 201.
- 442. R. Pati, L. Senapati, P. M. Ajayan and S. K. Nayak, *J. Appl. Phys.* **95** (2004) 694.
- 443. K. Hirahara, K. Suenaga, S. Bandow, H. Kato, T. Okazaki, H. Shinohara and S. Iijima, *Phys. Rev. Lett.* **85** (2000) 5384.
- 444. P. W. Chiu, G. Gu, G. T. Kim, G. Philipp, S. Roth, S. F. Yang and S. Yang, *Appl. Phys. Lett.* **79** (2001) 3845.
- 445. P. Launois, R. Moret, D. L. Bolloc'h, P. A. Albouy, Z. K. Tang, G. Li and J. Chen, *Solid State Commun.* **116** (2000) 99.
- 446. M. Otani, S. Okada and A. Oshiyama, *Phys. Rev. B* **68** (2003) 125424.

- 447. M.-H. Du and H.-P. Cheng, *Phys. Rev. B* **68** (2003) 113402.
- 448. X. Liu, T. Pichler, M. Knupfer, M. S. Golden, J. Fink, H. Kataura, Y. Achiba, K. Hirahara and S. Iijima, *Phys. Rev. Lett.* **65** (2002) 045419.
- 449. L. Kavan, L. Dunsch and H. Kataura, *Chem. Phys. Lett.* **361** (2002) 79.
- 450. L. Kavan, L. Dunsch, H. Kataura, A. Oshiyama, M. Otani and S. Okada, *J. Phys. Chem. B* **107** (2003) 7666.
- 451. A. Rochefort, *Phys. Rev. B* **67** (2003) 115401.
- 452. Y.-K. Kwon, D. Tomanek and S. Iijima, *Phys. Rev. Lett.* **82** (1999) 1470.
- 453. T. Takenobu, T. Takano, M. Shiraishi, Y. Murakami, M. Ata, H. Kataura, Y. Achiba and Y. Iwasa, *Nat. Mater.* **2** (2003) 683.
- 454. S. K. Bhatia and D. Nicholson, *J. Chem. Phys.* **119** (2003) 1719.
- 455. P. H. Nelson and S. M. Auerbach, *J. Chem. Phys.* **110** (1999) 9235.
- 456. D. G. Levitt, *Phys. Rev. A* **8** (1973) 3050.
- 457. D. S. Sholl and K. A. Fichthorn, *J. Chem. Phys.* **107** (1997) 4384.
- 458. D. S. Sholl, *Chem Eng J* **74** (1999) 25.
- 459. R. E. Tuzun, D. W. Noid, B. G. Sumpter and R. C. Merkle, *Nanotechnology* **7** (1996) 241.
- 460. Z. Mao and S. B. Sinnott, *J. Phys. Chem. B* **104** (2000) 4618.
- 461. K.-H. Lee and S. B. Sinnott, *J. Phys. Chem. B* **108** (2004) 9861.
- 462. K.-H. Lee and S. B. Sinnott, *Int. J. Multiscale Comp. Eng.* **3** (2005) 379.
- 463. M. Gitterman, *Phys. Rev. E* **62** (2000) 6065.
- 464. K. Ito and S. Miyazaki, *Prog. Theor. Phys.* **110** (2003) 875.
- 465. D. Alonso, A. Ruiz and I. d. Vega, *Phys. Rev. B* **66** (2002) 066131.
- 466. K.-H. Lee and S. B. Sinnott, *Nano Lett.* **5** (2005) 793.
- 467. S. Y. Bhide and S. Yashonath, *J. Am. Chem. Soc.* **125** (2003) 7425.
- 468. S. Supple and N. Quirke, *Phys. Rev. Lett.* **90** (2003) 214501.
- 469. M. W. Roth and J. Messentseva, *Mol. Simulat.* **30** (2004) 661.
- 470. Z. Mao and S. B. Sinnott, *Phys. Rev. Lett.* **89** (2002) 278301.
- 471. T. D. Power, A. I. Skoulidas and D. S. Sholl, *J. Am. Chem. Soc.* **124** (2002) 1858.
- 472. A. I. Skoulidas, D. M. Ackerman, J. K. Johnson and D. S. Sholl, *Phys. Rev. Lett.* **89** (2002) 185901.
- 473. D. M. Ackerman, A. I. Skoulidas, D. S. Sholl and J. K. Johnson, *Mol. Simulat.* **29** (2003) 677.
- 474. V. P. Sokhan, D. Nicholson and N. Quirke, *J. Chem. Phys.* **120** (2004) 3855.
- 475. D. Cao and J. Wu, *Langmuir* **20** (2004) 3759.
- 476. F. Zhang, *J. Chem. Phys.* **111** (1999) 9082.
- 477. G. Arora, N. J. Wagner and S. I. Sandler, *Langmuir* **20** (2004) 6268.
- 478. G. K. Papadopoulos, *J. Chem. Phys.* **114** (2001) 8139.
- 479. S. M. Cooper, H. F. Chuang, M. Cinke, B. A. Cruden and M. Meyyappan, *Nano Lett.* **3** (2003) 189.
- 480. K. G. Ayappa, *Langmuir* **14** (1998) 880.
- 481. Z. Mao and S. B. Sinnott, *J. Phys. Chem. B* **105** (2001) 6916.
- 482. L. Xu, M. G. Sedigh, T. T. Tsotsis and M. Sahimi, *J. Chem. Phys.* **112** (2000) 910.
- 483. E. Dujardin, T. W. Ebbesen, H. Hiura and K. Tanigaki, *Science* **265** (1994) 1850.
- 484. T. W. Ebbesen, *Ann. Rev. Mater. Sci.* **24** (1994) 235.

- 485. G. Hummer, J. C. Rasalah and J. P. Noworyta, *Nature* **414** (2001) 188.
- 486. A. Berezhkovskii and G. Hummer, *Phys. Rev. Lett.* **89** (2002) 064503.
- 487. M. S. P. Sansom and P. C. Biggin, *Nature* **414** (2001) 156.
- 488. Y. Gogotsi, J. A. Libera, A. Güvenç-Yazicioglu and C. M. Megaridis, *Appl. Phys. Lett.* **79** (2001) 1021.
- 489. A. Luzar and D. Chandler, *Nature* **397** (1997) 55.
- 490. R. J. Mashl, S. Joseph, N. R. Aluru and E. Jakobsson, *Nano Lett.* **3** (2003) 589.
- 491. K. Koga, G. T. Gao, H. Tanaka and X. C. Zeng, *Nature* **412** (2001) 802.
- 492. Y. Maniwa, H. Kataura, M. Abe, S. Suzuki, Y. Achiba, H. Kira and K. Matsuda, *J. Phys. Soc. Jpn.* **71** (2002) 2863.
- 493. A. Kolesnikov, J.-M. Zanoliti, C.-K. Loong, P. Thiyagarajan, A. Moravsky and R. O. Loutfy, *Phys. Rev. Lett.* **93** (2004) 035503.
- 494. J. Wang, Y. Zhu, J. Zhou and X.-H. Lu, *Phys. Chem. Chem. Phys.* **6** (2004) 829.
- 495. J. Martí and M. C. Gordillo, *Phys. Rev. B* **64** (2001) 021504.
- 496. J. Martí, E. Guàrdia and M. C. Gordillo, *Chem. Phys. Lett.* **365** (2002) 536.
- 497. A. Waghe, J. Rasaiah and G. Hummer, *J. Chem. Phys.* **117** (2002) 10789.
- 498. C. Dellago, N. M. Naor and G. Hummer, *Phys. Rev. Lett.* **90** (2003) 105902.
- 499. B. Huang, Y. Xia, M. Zhao, F. Li, X. Liu, Y. Ji and C. Song, *J. Chem. Phys.* **122** (2005) 084708.
- 500. A. Kalra, S. Garde and G. Hummer, *Proc. Natl. Acad. Sci. USA* **100** (2003) 10175.
- 501. B. J. Hinds, N. Chopra, R. Andrews, V. Gavalas and L. Bachas, *Science* **303** (2004) 62.
- 502. M. Majumder, N. Chopra and B. J. Hinds, *J. Am. Chem. Soc.* **127** (2005) 9062.
- 503. S. Joseph, R. J. Mashl, E. Jakobsson and N. R. Aluru, *Nano Lett.* **3** (2003) 1399.
- 504. D. J. Mann and M. D. Halls, *Phys. Rev. Lett.* **90** (2003) 195503.
- 505. R. Qiao and N. R. Aluru, *Nano Lett.* **3** (2003) 1013.
- 506. M. Krüger, I. Widmer, T. Nussbaumer, M. Buitelaar and C. Schönenberger, *New J. Phys.* **5** (2003) 138.
- 507. S. B. Cronin, R. Barnett, M. Tinkham, S. G. Chou, O. Rabin, M. S. Dresselhaus, A. K. Swan, M. S. Ünlü and B. B. Goldberg, *Appl. Phys. Lett.* **84** (2004) 2052.
- 508. P. Král and M. Shapiro, *Phys. Rev. Lett.* **86** (2001) 000131.
- 509. S. Ghosh, A. K. Sood and N. Kumarm, *Science* **299** (2003) 1042.
- 510. V. Sazonova, Y. Yaish, H. Ustunel, D. Roundy, T. A. Arias and P. L. McEuen, *Nature* **431** (2004) 284.
- 511. J. W. Kang and H. J. Hwang, *Nanotechnology* **15** (2004) 1633.
- 512. L. W. Nagel and D. O. Pederson, *Proceedings of the 16th Midwest Symposium Circuit Theory*, Waterloo, Canada, 1973.

## Chapter 14

### Aligned carbon nanotube membranes

B. Hinds

Department of Chemical and Materials Engineering, University of Kentucky, USA

#### 1. GRAND CHALLENGES AND APPLICATIONS OF MEMBRANE TECHNOLOGY

Membranes far more complex than anything that can be manufactured by humans are found in the walls of the simplest of cells. In general, a cell wall is similar to a soap bubble, a phospholipid bi-layer. However, it offers remarkable chemical selectivity due to the incorporated proteins known as chemical channels that span across the cell wall. Understanding how the channels work was achieved by decades of effort to form crystals of the proteins for crystallographic structure determination and careful measurement of ion transport. The 2003 Nobel Prize in Chemistry was awarded for this effort.

The basis for the operation of the channels relies on three critical components. These are (1) chemical selectivity at the entrance to the pore to attract ions of interest and exclude others, (2) the molecular interactions along the length of the pore to induce hydrogen bond ordering of the solvent, and (3) signaling from within the cell to control the conformation of the protein at the exit of the pore. This is schematically diagrammed in Figs. 1 and 2 showing the structure of the remarkable potassium [1] and aquaporin protein channels [2]. The understanding of how these channels work is critical to understanding the physiology of cells and discovering possible treatments for diseases through desired chemical interactions with the channel. Another approach would be to modify the channel itself. For instance, it is conceivable to design a protein channel that only finds cancer cell walls and then would allow a deadly concentration of Ca through that channel into the interior of the cancer cell. Further, applications would involve collecting a large number of these proteins and fabricate a selective membrane for chemical separations, sensing, or drug delivery. There are several critical challenges to this approach. The first is the growth and separation of these proteins at the kg scale, which is currently not possible. Second, micelle membranes (i.e. soap bubbles) are mechanically extremely fragile, making durable large-area membranes of bi-layers unfeasible at this time.

The elegance of the ion-channel systems found in nature is certainly worth of imitation in a human engineered composite structure. The four critical components required are: (1) an impermeable matrix film (i.e. a polymer or ceramic) with a high areal density of nanometer-scale pores, (2) selective 'gate-keeper' molecules that attract molecules of interest while excluding others, (3) a well-ordered hydrophobic

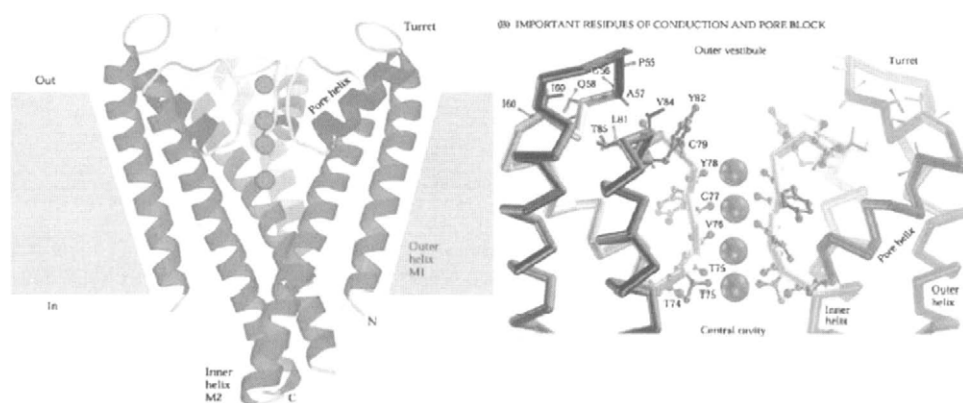


Figure 1. Schematic of the active region of bacterial  $K^+$  selective channel (KscA) from crystallographic structures [1]. The attractive chemistry at the entrance of the protein ion-channel attracts ions and forces them and their associated solvent molecules to order single file. The interactions are selective enough to distinguish between  $K^+$  and  $Ca^{2+}$ , an accomplishment not yet possible by human engineering. From Ref. [1], reproduced with permission from Sinaver Associates copyright 1984.

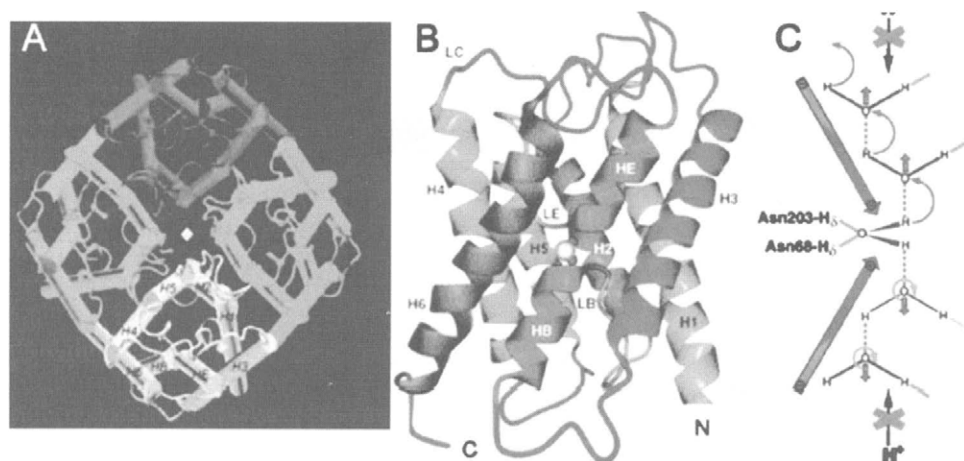


Figure 2. Schematic of aquaporin water channel. The channel excludes all ions, including hydronium ( $H_3O^+$ ). The physical basis for this is that the hydrophobic core between the for polypeptide helices forces H-bond ordering of the water in the column. The central ligand forces the mirror plane of H-bond ordering that prevents the rapid shuffling of  $H^+$  by concerted water rotation. From Ref. [2], reproduced with permission from Nature Publishing Group copyright 2000.



channel that promotes high rates of transport, and (4) a signaling 'gate keeper' that turns the channel on and off depending on the chemical conditions within the cell.

Outlined in this chapter are efforts to form the basis of an artificial ion channel using carbon nanotubes (CNTs) and containing the four critical components just described. For the first component, a high-density array of multi-walled carbon nanotubes (MWCNTs) was made to traverse across a solid polystyrene (PS) film. For the second component, by chemically functionalizing the tips of the CNTs, it is shown that the selectivity of differently sized permeates can be changed. For the third component, pressure-driven solvent flow is demonstrated to be 4–5 orders of magnitude faster than a simple Newtonian fluid. This possibly illustrates the dominance of hydrogen bond ordering. The fourth component is achieved by floating each side of the membrane on different functionalization solutions. This allows each side of the membrane to be independently functionalized with selective molecules.

## 2. CURRENT POROUS MEMBRANE SYSTEMS AND CHALLENGES

Membrane-based separation processes have many applications ranging from the separation of gases for fuel cells and pollution control to pharmaceuticals for medical treatments. Membrane separation is growing in importance with equipment sales of cross-flow filtration alone exceeding \$6.8 billion in 2005 for water purification and other nano/ultra-filtration applications [3]. The significant advantages of membrane separation include low-energy cost, low operation temperature, simple apparatus, flexibility with a variety of membrane media, and high selectivity in multi-component systems. Separations in the size regions from 1 to 10 nm are particularly interesting since they could be used to isolate macromolecules, such as proteins [4], which would be valuable to medicinal applications. Generally, membranes can be categorized as organic and inorganic films based on the separation mechanisms of size exclusion, chemical affinity, or diffusion.

Organic membranes are the most prevalent, primarily due to the ease and low cost of synthesizing mechanically strong films of large area. However, there are significant problems with the lack of precise pore size control, and the effects of solvent swelling changing this pore size. The most commonly used organic membranes include aromatic/polycarbonate co-polymers, cellulose acetate, aliphatic polyamides, polyimides, polydimethylsiloxane, and polysulfone. The choice of polymer system is a complex mix of pore size, mechanical strength, ability for surface chemical modification, and resistance to solvents. For size-exclusion separation mechanisms, co-polymers and polyamides have been optimized to reduce the distribution in pore size. However, there is a significant room for improvement, since selectivity is very sensitive to small changes in pore size.

Polysulfone materials are among the most studied systems, primarily due to the ability to chemically functionalize the surface to allow for affinity membranes [5,6]. With affinity membranes, the component of interest is attracted to the surface of the pore, which greatly enhances selectivity. There are many reported types of methods to immobilize amino acids, antigens, and other bioactive ligands to reactive sites on the support membrane [7]. However, polysulfone films are sensitive to solvent swelling, which significantly changes pore size and selectivity.

One solution is to functionalize micro-pores of hollow nylon fibers [8]. In a separation filter apparatus, this would allow significant packing density and optimal flow design. However, the relatively large pore size of hollow fibers significantly reduces selectivity as other species diffuse through the membrane. Thus, the affinity membranes tend to operate on the same principals as chromatography and generally have modest improvement over functionalized bead columns [6]. This makes it difficult to increase the scale for industrial separations, particularly when considering the detrimental effect of fouling, in which larger particles eventually block the pores. Also concern must be given to modifying the hydrophobic/philic nature of pores [9].

Inorganic porous ceramic membranes have demonstrated many applications in gas separation, beverage production water purification, and the separation of dairy products [10]. Porous membranes with pores greater than 0.5 nm usually act as size-excluding sieves and commercial materials including silica, alumina, zirconia, zeolite, and carbon membranes. All these types suffer from the difficulty of controlling pore size, except for zeolites. Zeolites have pore sizes determined by molecular structure and would be ideal for many low molecular weight gas separations, such as  $H_2/N_2/O_2$ . The primary difficulty with zeolites is in forming a crack-free coating over a porous support, though several research groups have recently claimed success [11,12].

Carbon-based membranes are particularly intriguing since they are easily synthesized from the pyrolysis of polymers over a porous support tube or fiber [13]. The pore size is typically determined by the escaping decomposition gases [14], which are not precisely controlled. However  $CO_2/CH_4$  selectivity of over 100 can be obtained [15], which is likely due to the affinity of  $CO_2$  absorption. This can be further modified by coating the porous carbon membrane with a chemical vapor deposition (CVD) deposited polymer, which further reduces the pore size and allows for  $N_2/O_2$  selectivity of 14 [16]. Other routes to control pore size by selective pyrolyzation of a polymer blend or fiber composites are being explored with mixed results, since initial microstructure is not well controlled nor are fibers of appropriate dimension easily aligned through the thickness of the membrane. The polarity of the pore is also an important factor but the pore surface can be functionalized to aid in separation processes [17,18].

In general, the critical issues to resolve for organic membranes are control of pore size and resistance to solvents and/or processing environment. In particular, swelling from solvent absorption can dramatically affect the selectivity and throughput. Inorganic membranes are very robust and do not suffer from solvent effects. However, high surface area inorganic membranes are expensive and there is no mechanism to finely control the distribution in pore sizes in the nanometer-scale. For both types of membranes, the issue of throughput, which is severely hampered by fouling, can be largely addressed by design. For example, hollow fiber membranes with countercurrent flow and cleaning cycles are currently the most promising designs. Usually, high-purity separations are difficult to achieve since a three-stage separation is a practical design limit and there is high osmotic pressure for low molecular weight solutes. Thus, the economics of the entire process is a complex issue of required purity, pre-filtering, and material costs.

Finer control of pore size (selectivity) and throughput can benefit overall process efficiency. For solutes, such as a specific protein, which must be separated from other physically similar proteins, selectivity is the dominant parameter. For membranes, the critical aspects to improve upon are controlled pore size with sub-nanometer size dispersion, imperviousness to solvent swelling, and the ability to functionalize for further selectivity. Fundamental limitations for high selectivity in affinity membranes are 'core-flow,' where undesired species will not interact with functionalized interface and site competition in which affinity sites are already occupied and do not interact with stream. These limitations can be addressed by reducing pore diameter and increasing pore length, but with significant detriment to flux rate.

An idealized membrane for chemical separation would have a high density of aligned pores, pore diameter controlled to the size of the target molecule, and selective chemical functionalization at the pore entrance. This would allow for a true 'gate-keeper' mechanism in which all molecules interact with a selective molecule before passing through the channel. With high areal density of pores, both high fluxes and selectivity would be attainable due to short diffusion path length and geometrically forced interaction with the affinity molecule.

### 3. ORDERED NANO-POROUS MEMBRANES

There has been significant progress with the synthesis of ordered nanometer-scale membrane structures in terms of uniform pore size and straight non-tortuous paths. Block co-polymers, composed of dissimilar polymers grafted together, segregate into well-ordered polymer domains on the scale of 10–20 nm. One of the polymer domains can be rendered soluble, by light exposure or chemical reaction, resulting in a nano-porous film with high areal density ( $\sim 10^{11}/\text{cm}^2$ ) [19]. These films must be thin for proper domain formation to traverse from the top to bottom of the polymer [16].

Making the pattern transfer to a robust substrate is the key challenge for the use of block co-polymers in separation applications. Fine control of pore size has been achieved with track-ion etch, where polymers are exposed to high-energy particles that leave a uniform track of broken bonds that can be easily etched. Typically, they have initial pore dimensions of  $\sim 20$ – $30$  nm. These can be reduced to  $\sim 1$  nm by an electrode-less plating of gold that can further be chemically functionalized to form an affinity membrane [20]. This approach demonstrates size exclusion, but suffers from a low areal density ( $10^8/\text{cm}^2$ ), subsequent low transport rate, and high fabrication expense.

Porous Al can be formed by the electrochemical oxidation of foils and has well ordered aligned pores (20–50 nm diameter). These are commercially produced, have high areal density ( $\sim 10^{10}/\text{cm}^2$ ), and can have a wide variety of surface functionalization [21]. Controlled sol–gel plating can further reduce the pore diameter, and subsequent surface functionalization results in the demonstration of enantiomeric separations [22]. Carbon has been deposited into porous alumina (PA) structures by the template method to make an aligned CNT membrane [23]. However, inner diameters are greater than 50 nm range, which is above many

molecular separation applications. Also, the CNT produced by this method appears to not have continuous ordered graphite sheets. The primary challenge in using pore plating to reduce inner pore diameter is that if the variations in initial pore diameters are larger than the target size, it is not possible to control plated pore size down to the molecular size scale. Thus, it is necessary to start with a membrane structure with initial pore diameter near the desired diameter with small dispersion and high areal density.

In principle, the inner core of CNTs can offer the finest control of nanometer-scale pore dimension. In CNT growth process, the size is set by diameter of the catalyst particle [24–28], offering a practical route for pore diameter control. CNTs have a broad theoretical base for predicting transport polar solvents, such as H<sub>2</sub>O [29–31]. In fact, the conductive nature of CNTs can be used to selectively transfer cationic species [32]. DNA oligonucleotides are also theoretically found to insert into in CNTs [33], which would have important biological separation/detection potential. A CNT-based membrane consisting of a single 100 nm inner core diameter CNT has been isolated to successfully show the transport measurements [34]. The challenge is to align large numbers ( $\sim 10^{11}/\text{cm}^2$ ) of well-controlled nanometer-scale inner diameter CNTs across a robust membrane structure. There are reports of single-walled carbon nanotube (SWCNT) alignment under extreme magnetic field but there is no microstructural characterization to show flux through the inner core of CNTs, as opposed to flow across a dense matting of CNTs [35]. A coating of aligned MWCNTs inside a tube furnace has been removed to form a free-standing tube ( $\sim 2$  cm diameter) where the tube wall consists of aligned MWCNTs. This can act as a cross-flow filter with absorption on the outer walls of the MWCNTs. However, fluids are not restricted to flow through the inner cores of those CNTs [36].

#### 4. CARBON NANOTUBE TRANSPORT THEORY

Fluid flow through the cores of CNTs is predicted to show enhanced transport of hydrocarbon gases and water [37]. For instance, one study [38] predicted that water flow through ‘hydrophobic’ SWCNTs should be possible because the process could induce H-bond ordering in a chain of water molecules. This can make-up for the energy cost to lose 2 of the 4 weak hydrogen bonds, as the water molecules separates from the bulk water. In order to preserve the H-bond ordering, that efficiently transfers momentum, it is critical to have nearly frictionless interaction of the water with the CNT graphite sheets. Using the study’s theoretical water flow volume-rate (which is comparable to that of the protein channel *aquaporin-1*) divided by the CNT cross sectional area, a remarkably fast water flow velocity of  $\sim 90$  cm/s is predicted.

High flow velocities of molecules were also predicted based on the frictionless nature of the CNT walls [39] as well as the fast diffusion rates for hydrocarbons [40,41]. In the latter case, favorable interactions of the methane with the CNT wall predict that the molecule will ‘skate’ down the tube wall and not scatter in random directions, as would conventionally happen in the case of Knudsen diffusion. The flow velocity of gaseous methane is predicted to be  $\sim 260$  cm/s at 1 bar [40]. Another molecular dynamics study [41] reports about an order of magnitude difference in

flux between methane and butane. This indicates that the flow through nanotubes is not just limited by the viscous forces, but also on  $n^2$  dependence of the hydrocarbon chain length [42]. Thus two interesting, yet opposed, interactions can result in enhanced flow velocity depending on the type of molecule going through the CNT core. In the first case, there is a nearly complete non-interaction of water (or polar molecules) with the graphitic sheets. This effectively eliminates van der Waals interactions making for a several angstrom thick gap between the water and the CNT wall. This results in an essentially frictionless surface and promotes hydrogen bond ordering. In the second case, there is a favorable interaction with the hydrocarbon on the CNT wall. However, this interaction is not localized to any particular carbon atom, thus allowing for a very low surface friction condition. This results in enhanced gas flow instead of the common case of inelastic gas scattering in random directions. In both models, the atomically flat nature of graphite sheets inherent to the CNT microstructure makes the enhanced flow possible over long-length scales.

## 5. APPROACH TO MAKING MWCNT MEMBRANES

Aligned growth of dense arrays of multi-walled CNTs has been demonstrated at the University of Kentucky [43,44] and elsewhere [45–47]. Although the outer diameters have significant variance ( $30 \pm 10$  nm), the hollow inner core diameter is well controlled to 7 nm. Since this is a thermal CVD process using xylene/ferrocene, it is an easily scalable process with an estimated cost of \$0.60/m<sup>2</sup>. The primary goal is to form a membrane structure taking advantage of the as-deposited alignment of MWCNTs to form a well-controlled nano-porous membrane structure [48]. Shown in Fig. 3a is a scanning electron microscope (SEM) micrograph of the as-grown MWCNT arrays. Particularly intriguing is the alignment of CNTs that is perpendicular to the substrate. If the space between CNTs could be filled with a polymer barrier, then a membrane with a rigid pore structure, high porosity, and small dispersion could be synthesized as diagrammed in Fig. 3 b. This would result in a wide variety of applications in membrane separation processes.

The as-deposited CNTs are grown for 30 min ( $\sim 5$   $\mu$ m length) on a quartz substrate using a CVD process with a ferrocene/xylene/Ar/H<sub>2</sub> feed at 700 °C [43]. The aligned CNT film then has a 50 wt% solution of PS and toluene spun coat over the surface. PS is known to have high wet ability with CNTs and readily impregnates into a CNT array [49,50]. Due to high viscous drag within the CNT array, only excess polymer on top of the structure is removed during the spin coating process. The film is dried in vacuum at 70 °C for 4 days. HF acid is then used to remove CNT/PS composite from the quartz substrate. Figs. 3b and 3c show the cleaved edge of the free-standing membrane structure with CNT alignment from top to bottom with the polymer film intact.

It is necessary to remove a thin layer of excess polymer on the top surface, and open the CNT tips to form a membrane structure. This is done using an H<sub>2</sub>O plasma enhanced oxidation process at 600 mTorr H<sub>2</sub>O pressure and 2.5 W/cm<sup>2</sup> for 7 min. These conditions are modified to a previous report [51] by Liming Dai's group that removed the Fe nanocrystal catalyst from the tips of CNTs. The overall processing scheme is shown in Fig. 4. The plasma oxidation process etches PS faster than the CNTs, leaving

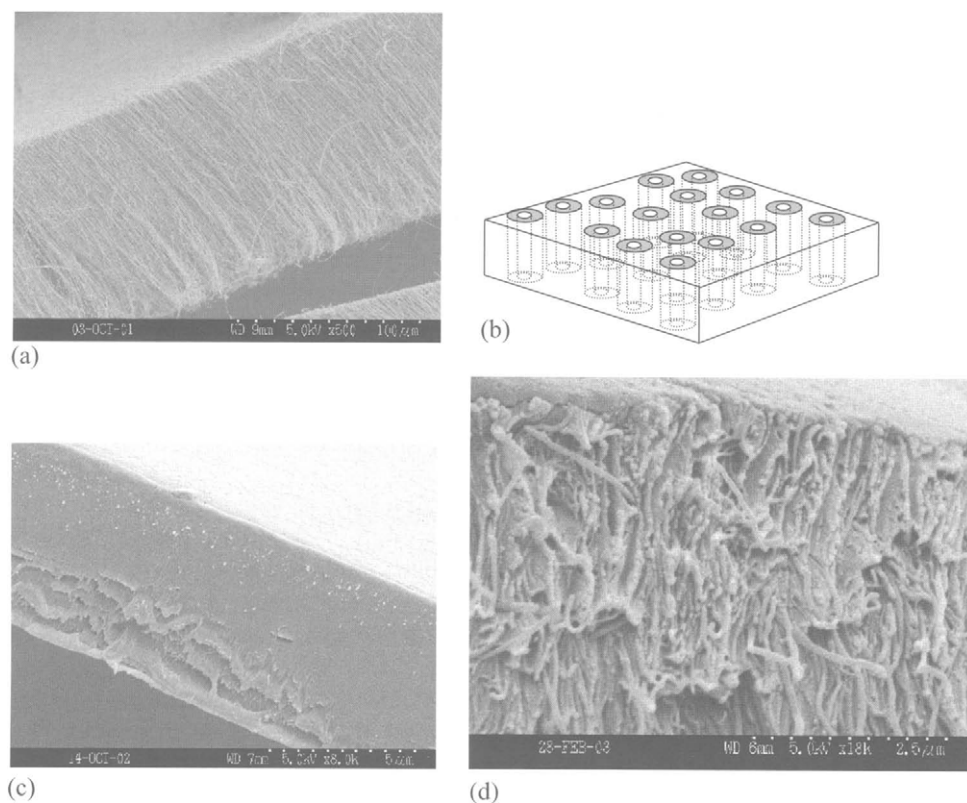


Figure 3. (a) As grown dense CNT array from Fe-catalyzed CVD process produced at UK CAER. (b) Schematic of target membrane structure. With a polymer impregnation between CNTs, a viable membrane structure can be readily produced with the pore being the rigid inner tube diameter of the CNT. (c) Cleaved film (upper bright area is top surface) with aligned sheets slightly pulled out from surface is shown. The polymer matrix is PS. (d) Another view of a cleaved edge after exposure to H<sub>2</sub>O plasma oxidation. PS matrix is slightly removed to contrast alignment of CNTs across the membrane.

CNT tips that are 10–50 nm above the polymer surface. The SEM analysis of this surface gives an estimated areal density of  $6 \times 10^{10}$  CNT-tips/cm<sup>2</sup>. Importantly, the plasma process leaves the tips of the CNTs functionalized with carboxylic acid that are readily functionalized with a selective receptor [52–55]. This idealized functionality is diagrammed in Fig. 5.

Transmission electron microscopy (TEM) of dissolved membranes (Fig. 6) demonstrated that about 70% of the CNT tips were opened by the plasma oxidation

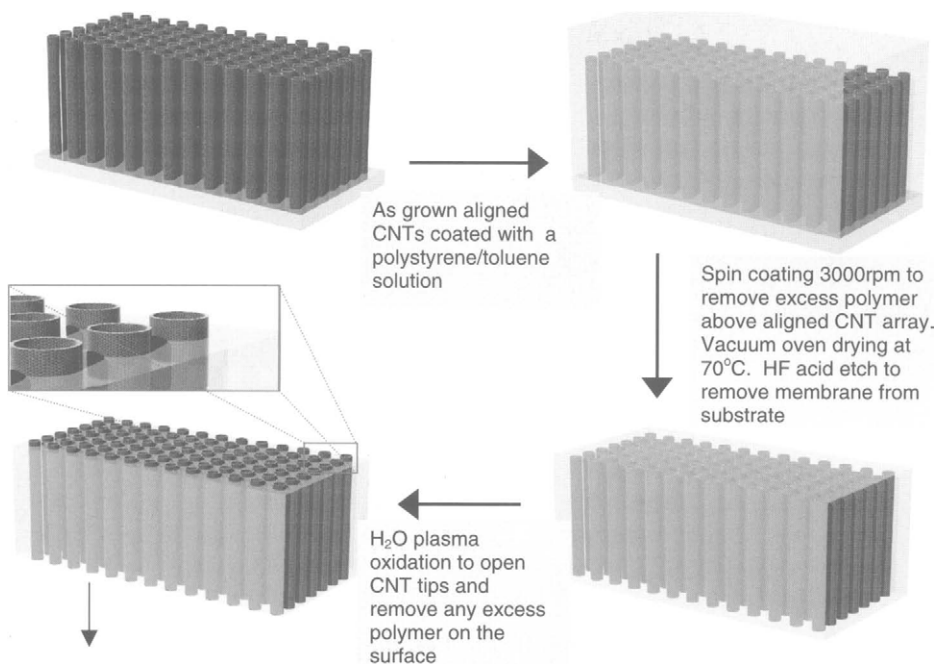


Figure 4. Processing steps involved in aligned CNT membrane fabrication process.

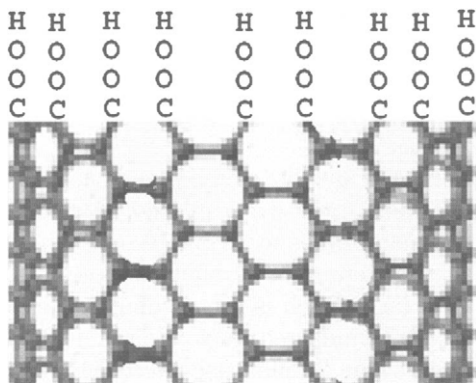


Figure 5. Idealized schematic of carboxylic acid termination on CNT at membrane surface after oxidative trimming. By carbodiimide condensation reactions, functionalized receptors can be attached resulting in a highly selective affinity membrane. CNT within the polymer film is protected from oxidative trimming.

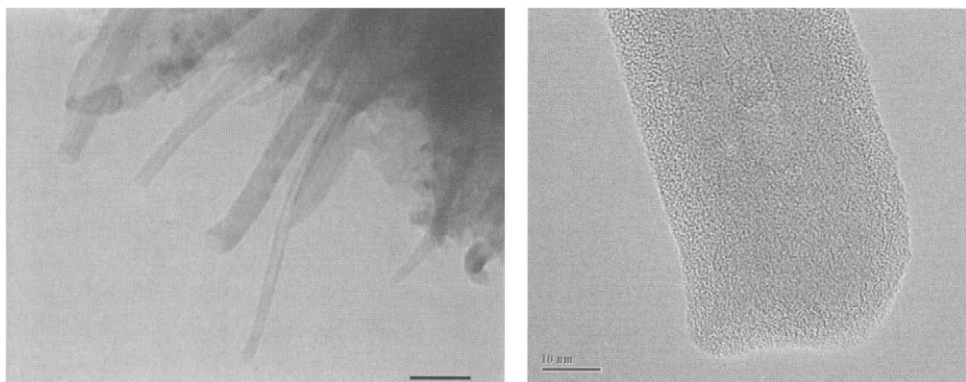


Figure 6. (a) TEM image of CNT tips after H<sub>2</sub>O plasma oxidation. The scale bar corresponds to 200 nm. (b) Higher magnification TEM image. The scale bar corresponds to 10 nm.

process under these conditions. Significant amounts of Fe catalyst were observed in the cores of the CNTs, but largely removed by 24 h HCl treatment. Electrical transport measurements also were consistent with highly conductive CNTs continuously spanning from the top to the bottom of the insulating polymer film. Conductivity from the top to the bottom of the membrane using Au film contacts, was 35.2/Ωcm. The 4-point probe measured sheet resistance gave an in-plane conductivity value of 2 orders of magnitude less at 0.32/Ωcm. A modest in-plane conductivity would be expected for the crossing of CNTs due to slight misalignment from idealized perpendicular growth from the substrate surface.

## 6. TRANSPORT THROUGH CNTS

Both, the pressure induced transport of gas/liquids and ionic diffusion transport through the aligned CNT membrane were studied. For room temperature N<sub>2</sub> gas flow measurements, CNT membranes were epoxy sealed between macro-PA filters and mounted in a gas flow system with a water manometer. Fig. 7a indicates a permeance of 2.6 μmol/(m<sup>2</sup> s Pa), which is quite comparable to nanometer-scale PA membrane structures [56]. In Knudsen diffusion, a gas molecule's mean free path is limited by pore radius and not the normal case of collision with other gases. The gas collisions rate with the pore wall, and subsequent random scattering, results in the molar flux ( $N_a$ ). This can be calculated using the formula:

$$N_a = \epsilon D_a (P_1 - P_2) / RTL$$

$$D_a = 0.97r(T/M_a)^{1/2}$$



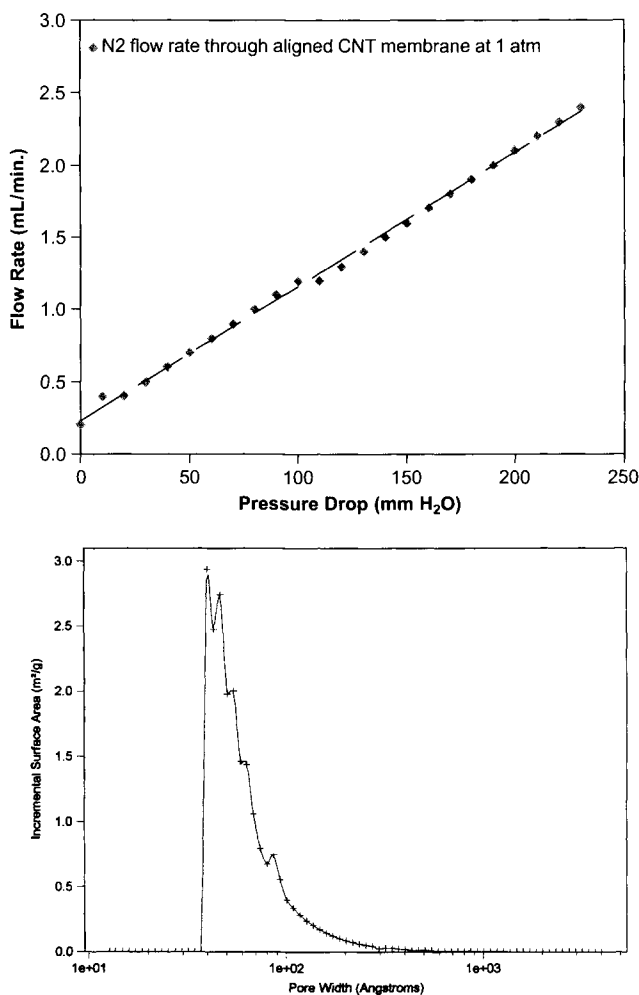


Figure 7. (a) N<sub>2</sub> gas flow through CNT membrane structure with 3.1 cm<sup>2</sup> surface area and 5 μm thickness. Slope of line indicates a permeance of 2.6 μmol/(m<sup>2</sup> s Pa). Offset from zero flow is due to manometer design. (b) N<sub>2</sub> porosity data at 77 K showing 6 ± 2 nm pore distribution consistent with TEM observation of inner CNT core diameter, thus supporting model of open CNT end exposed to surface of polymer film as in membrane structure.

In this formula,  $\varepsilon$  is the void fraction,  $P_1 - P_2$  the pressure difference,  $R$  the universal gas constant,  $T$  absolute temperature,  $L$  the pore length,  $r$  the mean pore radius, and  $M_a$  the molecular weight. By using the observed estimate of CNT areal density of  $6 \times 10^{10}/\text{cm}^2$ , mean pore diameter of 7.5 nm, and diffusion length of 5 μm,

a permeance of  $2.6 \mu\text{mol}/(\text{m}^2 \text{ s Pa})$  is calculated by Knudsen diffusion. This is consistent with the observed microstructure of open CNTs passing across PS film. Fig. 7b shows derived pore size distribution from  $\text{N}_2$  desorption at 77 K. Pore-size distribution matches that of the CNT inner core diameter that was observed by TEM. This is also consistent with the premise of an aligned CNT membrane structure. Observed pore volume from  $\text{N}_2$  desorption is  $0.073 \text{ cm}^3/\text{g}$ . This is consistent with the estimated pore volume calculated from the CNT areal density ( $6 \times 10^{10}/\text{cm}^2$ ), the inner core projected area ( $\pi r^2$ ,  $2r = 7.5 \text{ nm}$ ), the tube length ( $5 \mu\text{m}$ ), and PS density ( $1.05 \text{ g}/\text{cm}^3$ ) of  $0.025 \text{ cm}^3/\text{g}$ .

The aligned CNT membrane structure also allowed the transport of  $\text{Ru}(\text{NH}_3)_6^{3+}$  ions in aqueous solution. A  $10 \mu\text{m}$  thick membrane was epoxy-sealed to one end of a Pyrex tube, and  $400 \mu\text{L}$  of a  $0.01 \text{ M}$  KCl solution was placed inside the Pyrex tube. The membrane was submerged into a  $5 \text{ mM}$   $(\text{Ru}(\text{NH}_3)_6\text{Cl}_3)$ :  $0.01 \text{ M}$  KCl reference solution to establish an Ru concentration gradient. The inner solution was kept level with the outer reference solution to avoid any pressure-induced transport. The flux of Ru ions passing through membrane into the inner solution was then determined by cyclic voltammetry (CV). For the aligned CNT membrane after  $\text{H}_2\text{O}$  plasma oxidation, an  $\text{Ru}(\text{NH}_3)_6^{3+}$  flux of  $0.07 \mu\text{mol}/\text{cm}^2\text{h}$  was observed. Treatment of the membrane with HCl for 24 h aided the ionic flux significantly, increasing it to  $0.9 \mu\text{mol}/\text{cm}^2\text{h}$ . This is presumably due to dissolving the excess Fe not removed by the plasma process. The diffusion coefficient ( $D$ ) of  $\text{Ru}(\text{NH}_3)_6^{3+}$  through the membrane was found to be  $2.2 (\pm 0.9) \times 10^{-6} \text{ cm}^2/\text{s}$  from the measured flux, with the above-mentioned areal density, pore diameter, thickness, and tortuosity. This is near the bulk of aqueous solution diffusion for  $\text{Ru}(\text{NH}_3)_6^{3+}$  of  $7 \times 10^{-6} \text{ cm}^2/\text{s}$  indicating only modest interaction of the ion with the CNT tip and the core. It is expected that negatively charged carboxylate functional groups at the tips would reduce the observed  $D$  of a positively charged  $\text{Ru}(\text{NH}_3)_6^{3+}$  ion.

The observed gas and ionic flux were found to be consistent with the CNT membrane geometry and conventional flow models. However, it is important to examine the possibility of serendipitous transport through cracks or other defects. As a control experiment, membranes without  $\text{H}_2\text{O}$  plasma treatment did not show ionic transport. Therefore, diffusion through the solid polymer was not significant. Backlit optical microscopy after electrochemical characterization did not show any signs of microcracking. Diffusion experiments with Au nanocrystals ( $10 \text{ nm}$  diameter) showed no diffusion across the membrane, while small molecules in the same solution did diffuse across. This clearly indicates pore sizes less than  $10 \text{ nm}$ . Chemical modification of the CNT tips showed changes in selective transport, which would not be possible through microcracks (see Sec. 7 of this chapter). The selective attachment of streptavidin ( $15\text{--}20 \text{ nm}$  diameter) blocking pores also would not be possible with microcracks present. Thus, there is significant experimental evidence to show that transport is through the cores of CNTs.

Pressure-induced solvent flow through the aligned CNT membrane was measured in a syringe-pump pressure cell apparatus [57], where mass (hence volume) of the solvent passing through the membrane is directly measured on a pan balance as a function of time. Fig. 8 shows fluid volume as a function of time for a variety of

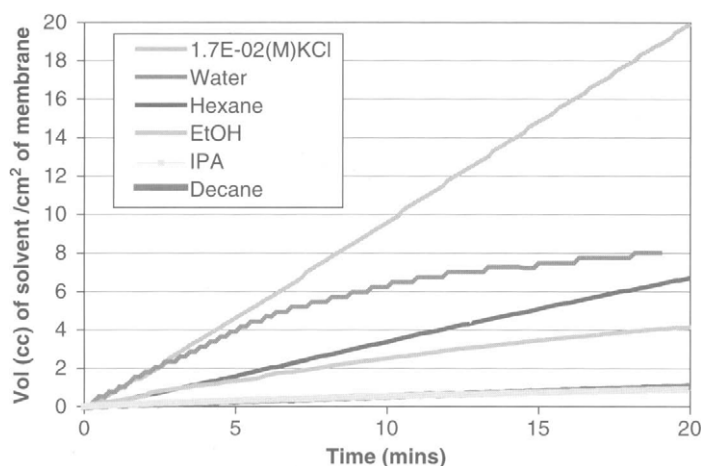


Figure 8. Cumulative volume of different solvents collected over a balance per unit area ( $\text{cm}^3/\text{cm}^2$ ) of the membrane flowing through the CNT membrane as a function of time at (0.7–1 bar applied pressure). Water flow data shown here has been normalized by permeable pore density (detailed parameters are shown in Table 1).

solvents with flow data summarized in Table 1. The flow rates are incredibly fast, with a remarkable 4–5 orders of magnitude increase in water flow over what would be seen in conventional nanoporous structures. This result has important practical applications since less than one ten thousandth the membrane will be needed for the same amount of chemical separation. Also the enhanced flow is the third critical component to mimicking protein channels as described in the beginning of this chapter.

Surprisingly, the initial flow of water is much higher than hexane. This is contrary to conventional expectations of a hydrophobic and lower viscosity liquid having higher flow through a hydrophobic CNT core. This suggests that hydrogen bond coupling of the fluid as well as minimal interactions with CNT wall may be dominant mechanisms for the enhanced fluid flow. Interestingly for the hydrogen-bonded liquids, the initial flow velocities also follow the same trend where water is faster than EtOH, which is faster than isopropylalcohol. This suggests that hydrogen bonding is the source of the initial high flow. Fig. 9 shows experimental observation of the reduction in flow with time, which suggests the role of flow-induced ordering for hydrogen-bonded liquids [58,59]. Experimental work has shown that the structure of water inside carbon nanopores has been found to be closer to solid than liquid [60]. The layering of water slowing the flow through nanotubes has been observed in molecular dynamics simulations [61]. ‘Liquid–vapor’ phase transitions and ice-like behavior inside CNTs have also been observed at low temperatures [62].

Table 1  
Summary of the observed pressure-driven flow through aligned MWCNT membrane.

Liquid	Permeable pore (# per cm <sup>2</sup> )	Membrane thickness (μm)	Initial permeability (cm <sup>3</sup> /cm <sup>2</sup> ) min bar	Flow velocity normalized at 1 bar (cm/s)	Viscosity (cP)	Calculated Newtonian velocity at 1 bar	Slip length (μm)
Hexane	3.4×10 <sup>9</sup>	126	0.44	5.6	0.3	5.16×10 <sup>-4</sup>	9.5
Decane	3.4×10 <sup>9</sup>	126	0.053	0.67	0.9	1.72×10 <sup>-4</sup>	3.4
Water	1×10 <sup>9</sup>	34	0.58	25	1.0	5.7×10 <sup>-4</sup>	54
			1.01	43.9		5.7×10 <sup>-4</sup>	68
0.017M KCl	3.4×10 <sup>9</sup>	126	0.72	9.5		1.5×10 <sup>-4</sup>	39
			1.25	19.6		1.5×10 <sup>-4</sup>	108
EtOH IPA	3.4×10 <sup>9</sup>	126	0.35	4.5	1.1	1.4×10 <sup>-4</sup>	28
			0.088	1.12	2	7.7×10 <sup>-4</sup>	13

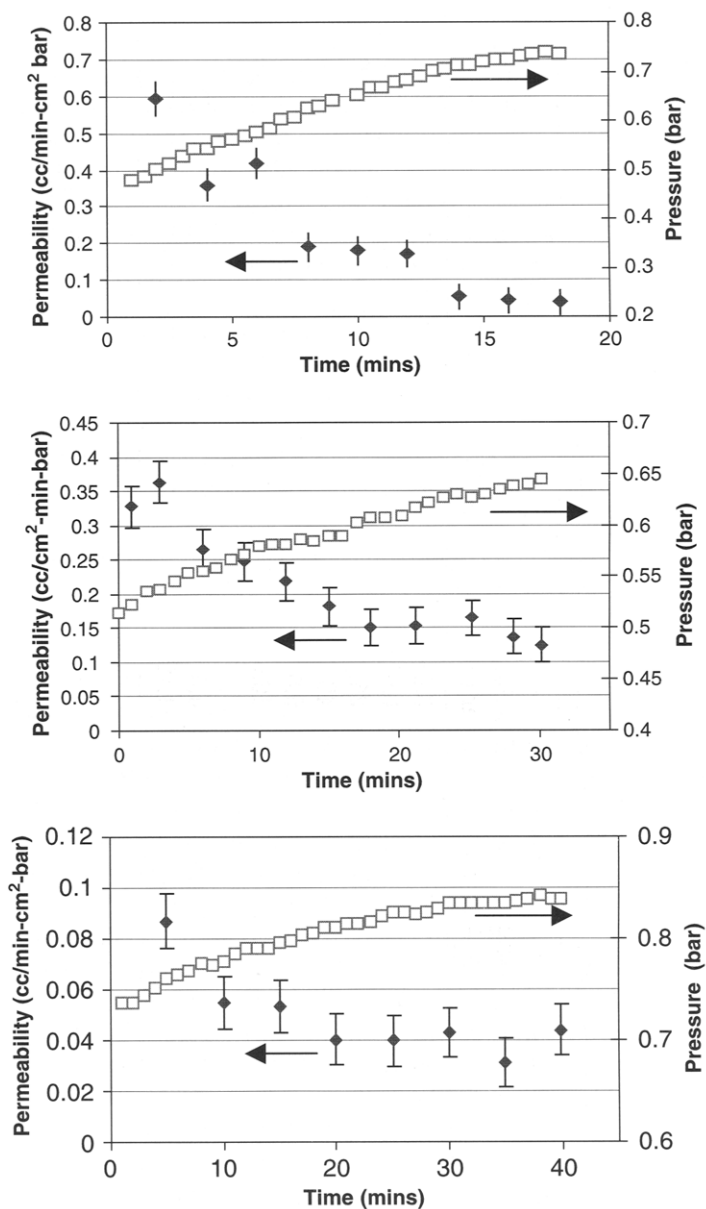


Figure 9. Pressure normalized permeability decay with time for associative liquids (a) water, (b) ethyl alcohol, and (c) iso-propyl alcohol. Reduced in the flow is accompanied by an increase in pressure, indicating the ordering of the liquids inside the CNTs. Error bars are derived from the mass of one drop that can be forming on effluent fitting.

Other possible experimental reasons for the observed decrease in flux can be the formation of bubbles on the hydrophobic solid–liquid interface, ‘fouling,’ or compaction of the pores by pressure. Solvents in these experiments were vacuum boiled to eliminate absorbed gasses. No reduction of flow was observed in PA nor polyacrylonitrile (PAN) ultrafiltration (UF) membranes under the same experimental conditions. Fouling was ruled out since diffusion experiments on membranes after pressure experiments showed no decline in permeability and the control membranes (PA and UF) showed no reduction in flow with time in the same experimental cell. Compaction was ruled out since the CNTs are some of the most mechanically stiff materials. Also, in other softer systems, compaction accounts was only about a 5% reduction in flow [63]. The addition of KCl (0.017 M) to water dramatically negates ordering that blocks flow through the CNT, with no reduction in flux seen with time. However, it is important to note that it is experimentally difficult to exclusively prove that air bubbles do not exist despite these accepted precautions with control experiments, and since KCl is also known to reduce the formation of air bubbles [64]. Thus, at present, there are indications of water ordering but no conclusive proof of the phenomena.

Conventionally, the flow of liquids ( $J$ ) through porous membranes can be predicted using the Haagen–Poiseuille equation [65] given by

$$J = (\varepsilon r^2 \Delta P) / (8 \mu \tau L)$$

In this formula,  $\varepsilon$  is the relative porosity,  $r$  the pore radius (7 nm for our system),  $P$  the pressure applied,  $\mu$  the dynamic viscosity,  $\tau$  the tortuosity (1.1), and  $L$  the length of the pore. The basic assumptions of this equation are laminar flow and ‘no-slip’ at the boundary layer, i.e. the velocity of the fluid at the CNT wall is zero. Observed flow rates are four to five orders of magnitude faster than conventional fluid prediction. In fact the observed flow velocity of water is close to the theoretical prediction of 90 cm/s (1 bar pressure) due to cooperative H-bond ordering and minimal CNT interaction [38]. It is necessary to mention that since the flow of water through the membrane is declining with time, there is a slight systematic underestimate of the initial flow rate. Three different measurements of H<sub>2</sub>O flow are shown in Table 1. This experimental observation of extremely high velocity supports the hypothesis that the transport of water through CNTs is frictionless and is independent of the length of the channel [66]. From previous studies [48,67], it was also found that the diffusivities of large molecules do not change significantly from bulk, suggesting a frictionless flow inside the smooth interiors of CNTs.

The slip lengths for the solvents on the CNTs can be calculated from the equation [68]:

$$V(\lambda) / V_{\text{ns}} = 1 + 4\lambda / r$$

In this formula,  $V(\lambda)$  is the experimentally observed flow velocity (cm/s),  $V_{\text{ns}}$  the ‘no-slip’ flow velocity calculated from the Haagen–Poiseuille equation,  $\lambda$  the slip length, and  $r$  the radius of the nanotube. Higher slip lengths were observed for the polar

molecules. Both for the polar and non-polar liquids, the slip lengths decrease with the chain length of the hydrocarbon. This is consistent with the fact that better wetting of the CNT wall decreases the slip length. The flow velocity of hexane through each nanotube was about 5.6 cm/s as compared to predictions of a flux of gaseous methane of  $\sim 260$  cm/s at 1 bar [69]. Another molecular dynamics study [70] reports about an order of magnitude difference in flux between methane and butane. It is difficult to calculate the flux values of butane from this work, as the pressures are experimentally too high. However, extrapolating another report [40] of butane flowing through CNTs results in velocities of  $\sim 26$  cm/s. This value is in close agreement with the flux of hexane found out in the experimental CNT study. Following the same trend [41], the experimental CNT study showed an order of magnitude difference in the flux of hexane and decane. This is despite the fact that hexane is only  $\sim 3$  times more viscous than decane. This indicates that the flow through nanotubes is not just limited by the viscous forces, but also on  $n^2$  dependence of hydrocarbon chain length [71].

In general, the transport through the CNT core shows minimal or modest enhancement in ionic diffusion and  $N_2$  gas flow, but incredible enhancement (4–5 orders of magnitude) of fluid flow. In the former case of ionic diffusion and Knudsen diffusion, the non-interacting CNTs offer no advantages, essentially acting like a mirror for ions and molecules to bounce off. This random scattering would not enhance transport rate and in fact with ions would closely correlate with bulk diffusivity. For gas flow, enhancement may occur with concentration of longitudinal momentum in scattering. In the case of the much denser fluid flow, dramatic enhancement is observed because of the nearly frictionless interface of the fluid and the CNT. This allows for very high wall velocity. The boundary condition of non-zero velocity at the CNT wall does not require the viscous transfer of momentum from a 'core' velocity, as is seen in conventional pores that have strong chemical interactions between pore and fluid and have high roughness at the atomic scale.

### 6.1. Gate-keeper functionality

Importantly, the open *tips* of CNTs have carboxyl end groups that are readily functionalized, forming the basis for 'gate keeper' controlled chemical separations or an ion-channel mimetic sensor. If a selective functional molecule is placed at the entrance of the CNT and is coordinated with a bulky receptor, the CNT pore would be blocked and the ionic flow through the CNT core would be reduced. Ionic flow can be easily detected electrochemically, which provides the basis of a selective sensor system. As a demonstration, the well-established biotin/streptavidin analyte/receptor system was chosen. (+)-Biotinyl-3,6 dioxaoctanediamine (Pierce Biotechnology EZ-link) was reacted with the carboxylate end groups of the CNT membrane using a carbodiimide-mediated reaction. This was subsequently coordinated with streptavidin to block the pore. The flux of  $Ru(NH_3)_6^{3+}$  ion through the membrane was measured for three different cases. The first case was the as-prepared aligned CNT membrane. The second was after biotin functionalization and the third was after coordination with streptavidin. With the attachment of the biotin tether (2.2 nm long), the  $Ru(NH_3)_6^{3+}$  flux was reduced by a factor of 5.5. Simple cross-sectional area reduction of the CNT inner core from 7.5 to 3.1 nm (reduction

of 4.4 nm) would predict a reduction of ionic flux by a factor of 6.2. This shows promise for using the dimensions of the attached molecules to further control pore dimensions. The ionic flux was further reduced by a factor of 15 upon streptavidin coordination with biotin. This approach of functionalizing the entrance to CNT cores could be generalized to a variety of biological affinity pairs to block ionic flow through the CNT core, when the analyte is present. Recently, it has been shown that a reversible biochemical pair can detect either the presence of bulky analyte (streptavidin) or the release agent of the streptavidin (biotin in solution) [72]. Essentially, this is a demonstration of two different general biomolecule detection methods. First is the presence of a large biomolecule and second is the detection of the release agent.

Besides demonstrating biochemical functionality, the chemistry at the CNT entrance was also systematically changed with molecules of desired length, hydrophilicity, or chemical functionality. This approach was necessary to investigate the hypothesis of a 'gate-keeper' mechanism for controlling the flow and selectivity of chemical transport through the CNT membranes. The relative selectivity of two similarly charged but differently sized permeate molecules was measured through the CNT membranes. The selectivity data were then analyzed using hindered diffusion models to demonstrate that selective transport occurred near the CNT tip entrances and not along the entire length of the CNT. This was found to be consistent with a 'gate-keeper' geometry [67].

The CNT membranes were functionalized using conventional carbodiimide chemistry with the functional molecules shown in Fig. 10.

Comparison of the transport of different molecules through a porous material is an effective method of probing the size and chemical state of pore interiors [73]. Hindered diffusion occurs in pores when the size of the permeating species is large enough to force significant interaction with the pore walls [74]. Transport of two molecules having similar charge but different sizes,  $\text{Ru}(\text{bi-py})_3^{2+}$  and  $\text{MV}^{2+}$ , show the relative hindrance provided by functional molecules at the entrance of the CNT cores. The summary of the transport properties through the membranes as a function of chemical functionalization are shown in Table 2.

It is also important to note that the Fe-catalyzed CVD process for synthesizing aligned CNTs can lead to the presence of iron nanoparticles in the CNT cores. This causes sample-to-sample variation in membrane transport. Plasma oxidation and HCl treatment are used to remove iron particles, but in extreme cases they remain to reduce the absolute flux values. As a control experiment, 'membranes' were made using identical process steps and thickness from regions of the deposition reactor where all CNTs are blocked by Fe. No flux of either  $\text{MV}^{2+}$  or  $\text{Ru}(\text{bi-py})_3^{2+}$  was detected, even after 3 days of diffusion experiments. The detection limit of the instrument was  $5.15 \times 10^{-8}$  M for  $\text{Ru}(\text{bi-py})_3^{2+}$ . Using the cell volume of 1.3 mL, the diffusion through the blocked membrane was less than 0.009 nmol/h. This indicated that diffusion through or defects in PS polymer film were not significant transport mechanisms. The selectivities are represented by  $\alpha$ , the ratio of the transport rates of the two species. In these simultaneous flux experiments, selectivities would not be affected by any CNTs that were blocked by Fe. Observed selectivities were greater than 1.5 calculated from the ratio of solution



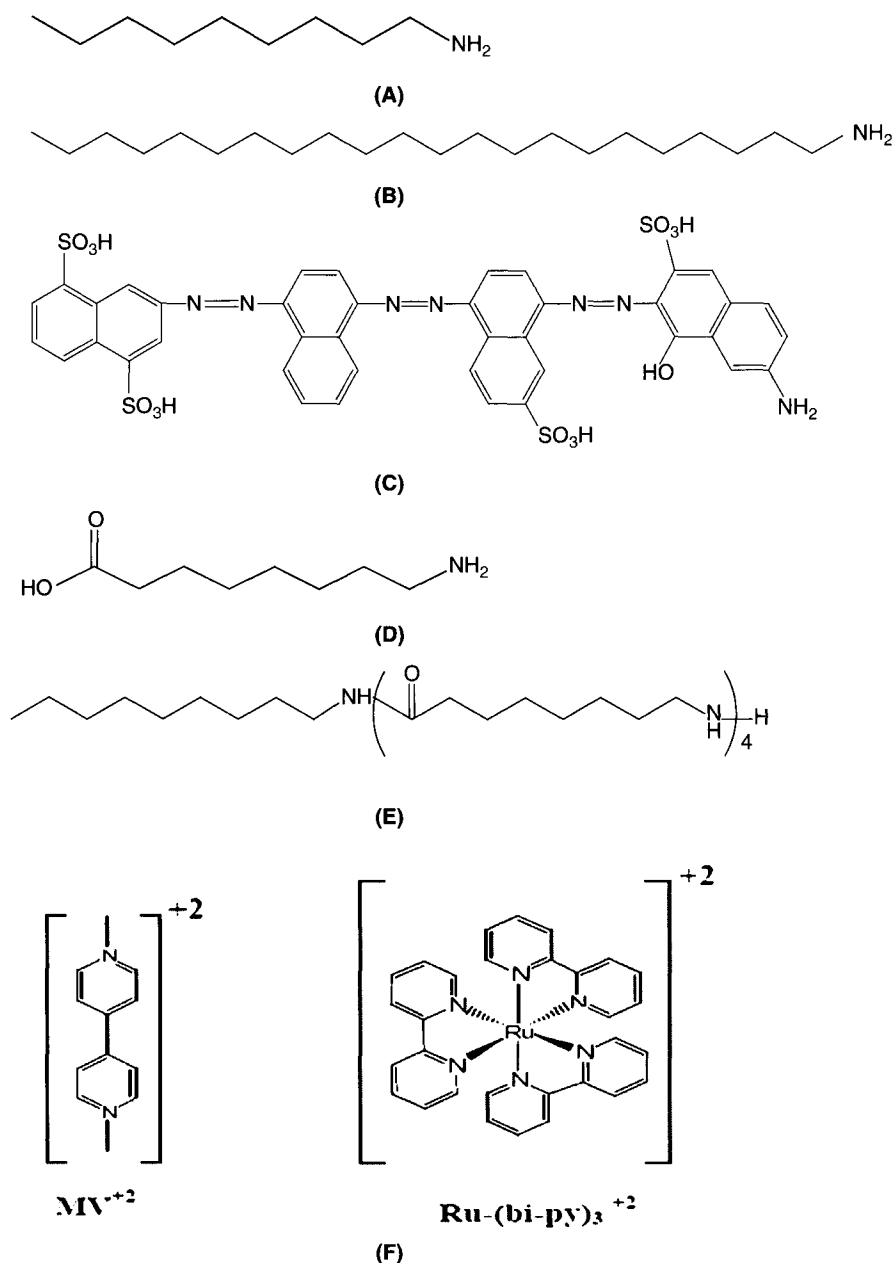


Figure 10. Schematic of the molecules used for functionalizing nanotube membrane (a) C9, (b) C22, (c) dye, (d) ACA, (e) C40 (polypeptide) (formed after four sequential reaction of ACA, followed by C9), and (f) different sized probe molecules to diffuse through CNT membrane, methyl viologen ( $MV^{2+}$ ) with equivalent spherical radius of 0.54 nm and  $Ru(bipyridine)_3^{2+}$  with spherical radius of 1.1 nm.

Table 2

Summary of transport measurements across CNT membranes (0.3 cm<sup>2</sup> area, 5 mmol of each source) from a 2-component source solution. Simultaneous flux of permeate is calculated from the linear fit of solute concentration vs. time. The separation factor ( $\alpha$ ) was experimentally measured for the membranes. Pore size was calculated from the observed separation factor ( $\alpha$ ) and using a hindered diffusion model of functionalization at the CNT entrance (model (i)).

Membrane tip functionality	Size of molecule (Å)	MV <sup>2+</sup> flux (nmol/h) (90% confidence)	Ru(bi-py) <sub>3</sub> <sup>2+</sup> flux (nmol/h) (90% confidence)	$\alpha$	Pore size calculated from $\alpha$ (Å)
CNT	0	4.21 ( $\pm$ 1.0)	2.45 ( $\pm$ 0.39)	1.7	67
CNT-C9	11.4	6.40 ( $\pm$ 2.18)	2.12 ( $\pm$ 0.90)	3.0	37
CNT-dye	26	21.05 ( $\pm$ 2.32)	9.57 ( $\pm$ 0.91)	2.2	47
CNT-C22	28	1.84 ( $\pm$ 0.48)	0.93 ( $\pm$ 0.22)	2.0	50
CNT-C40	52	0.65 ( $\pm$ 0.13)	0.18 ( $\pm$ 0.02)	3.6	33

diffusion coefficients. This indicates that the observed transport is not through microcracks in the CNT membranes.

In general the separation coefficients of MV<sup>2+</sup> and Ru-(bi-py)<sub>3</sub><sup>2+</sup> were modest (1.7–3.6) compared to PA, where separation coefficients were as high as 1500 [20]. In the alumina case, pore size reduction was accomplished by solid plating to sizes less than the diameter of Ru-(bi-py)<sub>3</sub><sup>2+</sup>. In the MV<sup>2+</sup> and Ru-(bi-py)<sub>3</sub><sup>2+</sup> cases, the areal density of the functionalized molecule may not be complete as it would be in the case of solid pore plating. In addition, the conformation of the molecules may change with solvent conditions. The observed selectivity is consistent with ‘gate-keeper’ functionality at the CNT tips. In optimized systems with high functional density, the tip functionality would have the advantage of short path length of hindered diffusion, thereby increasing overall chemical flux.

From established hindered diffusion studies, an increase in the separation factor ( $\alpha$ ) would be expected from a decrease in pore size by the attachment of a functional molecule. The separation factor for the initial CNT membrane with COOH functionality is 1.7, close to the bulk solution value. This increases to a separation factor of 3 in the CNT-C9 case. Purely geometric arguments using the diameter of the CNT core would give a pore size of 47 Å. This is derived from 7 nm nominal core diameter minus twice the molecule length.

Pore size reductions by depositing molecules in mesoporous silica materials using silane chemistry have been reported to be consistent with the length of the molecule [75]. However, when a longer aliphatic amine of length ~28 Å (CNT-C22), was attached to the CNT membrane, the selectivity actually declined to 2.0. The Ru-(bi-py)<sub>3</sub><sup>2+</sup> flux also decreased compared to that of CNT-C9, by a factor of about 2.2. The overall flux through CNT-C22 was reduced by increased hydrophobicity at the pore entrances. This has also been the case with C<sub>18</sub> modified PA [21] having very

little transport of water and hydrophilic permeates. Liquid permeation experiments in hydrophobic membranes have also shown lower permeability of polar molecules, such as water and alcohols as compared to alkanes. The reverse is true for hydrophilic membranes [76]. Since the separation factor is a function of the pore diameter at the CNT entrances, attachment of a larger molecule should ideally give a reduced pore size as was observed in hydrophilic mesoporous silica (as measured by BET) [74].

In other cases, it is possible that molecularly dense functionality was absent at the CNT core entrance due to a relatively small number of carboxylic acid groups at the CNT tips. This gave a reduced separation coefficient as compared to pore-plating methods. The reduction of the separation factor in CNT-C22 compared to CNT-C9 was consistent with the long hydrophobic alkyl chains preferring the surface of the hydrophobic CNTs and not protruding out into the aqueous channel. This was in contrast to the case of alumina or silica pores, where the long chain alkane interactions with the pore wall would be relatively weak.

## 6.2. Effect of charge and functional molecule aqueous solubility

Functionalization of the membrane with the anionically charged dye molecule (CNT-dye) led to increased flux of positively charged species. It increased approximately four-fold compared to the unmodified CNT membrane. Potential-dependent transport of charged species was demonstrated in gold nanotubule membranes [77]. Ru-(bi-py)<sub>3</sub><sup>2+</sup> flux increased approximately 2.8 times in 3.2 nm diameter and approximately 3.3 times in 1.5 nm diameter gold nanotube membranes when the applied potential was -0.4 V. Comparable increase of flux in CNT-dye indicated that there are electrostatic attractive forces acting on the positively charged permeate species by the negatively charged dye molecule.

Along with an increase in flux, an increase of separation factor in CNT-dye compared to CNT-C22 was also observed, despite the fact that the dye molecule is slightly smaller than C22. The presence of the charged functional molecule would not lead to an increase in the separation factor based on electrostatic attractions due to the identical charges on MV<sup>2+</sup> and Ru(bi-py)<sub>3</sub><sup>2+</sup>. Instead, the increase is due to the conformation of the charged, soluble dye molecule. In the case of long aliphatic chain lengths for C22, the separation factors do not increase significantly ( $\alpha = 2.0$ ) because the molecules prefer to be oriented along the CNT walls instead of protruding into the aqueous channel.

By functionalizing the entrance to the CNT core with an anionically charged dye molecule, the flux of cationic permeates dramatically increases. The length of space charge layer (ionic strength of the solution) should affect the flux of the permeates, and the separation factor. These observations are shown in Table 3.

There was nearly a three-fold decrease in Ru-(bi-py)<sub>3</sub><sup>2+</sup> flux when the electrolyte strength increased to 0.01 M KCl. This is consistent with short Debye screening lengths at high ionic strength. This reduced the Coloumbic attraction of the cationic permeate to the anionic functional groups, which reduced the overall flux. A theoretical study [32] of SWCNTs of 2.2 nm diameter found strong enhancement of ionic flux into CNT core with charged carboxylate groups.

Table 3

Transport measurements across CNT-dye in different concentration of electrolyte (KCl).

Electrolyte concentra tion (M) KCl	MV <sup>2+</sup> flux (nmol/h) (90% confidence)	Ru(bi-py) <sub>3</sub> <sup>2+</sup> flux (nmol/h)(90% confidence)	$\alpha$
0	21.1 ( $\pm 2.3$ )	9.57 ( $\pm 0.91$ )	2.2
0.01	8.88 ( $\pm 0.40$ )	3.24 ( $\pm 0.17$ )	2.7
0.1	10.36 ( $\pm 0.97$ )	4.12 ( $\pm 0.28$ )	2.5

### 6.3. Comparison of observed selectivity to hindered diffusion models

Observed separation coefficients between differently sized permeate molecules can give insight into the geometry of the membranes pores. The diffusivity ( $D_0$ ) of a solute in bulk solution is given by the Stoke–Einstein equation:

$$D_0 = kT/6\pi\eta R_s, \quad (1)$$

where  $k$  is the Boltzmann's constant,  $T$  the temperature,  $\eta$  the solvent viscosity, and  $R_s$  the Stokes–Einstein radius of the solute. The phenomena of the diffusion of solutes in the constrained space of pores causes the molecular friction to exceed the value in the bulk, thereby decreasing the effective diffusivity in the pores. Two correction factors [78] are used to model the phenomena of hindered diffusion, both of which can be expressed as a function of the reduced pore diameter,  $\lambda$ , given by

$$\lambda = \text{permeate molecule diameter/pore diameter}. \quad (2)$$

Hindered diffusion becomes dominant when  $\lambda$  approaches one. For  $\lambda$  greater than one, solute exclusion occurs. For purely steric interactions between the solute and the pore wall, the hindered diffusivity,  $D_h$ , can be expressed by Renkin's equation as [73]:

$$D_h = D_0(1 - \lambda)^2(1 - 2.104\lambda + 2.09\lambda^3 - 0.95\lambda^5) \quad (3)$$

It is of interest to compare experimental separation coefficients ( $\alpha$ ) to predictions of hindered diffusion at the CNT tip entrances in order to verify a 'gate-keeper' transport limited mechanism.

Two models were considered. The first had hindered diffusion only at distances  $L_1/2$  at the two ends of the CNT and normal diffusion along the length  $L_2$ . The total length of the nanotube in this case is thus  $L_1 + L_2$ . In the second case, there was hindered diffusion throughout the nanotube. Schematics for the two models are shown in Fig. 11a. Steady state conditions were assumed for this model. Since the cross-sectional area inside the nanotube is changing,  $W = N \times A$  is constant, where  $W$  is the molar transport rate,  $N$  the molecular flux (mol/cm<sup>2</sup> h), and  $A$  the pore area (cm<sup>2</sup>). It is also assumed that the concentration of a species changes

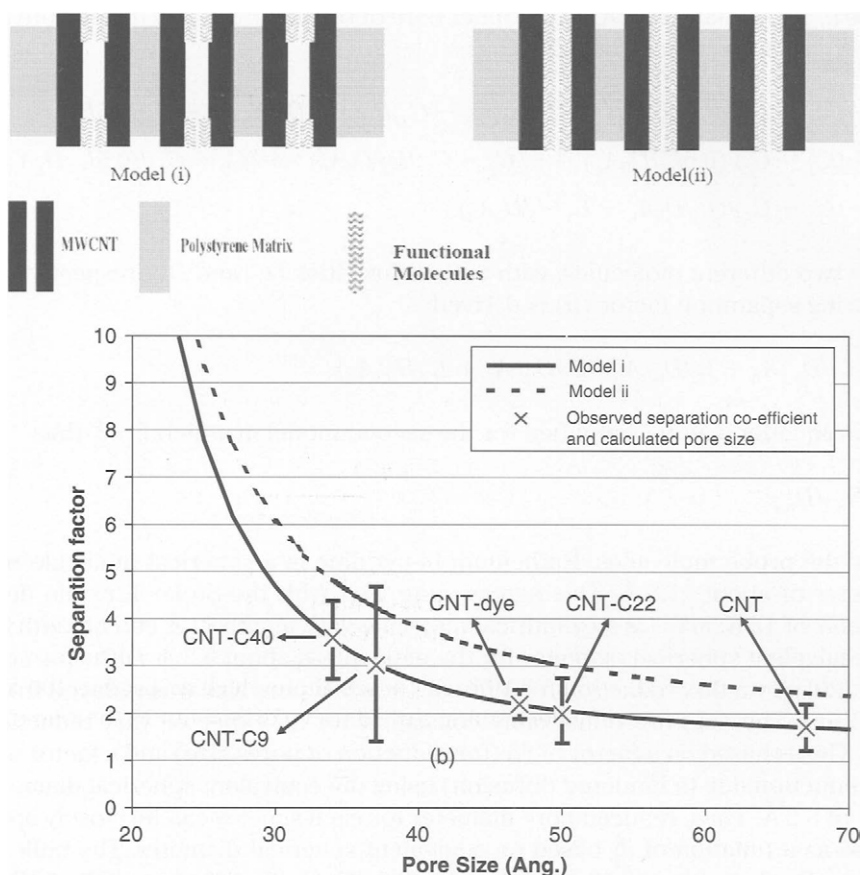


Figure 11. (a) Schematic, (b) separation factor, and  $(\alpha)$  with error bars (at 90% confidence) vs. pore size for (i) hindered diffusion at the entrance and exit to the nanotubes, (ii) hindered diffusion throughout the nanotube. Model (ii) predicts a higher  $\alpha$  than model (i) due to a longer hindered diffusion path length. From Ref. [67], reproduced with permission from American Chemical Society copyright 2005.

along the nanotube, with  $C_1$  (mol/cm<sup>3</sup>) at the entrance and  $C_4$  (mol/cm<sup>3</sup>) at the exit. These are the same as the feed and permeate concentration, respectively.  $C_2$  (mol/cm<sup>3</sup>) and  $C_3$  (mol/cm<sup>3</sup>) are the concentrations at the end of the first functional layer at the entrance and at the beginning of the second functional layer at the exit. The cross-sectional area of nonfunctionalized nanotube is  $A_0$  (cm<sup>2</sup>) and the area where hindered diffusion occurs is  $A_h$  (cm<sup>2</sup>). These areas are given by

$$A_0 = \pi d_0^2/4; A_h = \pi d_p^2/4, \quad (4)$$

where  $d_0$  is the diameter (Å) of the inner core of the nanotube and  $d_p$  the pore diameter (Å) at the entrance and exit. Thus,

$$\begin{aligned} W &= -D_{\text{r}A_{\text{h}}}(C_1 - C_2)/0.5L_1 = -D_0A_0(C_2 - C_3)/L_2 = -D_{\text{r}A_{\text{h}}}(C_3 - C_4)/0.5L_1 \\ &= -(C_1 - C_2)/(0.5L_1/D_{\text{r}A_{\text{h}}}) = -(C_2 - C_3)/L_2/D_0A_0 = -(C_3 - C_4)/(0.5L_1/D_{\text{r}A_{\text{h}}}) \\ &= -(C_1 - C_4)/(L_1/D_{\text{r}A_{\text{h}}} + L_2/D_0A_0). \end{aligned} \quad (5)$$

For two different molecules, with bulk diffusivities  $D_{0,1}$  and  $D_{0,2}$ , respectively, the following separation factor ( $\alpha$ ) is derived:

$$\alpha = (L_1/D_{\text{h},2}A_{\text{h}} + L_2/D_{0,2}A_0)/(L_1/D_{\text{h},1}A_{\text{h}} + L_2/D_{0,1}A_0). \quad (6)$$

This equation can be simplified for the second model in which  $L_2=0$ , thus

$$\alpha = D_{\text{h},1}/D_{\text{h},2}. \quad (7)$$

For the probe molecules, Ruthenium bi-pyridine is a spherical molecule with a diameter of about 11.8 Å. This agrees quite well with the Stoke–Einstein derived diameter of 12 Å.  $\text{MV}^{2+}$  is a cylindrical molecule with length 11 Å and breadth 3.3 Å. The equivalent spherical diameter for the molecule is about 5.2 Å. Diffusion studies in PA [20] saw a flux reduction for  $\text{MV}^{2+}$  of  $10^3$  when pore size was reduced from 5.5 to 0.6 nm. The data are remarkably consistent for an expected flux reduction of 1000. This is based on a factor of 83 (for reduction of pores size) and a factor of 13.8 (for reduction due to hindered diffusion) using the equivalent spherical diameter of  $\text{MV}^{2+}$  of 5.2 Å. Thus, reduced pore diameter for each species can be closely approximated as a function of  $d_p$  based on equivalent spherical diameter. The bulk diffusivity of  $\text{Ru}(\text{bi-py})_3^{2+}$  is  $5.16 \times 10^{-6} \text{ cm}^2/\text{s}$  [79]. The bulk diffusivity [80] of  $\text{MV}^{2+}$  is 1.5 times that of  $\text{Ru}(\text{bi-py})_3^{2+}$  (i.e. ).

In order to estimate the length of functionality ( $L_1$ ) in the first model, microscopy experiments were carried out on the CNTs from the membranes [81]. The CNTs were removed from the polymer matrix by dissolving the polymer in toluene solvent. The carboxylate end groups from the oxidation near CNT tips were converted to thiol functionality by the previously mentioned carboimide chemistry. This is easily decorated with the easily observed Au nanoparticles. The CNTs were functionalized at each end for a distance approximately 7% of the total length of the nanotube. These observations are further elaborated on in Sec. 8. Though the exterior of the CNTs were decorated with Au particles, it is assumed that the same oxidation process occurred inside during functionalization with molecules. Thus,  $L_1$  is approximately 14% and  $L_2$  86% of the total length of the nanotubes. At the tips, the surface coverage of nanocrystalline-Au (nc-Au) was  $\sim 52\%$ . This is consistent with the previous argument that the functional molecules at the tip CNTs is not so great as to be molecularly dense (functional molecules packed side-by-side). However, this Au nanoparticle decoration experiment is only a lower limit of functional density, since several functional molecules at the CNT tip may be attached to the same Au nanoparticle.

The selectivity vs. calculated pore size ( $d_p$ ) plots for the two models are shown in Fig. 11b. Consistent pore sizes of the different membranes can be calculated from the first model and the experimentally observed separation factors. These calculated values are also shown in Table 2. Importantly, in the case of the as-oxidized (carboxylate only functionality) membrane, the first model gives a calculated pore size of 67 Å. This is consistent with microscopic characterization of MWCNT cores giving a nominal inner core diameter of 7 nm. Using the second model, the calculated core diameter of as-oxidized CNTs is 20 nm. Importantly, the functional molecules would not be physically long enough to give the observed higher separation coefficients. That is, hindered diffusion calculated from a 20 nm initial pore diameter minus twice the functional molecule length would not give the observed enhancement in separation coefficient. The higher flux observed with anionic dye molecule also supports this model of tip functionalization. If the CNT cores were lined with an attractive anionic charge, a reduction in flux of cations would be expected. This is due to partitioning onto the pore wall with a decrease in the effective  $D$ . This marked decrease in diffusion flux is commonly seen in ion-exchange membranes [82]. A somewhat subtle point of the first model is the assumption of bulk diffusivity  $D_0$  in the non-functionalized region of the CNT core. This would indicate that the permeate molecules have little interaction with the CNT wall. Such phenomena would be expected since theoretical studies predicting that water molecules would have a several Å gap with the CNT wall due to large vander waals distance [29]. The data and model shown here are consistent but are not definitive proof of the nature of diffusive transport through the CNT. This is due to the experimental uncertainty of the number and the conformational state of the functionalized 'gate-keeper' molecules at the CNT core entrances.

## 7. ELECTROCHEMICAL OXIDATION AND BI-FUNCTIONALITY

Electrochemistry can also be used to tailor the aligned CNT membrane structure. Practical requirements to have usable membrane strength and aligned CNT growth require that the membrane must be at least 5  $\mu\text{m}$  thick. However, for large molecular separations based on gate-keeper selectivity, a short path length is desired since diffusion flux would increase. One possible route to trim the CNT length is to anodically oxidize them at + 1.7 V vs SCE [83]. Since the PS polymer is an insulator, the conductive CNTs are selectively etched within the polymer matrix. Thus, the pore length can be adjusted while maintaining the mechanical integrity of the thicker PS matrix.

Fig. 12a shows the surface of membrane films after  $\text{H}_2\text{O}$  plasma oxidation. The tips of the CNTs are extending above the surface because of the faster etching rate of PS by plasma treatment. Each bright area in Fig. 12a corresponds to tips of multiple (2–7) CNTs clustered together, resulting in outer diameters of  $\sim 50$  nm that are consistent with TEM observations. An areal density of  $6 (\pm 3) \times 10^{10}/\text{cm}^2$  can be estimated from this micrograph. Fig. 12b shows a schematic cross section illustration of how CNTs can be selectively oxidized electrochemically inside an insulating PS matrix.

Fig. 12c shows the surface after selective electrochemical oxidation. The PS surface pore size would be at least that of the 40 nm outer CNT diameter as

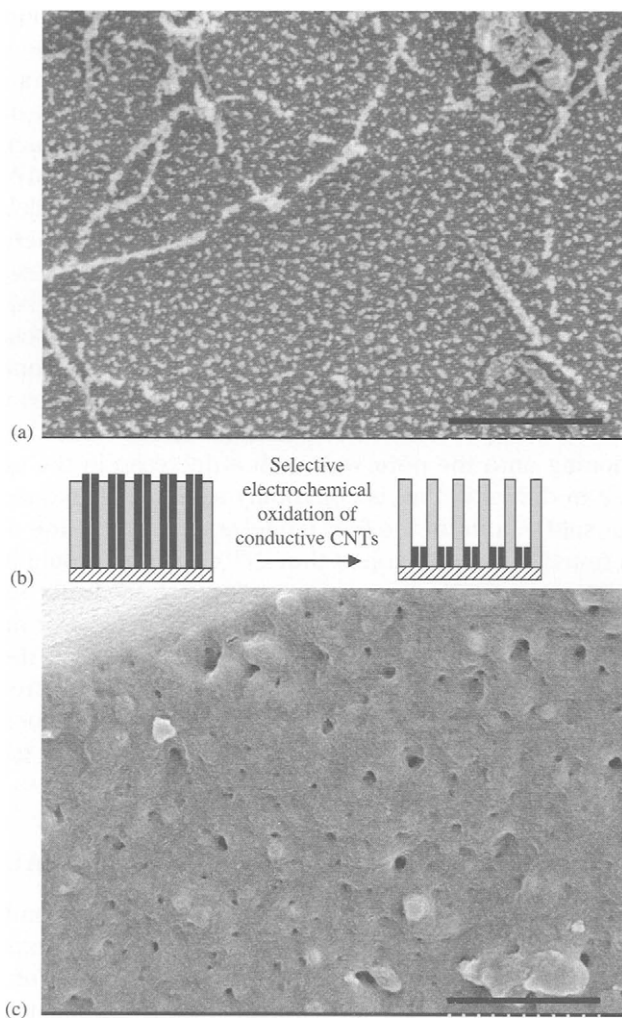


Figure 12. (a) Surface of CNT/PS membrane after  $\text{H}_2\text{O}$  plasma treatment. CNTs are above film surface due to faster etching rate of polymer. (b) Schematic for selective oxidation of only conductive CNTs. (c) Resultant film surface after electrochemical oxidation of CNT at +1.7 V vs. Ag/AgCl below surface of contiguous polymer film. Scale bar is 2.5  $\mu\text{m}$ . From Ref. [48], reproduced with permission from AAAS copyright 2004.

schematically diagrammed in Fig. 12b. Since the tips of CNTs tend to group together and there is the possibility of localized PS oxidation next to CNTs, the resulting PS surface pores are often greater than 100 nm. Selectively, reducing the length of CNT within the PS matrix can be a valuable tool for tuning membranes to give



required flux while keeping carboxylic functionalization at the tips of CNTs. These carboxylic end groups are then readily functionalized for selective molecular transport through the core of CNTs for separation or sensing applications.

Many 'bottom-up' nanofabrication techniques require diameter control and selective placement of CNTs. CNTs are chemically stable and highly hydrophobic in nature and therefore, they require surface modification in order to establish effective CNT-substrate interactions. There are various examples of sidewall functionalization, including coating with a polymer, surfactant, or DNA resulting in uniform dispersion or separation of CNTs [84–86]. In addition, oxidation of CNTs can result in tip and sidewall derivatization with phenolic and carboxylic groups, which can be further linked to a variety of molecules [87]. However, a common problem is functionalization along the CNT sidewalls, which results in unwanted reactive sites. These functionalization methods involve chemical oxidation processes, which not only oxidize the entire CNT area, but also uncontrollably cut the length of the CNTs. Carboxyl groups ( $-\text{COOH}$ ) can be derivatized with thiol terminal groups, such as  $\text{NH}_2-(\text{CH}_2)_{11}-\text{SH}$ . Then the CNTs can be decorated with gold nanoparticles to readily show the spatial location of chemical functionalization [88]. However, the selective functionalization of CNT tips without sidewall functionalization remains a major challenge.

Template-assisted growth of nanowires, followed by functionalization at nanowire tips, and removal of the membrane matrix, has demonstrated the ability to selectively functionalize nanowire tips [89]. This approach can be readily applied to aligned CNT membranes. A water ( $\text{H}_2\text{O}$ ) plasma oxidation process [51] opens the CNT tips, which is normally blocked with catalytic Fe nanocrystals. Oxidized CNT tips were exposed on both sides of the membrane. Importantly this oxidative chemistry affects only the tips of the CNTs, since the CNT sidewalls are protected by the PS matrix. As previously shown, these tips can be further derivatized by simple carbodiimide chemistry. In fact, it should be possible to derivatize each side of the membrane differently by floating the membrane on top of different reaction solutions. Interestingly, this approach was simultaneously explored unknowingly by two groups. [81,90].

To prove the spatial location of functional chemistry, carboxylate groups were converted to thiol functionality and decorated with nc-Au. An estimate of nanoparticle density can be obtained from TEM images by counting the number of Au nanoparticles (10 nm diameter) seen along a given length of a CNT. The density (particles/ $\mu\text{m}$  length) decreases from  $\sim 526$  particles/ $\mu\text{m}$  (in the first  $\sim 34$  nm of CNT length), to negligible values ( $< 7$  particles/ $\mu\text{m}$ ) at a location beyond 700 nm from the tip. Because PS etches faster than CNTs in plasma oxidation of membranes, tips of the CNTs were observed to be slightly above the polymer film in the membrane structure. Therefore, a small portion of the CNT sidewall on both sides of membrane is exposed to oxidation. For the average length of 34 nm starting from the CNT tip, the average nanoparticle coverage was approximately  $\sim 20\%$ . This is the ratio of total projection area of nanoparticles to total surface area of sidewall exposed to oxidation. The average coverage is the ratio of the total projection area of the nanoparticles to the total surface area at the tips. The average coverage at the CNT tips was approximately  $\sim 52\%$ .

With 10 nm diameter nc-Au, the maximum functionality detectable at saturation (i.e. 100% coverage) is  $10^{12}$  reactive sites/cm<sup>2</sup>. From nc-Au coverage, an estimate of surface functionality is  $5 \times 10^{11}$  sites/cm<sup>2</sup> at the tips and  $2 \times 10^{11}$  sites/cm<sup>2</sup> along sidewalls of CNT, above the PS matrix. Multiple reactive sites can be hidden under the nc-Au, so this TEM observation is a lower limit estimate of actual thiol functionality. As a reference, the density of broken C bonds at the edge of cleaved graphite is  $1.5 \times 10^{15}$ /cm<sup>2</sup>. On average, it appears that a small percentage of all possible carbon atoms at the tips and exposed CNT sidewalls are thiol functionalized. This relatively low functional density is consistent with the modest changes in the separation coefficient described in the previous section. A significant portion of the CNT is above PS matrix, and is thus subject to sidewall oxidation. However, it is possible to selectively electrochemically oxidize only the conductive CNT down into the insulating PS matrix, as previously described in this section. This allows selective functionalization of the etched MWCNTs only at the tips, since no CNT sidewall would be exposed above the PS.

Using MWCNT membranes, it is possible to functionalize only one side of membrane by floating the membrane on top of a reactive solution of 2-aminoethanethiol and EDC linker. The hydrophobic nature of PS allows sufficient surface tension to float the membrane on top of the aqueous solution. This approach, allowing exposed CNT tips on only one side of membrane to come in contact with the functionalization solution, is schematically shown in Fig. 13.

The Au nanocrystals in Fig. 14 shows the dramatic difference in functional density of the side of the membrane exposed to thiol functional chemistry, and the side not exposed. Fig. 14 also shows nanocrystalline-Fe in the core of the CNT, due to the higher amount of ferrocene in the CVD process. This CNT/PS composite came from a region of the substrate that had a relatively high concentration of nanocrystalline-Fe. Specific to this bi-functional derivatization of CNTs, chemical transport across the membrane is not required. An aligned CNT/polystyrene composite is preferred as a source of sidewall protected and tip-derivatized MWCNTs. Increasing ferrocene content in the CVD process can readily accomplish this over the entire substrate area, if desired. It is also noteworthy to mention that the approach shown here of floating a sidewall-protected film on top of a derivatization solution can similarly be applied to template-grown nanowire systems that utilize PA membranes.

## 8. FUTURE DIRECTIONS

A number of immediate scientific questions about the CNT membranes remain to be explored. How to understand the conformational roles of 'gate-keeper' ligands on selective separations? What is the role of fluid density between the extremes of extremely fast liquids and the conventionally described gas flow (Knudsen diffusion)? Can we unequivocally prove the flow-induced ordering of the polar solvents inside CNT cores? It is also important to increase the density of functional molecules at the tips of the CNTs. This provides selective interactions at the CNT entrances and promotes more efficient chemical separations. Methods to accurately assess the amount of functional density at the CNT tips must also be developed to

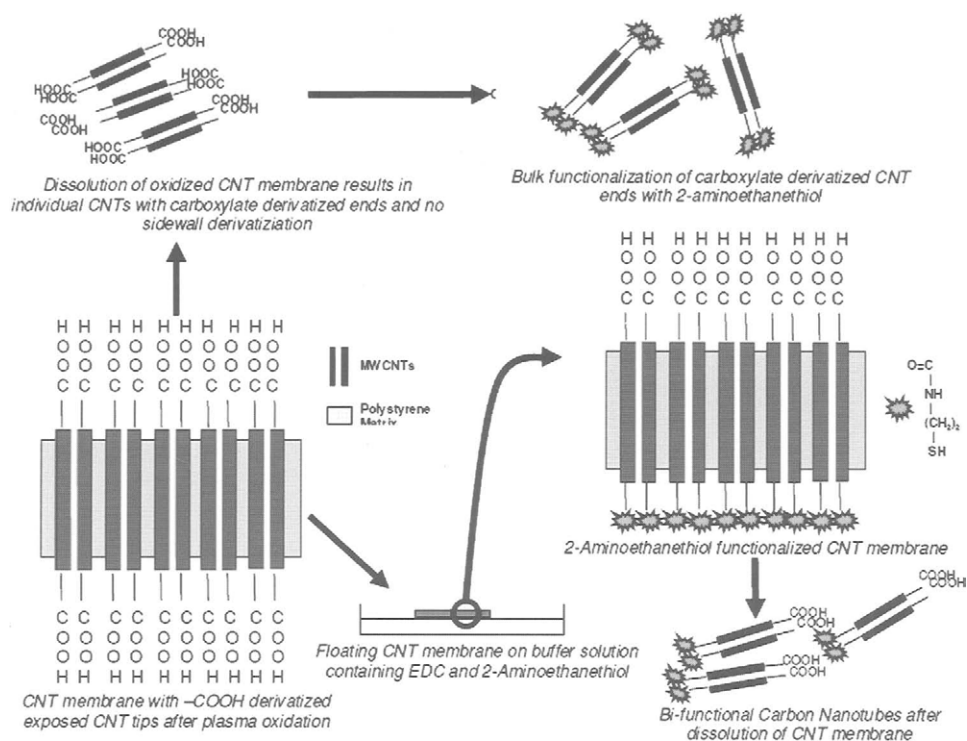


Figure 13. Scheme for selective functionalization of CNT tips and bi-functional CNTs using aligned CNT membrane precursor. Bi-functional (different chemistry at opposite ends of CNT) is achieved by floating the CNT membrane on top of functional carboiimide solution. From Ref. [81], reproduced with permission from Wiley-VCH Verlag GmbH & Co. copyright 2005.

properly model such interactions. A wide variety of important practical applications can be demonstrated with different specific functional chemistry at the CNT tips. This chemistry can be tailored to the desired application, such as sterically bulky ligands for gas and small molecule separations. Selective molecules (such as biotin) can be used for larger biomolecule separations. More specific bio-chemical pairs that can block the CNT cores can also be developed with this sensing platform. Catalyst can be directly coordinated with the CNT tips to allow simultaneous chemical reactions and separations. The conductive nature of the CNT membrane is also promising in terms of producing catalytic reactions with simultaneous separations. Also applied voltage can strongly affect transport rate for controlled drug delivery applications.

The aligned CNT membrane is a promising platform to mimic the complexity of nature's protein chemical channels. In particular, with this structure, it is possible to independently place 'gate-keeper' functional chemistry at each entrance of the

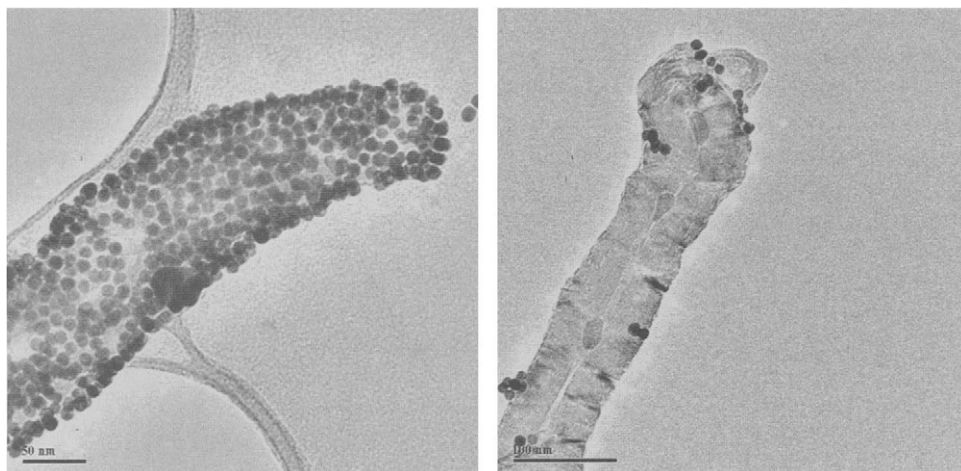


Figure 14. (Left) CNT tip from thiol functionalized side of membrane exposed to cystamine functionalization solution. 10 nm diameter nc-Au particles decorate thiol functionalized tips. (Right) Same CNT on side of membrane not exposed to functionalization solution.

nanometer-scale pores. Enhanced pressure-induced transport is seen through the core of the CNT due to nearly frictionless interface between the CNT and the fluid. In a significant measure, this membrane system achieves the four critical components to mimic nature's protein chemical channels. First, it is an impermeable matrix film with a high areal density of controlled nanometer-scale pores. Second, it has selective 'gate-keeper' molecules that attracts molecules of interest while excluding others. Third, it has a channel that promotes high transport rates, and fourth, it is possible to have different tip-functional chemistry than at the other side of the membrane.

## REFERENCES

1. B. Hille, *Ionic Channels of Excitable Membranes*, Sinauer Associates Inc, Sunderland, MA, 1984.
2. K. Murata, K. Mitsuoka, T. Hirai, T. Walz, P. Agre, J. B. Heymann, A. Engel and Y. Fujiyoshi, *Nature* **407** (2000) 599.
3. *Water and Waste Digest* **15**, (2005).
4. D. M. Considine and G. D. Considine, *Van Nostrand's Scientific Encyclopedia*, 6th ed., P2337-9 Van Nostrand Reinhold Co, New York (1983).
5. J. M. Henis, M. K. Tripodi and D. I. Stimpson, *Modified polymeric surfaces and processes for preparing same*, US Patent 4,794,002, 1988.
6. E. Klein, *J. Membr. Sci.* **179** (2000) 1.

7. C. Charcosset, *J. Chem. Technol. Biotechnol.* **71** (1998) 95.
8. D. J. Stimpson, *Polym. Prepr.* **27** (1986) 424.
9. M. Kim, K. Saito, S. Furusaki, T. Sugo and J. Okamoto, *J. Membr. Sci.* **56** (1991) 289.
10. K. Keizer and H. Verweij, *Chemtech* **26** (1996) 37.
11. J. C. Poshusta, V. A. Tuan, J. L. Falconer and R. D. Noble, *Ind. Eng. Chem. Res.* **37** (1998) 3924.
12. B. Oonkhanond and M. E. Mullins, *J. Membr. Sci.* **194** (2001) 3.
13. A. F. Ismail and L. I. B. David, *J. Membr. Sci.* **193** (2001) 1.
14. S. S. Wang, M. Y. Zeng and Z. H. Wang, *J. Membr. Sci.* **109** (1996) 267.
15. J. Hayashi, M. Yamamoto, K. Kusakabe and S. Morooka, *Ind. Eng. Chem. Res.* **34** (1995) 4364.
16. J. Hayashi, H. Mizuta, M. Yamamoto, K. Kusakabe and S. Morooka, *J. Membr. Sci.* **124** (1997) 243.
17. C. W. Jones and W. J. Koros, *Carbon* **32** (1994) 1427.
18. C. W. Jones and W. J. Koros, *Ind. Eng. Chem. Res.* **34** (1995) 158.
19. T. Thurn-Albrecht, R. Steiner, J. Derouchey, C. M. Stafford, E. Huang, M. Bal, M. Tuominen, C. J. Hawker and T. P. Russell, *Adv. Mater.* **12** (2000) 1138.
20. K. B. Jirage, J. C. Hulteen and C. R. Martin, *Science* **278** (1997) 655.
21. E. D. Steinle, D. T. Mitchell, M. Wirtz, S. B. Lee, V. Y. Young and C. R. Martin, *Anal. Chem.* **74** (2002) 2416.
22. S. B. Lee, D. T. Mitchell, L. Trofin, T. K. Nevanen, H. Soderlund and C. R. Martin, *Science* **296** (2002) 2198.
23. S. A. Miller and C. R. Martin, *J. Electroanal. Chem.* **522** (2002) 66.
24. H. Kanzow, C. Lenski and A. Ding, *Phys. Rev. B* **63** **12** (2001) 5402.
25. H. Ago, T. Komatsu, S. Ohshima, Y. Kuriki and M. Yumura, *Appl. Phys. Lett.* **77** (2000) 79.
26. Y. Li, J. Liu, Y. Q. Wang and Z. L. Wang, *Chem. Mater.* **13** (2001) 1008.
27. J. -M. Bonard, P. Chauvin and C. Klinke, *Nano Lett.* **2** (2002) 665.
28. C. L. Cheung, A. Kurtz, H. Park and C. M. Lieber, *J. Phys. Chem. B* **106** (2002) 2429.
29. G. Hummer, J. C. Rasaiah and J. P. Noworyta, *Nature* **414** (2001) 188.
30. A. Berezhkovskii and G. Hummer, *Phys. Rev. Lett.* **89** (2002) 064503.
31. J. H. Walther, R. Jaffe, T. Halicioglu and P. Koumoutsakos, *J. Phys. Chem. B* **105** (2002) 9980.
32. R. Qiao and N. R. Aluru, *Nano Lett.* **3** (2003) 1013.
33. H. J. Gao, Y. Kong, D. X. Cui and C. S. Ozkan, *Nano Lett.* **3** (2003) 471.
34. L. Sun and R. M. Crooks, *J. Am. Chem. Soc.* **122** (2000) 12340.
35. M. J. Casavant, D. A. Walters, J. J. Schmidt and R. E. Smalley, *J. Appl. Phys.* **93** (2003) 2153.
36. A. Srivastava, O. N. Srivastava, S. Talapatra, R. Vajtai and P. M. Ajayan, *Nat. Mater.* **3** (2004) 610.
37. T. Ohba, H. Kanoh and K. Kaneko, *Nano Lett.* **5** (2005) 227.
38. G. Hummer, J. C. Rasaiah and J. P. Noworyta, *Nature* **414** (2001) 188.
39. V. P. Sokhan, D. Nicholson and N. Quirke, *J. Chem. Phys.* **117** (2002) 8531.

40. A. I. Skoulidas, D. M. Ackerman, J. K. Johnson and D. S. Sholl, *Phys. Rev. Lett.* **89** (2002) 185901.
41. Z. G. Mao and S. B. Sinnott, *J. Phys. Chem. B* **105** (2001) 6916.
42. C. Y. Wei and D. Srivastava, *Phys. Rev. Lett.* **91** (2003) 235901.
43. R. Andrews, D. Jacques, A. M. Rao, F. Derbyshire, D. Qian, X. Fan, E. C. Dickey and J. Chen, *Chem. Phys. Lett.* **303** (1999) 467.
44. S. B. Sinnott, R. Andrews, D. Qian, A. M. Rao, Z. Mao, E. C. Dickey and F. Derbyshire, *Chem. Phys. Lett.* **315** (1999) 25.
45. Z. F. Ren, Z. P. Huang, J. W. Xu, J. H. Wang, P. Bush, M. P. Siegal and P. N. Provencio, *Science* **282** (1998) 1105.
46. V. I. Merkulov, A. V. Melechko, M. A. Guillorn, M. L. Simpson, D. H. Lowndes, J. H. Whealton and R. J. Raridon, *Appl. Phys. Lett.* **80** (2002) 4816.
47. Z. J. Zhang, B. Q. Wei, G. Ramanath and P. M. Ajayan, *Appl. Phys. Lett.* **77** (2000) 3764.
48. B. J. Hinds, N. Chopra, T. Rantell, R. Andrews, V. Gavalas and L. G. Bachas, *Science* **303** (2004) 62.
49. C. A. Mitchell, J. L. Bahr, S. Arepalli, J. M. Tour and R. Krishnamoorti, *Macromolecules* **35** (2002) 8825.
50. D. Qian, E. C. Dickey, R. Andrews and T. Rantell, *Appl. Phys. Lett.* **76** (2000) 2868.
51. S. M. Huang and L. M. Dai, *J. Phys. Chem. B* **106** (2002) 3543.
52. M. A. Hamon, H. Hui, P. Bhowmik, H. M. E. Itkis and R. C. Haddon, *Appl. Phys. A* **74** (2002) 333.
53. C. V. Nguyen, L. Delzeit, A. M. Cassell, J. Li, J. Han and M. Meyyappan, *Nano Lett.* **2** (2002) 1079.
54. J. L. Bahr and J. M. Tour, *Chem. Mater.* **13** (2001) 3823.
55. S. S. Wong, A. T. Woolley, E. Joselevich, C. L. Cheung and C. M. Lieber, *J. Am. Chem. Soc.* **120** (1998) 8557.
56. X. Pages, V. Rouessac, D. Cot, G. Nabias and J. Durand, *Sep. Purif. Technol.* **25** (2001) 399.
57. M. Majumder, N. Chopra, R. Andrews, B. J. Hinds, *Nature* **438** (2005) 44.
58. T. G. Knudstrup, I. A. Bitsanis and G. B. Westermannclark, *Langmuir* **11** (1995) 893.
59. J. Klein and E. Kumacheva, *J. Chem. Phys.* **108** (1998) 6996.
60. T. Iiyama, K. Nishikawa, T. Suzuki and K. Kaneko, *Chem. Phys. Lett.* **274** (1997) 152.
61. A. Kalra, S. Garde and G. Hummer, *Proc. Natl. Acad. Sci. USA* **100** (2003) 10175.
62. N. Naguib, H. H. Ye, Y. Gogotsi, A. G. Yazicioglu, C. M. Megaridis and M. Yoshimura, *Nano Lett.* **4** (2004) 2237.
63. V. E. Reinsch, A. R. Greenberg, S. S. Kelley, R. Peterson and L. J. Bond, *J. Membr. Sci.* **171** (2000) 217.
64. V. S. J. Craig, B. W. Ninham and R. M. Pashley, *J. Phys. Chem.* **97** (1993) 10192.
65. M. Mulder, *Basic Principles of Membrane Technology*, Kluwer Academic Publishers, Dordrecht (2006).
66. V. P. Sokhan, D. Nicholson and N. Quirke, *J. Chem. Phys.* **117** (2002) 8531.

67. M. Majumder, N. Chopra and B. J. Hinds, *J. Am. Chem. Soc.* **127** (2005) 9062–9070.
68. E. Lauga, M. P. Brenner, H. A. Stone, *Handbook of Experimental Fluid Dynamics*, Springer, Barlin, 2005.
69. A. I. Skoulidas, D. M. Ackerman, J. K. Johnson and D. S. Sholl, *Phys. Rev. Lett.* **89** (2002) 185901.
70. Z. G. Mao and S. B. Sinnott, *J. Phys. Chem. B* **105** (2001) 6916.
71. C. Y. Wei and D. Srivastava, *Phys. Rev. Lett.* **91** (2003) 235901.
72. P. Nednoor, N. Chopra, V. Gavalas, L. G. Bachas and B. J. Hinds, *Chem. Mater.* **17** (2005) 3595.
73. B. D. Bath, H. S. White and E. R. Scott, *Anal. Chem.* **72** (2000) 433.
74. I. A. Kathawalla, J. L. Anderson and J. S. Lindsey, *Macromolecules* **22** (1989) 1215.
75. J. Liu, Y. Shin, Z. M. Nie, J. H. Chang, L. Q. Wang, G. E. Fryxell, W. D. Samuels and G. J. Exarhos, *J. Phys. Chem. A* **104** (2000) 8328.
76. D. Bhanushali, S. Kloos, C. Kurth and D. Bhattacharyya, *J. Memb. Sci.* **199** (2001) 1–21.
77. M. S. Kang and C. R. Martin, *Langmuir* **17** (2001) 2753.
78. W. M. Deen, *AIChE J.* **33** (1987) 1409.
79. C. R. Martin, I. Rubinstein and A. J. Bard, *J. Electroanal. Chem.* **151** (1983) 267.
80. J. C. Hulteen and C. R. Martin, *J. Mater. Chem.* **7** (1997) 1075.
81. N. Chopra, M. Majumder and B. J. Hinds, *Adv. Funct. Mater.* **15** (2005) 858.
82. H. Miyoshi, *Sep. Sci. Technol.* **34** (1999) 231.
83. T. Ito, L. Sun and R. M. Crooks, *Electrochem. Solid State Lett.* **6** (2003) C4.
84. Y. P. Sun, W. J. Huang, Y. Lin, K. F. Fu, A. Kitaygorodskiy, L. A. Riddle, Y. J. Yu and D. L. Carroll, *Chem. Mater.* **13** (2001) 2864.
85. W. J. Huang, S. Taylor, K. F. Fu, Y. Lin, D. H. Zhang, T. W. Hanks, A. M. Rao and Y. P. Sun, *Nano Lett.* **2** (2002) 311.
86. M. Shim, N. W. S. Kam, R. J. Chen, Y. M. Li and H. J. Dai, *Nano Lett.* **2** (2002) 285.
87. Y. P. Sun, K. F. Fu, Y. Lin and W. J. Huang, *Acc. Chem. Res.* **35** (2002) 1096.
88. J. Liu, A. G. Rinzler, H. J. Dai, J. H. Hafner, R. K. Bradley, P. J. Boul, A. Lu, T. Iverson, K. Shelimov, C. B. Huffman, F. Rodriguez-Macias, Y. S. Shon, T. R. Lee, D. T. Colbert and R. E. Smalley, *Science* **280** (1998) 1253.
89. N. I. Kovtyukhova and T. E. Mallouk, *Chem.-Eur. J.* **8** (2002) 4355.
90. K. M. Lee, L. C. Li and L. M. Dai, *J. Am. Chem. Soc.* **127** (2005) 4122.

## Chapter 15

### **C<sub>60</sub> and carbon nanotube sensors**

Toshiyuki Ohashi<sup>a,b</sup> and Liming Dai<sup>a,c</sup>

<sup>a</sup>Department of Chemical and Materials Engineering,  
School of Engineering, The University of Dayton,  
300 College Park, Dayton, OH 45469-0240, USA

<sup>b</sup>Honda Research Institute USA, Inc.,  
1381 Kinnear Rd, Suite 116,  
Columbus, OH 43212, USA

<sup>c</sup>University of Dayton Research Institute (UDRI),  
The University of Dayton,  
300 College Park, Dayton, OH 45469, USA

#### **1. INTRODUCTION**

Measurement represents one of the oldest methods used by human beings to better understand and control the world. These measurements are often accomplished using a singular sensor or an array of sensors [1]. Chemical and biological sensors (i.e. biosensors) are the evolved products of physical measurement technologies [2]. Chemical sensors are measurement devices that convert a chemical or physical property of a specific analyte into a measurable signal, whose magnitude is normally proportional to the concentration of the analyte [3]. The principle of a biosensor employs a biological recognition process of the particular analyte [4]. Through a transduction mechanism, this biological recognition process is then converted into a measurable parameter that can be optical, electrical, or electrochemical or others. This measurable parameter can then be used to quantify the analyte presented. Obviously, the transduction mechanism serves an important role in the success of the advancement of a sensor or a sensor array. On the basis of the transduction principle, chemical and biological sensors can be classified into three major classes with different transducers: sensors with electrical transducers, sensors with optical transducers, and sensors with other transducers (e.g. mass change) [5].

The visit made by Kroto in 1985 to Smalley and Curl at Rice University led also to a Nobel-Prize-winning discovery of buckminsterfullerene C<sub>60</sub>—a *conjugated* molecule with a soccer-ball-like structure consisting of 12 pentagons and 20 hexagons facing symmetrically [6,7]. Just as the discovery of C<sub>60</sub> has created an entirely new branch of carbon chemistry [8], the subsequent discovery of carbon nanotubes by Iijima [9] in 1991 opened up a new era in material science and nanotechnology [5]. These elongated nanotubes consist of carbon hexagons arranged in a concentric manner with



both ends normally capped by fullerene-like structures containing pentagons. Having a *conjugated* all-carbon structure with unusual molecular symmetries, fullerenes and carbon nanotubes show interesting electronic, photonic, magnetic, and mechanical properties [10]. These unusual optoelectronic properties of  $C_{60}$  and carbon nanotubes make them attractive as transducer-active materials in various sensing devices. This chapter provides an overview of the recent research and development on  $C_{60}$  and carbon nanotube sensors.

## 2. FULLERENE $C_{60}$ SENSORS

Since the discovery of fullerene in 1985, almost two decades have passed. Along with the intensive research on fullerene chemistry worldwide, much effort has also been devoted to exploit a wide range of applications based on the unusual physicochemical properties characteristic of  $C_{60}$ . As we shall see below, one of the most important potential applications is  $C_{60}$  sensors.

### 2.1. Fullerene humidity sensors

By directly sublimating  $C_{60}$  onto a QCM quartz resonator, Radeva et al. [11] prepared a  $C_{60}$  sensor for sensing the relative air humidity. This is because the adsorption of water molecules from moisture onto the  $C_{60}$  film can be related directly to changes in the resonance frequency of the quartz resonator. Fig. 1 shows the dependence of the resonance frequency on the relative air humidity for the  $C_{60}$ -coated QCM resonator, recorded at between 10% and 98% relative humidity (RH) at a constant temperature of 30 °C. As can be seen, the sensitivity increases

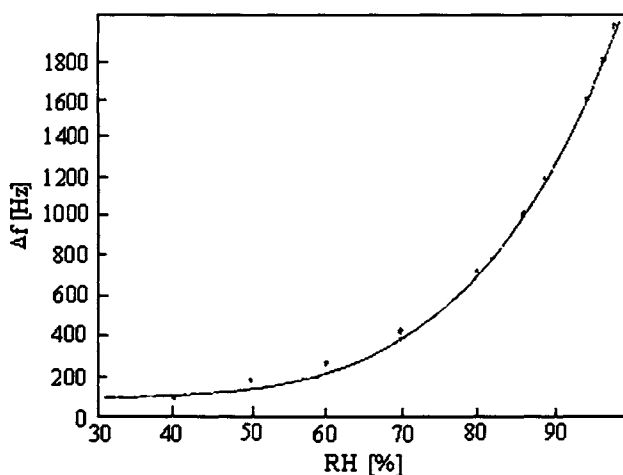


Figure 1. The dependence of the resonance frequency on the relative air humidity for a  $C_{60}$ -coated QCM resonator. (Reprinted with permission from Radeva et al. [11]. Copyright 1997 Elsevier.)

with the increase of the relative air humidity. A humidity sensitivity of ca. 11 Hz per% RH over the range of 30–70% RH was observed. This value of sensitivity corresponds to a sensitivity threshold of 0.01% for the humidity measurements, indicating that fullerene C<sub>60</sub> is one of the best water vapor sensitive materials.

The response of the C<sub>60</sub>-coated QCM resonator to a cyclic change of the air humidity in the range of 30–90% is shown in Fig. 2, which indicates that the interaction between the fullerene C<sub>60</sub> layer and water molecules is highly reversible. Furthermore, the response time was found to be less than a second. This value of the response time is considerably shorter than the corresponding values for similar quartz resonator humidity sensors based on other humidity adsorptive materials, including SiO<sub>2</sub> and polymer layers [11]. These results indicate that fullerene C<sub>60</sub> can be used to make advanced sensors for measuring relative air humidity.

## 2.2. Fullerene gas sensors

Sakurai and co-workers [12] have studied the gas-sensing characteristics of fullerene by measuring the electrical conductivity changes of a fullerene C<sub>60</sub> film formed on an Al substrate. In particular, these authors found that the conductivity of C<sub>60</sub>/C<sub>70</sub>-containing carbon soot increases upon exposure to NH<sub>3</sub>, (C<sub>2</sub>H<sub>5</sub>)N, and NO, whereas it decreases when exposed to CH<sub>3</sub>CHO [13]. The conductivity of a C<sub>60</sub> film also changes when exposed to H<sub>2</sub>, CH<sub>4</sub>, NO<sub>2</sub>, and CF<sub>4</sub>. These findings allowed them to develop highly selective gas sensors with reversible and fast responses. Their sensitivity to NO<sub>2</sub> can be improved by adding Ni to the carbon soot.

In addition to the conventional amperometric oxygen electrodes, various optical oxygen-sensing methods based on oxygen-induced luminescence quenching of

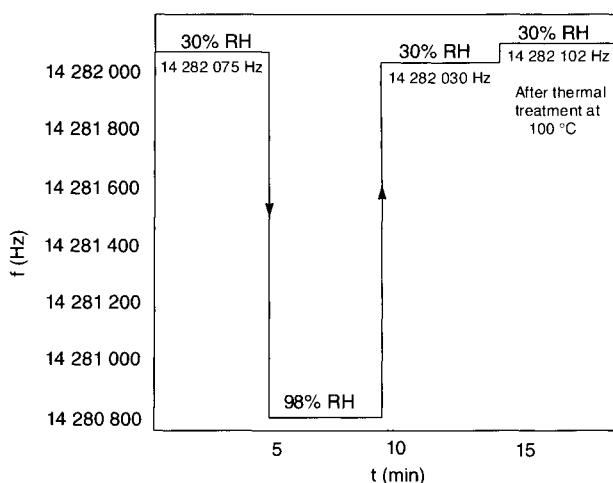


Figure 2. The frequency response to a cyclic change of the air humidity in the range of 30–90% for the C<sub>60</sub>-coated QCM resonator. (Reprinted with permission from Radeva et al. [11]. Copyright 1997 Elsevier.)

indicator molecules have been developed [14]. Among them, fullerene  $C_{60}$  and  $C_{70}$  were found to be highly desirable materials for sensing oxygen based on their optical property changes. The extremely long lifetime of the photoexcited triplet state of fullerenes (ca. 500  $\mu\text{s}$ ) indicates a very effective oxygen-quenching effect. Using the laser flash photolysis technique, Amao et al. [14] have measured the photoexcited triplet lifetime for fullerene  $C_{60}$  (Fig. 3a) and  $C_{70}$  (Fig. 3b) dispersed in a polystyrene (PS) film under various oxygen pressures. As can be seen in Fig. 3,  $C_{60}$ -PS is highly sensitive to oxygen throughout the whole range of the oxygen pressure, while  $C_{70}$ -PS is particularly sensitive to oxygen in the low-oxygen pressure region. Furthermore, it was demonstrated that fullerene-PS films are very stable to the irradiations used for the excitation (532 nm), and that the lifetime measurements (740 nm for  $C_{60}$  and 860 nm for  $C_{70}$ ) associated with oxygen sensing are highly reproducible.

Lin and Shih [15] reported the use of a fullerene  $C_{60}$ -di-propylamine-cryptand 22 ( $C_{60}$ -cryptand 22) coated surface acoustic wave (SAW) quartz crystal sensor for detecting various organic vapors. These authors claimed that this sensor has a high sensitivity to both polar and non-polar organic molecules by combining  $C_{60}$ , for example, with cryptands, which was previously reported [16,17] with a remarkable complexing ability for polar organic species.  $C_{60}$ -cryptand 22 was obtained from the reaction between 7,16-bis(3-aminopropyl)-1,4,10,13-tetraoxa-7,16-diaza cyclo-octadecane (di-propylamine-cryptand 22) and fullerene  $C_{60}$ . Di-propyl amine-cryptand 22 was synthesized according to the procedure described by Chiou and Shih [18],  $C_{60}$ -cryptand 22 was applied as a coating material for an SAW crystal as an SAW sensor. The SAW sensor has a basic resonant frequency of 250 MHz (the size: 8.0 mm  $\times$  2.0 mm) (Fig. 4).

The effect of the coating material on the frequency response was investigated by using  $C_{60}$ , cryptand 22, and  $C_{60}$ -cryptand 22 as adsorbents on the SAW crystal plate to adsorb and detect methanol molecules. As seen in Fig. 5, the SAW sensor with

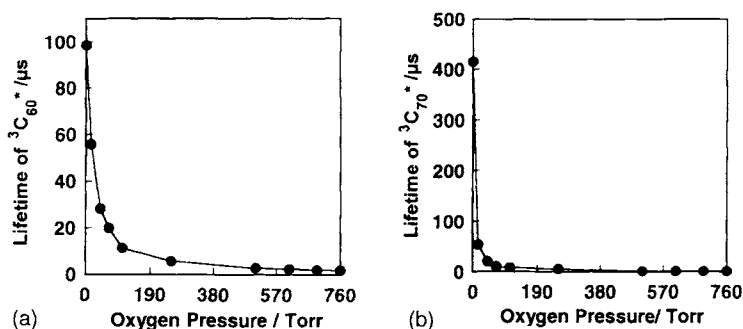


Figure 3. Dependence of the photoexcited triplet lifetime of (a)  $C_{60}$  and (b)  $C_{70}$  dispersed in a polystyrene (PS) film on the oxygen pressure. (Reprinted with permission from Amao et al. [14]. Copyright 1999 The Chemical Society of Japan.)

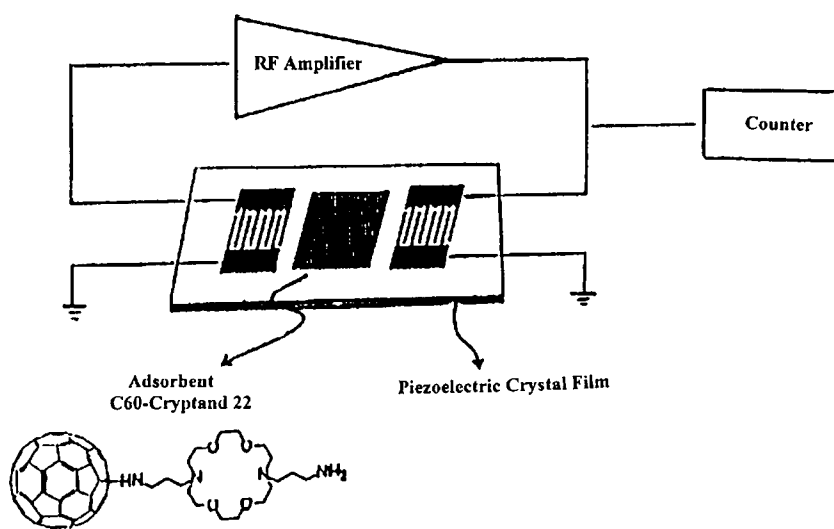


Figure 4. Fullerene C<sub>60</sub>-cryptand 22-coated surface acoustic (SAW) sensor. (Reprinted with permission from Lin and Shih [15]. Copyright 2003 Elsevier.)

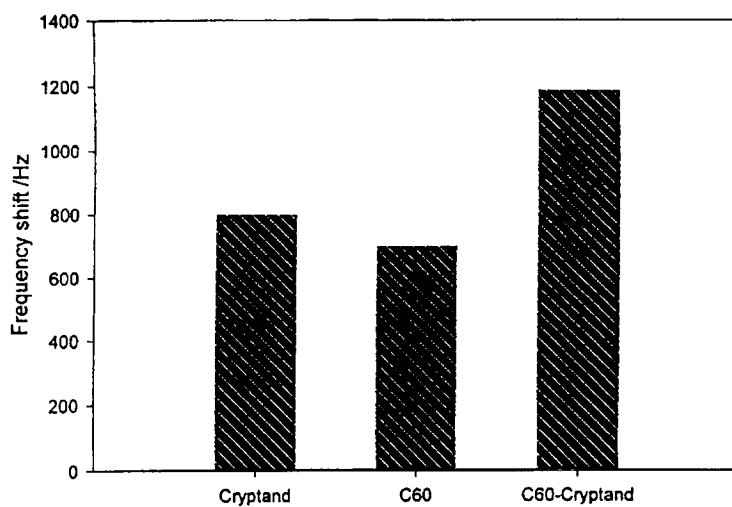


Figure 5. Effect of coating material on the SAW sensor for methanol (14 mg L<sup>-1</sup>). (Reprinted with permission from Lin and Shih [15]. Copyright 2003 Elsevier.)

C<sub>60</sub>-cryptand 22 coating for methanol exhibits a significantly better frequency response than C<sub>60</sub>-coated SAW sensor. It is not surprising to observe the smallest frequency shift for the C<sub>60</sub>-coated SAW sensor, because fullerene (C<sub>60</sub>) basically is an aromatic non-polar molecule and cannot strongly adsorb polar organic molecules such as methanol. The larger frequency shifts for the C<sub>60</sub>-cryptand 22- and cryptand 22-coated SAW sensors can be attributed to the hydrogen bonding formation between the macrocyclic polyether cryptand 22 and alcohol molecules. Further improvement in the frequency response by the attachment of C<sub>60</sub> to cryptand 22 may arise from the enhanced adsorption of methanol onto the C<sub>60</sub>-cryptand 22 molecule induced by the induction of the C<sub>60</sub> molecule with 60 $\pi$  electrons to cryptand 22.

Fig. 6 shows the response of C<sub>60</sub>-cryptand 22-coated SAW sensor to various polar organic vapors (propanol, propyl aldehyde, and acetone). The frequency responses for these organic vapors appear to be in the following order: propanol >> propyl aldehyde > acetone, presumably due to the formation of stronger hydrogen bonds of cryptand with propanol (ROH  $\cdots$  O-cryptand 22) or ROH  $\cdots$  N-cryptand 22) than propyl aldehyde (R  $\cdots$  HN-cryptand 22) and no hydrogen bond with acetone.

Fig. 7 shows the response of C<sub>60</sub>-cryptand 22-coated SAW sensor to various nonpolar organic vapors. As we can see in Fig. 7, the C<sub>60</sub>-cryptand 22 SAW crystal sensor exhibits a quite sensitive response to 1-hexene. The difference in the

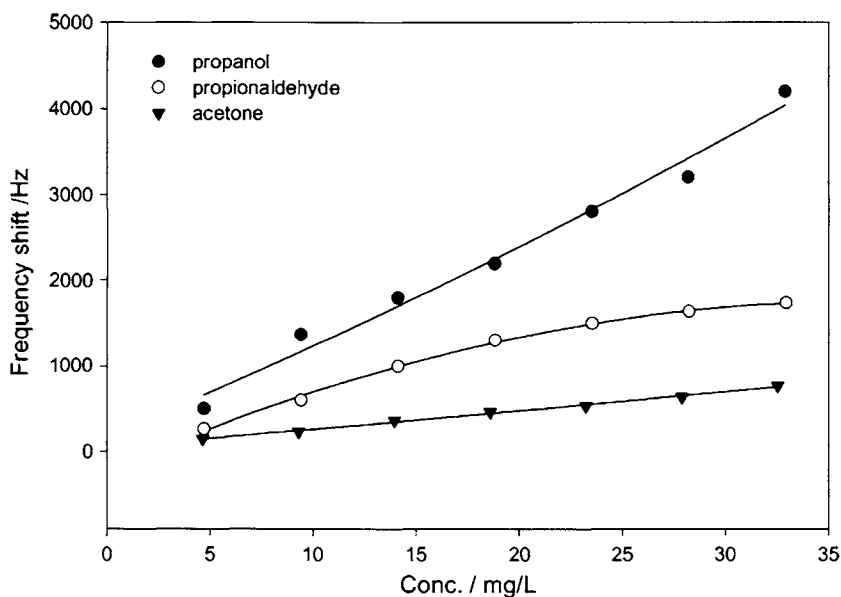


Figure 6. Frequency responses for propanol (solid circles), propyl aldehyde (open circles) and acetone (solid triangles) with the C<sub>60</sub>-cryptand 22 (0.4  $\mu$ g)-coated SAW sensor. (Reprinted with permission from Lin and Shih [15]. Copyright 2003 Elsevier.)

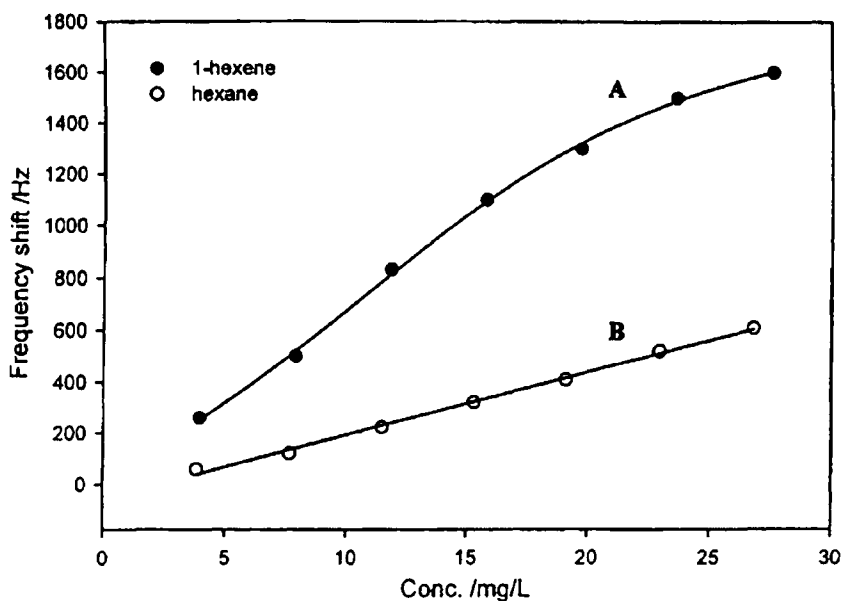


Figure 7. Frequency response of the  $C_{60}$ -cryptand 22-coated SAW sensor for 1-hexene (solid circles) and hexane (open circles). (Reprinted with permission from Lin and Shih [15]. Copyright 2003 Elsevier.)

frequency response to 1-hexene and hexane could be attributed to the different  $\pi$ - $\pi$  interaction strength of  $C_{60}$  with the organic vapors.

The  $C_{60}$ -cryptand 22-coated SAW sensor also exhibited the superior detection limits of  $0.2$ – $3.0 \text{ mg}^{-1}$  for various polar and nonpolar organic vapors. Moreover, a good reproducibility with a relative standard deviation of 4.2% for 20 repetitive injections of acetone vapor was demonstrated by using this SAW sensor as a detector for gas chromatography.

### 3. CARBON NANOTUBE SENSORS

Like fullerene  $C_{60}$ , carbon nanotubes also possess interesting optoelectronic properties. In particular, the electronic properties of carbon nanotubes are such that they may be metallic or semiconducting, depending on their diameter and the arrangement of graphitic rings in the walls [19]. Besides, they also show exceptionally good thermal and mechanical properties. The unique properties of carbon nanotubes have led to their use in areas as diverse as sensors, actuators, field-emitting flat panel displays as well as energy and gas storage [20]. The ability of carbon nanotubes and their derivatives to operate as gas sensors has been demonstrated recently [21,22,23]. As we shall see below, the principles for carbon nanotube sensors to detect the nature of gases and to determine their concentrations are based on changes in electrical

properties induced by charge transfer with the gas molecules (e.g.  $O_2$ ,  $H_2$ ,  $CO_2$ ) or in mass due to physical adsorption.

### 3.1. Carbon nanotube gas sensors

#### 3.1.1. Carbon nanotube ammonia and nitrogen dioxide sensors

Dai and co-workers [22] were the first to demonstrate that semiconducting single-walled carbon nanotubes (SWNTs) act as rapid and sensitive chemical sensors at ambient temperature. By so doing, these authors devised a simple sensing system, in which a single semiconducting SWNT was kept in contact with titanium and/or gold metal pads at the two ends (Fig. 8). Using the metal pads as the electrodes for electrical measurements, they found that the conductivity of the semiconducting SWNT changed rapidly over several orders of magnitude upon exposure to nitrogen dioxide and ammonia.

In particular, an increase in the conductivity by up to three orders of magnitude was observed within 10 s after exposing the semiconducting SWNT to 200 ppm  $NO_2$  (Fig. 9a) while the conductivity decreased by two orders of magnitude within 2 min upon exposure to 1%  $NH_3$  vapor (Fig. 9b).

These responses were attributed to the charge transfer between the *p*-type (i.e. hole doped) semiconducting SWNT and electron-donating  $NH_3$ , or electron-withdrawing  $NO_2$  gas. While the latter interaction increased the hole carriers in the SWNT, and hence enhanced conductance, the former interaction had an opposite effect. In principle, the semiconducting SWNT sensors could be applied to many other analytes of electron-donating or accepting capabilities ( $I_2$ ,  $AsF_5$ ,  $CO$ , etc.). With appropriate surface modification for gaining specific interactions with analytes of biological significance, they could even be used to detect biological systems in solution.

Commercial sensors based on semiconducting metal oxides have been developed for sensing  $NO_2$  and  $NH_3$ , but these sensors need to operate at temperatures of up to 600 °C for high sensitivity. The SWNT sensor, however, shows a strong response, much stronger than is typically recorded for a commercial counterpart, even at room temperature. Besides, the nanotube sensors are relatively simple to make, and their production can be easily scaled up. The nanotube sensors, however, need to take several hours to release the analyte at room temperature before they can be

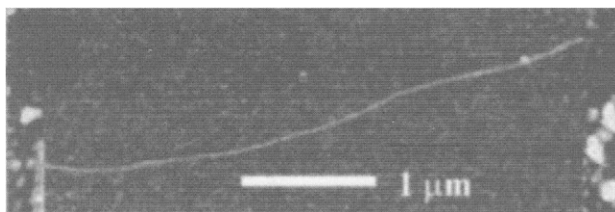


Figure 8. Atomic force microscopy image of a metal/SWNT/metal sample used for the gas-sensing application. (Reprinted with permission from Kong et al. [22]. Copyright 2000 The American Association for the Advancement of Science.)

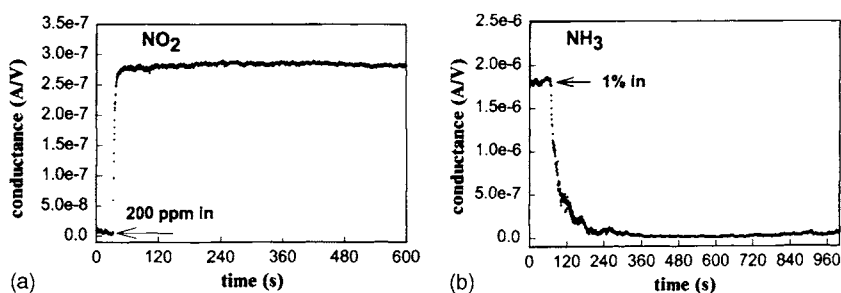


Figure 9. Electrical conductance response of a semiconducting SWNT to (a) 200 ppm NO<sub>2</sub> and (b) 1% NH<sub>3</sub> vapor. (Reprinted with permission from Kong et al. [22]. Copyright 2000 The American Association for the Advancement of Science.)

reused. Although the slow recovery of the sensor from the nanotube–analyte interaction can be expedited by heating, it remains as a major drawback.

### 3.1.2. Multiplex functionalized carbon nanotube sensors

Recently, Dai and co-workers [24] demonstrated detection of molecules in a gas mixture using the multiplexed (MT) nanotube sensors (Fig. 10). The sensor had highly sensitive multiple carbon nanotube molecular transistors and exhibited lower electrical noise than individual semiconducting SWNT devices.

Polymer functionalization was carried out to impart high sensitivity and selectivity to the sensors. The polyethyleneimine (PEI) functionalized *n*-type MT devices were ultrasensitive to NO<sub>2</sub>, responding to as low as 100 ppt of NO<sub>2</sub>, whereas as-grown MT devices were 10–50 ppb. PEI functionalization rendered as-grown SWNTs to be electron rich, leading to higher binding affinity and sticking coefficient for the electron-withdrawing NO<sub>2</sub>. The PEI-coated MT devices exhibited no response when exposed to NH<sub>3</sub>, a weakly electron-donating molecule. The PEI functionalized MT devices also exhibited no change in electrical conductance when exposed to many other molecules, including CO, CO<sub>2</sub>, CH<sub>4</sub>, H<sub>2</sub>, and O<sub>2</sub>. These results showed that PEI functionalized SWNTs are highly selective to strongly electron-withdrawing molecules. In contrast, Nafion-coated MT devices are highly sensitive to NH<sub>3</sub>. This is because Nafion is a polymer with Teflon backbone and sulfonic acid side groups, and is well known to be perm-selective to—OH-containing molecules, including NH<sub>4</sub>OH formed by reacting NH<sub>3</sub> with the environmental H<sub>2</sub>O.

These authors have further tried to use microspotting to coat MT devices in an array with different polymers, aiming at detecting NO<sub>2</sub> and NH<sub>3</sub> in gas mixtures by the multiplex-functionalized nanotube sensors. As shown in Fig. 11, microspotting of polymer solutions was done with commercial micropin (Telechem International Inc.) mounted on an in-house micromanipulator equipped with an optical microscope that allowed for positioning the pin over the MT devices. It was found that the conductance of a Nafion-coated device decreased (due to NH<sub>3</sub> electron donation to the *p*-type device reducing the majority hole carriers), while a PEI-coated device on the same chip



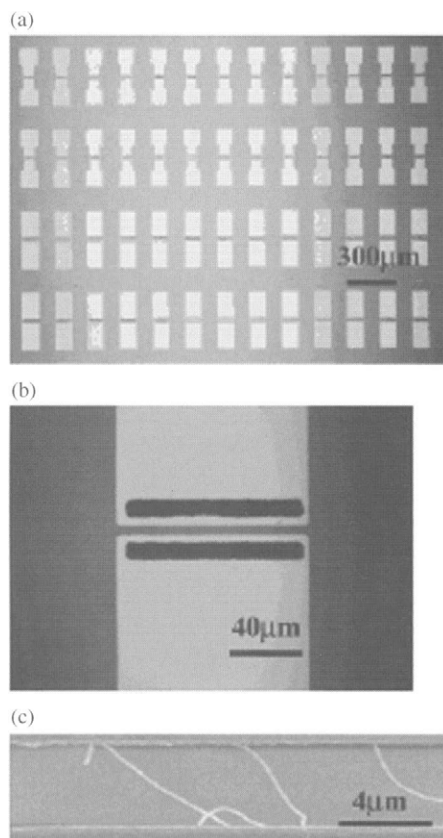


Figure 10. (a) Optical image of an array of multiple-SWNT devices. (b) Optical image of one device. The black regions (100  $\mu\text{m}$  long) contain catalyst patterned on top of opposing Mo source and drain electrodes. (c) Scanning electron microscopy (SEM) image of several nanotubes bridging two opposing Mo electrodes in a device. The nanotube appears bright and the apparent widths do not correspond to the true diameter of the nanotubes (average  $\sim 2$  nm measured by AFM and TEM). (Reprinted with permission from Qi et al. [24]. Copyright 2003 The American Chemical Society.)

showed no response to  $\text{NH}_3$ . However, the Nafion-coated device exhibited no response while the PEI-coated device showed a significant conductance decrease when 1 ppm of  $\text{NO}_2$  was introduced into the environment with the pressure of 500 ppm of  $\text{NH}_3$ . These results clearly demonstrate that multiplexed nanotube sensor arrays are promising for detecting mixture molecules in complex chemical environments.

### 3.1.3. Carbon nanotube hydrogen sensors

Dai and co-workers [23] have further demonstrated that certain chemical/physical modification could enhance the molecular specificity of carbon nanotube sensors. In

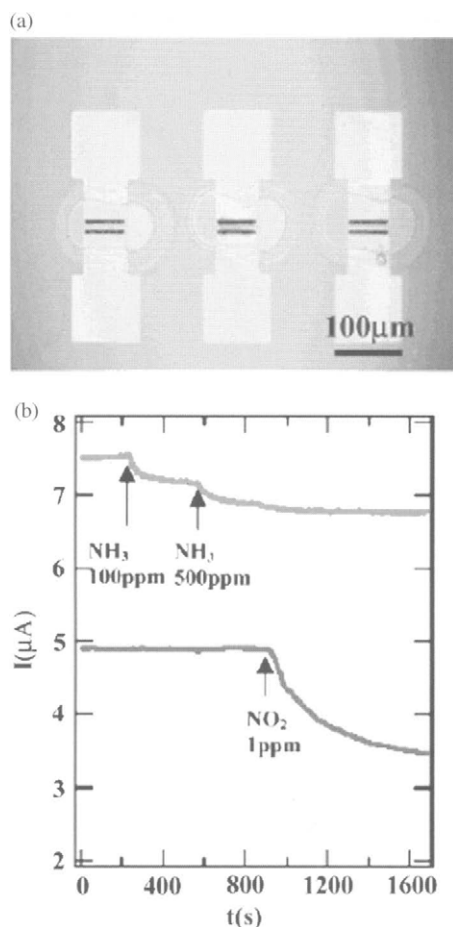


Figure 11. (a) Optical image showing three MT devices after micro spotting with droplets of polymer solutions. (b) Red (*top*) curve: a device coated with Nafion exhibits response to 100 and 500 ppm of NH<sub>3</sub> in air, and no response when 1 ppm of NO<sub>2</sub> was introduced to the environment. Blue (*bottom*) curve: a PEI-coated device exhibiting no response to 100 and 500 ppm of NH<sub>3</sub> and large conductance decrease to 1 ppm of NO<sub>2</sub>. (Reprinted with permission from Qi et al. [24]. Copyright 2003 The American Chemical Society.)

particular, these authors sputter-coated individual SWNT and its bundles with Pd nanoparticles. They observed up to 50% and 33% decrease in conductivity for the Pd-coated individual SWNT and nanotube bundles, respectively, upon exposure to a flow of air mixed with 400 ppm of hydrogen. This was followed by a rapid recovery of the conductivity after the hydrogen flow was turned off (Fig. 12). The response time, defined as the time required for half of the conductivity change, was found to be

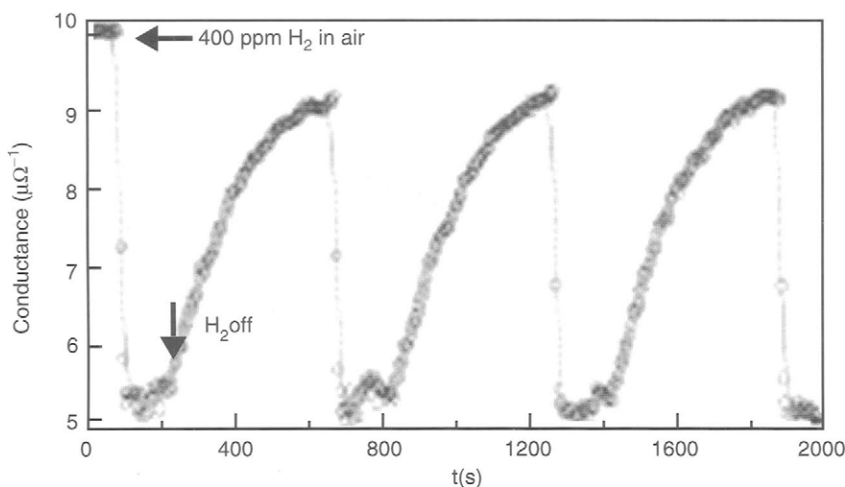


Figure 12. Electrical conductance of the SWNT coated with Pd nanoparticles *vs.* time in an air flow with 400 ppm  $H_2$  on and off. (Reprinted with permission from Kong et al. [23]. Copyright 2001 Wiley-VCH Verlag GmbH & Co.)

about 5–10 s, and the time for full recovery was ca. 400 s. The interaction between  $H_2$  and the Pd-SWNT is responsible for the sensing mechanism, whereas the corresponding interaction with  $O_2$  is the driving force for the recovery process.

As is well known, the interaction of the  $H_2$  and Pd surface at room temperature could cause atomic hydrogen to dissolve into Pd with a high solubility, leading to a decrease in the work function for Pd [25]. The decrease in Pd work function, in its turn, caused electron transfer from Pd to SWNTs to reduce the hole-carriers in the *p*-type nanotube, and hence a decreased conductivity. The recovery of the nanotube electrical characteristics was made by combining the dissolved atomic hydrogen in Pd with oxygen in air to form  $H_2O$ , when the hydrogen was turned off. The high sensitivity, fast response, and reversibility observed for the Pd-SWNT sensors at room temperature indicate that carbon nanotubes also are excellent new sensing materials for detecting low concentration of molecular hydrogen.

#### 3.1.4. Carbon nanotube oxygen sensors

In addition to the above studies, Zettl and co-workers [21] reported that SWNTs are extremely susceptible to oxygen adsorption. As shown in Fig. 13a, they found stepwise changes in the electrical resistance up to 10–15% by alternately exposing nanotube samples to air or a vacuum at 290 K. Identical changes were observed if pure dry oxygen was used to replace air, indicating that oxygen was responsible for the observed resistance change.

Similar changes were also observed for the thermoelectric power,  $S$  [26]. As seen in Fig. 13b, the  $S$  was positive with a value of ca.  $+20 \mu V K^{-1}$  for the SWNT in a pure

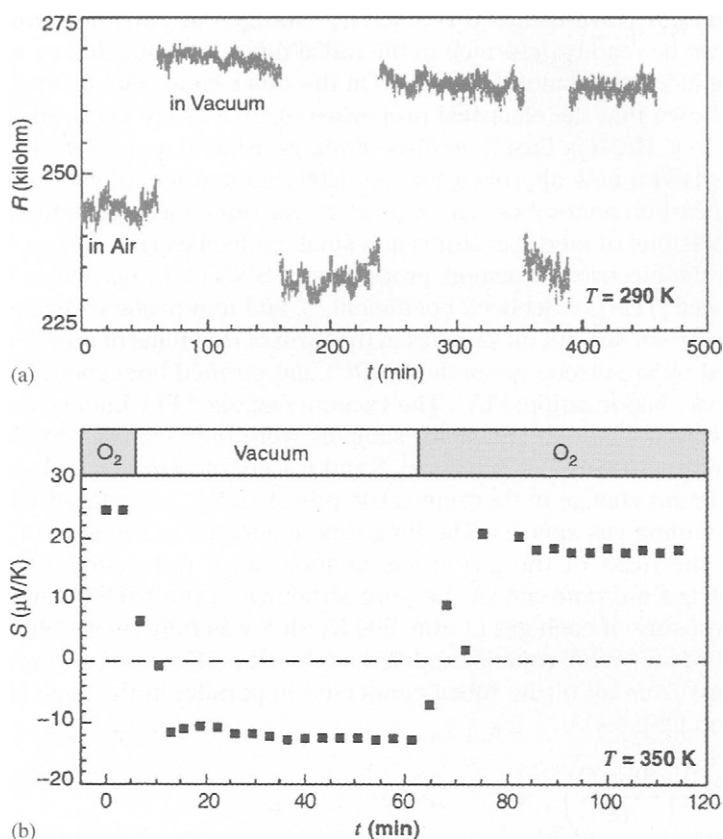


Figure 13. (a) Electrical resistance ( $R$ ) and (b) thermoelectric power responses of SWNT films to gas exposure. (Reprinted with permission from Collins et al. [21]. Copyright 2000 The American Association for the Advancement of Science.)

atmospheric pressure of oxygen environment at 350 K. The removal of oxygen from the system caused a continuous change in  $S$  from positive to negative, reaching an equilibrium value of ca.  $-10 \mu\text{VK}^{-1}$ . When the system was alternately cycled between pure oxygen and pure vacuum, stepwise changes in  $S$  were obtained. While the negative  $S$  indicates that the SWNT is an  $n$ -type semiconductor in a vacuum, the oxygen-exposed nanotube with a positive  $S$  is a  $p$ -type semiconductor.

Apart from the thermoelectric power measurements discussed above, Collins et al. [21] further used scanning tunneling spectroscopy and transport measurements to confirm that oxygen-exposed SWNTs behave as  $p$ -type semiconductors and the oxygen's electron affinity could cause these observed changes through charge transfer between the adsorbed oxygen and SWNTs. These results clearly indicate that carbon nanotubes can be used as sensing elements for making new oxygen sensors.

### 3.1.5. Atom collision-induced resistivity changes of carbon nanotubes

SWNTs can be readily deformed in the radial direction, though they are mechanically strong along the nanotube length. On the other hand, Eklund and co-workers [27] have shown that the electrical properties of SWNTs are very sensitive even to inert gases (e.g. He, N<sub>2</sub>). Based on these findings, Eklund and co-workers [28] have recently devised a new approach for the detection and identification of gas molecules using carbon nanotubes. These authors performed a systematic study on the effect of collisions of inert gas atoms and small molecules (He, Ne, Ar, Kr, Xe, CH<sub>4</sub>, and N<sub>2</sub>) on the electrical transport properties of SWNTs. In particular, the thermoelectric power (TEP) or Seebeck coefficient,  $S$ , and four-probe resistance,  $R$ , measurements were carried out on samples in the form of thin films of bundled nanotubes (synthesized by arc-discharge method; ARC) and purified buckypaper (synthesized by pulsed laser vaporization; PLV). The vacuum-degassed PLV buckypaper (Fig. 14a) and ARC-derived thin film (Fig. 14b) samples were then exposed to various gases under 1 atm pressure at  $T = 500$  K. So,  $S$  and  $R$  were measured simultaneously.

The maximum change in thermoelectric power ( $\Delta S_{\max}$ ) increased with the mass  $M$  of the colliding gas species. The long time constants of the system, which also depend on the mass of the gas atoms or molecules, were consistent with slow diffusion of gas into and out of the pore structure of the SWNT bundles, but the effect of exposure of each gas (1 atm, 500 K) on  $S$  was fully reversible.

The TEP of an SWNT rope is modeled as the sum of the conductance-weighted contributions from all of the tubes connected in parallel in the rope [29] with the Mott relation [25]:

$$S = \frac{-\pi^2 k_B^2 T}{3|e|} \left( \frac{d \ln \sigma E}{dE} \right)_{E_F} \quad (1)$$

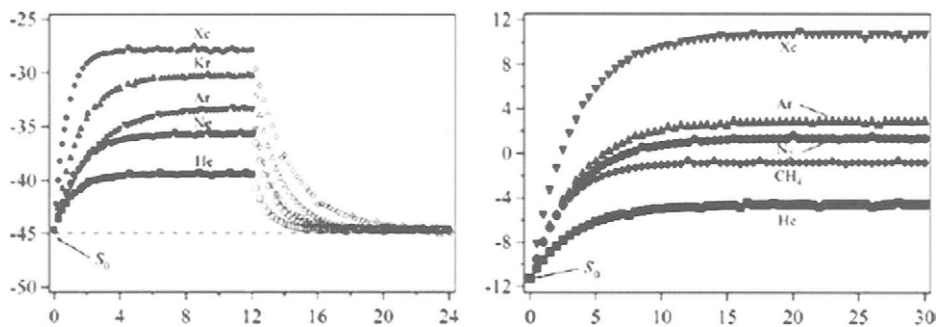


Figure 14. Time dependence of  $S$  at 500 K of (a) PLV buckypaper and (b) ARC-derived thin film to a sudden overpressure of 1 atm of inert gas (solid symbols). In (a), the open symbols show the TEP response after application of a vacuum over the sample. (Reprinted with permission from Romero et al. [28]. Copyright 2005 The American Association for the Advancement of Science.)

where  $\sigma$  is the electrical conductivity,  $e$  the electric charge,  $k_B$  the Boltzmann's constant, and  $T$  the temperature. The logarithmic derivative of  $\sigma$  is evaluated at the Fermi energy  $E_F$ . As predicted by Eq. (1),  $S$  for SWNT samples was observed to be roughly linear in temperature. Since these measurements were made at 500 K, a phonon drag contribution associated with a low-temperature effect [29,30] was ignored.

Here, the contributions that limit conductivity were separated into the following two parts: (i) carrier scattering intrinsically characteristic of the degassed metallic tubes (identified with phonons and permanent tube wall defects), and (ii) additional carrier scattering in the metallic tubes associated with the perturbation in the local tube wall potential caused by adsorbed gas molecules or collisions with gas molecules. Romero et al [27] assumed that the scattering contributions (i) and (ii) are additive [26]

$$\rho = \rho_0 + \rho_1 \quad (2)$$

where  $\rho_0$  is identified with the resistivity of the degassed metallic tubes and  $\rho_1$  is identified with the extra impurity scattering due to gas molecules interacting with the tube wall, and that

$$\sigma(E) = e^2 v(E)^2 D(E) \tau(E) \quad (3)$$

where  $v$ ,  $D$ , and  $\tau$  are the free carrier velocity, density of the states, and carrier lifetime, respectively.

By combining Eqs. (1)–(3), Eklund and co-workers obtained [27]:

$$S = S_0 - \frac{\pi^2 k_B^2 T}{3|e|} \left( \frac{\rho_1}{\rho_0 + \rho_1} \right) \times \left( \frac{1}{\tau_1} \frac{d\tau_1}{dE} - \frac{1}{\tau_0} \frac{d\tau_0}{dE} \right)_{E_F} \quad (4)$$

Depending on the sign and magnitude of the terms  $1/\tau_1(d\tau_1/dE)$  in Eq. (4), therefore, one can anticipate a positive or negative slope for the  $S$  vs.  $\rho_1$  plot at a fixed temperature  $T$ . By assuming that  $R_0 \gg \Delta R$  and that the gas collisions do not change the contact resistance between bundles in the SWNT samples, one can further correlate  $\rho_1/(\rho_0 + \rho_1)$  in Eq. (4) with the fractional change of the four-probe resistance  $\Delta R/R_0$ , where  $\Delta R = R - R_0$  represents the extra resistance caused by the colliding atoms and  $R_0$  is the initial sample resistance in the degassed state. The plots of  $S$  vs.  $\Delta R/R_0$  shown in Fig. 15 for the PLV buckypaper sample reveals a dependence of their slopes on the mass  $M$  of the particular gas. The same behavior was observed for the data measured at various pressures in the range of  $0 < p < 2$  atm;  $p$  is a measure of the collision frequency of the atoms with nanotube walls. The observed variation in slope with  $M$  (e.g. Fig. 15) suggested that the impulse delivered to the tube wall per collision is important to cause changes in the electrical properties.

The mass dependence of the colliding atoms or molecules on  $\Delta S_{\max}$  is considered in Fig. 16 (1 atm and 500 K; compare with Fig. 14). The straight solid lines in Fig. 16 represent the least square fit to the experimental  $\Delta S_{\max}$  vs.  $M$  (circles). Both solid lines exhibit an  $\sim M^{1/3}$  dependence. The solid and open circles represent the

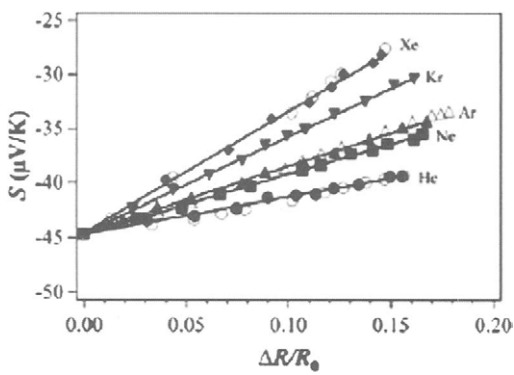


Figure 15.  $S$  vs.  $\Delta R/R_0$  curves showing the effect of inert gases on the transport properties of a SWNT buckypaper prepared from the PLV material. The solid symbols are from the time evolution of  $S$  and  $R$  to 1 atm of gas at 500 K, and the open symbols are from a pressure study at the same temperature, where the maximum response of  $S$  and  $R$  to a given pressure was measured. (Reprinted with permission from Romero et al. [28]. Copyright 2005 The American Association for the Advancement of Science.)

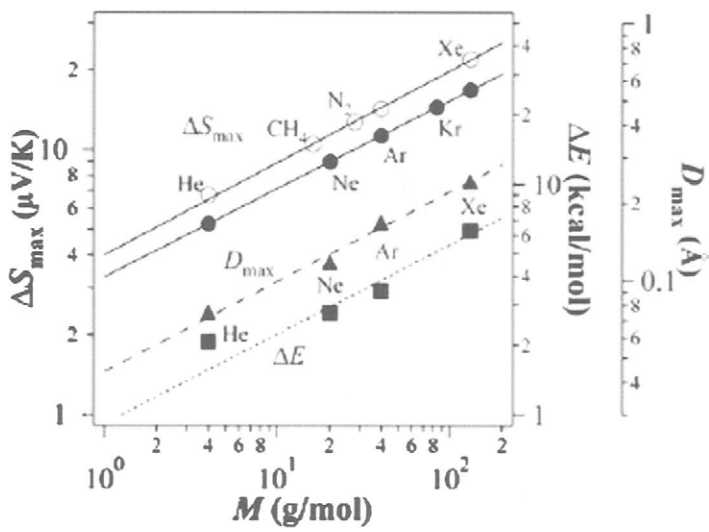


Figure 16. The maximum TEP change  $\Delta S_{\max}$  for two SWNT samples exposed to various gases (ARC: open circles, PLV: solid circles), calculated total energy gained by a (10, 0) nanotube upon collision with a gas atom ( $\Theta_i = 0^\circ$ ,  $E_i = 3.97 \text{ kcal mol}^{-1}$ , squares), and maximum radial displacement of the tube C atom immediately after impact with a gas atom ( $\Theta_i = 45^\circ$ ,  $E_i = 1.99 \text{ kcal mol}^{-1}$ , triangles) as a function of the atomic mass of the colliding inert gas. The lines are power-law fits to the data of the forms  $\Delta S_{\max} = 3.08M^{0.35}$ ,  $\Delta E = 0.91M^{0.39}$ , and  $\Delta D_{\max} = 0.04M^{0.35}$ . (Reprinted with permission from Romero et al. [28]. Copyright 2005 The American Association for the Advancement of Science.)

data for the PLV buckypaper and ARC-derived sample, respectively. For comparison, the mass dependence of the total energy transfer,  $\Delta E$  (squares), to a short (10, 0) nanotube upon collision (i.e. the total energy lost by the colliding atom) was plotted, along with the results from their molecular dynamics simulations. Also included is the maximum radial displacement,  $\Delta D_{\max}$  (triangles), of the tube C atom (with which the gas collides) on impact. The slopes of these theoretical lines were insensitive to the simulation conditions (i.e. incident angle, initial energy, and point of impact). Now, we can find that the perturbation of the transport properties, the total energy gained by the tube, and the maximum amplitude of the dent obtained from the simulations all share the same approximate power law on the colliding mass (i.e.  $M^{1/3}$ ).

Based on the above results, Eklund and co-workers proposed that the effects observed in *S* and *R* were caused by a new scattering channel for conduction electrons created by collision-induced transient dents in the tube wall. The above work clearly indicated that gas collisions at a high level can be easily detected by the nanotube sensors.

### **3.1.6. Resonant-circuit sensor**

Rao and co-workers[31] have recently reported the use of carbon nanotube-based microwave resonant sensor for monitoring ammonia gas. This sensor consists of a circular disk of an electromagnetic resonant circuit coated with nanotubes. Both single- or multi-walled carbon nanotubes (MWNTs) were physically coated on the top of the copper disk by conductive epoxy (Fig. 17). The sensing capability lies on the dielectric constant change of carbon nanotubes upon adsorption of ammonia molecules, which causes a downshift in the resonant frequency of the resonator.

It was found that the resonant frequency of the SWNT sensor changed by 4.375 MHz upon exposure to ammonia vapor for approximately 10 min. A relatively smaller downshift of 3.25 MHz was observed for the MWNT sensor. These sensors can be operated at room temperature with a good sensitivity to ammonia concentrations as low as 100 ppm (Fig. 18). A similar circular disk resonator without the nanotube coating showed no change in the resonant frequency when exposed to ammonia vapor under the same condition.

The nanotube resonant-circuit sensor has a much faster response than other  $\text{NH}_3$  sensors. For instance, SWNT chemical sensors based on resistance changes exhibit a fast response (a few minutes) with a slow recovery time (8–12 h) under exposure to 200 ppm of  $\text{NO}_2$  [22]. The nanotube resonant-circuit sensor also shows a better sensitivity (or the frequency shift) as compared to other types of resonant frequency detection sensors and is at least five times more sensitive than the recently reported humidity sensor based on a frequency shift mechanism [32]. The nanotube resonant-circuit sensors are attractive for designing remote sensor systems to monitor gases inside sealed packages and environmental conditions that does not allow physical wire connections.

### **3.1.7. Gas ionization sensor**

As schematically shown in Fig. 19, Ajayan and co-workers[33] have reported the ionization microsensors featuring the electrical breakdown of a range of gases and



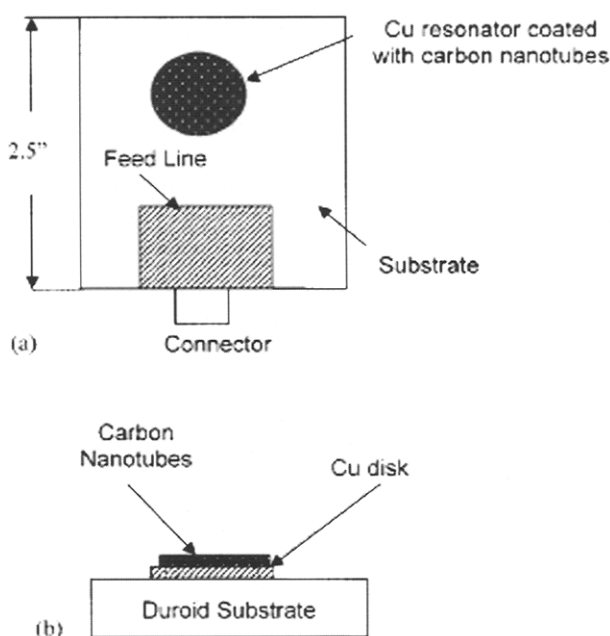


Figure 17. (a) Schematic representation of the resonator sensor. The shaded regions represent copper metal on which the nanotube coating is applied. (b) Cross-sectional view of the resonator sensor. (Reprinted with permission from Chopra et al. [31]. Copyright 2002 American Institute of Physics.)

gas mixtures at nanotube tips on the vertically aligned carbon nanotube array. It has been demonstrated that the sharp tips of nanotubes can generate very high electric fields at relatively low voltages, lowering breakdown voltages several-fold in comparison to traditional electrodes. This sensor could identify gases (e.g. He, Ar, N<sub>2</sub>, O<sub>2</sub>, CO<sub>2</sub>, NH<sub>3</sub>, and air) by determining distinct breakdown voltages for each of the gas at a given temperature and pressure (Fig. 20). On the other hand, the discharge current at the breakdown voltage was also found to be closely related to the nature and the number of gas molecules per unit volume. As such, it is also possible to identify the concentration of the species to be detected (Fig. 21). Moreover, the high discharge current characteristic of the nanotube field emission allows the detection of gas concentrations even down to a low ppm range ( $\sim 25$  ppm).

### 3.2. Carbon nanotube physical sensor

#### 3.2.1. Carbon nanotube chemical force sensors

Owing to their exceptional electrical and mechanical properties, carbon nanotubes (both SWNTs and MWNTs) have also been used as scanning probe microscope tips with a significantly better lateral resolution compared with commercial Si and SiN AFM tips [34,35]. Although these sharp nanotube tips offer

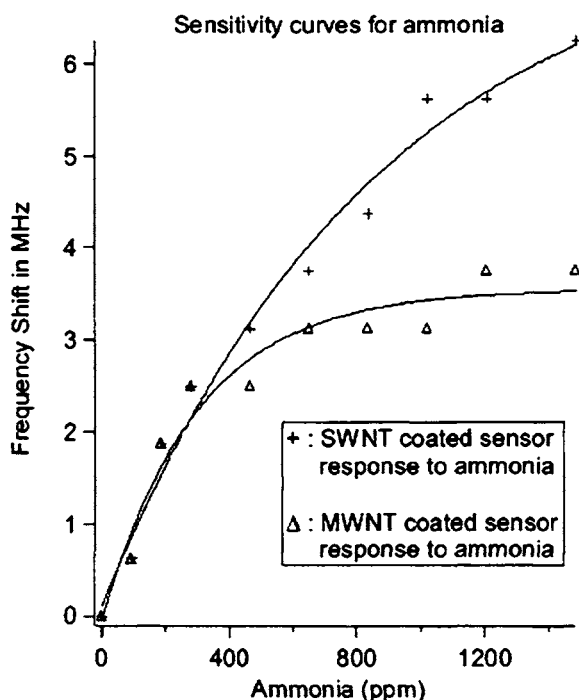


Figure 18. Comparison between the sensitivities of SWNT and MWNT coated sensors. (Reprinted with permission from Chopra et al. [31]. Copyright 2002 American Institute of Physics.)

advantages for high-resolution imaging, the unmodified nanotube tips, like most of the commercial tips, do not provide information about the chemical nature of the surface. Lieber and co-workers [36,37] have recently addressed this point by covalently modifying the ends of both SWNT and MWNT tips with chemically and/or biologically active functionalities for chemically sensitive mapping at molecular resolution. For example, these authors have introduced  $\text{-COOH}$  groups at the opened end of an SWNT tip by acid oxidation (Fig. 22) [38]. They then demonstrated the possibility to chemically attach an amine molecule,  $\text{RNH}_2$  (e.g. benzylamine) onto the terminal- $\text{-COOH}$  group through the amide linkage.

To demonstrate the chemically sensitive force mapping, Lieber and co-workers [36,37] first used a  $\text{-COOH}$  terminated SWNT AFM tip to image a micropatterned surface consisting of  $10\text{-}\mu\text{m}$  squares of a hexadecanethiol SAM (i.e.  $\text{CH}_3$ -rich surface) surrounded by a 16-mercaptohexadecanoic acid SAM (i.e.  $\text{-COOH}$ -rich surface). As shown in Fig. 23a, the tapping mode image recorded in ethanol shows a greater phase lap for tip- $\text{-COOH}$ /sample- $\text{-COOH}$  vs. tip- $\text{-COOH}$ /sample- $\text{CH}_3$  regions due to the stronger adhesion force for the former. The corresponding image obtained with the benzylamine-modified SWNT AFM tip shows the patterned feature, but with the opposite

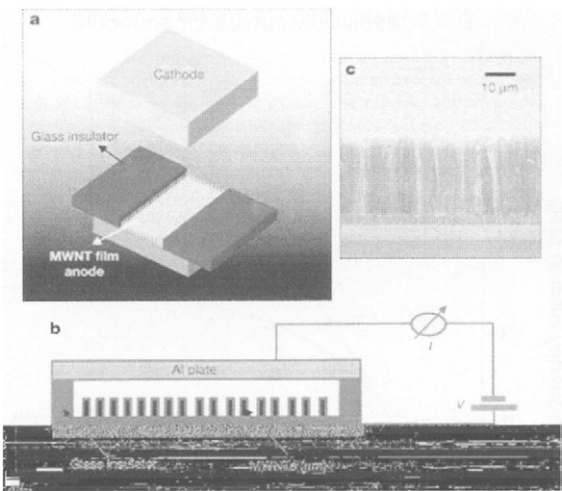


Figure 19. The nanotube sensor device: (a) showing MWNT film as the anode, 180- $\mu\text{m}$ -thick glass insulator plates, and Al plate as cathode, (b) diagram of the actual test set-up, and (c) SEM image of a CVD-grown, vertically aligned MWNT film used as the anode. (Reprinted with permission from Modi et al. [33]. Copyright 2003 Macmillan Publishers Ltd.)

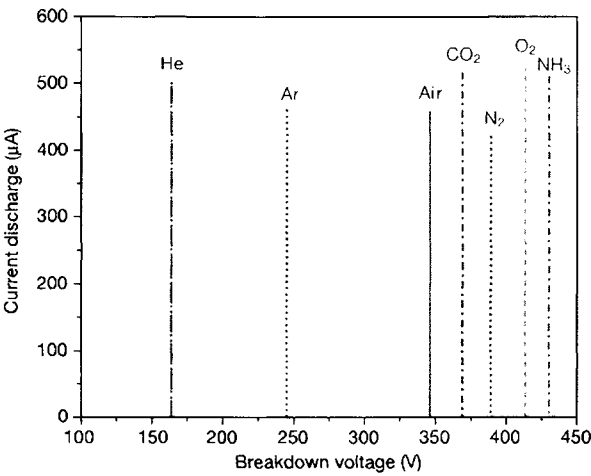


Figure 20. Current–voltage ( $I$ – $V$ ) curves for the electric breakdown.  $\text{NH}_3$ ,  $\text{CO}_2$ ,  $\text{N}_2$ ,  $\text{O}_2$ , He, Ar, and air have distinct breakdown voltages, ammonia displays the highest breakdown voltage, and helium the lowest. (Reprinted with permission from Modi et al. [33]. Copyright 2003 Macmillan Publishers Ltd.)

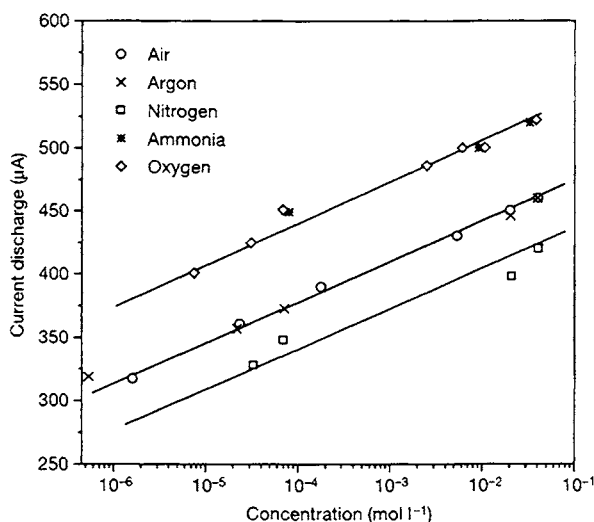


Figure 21. Effects of the gas concentration on the electrical breakdown: Plots of the discharge current at breakdown as a function of the gas concentration. The discharge current varies logarithmically with the concentration. (Reprinted with permission from Modi et al. [33]. Copyright 2003 Macmillan Publishers Ltd.)

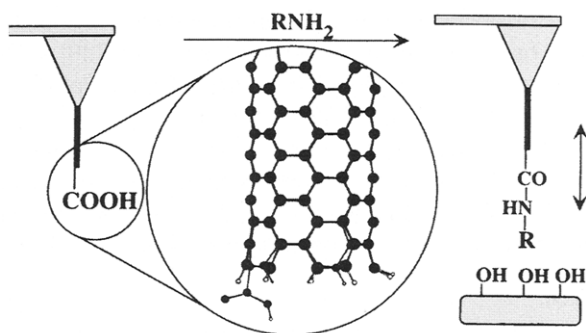


Figure 22. Schematic illustrating the SWNT tip modification via coupling an amine ( $\text{RNH}_2$ ) onto a terminal  $-\text{COOH}$  functionality, and the use of the tip-modified nanotube as an AFM probe to sense specific interactions between the functional group (R) and surface  $-\text{OH}$  group. (Reprinted with permission from Wong et al. [37]. Copyright 1998 The American Chemical Society.)

phase contrast (Fig. 23b) as this particular tip interacts more strongly with the  $-\text{CH}_3$ -rich surface in respect to the  $-\text{COOH}$  region. These results clearly demonstrate that chemically modified nanotube AFM tips can be used as sensing probes for chemically sensitive surface recognition.

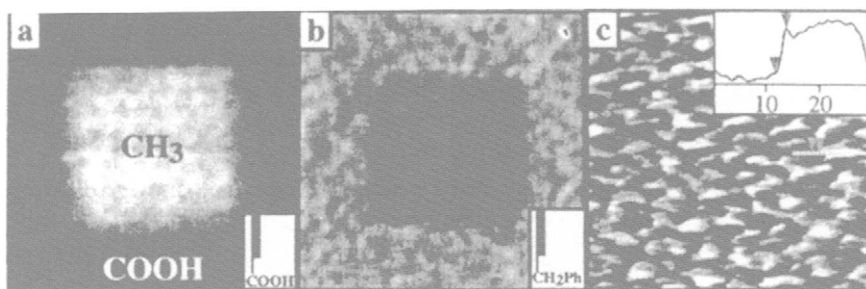


Figure 23. Tapping mode AFM images of a patterned sample with region-specific  $-\text{CH}_3$  and  $-\text{COOH}$  regions in ethanol recorded with (a) a  $-\text{COOH}$ -terminated SWNT tip, and (b) a benzylamine-functionalized SWNT tip. Dark regions indicate greater phase lag and the images are  $16\text{ }\mu\text{m} \times 16\text{ }\mu\text{m}$  in size. (c) tapping mode phase image recorded on a partial bilayer structure, indicating a lateral chemical resolution of ca. 3 nm. (Reprinted with permission from Wong et al. [37]. Copyright 1998 The American Chemical Society.)

### 3.2.2. Carbon nanotube pressure and temperature sensors

Wood and Wagner [39] have recently found that the disorder-induced Raman peak of SWNTs ( $D^*$  band,  $2610\text{ cm}^{-1}$  in air) shifts dramatically upon immersion of the nanotubes in a liquid or measured in a diamond-anvil cell [40] with respect to the corresponding peak observed in air (Fig. 24a). These authors, along with others, [41] have further found that the Raman peak of the nanotubes embedded in polymer matrices also shifts significantly with temperature (Fig. 24b). As shown in Fig. 24b, the wavenumber of the  $D^*$  band increases with decreasing temperature as the nanotubes experience compression. These changes are highly reversible, indicating the usefulness of carbon nanotubes as molecular sensors for pressure and temperature sensing.

### 3.2.3. Strain sensor

Further to the carbon nanotube pressure sensors discussed above, recent work has shown that stresses in polymer systems can be measured using single-walled carbon nanotubes (SWNTs) and Raman spectroscopy [42]. The disorder-induced  $D^*$  Raman peak of SWNTs represents a nanotube breathing vibrational mode, which is sensitive to changes in the strain condition of the nanotube. By monitoring the Raman spectrum of SWNTs mixed in a polymer matrix, therefore, a change in the stress state of the carbon nanotube can be determined, leading to novel carbon nanotube strain sensors for measuring stress fields around defects in polymers [42], tensile strain in materials [40,43], liquid molecular pressure [39], and polymeric morphology transitions [44].

Using SWNTs as stress sensors, Wagner and co-workers [45] have studied the interfacial strength between E-glass fibers and an isotactic polypropylene matrix. A schematic diagram of the micro-composite sample section is shown in Fig. 25.

The Raman spectrum of each coated fiber-composite system was evaluated during mechanical testing. Each micro-composite sample was strained parallel to the fiber

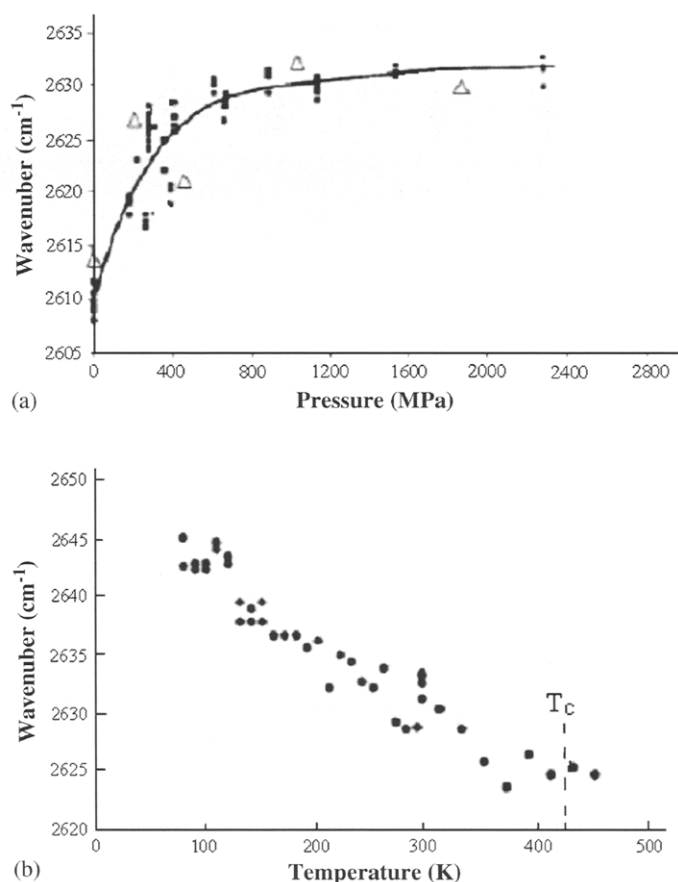


Figure 24. The peak position of the D\* Raman peak of (a) SWNTs as a function of the molecular (by immersion in liquids, black square) and macroscopic (using a diamond-anvil cell, open triangle) (After Wood and Wagner [39]), and (b) SWNTs embedded in polycarbonate upon cooling. (Reprinted with permission from Wood and Wagner [39]. Copyright 2000 American Institute of Physics.)

axis. While the fiber fragmented during straining, the SWNT D\* Raman peak (2630 cm<sup>-1</sup>) shifted to a lower wavenumber with applied strain by -2.5 cm<sup>-1</sup>/‰ (Fig. 26).

The D\* wavenumber change with applied strain for each coated polymer system is also related to the size of the fiber deforming in the polymer matrix. Fig. 27 shows that the Raman data correlate well with the fragmentation data (they were separately tested and plotted in Fig. 27) in reflecting the stress transfer capability of the polymer coatings in the glass fiber-polypropylene composites. These results show that SWNTs can be used as strain sensors to evaluate different levels of interfacial adhesion between sized E-glass fibers and the polypropylene matrix. Therefore, carbon nanotubes hold

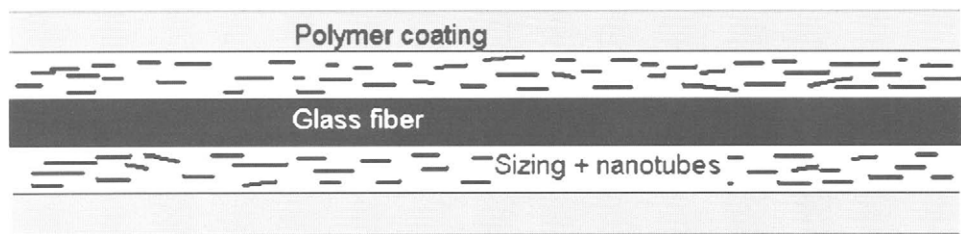


Figure 25. Schematic diagram of a sized and coated E-glass fiber-iPP micro-composite sample section. (Reprinted with permission from Barber et al. [45]. Copyright 2004 Elsevier.)

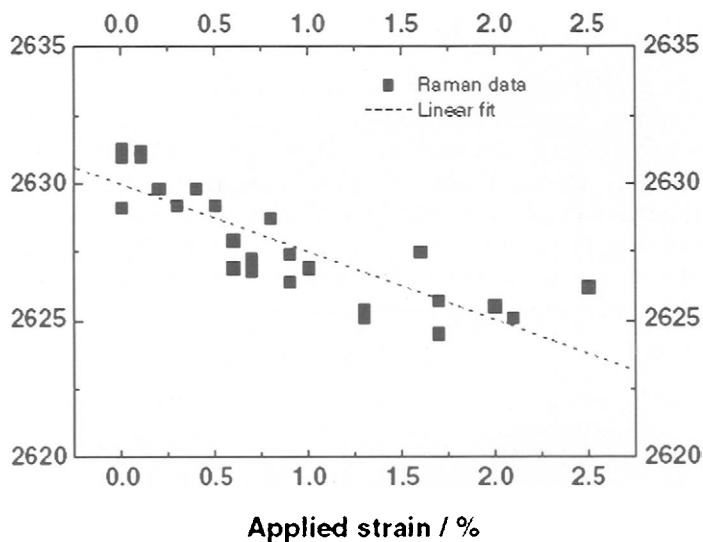


Figure 26. Calibration plot of the D\* wavenumber shift with applied strain for sized E-glass fibers. (Reprinted with permission from Barber et al. [45]. Copyright 2004 Elsevier.)

promise as strain sensors that can be used to evaluate composite interfaces in a non-destructive manner.

#### 3.2.4. Carbon nanotube flow sensor

Král and Shapiro [46] showed theoretically the generation of an electric current in a metallic carbon nanotube immersed in a flowing liquid. Later, the theoretical prediction

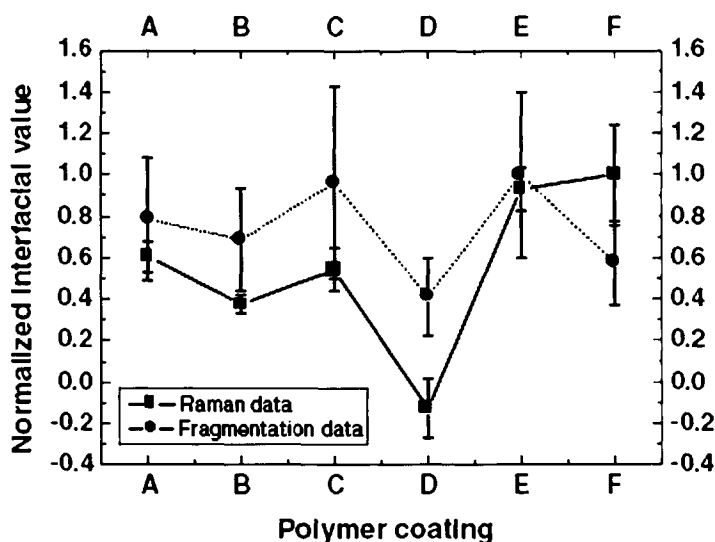


Figure 27. Normalized Raman data and fragmentation data ( $I_c$ ) for a variety of polymer coatings. The coatings promoting the highest interfacial adhesion between glass fibers and a polypropylene matrix have the highest normalized values. In the figure, A, B, C, D, E, and F show Vinyl-acetate-ethylene (Young's modulus: 1.13 MPa), Vinyl-acetate-ethylene (1.45 MPa), Methyl-methacrylate (1.11 MPa), Methyl-methacrylate (0.2 MPa), Styrene-methyl-methacrylate (1.29 MPa), and Styrene-methyl-methacrylate (0.956 MPa), respectively. (Reprinted with permission from Barber et al. [45]. Copyright 2004 Elsevier.)

was confirmed by an experimental observation of the voltage generated by the flow of a polar liquid over SWNT bundles [47]. In particular, Ghosh et al. [47] constructed the nanotube flow sensor by densely packing purified arc-generated SWNT bundles (an average tube diameter: 1.5 nm) between two metal electrodes. The nanotube sensor (dimension: 1 mm long along the flow, 0.2 mm thick, and 2 mm wide) was set in the center of a glass tube and immersed in water at rest, followed by the measurements of the flow-induced voltage. Fig. 28 shows the comparison of the voltage observed along the nanotube sensor as a function of the flow velocity for a series of fluid mixtures.

As shown in Fig. 28, a strong dependence of the flow-induced voltage on the ionic strength of the flowing liquid is observed. At a velocity of  $10^{-4} \text{ m s}^{-1}$ , the voltage for 1.2 M HCl is about five times that for water. Moreover, the voltage in the case of polar liquids (such as water) was greater than that in the case of the less polar liquids (such as methanol). By comparing the resultant voltages from two mixtures between water and glycerol, it was also found that the flow-induced voltage decreased with increasing fluid viscosity. The dominant mechanism responsible for this highly nonlinear response was proposed to involve a direct "pushing" of the free charge carriers in the nanotubes by the fluctuating Coulombic field of the liquid passing through the nanotubes.



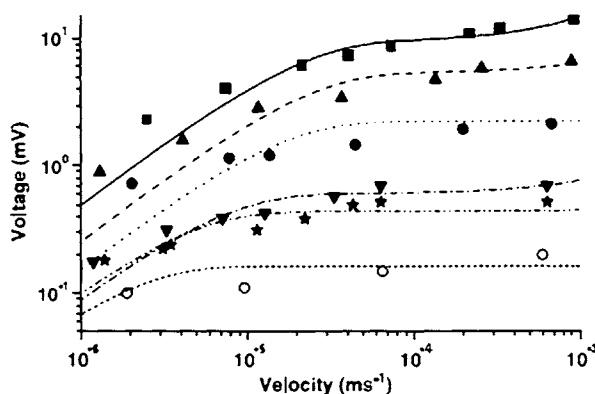


Figure 28. Induced voltage (V) as function of liquid velocities, for water (●); methanol (○); mixture of water:glycerol (75:25) (□); water:glycerol (88:12) (▼); 0.6 M HCl (▲); and 1.2 M HCl (■). The ratios for the water–glycerol mixtures are by volume. Lines show the fit of the data to idealized model of explanation for the mechanism of flow-induced voltage. (Reprinted with permission from Ghosh et al. [47]. Copyright 2003 The American Association for the Advancement of Science.)

### 3.3. Carbon nanotube optical sensor

#### 3.3.1. Carbon nanotube as receiver for electromagnetic waves

Ren and co-workers [48] performed optical measurements of random arrays of aligned carbon nanotubes (MWNTs) synthesized by a plasma-enhanced chemical vapor deposition (PECVD) process (Fig. 29).

These authors demonstrated the polarization effect using an Si wafer ( $2 \times 1 \text{ cm}^2$ ) consisting of a thin film of Cr in one-half surface and a random array of MWNTs in another half surface. As shown in Fig. 30, the suppression of the reflected signal was seen when the electric field of the incoming radiation was polarized perpendicular (polarization angle:  $\Theta = 90^\circ$ ) to the nanotube axis.

Fig. 31a shows a sample of a random array of nanotubes with gradually reduced lengths (from left to right) illuminated by white light. The strong interference colors of the reflected light from an array were observed, indicating the length matching antenna effect. The observed antenna length effect can be tuned by controlling the nanotube length and the array density during the growth process, making the devices' frequency to be selective. This antenna effect could be used in a variety of optoelectronic sensing devices, including THz and IR detectors.

#### 3.3.2. Optical resonances in carbon nanotubes

Strong electron–electron interactions have been demonstrated with the charge transport in SWNTs, leading to many phenomena such as Coulomb blockade [49,50], Kondo effects [51,52], and Luttinger liquid behavior [53,54]. Recent theoretical studies suggested that optically produced electron-hole pairs should, under their mutual

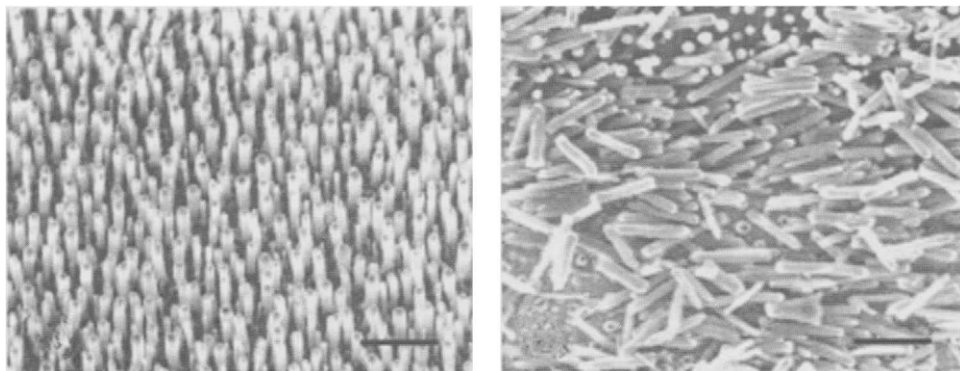


Figure 29. Aligned (a) and scratched (b) random arrays of MWNTs. Only the random array was used, to reduce the internanotube diffraction effects. Scale bars,  $1\mu\text{m}$ . (Reprinted with permission from Wang et al. [48]. Copyright 2004 American Institute of Physics.)

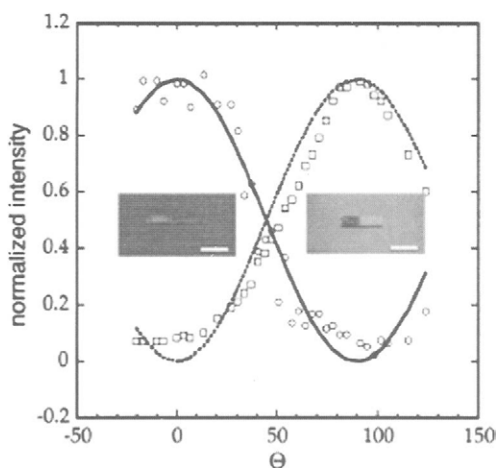


Figure 30. Polarization effect. Reflected, normalized light intensity vs. polarization angle  $\Theta$  for the sample shown in the insets. Circles represent the light intensity from the random array of nanotubes, and squares from the metallic film. Lines represent the expected functional dependencies:  $I = \cos^2\Theta$  for nanotubes (solid),  $I = \sin^2\Theta$  for metallic film (dotted). Left inset, sample viewed with the polarization plane parallel to nanotubes (p-polarization),  $\Theta = 0$ . Right inset, sample viewed through polarizer with the polarization plane perpendicular to nanotubes (s-polarization),  $\Theta = 90$ . Scale bars,  $1\text{ cm}$ . (Reprinted with permission from Wang et al. [48]. Copyright 2004 American Institute of Physics.)

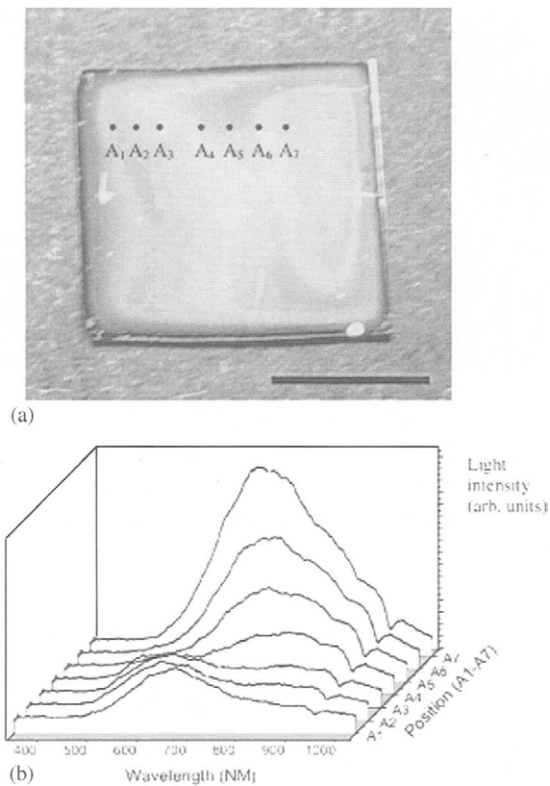


Figure 31. (Color) Antenna length effect. (a) Interference colors from the random array of MWNTs.  $A_1 - A_7$  are the selected positions where the length and optical measurements were carried out. Scale bar, 1 cm. (b) Reflected light intensity *vs.* radiation wavelength measured in selected points on the sample shown in (a). (Reprinted with permission from Wang et al. [48]. Copyright 2004 American Institute of Physics.)

Coulomb interaction, form strongly correlated electron–hole pairs known as excitons [55–61]. Although some evidence for the formation of excitons has emerged from studies of carbon nanotube optical spectra [62,63] and excited-state dynamics [64], it is difficult to rule out an alternative and widely used picture that attributes the optical resonances to van Hove singularities in the 1D density of states [65,66,67].

Wang et al. [68] demonstrated experimentally that the optically excited states of SWNTs are excitonic in nature. In so doing, these authors used a film of isolated SWNTs embedded in a poly(maleic acid/octyl vinyl ether) matrix for minimization of infrared absorption by water and identified excitons in carbon nanotubes using two-photon excitation spectroscopy (Fig. 32).

To detect the two-photon excitation process in the SWNTs, Wang et al. [68] did not directly measure the depletion of the pump beam, but monitored the induced

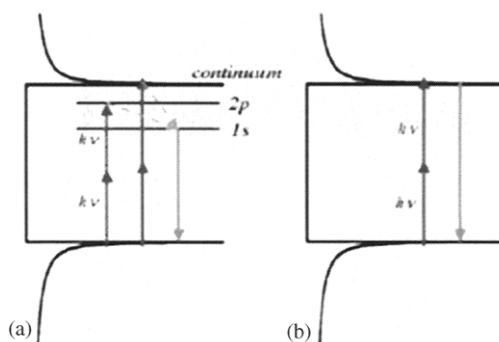


Figure 32. Schematic representation of the density of states for an SWNT, showing the two-photon excitation (blue arrows) with photon energy  $h\nu$  and subsequent fluorescence emission (red arrows) in the exciton and band pictures. (a) In the exciton picture, the 1s exciton state is forbidden under two-photon excitation. The 2p exciton and continuum states are excited. They relax to the 1s exciton state and fluoresce through a one-photon process. (b) In the band picture, the threshold for two-photon excitation lies at the band edge, where the relaxed fluorescence emission also takes place. (Reprinted with permission from Wang et al. [68]. Copyright 2005 The American Association for the Advancement of Science.)

light emission through the so-called two-photon-induced fluorescence excitation spectroscopy. The measured two-photon excitation spectra (Fig. 33) clearly show the strength of the fluorescence emission as a function of both the (two-photon) excitation energy and the (one-photon) emission energy.

From 2D contour plot in Fig. 33, distinct fluorescence emission features emerge at emission energies of 1.21, 1.26, 1.30, and 1.36 eV (circles in Fig. 33). These emission peaks have been assigned to SWNTs with chiral indices of (7,5), (6,5), (8,3), and (9,1), respectively [62]. It is apparent that none of the carbon nanotubes were excited when the two-photon excitation energy was the same as the emission energy (solid line in Fig. 33). Only when the excitation energy was substantially greater than the emission energy did two-photon absorption occur. The excitonic character of the optically excited state also has immediate implications for developing new electro-optical modulators and sensors.

### 3.3.3. Transparent and conductive carbon nanotube films

Transparent electrical conductors play an important role in modern technologies. Rinzler and co-workers [69] developed a class of SWNT-based transparent conducting films (t-SWNTs) as the active element of an optical modulator.

The production process for making the t-SWNT was quite simple, comprising three steps: (i) vacuum-filtering a dilute, surfactant-based suspension of purified nanotubes onto a filtration membrane (forming the homogeneous film on the membrane); (ii) washing away the surfactant with purified water; and (iii) dissolving the filtration

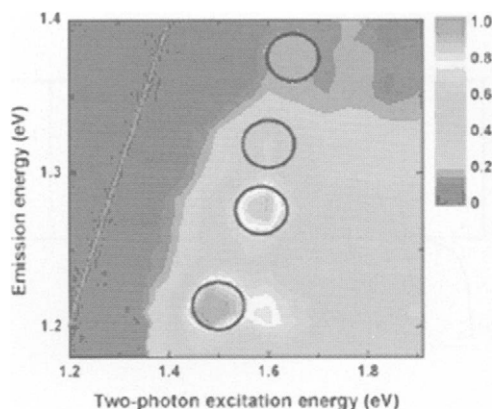


Figure 33. Contour plot of two-photon excitation spectra of SWNTs. The measured fluorescence intensity is shown in a false-color representation as a function of the (two-photon) excitation energy and the (one-photon) fluorescence peaks of different SWNT species [(7,5), (6,5), (8,3), and (9,1) with increasing emission energy] can be identified (black circles). The two-photon excitation peaks are shifted substantially above the energy of the corresponding emission feature, as is apparent by comparison with the solid line describing equal excitation and emission energies. The large shift arises from the excitonic nature of SWNT optical transitions. (Reprinted with permission from Wang et al. [68]. Copyright 2005 The American Association for the Advancement of Science.)

membrane in solvent. By so doing, Rinzler et al. produced t-SWNT films with a good homogeneity, extreme rigidity, and controllable thickness (Fig. 34). Fig. 35 shows the transmittance spectrum for a 240-nm-thick, free-standing t-SWNT film over a broad spectral range, along with the corresponding spectrum for a 50-nm-thick film on quartz over a more limited range. The as-prepared 50 nm film has transmittance greater than 70% over the visible part of the spectrum. In the near-IR at 2  $\mu\text{m}$ , this film has transmittance greater than 90%. The use of Beer's law to scale the transmittance of the 240 nm film to a thickness of 50 nm indicates that the transmittance should remain > 90% to just beyond 5  $\mu\text{m}$ . Hence, it is anticipated that the t-SWNT films can have a window of > 90% transmittance in a spectral band from 2 to 5  $\mu\text{m}$ .

The ease with which chemical charge transfer doping of carbon nanotubes will further optimize the transparency vs. conductivity by exposure of the nanotubes to vapors of appropriate chemicals provides an additional advantage for applications involving t-SWNTs. Unlike most *n*-type transparent conducting oxides (e.g. indium tin oxide, ITO), charge transport in these t-SWNTs is *p*-type. This should further permit new complementary applications and alternative photonic coupling schemes [70].

Just like chemical charge transfer doping shifts their Fermi levels by adding electrons into or removing them from the nanotubes, the application of electric fields can also induce such Fermi level shifts. In a nanotube-based FET (NFET), a

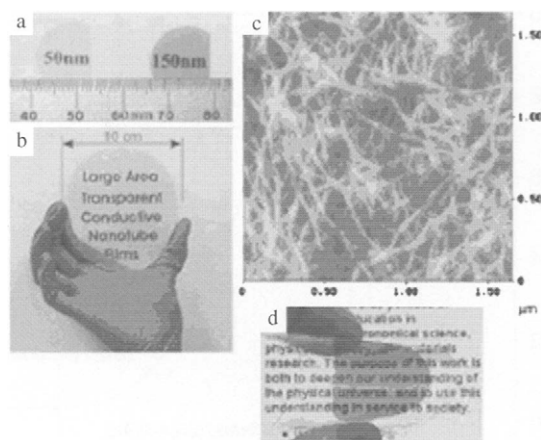


Figure 34. Transparent SWNT films. (a) Films of the indicated thickness on quartz substrates. (b) A large, 80-nm-thick film on a sapphire substrate 10 cm in diameter. (c) Flexed film on a Mylar sheet. (d) AFM image of a 150-nm-thick t-SWNT film surface (color scale: black to bright yellow, 30 nm). The text in (b) to (c) lies behind the films. (Reprinted with permission from Wu et al. [69]. Copyright 2004 The American Association for the Advancement of Science.)

semiconducting nanotube is electrically coupled to source and drain terminals while the field between the nanotube and an isolated gate electrode shifts the nanotube Fermi level, modulating its carrier concentration [71–74]. Fig. 36 shows a schematic representation of a device that constitutes an optical analog to the electrolyte-gated NFET, which modulates light transmission through the device as a function of the electrolyte “gate” potential. While the device was positioned horizontally, the nanotube films were saturated with the ionic liquid (IL) 1-ethyl-3-methylimidazolium-bis(trifluoromethylsulfonyl)imide. When the assembly was tipped up vertically, excess IL drained into the reservoir with a thin IL layer covered each of the nanotube film from the drain to reservoir through the wetting effect. Monochromatic light was passed through only one of the SWNT films. A negative potential applied to the gating (counterelectrode) film depleted electrons from the van Hove singularity associated with the S1 electronic transitions for the probed film. This results in a loss of the corresponding absorption and increased optical transmission through the device at the associated wavelength.

Fig. 37 shows the optical transmittance for the optical NFET (O-FET) illustrated in Fig. 36 as a function of voltage applied between the nanotube films. At the S1 absorbance maximum (1676 nm), the transmittance was modulated from 44% to 92% between “gate” (counterelectrode) potentials of + and –1.8 V [75,76]. Relative to the changes in the S1, S2, and M1 bands, transmittance changes at wavelengths greater than ~2000 nm occurred in the opposite direction with voltage. Negative counterelectrode potentials drew excess holes onto the probed film to increase the free carrier

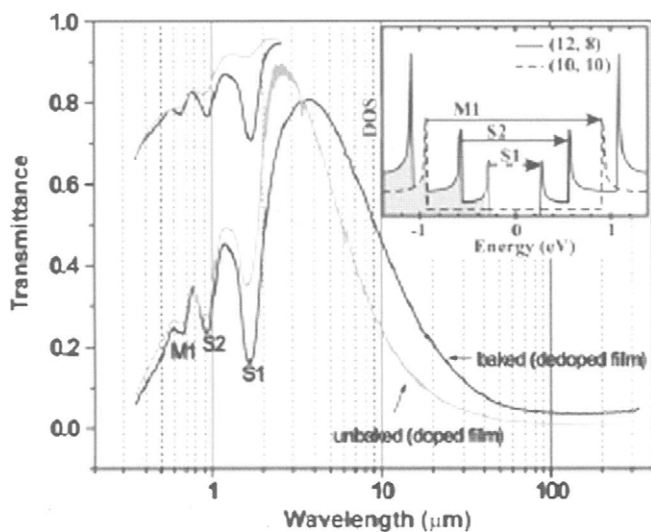


Figure 35. Transmittance spectra for two t-SWNT films (doped and dedoped) of thickness 50 nm (on quartz) and 240 nm (free-standing). The curves with greater transmittance (upper left) are for the 50-nm film. Gray curves denote the charge transfer, hole-doped films; black curves denote those films after dedoping. Inset shows the DOS for a representative (12,8) semiconducting nanotube (solid curve) within a tight binding model. Arrows between singularities represent electronic transitions responsible for the S1, S2, and M1 adsorption bands. Depletion of the first singularity (filled electronic states in gray) results in the loss of the corresponding electronic transition (dashed arrow) and loss of the associated S1 absorption intensity. The t-SWNT films consist of a mixture of semiconducting and metallic nanotubes with a distribution of diameters and chiral angles. The  $(n,m)$  index dependence of the spacing between van Hove singularities modulates the transition energies to yield the broad absorption bands seen in the spectra (also labeled S1, S2, and M1). Bundling of the nanotubes further broadens the observed absorption bands. (Reprinted with permission from Wu et al. [69]. Copyright 2004 The American Association for the Advancement of Science.)

absorption and reduce the transmission, whereas positive counterelectrodes potentials reduced the hole concentration to decrease the free carrier absorption and increase the transmission. These modulations in the transmittance were fully reversible, with no degradation observed after hundreds of cycles.

The simultaneous high transparency and good electrical conductivity of the t-SWNT films can be understood on the basis of three properties of the nanotubes: (i) low carrier density; (ii) high electric mobility; and (iii) the suppression of light absorption and reflection for polarization components perpendicular to the nanotube axis, which reduces the optical density of the disordered SWNT films for unpolarized incident light. Devices like this O-NFET optical modulator may find

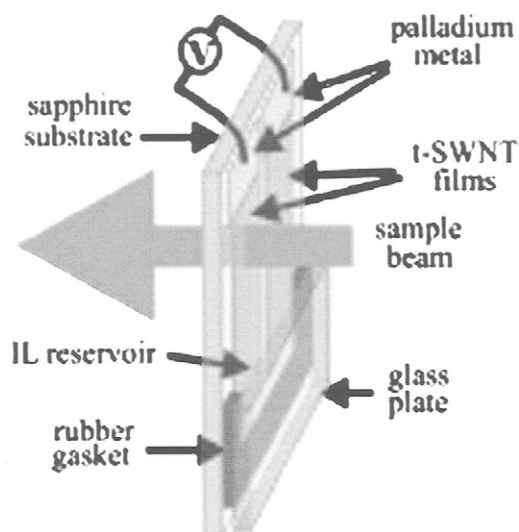


Figure 36. Optical analog to the electrolyte-gated NFET (O-FET). (Reprinted with permission from Wu et al. [69]. Copyright 2004 The American Association for the Advancement of Science.)

application in spacecraft thermal control, flexible/foldable displays, and military camouflage countermeasures [77].

### 3.4. Carbon nanotube biosensors

Apart from the many interesting sensing applications discussed above, carbon nanotubes have recently become promising functional materials for the development of novel biosensors. It has been shown that carbon nanotubes could promote electron transfer with various redox active proteins, including glucose oxidase, cytochrome *c*, and horseradish peroxidase. To demonstrate that carbon nanotubes can promote electron transfer with certain proteins and enzymes [78,79,80], for example, Li and co-workers [78] have investigated the electrochemical behavior of cytochrome *c* on an SWNT film electrode.

#### 3.4.1. Protein and enzyme biosensors

As can be seen in Fig. 38, cytochrome *c* gave no obvious electrochemical response at the bare GC electrode (Fig. 38a) whilst showed irreversible behavior with a difference between the anodic peak potential and the cathodic peak potential ( $\Delta E = 265$  mV) at the unactivated SWNT-modified electrode (Fig. 38b). However, a pair of well-defined redox peaks with  $\Delta E = 73.7$  mV was observed for cytochrome *c* at the same electrode after modification with an activated SWNT film (Fig. 38c). These results clearly indicate a significantly improved electron-transfer process for the carbon nanotube-modified electrode.

On the other hand, Wang et al. [81] have demonstrated that Nafion-coated carbon nanotube electrodes could enhance the redox activity of hydrogen peroxide so



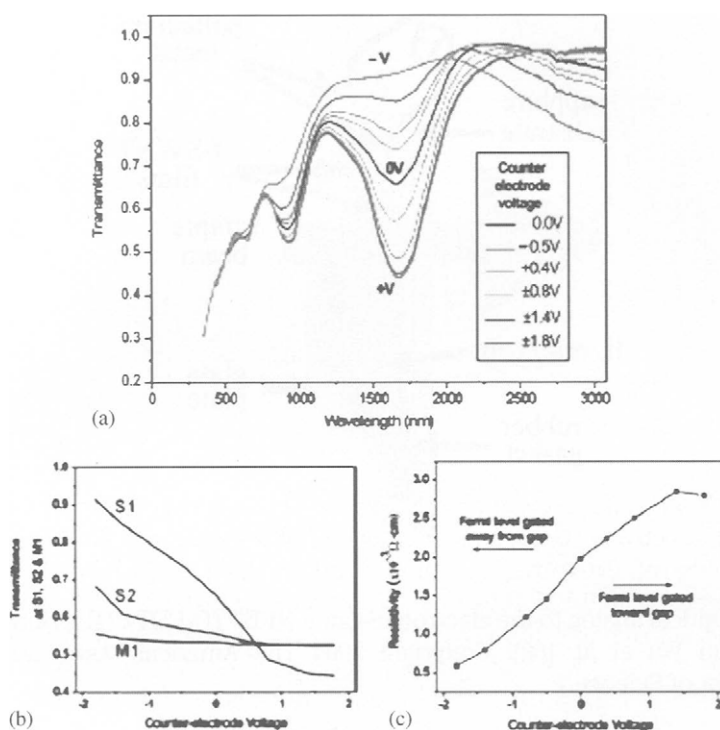


Figure 37. (a) Spectral transmittance of the O-NFET as a function of applied counter-electrode “gate” voltage. (b) Voltage-dependent transmittance at the S1 (1676 nm), S2 (932 nm), and M1 (656 nm) absorbances. (c) Four-probe resistivity of the t-SWNT film vs. the same counterelectrode “gate” voltages used in the spectral measurements. (Reprinted with permission from Wu et al. [69]. Copyright 2004 The American Association for the Advancement of Science.)

dramatically that a remarkable decrease in the over oxidation potential for hydrogen peroxide was observed. The accelerated electron transfer from hydrogen peroxide allowed for glucose measurements at very low potentials ( $-0.05$  V), where interfering reactions of acetaminophen, uric acid, and ascorbic acid were minimized. Similarly, Luong et al. [82] have used 3-aminopropyltriethoxysilane (APTES) as both a solubilizing agent for carbon nanotubes and an immobilization matrix for Glucose Oxidase (GOx) to construct a mediatorless, highly efficient glucose sensor. In this study, a well-defined redox response from glucose was observed at  $-0.45$  V (vs. Ag/AgCl) whereas no response was seen for three common interfering species, namely uric acid, ascorbic acid, and acetaminophen, at a concentration corresponding to the physiological level of  $0.1$  mM.

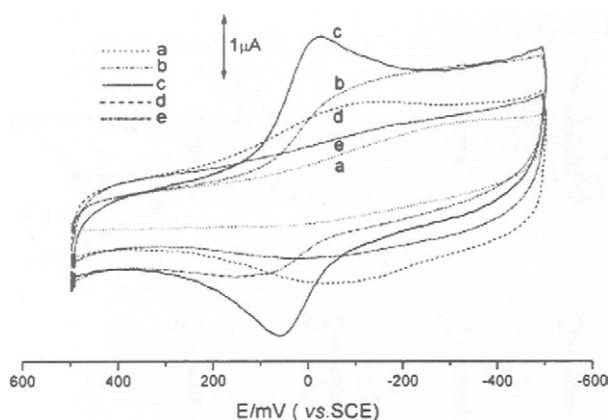


Figure 38. Cyclic voltammograms at a bare GC electrode (a), an unactivated SWNT-modified GC electrode (b, e), and an activated SWNT-modified GC electrode (c, d) in the absence of cytochrome *c* (d, e) and in the presence of  $5.0 \times 10^{-4}$  M cytochrome *c* (a–c) in 0.1 M phosphate buffer solution (pH 6.24). The potential scan rate is  $0.02 \text{ V s}^{-1}$ . The activation was achieved by scanning the SWNT-modified electrode in a fresh 0.1 M phosphate buffer solution (pH 6.24) over +1.5 to  $-1.0 \text{ V}$  at a scan rate of  $1 \text{ V s}^{-1}$  for 1.5 min. (Reprinted with permission from Wu et al. [78]. Copyright 2002 The American Chemical Society.)

Unlike the above glucose biosensors based on nonaligned carbon nanotubes, Ren and co-workers [83,84,85] developed a glucose biosensor by covalently immobilizing GOx onto an aligned carbon nanotube nanoelectrode ensemble (CNT-NEE) through the amide formation between the GOx and carboxylic acid groups on the aligned carbon nanotube tips (Fig. 39).

Due to the high surface packing density of the individual nanoelectrodes within the CNT-NEE assembly, the aligned carbon nanotube glucose biosensor thus prepared was found to be ultrasensitive with a high selectivity for electrochemical analysis of glucose over common interferents (e.g. acetaminophen, uric, and ascorbic acids) (Fig. 40).

Rusling and co-workers [86] have covalently linked myoglobin and horseradish peroxidase to an aligned SWNT electrode through the amide linkage. Quasi-reversible  $\text{Fe}^{3+}/\text{Fe}^{2+}$  voltammetry was observed for the iron heme enzymes myoglobin and horseradish peroxidase. The results demonstrated that the “trees” in the nanotube forest behaved electrically similar to a metal; conducting electrons from the external circuit to the redox sites of the enzymes. Willner and co-workers [87] have also investigated the long-range electron transfer from redox enzymes chemically bound onto the aligned SWNT structure.

Fig. 41 shows the procedure used by these authors to assemble the aligned SWNTs onto a gold electrode. As can be seen, the oxidized SWNTs were first covalently coupled with 2-thioethanol/cystamine mixed monolayer (3:1 ratio) assembled

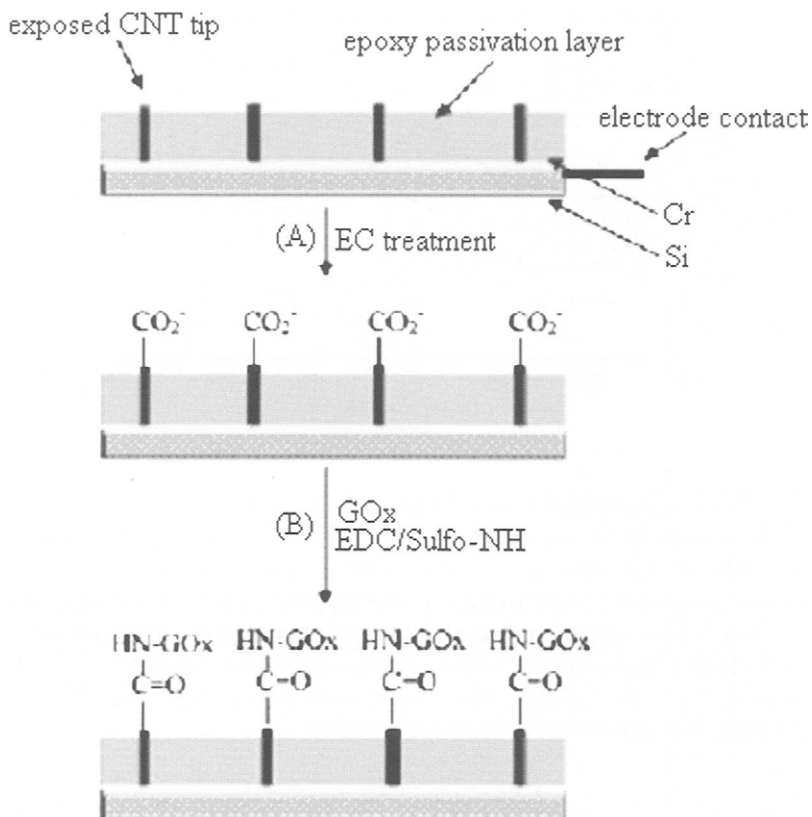


Figure 39. Fabrication of a glucose biosensor based on CNT nanoelectrode ensembles: (a) Electrochemical treatment of the CNT-NEE for functionalization (b) Coupling of the enzyme (GOx) to the functionalized CNT-NEE. (Reprinted with permission from Lin et al. [83]. Copyright 2004 The American Chemical Society.)

on an Au electrode. The incorporation of 2-thioethanol in the mixed monolayer was anticipated to prevent nonspecific adsorption of the surfactant-protected SWNTs onto the electrode surface. The amino derivative of flavin adenine dinucleotide (FAD) cofactor was then coupled to the carboxylic acid groups at the free top-ends of the aligned SWNTs. Finally, GOx was reconstituted on the FAD units linked to the ends of the aligned SWNTs for glucose sensing.

Figs. 42A and B show that the bioelectrocatalytic oxidation of glucose on the Au electrode modified with GOx-attached carbon nanotubes (average nanotube length of 25 nm) occurred at  $E > 0.18$  V, and the electrocatalytic anodic current became higher as the concentration of glucose increased. While Fig. 42C reproduces the calibration curves corresponding to the anodic currents generated by the GOx-reconstituted SWNT electrodes of different SWNT lengths in the presence of variable glucose

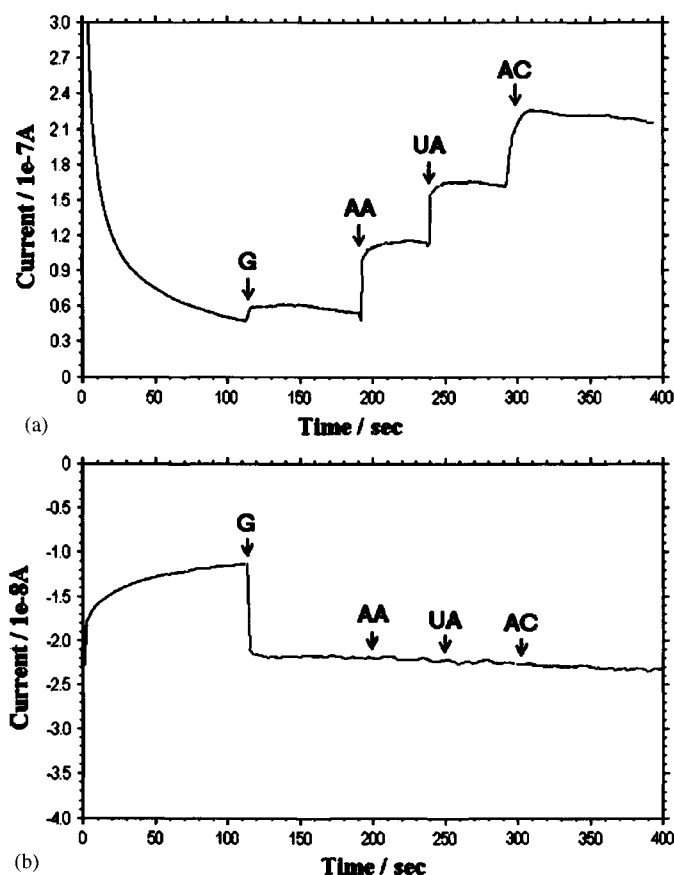


Figure 40. Amperometric responses of the CNT-NEE glucose biosensor to glucose (G), ascorbic acid (AA), uric acid (UA), and acetaminophen (AC) at potentials of +0.4 V (a) and -0.2 V (b). (Reprinted with permission from Lin et al. [83]. Copyright 2004 The American Chemical Society.)

concentrations, Fig. 42D shows a strong linear dependence between the turnover rate of electron transfer and  $L^{-1}$  ( $L$  is the nanotube length). The observed length-controlled electron transfer was further supported by examining the interfacial electron transfer to the FAD sites at the ends of the aligned SWNTs, though the mechanism for the tube-length-dependent electron transfer has not been fully understood. Given that no tube length dependence was observed in Gooding's study [88] (*vide supra*), the length-dependent charge transfer observed in Fig. 42 is most likely resulted from defect sites introduced along the nanotube wall during the oxidative shortening process. However, the detailed mechanism of the tube-length-dependent charge transfer deserves further investigation.

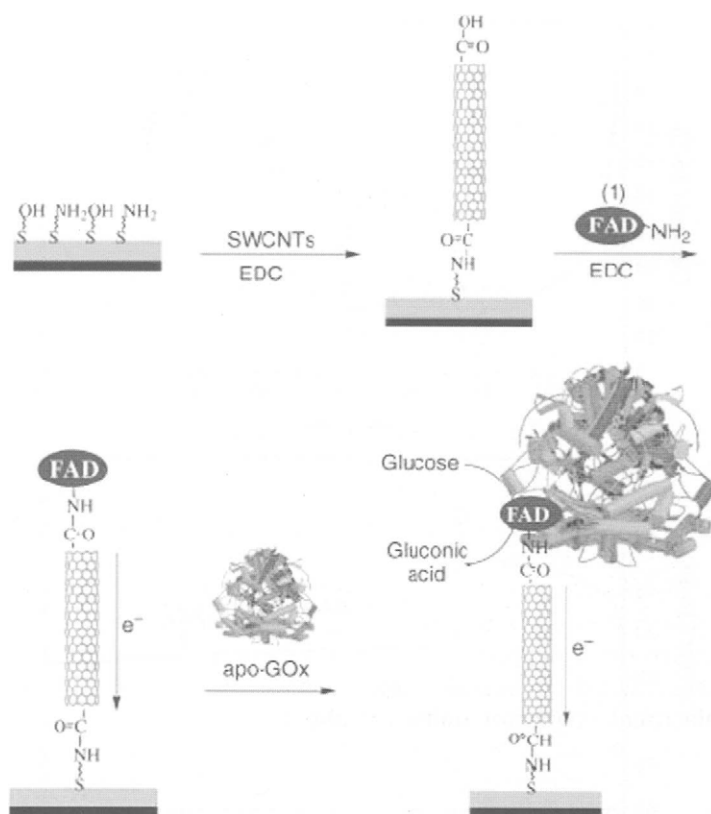


Figure 41. Assembly of the SWNT electrode with chemically bound glucose oxidase. (Reprinted with permission from Patolsky et al. [87]. Copyright 2004 Wiley-VCH Verlag GmbH & Co.)

To avoid the tedious processes for preparing aligned SWNTs, Dai et al. [89,90] have used the FePc-generated aligned MWNTs as a novel electrode platform for biosensing. In a typical experiment, these authors coated the aligned MWNTs with conducting polymers by electrochemically depositing a thin layer of polypyrrole or polyaniline onto individual carbon nanotubes along their tubular length in the presence of glucose oxidase. It was found that the detection of  $\text{H}_2\text{O}_2$  at these aligned MWNT electrodes coated with GOx-containing conducting polymers can also be achieved at low anodic potentials, leading to glucose sensors with a very high sensitivity and selectivity [91,92].

### 3.4.2. Carbon nanotube DNA sensors

A major feature of the Watson-Crick model of DNA is that it provides a vision of how a base sequence of one strand of the double helix can precisely determine the base sequence of the partner strand for passing the genetic information in all living

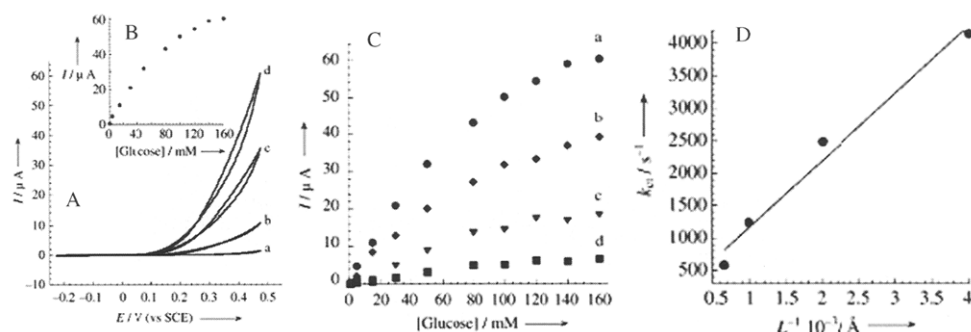


Figure 42. (A) Cyclic voltammograms corresponding to the electrocatalyzed oxidation of different concentrations of glucose by the GOx reconstituted on the 25-nm-long FAD-functionalized CNTs assembly: (a) 0 mM glucose, (b) 20 mM glucose, (c) 60 mM glucose, (d) 160 mM glucose. Data recorded in phosphate buffer, 0.1M, pH 7.4, scan rate 5 mV s<sup>-1</sup>. (B) Calibration curve corresponding to the amperometric responses of the reconstituted GOx/CNTs (25 nm) electrode (at  $E=0.45$  V) in the presence of different concentrations of glucose. (C) Calibration curves corresponding to the amperometric responses (at  $E = 0.45$  V) of reconstituted GOx–CNTs electrodes in the presence of variable concentrations of glucose and different CNT lengths as electrical connector units: (a) about 25 nm SWNTs, (b) about 50 nm SWNTs, (c) about 100 nm SWNTs, and (d) about 150 nm SWNTs. (D) Dependence of the electron-transfer turnover rate between the GOx redox center and the electrode on the lengths of the SWNTs comprising the enzyme electrodes (Reprinted with permission from Patolsky et al. [87]. Copyright 2004 Wiley-VCH Verlag GmbH & Co.)

species. The principle learned from this breakthrough has now been applied to the development of biosensors for DNA analysis and diagnosis through the very specific DNA pairing interaction [93,94]. Owing to their high sensitivity, facial data processing, great simplicity, and good compatibility with electronic detection technologies, DNA electrochemical biosensors are of great interest. The unique electronic properties and large surface area have made carbon nanotubes ideal electrodes for constructing advanced biosensors. This, coupled with various chemical reactions reported for the attachment of DNA chains onto carbon nanotubes has facilitated significantly the development of carbon nanotube DNA sensors.

Using a glass carbon electrode (GCE) modified with MWNTs, Fang et al. [95] observed an enhanced sensitivity for electrochemical DNA biosensor based on carbon nanotubes. Fig. 43 shows schematically the steps for constructing the nanotube-DNA biosensor. To start with, carboxylic acid functionalized multi-walled carbon nanotubes (COOH–MWNTs) were dropped on a GCE electrode, single-strand DNA oligonucleotides (ssDNAs) were then covalently bonded onto the COOH–MWNTs via the amide formation. The hybridization reaction on the

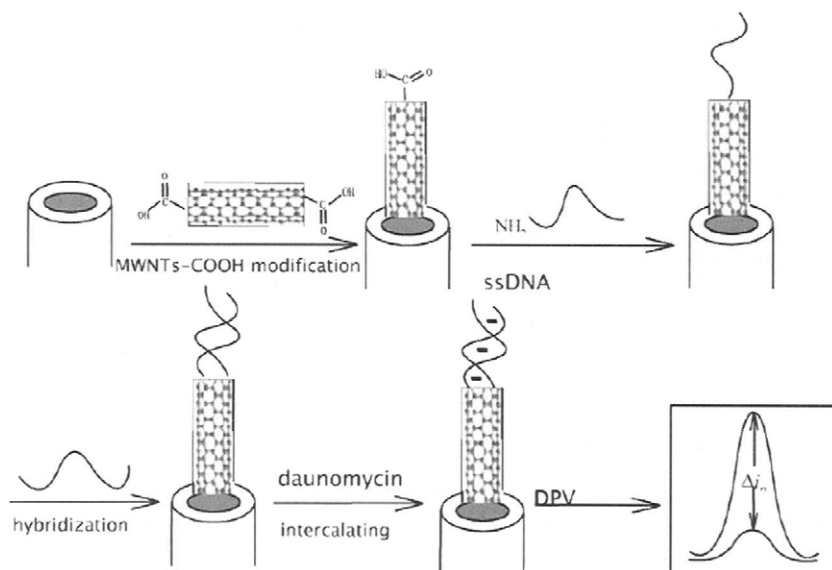


Figure 43. Schematic representation of the enhanced electrochemical detection of DNA hybridization by DNA biosensor based on the COOH-MWNTs. (Reprinted with permission from Cai et al. [95]. Copyright 2003 Springer-Verlag GmbH & Co.)

electrode was monitored by differential pulse voltammetry (DPV) analyses using an electroactive daunomycin intercalator as the indicator.

Compared with conventional DNA sensors with oligonucleotides being directly incorporated onto carbon electrodes, the carbon nanotube-based DNA sensor showed a dramatically increased DNA attachment density and complementary DNA detection sensitivity due to the large surface area and good charge-transport properties characteristic of carbon nanotubes. These promising results have further prompted these authors to develop novel biosensors for direct electrochemical detection of DNA hybridization by AC impedance measurements [96,97]. Fang and co-workers electrodeposited polypyrrole and oligonucleotide probe onto an MWNT-coated GCE electrode. The large surface area of carbon nanotubes allowed a large volume of polypyrrole/oligonucleotide to be deposited onto the electrode whilst the polypyrrole coating on individual carbon nanotubes remained sufficiently thin. Owing to their high electrical conductivity, carbon nanotubes can clearly reflect any resistance change in the polypyrrole/oligonucleotide thin film caused by hybridization reaction (Fig. 44).

In order to amplify electrical detection of DNA hybridization, Wang and co-workers [98,99,100] developed a carbon nanotube-based dual amplification route, in which carbon nanotubes play a dual amplification role (namely carrying numerous enzyme tags and accumulating the product of the enzymatic reaction), for dramatically amplifying enzyme tag numbers in sensing of DNAs and proteins (Fig. 45). The process

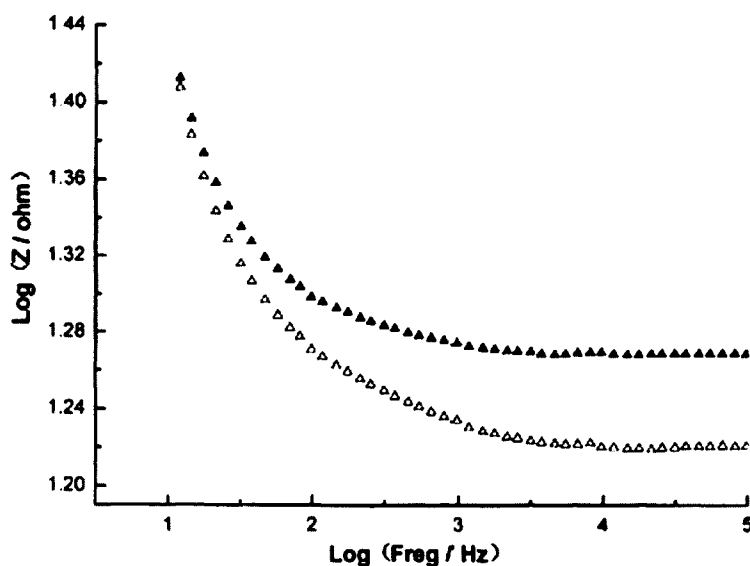


Figure 44. Impedance curves before (solid triangle) and after (hollow triangle) hybridization in 0.3 M PBS solution on an open circuit voltage. Frequency range, 10–10<sup>5</sup> Hz; amplitude: 5 mV vs. SCE. (Reprinted with permission from Cai et al. [96]. Copyright 2003 Wiley-VCH Verlag GmbH & Co.)

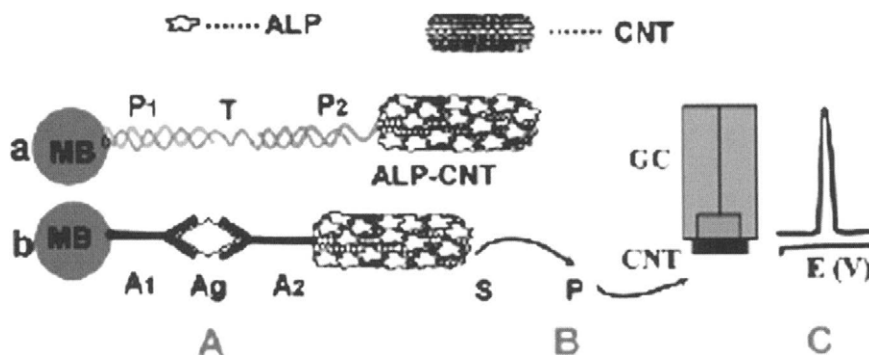


Figure 45. Schematic representation of the analytical protocol: (A) Capture of the ALP-loaded CNT tags to the streptavidin-modified magnetic beads by a sandwich DNA hybridization (a) or A<sub>1</sub>-Ag-A<sub>2</sub> interaction (b). (B) Enzymatic reaction. (C) Electrochemical detection of the product of the enzymatic reaction at the CNT-modified glassy carbon electrode; MB, Magnetic beads; P<sub>1</sub>, DNA probe 1; T, DNA target; P<sub>2</sub>, DNA probe 2; A<sub>1</sub>, first antibody; Ag, antigen; A<sub>2</sub>, secondary antibody; S and P, substrate and product, respectively, of the enzymatic reaction; GC, glassy carbon electrode; CNT, carbon nanotube layer. (Reprinted with permission from Wang et al. [98]. Copyright 2004 The American Chemical Society.)



shown in Fig. 45 involved the sandwich DNA hybridization (a) or antigen–antibody (b) binding along with magnetic separation of the analyte-linked magnetic-bead/CNT assembly (A), followed by enzymatic amplification (B), and chronopotentiometric stripping detection of the product at the CNT-modified electrode (C).

Fig. 46 shows the dramatic signal enhancement associated with the carbon nanotube-based dual amplification route for DNA hybridization (A) and Ag–Ab (B) bioassays. As can be seen in Fig. 46, the conventional protocols, based on the single-enzyme tag and a glassy-carbon electrode, were not responding to either  $10 \text{ pg mL}^{-1}$  DNA target (A, a) or  $80 \text{ pg mL}^{-1}$  IgG (B, a). The first amplification step based on the alkaline phosphatase (ALP) loaded carbon nanotubes (b) offered convenient detection of these low analyte concentrations. Further enhancements of the DNA and protein signals were observed in the second amplification path, employing the carbon

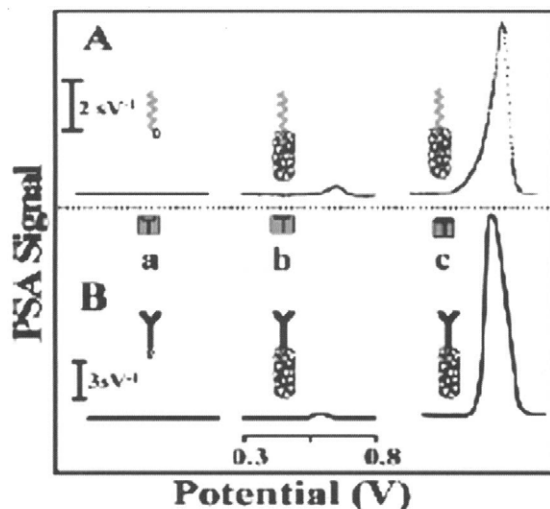


Figure 46. Chronopotentiometric signals for  $10 \text{ pg mL}^{-1}$  target oligonucleotide (A) and  $80 \text{ pg mL}^{-1}$  IgG (B) using the glassy carbon (GC) transducer and (a) a single ALP tag and (b) CNT-loaded with multiple ALP tags; (c) same as (b) but using the CNT modified GC electrode. Amount of magnetic beads,  $50 \text{ }\mu\text{g}$ ; sandwich assay with 20 and 30 min for each hybridization event and Ag/Ab association, respectively; sample volume,  $50 \text{ }\mu\text{L}$ . Detection, addition of  $50 \text{ }\mu\text{L}$  R-naphthyl phosphate ( $50 \text{ mM}$ ) solution with a 20-min enzymatic reaction. Measurements of the R-naphthol product were performed at the bare or modified GC electrodes, using a 2-min accumulation at  $+0.2 \text{ V}$  in a stirred phosphate buffer solution ( $0.05 \text{ M}$ ,  $\text{pH } 7.4$ ;  $1 \text{ mL}$ ), followed by a 10-s rest period (without stirring) and application of an anodic current of  $+5.0 \text{ }\mu\text{A}$ . See supporting information for the concentrations of the oligonucleotide probes and antibody, and sequence of oligonucleotide probes, levels, and preparation of the ALP-DNA-CNT and ALP streptavidin-CNT conjugates. (Reprinted with permission from Wang et al. [98]. Copyright 2004 The American Chemical Society.)

nanotube-modified electrode (c). The latter reflects the strong adsorptive accumulation of the liberated  $\alpha$ -naphthol on the carbon nanotube layer. Two series of six repetitive measurements of  $1 \text{ pg mL}^{-1}$  DNA target or  $0.8 \text{ ng mL}^{-1}$  IgG yielded reproducible signals with relative standard deviations of 5.6% and 8.9%, respectively.

Using aligned carbon nanotube electrodes, He and Dai [101] have recently developed novel nanotube–DNA sensors of a high sensitivity and selectivity by grafting ssDNA chains onto aligned carbon nanotubes generated from FePc [89]. In this study, aligned carbon nanotubes supported by gold substrate were first treated with acetic acid–plasma to introduce the surface carboxylic acid groups for grafting ssDNA chains with an amino group at the 5′-phosphate end (i.e. [AmC6]TTGACACCAGAC-CAACTGGT-3′, **I**). Complementary DNA (cDNA) chains labeled with ferrocene carboxaldehyde, FCA (i.e. [FCA-C6] ACCAGTTGGTCTGGTGTCAA-3′, **II**) were then used for hybridizing with the surface-immobilized oligonucleotides to form the double-strand DNA (dsDNA) helices on the aligned carbon nanotube electrodes (Fig. 47).

The performance of the aligned carbon nanotube–DNA sensors for sequence-specific DNA diagnoses is demonstrated in Fig. 48. The strong oxidation peak seen at 0.29 V in curve a of Fig. 48 is attributable to ferrocene and indicates the occurrence of hybridization of FCA-labeled cDNA (**II**) chains with the nanotube-supported ssDNA (**I**) chains, leading to a long-range electron transfer from the FCA probe to the nanotube electrode through the DNA duplex. In contrast, the addition of FCA labeled noncomplementary DNA chains (i.e. [FCA-C6]CTCCAGGAGTCG-TCGCCACC-3′, **III**) under the same conditions did not show any redox response of FCA (curve b of Fig. 48). Subsequent addition of target DNA chains

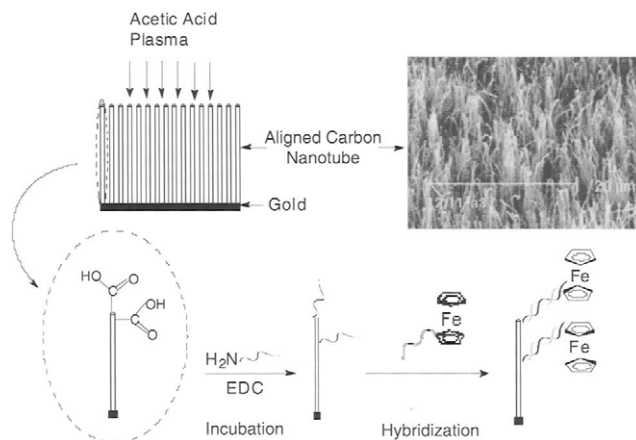


Figure 47. A schematic illustration of the aligned nanotube–DNA electrochemical sensor. The upper right SEM image shows the aligned carbon nanotubes after having been transferred onto a gold foil. For reasons of clarity, only one of the many carboxyl groups is shown at the nanotube tip and wall, respectively. (Reprinted with permission from He and Dai [101]. Copyright 2004 The Royal Society of Chemistry.)

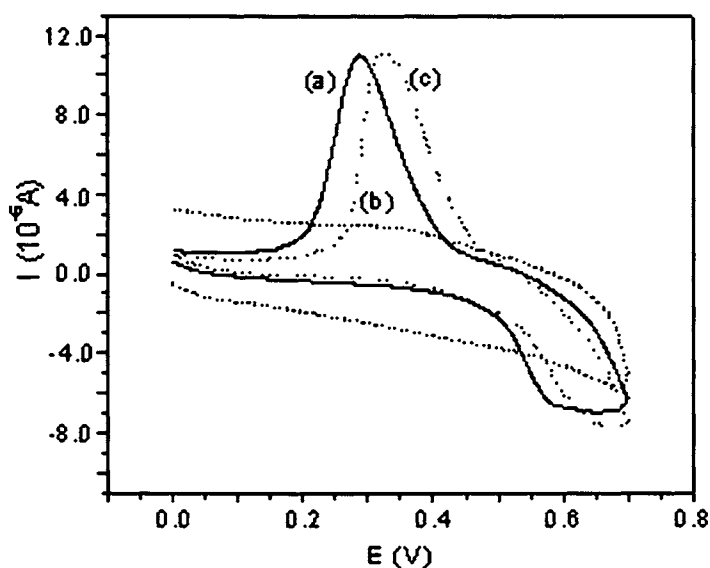


Figure 48. Cyclic voltammograms of the ssDNA (I)-immobilized aligned carbon nanotube electrode after hybridization with FCA-labeled complementary DNA (II) chains (a), in the presence of FCA-labeled noncomplementary DNA (III) chains (b), and after hybridization with target DNA (IV) chains in the presence of the FCA-labeled noncomplementary DNA (III) chains (c). All the cyclic voltammograms were recorded in 0.1 M  $\text{H}_2\text{SO}_4$  solution with a scan rate of  $0.1 \text{ V s}^{-1}$ . The concentration of the FCA-labeled DNA probes is  $0.05 \text{ mg mL}^{-1}$  (Reprinted with permission from He and Dai [101]. Copyright 2004 The Royal Society of Chemistry.)

(i.e. 5'-GAGGTCCTCAGCAGCGGTGGACCAGTTGGTCTGGTGTCAA-3', IV) into the above solution, however, led to a strong redox response from the FCA-labeled DNA (III) chains (curve c of Fig. 48) because the target DNA (IV) contains complementary sequences for both DNA (I) and DNA (III) chains.

### 3.4.3. DNA sensor based on platinum nanoparticles combined carbon nanotubes

Zhu et al. [102] presented DNA sensor based on platinum nanoparticles ( $\text{Pt}_{\text{nano}}$ ) combined with MWNTs. MWNTs and  $\text{Pt}_{\text{nano}}$  were dispersed in Nafion, which were used for modification of the GCE surface. Fig. 49 shows the electrochemical characteristics for three types of the electrodes. As can be seen in Fig. 49, the back current of the MWNTs/ $\text{Pt}_{\text{nano}}$ /GCE is the largest, indicating that the effective electrode surface of MWNTs/ $\text{Pt}_{\text{nano}}$ /GCE is larger than that of  $\text{Pt}_{\text{nano}}$ -modified GCE and MWNTs-modified GCE alone.

The immobilization of oligonucleotides (24-base) probe on the MWNTs/ $\text{Pt}_{\text{nano}}$ -modified GCE was carried out as shown in Fig. 50.

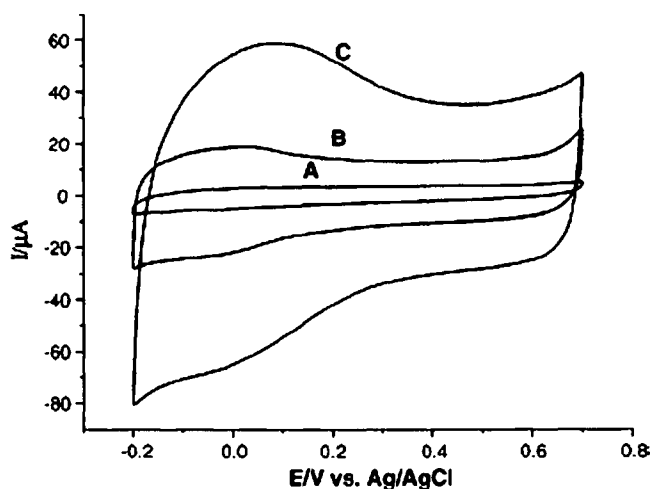


Figure 49. Cyclic voltammograms of Pt<sub>nano</sub>/GCE (A), MWNTs/GCE (B), and Pt<sub>nano</sub>/MWNTs/GCE (C) recorded in 0.3 mol L<sup>-1</sup> PBS blank solution (pH 7.2), scan rate: 0.1 V s<sup>-1</sup>. Scan range: -0.2 – 0.8 V (vs. Ag/AgCl). (Reprinted with permission from Zhu et al. [102]. Copyright 2005 Elsevier.)

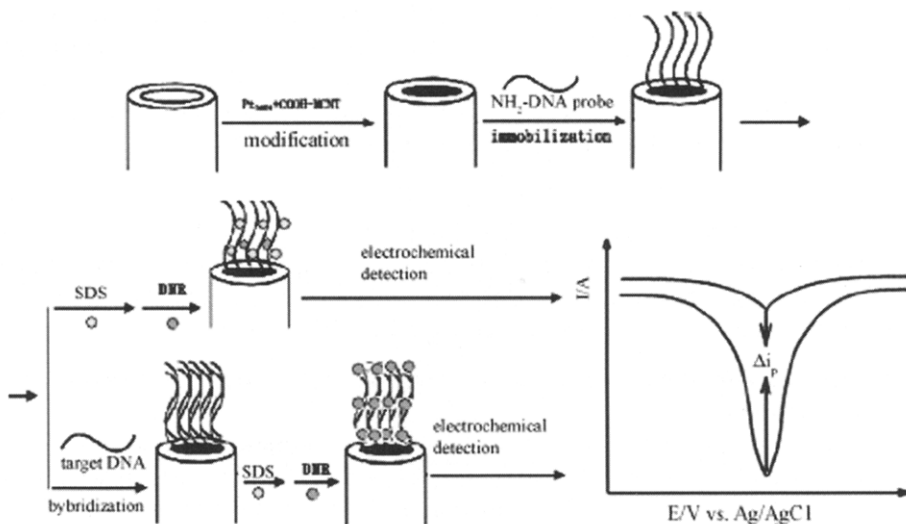


Figure 50. Schematic representation of the electrochemical detection of DNA hybridization based on platinum nanoparticles combined MWNTs. The reduction signal (+0.44 V) of Daunomycin (DNR) shown was used as indicator for electrochemical detection (Reprinted with permission from Zhu et al. [102]. Copyright 2005 Elsevier.)

The analytical performance of the DNA sensor based on MWNTs/Pt<sub>nano</sub> was also explored by using the immobilized probe to hybridize with the different concentrations of the complementary sequence, as shown in Fig. 51. The peak current in DPV response of intercalated daunomycin increases with the increase of the complementary target DNA concentrations. The average currents of daunomycin are linear with the logarithmic value of the complementary sequence concentration from  $2.25 \times 10^5$  to  $2.25 \times 10$  pM. The limit of detection derived from this result for probe/MWNTs/Pt<sub>nano</sub>/GCE to its complementary sequence is  $1.0 \times 10^{-11}$  mol L<sup>-1</sup>. The sensitivity of the electrochemical DNA biosensor is superior to that based on carbon nanotubes alone with the detection limit of  $1.0 \times 10^{-11}$  mol L<sup>-1</sup> for the same target sequence (24-base) detection [95,96].

Meyyappan and co-workers [103–105] have developed a more advanced micropatterned ultrasensitive DNA biosensor based on aligned carbon nanotubes. As shown in Fig. 52a, aligned MWNTs were directly grown on individual metal microcontacts, followed by encapsulating the MWNT arrays and the substrate surface with a spin-on glass (SOG) layer to only expose the nanotube ends at the surface. Each of the SOG-encapsulated individual MWNTs is like a nanoelectrode, and there are about 100 MWNT nanoelectrodes or more on each microcontact. Abundant carboxylic acid groups were produced at the end of MWNTs by electrochemical etching, and then functionalized with a specific oligonucleotide probe through the amide formation. Figs. 52b and c show schematically the mechanism of the MWNT nanoelectrode array for the DNA detection. A specific probe [Cy3]5'-CTTATTTCICAIITCCT-3'-[AmC7-Q]

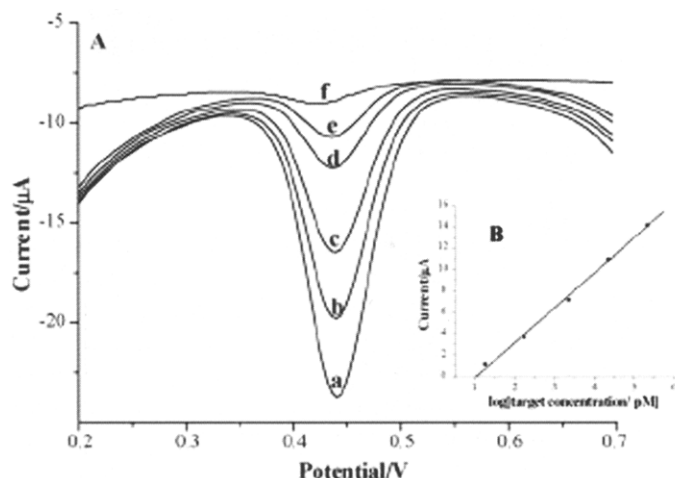


Figure 51. (A) DPV for different target concentrations: (a)  $2.25 \times 10^5$  pM; (b)  $2.25 \times 10^4$  pM; (c)  $2.25 \times 10^3$  pM; (d)  $2.25 \times 10^2$  pM; (e)  $2.25 \times 10^1$  pM; (f) 0.0 pM. (B) The resulting logarithmic standard plot. (Reprinted with permission from Zhu et al. [102]. Copyright 2005 Elsevier.)

was used in that study, which contains the sequence of the normal allele of the BRCA1 gene associated with the occurrence of several cancers. Electroactive guanine groups in the probe are replaced with nonelectroactive inosines. Genomic DNA from a healthy donor was used in PCR to amplify.

Fig. 52d shows the electrophoresis results of a DNA molecular weight standard ( $\phi$ X174RFDNA-*Hae*III digest) and the two PCR amplicons, respectively. The non-specific binding is removed through stringent washing in three steps using  $2 \times \text{SSC}/0.1\% \text{ SDS}$ ,  $1 \times \text{SSC}$ , and  $0.1\% \text{ SSC}$  respectively, by shaking the sample in each of the solutions at  $40^\circ\text{C}$  for 15 min.  $\text{Ru}(\text{bpy})_3^{2+}$  mediators were used to efficiently transport electrons from the guanine bases to the MWNT nanoelectrode and to provide an amplified guanine oxidation signal as long as target DNA molecules are within the three-dimensional diffusion layer.

#### 4. CONCLUSIONS

The concern of research for sensors using C<sub>60</sub> or carbon nanotube is increasing year by year. Especially, carbon nanotubes possess superior electronic, chemical, thermal,

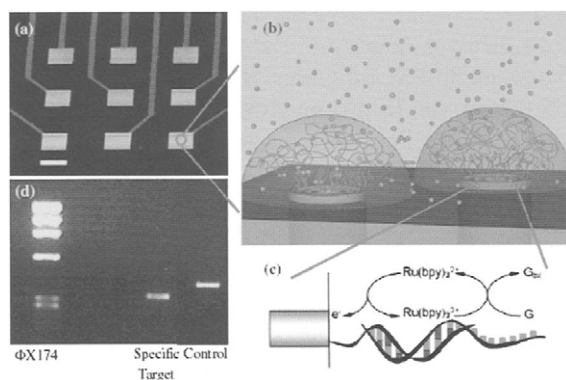


Figure 52. (a) An SEM image of an individually addressable  $3 \times 3$  microcontact array with an MWNT nanoelectrode array on each site. The scale bar is  $200 \mu\text{m}$ . (b) Schematic of the mechanism to detect DNA hybridization using an MWNT nanoelectrode array. The long single-stranded DNA PCR amplicons are hybridized to the short oligonucleotide probes which are functionalized at the very end of the MWNTs.  $\text{Ru}(\text{bpy})_3^{2+}$  mediators are used to transfer electrons from the guanine groups to the MWNT nanoelectrode for all target molecules within the hemispherical diffusion layer of the nanoelectrodes. (c) The schematic mechanism for the guanine oxidation amplified with  $\text{Ru}(\text{bpy})_3^{2+}$  mediators. (d) The gel electrophoresis. The lanes from left to right are DNA molecular weight standard ( $\phi$ X174RFDNA-*Hae*III digest), a specific PCR amplicon target with  $\sim 300$  bases, and a control sample with an unrelated PCR amplicon with  $\sim 400$  bases, respectively. (Reprinted with permission from Koehne et al. [103]. Copyright 2003 Institute of Physics and Iop Publishing Ltd.)

optical, and mechanical properties with a large surface area to be attractive for a wide range of potential applications. The infinite function (e.g. molecule selectivity) added by surface modification to nanotubes is only one of many advantages of sensors using nanotubes. Comparing carbon nanotube sensors with human five senses, we have already acquired or exceeded some human senses about a factor in sensitivity. The next key step to reach human senses will be the combination of the nanosensors with mother networks for signal detection or transmission, etc. For this purposes we may need bio-mimetic approach, because natural creatures remain a magnificent frontier for future sensing studies.

We have given a brief summary of the most recent research development in the field. Even this brief account has revealed the versatility of carbon nanotubes for making chemical and biosensors with a high sensitivity and selectivity. Of course, the potential also has shown extremely high as physical sensors. With continued research and development in this field, the possibility of producing carbon nanotube sensors for practical applications will soon be in sight.

## REFERENCES

1. J.W. Gardner and P.N. Bartlett (Eds.), *Sensors and Sensory Systems for an Electronic Nose*, Kluwer Academic Publishers, Dordrecht, 1992.
2. M. Butler, P. Vanysek and N. Yamazoe (Eds.), *Chemical and Biological Sensors and Analytical Methods II: Proceedings of the International Symposium*, Electrochemical Society, Pennington, 2001.
3. S. Büttgenbach (Ed.), *Chemical Microsensors and Applications*, SPIE – The International Society for Optical Engineering, Bellingham, 1998.
4. B.R. Eggins, *Biosensors: An Introduction*, Wiley, New York, 1996.
5. L. Dai, *Intelligent Macromolecules for Smart Devices: From Materials Synthesis to Device Applications*, Springer, London, 2004.
6. H.W. Kroto, J.R. Heath, S.C. Ó'Brien, R.F. Curl and R.E. Smalley, *Nature* **318** (1985) 162.
7. See, for example: R. Baum, *Chem. Eng. News* **74** (1996) 7.
8. T. Lin, V. Bajpai, T. Ji and L. Dai, *J. Aust. Chem.* **56** (2003) 63.
9. S. Iijima, *Nature* **354** (1991) 56.
10. P.J.F. Harris, *Carbon Nanotubes and Related Structures: New Materials for the Twenty-First Century*, Cambridge University Press, Cambridge, 1999.
11. E. Radeva, V. Georgiev, L. Spassov, N. Koprinarov, and St. Kanev, *Sensors. Actuators B.* **42** (1997) 11.
12. H. Koda, H. Nakajima, Y. Sakurai, and A. Okamoto, *Chem. Sens. (Japanese)* **16** (Suppl. B) (2000) 106.
13. T. Nosaka, Y. Sakurai, K. Natsukawa, T. Yotsuya, K. Nishida, and N. Akae, *Adv. Sci. Technol. (Faenza, Italy)*, **26** (Solid State Chemical and Biochemical Sensors) (1999) 255.
14. Y. Amao, K. Asai, and I. Okura, *Bull. Chem. Soc. Jpn.* **72** (1999) 2223; and references cited therein.
15. H. Lin, and J. Shih, *Sensors. Actuators B* **92** (2003) 243.

16. D.J. Cram, K. Blasius, K.P. Janzen, H. Luxenburger, V.B. Nguyen, H. Klotz and J. Stockemer, *J. Chromatogr.* **167** (1978) 307.
17. S.S. Tsai and J.S. Shih, *Sep. Sci. Tech.* **33** (1998) 1407.
18. C.S. Chiou and J.S. Shih, *Anal. Chim. Acta* **392** (1999) 125.
19. L. Dai, A. Patil, X. Gong, Z. Guo, L. Liu, Y. Liu and D. Zhu, *Chem. Phys. Chem.* **4** (2003) 1150.
20. L. Dai and A.W.H. Mau, *Adv. Mater.* **13** (2001) 899.
21. P.G. Collins, K. Bradley, M. Ishigami and A. Zettl, *Science* **287** (2000) 1801.
22. J. Kong, N.R. Franklin, C. Zhou, M.G. Chapline, S. Peng, K. Cho and H. Dai, *Science* **287** (2000) 622.
23. J. Kong, M.G. Chapline, and H. Dai, *Adv. Mater.* **13** (2001) 1384.
24. P. Qi, O. Vermesh, M. Grecu, A. Javey, Q. Wang, H. Dai, S. Peng and K.J. Cho, *Nano Lett.* **3** (2003) 347.
25. A. Mandelis and C. Christofides, *Physics, Chemistry and Technology of Solid State Gas Sensor Devices*, Wiley, New York, 1993.
26. R.D. Barnard, *Thermoelectricity in Metal and Alloys*, Wiley, New York, 1972.
27. C.K.W. Adu, G.U. Sumanasekera, B.K. Pradhan, H.E. Romero and P.C. Eklund, *Chem. Phys. Lett.* **337** (2001) 31.
28. H.E. Romero, K. Bolton, A. Rosén and P.C. Eklund, *Science* **307** (2005) 89.
29. H. E. Romero, G.U. Sumanasekera, G.D. Mahan and P.C. Eklund, *Phys. Rev. B* **65** (2002) 205410.
30. J. Vavro, M.C. Llaguno, J.E. Fischer, S. Ramesh, R.K. Saini, L.M. Ericson, V.A. Davis, R.H. Hauge, M. Pasquali and R.E. Smalley, *Phys. Rev. Lett.* **90** (2003) 065503-1.
31. S. Chopra, A. Pham, J. Gaillard, A. Parker and A.M. Rao, *Appl. Phys. Lett.* **80** (2002) 4632.
32. K.G. Ong and C.A. Grimes, *Smart Mater. Struct.* **9** (2000) 421.
33. A. Modi, N. Koratkar, E. Lass, B. Wei P.M. Ajayan, *Nature* **424** (2003) 171.
34. H. Dai, J.H. Hafner, A.G. Rinzler, D.T. Colbert and R.E. Smalley, *Nature* **384** (1996) 147.
35. S.S. Wong, J.D. Harper, P.T. Lansbury, Jr. and C.M. Lieber, *J. Am. Chem. Soc.* **120** (1998) 603.
36. S.S. Wong, E. Joselevich, A.T. Woolley, C. Cheung and C.M. Lieber, *Nature* **394** (1998) 52.
37. S.S. Wong, A.T. Woolley, E. Joselevich, C. Cheung and C.M. Lieber, *J. Am. Chem. Soc.* **120** (1998) 8557.
38. S.C. Tsang, Y.K. Chen, P.J.F. Harris and M.L.H. Green, *Nature* **372** (1994) 159.
39. J.R. Wood and H.D. Wagner, *Appl. Phys. Lett.* **76** (2000) 2883.
40. J.R. Wood, Q. Zhao, M.D. Frogley, E.R. Meurs, A.D. Prins, T. Peijs, D.J. Dunstan and H.D. Wagner, *Phys. Rev. B* **62** (2000) 7571.
41. O. Lourie and H.D. Wagner, *J. Mater. Res.* **13** (1998) 2418.
42. Q. Zhao, J.R. Wood and H.D. Wagner, *Appl. Phys. Lett.* **78** (2001) 1748.
43. M.D. Frogley, Q. Zhao and H.D. Wagner, *Phys. Rev. B* **65** (2002) 1134131.
44. Q. Zhao, J.R. Wood and H.D. Wagner, *J. Polym. Sci. B* **39** (2001) 1492.



45. A.H. Barber, Q. Zhao, H.D. Wagner and C.A. Baillie, *Comput. Sci. Technol.* **64** (2004) 1915.
46. P. Král and M. Shapiro, *Phys. Rev. Lett.* **86** (2001) 131.
47. S. Ghosh, A.K. Sood and N. Kumar, *Science* **299** (2003) 1042.
48. Y. Wang, K. Kempa, B. Kimball, J.B. Carlson, G. Benham, W.Z. Li, T. Kempa, J. Rybczynski, A. Herczynski and Z.F. Ren, *Appl. Phys. Lett.* **85** (2004) 2607.
49. M. Bockrath, D.H. Cobden, P.L. McEuen, N.G. Chopra, A. Zettl, A. Thess and R.E. Smalley, *Science* **275** (1997) 1922.
50. S.J. Tans, M.H. Devoret, H. Dai, A. Thess, R.E. Smalley, L.J. Geerligs and C. Dekker, *Nature* **386** (1997) 474.
51. T.W. Odom, J.L. Huang, C.L. Cheung and C.M. Lieber, *Science* **290** (2000) 1549.
52. J. Nygard, D.H. Cobden and P.E. Lindelof, *Nature* **408** (1999) 342.
53. M. Bockrath, D.H. Cobden, J. Lu, A.G. Rinzler, R.E. Smalley, L. Balents and P.L. McEuen, *Nature* **397** (1999) 598.
54. H. Ishii, H. Kataura, H. Shiozawa, H. Yoshioka, H. Otsubo, Y. Takayama, T. Miyahara, S. Suzuki, Y. Achiba, M. Nakatake, T. Narimura, M. Higashiguchi, K. Shimada, H. Namatame and M. Taniguchi, *Nature* **426** (2003) 540.
55. T. Ando, *J. Phys. Soc. Jpn.* **66** (1997) 1066.
56. T.G. Pedersen, *Phys. Rev. B* **67** (2003) 073401.
57. V. Perebeinos, J. Tersoff and Ph. Avouris, *Phys. Rev. Lett.* **92** (2004) 257402.
58. C.D. Spataru, S. Ismail-Beigi, L.X. Benedict and S.G. Louie, *Phys. Rev. Lett.* **92** (2004) 077402.
59. E. Chang, G. Bussi, A. Ruini and E. Molinari, *Phys. Rev. Lett.* **92** (2004) 196401.
60. C.L. Kane and E.J. Mele, *Phys. Rev. Lett.* **90** (2003) 207401.
61. H.B. Zhao and S. Mazumdar, *Phys. Rev. Lett.* **93** (2004) 157402.
62. S.M. Bachilo, M.S. Strano, C. Kittrell, R.H. Hauge, R.E. Smalley and R.B. Weisman, *Science* **298** (2002) 2361.
63. H. Htoon, M.J. O'Connell, P.J. Cox, S.K. Doorn and V.I. Klimov, *Phys. Rev. Lett.* **93** (2004) 027401.
64. Y.Z. Ma, J. Stenger, J. Zimmermann, S.M. Bachilo, R.E. Smalley, R.B. Weisman and G.R. Fleming, *J. Chem. Phys.* **120** (2004) 3368.
65. R. Saito, G. Dresselhaus and M.S. Dresselhaus, *Physical Properties of Carbon Nanotubes*, Imperial College Press, London, 1998.
66. A. Hagen and T. Hertel, *Nano Lett.* **3** (2003) 383.
67. M.S. Dresselhaus, G. Dresselhaus and A. Jorio, *Annu. Rev. Mater. Res.* **34** (2004) 247.
68. F. Wang, G. Dukovic, L.E. Brus and T.F. Heinz, *Science* **308** (2005) 838.
69. Z. Wu, Z. Chen, X. Du, J.M. Logan, J. Sippel, M. Nikolou, K. Kamaras, J.R. Reynolds, D.B. Tanner, A.F. Hebard and A.G. Rinzler, *Science* **305** (2004) 1273.
70. K. Lee, Z. Wu, Z. Chen, F. Ren, S.J. Pearton and A.G. Rinzler, *Nano Lett.* **4** (2004) 911.
71. S.J. Tans, R.M. Verschueren and C. Dekker, *Nature* **393** (1998) 49.
72. S. Heinze, J. Tersoff, R. Martel, V. Derycke, J. Appenzeller and Ph. Avouris, *Phys. Rev. Lett.* **89** (2002) 106801.
73. A. Javey, J. Guo, Q. Wang, M. Lundstrom and H. Dai, *Nature* **424** (2003) 654.

74. S. Rosenblatt, Y. Yaish, J. Park, J. Gore, V. Sazonova and P.L. McEuen, *Nano Lett.* **2**, (2002) 869.
75. S. Kazaoui, N. Minami, N. Matsuda, H. Kataura and Y. Achiba, *Appl. Phys. Lett.* **78** (2001) 3433.
76. L. Kavan, P. Raptá, L. Dunsch, M.J. Bronikowski, P. Willis and R.E. Smalley, *J. Phys. Chem. B* **105** (2001) 10764.
77. P. Chandrasekhar, B.J. Zay, T. McQueeney, A. Scara, D. Ross, G.C. Birur, B.S. Haapanen, L. Kauder, T. Swanson and D. Douglas, *Synth. Metals* **135** (2003) 23.
78. J.X. Wang, M.X. Li, Z.J. Shi, N.Q. Li, and Z.N. Gu, *Anal. Chem.* **74** (2002) 1993.
79. Y.D. Zhao, W.D. Zhang, H. Chen, Q.M. Luo and S.F.Y. Li, *Sensors. Actuators B* **87** (2002) 168.
80. A. Guiseppi-Elie, C. Lei and R.H. Baughman, *Nanotechnology* **13** (2002) 559.
81. J. Wang, M. Musameh and Y. Lin, *J. Am. Chem. Soc.* **125** (2003) 2408.
82. J.H.T. Luong, S. Hrapovic, D. Wang, F. Bensebaa and B. Simard, *Electroanalysis* **16** (2004) 132.
83. Y. Lin, F. Lu, Y. Tu and Z.F. Ren, *Nano Lett.* **4** (2004) 191.
84. Y. Tu, Y. Lin and Z.F. Ren, *Nano Lett.* **3** (2003) 107.
85. Y. Tu, Z.P. Huang, D.Z. Wang, J.G. Wen, and Z.F. Ren, *Appl. Phys. Lett.* **80** (2002) 4018.
86. X. Yu, D. Chattopadhyay, I. Galeska, F. Papadimitrakopoulos and J.F. Rusling, *Electrochem. Commun.* **5** (2003) 408.
87. F. Patolsky, Y. Weizmann and I. Willner, *Angew. Chem. Int. Ed.* **43** (2004) 2113.
88. J.J. Gooding, R. Wibowo, J. Liu, W. Yang, D. Losic, S. Orbons, F.J. Mearns, J.G. Shapter and D.B. Hibbert, *J. Am. Chem. Soc.* **125** (2003) 9006.
89. M. Gao, L. Dai and G.G. Wallace, *Electroanalysis* **15** (2003) 1089.
90. M. Gao, L. Dai and G.G. Wallace, *Synth. Met.* **137** (2003) 1393.
91. S.G. Wang, Q. Zhang, R. Wang and S.F. Yoon, *Biochem. Biophys. Res. Commun.* **311** (2003) 572.
92. S. Sotiropoulou and N.A. Chaniotakis, *Anal. Bioanal. Chem.* **375** (2003) 103.
93. W. C. I. Homs, *Anal. Lett.* **35** (2002) 1875.
94. J.J. Gooding, *Electroanalysis* **14** (2002) 1149.
95. H. Cai, X. Cao, Y. Jiang, P. He and Y. Fang, *Anal. Bioanal. Chem.* **375** (2003) 287.
96. H. Cai, Y. Xu, P. He and Y. Fang, *Electroanalysis* **15** (2003) 1864.
97. Y. Xu, Y. Jiang, H. Cai, P. He and Y. Fang, *Anal. Chim. Acta* **516** (2004) 19.
98. J. Wang, G. Liu and M.R. Jan, *J. Am. Chem. Soc.* **126** (2004) 3010.
99. J. Wang, G. Liu, M.R. Jan and Q. Zhu, *Electrochem. Commun.* **5** (2003) 1000.
100. J. Wang, A.N. Kawde and M. Musameh, *Analyst* **128** (2003) 912.
101. P. He, and L. Dai, *Chem. Commun.* **3** (2004) 348.
102. N. Zhu, Z. Chang, P. He, and Y. Fang, *Anal. Chim. Acta* **545** (2005) 21.
103. J. Koehne, H. Chen, J. Li, A. McCassell, Q. Ye, H.T. Ng, J. Han, and M. Meyyappan, *Nanotechnology* **14** (2003) 1239.
104. C.V. Nguyen, L. Delzeit, A.M. Cassell, J. Li, J. Han and M. Meyyappan, *Nano Lett.* **2** (2002) 1079.
105. J. Li, H.T. Ng, A. Cassell, W. Fan, H. Chen, Q. Ye, J. Koehne, J. Han and M. Meyyappan, *Nano Lett.* **3** (2003) 597.

## Chapter 16

### Carbon nanotubes for electron emitting devices

Kazuo Kajiwar<sup>a</sup> and Yahachi Saito<sup>b</sup>

<sup>a</sup>CNT-FED Research Consultant, Machida, Tokyo 195-0055, Japan

<sup>b</sup>Department of Quantum Engineering, Nagoya University, Furo-cho, Chikusa-ku, Nagoya-shi 464-8603, Japan

About a decade after the discovery of carbon nanotubes (CNTs), field emission displays (FEDs) using CNTs as electron sources have been actively studied and developed, since the use of CNTs as field emitters are based on the remarkable properties, e.g., high aspect ratio, high mechanical strength, high chemical stability, and high electrical and thermal conductivity, which are advantageous for electron emitting devices in vacuum nanoelectronics. In the last several years, CNT film emitters in FEDs have been developed in order to provide high current density, large-area emission uniformity, and long-term emission stability. In this review article, we describe, first, field emission phenomena from CNTs through field emission microscopy of CNTs with various morphologies. Secondly, we describe emission characteristics and degradation phenomena of CNT emitters through dynamic observation of field emission from CNTs by *in situ* transmission electron microscopy, revealing the robustness as well as the limitations of CNT emitters. Finally, applications of CNT-based field emitters to electron emitting devices, such as lamp devices and FEDs, are the major topics that are described in the following section.

#### 1. INTRODUCTION

About a decade after the discovery of carbon nanotubes (CNTs) in 1991, intense study of CNTs has been carried out for a wide range of applications owing to their unique properties. Among the applications proposed so far, field emission electron sources would be the most promising industrially and are nearly within the reach of practical use.

When a high electric field on the order of  $10^7$  V/cm is applied to a solid surface with a negative electrical potential, electrons inside the solid are emitted into vacuum by the quantum mechanical tunneling effect. This phenomenon is called field emission of electrons. Since the electric field concentrates at a sharp point, such an extremely high field can be obtained on a sharp tip of a very thin needle. CNTs with high aspect ratios (ca. 1000) have physical and chemical properties suitable for such field emitters. In 1995, field emission from a single multi-wall nanotube (MWNT) was first reported by Rinzler et al. [1], and an experiment using an MWNT film emitter was reported by de Heer et al. [2]. Saito et al. reported a field emission microscopy (FEM) study of CNTs in 1997 [3,4] and experimentally manufactured

cathode-ray tube (CRT)-type lighting elements with CNT field emitters [5]. In 1998, Uemura et al. reported the first CNT-based field emission display (FED) [6]. In 1999, Samsung SDI reported the fabrication of a prototype 4.5-inch color FED panel using single-wall carbon nanotube (SWNT) field emitters [7].

There are a wide variety of electron emitting devices, which utilize electron sources, ranging from industrial and analytical instruments to consumer products. In addition to FEDs, CNT field emitters are of great interest for other devices such as X-ray sources, gas discharge tube (GDT) protectors, microwave amplifiers, and so on. The advantages of field emission electron sources (cold cathodes) over thermionic electron sources (hot cathodes) are: (1) no need for heating sources, (2) potential of miniaturization of devices, (3) high current density, (4) narrow energy distribution, and (5) no need for preheating to emit quickly.

In the next section of this review, we describe the fundamentals of field emission phenomena of CNTs, revealed mainly by FEM. In the third section, we describe the fabrication, the emission characteristics and degradation phenomena of CNT film emitters, revealed mainly by dynamic observation of field emission from CNTs using *in situ* transmission electron microscopy (TEM). In Sec. 4, we describe their applications as field emitters to electron emitting devices that have been developed so far.

## 2. FIELD EMISSION FROM SINGLE CNTs

Electron field emission phenomena of CNTs studied mainly by FEM are described in this section.

### 2.1. Potential of CNTs as field emitters

The material of CNTs has the following properties advantageous for field emitters: (1) needle-like shape with a sharp tip, (2) high chemical stability, (3) high mechanical strength, (4) low carbon atom mobility, and (5) high electrical and thermal conductivity.

First, when an electric field is applied to a conductor with a sharp tip, it concentrates at the sharp point. The field strength at the tip surface is inversely proportional to the radius of curvature  $r$  of the tip [8]. Therefore, the sharper the tip of the emitter, the higher the electric field at the same applied voltage. This gives the first advantage to CNTs as field emitters, which have an extremely small radius of curvature  $r$  at their tip. Second, because of high chemical stability of CNTs, surfaces of CNTs are inert and stable against residual gas molecules in a vacuum vessel. Therefore, CNT emitters operate stably even in a vacuum of  $10^{-6}$  torr, in contrast to metal emitters such as tungsten and molybdenum needles, which require an ultrahigh vacuum (UHV) to operate stably. Third, high mechanical strength of CNT emitters enables them to endure the high stress caused by electrostatic forces (Maxwell tension). Fourth, together with this robustness, low carbon atom mobility of CNTs makes them keep their original shape (slender and sharp tip), even at a high electric field during prolonged operation. Finally, since CNTs, especially MWNTs formed by arc discharge, have high electrical and thermal conductivity, CNTs can transport and emit electrons of high current density (ca.  $10^9$  A/cm<sup>2</sup>) through their tubular walls into vacuum [9].

At present, however, the arc-discharge and laser ablation methods are utilized to produce ideal CNTs. The raw material prepared by these methods has to be purified using chemical and separation processes. None of these processes are scalable to make the industrial quantities needed for many applications (e.g., composites), and this has been a bottleneck in nanotube research and development. In recent years, work has focused on developing chemical vapor deposition (CVD) methods using catalyst particles and hydrocarbon precursors to grow CNTs; such methods have been used earlier to produce hollow carbon nanofibers in large quantities. The drawback of the catalytic CVD-based CNTs is the inferior quality of the structures that contain a number of defects, particularly because the structures are formed at much lower temperatures (600–1000 °C) in comparison to both the arc-discharge and laser ablation processes (ca. 2000 °C) [10].

## 2.2. Field emission microscopy

### 2.2.1. Emitter preparation and FEM apparatus

Saito et al. investigated six kinds of CNTs and nanofibers as field emitters: (1) as-grown MWNTs prepared in a helium arc (hereafter called “pristine MWNTs”), (2) as-grown MWNTs in a hydrogen arc (named “nanografibers” [11]), (3) purified MWNTs with open ends, (4) purified SWNTs (arc-produced), (5) vapor-grown carbon fibers (VGCFs, Showa Denko Co.), and (6) oxidized VGCFs [12]. TEM images of tips of the respective CNTs and nanofibers are shown in Figs. 1 and 2. Tips of pristine MWNTs are capped by graphitic layers (close ended, Fig. 1a), whereas purified MWNTs have open ends, which were obtained by an oxidation process (Fig. 1c). In contrast to MWNTs, purified SWNTs form bundles, and each bundle consists of about 100

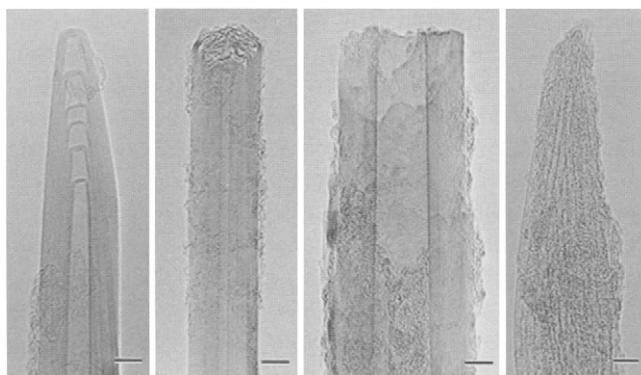


Figure 1. TEM images of tips of the four kinds of CNTs used for FEM study; (a) pristine MWNT with a capped end, (b) pristine nanografiber formed in a hydrogen arc, (c) MWNT with an open end, and (d) bundle of purified SWNTs. Scale bars, 5 nm. Reprinted with permission from Saito et al. [19], Elsevier Science.

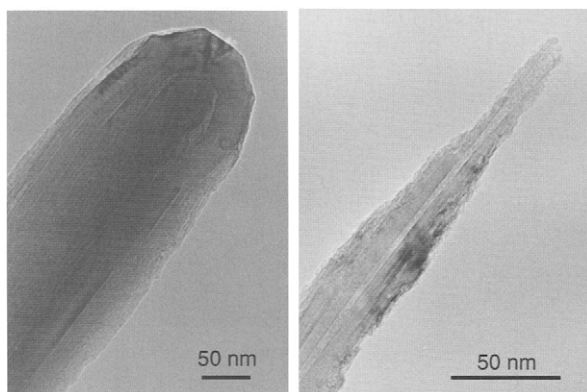


Figure 2. TEM images of tips of VGCFs; (a) as-obtained VGCF, and (b) oxidized VGCF after a heat treatment at 750 °C in air (mass reduction, 70 to 87%) [12].

nanotubes (Fig. 1d). On the other hand, nanografibers have an extremely narrow central channel, and the smallest diameter of the innermost layer is about 1 nm or less. Another structural feature of nanografibers produced by a hydrogen arc is that the tip of a nanografiber is partially broken or etched (Fig. 1b).

VGCFs are graphitic fibers with diameters of 100–500 nm (Fig. 2a), and their length exceeds 10  $\mu\text{m}$ . Their structure and morphologies are similar to those of MWNTs grown by arc discharge, though the diameter of VGCFs is about five times larger than that of the MWNTs. The VGCFs with thick diameter and dull tips are not suitable for a field emitter. However, the morphology of VGCFs can be modified to a sharp tip with a slender body by oxidizing them partially (Fig. 2b).

For FEM study, a bulk bundle of respective nanotubes was attached to the apex of a hairpin-shaped tungsten wire (0.15 mm in diameter) with a conductive paste. Two types of FEM apparatus were used in this study. Fig. 3 shows schematically the first apparatus, in which a probe hole (1 mm in diameter) was placed on a phosphor screen in order to accept electrons emitted from a selected region of a tip at the base pressure of  $10^{-8}$  to  $10^{-9}$  torr. The emitter tip of CNTs was placed at 60 mm distance in front of the screen. Field emission patterns could be observed on the phosphor screen. Electric current passed through the probe hole could be measured by a Faraday cup that was placed behind the probe hole. The acceptance half-angle of the probe hole was 17 mrad. In the second apparatus, an emission experiment could be carried out under a UHV of  $10^{-10}$  torr, though no probe hole was used. Details of the tip preparation and FEM apparatus were described in the previous publications [3,11,13,14].

### 2.2.2. Emission characteristics of CNTs

In the first FEM, regions where electrons are emitted from CNTs are imaged with large magnification (on the order of 1 million) as bright spots on the anode screen.

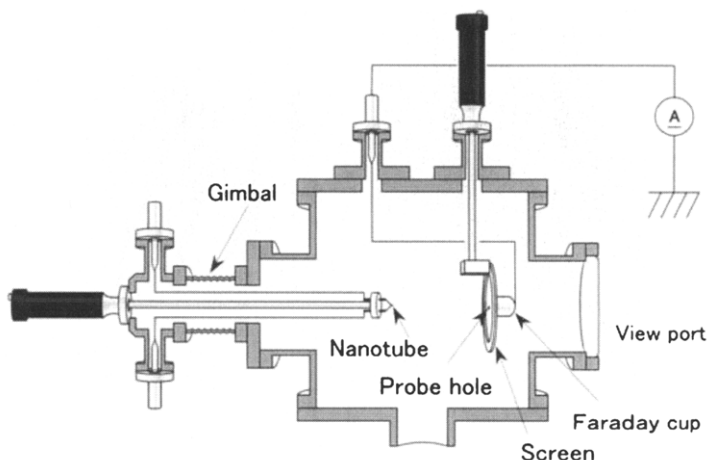


Figure 3. Schematic of an FEM apparatus with a probe hole. Reprinted with permission from Saito et al. [11], The Japan Society of Applied Physics.

Therefore, emission current from a single CNT can be measured by placing the probe hole of the screen within one of the bright spots. Emission current accepted by the probe hole,  $I_p$ , was measured as a function of voltage  $V$  applied to the tip. The  $I_p$ - $V$  characteristics for the six kinds of CNTs and nanofibers are shown in Fig. 4.

The threshold voltage and maximum current density are summarized in Table 1. The open-ended MWNTs began to emit electrons at the lowest tip voltage and sustained the highest current density. Nanografibers grown in hydrogen gave higher current than pristine MWNTs grown in helium. This was caused mainly by the cleanliness of nanografibers, i.e., a very tiny quantity of carbon debris, and partially by the structural defects of nanografiber tips, which might have a lower work function. VGCFs showed poor emission properties, though some improvement was obtained by sharpening their tips (oxidizing VGCFs).

These emission data were obtained with the first apparatus, which was not in an UHV and could not keep the emitter surfaces clean. Therefore, the emission did not probably come from clean surfaces but from adsorbates on the CNT surfaces, as explained below.

### 2.2.3. FEM patterns of MWNTs

FEM study using the first apparatus in a vacuum of  $10^{-8}$  torr or higher usually gave field emission patterns consisting of a number of bright spots with no inner structure [3,13], except for purified MWNTs whose tips were etched off. On the other hand, emission patterns from open-ended MWNTs showed bright “doughnut-like” annular rings [4,14].

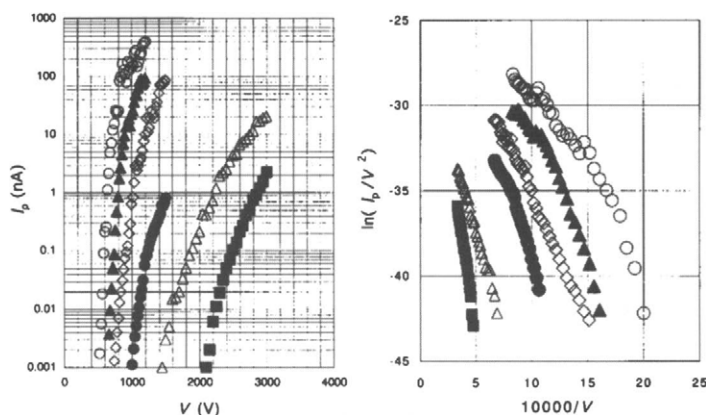


Figure 4. (a) Current vs. voltage characteristics and (b) F-N plots for various CNTs. Current was measured with a 1-mm probe hole. ●, A pristine MWNT; ◇, a nanografiber; ○, an open MWNT; ▲, a bundle of SWNTs; ■, as obtained VGCF; △, oxidized VGCF [12]. Reprinted with permission from Y. Saito, *Trans. MRS Jpn.* **25** (2000) 811, MRS, Japan.

Table 1

Field emission properties of six kinds of carbon nanotubes and nanofibers. Since emission current was measured by a 1-mm probe hole, the properties come from a single tube for MWNT and nanografiber, and from one bundle for SWNTs.

Carbon nanotubes	Threshold voltage <sup>1</sup> (V)	Maximum current density ( $\times 10^6$ A/cm <sup>2</sup> )
Capped MWNT	900–1000	0.1–1
Nanografiber	700–800	~1
Open MWNT	500–600	10–100
SWNTs	600–700	~10
As-obtained VGCF	~2000	~0.01
Oxidized VGCF	~1500	~0.1

<sup>1</sup>Threshold voltages represent tip voltages at which currents measured by the probe hole exceed 0.1 pA.

Recently, FEM experiments were performed in an UHV of about  $10^{-10}$  torr by using the second FEM apparatus [15]. MWNTs used in this study were produced by arc discharge. The MWNT emitters were heated to about 1300 K before the FEM study in order to clean their surfaces. A phosphor screen was placed at 30–40 mm distance from the emitter. The negative voltage of 0.9–1.6 kV was applied to the emitter relative to the screen. FEM patterns obtained from a capped MWNT with



clean surfaces are shown in Fig. 5. Six pentagonal rings arranged in fivefold- (Fig. 5a) and sixfold-symmetry (Fig. 5b) can be observed. Each pentagonal region contained a small dark spot at its center. It should also be noted that interference fringes were observed between the neighboring pentagons. Structural models of CNT tips that would give the FEM patterns in Figs. 5(a) and (b) are shown in Figs. 6(a) and (b), respectively [15].

These pentagonal rings can be explained as follows. When the voltage is applied to a nanotube, the electric field around the pentagons would be stronger than that on other flat regions because the pentagons are pointed like vertices of a polyhedron. In addition, it is theoretically estimated that the pentagon site has a higher density of states (DOS) near the Fermi level  $E_F$  than the normal hexagon site [16]. Therefore, the electron tunneling through the pentagons are expected to occur dominantly.

#### 2.2.4. Adsorption and desorption of molecules on MWNTs

In general, adsorption of residual gas molecules occurs on surfaces of CNTs, even in an UHV. The adsorbates may diffuse toward the tip of a CNT through field-enhanced surface migration; molecules are attracted to the direction of higher electric field by polarization forces. The adsorbates reside preferentially on the pentagonal sites, giving bright spots in the FEM patterns. These adsorbates could be removed easily by heating CNTs at about 1300 K for 3 min. Fig. 7 shows the change of FEM patterns during the desorption process by heating, together with the variation of emission current as a function of heating time [17]. Bright spots on the pentagons disappeared one by one with time, and concurrently the emission current decreased in a stepwise manner at about 90, 120, and 130 s. The stop of heating caused the final step at 160 s, i.e., the temperature of the tip decreased suddenly. Here it was recognized that the contrast (or visibility) of both the pentagonal rings and the interference fringes was low at 1300 K, whereas the contrast was high at

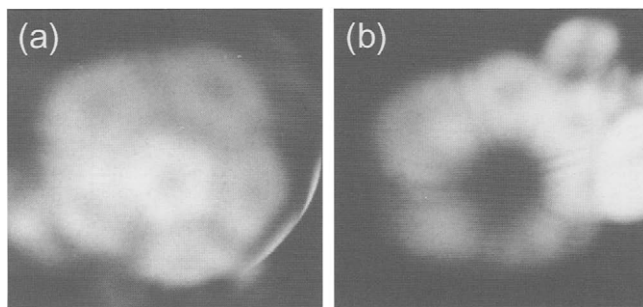


Figure 5. FEM patterns from capped MWNTs showing (a) fivefold- and (b) sixfold-symmetry. Reprinted with permission from Saito et al. [15], The Japan Society of Applied Physics.

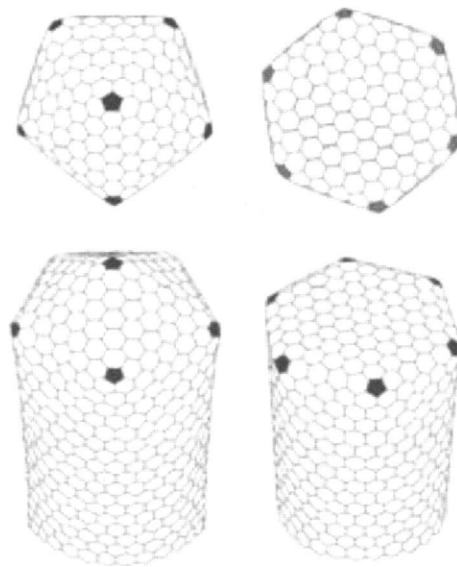


Figure 6. Geometries of nanotube caps exhibiting (a) fivefold- and (b) sixfold-symmetry. Reprinted with permission from Saito et al. [15], The Japan Society of Applied Physics.

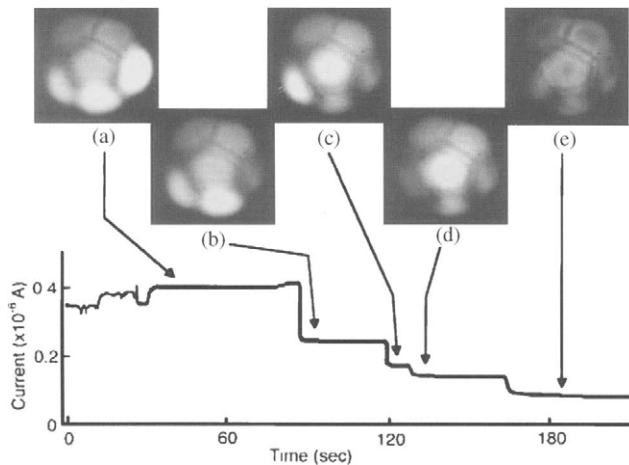


Figure 7. FEM patterns showing a desorption sequence of gas molecules and the corresponding changes in the emission current from an MWNT. Reprinted with permission from Hata et al. [17], Elsevier Science.

room temperature. This suggests that additional emission of incoherent thermionic electrons gives rise to the decrease in visibility at high temperature of 1300 K.

In the above experiment, adsorbate species could not be identified. To discriminate molecular species, a FEM study was carried out in a controlled atmosphere of various gases,  $H_2$ , CO,  $N_2$ , and  $O_2$  at  $1 \times 10^{-8}$  torr [18]. Field emission was enhanced by the adsorption of all of these molecular species, but the degree of enhancement was affected by the molecular species, e.g., the larger the molecular size was, the larger the enhancement. Behavior of CO molecules on the CNT cap was very similar to those described above, and CO was one of the dominant residual gas species in an UHV. This study suggests that CO molecules were probably the adsorbates observed in the above experiment.

In 1997, Saito et al. reported the stepwise fluctuation of emission current from CNTs [3,19]. Similar current fluctuations have been observed for the field emission from tips of glassy carbon since 1978 [20]. However, the origin of the stepwise fluctuation has not been clear so far. The study described here suggests that the adsorption and desorption of molecules on the surface of carbon emitters could cause the stepwise fluctuation of emission current from CNTs and also glassy carbons.

### 2.2.5. Effect of ambient gases on field emission from MWNTs

The influence of ambient gases on long-term variation of emission current (or lifetime as emitters) was examined in FEM. The CNT emitters used here were bulk bundles of MWNTs produced by arc discharge. The ambient gases studied were  $H_2$ , He,  $N_2$ ,  $O_2$ ,  $H_2O$ ,  $CH_4$ ,  $CO_2$ , and Ar at various pressures from  $10^{-7}$  to  $10^{-5}$  torr. The initial total current was set at 50  $\mu A$ , and the current variation was measured at a constant applied voltage. The emission current variations with time in various gas atmospheres at  $10^{-5}$  torr are shown in Fig. 8 [21]. The decrease of emission current with time occurred most sensitively in ambient gases of  $H_2O$ ,  $CO_2$ ,  $O_2$ , and  $CH_4$ . The ambient  $N_2$  and Ar also caused a small poisoning effect compared with those of reactive gases, whereas the poisoning effect of  $H_2$  and He was negligibly small. This suggests that the partial pressures of hazardous gases such as  $O_2$  and  $CH_4$  should be reduced as low as possible to prolong the lifetime of emitters, although CNT field emitters are very robust against residual gases.

### 2.2.6. Field emission from SWNTs

Enhanced field emission from adsorbates has been observed in the case of SWNTs as well. Dean et al. showed three distinct behavior states in field emission from SWNTs at temperatures ranging from 300 to 1800 K [22]. At room temperature, emission occurred through adsorbate states, which they considered to be correlated to the presence of water, since partial pressure of water is dominant in an unbaked vacuum chamber. These states were removed above 900 K. After adsorbate removal, the apparently clean CNT state showed a lower emission current and substantially reduced emission noise. Upon transition to the low current regime, the lobed patterns due to adsorbed states disappeared, and dimmer FEM patterns with finer structures were observed. The symmetry and the structure of these new images suggested that these were the FEM images of a clean SWNT cap. At extremely high currents and temperatures, the stable behavior of clean CNT states

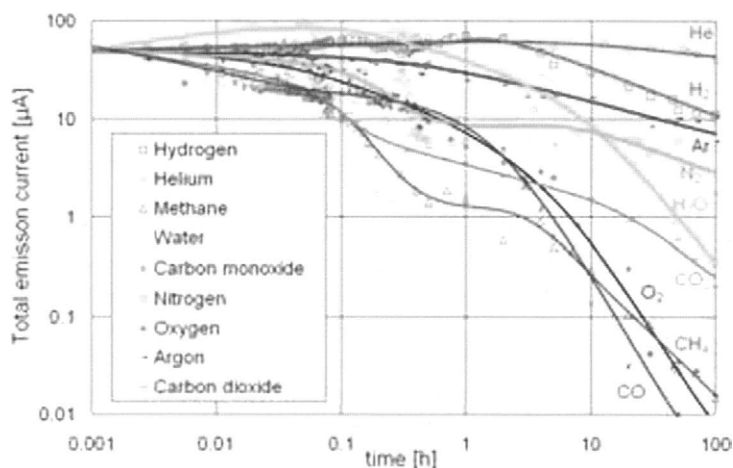


Figure 8. Emission current variation with time in various gas atmospheres ( $\text{H}_2$ , He,  $\text{N}_2$ ,  $\text{O}_2$ ,  $\text{H}_2\text{O}$ ,  $\text{CH}_4$ ,  $\text{CO}_2$ , and Ar) at  $10^{-5}$  torr.

broke down, and rings formed by rapid rotation of spots appeared instead. Similar ring patterns of SWNTs were observed by Zhu et al. [23].

Dean et al. also reported that an individual SWNT with adsorbates exhibited current saturation above 100 nA, and that the saturation resulted from the disappearance of adsorbates as the electric field and the current increased [24]. At these high fields and currents, the adsorbate states were completely removed from the CNT. On the other hand, a clean SWNT showed no evidence of current saturation for emission currents reaching 2  $\mu\text{A}$ .

### 2.3. Field emission energy distribution

One of the advantages of field emission electron sources (cold cathodes) is that the energy spread is much narrower than that for thermionic electron sources (hot cathodes). In macroscopic metal emitters, where the emitted electrons come from electrons in the conduction band, the width of the energy distribution is defined by the occupied electronic DOS around the Fermi level  $E_F$  and the tunneling barrier (i.e., tunneling probability). Above  $E_F$  the tunneling probability increases, but the population of electrons decreases very sharply. Below  $E_F$  the occupied DOS increases, but the tunneling probability decreases steeply. The resulting field emission energy distribution (FEED) of the electrons has the characteristic shape predicted by the Fowler–Nordheim (F–N) theory [25]. The FEED has a peak at  $E_F$  with exponential tails that depend on the temperature of the metal for the high-energy side and on the tunneling barrier width for the low-energy side. The F–N theory is valid for field emission from a flat surface of ideal metals. Therefore, deviations

from the F-N energy distribution are encountered in emitters with atomic-scale protrusions and/or nonmetallic emitters [26].

The full width at half-maximum (FWHM) of the FEED for a metal is typically about 0.2 eV. A measurement of the FEED of CNTs was first attempted by de Heer et al., who reported a narrow peak of 0.21 eV [27]. Fransen et al. observed two kinds of behavior on single MWNT emitters [28]; some spectra showed one peak of ca. 0.3 eV FWHM, and other spectra were composed of several peaks of about 0.15 eV FWHM. Loval et al. observed a fine structure in the low-energy tail of FEED spectra from a single SWNT at room temperature [29]. Small shoulders located at 0.64 and 1.05 eV below  $E_F$  were attributed to van Hove singularities in the DOS of the SWNT.

The early experimental spectra mentioned above are not guaranteed to have come from clean CNT surfaces. Takakura et al. carried out FEED measurements from clean MWNT caps and from an adsorbate on the cap [30]. FEM patterns from a clean MWNT cap exhibited pentagon rings, as described previously. Fig. 9 shows FEEDs from a central pentagon at the applied voltage of 780 V at room temperature. The FEEDs exhibited a few features different from those of typical metal emitters. First, a hump was observed at ca. 0.5 eV on the lower energy side of the main peak. Such fine structures below  $E_F$  have commonly been observed for metal emitters with an emission area at the atomic scale (called “nanotips” [31]), showing that the emission area of this CNT emitter was also at the atomic scale (i.e., size of a pentagon or a hexagon). Second, the descending slope of the main peak on the higher

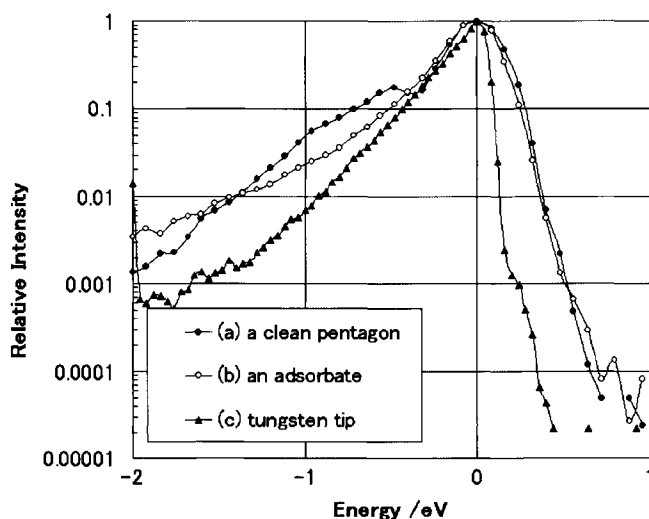


Figure 9. FEEDs from (a) a single pentagon and (b) an adsorbate on the clean cap of an MWNT. (c) FEED from a conventional tungsten emitter is also shown for easy comparison. Reprinted with permission from Takakura et al. [30], Elsevier Science.

energy side was not as steep as metal emitters. Third, the main peak was rather broad, 0.3 eV FWHM, compared with metal emitters (ca. 0.2 eV). All of the clean pentagons showed the same features as described here. Possible explanations for the last two features are the penetration of electric field into the emitter due to the semi-metallic nature of MWNTs and/or the temperature rise due to Joule heating, although the origin is not yet clear.

In FEED of electrons emitted through an adsorbate, the hump at the lower energy side disappeared, but the other two features (i.e., broad main peak and a slow decay at the higher energy side) found in the clean pentagons were retained. The species of adsorbates was not specified in this study, but it is speculated to be carbon monoxide (see the previous section).

### 3. CNT FILM EMITTERS

CNT film emitters are suitable for some applications such as the cathodes in FEDs. Considerable research and development on CNT film emitters have been made in the last several years. The fabrication methods of CNT films, emission characteristics of CNT film emitters, and *in situ* TEM are described in this section.

#### 3.1. Fabrication of film emitters

Several methods for preparing CNT films have been reported so far. MWNT films left on a filter after a purification process using filtration were the first ones reported for the preparation of CNT films [32]. We describe here (1) spray coating, (2) screen printing, (3) electrophoresis, and (4) CVD method, which are recently developed. The former three methods prepare films using CNTs produced beforehand by either arc-discharge or laser ablation, whereas the last one prepares CNT films directly on solid substrates with metal catalysts.

##### 3.1.1. Spray coating

CNT (MWNT or SWNT) films with various densities can be formed by spraying a CNT suspension onto solid substrates with a conventional airbrush. MWNTs (or SWNTs) prepared by arc discharge were first dispersed in ethanol, and then films were prepared by spraying the suspended solution onto the substrate. Figs. 10(a) and (b) show scanning electron microscope (SEM) images of spray-coated MWNT and SWNT films, respectively [21]. Much of the filamentous material was MWNTs, individually separated and in small bundles (Fig. 10a). Since the MWNTs used here were pristine, carbon debris such as graphitic nanoparticles existed on the film. Bundles of purified SWNTs, typically 20–30 nm in diameter and many micrometers long, were entangled in the SWNT film (Fig. 10b).

##### 3.1.2. Screen printing

Crude lumps of MWNTs taken out from an arc-discharge reactor were crushed and mixed with binders and surfactants to prepare pastes or slurries. The concentration of MWNTs can be adjusted by adding the conductive fillers and/or binders to the paste in this method. After being printed with the paste, the MWNT film was heated at 450 to 500 °C in air to vaporize organic binders and to form electrical and mechanical contact between MWNTs and the metal electrode on the substrate.

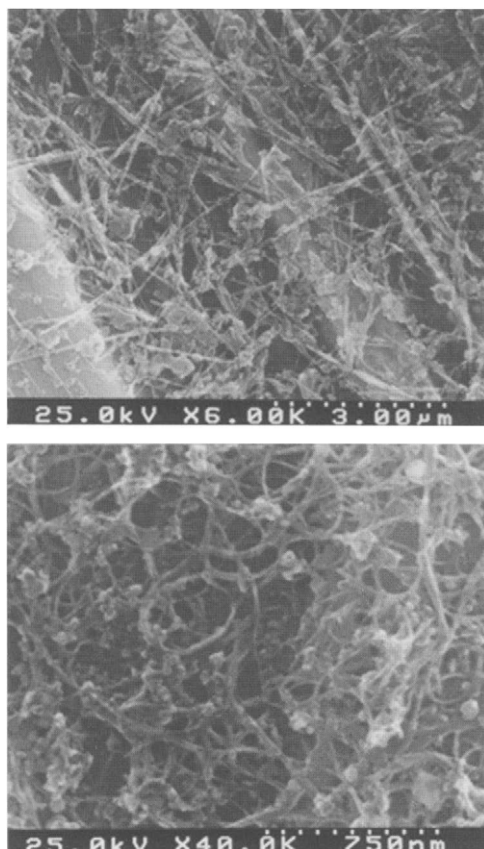


Figure 10. SEM images of spray-coated CNT films: (a) MWNTs and (b) SWNTs.

Since the CNTs were buried in the pristine films, the surface of the films had to be activated to expose tips of CNTs from the surface. After the calcination, surface materials such as graphite and fillers were removed by an appropriate surface treatment [33].

### 3.1.3. Electrophoresis

Nakayama et al. reported first the alignment and purification of MWNTs by using alternating current (ac) electrophoresis in isopropyl alcohol (IPA) [34]. MWNTs used here were produced by arc discharge, and were ultrasonically dispersed in IPA to make a suspension. This suspension was centrifuged to remove large particles. The suspension was dropped onto coplanar aluminum electrodes with a gap of 0.4 mm on glass substrates, and an ac electric field was applied to the electrodes until the IPA had evaporated completely at room temperature. The electric field was  $2 \times 10^3$  V/cm,

and the frequency was changed from 10 Hz to 10 MHz. They also attempted to deposit MWNTs on patterned conductive layers by electrophoresis [35].

Choi et al. deposited SWNTs by electrophoresis onto a patterned metal cathode for triode-type FEDs [36]. SWNTs used here were purified by using acid treatment and filtration. The purified SWNTs were uniformly mixed with distilled water during sonication.  $\text{Mg}(\text{NO}_3)_2 \cdot 6\text{H}_2\text{O}$  of  $10^{-6}$  to  $10^{-2}$  mol was added to the suspension to get a surface charge on the SWNTs. The electrophoresis was carried out to deposit SWNTs on a patterned metal cathode. A negative bias of direct current (dc) 10–50 V was applied on the patterned metal plate in this process.

### 3.1.4. CVD method

CVD is an alternative to the arc-discharge and laser ablation methods to produce CNTs. This method is based on the decomposition of a hydrocarbon gas over a catalytic metal to grow CNTs. In general, CNTs grown by this method have a larger diameter compared with the arc discharge, and are not perfectly graphitized, i.e., highly defective, or composed of grains [10]. Catalytic CVD method allows one to fabricate patterns of CNTs on the substrates such as glass plates by pre-patterning the substrate with a catalyst and subsequent growth of CNTs on the catalyst pattern [37–41]. Fe, Co, Ni, and their alloys are commonly used as catalysts, and hydrocarbon gases such as  $\text{CH}_4$ ,  $\text{C}_2\text{H}_2$ , and  $\text{C}_2\text{H}_4$  are used as carbon feedstock, sometimes with  $\text{NH}_3$  or  $\text{H}_2$  as carrier (or dilution) gas [42].

## 3.2. Emission characteristics of film emitters

### 3.2.1. Emission uniformity

One of the most challenging issues with CNT film emitters is the emission uniformity. Due to problems with the electric “screening effect” arising from closely packed nanotubes [43], variations in CNT structure and overall sample uniformity, only a very small fraction of the CNTs emit at a given time. The low emission site density means low resolution, low current density, and short lifetime in FEDs. An emission site density of the order of  $10^5/\text{cm}^2$  is often required for FEDs, which is not easy to accomplish. Emission from poorly made CNT cathodes is often dominated by edge emission and hot spots. Edge emission is due to concentration of the electric field at edges of the cathode, which can be eliminated by modifying the electric field distribution. Removing hot spots is also critical for achieving high emission uniformity. Several activation processes have been developed to eliminate these protrusions that dominate the emission process. These include plasma and mechanical treatments and aging process.

In 2004, Yotani et al. reported the emission enhancement by excimer-laser irradiation [44]. They carried out the surface treatment of the CNT emitter grown by thermal CVD. KrF-excimer light (248 nm, ca.  $50 \text{ mJ}/\text{cm}^2$ ) was irradiated over the CNT layer on the FeNiCr alloy substrate. The CNT tips formed by laser irradiation had sharp edges and clean surfaces. Therefore, the active emission area increased up to several times that of the initial emission area, resulting from the increase in the emission site density. This demonstrated that the laser irradiation is useful for the activation process of CNT film emitters and enhances the emission uniformity.



### 3.2.2. Emission stability

For any future applications, the prerequisite of the long-term stability of the field emitters must be fulfilled. The stability of emission performance can be readily evaluated by monitoring the evolution of total emission current at a fixed electric field. Zhou et al. reported the result from an SWNT film emitter measured using the parallel-plate geometry, as shown in Fig. 11(a) [45]. After the initial “burn-in”, under a constant

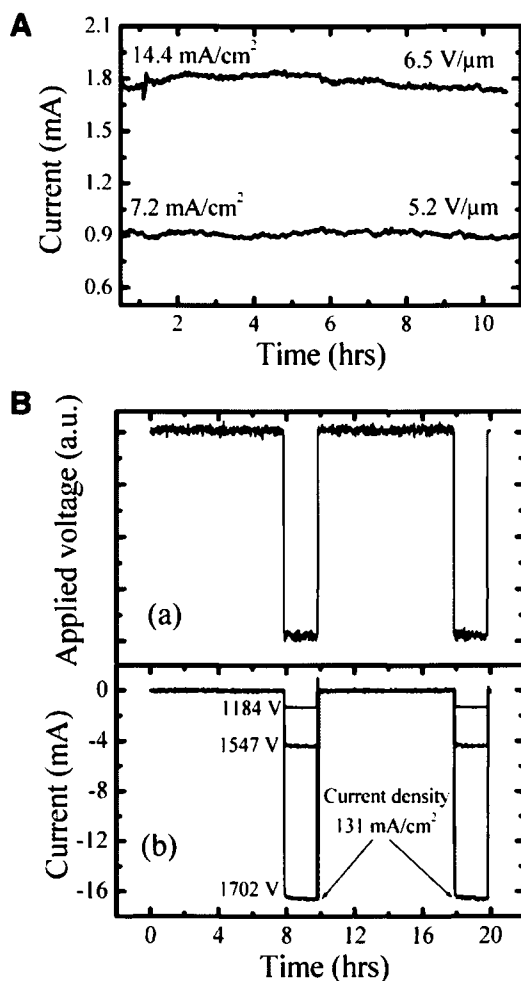


Figure 11. (A) Stability of the emission current measured under a constant applied electric field from an SWNT film using parallel plate geometry at 100% duty cycle, (B) pulsed emission current induced by a pulsed control voltage. Reprinted with permission from Zhou et al. [45], American Chemical Society.

dc voltage without feedback, no overall decay in the emission current was observed over 10 h period. They have demonstrated stable emission at comparable current level for over 300 h at 100% duty cycle. The standard deviation of the current fluctuation was 2–3%. The emission stability can be improved significantly by incorporation of a simple feedback loop. The threshold field measured from the film sample was larger than the value obtained using the small probe, which is related to the sample uniformity. A stable emission over more than 20 h was observed by several groups on MWNT films for current densities of ca. 1 mA/cm<sup>2</sup> [2,39]. The longest test up-to-date has been performed by Saito and Uemura who reported an increase of 11% of the applied field to maintain an emission current of 10 mA/cm<sup>2</sup> during 8000 h [19]. Other studies show nevertheless that degradation can occur on shorter time scales.

The emission current decay (degradation) of field emitters is usually due to several phenomena and can be either reversible or permanent. At present, it is summarized as follows: (1) Arcing gives the most serious irreversible damage to CNT emitters. (2) Local resistive (Joule) heating along the nanotube length due to the flow of emission current may “burn” the CNTs. A field emission electron spectroscopy study from an individual MWNT revealed that the temperature at the tip was up to 2000 K induced by an emission current of 1  $\mu$ A [46,47]. On the other hand, Joule heating of CNTs may help to remove adsorbates during field emission. (3) In the case of SWNTs, Dean et al. reported that “thermally assisted field evaporation” of carbon was found to result in the reduction of the length of the CNTs without catastrophic arcing events [48]. This process seems to define the upper limit for the field emission current that can be obtained from an individual CNT. (4) Besides, the bombardment of residual gas molecules ionized by the emitted electrons may also gradually modify the nanotubes. (5) For CNT film emitters, the adhesion of the CNTs to the substrate is also critical for stability. The strong electrostatic force exerted on the CNTs during emission can peel off the CNTs from substrate, causing current decay and arcing. (6) Electrostatic deflection or mechanical stresses can cause alterations in the shape and/or surroundings of the emitter and lead to a decrease of the local field enhancement. (7) Other degradation phenomena are of chemical origin, i.e., adsorption or desorption of residual gas molecules on the emitter surface (see the previous section), and modify the work function.

The origin of degradation of field emitters is not yet very clear. It seems that residual gases have a significant influence [7,21] and that the emitted current density is important as well [23]. In addition, the intrinsic properties of nanotubes also have an importance. A comparison between films of SWNTs and MWNTs at comparable chamber pressure ( $10^{-5}$  Pa) and emitted current density (0.2 mA/cm<sup>2</sup>) showed that the degradation was a factor of 10 faster for SWNTs [49]. The faster degradation of SWNTs was attributed to the fact that their single wall makes them more sensitive to ion bombardment and irradiation, while the multiple walls of MWNTs tend to stabilize their structure.

Finally, the configuration used for emission, i.e., parallel plates or plane-to-sphere configurations with distances of ca. 100  $\mu$ m, or field emission microscope setups with far larger interelectrode distances, may also play a role. Dean and Chalamala suggested that the poor vacuum conductance between two closely placed planes

leads to high local pressures of gases like  $\text{H}_2\text{O}$  or  $\text{O}_2$  that cause reactive etching and hence faster degradation [50].

In 2002, Yue et al. reported the pulsed emission current generated using a 100 Hz and 2 ms width square wave, as shown in Fig. 11(b) [51]. Since the field emission current is controlled by the applied voltage rather than temperature as in the case of thermionic emission, pulsed emission with variable pulse width and repetition rate can be readily obtained by programming the applied electric field. A peak emission current of ca. 25 mA was obtained from a  $0.2 \text{ cm}^2$  SWNT film ( $140 \text{ mA/cm}^2$ ), showing a clear one-by-one correspondence between the applied voltage and the emission current. The instantaneous response can be attractive for device applications.

### 3.3. *In situ* transmission electron microscopy

Few work have been carried out on dynamic observation of field emission from CNTs by using *in situ* TEM so far [52,53]. In 2004, Seko et al. reported on the mechanical behavior of CNTs as well as field emission from CNTs at high electric field, which were revealed by *in situ* TEM [54]. *In situ* observation of field emission from CNTs was performed by using TEM (JEM 2010, JEOL) with a special sample holder at 200 kV. This microscope was equipped with an image filter (GIF 200, GATAN), which allows one to record both TEM photographs and movies.

In the first experiment, MWNTs of ca. 20 nm in diameter were prepared by arc-discharge method. A bundle of MWNTs was attached onto a tungsten tip by ac electrophoresis [55], as shown in Figs. 12(a) and (b). An MWNT sample was placed on a special sample stage as a cathode, and a copper mesh was used as a counter-electrode (anode), which allows one to move along  $x$ -,  $y$ -, and  $z$ -directions by piezo-electric driving devices, as shown in Fig. 13.

As the applied field increased, a segment of a longer MWNT began to vibrate at ca.  $100 \text{ V}/\mu\text{m}$ , and the breaking of the longer MWNT suddenly occurred at ca.  $190 \text{ V}/\mu\text{m}$ , as shown in Figs. 14(a) and (b). This suggests that the continuous fast vibration of

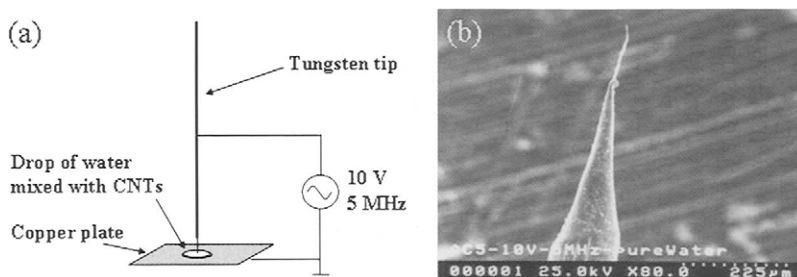


Figure 12. (a) Schematic illustrating the deposition method of MWNTs on a tungsten tip by ac electrophoresis and (b) SEM image of an MWNT bundle deposited on a tungsten tip.

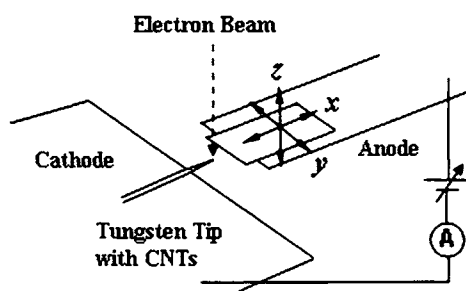


Figure 13. Schematic of a TEM sample stage with CNTs on a tungsten tip (cathode) and a metal plate (anode).

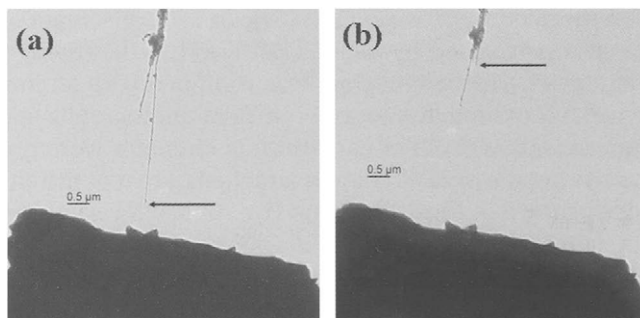


Figure 14. TEM images of MWNTs attached on a tungsten tip, (a) before and (b) after breakage by mechanical vibration at an electric field of ca. 190 V/μm.

the segment of MWNT caused the sudden breaking at the singular site of walls such as defects. From the simultaneous measurement of current–voltage ( $I$ – $V$ ) characteristics, the maximum current density of this MWNT prepared by arc discharge was ca.  $1.7 \times 10^5$  A/cm<sup>2</sup>.

In the second experiment, MWNTs of ca. 20 nm in diameter were directly prepared on a NiCrFe alloy substrate by thermal CVD at 650 °C. This MWNT sample was placed on a special sample stage as a cathode, and a NiCrFe alloy piece was used as a counter electrode, in a similar manner as previously shown in Fig. 13. As the applied voltage increased, randomly oriented MWNTs aligned gradually along the electric field direction. When the electric field reached ca. 95 V/μm, a segment of a longer MWNT sublimated in a very short time less than 0.01 s as shown in Figs. 15(a) and (b). In this *in situ* experiment,  $I$ – $V$  characteristics of the MWNT sample measured simultaneously are shown in Fig. 16. From this study, a sudden decrease of

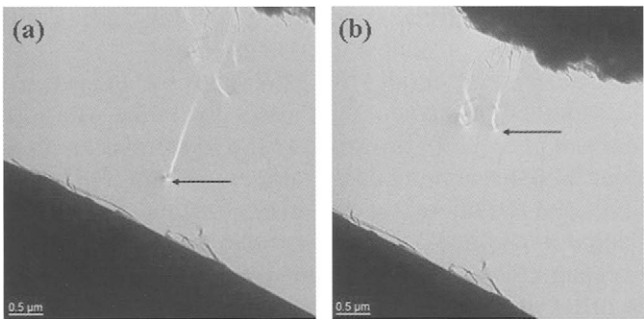


Figure 15. TEM images of MWNTs grown on a NiCrFe alloy substrate, (a) before and (b) after sublimation at an electric field of ca. 95 V/μm.

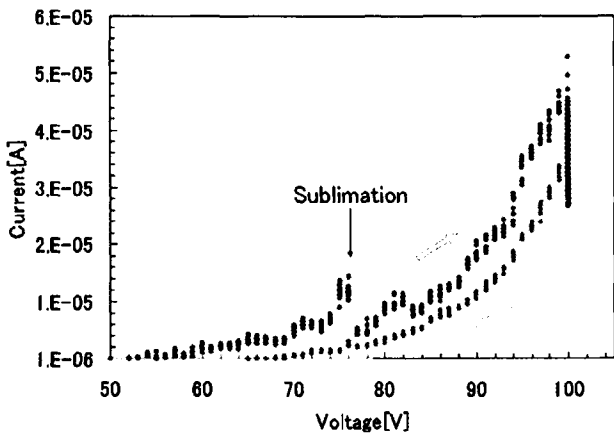


Figure 16. Current vs. voltage characteristics of an MWNTs cathode. A sudden decrease in current is due to the sublimation of an MWNT.

emission current was caused by the sublimation of the segment of longer MWNT, which results in the shortening of the MWNT length, followed by the decrease of electric field applied on the tip. Sublimation of MWNTs occurred probably by the local resistive heating at the singular site such as defects and impurities. In this case, the maximum current density of an MWNT grown by thermal CVD was ca.  $4.8 \times 10^6$  A/cm<sup>2</sup>. This current density, however, was lower by two orders of magnitude than that expected for an MWNT with higher degree of crystallinity [9]. This suggests that since many structural defects and catalytic metal impurities exist in MWNTs grown

by thermal CVD [10], the electrical conductivity and mechanical strength of these MWNTs were not as high as the almost ideal ones.

Only two kinds of failure modes in MWNTs were observed in this study: (1) mechanical breaking of a segment of MWNTs due to fast vibration, and (2) sublimation of a segment of MWNTs probably due to local resistive heating. However, it is supposed that there are a number of failure modes of CNTs, depending on the structures of CNTs and the operating conditions for field emitters. It is noted that, although arc-discharge grown MWNTs, in general, have a higher crystallinity than CVD grown ones, the breaking current density of an MWNT prepared by arc discharge was one order of magnitude lower than the sublimating current density of an MWNT grown by thermal CVD. This was probably caused by the vibratory stress along the axial direction and a higher contact resistance between an arc-discharge grown MWNT and a tungsten needle, compared with the MWNTs grown directly on the alloy substrate. Much work is needed to understand profoundly the failure mechanisms of MWNTs, and also of SWNTs, through *in situ* observation by using high-resolution TEM.

#### 4. APPLICATIONS OF CNT CATHODES TO ELECTRON EMITTING DEVICES

In this section, we describe applications of CNT-based cathodes to electron emitting devices that have been extensively developed so far, such as lamp devices and FED panels.

##### 4.1. Lamp devices

CRT lighting elements (light bulbs) equipped with hot filament cathodes are now used practically for giant outdoor displays. In 1997, Uemura et al. replaced a filament cathode with a CNT-based cold cathode and demonstrated for the first time that their performance was good enough for practical use [5,6].

##### 4.1.1. Fabrication of lighting elements

All parts other than cathodes were the same as those routinely used for manufacturing lighting elements in a plant. Fig. 17 shows a cross-sectional side view of a CRT-type lighting element with a CNT cathode. MWNTs produced by arc discharge were used for raw materials of CNT cathodes. In the first prototype fabrication, fibrous material containing abundant MWNTs was glued directly to a stainless-steel plate (cathode substrate) with a conductive paste [5]. Field emission was obtained in a vacuum-sealed glass bulb, even by this simple method. However, unstable emission such as flashing and discharge sometimes occurred, and dropping of CNTs also occurred due to the mechanical vibration. Moreover, this method was not suitable for industrial fabrication. Therefore, alternative methods were examined for fixing CNTs on a cathode substrate. Screen printing was found to be effective for industrial application. Fig. 18 shows a SEM image of a cathode surface prepared by the screen printing.

A phosphor screen was prepared by screen printing on a glass plate as an anode and coated with an aluminum reflective film (100 to 150 nm in thickness). ZnS:Cu,Al

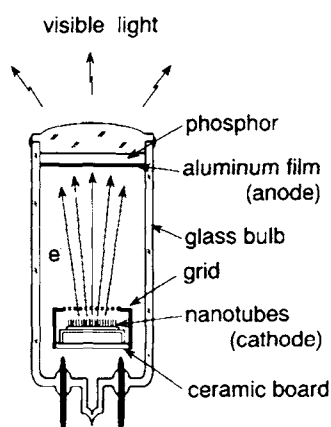


Figure 17. Cross-sectional side view of a CRT-type lighting element with a CNT cathode. The element is 20 mm in diameter and 74 mm in length. Reprinted with permission from Saito et al. [5], The Japan Society of Applied Physics.

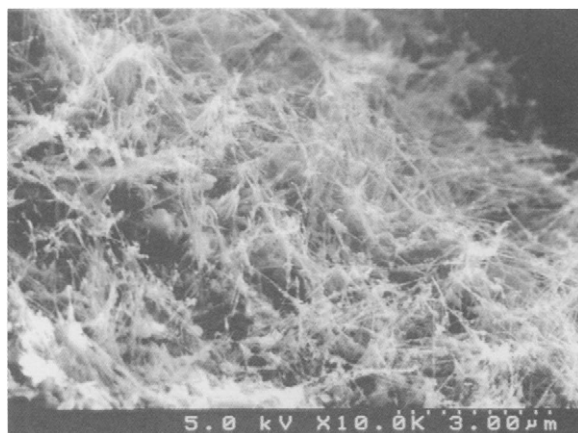


Figure 18. SEM image of a CNT cathode surface fabricated by screen printing. Reprinted with permission from Uemura et al. [6], Society for Information Display.

for green-emitting,  $\text{Y}_2\text{O}_3:\text{Eu}$  for red-emitting, and  $\text{ZnS}:\text{Ag}$  for blue-emitting phosphors were used in this study, respectively. After the vacuum tube was sealed, getter material was flashed to attain a high vacuum on the order of  $10^{-7}$  torr. The cathode-grid gap  $d_{\text{TG}}$  ranged from 0.2 to 1.0 mm. The CNT cathode was grounded (0 V), and

the control grid was biased to a positive voltage ranging from 0.2 to 1.2 kV to emit electrons from CNT tips. A high voltage of 10 kV was applied to the phosphor screen (anode).

#### 4.1.2. Emission characteristics

The total emission current from CNT cathodes as a function of the applied grid voltage for three different cathode-grid gaps,  $d_{T-G}$ , is shown in Fig. 19. For  $d_{T-G} = 0.2$  mm, a total emission current of ca. 200  $\mu\text{A}$  was obtained at the grid voltage of 300 V. Approximately 60% of the emission current passed through the grid and struck the anode. Since the effective cathode area was about 2 mm<sup>2</sup>, the current density was ca. 10 mA/cm<sup>2</sup> at 1.5 V/ $\mu\text{m}$  in this study. A typical emission current fluctuation at a fixed grid voltage is shown in Fig. 20, exhibiting a stable emission with

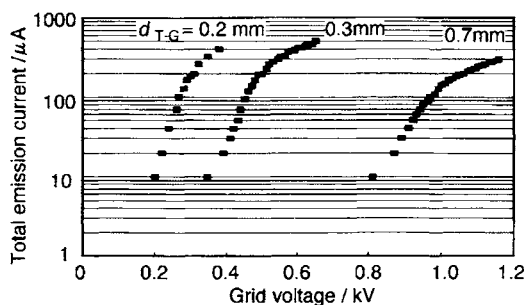


Figure 19. Total emission current as a function of the grid voltage for three different cathode-grid gaps,  $d_{T-G} = 0.2, 0.3$ , and  $0.7$  mm. Reprinted with permission from Uemura et al. [6], Society for Information Display.

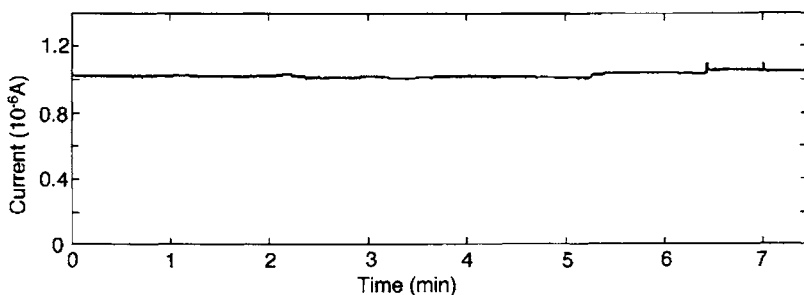


Figure 20. Total current fluctuation from a CNT cathode at a fixed grid voltage, exhibiting a stable emission with a fluctuation of only 4%. Reprinted with permission from Saito et al. [5], The Japan Society of Applied Physics.



only 4% fluctuation at 1.0  $\mu\text{A}$ . The CNT-based CRTs, which underwent a “knocking” treatment (a high voltage, e.g., 30 kV, was applied to remove the causes of discharge) and an “aging” process, sustained stable emissions without any notable decrease during a long-term operation of over 15,000 h (see below). This demonstrated that the robust and stable CNT emitters can be contrasted with delicate and sensitive metal (e.g., tungsten and molybdenum) emitters. This reliable operation is due to the remarkable properties of CNTs such as high chemical stability, high melting point, and high mechanical strength.

Fig. 21 shows three lighting devices with CNT cathodes in operation, which emit light in three colors: green, red, and blue. The luminance of the phosphor screens measured along the tube axis was  $6.3 \times 10^4 \text{ cd/m}^2$  for green,  $2.3 \times 10^4 \text{ cd/m}^2$  for red, and  $1.5 \times 10^4 \text{ cd/m}^2$  for blue at an anode current of 200  $\mu\text{A}$ , which was two times more intense than that of conventional thermionic CRT lighting devices [56]. The emitted light was brilliant and stable enough for practical use in giant outdoor displays. The luminance efficiency for green was 60 lm/W, which was as high as that of the fluorescent lamps. An aging test under a dc driving condition (12 kV and 210  $\mu\text{A}$ ) demonstrated that the CNT cathode had a lifetime of over 15,000 h, as shown in Fig. 22 [6,57].

In 2001, Yotani et al. reported ultrahigh luminance lamp devices by using special MWNTs, “nanografibers [11],” as field emitters [58]. A high current density of ca. 30 mA/cm<sup>2</sup> was obtained at a grid voltage of 2.9 kV with a cathode-grid gap of ca. 1.5 mm. An ultrahigh luminance of  $10^6 \text{ cd/m}^2$  was achieved for a green-emitting phosphor ZnS:Cu,Al under dc driving conditions of 30 kV and 400  $\mu\text{A}$ .

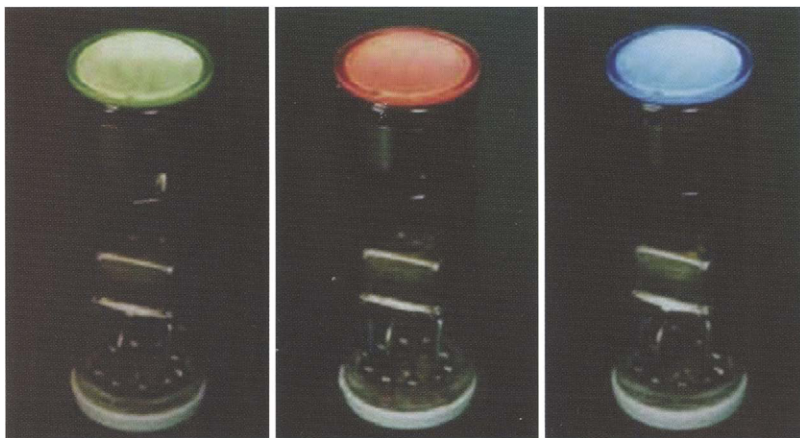


Figure 21. Photographs of CRT lighting devices in which phosphors used here are ZnS:Cu, Al for green,  $\text{Y}_2\text{O}_3\text{:Eu}$  for red, and ZnS:Ag for blue, from left to the right tubes, respectively. The anode voltage and current are 10 kV and 200  $\mu\text{A}$ , respectively. Reprinted with permission from Saito et al. [5], The Japan Society of Applied Physics.

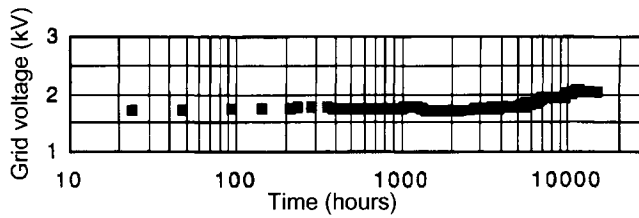


Figure 22. Life test of a CRT lighting element under a dc driving condition, anode voltage of 12 kV and constant emission current of 210  $\mu$ A. The temporal change in the grid voltage at constant emission current is shown [6]. Reprinted with permission from Yotani et al. [57], Society for Information Display.

## 4.2. Field emission displays

### 4.2.1. Prototype field emission display panels

In 1998, fabrication of prototype FED panels with CNT cathodes was reported by Uemura et al. [6] and Wang et al. [59], and in 1999 by Choi et al. [7,60]. These early panels had a diode-type structure, which consisted of two sets of glass plates: a CNT-based cathode and a phosphor-coated anode. The brightness of these diode-type FEDs was not so high (200–300  $\text{cd}/\text{m}^2$ ), similar to that of typical liquid crystal displays (LCDs). One of the advantages of FEDs is expected to be their potential to achieve high brightness that makes it possible to display characters and figures discernable even in daylight. To realize such high brightness and full gray scales, the FED panel should have a triode-type structure in which a control grid (or gate) is added between the cathode and the anode.

Fig. 23 shows schematically the structure of a triode-type panel with remote grids, which was fabricated by Noritake (Japan). One set of anodes, applied at a high voltage, consisted of lines of red-, green-, and blue-emitting (RGB) phosphors (1 mm width) with Al reflective film, just like a CRT screen [33]. In addition, many ribs were formed on the black matrix area between phosphor lines. These ribs (ca. 0.15 mm width) prevented stray electrons from misaddressing the RGB phosphor lines. One set of cathodes consisted of CNT layers formed on a glass substrate by screen printing. The CNT cathode was covered with a grid electrode, which was placed so as to be parallel to a phosphor line on the cathode ribs and controlled field emission from CNTs. The distances between the anode and grid and between the top of CNT tips and grid ( $d_{\text{TG}}$ ) ranged from 2.0 to 4.0 mm, and from 0.3 to 0.6 mm, respectively. After the panel was evacuated and sealed, getter material was flashed to attain a high vacuum on the order of  $10^{-7}$  torr.

The panel size was  $2.6 \times 2.6$  in., and the pixel size was  $0.12 \text{ (RGB)} \times 0.1$  in. ZnS:Cu,Al for green-,  $\text{Y}_2\text{O}_3\text{:Eu}$  for red-, and ZnS:Ag for blue-emitting phosphors were used in this panel. The luminance of phosphor screens was ca.  $7 \times 10^5 \text{ cd}/\text{m}^2$  for green, ca.  $1.8 \times 10^5 \text{ cd}/\text{m}^2$  for red, ca.  $1 \times 10^5 \text{ cd}/\text{m}^2$  for blue under a dc-driving

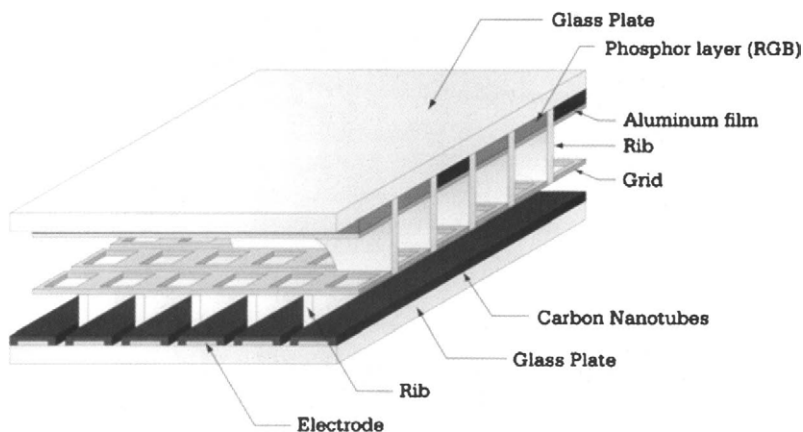


Figure 23. Structure of a triode-type CNT-FED panel with remote grids. Reprinted with permission from Y. Saito, *J. Nanosci. Nanotech.* **3** (2003) 39, American Scientific Publishers.

condition of anode voltage of 6 kV and current of ca. 1 mA/cm<sup>2</sup>. In 2001, a 14.5-inch diagonal FED panel with grid electrodes was successfully fabricated by Noritake [61].

In 1999, Samsung SDI (Korea) experimentally manufactured a 4.5-inch FED [7], and demonstrated a 9-inch FED displaying color images at the International Display Workshop in 1999 (IDW'99), as shown in Fig. 24 [62]. In 2000, the detailed technical specifications were reported at the 2000 Society for Information Display (SID'00) symposium [63]. These FED panels had a diode-type structure using SWNT field emitters. A 15-inch triode-type monochrome panel was also demonstrated at the SID'00, but the full-color gray control was not implemented, because of the high level of driving voltage. In 2001, Samsung developed a triode-type FED panel with an 8-bit gray scale control and demonstrated full-color moving pictures [64]. In this FED panel, gate electrodes near the SWNT cathodes were fabricated by microlithography. The gap between the cathode and gate was either 2 or 15  $\mu\text{m}$ , and the gate voltages were typically 40 and 80 V, respectively. A luminance of 500 cd/m<sup>2</sup> was obtained when the anode and the gate voltages were 1.5 kV and 100 V, respectively. Full-color moving images with 240 cd/m<sup>2</sup> were demonstrated under an anode voltage of 2 kV and a gate bias of  $\pm 36$  V.

While, in 2000 NEC (Japan) researchers also fabricated a 1-inch gated CNT-FED panel using SWNTs and photolithography [65]. The diameter of the gate hole was 100  $\mu\text{m}$ , and the insulating layer was 20  $\mu\text{m}$  thick, which separates the CNT cathode and gate. Emission current density of 0.5 mA/cm<sup>2</sup> was obtained at the anode voltage of 700 V and gate voltage of 80 V.

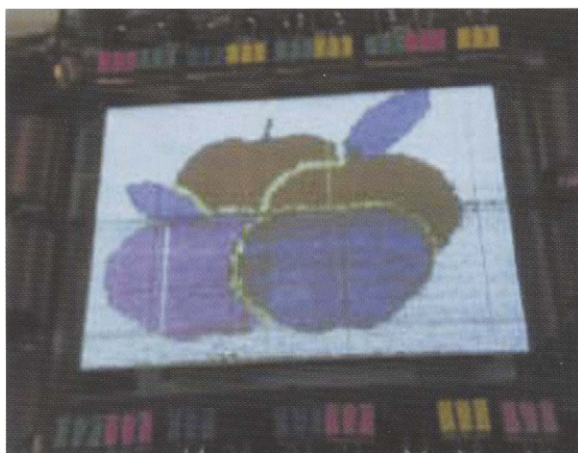


Figure 24. Moving image of a 9-inch CNT-FED. Reprinted with permission from Lee et al. [62], Elsevier Science.

#### 4.2.2. Large-size field emission displays

FEDs are expected to be utilized as display panels in the instrument and automotive industries (with sizes in the 5-inch range) as well as for flat TVs, where FEDs are supposed to bridge the size gap between 30-inch, the viable limit of active matrix LCDs foreseen a few years ago, and 40-inch, the lower limit of commercial plasma display panels (PDPs) [66].

In 2002, Noritake reported the experimental manufacturing of a 40-inch FED panel with CNT cathodes [67]. An electrophoresis method to form emitter electrodes was developed in order to reduce the driving voltage for FED panels. Double-wall carbon nanotubes (DWNTs) prepared by arc-discharge method were used and were coated on the metal electrode by electrophoresis. Fig. 25 shows an emission distribution profile from a DWNT-coated electrode, which was measured by a cathode emission profiler (CEPS-LW, Tokyo Cathode Lab). The profile was leveled at  $1.0 \text{ mA/cm}^2$  to evaluate emission uniformity. The current density was ca.  $5 \text{ mA/cm}^2$  at  $3.5 \text{ V}/\mu\text{m}$ . The 40-inch panel was assembled with four separated gate-insulator composite substrates. Thin insulator sheets with gate electrodes were made by screen printing method. In this method, the thickness of this sheet should be controlled down to ca.  $20 \mu\text{m}$ . The driving voltage could be reduced to less than 100 V by using this structure. The green-emitting luminance was ca.  $1.0 \times 10^5 \text{ cd/m}^2$  under dc-driving condition at the anode voltage of 5 kV. Fig. 26 shows characters displayed on a portion of the 40-inch FED panel. This demonstrated that the high luminance and good uniformity were obtained in a large-size CNT-FED.

In 2002, Samsung SDI reported a 32-inch FED panel with CNT cathodes [68]. Fig. 27 shows the total fabrication steps using a photosensitive CNT paste for the

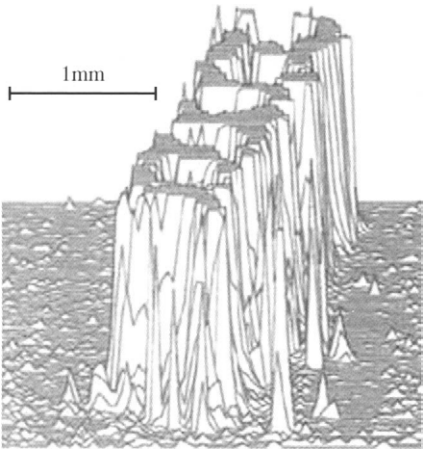


Figure 25. Emission distribution profile of a DWNT cathode. Current density in a range from 0.0 to 1.0 mA/cm<sup>2</sup> is displayed, i.e., portions exceeding 1.0 mA/cm<sup>2</sup> are cut off. Reprinted with permission from Uemura et al. [67], Society for Information Display.

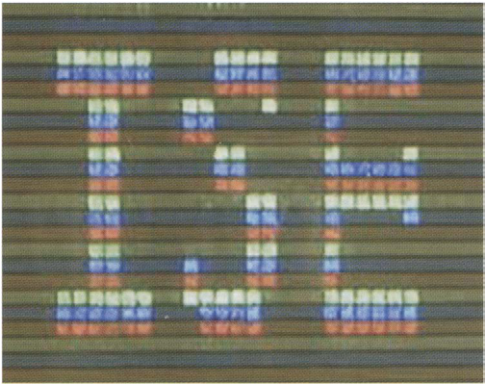


Figure 26. Displayed characters in a portion of a 40-inch CNT-FED panel [67]. Reprinted with permission from Uemura et al. [67], Society for Information Display.

triode-type structure of under-gated CNT cathode. The cross-sectional view of patterned CNT layers is shown in Fig. 28. The protruded length of the SWNTs was about 1  $\mu$ m, and they were partially oriented to the anode direction. The anode voltage was 1 kV, and the anode to cathode gap was 1.1 mm. The driving voltage of the

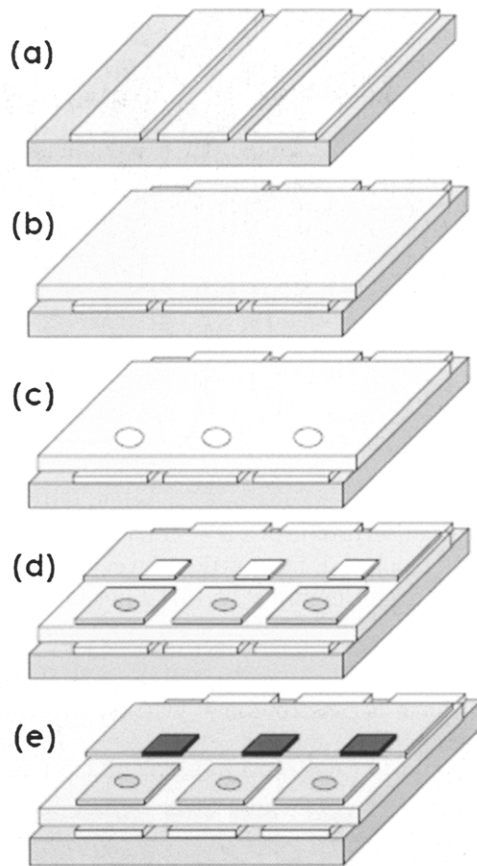


Figure 27. The fabrication steps of the 32-inch under-gated CNT cathode: (a) stripe-patterned under-gate formation, (b) thick-film insulator printing, (c) contact via hole formation, (d) cathode and counter-electrode formation, and (e) CNT emitting layer formation. Reprinted with permission from Lee et al. [68], Society for Information Display.

data lines was about 70 V, and the average brightness was ca. 150 cd/m<sup>2</sup> in the full white range at the peak current density of 1 mA/cm<sup>2</sup>. Even though the resistive layer was not adopted, the deviation of the brightness was within 15% on the whole area of the 32-inch panel. The emission uniformity (emission site density) seemed to be acceptable for large-size TV applications.

With such a large-size display, Samsung and Noritake intended to compete with PDPs for flat TV applications. Although the PDP acceptance for home entertainment and TV-on-the-wall applications is steadily growing, it seems that future PDP

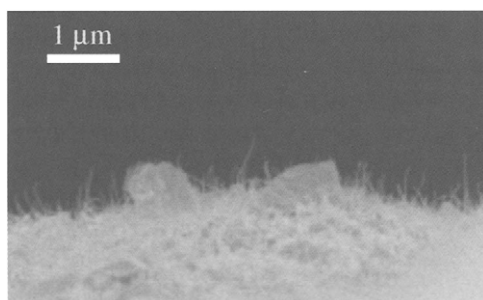


Figure 28. SEM image of a CNT emitting layer. Reprinted with permission from Lee et al. [68], Society for Information Display.

developments for the 40-inch range will be menaced by large-size active matrix LCDs rather than by FEDs.

In this landscape, what is the situation of FEDs? First of all, technical approaches different from the classical Spindt-type microtips such as CNTs are intended to be used for field emitters. The ideas behind such new approaches are to eliminate sophisticated process steps (such as sub-micron range lithography) and reduce driving voltage in order to have access to cheap LCD-type drivers, and also to aim at developing a low cost manufacturing technology based on non-sophisticated lithography such as screen printing. Clearly, a simple and cheap FED technology with low driving voltage can compete with PDPs in the large-size display range (above 40 to 60 in.). As the fabrication costs of PDPs and FEDs will end up as being very similar, the lower cost of the driving circuits could give a decisive advantage to FEDs.

### 4.3. Other devices

Applications of CNT field emitters to electron emitting devices other than displays are described in this subsection.

#### 4.3.1. X-ray sources

X-ray sources are widely used in industry, medical instruments, and scientific measurements. For the generation of X-rays, an energetic electron beam strikes a metal target from which electromagnetic radiation (X-rays) is emitted. An electron source and a metal target are sealed in a vacuum glass tube in most cases. In the X-ray tube, a primary electron beam is usually obtained by thermionic emission from tungsten filament (hot cathode), which works stably even in a moderate vacuum, because the emitter surface is kept clean during operation. However, the tungsten filament is sensitive to reactive residual gases such as  $O_2$  and  $H_2O$ , which produce volatile metal oxides, and subsequently the filament becomes thinner through sublimation or burn out during operation. Moreover, additional power is needed to heat the cathode above  $2000^\circ C$  in hot cathodes, which makes it difficult to produce a compact X-ray source.

These disadvantages of hot cathodes can be overcome by replacing them with field emitters (cold cathodes). Sugie et al. attempted to use CNT cathodes as a primary electron source in an X-ray tube in a high vacuum of  $2 \times 10^{-7}$  torr [69]. MWNTs were prepared by plasma-enhanced CVD method with acetylene and ammonia on a cobalt-coated tungsten wire (0.3 mm in diameter). CNTs were approximately aligned vertical to the surface of the wire and were capped by metal particles at the tips (covered by graphitic layers). The intensity of X-ray passing through a beryllium window was measured as a function of the target voltage from 20 to 60 kV at a constant emission current of  $10^{-7}$  A. The X-ray intensity increased almost exponentially with the increase of target voltage: 0.005 mSv/h at 20 kV and 4 mSv/h at 50 kV. At a pressure of  $2 \times 10^{-7}$  torr, the lifetime of the CNT cathodes was more than 1 h, and a clear X-ray image of a large-scale integrated circuit was obtained during operation.

Yue et al. also demonstrated an X-ray tube using an SWNT-based cathode [51]. A total emission current of 28 mA was obtained from a  $0.2 \text{ cm}^2$  area SWNT film emitters made by electrophoresis. The X-ray intensity was sufficient to image a human hand at 14 kVp and 180 mAs.

#### 4.3.2. Gas discharge tube

The GDT, usually consisting of two electrodes parallel to each other in a sealed ceramic case filled with noble gases, is one of the old methods used to protect against transient overvoltages in an electronic circuit. Rosen et al. first applied CNTs to gas-tube protectors [70]. The SWNTs used here were prepared by laser ablation method. Molybdenum electrodes were coated with uniform films of SWNTs by spray coating method. Adhesion between the substrate and the film was enhanced by introducing either a carbon-dissolving or a carbide-forming metal (e.g., iron) interlayer. A mean dc breakdown voltage of 448.5 V and a standard deviation of 4.8 V over 100 surges were observed in the CNT-based GDTs with a 1-mm gap between the electrodes. The breakdown voltage was about 30% lower, and the fluctuation of breakdown voltage was a factor of 4–20 better than those of commercial products measured. This enhanced performance demonstrated that CNT-based GDTs are attractive overvoltage protection units for advanced telecommunication networks.

### 5. CONCLUSIONS

Research on field emission from CNTs began only 10 years ago, and the progress has been very rapid. Now it has been proved that CNT-based cathodes are superior field emission electron sources, providing low-voltage operation and stable electron emission, even in an ordinary high vacuum on the order of  $10^{-6}$  torr. The potential of CNT cathodes for operation in a non-UHV is in strong contrast to that of metal field emitters, which require an UHV on the order of  $10^{-10}$  torr. This advantage is indispensable for the application of CNT cathodes to practical devices. Moreover, tremendous progress has been achieved in the development of FEDs during the last 5 years.

There are still important materials issues that need to be solved before they can be utilized in practical devices. These include emission uniformity, long-term emission stability (lifetime), and efficient refined processes for materials assembly and



integration. CNT-FEDs as well as PDPs may be suitable for large-size flat panel displays, e.g., TVs-on-the-wall, over several tens of inches, which can be hardly produced by LCDs. We can expect reliable and reproducible CNT cathodes to be fabricated, and CNT-based electron emitting devices can hopefully be utilized in our living rooms and offices in the near future.

## REFERENCES

1. A. G. Rinzier, J. H. Hafner, P. Nikolaev, L. Lou, S. G. Kim, D. Tomanek, P. Nordlander, D. T. Colbert, and R. E. Smalley, *Science* **269** (1995) 1550.
2. W. A. de Heer, A. Chatelain, and D. Ugarte, *Science* **270** (1995) 1179.
3. Y. Saito, K. Hamaguchi, T. Nishino, K. Hata, K. Tohji, A. Kasuya, and Y. Nishina, *Jpn. J. Appl. Phys.* **36** (1997) L1340.
4. Y. Saito, K. Hamaguchi, K. Hata, K. Uchida, Y. Tasaka, F. Ikazaki, M. Yumura, A. Kasuya, and Y. Nishina, *Nature* **389** (1997) 554.
5. Y. Saito, S. Uemura, and K. Hamaguchi, *Jpn. J. Appl. Phys.* **37** (1998) L346.
6. S. Uemura, T. Nagasako, J. Yotani, T. Shimojo, and Y. Saito, *SID1998 Digest*, 1998, pp. 1052–1055.
7. W. B. Choi, D. S. Chung, J. H. Kang, H. Y. Kim, Y. W. Jin, I. T. Han, Y. H. Lee, J. E. Jun, N. S. Lee, G. S. Park, and J. M. Kim, *Appl. Phys. Lett.* **75** (1999) 3129.
8. R. Gomer, *Field Emission and Field Ionization*, Harvard University Press, Cambridge, MA, 1961, p. 32.
9. B. Q. Wei, R. Vajtai, and P. M. Ajayan, *Appl. Phys. Lett.* **79** (2001) 1172.
10. H. Dai, in *Carbon Nanotubes Synthesis, Structure, Properties, and Applications*, eds. M. S. Dresselhaus, G. Dresselhaus, and P. Avouris, Springer, Berlin, 2001, pp. 29–53.
11. Y. Saito, R. Mizushima, S. Kondo, and M. Maida, *Jpn. J. Appl. Phys.* **39** (2000) 4168.
12. Y. Tanaka and Y. Saito, *Abstracts of the 17th Fullerene General Symposium*, Gifu, Japan, August 9–10, 1999, pp. 262–263.
13. Y. Saito, K. Hamaguchi, K. Hata, K. Tohji, A. Kasuya, Y. Nishina, K. Uchida, Y. Tasaka, F. Ikazaki, and M. Yumura, *Ultramicroscopy* **73** (1998) 1.
14. Y. Saito, K. Hamaguchi, S. Uemura, K. Uchida, Y. Tasaka, F. Ikazaki, M. Yumuar, A. Kasuya, and Y. Nishina, *Appl. Phys. A* **67** (1998) 95.
15. Y. Saito, K. Hata, and T. Murata, *Jpn. J. Appl. Phys.* **39** (2000) L271.
16. R. Tamura and M. Tsukada, *Phys. Rev. B* **52** (1995) 6015.
17. K. Hata, A. Takakura, and Y. Saito, *Surf. Sci.* **490** (2001) 296.
18. K. Hata, A. Takakura, and Y. Saito, *Ultramicroscopy* **95** (2003) 107.
19. Y. Saito and S. Uemura, *Carbon* **38** (2000) 169.
20. S. Yamamoto, S. Hosoki, S. Fukuhara, and M. Futamoto, *Surf. Sci.* **86** (1979) 734.
21. Y. Saito, T. Nishiyama, T. Kato, S. Kondo, T. Tanaka, J. Yotani, and S. Uemura, *Mol. Cryst. Liq. Cryst.* **387** (2002) 79.
22. K. A. Dean, P. von Allmen, and B. R. Chalamala, *J. Vac. Sci. Technol. B* **17** (1999) 1959.
23. W. Zhu, C. Bower, O. Zhou, G. Kochanski, and S. Jin, *Appl. Phys. Lett.* **75** (1999) 873.

24. K. A. Dean and B. R. Chalamala, *Appl. Phys. Lett.* **76** (2000) 375.
25. R. Gomer, Chapters 1 and 2 in *Field Emission and Field Ionization*, Harvard University Press, Cambridge, MA, 1961.
26. S. T. Purcell, V. T. Binh, and N. Garcia, *Appl. Phys. Lett.* **67** (1995) 436.
27. W. A. de Heer, J.-M. Bonard, K. Fauth, A. Chatelain, L. Forro, and D. Ugarte, *Adv. Mater.* **9** (1997) 87.
28. M. J. Fransen, T. L. von Rooy, and P. Kruit, *Appl. Surf. Sci.* **146** (1999) 312.
29. D. Loval, M. Buss, E. Graugnard, R. P. Andres, and R. Reifengerger, *Phys. Rev. B* **61** (2000) 5683.
30. A. Takakura, K. Hata, Y. Saito, K. Matsuda, T. Kona, and C. Oshima, *Ultramicroscopy* **95** (2003) 139.
31. V. T. Binh, S. T. Purcell, N. Garcia, and J. Doglioni, *Phys. Rev. Lett.* **69** (1992) 2527.
32. W. A. de Heer, W. S. Bacsa, A. Chatelain, T. Gerfin, R. Humphrey-Baker, L. Forro, and D. Ugarte, *Science* **268** (1995) 845.
33. S. Uemura, J. Yotani, T. Nagasako, Y. Saito, and M. Yumura, *Proceedings of Euro Display 1999*, 19th IDRC, 1999, pp. 93–96.
34. K. Yamamoto, S. Akita, and Y. Nakayama, *J. Phys. D* **31** (1998) L34.
35. Y. Nakayama, S. Akita, L. Pan, S. Yokoyama, and C. Chen, *Proceedings of the Japan–Korea Joint Symposium on Imaging Materials and Technology*, Osaka Prefecture University, Osaka, Japan, December 4, 1999.
36. W. B. Choi, Y. W. Jin, H. Y. Kim, S. J. Lee, M. J. Yun, J. H. Kang, Y. S. Choi, N. S. Park, N. S. Lee, and J. M. Kim, *Appl. Phys. Lett.* **78** (2001) 1547.
37. Z. F. Ren, Z. P. Huang, J. W. Xu, J. H. Wang, P. Bush, M. P. Siegal, and P. N. Provencio, *Science* **282** (1998) 1105.
38. S. Fan, M. G. Chapline, N. R. Franklin, T. W. Tombler, A. M. Cassell, and H. Dai, *Science* **283** (1999) 512.
39. H. Murakami, M. Hirakawa, C. Tanaka, and H. Yamakawa, *Appl. Phys. Lett.* **76** (2000) 1776.
40. H. Kind, J.-M. Bonard, C. Emmenegger, L.-O. Nilsson, K. Hernadi, E. Maillard-Schaller, L. Schlapbach, L. Forro, and K. Kern, *Adv. Mater.* **11** (1999) 1285.
41. N. R. Franklin and H. Dai, *Adv. Mater.* **12** (2000) 890.
42. G. S. Choi, Y. S. Cho, S. Y. Hong, J. B. Park, K. H. Son, and D. J. Kim, *J. Appl. Phys.* **91** (2002) 3847.
43. L. Nilsson, O. Groening, C. Emmenegger, O. Kuettel, E. Schaller, L. Schlapbach, H. Kind, J.-M. Bonard, and K. Kern, *Appl. Phys. Lett.* **76** (2000) 2071.
44. J. Yotani, S. Uemura, T. Nagasako, H. Kurachi, H. Yamada, T. Ezaki, T. Maesoba, T. Nakao, M. Ito, T. Ishida, and Y. Saito, *Jpn. J. Appl. Phys.* **43** (2004) L1459.
45. O. Zhou, H. Shimoda, B. Gao, S. Oh, L. Fleming, and G. Yue, *Acc. Chem. Res.* **35** (2002) 1045.
46. S. T. Purcell, P. Vincent, C. Journet, and V. T. Binh, *Phys. Rev. Lett.* **88** (2002) 105502.
47. P. Vincent, S. T. Purcell, C. Journet, and V. T. Binh, *Phys. Rev. B* **66** (2002) 075406.
48. K. A. Dean, T. P. Burgin, and B. R. Chalamala, *Appl. Phys. Lett.* **79** (2001) 1873.
49. J.-M. Bonard, J.-P. Salvetat, T. Stockli, W. A. de Heer, L. Forro, and A. Chatelain, *Appl. Phys. Lett.* **73** (1998) 918.

50. K. A. Dean and B. R. Chalamala, *Appl. Phys. Lett.* **75** (1999) 3017.
51. G. Z. Yue, Q. Qie, B. Gao, Y. Cheng, J. Zhang, H. Shimoda, S. Chang, L. P. Lu, and O. Zhou, *Appl. Phys. Lett.* **81** (2002) 355.
52. J. Cumings and A. Zettl, *Science* **289** (2000) 602.
53. Z. L. Wang, R. P. Gao, W. A. de Heer, and P. Poncharal, *Appl. Phys. Lett.* **80** (2002) 856.
54. K. Seko, J. Kinoshita, K. Kawakita, and Y. Saito, *Proceedings of 23rd Electronic Materials Symposium, Izunagaoka, Japan, July 7–9, 2004*, pp. 253–256.
55. Y. Nakayama, *Ultramicroscopy* **91** (2002) 49.
56. S. Uemura, Y. Seko, H. Kamogawa, M. Morikawa, and T. Shimojo, *ITE Tech. Rep.* **17** (1993) 31.
57. J. Yotani, S. Uemura, T. Nagasako, Y. Saito, and M. Yumura, *Proceedings of the 6th International Display Workshop, IDW'99, 1999*, pp. 971–974.
58. J. Yotani, S. Uemura, T. Nagasako, H. Kurachi, H. Yamada, T. Ezaki, Y. Saito, Y. Ando, and X. Zhao, *Proceedings of SID'01, 2001*, pp. 312–315.
59. Q. H. Wang, A. A. Setlur, J. M. Lauerhaus, J. Y. Dai, E. W. Seeling, and R. P. H. Chang, *Appl. Phys. Lett.* **72** (1998) 2912.
60. W. B. Choi, D. S. Chung, S. H. Park, and J. M. Kim, *SID'99 Digest, Society for Information Display, San Jose, CA, 1999*, pp. 1134–1137.
61. S. Uemura, J. Yotani, T. Nagasako, H. Kurachi, H. Yamada, T. Ezaki, T. Maesoba, and Y. Saito, *Proceedings of Asia Display/IDW'01, 2001*, pp. 1201–1204.
62. N. S. Lee, D. S. Chung, I. T. Han, J. H. Kang, Y. S. Choi, H. Y. Kim, S. H. Park, Y. W. Jin, W. K. Yi, M. J. Yun, J. E. Jung, C. J. Lee, J. H. You, S. H. Jo, C. G. Lee, and J. M. Kim, *Diam. Relat. Mater.*, **10** (2001) 265.
63. W. B. Choi, N. S. Lee, W. K. Yi, Y. W. Jin, Y. S. Choi, J. T. Han, D. S. Chung, H. Y. Kim, J. H. Kang, Y. J. Lee, M. J. Yun, S. H. Park, S. Yu, J. E. Jang, J. H. You, and J. M. Kim, *SID'00 Digest*, 2000, pp. 324–327.
64. J. E. Jung, Y. W. Jin, J. H. Choi, Y. J. Park, T. Y. Ko, D. S. Chung, J. W. Kim, J. E. Jang, S. N. Cha, W. K. Yi, S. H. Cho, M. J. Yoon, C. G. Lee, J. H. You, N. S. Lee, J. B. Yoo, and J. M. Kim, *Demonstration at the Tsukuba Symposium on Carbon Nanotubes, Tsukuba, Japan, October 3–5, 2001*.
65. F. Ito, Y. Tomihari, Y. Okada, K. Konuma, and A. Okamoto, *Proceedings of the 6th International Display Workshop, Kobe, Japan, 2000*, pp. 1177–1180.
66. D. Pribat, *IVMC 2002 Technical Digest, Lyon, France, K08, 2002*.
67. S. Uemura, J. Yotani, T. Nagasako, H. Kurachi, H. Yamada, T. Ezaki, T. Maesoba, T. Nakao, Y. Saito, M. Yumura, *SID'02 Digest*, 2002, pp. 1132–1135.
68. C. G. Lee, S. J. Lee, S. Y. Whang, E. J. Chi, T. I. Yun, J. S. Lee, J. W. Kim, J. E. Jang, S. H. Cho, B. G. Lee, S. J. Lee, H. S. Han, S. H. Ahn, K. S. Ryu, K. W. Jung, J. H. Kang, S. H. Jin, S. K. Jo, J. E. Jung, J. S. Choi, T. S. Oh, S. K. Kang, and J. M. Kim, *Proceedings of IDW'02, Hiroshima, Japan, December 4–6, 2002*, pp. 1021–1024.
69. H. Sugie, M. Tanemura, V. Filip, K. Iwata, K. Takahashi, and F. Okuyama, *Appl. Phys. Lett.* **78** (2001) 2578.
70. R. Rosen, W. Simendinger, C. Debbault, H. Shimoda, L. Fleming, B. Stoner, and O. Zhou, *Appl. Phys. Lett.* **76** (2000) 1668.

## Chapter 17

### Optical limiters and photovoltaic devices based on C<sub>60</sub>, carbon nanotubes and their nanocomposites

M. H.-C. Jin<sup>a</sup>, M. Durstock<sup>b</sup> and L. Dai<sup>c</sup>

<sup>a</sup>Materials Science and Engineering Program, University of Texas, Arlington, TX 76019, USA

<sup>b</sup>Materials and Manufacturing Directorate, Air Force Research Laboratory, AFRL/MLBP, Bldg 654, 2941 P St. Wright-Patterson AFB, OH 45433, USA

<sup>c</sup>Department of Chemical and Materials Engineering, University of Dayton, 300 College Park, Dayton, OH 45469, USA

Owing to their superior electronic, mechanical, and optical properties, carbon nanomaterials are of great interest for many important applications, including as optical limiters for eye protection and optical switching and as new charge transfer materials in organic photovoltaic (PV) devices that are light-weight and flexible. Carbon-based (carbon black, C<sub>60</sub>, and carbon nanotubes (CNTs)) optical limiting systems often take either a suspension or solution form with their optical limiting effects arising from the nonlinear scattering associated with opto-thermal properties of the constituents including liquid solvent or nonlinear absorption, respectively. Depending on the wavelength, the pulse width of a laser pulse, the type of solvent, and the size of the particles, optical limiting performance varies while concentration of the suspensions does not affect the limiting properties. C<sub>60</sub> and CNTs, with and without surface modification, can be dissolved in many solvents for a wide range of optical limiting applications. On the other hand, recent development in heterojunction devices indicates that highly efficient photo-induced charge transfer processes (e.g. exciton dissociation) occur at junctions between organic and carbon nanomaterials. Single junction devices based on a bulk composite of organic materials and carbon nanomaterials have provided proof of the concept to further improve the device performance via a dispersed bulk heterojunction configuration. Although monochromatic external quantum efficiency up to 70% was achieved, device performance is still limited by the low red-light absorption, poor carrier transport, and degradation of the materials. This chapter summarizes some of the new approaches toward advanced carbon-based optical limiters and PV devices.

#### 1. INTRODUCTION

The discoveries of fullerenes [1] and carbon nanotubes (CNTs) [2] have led to the rapid development in nanotechnology for the last decade. Extensive reviews on the fundamental and applied aspects of carbon nanomaterials have been given in other chapters of this book and some relevant publications [3–5]. Among the numerous

potential applications demonstrated for carbon nanomaterials, this chapter focuses on the recent developments of advanced optical limiters and organic photovoltaic (PV) devices based on carbon nanomaterials.

Historically, there has been a long-standing interest in developing high-power laser source for materials processing, biomedical applications, and long-range sensing and communications. Along with these developments, it is highly demanding to have health and safety measures for preventing these systems and the system operators from possible injury by laser beams. Although passive interference filters or shutters could be used for certain protections, as pointed out by Signorini et al. [6], these very simple devices cannot cover a broad range of wavelengths and their absorption saturates at relatively high input levels. A slow response time is also a problem when fast laser pulse is involved. Therefore, the design and development of new materials and/or devices with superior optical limiting properties become indispensable.

Ideal optical limiters should effectively transmit optical beams of a low input level with a rapid decrease in the transmittance for beams of a high input level in order to keep irradiance (or fluence) output under the damage threshold (Fig. 1) [7]. A large dynamic range together with fast (picoseconds) and wide spectral response (visible to near IR) is also highly desirable. The dynamic range is defined as the ratio of the transmittance at nonlinear threshold to that of damage threshold. A dynamic range of  $10^4$  or greater is often required for optical limiters used for the protection of the optical detecting system. Carbon nanomaterials, including fullerenes and CNTs, have attracted much attention as excellent optical limiting materials due to their nonlinear optical properties [6,7]. While carbon black suspensions (CBS) have

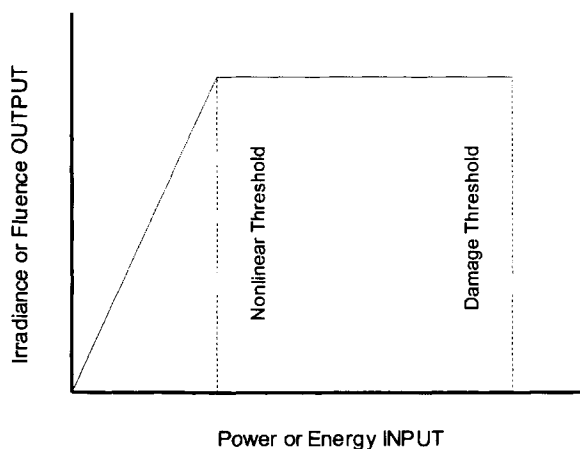


Figure 1. Schematic representation of the ideal behavior for a passive optical limiter. (After Signorini et al. [6].)

been considered as a benchmark in the development of optical limiting materials, fullerenes and CNTs showed great potential as new optical materials of superior performance. In Sec. 2, the optical limiting mechanisms will be described, followed by a detailed discussion on different optical limiting systems based on carbon nanomaterials.

While carbon nanomaterials has demonstrated excellent optical limiting properties, photo-induced electron transfer between organic materials and carbon nanomaterials [8] has also motivated the development of organic heterojunction PV devices [9]. Unlike solar cells from inorganic materials, organic PV devices suffer from high exciton dissociation energy (a few millielectronvolts vs. an order of 100 meV) associated with the conjugated semiconducting structure. As a consequence, the simple single-layer organic solar cells [10] cannot provide an effective exciton dissociation as the electric field established by the work function difference between the positive and negative electrodes or by the Schottky contact made between an organic material and an electrode was insufficient to break photo-generated excitons before their recombination (the diffusion length of excitons in typical conjugated molecules is in the order of 10 nm). In order to overcome this limitation, heterojunctions between various organic materials and carbon nanomaterials (Fig. 2) have been studied for PV applications with an expected more efficient exciton dissociation at the junction of the two materials due to the strong electron affinity of

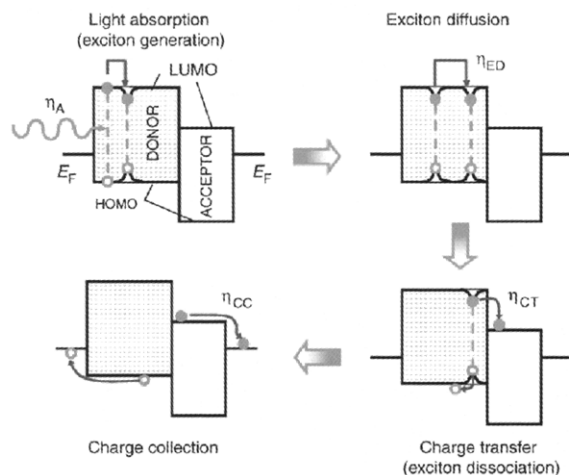


Figure 2. Steps in the photocurrent generation process. Excitons created by photons diffuse to the heterojunction between donor and acceptor. At the junction, excitons dissociate into free carriers to be collected at the opposite electrodes.  $\eta_{CC}$  is the charge collection efficiency and  $\eta_{CT}$  the charge transfer efficiency. (After Forrest [73].)

carbon nanomaterials [9,11]. In these cases, free electrons can rapidly reach the negative electrode through the carbon nanomaterial (electron-accepting (EA) material) while free holes generated from the exciton dissociation are effectively transported to the opposite electrode along conjugated organic molecules (electron-donating (ED) material). High electron mobility of fullerenes and CNTs further ensures that the solar cell performance is not limited by the electron current density.

A layered single heterojunction configuration with the junction between two dye layers was first introduced by Tang in 1986 for organic solar cells [10]. The first layered single heterojunction between conjugated polymer and carbon nanomaterial was devised by Sariciftci et al. in 1993 [9]. These authors used  $C_{60}$  as an EA carbon nanomaterial [9]. An alternative approach to advanced organic solar cells is to mix ED and EA materials to form dispersed bulk heterojunctions (Fig. 3) [11]. Compared to the layered heterojunction, the dispersed junctions with nanometer-scale feature size can maximize the harvest of photo-generated charges because of the large interfacial area and high cross-section of exciton dissociation. Most commonly used method for fabricating the bulk heterojunction is to spin-coat (or screen-print) a solution of ED and EA materials in an organic solvent onto a

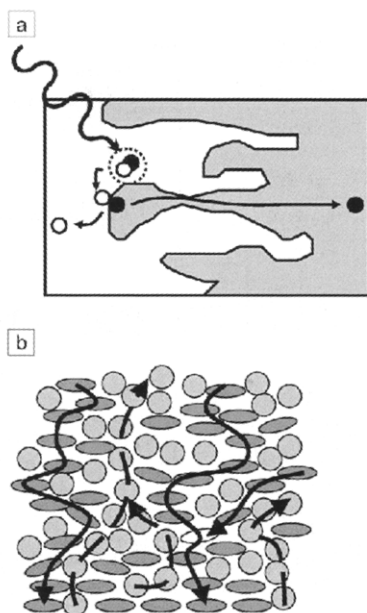


Figure 3. (a) A bulk heterojunction consisting of an entangled region of donor and acceptor materials, as indicated by open and shaded areas. Exciton is indicated by the complex of open and solid circles. (b) A mixed heterojunction shown on the microscopic scale, with percolating conducting pathways formed by acceptor and donor materials. (After Forrest [73].)

substrate. The solution process has great potential for large-area and cost-effective roll-to-roll production of even flexible devices. Various soluble derivatives of the carbon nanomaterials have been developed to promote better morphology of the active layers made by the solution process. Examples include the use of PCBM (1-(3-methoxycarbonyl) propyl-1-phenyl[6,6]C<sub>60</sub>) in organic solar cells based on soluble C<sub>60</sub> derivatives. Sec. 3 presents a comprehensive overview on carbon-based PVs of organic heterojunctions.

## 2. OPTICAL LIMITING PROPERTIES OF CARBON NANOMATERIALS

### 2.1. Mechanisms for optical limiting

Nonlinear optical materials play an important role in optical limiting systems. Depending on the nature of the nonlinearity, the nonlinear optical medium can be divided into two categories [6,12,13]. One is energy-spreading type optical limiting, including self-focusing, self-defocusing, induced aberration, nonlinear refraction, and nonlinear scattering. A properly designed aperture is normally used in front of the detector since the solid-angle of output beam from the medium increases over a nonlinear threshold (Fig. 4(a)–(e)). The other is nonlinear absorbing medium that

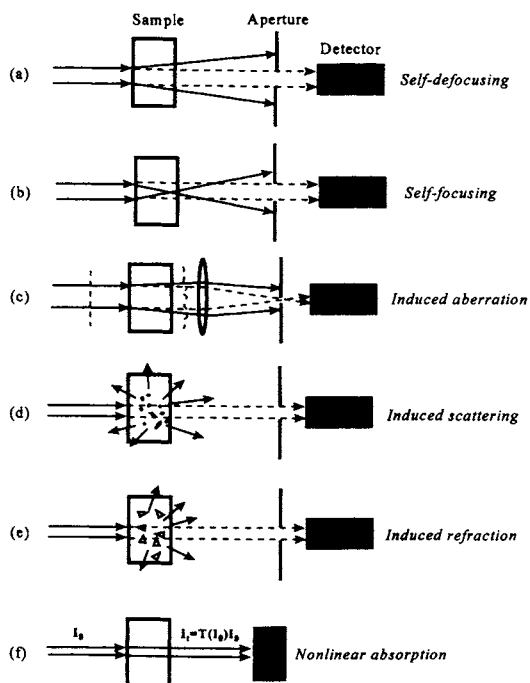


Figure 4. Schematic illustrations of optical limiting designs based on various mechanisms. (After He and Liu [12].)



simply changes the output irradiance at high input signal. Because the medium itself reduces the light intensity in the latter case, there is no need for an extra aperture to selectively collect the beam from the nonlinear absorbing medium as far as the beam size is smaller than the aperture of the detector itself (Fig. 4(f)).

The nonlinear absorbing process can be further explained by two different mechanisms—two-photon absorption (TPA) and excited state absorption (ESA). The TPA process involves molecular transition from the ground state to an excited state through the absorption of two consecutive photons. The first photon brings the system to a virtual state between the ground and excited states and the next photon brings it to the final excited state (Fig. 5(a)). Non-resonant virtual lifetime at the intermediate state is usually much shorter than the laser pulse width and is determined by the uncertainty principle and the energy mismatch between its energy and the input photon energy. With a strong dependence on the intensity (or irradiance) of the light, the TPA process is instantaneous. Inorganic semiconductors were studied as the earliest optical limiter materials, with which TPA is the primary mechanism for the optical limiting process [14]. Recently, certain organic compounds have been demonstrated to show promising results with high TPA cross sections [15,16]. Optical limiters based on the TPA mechanism offer many advantages, including (i) negligible linear absorption loss for a weak signal, (ii) extremely fast temporal response, and (iii) retaining high beam quality for the transmitted signal [12].

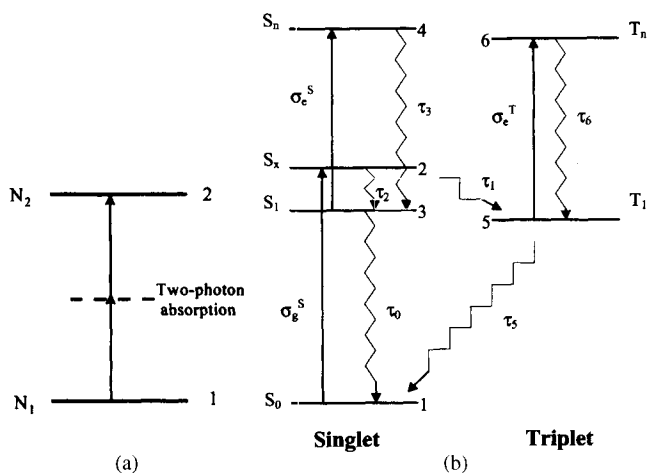


Figure 5. Schematic diagrams of nonlinear absorption mechanisms. (a) Two-photon absorption. (After He and Liu [12].) (b) Excited state absorption.  $S_0$  is the ground state,  $S_1$  the first singlet excited state,  $S_x$  a vibronic level of the first singlet excited state, and  $S_n$  a higher singlet excited state.  $T$  indicates triplet state,  $\sigma$  is absorption cross section and  $\tau$  the lifetime. (After Signorini et al. [6].)

On the other hand, ESA can be considered as a resonant TPA with a finite lifetime of the intermediate state longer than the pulse width. Within each laser pulse, the excited states are populated by the initial interaction with the input pulse and then the final interaction occurs between excited states and the pulse. In this slow cumulative ESA process, the fluence—integrated irradiance over a period of time—is more important than the intensity of the light. Depending on the relative magnitude of absorption cross sections for the ground and excited states, the system could show different nonlinearities. Saturable absorption (SA) occurs, for instance, when the absorption cross section of the excited state ( $\sigma_e$ ) is smaller than that of the ground state ( $\sigma_g$ ), leading to a transparent system. In contrast, absorption increases if  $\sigma_e$  is larger than  $\sigma_g$  and this is called reverse saturable absorption (RSA). Fig. 5(b) shows electronic level structure for the RSA process. While the singlet system is a common model for the RSA process when laser pulses shorter than sub-nanoseconds are used, the intersystem crossing can occur from the first singlet excited state to the triple state. An RSA occurs with large  $\sigma$  of triple excited states and sometimes it is larger than that of the single excited states. Optical limiting solutions containing carbon nanomaterials often show the RSA mechanism [6].

## 2.2. Carbon black suspension

Optical limiting properties of CBS has been extensively investigated since late 1980s, remaining as one of the best found optical limiting systems to date [7,13]. The preparation of CBS is easy and inexpensive, which only requires the dilution of the commercial India ink (black drawing ink) followed by filtration to remove large particles. The CBS solution is typically filtered by a filter with 0.2  $\mu\text{m}$  pore size and the resultant colloidal solution is stabilized by adding surfactant molecules. Fig. 6 shows the optical limiting response to nanosecond (ns) laser pulses for an aqueous CBS, which is comparable to that of  $\text{C}_{60}$  in toluene.

The driving force for optical limiting from CBS arises from nonlinear scattering, involving an avalanche ionization of carbon particles (microplasmas) when they interact with an incident laser pulse and subsequent bubble formation in host liquid (solvent) due to the heat released by expanding microplasmas. Consequently, the optical limiting performance depends on the pulse width of laser, nature of the solvent, solution concentration, and carbon black particle size. As the formation of scattering centers (microplasmas and bubbles) occurs over a period of several nanoseconds, CBS is the most effective for a laser pulse longer than nanoseconds. Vincent et al. [17] have recently obtained interesting optical limiting results with 0.2 ns laser pulses of the pulse energy up to a few hundreds of microjoules at 800 nm. In separate studies carried out by McEwan et al. [18] and Durand et al. [19], respectively, the effect of solvent and the correlation between limiting performance with the boiling point of the solvent were demonstrated. The optical limiting performance of CBS could be enhanced by increasing the concentration of carbon black, though the onset intensity for the optical limiting process showed no dependence on the solution concentration [20]. The nonlinear threshold can, however, be controlled by the particle size in suspensions [20].

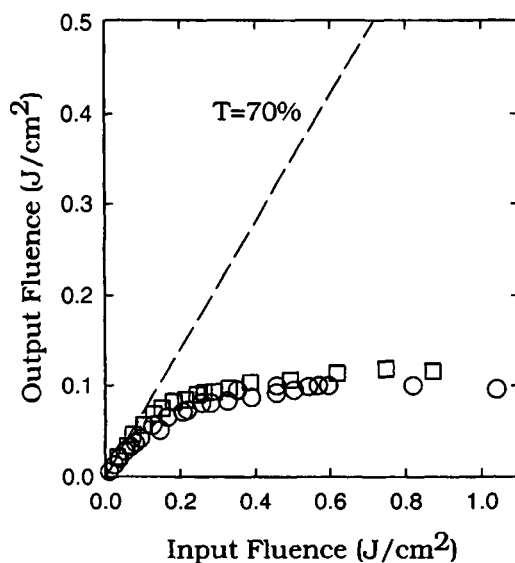


Figure 6. Optical limiting responses of aqueous CBS (□) compared with those of  $C_{60}$  in toluene solution (○) at the same linear transmittance of 70% at 532 nm. (After Sun et al. [7].)

A major drawback associated with the CBS optical limiter is that the breakdown (vaporization) of the carbon particles requires replenishment. For a relatively short operation time, this issue can be resolved by selecting small particles and appropriate solvents to improve the mixing by laser-induced convection currents [21].

### 2.3. Fullerene $C_{60}$

Since the first measurement of its optical limiting properties by Tutt and Kost in 1992 [22],  $C_{60}$  and its derivatives have been studied by many research groups as new optical limiting materials in suspensions, solutions, and solid-state composites [6]. Although a stronger excited-state absorption than the ground-state absorption makes to fulfill the conditions for a broadband RSA,  $C_{60}$ , unlike CBS, shows different optical limiting mechanisms under different conditions. For example,  $C_{60}$  suspended in water or polar organic solvents (alcohol) showed nonlinear scattering whereas  $C_{60}$  dissolved in aromatic solvents (toluene and benzene) exhibited nonlinear absorption [23]. Limiting response of  $C_{60}$  solutions in toluene taken at different wavelengths showed nonlinear absorption behavior over the entire visible region—ESA for short wavelengths (300–600 nm) and TPA for long wavelengths (~700 nm) [24]. Optical limiting performance of a hexakisadduct of  $C_{60}$  (HDTC<sub>60</sub>) with inner 12 triethylene glycols and peripheral 12 decyl chains was found to be greatly improved by the formation the HDTC<sub>60</sub>-Ag nanocomposites [25].

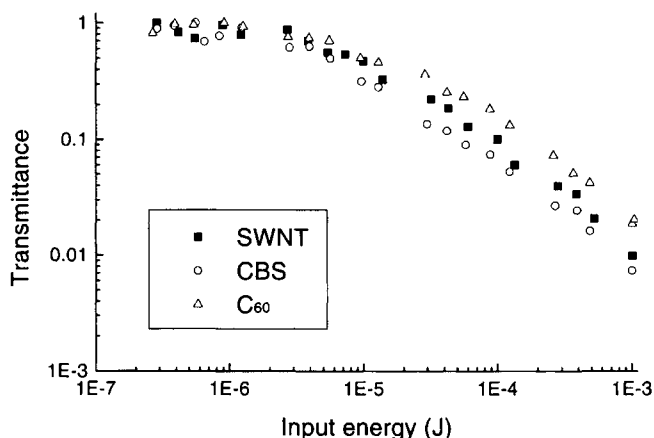


Figure 7. Optical limiting performances of an aqueous SWNT suspension,  $C_{60}$  in a toluene, and CBS in water for a 532 nm laser line. (After Vivien et al. [26].)

One of the shortcomings of liquid-based optical limiting systems is the presence of solvent, which could cause optical inhomogeneities through precipitation and/or convection currents of the solution.  $C_{60}$  in solid-state materials (polymers and inorganic oxide glasses) should provide a better stability. For readers interested in solid-state optical limiting devices based on  $C_{60}$ , we refer to the excellent review by Brusatin and Signorini [23].

## 2.4. Carbon nanotubes

Since pure single-wall carbon nanotubes (SWNTs) and multi-wall carbon nanotubes (MWNTs) are insoluble in any solvent, earlier studies on optical limiting applications of CNTs mainly focused on their suspensions [7]. Fig. 7 shows the comparison of the optical limiting performance for three different carbon-containing benchmark materials, which clearly indicates the strong optical limiting effect from a suspension of SWNTs in toluene at 532 nm laser pulses [26]. Significant optical limiting at 1064 nm has also been demonstrated for the SWNT suspension [26].

With the recent development in carbon nanomaterials and nanotechnology, CNTs (both SWNTs and MWNTs) can now be solubilized by either chemical or physical functionalization [27,28]. For instance, Sun and co-workers solubilized CNTs by attaching them to highly soluble copolymers, such as PPEI-EI (poly(propionylethylenimine-co-ethylenimine)) and poly(vinyl acetate-co-vinyl alcohol), and studied their optical limiting properties (Table 1) [29]. Due to the lack of photo-physical information on the functionalized CNTs, the optical limiting mechanism is still debatable, though it is believed to be dominant by nonlinear absorption. Like  $C_{60}$  suspensions and CBS, CNT suspensions have been demonstrated to show optical limiting properties through nonlinear scattering mechanism under certain

Table 1

Luminescence parameters of PPEI-EI/PVA-VA-bound CNTs in solution.  $\lambda_{\text{EX}}$ , excitation wavelength;  $\Phi$ , luminescence quantum yield;  $\tau$ , lifetime; and  $a$ , absorption cross section. (After Hirsch [27].)

Sample	Solvent	$\lambda_{\text{EX}}$ (nm)	$\phi^1$	$\tau_1$	$\tau_2$	$a_1/a_2$
S-MWNT-PPEI-EI	$\text{CHCl}_3$	632		2.2	5.6	1.2
		400	0.11	2.3	8.0	2.9
	Water	400	>0.03	2.3	8.9	4
S-SWNT-PPEI-EI	$\text{CHCl}_3$	632		1.9	5.8	1.2
		440	0.06			
SWNT-PPEI-EI	$\text{CHCl}_3$	400	>0.003	1.5	7.3	4.2
	Water	365		2.1	9.8	2.3
S-MWNT-PPEI-VA	$\text{CHCl}_3$	365	>0.03	1.6	6.0	7.3

<sup>1</sup>9,10-Bis(phenylethynyl)anthracene as the standard.

circumstances [7]. Despite the mechanistic similarities, CNT suspensions did not show dependency on the size of CNTs (length and diameter) [30] while Mishra et al. [31] showed that solvents with different boiling points affected the limiting response of SWNT suspensions. MWNTs have also been solubilized in organic solvents (e.g. chloroform, toluene) through the reaction of a secondary amine with the carboxylic acid groups bound to nanotubes. The solubilized MWNTs were demonstrated to exhibit good optical limiting performances to both 532 and 1064 nm nanosecond laser pulses [32].

### 3. ORGANIC PHOTOVOLTAIC DEVICES WITH CARBON NANOMATERIALS

#### 3.1. Fullerene as electron acceptors

Certain carbon nanomaterials studied for their use as optical limiters are also used for PV devices. The concept of photoinduced charge transfer at the interface of two semiconducting materials with different ionization energy and electron affinity was introduced for inorganic materials sensitized with organic dyes in the early 1950s [33,34]. Subsequently, these effects were exploited in two-layered organic heterojunction devices based on copper phthalocyanine (CuPc) and a perylene tetracarboxylic derivative (PV) [10]. The important role of the junction between two materials was demonstrated by the insensitivity of  $V_{\text{OC}}$  to a different set of top/bottom electrodes—the  $V_{\text{OC}}$  of CuPc/PV two-layer device differed only by 50 mV or less when a number of metals (In, Al, Cu, and Ag) with different work functions were used as a cathode and indium tin oxide (ITO) served as an anode.

More recently, Sariciftci et al. [8] demonstrated that a mixture of a conducting polymer and a more electronegative molecular semiconductor,  $\text{C}_{60}$ , possesses interesting photoinduced charge transfer properties, including (1) photoinduced optical absorption (PIA) related to  $\pi$ - $\pi^*$  absorption in the conducting polymer, (2) the

presence of conducting polymer cations and  $C_{60}$  anions, and (3) complete quench of the strong photoluminescence of the conducting polymer upon mixing with the  $C_{60}$ . Based on the above findings, these authors fabricated the first bi-layered PV device with a conjugated conducting polymer and  $C_{60}$  in 1993 [9]. A power conversion efficiency (PCE) of 0.04% was obtained under monochromatic (514 nm) illumination with an intensity of about 1 mW/cm<sup>2</sup>. Instead of using conjugated polymers, Xue et al. [35] fabricated layered heterojunctions from a vapor-deposited thin film of small molecules and  $C_{60}$ . They obtained a maximum PCE of  $(4.2 \pm 0.2)\%$  under 4–12 suns simulated AM1.5G illumination [35]. More recently, the same authors fabricated a tandem solar cell consisting of two stacked CuPc/ $C_{60}$  cells with a PCE up to  $(5.7 \pm 0.3)\%$  under 1 sun simulated AM1.5G illumination [36].

Despite the remarkable achievements from the layered heterojunction device with evaporated  $C_{60}$ , its quantum efficiency was still limited by the charge recombination due to a short diffusion length ( $\sim 10$  nm) of photogenerated excitons in the organic donor materials. In particular, the typical absorption length of conjugated polymers is in the order of 100 nm and only 10% of photons absorbed in the polymer layer contributes to the exciton dissociation at the interface between ED and EA materials. Monochromatic external quantum efficiencies (MEQE) only up to 25% have been reported for layered heterojunction devices with  $C_{60}$  [37].

The problem associated with low quantum efficiency due to the short exciton diffusion length of the organic molecules motivated the development of dispersed bulk heterojunction devices [11]. The new device construction entails the random mixing of ED and EA materials by solution processes, including spin-coating and screen printing. Soluble derivatives of  $C_{60}$  (e.g. PCBM (1-(3-methoxycarbonyl)propyl-1-phenyl[6,6] $C_{61}$ )) have been extensively used in the solution processes. Remarkably improved MEQE ( $\sim 70\%$ ) at about 500 nm has been reported for a dispersed heterojunction device based on P3HT (poly(3-hexylthiophene)) and PCBM after post-fabrication annealing and simultaneous external voltage bias [38]. A PCE value up to 3.5% was also demonstrated for the same device with white light (80 mW/cm<sup>2</sup>) (Fig. 8) [38].

The morphology and phase separation of a conducting polymer and PCBM composites randomly mixed by the solution process depend strongly on the solution processing conditions and post-fabrication treatment(s). A study on a bulk heterojunction of MDMO-PPV (poly[2-methoxy-5-(3,7-dimethyl-octyloxy)]-1,4-phenylenevinylene) and PCBM showed the best PCE and MEQE with 80 wt.% PCBM (Fig. 9). Although the  $V_{OC}$  depends less strongly on the PCBM content, a relatively high percentage content (over 67 wt.%) of PCBM is necessary to produce nanoscale phase separation, which reduces charge recombination by delocalizing electrons within the PCBM domains. Further increase in the PCBM content up to 80 wt.% could ensure the percolation of electrons through the PCBM domains.

Apart from PCBM, new  $C_{60}$  derivatives have also been searched in order to improve either the light absorption efficiency [40] or processibility [41,42]. In this context, methanofullerene derived from  $C_{70}$ , [70] PCBM, instead of  $C_{60}$ , was synthesized with a better match to the solar spectrum [40]. While the dispersed heterojunction with [70] PCBM indeed showed the highest EQE, the possible solvent effects on the film

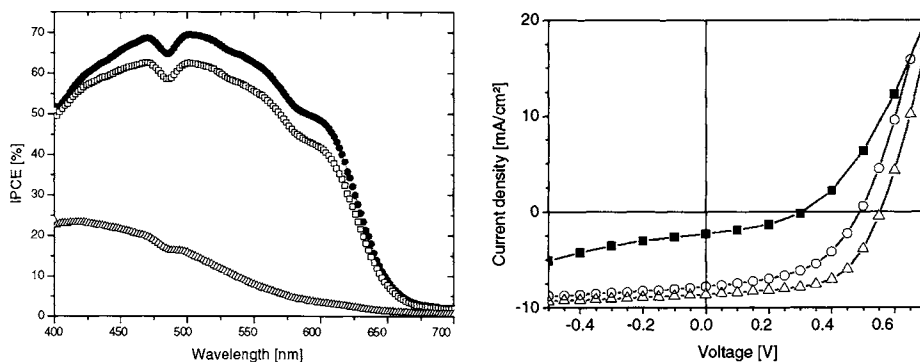


Figure 8. Characteristics of P3HT-PCBM dispersed heterojunction solar cells: (a) External quantum efficiency vs. photoexcitation wavelength; and (b) Current—voltage curves measured under white light with an irradiation intensity of 800 W/m<sup>2</sup>. As-produced solar cell (open triangles in (a) and filled squares in (b)), annealed solar cell (open squares in (a) and open circles in (b)), and cell simultaneously treated by annealing and applying an external voltage (filled circles in (a) and open triangles in (b)). (After Padinger et al. [38].)

morphology should not be underemphasized. Other C<sub>60</sub> derivatives (Fig. 10), including mono-functionalized C<sub>60</sub> (TDC<sub>60</sub> and TC<sub>60</sub>) [41] and anionically or cationically derivatized C<sub>60</sub> [43], were synthesized to improve solubility in a wide variety of organic solvents and self-assembling capability in an aqueous solution through the electrostatic interaction [42].

### 3.2. Polymer and carbon nanotube hybrid solar cells

Despite the high MEQEs (up to 70%) obtained from the dispersed heterojunction between PCBM and conjugated polymers, these PV devices still suffer from low short-circuit currents ( $I_{sc}$ ) (5–10 mA/cm<sup>2</sup>). Recent time-of-flight (TOF) photocurrent measurements of the charge transport in polyfluorene/PCBM [44] and PPV/PCBM [45] composites showed that the electron mobility ( $\mu_e$ ) (10<sup>-4</sup>–10<sup>-3</sup> cm<sup>2</sup>/Vs) was higher than the hole mobility ( $\mu_h$ ) (10<sup>-6</sup> cm<sup>2</sup>/Vs) at the optimized composition for the best cell performance (>75 wt.% PCBM), and that the PCBM-containing organic solar cells are characterized commonly by a percolation of electron currents. Electron mobilities of PCBM ranging from 10<sup>-6</sup> to 10<sup>-1</sup> cm<sup>2</sup>/Vs, calculated from TOF experiments and/or by analyses of field-effect transistors, were reported in literature [46,47], although these values depend somewhat on the experimental techniques used to determine the mobility and the processing conditions.

CNT has been considered to be a good alternative to C<sub>60</sub> (or PCBM) for the dispersed bulk heterojunction organic solar cells. As an extended form of C<sub>60</sub>, CNT is expected to provide higher  $\mu_e$  with a lower percolation threshold. In fact, CNT is

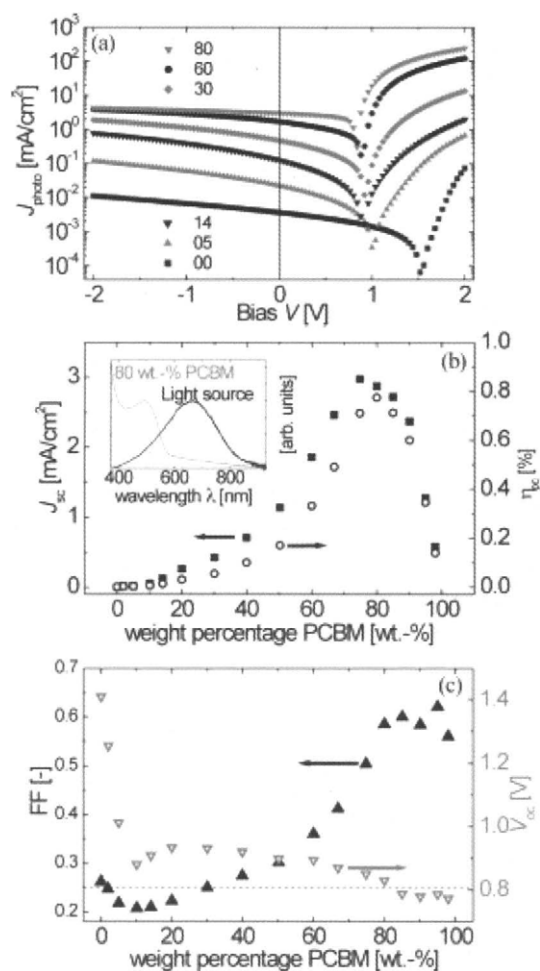


Figure 9. Effect of weight percentage of PCBM within MDMO-PPV on the solar cell characteristics. (a) Photocurrent, (b) short-circuit current density ( $J_{sc}$ ) and PCE ( $\eta_{pc}$ ), and (c) fill factor ( $FF$ ) and open-circuit voltage ( $V_{oc}$ ). Inset in (b) shows spectral overlap between light source used and an 80 wt.% PCBM film. The dotted line in (c) represents  $FF = 0.25$ . (After Duren et al. [39].)

known as an extremely electron-conductive semiconductor—field-effect electron mobility up to  $77000 \text{ cm}^2/\text{Vs}$  was recently reported for a SWNT [48]. The higher carrier mobility allows thicker devices to harvest more photons without sacrificing internal quantum efficiency. The first rectifying heterojunction between MWNTs and a commercially available soluble derivative of poly(*p*-phenylenevinylene) was



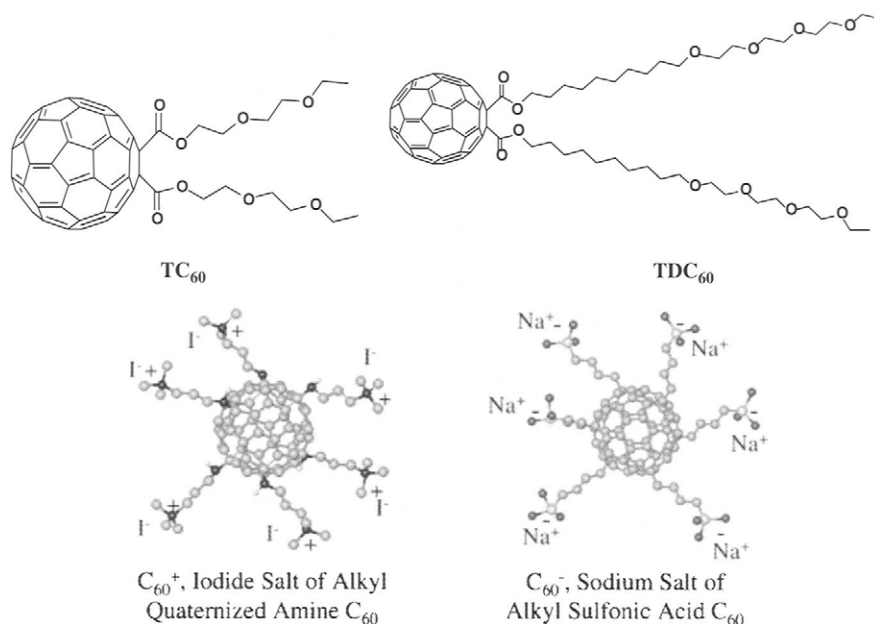


Figure 10. Molecular structures of nano-engineered photo-active materials for organic solar cells. (Top) Mono-functionalized methanofullerene derivatives:  $\text{TDC}_{60}$  contains an inner hydrophobic part (decyl chain) and an outer hydrophilic part (triethylene glycols) and  $\text{TC}_{60}$  is  $\text{C}_{60}$  substituted by hydrophilic chains only. (After Sun et al. [41].) (Bottom) Cationically (+) and anionically (−) derivatized  $\text{C}_{60}$  molecules for the electrostatic self-assembly process. (After Durstock et al. [42].)

reported by Romero et al. in 1996 [49]. The junction was made by filtering a solution of MEH-PPV onto a mat of CNTs. Their results showed that the nonlinear current injection was enhanced by a local field created at the interface between the two materials and the junction responded to light exposure. Another composite based on poly(*m*-phenylenevinylene-*co*-2,5-dioctoxy-*p*-phenylenevinylene) and MWNT prepared by mixing in toluene was reported by Curran et al. in 1998 [50]. It was found that the good wetting between polymer and the surface of MWNTs facilitated the measurements of conductivity, photoluminescence, and electroluminescence. The above work was quickly followed by the first report on the PV effect from MEH-PPV/CNT heterojunction [51]. In order to fabricate the polymer/CNT heterojunction PV cell, Ago et al. [51] spin-coated the PPV precursor (sulfonium salt) onto MWNTs, followed by heat treatment and sputtering Al as the top contact. This device showed an encouraging EQE of 1.8% between 390 nm and 430 nm while the EQE for an ITO/PPV counterpart was only about 0.7%.

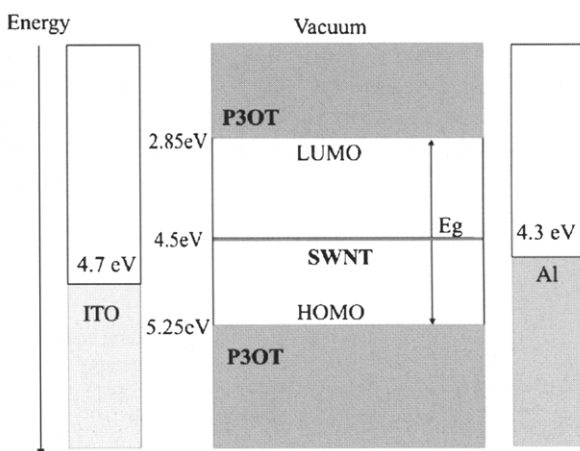


Figure 11. Potential energy diagram relative to vacuum level for a P3OT/SWNT bulk heterojunction under flat band conditions. (After Kymakis et al. [52].)

In somewhat related but independent work, Kymakis et al. [52–54] prepared a heterojunction device with P3OT (poly(3-octylthiophene)) and SWNTs. These authors illustrated the energy band alignment at the junction (Fig. 11) by assuming SWNT to be metallic overall (no bandgap) because there was no attempt to separate metallic and semiconducting CNTs during the preparation (It is not uncommon that the as-grown SWNTs contain both metallic and semiconducting CNTs with a small bandgap of 0.1–0.2 eV [54]). The junction was expected to be fully depleted with a typical polymer thickness of 100–200 nm, leading to a built-in-field of 0.75 eV at the junction determined by the difference between the highest occupied molecular orbital (HOMO) of the P3OT (5.25 eV) and the work-function of the CNT (4.5 eV). An efficient charge transfer at the junction was expected because the dissociation energy of the photo-induced excitons in P3OT is only about 0.4 eV [55]. Indeed, diodes with a structure of Al/P3OT-1 wt.% SWNTs/ITO showed a  $V_{OC}$  of 0.75 V, which is weakly dependent on the work function of various negative electrodes due to Fermi-level pinning between the negative electrode and SWNTs. It was noted that the percolation threshold was about 11 wt.%, and that the best cell performance was achieved with only 1 wt.% SWNTs [53]. However, the solar cell efficiency was lower than 1% in spite of the reasonably high  $V_{OC}$  (0.75 V). In order to improve the cell performance, the same group has recently carried out the dye sensitization of SWNTs in polymer matrix [56]. Improved light absorption in the UV and red region was achieved upon the addition of the dye molecules, leading to an increased  $I_{SC}$  by more than five times.

Highly efficient and light-weight organic solar cells might be an attractive power source for many different space missions. Collaboration among NASA Glenn

Research Center, NanoPower Research Laboratories in Rochester Institute Technology, and Ohio Aerospace Institute has realized P3OT/SWNTs/quantum dots (QDs) composites for solar cell applications [57,58]. Two different QDs, including CdSe and CuInS<sub>2</sub>, have been synthesized so far for the composite device [59]. Fig. 12 shows an idealized energy band diagram for the polymer solar cell with

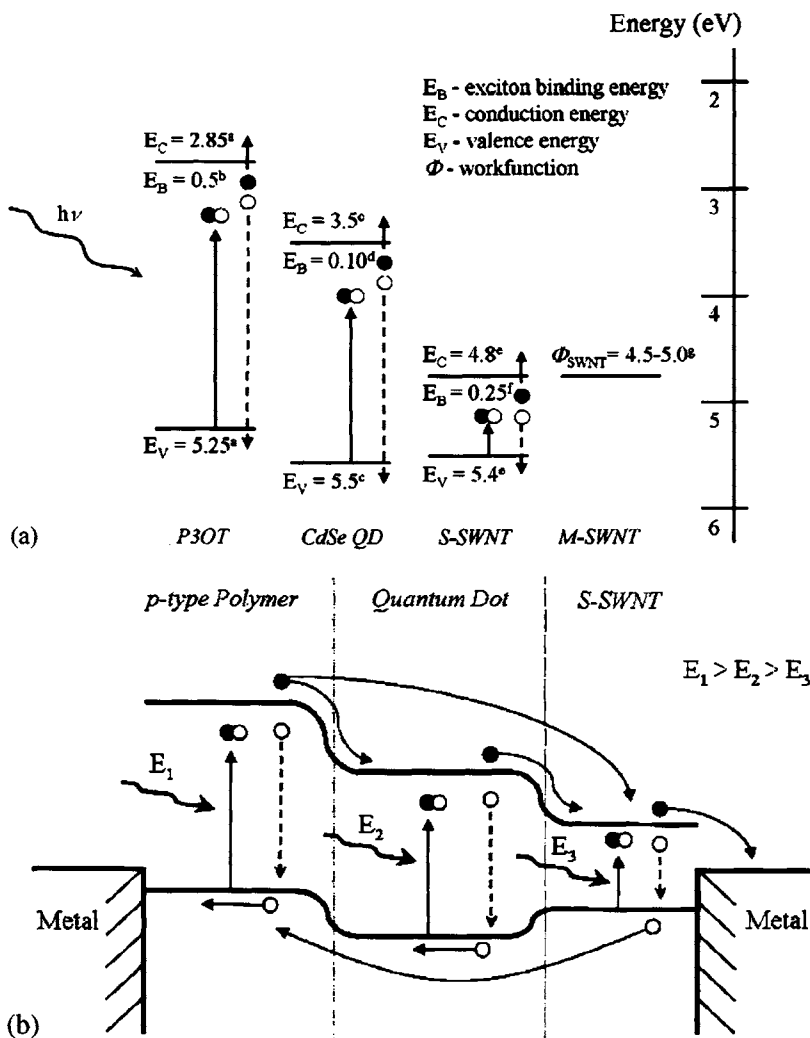


Figure 12. (a) Potential energy diagram relative to vacuum level of P3OT/CdSe quantum dots (QDs)/SWNT bulk heterojunction under flat band conditions; and (b) QD-SWNT-Polymer solar cell equilibrated at the Fermi energy. (After Landi et al. [58].)

QD–SWNT complexes [58]. A similar approach was made by incorporating MWNTs into the BBL (poly(benzimidazobenzophenanthroline ladder)) layer in PPV/BBL bi-layer heterojunction PV devices [60]. The addition of MWNTs sacrificed  $V_{OC}$  while  $I_{SC}$  was doubled.

## 4. OUTLOOK

### 4.1. Optical limiters

Despite its attractive broadband and flat absorption spectrum, CBS is not expected to be a strong optical limiter to sub-nanosecond laser pulses because the microplasma generation and subsequent bubble formation associated with the optical limiting process occur at nanosecond time scale. One recent study demonstrated that it is possible to enhance the optical limiting process with sub-nanosecond laser pulses by sending the pulse to the limiting medium (CBS) repeatedly to generate an accumulative effect [61]. On the other hand,  $C_{60}$  suspensions, with and without the assistance of a surfactant, often suffer a strong precipitation over time, leading to an even poorer optical limiting performance than CBS. A binary solvent mixture, which contains both fullerene-philic and fullerene-phobic components [62,63], has been devised to avoid large precipitates and stabilize the suspension over an extended period of time. Besides, chemically functionalized  $C_{60}$  derivatives have also been extensively studied for optical limiting applications over the past 10 years because of their improved solubility, strong near-IR absorption, and the ease with which solid-state materials can be prepared [23]. Just like modification of  $C_{60}$  has been demonstrated to enhance its optical limiting performance, coating of CNTs, for example, with amorphous  $Si_xN_y$  and SiC was shown to lead to a more stable broader band transmission [64].

### 4.2. Organic solar cells

As an EA component in organic solar cells, carbon nanomaterials have shown their excellent properties—i.e. efficient exciton dissociation, high carrier mobility, and flexible chemistry suitable for solution process. In the meantime, tremendous effort is being made in order to achieve a PCE value over 5% [65]. It is well known that stable organic materials with a low band gap are necessary for an enhanced photon harvesting with a long operation time [66]. Further increase in quantum efficiency could be achieved by improving carrier transport.

Along with the above efforts, several more unique approaches to fabricate dispersed heterojunction organic solar cells with carbon nanomaterials have recently been reported. For example, Lin et al. [67] fabricated solar cells with  $C_{60}$ -containing conjugated polymers while Wu et al. [68,69] synthesized functionalized CNTs (both SWNTs and MWNTs) to avoid the charge loss via exciton recombination. In the latter case, the irregularly formed long diffusion paths can be minimized because of the presence of very uniformly distributed close proximities between EA and ED molecules over the entire composite material. In this regard, vertically aligned EA nanotubes/wire arrays could be very effective in exciton dissociation and carrier transport [70]. Through a similar approach, a reasonably good PV response from a composite of P3HT and mesoporous titania has been

demonstrated [71]. Meanwhile, the potential of vertically aligned CNTs as electrode(s) in PV cells was recently pointed out by Jin and Dai [72], though it will require careful nano-engineering to realize the full potential of the vertically aligned CNTs.

## 5. SUMMARY

In this review, we have highlighted some important studies on the use of carbon nanomaterials in optical limiting and organic PV devices.  $C_{60}$  and CNTs used in the optical limiters as a form of either suspension or solution showed different nonlinear optical behavior. While  $C_{60}$  suspensions limit transmitted light by nonlinear scattering,  $C_{60}$  solutions showed nonlinear absorption mechanism. CBS as a benchmark material has limited flexibility due to the lack of chemical variations of carbon black even though a simple and inexpensive preparation makes it attractive to commercial applications. On the contrary,  $C_{60}$  and CNT can be chemically modified and composited with different materials to allow the construction of solid-state optical limiting devices.

Current organic solar cell technology requires highly conductive EA nanomaterials to promote exciton dissociation at the interface between the ED organic material and the nanomaterials. In the case of bulk dispersed heterojunction device, there is a conductive carrier path percolated through organic matrix to electrons freed from excitons. While there are many on-going research projects on the stability of composite materials with carbon nanomaterials, new architectures suggested for organic solar cells with improved performance require more advanced engineering of the carbon nanomaterials.

**Acknowledgment:** The authors gratefully acknowledge the National Aeronautics and Space Administration, Ohio Aerospace Institute, AFRL/ML, WBI, Dayton Development Collation, and University of Dayton for their financial support.

## REFERENCES

1. H. W. Kroto, J. R. Heath, S. C. O'Brien, R. F. Curl and R. E. Smalley, *Nature* **318** (1985) 162.
2. S. Iijima, *Nature* **354** (1991) 56.
3. D. M. Guldi and N. Martin, *Fullerenes: From Synthesis to Optoelectronic Properties*, Kluwer Academic Publishers, Boston, 2002.
4. M. Meyyappan, *Carbon Nanotubes: Science and Applications*, CRC Press, Boca Raton, 2005.
5. W. Andreoni, *The Physics of Fullerene-Based and Fullerene-Related Materials*, Kluwer Academic Publishers, Boston, 2000.
6. R. Signorini, R. Bozio and M. Prato, *Fullerenes: From Synthesis to Optoelectronic Properties*, Eds. D. M. Guldi and N. Martin, Kluwer Academic Publishers, Boston, 2002, pp. 295–326.
7. Y.-P. Sun, J. E. Riggs, K. B. Henbest and R. B. Martin, *J. Nonlin. Opt. Phys. Mat.* **9** (2000) 481.

8. N. S. Sariciftci, L. Smilowitz, A. J. Heeger and F. Wudl, *Science* **258** (1992) 1474.
9. N. S. Sariciftci, D. Braun, C. Zhang, V. I. Srdanov, A. J. Heeger, G. Stucky and F. Wudl, *Appl. Phys. Lett.* **62** (1993) 585.
10. C. W. Tang, *Appl. Phys. Lett.* **48** (1986) 183.
11. J. J. M. Halls and R. H. Friend, *Clean Electricity from Photovoltaics*, Eds. M. D. Archer and R. Hill, Imperial College Press, London, 2001, pp. 377–445.
12. G. S. He and S. H. Liu, *Physics of Nonlinear Optics*, World Scientific, New Jersey, 1999.
13. E. W. Van Stryland, D. J. Hagan, T. Xia and A. A. Said, *Nonlinear Optics of Organic Molecules and Polymers*, Eds. H. S. Nalwa and S. Miyata, CRC Press, Boca Raton, 1997, pp. 841–860.
14. J. M. Ralston and K. R. Chang, *Appl. Phys. Lett.* **15** (1969) 164.
15. M. Albota, D. Beljonne, J.-L. Brédas, J. E. Ehrlich, J.-Y. Fu, A. A. Heikal, S. E. Hess, T. Kogej, M. D. Levin, S. R. Marder, D. McCord-Maughon, J. W. Perry, H. Röckel, M. Rumi, G. Subramaniam, W. W. Webb, X.-L. Wu and C. Xu, *Science* **11** (1998) 1653.
16. B. A. Reinhardt, L. L. Brott, S. J. Clarson, A. G. Dillard, J. C. Bhatt, R. Kannan, L. Yuan, G. S. He and P. N. Prasad, *Chem. Mater.* **10** (1998) 1863.
17. D. Vincent, S. Petit and S. L. Chin, *Appl. Opt.* **41** (2002) 2944.
18. K. J. McEwan, P. K. Milsom and D. B. James, *Proc. SPIE-Int. Soc. Opt. Eng.* **3472** (1998) 42.
19. O. Durand, V. Grolier-Mazza and R. Frey, *Opt. Lett.* **23** (1998) 1471.
20. K. Mansour, M. J. Soileau and E. W. Van Stryland, *J. Opt. Soc. Am. B* **9** (1992) 1100.
21. D. Vincent, *Nonlin. Opt.* **21** (1999) 413.
22. L. W. Tutt and A. Kost, *Nature* **356** (1992) 225.
23. G. Brusatin and R. Signorini, *J. Mater. Chem.* **12** (2002) 1964.
24. S. V. Rao, D. N. Rao, J. A. Akkara, B. S. DeCristofano and D. V. G. L. N. K. Rao, *Chem. Phys. Lett.* **297** (1998) 491.
25. N. Sun, Z. Guo, L. Dai, D. Zhu, Y. Wang and Y. Song, *Chem. Phys. Lett.* **356** (2002) 175.
26. L. Vivien, E. Anglaret, D. Riehl, F. Bacou, C. Journet, C. Goze, M. Andrieux, M. Brunet, F. Lafonta, P. Bernier and F. Hache, *Chem. Phys. Lett.* **307** (1999) 317.
27. A. Hirsch, *Angew. Chem. Inter. Ed.* **41** (2002) 1853.
28. T. Lin, V. Bajpai, T. Ji and L. Dai, *Aust. J. Chem.* **56** (2003) 635.
29. J. E. Riggs, D. B. Walker, D. L. Carroll and Y.-P. Sun, *J. Phys. Chem. B* **104** (2000) 7071.
30. P. Chen, X. Wu, J. L. Sun, W. Ji and K. L. Tan, *Phys. Rev. Lett.* **82** (1999) 2548.
31. S. R. Mishra, H. S. Rawat, S. C. Mehendale, K. C. Rustagi, A. K. Sood, R. Bandyopadhyay, A. Govindaraj and C. N. R. Rao, *Chem. Phys. Lett.* **317** (2000) 510.
32. L. Liu, S. Zhang, T. Hu, Z. Guo, C. Ye, L. Dai and D. Zhu, *Chem. Phys. Lett.* **359** (2002) 191.
33. A. G. Gol'dman and I. A. Akimov, *Zhur. Fiz. Khim.* **27** (1953) 355.
34. R. C. Nelson, *J. Opt. Soc. Am.* **46** (1956) 13.

35. J. Xue, S. Uchida, B. P. Rand and S. R. Forrest, *Appl. Phys. Lett.* **84** (2004) 3013.
36. J. Xue, S. Uchida, B. P. Rand and S. R. Forrest, *Appl. Phys. Lett.* **85** (2004) 5757.
37. L. A. A. Pettersson, L. S. Roman and O. Inganäs, *J. Appl. Phys.* **86** (1999) 487.
38. F. Padinger, R. S. Rittberger and N. S. Sariciftci, *Adv. Func. Mater.* **13** (2003) 85.
39. J. K. J. van Duren, X. Yang, J. Loos, C. W. T. Bulle-Lieuwma, A. B. Sieval, J. C. Hummelen and R. A. J. Janssen, *Adv. Func. Mater.* **14** (2004) 425.
40. M. M. Wienk, J. M. Kroon, W. J. H. Verhees, J. Knol, J. C. Hummelen, P. A. van Hal and R. A. J. Janssen, *Angew. Chem. Int. Ed.* **42** (2003) 3371.
41. J. Li, N. Sun, Z.-X. Guo, C. Li, Y. Li, L. Dai, D. Zhu, D. Sun, Y. Cao and L. Fan, *Synth. Met.* **137** (2003) 1527.
42. M. F. Durstock, R. J. Spry, J. W. Baur, B. E. Taylor and L. Y. Chiang, *J. Appl. Phys.* **94** (2003) 3253.
43. Y. Chi, J. B. Bhonsle, T. Canteenwala, J. Shiea, B.-J. Chen and L. Y. Chiang, *Chem. Lett.* **5** (1998) 465.
44. R. Pacios, J. Nelson, D. D. C. Bradley and C. J. Brabec, *Appl. Phys. Lett.* **83** (2003) 4764.
45. S. A. Choulis, J. Nelson, Y. Kim, D. Poplavskyy, T. Kreouzis and J. R. Durrant, *Appl. Phys. Lett.* **83** (2003) 3812.
46. G. H. Bauer and P. Würfel, *Organic Photovoltaics: Concepts and Realization*, Eds. C. Brabec, V. Dyakonov, J. Parisi and N. S. Sariciftci, Springer, New York, 2003, pp. 118–158.
47. V. D. Mihailetschi, J. K. J. Duren, P. W. M. Blom, J. C. Hummelen, R. A. J. Janssen, J. M. Kroon, M. T. Rispens, W. J. H. Verhees and M. M. Wienk, *Adv. Func. Mater.* **13** (2003) 43.
48. T. Durkop, S. A. Getty, E. Cobas and M. S. Fuhrer, *Nano Lett.* **4** (2004) 35.
49. D. B. Romero, M. Carrard, W. De Heer and L. Zuppiroli, *Adv. Mater.* **8** (1996) 899.
50. S. A. Curran, P. M. Ajayan, W. J. Blau, D. L. Carroll, J. N. Coleman, A. B. Dalton, A. P. Davey, A. Drury, B. McCarthy, S. Maier and A. Strevens, *Adv. Mater.* **10** (1998) 1091.
51. H. Ago, K. Petritsch, M. S. P. Shaffer, A. H. Windle and R. H. Friend, *Adv. Mater.* **11** (1999) 1281.
52. E. Kymakis, I. Alexandrou and G. A. J. Amaratunga, *J. Appl. Phys.* **93** (2003) 1764.
53. E. Kymakis, I. Alexandrou and G. A. J. Amaratunga, *Synth. Met.* **127** (2002) 59.
54. E. Kymakis and G. A. J. Amaratunga, *Organic Photovoltaics: Mechanisms, Materials, and Devices*, Eds. S. Sun and N. S. Sariciftci, CRC Press, Boca Raton, FL, 2005, pp. 351–365.
55. E. M. Conwell and H. A. Mizes, *Phys. Rev. B* **51** (1995) 6953.
56. E. Kymakis and G. A. J. Amaratunga, *Sol. Energy Mater. Sol. Cells* **80** (2003) 465.
57. S. G. Bailey, S. L. Castro, B. J. Landi, H. J. Ruf, R. P. Raffaele, *Proceedings of 19th European Photovoltaic Solar Energy Conference and Exhibition WIP-Munich and ETA-Florence, Munich, Florence, 2004*, pp. 26–29.
58. B. J. Landi, S. L. Castro, H. J. Ruf, C. M. Evans, S. G. Bailey and R. P. Raffaele, *Sol. Energy Mater. Sol. Cells* **87** (2005) 733.
59. S. L. Castro, S. G. Bailey, R. P. Raffaele, K. K. Banger and A. F. Hepp, *Chem. Mater.* **15** (2003) 3142.

60. E. E. Donaldson, M. F. Durstock, B. E. Taylor, D. W. Tomlin, L. C. Richardson and J. W. Baur, *Proc. SPIE* **4465** (2001) 85.
61. N. M. Barbosa Neto, C. R. Mendonça, L. Misoguti and S. C. Zilio, *Appl. Phys. B* **78** (2004) 1.
62. Y.-P. Sun and C. E. Bunker, *Nature* **365** (1993) 398.
63. Y.-P. Sun, B. Ma, C. E. Bunker and B. Liu, *J. Am. Chem. Soc.* **117** (1995) 12705.
64. K. C. Chin, A. Gohel, H. I. Elim, W. Ji, G. L. Chong, K. Y. Lim, C. H. Sow and A. T. S. Wee, *Chem. Phys. Lett.* **383** (2004) 72.
65. S. Sun and N. S. Sariciftci, *Organic Photovoltaics: Mechanisms, Materials, and Devices*, CRC Press, Boca Raton, FL, 2005.
66. N. S. Sariciftci, *Mater. Today* **7** (2004) 36.
67. T. Lin, L. Dai, G. Wallace, A. Burrell and D. Officer, *Polymer Preprints* **43** (2002) 98.
68. W. Wu, J. Li, L. Liu, L. Yanga, Z.-X. Guo, L. Dai and D. Zhu, *Chem. Phys. Lett.* **364** (2002) 196.
69. W. Wu, S. Zhang, Y. Li, J. Li, L. Liu, Y. Qin, Z.-X. Guo, L. Dai, C. Ye and D. Zhu, *Macromolecules* **36** (2003) 6286.
70. B. Kannan, K. Castelino and A. Majumdar, *Nano Lett.* **3** (2003) 1729.
71. K. M. Coakley, Y. Liu, C. Goh and M. D. McGehee, *MRS Bull.* **30** (2005) 37.
72. M. H.-C. Jin and L. Dai, *Organic Photovoltaics: Mechanisms, Materials, and Devices*, Eds. S. Sun and N. S. Sariciftci, CRC Press, Boca Raton, FL, 2005, pp. 579–597.
73. S. R. Forrest, *MRS Bull.* **30** (2005) 28.



## Chapter 18

### Carbon nanotube and epoxy composites for military applications

Amanda M. Schrand<sup>a</sup> and Tia Benson Tolle<sup>b</sup>

<sup>a</sup>Department of Chemical and Materials Engineering  
and University of Dayton Research Institute, University of Dayton,  
300 College Park, Dayton, OH 45469, USA

<sup>b</sup>AFRL/MLBC, Air Force Research Laboratory,  
Wright-Patterson AFB, Dayton, OH 45433, USA

Carbon is of great engineering importance because of its ability to exist in many structural forms (e.g. amorphous carbon, graphite, diamond, carbon nanotube (CNT)). Depending on how the carbon atoms are arranged, their properties vary, for this reason, carbon has found many applications in military platforms. Although CNTs may be viewed as a graphite sheet that is rolled up into a nanoscale tube form, CNTs, unlike graphite, can exhibit semiconducting or metallic behavior. They also possess a high surface area per unit weight, high electrical and thermal conductivity, and good mechanical properties. On the other hand, epoxy is known for its ability to withstand high temperatures; chemical and corrosion resistance; high tensile strength, modulus and adhesion; and low cure shrinkage. Composites made from CNTs and epoxy have many potential applications due to their exceptional mechanical, electrical, and thermal properties, which are characteristic of the individual components with potential synergetic effects. Much of the available information on development of CNT/epoxy composites for military applications focuses on their use as reinforcements in structural materials, coatings, or integrated constituents in multifunctional or active materials. To realize the full potential of CNT/epoxy composites, however, many improvements need to be made in nanomaterials characterization for understanding the differences between nano and bulk counterparts, and tailoring of the interface between the matrix and nanomaterial. One major area of ongoing research is improving the interfacial characteristics of nanocomposites through chemical modifications to realize the ultimate properties predicted by theoretical models. The aim of this chapter is to summarize the recent research and development of CNT/epoxy structural composites that hold interest for military applications, along with some discussion on the component materials and structure–property characterization.

#### 1. INTRODUCTION

##### 1.1. Carbon fibers

Although carbon exists only in several forms (e.g. amorphous carbon, graphite, diamond, carbon nanotube (CNT)), many of the overall properties of a given carbon

material depend, apart from its atomic arrangement, also on its mesoscopic morphology. This provides a broad basis for the development of various carbon materials (e.g. carbon filaments, carbon fibers) with different properties from the same carbon constituents.

Vapor-grown carbon fibers have often been chosen as a precursor model fiber system for studying the basic role of nanoscale fibers in polymer systems [1,2]. Commercially produced carbon fibers can be prepared over a wide range of diameters (from less than 1000 Å to more than 100 µm), but generally have diameters exceeding 1 µm, and therefore they cannot take advantage of the enhanced mechanical, thermal, optical, and structural properties of nanostructured carbons [1]. Experimental results from Fan et al. [3] mention that vapor-grown carbon fibers with smaller diameters were stronger than those with larger diameters. Although carbon fibers are significantly larger than single-walled carbon nanotubes (SWNTs) with diameters on the order of 1 nm, carbon nanofibers with diameters 5–100 nm and lengths of 5–500 nm have been produced [2–4]. Carbon nanofibers are available commercially, but they are sold in small quantities relative to carbon fibers [1]. Having circular cross-sections with and without a hollow core [1], these carbon nanofibers are of particular interest because they are similar to CNTs in size, length, and structure. Because the focus of this chapter is given to CNTs, the readers are referred to some recent articles to explore the useful properties of carbon nanofibers alone and in composites [5–9].

## 1.2. Carbon nanotubes

CNTs are the most recent addition to the growing members of the carbon family. They can be viewed as a graphene sheet rolled up into a nanoscale tube form to produce the so-called SWNTs. There may be additional graphene tubes around the core of a SWNT to form multi-walled carbon nanotubes (MWNTs). These elongated nanotubes usually have a diameter in the range of a few angstroms to tens of nanometers and a length of several micrometers up to millimeters with both ends of the tubes normally capped by fullerene-like structures containing pentagons. Depending on their diameter and helicity of the arrangement of carbon atoms in the walls, CNTs can exhibit excellent electrical, thermal, and mechanical properties. These interesting properties make CNTs very attractive for a variety of potential applications. Since the discovery of CNTs by Iijima in 1991, there has been considerable interest in CNTs and their composites [10] compared to carbon nanofibers or traditional carbon fibers. However, most current theoretical [11–16] investigations on CNT nanocomposites primarily involve SWNTs due to their simplistic structure.

Both SWNTs and MWNTs are now readily available in relatively large quantities through simple, efficient, and inexpensive syntheses [17]. The production of MWNTs as yarns and sheets in scalable quantities for continuous high-rate production also has been accomplished [18,19]. By introducing twist during dry-state spinning, multi-ply, torque-stabilized two-ply yarns with impressive properties were produced that are not degraded by overhand knotting like ordinary fibers: strength of 460 MPa, electrical conductivity of 300 S/cm at room temperature, density of

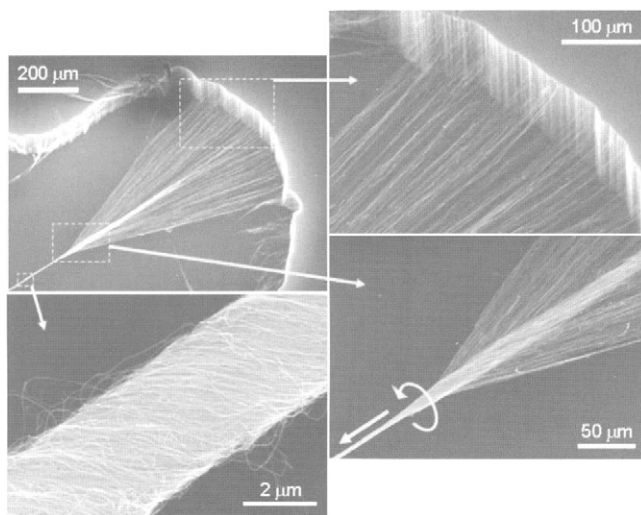


Figure 1. SEM images showing the structures formed during the draw twist process, which produces MWNT yarn. Partially bundled nanotubes are being simultaneously pulled and twisted from the forest wall. The draw twist process was interrupted and the sample was transferred to an SEM for image recording. (After Zhang et al. [18].)

0.8 g/cm<sup>3</sup>, failure stress up to 575 MPa/cm<sup>3</sup>, toughness of 20 J/g, and Poisson's ratio up to 4.2 can be produced. They are also not degraded by overhand knotting like ordinary fibers [18]. Fig. 1 shows the scanning electron microscope (SEM) images of CNT yarn being drawn and twisted from a "forest" in which the nanotubes were grown from a substrate in a manner resembling tree trunk in a dense bamboo forest with nearly identical heights [18]. The diameter and lengths of these MWNTs are approximately 10 nm and 10 μm, respectively [18]. It was suggested that small bundles of individual nanotubes move in and out of different bundles in the forest leading to three-dimensional connectivity, which is important to this spinning process [18].

In the case of transparent, self-supporting, meter-long, electronically conductive MWNT sheets, up to 10 m of sheet per minute can be produced by drawing and winding MWNTs from a forest onto a rotating plastic cylinder [19]. As in the previous production of MWNT yarns, intermittent bundling within the forest where individual nanotubes migrate from one bundle to another seems to be important. Fig. 2 shows some examples of MWNT forest conversion and assembly into sheets. The properties of a sheet produced from a 245 μm high forest include: a thickness of 18 μm with an areal sheet density of approximately 2.7 μg/cm<sup>2</sup> and a volumetric density of 0.0015 g/cm<sup>3</sup>. Highly oriented 50-nm thick sheets have densities of 0.5 g/cm<sup>3</sup>, resistivities of 700 Ω/in<sup>2</sup> in the draw direction; work functions of 5.2 eV; and when stacked (Fig. 2D), have tensile strengths up to 465 MPa/(g/cm<sup>3</sup>), which is comparable to aforementioned nanotube yarns (575 MPa/(g/cm<sup>3</sup>)). These sheets have been demonstrated to

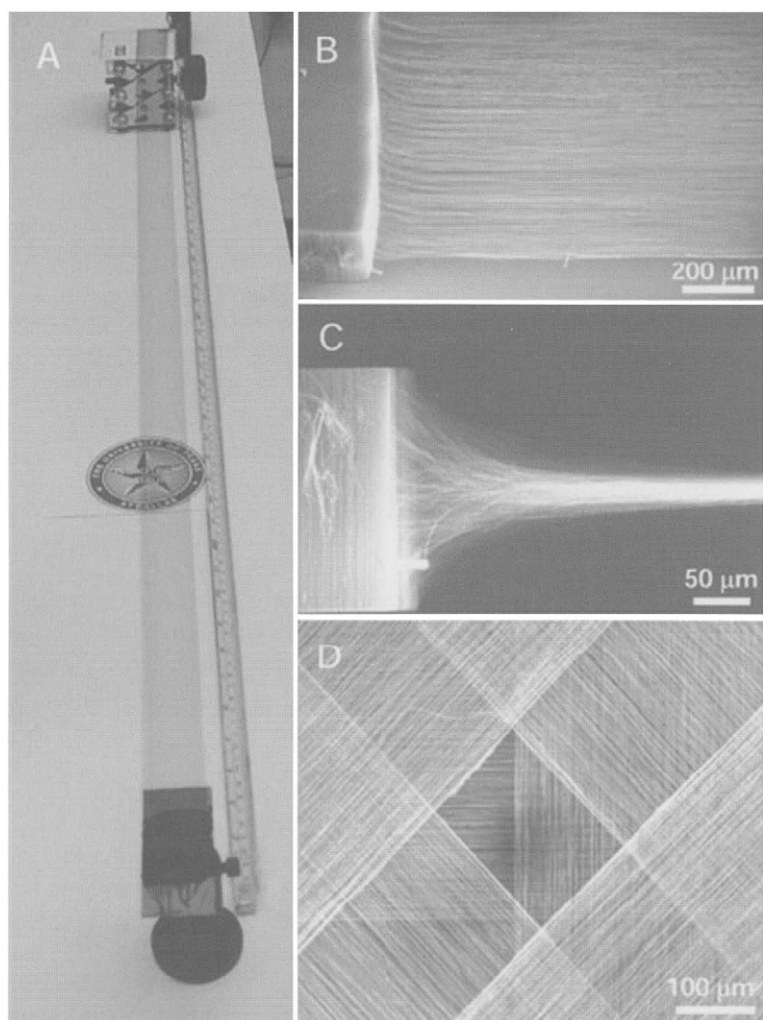


Figure 2. MWNT forest conversion and assembly into sheets. (A) Photograph of a self-supporting 3.4-cm wide, meter-long MWNT sheet that has been hand drawn from a nanotube forest at an average rate of 1 m/min. Its transparency is illustrated by the visibility of the NanoTech Institute logo beneath the MWNT sheet. (B) SEM image at a 35° angle with respect to the forest plane, capturing an MWNT forest being drawn into a sheet. (C) SEM image showing the cooperative 90° rotation of MWNTs in a forest to form a sheet. (D) SEM image of a two-dimensionally re-reinforced structure fabricated by overlaying four nanotube sheets with a 45° shift in orientation between successive sheets. The dark circle is the shadow of the in-lens detector. (After Zhang et al. [19].)

be useful for microwave bonding of plastics and for making transparent, highly elastomeric electrodes; planar sources of polarized broadband radiation; conducting appliqué; and flexible organic light-emitting diodes [19]. Additional experiments will focus on polymer infiltration to further increase the strength and applications of nanotube-reinforced materials and ongoing research into SWNT films and fibers is currently being pursued [19].

### 1.3. Epoxy

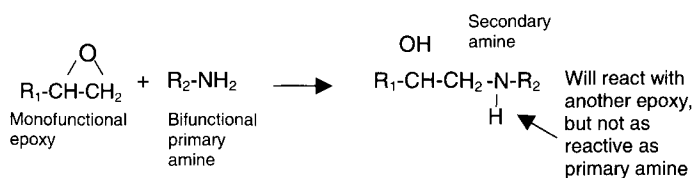
Among many polymer matrices used in composites, thermosets are most widely used in military applications and epoxy represents a workhorse matrix for aerospace composites. Epoxies have reached this position due to their well-known ability to withstand moderately high temperatures ( $T_g$  between 200 and 225 °C), good chemical and corrosion resistance, high tensile strength (10–18 ksi), high modulus, high adhesion, low percent shrinkage in cure, excellent adhesion to various substrates, and reasonably low toxicity [20,21]. For these reasons, epoxies have been the matrix of choice for many aerospace and military composites [22a–b].

The three basic parts of an epoxy resin formulation are the base epoxy resin, curing agents, and modifiers, which all contribute to the physical and mechanical properties of the resulting composite [21a–b]. The three primary classes of epoxies used in composite applications are phenolic glycidyl ethers, aromatic glycidyl amines, and cycloaliphatics [21a–b], as shown in Table 1. These base epoxy resins will react with a large number of chemical species called cure agents or hardeners with the most common classes being amines, amine derivatives, and anhydrides [21a–b]. The simplest epoxy formulations combine a single epoxy resin with a single curative. More complex formulations can include multiple resins; modifiers for toughness, flexibility, or flame/smoke suppression; inert fillers for producing color; and multiple curing agents that drive specific reactions at certain times [21a–b]. The development of carbon fiber-reinforced epoxy materials has reached a level of maturity through developments for military and aerospace applications. Today, such composites are base-lined on many satellites, military aircraft, and

Table 1

Three basic parts of epoxy resin are base resin, curing agents, and modifiers; “epoxy resin” = “epoxy resin (Part A)” + “curing agent (Part B)” + catalysts, diluents, and modifiers (optional).

Epoxy resins (Part A)	Curing agents (Part B)	Modifiers (optional)
Phenolic glycidyl ethers	Amines	Tougheners
Aromatic glycidyl amines	Amidoamines	Diluents
Cycloaliphatics	Polyamides	Catalysts
	Ionic curing agents	Plasticizers
	Anhydride	Pigments
	Polysulfides, thiols, mercaptans	Dyes



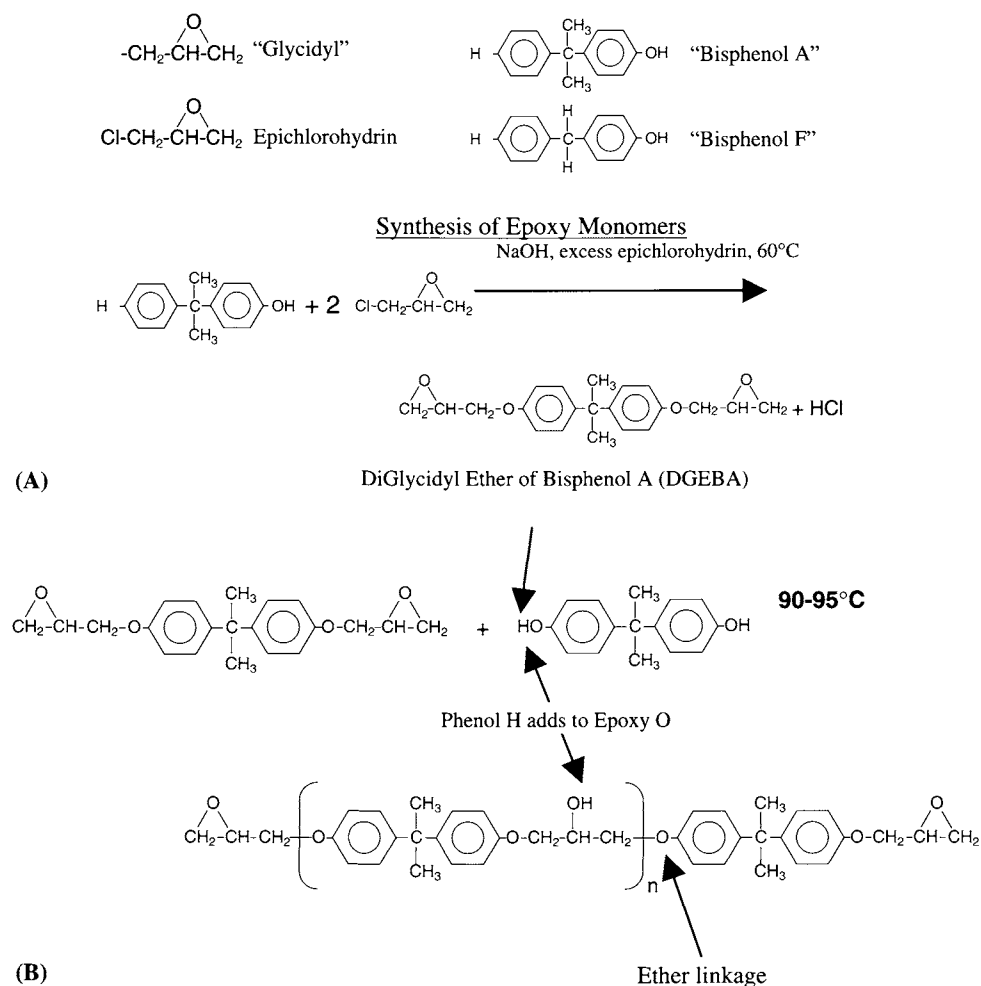
Scheme 1. Reactive groups involved in step polymerization of epoxy. (After May or Klosterman [21b, 25].)

commercial aircraft as well as being transitioned to many non-aerospace applications [22c–d]. Processes for curing and manufacturing have been optimized in industry. In addition to autoclave curing, which relies upon heat and pressure for polymerization, alternative curing methods such as radiation, ultraviolet, infrared, magnetic field [23], or electron beam [24] can be used.

Epoxies can exist in many physical forms from low viscosity liquids to high melting point solids. This makes them convenient for many types of processing and applications with a wide variety of curing agents or with itself via homopolymerization [21a–b]. For these reasons, epoxies are used in many aerospace applications such as adhesives, coatings, encapsulates, casting materials, potting compounds, and binders for flooring panels, ducting, vertical and horizontal stabilizers, wings, and fuselages as well as for high performance aerospace structures [21a–b]. The primary crosslinking reaction occurs through an epoxide group, as shown in Schemes 1 and 2 [21b, 25].

#### 1.4. Carbon Nanotube/Epoxy Composites

Carbon fibers have been used for their strength and lightness to reinforce polymeric materials for a variety of applications ranging from tennis racquets to aircraft parts. Because of their high resilience, large surface area, and good electronic properties, many believe that CNTs may work well in addition to, or become preferred alternative to, carbon fibers for creating novel carbon/polymer (e.g. epoxy) nanocomposites with enhanced mechanical and electrical properties. A number of methods ranging from extrusion to molding have been devised to prepare CNT and epoxy nanocomposites. The potential for multifunctional composites based on the thermal and electrical properties of CNTs motivates much research today. The high specific strength, specific stiffness, and good chemical resistance of carbon-reinforced composites also makes them attractive for structural applications for a variety of products [26]. The primary application of carbon-reinforced composites in aerospace applications is for improving the performance of lightweight, high-strength carbon-fiber structural composites as the current structural properties imparted by aerospace grade carbon fibers is already quite high. Along with much research on other polymer matrices, including poly(methyl methacrylate) (PMMA) [27–31], polypropylene (PP) [31–36], polystyrene (PS) [37–40], polyurethane (PU) [41–43], phenolic [44,45], and other polymers [31,35,36,45–60], reinforced with carbon nano-platelets [61], nanoclays [45,57,58,62–64], or nanosilicates [45,58],



Scheme 2. Common chemical reaction schemes for base epoxy resins and curing agents (A) epoxy resin terminology for diglycidyl ether of bisphenol A (DGEBA) or F (DGEBF); (B) higher molecular weight analogs of DGEBA where a phenol H add to an epoxy O to create an ether linkage. (After May or Klosterman [21b, 25].

there are recent review articles on CNT/epoxy composites [64–73a–c]. At the present time, however, the predicted enhancement in properties of nanoscale-reinforced carbon/epoxy composites has yet to be realized.

### 1.5. Interface engineering

Surface and interface play an important role in controlling the properties of a broad range of composite materials including CNT/epoxy nanocomposites. Similar

to conventional composites, improvements that could enhance CNT/epoxy composites include: optimal bonding between the epoxy and CNT at the interface, reduced MWNT interwall sliding under tension, uniform CNT dispersion, increased CNT alignment, and reduced polymer shrinkage during processing [74,75]. Unlike aerospace grade carbon fibers, modification of the surface of carbon nanotubes may represent significant impact to the nanotubes itself. Interface tailoring represents the opportunity to impart significant modifications to their performance. The functionalization of CNTs through surface treatments has become of great importance for tailoring interface properties [76]. If CNTs behave similarly to carbon fibers, the adhesive strength at the interface and interlaminar shear strength of the composite could be improved with increased oxygen-containing functional groups [77–81]. Typically reported oxidative treatments include dry/gaseous, anodic, liquid phase/chemical, plasma [82], and whiskerization, as well as carbon and polymer coatings [26,79,80,83–86]. Recent oxidative treatments have included: NaOH, NaHCO<sub>3</sub>, Na<sub>2</sub>CO<sub>3</sub>, H<sub>2</sub>SO<sub>4</sub>, NH<sub>4</sub>HCO<sub>3</sub>, (NH<sub>4</sub>)<sub>2</sub>CO<sub>3</sub>, HNO<sub>3</sub>, H<sub>3</sub>PO<sub>4</sub>, NaHCO<sub>3</sub>, and mixtures of F<sub>2</sub>/O<sub>2</sub> gases. Among them, acid oxidization (e.g. nitric acid) is the predominant type of surface treatment used because it removes amorphous carbon impurities such as carbon black and graphite leading to a mixture of covalent and ionic bonds between the surface of the nanotube and epoxy matrix, possible for scale up applications [78]. The functional groups that form after oxidation can include carboxyl, hydroxyl, carbonyl, and carboxylic groups among others, which are expected to chemically interact with epoxy [79,81].

The role of the interface between fiber and matrix is key for many properties of the resultant composite. This concept is well understood in the aerospace composites field and provides the foundation from which most of the current research is drawn. For example, weak adhesion leads to debonding under load and very strong interactions lead to brittleness in some cases [73a, 81]. For this reason and others, research on carbon fiber/epoxy composites as well as CNT/epoxy composite interfacial properties continues. There does, however, seem to be a direct correlation between surface chemistry and interfacial interaction. Surface functionalization has been reported to aid in the dispersion of CNTs within polymers, a key challenge for composites in which certain morphologies are desired [81b]. The use of SWNTs “bucky paper”, similar to a nanomesh fabric of SWNTs, in epoxy composites may improve some of these challenges by allowing a controlled nanostructure with high nanotube loading [87–91]. SWNT/polymer composites are also being used as nanocomposite fibers through melt spinning [92] and as spray coatings [93], which introduces variability in their interfacial characteristics.

An alternative way to enhance the interface strength may be the presence of a helical conformation of the polymer around the nanotube [94]. This strength may result from the molecular entanglement of two phases and force the long-range order of the polymer. However, the interface is not the only structural issue that exists in CNT/epoxy composites. The structure of the CNT itself introduces a variable. SWNTs have distinct chiralities that dictate their dielectric properties and MWNTs have been reported to have several morphologies [Ref Huang S and Dai L]. Selection of the particular carbon nanotubes must be based on the desired final



composite properties. For CNT/epoxy composites consisting of MWNTs, only very weak van der Waals forces exist to link the individual graphene shells together [95]. Even without imposing any large forces, the inner shells could rotate and slide freely. Therefore, using MWNTs in composites may not allow the maximum strength to be achieved. In this case, the use of SWNTs may prove beneficial to the overall composites properties.

Uniform dispersion of CNTs throughout the matrix is also a challenge. Previous studies with epoxy/carbon fiber composites have found that surface oxidation of the carbon fibers leads to better dispersion and mechanical properties in epoxy matrices [78,96]. However, oxidation-induced damage to the CNTs can lead to structural defects, which decrease the potential reinforcement strength and final properties of the composite [78]. Therefore, future studies need to investigate the optimization of surface oxidative treatments. Better ways to disperse CNTs in epoxy composites are currently being pursued through end functionalization without damaging the defect-free surface of the CNTs [97,98].

## **2. STRUCTURE-PROPERTY RELATIONSHIPS**

### **2.1. Structure and property characterization**

Compared with the vast amount of publications on the epoxy/carbon fiber composites [26,79–86,99–109], structure–property relationships for CNT/epoxy composites have been much less discussed in the literature [20,52,77,78,110–113]. In this section, experiment characterization methods used for epoxy and CNT composites are described, though reference is also made to some complementary work on carbon fiber/epoxy composites as appropriate.

Characterization of nanoscale morphology is difficult to capture with current characterization tools and more than one approach is typically required to gain sufficient insight upon which to base descriptions and models, while the models themselves are being modified [113c]. X-ray, light, and neutron scattering studies are uniquely suited to capturing averaged information about morphology real-space imaging such as transmission electron microscopy (TEM) complements scattering data with specific local morphology information. As neither method alone provides information on a sufficient volume of material from which to draw overall morphology conclusions, especially in light of the multiple combinations and scales on which morphologies can occur, their combined use is of value.

SEM is a useful tool for visualizing the fiber or CNT at resolutions down to approximately 1 nm [113b]. The majority of SEM studies involve the interpretation of composite fracture surfaces, though SEM has also been used by many groups to qualitatively describe the changes in fiber morphology after surface oxidation [26,79,80,85]. Fracture studies provide valuable insight into interface and toughening mechanisms and have been used extensively in conventional composite research. The fracture surface of 5wt% SWNT bundle/epoxy composites, that were loaded axially in tension and compression, was examined in detail as shown in Fig. 3. For example, 5 wt% SWNT/epoxy bundle composites were loaded axially in tension and compression and the fracture surface was examined in detail with SEM as shown in Fig. 3 [111].

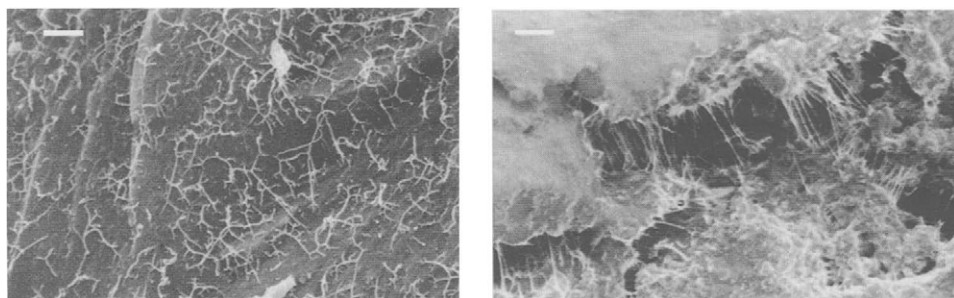


Figure 3. (a) SEM micrograph showing a network of single-walled CNT aggregates collapsed on the surface of a fractured nanotube–epoxy composite. (b) SEM micrograph of single-walled CNT bundles stretched across a crack opening in a nanotube–epoxy composite. Scale bars = 1  $\mu\text{m}$ . (After Ajayan et al. [111].)

A typical fracture surface consisted of a network of SWNT bundles that appeared to have been pulled out of the matrix and then collapsed back to cover the surface, as shown in Fig. 3a. In contrast, other areas of the fracture surface displayed fully stretched SWNTs as shown in Fig. 3b. Both the load transfer to the CNTs and falling apart of the bundles suggest that nanotube sliding is responsible for the fracture and that the low modulus features of the SWNT bundles and not the axial modulus of individual tubes is what controls the mechanical stability and strength of the composites. To prepare CNT/epoxy nanocomposites with desirable mechanical properties, CNTs must not only be optimally bonded to the matrix, but the CNTs themselves must maintain intact.

Epoxy filled with oxidized MWNTs leads to a stronger interfacial bonding than its pristine nanotube counterpart, as indicated by the SEM fracture surface images in Fig. 4 [114]. Poor adhesion between the pristine CNTs and epoxy matrix is evident by the nanotube pullout seen in Fig. 4a. In the epoxy/oxidized nanotube composites, however, the nanotubes break instead of slipping, suggesting that the interfacial adhesion is strong (Fig. 4b).

TEM is another powerful tool for examining the internal structure and interfaces of ultrathin composite sections (typically <100 nm) at very high magnifications and resolutions. Efforts are currently underway to increase the resolving capability to 0.5 Å, approximately one-third the size of a carbon atom, a key dimension for atomic level research [115b]. TEM can provide complementary information to SEM such as size, morphology, distribution, and interface phenomena of CNTs in an epoxy matrix. In addition, the TEM can be modified for visualizing in-situ mechanical deformations, such as the buckling and collapse of CNT/epoxy composites [115], the fracture of SWNTs in an epoxy resin under axial tension [116], interfacial shear strength (IFSS) [117], and the results of surface treatment on dispersion and interfacial characteristics [78].

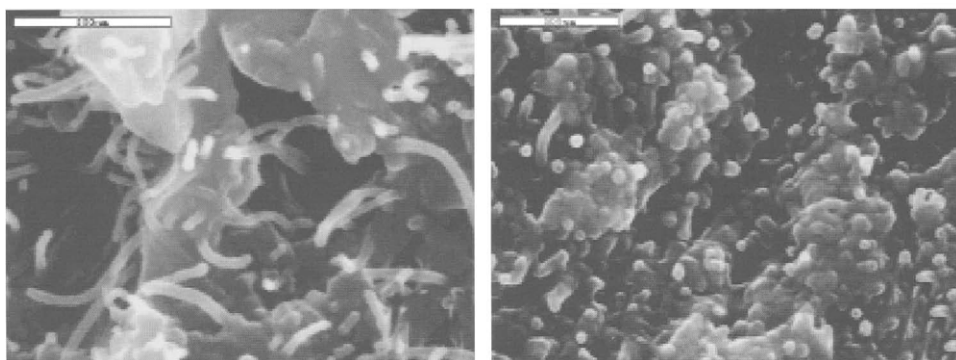


Figure 4. Fracture surfaces of composites filled with (a) pristine and (b) oxidized 6% MWNTs. They show the effect of MWNT surface groups on interfacial bonding. Scale bars on the images correspond to 500 nm. (After Breton et al. [114].)

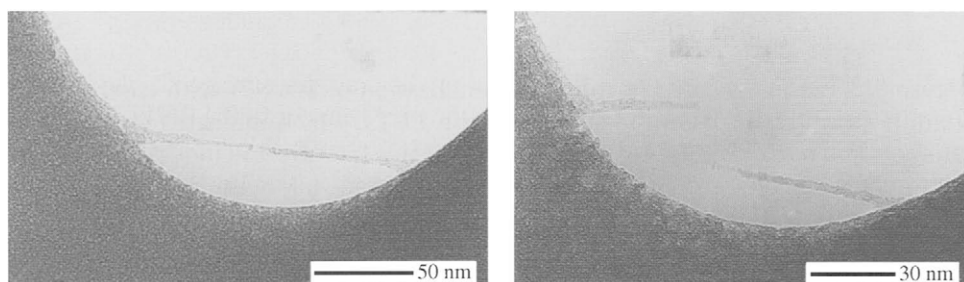


Figure 5. Experimental evidence of the full real-time rupture of a SWNT, as seen in the TEM. The expansion of elliptical holes in the epoxy film results in a tensile force within a bridging nanotube rope: (a) polymer wets the nanotube rope very well, and upon the application of stresses, the rope draws the polymers out; (b) fracture of the rope occurs in tension within the polymer hole region rather than in shear within the gripping polymer region at the ends of the bundles. (After Lourie and Wagner [116].)

For example, the fracture of SWNTs in an epoxy resin under axial tension can be observed by TEM [116]). The polymer matrix at both ends of the well-aligned SWNT bundles extensively deforms under tension (Fig. 5). The fracture of the CNTs occurs in tension within the polymer hole region rather than in shear within the gripping polymer region at the ends of the CNT bundles, providing evidence for strong polymer–CNT wetting and interfacial adhesion in this particular case.

Similar to the SEM study mentioned earlier [114], improved interfacial adhesion was observed in MWNT/epoxy composites where the nanotubes were first oxidized by refluxing with triethylenetetramine [78]. The resulting composites were investigated with TEM imaging, in which oxidation of the CNTs was associated with the reduced agglomeration and improved interfacial interaction as shown in Fig. 6 compared to MWNTs only treated with a mixture of sulfuric and nitric acids (Fig. 7).

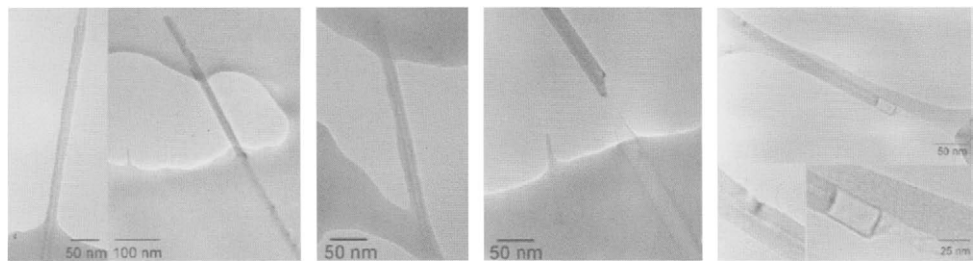


Figure 6. TEM image after further functionalization of MWNTs with triethylenetetramine (a) matrix covers the surface of the CNTs, which indicates an improved interaction. (b, c) Nanotubes should improve the fracture toughness by bridging micro-cracks and pores in the matrix. (d, e) Telescopic pullouts substantiate the evidence of improved interactions. (After Gojny et al. [78].)

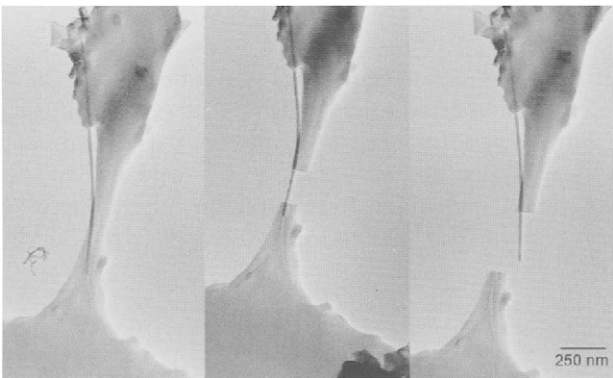


Figure 7. A weak interaction still exists between an epoxy matrix and MWNTs treated with oxidizing inorganic acids, which leads to nanotube pullout. (After Gojny et al. [78].)

## 2.2. Mechanical properties

In what follows, we will summarize recent work on the mechanical properties of CNT/epoxy composites, including tensile strength, yield strength, impact strength, Young's modulus, IFSS, shear stress, fracture toughness, and hardness.

### 2.2.1. Strength and stiffness

The extremely high modulus and strength predicted for carbon nanotubes has inspired some to explore the translation of such properties into polymer based composites [73a]. It has been demonstrated that the mechanical strength and stiffness increased significantly by incorporating even a small amount of CNTs in epoxy-based composites [23,118–120]. As seen in Fig. 8, the Young's modulus and yield

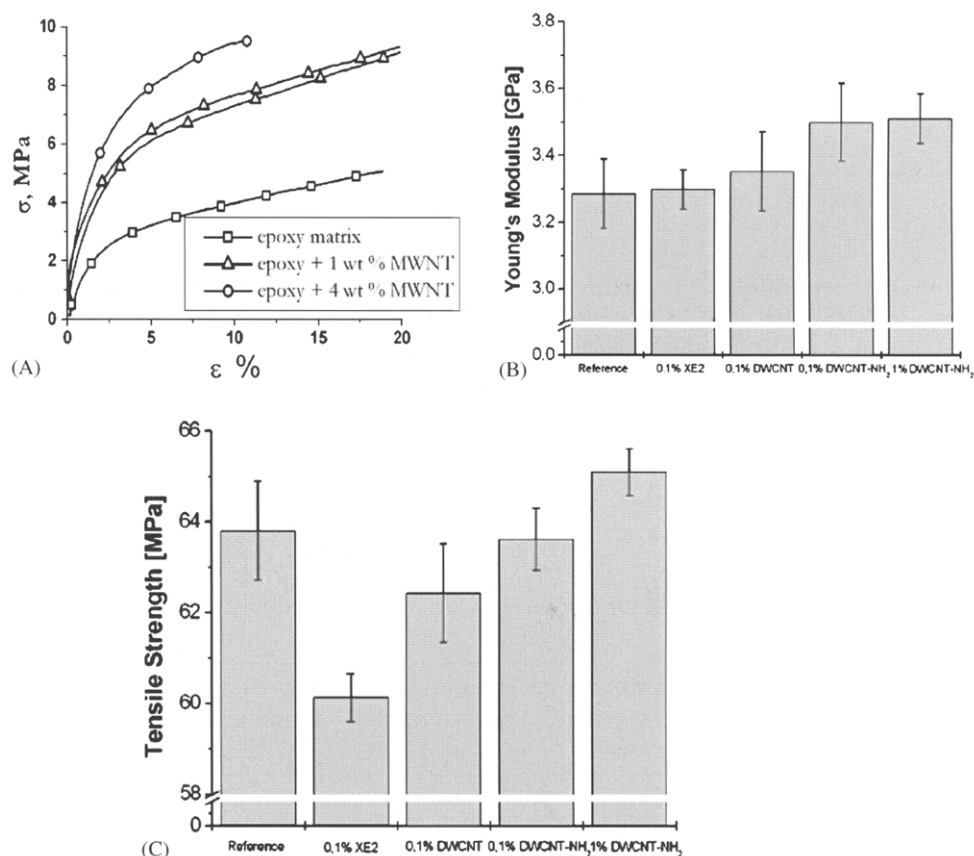


Figure 8. (a) Tensile test stress–strain curves of the resin and its composites and the resulting Young's modulus at different strain levels. Mechanical properties of nanoparticle-reinforced composites (b) Young's modulus, and (c) tensile strength. (After Allaoui et al. [118].)

strength of 1 and 4 wt% CNT/epoxy composites were doubled and quadrupled compared to pure resin samples [118].

Another study showed increases in many additional mechanical properties in bisphenol A MWNT/epoxy composites, as shown in Table 2 [96]. Composites composed of 0.5 wt% CNTs treated with 35 wt%  $\text{HNO}_3$  for 30 min (No. 3) compared to either control (No. 1) or 0.5 wt% untreated CNTs (No. 2) showed higher tensile strength, elongation at break, flexural strength, and impact toughness.

Because the orientation of fibers affects fiber-dominated properties, the exploration of methods to align or control the orientation of carbon nanotubes within polymers have recently become of interest. Composite properties have been reported to be further enhanced by curing in a magnetic field [23]. As shown in Table 3, simply

Table 2

Summary of mechanical properties of CNT/epoxy composites bisphenol A epoxy mixed with 0.5wt% CNTs.

No.	$\sigma_t$ (MPa)	$E_t$ (GPa)	$\epsilon(\%)$	$\sigma_f$ (MPa)	$E_f$ (GPa)	$\alpha_k$ (N/mm)
1	77	2.7	3.6	199	3.1	1.5
2	88	2.8	4.5	224	3.4	2.6
3	96	2.7	7	244	3.1	2.8

*Note:* The majority of desirable properties are for the treated [3] nanotube-based composite. 1, control; 2, untreated; 3, treated.

$\sigma_t$ , tensile strength (MPa);  $\sigma_f$ , flexural strength (MPa);  $E_t$ , tensile modulus (GPa);  $E_f$ , flexural modulus (GPa);  $\epsilon$ , elongation at break (%);  $\alpha_k$ , impact toughness (N/mm).

*Source:* After Li et al. [96].

Table 3

Compressive response of polymer cured in a magnetic field at a magnetic strength of 21 T.

Material	Magnetic cure time (h)	Compressive strength (MPa)	Gain/loss in strength (%)	Compressive modulus (GPa)	Gain/loss in modulus (%)
Neat SC-15	0	58.57	—	1.46	—
Neat SC-15	3	70.46	20.3	2.17	48.63
1% CNF	0	68.35	16.7	2.19	50
1% CNF	3	81.74	39.56	2.26	54.79
1% CNT	0	97.93	67.2	2.69	84.25
1% CNT	3	132.34	126.09	3.89	166.44

*Source:* After Mahfuz et al. [23].

by curing the neat polymer in a uniform magnetic field significantly enhanced the strength and stiffness by 20 and 49%, respectively over the neat control (not magnetically cured) polymers [23]). A more pronounced increase in mechanical properties was realized when CNT/epoxy carbon nanofiber (CNF) composites were cured under high magnetic fields of 21 teslas (T). Quasi-static compression results showed that composite strength and stiffness increased by 126 and 166%, respectively, compared to the neat epoxy control system under zero field [23]. These studies suggest that additional procedures are likely to be developed to further increase the mechanical properties of nanotube-based composites at many stages of their fabrication.

### 2.2.2. Interfacial shear strength and stress

The role of the interface is critical for structural properties. Developing and utilizing any composite not only requires quality constituents, but also strong interfacial bonding and a favorable mechanism of load transfer [38]. In CNT and polymer composites, stresses are transferred from the nanotubes to the matrix through an interface, which has properties distinct from both the fiber and the matrix. Therefore, good adhesion between carbon nanotube and matrix is crucial for high performance carbon nanotube-reinforced composites. The adhesion between the reinforcing nanotubes and the matrix determines the amount of load, transferred through shear, that can be distributed among the nanotubes, ultimately determining the maximum load-bearing capacity of the composite structures (121). Several methods are available to interrogate the adhesion between matrices and aerospace carbon fibers; however, the size of the carbon nanotubes poses significant challenges for such characterization [121b-c].

A fragmentation test has been used to determine the IFSS between a single carbon fiber and epoxy matrix in dog-bone-shaped specimens [79–81]. However, the existing tools are inapplicable to the manipulation of CNTs due to their small sizes. Fortunately, a few novel ways of measuring IFSS in CNT/epoxy composites have been recently developed.

There are also methods that have been developed to measure the interface between single fibers and a polymeric matrix through the use of a unique cruciform specimen. However, the size and handling challenges associated with carbon nanotubes currently make adapting such a test to this class of fibers extremely difficult [121d]. Atomic force microscopy, microfabrication facilities, and new microinstrumentation fabrication may provide tools more appropriate for characterization of interfaces on the nanoscale [121c].

The relative modulus between the constituents of composites, such as an epoxy and an aerospace carbon fiber, plays strongly into final composite properties. Although epoxies are considered to have low shrinkage among other polymer matrices, compressive stresses in the CNTs can cause them to bend and kink [115]. Therefore, intrinsic differences related to the brittleness of epoxy compared to the flexibility of CNTs can sometime cause difficulties in realizing optimal composite properties. CNT/epoxy IFSS can be approximated by using a scanning probe microscope (SPM) and TEM tip to draw out single CNTs bridging holes [28]. Both SWNT bundles and MWNTs were imaged and measured for interfacial adhesion providing

a direct way to measure the shear strength of CNT/polymer composites, which was found to inversely correlate with the embedded length of the CNT. In Fig. 9, a MWNT with a diameter of 8.2 nm is bridging a hole in an epoxy matrix (Image A). The image to the right (B) is an image of the same specimen following partial pullout by means of a SPM tip. The larger arrow shows the direction of the tip movement and the small arrow indicates the empty cylindrical hole left behind after partial pullout. A force–distance curve is obtained in (C) that shows the dependence of the lateral force on distance traveled by the SPM tip. The force–distance curve for an empty hole scanned by the SPM is also shown on the same plot. Fig. 10 also shows that the IFSS inversely correlated with the embedded length of the CNT.

### 2.2.3. Fracture toughness and hardness

Although the general trends and summaries for the properties of fracture toughness and hardness of surface-modified carbon nanotubes in epoxy-based composites have yet to be validated, the resulting composite properties have been observed to increase upon the addition of carbon nanotubes. For example, an enhanced fracture toughness was found with the addition of low levels of double-walled carbon nanotubes (DWNs) either “as-is” or in an amino-functionalized form ( $-\text{NH}_2$ ) in epoxy composites as shown in Fig. 11 [119].

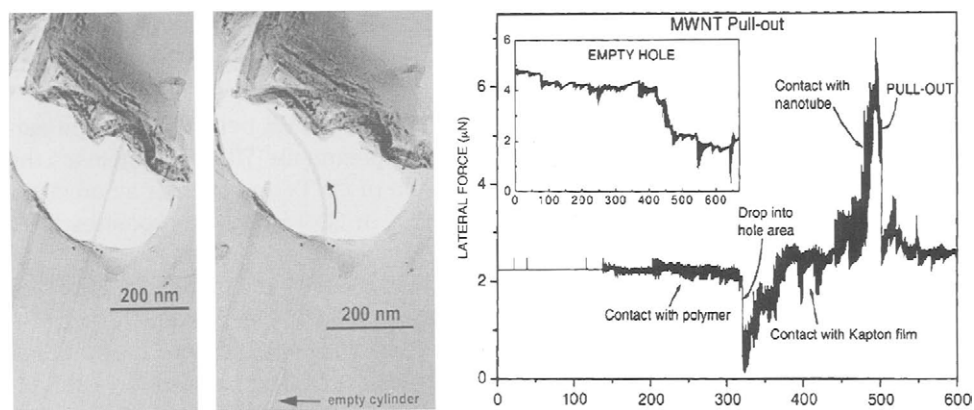


Figure 9. TEM images of a multi-walled CNT crossing a hole in an epoxy resin matrix. (A) TEM image of nanotube bridging matrix hole. The bridging nanotube in these images has a diameter of 8.2 nm. (B) TEM image of the same specimen following partial pullout by means of an SPM tip. The larger arrow shows the direction of the tip movement; the small arrow indicates the empty cylindrical hole left behind after partial pullout. (C) Force–distance curve obtained for this specimen shows the dependence of the lateral force on distance traveled by the SPM tip. The force–distance curve for an empty hole scanned by the SPM tip is also shown on the same plot. (After Cooper et al. [28].)



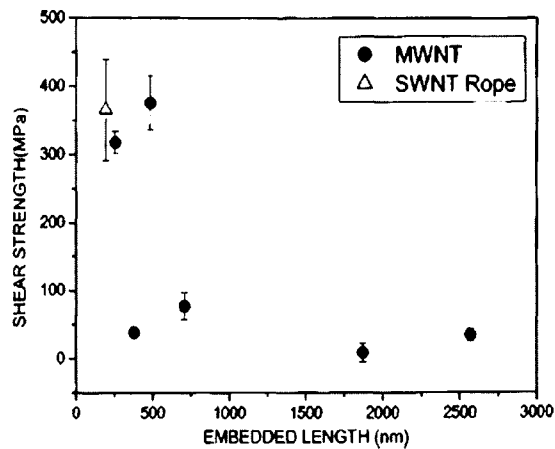


Figure 10. Correlation between shear strength and embedded nanotube length. (After Cooper et al. [28].)

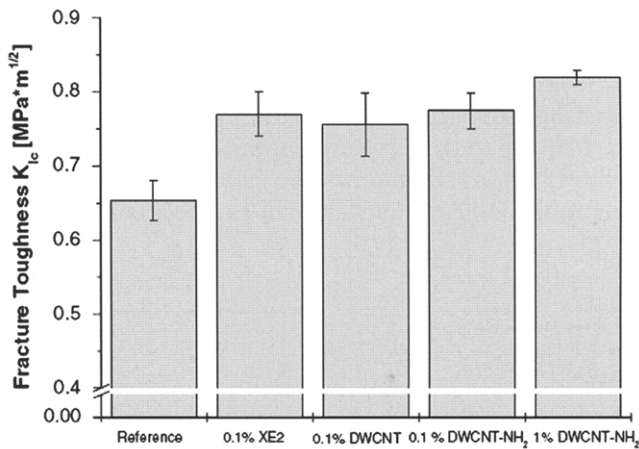


Figure 11. The fracture toughness showed a general increase caused by the nano-scaled reinforcements. Shown are the experimentally obtained  $K_{IC}$  values. (After Gonjy et al. [119].)

Similarly, epoxy nanocomposites containing MWNTs treated by oxyfluorination at 100 °C possess a greater fracture toughness ( $K_{IC}$ ) value of 3.05 MPa m<sup>1/2</sup> compared to 2.45 MPa m<sup>1/2</sup> for untreated CNT composites [122]. The fracture toughness of linseed DGEBF epoxy/fluorinated SWNT composites increased by approximately 43% after

the addition of 0.20 wt% CNTs, whereas it decreased after adding 60–80 wt% of epoxidized linseed oil into the epoxy resin mixture [123].

However, several studies have provided somewhat disappointing results where the mechanical properties of the composites were reduced after the addition of nanotubes. For example, epoxy composites containing 2 wt% MWNTs had increased hardness but reduced strengths compared to control resin [124], as exemplified in Fig. 12. The decrease of flexural strength was unlikely to be caused by CNTs as many experimental studies have demonstrated that nanotubes are very strong. It was hypothesized that the cause of the strength reduction with the addition of the nanotubes may be due to structural non-homogeneity and/or the presence of a weakly bonded interface. The hardness was likely improved due to the high aspect ratio and mesh-like reinforcement, which would not necessarily improve the flexural strength that is mainly determined by the nanotube/matrix interface strength. In a separate study, the influence of solvents for CNT dispersion on the mechanical properties of SWNT/epoxy composites was examined in terms of Vicker's hardness [125]. Composites prepared from *N,N*-dimethylformamide (DMF) had the lowest hardness compared to its ethanol and acetone counterparts likely due to the presence of residual solvent. In any discussion of toughness it is important to note that a polymer's yield strength and flow ability is time and temperature dependent, as is its relaxation and response to stress. Different test rates will illicit different responses and crack propagation behavior within polymer based composites, therefore caution should be exercised when comparing data obtained through impact tests with fracture toughness tests.

As can be seen from the above discussion, the mechanical properties of epoxy resins, including tensile strength, yield strength, impact strength, Young's modulus, IFSS, shear stress, fracture toughness, and hardness, may be improved significantly by compositing with CNTs, as summarized in Table 4. Such benefits may not translate to carbon nanotube-modified conventional carbon fiber-reinforced composites

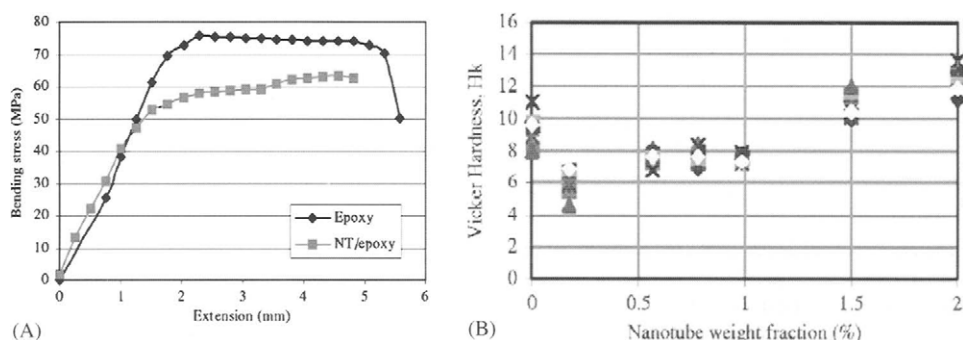


Figure 12. Results from the (A) flexural strength test and (B) hardness (measured by a micro-hardness tester) of CNT composites with different CNT weight fractions. A total of 10 points were taken on each of the CNT composites in order to get average readings as represented by various symbols at each wt% in (B). (After Lau and Shi [124].)

Table 4

Summary of maximum mechanical properties of epoxy/CNT composites.

Modulus	Strength	Stress	Hardness	Impact/fracture properties	Reference
465 MPa	6 MPa (yield)	—	—		[118]
3.51 GPa	65 MPa (tensile)	—	—	7.65% fracture strain, 0.82 MPa m <sup>1/2</sup> for $K_{IC}$	[119]
2.8 GPa (tensile), 3.4 GPa	96 MPa (tensile), 244 MPa (flexural)	—	—	2.8 N/mm impact toughness, 7% elongation at break	[96]
—	2223 kPa MPa	—	—	>20 J/m for Izod impact strength	[126]
—	—	—	—	3.05 MPa m <sup>1/2</sup> for $K_{IC}$	[122]
4.13 GPa	80 MPa	—	—		[114]
>75 MPa	376 MPa (shear)	—	—	0.025% elongation at break	[120]
—	—	—	—		
—	>60 MPa	12 GPa (tensile, model)	—		[127]
—	—	—	14 $H_k$		[95]
>2 MPa [128]		(fracture)		0.45 fracture strain	
—	75.6 MPa (flexural)	—	—	0.8 MPa m <sup>1/2</sup> for $K_{IC}$	[123]
		—	18		[125]

due to the extremely high modulus and strength of the conventional carbon fibers. Since focus is given to mechanical properties related to military applications, with no intention for a comprehensive literature survey of the subject, this table is not intended to exhaust all significant work reported in literature.

### 2.3. Electrical properties

Aerospace epoxy-based composites typically rely upon laminates of carbon fibers, providing good x-y in-plane properties associated with the carbon fibers. However, in the z direction, certain properties such as conductivity rely upon the performance of the epoxy. In applications where high electrical conductivity is required, the transition from metallic materials to epoxies can be hindered by the low electrical conductivity of the epoxy. Apart from the numerous studies on the mechanical properties of CNT/epoxy composites discussed above, the AC and DC electrical

conductivity of CNT/epoxy composites have also been investigated. Many studies have shown that the addition of CNTs to an epoxy matrix increases the electrical conductivity and decreases electrostatic charging. However, there is some debate over whether surface treatments, addition of CNTs over a critical level, and alignment or uniform dispersion of CNTs play an imperative role in conferring these beneficial electrical properties [77,118,120,129–132]. Interestingly, the use of acid-oxidized CNTs [77] did not increase the electrical conductivity compared to untreated CNT/epoxy composites, suggesting that the electrical conductivity of the CNT/epoxy composites is dependent on the intrinsic electrical conductivity of the CNTs.

An electrical conductivity greater than  $10^{-6}$  S/m is normally needed for anti-electrostatic charging and CNT/epoxy composites with conductivities of  $10^{-2}$  S/m at filler volume fractions as low as 0.1 vol% have been prepared [132]. However, there is a percolation threshold where the composite electrical conductivity is not further enhanced above  $1 \times 10^{-4}$  S/cm [118,131]. A representative AC/DC study of an MWNT/epoxy composite is shown in Fig. 13, where the percolation threshold was estimated to be between 0.5 and 1 wt% MWNT content [118]. Other significant studies on electrical properties with various forms of carbon nanotubes have demonstrated significant opportunities for electromagnetic interference (EMI) shielding and electrostatic discharge (ESD) control for aerospace applications [131b].

Similar to the alignment of CNTs in a magnetic field and the increased mechanical properties of the composite, the application of an electric field induced the alignment of MWNTs in epoxy composites and increased AC electrical conductivity [132]. Alignment was evaluated with in-situ optical microscopy and multiple methods to determine the conductivity [132]. The application of both AC and DC electric fields during composite curing induced the formation of aligned conductive CNT networks between the electrodes (Fig. 14). The CNT agglomeration was dominated by electric field-induced forces acting on the CNTs, which have a negative surface charge after processing in the epoxy. The network structure formed in AC composite samples was more uniform and aligned compared to DC fields, as evident in Figs. 14–16, where increasing the wt% of CNTs and the application of AC resulted in better electrical properties. A summary of the electrical conductivity of selected nanotube composites is in Table 5.

## 2.4. Thermal properties

Thermal properties of interest to aerospace and military applications include structural performance within high temperature environments and thermal conductivity. Carbon nanotubes offer much potential due to their significant property enhancements to epoxies at very low loading levels thus minimally perturbing conventional processing techniques or affecting the structural properties of the epoxy. Thermal properties of CNT/epoxy composites have recently been investigated with the use of instrumentation such as dynamic scanning calorimetry (DSC), dynamic mechanical thermal analysis (DMA or DMTA), thermogravimetric analysis (TGA), and thermomechanical analysis (TMA). The cure behavior of CNT/epoxy composites displays several trends and is typically examined with DSC. Several studies show that CNTs either untreated [133,134] or surface treated [20] increase the rate of the cure reaction, but the decomposition time is lowered

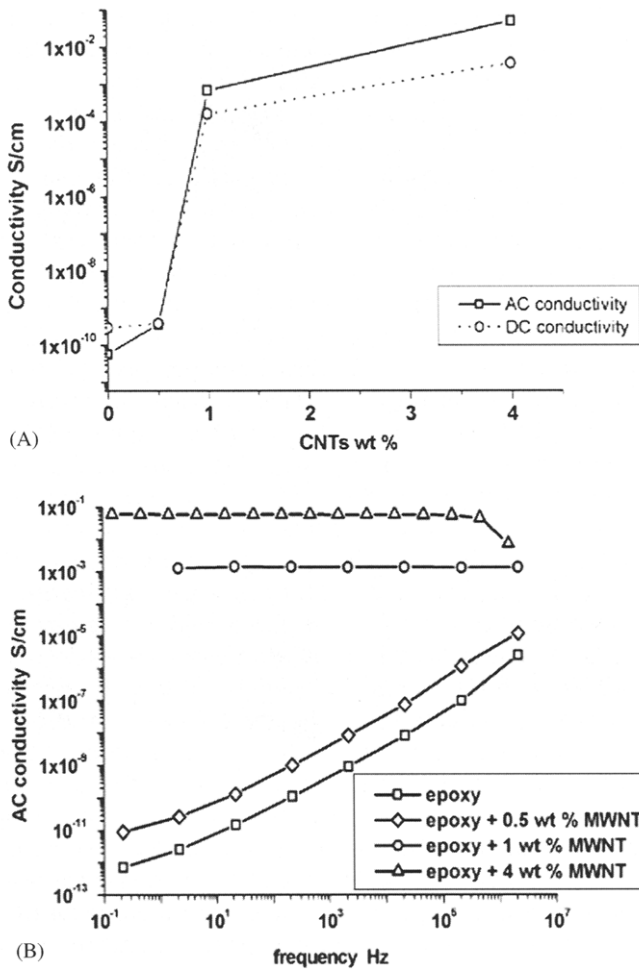


Figure 13. (A) AC and DC conductivity as a function of CNT weight percentage at 100 Hz. (B) AC conductivity as a function of the frequency. (After Allaoui et al. [118].)

[133]. Another study shows that magnetic field curing increases the storage modulus, glass transition temperature ( $T_g$ ), and decomposition temperature compared to neat resins [23].

The properties of polymer nanocomposites depend primarily on the dispersion of nanoparticles and their interaction with the polymer matrix. Surface treatments in order to disperse carbon nanotubes more effectively in composites or to increase their binding to epoxy have different effects on the resulting properties of the composite [135]. Several studies, however, suggest that the removal of residual solvent [125], surface oxidation [77], fluorination [126], surface functionalization via

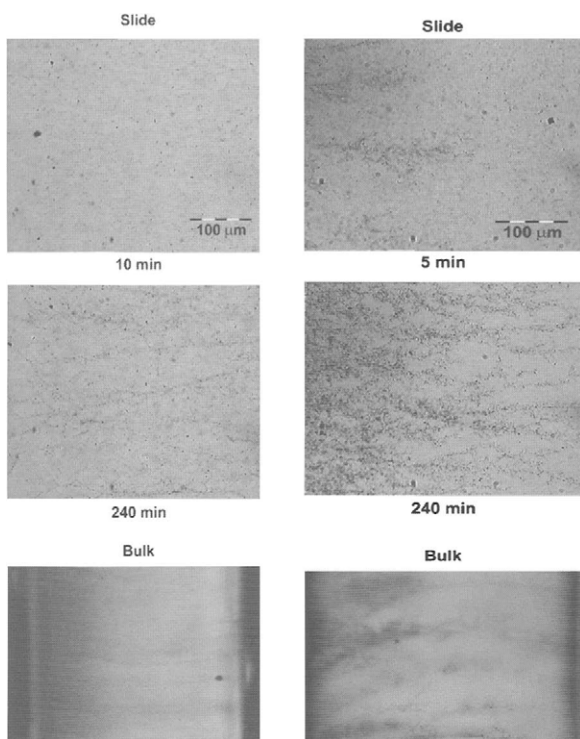


Figure 14. Transmission optical micrographs of epoxy composites containing 0.01 wt% MWNTs during curing at 80 °C after 10 or 240 min in (A) AC or (B) DC field of 100 V/cm. The bottom images show the resulting CNT network structure in a fully processed bulk composite cured under these conditions. (After Martin et al. [132].)

attachment of organic groups to the surface [135], and the amount of dispersion [120] can all enhance the resulting thermal properties of the composites. A few representative experiments will be mentioned below.

The shape of the carbon nano-reinforcement (single-walled, coiled, or bamboo CNT) affects the heat absorbability and cure behavior of the resulting composite including its  $T_g$  [48]. As shown in Fig. 17, the exothermic peak disappears at 44.33 °C in the composite samples, which indicates that the CNTs prevented the epoxy from releasing heat energy at this temperature. The endothermic peak at approximately 50 °C in each curve represents the  $T_g$  for the corresponding composite. Interestingly, the surface configuration of the CNT plays a major role in the  $T_g$  behavior of the composite with a higher  $T_g$  in straight SWNTs and bamboo MWNTs compared to a lower  $T_g$  in coiled MWNTs. It is hypothesized that CNTs with different

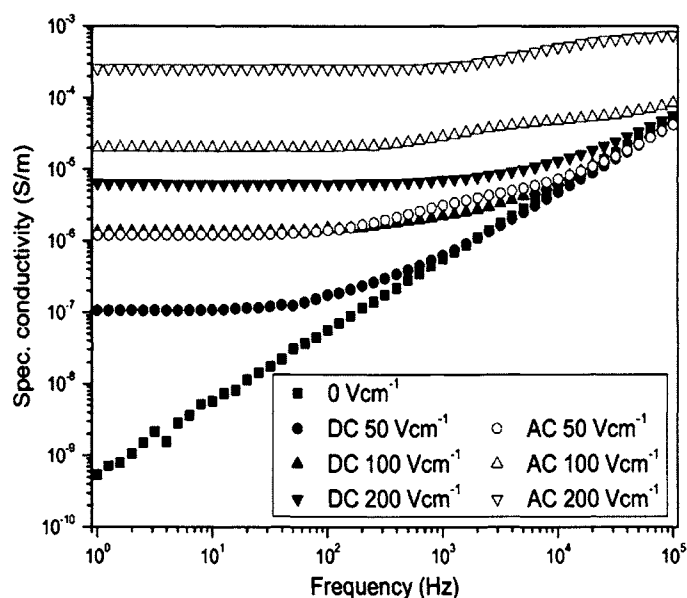


Figure 15. Specific AC conductivity as a function of frequency for fully processed bulk epoxy composites containing 0.01 wt% MWNTs exposed to AC and DC electric fields during curing. (After Martin et al. [132].)

shapes should have different steric hindrances on the curing reaction between the epoxy and hardener. The helical shape of the coiled MWNTs should have a larger steric hindrance than the straight CNTs.

The role of different solvents for CNT dispersion on the thermal properties of SWNT/epoxy composites was studied with DSC and TGA [125]. DSC results indicated that even small traces of residual solvent in the composite processing had a great impact on the cure reaction and subsequently affected the endothermic behaviors of the composites (Fig. 18a). The corresponding TGA results showed the existence of residual solvent in the resulting composites (Fig. 18b).

The thermal effect of surface treatment on CNT/epoxy composites was studied with DSC, DMTA, and TGA [77]. Surface oxidation of CNTs improved the thermal stability of CNT/epoxy composites [77]. The initial degradation temperatures via TGA of the CNT/epoxy composites were slightly higher than that of the neat resin and thermal degradation temperature was independent of CNT content. However, the thermal degradation temperature was higher for oxidized CNT/epoxy composites compared to untreated CNT/epoxy composites. It was suggested that the generation of functional groups on the CNT surface as a result of oxidative surface treatment induced polar interactions with the electrophilic epoxide groups. Nucleophile–electrophile complexes could then be formed between functional

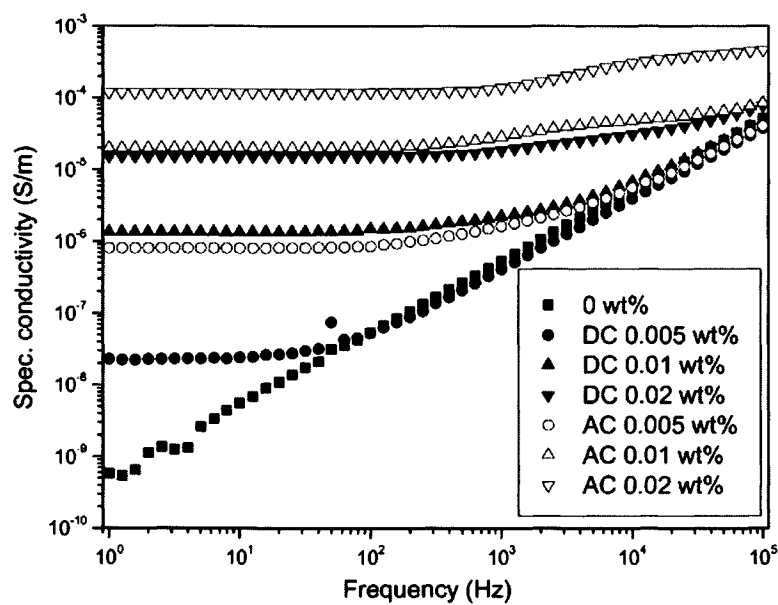


Figure 16. Specific AC conductivity as a function of frequency for fully processed bulk epoxy composites containing different weight fractions of MWNTs exposed to AC and DC electric fields of 100 V/cm during curing. (After Martin et al. [132].)

Table 5

Summary of electrical conductivity of CNT/epoxy composites.

Conductivity	CNT volume	Reference
$10^{-2}$ S/m	0.1 vol%	[129]
$10^{-3}$ S/cm	1 wt%	[118]
$6 \times 10^{-2}$ S/cm	4 wt%	[118]
$10^{-2}$ – $10^{-1}$ S/cm	50 wt%	[77]
$1 \times 10^{-4}$ S/cm	0.4 wt%	[131]
$10^{-2}$ S/cm	1.5 wt%	[120]
$10^{-4}$ – $10^{-3}$ S/m	0.01 wt%	[132]
$10^{-4}$ – $10^{-3}$ S/m	0.02 wt%	[132]
$10^{-5}$ – $10^{-3}$ S/cm	3 vol%	[130]

groups and epoxides due to these polar interactions. This may not only aid CNT dispersion, but may also improve the thermal stability of the CNT/epoxy composites. A summary of the maximum thermal property values obtained for various CNT/epoxy composites is shown in Table 6.



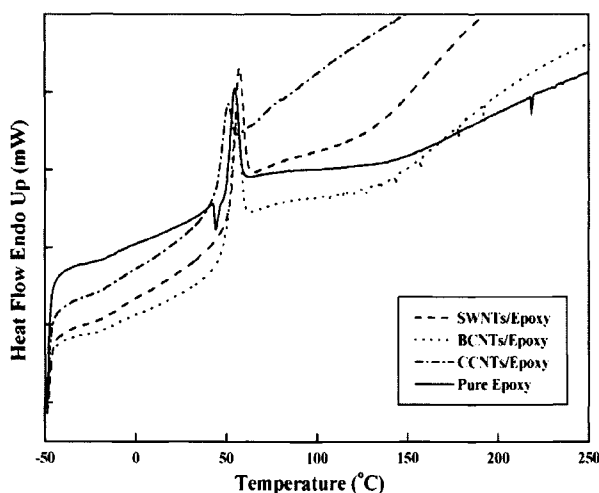


Figure 17. DSC curves at a heating rate of 10 °C/min for different types of CNT/epoxy composites and pure epoxy. (After Lau et al. [48].)

Thermal management is a growing need for military and non-military applications alike. As device engineers continue to maintain Moore's Law, and devices get smaller and more powerful, the management of heat has become a serious issue. For those applications that rely upon epoxy-based composites and do not want the associated weight impact associated with converting to a metallic material, the addition of CNTs to improve thermal conductivity without significantly perturbing the structural properties or manufacturing processes offers a potential solution [135b]. However, thermal transport in nanostructures requires an understanding of heat transport beyond that gained at the continuum level and necessitates advances in measurement methods. This arena is one that offers many opportunities for exploration. An excellent summary of the challenges to our current understanding can be found in Cahill et al., 2005. Pop et al., 2005 provide an example of the thermal properties of a suspended metallic SWNT [121c, 135c]. The characteristics of a SWNT with a length of 2.6 microns and a diameter of 1.7nm were extracted from its high-bias electrical characteristics over the 300-800 K temperature range and show a thermal conductance of approximately  $2.4 \text{ nWK}^{-1}$  and thermal conductivity of nearly  $3500 \text{ Wm}^{-1}\text{K}^{-1}$  at room temperature [135c]. By adding SWNT to polymers, composites with improvements in thermal conductivity have also been achieved [73a-c]. Through the increased understanding of interface, dispersion, and percolation networks/morphology characteristics is expected to provide pervasive and significant advances in the field of nanocomposites.

All properties rely on morphology and morphology relies on processing. For the class of CNT/epoxy composites, current technical challenges to achieving

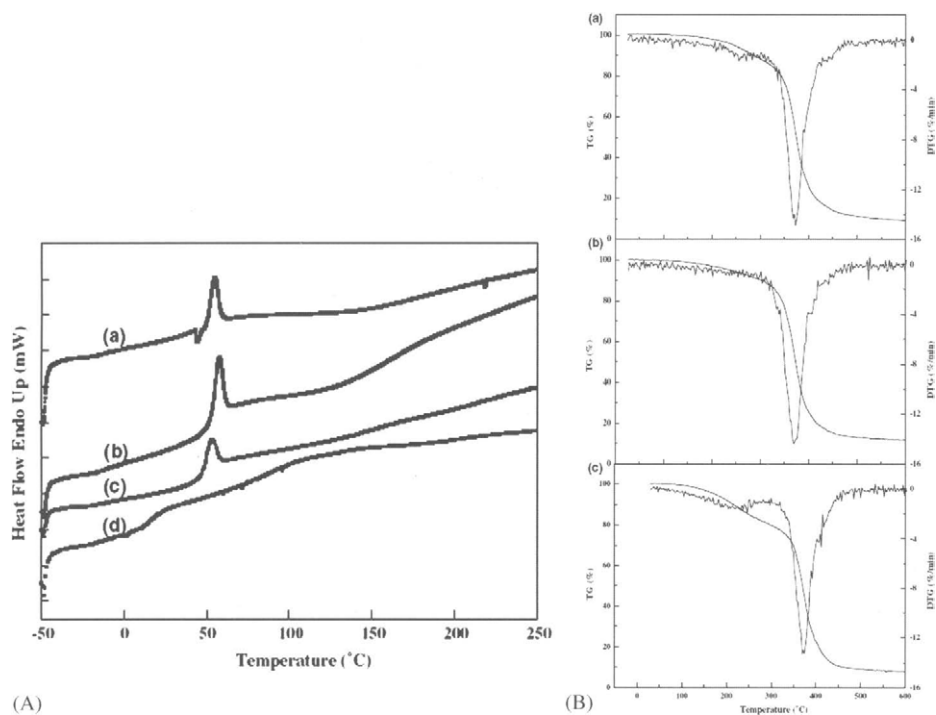


Figure 18. (a) DSC curves at a heating rate of 10 °C/min obtained from the samples S1 (a, epoxy only), S2 (b, SWNT/epoxy, acetone), S3 (c, SWNT/epoxy, ethanol), and S4 (d, SWNT/epoxy, DMF). (b) TGA of the samples S2 (a, SWNT/epoxy, acetone), S3 (b, SWNT/epoxy, ethanol), and S4 (c, SWNT/epoxy, DMF). (After Lau et al. [125].)

predictable, controllable properties of interest to aerospace and military applications include: dispersion of the carbon nanotubes, orientation control, and interface characteristics. All of these properties are impacted by surface modification. Apart from the microscopic, mechanical, electrical, and thermal characterization discussed above, X-ray photoelectron spectroscopy (XPS) [26,79,80,83–85,96,137] and Fourier-transform infrared (FTIR) spectroscopy [122,125,130,134,138], have also been used for characterization of surface and interfacial chemistry of CNTs and their derivatives blended with and without polymers. Various surface modification and dispersion methods used for CNTs in epoxy composites are listed in Table 7.

3. MILITARY APPLICATIONS

This section briefly discusses military systems that incorporate epoxy-carbon composites into their structural components or adhesives as new materials with improved properties (e.g. mechanical, electrical, or thermal).

Table 6  
Summary of maximum thermal property values obtained for the glass transition temperature ( $T_g$ ) and storage modulus of CNT/epoxy composites.

Composite	Special treatment	$T_g$ (°C)	Storage modulus	Reference
1 wt% CNT/Epoxy	Magnetic field curing	105	2500 MPa	[23]
SWNT/Epoxy	Acetone sonication	57.338	—	[48]
coiled CNT/Epoxy	Acetone sonication	55.291	—	[48]
Bamboo CNT/Epoxy	Acetone sonication	55.278	—	[48]
0.2–0.3 wt% SWNT/ Epoxy	Fluorination	139	0.63 GPa	[126]
SWNT/Epoxy	Acetone and tip sonication	104.21	2249 MPa	[136]
CNT/Epoxy	Ethanol sonication	—	0.83 GPa	[120]
Epoxidized linseed	Fluorination	118	3.7 GPa	[123]
0.2 wt% SWNT/oil/ DGEBF				
SWNT/Epon 862 (B3-O12)	Oxidized	145	—	[91]

3.1. Enhanced mechanical properties

The use of CNT/epoxy composites for enhanced mechanical properties in military applications can be divided into three categories: structural nano composites/adhesives, coatings, and multifunctional/smart materials.

3.1.1. Structural Nanocomposites/adhesives

In their most general form, as engineered materials, composites offer the greatest opportunities for significant advances in material design and function. Over the years, the use of composites has steadily increased as shown in Fig. 19. The first expected use of over 50% composite materials in the primary structure of a commercial passenger airliner, the Boeing 787 *Dreamliner*, is currently underway. It will carry between 200 and 350 passengers, depending on the seating configuration, and will be more fuel-efficient than comparable earlier airliners due primarily to a reduction in its weight. For example, by manufacturing a one-piece fuselage section, 1,500 aluminum sheets and 40,000 to 50,000 fasteners will be eliminated. In addition, the incorporation of health-monitoring systems that will allow the airplane to self-monitor and report maintenance requirements to ground-based computer systems are being considered [140b].

The US Department of Defense (DoD) has been utilizing polymer matrix composites and structural adhesive materials in military equipment for over 20 years due to their high strength-to-weight and stiffness-to-weight ratios for use in load-bearing structures and adhesives (139). For example, advanced composites

Table 7

Summary of dispersion and surface functionalization treatments for carbon nanotubes used in epoxy composites.

Solvent for dispersion	Chemical surface treatment	Other treatment	Reference
Ethanol	Untreated	Sonicate 2 h	[116]
Ethanol	Untreated	Ultrasonicate 1 h	[129]
Methanol	Untreated	Magnetic agitation	[118]
None	Untreated	Ultrasonicate	[117]
Acetone	60–65% nitric acid at 100–110 °C for 30 min	Sonicate 1 h	[20]
None	Untreated	Sonicate 2 h	[133]
Ethanol	Untreated	Sonicate 2 h	[110]
Acetone	Mixture of sulfuric/nitric acid/triethylenetetramine	Sonicate 30 min	[78]
Acetone	50–60% nitric acid at 100 °C for 30 min	Ultrasonicate 1 h	[77]
None	Untreated	Roll milled	[96]
Triton X-100 surfactant	28–40% HNO <sub>3</sub> and 28.5% H <sub>2</sub> O <sub>2</sub> /NH <sub>4</sub> OH	H <sub>2</sub> O <sub>2</sub> /NH <sub>4</sub> OH	[130]
Ethanol	Untreated	Ultrasonicate 5 min	[128]
Acetone	Fluorination	Sonicate 5 h	[126]
None	Oxyfluorination with F <sub>2</sub> , O <sub>2</sub> , N <sub>2</sub> gases at 0.2 MPa 15 min	Sonicate 3 h	[122]
None	Oxidation in sodium hypochlorite at ambient temperature	Sonicate	[114]
Acetone, BYK-9076 surfactant	Untreated	Tip or bath sonicate	[136]
Water (for storage)	HCl	Sonicate 1 h	[131]
None	Untreated	Sonicate 2 h	[134]
Acetone	Untreated	Sonicate 1 h	[48]
Ethanol	Untreated	Sonicate 2 h	[120]
Acetone	Fluorination	Sonicate 5 h	[123]
Acetone, ethanol, DMF	Untreated	Sonicate 1 h	[125]

DMF = *N,N*-dimethylformamide; Triton X-100=0.9 wt% polyoxyethylene octylphenyl-ether in acetone.

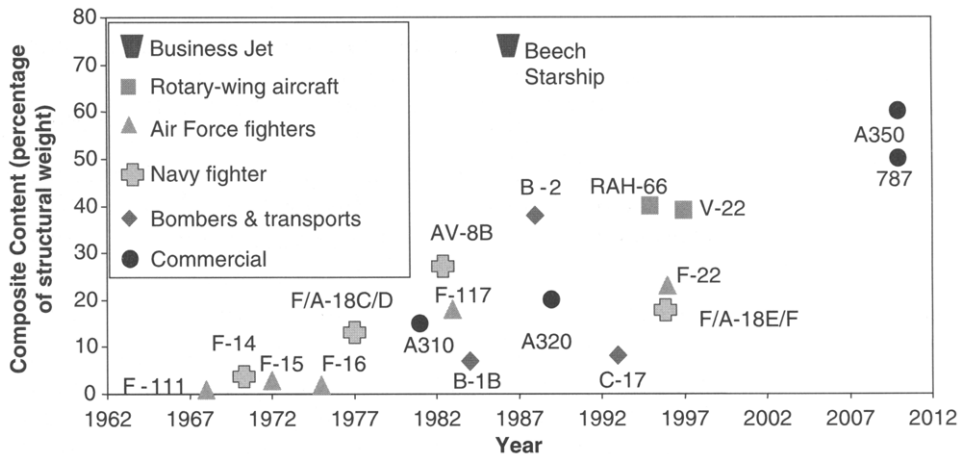


Figure 19. The increasing use of composites (as a percentage of their structural weight) in aircrafts over time.

have been incorporated into armor for vehicles developed under the Composite Armored Vehicle program (141). For this application, a combination of ceramics, metals, and polymeric composites provide unmatched mass efficient protection to the vehicle. The multi-layered protective outer structure also allows for the incorporation of additional functional layers for features such as electromagnetic ground planes and signature control (141). Other structural composite materials developed for military applications have included: lighter weight personnel armor; transparent armor for windows and windshields, visors, blast shields, lookdown windows, lenses, goggles, face shields; and canopies for aircraft (142).

Epoxy has been shown to be a good candidate for replacing some mechanical parts (e.g. fasteners) in systems such as the Future Combat Systems Multi-role Armament and Ammunition System (FCS-MRAAS) due to its high-strength and durability (22,139,143–150). The FCS-MRAAS provides both direct and indirect fire at firing rates as high as 20 rounds/min while weighing less than 18 tons (16 300 kg) [143]. Its lightweight tube support is currently designed from IM7 and M55J carbon fibers in an epoxy matrix with titanium fittings [143]. Studies have indicated that 10–20% weight reductions and 30–50% fabrication cost reductions are possible if new technologies could be developed to minimize or eliminate the number of fasteners and mechanical attachment systems currently being used with composite materials [151a]. Drilling bolt holes into a composite not only reduces the load bearing capacity of the structure, but it also greatly increases the overall manufacturing costs due to machining, cleaning, fastener installation, and assembly

steps [151a]. The remedy to this problem is better designs that minimize or eliminate the need for traditional mechanical fasteners and new process and fastening technologies that are compatible with composite materials [151a].

Although nanocomposites found early commercial application in automobiles and sporting equipment, recently, the DoD has established strategic goals that will necessitate the use of lightweight nanocomposites in order to meet performance requirements. For military applications, nanocomposites may offer a level of tailorability and material design that satisfies needs across platforms ranging from satellites to launch, aircraft and land vehicles [151b].

### 3.1.2. Coatings

Coatings are of great significance to many potential military applications. Various advanced composite coatings have been used to improve durability, reliability, and performance of many aircraft and armored vehicle components [152]. Multi-functional nanocoatings currently in development for aerospace applications include environmentally safe materials for corrosion sensing and protection using and aircraft skins for sensing mechanical damage [152].

Conventional paints are often not only health hazards, but also labor intensive to develop and to apply. Currently, up to 20% of army vehicles are out of service due to coatings damage and repainting needs, which amounts to an estimated \$2 billion for repainting and paint-scraping repair. CNTs could be used to replace carbon black in powder paints as conductive fillers for electrostatic spray painting of body parts, leading to more durable, corrosion-resistance paints and surfaces [152].

Carbon nanofibers, MWNTs, or SWNTs have been used to exploit the intrinsic properties of carbon nanomaterials for improved epoxy composites. Zyvex currently offers these materials in production quantities for global markets [153]. Fig. 20 shows some of the current and potential applications of Zyvex Nanosolve additives [154].

CNT/epoxy composite coatings have also been used as high radar transparency [155] or radar absorbing coatings [156] to disguise or reflect objects from an enemy's night-vision equipment. Alternatively, SWNT/epoxy mixtures can be used as sprays or sizing agents for other composite materials to enhance the interphase/interface between reinforcements and the matrix, as shown in Fig. 21 [93].

### 3.1.3. Multifunctional/smart materials

In the past, the Army has segregated ballistic and structural requirements, but now these two requirements are combined in certain composite systems such as sensors and radomes [151]. Current efforts are focused on combining power, sensor, communication, and health-monitoring systems with structural composite elements. The best way to accomplish these tasks is to take a holistic approach to developing systems for the Army. The total requirements for the system have to be considered while the designer is selecting materials. In addition, the tooling schemes and manufacturing processes should be considered to ensure that the



Figure 20. Current and Potential applications of Zyvex Nanosolve additives. (After [http://www.zyvex.com/Products/NASO\\_001a.html](http://www.zyvex.com/Products/NASO_001a.html) [154].)

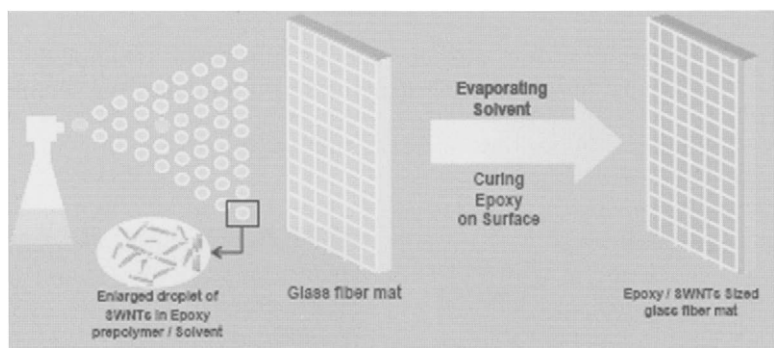


Figure 21. Schematic representation of SWNT/epoxy sizing by spraying on a glass fiber fabric. (After Kim et al. [93].)

most cost-effective material solution is chosen. Through developing neat performs and hybridizing the reinforcement, material waste could be reduced or eliminated [157]. A truly multi-functional composite system could provide armor, structural support, electromagnetic interference (EMI) shielding, lightning strike protection, and communication hardware [151]. An example of a multi-functional composite is

shown in Fig. 22 [151]. A braiding technique was used to form both the structural radome component and simultaneously co-locate with a high degree of accuracy a series of fiber optic sensors [151]. The use of such structural health-monitoring sensors in missile structures has the potential to assess if there has been any damage to the missile components during transport, use, or storage [151]. Fig. 23 shows a piezo-electric and optical sensor system that could be embedded and surface mounted to a large-scale composite fuselage to monitor the structure’s loading environment in order to extend service life while increasing overall safety [140].

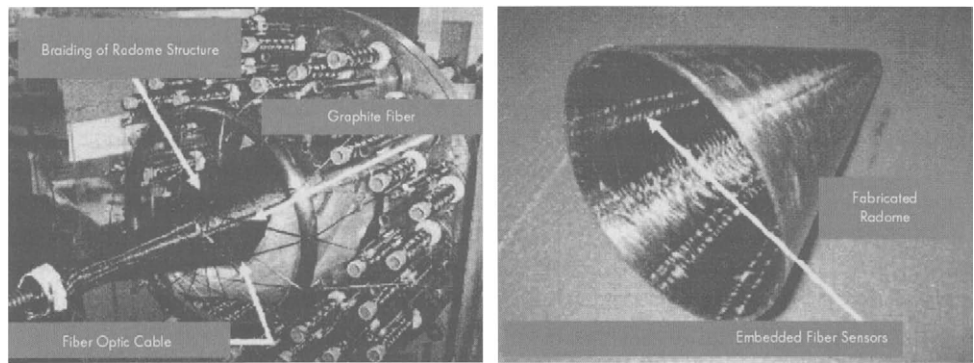


Figure 22. Mentis Sciences Inc. missile radome fabrication technology, where a braiding process is used for embedding structural health-monitoring sensors. (After Walsh [151].)

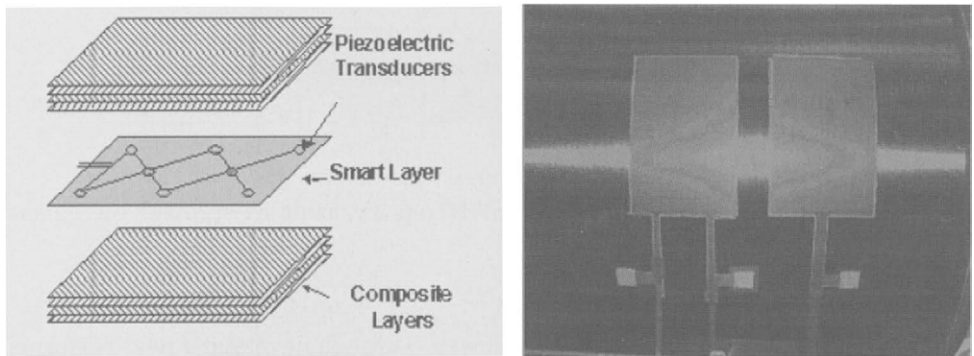


Figure 23. Structural health-monitoring system with a multi-layer structure. (After Jenks [140].)



Ideally, CNTs could individually be used in sensors to detect the presence of chemical weapons due to the small changes in their conductance when they come in contact with such chemical species [158–160] or they could be incorporated into electrode or membrane-based biosensors replacing the existing materials to enhance sensitivity and selectivity [161–163]. Self-healing of epoxy composites [164] with catalyzed monomers or catalysts embedded directly in the matrix has been recently studied. Other proposed areas of application of CNT/epoxy composites are military protective uniforms that are stronger, more durable, lighter, self-cleaning, self-healing, that can automatically seal its own pores, and decontaminate itself. These smart materials could be made into a variety of materials such as woven fiber cloth, coatings, or components of structural parts that perform other sensory functions.

### 3.2. Enhanced electrical properties

Transparent conductive coatings that contain CNTs for electrostatic charge mitigation can be used both for military [165f] and space applications [59] and are covered in more detail in Chapter 19 [166]. An electrical conductivity exceeding  $10^{-6}$  S/m is normally required to dissipate electrostatic charge [132], whereas the electrical conductivity needs to only be on the order of  $10^{-8}$  S/cm for anti-static applications. The latter value of electrical conductivity is much lower than that of CNT/epoxy composites (see Table 5 on Electrical Conductivity), indicating that CNT/epoxy composites can be used to replace carbon fiber or nanofiber/polymer alcohol (PVA) composites, such as poly vinyl alcohol (PVA)/nanofiber, metal-coated carbon fiber/acrylonitrile-butadiene styrene (ABS), or poly vinylidene fluoride/nanofiber composites, for EMI shielding and lightening strike protection (Fig. 24) [140,167–170]. In addition, conducting CNT/epoxy nanocomposites have also been used as material coatings for military aircraft canopies, for self-passivation to aggressive environments [171], electromechanical actuators [113], and artificial muscles.

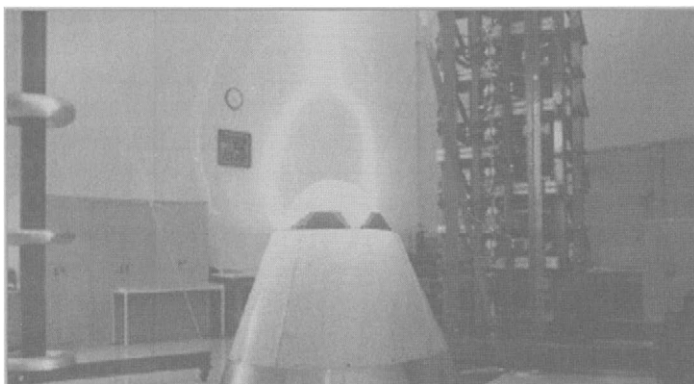


Figure 24. Lightning strike/EME performance testing. (After Jenks [140].)

The DoD has recently reviewed composites for use in orbiting platforms such as satellites [172a] and the potential application of fullerenes and carbon nanotubes in polymer nanocomposites for solar cell future power generation [172b–177] and other power applications has been explored [178]. Lightweight materials and structures for space solar power systems (SSPS) are being examined by Mitsubishi Electric Corporation [179]. Fig. 25 shows the three main parts of the SSPS: a large mirror to concentrate rays of sunlight, solar cells to generate electrical power from sunlight, and a large transmitter to convert the power into microwaves or laser beams to send power to earth. During power generation and conversion into microwaves or laser beams, waste energy is converted into heat. The quantity of heat produced during the generation and conversion processes is too large to be radiated from the SSPS structure. In order to radiate excess heat to space, a SSPS will need an extremely large radiator. The weight of the radiator must be as low as possible. This can be achieved by optimizing the thermal conductance and reducing the weight of cooling devices such as heat pipes. Fig. 26 shows one example of a lightweight radiator panel, which consists of carbon fiber-reinforced plastic (CFRP) skins, an aluminum core, and aluminum heat pipes. CFRP used in the panel skins has twice the thermal conductivity and one-fifth the density of copper. The design used here reduced the weight of the heat pipe in half and the recent development of CFRP materials with even higher thermal conductivity should enable even lighter heat pipe radiator panels in the coming years [179].

### 3.3. Enhanced Thermal Properties

Polymer–clay nanocomposites have been researched for enhanced fire retardancy and anti-flammability in aircraft interiors for many years [180–186]. However, the

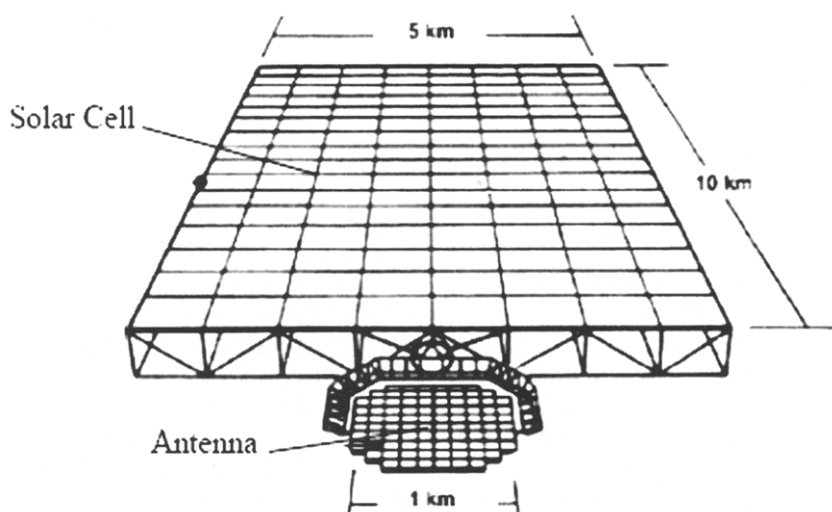


Figure 25. Space solar power satellite (SSPS) system. (After Ishii et al. [179].)

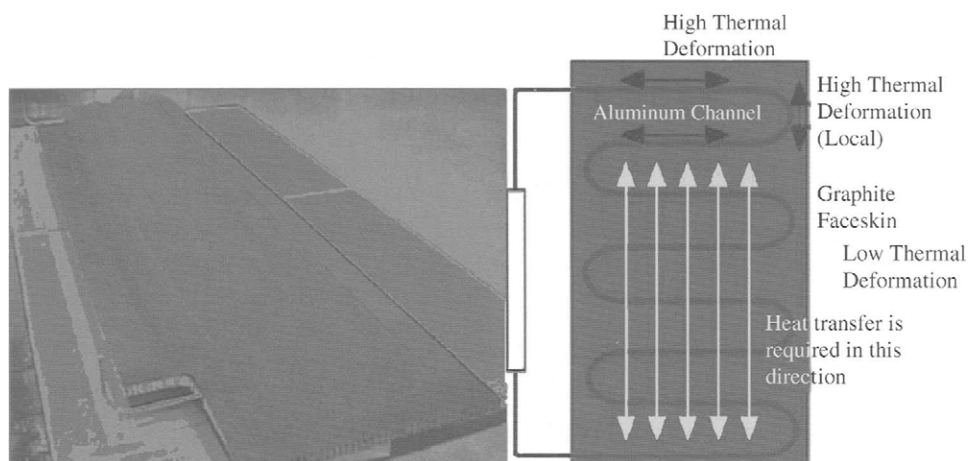


Figure 26. Heat pipe embedded radiator panel (CFRP Face skin/aluminum core). (After Ishii et al. [179].)

CNT is a recent addition to the fire retardant polymer nanocomposites. For instance, nanocomposites have been prepared with both nanoclay and CNTs for flame retardancy [187]. In addition to significantly reducing the heat release rate of PP or PMMA [181,188], it was shown that the addition of CNTs modify the thermal and oxidative degradation properties of the polymer. Relevant studies on modifying epoxies for flame retardant properties, for example, by incorporating phosphorus into the backbone of the resin [189] and advanced composites for thermal protection via ablation in military applications continue to be developed [190].

#### 4. SUMMARY

The characterization techniques of SEM, TEM, XPS, and FTIR reveal new and interesting properties of CNT/epoxy composites such as their fracture mechanism, interfacial bonding quality, and effect of functionalizing treatments on the CNTs. Mechanical, electrical, and thermal tests reveal that CNT/epoxy composites have many desirable properties including enhanced strength, stiffness, conductivity, and thermal stability with very low CNT content. Therefore, the number of applications for CNT/epoxy composites in both military applications and many other areas is rapidly expanding. The National Science Foundation (NSF) predicts that the total market for nanotech products and services will reach \$1 trillion in US dollars by the year 2015. The accuracy of this claim is difficult to assess, but some theorize that the peak of scientific activity is still to come, possibly in three to five years from now, and large-scale exploitation of nanotechnological results might arise 10 years from now. However, it seems reasonable to assume that during the next two to

three years most activity in nanotechnology will still be in the area of research, rather than completed projects or products [191].

## REFERENCES

1. M. S. Dresselhaus and G. Dresselhaus, *J. Electroceram.* **1** (1997) 273–286.
2. K. Lozano, J. Bonilla-Rios and E. V Barrera, *J. Appl. Polym. Sci.* **80** (2000) 1162–1172.
3. Y. Y. Fan, H. M. Cheng, Y. L. Wei, G. Su and Z. H. Shen, *Carbon* **38** (2000) 921–927.
4. H. Ma, J. Zeng, M. Realff, S. Kumar and D. A. Schiraldi, *Compos. Sci. Technol.* **63** (2003) 1617–1628.
5. G. B. Zheng, H. Sano and Y. Uchiyama, *Carbon* **41** (2003) 853–856.
6. Y. Yoon and H. Baik, *Diamond Relat. Mater.* **10** (2001) 1214–1217.
7. Y. Shyu and C. Hong, *Diamond Relat. Mater.* **10**(2001) 1241–1245.
8. W. Ren and H. Cheng, *Carbon* **41** (2002) 1645–1687.
9. Y. Wang, S. Serrano and J. Santiago-Aviles, *Synth. Met.* **138** (2003) 423–427.
10. S. Iijima, *Nature* **354** (1991) 56–58.
11. Y. Liu and X. Chen, *Mech. Mater.* **35** (2003) 69–81.
12. F. Fisher, R. Bradshaw and L. Brinson, *Compos. Sci. Technol.* **63** (2003) 1–15.
13. E. Saether, S. Frankland and R. Pipes, *Compos. Sci. Technol.* **63** (2003) 1543–1550.
14. J. Gou, S. Jiang, B. Minaie, K. Hsiao, Z. Liang, C. Zhang and B. Wang, *SAMPE Proceedings*, May 2004.
15. I. Guz and Y. Rushchitskii, *Mech. Compos. Mater.* **40** **3** (2004) 179–190.
16. K. T. Lau, C. Gu, G. H. Gao, H. Y. Ling and S. Reid, *Carbon* **42** (2004) 423–460.
17. M. Perez-Cabero, I. Rodriguez-Ramos and A. Guerrero-Ruiz, *J. Catal.* **215** (2003) 305–316.
18. M. Zhang, K. Atkinson and R. Baughman, *Science* **306** (2004) 1358–1361.
19. M. Zhang, S. Fang, A. Zakhidov, S. Lee, A. Aliev, C. Williams, K. Atkinson and R. Baughman, *Science* **309** (2005) 1215–1219.
20. J. Bae, J. Jang and S. H. Yoon, *Macromol. Chem. Phys.* **203** (2002) 2196–2204.
21. (a) M. Boyle <http://www.hexcel.com>, (b) C. May Marcel Dekker, Inc. Publishers (1988).
22. (a) B. Maruyama, and K. Alam, *SAMPE Journal* **38** (2002) 3: 59–68, (b) C. Martin, J. Sandler, M. Shaffer, M. Schwarz, W. Bauhofer, K. Schulte, and A. Windle, *Composites Science and Technology* **64** (2004) 2309–2316, (c) *Handbook of Composites 2nd Edition*, edited by S.T. Peters, Chapman and Hall Publishers (1997), (d) *Composite Airframe Structures* edited by M. Niu, (1992).
23. H. Mahfuz, S. Zainuddin, V. Rangari, S. Jeelani, M. Parker and T. Al-Saadi, *SAMPE Proceedings*, May 2005.
24. L. Bykanova, C. Byrne, A. Bykanov and D. Goodman, *SAMPE Proceedings*, May 2003.

25. D. Klosterman, MAT510 Class Handouts, University of Dayton, Dayton, OH, Spring 2004.
26. S. Park, M. Seo and K. Rhee, *Mater. Sci. Eng. A* **356** (2003) 219–226.
27. Z. Jin, K. Pramoda, G. Zu and S. Goh, *Chem. Phys. Lett.* **337** (2001) 43–47.
28. C. Cooper, S. Cohen, A. Barber and H. Wagner *Appl. Phys. Lett.* **81** (2002) 3873–3875.
29. R. W. Siegel, S. K. Chang, B. J. Ash, J. Stone, P. M. Ajayan, R. W. Doremus and L. S. Schadler, *Scripta Mater.* **44** (2001) 2061–2064.
30. Z. Jia, Z. Wang, C. Xu, J. Liang, B. Wei, D. Wu and S. Zhu, *Mater. Sci. Eng. A* **271** (1999) 395–400.
31. S. Kumar, T. Uchida, T. Dang, X. Zhang and Y. Park, *SAMPE Proceedings*, May 2004.
32. R. Andrews, D. Jacques, M. Minot and T. Rantell, *Macromol. Mater. Eng.* **287** (2002) 395–403.
33. S. Kumar, H. Doshi, M. Srinivasarao, J. Park and D. A. Schiraldi, *Polymer* **43** (2002) 1701–1703.
34. P. Cortes, K. Lozano, E. V. Barrera and J. Bonilla-Rios, *J. Appl. Polym. Sci.* **89** (2002) 2527–2534.
35. S. Kumar, T. Liu, T. Sreekumar, T. Uchida, X. Zhang and Y. Park, *SAMPE Proceedings*, May 2004.
36. D. Glasgow, G. Tibbetts, M. Matuszewski, K. Walters and M. Lake, *SAMPE Proceedings*, May 2004.
37. D. Qian and E. C. Dickey, *J. Microsc.* **204** (2001) 39–45.
38. E. T. Thostenson and T. W. Chou, *J. Phys. D: Appl. Phys.* **35** (2002) L77–L80.
39. E. T. Thostenson and T. W. Chou, *J. Appl. Phys. D: Appl. Phys.* **36** (2003) 573–582.
40. B. Safadi, R. Andrews and E. A. Grulke, *J. Appl. Polym. Sci.* **84** (2001) 2660–2669.
41. J. Cho, J. Kim, Y. Jung and N. Goo, *Macromol. Rapid Commun.* **26** (2005) 412–416.
42. J. Kwon and H. Kim, *J. Appl. Polym. Sci.* **96** (2005) 595–604.
43. H. Wagner, O. Lourie and X. Zhou, *Composites: Part A* **30** (1999) 59–66.
44. C. Li, D. Wang, X. Wang and J. Liang, *Carbon* **43** (2005) 1557–1583.
45. J. Koo, Z. Luo and L. Pilato, *SAMPE Proceedings*, May 2004.
46. Z. X. Jin, S. H. Goh, G. Q. Xu and Y. W. Park, *Synth. Met.* **135–136** (2003) 735–736.
47. S. Curran, A. P. Davey, J. Coleman, A. Dalton, B. McCarthy, S. Maier, A. Drury, D. Gray, M. Brennan, K. Ryder, M. Lamy de la Chapell, C. Journet, P. Bernier, H. J. Byrne, D. Carroll, P. M. Ajayan, S. Lefrant and W. Blau, *Synth. Met.* **103** (1999) 2559–2562.
48. K. Lau, M. Lu, H. Li, L. Zhou and D. Hui, *J. Mater. Sci.* **39** (2004) 5861–5863.
49. S. Park and Y. Jang, *J. Colloid Interface Sci.* **237** (2001) 91–97.
50. E. Tamburri, S. Orlanducci, M. Terranova, F. Valentini, G. Palleschi, A. Curulli, F. Brunetti, D. Passeri, A. Alippi and M. Rossi, *Carbon* **43** (2005) 1213–1221.
51. J. Smith, J. Connell, K. Watson and P. Danehy, *Polymer* **46** (2005) 2276–2284.

52. M. Frogley, D. Ravich and H. Wagner, *Compos. Sci. Technol.* **63** (2003) 1647–1654.
53. D. A. Brune and J. Bicerano, *Polymer* **43** (2002) 369–387.
54. J. Park and S. Jana, *Polymer* **44** (2003) 2091–2100.
55. S. Yang, A. Lomeli, M. Borrego, R. Jones and K. Lozano, *SAMPE Proceedings*, September 2003.
56. R. Vaidyanathan, C. Green, T. Phillips, E. Barrera, M. Shofner, R. Wilkins and S. Thiebault, *SAMPE Proceedings*, September 2003.
57. C. Shiner, J. Timmerman, E. Williams and J. Seferis, *SAMPE Proceedings*, May 2003.
58. J. Koo, L. Pilato, G. Wissler, A. Lee, A. Abusafieh and J. Weispfenning, *SAMPE Proceedings*, May 2005.
59. K. Watson, J. Smith Jr. and W. Connell, *SAMPE Proceedings*, May 2003.
60. K. Ishiguro, T. Karaki, S. Sangari and J. Seferis, *SAMPE Proceedings*, November 2004.
61. L. Drzal and H. Fukushima, *SAMPE Proceedings*, May 2003.
62. C. Chen and D. Curliss, *J. Appl. Polym. Sci.* **90** (2003) 2276–2287.
63. C. Chen, *SAMPE Proceedings*, September 2003.
64. R. Vaia *The AMPTIAC Newslett.* **6** (2002) 17–24.
65. (a) L. Dai, *Polym. Adv. Technol.* **10** (1999) 357–420, (b) J. Burghardt, H. Hansen, L. Hansen and G. Hansen, *Proceedings of SAMPE Conference – ISSE 2006* (in press), (c) T. Gibson, B. Rice, W. Ragland, E. Silverman, H. Peng, K. Strong and D. Moon, *Proceedings of SAMPE Conference-ISSE 2005*, (d) D. Dummer and D. Radford, *Proceedings of SAMPE Conference-ISTC 2004*, (e) G. Hansen, *Proceedings of SAMPE Conference-ISTC 2005*, and (f) R. Jacobsen, K. Walters, M. Matuszewski, D. Glasgow and C. Wang, *Proceedings of SAMPE Conference-ISSE 2004*.
66. J. Salvétat, J. Bonard, N. Thomson, A. Kulik, L. Forro, W. Benoit and L. Zuppiroli, *Appl. Phys. Mater. Sci. Eng.* **69** (1999) 255–260.
67. L. Dai and A. Mau, *Adv. Mater.* **13** (2001) 899–913.
68. E. G. Rakov, *Russ. Chem. Rev.* **70** (2001) 827–863.
69. E. T. Thostenson, Z. Ren and T. W. Chou, *Compos. Sci. Technol.* **61** (2001) 1899–1912.
70. H. Dai, *Surf. Sci.* **500** (2002) 218–241.
71. S. Iijima, *Physica B* **323** (2002) 1–5.
72. J. Salvétat-Delmotte and A. Rubio, *Carbon* **40** (2002) 1729–1734.
73. (a) E. Thostenson, C. Li and T. Chou T, *Compos. Sci. and Technol.* **65** (2005) 491–516, (b) X. Xie, Y. Mai and X. Zhou, *Mater. Sci. Eng. R* **49** (2005) 89–112, and (c) D. Qian, G. Wagner, W. Liu, M. Yu and R. Ruoff, *American Society of Mechanical Engineers* (2002) 495–533.
74. K. T. Hilo, J. Alms and S. G. Advent, *Nanotechnology* **14** (2003) 791–793.
75. L. Jin, C. Bower and O. Shout, *Appl. Phys. Lett.* **73** (1998) 1197–1199.
76. A. Garg and S. B. Sinnott, *Chem. Phys. Lett.* **295** (1998) 273–278.
77. J. Jang, J. Bae and S. H. Yoon, *J. Mater. Chem.* **13** (2003) 676–681.
78. F. Gojny, J. Nastalczyk, Z. Roslaniec and K. Schulte, *Chem. Phys. Lett.* **370** (2003) 820–824.

79. S. Yumitori and Y. Nakanishi, *Composites Part A* **27A** (1996) 1051–1058.
80. S. Yumitori and Y. Nankanishi, *Composites Part A* **27A** (1996) 1059–1066.
81. (a) J. Gulyas, E. Foldes, A. Lazar and B. Pukanszky, *Surface Chemistry and Adhesion. Composites Part A* **32** (2001) 353–360 and (b) J. Zhao, D. Schaefer, D. Shi, J. Lian, J. Brown, G. Beaucage, L. Wang and R. Ewing, *J. Phys. Chem. B* **109** (2005) 23351–23357.
82. N. Dilsiz, E. Ebert, W. Weisweiler and G. Akovali, *J. Colloid Interface Sci.* **170** (1995) 241–248.
83. S. Park, M. Seo and J. Lee, *J. Colloid Interface Sci.* **268** (2003) 127–132.
84. S. Park, M. Seo and Y. Lee, *Carbon* **41** (2003) 723–730.
85. S. Park and M. Kim *J. Mater. Sci.* **35** (2000) 1901–1905.
86. S. Park and B. Park, *J. Mater. Sci. Lett.* **18** (1999) 47–49.
87. Z. Liang, K. Shankar, K. Barefield, C. Zhang, B. Wang and L. Kramer, *SAMPE Proceedings*, May 2003.
88. J. Gou, B. Minaie, Z. Liang, C. Zhang and B. Wang, *SAMPE Proceedings*, May 2003.
89. Z. Wang, Z. Liang, B. Wang, C. Zhang and L. Kramer, *Composites Part A*: **35** (2004) 1225–1232.
90. B. Wang, Z. Liang, R. Shankar and C. Zhang, *SAMPE Proceedings*, May 2004.
91. Z. Liang, P. Gonnet, E. Choi, R. Kadambala, C. Zhang, J. Brooks, B. Wang and L. Kramer, *SAMPE Proceedings*, May 2005.
92. M. Jose, J. Tyner, E. Nyairo and D. Dean, *SAMPE Proceedings*, May 2004.
93. J. Kim, E. Barrera and C. Armeniades, *SAMPE Proceedings*, September 2003.
94. (a) V. Lordi and N. Yao, *J. Mater. Res.* **15** (2000) 2770–2779 and (b) S. Huang and L. Dai, *J. Nano. Res.* **4** (2002) 145–155.
95. K. Lau and D. Hui, *Carbon* **40** (2002) 1597–1617.
96. D. Li, X. Zhang, G. Sui, D. Wu and J. Liang, *J. Mater. Sci. Lett.* **22** (2003) 791–793.
97. K. Lee, L. Li and L. Dai, *J. Am. Chem. Soc.* **127** (2005) 4122–4123.
98. W. Chen, L. Dai, H. Jian and T. Bunning, *Plasma Process. Polym.* **2** (2005) 279–292.
99. N. Lopattananon, A. Kettle, D. Tripathi, A. Beck, E. Duval, R. France, R. Short and F. Jones, *Composites Part A* **30** (1999) 49–57.
100. P. Varelidis, R. McCullough and C. Papaspyrides, *Compos. Sci. Technol.* **59** (1999) 1813–1823.
101. Y. Basova, H. Hatori, Y. Yamada and K. Miyashita, *Electrochem. Commun.* **1** (1999) 540–544.
102. K. Atkinson, G. Farrow and C. Jones, *Composites Part A* **27A** (1996) 799–804.
103. J. Kikuma, T. Konishi and T. Sekine, *J. Electron Spectrosc. Relat. Phenomena* **69** (1994) 141–147.
104. M. Alexander and F. Jones, *Carbon* **33** (1995) 569–580.
105. S. Gardner, C. Singamsetty, G. Booth, G. He and C. Pittman, *Carbon* **33** (1995) 587–595.
106. C. Weitzsacker, M. Xie and L. Drzal, *Surf. Interface Anal.* **25** (1997) 53–63.

107. K. Liu and M. Piggott, *Composites* **26** (1995) 841–848.
108. I. Park, D. Lee and J. Nam, *J. Appl. Polym. Sci.* **84** (2002) 144–154.
109. H. Choi, K. Ahn, J. Nam and H. Chun, *Composites Part A* **32** (2001) 709–720.
110. K. Lau, S. Shi and H. Cheng, *Compos. Sci. Technol.* **63** (2003) 1161–1164.
111. P. M. Ajayan, L. S. Schadler, C. Giannaris and A. Rubio, *Adv. Mater.* **12** (2000) 750–753.
112. R. Pipes, S. Frankland, P. Hubert and E. Saether, *Compos. Sci. Technol.* **63** (2003) 1349–1358.
113. (a) M. Tahhan, V. Truong, G. Spinks and G. Wallace, *Smart Mater. Struct.* **12** (2003) 626–632, (b) J. Goldstein, D. Newbury, D. Joy, C. Lyman, P. Echlin, E. Lifshin, L. Sawyer and J. Michael, *Kluwer Academic/Plenum Publishers* (2003) and (c) T. Liu and S. Kumar, *Nano. Lett.* **3** (2003) 647–650.
114. Y. Breton, G. Desarmot, J. Salvétat, S. Delpeux, C. Sinturel, F. Beguin and S. Bonnamy, *Carbon* **42** (2004) 1027–1030.
115. (a) E. Lourie, D. M. Cox and H. D. Wagner, *Phys. Rev. Lett.* **81** (1998) 1638–1641 and (b) <http://www.prnewswire.com/cgi-bin/stories.pl?ACCT=109&STORY=/www/story/11-29-2004/0002551037&EDATE=>.
116. O. Lourie and H. Wagner, *Appl. Phys. Lett.* **73** (1998) 3527–3529.
117. C. Cooper, S. Cohen, A. Barber and H. Wagner, *Appl. Phys. Lett.* **81** (2002) 20.
118. A. Allaoui, S. Bai, H. Cheng and J. Bai, *Compos. Sci. Technol.* **62** (2002) 1993–1998.
119. F. Gonjy, M. Wichmann, U. Kopke, B. Fiedler and K. Schulte, *Compos. Sci. Technol.* **64** (2004) 2363–2371.
120. Y. Song and J. Youn, *Carbon* **43** (2005) 1378–1385.
121. (a) L. Drzal and M. Madhukar, *J. Mater. Sci.* **28** (1993) 569–610, (b) V. Buryachenko, A. Roy, K. Lafdi, K. Anderson and S. Chellapilla, *Compos. Sci. Technol.* **65** (2005) 2435–2465, (c) D. Cahill, W. Ford, K. Goodson, G. Mahan, A. Majumdar, H. Maris, R. Merlin and S. Phillpot, *J. Appl. Phys.* **93** (2003) 2: 793–818, (d) G. Tandon, R. Kim, and V. Bechel *Compos. Sci. Technol.* **60** (2000) 2281–2295.
122. S. Park, H. Jeong and C. Nah, *Mater. Sci. Eng. A* **385** (2004) 13–16.
123. H. Miyagawa, A. Mohanty, L. Drzal and M. Misra, *Nanotechnology* **16** (2005) 118–124.
124. K. T. Lau and S. Q. Shi, *Carbon* **40** (2002) 2961–2973.
125. K. Lau, M. Lu, C. Lam, H. Cheung, F. Sheng and H. Li, *Compos. Sci. Technol.* **65** (2005) 719–725.
126. H. Miyagawa and L. Drzal, *Polymer* **45** (2004) 5163–5170.
127. K. Xiao and L. Zhang, *J. Mater. Sci.* **39** (2004) 4481–4486.
128. A. Li, M. Zaiser and V. Koutsos, *Phys. Status Solidi* **13** (2004) R89–R91.
129. J. Sandler, M. Shaffer, T. Prasse, W. Bauhofer, K. Schulte and A. Windle, *Polymer* **40** (1999) 5967–5971.
130. Y. Kim, T. Shin, H. Choi, J. Kwon, Y. Chung and H. Yoon, *Carbon* **43** (2005) 23–30.
131. (a) S. Barrau, P. Demont, C. Maraval, A. Bernes and C. Lacabanne, *Macromol. Rapid Commun.* **26** (2004) 390–394 and (b) H. Koerner, W. Liu, M. Alexander, P. Mirau, H. Dowty and R. Vaia, *Polymer* **46** (2005) 4405–4420.



132. C. Martin, J. Sandler, A. Windle, M. Schwartz, W. Bauhofer, K. Schulte and M. Shaffer, *Polymer* **46** (2005) 877–886.
133. D. Puglia, L. Valentini and J. Kenny, *J. Appl. Polym. Sci.* **88** (2002) 452–458.
134. H. Xie, B. Liu, Z. Yuan, J. Shen and R. Cheng, *J. Polym. Sci. Part B: Polym. Phys.* **42** (2004) 3701–3712.
135. (a) H. Lu, H. Shen, Z. Song and S. Nutt, SAMPE Proceedings, May 2004, (b) R. Watts, SAMPE Proceedings May 2005 and (c) E. Pop, D. Mann, Q. Wang, K. Goodson and H. Dai, *Nano. Lett.* **6** (2005) 96–100.
136. Y. Liao, O. Mariett-Tondin, Z. Liang, C. Zhang and B. Wang, *Mater. Sci. Eng. A* **385** (2004) 175–181.
137. <http://www.uksaf.org/tech/xps.html>.
138. <http://www.mse.arizona.edu/classes/mse480/FTIR/Images/Nicolet.pdf>.
139. J. Sands, B. Fink, S. McKnight, C. Newton, J. Gillespie Jr. and R. Palmese, *Clean Products Process.* **2** (2001) 228–235.
140. <http://www.boeing.com/commercial/787family/background.html>
141. B. Cheeseman, R. Jensen and C. Hoppel AMPTIAC **8** (2004) 37–43.
142. J. Sands, P. Patel, P. Dehmer, A. Hsieh and M. Boyce, APTIAC **8** (2004) 28–36.
143. A. Littlefield, J. Root and M. Leach, SAMPE Proceedings, November 2004.
144. K. Hsiao, J. Alms and S. Advani, *Nanotechnology* **14** (2003) 791–793.
145. S. Zhou and M. Hawley, *Compos. Struc.* **61** (2003) 303–309.
146. W. Lim and H. Mizumachi, *J. Appl. Polym. Sci.* **66** (1997) 525–536.
147. L. Amirova, K. Shageeva and V. Stroganov, *Russ. J. Appl. Chem.* **74** (2001) 1364–1367.
148. I. Ashcroft, D. Hughes and S. Shaw, *Assem. Automat.* **20** (2000) 150–161.
149. R. Balkova, S. Holcnerova and V. Cech, *Intl. J. Adhesion Adhesives* **22** (2002) 291–295.
150. A. Baldan, *J. Mater. Sci.* **39** (2004) 1–49.
151. (a) S. Walsh, AMPTIAC **8** (2004) 44–48 and (b) Materials Research to Meet 21st-Century Defense Needs, Committee on Materials Research for Defense, National Research Council Report, 2003.
152. <http://www.azonano.com/details.asp?ArticleID=568> (author website nano.org.uk).
153. <http://www.azonano.com/news.asp?newsID=777>.
154. [http://www.zyvex.com/Products/NASO\\_001a.html](http://www.zyvex.com/Products/NASO_001a.html).
155. <http://journals.ohiolink.edu/local-cgi/send-pdf/050524160611195667.pdf>.
156. J. Oh, K. Oh, C. Kim and C. Hong, *Composites: Part B* **35** (2004) 49–56.
157. S. Walsh, D. Spagnuolo and B. Scott, SAMPE Proceedings, May 2005.
158. L. Dai, *Energeia* **16** (2005) 1–4.
159. M. Gao, L. Dai and G. Wallace, *Electroanalysis* **15** (2002) 1089–1094.
160. M. Terrones, A. Jorio, M. Endo, A. Rao, Y. Kim, T. Hayashi, H. Terrones, J. Charlier, G. Dresselhaus and M. Dresselhaus, *Mater. Today* **7** (2004) 30–45.
161. P. Mulchandani, Y. Lei, W. Chen, J. Wang and A. Mulchandani, *Analyt. Chim. Acta* **470** (2002) 79–86.
162. A. Vilkanauskys, T. Erichsen, L. Marcinkeviciene, V. Laurinavicius and W. Schuhmann *Biosensors Bioelectron.* **17** (2002) 1025–1031.

163. A. Abdelghani, C. Abdelghani-Jacquín, H. Hillebrandt and E. Sackmann, *Mater. Sci. Eng.* **C22** (2002) 67–72.
164. M. Kessler and S. White, *Composites Part A* **32** (2001) 683–699.
165. P. Glatkowski, *SAMPE Proceedings*, May 2003.
166. K. Watson and J. Connell, *Space Applications*, This book, Chapter 19, Carbon Nanotechnology, Elsevier B.V.
167. B. Lee, W. Woo and M. Kim, *Macromol. Mater. Eng.* **286** (2001) 114–118.
168. S. Tzeng and F. Chang, *Mater. Sci. Eng.* **A302** (2001) 258–267.
169. C. Huang and J. Pai, *Eur. Polym. J.* **34** (1998) 261–267.
170. (a) B. Lee, W. Woo, H. Park, H. Hahm, J. Wu and M. Kim, *J. Mater. Sci.* **37** (2002) 1839–1843, (b) J. Fielding, J. Gordon, M. Alexander, M. Kistner, J. Horwath, J. Borges, A. Loff and D. Widauf, *SAMPE Proceedings 2005-ISSE* and (c) G. Hansen, *Proceedings of SAMPE Conference – ISSE 2006* (in press).
171. H. Fong, R. Vaia, J. Sanders and D. Lincoln, *Chem. Mat.* **13** (2001) 4123–4129.
172. (a) J. Guthrie, T. Benson Tolle and D. Rose, *AMPTIAC* **8** (2004) 51–58 and (b) E. Katz et al.
173. E. Kymakis and G. Amaratunga, *Solar Energy Mat. Solar Cells* **80** (2003) 465–472.
174. N. Koprinarov, R. Stefanov, G. Pchelarov, M. Konstantinova and I. Stambolova, *Synth. Metals* **77** (1996) 47–49.
175. J. Rud, S. Lovell, J. Senn, Q. Qiao and J. McLeskey, *J. Mater. Sci.* **40**: (2005) 1455–1458.
176. B. Landi, S. Castro, H. Ruf, C. Evans, S. Bailey and R. Rafaelle, *Solar Energy Mater. Solar Cells* **87** (2005) 733–746.
177. B. Landi, R. Rafaelle, S. Castro and S. Bailey, *Progr. Photovolt.: Res. Appl.* **13** (2005) 165–172.
178. R. Rafaelle, B. Landi, J. Harris, S. Bailey and A. Hepp, *Mater. Sci. Eng. B* **116** (2005) 233–243.
179. H. Ishii, T. Ozaki and S. Hahn, *SAMPE Conference Proceedings*, May 2004.
180. J. Borchardt, *Mater. Today* **7** (2004) 29.
181. T. Kashiwagi, E. Grulke, J. Hilding, R. Harris, W. Awad and J. Douglas, *Macromol. Rapid Commun.* **23** (2002) 761–765.
182. T. Kashiwagi, E. Grulke, J. Hilding, K. Groth, R. Harris, K. Butler, J. Shields, S. Kharchenko and J. Douglas, *Polymer* **45** (2004) 4227–4239.
183. J. Gilman, *Appl. Clay Sci.* **15** (1999) 31–49.
184. F. Dabrowski, M. Bras, R. Delobel, J. Gilman and T. Kashiwagi, *Macromol. Symp.* **194** (2003) 201–206.
185. S. Bourbigot, M. Bras, F. Dabrowski, J. Gilman and T. Kashiwagi, *Fire Mater.* **24** (2000) 201–208.
186. A. Morgan, R. Harris Jr., T. Kashiwagi, L. Chyall and J. Gilman, *Fire Mater.* **26** (2002) 247–253.
187. G. Beyer, *Fire Mater.* **29** (2005) 61–65.
188. T. Kashiwagi, F. Du, K. Winey, K. Groth, J. Shields, S. Bellayer, H. Kim and J. Douglas, *Polymer* **46** (2005) 471–481.

189. C. Thompson, J. Smith Jr., W. Connell, P. Hergenrother and R. Lyon, SAMPE Proceedings, May 2004.
190. R. Vaia, G. Price, P. Ruth, H. Nguyen and J. Lichtenhan, Appl. Clay Sci. **15** (1999) 67–92.
191. A. Arnall, A technical, political and institutional map of emerging technologies. Greenpeace Report, 2003. [www.greenpeace.org.uk/MultimediaFiles/Live/FullReport/5886.pdf](http://www.greenpeace.org.uk/MultimediaFiles/Live/FullReport/5886.pdf)

## Chapter 19

### Polymer and carbon nanotube composites for space applications

Kent A. Watson<sup>a</sup> and John W. Connell<sup>b</sup>

<sup>a</sup>National Institute of Aerospace, 100 Exploration Way, Hampton, VA 23666-6147

<sup>b</sup>National Aeronautics and Space Administration, Langley Research Center, MS 226 Hampton, VA 23681-2199, USA

Polymer and carbon nanotube (CNT) composite materials are potentially useful for space applications because of their unique combination of electrical, thermal, and mechanical properties. Much of the research has focused on using carbon nanotubes (CNTs) as electrically conductive additives for polymers to mitigate electrostatic charged build-up. This addresses a problem that is particularly relevant to large, deployable spacecraft comprised primarily of polymer materials such as Gossamer structures. These spacecraft are constructed of compliant polymeric materials that can be folded into compact volumes for launch. Transparent, conductive coatings are needed that can tolerate folding and subsequent deployment. Other concepts for polymer and CNT composites include lightweight, radiation shielding (heavy ion and electromagnetic radiation), high thermal conductivity matrices and coatings, and structural matrix systems. Space environment survivability is an important factor in the development of nanocomposite materials. The effect of space environmental exposure on the properties of CNTs is not known. In practice, polymer nanocomposites will undoubtedly suffer from environmentally induced degradation due to particulate radiation, atomic oxygen (in low Earth orbit), ultraviolet radiation, thermal cycling, micrometeoroid impacts, and synergistic effects due to combinations thereof. Topics covered include the space environment, the effects (including synergistic) of the space environment on polymer nanocomposites, and potential applications of polymer nanocomposites.

#### 1. INTRODUCTION

No longer sheltered by the Earth's protective atmosphere, space becomes a hostile environment to both humans and spacecraft and it is imperative to consider the damaging effects of the space environment when designing materials for use in low Earth orbit (LEO) and beyond. Factors that determine the environmental exposure of spacecraft are altitude, attitude, orbit, mission duration, and inclination. In general, materials in space are subjected to atomic oxygen (AO), ultraviolet (UV) radiation, vacuum UV (VUV) radiation, micrometeoroids, debris, ionizing radiation, thermal cycling, and other environmental conditions depending on orbit.

Table 1.  
Summary of orbital environments.

Orbit	Altitude	Primary environmental hazards
LEO	Upto 1,000 km	AO, meteoroids, space debris, UV/VUV radiation, thermal cycling
MEO	1,000–35,000 km	Van Allen radiation, UV/VUV radiation, meteoroids, thermal cycling
GEO	~35,000 km	Solar flare protons, spacecraft charging, UV/VUV radiation, thermal cycling

There are four representative orbital regions in space: LEO, mid-Earth orbit (MEO), geosynchronous orbit (GEO), and interplanetary/deep space. Materials in LEO are especially prone to attack from AO. At higher altitudes (MEO, GEO, deep space), AO and orbital debris become negligible but UV, VUV, electrons, protons, and other particulate radiation are of concern. However, spacecraft destined for MEO, GEO, or beyond may spend extended periods of time in LEO where the craft may undergo system checks and be serviced, if necessary, before being boosted to a higher orbit or beyond Earth. AO may also be problematic in orbits around other planets (i.e. Mars) that have an atmosphere containing oxygen. Table 1 is a summary of important orbital environments and the predominant environmental hazards.

Spacecraft and vehicles come in many different forms ranging from large, thin-film based structures—also called Gossamer structures—to interplanetary probes to multifaceted complex structures (i.e. the International Space Station, ISS). Each spacecraft is often constructed from a variety of materials with an assortment of different requirements and each material must be designed with the final orbital environment in mind. A brief introduction to the space environment, its effects on materials, and potential space applications where CNTs and nanocomposites may be useful is offered in this chapter.

## 2. SPACE ENVIRONMENT

### 2.1. Atomic oxygen

Spacecraft orbiting in LEO are exposed to a residual atmosphere composed predominately of highly reactive AO atoms. In LEO, AO is formed as a result of photo dissociation of molecular oxygen ( $O_2$ ) due to exposure from ultraviolet solar radiation at wavelengths less than 243 nm. The probability of recombination of AO molecules to reform molecular oxygen is negligible due to the low atmospheric density of AO molecules. Thus, the formation of AO occurs in ~99% yield as shown:

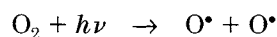


Fig. 1 shows the density of gaseous species from 100 to 700 km [1]. The composition of the upper atmosphere shown is an average, as it varies with temperature,

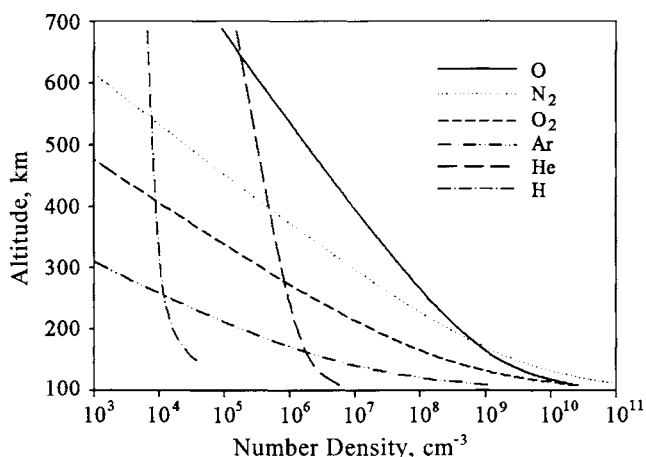


Figure 1. Density of gaseous species as a function of altitude [1].

solar activity, variations in the Earth's magnetic field, latitude, and season. AO is the most abundant and most reactive species at altitudes from about 200 to 650 km and although other gaseous species are present, including nitrogen and atomic hydrogen, their reactivity toward typical spacecraft materials is negligible.

Although the concentration of AO in LEO is low (pressures of  $\sim 10^{-7}$  torr), the high orbital velocity of spacecraft in LEO causes the flux of AO on ram-orientated spacecraft surfaces to be very high—with collisional energies of  $\sim 5$  eV ( $\sim 480$  kJ/mol). (Orbiting spacecraft in LEO typically travel at velocities of 8–12 km/s depending on eccentricity and orbital inclination.) The total amount of AO exposure depends on many factors including spacecraft altitude, orbital inclination, attitude, mission duration, and solar activity [2]. As an example, the ISS is bombarded with AO at about  $10^{14}$  atoms/cm<sup>2</sup> s for normal incident ram surfaces. Also, because AO formation is dependent upon solar radiation, its concentration is dependent upon solar activity. Fig. 2 shows AO flux as a function of solar cycle activity at altitudes ranging from 300 to 900 km [3]. Spacecraft in LEO orbit will be exposed to less AO during periods of low solar activity than one orbiting during periods of high activity. Fig. 3 shows the history of sunspot variation throughout the 11-year solar cycle from 1850 to 2005 [4]. For short missions in LEO, solar activity is an important factor and the solar cycle should be taken into consideration when selecting spacecraft materials. The Sun emits more energy, including UV radiation, during times of solar maximum. The increase in radiation may increase the damaging effects on spacecraft materials and the increase in energy also expands the upper atmosphere due to thermal expansion which in turn increases the concentration of AO at LEO altitudes [5].

Erosion and material property changes due to AO are generally insignificant for short periods of exposure. However, as the typical lifetime of spacecraft increases

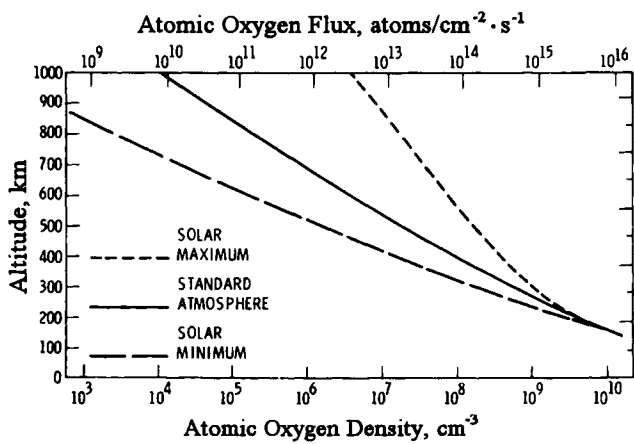


Figure 2. AO flux as a function of altitude [3].

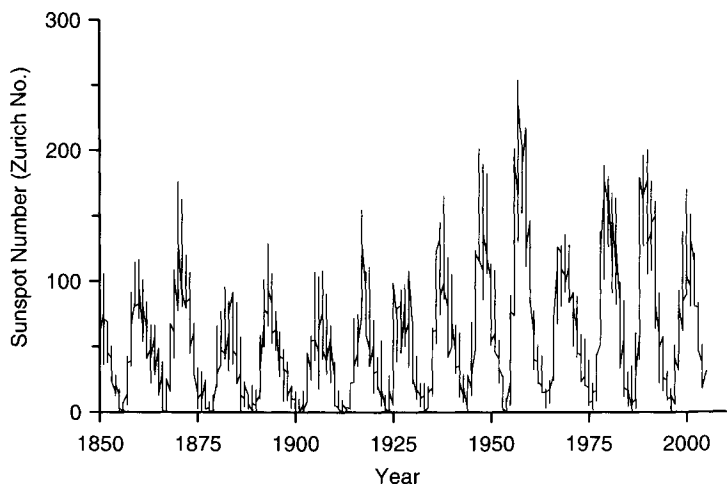


Figure 3. History of sunspot variation.

to 10 years and greater (space station, etc.), the stability of material properties important to the function of the spacecraft becomes a major consideration.

**2.2. Effect of atomic oxygen on materials**

Many spacecraft materials, including carbon-based materials and organic polymers, are subject to degradation when exposed to highly reactive AO [6,7]. Further

complicating the issue are synergistic effects caused by concurrent exposure to UV and VUV radiation. Combined, the presence of these elements in LEO is at sufficient concentrations and energy levels to cause chemical bond cleavage. The resulting bond cleavage can give rise to further chemical reactions that can cause adverse physical, mechanical, and optical property changes in the material. Chemical reactions can also lead to small molecule formation and subsequent off-gassing, and these newly formed gaseous species can further erode materials, contaminate surfaces, or degrade optical properties of telescope lenses, reflectors, solar concentrators, etc. The chemistry and mechanism of material degradation due to AO attack is complex and not fully understood. In general, the degradation process can be described as the removal of carbon, hydrogen, or other atoms in the material through processes involving abstraction, addition, or replacement of atoms [8].

The effects of AO on CNTs can be speculated from in-orbit studies done on organic materials and carbon forms such as pyrolytic graphite and carbon fiber due to their similarities in composition and/or structure. The effects of AO flux and the space environment on several hundred different materials have been investigated in three Space Shuttle experiments, one satellite recovery (Long Duration Exposure Facility, LDEF), experiments aboard Russia's Mir Space Station, servicing missions on the Hubble Space Telescope, and observations on the ISS [5,7,9–17]. AO erosion yields (the volume of material that is lost per incident AO atom) of selected commonly used materials are shown in Table 2. Gold and aluminum are apparently unaffected by AO exposure. Many organic polymers are readily degraded as indicated from the data as well as Fig. 4. Fig. 4 shows unprotected Kapton® before and after exposure to AO in LEO aboard LDEF (10 months exposure) [18]. The “before” image shows a relatively smooth film surface and after AO exposure, pitting and erosion of material is readily observed. Left unprotected, exposure of Kapton® and many other organic polymers to AO would eventually lead to complete mass loss which would have obvious catastrophic effects.

Table 2.  
Erosion yield of various materials exposed to LEO environment.

Material	Erosion yield, $\times 10^{-24}$ $\text{cm}^{-3} \text{atom}^{-1}$	Reference
Aluminum	0.00	19
Diamond	0.021	20
Gold	0.0	8
Kevlar 49	5.0	6
Kapton	3.0	21
Polyethylene	3.3–3.7	21
Polycarbonate	6.0	21
Polymethylmethacrylate	3.1	21



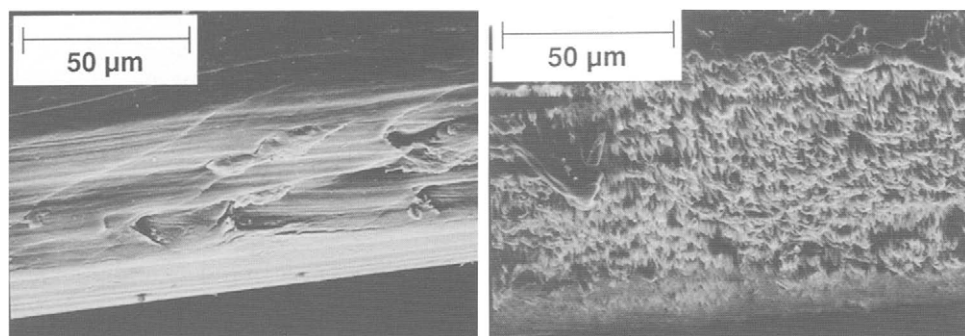


Figure 4. Effect of AO on Kapton®.

Table 3.

Erosion yield of carbon and carbon composites exposed to LEO environment.

Graphite/resin	Erosion yield, $\times 10^{-24}$ $\text{cm}^{-3} \text{atom}^{-1}$	Reference
Carbon film	1.4–4.3	6
Graphite, basal orientated	0.63	6
Glassy carbon	1.3	6
Highly oriented pyrolytic graphite	1.04–1.07	20
T300 carbon/1034C epoxy	2.1	21
T300 carbon/5208 epoxy	2.6	21
Epoxy	1.7	22
T300 carbon/934 epoxy	0.99–1.35	21
AS-4/3501-6 Epoxy	0.8	21
C6000/PMR-15 polyimide	0.9	21
HMS/934 epoxy	1.0	21
P75S/934 epoxy	1.0	21

Materials aboard LDEF included several carbon fiber/polymer matrix composites. Table 3 shows the AO erosion yields for selected carbon materials and carbon composites. In general, erosion due to AO was much greater for the organic matrix resin than for the carbon fibers. In-flight LEO experiments on materials containing nanotubes are currently being conducted on MISSE (Materials International Space Station Experiment) and additional samples are scheduled to be placed on the ISS when the Space Shuttle resumes space flight.

Although in-flight space environmental effects on single-wall carbon nanotubes (SWNTs) and multi-wall carbon nanotubes (MWNTs) are unknown at this time, it is

probable that the nanotubes will be eroded to some extent due to AO exposure. For composite [23] and nanocomposite materials, the matrix (typically organic in nature) will be damaged if left unprotected when exposed to AO and UV, and mechanical and other properties of the composites will suffer.

CNTs will likely exhibit similar erosion yields to graphite and other similar forms of carbon since both CNTs and graphite consist of  $sp^2$ -hybridized carbons. Graphite consists of layered sheets of  $sp^2$  carbons whereas CNTs can be viewed as sheets of  $sp^2$  carbons rolled up into long tubes or cylinders. A HRSEM image of graphite is shown in Fig. 5 and the cylindrical shape of SWNTs and MWNTs can be seen in Figs. 6 and 7, respectively. MWNTs can have diameters ranging from 50 to over 400 nm depending on the manufacturing process whereas SWNTs typically have much smaller diameters on the order of 1.2–1.4 nm.

AO apparently reacts with graphite and similar forms of carbon forming oxygen-carbon complexes. Due to the vacuum of space, the resulting carbon complexes evaporate into the gaseous phase resulting in mass loss and depression of mechanical properties [24]. In-flight AO erosion yields of pyrolytic graphite range from 1.04 to  $1.7 \times 10^{-24} \text{ cm}^3/\text{atom}$  [20]. Stark et al. [25] studied the effect of AO on the mechanical properties of highly graphitized carbon fibers and found that Young's modulus and tensile strengths decreased with increasing exposure time. Scanning electron microscopy (SEM) images of the exposed graphitized carbon fibers revealed severe surface degradation. Other studies [26–30] also show similar degradation of carbon and graphite materials due to AO, presumably because AO reacts preferentially with delocalized  $\pi$  electrons in the graphite. Similar chemistry is expected to occur with SWNT and MWNTs.

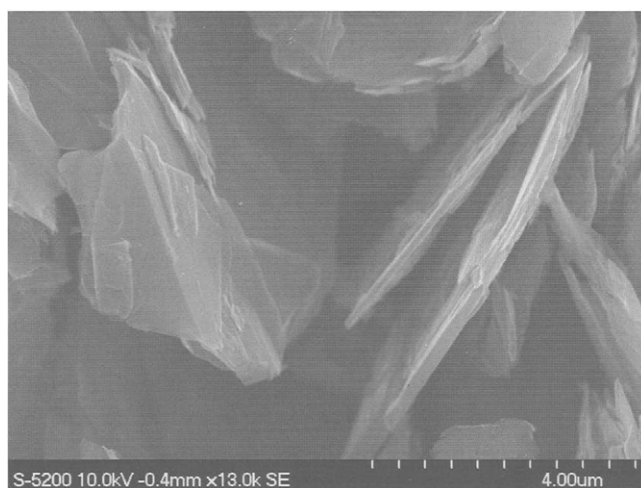


Figure 5. HRSEM image of graphite.

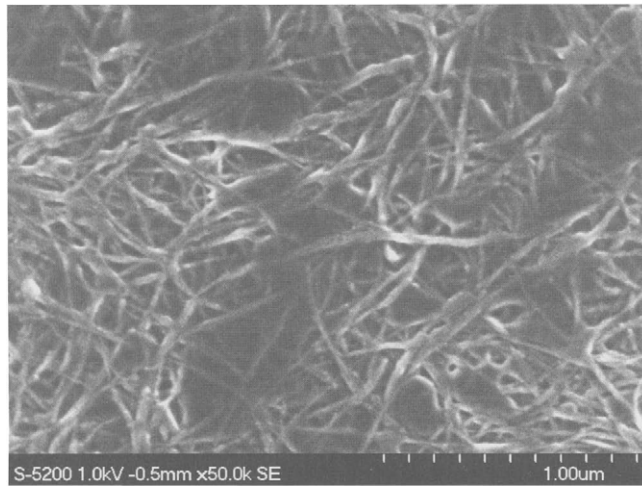


Figure 6. HRSEM image of SWNTs.



Figure 7. HRSEM image of MWNTs.

Due to greater bond strain (smaller diameter tube), it is hypothesized that SWNTs may be more reactive towards AO compared to MWNTs and graphite. Regardless of reaction rates, as with carbon fiber composites the limiting factor with regards to AO degradation will likely be the organic matrix and not the CNTs.

### 2.3. Protection against atomic oxygen

Present methods for the elimination or reduction of erosion due to AO on commercial materials involve coating the material with metal oxides such as aluminum oxide, titanium oxide, chromium oxide, tin oxide, silicon compounds, fluorinated polymers, and combinations thereof [7,31,32]. Application of the AO coating usually requires a specialized facility and a separate processing step. In addition, there are limitations on the shape and size of structure that can be coated. Other problems associated with the use of coatings include difficulty in uniformly coating complex shapes and the risk of damage to the coating from manufacturing, handling, storage, and from space-based particle impact. Another problem that arises is when there is a mismatch between the coefficient of thermal expansion (CTE) of the substrate material and the coating. Upon thermal cycling this can cause cracking or peeling (dis-bonding). Once damage occurs to the protective coating, the underlying polymer becomes exposed to the space environment (AO, UV, etc.) and erosion may resume leading to the loss of mechanical, optical, or other properties.

Developing thin polymeric films for space applications is very challenging. In many of these cases the material must be folded for stowage prior to launch (i.e. inflatable structures) and the use of an AO protective coating may not be viable as it will likely be damaged due to folding and unfolding of the coated film.

An alternative to coatings is to use materials inherently resistant to AO. AO resistant polymer development has recently focused on incorporating phenylphosphine oxide (PPO) [33–40] groups or silicon [41,42] into the backbone of polymers. X-ray photoelectron spectroscopy studies have shown that polymers containing chemically bound PPO units [33–38] or phosphazene groups [43,44] have significantly increased AO and oxygen plasma resistance due to formation of a phosphate surface layer. Other work using X-ray Adsorption Near Edge Structure Spectroscopy indicates that a polyphosphate surface layer forms upon exposure of these materials to AO, subsequently inhibiting erosion of the underlying polymer [45].

Several protective coatings for carbon composites have undergone space-flight testing, primarily on LDEF. Coatings tested included metals and metal oxides such as nickel, aluminum,  $\text{TiO}_2$ ,  $\text{ZnO}$ ,  $\text{Al}_2\text{O}_3$ ,  $\text{Ni/SiO}_2$ ,  $\text{Al/Al}_2\text{O}_3$ ,  $\text{In-Sn}$ ,  $\text{Al/Ni}$ ,  $\text{SiO}_2/\text{Cr}$ , and others [46–49]. The metallic coatings were sputter-deposited onto graphite/epoxy composites and post-flight analysis indicated good to excellent AO protection. Metal and metal oxide coatings would conceivably protect CNTs composites with similar effectiveness.

### 2.4. UV and VUV radiation

Ground-based objects and aircraft flying at standard altitudes (typically under 12.8 km) are largely protected from UV radiation (approximate wavelengths between 0.1 and 0.4  $\mu\text{m}$ , with VUV between 0.1 and 0.2  $\mu\text{m}$ ) by the Earth's atmosphere [50]. Spacecraft operating at LEO and above are beyond protection and are subjected to UV radiation as part of being exposed to the full on-orbit solar spectrum (Fig. 8) [51].

### 2.5. Effects of UV radiation on materials

UV radiation present in the space environment can degrade organic polymer matrices of composites and nanocomposites. This may lead to loss of mechanical,

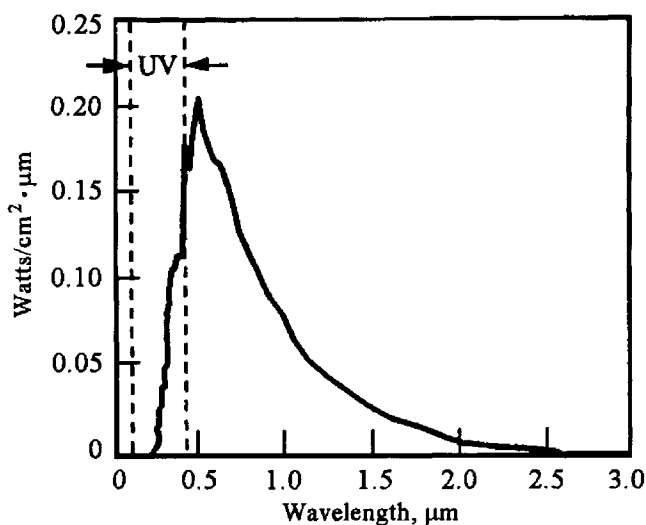


Figure 8. ASTM solar air mass zero curve [51].

thermo-optical, and optical properties of structural components and subsystems. Organic polymers in particular are vulnerable because many organic bonds absorb UV radiation, which can lead to radical formation, subsequent chemical reactions (crosslinking, etc.), bond breakage, and polymer chain scission. As an example, exposure of a graphite epoxy composite to UV radiation can initiate microcracking in the composites, which can be further aggravated by thermal cycling [52]. (Thermal cycling will be discussed later in this chapter.) In addition, synergism between UV radiation and AO exposure can cause increased reaction efficiencies as compared to UV or AO exposure alone. Although CNTs may not be affected directly by exposure to UV radiation, loss of mechanical or optical properties of the composite can occur due to matrix degradation.

## 2.6. Ionizing radiation

Spacecraft are exposed to numerous ionizing radiation sources including electrons, protons, X-rays, gamma rays, and nuclei of many elements. Solar flares produce electromagnetic radiation energy spikes ranging from radio waves to gamma waves. As with AO density, X-ray emission peaks also occur at times of high solar activity and are tied in with the solar cycle [53]. Charged particle radiation (electrons, protons,  $\alpha$  particles, nuclei) originates from three main sources: galactic cosmic rays, solar events, and the trapped radiation belts (Van Allen belts). Table 4 summarizes the source, types of particles, and energies of ionizing radiation [54].

## 2.7. Effects of ionizing radiation on materials

In addition to composite degradation, ionizing radiation is potentially hazardous to crew members and electronics [55]. Space radiation studies performed on CNTs

Table 4.  
Summary of ionizing radiation.

Source	Radiation	Approximate energies
Galactic cosmic rays	Protons, alpha particles, electrons, atomic nuclei	$10^8$ – $10^{19}$ eV
Solar proton events	Protons, electrons, heavy ions	$10$ – $>100$ MeV/n
Solar flares	Energetic photons	Radio waves through gamma waves with notable increase in X-rays
Van Allen belts	Protons, electrons, heavier ions	$10$ – $>100$ MeV

have been limited but early tests indicate that CNTs have some radiation tolerance [56–59]. In a recent paper, the effects of ground-based radiation sources on polyethylene/SWNT composites were studied [60]. The simulated radiation included secondary neutrons, protons in LEO, and protons and heavy ions typical of galactic cosmic rays. The study indicated that SWNTs are radiation tolerant for medium energy protons typical of an LEO orbit and high-energy protons and iron ions typically found in interplanetary space. The results also suggested that, as with other space environment effects, the consequences of matrix exposure to ionizing radiation might be the weak link when considering CNT composites for space applications.

Another recent study by Tatro et al. examined MWNT/poly(methyl methacrylate) (PMMA) composites after being  $\gamma$ -irradiated via a  $^{137}\text{Cs}$  source [61]. The results indicated that the radiation resistance of PMMA may be increased through the addition of small amounts (0.50%) of MWNT. Conjugated bonds of the nanotubes may absorb some of the radiation energy, become excited, and subsequently return to the ground state, thereby limiting radiation damage to the PMMA.

Najafi et al. [62] exposed PMMA/SWNT composites to electron beam radiation. The results indicate that the addition of SWNTs at concentrations of  $\sim 0.5$  wt% reinforced the PMMA against irradiation-induced degradation. The rationale is that the SWNT networks disperse irradiated electrons throughout the PMMA matrix, preventing free radical formation and subsequent polymer degradation. In another study, MWNTs and SWNTs were irradiated with low-energy electron beams of 30 keV [63]. The SWNTs showed an apparent collapse on prolonged exposure as well as irreversible damage. These preliminary studies highlight the need for long duration in-flight testing of carbon nanocomposites.

## 2.8. Thermal cycling

Spacecraft in LEO can experience severe temperature extremes as they pass from Sun exposure to shadow (behind Earth). The atmospheric temperature at altitudes from  $\sim 200$  to 500 km is typically greater than  $400^\circ\text{C}$  (full Sun exposure); however, due to the extremely low atmospheric pressures at LEO altitudes, little conductive

heat transfer occurs to spacecraft. The temperature of spacecraft and other objects in LEO is primarily dependent upon the gain or loss of radiant energy. Spacecraft in LEO receive radiant thermal energy from three primary sources: solar radiation from the Sun, solar energy reflected from Earth's surface (albedo), and outgoing long-wave radiation emitted by Earth's atmosphere. Spacecraft in an LEO have orbital periods of  $\sim 90$  min and move in and out of direct sunlight once for every orbit. In GEO, spacecraft are exposed to solar radiation for most of the year, hence thermal cycling is less severe because the satellite spends the majority of the time fully exposed to solar energy leading to fewer temperature fluctuations. Also, since a GEO orbit is much farther away from Earth than LEO, thermal energy from Earth received by spacecraft has less influence.

Spacecraft materials must be able to withstand thermal cycling from one temperature extreme to the other. Over a period of 30 years, a structure in LEO can be subjected to over 500,000 thermal cycles. Differences in CTE between composite material components can cause microcrack formation due to repetitive thermal cycling [64]. Microcracks can result in degradation due to AO and UV exposure of the interior of the composite and subsequent loss of mechanical properties. In addition, thermal fatigue can lead to detrimental inter-lamina shear and bending properties [65]. Coated structures with CTE differentials are susceptible to thermal cycling effects as well. CTE differentials are especially important to consider when using coatings on materials that will undergo thermal cycling.

## **2.9. Meteoroids, micrometeoroids, and space-debris**

Meteoroids, micrometeoroids, and human-made space debris provide a unique space environmental hazard. Impacts upon spacecraft may puncture pressurized compartments, damage solar array panels (causing electrical failure), cause mechanical failure of composites, or cause a multitude of other damaging effects. Fig. 9 shows the predicted micrometeoroid and debris spacecraft impact fluxes with varying particle sizes [66]. Micrometeoroids ranging from 50  $\mu\text{m}$  to 1 mm in diameter are the predominate concern. Collision velocities for meteoroids and micrometeoroids range from approximately 3 to 72 km/s, depending on spacecraft orbital velocity, velocity, and angle of impact [21]. For orbital debris, collision velocities can vary from 3 to 15 km/s. Micrometeoroid and debris damage to composites can be intensified due to subsequent exposure of underlying material to AO, UV, VUV, charged particles, and thermal cycling. The frequencies of impacts, although rare, are expected to increase in the future as the population of human-made debris increases.

## **2.10. Synergistic effects**

Materials in space are concurrently exposed to numerous harsh conditions and synergism between these space environmental components can cause accelerated damage and degradation. As an example, perfluorinated materials such as copoly(fluoroethylene propylene) exhibit good resistance to AO, but dramatic increases in the erosion rate are observed when the polymer is exposed simultaneously to AO and UV radiation [67–70].

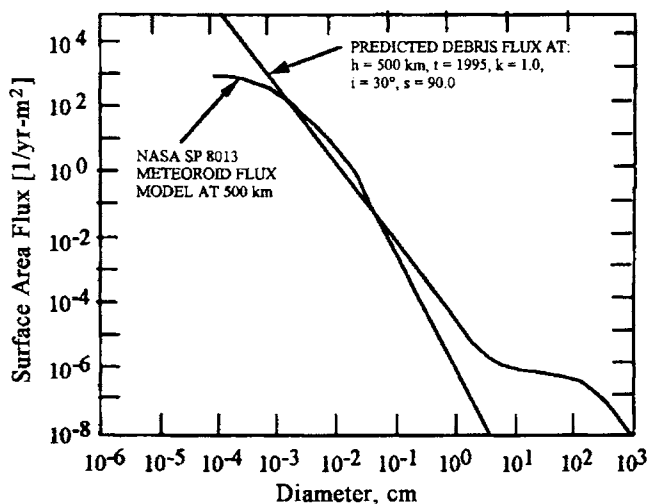


Figure 9. Predicted micrometeoroid fluxes [66].

A recent study by Han and Kim [71] involved exposing graphite/epoxy composites to ground-based LEO simulated environments. After exposure to simulated AO under vacuum conditions, erosion of the composite surface resulted in mass loss and degradation in tensile properties. Synergistic conditions caused additional harmful effects. When the composites were exposed to UV radiation, thermal cycling, simulated AO, and vacuum, more surface erosion was reported as well as microcracks. Recognizing potential synergistic effects is critical when considering spacecraft materials and design.

### 3. POTENTIAL SPACE APPLICATIONS OF CARBON NANOTUBE COMPOSITES

#### 3.1. Structural uses for nanotubes composites

Nanotube composites for non-space use (i.e. taking advantage of their theoretical mechanical properties) are covered in more detail in the chapter entitled "Nanotube and epoxy composites for military applications" [72]. Weight loss in generic space structures leads to reduced launch weight with the end result being cost savings. Stronger and lighter materials are suitable for reusable launch vehicles, air frames, fuel tanks, spacesuits, crew exploration vehicles, and lunar and planetary habitats. Multifunctional nanocomposite materials can reduce weight by performing several functions. Such technologies will be instrumental to achieving a sustained human presence in space.

#### 3.2. Clear, conductive coatings for electrostatic discharge

One potential application for CNTs takes advantage of their excellent electrical conductive properties, small size, and high aspect ratio. As an example, SWNTs can



be used to make clear, conductive coatings for spacecraft surfaces. Low color, space environmentally durable polymeric films with sufficient electrical conductivity to mitigate electrostatic charge (ESC) build-up are needed for applications on advanced spacecraft, particularly on large, ultra-light weight space structures [73]. For these applications, the films must exhibit sufficient electrical conductivity to prevent static charge build-up.

Particles prevalent in the Earth's orbital environment include electrons, solar flare protons, and galactic cosmic rays [74–76]. The high energies of these particles allow them to penetrate spacecraft surface layers and cause chemical reactions that can ultimately degrade optical and/or mechanical properties of organic polymers and composites. Furthermore, energetic charged particles—particularly electrons—can penetrate surface layers, depositing a charge on to insulating materials and other electrically isolated surfaces on a spacecraft. ESC build-up and development of large electric fields can result. Consequent discharging can potentially cause catastrophic damage to sensitive spacecraft electronics [77,78]. The surface resistivity required to dissipate ESC build-up on insulators (such as polymer films) is in the range of  $10^6$ – $10^{10}$   $\Omega/\text{sq}$ .

Many applications for polymers on spacecraft require only surface resistivity to mitigate ESC (volume conductivity is not necessary) [79,80]. The amount of SWNTs required to mitigate ESC build-up is greatly reduced when only surface resistivity is required as compared to films containing SWNTs dispersed throughout the bulk. The advantage of using coatings is that the use of a lower amount of SWNTs has negligible effects on the optical and thermo-optical properties of the films.

In a recent study, transparent, flexible films with surface resistivities sufficient to mitigate ESC were prepared by surface coating three different space durable polyimides (LaRC™ CP2, TOR-NC, and PPO-6FDA, Fig. 10) with a thin layer of SWNTs [81]. In general, it was found that films coated with SWNTs exhibited surface resistivities sufficient for ESC mitigation with negligible degradation of the thermo-optical properties.

Fig. 11 is a high-resolution scanning electron microscope image of two polymers coated with SWNTs [81]. The sample on the left (coated TOR-NC) has a surface resistivity of  $2.0 \times 10^7$   $\Omega/\text{sq}$ , and the sample on the right (coated PPO-6FDA) has a surface resistivity of  $1.4 \times 10^7$   $\Omega/\text{sq}$ . Both values are within the range required for electrostatic charge mitigation.

The effect of SWNT spray-coating on the solar absorptivity ( $\alpha$ ) and thermal emissivity ( $\varepsilon$ ) is of interest since these properties are important for some applications on Gossamer spacecraft [82]. Solar absorptivity pertains to the fraction of incoming solar energy that is absorbed by the film and is typically below 0.1 for a low color/colorless film. Thermal emissivity is a measure of the films ability to radiate energy from the film surface. Table 5 shows  $\alpha$  and  $\varepsilon$  values of the samples shown in Fig. 11 as well as the values for the control samples [81]. Overall,  $\varepsilon$  values were not greatly affected after application of SWNTs to the film surface. Solar absorptivity values increased somewhat with increased amount of SWNTs.

Conductive coatings that are robust and can withstand folding and/or bending are also sought after for use on spacecraft. Indium tin oxide (ITO) is the current state

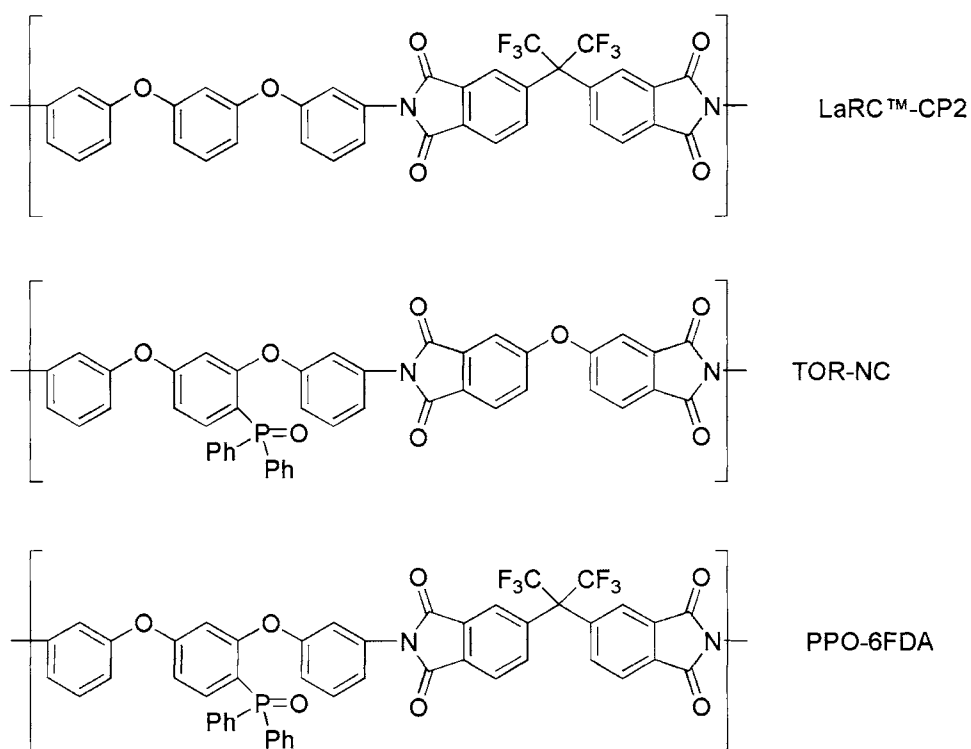


Figure 10. Space durable polyimides.

of the art material used for clear conductive coatings; however, an ITO coating is fragile and cannot withstand bending or folding when applied to a flexible substrate. Coatings using SWNTs are robust and can withstand numerous foldings as well as being crumpled into a ball. Tests indicated that films coated with SWNTs retained their surface resistivities after harsh manipulation [81,83]. Comparable tests applied to an ITO-coated film would result in immediate loss of conductivity due to fracture of the coating upon bending [84].

As part of a future MISSE experiment, films coated with SWNTs will be exposed to the LEO environment. To determine the effect of AO on the SWNT coating, samples will be placed with the SWNT coating facing the AO flux as well as facing away from the AO flux. One of the polymers coated with SWNTs contains phosphorus, which provides inherent AO protection [40].

### 3.3. Thermal conductivity

Researchers at NASA Langley Research center, together with Clemson University and NASA Johnson Space Center, are currently investigating the use of CNTs as additives to improve the thermal conductivity (TC) of polymeric materials. The objective

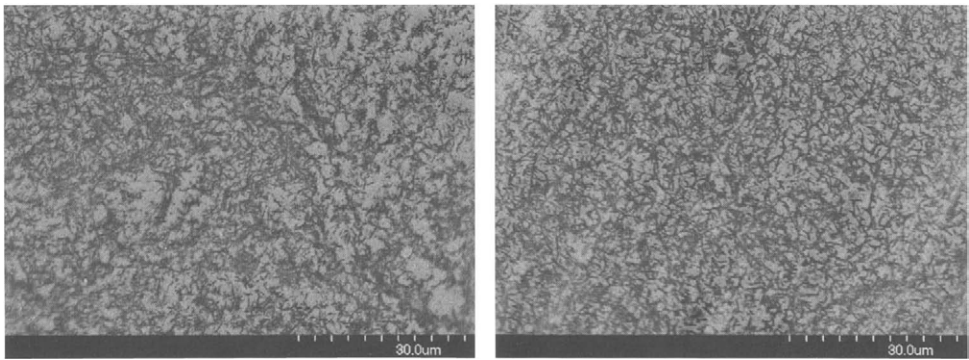


Figure 11. High-resolution SEM of PPO-6FDA (left) and TOR-NC (right) both coated with SWNT (magnification = 1500x).

Table 5.  
Solar absorptivity and thermal emissivity values of PPO-6FDA and TOR-NC polymers coated with SWNTs.

Sample	Solar absorptivity	Thermal emissivity
PPO-6FDA, neat	0.05	0.54
PPO-6FDA coated	0.09	0.56
TOR-NC, neat	0.05	0.60
TOR-NC coated	0.08	0.58

of this work is to reduce spacesuit weight and improve astronaut mobility, comfort, and safety by improving the thermal conductivity of the fabric and tubing used for the liquid cooling ventilation garment (LCVG). CNTs are among the most thermally conductive materials known with conductivities in the range of 3000 W/mK (multi-walled CNTs) [85]. In comparison, silver has a TC of 430 W/mK. Currently, the LCVG weighs approximately 3.3 kg including the water circulating in the cooling tubes. By increasing the TC of the materials, the weight of the LCVG can be reduced.

Today’s spacesuits are adequate for current astronaut needs, primarily for work in a vacuum. Examples include space walks in LEO as well as astronauts walking on the surface of the Moon. However, the current technology used on spacesuits will not work on Mars or other planetary systems that have an atmosphere and significant gravity. Advanced astronaut spacesuits with improved TC fabrics are essential to the success of future Mars and other planetary missions.

3.4. Radiation/heavy ion shielding

Galactic cosmic rays are a significant source of radiation for spacecraft, particularly in deep space missions [86,87]. Space exploration requires radiation protection

to protect astronauts and electronic equipment for applications such as space suits, lunar/planetary rovers, lunar/planetary habitats, interplanetary space vehicles, etc. Heavy ion radiation poses significant dangers such as increased cancer risk in astronauts and memory damage in sensitive computer components. A current method to impart heavy ion radiation protection on the ISS uses polyethylene (PE), which is known to possess excellent heavy ion radiation protection, positioned at critical locations within the aluminum framework of the station. Aluminum is lightweight and strong and therefore is a good choice for vehicle construction; however, its heavy-ion radiation protection is poor. Combining the aluminum structure with high hydrogen-containing PE compensates for aluminum's limitations. However, PE is a parasite: it carries a weight penalty, takes up valuable space, and is a flammable material creating a safety hazard. The combination of these problems makes this approach impractical for radiation protection in future exploration systems.

Elements with low atomic numbers, primarily hydrogen but includes elements up to carbon and oxygen, offer improved shielding properties over aluminum [86]. Therefore, a potential use in space for nanotubes is composites for intrinsic heavy ion radiation protection. Nanotubes can be combined with high hydrogen-containing polymers to impart heavy ion radiation resistance.

### 3.5. Space elevator

First proposed as science fiction, the emergence of a material with the theoretical strength of CNTs makes the thought of a space elevator plausible. The first publication of a space elevator taking advantage of a geosynchronous orbit appeared in 1960 [88] and Pearson [89] conveyed the space elevator concept to the aerospace community in 1975. The basic concept of a space elevator is to construct a cable from a base on Earth to a GEO altitude or beyond. Once deployed, the cable could be ascended and descended by mechanical means, allowing space access without the need for rockets. Payloads, including people, supplies, and interplanetary spacecraft, could ascend and descend between the Earth and space via the cable. A material with a very high tensile strength/density ratio must be used in the fabrication of the cable, and CNTs, with a theoretical tensile strength of 130 GPa, offer a material with a low density and high strength necessary for this futuristic project.

As with spacecraft already in orbit via typical launch methods, the cable and other components used for the space elevator would be susceptible to space environmental hazards as outlined in this chapter. The main environmental concerns for the cable are meteoroid/debris impact, AO degradation, radiation damage, and even a remote chance of an impact by a spacecraft/satellite already in LEO. AO resistance, predominately needed on the ram-facing side of the cable, could be protected via AO resistant coatings and materials include aluminum or ceramics.

Ionizing radiation is a concern, particularly with the cable. Calculations for energetic electrons and protons indicate that the segment of the cable in Earth's radiation belts will experience less than 3 Mrad per year [90]. Studies of epoxy/carbon fiber composites (epoxy/nanotube composites would be expected to have comparable properties) have found them to be radiation hard to greater than 104 Mrad [91,92]. The predicted radiation resistance would allow the composite cable to

survive more than 1000 years in the expected space environment [93]. See Refs. [94–97] for additional information on the space elevator.

### 3.6. Solar sails

The concept of a solar sail is to use a large, film-based polymeric material as a sail that exploits the tiny but constant force exerted by solar photons to provide forward momentum [73]. Lightweight, strong, and space environmentally durable materials are critical to the success of these types of spacecraft. CNT composites could be used for the two main parts of a solar sail: the boom (structural support) and the sail itself. In both cases, strong and lightweight materials are a necessity. The most important aspect of solar sails is the average areal density (AAD) and in order to reduce the AAD it is necessary to use lightweight, very thin films, and nanocomposites—possibly CNT composites [98].

One current problem associated with the manufacturing of thin films is static charge build-up. However, the methods described previously in the chapter (Sec. 3.2.) may be used to mitigate ESC.

## 4. SUMMARY

Space presents a unique and harsh environment that can degrade or otherwise impair spacecraft materials and their properties. Synergistic effects between AO, UV, ionizing radiation, thermal cycling, meteoroids, space debris, and other threats should be taken into consideration when selecting or developing materials for use on spacecraft. The three main areas where nanocomposites have potential use in space applications are: ESC mitigation, enhanced thermal conductivity, and improved mechanical properties. The first use in space will likely be for ESC mitigation.

The effect of the space environment on carbon nanocomposites is not known at this time. However, the anticipated uses of nanocomposites for space applications highlight the critical need for short- and long-term testing of material in the space environment. The process to space-qualify a material is long, expensive, and usually application specific. Until then the effects of the space environment on CNTs and composites can be estimated from ground-based experiments and the effects on carbon material similar in structure such as pyrolytic graphite and other carbon composites.

## REFERENCES

1. U.S. Standard Atmosphere, NASA Technical Memo TMX-74335 (1976) 30.
2. T. F. Tascione, *Introduction to the Space Environment*, Orbit Book Company, Malabar, FL, USA, 1988.
3. D. R. Peplinski, G. S. Arnold and E. N. Borson, Thirteenth Space Simulation Conference. The Payload: Testing for Success, NASA CP-2340, NASA Goddard Space Flight Center, Greenbelt, MD, USA, 1984, pp. 133–145.
4. Sunspot Data Obtained from National Geophysical Data Center, Boulder, CO, <http://www.ngdc.noaa.gov/stp/SOLAR/ftpsunspotnumber.html>.

5. J. Visentine, NASA SDIO Space Environmental Effects on Materials Workshop, NASA CP-3035, Part 1, NASA Langley Research Center, Hampton, VA, USA, 1989, pp. 179–195.
6. M. R. Reddy, *J. Mater. Sci.* **30** (1995) 281–307.
7. S. Packirisamy, D. Schwam and M. H. Litt, *J. Mater. Sci.* **30** (1995) 308–320.
8. B. A. Banks, S. K. Rutledge, J. A. Brady and J. E. Merrow, NASA SDIO Space Environmental Effects on Materials Workshop, NASA CP-3035, Part 1, NASA Langley Research Center, Hampton, VA, USA, 1989, pp. 197–239.
9. B. A. Stein and P. R. Young (Eds.), LDEF Materials Data Analysis Workshop, NASA CP-10046, NASA Langley Research Center, Hampton, VA, USA, 1990.
10. B. A. Stein and P. R. Young (Eds.), LDEF Materials Workshop '91, NASA CP-3162, NASA Langley Research Center, Hampton, VA, USA, 1992.
11. A. S. Levine (Ed.), Proceedings of the First LDEF Post-retrieval Symposium, NASA CP-3134, NASA Langley Research Center, Hampton, VA, USA, 1992.
12. A. S. Levine (Ed.), Proceedings of the Second LDEF Post-retrieval Symposium, NASA CP-3194, NASA Langley Research Center, Hampton, VA, USA, 1993.
13. A. S. Levine (Ed.), Proceedings of the Third LDEF Post-retrieval Symposium, NASA CP-3275, NASA Langley Research Center, Hampton, VA, USA, 1993.
14. W. S. Slemple, AIAA Paper 83-2633, 1983.
15. R. C. Tennyson, W. D. Morison, J. E. Klemberg, L. Martinu, M. R. Wertheimer and D. G. Zimick, AIAA Paper 92-2152, 1992.
16. T. M. Zubly, K. K. de Groh and D. C. Smith, Proceedings of the Hubble Space Telescope Solar-Array Workshop, ESA WPP-77, European Space Agency, Paris, France, 1995 p. 385.
17. J. A. Townsend, P. A. Hansen, J. A. Dever, K. K. de Groh, B. A. Banks, L. Wang and C. He, *High Perform. Polym.* **11** (1999) 81–99.
18. P. R. Young, Unpublished work, 1992.
19. A. F. Whitaker, Proceedings of the Second LDEF Post-retrieval Symposium, NASA CP-3194, NASA Langley Research Center, Hampton, VA, USA, 1993, pp. 1125–1135.
20. B. A. Banks, S. K. Rutledge, P. E. Paulsen and T. J. Steuber, NASA TM-101971, National Aeronautics and Space Administration, Washington, DC, USA, 1989.
21. E. M. Silverman, NASA CR-4661, National Aeronautics and Space Administration, Washington, DC, USA, 1995.
22. L. J. Leger, B. Santos-Mason, J. T. Visentine and J. F. Kuminecz, Proceedings of the NASA Workshop on Atomic Oxygen Effects, NASA CR-181163, National Aeronautics and Space Administration, Washington, DC, USA, 1987, pp. 1–10.
23. P. E. George and H. W. Dursch, *J. Adv. Mater.* **25** (1994) 10–19.
24. C. Park, *AIAA J.* **14** (1976) 1640.
25. A. K. Stark, L. A. Berglund, M. Tagawa and N. Ohmae, *Carbon* **32** (1994) 641–644.
26. H. Marsh, E. O'Hair and W. F. K. Wynne-Jones, *Nature* **198** (1963) 1195.
27. H. Marsh, E. O'Hair and R. Reed, *Trans. Farad. Soc.* **61** (1965) 285.
28. H. Harsh, R. Reed, E. O'Hare and W. F. K. Wynne-Jones, *Trans. Farad. Soc.* **61** (1965) 274.

29. P. Pattabiraman, N. M. Rodriguez, B. Z. Jang and R. T. K. Baker, *Carbon* **28** (1990) 867–878.
30. H. Kinoshita, M. Umeno, M. Tagawa and N. Ohmae, *Surf. Sci.* **440** (1999) 49–59.
31. B. A. Banks, M. J. Mirtich, S. K. Rutledge and D. M. Swec, NASA TM-83706, National Aeronautics and Space Administration, Washington, DC, USA, 1984.
32. S. K. Rutledge and J. A. Mihelcic, in *Materials Degradation in Low Earth Orbit*, Eds. V. Srinivasan and B. A. Banks, TMS, Warrendale, Pa, USA, 1990 pp. 35–48.
33. C. D. Smith, H. Grubbs, H. F. Webster, A. Gungor, J. P. Wightman and J. E. McGrath, *High Perform. Polym.* **3**(4) (1991) 211.
34. J. G. Smith Jr., J. W. Connell and P. M. Hergenrother, *Polymer* **35** (1994) 2834.
35. J. W. Connell, J. G. Smith Jr. and P. M. Hergenrother, *Polymer* **36** (1995) 5.
36. J. W. Connell, J. G. Smith Jr. and J. L. Hedrick, *Polymer* **36** (1995) 13.
37. J. W. Connell, J. G. Smith Jr., C. G. Kalil and E. J. Siochi, *Polym. Adv. Technol.* **9** (1998) 11.
38. J. W. Connell, J. G. Smith Jr. and P. M. Hergenrother, *J. Fire Sci.* **11** (1993) 137.
39. J. W. Connell and K. A. Watson, *High Perform. Polym.* **13** (2001) 23.
40. K. A. Watson, F. L. Palmieri and J. W. Connell, *Macromolecules* **35** (2002) 4968.
41. J. W. Connell, J. V. Crivello and D. Bi, *J. Appl. Poly. Sci.* **57** (1995) 1251–1259.
42. J. W. Connell, D. C. Working, T. L. St. Clair and P. M. Hergenrother, in *Polyimides: Materials, Chemistry, and Characterization*, Ed. C. Feger, Technomic, Lancaster, Pa, USA, 1993, pp. 152–164.
43. L. L. Fewell, *J. Appl. Polym. Sci.* **41** (1990) 391.
44. L. L. Fewell and L. Finney, *Polymer* **32** (1991) 393.
45. J. Sanders, J. Cuttler, J. W. Connell, K. A. Watson and S. Choi, Unpublished results, 1998.
46. W. S. Slemp, B. Santos-Mason, G. Y. Sykes Jr. and W. G. Witte Jr., NASA TM-100459 Part I, National Aeronautics and Space Administration, Washington, DC, USA, 1988, p. 5.1.
47. G. L. Steckel, T. Cookson and C. Blair, LDEF Materials Workshop '91, NASA CP-3162, NASA Langley Research Center, Hampton, VA, USA, 1992, p. 515.
48. P. E. George, H. W. Dursch and S. G. Hill, *Proceedings of the 2nd LDEF Post-retrieval Symposium*, NASA CP-3194 Part 3, Ed. A. S. Levine, NASA Langley Research Center, Hampton, VA, USA, 1993, p. 923.
49. W. S. Slemp and P. R. Young, *Proceedings of the Second LDEF Post-retrieval Symposium*, NASA CP-3194, NASA Langley Research Center, Hampton, VA, USA, 1993, p. 1093.
50. M. A. Seeds, *Foundations of Astronomy*, Wadsworth Publishing Company, Belmont, CA, USA, 1986.
51. W. S. Slemp, NASA SDIO Space Environmental Effects on Materials Workshop, NASA CP-3035, NASA Langley Research Center, Hampton, VA, 1989, pp. 425–446.
52. W. B. Liau and F. P. Tseng, *Polym. Composites* **19** (1998) 440–445.
53. A. C. Tribble, *The Space Environment: Implications for Spacecraft Design*, Princeton University Press, Princeton, 1995.
54. T. W. Armstrong and B. L. Colborn, Contract No. NAS8-38427 for NASA Marshall Space Flight Center, Science Applications International Corporation, 1990.

55. J. A. Dever, K. K. de Groh, B. A. Banks, J. A. Townsend, J. L. Barth, S. Thompson and W. Savage, *High Perform. Polym.* **12**(1) (2000) 125–139.
56. M. O'Rourke, L. Clayton, D. D'Angelo and J. P. Harmon, *J. Mater. Res.* **17** (2002) 10.
57. V. V. Klimov and V. S. Letokhov, *Phys. Lett. A* **226** (1997) 244–252.
58. F. Z. Cui, Z. H. Chen, J. Ma, G. R. Xia and Y. Zhai, *Phys. Lett. A* **295** (2002) 55–59.
59. E. Salonen, A. V. Krasheninnikov and K. Nordlund, *Nucl. Instrum. Methods Phys. Res. B* **193** (2002) 603–608.
60. R. Wilkins, M. X. Pulikkathara, V. N. Khabashesku, E. V. Barrera, R. K. Vaidyanathan and S. A. Thibeault, *Mater. Res. Soc. Symp. Proc.* **851** (2004) NN6.5.1.
61. S. R. Tatro, L. M. Clayton, P. A. O'Rourke Muisener, A. M. Rao and J. P. Harmon, *Polymer* **45** (2004) 1971–1979.
62. E. Najafi, J.-O. Lee and K. Shin, *Mater. Res. Soc. Symp. Proc.* **851** (2004) NN6.6.1.
63. S. Gupta, R. J. Patel and N. D. Smith, *Mater. Res. Soc. Symp. Proc.* **851** (2004) NN6.3.1.
64. K. K. de Groh, B. A. Banks and D. C. Smith, *Sol. Eng.* **2** (1995) 939.
65. D. R. Tenney, G. F. Sykes and D. E. Bowles, *Third European Symposium on Spacecraft Materials in the Space Environment*, ESA Publications Division, ESTEC, Noordwijk, The Netherlands, 1985, pp. 9–21.
66. D. J. Kessler, R. C. Reynolds and P. D. Anz-Meador, NASA-TM 100471, National Aeronautics and Space Administration, Washington, DC, USA, 1988.
67. L. Leger, J. Visentine and B. Santos-Mason, *SAMPE Q* **18**(2) (1987) 38.
68. A. E. Stiegman, D. E. Brinza, M. S. Anderson, T. K. Minton, G. E. Laue and R. H. Liang, *Jet Propulsion Laboratory Publication 91-10*, Jet Propulsion Laboratory, Pasadena, CA, USA, 1991.
69. R. C. Tennyson, *J. Surf. Coat. Technol.* **68/69** (1994) 519–527.
70. H. W. Dursch and H. G. Pippin, in *Materials Degradation in Low Earth Orbit*, Eds., V. Srinivasan and B. A. Banks, TMS, Warrendale Pa, USA, 1990, pp. 207–218.
71. J.-H. Han and C.-G. Kim, *Composite Structures* **72** (2006) 218–226.
72. A. M. Schrand and T. Benson Tolle, *This Volume*.
73. C. H. M. Jenkins (Ed.), *Gossamer Spacecraft: Membrane and Inflatable Structures Technology for Space Applications*, Vol. 191, American Institute of Aeronautics and Astronautics, Reston, VA, USA, 2001.
74. R. E. Smith and G. S. West (Eds.), NASA TM 82478, National Aeronautics and Space Administration, Washington, DC, USA, 1982.
75. A. S. Jursa, *Handbook of Geophysics and the Space Environment*, NTIS Document ADA 167000, Air Force Geophysics Laboratory, Air Force Systems Command USAF, Washington, DC, USA, 1981.
76. *The Radiation Design Handbook*, ESA PSS-01-609, ESA Publications Division, ESTEC, Noordwijk, The Netherlands, 1989.
77. P. A. Robinson Jr., *Spacecraft Environmental Anomalies Handbook*, GL-TR-89-0222, Geophysics Laboratory, Air Force Systems Command, USAF, Washington, DC, USA, 1989.



78. A. R. Frederickson, L. Levy and C. L. Enloe, IEEE Transactions on Electrical Insulation, IEEE Publishing, New York, NY, USA, 1992 p. 1166.
79. P. J. Glatkowski, P. Mack, J. L. Conroy, J. W. Piche and P. Winsor, U.S. Patent 6,265,466 B1, issued to Eikos, Inc., Franklin, MA, USA, 2001.
80. P. J. Glatkowski, Sci. Adv. Mat. Proc. Eng. Proc. **48** (2003) 2146.
81. K. A. Watson, S. Ghose, D. M. Delozier, J. G. Smith Jr. and J. W. Connell, Polymer **46** (2005) 2076–2085.
82. J. G. Smith Jr., J. W. Connell, K. A. Watson and P. M. Danehy, Polymer **46** (2005) 2276–2284.
83. J. G. Smith Jr., K. A. Watson, J. W. Connell, D. M. Delozier, P. T. Lillehei, Y. Lin, B. Zhou and Y.-P. Sun, Polymer **45** (2004) 825–836.
84. D. R. Cairns, R. P. Witte II, D. K. Sparacin, S. M. Sachsman, D. C. Paine and G. P. Crawford, Appl. Phys. Lett. **76** (2000) 1425–1427.
85. P. Kim, L. Shi, A. Majumadar and P. McEuen, Phys. Rev. Lett. **87** (2001) 215502-1–215502-4.
86. W. Schimmerling, Radiat. & Environ. Biophys. **31** (1992) 197.
87. W. Schimmerling, J. W. Wilson, J. E. Nealy, S. A. Thibeault, F. A. Cucinotta, J. L. Shinn, M. Kim and R. Kiefer, Adv. Space Res. **17** (1996) (2)31–(2)36.
88. Y. Artsutanov, Science **158** (1960) 946.
89. J. Pearson, Acta Astronautica **2** (1975) 785.
90. E. J. Daly, J. Lemaire, D. Heynderickx and D. J. Rogers, IEEE Trans. Nucl. Sci. **43**(2) (1996) 403.
91. S. Egusa, J. Mater. Sci. **25** (1990) 1863.
92. F. L. Bouquet, W. E. Price and D. M. Newell, IEEE Trans. Nucl. Sci. NS-**26**(4) (1979) 4660.
93. B. C. Edwards, Acta Astronautica **10** (2000) 735.
94. D. V. Smitherman Jr., NASA CP-2000-210429, National Aeronautics and Space Administration, Washington, DC, USA, 2000.
95. B. C. Edwards and E. A. Westling, The Space Elevator, BC Edward, Houston, TX, USA, 2003.
96. A. C. Clarke, Adv. Earth Oriented Appl. Sci. Techn. **1** (1979) 39.
97. J. D. Isaacs, A. C. Vine, H. Bradner and G. E. Bachus, Science **151** (1966) 682.
98. D. L. Edwards and M. Chipara, Mater. Res. Soc. Symp. Proc. **851** (2004) NN1.6.1.

## Chapter 20

### **From carbon nanotechnology to bionanotechnology: Protein and peptide nanofibrils and nanowires**

Oleg I. Kiselev

Institute of Influenza Russian Academy of Medical Sciences,  
Department of Molecular Virology and Genetic Engineering, Russia, Saint Petersburg

#### **1. BIONANOTECHNOLOGY**

As can be seen from preceding chapters, nanotechnology is no longer a merely social talking point and is beginning to affect the lives of everyone. With the revolutionary discoveries of the C molecule and carbon nanotubes, carbon nanotechnology has become the building block of the entire field of nanotechnology. Whether it is deoxyribonucleic acid (DNA) or synthetic polymers, all are based on carbon backbones. Nature has been doing remarkably well by systematically organizing of matter at nanometer-length scale in biological systems. For example, the well-known proteins collagen and insulin form nanofibrils and the Sup35 yeast protein forms nanowires. Either by using these naturally occurring proteins or creating synthetic derivatives of these molecules, nanotools and nanoelements can be fabricated for molecular recognition, electronic transmission, or for disease diagnosis and treatment. Progress in understanding the molecular basis of human diseases has prompted a new wave of studies in bionanotechnology.

Bionanotechnology is a field of science and technology that has resulted from advances in the disciplines of biochemistry, molecular biology, cytology, genetic engineering, and biotechnology. Bionanotechnology takes advantage of the unique properties of biological macromolecules such as peptides, proteins, and prions by using their self-assembling nature for the nano-engineering of molecular templates and supra-molecular structures [1]. The self-assembling of biological macromolecules including nucleic acids such as DNA is based on the recognition of complementary regions. Through complementary binding, these macromolecules naturally link and construct the body's tissues and organs through fiber-like structures. Many proteins are amphiphilic and maintain their structure and conformation in both hydrophilic and hydrophobic environments, which makes them attractive candidates for attachment to various materials for biocompatibility. In general, the advantages to use proteins and peptides as building blocks in bionanotechnology include, but not limit to: (1) Proteins are produced in large quantities for many purposes in mild and non-consumptive conditions; (2) Proteins and peptides are more stable and resistant to temperature, irradiation, enzymes etc.; (3) Proteins and

peptides have many conformations and conformational transitions, which is important for the construction of molecular memory tools based on molecular plasticity; (4) Proteins and peptides undergo folding and many intermediate states; (5) Self-assembling is an intrinsic property of many proteins and peptides. Some of them are capable of forming nanofibrils and nanotubes; (6) Proteins and peptides can be galvanized by metals such as Ag, Au, Zn, Cd, Se, Cu etc.; (7) Polypeptides may have recognition patterns and specific domains for ligand binding; (8) Proteins and peptides can be used for the design of nanowires and manufacturing in very mild conditions; (9) Natural and synthetic peptides are biocompatible for use in the design of retina, neurons, wires, etc.; (10) Using peptide and protein genetic code as an operating system for other types of memory and information operation; (11) Protein-based devices may be able to replace human structures such as the eye lens and retina, skin, bones etc.; and (12) Proteins are capable of forming tight complexes with many other molecules and artificial nanomaterials.

Areas of bionanotechnology where applications are beginning to be developed include the assembling of the eye's lens, retina, nerves, as well as chips for the treatment of brain disorders. Devices and approaches that are covered in this chapter include the creation of nanoscale components such as protein nanotubes, nanowires, and nanotools. Synthetic peptides and proteins are discussed as leading materials in bionanotechnology as the nearest materials to be incorporated into practical and commercial applications in medicine.

## 2. SIMILARITIES BETWEEN FULLERENE C AND VIRUSES

Viruses are autonomous genetic machines that reproduce inside cell, and subsequently kill the cells that they infect. Because viruses are very small, difficult to detect, and highly capable of infecting a large number of people or animals, there is a threat for use of viruses as biological warfare agents. Interestingly,  $C_{60}$  fullerenes and many viruses share similar morphologies as shown in Fig. 1.

Fig. 2 shows how the structure of proteins exists on many levels. For example, different types of Hemagglutinin (HA) exist, each binding to a slightly different type of host molecule. HA is like a key that allows the virus to enter those cells

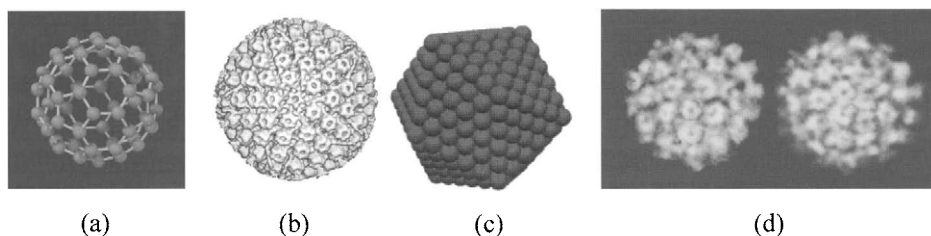


Figure 1. Structure of (a) C fullerene, (b) Herpes virus, (c) model of polio virus, and (d) microscopic images of herpes virus.

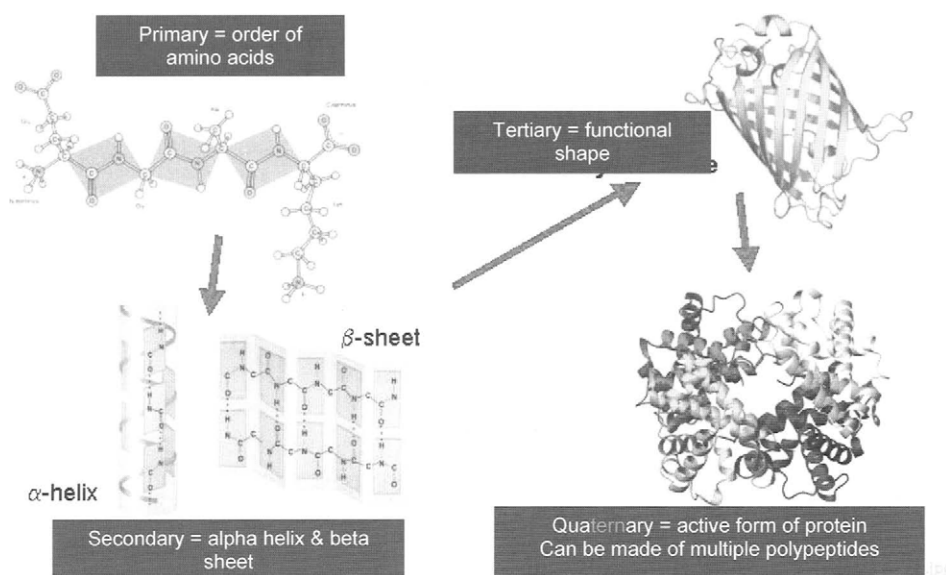


Figure 2. Formation of secondary, tertiary, and quaternary structures by bio-molecules.

with a matching lock. Bird flu HA binds to molecules found on birds' intestinal cells. Human flu HA binds to slightly different molecules on human lung cells. Birds are natural hosts to all flue strains while humans are only infected by strains that have adapted to recognize epithelium cell in upper inhalation tract and lungs.

Recently humans have been infected by the bird flu H5N1. The HA associated with the virus makes it particularly lethal because people have no natural immunity to it. That is, their antibodies do not recognize this new HA antigen [2]. The protein structure of a flu virus, HA tertiary structure and its physical map are shown in Figs. 3 and 4.

Many stages of viral replication are dependent on translocation across the plasma membrane. C fullerenes are also capable of penetrating the lipid bilayer of the plasma membrane as shown in Fig. 5. In addition, fullerenes can be used as free radical generators under light irradiation where they initially select and target proteins and membranes. Viral proteins containing the amino acids Cys, Tyr, and Met. are damaged by free radical oxidation, which leads to cross-linking, catalytic inactivation, blocking of conformational transitions, and fusion with cellular membranes. Therefore, many of the similarities between fullerene C and viruses can be used in biology and medicine in both damaging and beneficial ways.

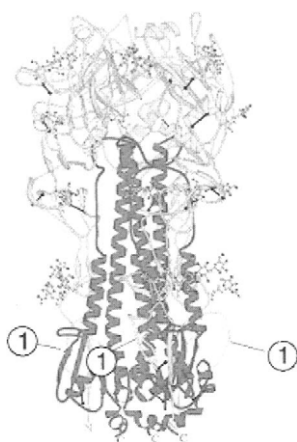


Figure 3. The HA molecule with the sites used to bind with the host cell membrane indicated by the number one.

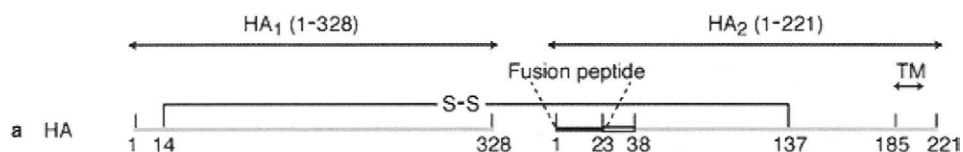


Figure 4. Influenza HA physical map.

### 3. FULLERENE-BINDING PEPTIDE DOMAIN

Fullerenes and carbon nanotubes are the two major constituent members of the carbon family, but the two carbon materials are very different in their properties. The chemistry of fullerene molecules has provided many derivatives for a variety of purposes during the past 5 years. Now, the chemical modification of carbon nanotubes is a growing area in research and technology development. Further developments in nanotechnology will likely rely upon the manufacturing of materials that can have closer interface with biological materials. For example, fullerenes are capable of interacting with proteins [3] and computer modeling of fullerene-peptide complexes showed that the fullerene molecule specifically interacts with the domain containing duplicated phenylalanine residues [4,5]. Unexpected data were obtained in studies of fullerene complexes with insulin fibers. In Fig. 6, the complexes have fullerene molecules clustered inside bundles of protein fibrils. These bundles

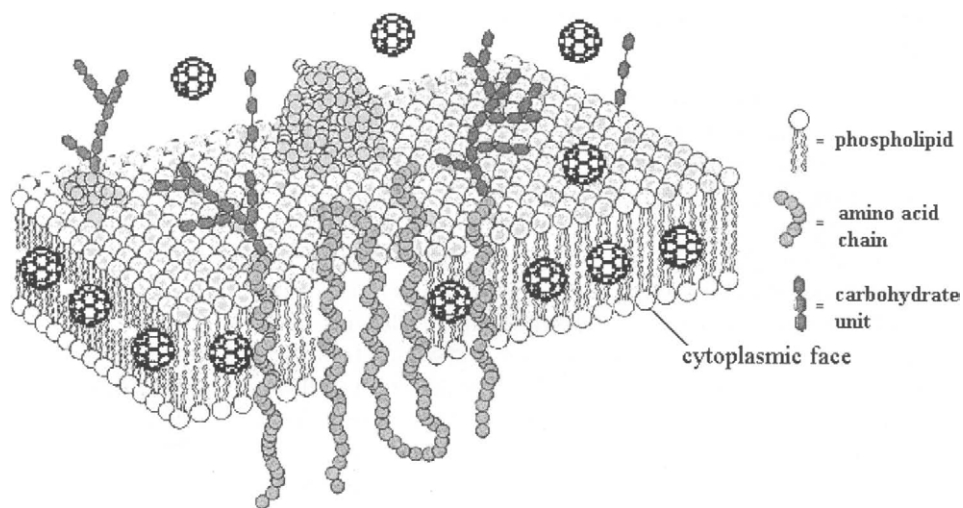


Figure 5. Fullerenes in PVP complexes are capable of penetrating into the lipid bilayer of a cell's plasma membrane.

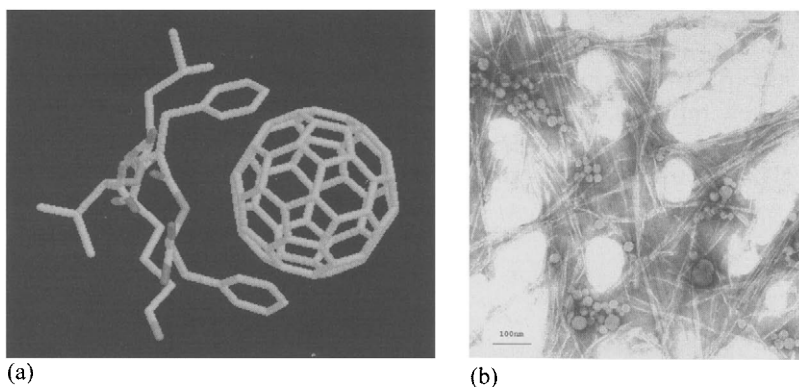


Figure 6. (a) Computer modeling of peptide (Lys-Leu-Val-Phe-Phe), specifically recognize single fullerene molecule and (b) interaction of insulin fibrils with fullerene clusters.

include nucleation sequences of the insulin B-subunits such as the C-terminal domain, containing duplicated phenylalanine residues (Fig. 6b). If carbon nanotubes can be functionalized to bind or recognize similar domains, a multitude of new bio-compatible complexes could be formed with great potential applications.

#### 4. BIOLOGICAL MACROMOLECULES: PROTEINS, PEPTIDES, AND PRIONS

Carbon, hydrogen, nitrogen, and oxygen, along with sulfur, phosphorus, iron, or iodine, are basic elements for generating biological macromolecules. When these elements are combined into basic amino groups and one or more acidic carboxyl groups, they can form an amino acid, which is the building block of peptides and proteins. Peptides are compounds that are composed of two or more amino acids joined by peptide bonds. Proteins are polypeptides composed of large groups of amino acids that form the human body's hormones, enzymes, antibodies, tissues, and organs. Some symptoms of defects or deficiencies in proteins are: abnormal tissue development, poor resistance to infection, and delayed healing. Proteins in the body are capable of recognizing millions of molecules, which can lead to beneficial interactions such as triggering an immune response to inactivate and destroy viruses. However, not all natural biological macromolecules are beneficial. Proteinaceous particles called prions are believed to be responsible for transmissible neurodegenerative diseases. They can cause damage to the body because they go undetected as foreign material by the immune system due to their lack of nucleic acid, which is the material responsible for genetic encoding.

#### 5. NATURAL NANOSTRUCTURES: NANOFIBRILS AND NANOWIRES

##### 5.1. Collagen

Collagen is a rather heterogeneous protein secreted by cells into the extracellular matrix [6]. It is found throughout the human body where it forms tissues such as bones, tendons, and skin. Its conformation allows it to make long, thin, and mechanically resistant fibrils that become organized as a microfilm as shown in Fig. 7. This structure results in complicated visco-elastic mechanical behavior [6,7].

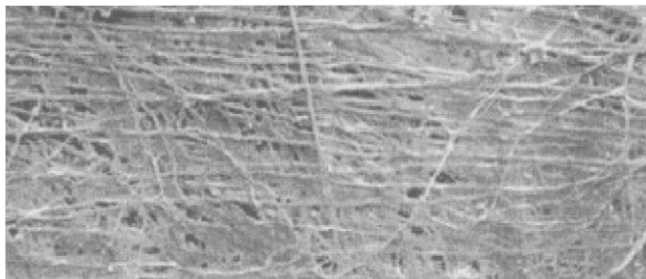


Figure 7. Transmission electron micrograph of collagen fibrils where the diameter of the collagen fibrils is 10–50 nm.

Collagen is also a target of many post-translational modifications including ion-filling and cross-linking because it is enriched with proline and glycine amino acid residues in repeated motifs as shown in Fig. 8. These post-translational modifications result in triple-helix fibrils that are 50–200 nm in length as shown in Fig. 9. Collagen is widely used in medicine and cosmetics, but it has not been used in molecular and nano design at this point. However, understanding the structure of this protein may provide information for modeling other biomolecules with similar structures and properties.

## 5.2. Prions and prion-like proteins

Many proteins are able to form fibrils in a wide range of physiological and pathological conditions [7–12]. Some of these proteins have native structures, but have lost their stability in a specific environment whereas others are mutants. All of these proteins are unified in groups of prion-like proteins, which are characterized by their ability to form protein fibrils [7,8]. Prions are infectious proteins having the intrinsic capability to form nanofibrils during their life cycle and biogenesis in infected cells. Fig. 10a shows an example of image of the fibrils that prions form via transmission electron microscopy (TEM) and Fig. 10b shows prion peptides from an amyloidogenic region grown on a solid surface. Prions consist of polypeptide chains that are 254 amino acids in length. The mapping of these molecules has led to the identification of rather short amyloidogenic sequences involved in conformation transformation such as:

06-KTNMKHMAGAAAAGAVVGGLG-126

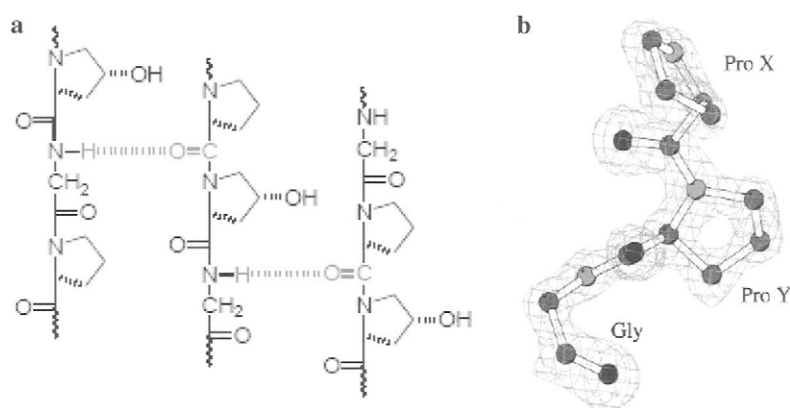


Figure 8. Primary structures of collagen fragments and inter chain hydrogen bounds. Hydrogen bonding in triple-helical collagen. (a) Ladder of intrastrand ProC=OHGly hydrogen bonds and (b) Electrostatic field of tripeptide Gly-Pro-Hyp segment of collagen molecule.



## Pathway

❖ Following exocytosis:

- Propeptides cleaved off by extracellular enzymes
- Triple-helix molecules polymerize into fibrils 50-200 nm long
- Fibrils pack into fibers (stronger than steel of same size)

❖ When denatured, forms gelatin (missing propeptides lead to unordered cross-linking)

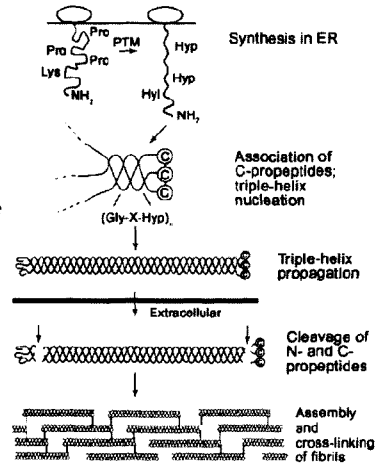


Figure 9. Biosynthesis and assembling of collagen fibrils.

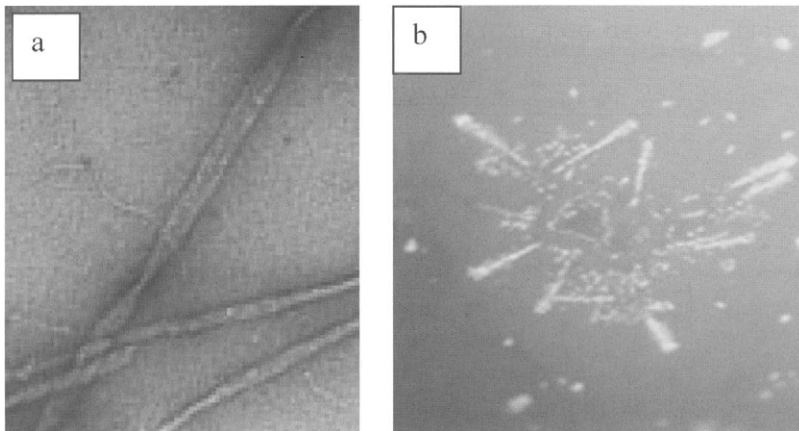


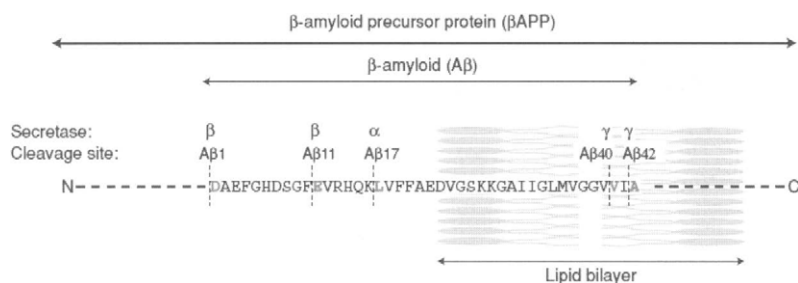
Figure 10. Structural organization of prion fibrils. (a) TEM of prion fibrils and (b) Self-assembling of prion peptides (from amyloidogenic region) on a solid surface.

During the multiplication of prions, the formation of fibrils in infected brain tissue causes the destruction of the brain's neuronal network. This results in the disruption of proper function as expressed by progressive psychoneurotic disease, which can be fatal [7,8]. In addition,  $\text{Cu}^{2+}$ -binding domains were identified in the N-terminal

portions of prion proteins. However, the physiological role of  $\text{Cu}^{2+}$  binding by prion proteins is not clearly understood. The affinity of fibrils to ions of various metals could contribute to the development of conductive-like elements inside the brain leading to severe disturbances in the local brain tissue conductivity. The general neuropathological sign of Alzheimer's disease is low and chaotic electrical activity of a brain in electroencephalography (EEG) observation. Thus, in situ mineralized prion fibrils may have local conductivity that disrupts normal signaling pathways in the brain. This hypothesis led to the testing of protein fibrils for the assembly of bio-compatible protein-containing nanowires [8,11].

### 5.3. $\text{A}\beta$ -peptides

Small  $\text{A}\beta$ -peptides have lengths from 40 to 42 amino acids and are proteolytic fragments of the huge membrane-bound amyloid precursor protein (APP) shown in Fig. 11. A nucleation domain was identified as the primary attachment of the peptides to each other and the initiation of fibril biogenesis. Short A-peptide homologous peptide fragments specifically bind to  $\text{A}\beta$ -42 and prevent fibril assembling. This is the most important evidence that the short sequence of the  $\text{A}\beta$ -42 is involved in fibril assembling [8–10]. Secretase ( $\alpha$ ,  $\beta$ ,  $\gamma$ ) are a set of proteases, which cleaves  $\text{A}\beta$ -40–42 peptide in different positions. When  $\text{A}\beta$ -40–42 peptide escapes cleavage, it is capable of forming tight fibril aggregates that are found as deposits inside destroyed brain tissue. In water, the  $\text{A}\beta$ -peptide has a complicated conformation including  $\alpha$ -helices and  $\beta$ -structures, which is modeled in Fig. 12. The assembly of the native peptide into fibrils leads to a complete transformation of the peptide from an  $\alpha$ -helical to an entirely  $\beta$ -stranded structure. Usually  $\beta$ -sheet peptides interact with each other along their entire length in order to form very tight structures [9,11]. Further investigation into the structure of these peptide fibrils showed that there is a special arrangement of peptides inside the fibrils.



Schematic diagram of the  $\beta$ -amyloid precursor protein (βAPP)

Figure 11. Primary sequence and proteolytic sites of  $\text{A}\beta$ -40–42 peptide, partially integrated into lipid membrane. Secretase  $\alpha$ ,  $\beta$  and  $\gamma$  cleavage sites are pointed along polypeptide sequence. N, NH<sub>2</sub>-terminus; C, COOH-terminus [14,15].

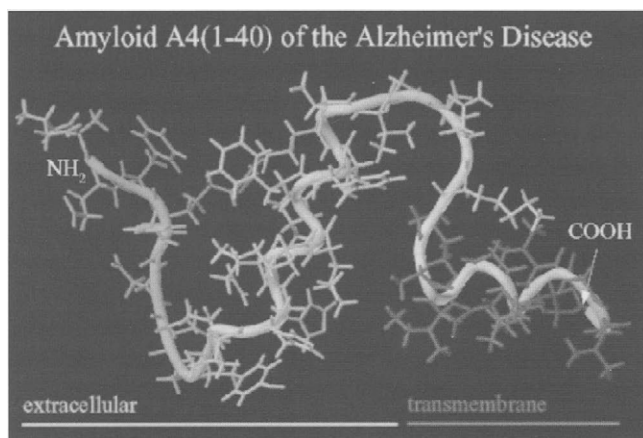


Figure 12. Computer model of  $A\beta$ -40 peptide. The peptide consist of extracellular and transmembrane parts, that is shown here. The sequence of  $A\beta$ -40 peptide is deciphered in Fig. 11.

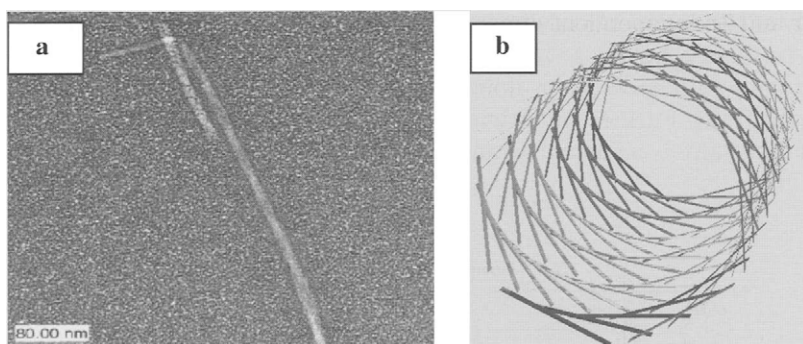


Figure 13. Structure and modeling of  $A\beta$ -peptide nanotube: (a) TEM of single  $A\beta$ -peptide fibril and (b) computer model of  $A\beta$ -peptide nanotube.

According to X-ray analysis, peptides form water-filled nanotubes that are assembled by peptides like stick pieces resulting from interactions between short clusters of amino acid residues as shown by a model in Fig. 13b. According to a generic statistical mechanical model [12–14], the self-assembling of the peptide starts from chiral rod-like units into helical tapes, then under increasing concentration it forms into twisted ribbons or double tapes. Fibrils, as an additional step, represent

twisted stacks of ribbons, which lead to the final stage in fibrillogenesis where fibers are produced. According to this model, the sequential transformation of peptides provides many opportunities for chemical modification, as can be seen from the morphology of A $\beta$ -peptide deposits in damaged tissue [8,12,14–16]. It is hoped that understanding the further modifications that are made to peptides or proteins by metal ions may elucidate the mechanisms involved in making conductive fibers [8,12–16].

#### 5.4. Insulin

Insulin is a protein hormone widely used in the treatment of diabetes [14]. It consists of two subunits: A and B, associated by Cys–Cys binding. It can exist in several different molecular forms such as monomers, dimers, and hexamers. Zn<sup>2+</sup> is necessary for assembling of the hexamer storage form of insulin [4,5]. The insulin dimer is primarily stabilized by  $\beta$ -sheet domains located in subunit B as shown in Fig. 14.

Denaturing and assembling fibrils on insulin molecules were dependent upon an acidic pH, hydration, and Zn<sup>2+</sup> ions. As a result, a high yield of insulin nanofibers was achieved as shown in Fig. 15. In solution at neutral pH and at physiological concentrations (about 1 ng/ml), insulin exists as a monomer and is in the active form of the hormone. At higher concentrations, at acid or neutral pH, and in the absence of zinc, the insulin monomer self-associates to form dimers. In the presence of zinc, insulin forms hexamers. Studies of insulin analogues demonstrate that its activity is dependent upon the integrity of the insulin fold. Insulin domains involved in Zn-dependent hexamer and Zn-independent dimer formation have different locations. The central

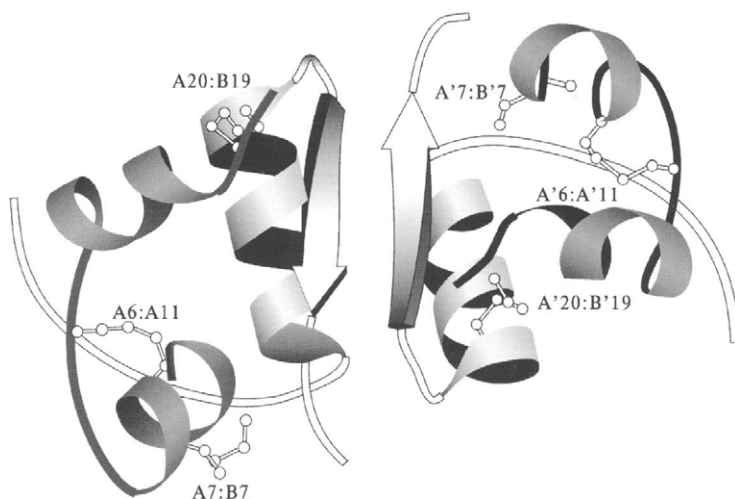


Figure 14. Computer model of insulin dimer. Arrows:  $\beta$  strands are shown between two monomers as an interface region.

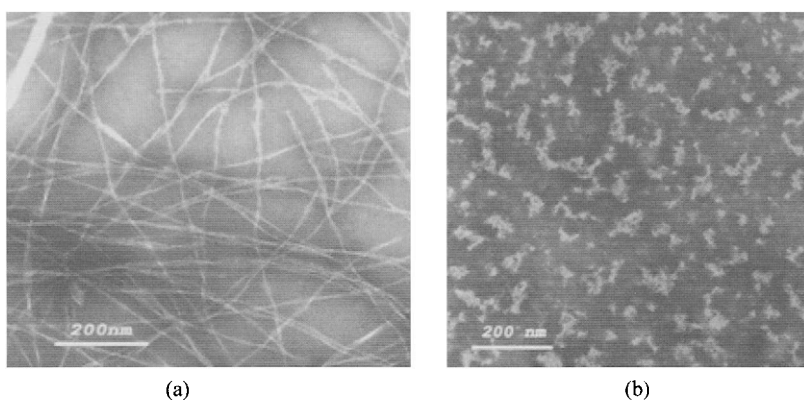


Figure 15. TEM of insulin fibers. (a) Amorphous aggregates of insulin from acetonitrile solution. (b) Insulin fibers formed in water buffer, contained 1 mM  $\text{ZnSO}_4$ .

residues responsible for hexamer formation include B10 His, which binds Zn ions as well as B14 Ala, B17 Leu, B20 Gly, and A13 Leu, which are involved in close-packed hydrophobic interactions. The ability to form dimers is mediated by hydrophobic interactions involving B8 Gly, B9 Ser, B12 Val, B13 Glu, B16 Tyr, B24 Phe, B25 Phe, B26 Tyr, B27 Thr, and B28 Pro. The B chain of one monomer packs against the B chain of the second monomer and further stability is provided by hydrogen bonding between the anti-parallel  $\beta$ -strands B24–B26 of each molecule. The packing arrangement in the dimer results in perturbations of the side-chain and main-chain structure slightly changing the resulting monomer conformation. The B25 Phe side-chain is important for stabilizing the native dimer structure. However, decreasing the pH and increasing the concentration of the protein fatally lead to insulin aggregation and fibril formation, which have been described in many studies [4].

### 5.5. Sup35 yeast protein

Many studies have been performed with phospholipids, tubules, DNA, bacteriophages, and cellular microtubules [1,9]. However, individual proteins are the best materials for designing conductive macromolecular units and wires due to their availability, consistency, and self-assembling nature. Proteins with similar behavior, structure, and the capability to form intracellular fibrils were identified in brewer yeast by the yeast geneticist S. Lindquist. During the past decade, she discovered and studied a unique protein called Sup35. This protein is similar both in structure and function to prion-like proteins, so it has become a quite simple, safe (non-infectious), and available model for basic studies in this field.

Fragments of yeast *Saccharomyces cerevisiae* protein Sup35 were selected for use in a conducting nanowire design [9,12]. Recombinant Sup35 protein contains N-terminal and middle region (NM) of native Sup35p. NM forms self-assembling

$\beta$ -sheet-rich amyloid fibers that have a suitable size and shape for nanocircuitry with diameters of 9–11 nm. In water, NM is a soluble protein and with a flexible, unordered structure. Under the appropriate conditions, NM rapidly converts to insoluble amyloid fibers. This process is primed by the addition of preformed fibrils. The fibers grow into two directions and form varied fiber patterns. These fibers are also resistant to proteases and denaturing conditions and reagents, which makes them suitable for the fabrication and processing of electrical wires. The kinetics of fiber formation by NM is slow and it does not make aggregates as other amyloids and prion-like proteins. Moreover, NM fibers form under physiological conditions such as a neutral pH and at room temperature. The secondary structure of NM was determined by UV-CD and showed that in solution NM has a random coil-rich structure and a sheet-like appearance when it is in fibers. This is important because the industrial fabrication process of nanoscale devices requires mechanically stable and chemically resistant materials. NM fibers can be incubated in phosphate buffer with different ionic strengths, at temperatures from 25 °C to 98 °C, and in denaturing agents such as 8M urea and 2M guanidinium hydrochloride. NM fibers were completely stable in the absence of salt and in 2.5 M NaCl. Moreover, NM fibers can be used after storing frozen for 3 months at –20 °C and –80 °C. Chemical stability in alkaline, acidic, and organic solvents was also demonstrated. NM fibers with variable lengths can be repeatedly produced and the average size of the fibers was approximately 500 nm. Increasing the concentration of the soluble NM increased the fiber length.

NM fibers conductive properties are tailorable. They can be both good insulators or using multi-step processing, NM fibers can be converted to conducting nanowires with low Ohmic resistance. For conductivity purposes, specially engineered NM was used. By site-specific mutagenesis, the Cys derivative of NM was obtained. Moreover, this Cys residue in engineered NM remains accessible after fiber formation in the derivative NM K184C. This derivative, NM K184C, was used as the starting recombinant NM. Using monomaleimido nanogold nanoprobe, gold nanoparticles were covalently attached to the fibers. After this modification, NM K184C displayed the same morphology as the original protein. The distance between cysteine residues in the fibers was 3–5 nm where the nanogold particle diameters were only 1.4 nm. In order to bridge the particles with metal to gain conductivity, GoldEnhancer was used. This process was inefficient because some gaps remain unfilled. A special gold toning procedure was developed to create a final conductive nanowire. Nanogold particles on the labeled fibers elicited a reducing activity when reacted with silver ions. The silver-modified fibers in Fig. 16 become thicker and have diameters from 80–200 nm compared to bare fibers with diameters from 9–11 nm.

The electrical behavior of NM-template metallic fibers was assessed by randomly depositing fibers. Nanogold particles on patterned electrodes were then covalently attached. Then, the gold toning procedure allowed the formation of metallically continuous gold nanowires. The 100 nm nanowires had a very low resistance of  $R=86\ \Omega$ . This is the first successful design of proteinaceous nanowires of natural origin with modifications inserted by genetic engineering.

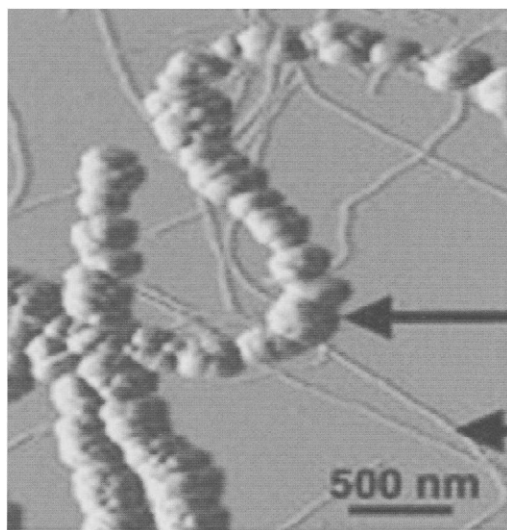


Figure 16. Metallic fiber of yeast prion-like protein. Bare and toner-labeled fibers: diameters 9–11 and 80–200 nm, respectively.

Short domains in Sup35 were also studied for forming fibers with assigned properties such as in the creation of peptide nanotubes as shown in Fig. 17. There are many successful examples of experimentally designing nanomaterials using short peptides with specific functions [3,9,17–20]. However, many studies in peptide technology for the creation of nanotools have shifted from the applications of natural polypeptides to the applications of specially designed synthetic polypeptides. A synthetic peptide is completely homogenous in its structure and could be modified or prepared for modification during its synthesis. The size of these peptide fibers provides the possibility of creating very small components for nanoelectronics. For example, the short peptide sequence GNNQQNY is capable of forming highly ordered fibers and nanotubes. However, Sup35 yeast protein was the first subject for the design of metal-filling protein nanowires [9,12,17].

The existence of sequence diversity among prion-like proteins capable of forming highly ordered fibrils creates an even wider range of starting materials than currently exist in the electronics industry [8,11]. All of the proteins and peptides listed in Table 1 are prion-like proteins that can be used for the creation of protein nanotubes and galvanized nanowires. It is important to note that they have very different primary sequences, but are similar in secondary structure. Additionally, these prion-like proteins have similar aromatic amino acid residues usually located in nucleation regions where fibril formation is initiated.

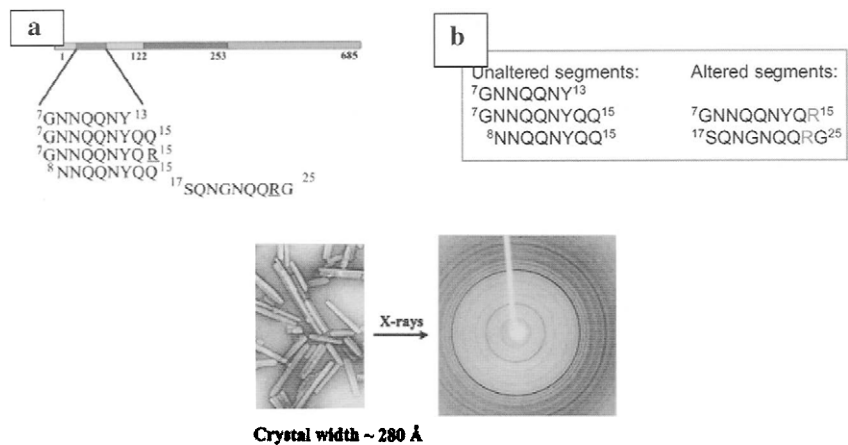


Figure 17. Yeast Sup35 protein physical map and peptides active in fibrillogenesis. (a) Amyloidogenic sequences are located on the map of Sup35p in N-terminus and in the middle part of the protein. Minimal length of peptide capable to form fibrils is heptapeptide: GNNQQNY. (b) Sequences of short peptides trialed as an N-terminal nucleation domain of Sup35p [17].

Table 1

Structure and properties of fibril forming protein sequences [9,10].

Name of natural peptide	Disorder or natural condition	Short fibrillogenic sequence
1. A $\beta$ -amyloid peptide	Alzheimer disease	KLVFFFA LVFFFA LPFFD KLVFFFAE
2. Islet amyloid precursor protein	Type II diabetes	TNVGSNTY
3. Lactadherin	Aortic medial amyloid	NFGSVQFV
4. Gelsolin	Finnish hereditary Amyloidosis	SFNNGDCCFILD
5. Serum amyloid A	Chronic systemic inflammation amyloidosis	SFFSFLGEAFD PHGGGWGQ
6. PrP <sup>Sc</sup>	Creutzfeld–Jakob disease (CJD)	
7. Sup35p yeast protein	Yeast prion protein	PQGGYQQYN GNNQQNY



## 6. HUMAN PATHOLOGY AND PROTEIN GALVANIZATION

### 6.1. Metal-filled nanowires

Many studies have tried to clarify the role of metal ions in the assembly and catalytic activity of A-peptides and their fibrils. In Fig. 18, a schematic of ion modification is described where  $\text{Cu}^{2+}$  and  $\text{Zn}^{2+}$  ions are attached to A $\beta$ -peptides. This process was termed protein galvanization [13]. Moreover, data obtained in this study support the idea that amyloid fibril galvanization is principally caused by  $\text{Zn}^{2+}$  released during neurotransmission as shown in Fig. 18.

During active synaptic transmission, the concentration of  $\text{Zn}^{2+}$  ions reaches 300  $\mu\text{M}$ . This local concentration is very high and sufficient for peptide galvanization of the localized A $\beta$ -peptides. The galvanization of A $\beta$ -peptides leads to the precipitation of the oxidized form of the peptides and rapidly induces amyloid fibril development as shown in Fig. 18. The biogenesis of amyloid fibrils includes free radical generation and oxidation of the protein and its fragments. The main consequence of free radical generation is intra-molecular networks or fiber cross-linking. The cross-linking of generated fibrils leads to the assembly of high molecular mass aggregates and intra-tissue deposits called plaques. A similar process could be reproduced in experimental conditions [8,12,14–16]. In our opinion,  $\text{Zn}^{2+}$ -saturated peptides become the prototype of a conductive peptide element generated during the development of disease in the human brain [4,9]. Moreover, during aggregation this protein can form bundles and branched bundles of dendrimer-like structures.

### 6.2. Natural protein galvanization: Zinc-binding motifs

Proteins have  $\text{Zn}^{2+}$ -binding sites. However,  $\text{Zn}^{2+}$  ions can be replaced by many other ions. In conditions where the polypeptide chain is saturated by those ions, the protein dramatically changes its properties and can then be used in nanoelectronic design. In Fig. 19, the Zn-finger motif of a DNA-binding protein is shown. This Zn-finger motif usually contains His and Cys residues in a specific polypeptide loop [8].

Many proteins contain more than 10 Zn-finger motifs per molecule that bind with high affinity. Zinc-dependent galvanization of other proteins may occur in aggregates of peptides that contain out of order Cys or His residues, but that interact through interchain binding. In vitro experiments with a high molar access of  $\text{Zn}^{2+}$

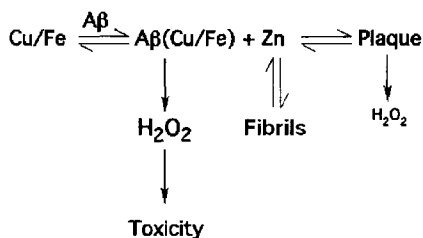


Figure 18. Metabolic galvanization of A $\beta$ -peptide [12].

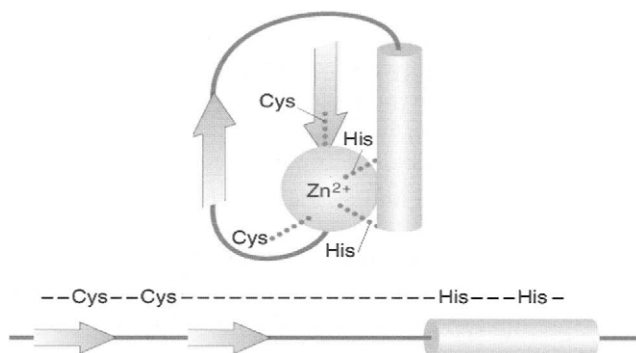
**(b) Zinc-finger motif**

Figure 19. Structural organization of a DNA-binding domain and Zn-finger motif. Arrows are  $\beta$ -sheet domain; cylinder is  $\alpha$ -helix; Cys, cysteine; His, Histidine.  $Zn^{2+}$  binds usually to specific consensus sequence in many proteins involved in transcriptional regulation.

ions lead to saturation of the protein by tightly bound  $Zn^{2+}$ . The same saturation binding was detected for other metals. This property of natural proteins is currently being used for the design of metal-binding short peptides as conducting wires [9].

## 7. APPLICATIONS OF BIONANOTECHNOLOGY: DIAGNOSTICS, TREATMENTS, AND FUTURE DIRECTIONS

Many infectious agents are rapidly being distributed throughout the world and causing epidemic outbreaks with a high death rate. Diseases such as the avian flu, SARS, Dengue, Ebola are some of the most dangerous infections. Therefore, there is a great demand for special tools that can rapidly and specifically diagnose these threats [2,9].

Many diagnostics, including enzyme-linked immunoassays, are based on an adsorption of antigens or antibodies onto the bottom of plastic plates. Using current technology, antibodies could be localized in an exact place or spot by techniques such as nanolithography. However, the main problems associated with this type of set-up are nonspecific background binding of the proteins and insufficient detection sensitivity. Nanotechnology provides a novel opportunity to construct devices for the specific detection of single viral particles. This high sensitivity is needed because only 5–10 individual HIV viral particles are enough to infect a sexual partner or drug user. Moreover, these infectious agents are rather stable and aggressive and could be transmitted in trace amounts to other hosts. Prions and other infectious amyloidoses could be transmitted on the level of femto molar concentrations. Therefore, diagnostic devices need to be extremely sensitive in order to detect single viral particles or single molecules of infectious agents. Fig. 20 shows a novel approach and sensor for the detection of single viral particles.

Lasers are widely used in medicine for simple skin cosmetic treatments to more advanced surgical operations on the eye or brain. Specialized semiconductor lasers are used in applications such as telecommunications, informational storage, and the fabrication of integrated electrically driven devices. The problem is to understand how to combine the current silicon technology of microelectronics to other materials such as organic molecules, synthetic and natural polymers, and inorganic nanostructures. Recently, amplified stimulated emission and laser irradiation have been used in optically pumped organic systems and as inorganic nanocrystals or nanowires. For example, single-crystal cadmium sulfide nanowires were used in an electrically driven laser [22]. Small and compact distantly driven lasers are very important in medicine to replace radioactive materials in treatment of tumors and other diseases. The creation of a biocompatible type of single nanowire laser would be beneficial in the treatment of metastasis in hard to access organs of the human body [23].

The recent discovery of the heat absorptive properties of carbon nanotubes for use in laser irradiation opens up new possibilities in the treatment of tumor diseases [22–24]. Irradiation of a carbon nanotube suspension by a near-infrared laser beam leads to the heating of the solution up to 70 °C within 2 min. Electrons in the nanotubes become excited and begin releasing energy in the form of heat. By using an intrinsic property of nanotubes, a weapon that kills cancer can be developed. The main problem with this system is precise targeting. It is well known that tumor cells contain surface clusters of folate receptors and depend on a folic acid substrate for their proliferation. This difference between normal and cancer cells makes possible

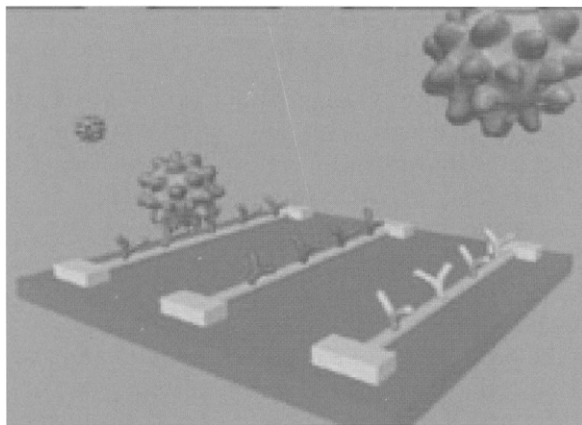


Figure 20. Solid phase sensor for detection of single viral particles. Antibodies (cyan, red, green) are covalently attached to nanoelectrode. Viruses (brown) are specifically attached to antibodies and could be detected by signal registration immediately after interaction. This approach increases sensitivity of viral detection until single viral particle identification and can be used simultaneously for detection of hundred viruses [21].

selective targeting through “labeling” of carbon nanotubes by folate. Folate-labeled nanotubes have been taken up by cancer cells with high efficiency. Then, the treated cancer cells were illuminated with a near-infrared laser, which soon heated and completely killed the cells containing the folate-labeled carbon nanotubes. This type of local heating induces the apoptosis of cancer cells, which is better known as hypothermal cancer treatment [22]. Many other tools for targeting can be used in further studies and for clinical applications. Thus, the combination of lasers with the intrinsic properties fullerenes and functionalized nanotubes is a rapidly growing area of research and design for novel technologies in cancer treatment.

Bionanotechnology can be defined by its utility for creating devices of enhanced sensitivity or function that are useful in biomedical research, drug discovery, and clinical therapy. The successful study of human conformational pathology has opened up new opportunities in the experimental design of protein fibrils and their application as nanoparts of bionanotechnology devices for use in revolutionary technology as shown in Fig. 21. Biomolecules and their derivatives all have dimensions in the nanometer range, but there is nothing to be gained by re-classifying all of biotechnology as nanotechnology. When biomolecules are combined with manufactured nanoscale items or are significantly re-engineered, they can be considered for use in nanoelectronic tools. Likewise, some protein wires and semiconductor chips

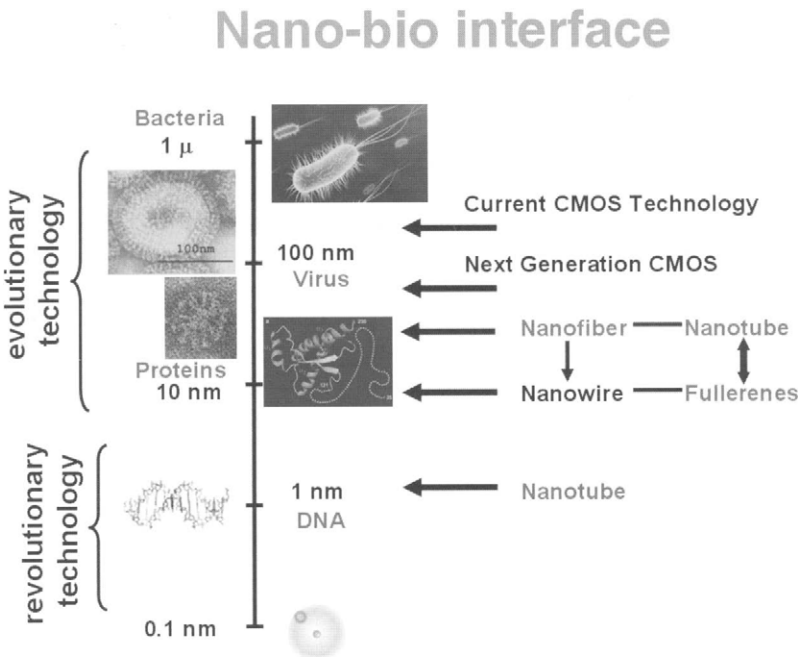


Figure 21. Scheme of further development of bionanotechnology.

now have features with dimensions smaller than 90 nm. Biotechnology and genetic engineering as well as chemical growth of nanoscale could provide the necessary complexity for the basic components of nanotools. The most important question in the further development of this unique field is to find accurate and outstanding wide spread application. In the near future, nanodiagnostic devices could revolutionize the screening and detection of viruses.

## REFERENCES

1. S. Zhang, *Nat. Biotechnol.* **21** (2003) 1171–1177.
2. <http://www.omedon.co.uk/influenza/influenza/>.
3. L. B. Piotrovsky, *Fundamental Directions in Molecular Medicine*, Eds. O. I. Kiselev and U. P. Golikov, Rostok publishers, Saint-Petersburg, 2005, 197–267.
4. J. Brange, J. WhittinghamDonald, D. Edwards, Y.-S. Zhang, A. Wollmer. D. Brandenburg, G. Dodson and J. Finch, *Current Science* **72** (1997) 470–476.
5. M. R. H. Krebs, C. A. MacPhee, A. F. Miller, I. E. Dunlop and C. M. Dobson, *Proc. Natl. Acad. Sci. USA* **101** (2004) 14420–14424.
6. K. Misof, G. Rapp and P. Fratzl, *Biophys. J.* **72** (1966) 1367–1381.
7. R. Valuzzi and D. L. Kaplan, *Biopolymers* **53** (2000) 350–362.
8. S. B. Pruziner, *Science* **252** (1991) 1515–1522.
9. V. I. Pokrovskii, O. I. Kiselev and B. L. Cherkasskii, *Prions and Prion's Diseases*, MedAcadem Publishers, Moscow, 2004, p. 398 (in Russian).
10. E. Gazit, A possible role for  $\pi$ -stacking in the self-assembly of amyloid fibrils, *FASEB J.* **16** (2002) 77–82.
11. R. W. Carrel and D. A. Lomas, *Lancet* **350** (1997) 94–98.
12. Sheibel, Th., R. Parthasarathy, G. Sawicki, X.-M. Lin, H. Jaeger and S. L. Lindquist, Conducting nanowires built by controlled self-assembly of amyloid fibers and selective metal deposition, *Proc. Natl. Acad. Sci. USA* **100** (2003) 4527–4532.
13. A. I. Bush and R. E. Tanzi, *Proc. Natl. Acad. Sci.* **99** (2002) 7317–7319.
14. D.-Sh. Yang, J. McLaurin, K. Qin, D. Westaway and P. E. Fraser, *Eur. J. Biochem.* **267** (2000) 6692–6698.
15. M. F. Perutz, J. T. Finch, J. Berriman and A. Lesk, *Proc. Natl. Acad. Sci. USA* **99** (2002) 5591–5595.
16. A. Aggeli, I. A. Nyrkova, M. Bell, R. Harding, L. Carrick, T. C. B. McLeish, A. N. Semenov and N. Boden, *Proc. Natl. Acad. Sci. USA* **98** (2001) 11857–11862.
17. M. Balbirnie, R. Grothe and D. Eisenberg, *Proc. Natl. Acad. Sci. USA* **98** (2001) 2375–2380.
18. C. Valery, F. Artzner, B. Robert, T. Gulick, G. Keller, C. Grabielle-Madelmont, M.-L. Torres, R. Cherif-Cheich and M. Paternostre, *Biophys. J.* **86** (2004) 2484–2501.
19. M. L. De la Paz, K. Goldie, J. Zurdo, E. Lacroix, C. M. Dobson, A. Hoenger and L. Serrano, *Proc. Natl. Acad. Sci. US* **99** (2002) 16052–16057.
20. I. A. Banerjee, L. Yu and H. Matsui, *Proc. Natl. Acad. Sci. USA* **100** (2003) 14678–14682.

21. N. D. Lazo, M. A. Grant, M. C. Condon, A. C. Rigby and D. B. Teplow, On the nucleation of amyloid  $\beta$ -protein monomer folding, *Protein Science* **14** (2005) 1581–1596.
22. E. Smalley, Biochip spots single viruses, *Technology Research News (TRN)* **Oct. 20/27** (2004). <http://www.trnmag.com>.
23. M. Schwartz, Scientists develop nanotech-laser treatment that kills cancer cells harming healthy tissue. [http://www.eurekalert.org.pub\\_releases](http://www.eurekalert.org.pub_releases).
24. X. Duan, Huang Yu, R. Agarwal and C. M. Lieber, *Nature* **421** (2003) 241–245.

## Author Index

- Abe, M., 35  
Ago, H., 39, 624  
Ajayan, P.M., 198, 215, 339, 340, 443, 541  
Alain, E., 329  
Aluru, N.R., 361, 465  
Amao, Y., 528  
Amaratunga, G.A.J., 224  
Amelinckx, S., 37  
Arnold, M.S., 273  
Avouris, P., 396, 411, 435
- Bøggild, P., 272  
Bae, S.Y., 54  
Baik, S., 271  
Baker, R.T.D., 35  
Balasubramanian, K., 277  
Bandow, S., 35, 39  
Banerjee, S., 276  
Bard, A.J., 110  
Barisci, J.N., 306  
Basiuk, V.A., 286, 287  
Baughman R.H., 299, 307, 469  
Benson Tolle, T., 633, 685  
Berezhkovskii, A., 446  
Bethune, D.S., 109  
Bhide, S.Y., 439  
Binnig, G., 4  
Bonifazi, D., 155  
Bradley, K., 435  
Brenner, D.W., 386  
Britto, P.J., 351  
Broughton, J.Q., 337  
Buldum, A., 386  
Byl, O., 428
- Cai, H., 303  
Cao, D., 442  
Che, G.L., 347  
Che, T., 415, 420  
Chen, H.M., 87  
Chen, J., 197, 281
- Chen, J.H., 349  
Chen, Y., 53  
Cheng, H.-M., 323, 339, 340  
Chikkannanavar, S.B., 34  
Chiou, C.S., 528  
Choi, W.B., 600  
Cole, M.W., 325, 426, 432  
Collins, P.G., 269, 434, 435, 537  
Connell, J.W., 673  
Curl, R.F., 525  
Curran, S.A., 223, 624
- Dai, H., 7, 35, 37, 91, 532, 534  
Dai, L., 3, 191, 195, 206, 213, 215, 525, 561, 567, 611  
de Heer, W.A., 577  
Dean, K.A., 585, 586  
Dellago, C., 457  
Dillon, A.C., 325, 343  
Dimaki, M., 272  
Dresselhaus, M.S., 344  
Drexler, E., 4  
Drocco, J.A., 435  
Durand, O., 617  
Durstock, M., 611  
Dyke, C.A., 276
- Ebbesen, T.W., 35, 37  
Eigler, D.M., 4  
Eklund, P.C., 336, 538  
El Khakani, M.A., 28  
Endo, M., 30, 35
- Falvo, M.R., 386  
Fan, Y.Y., 634  
Fang, H.T., 43  
Fang, Y., 563, 564  
Feng, W., 215  
Fernando, K.A.S., 255, 286  
Feynman, R., 3  
Frackowiak, E., 348  
Fu, Q., 81

- Gao, B., 347  
Gerber, C., 4  
Ghosh, S., 468, 549  
Gilbert, K.E.H., 42  
Goldoni, A., 435  
Gooding, J.J., 561  
Gordillo, M.C., 432, 449  
Gordillo, M.W., 326  
Govindaraj, A., 15  
Govinkdjee, S., 368  
Green, M.L.H., 26, 338
- Hafner, J.H., 93  
Hamada, N., 387  
Harris, P.S., 35  
Hassanien, A., 280  
Hata, K., 31  
He, P., 567  
Hinds, B.J., 195, 491  
Homan, K.H., 134  
Hongo, H., 97  
Hou, P.X., 346, 347  
Huang, L.M., 96  
Hughes, M., 313  
Hummelen, J.C., 174  
Hummer, G., 446, 456  
Huxtable, S.T., 423  
Hwang, H.J., 470
- Iijima, S., 6, 7, 35, 72, 297, 337, 339, 361, 525, 634,  
Itkis, M.E., 26, 42
- Jin, M. H.-C., 611  
Johnson, J.K., 432  
Joselevich, E., 269  
Joseph, S., 465  
Jurewicz, K., 349
- Kajiwara, K., 577  
Kalra, A., 460  
Kaneko, K., 327  
Kang, J.W., 470  
Keller, T.M., 20
- Kiang, C.H., 340  
Kiselev, O.I., 697  
Kitaygorodskiy, A., 266  
Kock, C.C., 55  
Kolesnikov, A., 456  
Kong, J., 350, 435  
Kooi, S.E., 205  
Kost, A., 618  
Král, P., 548  
Kr?tschmer, W., 6  
Kroto, H.R., 134, 149  
Kroto, H.W., 6, 35, 525  
Krüger, M., 466  
Krupke, R., 44  
Kymakis, E., 224, 625  
Kyotani, T., 340
- Labedkin, S., 340  
Laplaze, D., 33  
Lee, J.S., 54  
Lee, K.M., 191  
Lee, S.M., 344  
Lee, Y.H., 344  
Lefrant, S., 305  
Li, H., 283, 284, 287  
Li, L.X., 35  
Li, M.X., 557  
Li, Q.W., 29, 86  
Li, S.L., 54  
Li, Y., 255, 269, 270  
Li, Y.L., 30, 90  
Lieber, C.M., 269  
Lin, H., 528  
Lin, Y., 215  
Liu, C., 346  
Liu, J., 81, 94  
Lu, J.P., 386  
Luong, J.H.T., 558  
Luzzi, D.E., 34, 338
- Mackay, A.L., 142, 147  
Maehashi, K., 280  
Maiti, A., 37  
Marrazza, G., 304



- Martí, J., 449, 452  
 Martin, C.R., 220  
 Martin, N., 174  
 Martinez, M.T., 40  
 Mashl, R.J., 455  
 Matranga, C., 428  
 Mateo-Alonso, A., 155  
 McEwan, K.J., 617  
 Menon, M., 398  
 Messentseva, J., 441  
 Mesyats, G.A., 140  
 Meunier, V., 348  
 Meyyappan, M., 570  
 Minett, A.I., 297  
 Mintmire, J.W., 387  
 Mishra, S.R., 620  
 Miura, K., 386  
 Mizuno, K., 30  
 Moisala, A., 38  
 Moreland, J.F., 415  
 Moulton, S.E., 297  
  
 Nakayama, Y., 589  
 Ni, B., 386, 387  
 Nikolaev, P., 32  
 Noya, E.G., 423  
 Nützenadel, C., 343  
  
 O'Brien, S.P., 91  
 O'Connell, M.J., 224  
 Oberlin, A., 35  
 Ohashi, T., 525  
 Okazaki, T., 31  
 Ōsawa, E.J., 6, 127  
 Osman, M.A., 415  
 Ozawa, M., 127  
  
 Paillet, M., 30  
 Papadakis, S.J., 470  
 Park, J.H., 306  
 Pederson, M.R., 337  
 Pender, M.J., 30  
 Peng, L.M., 31  
 Piotrovsky, L. B., 235  
  
 Power, T.D., 442  
 Prato, M., 155  
  
 Qadri, S.B., 20  
 Qiao, R., 465  
 Qu, L., 191, 206  
 Quate, C., 4  
 Quirke, N., 439  
  
 Radeva, E., 526  
 Rao, A.M., 541  
 Rao, C.N.R., 15  
 Raymundo-Pinero, E., 341  
 Ren, Z.F., 550, 558  
 Ricca, A., 435  
 Rinzler, A.G., 553, 577  
 Rohrer, H., 4  
 Romero, H.E., 539  
 Roth, M.W., 441  
 Rusling, J.F., 559  
  
 Sackman, J.L., 368  
 Saito, R., 387  
 Saito, Y., 35, 577  
 Sakurai, Y., 527  
 Samsonidze, Ge.G., 43  
 Sariciftci, N.S., 614  
 Sazonova, V., 469  
 Schall, J.D., 386  
 Schrand, A.M., 633  
 Seko, K., 593  
 Sen, R., 40  
 Seo, K., 280  
 Shapiro, M., 548  
 Shen, T.D., 64  
 Shengogin, S., 415  
 Shi, W., 432  
 Shih, J., 528  
 Shinohara, H., 31  
 Sholl, D.S., 442  
 Sinnott, S.B., 361, 386, 387, 437  
 Smalley, R.E., 6, 7, 26, 525,  
 Smith, B.W., 33  
 Sokhan, V.P., 442

Spinks, G.M., 309, 313  
Srivastava, D., 398, 415  
Stan, G., 325  
Stark, A.K., 679  
Strano, M.S., 44  
Su, M., 86  
Sudak, L.J., 368  
Sun, C.H., 333  
Sun, L.F., 339  
Sun, Y., 198  
Sun, Y.-P., 255  
  
Tan, S., 280  
Tang, B.Z., 202  
Tang, C.C., 54  
Tang, C.W., 614  
Tang, J., 64  
Taniguchi, N., 4  
Tans, S.T., 388  
Teizer, W., 432  
Tour, J.M., 276  
Tsang, S.C., 192, 340  
Tutt, L.W., 618  
  
Uemura, K., 140  
Uemura, S., 596, 600  
Ugarte, D., 131, 350  
Urbiet, A., 54  
  
Vavro, J., 423  
Vincent, D., 617  
Vivekchand, S.R.C., 40, 42  
  
Wagner, H.D., 546  
Wallace, G.G., 297  
Wan, L.-J., 109  
Wang, F., 552  
Wang, J., 304, 557, 564  
Wang, W., 255

Wang, S.S., 276  
Wang, X., 30  
Watson, K.A., 673  
Watt, J., 3  
Weaver, M.J., 109  
Williams, K.A., 336  
Willner, I., 559  
Wiltshire, J.G., 40  
Wood, J.R., 546  
Wu, J., 442  
  
Xiao, H.D., 54  
Xu, H., 202  
Xu, W.H., 343  
Xu, Y.-Q., 42  
  
Yang, Q.-H., 323, 327, 328, 333, 335, 336, 340, 343  
Yang, Z.H., 306  
Yao, Z., 415  
Yashonath, S., 439  
Yemini, M., 304  
Yin, L.W., 54  
Yin, Y.F., 346  
Yoon, B.J., 349  
Yotani, J., 590  
Yue, G.Z., 593  
  
Zettl, A., 536  
Zhang, B., 95  
Zhang, H.-M., 109  
Zhang, M.F., 28  
Zhang, W., 415  
Zhang, X.F., 72  
Zhang, Y.Q., 368  
Zheng, L.X., 96  
Zheng, M., 44, 45, 273  
Zhu, H.W., 89  
Zhu, W., 586

## Subject Index

- Absorption, 260, 262, 273–278,  
283–286, 289
- Acetic acid plasma, 567
- Activation process, 590
- Actuators, 191, 307, 309
- Adhesive, adhesive strength, 640
- Adsorbate species, 585
- Adsorption of gases, 425–426
- Adsorption, 323–337, 340–341,  
343–348, 350, 352, 583, 585, 592
- Aerogel-supported CVD, 18
- Agglutination, 136, 138
- Alcohol catalytic CVD, 18, 31
- Alcohols, 86, 88, 92, 95
- Aligned carbon nanotube–DNA  
sensors, 567
- Aligned carbon nanotubes, 208, 214,  
542, 550, 559, 567, 570
- Aligned MWNTs, 20, 24
- Aligned nanotube, 15, 31
- Alkaline phosphatase (ALP), 566
- ALP-I, 565
- Amines, 279
- Ammonia, 532, 541, 544
- Annealing, 53–54, 59, 65, 67–77
- Antioxidant, 236–238, 241, 244–246
- Antiviral activity, 247–248
- Arc-discharge, 16–17, 22–26, 28, 34–35,  
40–43
- Arcing, 592
- Arc-vaporization, 15, 36
- Artificial muscles, 8
- Asymmetric end-functionalization, 195
- Atomic force, 4
- Atomic oxygen, 677–678, 680, 685
- Attachment of dichlorocarbene, 198
- Ball milling, 53–59, 61–67, 69, 71–74,  
77
- Band-gap, 255, 260–261, 263, 274, 286
- Batteries, 54, 115, 306
- Benzylamine, 543, 546
- Biosensors, 218, 525, 557, 559–561,  
563–564, 570, 572
- Bottom up, 4–5
- Boudouard reaction, 32
- Buckminsterfullerene  $C_{60}$ , 6–7, 525
- Bulk growth, 85, 95
- Bulk heterojunction, 611, 614,  
621–622, 626
- Bulk, 259, 261, 264, 266, 269, 276, 279,  
283, 289
- $C_{60}$ , 155–164, 166–171, 173, 175–180,  
611, 614–615, 617–622, 624,  
627–628
- Carbon blacks, 127–133, 137–142, 148,  
611–612, 617
- Carbon monoxide, 86, 95
- Carbon nano-onions, 127–128,  
132–134, 139–142, 149
- Carbon nanotube fluorescence, 222
- Carbon nanotube, 15, 22, 27, 31–35,  
39, 43–44, 191–193, 195–196, 200,  
202–206, 208, 211, 213–214, 216,  
218, 220, 222–223, 225, 227, 297,  
323–325, 328, 333–334, 337,  
339–340, 342–344, 347, 611, 619,  
622
- Carbon nanotubes, 255–256, 270, 273,  
281
- double-walled (DWNT), 285, 287
- metallic, 255–257, 259–263,  
265–267, 269–277, 279,  
281–285, 287–289
- multi-wall carbon nanotubes  
(MWNTs), 255
- semiconducting, 255–257, 259–263,  
265–277, 279, 281–289
- semi-metallic, 255, 259–260
- single-walled (SWNT), 255
- Carbon nanotubes, 53
- closing, 26, 37
- filling, 34

- multi-walled (see multi-walled carbon nanotubes), 15
- single-walled (see single-walled nanotubes), 15, 22
- synthesis, 15
- Carboxylic acid, 559–560, 563, 567, 570
- Catalytic CVD, 579, 590
- cDNA, 567
- Chemical force sensors, 215
- Chemical functionalization, 376, 397–398, 495, 508, 517
- Chemical polymerization, 214–215
- Chemical sensors, 220, 525, 532, 541
- Chemical separation, 495
- Chemical vapor deposition (CVD), 18–19, 29, 31–32, 81, 85, 579
- Chips, 702, 719
- Chiral angle, 255, 260
- Chirality, 255, 257, 263, 267, 269, 277, 280, 287, 365, 378, 387–388, 390–391, 395, 397, 404, 406, 408, 411, 421, 439, 442, 448–449
- CNT, 619–620, 622, 624–625, 628
- CO<sub>2</sub> laser, 28, 32
- Coatings, 677, 685, 688–691, 693
- Cobaltocene, 20–21
- Colloidal solution, 8, 239, 617
- Combustion engine, 3
- Complementary DNA (cDNA), 567
- Computer, 3–4
- Conditioning catalyst, 35–36
- Conductivity, 259, 266, 283, 527, 532, 535–536, 539, 554, 556, 564, 677, 690–692, 694
- Confinement, 5
- Conjugated polymer, 614, 621–622, 627
- Contact resistance, 596
- Continuous laser, 28
- Coulomb interaction, 552
- Covalent coupling, 192
- Covalent functionalization, 192, 202
- Cryptand, 528–531
- Cycloaddition, 157–163, 165–168, 173, 178
- Cytochrome, 557, 559
- Daunomycin, 564, 569–570
- Defects, 362, 378–380, 393–395, 398, 400, 409, 421–423, 434–435, 439, 457, 471
- Deformation, 363, 366–368, 371, 377–379, 381, 383–384, 386, 398, 402, 405–406, 408
- Degradation of field emitters, 592
- Desorption, 583–585, 592
- Detonation, 8
- Diameter control, 98, 100
- Diameters of SWNTs, 84
- Diamond, 4, 6–8, 140–141, 143, 148
- Diazonium, 276–277
- Dielectric constant, 8
- Dielectrophoresis, 44, 270
- Differential pulse voltammetry (DPV), 564
- Diffusion coefficient, 442, 456–457
- Diode-type structure, 600–601
- Dipole moment, 448, 451, 454, 463–465
- Dissipation factor, 8
- DNA sensors, 562–564, 567
- DNA, 272, 274
- DNA-CNT hybrid, 44–45
- Doping, 256, 260, 273–274, 285
- Double-walled carbon nanotubes (DWNTs), 34
- Elastic response, 367, 379
- Electric generator, 3
- Electrical breakdown strength, 8
- Electrochemical cell, 225–226
- Electrochemical, 15, 43, 297, 299
  - synthesis, 15
  - oxidation, 43
- Electrochemistry, 122
- Electrodes, 297–299
- Electroless deposition, 206
- Electrolysis, 18
- Electrolyte, 446, 464–468
- Electromagnetic interference
  - shielding (EMI), 652, 663, 665
- Electron field emitting, 8
- Electron transfer glucose biosensors, 559

- Electronic band structures of SWNTs, 83
- Electronic devices, 378, 388, 397–398, 401–402, 411
- Electronic properties, 363, 387–391, 393, 395, 397–398, 400, 405–406, 408–409, 433, 437, 463
- Electronic structure, 34, 44
- Electrophoresis, 43
- Electrophoresis, 588–590, 593, 602, 606
- Electrostatic charging/spray painting, 662
- Electrostatic discharge, 689
- Emission site density, 590, 604
- Emission stability, 577, 591–592
- Emission uniformity, 577, 590, 602, 604, 606
- Encapsulation, 203, 220
- End functionalization, 192, 220
- Energy storage, 323–324
- Enrichment, 257, 263, 265–267, 269, 275, 279, 281, 283
- Environmental stability, 8
- Enzyme biosensors, 557
- Enzymes, 557, 559
- Epoxy, 633, 637–663, 665, 667
- ESA, 616–618
- Ethanol, 543, 546
- Excited state absorption, 616
- Exciton dissociation, 611, 613–614, 621, 627–628
- Excitonic, 552–554
- Excitons, 552
- Explosive electron emission, 140
- Failure modes, 596
- $\text{Fe}(\text{CO})_5$ , 21, 29, 32
- Fermi levels, 554
- Ferrocene, 20–22, 24, 29
- FET devices, 256, 277, 281
- Field emission displays (FEDs), 6, 8, 26, 577
- Field emission energy distribution (FEED), 586
- Field emission microscopy (FEM), 577
- Field emission, 577–582, 585–586, 592–593, 596, 600, 602, 606
- Flame synthesis, 33
- Flavin adenine dinucleotide (FAD), 560
- Flexural strength of epoxy/CNT composites, 646, 651
- Floating catalyst, 85–89, 91
- Flow sensor, 548–549
- Fluid viscosity, 549
- Fluidized-bed method, 30
- Fluorescence, 261, 263, 268, 272, 274
- Fowler–Nordheim (F–N) theory, 586
- Fracture of CNTs, 643
- Fracture toughness, 644–645, 648–650
- Free electron laser, 28
- Fullerene  $\text{C}_{60}$ , 6–7
- Fullerene gas sensors, 527
- Fullerene humidity sensors, 526
- Fullerenes, 6–7, 15, 34, 36–37, 109–111, 119–120, 122–123, 155–164, 167–180, 526–531, 618, 620, 627, 702–705
- Functional groups, 363, 427, 465
- Functionalisation, 297, 300
- Functionalization of carbon nanotube, 192, 196, 200, 202, 204
- Functionalization, 44, 274–277, 279, 281, 287
- Gas sensors, 527, 531–532
- Gaseous adsorption, 433
- Gatekeeper, 510
- Glass carbon, 563
- Glassy carbon, 565–566
- Glucose biosensor, 559–561
- Glucose oxidase, 557–558, 562
- Glucose, 557–563
- Graphene, 36–37
- Graphite, 6–8, 15, 17–18, 23, 25–28, 33, 35–37
- Graphitized carbon black, 138
- Guanine, 571

- Hardness, 645, 648, 650–651  
Hexadecanetriol, 543  
Hexane, 531  
Hexene, 530–531  
HFCVD, 31  
High pressure CO disproportionation process, 32  
High-resolution electron microscopy, 15  
HiPco, see High pressure CO disproportionation process, 32  
Histogram, 405  
Horseradish peroxidase, 557, 559  
Humidity sensor, 526–527, 541  
Hybridization, 563–569, 571  
Hydrogen bonding (HB), 446  
Hydrogen peroxide, 557–558  
Hydrogen sensors, 534  
Hydrophilic, 171  
Hydrothermal, 18, 39  
  
Immobilization, 558, 568  
*In situ* transmission electron microscopy, 577–578, 593  
Industrial revolutions, 3  
Information technology, 3  
Innerwall modification, 200  
Intercalation, 43  
Interfacial adhesion, 547, 549  
Interfacial shear strength (IFSS) of epoxy/CNT composites, 642, 645, 647  
Internal, 3  
Ion bombardment, 592  
Ionic strength, 549  
  
Junctions, 395, 397–400  
  
Kataura plot, 260–261, 263, 281, 283  
  
Large-size field emission displays, 602  
Laser ablation, 27–28, 33  
Laser assisted thermal CVD, 18  
Laser vaporization, 26, 28  
Length control, 101  
Lighting elements, 578, 596  
  
Long nanotubes, 101  
Low earth orbit, 677  
  
Mackay crystals, 127, 142–143, 146–147  
Magnetic field, 17  
Mechanism of soot and fullerene formation, 135  
Mechanochemical reactions, 204  
Medicinal chemistry, 235–236  
Membrane, 491, 493–504, 506–511, 515–520  
Membranotropic action, 247  
Metallicity, 255, 277, 287  
Metallocene, 20–22, 29, 37  
Methanol, 528–530, 549–550  
Micelles, 44  
Microelectromechanical systems (MEMS), 8, 470, 471  
Microfiltration, 40  
Microscope (AFM), 4  
Microscopy, 257  
Military applications, 633, 637, 651–652, 657–659, 661–662, 667  
Mobility, 396, 443, 456–457  
Molecular machine, 5  
Molecular transport, 437–439, 443, 462  
Molecular-filtration membranes, 8  
Multi-wall carbon nanotubes (MWNTs), 8, 15, 53, 81, 191, 323, 541, 619, 634, 684  
Multi-walled (see multi-walled carbon nanotubes), 15, 16, 18, 31, 32  
MWNT, 620, 624  
Myoglobin, 559  
  
Nafion, 533–535, 557, 568  
Nanobiotechnology, 701  
Nanocomposite, 191, 226–227  
Nanodiamonds, 6, 8  
Nanopore, 220  
Nanostructure, 37, 38, 139, 308, 351, 640  
Nanotechnology, 3–6, 8–9  
Nanotube-based FET (NFET), 554  
Nanowire, 712–713, 718

- NASA, 625  
Near-infrared spectroscopy, 26, 40  
Nebulized spray pyrolysis, 20, 23  
Negative Gaussian curvatures, 146–147  
 $\text{NH}_3$ , 527, 532–535, 541–542, 544  
Nickelocene, 20–22, 29  
Nitrogen dioxide, 532  
Nitronium, 277–278  
NMR, 265–266  
 $\text{NO}_2$ , 527, 532–535, 541  
Nobel laureate, 3  
Nobel Prize, 4, 6  
Nonlinear absorbing, 615–616  
Nonlinear optical properties, 612  
Nonlinear scattering, 611, 615, 617–619, 628  
*n*-type, 533, 537, 554  
Nucleic acids, 701  
  
Octadecylamine, 43–44  
Oligonucleotides, 563–564, 567–568  
Optical limit, 611–613, 615–620, 627–628  
Optoelectronic devices, 222, 227  
Organic photovoltaic device, 620  
Organic solar cell, 613–615, 622, 624–625, 627–628  
Organometallic precursor, 37  
Orientation control, 101  
Osmylation, 277  
Outerwall functionalization, 196  
Oxidant, 236–238, 240–241, 244  
Oxidation of carbon nanotubes, 192  
Oxygen pressures, 528  
  
P3OT, 625–626  
PCBM, 615, 621, 622  
Pd, 535–536  
Peapod, 33–34, 377, 423  
PECVD, 19, 31  
PEI, 533–535  
Phonons, 392, 415, 418, 420, 422, 424  
Photo-induced electron transfer, 613  
Phototoxicity, 245  
Photovoltaic device, 611, 620  
Photovoltaics, 175  
  
Physical wrapping, 202  
Plasma rotating electrode, 17  
Plasma, 195, 212–214, 220  
Plasma-enhanced chemical vapor deposition (PECVD), 550, 606  
Plastic response, 378  
Platinum, 568–569  
Poisoning effect, 585  
Polar organic molecules, 528, 530  
Pollution, 3  
Polyaniline, 562  
Polyethyleneimine (PEI), 533  
Polyimides, 690–691  
Polypyrrole, 562, 564  
Polypyrrole/oligonucleotide, 564  
Porous materials, 323, 333  
Porphyrin, 282, 284, 286  
PPV, 621–624, 627  
Prions, 701, 706–708, 717  
Pristine fullerene, 235–239, 244–249  
Production costs of major nano-carbon materials, 128  
Protein channel mimick, 491, 496  
Protein fibril, 704, 707, 709, 719  
Proteins, 5, 9, 557, 564, 701–704, 706–707, 709, 711–717, 719  
*p*-type, 532–533, 536–537, 554  
Pulsed laser, 27–28  
Purification, 15, 24, 30, 34, 39–43  
PV, 611–613, 620–622, 624, 627–628  
Pyrene, 281, 283–285  
Pyrolysis, 15, 18, 20–24, 29, 31–32, 36–38  
Pyrolytic synthesis of  $\text{C}_{60}$ , 127, 142–143  
  
Quantization effect, 5  
Quantum dot, 626  
  
Radial breathing mode, 44  
Radiation effects, 685  
Radiation shielding, 677  
Raman spectroscopy, 29, 35, 42–45, 546  
Raman, 262–265, 270–273, 276–279, 281, 283, 285, 289  
Resistive (Joule) heating, 592  
Resonance frequency, 526

- Reverse saturable absorption, 617  
Roll-to-roll, 615  
RSA, 617–618
- SA, 617  
Saturable absorption, 617  
SAW, 528–531  
Scanning electron microscopy (SEM),  
24, 62, 86, 89, 109  
Scanning probe microscopy, 4  
Scanning tunneling microscope  
(STM), 4, 109  
Schwarzites, 147–148  
Screen printing, 588, 596–597, 600,  
602, 605, 621  
Screening effect, 590  
Seebeck coefficient, 538  
Self-assembling, 4  
Self-assembly, 109, 206–207  
Self-healing, 665  
Semiconducting states, 220  
Semiconducting, 255–257, 259–263,  
265–277, 279, 281–289  
Semi-metallic, 255, 259–260  
Sensing applications, 517  
Sensors, 7–9  
Separation, 255–257, 260, 266, 269,  
271, 273–274, 276–277, 279, 281,  
283–285, 287, 289  
Sidewall fluorination, 196  
Sidewall functionalization, 196–197  
Single wall carbon nanotube, 7  
Single-molecular transistor, 8  
Singlestrand DNA oligonucleotides  
(ssDNAs), 567  
Single-walled carbon nanotubes  
(SWNTs), 8, 15, 17, 22, 23, 32, 33,  
34, 43, 619  
sidewall, 26, 40  
synthesis, 22, 24, 26, 28, 30–31, 38  
Single-walled nanohorns (SWNHs), 17,  
326  
Size of catalyst nanoparticles, 94  
Size-dependent properties, 3, 5  
Smart materials, 659, 662  
Solar cell, 613–615, 621–628  
Solar energy, 33  
Solar sails, 694  
Solid state formation, 53, 67, 72, 73, 77  
Solvent ordering, 491  
Space elevator, 693–694  
Space, 677–678, 680–683, 685–694  
Spatial velocity hodograph, 37  
Specific heat, 415, 417–419, 432  
Spin-coating, 619  
Spin-on glass, 209  
Spiroid, 132–136, 142  
Spiroid-to-onion transformation, 133  
Steam engine, 3  
Stirred-media milling, 8  
STM, 4–5  
Stone–Wales rearrangement, 134, 136,  
145, 146  
Strand DNA (dsDNA), 567  
Superhard carbons, 127, 143  
Supported catalyst, 85–86, 88  
Supramolecular, 172, 174–175, 178,  
180  
Surface charge, 446–447, 458, 465  
Surface growth, 85, 88–89, 95–96  
Surface modification, 532, 572  
Surface, 323–324, 326–327, 331–337,  
339–341, 343–344, 347–352  
Suspension, 611, 617, 619, 627–628  
Synthesis, 13, 15, 17–18, 20–22, 24, 26,  
28, 30–31, 33, 35, 38–40, 43
- Tensile strength of CNTs, 650, 651  
Tensile strength of epoxy, 650  
Tensile strength of epoxy/CNT  
composites, 651  
Thermal conductivity, 24, 28, 365, 415,  
418–423, 677, 691–692, 694  
Thermal evaporation, 33  
Thermal properties, 361, 415  
Thermally assisted field evaporation,  
592  
Thermoelectric power (TEP), 538  
Thermopower, 415, 424–425  
Top down, 4–5  
Toxicity, 235, 245–246  
TPA, 616–618



- Transmission electron microscope (TEM), 7
- Transparent electrical conductors, 553
- Transportation, 220
- Triode-type structure, 600, 603
- Triton X-100, 44
- Tunneling probability, 586
- Two-photon excitation, 552–554, 616
  
- van Hove singularity, 555
- Vapor phase deposition, 29, 34
- Vapor-phase-growth, 20
- Virucidal action, 243
  
- Water and carbon nanotubes, 447
- Wetting, 445–446
- Work function, 581, 592
  
- X-ray sources, 578, 605
  
- Yarmulke, 36–37
- Young's modulus of epoxy/CNT composites, 641
- Young's modulus, 365, 367–368, 373, 377–378
  
- Zeolite, 147, 201, 267, 339, 442, 494